STATE OF NEW MEXICO
OIL CONSERVATION COMMISSION

IN THE MATTER OF APPLICATION OF THE OIL CONSERVATION DIVISION TO ADOPT 19.15.41 NMAC, 19.15.42 NMAC, AND 19.15.43 NMAC **CASE NO. 25875**

DÍNE C.A.R.E., EARTHWORKS, SAN JUAN CITIZENS ALLIANCE, SIERRA CLUB RIO GRANDE CHAPTER, TÓ NIZHÓNÍ ÁNÍ, AND WESTERN ENVIRONMENTAL LAW CENTER'S
PRE-HEARING STATEMENT

Pursuant to 19.15.4.11.B NMAC and the Hearing Officer's Prehearing Procedural Order in this matter, the Diné C.A.R.E., Earthworks, San Juan Citizens Alliance, Sierra Club Rio Grande Chapter, Tó Nizhóní Áni, and Western Environmental Law Center ("WELC") (collectively, "Conservation Groups") hereby submit their Prehearing Statement in this matter with the following information:

1. The person's name and its attorney's name: WELC represents all parties in the proceeding, identified above.

2. The names of all witnesses the person will call to testify: Conservation Groups will present:

   a. Peter Morgan, J.D., Legal and Policy Director, Center for Asset Retirement and Accountability; and

   b. Charles Harvey, PhD, Professor of Civil Engineering, Massachusetts Institute of Technology.

2. All witnesses' full direct testimony, their qualifications including a description of their education and experience, and the approximate time to present a summary of the witness's direct testimony: All witnesses' full direct testimony and qualifications are set forth in this Prehearing Statement as follows:

a. Direct testimony of Peter Morgan is Conservation Groups' Exhibit 3 and his resume is Exhibit 2; the approximate time for a summary of his testimony is 30 minutes.

b. Direct testimony of Charles Harvey, PhD, is Conservation Groups' Exhibit 5 and his resume is Exhibit 4; the approximate time for a summary of his testimony is one hour.

3. Any proposed modifications to the proposed rule change with reasons for adopting the modifications: Conservation Groups' proposed modifications are set forth in their Exhibit 1 and their reasons for adopting the modifications are set forth in their exhibits, a list of which appears below.

5. All exhibits the person plans to offer as direct exhibits in the hearing:

Conservation Groups' list of exhibits is set forth below, and the exhibits are attached. Conservation Groups provide a Bates stamp number for each exhibit to facilitate accessing the exhibits.

Exhibit	Description	Bates Stamped Page
1	Proposed amendments	CG-001
1-A	Proposed amendments to 19.15.41 NMAC	CG-002
1-B	Proposed amendments to 19.15.42 NMAC	CG-010
1-C	Proposed amendments to 19.15.43 NMAC	CG-027
2	Resume of Peter Morgan	CG-053
3	Direct testimony of Peter Morgan	CG-055
4	Resume of Charles Harvey, PhD	CG-075
5	Direct testimony of Charles Harvey, PhD	CG-089
6	Bukar Report	CG-185
7	Burton-Kelly Report	CG-197
8	Carroll Report	CG-208
9	Cavanagh Report	CG-221
10	Chen Report	CG-234
11	Choi Report	CG-249
12	Crain Report	CG-263
13	Gholami Report	CG-279
14	Jahan Report	CG-298
15	Langenbruch Report	CG-316
16	Pan Report	CG-327
17	Saló-Salgado Report	CG-342
18	Snider Article	CG-385
19	Sun Report	CG-392
20	Tian Report	CG-414

21	White Report	CG-427
22	Zoback Report	CG-434
23	Zoback Report	CG-440

Respectfully submitted,

/s/ Morgan O'Grady

Morgan O'Grady, Staff Attorney
Rose Rushing, Staff Attorney
Daniel Timmons, Senior Attorney
Western Environmental Law Center
409 East Palace Avenue, #2
Santa Fe, New Mexico 87501
ogrady@westernlaw.org
rushing@westernlaw.org
timmons@westernlaw.org

Attorneys for Diné C.A.R.E., Earthworks, San Juan Citizens Alliance, Sierra Club Rio Grande Chapter, Tó Nizhóní Áni, and Western Environmental Law Center

Certificate of Service

I certify that on June 29, 2026, I served a copy of this pleading to the following via email:

Jesse Tremaine
Legal Director
New Mexico Energy, Minerals and Natural Resources Department,
Oil Conservation Division
1220 South St. Francis Drive
Santa Fe, New Mexico 87505
jessek.tremaine@emnrd.nm.gov

Attorney for the New Mexico Oil Conservation Division

Sheila Apodaca
Oil Conservation Commission Clerk
New Mexico Energy, Minerals, and Natural Resources Department
Wendell Chino Building
1220 South St. Francis Drive 3rd Floor
Santa Fe, New Mexico 87505
505-699-8358
occ.hearings@emnrd.nn.gov
sheila.apodaca@emnrd.nm.gov

Oil Conservation Commission Clerk

Zachary A. Shandler
Assistant Attorney General
New Mexico Department of Justice
P.O. Box 1508
Santa Fe, New Mexico 87504
zshandler@nmdoj.gov

Oil Conservation Commission Counsel

Adam Rankin
Paula Vance
A. Raylee Starnes
P.O. Box 2208
Santa Fe, New Mexico 87504
(505) 988-4421
agrankin@hollandhart.com
pmvance@hollandhart.com
arstarnes@hollandhart.com

Aaron B. Tucker
555 17th Street, Suite 3200
(303) 295-8369
abtucker@hollandhart.com

Attorneys for Oxy USA, Inc

Ana Maria Gutierrez
Jessica Portmess
Womble Bond Dickinson (US) LLP
1899 Wynkoop St., Ste. 750
Denver, CO 80202
(720) 983-1350
ana.gutierrez@wbd-us.com
jessica.portmess@wbd-us.com

Amanda Thatcher
Womble Bond Dickinson (US) LLP
Phoenix, AZ 85004
(602) 262-5311
amanda.thatcher@wbd-us.com

Attorneys for the New Mexico Oil and Gas Association

/s/ Morgan O'Grady
Morgan O'Grady

EXHIBIT 1

EXHIBIT 1-A

TITLE 19 NATURAL RESOURCES AND WILDLIFE
CHAPTER 15 OIL AND GAS
PART 41 PROCEDURES FOR DECISION MAKING

19.15.41.1 ISSUING AGENCY: Oil Conservation Commission.
[19.15.41.1 NMAC – N, xx/xx/2026]

19.15.41.2 SCOPE: 19.15.41 NMAC applies to persons constructing, operating or closing a sequestration facility or engaged in the injection of carbon dioxide for the purposes of geologic sequestration under the Geologic Carbon Dioxide Storage Stewardship Act.
[19.15.41.2 NMAC – N, xx/xx/2026]

19.15.41.3 STATUTORY AUTHORITY: 19.15.41 NMAC is adopted pursuant to the Geologic Carbon Dioxide Storage Stewardship Act, Sections 74-14-1 through 74-14-7 and the Oil and Gas Act, Section 70-2-6, 70-2-11, and Paragraph (15) of Subsection B of Section 70-2-12 NMSA 1978.
[19.15.41.3 NMAC – N, xx/xx/2026]

19.15.41.4 DURATION: Permanent.
[19.15.41.4 NMAC – N, xx/xx/2026]

19.15.41.5 EFFECTIVE DATE: Day, Month, Year, unless a later date is cited at the end of a section.
[19.15.41.5 NMAC – N, xx/xx/2026]

19.15.41.6 OBJECTIVE: To regulate the permitting, construction, operation and closure of sequestration facilities, the injection of carbon dioxide for the purposes of geologic sequestration and to maintain primary enforcement authority for Safe Drinking Water Act (42 U.S.C. 300f et seq.) Underground Injection Control (UIC) program for UIC Class VI wells.
[19.15.41.6 NMAC – N, xx/xx/2026]

19.15.41.7 DEFINITIONS: The following definitions apply to this part for underground injection control programs:

A. Definitions beginning with the letter "A".

(1) "Administrator" means the Administrator of the United States Environmental Protection Agency (U.S. EPA), or an authorized representative.

(2) "Application" means a submission by an individual or entity, using the prescribed forms, to request authorization for underground injection activities, inclusive of any subsequent amendments, updates, or supplements to the original submission.

(3) "Aquifer" means a geological "formation," group of formations, or part of a formation that is capable of yielding a significant amount of water to a well or spring.

(4) "Area of review" means the area surrounding an injection well described according to the criteria set forth in § 40 CFR 146.06 ~~or in the case of an area permit, the project area plus a circumscribing area the width of which is either one-quarter of a mile or a number calculated according to the criteria set forth in § 40 CFR 146.06~~.

B. Definitions beginning with the letter "B". [RESERVED].

C. Definitions beginning with the letter "C".

(1) "Cesspool" means a "drywell" that receives untreated sanitary waste containing human excreta, and which sometimes has an open bottom or perforated sides.

(2) "Contaminant" means any physical, chemical, biological, or radiological substance or matter in water.

D. Definitions beginning with the letter "D".

(1) "Director" means the director of the New Mexico Energy, Minerals and Natural Resources Department, Oil Conservation Division.

(2) "**Draft permit"** means a document prepared under Subsection B of 19.15.41.8 NMAC indicating the director's decision to issue or deny, modify, revoke and reissue, terminate, or reissue a "permit." A notice of intent to terminate a permit, and a notice of intent to deny a permit, as discussed in Subsection A

of 19.15.41.8 NMAC are types of "draft permits." A denial of a request for modification, revocation and reissuance, or termination, as discussed in Subsection A of 19.15.41.8 NMAC is not a "draft permit."

(3) "Drilling mud" means a heavy suspension used in drilling an "injection well," introduced down the drill pipe and through the drill bit.

(4) "Drywell" means a well, other than an improved sinkhole or subsurface fluid distribution system, completed above the water table so that its bottom and sides are typically dry except when receiving fluids.

E. Definitions beginning with the letter "E".

(1) "Eligible Indian Tribe" is a Tribe that meets the statutory requirements established at 42 U.S.C. 300j-11(b)(1).

(2) "Emergency permit" means a UIC "permit" issued in accordance with Section 40 CFR 144.34.

(3) "Environmental protection agency" ("EPA") means the United States environmental protection agency.

(4) "Exempted aquifer" means an "aquifer" or its portion that meets the criteria in the definition of "underground source of drinking water" but which has been exempted according to the procedures in Subsection D of 19.15.42.8 NMAC.

(5) "Existing injection well" means an "injection well" other than a "new injection well."

F. Definitions beginning with the letter "F".

(1) "Facility or activity" means any UIC "injection well," or any other facility or activity that is subject to regulation under these regulations.

(2) "Fluid" means any material or substance which flows or moves whether in a semisolid, liquid, sludge, gas, or any other form or state.

(3) "Formation" means a body of consolidated or unconsolidated rock characterized by a degree of lithologic homogeneity which is prevailingly, but not necessarily, tabular and is mappable on the earth's surface or traceable in the subsurface.

(4) "Formation fluid" means "fluid" present in a "formation" under natural conditions as opposed to introduced fluids, such as "drilling mud."

G. Definitions beginning with the letter "G".

(1) "Generator" means any individual or entity, identified by a specific site location, whose actions or operations result in the creation of hazardous waste as defined under the New Mexico Hazardous Waste Management Regulations (Section 20.4.1 NMAC), or who is responsible for producing or causing the production of any fluid intended for subsurface injection under applicable New Mexico Oil Conservation Division rules (Chapter 19.15 NMAC).

(2) "Geologic sequestration" means the long-term containment of a gaseous, liquid, or supercritical carbon dioxide stream in subsurface geologic formations. This term does not apply to carbon dioxide capture or transport.

(3) "Groundwater" means water below the land surface in a zone of saturation.

H. Definitions beginning with the letter "H".

(1) "Hazardous waste" means a hazardous waste as defined in 40 CFR 261.3.

(2) "Hazardous waste management facility ("HWM facility")" means all contiguous land, and structures, other appurtenances, and improvements on the land used for treating, storing, or disposing of hazardous waste. A facility may consist of several treatment, storage, or disposal operational units (for example, one or more landfills, surface impoundments, or combination of them).

I. Definitions beginning with the letter "I".

(1) "Improved sinkhole" means a naturally occurring karst depression or other natural crevice found in volcanic terrain and other geologic settings which have been modified by man for the purpose of directing and emplacing fluids into the subsurface.

(2) "Indian lands" means "Indian country" as defined in Section 18 U.S.C. 1151. That section defines Indian country as: (a) All land within the limits of any Indian reservation under the jurisdiction of the United States government, notwithstanding the issuance of any patent, and, including rights-of-way running through the reservation; (b) All dependent Indian communities within the borders of the United States whether within the original or subsequently acquired territory thereof, and whether within or without the limits of a State; and (c) All Indian allotments, the Indian titles to which have not been extinguished, including rights-of-way running through the same.

(3) "Indian tribe" means any Indian tribe having a federally recognized governing body carrying out substantial governmental duties and powers over a defined area.

(4) "Injection well" means a "well" into which "fluids" are being injected.

(5) "Injection zone" means a geological "formation," group of formations, or part of a formation receiving fluids through a "well."

J. Definitions beginning with the letter "J". [RESERVED].

K. Definitions beginning with the letter "K". [RESERVED].

L. Definitions beginning with the letter "L". [RESERVED].

M. Definitions beginning with the letter "M".

(1) "Major facility" means any UIC "facility or activity" classified as such by the director, in conjunction with the EPA regional administrator.

(2) "Manifest" means the shipping document EPA Form 8700-22 (including, if necessary, EPA Form 8700-22A), originated and signed in accordance with the applicable requirements of Section 20.4.1.500 NMAC (incorporating 40 CFR Part 262).

N. Definitions beginning with the letter "N". "New Injection Well" means a well which began injection after the New Mexico Class VI Underground Injection Control program is approved and the applicable New Mexico Oil Conservation Division rules and regulations are promulgated.

O. Definitions beginning with the letter "O". "Owner or operator" means the owner or operator of any "facility or activity" subject to regulation under the UIC program.

P. Definitions beginning with the letter "P".

(1) "Permit" means an authorization, license, or equivalent control document issued by EPA or an approved State to implement the requirements of this part, parts 145, 146 and 124. Excluding Class VI UIC, "Permit" includes an area permit or any permit which has not yet been the subject of final agency action, such as a "draft permit."

(2) "Person" means an individual, association, partnership, corporation, municipality, state, federal, or tribal agency, or an agency or employee thereof.

(3) "Plugging" means the act or process of stopping the flow of water, oil or gas into or out of a formation through a borehole or well penetrating that formation.

(4) "Point of injection" means the last accessible sampling point prior to waste fluids being released into the subsurface environment through a Class V injection well. For example, the point of injection of a Class V septic system might be the distribution box—the last accessible sampling point before the waste fluids drain into the underlying soils. For a dry well, it is likely to be the well bore itself.

(5) "Project" means a group of wells in a single operation.

Q. Definitions beginning with the letter "Q". [RESERVED].

R. Definitions beginning with the letter "R".

(1) "Radioactive Waste" means any waste which contains radioactive material in concentrations which exceed those listed in Section 10 CFR 20, Appendix B, Table II, column 2.

(2) "RCRA" means the Solid Waste Disposal Act as amended by the Resource Conservation and Recovery Act of 1976 (Pub. L. 94–580, as amended by Pub. L. 95–609, Pub. L. 96–510, 42 U.S.C. 6901 et seq.).

S. Definitions beginning with the letter "S".

(1) "SDWA" means the Safe Drinking Water Act (Pub. L. 93– 523, as amended; 42 U.S.C. 300f et seq.).

(2) "Site" means the land or water area where any "facility or activity" is physically located or conducted, including adjacent land used in connection with the facility or activity.

(3) "State" means any of the 50 States, the District of Columbia, Guam, the Commonwealth of Puerto Rico, the Virgin Islands, American Samoa, the Trust Territory of the Pacific Islands, the Commonwealth of the Northern Mariana Islands, or an Indian tribe treated as a state.

(4) "Stratum" (plural strata) means a single sedimentary bed or layer, regardless of thickness, that consists of generally the same kind of rock material.

Subsurface fluid distribution system means an assemblage of perforated pipes, drain tiles, or other similar mechanisms intended to distribute fluids below the surface of the ground.

T. Definitions beginning with the letter "T".

(1) "Total dissolved solids" means total dissolved (filterable) solids as determined by the use of the method specified in Section 40 CFR Part 136.

(2) "Transferee" means the owner or operator receiving ownership or operational control of the well.

(3) **"Transferor"** means the owner or operator transferring ownership or operational control of the well.

U. Definitions beginning with the letter "U".

(1) **"UIC**" means the Underground Injection Control program under Part C of the Safe Drinking Water Act, including an "approved State program."

(2) **"Underground injection"** means a "well injection."

(3) **"Underground source of drinking water (USDW)"** means an aquifer or its portion:

(a) which supplies any public water system; or

(b) which contains a sufficient quantity of groundwater to supply a public water system; and

(i) currently supplies drinking water for human consumption; or

(ii) contains fewer than 10,000 mg/l total dissolved solids; and

(iii) which is not an exempted aquifer.

V. Definitions beginning with the letter "V". [RESERVED].

W. Definitions beginning with the letter "W".

(1) **"Well"** means a bored, drilled, or driven shaft whose depth is greater than the largest surface dimension; or, a dug hole whose depth is greater than the largest surface dimension; or, an improved sinkhole; or, a subsurface fluid distribution system.

(2) **"Well injection"** means the subsurface emplacement of fluids through a well.

X. Definitions beginning with the letter "X". [RESERVED].

Y. Definitions beginning with the letter "Y". [RESERVED].

Z. Definitions beginning with the letter "Z". [RESERVED].

[19.15.41.7 NMAC – N, xx/xx/2026]

19.15.41.8 PROCEDURES FOR DECISION MAKING:

A. Application for a permit.

(1) Any person who requires a permit under the UIC programs shall complete, sign, and submit to the Director an application for each permit required under Section 19.15.42.11 NMAC.

(2) The director shall not begin the processing of a permit until the applicant has fully complied with the application requirements for that permit. See Subsection A of 19.15.42.11 NMAC.

(3) Permit applications must comply with the signature and certification requirements of Subsection B of 19.15.42.11 NMAC.

B. Modification, revocation and reissuance, or termination of permits.

(1) Permits may be modified, revoked and reissued, or terminated either at the request of any interested person (including the permittee) or upon the Director's initiative. However, permits may only be modified, revoked and reissued, or terminated for the reasons specified in Subsection H of 19.15.42.11 NMAC or Subsection I of 19.15.42.11 NMAC and Subsection J of 19.15.42.11 NMAC. All requests shall be in writing and shall contain facts or reasons supporting the request. The permittee must furnish any relevant information within 30 days to support the director's review of potential grounds for permit modification, termination, or reissuance, or to verify compliance with permit conditions.

(2) If the director decides the request is not justified, the director shall send the requester a brief written response giving a reason for the decision. Denials of requests for modification, revocation and reissuance, or termination are not subject to public notice, comment, or hearings.

(3) If the director tentatively decides to modify or revoke and reissue a permit under Subsection H of 19.15.42.11 NMAC, the director shall prepare a draft permit under Subsection C of 19.15.41.8 NMAC incorporating the proposed changes. The director may request additional information and, in the case of a modified permit, may require the submission of an updated application. In the case of revoked and reissued permits, the director shall require the submission of a new application.

(4) In a permit modification under this section, only those conditions to be modified shall be reopened when a new draft permit is prepared. All other aspects of the existing permit shall remain in effect for the duration of the unmodified permit. When a permit is revoked and reissued under this section, the entire permit is reopened just as if the permit had expired and was being reissued. During any revocation and reissuance proceeding, the permittee shall comply with all conditions of the existing permit until a new final permit is reissued.

(5) ''Minor modifications'' as defined in Subsection J of 19.15.42.11 NMAC are not subject to the requirements of this section.

(6) If the director tentatively decides to terminate a permit under Subsection I of 19.15.42.11 NMAC of this chapter, he or she shall issue a notice of intent to terminate. A notice of intent to terminate is a type of draft permit which follows the same procedures as any draft permit prepared under Subsection C of 19.15.41.8 NMAC.

C. Draft permits.

(1) Once an application is complete, the director shall prepare a draft permit or deny the application.

(2) If the director decides to prepare a draft permit, he or she shall prepare a draft permit that contains the following information:

(a) all conditions under Subsection A of 19.15.42.12 NMAC;

(b) all compliance schedules under Subsection C of 19.15.42.12 NMAC;

(c) all monitoring requirements under Subsection D of 19.15.42.12 NMAC; and

(d) UIC permits, permit conditions under Subsection B of 19.15.42.12 NMAC.

(3) Draft permits prepared by a state shall be accompanied by a fact sheet if required under Subsection D of 19.15.41.8 NMAC.

D. Fact sheet.

(1) A fact sheet shall be prepared for every draft permit for a major UIC facility or activity, and for every draft permit which the director finds is the subject of wide-spread public interest or raises major issues. The fact sheet shall briefly set forth the principal facts and the significant factual, legal, methodological and policy questions considered in preparing the draft permit. The director shall send this fact sheet to the applicant and, on request, to any other person.

(2) The fact sheet shall include, when applicable:

(a) brief description of the type of facility or activity which is the subject of the draft permit;

(b) the type and quantity of wastes, fluids, or pollutants which are proposed to be or are being treated, stored, disposed of, injected, emitted, or discharged;

(c) a brief summary of the basis for the draft permit conditions including references to applicable statutory or regulatory provisions;

(d) reasons why any requested variances or alternatives to required standards do or do not appear justified;

(e) a description of the procedures for reaching a final decision on the draft permit including:

(i) the beginning and ending dates of the comment period under Subsection E of 19.15.41.8 NMAC and the address where comments will be received;

(ii) procedures for requesting a hearing and the nature of that hearing; and

(iii) any other procedures by which the public may participate in the final decision; and

(f) name and telephone number of a person to contact for additional information.

E. Public notice of permit actions and public comment period.

(1) The director shall give public notice that the following actions have occurred:

(a) a permit application has been tentatively denied under Subsection I of 19.15.42.11 NMAC;

(b) a draft permit has been prepared under Paragraph (2) of Subsection C of 19.15.41.8 NMAC;

(c) a hearing has been scheduled under Subsection G of 19.15.41.8 NMAC;

(d) an appeal has been granted.

(2) No public notice is required when a request for permit modification, revocation and reissuance, or termination is denied under Paragraph (2) of Subsection B of 19.15.41.8 NMAC. Written notice of that denial shall be given to the requester and to the permittee.

(3) Public notice of the preparation of a draft permit (including a notice of intent to deny a permit application) required under Paragraph (1) of this subsection shall allow at least 30 days for public comment.

(4) Public notice of a public hearing shall be given at least 30 days before the hearing. (Public notice of the hearing may be given at the same time as public notice of the draft permit and the two notices may be combined.)

(5) Public notice of activities described in Subparagraph (a) of Paragraph (1) of this subsection shall be given by the following methods:

(a) electronic mailing (email) or by mailing a copy of a notice to the following persons (any person otherwise entitled to receive notice under this paragraph may waive his or her rights to receive notice for any classes and categories of permits):

(i) the applicant;

(ii) any other agency which the Director knows has issued or is required to issue a RCRA, UIC, PSD (or other permit under the Clean Air Act), NPDES, 404, sludge management permit, or ocean dumping permit under the Marine Research Protection and Sanctuaries Act for the same facility or activity (including the EPA).

(iii) Federal and state agencies with jurisdiction over fish, shellfish, and wildlife resources and over coastal zone management plans, the Advisory Council on Historic Preservation, the New Mexico Energy, Minerals, and Natural Resources Department (EMNRD), State Historic Preservation Officers, including any affected States (Indian Tribes). (For purposes of this paragraph, and in the context of the Underground Injection Control Program only, the term State includes Indian Tribes treated as States.)

(iv) Persons on a mailing list developed by (a) including those who request in writing to be on the list; (b) soliciting persons for "area lists" from participants in past permit proceedings in that area; and (c) notifying the public of the opportunity to be put on the mailing list through periodic publication in the public press and in such publications as regional and state funded newsletters, environmental bulletins, or State law journals. (The director may update the mailing list from time to time by requesting written indication of continued interest from those listed. The director may delete from the list the name of any person who fails to respond to such a request.)

(v) Any unit of local government having jurisdiction over the area where the facility is proposed to be located;

(vi) each State agency having any authority under State law with respect to the construction or operation of such facility.

(b) For Class VI injection well UIC permits, mailing or emailing a notice to state and local oil and gas regulatory agencies and State agencies regulating mineral exploration and recovery, the Director of the Public Water Supply Supervision program in the state, the BLM, the office of the state engineer, the state land office, all tribal authorities, and all agencies that oversee injection wells in the State.

(c) For major permits, publication of a notice in a daily or weekly newspaper within the area affected by the facility or activity.

(d) When the program is being administered by an approved state, in a manner constituting legal notice to the public under State law.

(e) Any other method reasonably calculated to give actual notice of the action in question to the persons potentially affected by it, including press releases or any other form or medium to elicit public participation.

(6) All public notices issued under this part shall contain the following minimum information:

(a) name and address of the Division of EMNRD office processing the permit action for which notice is being given;

(b) name and address of the permittee or permit applicant and, if different, of the facility or activity regulated by the permit;

(c) a brief description of the business conducted at the facility or activity described in the permit application or the draft permit;

(d) name, address and telephone number of a person from whom interested persons may obtain further information, including copies of the draft permit, fact sheet, and the application;

(e) a brief description of the comment procedures required by Subsection F of 19.15.41.8 NMAC and Subsection G of 19.15.41.8 NMAC and the time and place of any hearing that will be held, including a statement of procedures to request a hearing (unless a hearing has already been scheduled) and other procedures by which the public may participate in the final permit decision; and

(f) Any additional information considered necessary or proper.

(7) In addition to the general public notice described in Paragraph (5) of this subsection, the public notice of a hearing under Subsection G of 19.15.41.8 NMAC shall contain the following information:

(a) reference to the date of previous public notices relating to the permit;

(b) date, time, and place of the hearing; and

(c) a brief description of the nature and purpose of the hearing, including the applicable rules and procedures.

(8) In addition to the general public notice described in Paragraph (5) of this subsection, all persons identified in Subparagraph (a) of Paragraph (5) of this subsection shall be mailed a copy of the fact sheet, the permit application (if any), inclusive of the third-party verification of the modeling ensemble, and the draft permit (if any).

F. Public comments and requests for public hearings. During the public comment period provided under Subsection E of 19.15.41.8 NMAC, any interested person may submit written comments on the draft permit and may request a public hearing, if no hearing has already been scheduled. A request for a public hearing shall be in writing and shall state the nature of the issues proposed to be raised in the hearing. All comments shall be considered in making the final decision and shall be answered as provided in Subsection I of 19.15.41.8 NMAC.

G. Public hearings.

(1) The director shall hold a public hearing whenever he or she finds, on the basis of requests, a significant degree of public interest in a draft permit(s).

(2) The director may also hold a public hearing at his or her discretion, whenever, for instance, such a hearing might clarify one or more issues involved in the permit decision.

(3) Public notice of the hearing shall be given as specified in Subsection E of 19.15.41.8 NMAC.

(4) Any person may submit oral or written statements and data concerning the draft permit. Reasonable limits may be set upon the time allowed for oral statements, and the submission of statements in writing may be required. The public comment period under Subsection E of 19.15.41.8 NMAC shall automatically be extended to the close of any public hearing under this section. The hearing officer may also extend the comment period by so stating at the hearing.

(5) A tape recording or written transcript of the hearing shall be made available to the public.

H. Issuance and effective date of permit.

(1) After the close of the public comment period under Subsection E of 19.15.41.8 NMAC on a draft permit, the director shall issue a final permit decision. The director shall notify the applicant and each person who has submitted written comments or requested notice of the final permit decision. This notice shall include reference to the procedures for appealing a decision on a UIC permit under Section 40 CFR 124.19. For the purposes of this section, a final permit decision means a final decision to issue, deny, modify, revoke, and reissue, or terminate a permit.

(2) A permit to construct a Class VI injection well issued by the oil conservation division (OCD) shall be valid for a period of two years from the date of issuance. If drilling operations have not commenced within the two-year period, the permit shall automatically terminate without further notice. The owner or operator may request an extension by submitting a written request to the OCD engineering bureau at least 30 days prior to the expiration of the initial two-year period. Such a request must demonstrate good cause for the delay and include a revised timeline for drilling, a detailed explanation of the circumstances necessitating the extension, and any relevant supporting documentation. The OCD may approve the extension if it determines that the delay is justified and consistent with the objectives of the Class VI program.

I. Response to comments.

(1) At the time that a final permit is issued, the Director shall issue a response to comments. This response shall:

(a) specify which provisions, if any, of the draft permit have been changed in the final permit decision, and the reasons for the change; and

(b) briefly describe and respond to all significant comments on the draft permit raised during the public comment period, or during any hearing.

(2) The response to comments shall be available to the public.

[19.15.41.8 NMAC – N, xx/xx/2026]

History of 19.15.41 NMAC: [RESERVED]

EXHIBIT 1-B

TITLE 19 NATURAL RESOURCES AND WILDLIFE
CHAPTER 15 OIL AND GAS
PART 42 UNDERGROUND INJECTION CONTROL PROGRAM

19.15.42.1 ISSUING AGENCY: Oil Conservation Commission.
[19.15.42.1 NMAC – N, XX/XX/XXXX]

19.15.42.2 SCOPE: 19.15.42 NMAC applies to persons constructing, operating or closing a sequestration facility or engaged in the injection of carbon dioxide for the purposes of geologic sequestration under the Geologic Carbon Dioxide Storage Stewardship Act.
[19.15.42.2 NMAC – N, XX/XX/XXXX]

19.15.42.3 STATUTORY AUTHORITY: 19.15.42 NMAC is adopted pursuant to the Geologic Carbon Dioxide Storage Stewardship Act, Sections 74-14-1 through 74-14-7 and the Oil and Gas Act, Section 70-2-6, 70-2-11, and Paragraph (15) of Subsection B of Section 70-2-12 NMSA 1978.
[19.15.42.3 NMAC – N, XX/XX/XXXX]

19.15.42.4 DURATION: Permanent.
[19.15.42.4 NMAC – N, XX/XX/XXXX]

19.15.42.5 EFFECTIVE DATE: [**RESERVED**].
[19.15.42.5 NMAC – N, XX/XX/XXXX]

19.15.42.6 OBJECTIVE: To regulate the permitting, construction, operation and closure of sequestration facilities, the injection of carbon dioxide for the purposes of geologic sequestration and to maintain primary enforcement authority for Safe Drinking Water Act (42 U.S.C. 300f et seq.) Underground Injection Control (UIC) program for UIC Class VI wells.
[19.15.42.6 NMAC – N, XX/XX/XXXX]

19.15.42.7 DEFINITIONS: The following definitions apply to this subpart for underground injection control programs:

A. Definitions beginning with the letter "A".

(1) "Application" means a submission by an individual or entity, using the prescribed forms, to request authorization for underground injection activities, inclusive of any subsequent amendments, updates, or supplements to the original submission.

(2) "Aquifer" means a geological "formation," group of formations, or part of a formation that is capable of yielding a significant amount of water to a well or spring.

(3) "Area of review" means the area surrounding an injection well described according to the criteria set forth in § 40 CFR 146.06 ~~or in the case of an area permit, the project area plus a circumscribing area the width of which is either ¼ of a mile or a number calculated according to the criteria set forth in Section 40 CFR 146.06~~.

B. Definitions beginning with the letter "B". [RESERVED].

C. Definitions beginning with the letter "C".

(1) "Cesspool" means a "drywell" that receives untreated sanitary waste containing human excreta, and which sometimes has an open bottom and/or perforated sides.

(2) "Contaminant" means any physical, chemical, biological, or radiological substance or matter in water.

D. Definitions beginning with the letter "D".

(1) "Director" means the director of the New Mexico energy, minerals and natural resources department, oil conservation division.

(2) "Draft permit" means a document prepared under Subsection C of 19.15.41.8 NMAC indicating the director's decision to issue or deny, modify, revoke and reissue, terminate, or reissue a "permit." A notice of intent to terminate a permit, and a notice of intent to deny a permit, as discussed in Subsection B of 19.15.41.8 NMAC are types of "draft permits." A denial of a request for modification, revocation and reissuance, or termination, as discussed in Subsection B of 19.15.41.8 NMAC is not a "draft permit."

(3) "Drilling mud" means a heavy suspension used in drilling an "injection well," introduced down the drill pipe and through the drill bit.

(4) "Drywell" means a well, other than an improved sinkhole or subsurface fluid distribution system, completed above the water table so that its bottom and sides are typically dry except when receiving fluids.

E. Definitions beginning with the letter "E".

(1) "Eligible indian tribe" is a tribe that meets the statutory requirements established at 42 U.S.C. 300j-11(b)(1).

(2) "Emergency permit" means a UIC "permit" issued in accordance with Section 40 CFR 144.34.

(3) "Environmental protection agency ("EPA")" means the United States Environmental Protection Agency.

(4) "Exempted aquifer" means an "aquifer" or its portion that meets the criteria in the definition of "underground source of drinking water" but which has been exempted according to the procedures in Subsection D of 19.15.42.8 NMAC.

(5) "Existing injection well" means an "injection well" other than a "new injection well."

F. Definitions beginning with the letter "F".

(1) "Facility or activity" means any UIC "injection well," or any other facility or activity that is subject to regulation under these regulations.

(2) "Fluid" means any material or substance which flows or moves whether in a semisolid, liquid, sludge, gas, or any other form or state.

(3) "Formation" means a body of consolidated or unconsolidated rock characterized by a degree of lithologic homogeneity which is prevailingly, but not necessarily, tabular and is mappable on the earth's surface or traceable in the subsurface.

(4) "Formation fluid" means "fluid" present in a "formation" under natural conditions as opposed to introduced fluids, such as "drilling mud."

G. Definitions beginning with the letter "G".

(1) "Generator" means any individual or entity, identified by a specific site location, whose actions or operations result in the creation of hazardous waste as defined under the New Mexico Hazardous Waste Management Regulations (Section 20.4.1 NMAC), or who is responsible for producing or causing the production of any fluid intended for subsurface injection under applicable New Mexico Oil Conservation Division rules (Section 19.15 NMAC).

(2) "Geologic sequestration" means the long-term containment of a gaseous, liquid, or supercritical carbon dioxide stream in subsurface geologic formations. This term does not apply to carbon dioxide capture or transport.

(3) "Groundwater" means water below the land surface in a zone of saturation.

H. Definitions beginning with the letter "H".

(1) "Hazardous waste" means a hazardous waste as defined in Section 40 CFR 261.3.

(2) "Hazardous waste management facility ("HWM facility")" means all contiguous land, and structures, other appurtenances, and improvements on the land used for treating, storing, or disposing of hazardous waste. A facility may consist of several treatment, storage, or disposal operational units (for example, one or more landfills, surface impoundments, or combination of them).

I. Definitions beginning with the letter "I".

(1) "Improved sinkhole" means a naturally occurring karst depression or other natural crevice found in volcanic terrain and other geologic settings which have been modified by man for the purpose of directing and emplacing fluids into the subsurface.

(2) "Indian lands" means "Indian country" as defined in Section 18 U.S.C. 1151. That section defines Indian country as: (a) All land within the limits of any Indian reservation under the jurisdiction of the United States government, notwithstanding the issuance of any patent, and, including rights-of-way running through the reservation; (b) All dependent Indian communities within the borders of the United States whether within the original or subsequently acquired territory thereof, and whether within or without the limits of a State; and (c) All Indian allotments, the Indian titles to which have not been extinguished, including rights-of-way running through the same.

(3) "Indian tribe" means any Indian tribe having a federally recognized governing body carrying out substantial governmental duties and powers over a defined area.

(4) "Injection well" means a "well" into which "fluids" are being injected.

(5) "Injection zone" means a geological "formation," group of formations, or part of a formation receiving fluids through a "well."

J. Definitions beginning with the letter "J". [RESERVED].

K. Definitions beginning with the letter "K." [RESERVED].

L. Definitions beginning with the letter "L". [RESERVED].

M. Definitions beginning with the letter "M".

(1) "Major facility" means any UIC "facility or activity" classified as such by the director, in conjunction with the EPA regional administrator.

(2) "Manifest" means the shipping document EPA Form 8700-22 (including, if necessary, EPA Form 8700-22A), originated and signed in accordance with the applicable requirements of Section 20.4.1.500 NMAC (incorporating Section 40 CFR Part 2362).

N. Definitions beginning with the letter "N". "**New injection well"** means a well which began injection after the New Mexico Class VI Underground Injection Control program is approved and the applicable New Mexico Oil Conservation Division rules and regulations are promulgated.

O. Definitions beginning with the letter "O". "Owner or operator" means the owner or operator of any "facility or activity" subject to regulation under the UIC program.

P. Definitions beginning with the letter "P".

(1) "Permit" means an authorization, license, or equivalent control document issued by the EPA or an approved State to implement the requirements of Sections 19.15.41 NMAC, 19.15.42 NMAC and 19.15.43 NMAC. Excluding Class VI UIC, "permit" includes an area permit or any permit which has not yet been the subject of final agency action, such as a "draft permit."

(2) "Person" means an individual, association, partnership, corporation, municipality, state, federal, or tribal agency, or an agency or employee thereof.

(3) "Plugging" means the act or process of stopping the flow of water, oil, or gas into or out of a formation through a borehole or well penetrating that formation.

(4) "Point of injection" means the last accessible sampling point prior to waste fluids being released into the subsurface environment through a Class V injection well. For example, the point of injection of a Class V septic system might be the distribution box—the last accessible sampling point before the waste fluids drain into the underlying soils. For a dry well, it is likely to be the well bore itself.

(5) "Project" means a group of wells in a single operation.

Q. Definitions beginning with the letter "Q". [RESERVED].

R. Definitions beginning with the letter "R".

(1) "Radioactive waste" means any waste which contains radioactive material in concentrations which exceed those listed in Section 10 CFR 20, Appendix B, Table II, column 2.

(2) "RCRA" means the Solid Waste Disposal Act as amended by the Resource Conservation and Recovery Act of 1976 (Pub. L. 94–580, as amended by Pub. L. 95–609, Pub. L. 96–510, 42 U.S.C. 6901 et seq.).

S. Definitions beginning with the letter "S".

(1) "SDWA" means the Safe Drinking Water Act (Pub. L. 93– 523, as amended; 42 U.S.C. 300f et seq.).

(2) "Site" means the land or water area where any "facility or activity" is physically located or conducted, including adjacent land used in connection with the facility or activity.

(3) "State" means any of the 50 States, the District of Columbia, Guam, the Commonwealth of Puerto Rico, the Virgin Islands, American Samoa, the Trust Territory of the Pacific Islands, the Commonwealth of the Northern Mariana Islands, or an Indian Tribe treated as a State.

(4) "Stratum" (plural strata) means a single sedimentary bed or layer, regardless of thickness, that consists of generally the same kind of rock material.

(5) "Subsurface fluid distribution system" means an assemblage of perforated pipes, drain tiles, or other similar mechanisms intended to distribute fluids below the surface of the ground.

T. Definitions beginning with the letter "T".

(1) "Total dissolved solids" means total dissolved (filterable) solids as determined by the use of the method specified in 40 CFR Part 136.

(2) "Transferee" means the owner or operator receiving ownership and/or operational control of the well.

(3) "Transferor" means the owner or operator transferring ownership and/or operational control of the well.

U. Definitions beginning with the letter "U".

(1) **"UIC"** means the Underground Injection Control program under Part C of the Safe Drinking Water Act, including an "approved State program."

(2) **"Underground injection"** means a "well injection."

(3) **"Underground source of drinking water (USDW)"** means an aquifer or its portion:

(a) Which supplies any public water system; or

(b) Which contains a sufficient quantity of groundwater to supply a public water system; and

(i) Currently supplies drinking water for human consumption; or

(ii) Contains fewer than 10,000 mg/l total dissolved solids; and

(iii) Which is not an exempted aquifer.

V. Definitions beginning with the letter "V". [RESERVED].

W. Definitions beginning with the letter "W".

(1) **"Well"** means a bored, drilled, or driven shaft whose depth is greater than the largest surface dimension; or, a dug hole whose depth is greater than the largest surface dimension; or, an improved sinkhole; or, a subsurface fluid distribution system.

(2) **"Well injection"** means the subsurface emplacement of fluids through a well.

X. Definitions beginning with the letter "X". [RESERVED].

Y. Definitions beginning with the letter "Y". [RESERVED].

Z. Definitions beginning with the letter "Z". [RESERVED].

[19.15.42.7 NMAC – N, XX/XX/XXXX]

19.15.42.8 GENERAL PROVISIONS:

A. General provisions for underground injection control programs.

(1) Note that Section 19.15.43.9 NMAC sets forth requirements for owners or operators of Class VI injection wells.

(2) Such aquifers are those which would otherwise qualify as "underground sources of drinking water" to be protected, but which have no real potential to be used as drinking water sources. Therefore, they are not USDWs. No aquifer is an exempted aquifer until it has been affirmatively designated under the procedures at Subsection D of 19.15.42.8 NMAC. Aquifers which do not fit the definition of "underground source of drinking water" are not "exempted aquifers." They are simply not subject to the special protection afforded USDWs. During initial Class VI program development, the director shall not expand the areal extent of an existing Class II enhanced oil recovery or enhanced gas recovery aquifer exemption for Class VI injection wells and EPA shall not approve a program that applies for aquifer exemption expansions of Class II-Class VI exemptions as part of the program description. All Class II to Class VI aquifer exemption expansions previously issued by EPA must be incorporated into the Class VI program descriptions pursuant to requirements at Section 40 CFR 145.23(f)(9).

B. Confidentiality of information.

(1) Any information submitted pursuant to these regulations may be claimed as confidential by the submitter in accordance with applicable provisions of state law. A claim of confidentiality must be made at the time of submission, either in the manner prescribed by the applicable application form or instructions, or by clearly marking each page containing such information with the phrase "confidential business information." Failure to assert a confidentiality claim at the time of submission may result in the division making the information available to the public without further notice. Information properly designated as confidential shall be handled in accordance with the procedures set forth in applicable state law and any incorporated federal confidentiality provisions, including but not limited to Section 40 CFR Part 2.

(2) Claims of confidentiality for the following information will be denied:

(a) The name and address of any permit applicant or permittee.

(b) Information which deals with the existence, absence, or level of contaminants in drinking water or zones other than the approved injection zone.

(c) Information already in the public record.

C. Classification of wells.

(1) *Class VI* Injection wells are classified as follows: Wells that are not experimental in nature that are used for geologic sequestration of carbon dioxide beneath the lowermost formation containing a USDW or wells used for geologic sequestration of carbon dioxide that have been granted a waiver of the injection depth requirements pursuant to requirements at Subsection P of 19.15.43.9 NMAC or wells used for geologic sequestration of carbon dioxide that have received an expansion to the areal extent of an existing Class II enhanced

oil recovery or enhanced gas recovery aquifer exemption pursuant to Subsection A of 19.15.43.8 NMAC and Section 40 CFR 144.7(d).

D. Identification of underground sources of drinking water and exempted aquifers.

(1) The director may identify (by narrative description, illustrations, maps, or other means) and shall protect as underground sources of drinking water, all aquifers and parts of aquifers which meet the definition of ‘‘underground source of drinking water’’ in Section 19.15.42.7 NMAC, except to the extent there is an applicable aquifer exemption under Paragraph (2) of this section or an expansion to the areal extent of an existing Class II enhanced oil recovery or enhanced gas recovery aquifer exemption for the exclusive purpose of Class VI injection for geologic sequestration under Paragraph (4) of this section. Other than EPA approved aquifer exemption expansions that meet the criteria set forth in Subsection A of 19.15.43.8 NMAC, new aquifer exemptions shall not be issued for Class VI injection wells. Even if an aquifer has not been specifically identified by the Director, it is an underground source of drinking water if it meets the definition in Section 19.15.42.7 NMAC.

(2) The director may identify (by narrative description, illustrations, maps, or other means) and describe in geographic or geometric terms (such as vertical and lateral limits and gradient) which are clear and definite, all aquifers or parts thereof which the director proposes to designate as exempted aquifers using the criteria in Subsection A of 19.15.43.8 NMAC.

(3) No designation of an exempted aquifer submitted as part of a UIC program shall be final until approved by the administrator as part of a UIC program. No designation of an expansion to the areal extent of a Class II enhanced oil recovery or enhanced gas recovery aquifer exemption for the exclusive purpose of Class VI injection for geologic sequestration shall be final until approved by the administrator as a revision to the applicable Federal UIC program under Part 147 or as a substantial revision of an approved State UIC program in accordance with Section 40 CFR 145.32 and Section 19.15.42.13 NMAC.

(4) Expansion to the areal extent of existing Class II aquifer exemptions for Class VI wells. Owners or operators of Class II enhanced oil recovery or enhanced gas recovery wells may request that the director approve an expansion to the areal extent of an aquifer exemption already in place for a Class II enhanced oil recovery or enhanced gas recovery well for the exclusive purpose of Class VI injection for geologic sequestration. Such requests must be treated as a substantial revision to the state’s UIC program and will not be final until approved by EPA.

(a) The owner or operator of a Class II enhanced oil recovery or enhanced gas recovery well that requests an expansion of the areal extent of an existing aquifer exemption for the exclusive purpose of Class VI injection for geologic sequestration must define (by narrative description, illustrations, maps, or other means) and describe in geographic and/or geometric terms (such as vertical and lateral limits and gradient) that are clear and definite, all aquifers or parts thereof that are requested to be designated as exempted using the criteria in Subsection A of 19.15.43.8 NMAC.

(b) In evaluating a request to expand the areal extent of an aquifer exemption of a Class II enhanced oil recovery or enhanced gas recovery well for the purpose of Class VI injection, the director must determine that the request meets the criteria for exemptions. In making the determination, the director shall consider:

(i) current and potential future use of the USDWs to be exempted as drinking water resources;

(ii) the predicted extent of the injected carbon dioxide plume, and any mobilized fluids that may result in degradation of water quality, over the lifetime of the GS project, as informed by computational modeling performed pursuant to Section 40 CFR 146.84(c)(1), in order to ensure that the proposed injection operation will not at any time endanger USDWs including non-exempted portions of the injection formation;

(iii) whether the areal extent of the expanded aquifer exemption is of sufficient size to account for any possible revisions to the computational model during reevaluation of the area of review.

(c) Any information submitted to support a waiver request made by the owner or operator, if appropriate.

E. Noncompliance and program reporting by the director. The director shall submit any reports required under this section to the regional administrator.

(1) Quarterly reports. The director shall submit quarterly narrative reports for major facilities as follows:

(a) Provide an alphabetized list of permittees. When two or more permittees have the same name, the lowest permit number shall be entered first.

(b) For each entry on the list, include the following information in the following order:

(i) Name, location, and permit number of the noncomplying permittees.

(ii) A brief description and date of each instance of noncompliance for that permittee. Instances of noncompliance may include one or more of the kinds set forth in Paragraph (2) of this section. When a permittee has noncompliance of more than one kind, combine the information into a single entry for each such permittee.

(iii) The date(s) and a brief description of the action(s) taken by the Director to ensure compliance.

(iv) Status of the instance(s) of noncompliance with the date of the review of the status or the date of resolution; and

(v) Any details which tend to explain or mitigate the instance(s) of noncompliance.

(2) Instances of noncompliance to be reported. Any instances of noncompliance within the following categories shall be reported in successive reports until the noncompliance is reported as resolved. Once noncompliance is reported as resolved it need not appear in subsequent reports.

(a) Failure to complete construction elements. When the permittee has failed to complete, by the date specified in the permit, an element of a compliance schedule involving either planning for construction or a construction step (for example, begin construction, attain operation level); and the permittee has not returned to compliance by accomplishing the required elements of the schedule within 30 days from the date a compliance schedule report is due under the permit.

(b) Modifications to schedules of compliance. When a schedule of compliance in the permit has been modified under Subsection H of 19.15.42.11 NMAC or Subsection J of 19.15.42.11 NMAC because of the permittee's noncompliance.

(c) Failure to complete or provide compliance schedule or monitoring reports. When the permittee has failed to complete or provide a report required in a permit compliance schedule (for example, progress report or notice of noncompliance or compliance) or a monitoring report; and the permittee has not submitted the complete report within 30 days from the date it is due under the permit for compliance schedules, or from the date specified in the permit for monitoring reports.

(d) Deficient reports. When the required reports provided by the permittee are so deficient as to cause misunderstanding by the director and thus impede the review of the status of compliance.

(e) Noncompliance with other permit requirements. Noncompliance shall be reported in the following circumstances:

(i) Whenever the permittee has violated a permit requirement (other than reported under Subparagraph (a) or (b) of paragraph (2) of this section), and has not returned to compliance within 45 days from the date reporting of noncompliance was due under the permit; or

(ii) When the director determines that a pattern of noncompliance exists for a major facility permittee over the most recent four consecutive reporting periods. This pattern includes any violation of the same requirement in two consecutive reporting periods, and any violation of one or more requirements in each of four consecutive reporting periods; or

(iii) When the director determines significant permit noncompliance or other significant event has occurred, such as a migration of fluids into a USDW.

(f) All other. Statistical information shall be reported quarterly on all other instances of noncompliance by major facilities with permit requirements not otherwise reported under Paragraph (2) of this section.

(3) Annual reports.

(a) Annual noncompliance report. Statistical reports shall be submitted by the Director on nonmajor UIC permittees indicating the total number reviewed, the number of noncomplying nonmajor permittees, the number of enforcement actions, and number of permit modifications extending compliance deadlines. The statistical information shall be organized to follow the types of noncompliance listed in Paragraph (2) of this section.

(b) In addition to the annual noncompliance report, the state director shall submit each year a program report to the administrator (in a manner and form prescribed by the administrator) consisting of the following:

(i) A detailed description of the State's implementation of its program;

(ii) Suggested changes, if any to the program description (see Section 40 CFR 145.23(f)) which are necessary to reflect more accurately the State's progress in issuing permits;

(iii) An updated inventory of active underground injection operations in the State.

(c) For all annual reports. The period for annual reports shall be for the calendar year ending December 31, with reports completed and available to the public no more than 60 days later.

(4) In addition to complying with the requirements of Subparagraph (b) of Paragraph (3) this section, the director shall provide the administrator, on February 28 and August 31 of each of the first two years of program operation, the information required in Sections 40 CFR 146.13, 146.23, and 146.33.

(5) All Class VI program reports shall be consistent with reporting requirements set forth in Subsection L of 19.15.43.9 NMAC.

(6) Schedule. For all quarterly reports. On the last working day of May, August, November, and February, the state director shall submit to the regional administrator information concerning noncompliance with permit requirements by major facilities in the state in accordance with the following schedule. The regional administrator shall prepare and submit information for EPA-issued permits to EPA Headquarters in accordance with the same schedule. Dates for completion of reports are as follows: January, February, and March: 1, May 31, April, May, and June: 1 Aug. 31, July, August, and September: 1, Nov. 30, October, November, and December: 1, Feb. 28. Reports must be made available to the public for inspection and copying on this date.

[19.15.42.7 NMAC – N, XX/XX/XXXX]

19.15.42.8 GENERAL PROGRAM REQUIREMENTS:

A. Prohibition of unauthorized injection. Any underground injection, except into a well authorized by rule or except as authorized by permit issued under the UIC program, is prohibited. The construction of any well required to have a permit is prohibited until the permit has been issued.

B. Prohibition of movement of fluid into underground sources of drinking water.

(1) No owner or operator shall construct, operate, maintain, convert, plug, abandon, or conduct any other injection activity in a manner that allows the movement of fluid containing any contaminant into underground sources of drinking water, if the presence of that contaminant may cause a violation of any primary drinking water regulation under Section 40 CFR 141 or may otherwise adversely affect the health of persons. The applicant for a permit shall have the burden of showing that the requirements of this paragraph are met.

(2) For Class I, II, III, and VI wells, if any water quality monitoring of an underground source of drinking water indicates the movement of any contaminant into the underground source of drinking water, except as authorized under Section 19.15.43 NMAC, the director shall prescribe such additional requirements for construction, corrective action, operation, monitoring, or reporting (including closure of the injection well) as are necessary to prevent such movement. In the case of wells authorized by permit, these additional requirements shall be imposed by modifying the permit in accordance with Subsection H of 19.15.42.11 NMAC, or the permit may be terminated under Subsection I of 19.15.42.11 NMAC if cause exists, or appropriate enforcement action may be taken if the permit has been violated. In the case of wells authorized by rule, see Sections 40 CFR 144.21 through 144.24 and Subsection A of 19.15.42.10 NMAC.

(3) Notwithstanding any other provision of this section, the director may take emergency action upon receipt of information that a contaminant which is present in or likely to enter a public water system or underground source of drinking water may present an imminent and substantial endangerment to the health of persons.

C. Prohibition of non-experimental Class V wells for geologic sequestration. The construction, operation or maintenance of any non-experimental Class V geologic sequestration well is prohibited.

D. Records. The director may require, by written notice on a selective well-by-well basis, an owner or operator of an injection well to establish and maintain records, make reports, conduct monitoring, and provide other information as is deemed necessary to determine whether the owner or operator has acted or is acting in compliance with Part C of the SDWA or its implementing regulations.

E. Requirements for Class VI wells. Owners or operators of Class VI wells must obtain a permit. Class VI wells cannot be authorized by rule to inject carbon dioxide.

F. Transitioning from Class II to Class VI.

(1) Owners or operators that are injecting carbon dioxide for the primary purpose of long-term storage into an oil and gas reservoir or for which there is an increased risk of USDWs compared to Class II operations must apply for and obtain a Class VI geologic sequestration permit ~~when there is an increased risk to~~

~~USDWs compared to Class II operations~~. In determining if there is an increased risk to USDWs, the owner or operator must consider the factors specified within this section.

(2) The director shall determine when there is an increased risk to USDWs compared to Class II operations and a Class VI permit is required. In order to make this determination the Director must consider the following:

(a) increase in reservoir pressure within the injection zone(s);
(b) increase in carbon dioxide injection rates;
(c) decrease in reservoir production rates;
(d) distance between the injection zone(s) and USDWs;
(e) suitability of the Class II area of review delineation;
(f) integrity of the caprock seal for long-term containment;
~~(f)~~(g) quality of abandoned well plugs within the area of review;
~~(g)~~(h) the owner's or operator's plan for recovery of carbon dioxide at the cessation of injection;
~~(h)~~(i) the source and properties of injected carbon dioxide; and
~~(i)~~(j) any additional site-specific factors as determined by the director.

19.15.42.9 AUTHORIZATION OF UNDERGROUND INJECTION BY RULE:

Existing Class II enhanced recovery and hydrocarbon storage wells. Injection of carbon dioxide through Class VI wells shall not be authorized by rule. A permit must be secured by the owner or operator prior to conducting injection operations under this well classification. For any existing Class II enhanced recovery or hydrocarbon storage well that is authorized by rule, such authorization shall terminate upon the effective date of a Class VI permit issued in accordance with Subsection F of 19.15.42.9 NMAC upon approved plugging and abandonment of the well, or at the time the well is converted to another use.
[19.15.42.9 NMAC – N, XX/XX/XXXX]

19.15.42.10 AUTHORIZATION BY PERMIT:

A. Application for a permit; authorization by permit.

(1) No person shall conduct any underground injection activity unless authorized by a permit issued pursuant to these regulations. Effective on the date these regulations become enforceable, the construction or operation of any well for which a permit is required under this part is strictly prohibited unless and until such permit has been duly issued by the director.

(2) **Who applies?** When a facility or activity is owned by one person but is operated by another person, it is the operator's duty to obtain a permit.

(3) **Time to apply.** Any person who performs or proposes an underground injection for which a permit is or will be required shall submit an application to the director in accordance with the UIC program as follows: For new injection wells, except new wells in projects authorized under Section 40 CFR 144.21(d) or authorized by an existing area permit under Section 40 CFR 144.33(c), a reasonable time before construction is expected to begin.

(4) **Completeness.** The director shall not issue a permit before receiving a complete application for a permit. An application for a permit is complete when the director receives an application form and any supplemental information which are completed to his or her satisfaction. The completeness of any application for a permit shall be judged independently of the status of any other permit application or permit for the same facility or activity.

(5) **Information requirements.** All applicants for Class VI permits shall provide the following information to the director, using the application form provided by the director.

(a) The activities conducted by the applicant which require it to obtain permits under RCRA, UIC, the National Pollution Discharge Elimination System (NPDES) program under the Clean Water Act, or the Prevention of Significant Deterioration (PSD) program under the Clean Air Act.

(b) Name, mailing address, and location of the facility for which the application is submitted.

(c) Up to four SIC codes which best reflect the principal products or services provided by the facility.

(d) The operator's name, address, telephone number, ownership status, and status as Federal, State, private, public, or other entity.

(e) Whether the facility is located on Indian lands.

(f) A listing of all permits or construction approvals received or applied for under any of the following programs:

(i) Hazardous Waste Management program under RCRA.

(ii) UIC program under SDWA.

(iii) NPDES program under CWA

(iv) Prevention of Significant Deterioration (PSD) program under the Clean Air Act.

(v) Nonattainment program under the Clean Air Act.

(vi) National Emission Standards for Hazardous Pollutants (NESHAPS) preconstruction approval under the Clean Air Act.

(vii) Ocean dumping permits under the Marine Protection Research and Sanctuaries Act.

(viii) Dredge and fill permits under section 404 of CWA.

(ix) Other relevant environmental permits, including State permits.

(g) A brief description of the nature of the business.

(h) The names and addresses of all property owners within the area of review and ¼ mile of the Class VI well or project.

B. Signatories to permit applications and reports.

(1) Applications. All permit applications shall be signed as follows:

(a) For a corporation, by a responsible corporate officer. For the purpose of this section, a responsible corporate officer means:

(i) A president, secretary, treasurer, or vice president of the corporation in charge of a principal business function, or any other person who performs similar policy- or decision-making functions for the corporation, or

(ii) The manager of one or more manufacturing, production, or operating facilities employing more than 250 persons or having gross annual sales or expenditures exceeding $25 million (in second-quarter 1980 dollars), if authority to sign documents has been assigned or delegated to the manager in accordance with corporate procedures.

(b) For a partnership or sole proprietorship, by a general partner or the proprietor, respectively.

(c) For a municipality, state, federal, or other public agency, by either a principal executive officer or ranking elected official.

(d) The chief executive officer of the agency, or

(e) A senior executive officer having responsibility for the overall operations of a principal geographic unit of the division.

(2) Reports. All reports required by permits, other information requested by the director, and all permit applications submitted for Class II wells under Subsection A of 19.15.42.11 NMAC shall be signed by a person described in Paragraph (1) of this section, or by a duly authorized representative of that person. A person is a duly authorized representative only if:

(a) The authorization is made in writing by a person described in Paragraph (1) of this section;

(b) The authorization specifies either an individual or a position having responsibility for the overall operation of the regulated facility or activity, such as the position of plant manager, operator of a well or a well field, superintendent, or position of equivalent responsibility. A duly authorized representative may thus be either a named individual or any individual occupying a named position; and

(c) The written authorization is submitted to the director.

(3) Changes to authorization. If an authorization under Paragraph (1) of this section is no longer accurate because a different individual or position has responsibility for the overall operation of the facility, a new authorization satisfying the requirements of Paragraph (1) of this section must be submitted to the director prior to or together with any reports, information, or applications to be signed by an authorized representative.

(4) Certification. Any person signing a document under Paragraph (1) or (2) of this section shall make the following certification: "I certify under penalty of law that this document and all attachments were prepared under my direction or supervision in accordance with a system designed to assure that qualified personnel properly gather and evaluate the information submitted. Based on my inquiry of the person or persons who manage the system, or those persons directly responsible for gathering the information, the information submitted is, to the

best of my knowledge and belief, true, accurate, and complete. I am aware that there are significant penalties for submitting false information, including the possibility of fine and imprisonment for knowing violations."

C. Area permits. The director may issue a permit on an area basis, rather than for each well individually, provided that the permit is for injection wells other than Class VI wells. Area permits are expressly prohibited for Class VI injection wells.

D. Effect of a permit.

(1) Compliance with a permit during its term constitutes compliance, for purposes of enforcement, with Part C of the SDWA. However, a permit may be modified, revoked and reissued, or terminated during its term for cause as set forth in Subsections H and I of 19.15.42.11 NMAC.

(2) The issuance of a permit does not convey any property rights of any sort, or any exclusive privilege.

(3) The issuance of a permit does not authorize any injury to persons or property or invasion of other private rights, or any infringement of State or local law or regulations.

E. Duration of permits.

(1) Permits for Class VI UIC wells shall remain in effect for the duration of the facility's operational life and the post injection site care period. The director shall conduct a permit review no less frequently than once every five years to assess whether the permit requires modification, revocation and reissuance, termination, or the incorporation of minor modifications, consistent with applicable permitting standards and procedures.

(2) The term of a permit shall not be extended by modification beyond the maximum duration specified in Subsection F of 19.15.42.11 NMAC.

(3) The director may issue any permit for a duration that is less than the full allowable term under this section.

F. Continuation of expiring permits.

(1) Continuation of permits. The conditions of an expired permit may continue in force until the effective date of a new permit if the permittee has submitted a timely and a complete application for a new permit or, if the Director, through no fault of the permittee, does not issue a new permit with an effective date on or before the expiration date of the previous permit (for example, when issuance is impracticable due to time or resource constraints).

(2) Effect. Permits continued under this section remain fully effective and enforceable.

(3) Enforcement. When the permittee is not in compliance with the conditions of the expiring or expired permit the Director may choose to do any or all of the following:

(a) Initiate enforcement action based upon the permit which has been continued;

(b) Issue a notice of intent to deny the new permit. If the permit is denied, the owner or operator would then be required to cease the activities authorized by the continued permit or be subject to enforcement action for operating without a permit;

(c) Issue a new permit under this chapter with appropriate conditions; or

(d) Take other actions authorized by these regulations.

G. Transfer of permits.

(1) Transfers by modification. Except as provided in Paragraph (2) of this section, a permit may be transferred by the permittee to a new owner or operator only if the permit has been modified or revoked and reissued (under Subsection H of 19.15.42.11 NMAC), or a minor modification made (under Subsection J of 19.15.42.11 NMAC), to identify the new permittee and incorporate such other requirements as may be necessary under the Safe Drinking Water Act.

(2) Automatic transfers of Class VI permits are prohibited.

H. Modification or revocation and reissuance of permits. When the director receives any information (for example, inspects the facility, receives information submitted by the permittee as required in the permit (see Subsection A of 19.15.42.12 NMAC of this chapter), receives a request for modification or revocation and reissuance under Subsection B of 19.15.41.8 NMAC, or conducts a review of the permit file) he or she may determine whether or not one or more of the causes listed in Paragraphs (1) and (2) of this section for modification or revocation and reissuance or both exist. If cause exists, the director may modify or revoke and reissue the permit accordingly, subject to the limitations of Paragraph (3) of this section and may request an updated application if necessary. When a permit is modified, only the conditions subject to modification are reopened. If a permit is revoked and reissued, the entire permit is reopened and subject to revision and the permit is reissued for a new term. See Subsection B of 19.15.41.8 NMAC. If cause does not exist under this section or Subsection J of 19.15.42.11 NMAC, the director shall not modify or revoke and reissue the permit. If a permit modification satisfies the criteria

in Subsection J of 19.15.42.11 NMAC for ‘‘minor modifications’’ the permit may be modified without a draft permit or public review. Otherwise, a draft permit must be prepared (Subsection C of 19.15.41.8 NMAC).

(1) Causes for Modification. The following are causes for modification and may be causes for revocation and reissuance of permits:

(a) Alterations. There are material and substantial alterations or additions to the permitted facility or activity which occurred after permit issuance which justify the application of permit conditions that are different or absent in the existing permit.

(b) Information. The director has received information. Permits other than for Class II and III wells may be modified during their terms for this cause only if the information was not available at the time of permit issuance (other than revised regulations, guidance, or test methods) and would have justified the application of different permit conditions at the time of issuance. For UIC area permits (Section 40 CFR 144.33), this cause shall include any information indicating that cumulative effects on the environment are unacceptable.

(c) New regulations. The standards or regulations on which the permit was based have been changed by promulgation of new or amended standards or regulations or by judicial decision after the permit was issued. Permits for Class VI wells may be modified during their terms only as follows:

(i) the permit condition requested to be modified was based on a promulgated regulation or guideline;

(ii) there has been a revision, withdrawal, or modification of that portion of the rule or regulation on which the permit condition was based, and

(iii) a permittee requests modification within 90 days after New Mexico Register notice of the action on which the request is based.

(d) For judicial decisions, a court of competent jurisdiction has remanded and stayed oil conservation division regulations if the remand and stay concern that portion of the regulations on which the permit condition was based and a request is filed by the permittee in accordance with Subsection B of 19.15.41.8 NMAC within 90 days of judicial remand.

(e) Compliance schedules. The director determines good cause exists for modification of a compliance schedule, such as an act of God, strike, flood, or materials shortage or other events over which the permittee has little or no control and for which there is no reasonably available remedy.

(f) Basis for modification of Class VI permits. Additionally, for Class VI wells, whenever the Director determines that permit changes are necessary based on:

(i) Area of review reevaluations under Subsection E of 19.15.43.9 NMAC;

(ii) Any amendments to the testing and monitoring plan under Subsection K of 19.15.43.9 NMAC;

(iii) Any amendments to the injection well plugging plan under Subsection M of 19.15.43.9 NMAC;

(iv) Any amendments to the post-injection site care and site closure plan under Subsection N of 19.15.43.9 NMAC;

(v) Any amendments to the emergency and remedial response plan under Subsection O of 19.15.43.9 NMAC; or

(vi) A review of monitoring and testing results conducted in accordance with permit requirements.

(2) Causes for modification or revocation and reissuance. The following are causes to modify or, alternatively, revoke and reissue a permit:

(a) Cause exists for termination under Subsection I of 19.15.42.11 NMAC, and the director determines that modification or revocation and reissuance is appropriate.

(b) The director has received notification of a proposed transfer of the permit. A permit also may be modified to reflect a transfer after the effective date of an automatic transfer (Subsection G(2) of 19.15.42.11 NMAC) but will not be revoked and reissued after the effective date of the transfer except upon the request of the new permittee.

(c) A determination that the waste being injected is a hazardous waste as defined in Section 40 CFR 261.3 either because the definition has been revised, or because a previous determination has been changed.

(3) Facility siting. Suitability of the facility location will not be considered at the time of permit modification or revocation and reissuance unless new information or standards indicate that a threat to human health or the environment exists which was unknown at the time of permit issuance.

I. Termination of permits.

(1) The director may terminate a permit during its term, or deny a permit renewal application for the following causes:

(a) noncompliance by the permittee with any condition of the permit;

(b) the permittee's failure in the application or during the permit issuance process to disclose fully all relevant facts, or the permittee's misrepresentation of any relevant facts at any time; or

(c) a determination that the permitted activity endangers human health or the environment and can only be regulated to acceptable levels by permit modification or termination.

(2) The director shall follow the applicable procedures in Subsection C of 19.15.41.8 NMAC in terminating any permit under this section.

J. Minor modifications of permits. Upon the consent of the permittee, the director may modify a permit to make the corrections or allowances for changes in the permitted activity listed in this section, without following the procedures of Subsection B of 19.15.41.8 NMAC. Any permit modification not processed as a minor modification under this section must be made for cause and with Subsections C and E of 19.15.41.8 NMAC draft permit and public notice as required in Subsection H of 19.15.42.11 NMAC. Minor modifications may only:

(1) correct typographical errors;

(2) require more frequent monitoring or reporting by the permittee;

(3) change an interim compliance date in a schedule of compliance, provided the new date is not more than 120 days after the date specified in the existing permit and does not interfere with attainment of the final compliance date requirement;

(4) Allow for a change in ownership or operational control of a facility where the director determines that no other change in the permit is necessary, provided that a written agreement containing a specific date for transfer of permit responsibility, coverage, and liability between the current and new permittees has been submitted to the director;

(5) Change quantities or types of fluids injected which are within the capacity of the facility as permitted and, in the judgment of the director, would not interfere with the operation of the facility or its ability to meet conditions described in the permit and would not change its classification;

(6) Change construction requirements approved by the director pursuant to Subsection B of 19.15.42.12 NMAC (establishing UIC permit conditions), provided that any such alteration shall comply with the requirements of this part and Section 19.15.43 NMAC;

(7) Amend a Class VI injection well testing and monitoring plan, plugging plan, post-injection site care and site closure plan, or emergency and remedial response plan where the modifications merely clarify or correct the plan, as determined by the Director.

[19.15.42.10 NMAC – N, XX/XX/XXXX]

19.15.42.11 PERMIT CONDITIONS:

A. Conditions applicable to all permits. The following conditions apply to all UIC permits. All conditions applicable to all permits shall be incorporated into the permits either expressly or by reference. If incorporated by reference, a specific citation to these regulations.

(1) **Duty to comply.** The permittee must comply with all conditions of this permit. Any permit noncompliance constitutes a violation of the Safe Drinking Water Act and is grounds for enforcement action; for permit termination, revocation and reissuance, or modification; or for denial of a permit renewal application.

(2) **Duty to reapply.** If the permittee wishes to continue an activity regulated by this permit after the expiration date of this permit, the permittee must apply for and obtain a new permit.

(3) **Duty to halt or reduce activity.** It shall not be a defense for a permittee in an enforcement action that it would have been necessary to halt or reduce the permitted activity in order to maintain compliance with the conditions of this permit.

(4) **Duty to mitigate.** The permittee shall take all reasonable steps to minimize or correct any adverse impact on the environment resulting from noncompliance with this permit.

(5) **Proper operation and maintenance.** The permittee shall at all times properly operate and maintain all facilities and systems of treatment and control (and related appurtenances) which are installed or used by the permittee to achieve compliance with the conditions of this permit. Proper operation and maintenance includes effective performance, adequate funding, adequate operator staffing and training, and adequate laboratory and process controls, including appropriate quality assurance procedures. This provision requires the operation of backup or auxiliary facilities or similar systems only when necessary to achieve compliance with the conditions of the permit.

(6) Permit actions. This permit may be modified, revoked and reissued, or terminated for cause. The filing of a request by the permittee for a permit modification, revocation and reissuance, or termination, or a notification of planned changes or anticipated noncompliance, does not stay any permit condition.

(7) Property rights. This permit does not convey any property rights of any sort, or any exclusive privilege.

(8) Duty to provide information. The permittee shall furnish to the Director, within 30 days, any information which the Director may request to determine whether cause exists for modifying, revoking and reissuing, or terminating this permit, or to determine compliance with this permit. The permittee shall also furnish to the Director, upon request, copies of records required to be kept by this permit.

(9) Inspection and entry. The permittee shall allow the Director, or an authorized representative, upon the presentation of credentials and other documents as may be required by law, to:

(a) Enter upon the permittee's premises where a regulated facility or activity is located or conducted, or where records must be kept under the conditions of this permit;

(b) Have access to and copy, at reasonable times, any records that must be kept under the conditions of this permit;

(c) Inspect at reasonable times any facilities, equipment (including monitoring and control equipment), practices, or operations regulated or required under this permit; and

(d) Sample or monitor at reasonable times, for the purposes of assuring permit compliance or as otherwise authorized by the SDWA, any substances or parameters at any location.

(10) Monitoring and records.

(a) Samples and measurements taken for the purpose of monitoring shall be representative of the monitored activity.

(b) The permittee shall retain records of all monitoring information, including the following:

(i) Calibration and maintenance records and all original strip chart recordings for continuous monitoring instrumentation, copies of all reports required by this permit, and records of all data used to complete the application for this permit, for a period of at least 3 years from the date of the sample, measurement, report, or application. This period may be extended by request of the Director at any time; and

(ii) The nature and composition of all injected fluids until 3 years after the completion of any plugging and abandonment procedures specified under Subsection B of 19.15.42.12 NMAC, or under 40 CFR 146, Subpart G as appropriate. The director may require the owner or operator to deliver the records to the director at the conclusion of the retention period.

(c) Records of monitoring information shall include:

(i) the date, exact place, and time of sampling or measurements;

(ii) the individual(s) who performed the sampling or measurements;

(iii) the date(s) analyses were performed;

(iv) the individual(s) who performed the analyses;

(v) the analytical techniques or methods used; and

(vi) the results of such analyses.

(d) Owners or operators of Class VI wells shall retain records as specified in Section 19.15.43.9 NMAC, including Subsection E of 19.15.43.9 NMAC, Subsection L of 19.15.43.9 NMAC, and Subsection M of 19.15.43.9 NMAC.

(11) Signatory requirement. All applications, reports, or information submitted to the Director shall be signed and certified (See Subsection B of 19.15.42.11 NMAC).

(12) Reporting requirements.

(a) Planned changes. The permittee shall give notice to the director as soon as possible of any planned physical alterations or additions to the permitted facility.

(b) Anticipated noncompliance. The permittee shall give advance notice to the Director of any planned changes in the permitted facility or activity which may result in noncompliance with permit requirements.

(c) Transfers. This permit is not transferable to any person except after notice to the Director. The Director may require modification or revocation and reissuance of the permit to change the name of the permittee and incorporate such other requirements as may be necessary under the Safe Drinking Water Act (See Subsection G of 19.15.42.11 NMAC); in some cases, modification or revocation and reissuance is mandatory.

(d) Monitoring reports. Monitoring results shall be reported at the intervals specified elsewhere in this section.

(e) Compliance schedules. Reports of compliance or noncompliance with, or any progress reports on, interim and final requirements contained in any compliance schedule of this permit shall be submitted no later than 30 days following each schedule date.

(f) 24-hour reporting. The permittee shall report any noncompliance which may endanger health or the environment, including:

(i) Any monitoring or other information which indicates that any contaminant may cause an endangerment to a USDW; or

(ii) Any noncompliance with a permit condition or malfunction of the injection system which may cause fluid migration into or between USDWs.

(g) Any information shall be provided orally within 24 hours from the time the permittee becomes aware of the circumstances. A written submission shall also be provided within 5 days of the time the permittee becomes aware of the circumstances. The written submission shall contain a description of the noncompliance and its cause, the period of noncompliance, including exact dates and times, and if the noncompliance has not been corrected, the anticipated time it is expected to continue; and steps taken or planned to reduce, eliminate, and prevent reoccurrence of the noncompliance.

(h) Other noncompliance. The permittee shall report all instances of noncompliance not reported under Subparagraphs (a) (d), (e), and (f) of this section, at the time monitoring reports are submitted. The reports shall contain the information listed in Subparagraph (f) Paragraph (12) of this section.

(i) Other information. Where the permittee becomes aware that it failed to submit any relevant facts in a permit application, or submitted incorrect information in a permit application or in any report to the director, it shall promptly submit such facts or information.

(13) Requirements prior to commencing injection. Except for all new wells authorized by an area permit under Section 40 CFR 144.33(c), a new injection well may not commence injection until:

(a) construction is complete; and

(b) the permittee has submitted notice of completion of construction to the director; and

(c) the director has inspected or otherwise reviewed the new injection well and finds it is in compliance with the conditions of the permit; or

(d) the permittee has not received notice from the director of his or her intent to inspect or otherwise review the new injection well within 13 days of the date of the notice in Subparagraph (b) of Paragraph (13) of this section, in which case prior inspection or review is waived and the permittee may commence injection. The director shall include in his notice a reasonable time period in which he shall inspect the well.

(14) The permittee shall notify the director at such times as the permit requires before conversion or abandonment of the well or in the case of area permits before closure of the project.

(15) A Class VI permit shall include conditions which meet the requirements set forth in Subsection M of 19.15.43.9 NMAC. Where the plan meets the requirements of Subsection M of 19.15.43.9 NMAC, the director shall incorporate it into the permit as a permit condition. For purposes of this paragraph, temporary or intermittent cessation of injection operations is not abandonment.

(16) Duty to establish and maintain mechanical integrity.

(a) The owner or operator of a Class VI well permitted under this part shall establish mechanical integrity prior to commencing injection or on a schedule determined by the director. The owner or operator of Class VI wells must maintain mechanical integrity as defined in Subsection J of 19.15.43.9 NMAC.

(b) When the director determines that a Class VI well lacks mechanical integrity pursuant to Section 40 CFR 146.89 or Subsection J of 19.15.43.9 NMAC for Class VI, the director shall give written notice of his/her determination to the owner or operator. Unless the director requires immediate cessation, the owner or operator shall cease injection into the well within 48 hours of receipt of the director's determination. The director may allow plugging of the well pursuant to the requirements of Section 40 CFR 146.92 or require the permittee to perform such additional construction, operation, monitoring, reporting and corrective action as is necessary to prevent the movement of fluid into or between USDWs caused by the lack of mechanical integrity. The owner or operator may resume injection upon written notification from the director that the owner or operator has demonstrated mechanical integrity pursuant to Section 40 CFR 146.89.

(c) The director may allow the owner or operator of a well which lacks mechanical integrity pursuant to Section 40 CFR 146.8(a)(1) to continue or resume injection, if the owner or operator has made a satisfactory demonstration that there is no movement of fluid into or between USDWs.

B. Establishing permit conditions.

(1) In addition to conditions required in Subsection A of 19.15.42.12 NMAC, the director shall establish conditions, as required on a case-by-case basis under § 19.15.42.11.E NMAC (duration of permits), Subsection C of 19.15.42.12 NMAC (schedules of compliance), Subsection D of 19.15.42.12 NMAC (monitoring).

(2) Permits for owners or operators of Class VI injection wells shall include conditions meeting the requirements of 19.15.43.9 NMAC. Permits for other wells shall contain the following requirements, when applicable:

(a) **Construction requirements as set forth in 19.15.43 NMAC.** Existing wells shall achieve compliance with such requirements according to a compliance schedule established as a permit condition. The owner or operator of a proposed new injection well shall submit plans for testing, drilling, and construction as part of the permit application. Except as authorized by an area permit, no construction may commence until a permit has been issued containing construction requirements (see Subsection A of 19.15.42.9 NMAC). New wells shall be in compliance with these requirements prior to commencing injection operations. Changes in construction plans during construction may be approved by the administrator as minor modifications (Subsection J of 19.15.42.11 NMAC). No such changes may be physically incorporated into construction of the well prior to approval of the modification by the director.

(b) **Corrective action** as set forth in Section 40 CFR 144.55 and 146.7 and Subsection E of 19.15.43.9 NMAC.

(c) **Operation requirements** as set forth in 19.15.43 NMAC. The permit shall establish any maximum injection volumes and/or pressures necessary to assure that fractures are not initiated in the confining zone, that injected fluids do not migrate into any underground source of drinking water, that formation fluids are not displaced into any underground source of drinking water, and to assure compliance with the 19.15.43 NMAC operating requirements.

(d) **Monitoring and reporting requirements** as set forth in 19.15.43 NMAC. The permittee shall be required to identify types of tests and methods used to generate the monitoring data.

(e) **Financial responsibility.**

(i) The permittee, including the transferor of a permit, is required to demonstrate and maintain financial responsibility and resources to close, plug, and abandon the underground injection operation in a manner prescribed by the director until (a) the well has been plugged and abandoned in accordance with an approved plugging and abandonment plan pursuant to Subsection A of 19.15.42.12 NMAC, Subsection M of 19.15.43.9 NMAC, and 40 CFR 146.10, and submitted a plugging and abandonment report pursuant to Subsection A of 19.15.42.12 NMAC; or (b) the well has been converted in compliance with the requirements of Subsection A of 19.15.42.12 NMAC; or (c) the transferor of a permit has received notice from the director that the owner or operator receiving transfer of the permit, the new permittee, has demonstrated financial responsibility for the well.

(ii) The permittee shall show evidence of such financial responsibility to the director by the submission of a surety bond, or other adequate assurance, such as a financial statement or other materials acceptable to the director. The owner or operator of a well injecting hazardous waste must comply with the financial responsibility requirements of Section 40 CFR 144, Subpart F.

(iii) For Class VI wells, the permittee shall show evidence of such financial responsibility to the director by the submission of a qualifying instrument (see Subsection F of 19.15.43.9 NMAC), such as a financial statement or other materials acceptable to the director. The owner or operator of a Class VI well must comply with the financial responsibility requirements set forth in Subsection F of 19.15.43.9 NMAC.

(f) **Mechanical integrity.** A permit for any Class VI well which lacks mechanical integrity shall include a condition prohibiting injection operations until the permittee shows to the satisfaction of the director that the well has mechanical integrity.

(g) **Additional conditions.** The director shall impose on a case-by-case basis such additional conditions as are necessary to prevent the migration of fluids into underground sources of drinking water.

(3) In addition to conditions required in all permits the director shall establish conditions in permits as required on a case-by-case basis, to provide for and assure compliance with all applicable requirements of the SDWA and Parts 144, 145, 146 and 124.

(4) An applicable requirement refers to any State statutory or regulatory provision that becomes effective prior to the final administrative action on a permit application. An applicable requirement also includes any provision that becomes effective prior to the modification or revocation and reissuance of a permit, consistent with the authority provided under Subsection H of 19.15.42.11 NMAC.

(5) New or reissued permits, and to the extent allowed under Subsection H of 19.15.42.11 NMAC modified or revoked and reissued permits, shall incorporate each of the applicable requirements referenced in Subsection B of 19.15.42.12 NMAC.

(6) Incorporation. All permit conditions shall be incorporated either expressly or by reference. If incorporated by reference, a specific citation to the applicable regulations or requirements must be given in the permit.

C. Schedule of compliance.

(1) General. The permit may, when appropriate, specify a schedule of compliance leading to compliance with the SDWA and Sections 19.15.41 NMAC, 19.15.42 NMAC, 19.15.43 NMAC, and 40 CFR 145.

(2) Time for compliance. Any schedules of compliance shall require compliance as soon as possible, and in no case later than three years after the effective date of the permit.

(3) Interim dates. Except as provided in paragraph (b)(1)(ii) of 40 CFR 144.53, if a permit establishes a schedule of compliance which exceeds 1 year from the date of permit issuance, the schedule shall set forth interim requirements and the dates for their achievement.

(a) The time between interim dates shall not exceed one year.

(b) If the time necessary for completion of any interim requirement is more than 1 year and is not readily divisible into stages for completion, the permit shall specify interim dates for the submission of reports of progress toward completion of the interim requirements and indicate a projected completion date.

(4) Reporting. The permit shall be written to require that if Paragraph (2) of this subsection is applicable, progress reports be submitted no later than 30 days following each interim date and the final date of compliance.

D. Requirements for recording and reporting of monitoring results. All permits shall specify:

(1) Requirements concerning the proper use, maintenance, and installation, when appropriate, of monitoring equipment or methods (including biological monitoring methods when appropriate);

(2) Required monitoring including type, intervals, and frequency sufficient to yield data which are representative of the monitored activity including when appropriate, continuous monitoring;

(3) Applicable reporting requirements based upon the impact of the regulated activity and as specified in Section 19.15.43 NMAC. Reporting shall be no less frequent than specified in the above regulations.

[19.15.42.11 NMAC – N, XX/XX/XXXX]

19.15.42.12 STATE UIC PROGRAM REQUIREMENTS:

A. Requirements for enforcement authority.

(1) The energy, minerals and natural resources department oil conservation division shall have available the following remedies for violations of State program requirements:

(a) To restrain immediately and effectively any person by order or by suit in State court from engaging in any unauthorized activity which is endangering or causing damage to public health or environment;

(b) To sue in New Mexico district court to enjoin any threatened or continuing violation of any program requirement, including permit conditions, without the necessity of a prior revocation of the permit, as authorized under Subsection A of Section 70-2-6 and Paragraph (2) of Subsection A of Section 70-2-31 NMSA 1978.

(c) To assess or sue to recover in court civil penalties and to seek criminal remedies, including fines, as follows:

(i) For all wells except Class II wells, civil penalties shall be recoverable for any program violation in at least the amount of $2,500 per day. For Class II wells, civil penalties shall be recoverable for any program violation in at least the amount of $1,000 per day.

(ii) Criminal fines shall be recoverable in at least the amount of $5,000 per day against any person who willfully violates any program requirement, or for Class II wells, pipeline (production) severance shall be imposable against any person who willfully violates any program requirement.

(2) Enforcement related to Parts 41, 42 and 43 of Title 19, Chapter 15 shall be conducted pursuant to the processes and penalties described in Section 19.15.5.10 NMAC.

[19.15.42.12 NMAC – N, XX/XX/XXXX]

History of 19.15.42 NMAC: [RESERVED]

EXHIBIT 1-C

TITLE 19 NATURAL RESOURCES AND WILDLIFE
CHAPTER 15 OIL AND GAS
PART 43 UNDERGROUND INJECTION CONTROL PROGRAM: CRITERIA AND STANDARDS

19.15.43.1 ISSUING AGENCY: Oil Conservation Commission.
[19.15.43.1 NMAC – N, XX/XX/XXXX]

19.15.43.2 SCOPE: 19.15.43 NMAC applies to persons constructing, operating or closing a sequestration facility or engaged in the injection of carbon dioxide for the purposes of geologic sequestration under the Geologic Carbon Dioxide Storage Stewardship Act.
[19.15.43.2 NMAC – N, XX/XX/XXXX]

19.15.43.3 STATUTORY AUTHORITY: 19.15.43 NMAC is adopted pursuant to the Geologic Carbon Dioxide Storage Stewardship Act, Sections 74-14-1 through 74-14-7 and the Oil and Gas Act, Section 70-2-6, 70-2-11, and Paragraph (15) of Subsection B of Section 70-2-12 NMSA 1978.
[19.15.43.3 NMAC – N, XX/XX/XXXX]

19.15.43.4 DURATION: Permanent.
[19.15.43.4 NMAC – N, XX/XX/XXXX]

19.15.43.5 EFFECTIVE DATE: Month, Day, Year, unless a later date is cited at the end of the section.
[19.15.43.5 NMAC – N, XX/XX/XXXX]

19.15.43.6 OBJECTIVE: To regulate the permitting, construction, operation and closure of sequestration facilities, the injection of carbon dioxide for the purposes of geologic sequestration and to maintain primary enforcement authority for Safe Drinking Water Act (42 U.S.C. 300f et seq.) Underground Injection Control (UIC) program for UIC Class VI wells.
[19.15.43.6 NMAC – N, XX/XX/XXXX]

19.15.43.7 DEFINITIONS: The following definitions apply to this part:

A. Definitions beginning with the letter "A". "Abandoned well" means a well whose use has been permanently discontinued or which is in a state of disrepair such that it cannot be used for its intended purpose or for observation purposes.

B. Definitions beginning with the letter "B". [RESERVED].

C. Definitions beginning with the letter "C".

(1) "Casing" means a pipe or tubing of appropriate material, of varying diameter and weight, lowered into a borehole during or after drilling in order to support the sides of the hole and thus prevent the walls from caving, to prevent loss of drilling mud into porous ground, or to prevent water, gas, or other fluid from entering or leaving the hole.

(2) "Catastrophic collapse" means the sudden and utter failure of overlying "strata" caused by removal of underlying materials.

(3) "Cementing" means the operation whereby a cement slurry is pumped into a drilled hole and/or forced behind the casing.

(4) "Confining bed" means a body of impermeable or distinctly less permeable material stratigraphically adjacent to one or more aquifers.

(5) "Confining zone" means a geological formation, group of formations, or part of a formation that is capable of limiting fluid movement above an injection zone.

(6) "Conventional mine" means an open pit or underground excavation for the production of minerals.

D. Definitions beginning with the letter "D". "Disposal well" means a well used for the disposal of waste into a subsurface stratum.

E. Definitions beginning with the letter "E".

(1) "Effective date" of a UIC program means the date that a State UIC program is approved or established by the Administrator.

(2) "Experimental technology" means a technology which has not been proven feasible under the conditions in which it is being tested.

F. Definitions beginning with the letter "F".

(1) "Fault" means a surface or zone of rock fracture along which there has been displacement.

(2) "Flow rate" means the volume per time unit given to the flow of gases or other fluid substance which emerges from an orifice, pump, turbine or passes along a conduit or channel.

G. Definitions beginning with the letter "G". [RESERVED].

H. Definitions beginning with the letter "H". [RESERVED].

I. Definitions beginning with the letter "I". [RESERVED].

J. Definitions beginning with the letter "J". [RESERVED].

K. Definitions beginning with the letter "K". [RESERVED].

L. Definitions beginning with the letter "L". "Lithology" means the description of rocks on the basis of their physical and chemical characteristics.

M. Definitions beginning with the letter "M". [RESERVED].

N. Definitions beginning with the letter "N". [RESERVED].

O. Definitions beginning with the letter "O". "Owner or operator" means the owner or operator of any facility or activity subject to regulation under the RCRA, UIC, NPDES, or 404 programs.

P. Definitions beginning with the letter "P".

(1) "Packer" means a device lowered into a well to produce a fluid-tight seal.

(2) "Permit" means an authorization, license, or equivalent control document issued by EPA or an "approved State" to implement the requirements of this part and Section 19.15.41 NMAC, Section 19.15.42 NMAC, and Section 40 CFR 145. Permit does not include RCRA interim status (Section 40 CFR 122.23), UIC authorization by rule (Subsection C of 19.15.42.9 NMAC and Subsection A of 19.15.42.10 NMAC), or any permit which has not yet been the subject of final agency action, such as a "draft permit" or a "proposed permit."

(3) "Plugging" means the act or process of stopping the flow of water, oil or gas into or out of a formation through a borehole or well penetrating that formation.

(4) "Plugging record" means a systematic listing of permanent or temporary abandonment of water, oil, gas, test, exploration and waste injection wells, and may contain a well log, description of amounts and types of plugging material used, the method employed for plugging, a description of formations which are sealed and a graphic log of the well showing formation location, formation thickness, and location of plugging structures.

(5) "Pressure" means the total load or force per unit area acting on a surface.

Q. Definitions beginning with the letter "Q". [RESERVED].

R. Definitions beginning with the letter "R". [RESERVED].

S. Definitions beginning with the letter "S".

(1) "Sole or principal source aquifer" means an aquifer which has been designated by the U.S. EPA Regional Administrator pursuant to section 1424 (a) or (e) of the SDWA.

(2) "Subsidence" means the lowering of the natural land surface in response to: Earth movements; lowering of fluid pressure; removal of underlying supporting material by mining or solution of solids, either artificially or from natural causes; compaction due to wetting (hydrocompaction); oxidation of organic matter in soils; or added load on the land surface.

(3) "Surface casing" means the first string of well casing to be installed in the well.

T. Definitions beginning with the letter "T". [RESERVED].

U. Definitions beginning with the letter "U". [RESERVED].

V. Definitions beginning with the letter "V". [RESERVED].

W. Definitions beginning with the letter "W".

(1) "Well plug" means a watertight and gastight seal installed in a borehole or well to prevent movement of fluids.

(2) "Well stimulation" means several processes used to clean the well bore, enlarge channels, and increase pore space in the interval to be injected thus making it possible for wastewater to move more readily into the formation, and includes (a) surging, (b) jetting, (c) blasting, (d) acidizing, and (e) hydraulic fracturing.

(3) "Well monitoring" means the measurement, by on-site instruments or laboratory methods, of the quality of water in a well.

X. Definitions beginning with the letter "X". [RESERVED].

Y. Definitions beginning with the letter "Y". [RESERVED].

Z. Definitions beginning with the letter "Z". [RESERVED].

[19.15.43.7 NMAC – N, XX/XX/XXXX]

19.15.43.8 GENERAL PROVISIONS:

A. Criteria for exempted aquifers.

(1) An aquifer or a portion thereof which meets the criteria for an "underground source of drinking water" in Subsection YY of 19.15.41.7 NMAC may be determined under Section 40 CFR 144.7 to be an "exempted aquifer" for Class VI wells if it meets the following criteria:

(a) it does not currently serve as a source of drinking water; and

(b) it cannot now and will not in the future serve as a source of drinking water because:

(i) it is mineral, hydrocarbon or geothermal energy producing, or can be demonstrated by a permit applicant as part of a permit application for a Class II or III operation to contain minerals or hydrocarbons that considering their quantity and location are expected to be commercially producible;

(ii) it is situated at a depth or location which makes recovery of water for drinking water purposes economically or technologically impractical;

(iii) it is so contaminated that it would be economically or technologically impractical to render that water fit for human consumption; or

(iv) it is located over a Class III well mining area subject to subsidence or catastrophic collapse; or

(v) the total dissolved solids content of the ground water is more than 3,000 and less than 10,000 mg/l and it is not reasonably expected to supply a public water system.

(2) The areal extent of an aquifer exemption for a Class II enhanced oil recovery or enhanced gas recovery well may be expanded for the exclusive purpose of Class VI injection for geologic sequestration under Section 40 CFR 144.7 if it meets the following criteria:

(a) it does not currently serve as a source of drinking water; and

(b) the total dissolved solids content of the ground water is more than 3,000 mg/l and less than 10,000 mg/l; and

(c) it is not reasonably expected to supply a public water system.

[19.15.43.8 NMAC – N, XX/XX/XXXX]

19.15.43.9 CRITERIA AND STANDARDS APPLICABLE TO CLASS VI WELLS:

A. Applicability. This subpart establishes criteria and standards for underground injection control programs to regulate any Class VI carbon dioxide geologic sequestration injection wells.

(1) This subpart applies to any wells used to inject carbon dioxide specifically for the purpose of geologic sequestration, i.e., the long-term containment of a gaseous, liquid, or supercritical carbon dioxide stream in subsurface geologic formations.

(2) This subpart also applies to owners or operators of permit- or rule-authorized Class I, Class II, or Class V experimental carbon dioxide injection projects who seek to apply for a Class VI geologic sequestration permit for their well or wells. Owners or operators seeking to convert existing Class I, Class II, or Class V experimental wells to Class VI geologic sequestration wells must demonstrate to the director that the wells were engineered and constructed to meet the requirements at Subsection P of 19.15.43.9 NMAC and ensure protection of underground sources of drinking water (USDWs), in lieu of requirements at Paragraph (2) of Subsection G of 19.15.43.9 NMAC and Paragraph (1) of Subsection H of 19.15.43.9 NMAC. By December 10, 2011, owners or operators of either Class I wells previously permitted for the purpose of geologic sequestration or Class V experimental technology wells no longer being used for experimental purposes that will continue injection of carbon dioxide for the purpose of carbon sequestration must apply for a Class VI permit. A converted well must still meet all other requirements under 19.15.43.9 NMAC.

B. Definitions. The following definitions apply to this subpart. To the extent that these definitions conflict with those in Section 19.15.41.7 NMAC or Section 19.15.43.7 NMAC, these definitions govern for Class VI wells:

(1) "**Area of review"** means the region surrounding the geologic sequestration project where USDWs may be endangered by the injection activity. The area of review is delineated using computational modeling that accounts for the physical and chemical properties of all phases of the injected carbon dioxide stream and displaced fluids, and is based on available site characterization, monitoring, and operational data as set forth in Subsection I of 19.15.43.9 NMAC.

(2) "**Carbon dioxide plume"** means the extent underground, in three dimensions, of an injected carbon dioxide stream.

(3) "**Carbon dioxide stream"** means carbon dioxide that has been captured from an emission source (e.g., a power plant), plus incidental associated substances derived from the source materials and the capture process, and any substances added to the stream to enable or improve the injection process. This subpart does not apply to any carbon dioxide stream that meets the definition of a hazardous waste under Section 40 CFR 261.

(4) **"Confining zone"** means a geologic formation, group of formations, or part of a formation stratigraphically overlying the injection zone(s) that acts as barrier to fluid movement. For Class VI wells operating under an injection depth waiver, confining zone means a geologic formation, group of formations, or part of a formation stratigraphically overlying and underlying the injection zone(s).

(5) **"Corrective action"** means the use of director-approved methods to ensure that wells within the area of review do not serve as conduits for the movement of fluids into USDWs.

(6) **"Geologic sequestration"** means the long-term containment of a gaseous, liquid, or supercritical carbon dioxide stream in subsurface geologic formations. This term does not apply to carbon dioxide capture or transport.

(7) **"Geologic sequestration project"** means an injection well or wells used to emplace a carbon dioxide stream beneath the lowermost formation containing a USDW; or, wells used for geologic sequestration of carbon dioxide that have been granted a waiver of the injection depth requirements pursuant to requirements at Subsection P of 19.15.43.9 NMAC; or, wells used for geologic sequestration of carbon dioxide that have received an expansion to the areal extent of an existing Class II enhanced oil recovery or enhanced gas recovery aquifer exemption pursuant to Subsection A of 19.15.43.8 NMAC and Section 40 CFR 144.7(d). It includes the subsurface three-dimensional extent of the carbon dioxide plume, associated area of elevated pressure, and displaced fluids, as well as the surface area above that delineated region.

(8) **"Injection zone"** means a geologic formation, group of formations, or part of a formation that is of sufficient areal extent, thickness, porosity, and permeability to receive carbon dioxide through a well or wells associated with a geologic sequestration project.

(9) **"Intensive Corrective Action Area**" means the area into which brine with supercritical carbon dioxide will potentially intrude, defined radially from the injection well location as the maximum plume boundary extent across all model simulations, with an additional buffer of half the distance of the maximum plume boundary extent.

(10) "**Plume stabilization"** mean the state when the carbon dioxide stream that has been injected subsurface essentially no longer expands vertically or horizontally, as demonstrated by a minimum of five consecutive years of monitoring data.

~~(9)~~**(11)** **"Post-injection site care"** means appropriate monitoring and other actions (including corrective action) needed following cessation of injection to ensure plume stabilization has occurred and that USDWs are not endangered, as required under Subsection N of 19.15.43.9 NMAC.

~~(10)~~**(12)** **"Pressure front"** means the zone of elevated pressure that is created by the injection of carbon dioxide into the subsurface. For the purposes of this subpart, the pressure front of a carbon dioxide plume refers to a zone where there is a pressure differential sufficient to cause the movement of injected fluids or formation fluids into a USDW.

~~(11)~~**(13)** **"Site closure"** means the point/time, as determined by the director following the requirements under Subsection N of 19.15.43.9 NMAC, at which the owner or operator of a geologic sequestration site is released from post-injection site care responsibilities.

~~(12)~~**(14)** **"Transmissive fault or fracture"** means a fault or fracture that has sufficient permeability and vertical extent to allow fluids to move between formations.

C. Required Class VI permit information. This section sets forth the information which must be considered by the director in authorizing Class VI wells. For converted Class I, Class II, or Class V experimental wells, certain maps, cross-sections, tabulations of wells within the area of review and other data may be included in the application by reference provided they are current, readily available to the director, and sufficiently identified to be retrieved. In cases where EPA issues the permit, all the information in this section must be submitted to the Regional Administrator.

(1) Prior to the issuance of a permit for the construction of a new Class VI well or the conversion of an existing Class I, Class II, or Class V well to a Class VI well, the owner or operator shall submit, pursuant to Paragraph (5) of Subsection L of 19.15.43.9 NMAC, and the director shall consider the following:

(a) Information required in Subsection A of 19.15.42.11 NMAC;

(b) A map showing the injection well for which a permit is sought and the applicable area of review consistent with Subsection E of 19.15.43.9 NMAC. Within the area of review, the map must show the number or name, and location of all injection wells, producing wells, abandoned wells, plugged wells or dry holes, deep stratigraphic boreholes, state- or EPA-approved subsurface cleanup sites, surface bodies of water, springs, mines (surface and subsurface), quarries, water wells, other pertinent surface features including structures intended for human occupancy, state, tribal, and territory boundaries, and roads. The map should also show faults, if known or suspected. Only information of public record is required to be included on this map;

(c) Information on the geologic structure and hydrogeologic properties of the proposed storage site and overlying formations, including:

(i) maps and cross sections of the area of review;

(ii) the location, orientation, and properties of known or suspected faults and fractures that may transect the confining zone(s) in the area of review and a determination that they would not interfere with containment under anticipated changes in pressure associated with injection;

(iii) data on the depth, areal extent, thickness, mineralogy, porosity, permeability, and capillary pressure of the injection and confining zone(s); including geology/facies changes based on field data which may include geologic cores, outcrop data, seismic surveys, well logs, and names and lithologic descriptions;

(iv) geomechanical information on fractures, stress, ductility, rock strength, and in situ fluid pressures within the confining zone(s);

(v) information on the seismic history including the presence and depth of seismic sources and a determination that the seismicity would not interfere with containment under anticipated changes in pressure associated with injection; and

(vi) geologic and topographic maps and cross sections illustrating regional geology, hydrogeology, and the geologic structure of the local area.

(d) A comprehensive tabulation of all wells within the area of review. The tabulation shall include, at a minimum, each well's type, construction, date drilled, location, total depth, plugging and/or completion record, and any other information the director may require. For all wells that penetrate the confining zone and/or injection zone, the operator shall provide additional documentation sufficient to evaluate the potential for fluid migration along the wellbore. This may include, but is not limited to, casing and cement integrity records, mechanical integrity test results, and any relevant historical or geophysical data necessary to assess the risk to underground sources of drinking water.

(e) Maps and stratigraphic cross sections indicating the general vertical and lateral limits of all USDWs, water wells and springs within the area of review, their positions relative to the injection zone(s), and the direction of water movement, where known;

(f) Baseline geochemical data on subsurface formations, including all USDWs in the area of review;

(g) Proposed operating data for the proposed geologic sequestration site:

(i) average and maximum daily rate and volume and/or mass and total anticipated volume and/or mass of the carbon dioxide stream;

(ii) average and maximum injection pressure;

(iii) the source(s) of the carbon dioxide stream; and

(iv) an analysis of the chemical and physical characteristics of the carbon dioxide stream.

(h) Proposed pre-operational formation testing program to obtain an analysis of the chemical and physical characteristics of the injection zone(s) and confining zone(s) and that meets the requirements at Subsection H of 19.15.43.9 NMAC;

(i) proposed stimulation program, a description of stimulation fluids to be used and a determination that stimulation will not interfere with containment;

(j) proposed injection operation procedures;

(k) schematics or other appropriate drawings of the surface and subsurface construction details of the well;

(l) injection well construction procedures that meet the requirements of Subsection G of 19.15.43.9 NMAC;

(m) proposed area of review and corrective action plan that meets the requirements under Subsection E of 19.15.43.9 NMAC;

(n) a demonstration, satisfactory to the director, that the applicant has met the

financial responsibility requirements under Subsection F of 19.15.43.9 NMAC;

(o) proposed testing and monitoring plan required by Subsection K of 19.15.43.9 NMAC;

(p) proposed injection well plugging plan required by Paragraph (2) of Subsevtion M of 19.15.43.9 NMAC;

(q) proposed post-injection site care and site closure plan required by Paragraph (1) of Subsection N of 19.15.43.9 NMAC;

(r) At the director's discretion, a demonstration of an alternative post-injection site care timeframe required by Paragraph (3) of Subsection N of 19.15.43.9 NMAC;

(s) Proposed emergency and remedial response plan required by Paragraph (1) of Subsection O of 19.15.43.9 NMAC;

(t) A list of contacts, submitted to the director, for those states, tribes, and territories identified to be within the area of review of the Class VI project based on information provided in Subparagraph (b) of Paragraph (1) of this Subsection;

(u) A summary of community outreach activities conducted with communities located within the AoR prior to submittal of the permit application; and

(v) Any other information requested by the director.

(2) The director shall notify, in writing, any states, tribes, or territories within the area of review of the Class VI project based on information provided in Subparagraphs (b) and (t) of Paragraph (1) of this Subsection of the permit application and pursuant to the requirements at Section 40 CFR 145.23(f)(13).

(3) Prior to granting approval for the operation of a Class VI well, the director shall consider the following information:

(a) The final area of review based on modeling, using data obtained during logging and testing of the well and the formation as required by Subparagraphs (b), (c), (d), (e), (f), and (j) of Paragraph (3) this Subsection;

(b) Any relevant updates, based on data obtained during logging and testing of the well and the formation as required by Subparagraphs (c), (d), (f), (g), and (j) of Paragraph (3) of this Subsection, to the information on the geologic structure and hydrogeologic properties of the proposed storage site and overlying formations, submitted to satisfy the requirements of Subparagraph (c) of Paragraph (1) of this Subsection;

(c) Information on the compatibility of the carbon dioxide stream with fluids in the injection zone(s) and minerals in both the injection and the confining zone(s), based on the results of the formation testing program, and with the materials used to construct the well;

(d) The results of the formation testing program required at Subparagraph (h) of Paragraph (1) of this Subsection;

(e) Final injection well construction procedures that meet the requirements of Subsection G of 19.15.43.9 NMAC;

(f) The status of corrective action on wells in the area of review;

(g) All available logging and testing program data on the well required by Subsection H of 19.15.43.9 NMAC;

(h) A demonstration of mechanical integrity pursuant to Subsection J of 19.15.43.9 NMAC;

(i) Any updates to the proposed area of review and corrective action plan, testing and monitoring plan, injection well plugging plan, post-injection site care and site closure plan, or the emergency and remedial response plan submitted under Paragraph (1) of this Subsection, which are necessary to address new information collected during logging and testing of the well and the formation as required by all paragraphs of this section, and any updates to the alternative post-injection site care timeframe demonstration submitted under Paragraph (1) of this Subsection, which are necessary to address new information collected during the logging and testing of the well and the formation as required by all paragraphs of this section; and

(j) Any other information requested by the director.

(4) Owners or operators seeking a waiver of the requirement to inject below the lowermost USDW must also refer to Subsection P of 19.15.43.9 NMAC and submit a supplemental report, as required at Paragraph (1) of Subsection P of 19.15.43.9 NMAC. The supplemental report is not part of the permit application.

D. Minimum criteria for siting.

(1) Owners or operators of Class VI wells must demonstrate to the satisfaction of the director that the wells will be sited in areas with a suitable geologic system. The owners or operators must demonstrate that the geologic system comprises:

(a) An injection zone(s) of sufficient areal extent, thickness, porosity, and permeability to receive the total anticipated volume of the carbon dioxide stream;

(b) Confining zone(s) free of transmissive faults or fractures and of sufficient areal extent and integrity to contain the injected carbon dioxide stream and displaced formation fluids and allow injection at proposed maximum pressures and volumes without initiating or propagating fractures in the confining zone(s).

(2) The director may require owners or operators of Class VI wells to identify and characterize additional zones that will impede vertical fluid movement, are free of faults and fractures that may interfere with containment, allow for pressure dissipation, and provide additional opportunities for monitoring, mitigation, and remediation.

E. Area of review and corrective action.

(1) The area of review is the region surrounding the geologic sequestration project where USDWs may be endangered by the injection activity. The area of review is delineated using computational modeling that accounts for the physical and chemical properties of all phases of the injected carbon dioxide stream and is based on available site characterization, monitoring, and operational data.

(2) The owner or operator of a Class VI well must prepare, maintain, and comply with a plan to delineate the area of review for a proposed geologic sequestration project, periodically reevaluate the delineation, and perform corrective action that meets the requirements of this section and is acceptable to the director. The requirement to maintain and implement an approved plan is directly enforceable regardless of whether the requirement is a condition of the permit. As a part of the permit application for approval by the director, the owner or operator must submit an area of review and corrective action plan that includes the following information:

(a) The method for delineating the area of review that meets the requirements of Paragraph (3) of this Subsection, including the model to be used, assumptions that will be made, and the site characterization data on which the model will be based;

(b) A description of:

(i) The fixed frequency between AoR reevaluations, which must include an initial reevaluation two years after injection begins, and at no time may exceed four years;

(ii) The monitoring and operational conditions that would warrant a reevaluation of the area of review prior to the next scheduled reevaluation as determined by the minimum fixed frequency established in item (i) of Subparagraph (b) of Paragraph (2) of this Subsection, including pre-specified, well-specific exceedance thresholds in pressure monitoring data and geochemical monitoring data and the discovery of a previously unidentified artificial penetration;

(iii) How monitoring and operational data (e.g., injection rate and pressure) will be used to inform an area of review reevaluation; ~~and~~

(iv) How corrective action will be conducted to meet the requirements of Paragraph (4) of this Subsection, including what corrective action will be performed prior to injection and what, if any, portions of the area of review will have corrective action addressed on a phased basis and how the phasing will be determined; how corrective action will be adjusted if there are changes in the area of review; and how site access will be guaranteed for future corrective action; and

(c) Findings of independent, certified third-party verification of the modeling ensemble used to delineate the area of review.

(3) Using a qualified professional expert, owners ~~Owners~~ or operators of Class VI wells must perform the following actions to delineate the area of review and identify all wells that require corrective action:

(a) Predict, using existing site characterization, monitoring and operational data, and computational, peer-reviewed or commercially-available modeling, the projected lateral and vertical migration of the carbon dioxide plume ~~and formation fluids in the subsurface from the commencement of injection activities~~ until the plume movement ceases~~, until pressure differentials sufficient to cause the movement of injected fluids or formation fluids into a USDW are no longer present, or until the end of a fixed time period as determined by the Director~~, calculate the area over which induced pressure differentials could drive movement of formation fluids or injected fluids into a USDW over the maximum duration of injection, and define the AoR as the union of these two areas. The model must:

(i) Use an ensemble approach that considers the full range of realistic variation in and interaction among key parameters, including permeability-field parameters, kv/kh ratio, porosity, and relative permeability curves and hysteresis;

~~(i)~~(ii) Be based on detailed geologic data collected from at least three wells to characterize the injection zone(s), confining zone(s) and any additional zones; and anticipated operating data, including injection pressures, rates, and total volumes over the proposed life of the geologic sequestration project;

(iii) Calculate the project AoR as the union of all potential AoRs computed using pressure-driven methods, the areal CO2 plume extent, and a simple scalar factor for estimating distance of pressure front based on maximum plume extent;

~~**(ii)**~~ **(iv)** Evaluate and incorporate considerations of any geologic heterogeneities, other discontinuities, data quality, and their possible impact on model predictions;

(v) Evaluate reactive transport to account for the geochemical reactions and lithology of the target reservoir and caprocks;

(vi) Identify the Intensive Corrective Action Area;

~~**(iii)**~~ **(vii)** Consider potential migration through faults, fractures, and artificial penetrations, using 3D seismic characterization; and

(viii) Consider pressure and chemical interactions with all other operational or historic injection projects within a ten-mile radius.

(b) Confirm the model's validity by placement of a monitoring well where plume is modeled to be after one year of commencement of injection.

~~**(b)**~~**(c)** Using ~~methods approved by the director~~ state oil and gas, water, and geological agency databases, county records, and private well-databases, identify all penetrations, including active and abandoned wells and underground mines, in the area of review that may penetrate the confining zone(s). When plugging records are incomplete, use field testing to identify all penetrations. Provide a ~~description~~ record of each well's type, construction, date drilled, location, depth, record of plugging and/or completion, and any additional information the director may require.

~~**(c)**~~**(d)** Determine which abandoned wells in the area of review have been plugged in a manner that prevents the movement of carbon dioxide or other fluids that may endanger USDWs, including use of materials compatible with the carbon dioxide stream.

(e) Use independent, certified third-party verification of modeling ensemble.

(4) Owners or operators of Class VI wells must perform corrective action on all wells in the area of review that are determined to need corrective action or breach any layer of the confining layer, or that are located in the Intensive Corrective Action Area, using methods designed to prevent the movement of fluid into or between USDWs, including use of materials compatible with the carbon dioxide stream and re-plugging with carbon dioxide resistant cement at all depths~~, where appropriate~~.

(5) An initial AoR reevaluation shall occur no later than two years following the commencement of injection operations, or if the owners or operators fail to confirm the model's validity as specified in Subparagraph (b) of Paragraph (3) of Subsection E of 19.15.43.9 NMAC, the difference between the measured and modeled increases in pressure exceeds either 20 percent of the modeled increase in pressure or 50 kilopascals, the plume is detected in a monitoring well the plume was not expected to reach or more than one month earlier than expected, a seismic event greater than or equal to moment magnitude 2.0 occurs within the modeled pressure footprint, a pressure fall-off test results yielding formation properties materially inconsistent with model-assumed values, injection commences by another operator in the same formation or a hydraulically connected zone within the pressure footprint, or the owner, operator, or regulator discovers a previously unidentified well, fault, or fracture within the AoR. This early reevaluation must be used to confirm the accuracy and reliability of predictive modeling results submitted as part of the original permit application. Upon demonstration to the director, in accordance with Subparagraph (d) of Paragraph (5) of Subsection E of 19.15.43.9 NMAC, that the predictive modeling appropriately represents site conditions, AoR reevaluation frequency may be reduced to a minimum of once every four years. When conducting an AoR reevaluation an owner or operator must:

(a) Reevaluate the area of review in the same manner specified in Subparagraph (a) of Paragraph (3) and Paragraph (5) of this Subsection;

(b) Identify all wells in the reevaluated area of review that require corrective action in the same manner specified in Paragraph (3) of this Subsection;

(c) Perform corrective action on wells requiring corrective action in the reevaluated area of review in the same manner specified in Paragraph (4) of this Subsection; and

(d) Submit an amended area of review and corrective action plan or demonstrate to the director through monitoring data and modeling results that no amendment to the area of review and corrective action plan is needed. Any amendments to the area of review and corrective action plan must be approved by the director, must be incorporated into the permit, and are subject to the permit modification requirements at Subsection H of 19.15.42.11 NMAC or Subsection J of 19.15.42.11 NMAC, as appropriate.

(6) The emergency and remedial response plan (as required by Subsection O of 19.15.43.9 NMAC) and the demonstration of financial responsibility (as described by Subsection F of 19.15.43.9 NMAC) must

account for the area of review delineated as specified in Subparagraph (a) of Paragraph (3) of this Subsection or the most recently evaluated area of review delineated under Paragraph (5) of this Subsection, regardless of whether or not corrective action in the area of review is phased.

(7) All modeling inputs and data used to support area of review reevaluations under Paragraph (5) of this Subsection shall be retained for 10 years after site closure.

F. Financial responsibility.

(1) The financial responsibility instrument(s) used by the owner or operator must be selected from the list of qualifying instruments approved under this section and shall also comply with Subsection B of 19.15.8.8 NMAC. All financial assurance documents must be submitted on forms prescribed by, or otherwise acceptable to, the division:

(a) The financial responsibility instrument(s) used must be from the following list of qualifying instruments:

(i) Trust funds.

(ii) Surety bonds that satisfy all applicable requirements set forth in Sections 19.15.8.9-10 NMAC.

(iii) Letter of credit that satisfies all applicable requirements set forth in Section 19.15.8.9 and Subsections A-E of 19.15.8.11 NMAC.

(iv) Insurance.

~~**(v)** Self insurance (i.e., Financial Test and Corporate Guarantee).~~

(vi) Escrow account adhering to the requirements under Section 19.15.8.10 NMAC.

~~**(vii)** Any other instrument(s) satisfactory to the director.~~

(b) The qualifying instrument(s) must be sufficient to cover the cost of:

(i) Corrective action (that meets the requirements of Subsection E of 19.15.43.9 NMAC;

(ii) Injection well plugging (that meets the requirements of Subsection M of 19.15.43.9 NMAC and all additional requirements under Paragraph (1) and Subparagraphs (a)-(c) of Paragraph (2) of Subsection C of 19.15.8.15 NMAC;

(iii) Post injection site care and site closure (that meets the requirements of Subsection N of 19.15.43.9 NMAC, all additional requirements under Subsections A, B, C, D, E, F and Paragraphs (1)-(3) of Subsection G of 19.15.8.15 NMAC; and

(iv) Emergency and remedial response (that meets the requirements of Subsection O of 19.15.43.9 NMAC).

(c) The financial responsibility instrument(s) must be sufficient to address endangerment of underground sources of drinking water.

(d) The qualifying financial responsibility instrument(s) must comprise protective conditions of coverage.

(i) Protective conditions of coverage must include at a minimum cancellation, renewal, and continuation provisions, specifications on when the provider becomes liable following a notice of cancellation if there is a failure to renew with a new qualifying financial instrument, and requirements for the provider to meet a minimum rating, minimum capitalization, and ability to pass the bond rating when applicable.

(ii) Cancellation—for purposes of this part, an owner or operator must provide that their financial mechanism may not cancel, terminate or fail to renew except for failure to pay such financial instrument. If there is a failure to pay the financial instrument, the financial institution may elect to cancel, terminate, or fail to renew the instrument by sending notice by certified mail to the owner or operator and the director. The cancellation must not be final for 120 days after receipt of cancellation notice. The owner or operator must provide an alternate financial ~~responsibility demonstration~~ mechanism within 60 days of notice of cancellation, and if an alternate financial ~~responsibility demonstration~~ mechanism is not acceptable (or possible), ~~any funds from the instrument being cancelled must be released~~ the provider of the financial instrument being canceled must release all funds from that instrument to the Director within 60 days of notification by the Director.

(iii) Renewal—for purposes of this part, owners or operators must renew all financial instruments, if an instrument expires, for the entire term of the geologic sequestration project. The instrument may be automatically renewed as long as the owner or operator has the option of renewal at the face amount of the expiring instrument. The automatic renewal of the instrument must, at a minimum, provide the holder with the option of renewal at the face amount of the expiring financial instrument.

(iv) Cancellation, termination, or failure to renew may not occur

and the financial instrument will remain in full force and effect in the event that on or before the date of expiration: The director deems the facility abandoned; or the permit is terminated or revoked or a new permit is denied; or closure is ordered by the Director or a U.S. district court or other court of competent jurisdiction; or the owner or operator is named as debtor in a voluntary or involuntary proceeding under Title 11 (Bankruptcy), U.S. Code; or the amount due is paid.

(e) The qualifying financial responsibility instrument(s) must be approved by the director.

(i) The director shall consider and approve the financial responsibility demonstration for all the phases of the geologic sequestration project prior to issue a Class VI permit (Subsection C of 19.15.43.9 NMAC).

(ii) The owner or operator must provide any updated information related to their financial responsibility instrument(s) on an annual basis and if there are any changes, the director must evaluate, within a reasonable time, the financial responsibility demonstration to confirm that the instrument(s) used remain adequate for use. The owner or operator must maintain financial responsibility requirements regardless of the status of the director's review of the financial responsibility demonstration.

(iii) The director may disapprove the use of a financial instrument if he determines that it is not sufficient to meet the requirements of this section.

(f) The owner or operator may demonstrate financial responsibility by using one or multiple qualifying financial instruments for specific phases of the geologic sequestration project.

(i) In the event that the owner or operator combines more than one instrument for a specific geologic sequestration phase (e.g., well plugging), such combination must be limited to instruments that are not based on financial strength or performance (i.e., ~~self insurance or~~ performance bond), for example trust funds, surety bonds guaranteeing payment into a trust fund, letters of credit, escrow account, and insurance. In this case, it is the combination of mechanisms, rather than the single mechanism, which must provide financial responsibility for an amount at least equal to the current cost estimate.

(ii) When using a third-party instrument to demonstrate financial responsibility, the owner or operator must provide a proof that the third-party providers either have passed financial strength requirements based on credit ratings; or has met a minimum rating, minimum capitalization, and ability to pass the bond rating when applicable.

(iii) An owner or operator using certain types of third-party instruments must establish a standby trust to enable the oil conservation division to be party to the financial responsibility agreement without being the beneficiary of any funds. The standby trust fund must be used along with other financial responsibility instruments (e.g., surety bonds, letters of credit, or escrow accounts) to provide a location to place funds if needed.

(iv) An owner or operator may deposit money to an escrow account to cover financial responsibility requirements; this account must segregate funds sufficient to cover estimated costs for Class VI (geologic sequestration) financial responsibility from other accounts and uses.

~~**(v)** An owner or operator or its guarantor may use self insurance to demonstrate financial responsibility for geologic sequestration projects. In order to satisfy this requirement the owner or operator must meet a Tangible Net Worth of an amount approved by the director, have a net working capital and tangible net worth each at least six times the sum of the current well plugging, post injection site care and site closure cost, have assets located in the United States amounting to at least 90 percent of total assets or at least six times the sum of the current well plugging, post injection site care and site closure cost, and must submit a report of its bond rating and financial information annually. In addition the owner or operator must either: Have a bond rating test of AAA, AA, A, or BBB as issued by Standard & Poor's or Aaa, Aa, A, or Baa as issued by Moody's; or meet all of the following five financial ratio thresholds: A ratio of total liabilities to net worth less than 2.0; a ratio of current assets to current liabilities greater than 1.5; a ratio of the sum of net income plus depreciation, depletion, and amortization to total liabilities greater than 0.1; A ratio of current assets minus current liabilities to total assets greater than −0.1; and a net profit (revenues minus expenses) greater than 0.~~

~~**(vi)** An owner or operator who is not able to meet corporate financial test criteria may arrange a corporate guarantee by demonstrating that its corporate parent meets the financial test requirements on its behalf. The parent's demonstration that it meets the financial test requirement is insufficient if it has not also guaranteed to fulfill the obligations for the owner or operator.~~

(vii) An owner or operator may obtain an insurance policy to cover the estimated costs of geologic sequestration activities requiring financial responsibility. This insurance policy must be obtained from a third party provider.

(2) The requirement to maintain adequate financial responsibility and resources is directly enforceable regardless of whether the requirement is a condition of the permit.

(a) The owner or operator must maintain financial responsibility and resources until:

(i) the director receives and approves the completed post-injection site care and site closure plan; and

(ii) the director approves site closure.

(b) The owner or operator may be released from a financial instrument in the following circumstances:

(i) The owner or operator has completed the phase of the geologic sequestration project for which the financial instrument was required and has fulfilled all its financial obligations as determined by the director, including obtaining financial responsibility for the next phase of the GS project. As set forth in Subsection A of 19.15.8.12 NMAC, the division shall release a financial assurance document upon the operator's or surety's written request if all wells drilled or acquired under that financial assurance have been plugged and abandoned and the location restored and remediated and released pursuant to Subsection M of 19.15.43.9 NMAC, Sections 19.15.25.9 NMAC through 19.15.25.11 NMAC; or

(ii) The owner or operator has submitted a replacement financial instrument and received written approval from the director accepting the new financial instrument and releasing the owner or operator from the previous financial instrument.

(3) The owner or operator must have a detailed written estimate, in current dollars, of the cost of performing corrective action on wells in the area of review, plugging the injection well(s), post-injection site care and site closure, and emergency and remedial response.

(a) The cost estimate must be performed for each phase separately and must be based on the costs to the regulatory agency of hiring a third party to perform the required activities. A third party is a party who is not within the corporate structure of the owner or operator.

(b) During the active life of the geologic sequestration project, the owner or operator must adjust the cost estimate for inflation within 60 days prior to the anniversary date of the establishment of the financial instrument(s) used to comply with Paragraph (1) of this Subsection and provide this adjustment to the director. The owner or operator must also provide to the director written updates of adjustments to the cost estimate within 60 days of any amendments to the area of review and corrective action plan (Subsection E of 19.15.43.9 NMAC), the injection well plugging plan (Subsection M of 19.15.43.9 NMAC), the post-injection site care and site closure plan (Subsection N of 19.15.43.9 NMAC), and the emergency and remedial response plan (Subsection O of 19.15.43.9 NMAC).

(c) The director must approve any decrease or increase to the initial cost estimate. During the active life of the geologic sequestration project, the owner or operator must revise the cost estimate no later than 60 days after the director has approved the request to modify the area of review and corrective action plan (Subsection E of 19.15.43.9 NMAC), the injection well plugging plan (Subsection M of 19.15.43.9 NMAC), the post-injection site care and site closure plan (Subsection N of 19.15.43.9 NMAC), and the emergency and response plan (Subsection O of 19.15.43.9 NMAC), if the change in the plan increases the cost. If the change to the plans decreases the cost, any withdrawal of funds must be approved by the director. Any decrease to the value of the financial assurance instrument must first be approved by the director. The revised cost estimate must be adjusted for inflation as specified at Subparagraph (b) of Paragraph (3) of this Subsection.

(d) Whenever the current cost estimate increases to an amount greater than the face amount of a financial instrument currently in use, the owner or operator, within 60 days after the increase, must either cause the face amount to be increased to an amount at least equal to the current cost estimate and submit evidence of such increase to the director, or obtain other financial responsibility instruments to cover the increase. Whenever the current cost estimate decreases, the face amount of the financial assurance instrument may be reduced to the amount of the current cost estimate only after the owner or operator has received written approval from the director.

(4) The owner or operator must notify the director by certified mail of adverse financial conditions such as bankruptcy that may affect the ability to carry out injection well plugging and post-injection site care and site closure.

(a) In the event that the owner or operator or the third party provider of a financial responsibility instrument is going through a bankruptcy, the owner or operator must notify the director by certified mail of the commencement of a voluntary or involuntary proceeding under Title 11 (Bankruptcy), U.S. Code, naming the owner or operator as debtor, within 10 days after commencement of the proceeding.

(b) A guarantor of a corporate guarantee must make such a notification to the director if the guarantor is named as debtor, as required under the terms of the corporate guarantee.

(c) An owner or operator who fulfills the requirements of Paragraph (1) of this Subsection by obtaining a trust fund, surety bond, letter of credit, escrow account, or insurance policy will be deemed to be without the required financial assurance in the event of bankruptcy of the trustee or issuing institution, or a suspension or revocation of the authority of the trustee institution to act as trustee of the institution issuing the trust fund, surety bond, letter of credit, escrow account, or insurance policy. The owner or operator must establish other financial assurance within 60 days after such an event.

(5) The owner or operator must provide an adjustment of the cost estimate to the director within 60 days of notification by the director, if the director determines during the annual evaluation of the qualifying financial responsibility instrument(s) that the most recent demonstration is no longer adequate to cover the cost of corrective action (as required by Subsection E of 19.15.43.9 NMAC), injection well plugging (as required by Subsection M of 19.15.43.9 NMAC), post-injection site care and site closure (as required by Subsection N of 19.15.43.9 NMAC), and emergency and remedial response (as required by Subsection O of 19.15.43.9 NMAC).

(6) The director must approve the use and length of pay-in-periods for trust funds or escrow accounts.

G. Injection well construction requirements.

(1) General. The owner or operator must ensure that all Class VI and monitoring wells are constructed and completed to:

(a) Prevent the movement of fluids into or between USDWs or into any unauthorized zones;

(b) Permit the use of appropriate testing devices and workover tools; and

(c) Permit continuous monitoring of the annulus space between the injection tubing and long string casing.

(2) Casing and cementing of Class VI wells.

(a) Casing and cement or other materials used in the construction of each Class VI well and monitoring wells must have sufficient structural strength and be designed for the life of the geologic sequestration project. All well materials must be compatible with fluids with which the materials may be expected to come into contact and must meet or exceed standards developed for such materials by the American Petroleum Institute, ASTM International, or comparable standards acceptable to the director. The casing and cementing program must be designed to prevent the movement of fluids into or between USDWs. In order to allow the Director to determine and specify casing and cementing requirements, the owner or operator must provide the following information:

(i) depth to the injection zone(s);

(ii) injection pressure, external pressure, internal pressure, and axial loading;

(iii) hole size;

(iv) size and grade of all casing strings (wall thickness, external diameter, nominal weight, length, joint specification, and construction material);

(v) corrosiveness of the carbon dioxide stream and formation fluids;

(vi) down-hole temperatures;

(vii) lithology of injection and confining zone(s);

(viii) specified cement type or grade, including all proposed additives, as well as the anticipated slurry density (lb/gal) and volumetric yield (cu ft/sack); and

(ix) quantity, chemical composition, and temperature of the carbon dioxide stream.

(b) Surface casing for all Class VI wells and monitoring wells shall be set and cemented through the base of the deepest known USDW and must extend into an underlying confining unit, such as a competent shale formation. The casing must be cemented with a volume sufficient to achieve full cement return from the casing shoe to the surface.

(c) At least one long string casing, using a sufficient number of centralizers, must extend to the injection zone and must be cemented by circulating cement to the surface in one or more stages.

(d) Circulation of cement may be accomplished by staging. The director may approve an alternative method of cementing in cases where the cement cannot be recirculated to the surface, provided the owner or operator can demonstrate by using logs that the cement does not allow fluid movement behind the well bore.

(e) Cement and cement additives must be compatible with the carbon dioxide stream and formation fluids and of sufficient quality and quantity to maintain integrity over the design life of the geologic sequestration project. The integrity and location of the cement shall be verified using technology capable of evaluating cement quality radially and identifying the location of channels to ensure that USDWs are not endangered.

(3) Tubing and packer.

(a) Tubing and packer materials used in the construction of each Class VI well and monitoring wells must be compatible with fluids with which the materials may be expected to come into contact across all zones for all depths and must meet or exceed standards developed for such materials by the American Petroleum Institute, ASTM International, or comparable standards acceptable to the director.

(b) All owners or operators of Class VI wells must inject fluids through tubing with a packer set at a depth opposite a cemented interval at the location approved by the director.

(c) In order for the director to determine and specify requirements for tubing and packer, the owner or operator must submit the following information:

(i) depth of setting;

(ii) characteristics of the carbon dioxide stream (chemical content, corrosiveness, temperature, and density) and formation fluids;

(iii) maximum proposed injection pressure;

(iv) maximum proposed annular pressure;

(v) proposed injection rate (intermittent or continuous) and volume and/or mass of the carbon dioxide stream;

(vi) size of tubing and casing; and

(vii) tubing tensile, burst, and collapse strengths.

H. Logging, sampling, and testing prior to injection well operation.

(1) During the drilling and construction of a Class VI injection well, the owner or operator must run appropriate logs, surveys and tests to determine or verify the depth, thickness, porosity, permeability, and lithology of, and the salinity of any formation fluids in all relevant geologic formations to ensure conformance with the injection well construction requirements under Subsection G of 19.15.43.9 NMAC and to establish accurate baseline data against which future measurements may be compared. In order to obtain approval for injection, the owner or operator must submit the appropriate forms to the Director along with all required attachments including a descriptive report prepared by a knowledgeable log analyst that includes an interpretation of the results of such logs and tests. At a minimum, such logs and tests must include:

(2) Deviation checks during drilling on all holes constructed by drilling a pilot hole which is enlarged by reaming or another method. Such checks must be at sufficiently frequent intervals to determine the deviation from the original pilot hole to ensure that vertical avenues for fluid movement in the form of diverging holes are not created during drilling; and

(a) before and upon installation of the surface casing:

(i) Gamma ray, resistivity, spontaneous potential, and caliper logs before the casing is installed; and

(ii) a cement bond and variable density log to evaluate cement quality radially, and a temperature log after the casing is set and cemented.

(b) Before and upon installation of the long string casing:

(i) Gamma ray, resistivity, spontaneous potential, porosity, caliper, fracture finder logs, and any other logs the director requires for the given geology before the casing is installed; and

(ii) a cement bond and variable density log, and a temperature log after the casing is set and cemented.

(c) A series of tests designed to demonstrate the internal and external mechanical integrity of injection wells, which may include:

(i) a pressure test with liquid or gas;

(ii) a tracer survey such as oxygen-activation logging;

(iii) a temperature or noise log;

(iv) a casing inspection log; and

(d) any alternative methods that provide equivalent or better information and that are required by or approved of by the director.

(3) The owner or operator must take whole cores or sidewall cores of the injection zone and confining system and formation fluid samples from the injection zone(s), and must submit to the director a detailed

report prepared by a log analyst that includes: Well log analyses (including well logs), core analyses, and formation fluid sample information. The director may accept information on cores from nearby wells if the owner or operator can demonstrate that core retrieval is not possible and that such cores are representative of conditions at the well. The director may require the owner or operator to core other formations in the borehole.

(4) The owner or operator must record the fluid temperature, pH, conductivity, reservoir pressure, and static fluid level of the injection zone(s).

(5) At a minimum, the owner or operator must determine or calculate the following information concerning the injection and confining zone(s):

(a) fracture pressure;

(b) other physical and chemical characteristics of the injection and confining zone(s); and

(c) physical and chemical characteristics of the formation fluids in the injection zone(s).

(6) Upon completion, but prior to operation, the owner or operator must:

(a) ~~conduct~~ Conduct the following tests to verify hydrogeologic characteristics of the injection zone(s):

~~(a)~~(i) a pressure fall-off test; and

~~(b)~~(ii) a pump test; or

~~(c)~~(iii) injectivity tests.

(7) The operator shall provide the division with the opportunity to witness all planned well workovers, stimulation activities and any testing or logging operations. A proposed schedule of these activities must be submitted to the division no less than 30 days prior to the commencement of the first such activity. Additionally, the operator must provide at least 48 hours of advance notice before initiating any specific activity. No activity may begin before the 30-day review period has concluded unless prior written authorization is granted by the director.

I. Injection well operating requirements.

(1) Except during stimulation, the owner or operator must ensure that injection pressure does not exceed 90 percent of the fracture pressure of the injection zone(s) so as to ensure that the injection does not initiate new fractures or propagate existing fractures in the injection zone(s). In no case may injection pressure initiate fractures in the confining zone(s) or cause the movement of injection or formation fluids that endangers a USDW. Pursuant to requirements at Subparagraph (i) of Paragraph (1) of Subsection C of 19.15.43.9 NMAC, all stimulation programs must be approved by the director as part of the permit application and incorporated into the permit.

(2) Injection between the outermost casing protecting USDWs and the well bore is prohibited.

(3) The owner or operator must fill the annulus between the tubing and the long string casing with a non-corrosive fluid approved by the director. The owner or operator must maintain on the annulus a pressure that exceeds the operating injection pressure, unless the director determines that such requirement might harm the integrity of the well or endanger USDWs.

(4) Other than during periods of well workover (maintenance) approved by the director in which the sealed tubing-casing annulus is disassembled for maintenance or corrective procedures, the owner or operator must maintain mechanical integrity of the injection well at all times.

(5) The owner or operator must install, use, and maintain:

(a) continuous recording devices adhering to the standards set forth in Section 19.15.26.11 NMAC, to monitor the injection pressure; the rate, volume and mass, and temperature of the carbon dioxide stream; and the pressure on the annulus between the tubing and the long string casing and annulus fluid volume; and

(b) alarms and automatic surface shut-off systems or, at the discretion of the director, down-hole shut-off systems (e.g., automatic shut-off, check valves) for onshore wells or, other mechanical devices that provide equivalent protection; and

(c) alarms and automatic down-hole shut-off systems for wells located offshore but within State territorial waters, designed to alert the operator and shut-in the well when operating parameters such as annulus pressure, injection rate, or other parameters diverge beyond permitted ranges and/or gradients specified in the permit.

(d) All alarms shall be integrated with an automated shutdown system to ensure immediate response to critical operating conditions.

(e) The operator shall function test all automated emergency shutdown systems at least once every six months.

(6) If a shutdown (i.e., down-hole or at the surface) is triggered or a loss of mechanical integrity is discovered, the owner or operator must immediately investigate and identify as expeditiously as possible the cause of the shutoff. If, upon such investigation, the well appears to be lacking mechanical integrity, or if monitoring required under Paragraph (5) of this Subsection otherwise indicates that the well may be lacking mechanical integrity, the owner or operator must:

(a) immediately cease injection;

(b) take all steps reasonably necessary to determine whether there may have been a release of the injected carbon dioxide stream or formation fluids into any unauthorized zone;

(c) notify the director within 24 hours;

(d) restore and demonstrate mechanical integrity to the satisfaction of the director prior to resuming injection; and

(e) notify the director when injection can be expected to resume.

J. *Mechanical integrity*.

(1) A Class VI well has mechanical integrity if:

(a) there is no significant leak in the casing, tubing, or packer; and

(b) there is no significant fluid movement into a USDW through channels adjacent to the injection well bore.

(2) To evaluate the absence of significant leaks under Subparagraph (a) of Paragraph (1) of this Subsection, owners or operators must, following an initial annulus pressure test, continuously monitor injection pressure, rate, injected volumes; pressure on the annulus between tubing and long-string casing; and annulus fluid volume as specified in Paragraph (5) of Subsection I of 19.15.43.9 NMAC.

(3) At least once per year, the owner or operator must use one of the following methods to determine the absence of significant fluid movement under Subparagraph (b) of Paragraph (1) of this subsection:

(a) An approved tracer survey such as an oxygen-activation log; or

(b) A temperature or noise log.

(4) ~~If required by the director, at a frequency specified in the testing and monitoring plan pursuant to Subsection K of 19.15.43.9 NMAC, the~~ The owner or operator must run a casing inspection log monthly to evaluate the presence or absence of corrosion or other signs of degradation in the long-string casing. The frequency and scope of subsequent casing inspection logs may be modified by the director based on the results of the most recent inspection, or if the well has been compromised and requires a workover or significant remedial action.

(5) The director may require any other test to evaluate mechanical integrity under Subparagraphs (a) or (b) of Paragraph (1) of this Subsection. Also, the director may allow the use of a test to demonstrate mechanical integrity other than those listed above with the written approval of the EPA. To obtain approval for a new mechanical integrity test, the director must submit a written request to the EPA setting forth the proposed test and all technical data supporting its use.

(6) In conducting and evaluating the tests enumerated in this section or others to be allowed by the director, the owner or operator and the director must apply methods and standards generally accepted in the industry. When the owner or operator reports the results of mechanical integrity tests to the director, a description of the test(s) and the method(s) used must be included. In making the evaluation, the director must review monitoring and other test data submitted since the previous evaluation.

(7) The director may require additional or alternative tests if the results presented by the owner or operator under Paragraphs (1) through (4) of this Subsection are not satisfactory to the director to demonstrate that there is no significant leak in the casing, tubing, or packer, or to demonstrate that there is no significant movement of fluid into a USDW resulting from the injection activity as stated in Subparagraphs (a) and (b) of Paragraph (1) of this Subsection.

K. Testing and monitoring requirements. The owner or operator of a Class VI well must prepare, maintain, and comply with a testing and monitoring plan to verify that the geologic sequestration project is operating as permitted and is not endangering USDWs. The requirement to maintain and implement an approved plan is directly enforceable regardless of whether the requirement is a condition of the permit. The testing and monitoring plan must be submitted with the permit application, for director approval, and must include a description of how the owner or operator will meet the requirements of this section, including accessing sites for all necessary monitoring and testing during the life of the project and the specific statistical test to be used for groundwater monitoring before collecting data. The statistical test for groundwater monitoring must include the number and kinds of samples

collected to establish background appropriate for the form of statistical test employed, a sample size as large as necessary to ensure with reasonable confidence that a contaminant release to ground water from a facility will be detected, a statistical method appropriate for the distribution of chemical parameters or hazardous constituents, an accounting for data below the limit of detection with one more statistical procedures that are protective of human health and the environment, inclusion of procedures to control or correct for seasonal and spatial variability as well as temporal correlation in the data, and a determination of an appropriate sampling procedure and interval for each hazardous constituent listed in the facility permit. It must also include a summary of community engagement activities conducted to develop a plan that addresses project-related risks. Testing and monitoring associated with geologic sequestration projects must, at a minimum, include:

(1) analysis of the carbon dioxide stream with sufficient frequency to yield data representative of its chemical and physical characteristics;

(2) installation and use, except during well workovers as defined in Paragraph (4) of Subsection I of 19.15.43.9 NMAC, of continuous recording devices to monitor injection pressure, rate, and volume; the pressure on the annulus between the tubing and the long string casing; and the annulus fluid volume added;

(3) corrosion monitoring of the well materials for loss of mass, thickness, cracking, pitting, and other signs of corrosion, which must be performed on a quarterly basis to ensure that the well components meet the minimum standards for material strength and performance set forth in Paragraph (2) of Subsection G of 19.15.43.9 NMAC, by:

(a) analyzing coupons of the well construction materials placed in contact with the carbon dioxide stream; or

(b) routing the carbon dioxide stream through a loop constructed with the material used in the well and inspecting the materials in the loop; or

(c) using an alternative method approved by the director.

(4) Quarterly monitoring of the groundwater quality and geochemical changes above the confining zone(s) that may be a result of carbon dioxide movement through the confining zone(s) or additional identified zones including:

(a) the location and number of monitoring wells based on specific information about the geologic sequestration project, including injection rate and volume, geology, the presence of artificial penetrations, and other factors; and

(b) the monitoring frequency and spatial distribution of no fewer than four monitoring wells based on baseline geochemical data that has been collected under Subparagraph (f) of ~~Pararaph~~ Paragraph (1) of Subsection C of 19.15.43.9 NMAC, ~~and~~ on any modeling results in the area of review evaluation required by Paragraph (3) of Subsection E of 19.15.43.9 NMAC, a maximum-risk scenario simulation, and two simulations in which computational model grid spacing is increased and decreased by a factor of two. The monitoring plan must describe how the proposed monitoring will yield useful information on the area of review delineation and/or compliance with standards under Section 40 CFR 144.12.

(5) A demonstration of external mechanical integrity pursuant to ~~Pargraph~~ Paragraph (3) of Subsection J of 19.15.43.9 NMAC, adhering to the methods prescribed in Section 19.15.26.11 NMAC, at least once per year until the injection well is plugged; and, if required by the director, a casing inspection log pursuant to requirements at Paragraph (4) of Subsection J of 19.15.43.9 NMAC at a frequency established in the testing and monitoring plan;

(6) a pressure fall-off test based on site-specific data and run to completion at least once every five years unless more frequent testing is required by the Director based on site-specific information.

(7) Testing and continuous monitoring to track the extent of the carbon dioxide plume and the presence or absence of elevated pressure (e.g., the pressure front) and identification of excess pressure by calculating the absolute and excess pressure divided by hydrostatic pressure, by using:

(a) direct methods in the injection zone(s); and

(b) indirect methods (e.g., seismic, electrical, gravity, or electromagnetic surveys and/or down-hole carbon dioxide detection tools), unless the director determines, based on site-specific geology, that such methods are not appropriate.

(8) Soil gas monitoring is required to detect movement of carbon dioxide that could endanger a USDW;

(9) ~~the director may require~~ surface air monitoring is required to detect movement of carbon dioxide that could endanger a USDW, including in oil and gas fields or other areas with a high density of legacy wellbores.

(a) Design of Class VI soil gas and surface air (if required) monitoring must be based on potential risks to USDWs within the area of review.

(b) The monitoring frequency and spatial distribution of soil gas and surface air monitoring (if required) must be based on baseline geochemical data that has been collected under Subparagraph (f) of Paragraph (1) of Subsection C of 19.15.43.9 NMAC and on any modeling results in the area of review evaluation required by Paragraph (3) of Subsection E of 19.15.43.9 NMAC. The monitoring plan must describe how the proposed monitoring will yield useful information on the area of review delineation and/or compliance with standards under Subsection B of 19.15.42.9 NMAC.

(c) If an owner or operator demonstrates that monitoring employed under Section 40 CFR 98.440 to 98.449 (Clean Air Act, 42 U.S.C. 7401 et seq.) accomplishes the goals of paragraphs (9)(a) and (b) of this section, and meets the requirements pursuant to Subparagraph € of Paragraph (3) of Subsection L of 19.15.43.9 NMAC, a director that requires surface air/soil gas monitoring must approve the use of monitoring employed under Sections 40 CFR 98.440 to 98.449. Compliance with Section 40 CFR 98.440 to 98.449 pursuant to this provision is considered a condition of the Class VI permit;

(10) seismicity monitoring is required as part of the operational and post-injection monitoring requirements for all Class VI injection projects. The owner or operator must design and implement a site-specific seismic monitoring program capable of detecting and characterizing induced seismicity that may result from carbon dioxide injection activities. Responses to seismic events shall be conducted in accordance with protocols established by the oil conservation division.

(a) Design of Class VI seismicity monitoring program must be based on the potential risk of disturbing the confinement efficiency and endangering USDWs within the area of review.

(b) The owner or operator shall purchase a state-owned, distributed acoustic network of seismic sensors, the resulting data of which shall be owned by the state.

~~(b)~~(c) The spatial distribution of the monitoring network must be decided using baseline data and must incorporate the Seismic Hazard Assessment and other findings pursuant to Item (v) of Subparagraph (c) of Paragraph (1) of Subsection C of 19.15.43.9 NMAC to establish baseline microseismic activity.

(d) The seismic threshold metric must use Peak Ground Velocity or Peak Ground Acceleration.

(11) Any additional monitoring, as required by the director, necessary to support, upgrade, and improve computational modeling of the area of review evaluation required under Paragraph (3) of Subsection E of 19.15.43.9 NMAC and to determine compliance with standards under Subsection B of 19.15.42.9 NMAC.

(12) The owner or operator shall periodically review the testing and monitoring plan to incorporate monitoring data collected under this Part, operational data collected under Subsection I of 19.15.43.9 NMAC, ~~and~~ the most recent area of review reevaluation performed under Paragraph (5) of Subsection E of 19.15.43.9 NMAC, and new EPA standards regarding material compatibility for well infrastructure. An initial review of the testing and monitoring plan shall occur two years after injection begins, and at no time may exceed four years. Based on this review, the owner or operator shall submit an amended testing and monitoring plan or demonstrate to the director that no amendment to the testing and monitoring plan is needed. Any amendments to the testing and monitoring plan must be approved by the director, must be incorporated into the permit, and are subject to the permit modification requirements at Subsection H of 19.15.42.11 NMAC or Subsection J of 19.15.42.11 NMAC, as appropriate. Amended plans or demonstrations shall be submitted to the director as follows:

(a) within one year of an area of review reevaluation;

(b) following any significant changes to the facility, such as addition of monitoring wells or newly permitted injection wells within the area of review, on a schedule determined by the director; or

(c) when required by the director.

(13) A quality assurance and surveillance plan for all testing and monitoring requirements.

L. Reporting requirements. The owner or operator must, at a minimum, provide, as specified in Paragraph (5) of this Subsection, the following reports to the director and the EPA, for each permitted Class VI well:

(1) semi-annual reports containing:

(a) any changes to the physical, chemical, and other relevant characteristics of the carbon dioxide stream from the proposed operating data;

(b) monthly average, maximum, and minimum values for injection pressure, flow rate and volume, and annular pressure;

(c) a description of any event that exceeds operating parameters for annulus pressure or injection pressure specified in the permit;

(d) a description of any event which triggers a shut-off device required pursuant to Paragraph (5) of Subsection I of 19.15.43.9 NMAC and the response taken;

(e) the monthly volume and mass of the carbon dioxide stream injected over the reporting period and the volume injected cumulatively over the life of the project;

(f) monthly annulus fluid volume added; and

(g) the results of monitoring prescribed under Subsection K of 19.15.43.9 NMAC.

(2) Report, within 30 days, the results of:

(a) periodic tests of mechanical integrity;

(b) gauge malfunction or instrumentation failure;

~~**(b)**~~**(c)** any well workover; and,

~~**(c)**~~**(d)** any other test of the injection well conducted by the permittee if required by the director.

(3) Report, within 24 hours:

(a) any evidence that the injected carbon dioxide stream or associated pressure front may cause an endangerment to a USDW;

(b) any noncompliance with a permit condition, or malfunction of the injection system, which may cause fluid migration into or between USDWs;

(c) any triggering of a shut-off system (i.e., down-hole or at the surface);

(d) any failure to maintain mechanical integrity; or

(e) pursuant to compliance with the requirement at Paragraph (8) of Subsection K of 19.15.43.9 NMAC for surface air/soil gas monitoring or other monitoring technologies, if required by the director, any release of carbon dioxide to the atmosphere or biosphere.

(4) Owners or operators must notify the director in writing 30 days in advance of:

(a) any planned well workover;

(b) any planned stimulation activities, other than stimulation for formation testing conducted under Subsection C of 19.15.43.9 NMAC; and

(c) any other planned test of the injection well conducted by the permittee.

(5) Regardless of whether a state has primary enforcement responsibility, owners or operators must submit all required reports, submittals, and notifications under this Part to the director and EPA in an electronic format approved by EPA.

(6) Records shall be retained by the owner or operator as follows:

(a) All data collected under Subsection C of 19.15.43.9 NMAC for Class VI permit applications shall be retained throughout the life of the geologic sequestration project and for at least 10 years following site closure.

(b) Data on the nature and composition of all injected fluids collected pursuant to Paragraph (1) of Subsection K of 19.15.43.9 NMAC shall be retained for at least 10 years after site closure. The director may require the owner or operator to deliver the records to the director at the conclusion of the retention period.

(c) Monitoring data collected pursuant to Paragraphs (2)-(11) of Subsection K of 19.15.43.9 NMAC shall be retained for at least 10 years after it is collected.

(d) Well plugging reports, post-injection site care data, including, if appropriate, data and information used to develop the demonstration of the alternative post-injection site care timeframe, and the site closure report collected pursuant to requirements at Paragraphs (6) and (8) of Subsection N of 19.15.43.9 NMAC shall be retained for at least 10 years following site closure.

(e) The director has authority to require the owner or operator to retain any records required by these regulations for longer than 10 years after site closure.

M. Injection well plugging.

(1) Prior to the well plugging, the owner or operator must flush each Class VI injection well with a buffer fluid, determine bottom-hole reservoir pressure, and perform a final external mechanical integrity test.

(2) **Well plugging plan.** The owner or operator of a Class VI well must prepare, maintain, and comply with a plan that is acceptable to the director. The requirement to maintain and implement an approved plan is directly enforceable regardless of whether the requirement is a condition of the permit. The well plugging plan must be submitted as part of the permit application, must be designed to prevent the migration of fluid into or between USDWs or outside of the injection zone, and must include the following information:

(a) appropriate tests or measures for determining bottom-hole reservoir pressure;

(b) appropriate testing methods to ensure external mechanical integrity as specified in Subsection J of 19.15.43.9 NMAC;

(c) a detailed description of the size and quantity of casing, tubing, and any other well construction materials proposed for removal prior to well closure;

(d) the type and number of plugs to be used;

(e) the placement of each plug, including the elevation of the top and bottom of each plug;

(f) the type, grade, and quantity of material, such as cement, to be used in plugging. The material must be compatible with the carbon dioxide stream;

(g) the method of placement of the plugs;

(h) pre-closure and post-closure well schematics; and

(i) any additional information requested by the director.

(j) Upon successful completion of well closure, the owner or operator shall comply with Section 19.15.25.10 NMAC to properly abandon the well and location.

(3) Notice of intent to plug. The owner or operator must notify the director in writing pursuant to Paragraph (5) of Subsection L of 19.15.43.9 NMAC, at least 60 days before plugging of a well. If any modifications have been made to the approved well plugging plan at the time of this notice, a revised plan must be submitted for review. The director may authorize a shorter advance notice period, if warranted. In addition to this notice, the owner or operator must also provide a minimum of 24 hours of notice to the director prior to commencing physical plugging operations. Any amendments to the well plugging plan must be approved by the director, incorporated into the permit, and processed in accordance with the applicable permit modification requirements at Subsection H of 19.15.42.11 NMAC or Subsection J of 19.15.42.11 NMAC.

(4) Well plugging report. Within 30 days after well plugging and abandonment, the owner or operator must submit, pursuant to Paragraph (4) of Subsection M of 19.15.43.9 NMAC, a well plugging report to the director. The report must be certified as accurate by the owner or operator and by the person who performed the well and location inspection pursuant to Subsection F of 19.15.25.10 NMAC. The owner or operator shall retain the well plugging report for 10 years following site closure. The report shall contain the following information:

(a) a detailed description of the site closure procedures, clearly identifying any deviations from the submitted plan during the closure process;

(b) all state regulatory reporting forms and correspondence related to site closure; and

(c) any relevant information related to closure activities including well schematics, monitoring data, and mechanical integrity test results.

N. Post-injection site care and site closure.

(1) The owner or operator of a Class VI well must prepare, maintain, and comply with a plan for post-injection site care and site closure that meets the requirements of Subparagraph (b) of Paragraph (1) of this Subsection and is acceptable to the director. The requirement to maintain and implement an approved plan is directly enforceable regardless of whether the requirement is a condition of the permit.

(a) The owner or operator must submit the post-injection site care and site closure plan as a part of the permit application to be approved by the director.

(b) The post-injection site care and site closure plan must include the following information:

(i) the pressure differential between pre-injection and predicted post-injection pressures in the injection zone(s);

(ii) the predicted position of the carbon dioxide plume and associated pressure front at site closure as demonstrated in the area of review evaluation required under Subparagraph (a) of Paragraph (3) of Subsection E of 19.15.43.9 NMAC;

(iii) a description of post-injection monitoring location, methods, and proposed frequency;

(iv) a proposed schedule for submitting post-injection site care monitoring results to the director pursuant to Paragraph (5) of Subsection L of 19.15.43.9 NMAC; and

(v) the duration of the post-injection site care timeframe and, if approved by the director, the demonstration of the alternative post-injection site care timeframe that ensures non-endangerment of USDWs.

(c) Upon cessation of injection, owners or operators of Class VI wells must either submit an amended post-injection site care and site closure plan or demonstrate to the director through monitoring

data and modeling results that no amendment to the plan is needed. Any amendments to the post-injection site care and site closure plan must be approved by the director, be incorporated into the permit, and are subject to the permit modification requirements at Subsection H or J of 19.15.42.11 NMAC.

(d) At any time during the life of the geologic sequestration project, the owner or operator may modify and resubmit the post-injection site care and site closure plan for the director's approval within 30 days of such change.

(2) The owner or operator shall monitor the site following the cessation of injection to show the position of the carbon dioxide plume and pressure front and demonstrate that USDWs are not being endangered.

(a) Following the cessation of injection, the owner or operator shall continue to conduct monitoring as specified in the director-approved post-injection site care and site closure plan for at least 50 years or for the duration of the alternative timeframe approved by the director pursuant to requirements in Paragraph (3) of this subsection, unless the owner or operator makes a demonstration under Subparagraph (b) of Paragraph (2) of this Subsection. The monitoring must continue until the geologic sequestration project no longer poses an endangerment to USDWs and the demonstration under Subparagraph (b) of Paragraph (2) of this subsection is submitted and approved by the director.

(b) If the owner or operator can demonstrate to the satisfaction of the director before 50 years or prior to the end of the approved alternative timeframe based on monitoring and other site-specific data, that the geologic sequestration project no longer poses an endangerment to USDWs, the director may approve an amendment to the post-injection site care and site closure plan to reduce the frequency of monitoring or may authorize site closure before the end of the 50-year period or prior to the end of the approved alternative timeframe, where he or she has substantial evidence that the geologic sequestration project no longer poses a risk of endangerment to USDWs.

(c) Prior to authorization for site closure, the owner or operator must submit to the Director for review and approval a demonstration, based on monitoring and other site-specific data, that no additional monitoring is needed to ensure that the geologic sequestration project does not pose an endangerment to USDWs.

(d) If the demonstration in Subparagraph (c) of Paragraph (2) of this subsection cannot be made (i.e., additional monitoring is needed to ensure that the geologic sequestration project does not pose an endangerment to USDWs) at the end of the 50-year period or at the end of the approved alternative timeframe, or if the director does not approve the demonstration, the owner or operator must submit to the director a plan to continue post-injection site care until a demonstration can be made and approved by the director.

(3) **Demonstration of alternative post-injection site care timeframe.** The director may approve, in consultation with EPA, an alternative post-injection site care timeframe other than the 50 year default, if an owner or operator can demonstrate ~~during the permitting process~~ after injection operations cease that an alternative post-injection site care timeframe is appropriate and ensures non-endangerment of USDWs. The demonstration must be based on significant, site-specific data and information including all data and information collected pursuant to Subsections C and D of 19.15.43.9, and must contain substantial evidence that the geologic sequestration project will no longer pose a risk of endangerment to USDWs at the end of the alternative post-injection site care timeframe.

(a) A demonstration of an alternative post-injection site care timeframe must include consideration and documentation of:

(i) the results of computational modeling performed pursuant to delineation of the area of review under Subsection E of 19.15.43.9 NMAC;

(ii) the predicted timeframe for pressure decline within the injection zone, and any other zones, such that formation fluids may not be forced into any USDWs; and the timeframe for pressure decline to pre-injection pressures;

(iii) the predicted rate of carbon dioxide plume migration within the injection zone, and the predicted timeframe for the cessation of migration;

(iv) a description of the site-specific processes that will result in carbon dioxide trapping including immobilization by capillary trapping, dissolution, and mineralization at the site;

(v) the predicted rate of carbon dioxide trapping in the immobile capillary phase, dissolved phase, and mineral phase;

(vi) the results of laboratory analyses, research studies, and field or site-specific studies to verify the information required in Items (iv) and (v) of this Subparagraph;

(vii) a characterization of the confining zone(s) including a demonstration that it is free of transmissive faults, fractures, and micro-fractures and of appropriate thickness, permeability, and integrity to impede fluid (e.g., carbon dioxide, formation fluids) movement;

(viii) the presence of potential conduits for fluid movement including planned injection wells and project monitoring wells associated with the proposed geologic sequestration project or any other projects in proximity to the predicted/modeled, final extent of the carbon dioxide plume and area of elevated pressure;

(ix) a description of the well construction and an assessment of the quality of plugs of all abandoned wells within the area of review;

(x) the distance between the injection zone and the nearest USDWs above or below the injection zone; and

(xi) any additional site-specific factors required by the director.

(b) Information submitted to support the demonstration in Subparagraph (a) of Paragraph (3) of this Subsection must meet the following criteria:

(i) all analyses and tests performed to support the demonstration must be accurate, reproducible, and performed in accordance with the established quality assurance standards;

(ii) estimation techniques must be appropriate and EPA-certified test protocols must be used where available;

(iii) predictive models must be appropriate and tailored to the site conditions, composition of the carbon dioxide stream and injection and site conditions over the life of the geologic sequestration project;

(iv) predictive models must be calibrated using existing information (e.g., at Class I, Class II, or Class V experimental technology well sites) where sufficient data are available;

(v) reasonably conservative values and modeling assumptions must be used and disclosed to the director whenever values are estimated on the basis of known, historical information instead of site-specific measurements;

(vi) an analysis must be performed to identify and assess aspects of the alternative post-injection site care timeframe demonstration that contribute significantly to uncertainty. The owner or operator must conduct sensitivity analyses to determine the effect that significant uncertainty may contribute to the modeling demonstration.

(vii) an approved quality assurance and quality control plan must address all aspects of the demonstration; and,

(viii) any additional criteria required by the director.

(4) **Notice of intent for site closure.** The owner or operator must notify the director in writing at least 120 days before site closure. At this time, if any changes have been made to the original post-injection site care and site closure plan, the owner or operator must also provide the revised plan. The director may allow for a shorter notice period.

(5) After the director has authorized site closure, the owner or operator must plug all monitoring wells in a manner which will not allow movement of injection or formation fluids that endangers a USDW.

(6) The owner or operator must submit a site closure report to the director within 90 days of site closure, which must thereafter be retained at a location designated by the director for 10 years. The report must include:

(a) documentation of appropriate injection and monitoring well plugging as specified in Subsection M of 19.15.43.9 NMAC and Paragraph (5) of this Subsection. The owner or operator must provide a copy of a survey plat which has been submitted to the local zoning authority designated by the director. The plat must indicate the location of the injection well relative to permanently surveyed benchmarks. The owner or operator must also submit a copy of the plat to the appropriate EPA Regional Office per Subsection M of 19.15.43.9 NMAC;

(b) documentation of appropriate notification and information to such State, local and tribal authorities that have authority over drilling activities to enable such state, local, and tribal authorities to impose appropriate conditions on subsequent drilling activities that may penetrate the injection and confining zone(s); and

(c) records reflecting the nature, composition, and volume of the carbon dioxide stream.

(7) Each owner or operator of a Class VI injection well must record a notation on the deed to the facility property or any other document that is normally examined during title search that will in perpetuity provide any potential purchaser of the property the following information:

(a) the fact that land has been used to sequester carbon dioxide;

(b) the name of each State agency, local authority, or tribe with which the survey plat was filed, as well as the address of the EPA Regional Office to which it was submitted; and

(c) the volume of fluid injected, the injection zone or zones into which it was injected, and the period over which injection occurred.

(8) The owner or operator must retain for 10 years following site closure, records collected during the post-injection site care period. The owner or operator must deliver the records to the director at the conclusion of the retention period, and the records must thereafter be retained at a location designated by the director for that purpose.

O. Emergency and remedial response.

(1) As part of the permit application, the owner or operator must provide the director with an emergency and remedial response plan that describes actions the owner or operator must take to address movement of the injection or formation fluids that may cause an endangerment to a USDW during construction, operation, and post-injection site care periods. The requirement to maintain and implement an approved plan is directly enforceable regardless of whether the requirement is a condition of the permit.

(2) The owner or operator must conduct outreach with communities located within the AoR during development of the emergency and remedial response plan. This outreach must identify the chain of command for notifying the public in the event of an emergency and incorporate this information into the plan, and to develop protocols for notifying the public about well-related issues and emergencies, taking into account local language needs and the needs of persons with disabilities. The emergency and remedial response plan must describe how the owner or operator will provide training for local emergency responders, include a summary of community outreach activities conducted prior to the plan's submittal, and explain how community outreach will be maintained throughout the life of the project.

(3) The owner or operator must have at least one employee on the premises or otherwise available at all times with the authority to carry out the emergency and remedial response plan.

~~(3)~~**(4)** If the owner or operator obtains evidence that the injected carbon dioxide stream and associated pressure front may cause an endangerment to a USDW, a significant seismic event has occurred, a statistically significant geochemical change is detected above the confining zone, a release of carbon dioxide is detected by surface air monitoring, fluid has migrated into an unauthorized zone, or a gauge has malfunctioned for longer than one week, the owner or operator must:

(a) immediately cease injection;

(b) take all steps reasonably necessary to identify and characterize any release, migration, or malfunction;

(c) notify the director within 24 hours; and

(d) implement the emergency and remedial response plan approved by the director.

~~(4)~~**(5)** The director may allow the operator to resume injection prior to remediation if the owner or operator demonstrates that the injection operation will not endanger USDWs.

~~(5)~~**(6)** The owner or operator shall periodically review the emergency and remedial response plan developed under Paragraph (1) of this Subsection at least once every three years. Based on this review, the owner or operator shall submit an amended emergency and remedial response plan or demonstrate to the director that no amendment to the emergency and remedial response plan is needed. Any amendments to the emergency and remedial response plan must be approved by the director, must be incorporated into the permit, and are subject to the permit modification requirements at Subsection H or J of 19.15.42.11 NMAC, as appropriate. Amended plans or demonstrations shall be submitted to the director as follows:

(a) within one year of an area of review reevaluation;

(b) following any significant changes to the facility, such as addition of injection or monitoring wells, on a schedule determined by the director; or

(c) when required by the director.

P. Class VI injection depth waiver requirements. This section sets forth information which an owner or operator seeking a waiver of the Class VI injection depth requirements must submit to the director; information the director must consider in consultation with all affected Public Water System Supervision Directors; the procedure for director—Regional Administrator communication and waiver issuance; and the additional

requirements that apply to owners or operators of Class VI wells granted a waiver of the injection depth requirements.

(1) In seeking a waiver of the requirement to inject below the lowermost USDW, the owner or operator must submit a supplemental report concurrent with permit application. The supplemental report must include the following:

(a) a demonstration that the injection zone(s) is/are laterally continuous, is not a USDW, and is not hydraulically connected to USDWs; does not outcrop; has adequate injectivity, volume, and sufficient porosity to safely contain the injected carbon dioxide and formation fluids; and has appropriate geochemistry.

(b) a demonstration that the injection zone(s) is/are bounded by laterally continuous, impermeable confining units above and below the injection zone(s) adequate to prevent fluid movement and pressure buildup outside of the injection zone(s); and that the confining unit(s) is/are free of transmissive faults and fractures. The report shall further characterize the regional fracture properties and contain a demonstration that such fractures will not interfere with injection, serve as conduits, or endanger USDWs.

(c) a demonstration, using computational modeling, that USDWs above and below the injection zone will not be endangered as a result of fluid movement. This modeling should be conducted in conjunction with the area of review determination, as described in Subsection E of 19.15.43.9 NMAC, and is subject to requirements, as described in Paragraph (3) of Subsection E of 19.15.43.9 NMAC, and periodic reevaluation, as described in Paragraph (5) of Subsection E of 19.15.43.9 NMAC.

(d) A demonstration that well design and construction, in conjunction with the waiver, will ensure isolation of the injectate in lieu of requirements at Subparagraph (a) of Paragraph (1) of Subsection G of 19.15.43.9 NMAC and will meet well construction requirements in Paragraph (6) of this Subsection.

(e) A description of how the monitoring and testing and any additional plans will be tailored to the geologic sequestration project to ensure protection of USDWs above and below the injection zone(s), if a waiver is granted.Information on the location of all the public water supplies affected, reasonably likely to be affected, or served by USDWs in the area of review.

(f) Any other information requested by the director to inform the Regional Administrator's decision to issue a waiver.

(2) To inform the Regional Administrator's decision on whether to grant a waiver of the injection depth requirements at Sections 40 CFR 144.6, 40 CFR 146.5(f), and Subparagraph (a) of Paragraph (1) of Subsection G of 19.15.43.9 NMAC, the director must submit, to the Regional Administrator, documentation of the following:

(a) an evaluation of the following information as it relates to siting, construction, and operation of a geologic sequestration project with a waiver:

(i) the integrity of the upper and lower confining units;

(ii) the suitability of the injection zone(s) (e.g., lateral continuity; lack of transmissive faults and fractures; knowledge of current or planned artificial penetrations into the injection zone(s) or formations below the injection zone);

(iii) the potential capacity of the geologic formation(s) to sequester carbon dioxide, accounting for the availability of alternative injection sites;

(iv) all other site characterization data, the proposed emergency and remedial response plan, and a demonstration of financial responsibility;

(v) community needs, demands, and supply from drinking water resources;

(vi) planned needs, potential and/or future use of USDWs and non- USDWs in the area;

(vii) planned or permitted water, hydrocarbon, or mineral resource exploitation potential of the proposed injection formation(s) and other formations both above and below the injection zone to determine if there are any plans to drill through the formation to access resources in or beneath the proposed injection zone(s)/formation(s);

(viii) the proposed plan for securing alternative resources or treating USDW formation waters in the event of contamination related to the Class VI injection activity; and

(ix) any other applicable considerations or information requested by the director.

(b) Consultation with the public water system supervision directors of all states and tribes having jurisdiction over lands within the area of review of a well for which a waiver is sought.

(b) Consultation with the state engineer.

(c) Any written waiver-related information submitted by the public water system supervision director(s) to the (UIC) director.

(3) Pursuant to requirements at Subsection E of 19.15.41.8 NMAC and concurrent with the Class VI permit application notice process, the director shall give public notice that a waiver application has been submitted. The notice shall clearly state:

(a) the depth of the proposed injection zone(s);

(b) the location of the injection well(s);

(c) the name and depth of all USDWs within the area of review;

(d) a map of the area of review;

(e) the names of any public water supplies affected, reasonably likely to be affected, or served by USDWs in the area of review; and

(f) the results of UIC-Public Water System Supervision consultation required under Subparagraph (b) of Paragraph (2) of this Subsection.

(4) Following public notice, the director shall provide all information received through the waiver application process to the regional administrator. Based on the information provided, the regional administrator shall provide written concurrence or non-concurrence regarding waiver issuance.

(a) If the regional administrator determines that additional information is required to support a decision, the director shall provide the information. At his or her discretion, the regional administrator may require that public notice of the new information be initiated.

(b) In no case shall a director of a state-approved program issue a waiver without receipt of written concurrence from the regional administrator.

(5) If a waiver is issued, within 30 days of waiver issuance, EPA shall post the following information on the Office of Water's Web site:

(a) the depth of the proposed injection zone(s);

(b) the location of the injection well(s);

(c) the name and depth of all USDWs within the area of review;

(d) a map of the area of review;

(e) the names of any public water supplies affected, reasonably likely to be affected, or served by USDWs in the area of review; and

(f) the date of waiver issuance.

(6) Upon receipt of a waiver of the requirement to inject below the lowermost USDW for geologic sequestration, the owner or operator of the Class VI well must comply with:

(a) All requirements at Subsections E, F, H, I, J, L, M, and O of 19.15.43.9 NMAC;

(b) All requirements at Subsection G of 19.15.43.9 NMAC with the following modified requirements:

(i) The owner or operator must ensure that Class VI wells with a waiver are constructed and completed to prevent movement of fluids into any unauthorized zones including USDWs, in lieu of requirements at Subparagraph (a) of Paragraph (1) of Subsection G of 19.15.43.9 NMAC.

(ii) The casing and cementing program must be designed to prevent the movement of fluids into any unauthorized zones including USDWs in lieu of requirements at Subparagraph (a) of Paragraph (2) of Subsection G of 19.15.43.9.G NMAC.

(iii) The surface casing must extend through the base of the nearest USDW directly above the injection zone and be cemented to the surface; or, at the director's discretion, another formation above the injection zone and below the nearest USDW above the injection zone.

(c) All requirements at Subsection K of 19.15.43.9 NMAC with the following modified requirements:

(i) The owner or operator shall monitor the groundwater quality, geochemical changes, and pressure in the first USDWs immediately above and below the injection zone(s); and in any other formations at the discretion of the director.

(ii) Testing and monitoring to track the extent of the carbon dioxide plume and the presence or absence of elevated pressure (e.g., the pressure front) by using direct methods to monitor for pressure changes in the injection zone(s); and, indirect methods (e.g., seismic, electrical, gravity, or electromagnetic surveys and/or down-hole carbon dioxide detection tools), unless the director determines, based on site-specific geology, that such methods are not appropriate.

(d) All requirements at Subsection N of 19.15.43.9 NMAC with the following, modified post-injection site care monitoring requirements:

(i) The owner or operator shall monitor the groundwater quality, geochemical changes and pressure in the first USDWs immediately above and below the injection zone; and in any other formations at the discretion of the director.

(ii) Testing and monitoring to track the extent of the carbon dioxide plume and the presence or absence of elevated pressure (e.g., the pressure front) by using direct methods in the injection zone(s); and indirect methods (e.g., seismic, electrical, gravity, or electromagnetic surveys and down-hole carbon dioxide detection tools), unless the director determines based on site-specific geology, that such methods are not appropriate.

(e) Any additional requirements requested by the director designed to ensure protection of USDWs above and below the injection zone(s).

[19.15.43.9 NMAC – N, XX/XX/XXXX]

History of 19.15.43 NMAC: [RESERVED]

EXHIBIT 2

PETER M. MORGAN
peter@thecara.org

EMPLOYMENT

CENTER FOR ASSET RETIREMENT ACCOUNTABILITY (CARA), Denver, CO
Legal and Policy Director, September 2024-Present

- Develop policy and legal solutions to address well plugging and other aspects of extractive industry decommissioning.

THE SIERRA CLUB, Environmental Law Program
Senior Attorney, January 2017–September 2024, Denver, CO

- Led Sierra Club's work to secure the timely clean-up of coal mines and oil and gas wells

Staff Attorney, July 2010–December 2016, Denver, CO
Law Fellow, September 2008–June 2010, San Francisco, CA

THE SUPREME COURT OF ALASKA, Justice Walter Carpeneti, Juneau, AK
Law Clerk, August 2007–August 2008

THE NATURAL CAPITAL PROJECT, Stanford, CA
Postdoctoral Policy Fellow, Hawaii Site, January 2007–August 2007

THE NATURE CONSERVANCY, Martha's Vineyard, MA
Program Manager, Massachusetts Islands Program, 2002–2003
Office Manager, Massachusetts Islands Program, 2001–2002

EDUCATION

STANFORD LAW SCHOOL, Stanford, CA
J.D., *January 2007*

STANFORD UNIVERSITY, Stanford, CA
M.S., Interdisciplinary Graduate Program in Environment and Resources, *January 2007*

MIDDLEBURY COLLEGE, Middlebury, VT
B.A., *magna cum laude, phi beta kappa*, with High Honors in American Literature, *May 2001*

TESTIMONY AND SPEAKING APPEARANCES

Witness, New Mexico Oil Conservation Commission, Rulemaking on Proposed Amendments to Oil and Gas Regulatory Program, October 2025
Witness, U.S. House of Representatives, Natural Resources Committee, Hearing on Examining the Biden Administration's Abandoned Mine Lands and Active Mining Programs, November 2023
Panelist, *US Coal in the 21st Century: Bankruptcy, Ownership and Financing*, Columbia University Law School, September 2016

MEDIA ENGAGEMENT

Quoted on issues related to fossil fuel clean-up and decommissioning in the *New York Times, Washington Post, Wall St. Journal, Science, Slate, Greenwire*.
Letters to the editor published in the *New Yorker* and the *Atlantic Monthly*.

EXHIBIT 3

STATE OF NEW MEXICO
NEW MEXICO OIL CONSERVATION COMMISSION

IN THE MATTER OF PROPOSAL TO ADOPT 19.15.41, 19.15.42, and 19.15.43 NMAC; STATEWIDE **CASE NO. 25875**

DIRECT TESTIMONY OF PETER MORGAN

Background and Qualifications

Q: Please state your name.

A: Peter Morgan.

Q: Where are you employed and what is your position?

A: I am Legal and Policy Director for the Center for Asset Retirement Accountability (CARA). I helped found CARA in September 2024. CARA's mission is to address the national problem of unplugged oil and gas wells and other aging infrastructure, including through regulatory solutions. This work involves understanding existing regulatory requirements at the federal and state level, identifying gaps and flaws with those requirements that lead to clean-up and decommissioning obligations being passed on to the public, and proposing solutions to address those gaps and flaws.

Q: What is your educational background?

A: I have a Bachelor of Arts from Middlebury College. I have a J.D. from Stanford Law School and a Master of Science degree from Stanford's Emmet Interdisciplinary Program in Environment and Resources.

Q: Can you briefly describe your work background?

A: Prior to my current position with CARA, I worked for 16 years as an attorney for the Sierra Club. My work at Sierra Club focused on issues around the operation and cleanup of fossil fuel extraction facilities nationwide, with a concentration on oil and gas operations and coal

mines. Through this work I have expertise in understanding state and federal regulatory requirements for financial assurance from industrial operators for plugging and abandonment and site remediation, the strengths and weaknesses in these regulatory schemes, industrial operators' failure to comply with regulatory requirements and best practices, and the fiscal, environmental, and public health problems resulting from orphaned and abandoned wells and infrastructure across the nation, including in New Mexico.

I testified before Congress at a 2023 hearing of the U.S. House of Representatives Natural Resources Committee's Subcommittee on Energy and Mineral Resources on the need for improved regulations to strengthen financial assurances, restrict transfer of obligations, and address other issues related to cleaning up fossil fuel extraction sites. I have drafted and submitted multiple sets of comments to federal authorities including the U.S. Bureau of Land Management regarding best regulatory practices to ensure prompt cleanup of fossil fuel extraction infrastructure and to avoid the creation of orphaned infrastructure. In 2025, I testified before this body on the need for improved financial assurance requirements for oil and gas operators in New Mexico.

Q: Is Conservation Groups' Exhibit 2 an accurate copy of your resume?

A: Yes.

Q: In preparing your testimony, what sources did you review?

A: I reviewed OCD's Application, including the proposed new rules at Parts 41, 42, and 43 of Title 19, Chapter 15 of the New Mexico Administrative Code. I am also familiar with the federal Class VI regulations at 40 C.F.R. Parts 124, 144, and 146, on which OCD's application is based. In addition, I reviewed various materials that are included as references at the end of my testimony.

Summary of Opinions

Q: Can you summarize the opinions you will provide in your testimony?

A: Yes. I will provide testimony and opinions on the Conservation Groups' proposed amendments to 19.15.43.9.F NMAC. Specifically, I will cover the following areas:

First, self-insurance is a flawed approach that would expose the state to significant risk.

Second, corporate guarantees similarly carry risks.

Third, cancellation of financial assurance in the event of failure to pay transfers risk from providers to the state and taxpayer.

Overall, my recommendations are intended to help prevent carbon dioxide injection wells being orphaned without adequate financial assurance in place to provide for their plugging. My goal is to ensure the agency has access to adequate resources to plug any wells that have been orphaned.

19.15.43.9 – Criteria and Standards Applicable to Class VI Wells

Q: Mr. Morgan, before you discuss Conservation Groups' specific proposals at 19.15.43.9 NMAC, please discuss the role of financial assurance in general and the problems that arise when financial assurance is not adequate, beginning with why adequate financial assurance is an important component of effective carbon sequestration regulations?

A: Effective financial assurances are a critical component of a successful Class VI injection well permitting program because they help ensure that injection wells will not be left in a condition that will allow fluid movement that could endanger underground sources of drinking water, either during operations or during the required post-plugging monitoring period. The federal Class VI program emphasizes that the role of financial assurances is "to ensure that

financial resources would be available for corrective action, injection well plugging, post-injection site care (PISC), site closure, and emergency and remedial response."[1]

Although Class VI injection wells constitute a relatively new class of industrial activity, regulators can look to other industries with similar physical impacts and life-cycles—including both the coal and oil and gas industries—to anticipate problems that might arise when financial assurance is inadequate. As with oil and gas wells, carbon dioxide injection wells provide access to a finite resource. In this case, that resource is pore space. Once the available pore space has been filled, or the operator otherwise decides to cease injection, the well must be plugged and the site monitored—typically for decades. Carbon dioxide injection wells are also similarly subject to changes in commodity prices and to broader changes in the regulatory landscape that can impact an operator's profitability and solvency.

Just as in oil and gas operations, significant costs associated with operating a carbon dioxide injection well persist long after the operation has stopped generating revenue, whether through tax credits or other sources. At the same time, plugging and decommissioning is expensive and represents a pure cost with no potential to produce additional revenue.[2] And Class VI wells have significant additional post-plugging costs not typically encountered with oil and gas wells, such as the requirement for long-term monitoring. Class VI wells may need to be monitored for 50 years or more after they are plugged, at the operator's expense.[3] It is

---

[1] U.S. Environmental Protection Agency, "Federal Requirements Under the Underground Injection Control (UIC) Program for Carbon Dioxide (CO_2) Geologic Sequestration (GS) Wells," 75 Fed. Reg. 77,230, 77,233 (December 10, 2010).

[2] *See* J. Weber et al., Identifying the End: Minimum Production Thresholds for Natural Gas Wells, University of Pittsburgh Graduate School of Public and International Affairs Working Paper No. 21-500 at p. 4 (May 27, 2021) (discussing decommissioning in the oil and gas industry).

[3] 75 Fed. Reg. at 77,268.

foreseeable that some operators may go out of business or abandon their obligations before completing plugging, or during the lengthy post-plugging monitoring period where costly corrective action may be required, leaving the regulator with no assets to claim.[4] Class VI wells also implicate concerns similar to those encountered with oil and gas wells regarding the potential for a well to become inactive, with uncertainty as to whether operations will resume and concerns around well integrity during such periods. Regulators can address all of these dynamics and concerns by requiring operators to post third-party financial assurance instruments—prior to drilling or acquiring a well—sufficient to cover the costs of plugging, monitoring, and any needed corrections actions, or at least sufficient to shift the incentives so that operators prioritize well plugging.[5]

Financial assurance requirements for resource extractors and other industrial activities provide a mechanism for ensuring ultimate compliance with decommissioning requirements.[6] The operator posts the financial assurance, which is only released when plugging and post-plugging activities are successfully completed.[7] If plugging and required post-plugging activities are not successfully completed, the operator forfeits the financial assurance and the proceeds are used by the state to pay a third party to complete the plugging or conduct any additional required activities, including long-term monitoring.[8]

Effective financial assurance programs facilitate timely and effective decommissioning in

---

[4] *See* David Gerard, The Law and Economics of Reclamation Bonds, Resources Policy 26 (4): 189–97 at p. 191, Oct. 2, 2000.
[5] *Id.* at p. 191 ("An approach to the judgment-proof problem is to require collateral (such as a bond), thus providing the agent with a direct monetary incentive to comply with the regulations. If the agent fails to perform, the forfeited collateral is used to remedy the performance failure.").
[6] *Id.* at p. 189.
[7] *Id.*
[8] *Id.*

three primary ways.

First, the financial assurance "assures that some resources will be available for reclamation if the firm fails to clean up the site."[9] Recent changes to the tax credits for which injection wells are eligible support this financial backstop, as policy changes or the expiration of existing tax credits may greatly impact the financial viability of a project before plugging and decommissioning is complete.[10] Adequate financial assurance requirements insulate a prudent regulator from the risks of the industry.

Second, maintaining the financial assurance imposes an ongoing cost on the operator that is only released once the operator has fulfilled the obligations covered by that financial instrument. The obligations that must be covered by an operator's financial responsibility instruments are: corrective action; injection well plugging; post injection site care and site closure; and emergency and remedial response.[11] The proposed rules contemplate that a financial instrument may be specific to a particular phase of the project, such as plugging, and that an "owner or operator may be released from a financial instrument" once it has "completed the phase of the geologic sequestration project for which the financial instrument was required."[12] The requirement that an operator maintain a third-party financial instrument to cover plugging costs thereby creates an incentive for the operator to complete plugging as quickly as possible so that the financial instrument covering plugging costs may be released. Financial assurances such as surety bonds "can impose liquidity constraints on firms" and "can tie up a firm's operating

---

[9] *Id.*

[10] *See* https://www.eia.gov/todayinenergy/detail.php?id=65764; https://www.globalccsinstitute.com/u-s-preserves-and-increases-45q-credit-in-one-big-beautiful-bill-act/. Specifically, parity between tax credits used for geologic sequestration and enhanced oil recovery lessen the competitiveness of Class VI projects.

[11] 40 C.F.R. 146.85(a)(2); proposed section 19.15.43.9.F.1.b. NMAC.

[12] Proposed section 19.15.43.9.F.2.b. NMAC.

capital,"[13] such that the operator will be motivated to seek release sooner than later. In addition to imposing collateral requirements, surety bond providers also charge annual premiums and other regular fees. The desire to free up capital and avoid these ongoing costs should offset an operator's desire to avoid or delay the cost of plugging. Once plugging is complete and the associated financial instrument is released, the remaining financial instruments will provide similar incentives for operators to timely complete obligations associated with the remaining phases of the geologic sequestration project.

Third, financial assurance requirements shift risk away from the state and onto a third party such as a surety bond provider, with the third party conducting its own analysis of an operator's reliability and likelihood of default.[14] Financial assurance providers will screen operators and set premiums and other fees based on "observable indicators" of factors including "regulatory compliance."[15] This prevents firms from accumulating unsustainable environmental costs over time and eventually declaring bankruptcy.[16] For a carbon dioxide injection well, a surety provider may offer more favorable terms to an operator who has established a very low risk of needing to conduct additional costly corrective actions.

Q: Why isn't it sufficient to rely on the regulatory requirements included in OCD's proposed rules that require operators to plug injection wells once injection ceases?

A: The significant costs of plugging and monitoring an injection well, including any

---

[13] David Gerard, The Law and Economics of Reclamation Bonds, Resources Policy 26 (4): 189–97, Oct. 2, 2000, at p. 191.

[14] *Id.* at 189-90 ("The use of a third party further reduces public exposure by increasing the number of parties potentially liable for the cleanup. Moreover, the third party assumes an enforcement role, which encourages contractual or regulatory compliance.").

[15] Judson Boomhower, Drilling Like There's No Tomorrow: Bankruptcy, Insurance, and Environmental Risk, American Economic Review Vol. 109, No. 2 at p. 401, Feb. 2019.

[16] *Id.* at p. 418 (noting that "Insurers in this market described this type of monitoring in interviews").

necessary post-plugging corrective actions, will typically come due for an operator after the project has stopped qualifying for tax credits or otherwise generating revenue. This creates a powerful incentive for the operator to avoid those costs, regardless of what the regulations require, including by filing for bankruptcy.

As described above, financial instruments can be specific to particular phases of the project, including plugging. This creates its own incentive that promotes prompt plugging in order to have that financial instrument released and bring down the operation's ongoing costs. Remaining financial assurance instruments for obligations such as ongoing monitoring and potential corrective action should be less expensive and can be balanced against the costs and disadvantages of bankruptcy.

Q: In addition to the financial assurance requirements, New Mexico will maintain a Geologic Carbon Dioxide Long-Term Storage Stewardship Fund. Why not just rely on the Stewardship Fund to make up any shortfall, rather than amend the financial assurance requirements?

The New Mexico legislature established the Stewardship Fund in the 2025 legislative session for the "sole purpose of ensuring the long-term storage security of geologic sequestration facilities."[17] Although the plugging of abandoned injection wells is a permitted use of the Stewardship Fund, it is one of many uses that all draw from the same pot.[18] Moreover, the adequacy of the Stewardship Fund is entirely unknown at this point, both because estimates of future Class VI projects in New Mexico are entirely speculative and because the Oil Conservation Commission has not yet established by rule a fee schedule "sufficient to meet the

[17] Section 74-14-5(A) NMSA 1978.
[18] Section 74-14-5(B) NMSA 1978.

projected needs of the fund."[19] Unfortunately, funds of this type are also sometimes raided by legislatures to cover shortfalls in a state's general fund, meaning even the collected money may not actually be available for the intended purpose.[20] There is too much uncertainty around the Stewardship Fund to rely on it to make up any shortfall.

In addition, reliance on a general fund of this type fails to provide any incentive to an operator to timely plug its wells and effectively manage post-injection site care. In fact, such funds can pose a moral hazard, with operators concluding that they are better off avoiding the cost of plugging and turning their wells over to the state to plug using the fund. Such a practice is self-reinforcing in a vicious cycle. Once an operator sees its competitors avoiding plugging costs, it will similarly seek to externalize those costs. The result is a dramatic and unsustainable increase in the burden on the fund.

Q: Mr. Morgan, let's turn to Conservation Groups' proposed amendments at 19.15.43.9 NMAC. OCD's proposed amendments are redlined in blue underline, and Conservation Groups' proposed amendments are shown in red redline and strikeout in their Exhibit 1.

Beginning with 19.15.43.9.F(1)(a)(v) NMAC, relating to use of self-insurance, what is the basis for the proposed amendment, as shown below?

~~**19.15.43.9.F.1(a)(v)** Self Insurance (i.e., Financial Test and Corporate Guarantee).~~

A: "Self-insurance," sometimes referred to as "self-bonding," is a fundamentally flawed approach, as no matter how financially secure a company appears, it can always fail. And when

[19] Section 74-14-5(A) NMSA 1978.

[20] *See* https://www.canarymedia.com/articles/enn/ohio-diverts-money-from-coal-mine-cleanup-fund-as-risk-of-closures-rises (describing Ohio lawmakers' transfer of $5 million from a coal mine clean-up fund to address shortfalls in the state's general budget).

it does, the absence of any third-party financial assurance, and prospect for plugging or other decommissioning costs reverting to the state, significantly compromise the regulator's ability to pursue necessary enforcement.

The experience of another regulatory program that relied on self-bonding provides an instructive example. The Surface Mining Control and Reclamation Act (SMCRA), which governs coal mining, allows the use of self-bonding in certain circumstances.[21] In 2015 and 2016, the three largest coal mine operators in the United States—Alpha Natural Resources, Arch Coal, and Peabody Energy—had been allowed to self bond following a review of their financial condition.[22] Collectively, they had over a billion dollars in self-bonded clean-up liabilities.[23] All went bankrupt following a drop in commodity prices that left them unable to service their debt. When the three companies went into bankruptcy, they had enormous leverage over the regulators because there was no bonding in place.[24]

The Government Accountability Office assessed the use of self-bonding in the wake of the coal mine operator bankruptcies and concluded that "[s]elf-bonding presents a risk to the government."[25] The GAO found that self-bonding is not an effective financial assurance for three reasons:

---

[21] 30 C.F.R. § 800.23; see also Joshua C. Macey & Jackson Salovaara, Bankruptcy as Bailout, 71 STAN. L. REV. 879, 895 (2019).

[22] Specifically, coal mine operators were allowed to self-bond if they had been in continuous operation for five years, had an "A" rating or higher from Moody's or S&P, had a ratio of total liabilities to net worth of 2.5 or less, and a ratio of current assets to current liabilities of 1.2 or greater. 30 C.F.R. § 800.23.

[23] Joshua C. Macey & Jackson Salovaara, *Bankruptcy as Bailout*, 71 STAN. L. REV. at 895-96.

[24] *See* Joshua Macey, Jackson Salovaara, *Bankruptcy as Bailout: Coal Company Insolvency and the Erosion of Federal Law*, 71 Stan. L. Rev. 879, 897-98 (2019) for more discussion on the inherent flaws with self-bonding.

[25] U.S. Gov't Accountability Off., COAL MINE RECLAMATION: Federal and State Agencies Face Challenges in Managing Billions in Financial Assurances, GAO-18-305 (March 6, 2018), https://www.gao.gov/assets/gao-18-305.pdf

> because it is difficult to (1) ascertain the financial health of an operator, (2) determine whether the operator qualifies for self-bonding, and (3) obtain a replacement for existing self-bonds when an operator no longer qualifies.[26]

Foregoing third-party financial assurances in favor of reliance on an obligated party's financial health creates a scenario where the obligated party has profound financial leverage over the regulator should the obligated party's financial condition deteriorate. Two factors contribute to this dynamic.

First, regulators are unable to demand additional financial assurances from a financially distressed operator, which will claim that it will liquidate rather than provide the additional financial assurance. As the GAO found, "if a company passes a financial strength test but subsequently files for bankruptcy or becomes insolvent, the company in essence is no longer providing financial assurance because it may no longer have the financial capacity to meet its obligations. *Such financial deterioration can occur quickly.* While companies no longer meeting the financial test are to obtain other financial assurance, they may not be able to obtain or afford to purchase it."[27]

Because the regulator knows that there is no third-party financial assurance instrument in place, or that the financial assurance covers only a fraction of the anticipated cost, their approach to enforcement will be significantly constrained. As the Executive Director of the Interstate Mining Compact Commission has observed, this situation amounts to "a classic Catch-22: if the state chooses to insist on alternative financial assurances or collateral as a result of the

---

[26] *Id.*

[27] U.S. Gov't Accountability Off., Offshore Oil and Gas Resources: Actions Needed to Better Protect Against Billions of Dollars in Federal Exposure to Decommissioning Liabilities, GAO-16-40, at 27 (Dec. 18, 2015), https://www.gao.gov/products/gao-16-40.

company's diminished financial situation, the threat to the company's financial solvency would only increase."[28]

Second, once the company is in bankruptcy, the regulator may be forced to accept concessions to which it would not otherwise agree. Bankruptcy courts frequently allow resource extractors to abandon property without satisfying decommissioning obligations, and reduce demands for cost reimbursements to unsecured claims that can be discharged. For example, in the case of the self-bonded coal mine operators, regulators were forced to significantly reduce their claims for decommissioning and clean-up activities in bankruptcy, settling one clean-up claim of $150 million for just $5.4 million, and another claim of $100 million for just $3.4 million.[29]

The GAO specifically highlighted the compromised position that self-bonding puts regulators in once a self-bonded operator is in financial distress, noting that:

> if a self-bonded operator were to enter bankruptcy and did not secure a financial assurance to replace the self-bond or complete the required reclamation, the state regulatory authority would have to work through the bankruptcy proceedings to obtain funds for reclamation, . . . [and] [a]s a result, the state may recover only some, or possibly none, of the funds promised through the selfbond, and the cost of reclamation could fall on taxpayers.[30]

These concerns about the potential for self-bonded operators to become insolvent and enter bankruptcy have led the U.S. Bureau of Land Management to eliminate the use of self-bonding for the hardrock mining industry. The GAO reports that BLM "determined that a self-bond is less secure than other types of financial assurances, especially in cases where commodity

---

[28] Gregory E. Conrad, Interstate Mining Compact Comm'n, Mine Reclamation Bonding—From Dilemma to Crisis to Reinvention: What's a State Regulator to Do? 9 (2014), https://perma.cc/2V7E-R8BG (quoted in Bankruptcy as Bailout, 71 Stan. L. Rev. 879, 898 (2019)).

[29] Bankruptcy as Bailout, 71 Stan. L. Rev. at 883 n.12.

[30] GAO-18-305 at p. 22.

prices fluctuate."[31] BLM also found that "operators that would otherwise be eligible to self-bond should not have a significant problem obtaining another type of financial assurance."[32]

Q: Are there elements of a Class VI program that make it particularly ill-suited to the use of self-bonding?

A: Yes. Class VI facilities require financial assurance coverage for much longer than typical industrial projects, with the longest period coming after the point where the well is plugged and the facility is no longer generating revenue. This means there is a very high likelihood that an operator will go out of business before operations are concluded and the financial assurance is released. In such a circumstance, third-party financial instruments are much more reliable than self-bonding.

Development and management of a Class VI well involves at least the following stages: drilling, injection, testing and monitoring, corrective action (as needed), plugging, post-injection site care and monitoring, and site closure.[33] Class VI wells must be plugged and monitored "in order to ensure that the well itself does not become a conduit for movement into [underground sources of drinking water]."[34] Monitoring and site care must continue "until it can be demonstrated that movement of the CO_2 plume and pressure front no longer pose a risk of endangerment to [underground sources of drinking water]."[35] The monitoring stage alone is expected to last at least 50 years.[36]

The risk of an operator going out of business over the many decades where ongoing

---

[31] *Id*. at pp. 23–24.
[32] *Id*.
[33] *See* 75 Fed. Reg. at 77,232–23.
[34] *Id*. at 77,266.
[35] *Id*.
[36] *Id*. at 77,268.

monitoring and maintenance are required, and where emergency response and corrective action are likely, is too high to allow the use of self-bonding. As discussed above, once a self-bonded operator shows signs of financial distress, it is typically too late to secure a replacement financial assurance.

Q: Don't EPA's rules for Class VI regulatory programs expressly authorize the use of self-insurance?

A: EPA's Class VI injection rules, including the provisions authorizing the use of self-bonding, were finalized in 2010, prior to the collapse of the self-bonded coal mine operators. Accordingly, EPA did not have the opportunity to incorporate the lessons of those bankruptcies into its final rule. But New Mexico does have that opportunity and should learn from those failures. Notably, both Colorado[37] and Louisiana[38] declined to adopt self-bonding in their Class VI primacy rules.

Q: What is the basis for the proposed amendment to 19.15.43.9.F(1)(a)(vii), relating to other forms of financial assurance that may be used, as shown below?

~~**19.15.43.9.F.1(a)(vii)** Any other instrument(s) satisfactory to the Director.~~

A: This provision is unnecessary, because the other instruments specified in the draft rule are adequate.

Q: What is the basis for the proposed amendment to 19.15.43.9.F(1)(d)(i)(A), relating to cancellation of financial assurance, as shown below?

19.15.43.9.F(1)(d)(ii) Cancellation—for purposes of this part, an owner or operator must provide that their financial mechanism may not cancel, terminate or fail to renew except for failure to pay such financial instrument. If there is a failure to pay the financial instrument, the financial institution may elect to cancel, terminate, or fail to renew the instrument by sending notice by certified mail to the owner or operator and the Director.

[37] 2 COLO. CODE REGS § 404-1-1415(a)(1).
[38] LAC 43:XVII § 3609.C.

> The cancellation must not be final for 120 days after receipt of cancellation notice. The owner or operator must provide an alternate financial ~~responsibility demonstration~~ mechanism within 60 days of notice of cancellation, and if an alternate financial ~~responsibility demonstration~~ mechanism is not acceptable (or possible), ~~any funds from the instrument being cancelled must be released~~ the provider of the financial instrument being canceled must release all funds from that instrument to the Director within 60 days of notification by the Director.

A: As written, the rule is ambiguous regarding what follows if a financial institution seeks to cancel a financial assurance instrument and no replacement financial instrument is provided. The proposed amendment would clarify that if no replacement financial instrument is provided, the original financial instrument is forfeit and the financial institution must release the funds to the Director. The amendment therefore avoids any scenario where the owner or operator is in financial distress and there is no financial instrument in place to cover costs associated with plugging, monitoring, or corrective action.

Leaving the language ambiguous, or adopting a reading allowing complete cancellation without payment, would defeat the purpose of requiring financial assurances. The only circumstance under which cancellation should be possible is if a replacement financial assurance is already in place. Surety providers and other providers of financial assurances assume the risk of operator default. In exchange, they get to collect premiums and secure collateral. Allowing a provider to cancel an instrument for failure to pay defeats the entire purpose. Under that scenario, if an operator were to go out of business and fail to pay to maintain the financial instrument, the provider could cancel the instrument. But that's exactly the time when it's most critical for the financial assurance to be in place. And no other provider is going to be willing to provide a replacement financial assurance at that time, given the operator's failure to pay.

North Dakota's approved Class VI program incorporates a similar clarifying edit. The relevant language from the North Dakota program states "The storage operator shall provide an

alternate qualifying financial responsibility demonstration within sixty days of notice of cancellation, and if it is not acceptable or possible, any funds from the instrument being canceled must be released to the commission within sixty days of notification by the commission."[39] North Dakota's regulation makes clear that in the event no replacement financial instrument is provided, the "funds from the instrument being canceled" will be released "to the commission."

Q: What is the basis for the proposed amendment to 19.15.43.F(1)(f)(i), relating to combination of instruments, as shown below?

> **19.15.43.F(1)(f)(i)** In the event that the owner or operator combines more than one instrument for a specific geologic sequestration phase (e.g., well plugging), such combination must be limited to instruments that are not based on financial strength or performance (i.e., ~~self insurance or~~ performance bond), for example trust funds, surety bonds guaranteeing payment into a trust fund, letters of credit, escrow account, and insurance. In this case, it is the combination of mechanisms, rather than the single mechanism, which must provide financial responsibility for an amount at least equal to the current cost estimate.

A: As discussed above, self-insurance is a fundamentally flawed approach that the OCC should decline to adopt. The reference in 19.15.43.F(1)(f)(i) NMAC to self-insurance should be removed.

Q: What is the basis for the proposed amendment to 19.15.43.F(1)(f)(v), relating to use of self-insurance, as shown below?

> ~~**19.15.43.9.F(1)(f)(v)** An owner or operator or its guarantor may use self insurance to demonstrate financial responsibility for geologic sequestration projects. In order to satisfy this requirement the owner or operator must meet a Tangible Net Worth of an amount approved by the Director, have a net working capital and tangible net worth each at least six times the sum of the current well plugging, post injection site care and site closure cost, have assets located in the United States amounting to at least 90 percent of total assets or at least six times the sum of the current well plugging, post injection site care and site closure cost, and must submit a report of its bond rating and financial information annually. In addition the owner or operator must either: Have a bond rating test of AAA, AA, A, or BBB as issued by Standard & Poor's or Aaa, Aa, A, or Baa as issued by Moody's; or meet all of the following five financial ratio thresholds: A ratio of~~

[39] N.D. Admin. Code 43-05-01-09.1(1)(d)(2).

~~total liabilities to net worth less than 2.0; a ratio of current assets to current liabilities greater than 1.5; a ratio of the sum of net income plus depreciation, depletion, and amortization to total liabilities greater than 0.1; A ratio of current assets minus current liabilities to total assets greater than −0.1; and a net profit (revenues minus expenses) greater than 0.~~

A: As discussed above, self-insurance is a fundamentally flawed approach that the OCC should decline to adopt.

In the coal mining example discussed above, the self-bonding criteria provided under SMCRA was at least as stringent as the criteria proposed here and still failed to predict or prevent the failure of operators holding hundreds of millions of dollars of reclamation liability. The SMCRA criteria allowed an operator to self-bond if they had been in continuous operation for five years, had an "A" rating or higher from Moody's or S&P, had a ratio of total liabilities to net worth of 2.5 or less, and a ratio of current assets to current liabilities of 1.2 or greater.[40] This includes a higher credit rating and a higher ratio of total liabilities to net worth than what's found in the proposed rule. Even though the financial condition criteria under SMRCA were more stringent than the criteria contemplated in the proposed rule, they failed to predict the future bankruptcies of the coal mine operators, leaving regulators at an enormous disadvantage.

Q: What is the basis for the proposed amendment to 19.15.43.9.F(1)(f)(vi), relating to corporate guarantees, as shown below?

~~**19.15.43.9.F(1)(f)(vi)** An owner or operator who is not able to meet corporate financial test criteria may arrange a corporate guarantee by demonstrating that its corporate parent meets the financial test requirements on its behalf. The parent's demonstration that it meets the financial test requirement is insufficient if it has not also guaranteed to fulfill the obligations for the owner or operator.~~

A: This provision allows an owner or operator not able to meet corporate financial test

[40] 30 C.F.R. § 800.23; *see also* Joshua C. Macey & Jackson Salovaara, *Bankruptcy as Bailout*, 71 STAN. L. REV. 879, 895 (2019).

criteria to arrange a corporate guarantee by demonstrating that its corporate parent meets the financial test requirements on its behalf. For the reasons discussed above regarding self insurance, this provision should be eliminated. Corporate parents are subject to the same dynamics and risks as their subsidiaries, and financial condition criteria are similarly inadequate to predict or prevent bankruptcies or other failures.

Both Colorado and Louisiana opted to omit corporate guarantees as a financial responsibility option in their respective Class VI programs.[41]

This concludes my testimony, which is accurate to the best of my knowledge.



Peter Morgan

6/26/2026
Date

[41] LAC 43:XVII § 3609.C; 2 COLO. CODE REGS § 404-1-1415(a)(1).

List of References

Judson Boomhower, Drilling Like There's No Tomorrow: Bankruptcy, Insurance, and Environmental Risk, American Economic Review Vol. 109, No. 2, Feb. 2019.

Gregory E. Conrad, Interstate Mining Compact Comm'n, Mine Reclamation Bonding—From Dilemma to Crisis to Reinvention: What's a State Regulator to Do? 9 (2014), https://perma.cc/2V7E-R8BG (quoted in Bankruptcy as Bailout, 71 Stan. L. Rev. 879, 898 (2019)).

David Gerard, The Law and Economics of Reclamation Bonds, Resources Policy 26 (4): 189–97, Oct. 2, 2000.

Joshua C. Macey & Jackson Salovaara, Bankruptcy as Bailout, 71 STAN. L. REV. 879, 895 (2019).

U.S. Environmental Protection Agency, "Federal Requirements Under the Underground Injection Control (UIC) Program for Carbon Dioxide (CO_2) Geologic Sequestration (GS) Wells," 75 Fed. Reg. 77,230, 77,233 (December 10, 2010).

U.S. Gov't Accountability Off., Offshore Oil and Gas Resources: Actions Needed to Better Protect Against Billions of Dollars in Federal Exposure to Decommissioning Liabilities, GAO-16-40, at 27 (Dec. 18, 2015), https://www.gao.gov/products/gao-16-40.

U.S. Gov't Accountability Off., COAL MINE RECLAMATION: Federal and State Agencies Face Challenges in Managing Billions in Financial Assurances, GAO-18-305 (March 6, 2018), https://www.gao.gov/assets/gao-18-305.pdf

U.S. Gov't Accountability Office, Oil and Gas: Bureau of Land Management Should Address Risks from Insufficient Bonds to Reclaim Wells, GAO-19-615 (Sept. 2019).

J. Weber et al., Identifying the End: Minimum Production Thresholds for Natural Gas Wells, University of Pittsburgh Graduate School of Public and International Affairs Working Paper No. 21-500 at p. 4 (May 27, 2021).

EXHIBIT 4

CHARLES FRANKLIN HARVEY

Department of Civil and Environmental Engineering
Building 48, MIT, Cambridge, MA 02139

email: charvey@mit.edu
phone: (617) 258-0392

Web page: **https://harveylab.mit.edu**

CARBON and WATER: Integrated Field, Modeling, and Management

- Peatlands: Ecology, hydrology, and carbon stores (Borneo and Massachusetts).
- Coastal Hydrology: Water and chemical exchanges between land and oceans (Plum Island, Massachusetts)
- Geologic sequestration of carbon dioxide
- Natural Methane Fluxes (Harvard Forest, Plum Island, Massachusetts)
- Arsenic contamination of groundwater (Bangladesh, Vietnam, and West Bengal)

EMPLOYMENT

MIT, 1998 - present.
Full Professor (2011), Tenured (2006), Associate Professor (2003), Civil and Environmental Engineering.

Harvard University, 1996 - 1998.
Gordon McKay Assistant Professor of Environmental Engineering (tenure track), Earth and Planetary Science.

U. S. Geological Survey, 1988 - 1990. Menlo Park, CA, Hydrologist.

U. S. Geological Survey, 1987 - 1988. Richmond, VA, Hydrologist.

EDUCATION

Stanford, **Ph.D., 1996**, Geological and Environmental Sciences. Advisor: Steven Gorelick
National Science Foundation Graduate Fellowship.
Student Appointment, U.S. Geological Survey, Menlo Park.

Ohio State University, 1987-88, School of Medicine.
Completed the first year of medical school (MD) with honors in physiology.

Oberlin College, **B.A., 1986**, Mathematics.

AWARDS/HONORS

National Academy of Engineering

Fellow, American Geophysical Union

Fellow, Geological Society of America

Geological Society of America, Meinzer Award, 2014, advancing the science of Hydrogeology.

Prince Sultan bin Abdulaziz International Prize for Water, 2012**,** Fifth Award Groundwater Prize, for contributions to understanding groundwater contamination.

M. King Hubbert Award, 2008, National Groundwater Association (NGWA) prize for science or engineering contributions to the groundwater industry.

Wonking-Class Hero, Miller-McCune Magazine.

Oliver Lectureship, Jackson School of Geosciences, University of Texas, 2009.

Freeman Lecturer, Boston Society of Civil Engineers and Mass. Inst. of Technology, 2003.

Science Prize for Online Resources for Education, American Association of the Advancement of Sciences (AAAS). Member of Harvard-Smithsonian team that produced the environmental science curriculum, *The Habitable Planet,* funded by the Annenberg Foundation, 2010.

National Science Foundation Career Award, 1999.

ACTIVITIES and SERVICES

- Editorials and Policy Critiques:
  New York Times OpEd, *Every Dollar Spent on this Climate Technology is a Waste*
  Wall Street Journal, *What Is the Future for Carbon Capture Technology?*
  Bulletin of Atomic Scientists, *Direct air capture: An expensive distraction from real climate solutions*
  PBS Frontline, *The Power of Big Oil*, April 2022
  BBC This World, *Big Oil Versus the World*, August 2022
  CBS News, Nano (German science TV show), Norwegian TV interview
- Founding member, *Science Roundtable on Carbon Capture and Storage*. Presentations and Convenings: *Funders Collaborative on Oil and Gas, Texas Funders Event, Ohio River Valley Funders, Society of Environmental Journalists, Climate Strategy Group, Environmental Grantmakers Association, Gulf Coast CCS*
- Co-developed curriculum for high school, Massachusetts Humanities, *Narrating Local Climate Change: Telling Current and Future MA Stories with Eco Memoir and Eco Speculation*,
- Oversight Panel for Critical Zone Observatories, National Science Foundation.
- National Academy of Science committee to review the everglades aquifer storage and recovery program.
- Visiting committee to review the department of Earth Systems Science in the school at Stanford.
- Content for the film “Haze, It’s Complicated” a documentary film about peat fires in Southeast Asia. Best Feature, 11th Kuala Lumpur Eco Film Festival, 2018; Award of Excellence, IndiFest 2018 Film Awards
- AAAS expert panel to evaluate and guide the Vermont Experimental Program to Stimulate Competitive Environmental Research (EPSCOR).
- Faculty Policy Committee, MIT.
- Board of Directors *the Arsenic Foundation* (residing at Harvard University)
- Board of Directors *Sea Change* (a nonprofit organization mediating environmental disputes).
- Panel member for the Department of Energy’s workshop *Basic Research for Geosciences; Facilitating 21st Century Energy Systems*.
- Technical Outreach in Service to Communities (TOSC) appointed by EPA for Cape Cod.
- Organizer of National Science Foundation sponsored workshop on the future of the Ganges-Brahmaputra Delta, held in Bangladesh.
- Member of National Science Foundation expert panel to assess the effects of the 2004 tsunami on Sri Lanka’s groundwater.
- Associate Editor for *Water Resources Research* and *Hydrogeology*.
- Reviewer for *Nature*, *Science*, *Proceedings of the National Academy of Science*, and many journals.
- Organizer for conferences and workshops including: Asian School of the Environment Workshop, *Peatlands of Southeast Asia*, 2020, Chapman Conference, *Arsenic in Asian Environments,* 2009;

Bringing Groundwater Quality Research to the Watershed Scale, IAH/AIH, IAHS/AISH, Ontario, 2004; *International Conference on Finite Element Models, Solving Groundwater Problems*, Czech Republic, 2004; *Reactive Transport*, AGU/EGU/HIS *International Workshop on Groundwater Hydrology*, Berkeley, 2002; Gordon Conference on *Flow in Porous Media*, 2002.

START-UP ENGAGEMENT

- C12, a private venture for geologic carbon sequestration that raised over $200 million. Flamed out after the precipitous drop in the cost of renewables made carbon capture and sequestration uneconomic and unnecessary for emissions reduction.
- Graphyte, a private venture for sequestering carbon in farm waste
- KoBold Metals, a private venture for finding critical minerals using advanced statistical methods

CONSULTING

- Expert witness for water rights in case in Santa Barbara.
- Government of Singapore (PUB), oversight of the assessment of Singapore's groundwater resources.
- Analysis of coal ash basins in the Southeast US, NAACP.
- Review of US Army's plan for remediating arsenic contamination.
- World Bank, India, development of hydrologic modeling capabilities in India, member of Hydrology Expert Facility.
- Kronick, Moskovitz, Tiedemann and Girard, expert testimony to the California Water Board.
- Industrial Economics, Cambridge Massachusetts, evaluation of proposed EPA regulations for: (i) the paint industry, (ii) fly ash disposal from power plants, and; (iii) Re-use of waste foundry sands.

PATENTS

Characterization of Subsurface CO_2 Sequestration Reservoirs by Air Injection, U.S. Patent No. 61/241,504, used to test potential sites for CO_2 sequestration.

High-Resolution Differential Pressure Sensor, U.S. Patent No. 12/611,454, used to record continuous measurements of groundwater fluxes.

JOURNAL PUBLICATIONS SINCE 2000

Peatlands and Wetlands

Insights into the persistence and vulnerability of tropical peat carbon stocks from a long-term field decomposition experiment. *Global Biogeochemical Cycles*. (2026). (CR Perryman, MR Baysinger, AR Cobb, L Gandois, JP Chanton, T Evans, A Chua, J Eri, Haji Bohari bin Haji Idi, J M Incham, J P Pu, A Teo, Ramasamy Anak Zulkiflee, CF Harvey, AM Hoyt)

Quantifying Subsidence in Tropical Peatlands, Remote Sensing for Characterization of Geohazards and Natural Resources. 2024. (AM Hoyt, E Chaussard, SS Seppalainen, CF Harvey).

A Unified Explanation for the Morphology and Carbon Storage of Raised Peatlands. *Nature*. 2024. (Cobb, A.R. Dommain, R. Yeap, K. Cao, H. Dadap, N.C. Bookhagen, B. Glaser, P.H. Harvey, C.F.).

Improved terrain estimation from spaceborne lidar in tropical peatlands using spatial filtering. *Science of Remote Sensing*. 2023. (AR Cobb, R Dommain, RS Sukri, F Metali, B Bookhagen, CF Harvey).

Processes Controlling Methane Emissions from a Tropical Peatland Drainage Canal. *JGR Biogeosciences*. 2023. (Sommers L, Hoyt A. Cobb A. Isnin S. Suhip, M. A, Sukri R. Ganois L. Harvey C.).

Latitude, elevation, and mean annual temperature predict peat organic matter chemistry at a global scale. *Global Biogeochemical Cycles*. 2022. (Verbeke, B.A et al.).

Variation in carbon and nitrogen concentrations among peatland categories at the global scale. *PLOS ONE.* 2022*. (Watmough, S.A et al.)*.

Climate change-induced peatland drying in Southeast Asia. *Environmental Research Letters* 2022*. (Nathan C Dadap, Alexander R Cobb, Alison M Hoyt, Charles F Harvey, Andrew F Feldman, Eun-Soon Im, Alexandra G Konings)*.

Drainage Canals in Southeast Asian Peatlands Increase Carbon Emissions. *AGU Advances*. 2021. (Nathan C. Dadap, Alison M. Hoyt, Alexander R. Cobb, Doruk Oner, Mateusz Kozinski, Pascal V. Fua, Krishna Rao, Charles F. Harvey, Alexandra G. Konings).

Carbon Storage Capacity of Tropical Peatlands in Natural and Artificial Drainage Networks. *Environmental Research Letters*. 2020. (Cobb, Alexander R. Rene Dommain, Fangyi Tan, Hwee En Heng, C.F. Harvey).

Widespread Subsidence and Carbon Emissions across Southeast Asian Peatlands. *Nature Geoscience*. 2020. (Alison Hoyt, E. Chaussard, and Charles F Harvey).

Scalar Simulation and Parameterization of Water-Table Dynamics in Tropical Peatlands.*Water Resources Research*. 2019. (Alexander Cobb and Charles F Harvey).

Satellite Soil Moisture Observations Predict Burned Area in Southeast Asian Peatlands. *Environmental Research Letters*. 2019. (Dadap, Nathan C, Alexander R Cobb, Alison M Hoyt, Charles F Harvey, and Alexandra G Konings.).

From Canals to the Coast: Dissolved Organic Matter and Trace Metal Composition in Rivers Draining Degraded Tropical Peatlands in Indonesia. *Biogeosciences Discussions*. 2020. (Gandois, Laure, Alison M Hoyt, Stéphane Mounier, Gaël Le Roux, Charles Franklin Harvey, Adrien Claustres, Mohammed Nuriman, and Gusti Anshari).

CO2 Emissions from an Undrained Tropical Peatland: Interacting Influences of Temperature, Shading and Water Table Depth.*Global Change Biology*. 2019. (Alison M. Hoyt, Laure Gandois, Jangarun Eri, Fuu Ming Kai, Charles F. Harvey, Alexander R. Cobb).

Tropical Peatland Carbon Storage Linked to.*Global Latitudinal Trends in Peat Recalcitrance. 20, Nature Communications.* 2018*.* (Hodgkins, S.B. C.J. Richardson, R. Dommain, H. Wang, P.H. Glaser, B. Verbeke, B. Winkler, B. Rose, A.R Cobb, V.I. Rich, M. Missilmani, C.F. Harvey).

Smoke Radiocarbon Measurements from Indonesian Fires Provide Evidence for Burning of Millennia-Aged Peat. *Proceedings of the National Academy of Sciencesss*. 2018. (Wiggins, E. Czimczik, G.M. Santos, Y. Chen, X. Xu, S.R. Holden, J.T. Randerson, C.F. Harvey, F.M Kai, E.Y. Liya).

How Temporal Patterns in Rainfall Determine the Geomorphology and Carbon Fluxes of Tropical Peatlands, Proceedings of the National Academy of.*Sciencess*. 2017. (Cobb, A. R. A. Hoyt, L. Gandois, J. Eri, R. Dommain, K. A. Salim, Fuu Ming Kai, Nur Haji Su'ut, C. F. Harvey).

Denial of Long-Term Issues with Agriculture on Tropical Peatlands Will Have Devastating Consequences.*Global Change Biology.* 2017. (Wijedasa, L. S. et al.).

Temperature and Burning History Affect Emissions of Greenhouse Gases and Aerosol Particles from Tropical Peatland Fire.*Journal of Geophysical Research-Atmospheres.* 2017. (Kuwata, Mikinori, Fuu Ming Kai, Liudongqing Yang, Masayuki Itoh, Haris Gunawan, and Charles F Harvey).

Review of the Everglades Aquifer Storage and Recovery Regional Study, National Academies Press. 2015. (Saiers, J. Harvey, C. F. Hopkins, W. Potter, K.W. Price, R. Pyne, R. Robinson, L. Screaton, E. Trussell, R.).

Forest dynamics and tip-up pools drive pulses of high carbon accumulation rates in a tropical peat dome in Borneo. *Biogeochemistry.* 2015*. (Dommain R. A. R. Cobb, H. Joosten, P. H. Glaser, A. F.L. Chua, L. Gandois, F. M. Kai, A. Noren, K. Abu Salim, N. S.H. Su'ut, C. F. Harvey)*

Crab Burrows as Conduits for Groundwater-Surface water Exchange in Bangladesh. *Geophysical Research Letters*. 2014. (M. Stahl, M. H. Tarek, D. Yeo, A. B. M. Badruzzaman, C. F. Harvey).

Carbon fluxes from an urban tropical grassland.*Environmental Pollution*. 2014. (Ng BJL, Hutyra LR, Nguyen H, Cobb AR, Kai FM, Harvey C F, Gandois L).

Origin, composition, and transformation of dissolved organic matter in tropical peatlands,*Geochimica et Cosmochimica Acta*. 2014. (Gandois, L. R. Teisserenc, A. R. Cobb, H. I. Chieng, L. Lim, A. S. Kamariah and C. F. Harvey).

An Off-Grid PV Power System for Meteorological and Eddy Covariance Flux Station in Kranji, Singapore,*Energy Procedia*. 2013. (FM Kai, A Cobb, AFL Chua, MH Tee, B Ng, L Gandois, C Harvey).

Impact of Deforestation on Solid and Dissolved Organic Matter Characteristics of Tropical Peat Forests: Implications for Carbon Release. *Biogeochemistry*. 2012. (L. Gandois, A. R. Cobb, I. Chieng Hei, L. B. L. Lim, K. Abu Salim, C. F. Harvey).

Carbon Capture

Tracing sources of funds used to lobby the US government about carbon capture, use, and storage. *Environmental Science & Policy*. (2025) (L E Gulden, C Harvey.

Which Climate Subsidy Is the Best Return on U.S. Federal Investment: CCS or Rooftop Solar? *Journal of Climate Resilience and Justice.* 2025. (L Gulden, D Wamsted, C F Harvey)

Philanthropy Is Wasting Time and Money on Carbon Capture. *Inside Philanthropy*. 2024. (Robert D. Bullard Charles F. Harvey and Bakeyah S. Nelson).

Every Dollar Spent on This Climate Technology Is a Waste. *New York Times, guest editorial*. 2022. (C Harvey, K House).

Direct air capture: An expensive distraction from real climate solutions. *Bulletin of Atomic Scientists.* 2021. (*K. House,J. Goldman, CF. Harvey*).

The Immobility of CO2 in Marine Sediments Beneath 1500 Meters of Water. *Chem Sus Chem*. 2010. (House, K.Z. A. Bilgin. C. F. Harvey, D. P. Schrag).

The Energy Penalty of Post-Combustion CO2 Capture and Storage and Implications for Retrofitting the Installed Base,*Energy and Environmental Science*. 2009. (K. House, C. F. Harvey, M. Aziz, D. Schrag).

Permanent Carbon Dioxide Storage in Deep-Sea Sediments,*Proceedings of the National Academy of Science.*2006. (K. House, D. Schrag, C. F. Harvey, K. Lackner).

Coastal Groundwater

Transient Groundwater Dynamics in a Coastal Aquifer: Tides, the Lunar Cycle and the Beach Profile. *Water Resources Research*. 2013. (E. Abarca, H Karam, H. F. Hemond, C. F. Harvey).

Patterns and Variability of Groundwater Flow and Radium Activity at the Coast: A Case Study from Cape Cod. *Marine Chemistry*. 2011. (Michael, H. M. Charette, C. F. Harvey).

Marine Electrical Resistivity Imaging of Submarine Ground-Water Discharge: Sensitivity Analysis and Application in Waquoit Bay, Massachusetts, USA. *Hydrogeology*. 2010. (R. D. Henderson, F. D. Day-Lewis, E. Abarca, C. F. Harvey, H. N. Karam, L. Liu, J.W. Lane, Jr.).

Investigation of Aquifer-Estuary Interaction Using Wavelet Analysis of Fiber-Optic Temperature Data.*Geophysical Research Letters*. 2009. (R.D. Henderson, F.D. Day-Lewis, C.F. Harvey).

A Differential Pressure Instrument with Wireless Telemetry for In-Situ Measurement of Fluid Flow across Sediment-Water Boundaries. *Sensors*. 2009. (A. Gardner, H. Karam, A. Mulligan, C.F. Harvey, T. Hammar, and H. F. Hemond).

Seasonal Water Exchange between Aquifers and the Coastal Ocean. *Nature,*2005. (H. Michael, A. Mulligan

and C. F. Harvey).

Characterizing Submarine Groundwater Discharge. *Geophysical Research Letters.* 2003. *(Michael, H. Lubetsky, J. and Harvey, C. F.)*.

Bangladesh, Vietnam, and Arsenic Contamination

Radiocarbon analysis of RNA, DIC, DOC and CH4 to constrain the sustainability of pumping Pleistocene aquifers in Bangladesh. *Arsenic in the Environment: Bridging Science to Practice for Sustainable Water Supply*. 2023. (BJ Mailloux, MR Mozumder, BC Bostick, T Ellis, C Harvey, G Slater).

Shift in groundwater recharge of the Bengal Basin from rainfall to surface water. *Communications Earth & Environment*. 2023. (Y Jameel, M Stahl, H Michael, BC Bostick, MS Steckler, P Schlosser, CF Harvey).

Evaluation of a Field Kit for Testing Arsenic in Paddy Soil Contaminated by Irrigation Water.*Geoderma*. 2021. (Linden B. Huhmann and Charles F. Harvey and Jason Gross and Anjal Uddin and Imtiaz Choudhury and Kazi M. Ahmed and John M. Duxbury and Benjamin Bostick and Alexander Van Geen).

A mass-balance approach to evaluate arsenic intake and excretion in different populations. *Environment International.* 2022. (D Beene, P Collender, A Cardenas, C Harvey, L Huhmann, Y Lin, J Lewis).

Well-Switching to Reduce Arsenic Exposure in Bangladesh: Making the Most of Inaccurate Field Kit Measurements.*Geo Health*. 2021. (Yusuf Jameel, Rajib Mozumder, Alexander van Geen, and Charles F. Harvey).

A Mass-Balance Model to Assess Arsenic Exposure from Multiple Wells in Bangladesh. *Journal of Exposure Science & Environmental Epidemiology*. 2022. (Linden Huhmann, Charles F Harvey, Ana Navas-Acien, Joseph Graziano, Vesna Slavkovich, Yu Chen, Maria Argos, Habibul Ahsan, Alexander van Geen).

Quantifying Riverine Recharge Impacts on Redox Conditions and Arsenic Release in.Groundwater Aquifers Along the Red River, Vietnam*. Water Resources Research*. 2019. (Nghiem, Athena A, Mason O Stahl, Brian J Mailloux, Tran Thi Mai, Pham Thi Trang, Pham Hung Viet, Charles F Harvey, Alexander Van Geen, and Benjamin C Bostick).

Inversion of High-Arsenic Soil for Improved Rice Yield in Bangladesh. *Environmental Science & Technology*. 2019. (Huhmann, B. C. F Harvey, Anjal Uddin, I. Choudhury, Kazi Matin Ahmed, J. Duxbury, T. Ellis, and A. Van Geen.).

Changes in Arsenic Exposure in Araihazar, Bangladesh from through 2015 Following a Blanket Well Testing and Education Campaign.*Environment International,*2019. (Huhmann, Brittany L, Charles F Harvey, Ana Navas-Acien, Joseph Graziano, Faruque Parvez, Yu Chen, Maria Argos, Alauddin Ahmed, A K M Rabiul Hasan, and Habibul Ahsan).

Field Study of Rice Yield Diminished by Soil Arsenic in Bangladesh. *Environmental Science and Technology*. 2017. (Huhmann, B. L. C. F. Harvey, Anjal Uddin, I. Choudhury, Kazi M Ahmed, J. M Duxbury, B. C Bostick, and A. Van Geen.).

Geochemical Transformations beneath Man-Made Ponds: Implications for Arsenic Mobilization in South Asian Aquifers. *Geochimica et Cosmochimica Acta*. 2008, (M. Stahl and C.F. Harvey).

Origin of. Groundwater Arsenic in a Rural Pleistocene Aquifer in Bangladesh Depressurized by Distal Municipal Pumping*. Water Resources Research*. *2019.* (Mozumder, M. R. H. Michael, H. A. Mihajlov, I. Khan, M. R. Knappett, P. S. K. Bostick, B. C. Mailloux, B. J. Ahmed, K. M. Choudhury, I. Koffman, T. Ellis, T. Whaley-Martin, K. San Pedro, R. Slater, G. Stute, M. Schlosser, P. & Geen, A.).

High-Arsenic.Groundwater in the Southwestern Bengal Basin Caused by a Controlled Deep Flow System. *Geophysical Research Letters.* 2019*.* (Khan, Mahfuzur R, H. A. Michael, B. Nath, B. L. Huhmann, C. F. Harvey, A. Mukherjee, I. Choudhury, M. Chakraborty, M. S. Ullah, K. M. Ahmed, S. L. Goodbred, P. Schlosser, B. C. Bostick, B. J. Mailloux, T. Ellis, A. van Geen).

Arsenic Oxyanion Binding to NOM from Dung and Aquaculture Pond Sediments in Bangladesh: Importance of Site-Specific Binding Constants. *Applied Geochemistry.* 2017. (Lin, Tiffany Y, S. Hafeznezami, L. Rice, J. Lee, A. Maki, T. Sevilla, M. Stahl, R. Neumann, C.F. Harvey, and IH M. Suffet. “).

Megacity Pumping and Preferential Flow Threaten Groundwater Quality, *Nature Communications*. 2016. (Khan, M. R. et al.).

Vulnerability of Low-Arsenic Aquifers to Municipal Pumping in Bangladesh, *Journal of Hydrology.*2016. (Knappett, P. et al.).

River Bank Geomorphology Controls Groundwater Arsenic Concentrations in Aquifers Adjacent to the Red River, Hanoi Vietnam. *Water Resources Research*. 2016. (Stahl, M. O. Harvey, C. F. Van Geen, A. Sun, J. Thi Kim Trang, P. Mai Lan, V. et al.).

Retardation of arsenic transport through a Pleistocene aquifer. *Nature*. 2013. (A. van Geen, B. Bostick, P. Trang, V. Lan, N. Mai, P. Manh, P. Viet, K. Radloff, Z. Aziz, J. Mey, M. Stahl, C. F. Harvey, P. Oates, B. Weinman, C. Stengel, F. Frei, R. Kipfer, M. Berg).

Rice Field Geochemistry and Hydrology: An Explanation for Why Groundwater Irrigated Fields in Bangladesh are Net Sinks of Arsenic from Groundwater, Environmental.*Science and Technology*. 2011. (Neumann, R.B. A.P. St. Vincent, L. C. Roberts, A. B. M. Badruzzaman, A. Ali, and C. F. Harvey).

Anthropogenic Influences on Groundwater Arsenic Concentrations in Bangladesh. *Nature Geoscience*. 2010. (R. B. Neumann, K. N. Ashfaque, A. B. M. Badruzzaman, M. Ashraf Ali, J. K. Shoemaker and C. F. Harvey).

The Hydrology of a Groundwater-Irrigated Rice Field in Bangladesh: Seasonal and Daily Mechanisms of Infiltration. *Water Resources Research*. 2009. (R. B. Neumann, M. L. Polizzotto, A. B. M. Badruzzaman, M. Ashraf Ali, Z. Zhang, Zhongyuan Zhang1, C. F. Harvey).

Environmental Science: Poisoned Waters Traced to Source. *Nature*. 2008. (C. F. Harvey).

Groundwater Dynamics and Arsenic Contamination in Bangladesh. *Chemical Geology*. 2006. (Harvey, C. F. K. N. Ashfaque, W. Yu, A.B.M. Badruzzaman, M. Ashraf Ali, P. M. Oates, H. A. Michael, R. B. Neumann, R. Beckie, S. Islam and M. F. Ahmed).

Solid-Phases and Desorption Processes of Arsenic within Bangladesh Sediments, *Chemical Geology*. 2006. (M. L. Polizzotto, C. F. Harvey, G. Li, B. Badruzzman, A. Ali, M. Newville, S. Sutton and S. Fendorf).

Groundwater Dynamics and Arsenic Mobilization in Bangladesh Assessed Using Noble Gases and Tritium, Environmental. *Science and Technology.* 2006. *(S. Klump, R. Kipfer, O. Cirpka, C. F. Harvey, K. Ashfaque, A.B.M. Badruzzaman, S. Hug and D. Imboden)*.

Processes Conducive to the Release and Transport of Arsenic into Aquifers of Bangladesh. *Proceedings of the National Academy of Science.* 2005. *(M. L. Polizzotto, C. F. Harvey, S. R. Sutton and S. Fendorf)*.

Arsenic: Its Biogeochemistry and Transport in Groundwater, in "Biogeochemical Cycles of the Elements", Vol. 43 of Met. Ions Biol. Syst. A. Sigel, H. Sigel, and R. K. O. Sigel, eds. M. Dekker, New York. 2005. (C.F. Harvey, and R. Beckie).

Groundwater Arsenic Contamination onthe Ganges Delta: Biogeochemistry, Hydrology, Human Perturbations, and Human Suffering on a Large Scale*. Comptes-Rendus: Geoscience.* 2005. (Harvey, C. F. C. Swartz, B. Badruzzman, N. Keon, W. Yu, A. Ali, J. Jay, R. Beckie)

Subsurface Geochemistry and Arsenic Mobility in Bangladesh*, Geochimica Acta.* 2004. *(Swartz, C.H. Keon, N.E. Badruzzman, B. Ali, A. Brabander, D, Jay, J. Islam, S. Hemond, H.F. Harvey, C.F.)*.

Arsenic in Groundwater in Bangladesh: A Geostatistical and Epidemiological Framework for Evaluating Health Effects and Potential Remedies. *Water Resources Research.* 2003. (Yu, W. Harvey, C. F. and Harvey, C.M.).

Arsenic Mobility and Groundwater Extraction in Bangladesh. *Science. 2*002. (Harvey, C. F. Swartz, C.H.

Badruzzman, B. Keon, N.E. Yu. W. Ali, A. Jay, J. Beckie, R. Niedan, V. Brabander, D, Oates, P. Ahsfaque, K. Islam, S. Hemond, H.F. Ahmed, F.).

Groundwater Flow in the Ganges Delta. *Science, Technical Comment.* 2002. (Harvey, C. F.).

Possible Causes of High Arsenic Concentrations in the Well Water of Bangladesh,*Environmental Sciences,*2001. *(Harvey, C.F.)*.

Evaluation of an Arsenic Sequential Extraction Method for Evaluating Mobility in Sediments. *Environmental Science and Technology.* 2001. (Keon, N. E. Swartz, C. H. Brabander, D. J. Harvey, C. F. Hemond, H. F.).

Hydrogeology and Reactive Transport

Detecting Well Casing Leaks in Bangladesh Using a Salt Spiking Method. *Groundwater*. 2014. (M.O. Stahl, J. B. Ong, C.F. Harvey, C. D. Johnson, A.B.M. Badruzzaman, M.H. Tarek, A. van Geen, J. A. Anderson, J. W. Lane).

Using Performance Reference Compounds in Polyethylene Passive Samplers to Deduce Sediment Porewater Concentrations for Numerous Target Chemicals,*Environmental Science and Technology*. 2009. (L. Fernandez, C.F. Harvey, P.M. Gschwend).

Acceptance of M.*King Hubbert Award, Groundwater*. 2009. (C. F. Harvey).

The Effects of Dual-Domain Mass Transfer on the Tritium-Helium-3 Groundwater Dating Method. *Environmental Science and Technology*. 2008. (R. Neumann, E. La Bolle and C. F. Harvey).

A Colorimetric Reaction to Quantify Fluid Mixing, *Experiments in Fluids.* 2006. (P. M. Oates and C. F. Harvey).

Comment on Investigating the Macrodispersion Experiment(MADE)site in Columbus, Mississippi, using a three-dimensional inverse flow and transport model. *Water Resources Research.* 2006. *(Molz, F. J. C. Zheng, S. M. Gorelick, and C. F. Harvey)*.

Shedding Light on Reactive Microbial Transport in Porous Media: Experimental Visualization and Numerical Modeling of Pseudomonas Fluorescens 5RL Bioluminescence, *Contaminant Hydrology*. 2005. (P. M. Oates, C. Castenson, C. F. Harvey, M. Polz, and P. Culligan).

Experimental Visualization of Solute Transport and Mass Transfer Processes in Spatially Heterogeneous Porous Media, *Environmental Science and Technology.* 2004. *(Zinn, B. C. F. Harvey, L. Meigs, R. Haggerty, W. Peplinski, and C. Freiherr von Schwerin)*.

What Controls the Apparent Timescale of Solute Mass Transfer in Aquifers and Soils? A Comparison of Diverse Experimental Results.*Water Resources Research*. 2004. (Haggerty, R. Harvey, C.F. Freiherr von Schwerin, C. Meigs, L.).

GRANTS AND FELLOWSHIPS

Ecosystem on the Edge: How Coastal Marsh Plants and Microbes Thrive in an Oscillating Environment, **Simons Foundation**, (2024-2028)

Environmental Justice and Industrial Carbon Capture and Storage, **Rockefeller Foundation**, (2024-2025)

Cross-scale methane dynamics at terrestrial-aquatic interfaces in temperate forests, **Dept. of Energy,** (2023-2027)

Supply Chain Analysis to Thwart Illegal Logging: Machine Learning-based Monitoring and Strategic Network Inspection, **National Science Foundation**, (2021-2025).

Collaborative Research: Hydrologic Disturbance in Tropical Peatlands: Linking Drainage, Soil Moisture, Flammability, and Carbon Fluxes, **National Science Foundation**, (2019-2024).

Tools for Managing Tropical Peatlands and Controlling Haze in Southeast Asia, **Singapore National Research Foundation**, (2017–2023).

Competing Demands and Future Vulnerability of Groundwater: Drinking Water Quality and Food Security in Arsenic-Impacted South and Southeast Asia, Coupled Human Natural Processes (CHN), **National Science Foundation**, (2015-2020).

Changes in river-aquifer exchange induced by groundwater pumping, and their effect on arsenic contamination in the Red River Delta, Vietnam, **National Science Foundation**, (2015–2018).

Health Effects and Geochemistry of Arsenic and Manganese, National Institute for Environmental Health, (2012-2017).

Center for Environmental Modeling and Sensing (CENSAM), Carbon Fluxes in and out of Tropical Forests, **Singapore National Research Foundation**, (2008–2017).

Water and Carbon Dynamics in Tropical Peat Lands, **National Science Foundation**, (2011–2014).

Collaborative Research: Enhancing the sustainability of groundwater pumping from low-arsenic aquifers in southern Asia - a case-study in Vietnam south of Hanoi, **National Science Foundation**, (2009–2012).

Hydrogeology of Kuwait, **Kuwait-MIT Center for Natural Resources and Environment**, (2009).

Environmental Sensor Networks in Asian Rice Fields, **National Science Foundation**, (2006–2009).

Saltwater and Freshwater Fluxes through Coastal Aquifers: Multiple Time Scales of Terrestrial and Oceanic Forcing, **National Science Foundation**, (2006–2009).

CO_2 Sequestration Beneath the Deep-Sea Floor, **Department of Energy**, (2006 –2007).

Freshwater/Saltwater Interaction at the Coast, **Sea Grant, Woods Hole Oceanographic Institute,** (2006 –2008).

Groundwater Dynamics and Arsenic Contamination in the Ganges Delta: Irrigated Agriculture, Solute Transport, and Aquifer Flushing, **National Science Foundation**, (2005 –2009).

Collaborative Research: Mathematical and Experimental Analysis of Transport Phenomena in Highly Heterogeneous Porous Media, **National Science Foundation,** (2003 –2006).

Rotting Foundations and Groundwater Dynamics Beneath Boston, **City of Boston**, (2003).

Tracking Arsenic through the Food Chain, **National Institute of Health**, (2002 – 2003).

Arsenic Contaminated Groundwater in Bangladesh: Characterizing the Source, Mobilization, and Transport, **National Science Foundation**, (2000 - 2003).

A Sustainable Water Supply System in an Arsenic-Contaminated Asian Environments, **Alliance for Global Sustainability**, (2000 - 2002).

Revisiting two Basic Processes in Hydrogeology: Solute Transport in Heterogeneous Formations and Chemical Mixing in Porous Media, **National Science Foundation CAREER**, (1999 - 2004)**.**

Transport Visualization for Studying Mass Transfer and Solute Transport in Permeable Media Upscaling the Effects of Diffusion in Natural Soils and Aquifers, **Department of Energy (Basic Energy Science),** (2000 - 2003).

Investigating Contaminant inputs via Submarine Groundwater Discharge to Coastal Waters using Radium Isotopes, **Office of Naval Research** (1999 – 2001).

A Decision Analysis Framework for Groundwater Remediation, **Environmental Protection Agency (NCERQA)**, (1997 - 2000).

Arsenic Transport through Heterogeneous Sediments, **National Institute of Health**, (1998 - 2000).

Upscaling Diffusion in Natural Soils and Aquifers, **Department of Energy**, (1998 – 2001).

Water Resources, **Merck Foundation Grant**, (1996 - 1997).

SELECTED INVITED TALKS

Peatland Hydrology, Ecology, and Carbon Dynamics, Dartmouth, 2025.

Controlling Greenhouse Gases, Moore Lecture, University of Virginia, 2024.

Carbon Capture & Storage: More Useful for Producing Oil than Cutting Greenhouse Gas Emissions?, Cornel University, Atkinson Center for Sustainability, Cornell, 2023.

Managing Tropical Peatlands, Cornel University, Ecology Symposium, 2023.

The Necromass of Borneo, Harvard University, Earth and Planetary Science Colloquium, 2022.

The Mathematical Simplicity of Peatlands, Princeton University, CEE Seminar, 2022.

Carbon Capture and Sequestration: Better for Producing Oil than Reducing Emissions? DOER School of Sustainability, Stanford University, 2022.

Carbon Capture and Sequestration: What Value for Fighting Climate Change?, MIT Energy Initiative Annual Research Conference, 2022.

Unresolved Scientific Questions are the Largest Barrier to Successful Natural Climate Solutions, Imperial College, 2022.

Peatland Geomorphology and Carbon Fluxes, University of Virginia, 2020.

Physical Controls on Methane Fluxes from Peatlands across the World, University of British Columbia, 2018.

What Drives Saline Circulation Cells in Coastal Aquifers? An Energy Balance for Density-Driven Groundwater Systems, 21st Hubbert Quorum, 2018.

Carbon Dynamics and Hydrologic Processes in Peatlands, Columbia University, Workshop on the Future of Peatlands, 2015.

The Mathematical Simplicity of Tropical Peat Swamp Forests, U. Cal. Berkeley, Earth Sciences Lecture Series, 2014; Stanford University, Woods Institute for the Environment, 2014.

Tropical Peat Forests: Where the Water Table Creates the Land Surface, 20th Hubbert Quorum, USGS Menlo Park, 2012.

Tropical Peat Forests, Presentation to the Minister of Industry and Primary Resources, and the Minister of Forestry of Brunei and the Heart of Borneo Commission, 2012.

Oliver Lectures, University of Texas, 2010:

Origins and Solutions of the Arsenic Crisis in Southeast Asia
Coastal Groundwater Dynamics and Biogeochemistry
Geologic Carbon Sequestration: Comparing Terrestrial and Submarine Injection

Lectures at Marie Curie Symposium (European Union), Corsica, 2010:

Reactive Solute Transport: Laboratory Visualization Experiments to Construct and Test Stochastic Theory
Coastal Groundwater Dynamics and Biogeochemistry
Geologic Carbon Sequestration: Comparing Terrestrial and Submarine Injection

The Cause of Severe Arsenic Contamination in Bangladesh, Chapman Conference, *Arsenic in Asian Environments,* 2009.

Hydrogeology is the Key to Understanding the Arsenic Crisis on the Ganges Delta, Consortium of Universities for the Advancement of Hydrologic Science, Cyberseminars (on-line live seminar archived at: http://www.cuahsi.org/sem-archive.html), 2008.

Toxics in Groundwater, Symposium on the Future of Environmental Science, Harvard School of Public Health, 2008.

Chemical Spreading, Mixing and Reaction in Groundwater, Gordon Research Conference on Flow in Porous Media, 2006.

The Hydrology and Biogeochemistry of the Arsenic Crisis in Bangladesh, Harvard University, Series on the Global Environment, 2006.

The Arsenic Crisis in Bangladesh, U.S. Geological Survey, Reston VA, 2006.

Reactive Transport in Porous Media, Harvard Geophysics and Rock Mechanics Series, 2006.

Solute Mixing and Chemical Reaction in Porous Media, DFG-NSF Workshop on Geochemical Gradients, sponsored by the Deutsche Forschungsgemeinschaft, 2004.

The Crisis of Arsenic Contamination in Bangladesh, World Water Symposium, Davis CA, 2004.
Water Quality and Human Health: Bangladesh as a Case Study, Public and Private Sector Collaboration in Addressing the UN Millennium Water and Sanitation Goals, American Academy of Arts and Sciences Cambridge, MA, 2003.
The Arsenic Crisis on the Ganges Delta: Hydrology, Biogeochemistry, Human Perturbations, and Human Suffering on a Large Scale, Colloque sur l'EAU, French Academy of Science, 2003.
The Arsenic Crisis in Bangladesh, ETH (EAWAG), Dubendorf, Switzerland, 2003.
Solute Transport and Reaction in Groundwater, Henry Darcy's 200th Birthday: Fundamental Advancements, Observation and Analysis, Geological Society America, Seattle, 2003.
Direct Visualization of Reactive Transport: Mixing at the Pore-Scale and at the Darcy-Scale, Conceptual Model Development for Subsurface Reactive Transport Modeling of Inorganic Contaminants, Radionuclides, and Nutrients, Federal Interagency Steering Committee on Multimedia Environmental Modeling Workshop, Albuquerque, NM, 2003.

GRANTS AND FELLOWSHIPS

Ecosystem on the Edge: How Coastal Marsh Plants and Microbes Thrive in an Oscillating Environment, **Simons Foundation**, (2024-2028)
Environmental Justice and Industrial Carbon Capture and Storage, **Rockefeller Foundation**, (2024-2025)
Cross-scale methane dynamics at terrestrial-aquatic interfaces in temperate forests, **Dept. of Energy,** (2023-2027)
Supply Chain Analysis to Thwart Illegal Logging: Machine Learning-based Monitoring and Strategic Network Inspection, **National Science Foundation**, (2021-2025).
Collaborative Research: Hydrologic Disturbance in Tropical Peatlands: Linking Drainage, Soil Moisture, Flammability, and Carbon Fluxes, **National Science Foundation**, (2019-2024).
Tools for Managing Tropical Peatlands and Controlling Haze in Southeast Asia, **Singapore National Research Foundation**, (2017–2023).
Competing Demands and Future Vulnerability of Groundwater: Drinking Water Quality and Food Security in Arsenic-Impacted South and Southeast Asia, Coupled Human Natural Processes (CHN), **National Science Foundation**, (2015-2020).
Changes in river-aquifer exchange induced by groundwater pumping, and their effect on arsenic contamination in the Red River Delta, Vietnam, **National Science Foundation**, (2015–2018).
Health Effects and Geochemistry of Arsenic and Manganese, National Institute for Environmental Health, (2012-2017).
Center for Environmental Modeling and Sensing (CENSAM), Carbon Fluxes in and out of Tropical Forests, **Singapore National Research Foundation**, (2008–2017).
Water and Carbon Dynamics in Tropical Peat Lands, **National Science Foundation**, (2011–2014).
Collaborative Research: Enhancing the sustainability of groundwater pumping from low-arsenic aquifers in southern Asia - a case-study in Vietnam south of Hanoi, **National Science Foundation**, (2009–2012).
Hydrogeology of Kuwait, **Kuwait-MIT Center for Natural Resources and Environment**, (2009).
Environmental Sensor Networks in Asian Rice Fields, **National Science Foundation**, (2006–2009).
Saltwater and Freshwater Fluxes through Coastal Aquifers: Multiple Time Scales of Terrestrial and Oceanic Forcing, **National Science Foundation**, (2006–2009).
CO_2 Sequestration Beneath the Deep-Sea Floor, **Department of Energy**, (2006 –2007).
Freshwater/Saltwater Interaction at the Coast, **Sea Grant, Woods Hole Oceanographic Institute,** (2006 –2008).

Groundwater Dynamics and Arsenic Contamination in the Ganges Delta: Irrigated Agriculture, Solute Transport, and Aquifer Flushing, **National Science Foundation**, (2005 –2009).
Collaborative Research: Mathematical and Experimental Analysis of Transport Phenomena in Highly Heterogeneous Porous Media, **National Science Foundation,** (2003 –2006).
Rotting Foundations and Groundwater Dynamics Beneath Boston, **City of Boston**, (2003).
Tracking Arsenic through the Food Chain, **National Institute of Health**, (2002 – 2003).
Arsenic Contaminated Groundwater in Bangladesh: Characterizing the Source, Mobilization, and Transport, **National Science Foundation**, (2000 - 2003).
A Sustainable Water Supply System in an Arsenic-Contaminated Asian Environments, **Alliance for Global Sustainability**, (2000 - 2002).
Revisiting two Basic Processes in Hydrogeology: Solute Transport in Heterogeneous Formations and Chemical Mixing in Porous Media, **National Science Foundation CAREER**, (1999 - 2004)**.**
Transport Visualization for Studying Mass Transfer and Solute Transport in Permeable Media Upscaling the Effects of Diffusion in Natural Soils and Aquifers, **Department of Energy (Basic Energy Science),** (2000 - 2003).
Investigating Contaminant inputs via Submarine Groundwater Discharge to Coastal Waters using Radium Isotopes, **Office of Naval Research** (1999 – 2001).
A Decision Analysis Framework for Groundwater Remediation, **Environmental Protection Agency (NCERQA)**, (1997 - 2000).
Arsenic Transport through Heterogeneous Sediments, **National Institute of Health**, (1998 - 2000).
Upscaling Diffusion in Natural Soils and Aquifers, **Department of Energy**, (1998 – 2001).
Water Resources, **Merck Foundation Grant**, (1996 - 1997).

TEACHING and MENTORING

Co-Director of Terrascope, began 2008- 2011. Terrascope is an undergraduate learning community at MIT built on a sequence of classes that investigate a different global environmental issue each year.

Courses Taught

• Graduate Level: *Hydrogeology, Hydrology, Stochastic Hydrology, Geostatistics*
Doctoral Seminars -- *Terrestrial Carbon Fluxes, Reactive Transport, Coastal Hydrology, Mass-Transfer Processes in Groundwater and Soils*

• Undergraduate: *Senior Design Capstone*, *Introduction to Operations Research,*
Ecology II: Engineering for Sustainability,
Mission 2011: Solving Water Crises, Mission 2012: Fixing the Carbon Cycle;
Mission 2013: Solving Food Security; Mission 2015: Strategic Minerals

• Short Courses and Workshops:
Mass Transfer in Groundwater and Soil, Technical University of Denmark
Advanced Groundwater Hydrology, University of Florence
Environmental Challenges for the Bengal Delta, Dhaka Bangladesh, (NSF funded)
Tropical Peat Workshop, Asian School of the Environment, Nanyang Technical University, Singapore, included four-day field trip to Borneo

Doctoral Advisees

• Completed PhD's: Brittany Huhmann, Neha Mehta, Alison Hoyt (Faculty, Stanford University), Mason Stahl (Faculty, Union College), Hanan Karam (Hydrogeologist, ESI UK), Rebecca Neumann (Faculty, University of Washington), Khandaker Ashfaque (Project Engineer, ARCADIS), Peter

Oates (Principle Scientist, QEA), Kurt House (CEO, C12 Energy), Holly Michael (Faculty, Univ. Delaware), Winston Yu (Senior Water Resources Specialist at the World Bank.), Brendan Zinn, Kāʻeo Duarte (Vice president of community engagement and resources, Kamehameha Schools)

- Post-Doctoral Researchers: Lauren Somers, Yusuf Jameel, Christopher Swartz, Jenny Jay, Elena Abarca, Alex Cobb, Kurt House, Laure Gandois, Kai Fu-Ming, Yusuf Jameel, Lauren Somers

EXHIBIT 5

STATE OF NEW MEXICO
NEW MEXICO OIL CONSERVATION COMMISSION

IN THE MATTER OF PROPOSAL TO ADOPT 19.15.41, 19.15.42, and 19.15.43 NMAC; STATEWIDE **CASE NO. 25875**

DIRECT TESTIMONY OF DR. CHARLES HARVEY

Background and Qualifications

Q: Please state your name.

A: Dr. Charles Harvey.

Q: Where are you employed and what is your position?

A: I am a professor at the Massachusetts Institute of Technology (MIT) in Cambridge, Massachusetts.

Q: What is your educational background?

A: I have an undergraduate degree in mathematics from Oberlin College, as well as a Master of Science in applied earth science and Ph.D. in geological and environmental sciences from Stanford University.

Q: Would you please summarize your work experience background?

A: In the late 80's I worked in the Richmond, Virginia office of the US Geological Survey (USGS) for a year before moving to the Menlo Park, California branch of the USGS where I worked for several more years as I pursued graduate degrees at Stanford. After graduating from Stanford I joined the faculty at Harvard, then moved to MIT where I have held a faculty position for 27 years in the Department of Civil and Environmental Engineering. In addition to my research, I have also worked as a consultant across a variety of hydrogeology issues including coal-ash contamination of groundwater, determination of the source of water to deep production

wells, and groundwater resource evaluation. Of most relevance, I consulted for five years with C12 Energy, a start-up carbon capture and storage (CCS) company that my former post-doc, Kurt House, founded in 2008.

Q: Could you summarize your research focus as it relates to subsurface fluid flow, geologic carbon sequestration, and the behavior of carbon dioxide ("CO_2") plumes in saline and hydrocarbon reservoirs?

A: My work focuses on groundwater and spans a range of scientific, engineering, and policy issues. This focus has taken me from the basic physics of porous media flow and reactive solute transport, to geologic carbon storage, to arsenic contamination of groundwater, to groundwater/seawater interaction at the coast, to the ecology of peatlands. In all of these areas, I have experience with both field experiments and numerical-model development. My research on subsurface fluid flow and groundwater contamination was highlighted as a key contribution leading to my recent election to the National Academy of Engineering.

Q: Have you published peer-reviewed work on the risks, monitoring requirements, or long-term performance of geologic carbon storage?

A: Yes.

Q: Please describe your published, peer-reviewed work.

A: I have published over 60 peer-reviewed scientific articles across topics in hydrogeology.

I have published eight articles, including one editorial, on CCS:

- Permanent Carbon Dioxide Storage in Deep-Sea Sediments, *Proceedings of the National Academy of Science.*2006. (K. House, D. Schrag, C. F. Harvey, K. Lackner).
- The Energy Penalty of Post-Combustion CO_2 Capture and Storage and Implications for Retrofitting the Installed Base, *Energy and Environmental Science*. 2009. (K. House, C. F. Harvey, M. Aziz, D. Schrag).
- The Immobility of CO_2 in Marine Sediments Beneath 1500 Meters of Water. *Chem Sus Chem*. 2010. (K. House., A. Bilgin. C. F. Harvey, D. P. Schrag).

- Direct air capture: An expensive distraction from real climate solutions. *Bulletin of Atomic Scientists.* 2021. (K. House, J. Goldman, C. F. Harvey).
- Every Dollar Spent on This Climate Technology Is a Waste. *New York Times, guest editorial*. 2022. (C. Harvey, K. House).
- Philanthropy Is Wasting Time and Money on Carbon Capture. *Inside Philanthropy*. 2024. (Robert D. Bullard, Charles F. Harvey, and Bakeyah S. Nelson).
- Tracing sources of funds used to lobby the US government about carbon capture, use, and storage. *Environmental Science & Policy*. (2025) (L. E. Gulden, C. Harvey).
- Which Climate Subsidy Is the Best Return on U.S. Federal Investment: CCS or Rooftop Solar? *Journal of Climate Resilience and Justice.* 2025. (L. Gulden, D. Wamsted, C. F. Harvey).

In another relevant paper, we showed that conventional methods for generating ensembles of subsurface parameters do not generate preferential conduits.

> When Good Statistical Models of Aquifer Heterogeneity Go Bad: A Comparison of Flow, Dispersion and Mass Transfer in Multigaussian and Connected Conductivity Fields. *Water Resources Research.* 2003. (Zinn, B. and Harvey, C. F.).

The consequence of the findings described in this paper is that the variogram approach as detailed in the United States Environmental Protection Agency's ("EPA") Underground Injection Control Program Class VI Well Site Characterization Guidance will fail to generate realistic permeability fields that create the most risk of CO_2 migration. The underlying statistical model that is used to generate random fields does not allow for connected features of high value.

I have also published on the coupled physics and chemistry of reactive transport in groundwater, relevant to understanding the geochemical effects of plumes of dissolved CO_2:

- Shedding Light on Reactive Microbial Transport in Porous Media: Experimental Visualization and Numerical Modeling of Pseudomonas Fluorescens 5RL Bioluminescence, *Contaminant Hydrology*. 2005. (P. M. Oates, C. Castenson, C. F. Harvey, M. Polz, and P. Culligan).
- Experimental Visualization of Solute Transport and Mass Transfer Processes in Spatially Heterogeneous Porous Media, *Environmental Science and Technology.* 2004. (Zinn, B. C. F. Harvey, L. Meigs, R. Haggerty, W. Peplinski, and C. Freiherr von Schwerin).
- What Controls the Apparent Timescale of Solute Mass Transfer in Aquifers and Soils? A Comparison of Diverse Experimental Results. *Water Resources Research*. 2004. (Haggerty, R. Harvey, C.F. Freiherr von Schwerin, C. Meigs, L.).

- Temporal Moment-Generating Equations: Modeling Transport and Mass Transfer in Heterogeneous Aquifers. *Water Resources Research.* 1995. (Harvey, C. F. and S. M. Gorelick).
- Reactive Transport in Porous Media: A Comparison of Model Prediction with Laboratory Visualization, *Environmental Science and Technology.* 2002. (Gramling, C. Harvey, C.F. Meigs, L.).

Q: Is Conservation Groups' Exhibit 4 an accurate copy of your resume?

A: Yes.

Q: In preparing your testimony, what sources did you review?

A: I reviewed OCD's Application, including the proposed new rules at Parts 41, 42, and 43 of Title 19, Chapter 15 of the New Mexico Administrative Code. I am also familiar with the federal Class VI regulations at 40 C.F.R. Parts 124, 144, and 146, on which OCD's application is based. In addition, I reviewed various materials that are included as references at the end of my testimony.

Summary of Opinions

Q: Can you summarize the opinions you will provide in your testimony?

A: Yes. My testimony addresses three themes, each grounded in peer-reviewed scientific literature and each driving proposed amendments to OCD's rules. Before elaborating on those themes, I want to state the factual context that motivates them.

Relatively few CCS projects have injected CO_2 into deep saline aquifers; most projects inject CO_2 into oil fields for the purpose of enhanced oil recovery. Of the approximately 50 CCS facilities now operational worldwide, no more than 12 inject CO_2 into saline aquifers (Global CCS Institute, 2025). Pre-injection model predictions have been proven materially wrong at saline-aquifer facilities for which there is published operational data, including at the Archer Daniels Midland (ADM) facility in Decatur, Illinois (Senel & Chugunov, 2013; Bukar et al.,

2025), at the CCS facility at In Salah in Algeria (Rutqvist et al., 2016; White et al., 2014), and at Snøhvit in Norway (Hansen et al., 2013). EPA-permitted monitoring wells at Decatur developed corrosion leaks within seven years of construction (Snider & Lefebvre, 2024). A comprehensive review of two decades of risk assessment practice for geologic carbon storage concludes that feasibility evaluation demands a thorough risk and uncertainty assessment, because the long-term safety of CO_2 storage is a prerequisite for project success (Xiao et al. 2024). The consequences of containment failure are likely irreversible on any human timescale: once an aquifer has been contaminated by CO_2-mobilized metals or displaced brine, it cannot be restored. This factual context demands a regulatory framework designed for uncertainty and failure, not one that assumes success.

The first theme of my testimony drives toward a full understanding of the hazards posed by injection of CO_2 into saline aquifers. CO_2 injection creates two zones of potential endangerment: a typically larger zone of increased pressure and an inner CO_2-plume zone, which each pose qualitatively different threats. The reservoir simulation models used to predict the extent of both zones are inherently unreliable. Even in the oil and gas industry, where calibration data are comparatively abundant, subsurface predictions carry large uncertainty: an analysis of over 500 ExxonMobil exploration wells drilled over two decades found that more than 20% of the failures to find oil and gas in near-field wildcats (i.e., in regions with a known hydrocarbon system) were a direct result of a mischaracterization of the trap and seal, meaning that even with best-in-class skill and plentiful site data, 20% of the time reservoir geologists incorrectly surmised that a cap rock would contain the buoyant oil and gas (Rudolph and Goulding, 2017). For CO_2 storage in saline aquifers, where no production history exists against which to calibrate models, where data are sparse, and where the stakes of prediction error are higher, the reliability

of pre-injection models is even lower. In most regions where CCS is considered, including in New Mexico, legacy oil and gas wells provide leakage pathways, but existing well inventories are incomplete. Furthermore, the subsurface properties governing CO_2 migration are site-specific and scale-dependent, meaning that analog data from other formations cannot substitute for direct measurement. Recognizing both zones in the regulations and grounding the safety case in site-specific data validated against field observations ensures that the regulatory framework reflects the actual physical reality of CO_2 injection rather than optimistic modeling assumptions. Furthermore, given the interest in expanding CO_2 storage in saline aquifers across New Mexico, it is also essential that we consider the injection of CO_2 within the larger context of a multi-project landscape where patterns of induced pressure overlap across projects.

The second theme of my testimony addresses the designing of enforceable protections. The Area of Review ("AoR") is the master regulatory parameter from which monitoring, corrective action, and seismicity coverage all derive; defining it conservatively from the outset ensures that downstream safeguards are appropriately scoped. Action thresholds must be defined quantitatively and before the permit is issued, because a regulatory standard without a pre-specified threshold cannot be consistently measured or reliably enforced. The mature precedent is the RCRA groundwater monitoring framework at 40 CFR 264.97, which requires pre-specification of statistical methods and significance levels and which was developed because post-hoc threshold selection proved vulnerable to manipulation. Safety-critical decisions must be automatic rather than discretionary because the consequences of delayed action in CO_2 storage are irreversible and operators face economic incentives that run counter to precautionary response. Scientific transparency — including disclosure of modeling assumptions, code validation, calibration metrics, and raw operating data — is essential because a regulator who

cannot see the data and reasoning behind a model's predictions cannot evaluate the safety case. Where CO_2 injection volumes or pressures in a Class II enhanced-recovery operation create risks equivalent to a dedicated storage project, the operation must be subject to Class VI requirements, because the Class II framework was not designed to manage the risks of long-term CO_2 storage.

The third theme of my testimony is ensuring the long-term containment of injected CO_2. The time horizon of regulatory protection must match the time horizon of the hazard: stored CO_2 plumes persist for centuries to millennia, infrastructure degrades on a timescale of years to decades, and water resources that are impractical to develop today may become essential to New Mexico communities in the future. Materials historically used for well construction and plugging — conventional Portland cement and carbon steel — degrade on contact with CO_2-bearing brine: CO_2-resistant materials must be required at all depths in wells that may encounter the CO_2 plume and should not be required in the injection zone alone. Plume stabilization — the point at which the CO_2 plume has essentially ceased migrating — must be demonstrated through sustained monitoring before any reduction in post-injection oversight, rather than assumed from model predictions or tied to a fixed calendar period. The option to petition for a shortened post-injection site care (PISC) period before injection has even ceased must be eliminated. The state must build independent, durable oversight capacity, including its own seismic monitoring infrastructure and technically trained staff, so that New Mexico can detect and respond to problems on its own terms rather than depending on operator self-reporting. This capacity must be designed to outlast any individual project or operator, because the state's responsibility to protect its drinking water resources does not expire when a permit does.

Overview of key concepts underlying recommendations for improved CCS safety

Q: Dr. Harvey, can you explain why CO_2 injection creates two distinct zones of concern, and why the regulations should recognize both?

A: Yes. There are two distinct zones of endangerment to underground sources of drinking water, and both zones grow as injection continues. The first is the increased-pressure zone, which typically contains and extends far beyond the CO_2 plume itself and is the region across which formation pressures are substantially elevated by CO_2 injection. The second zone, encompassed within the first increased-pressure zone, is the CO_2-plume zone which comprises the region where injected CO_2 exists as a separate phase or dissolved in the formation brine. These two zones differ in spatial extent, in the mechanisms by which they threaten groundwater, and in the regulatory responses they require. An effective regulatory framework must recognize both.

In the first zone, pressurization of the storage aquifer may drive contamination of shallower groundwater. When CO_2 is injected into the subsurface, it displaces water (contrary to a common misconception, there is no "empty" gas-filled pore space for the CO_2 to fill). CO_2 must be injected at a higher pressure than the pore water it displaces. The higher pressure forces CO_2 into the aquifer, driving water away from the injection well and pressurizing pore water throughout the aquifer. As pore water flows away from the well, pressure is transmitted throughout the entire aquifer, much farther than either the CO_2 plume or the travel distance of water directly displaced by the CO_2 plume. The resulting pattern of pore pressure has no distinct front or edge; rather, it falls off continuously with distance from the injection well. The entire subsurface experiences rising pressures that continue to increase everywhere for the duration of injection. For this reason, delineating the first zone requires a subjective choice of how much

increased pressure to allow. The problem with defining this zone is not only predicting the pattern of increased pressures but also choosing what threshold is acceptable.

The increased-pressure zone is almost always substantially larger than the CO_2 plume zone. Birkholzer and Zhou (2009) report that a CO_2 plume with linear dimensions of approximately 10 km can generate a 0.1-MPa pressure front extending more than 100 km, and their own modeling of the Illinois Basin confirmed pressure propagation beyond 100 km from the core injection area. White et al. (2020) demonstrate that the pressure-defined AoR at one study site was 278 km², far exceeding the footprint of the CO_2 plume itself. The EPA's own AoR guidance recommends that operators delineate both boundaries separately (EPA, 2013).

Delineating this zone of increased pressures is important because elevated formation pressure can drive native brine upward through legacy wells, faults, or fractures into overlying drinking water aquifers (Tsang et al., 2008). This brine displacement can contaminate underground sources of drinking water ("USDW") even in areas the CO_2 plume will never reach. Pressure increases on pre-existing faults can also trigger induced seismicity (Zoback and Gorelick, 2012; Langenbruch et al., 2018). Ranaee et al. (2022) demonstrate that pressure buildup, not volumetric displacement, is the binding constraint on safe CO_2 storage, and that it must be limited to avoid fault reactivation and caprock failure.

Delineating the second zone, the zone that may contain injected CO_2, is important because this zone defines the region from which CO_2 may escape and within which dissolved CO_2 may corrode and damage key infrastructure and/or weaken cap rock. This second zone may be very difficult to predict if the buoyant plume migrates away from the point of injection or if the plume rises along the inverted topography of the "roof" imposed by the overlying confining

unit. If the zone is defined by an anticline or a structural trap where injected CO_2 accumulates it will be relatively easier to predict.

Within the inner CO_2 plume zone, risks of pressure and buoyancy driven escape are compounded by potential geochemical degradation. CO_2 dissolved in brine forms carbonic acid, which can degrade the cement matrix when reacting with Portland cement, especially when coupled with defects in the cementing (Carroll et al., 2016; Gholami et al., 2021). Gholami et al. (2021) identify deficient cement installations as a cause of CO_2 migration and leakage from the near-wellbore region, and they document multiple pathways through which CO_2 can compromise the integrity of abandoned wells. CO_2-bearing brine also corrodes steel casing through mechanisms that remain poorly understood, particularly under supercritical conditions (Sun et al., 2023). Ilgen et al. (2018) show that geochemical interactions between CO_2, brine, and carbonate-rich shale can cause localized mechanical weakening in confining formations over time: such weakening can be reasonably inferred to reduce the formations' sealing capacity. These geochemical risks may not exist in the outer pressure zone, where CO_2 is not present, but all of them must be addressed within the plume zone through more stringent material and corrective action requirements.

If the regulations define only a single zone by which to guide regulations, operators will have an incentive to use the smaller plume-based boundary, leaving the much larger pressure zone outside the regulatory perimeter. Legacy wells, faults, and USDWs within that unregulated pressure zone would receive no corrective action, no monitoring, and no seismicity assessment. The proposed amendments establish a dual-zone regulatory structure: a pressure-based outer boundary that governs seismicity monitoring, fault stability analysis, and identification of all legacy wells requiring evaluation; and a CO_2-plume-based inner boundary that governs

requirements for CO_2-resistant materials, intensive corrective action, and monitoring well management. I will describe the specific amendments implementing this structure in the sections that follow.

Q: Dr. Harvey, could you please outline why the AoR is such a consequential determination, and what happens downstream if it is undersized?

A: Determining the AoR is consequential in a Class VI permit because nearly all other regulatory safeguards are tied to it. The AoR defines the geographic boundary within which the operator must identify and evaluate legacy wells, assess fault systems, place monitoring wells, design corrective action plans, and conduct seismicity monitoring. If the AoR is correctly sized, these downstream protections have a reasonable chance of covering the area affected by injection; if the AoR is undersized, each protection is correspondingly undersized, and the regulatory framework is left with gaps that cannot be corrected after the fact.

Consider what flows from the AoR boundary. Under the EPA's Class VI framework and OCD's proposed rules, the operator must identify all artificial penetrations within the AoR, evaluate their construction and plugging status, and perform corrective action on any that could serve as leakage pathways (EPA, 2013). Arbad et al. (2024) assessed 151 legacy wells within a single AoR in the Illinois Basin and found that many lacked adequate records of plugging condition, completion depth, and cement integrity. Wells outside the AoR boundary receive none of this scrutiny. The operator must also characterize faults within the AoR and assess their stability under the changed pressure regime that injection will create (Zoback and Gorelick, 2012; Cheng et al., 2023). Faults outside the AoR receive no stability analysis, even if injection-driven pressure changes reach them. Monitoring well placement, seismicity network coverage, and the geographic scope of the testing and monitoring plan all derive from the AoR. An

undersized AoR systematically excludes from regulatory oversight the wells, faults, and formations that lie between the permit boundary and the actual extent of pressure influence.

There are several reasons why AoRs are prone to undersizing. First, the pressure front almost always extends far beyond the CO_2 plume. If an operator delineates the AoR based primarily on the plume footprint rather than the pressure front, which is possible under Class VI regulations because the AoR is defined only in the Division's proposed regulations as "the region surrounding the geologic sequestration project where USDWs may be endangered by the "injection activity," the result will underestimate the area of potential endangerment. Second, the reservoir simulation models used to predict both plume extent and pressure propagation are subject to large uncertainties. Oliver and Chen (2011) demonstrated that the inverse problem is ill-posed for reservoir models: multiple parameter combinations can match available data while producing uncertain predictions. Subbey et al. (2004) also demonstrate how a model cannot be uniquely determined by showing that many different geological models can reproduce the same calibration data but simulate different forecasts. For a Class VI permit application, where the plume-simulation model has typically never been tested against injection data at the site, these uncertainties can be extreme. A single deterministic model run, which is what most Class VI permit applications currently use to define their AoRs, gives no indication of how sensitive the predicted AoR boundary is to the assumptions embedded in the model.

Third, and of relevance to New Mexico, under the existing Class VI framework, the AoRs across disparate projects risk being modeled in isolation. The compounding effects of multiple adjacent CCS projects warrant a coherent regulatory framework. Wang et al. (2025) analyzed GCS projects along the Gulf Coast and found that when multiple projects were modeled together, their individual pressure fields overlapped and merged, producing combined

pressure-field-determined AoRs that vastly exceeded the sum of the individually calculated boundaries. Even under base-case assumptions, several clusters of projects shared a single expanded AoR, and under worst-case conditions, the merged AoR encompassed multiple projects and large numbers of legacy wells that no individual operator had evaluated. Birkholzer and Zhou (2009) reached a similar conclusion modeling 20 injection sites in the Illinois Basin: cumulative pressure buildup extended across much of the basin, far exceeding what any single project's model would have predicted. If New Mexico permits multiple Class VI projects targeting the same geologic formations without requiring that their models account for each other's pressure contributions, the individual AoRs will be undersized and fail to account for risks to New Mexico's drinking water.

The practical consequences of an undersized AoR can be severe and, in many cases, are irreversible. Legacy wells that should have been evaluated and remediated before injection begins will instead be discovered only after pressure-driven brine migration or CO_2 leakage has already occurred. Faults that should have been assessed for reactivation potential will instead manifest as induced seismicity events that the monitoring network was not positioned to detect in advance. Monitoring wells placed to track the predicted plume boundary will fail to capture brine displacement occurring outside their coverage area. The Corrective Action Plan ("CAP"), which is written to address risks to drinking water within the permitted AoR, will contain no provisions for responding to problems outside it. Because the AoR is established before injection begins, and revised only periodically thereafter, an initial undersizing propagates error through the entire permit lifecycle.

For these reasons, I support amendments that define the AoR conservatively from the outset: explicitly using pressure-based rather than plume-based delineation, requiring ensemble

modeling to characterize the uncertainty in the AoR boundary, requiring a unified modeling framework when multiple projects target the same formation, and mandating early reevaluation against monitoring data so that errors in the initial AoR can be identified and corrected before they cause harm. I will address each of these amendments in detail in the sections that follow.

Q: Dr. Harvey, can you explain the limitations of modeling and why they're relevant to this rulemaking?

A: Reservoir simulation models are the primary tool for predicting where injected CO_2 will migrate, how far pressure will propagate, and whether containment will hold. Every major element of a Class VI permit depends on these predictions. The models are indispensable, but the peer-reviewed literature establishes that they carry large and irreducible uncertainties that the regulatory framework must account for.

The limitations are structural. Oliver and Chen (2011) establish that calibrating a reservoir model to observed data is almost always ill-posed: many different parameter combinations can reproduce the same observations while yielding uncertain predictions of future behavior. Subbey et al. (2004) demonstrate this non-uniqueness quantitatively. Arnold et al. (2019) and Demyanov et al. (2019) extend this finding to show that the choice of geological scenario itself, which the modeler makes before running a single simulation, introduces uncertainty that propagates through every subsequent prediction. Demyanov et al. (2019) conclude that this scenario uncertainty cannot be adequately captured without testing multiple conceptual models, a step that most Class VI permit applications do not take. Beyond geological scenario choice, the choice of simulation method itself affects results: Cusini et al. (2019) show that a widely used upscaling method, even after calibration, was highly sensitive to changes in simulation conditions, and Nilsen et al. (2011) show that different simulation approaches

produce different predictions for the same site. These structural limitations are compounded by the site-specific parameter uncertainties I describe in my testimony on site-specific data requirements.

The operational record confirms these concerns. At Decatur, pre-injection modeling projected with high confidence that CO_2 would remain well below the primary seal (Senel and Chugunov, 2013). However, subsequent imaging revealed CO_2 had migrated along faults to reach the cap rock (Bukar et al., 2025). The cap rock may still be sealing, but the model was wrong about where the CO_2 would go, which is the very prediction on which the AOR was based. At Snøhvit, pressure rose faster than anticipated, approaching fracture limits (Hansen et al., 2013). At In Salah, unexpected hydrofracturing of the lower caprock led to halting of injection (White et al., 2014). At Sleipner, plume behavior was dominated by geological features that only became apparent during injection (Eiken et al., 2011). These are not isolated failures; they represent the full set of saline-aquifer CCS sites with published operational data.

A fundamental reason for this poor performance is the absence of calibration data. In oil and gas, models are built with information from multiple site wells and 3D seismic surveys and are tuned against production data accumulated over years. Even in this oil-and-gas-industry case marked by plentiful data, Rudolph and Goulding (2017) found substantial prediction errors for key reservoir parameters across over 500 wells. For CCS in saline aquifers, there is no production history to calibrate against.

The oil and gas industry can remain profitable even when a substantial fraction of their model predictions about oil and gas extraction prove inaccurate; for CO_2 storage, a 10% failure rate is unacceptable. The model submitted with a permit application is a hypothesis about subsurface behavior based on limited data that has not yet been tested.

The regulatory implications follow directly: ensemble modeling to capture the range of plausible outcomes (Tuczynski and Stopa, 2023); early validation against monitoring data (Saló-Salgado et al., 2024; Freeman et al., 2025); full transparency of modeling assumptions for meaningful regulatory review; and qualified professionals performing the work. As I describe in my testimony on the Area of Review, these modeling limitations have direct consequences for how the Area of Review is delineated and why single deterministic model runs are inadequate for that purpose.

Q: Dr. Harvey, could you please explain why oil and gas companies' extensive experience using multiphase flow models to simulate reservoirs does not directly inform Class VI permitting?

A: One of the dominant narratives one hears when listening to CCS advocates' reasoning regarding use of reservoir-simulation models to ensure Class VI project safety is that this class of models has been used in the oil and gas industry for decades. The fact that oil companies find multiphase flow models useful does not mean they have the same value for analyzing Class VI permits. First, oil companies invest vastly more resources and expertise into the models than is possible for Class VI permit applications. Second, oil companies find the output of these models useful even if it is incorrect a significant fraction of the time. The oil business is built on playing the odds. Third, unlike Class VI permit seekers, oil companies generally do not use the models to prove an outcome that they prefer; rather, they seek statistically meaningful output so that they can make investments that best manage risk. For all three of these reasons, the fact that these models exist and are used by industry does not imply that they are useful for modeling the safety of CO_2 storage. Application of these models, which are indeed invaluable tools for understanding multiphase flow in porous media, must be tailored to the use case at hand.

Q: Dr. Harvey, why do you believe legacy wells are such a significant concern?

A: The peer-reviewed literature identifies legacy wells as a significant real-world leakage pathway for geological carbon storage projects. Celia and Nordbotten (2009) explain why: in mature sedimentary basins that have undergone decades of oil and gas development, the number of existing wellbore penetrations is enormous and creates numerous potential conduits through confining formations. According to the New Mexico Bureau of Geology and Mineral Resources, oil and gas was first produced in New Mexico in the 1920s, and at least 110,000 wellbores exist across the sedimentary basins in the state. [1] Each of these wells, whether active, suspended, or plugged and abandoned, creates an artificial conduit through the confining formations that are supposed to prevent upward migration of buoyant CO_2 and pressure-displaced brine. Gasda et al. (2004) estimate that a CO_2 plume with a radius of roughly 5 km in a well-dense area could come into contact with several hundred existing wells. Xiao et al. (2024), reviewing two decades of risk assessment practice, report that wells are the primary leakage pathway for geologic carbon storage projects and that up to 15% of legacy wells in studied areas have exhibited well integrity concerns.

The problem is compounded by the fact that existing well inventories are systematically incomplete. Boutot et al. (2022) compiled the first comprehensive national dataset of documented orphaned wells and found at least 123,318 as of April 2022, yet this represented only about 3% of all estimated abandoned wells in the United States. Critically, even among these documented wells, only 49% had depth information and only 16% had a recorded last production date, meaning the data needed to assess whether a given well poses a leakage risk are frequently unavailable. Jahan et al. (2025) extended this work by estimating the number of

[1] Ron Broadhead and Shari Kelley, *Frequently Asked Questions About Oil and Gas*, New Mexico Bureau of Geology & Mineral Resources, https://geoinfo.nmt.edu/faq/energy/petroleum/home.html.

undocumented orphan wells using historical production records and found approximately 340,000 in Pennsylvania and 309,000 in Oklahoma alone. Validation using aeromagnetic surveys in western Pennsylvania confirmed that at least two undocumented wells existed for every documented well. The authors note that other oil-producing states may have much higher numbers than current official estimates, particularly states like New Mexico and Texas with long production histories. Kim et al. (2024) compile an aerial imagery dataset to support automated detection and note that the locations of hundreds of thousands of wells remain unknown in the United States. Taken together, these studies establish that any operator relying on a database search to identify all artificial penetrations within an AOR will miss wells that exist but are not recorded, and will lack critical information about many wells that are recorded.

The materials used to construct and plug legacy wells present a separate concern. Most wells in New Mexico were completed with conventional Portland cement, which was designed for hydrocarbon service, not for sustained exposure to CO_2. Carroll et al. (2016) document that CO_2-bearing brine reacts with Portland cement through carbonation reactions that are governed by coupled chemical, mechanical, and transport processes whose outcome depends on site specific defects that cannot be understood from records alone. Gholami et al. (2021) identify deficient cementing as a likely cause of CO_2 migration from the near-wellbore region and document multiple pathways through which CO_2 can compromise well integrity, including along the casing-cement interface, through the cement matrix itself, and through the annular space between cement and formation rock. Steel components are also vulnerable. Sun et al. (2023) review the state of knowledge on corrosion under CO_2 storage conditions and note that the corrosion mechanisms, particularly under supercritical conditions and in high-chloride brines, remain incompletely understood.

At ADM's Decatur facility, EPA-permitted monitoring wells built under modern Class VI requirements developed corrosion leaks within a few years of construction (Snider and Lefebvre, 2024). If wells built to current standards and inspected by EPA corroded this quickly, the integrity of decades-old legacy wells completed under far less stringent standards and never designed for CO_2 exposure cannot be assumed. Furthermore, records describing well completions may not even exist: Arbad et al. (2024) assessed 151 legacy wells within a single AOR in the Illinois Basin and found that many lacked adequate records of plugging condition, completion depth, and cement integrity. A substantial number of these wells could not be categorized with confidence because the data needed to evaluate whether they present a leakage risk simply did not exist.

In New Mexico, the geologic formations being considered for CO_2 storage are, in many cases, the same formations that have been drilled extensively for hydrocarbon extraction over the past century (e.g., the Permian Basin and the San Juan Basin). The proposed regulations must account for the reality that any AoR delineated for a Class VI project in the state is likely to contain legacy wells with conventional materials vulnerable to CO_2 degradation, incomplete records, and/or uncertain plugging status. I therefore support requiring operators to cross-reference multiple databases when identifying artificial penetrations, because no single database is complete (Jahan et al., 2025). Wells with incomplete plugging records must be field-tested rather than assumed sound. Corrective action within the area where the CO_2 plume may travel must use CO_2-resistant materials throughout, not conventional Portland cement that will degrade with exposure to CO_2-bearing brine. Mandatory surface-air monitoring should be required in areas with high wellbore density because the ability to predict which specific legacy well will

serve as a leakage pathway is inherently limited by subsurface uncertainty. I will address the specific amendments implementing each of these requirements in the sections that follow.

Q: Dr. Harvey, please provide context to explain why site-specific data are essential to effective regulation.

A: The subsurface properties that control CO_2 migration and pressure propagation vary over short distances and cannot be reliably inferred from measurements made elsewhere. This is a specific, well-documented finding across multiple parameters that are critical to Class VI permit decisions.

Ni et al. (2025) demonstrate that capillary heterogeneity, which influences how CO_2 moves vertically through layered formations, is formation-specific and scale-dependent. The nature of heterogeneity itself means that measurements from one location within a reservoir cannot be assumed representative of the full formation, and transferring constitutive relationships from analog formations elsewhere is not scientifically supportable. Moodie et al. (2021) show that the choice of relative permeability curve substantially changes model predictions of CO_2 trapping efficiency and phase behavior, and that if measured laboratory data are not available for the site, relative permeability must be considered as a significant source of uncertainty. Vilarrasa et al. (2019) emphasize that the in-situ stress state must be measured at each candidate storage site to establish the maximum sustainable injection pressure and the thermal limits for safe operation. Chiyonobu et al. (2013) provide a concrete demonstration from the Nagaoka CCS pilot site in Japan: a geological model built at 10-centimeter resolution, informed by detailed core analysis, was needed to match observed CO_2 migration. Thin siltstone barriers that controlled plume behavior are unlikely to have been identified without site-specific characterization at that resolution.

The difficulty of modeling CO_2 plumes is demonstrated most directly by Saló-Salgado et al. (2024), who attempted to model a two-dimensional laboratory experiment in which the porous material was constructed with known flow parameters and an engineered spatial structure visible behind glass walls. Their model produced inaccurate predictions of plume evolution after a controlled injection of CO_2 even though the experimental tank was engineered to have a specific spatial pattern of granular material with laboratory characterizations of multiphase flow properties. Salo-Salgado state, "The sand–water–CO_2(g) system is very sensitive to effective permeability and capillary pressure changes; where heterogeneous structures are present, accurate deterministic estimates of CO_2 migration are difficult to obtain." These two-dimensional results point to the great uncertainty that is inherent to model predictions of the long-term evolution of CO_2 plumes in three-dimensional spatial structures where flow characteristics are not known. The operational record at Sleipner confirms this at field scale: plume behavior was dominated by geological features that became apparent only during injection, not during pre-injection characterization (Eiken et al., 2011). A model built on analog data would have missed those features entirely.

However, several existing Class VI permit applications have relied heavily on analogs from distant sites and/or data from only a single characterization well (see, for example, the One Earth Sequestration CCS permit application in Illinois and the Pratt Zero Carbon permit application in Kansas). Ni et al. (2025) establish that capillary heterogeneity operates across spatial scales from millimeters to kilometers, and even small-scale variations can dramatically impact CO_2 mobility and trapping at the field scale. Saló-Salgado et al. (2024) confirm this experimentally: models calibrated against one stratigraphic section were not accurate when applied to a different section with different heterogeneous structures, demonstrating that site-

specific characterization cannot be replaced by calibration from elsewhere. I support amendments that increase the amount of site-specific data used to support the safety case for Class VI injection, including requiring on-site diagnostic fracture injection tests ("DFIT") run to completion, minimum data density standards for site characterization, 3D seismic coverage of the full AOR, and site-specific dynamic fault stability analyses.

Q: Dr. Harvey, can you explain why pre-specified quantitative thresholds and automatic responses are necessary?

A: A quantitative threshold defined before injection commences converts a discretionary judgment into an objective test. Without pre-specified thresholds, every anomalous reading requires an evaluation of whether conditions are serious enough to warrant action. That evaluation introduces delay at precisely the points where the potential consequences of delay (e.g., contamination of an aquifer, escalation of fault slip, loss of seal integrity) may be irreversible. Pre-specification and corresponding public review of thresholds also lowers the chance that thresholds are selected to minimize the likelihood of triggering a costly response. This is the lesson of the RCRA groundwater monitoring framework at 40 CFR 264.97, which requires operators to specify the statistical test, the data to be evaluated, and the significance level before permit issuance, because post-hoc selection proved unreliable (EPA, 2009). The EPA's Class VI AoR guidance applies the same principle, recommending that specific criteria for triggering an AoR reevaluation be included in the permit (EPA, 2013).

The same logic requires that responses to threshold exceedances be automatic rather than discretionary. Once a threshold is crossed, a discretionary process reintroduces the delay and economic pressure that pre-specification was designed to eliminate. At In Salah, anomalous surface deformation signaled that injection pressures were compromising the lower caprock, but

the decision to suspend injection was made by the operator after a period of assessment, not by an automatic trigger (White et al., 2014). The outcome was acceptable because the operator chose to act; a different operator facing different economic pressures might not have. At Snøhvit, reservoir pressure approached fracture limits faster than anticipated, requiring operational changes that had not been pre-planned (Hansen et al., 2013).

Pre-specification is also necessary for monitoring system design. A monitoring network cannot be evaluated for adequacy without knowing what signal it must detect. Detection probability depends on the interaction between the number of monitoring wells, aquifer heterogeneity, and sampling frequency (Sarris et al., 2022), and the widely applied minimum of three monitoring wells in the predicted direction of plume movement is inadequate for reliable detection in heterogeneous formations (Yenigül et al., 2005).

The proposed amendments apply this principle across all safety-critical decisions: injection ceases upon evidence of unauthorized fluid migration; injection stops when continuous monitoring gauges malfunction for more than one week; seismicity above a pre-specified ground-motion threshold triggers an operational pause; and pressure and geochemical thresholds for AoR reevaluation are defined in the permit rather than left to post-hoc interpretation. In each case, the threshold is defined by site-specific science, specified before injection begins, and enforced without requiring a judgment call in a moment of crisis.

Q: Dr. Harvey, why does scientific transparency matter for the effectiveness of this regulatory program?

A: Scientific transparency is a prerequisite for accountability. Every Class VI permit decision rests on the output of myriad scientific and engineering decisions. For example, in the case of reservoir simulation models, development of those models involves consequential

choices at every stage: Which simulation code to use? How to discretize the domain? What constitutive relationships to apply? Which geological scenario to adopt? How and with what metrics to calibrate the model against available data? The peer-reviewed literature establishes that these choices materially affect results. Cusini et al. (2019) show that a widely used upscaling method, even after calibration, was highly sensitive to changes in simulation conditions. Nilsen et al. (2011) show that different simulation approaches produce different predictions for the same site. Cheng et al. (2023) identify accurate characterization of the stress state and correct identification of fault systems as key challenges for forecasting CO_2 injection-induced seismicity, noting that the complexity of coupled thermal, hydraulic, mechanical, and chemical processes makes reliable prediction difficult even with site-specific data. A regulator who cannot see what choices were made is reviewing a conclusion without access to the reasoning behind it.

The same principle applies to operational data. Raw time-series records from pressure gauges and geochemical sensors contain information that quarterly summary statistics do not preserve (e.g., instrument drift, short-duration pressure events, etc.). Requiring operators to provide raw monitoring data does not impose a new collection burden, since the data are already being recorded; it simply ensures the regulator can conduct independent analysis rather than relying solely on operator-prepared summaries. Where confidential business information (CBI) claims prevent access to the modeling assumptions, calibration data, or code validation results on which the safety case depends, the effect is to place the scientific basis of a permit decision beyond independent review. Safety-relevant data must be exempt from CBI protection to ensure fully scientific transparency and accountability.

I support the requirement of full disclosure of code assumptions and constitutive relationships, peer-reviewed computational codes with documented test cases, reporting of

calibration metrics, provision of raw operating data to OCD, exemption of safety-relevant data from CBI claims, and independent third-party verification of the modeling ensemble.

Q: Dr. Harvey, can you explain why the state needs its own independent oversight capacity for CO_2 storage projects?

A: CO_2 storage projects inject for years to decades, the hazard persists for centuries to millennia, and the state's responsibility to protect drinking water resources does not expire when an operator's permit does. The long time horizons involved require oversight structures that outlast any individual project or operator. If New Mexico's oversight capability depends entirely on operator-funded consultants and operator-submitted analyses, that capability disappears when the operator ceases operations, loses solvency, or transfers the permit.

The technical demands of Class VI oversight reinforce this point. Evaluating a permit application requires the ability to independently understand a range of scientific data, assess reservoir simulation models, review calibration quality, scrutinize geological interpretations, and judge whether an AOR delineation is adequate. As I have described, these models embed consequential choices that materially affect predictions, and the peer-reviewed literature shows that different choices produce different results (Cusini et al., 2019; Nilsen et al., 2011; Oliver and Chen, 2011). A regulator who lacks the technical capacity to interrogate those choices is in the position of accepting or rejecting the operator's conclusions without being able to evaluate the reasoning. Independent third-party verification of modeling ensembles, which the proposed amendments require, is only meaningful if the state has staff with the expertise to commission, interpret, and act on that verification.

Seismicity monitoring is a clear example of where independent state capacity is not optional. Induced seismicity from injection operations can develop rapidly and requires real-time

detection to support timely operational decisions (Langenbruch et al., 2018; Zoback and Hennings, 2025). Ground motion analysis requires site-specific input parameters, model calibration, and dynamic wave propagation analysis — work that demands trained expertise. If the state relies solely on operator-reported seismic data, it cannot independently verify whether a seismic event has exceeded a threshold, whether the operator's seismic network is functioning correctly, or whether the reported ground motion measurements are accurate. A state-owned seismic monitoring network with trained staff ensures that New Mexico can detect and characterize induced seismicity on its own terms.

I support amendments ensuring the state has independent seismic monitoring infrastructure and the authority to commission independent verification of operator-submitted models and data.

Q: Dr. Harvey, could you please define inter-wellbore interference, and explain why it's relevant to the proposed rules?

A: Inter-wellbore interference refers to the overlap and superposition of pressure fields created by multiple injection wells operating in the same geologic formation. When CO_2 is injected at a single well, it displaces pore fluids and increases formation pressure across a wide area. When multiple wells inject simultaneously, their individual pressure fields combine, producing cumulative pressure effects that exceed what any single well would generate in isolation.

Birkholzer and Zhou (2009) modeled a regional CCS program with 20 injection sites in the Illinois Basin and found that cumulative pressure buildup extended across much of the basin, far beyond what any individual project's model would have predicted. Wang et al. (2025) extended this finding using announced GCS projects along the Gulf Coast and found that

individually calculated pressure plumes merged into larger combined pressure footprints when multiple projects were modeled together. Even under base-case assumptions, several clusters of projects shared a single expanded zone of increased pressure, and under worst-case conditions, the merged AOR encompassed multiple projects and large numbers of legacy wells. Wang et al. observe that responsibility for pressure interference remains unclear and that the assignment of responsibility remains an open question. This is a regulatory gap with direct implications for drinking water protection.

Accounting for pressure interference between CCS projects is directly relevant to New Mexico because the state may ultimately host multiple Class VI projects targeting the same geologic formations. If each project models its AoR independently, without accounting for pressure contributions from neighboring projects, the individual AoRs will be undersized in comparison to the true zone of increased danger to drinking water sources. Monitoring networks will be scoped too narrowly, corrective action plans will miss at-risk wells in the inter-project areas, and induced seismicity hazards from cumulative pressure loading will be underestimated. Frequent measurements are essential to distinguish a project's own pressure signature from regional interference effects. I support amendments requiring a unified modeling framework for multi-well projects, more frequent pressure fall-off testing, and more frequent AOR reevaluation to account for evolving pressure conditions across the basin.

Q: Dr. Harvey, can you explain the mechanisms by which CO_2 injection can cause earthquakes, and why the proposed seismicity amendments are necessary?

A: CO_2 injection increases pore pressure in the target formation, and that pressure increase propagates outward well beyond the CO_2 plume. When elevated pore pressure reaches a pre-existing fault, it reduces the effective normal stress clamping the fault surfaces together, which

can allow the fault to slip. This is one fundamental mechanism of injection-induced seismicity. Another common mechanism is simply hydrofracking: when the injection pressure exceeds the least compressive stress, the rock fractures, and this opening facture can then serve as a conduit for CO_2 escape.

The critical point for regulation is that induced seismicity is governed by the pressure front, not the CO_2 plume. A fault can be reactivated by pressure changes alone, without any contact with CO_2. Langenbruch et al. (2018) show that seismic event rates correlate with rate and volume of injection as well as with the proximity of faults to the pressure front. Vilarrasa et al. (2019) emphasize that both pressure and temperature changes from injection affect fault stability, and that the in-situ stress state must be measured at each site to determine the maximum sustainable injection pressure.

The operational record shows that induced seismicity is likely where fluids such as CO_2 are injected at pressure into the subsurface. Zoback and Gorelick (2012) argue that there is a high probability that earthquakes will be triggered by injection of large volumes of CO_2 into brittle continental interior rocks. Zoback and Hennings (2025) review the analogous record or large-scale saltwater disposal and report that every case of large-scale injection into deep saline aquifers in hydraulic communication with crystalline basement has induced significant seismicity. At CO_2 injection sites specifically, Williams-Stroud et al. (2020) documented microseismicity associated with CO_2 injection in the Illinois Basin. The risk is sufficiently well-established that Bommer et al. (2006) developed and deployed a real-time traffic light system using peak ground velocity thresholds to manage induced seismicity during a fluid injection project, providing an operational precedent for the ground-motion-based response protocols proposed in these amendments. As noted by Bommer et al. (2006), the relevant metric for

potential damage is ground motion (peak ground velocity or acceleration), not earthquake magnitude alone, because the same magnitude event at different depths and distances produces different ground shaking. I support amendments requiring site-specific dynamic fault stability analysis, pre-specified ground-motion thresholds for operational pauses, state-owned seismic monitoring infrastructure with trained staff, and worst-case scenario modeling that accounts for sub-seismic faults.

Q: Dr. Harvey, can you explain what plume stabilization means and why the post-injection site care period should be tied to it?

A: After injection ceases, the CO_2 plume does not immediately stop moving. Buoyancy forces continue to drive supercritical CO_2 upward against the caprock, residual trapping gradually immobilizes portions of the plume, and dissolution into formation brine slowly reduces the mobile CO_2 mass. The pressure field also continues to evolve as overpressure dissipates outward. Plume stabilization refers to the point at which the plume's geographic footprint and vertical extent have essentially ceased changing. The timescale for this process depends on site-specific factors including formation dip, mineralogy, permeability heterogeneity, residual trapping capacity, and the volume injected. Pawar et al. (2020) show that plume migration continues during the post-injection phase, with the plume centroid, spreading rate, and shape all continuing to evolve, driven by buoyancy and reservoir geology. Pawar et al. (2020) also find that the overpressure area and the CO_2 plume area can differ significantly, with overpressure remaining for a considerable period after injection stops. Bandilla et al. (2012) reach a similar conclusion at regional scale, showing that pressure dissipation occurs on different timescales than plume stabilization, meaning that even after the plume stops migrating, the pressure field may still be evolving and driving brine displacement.

Pawar et al. (2020) also find that the absence of plume stability does not by itself imply groundwater endangerment: leakage risk depends on whether the mobile plume encounters a wellbore or other conduit. However, as long as the plume is migrating, it may encounter new pathways outside the initial risk assessment. The proposed amendments require that any reduction in monitoring obligations be tied to demonstrated plume stabilization over at least five consecutive years of monitoring data, rather than a calendar period or model prediction. This ensures that the decision to reduce oversight is based on observed behavior, not on a forecast from the same class of models that have been proven unreliable at operational sites.

Q: Dr. Harvey, can you explain why CO_2-resistant materials are needed at all depths in wells that may encounter the CO_2 plume, not just in the injection zone?

A: The conventional well construction materials used throughout the oil and gas industry (Portland cement and carbon steel) were designed for hydrocarbon service, not for sustained exposure to CO_2-bearing brine, and the peer-reviewed literature documents that they degrade under those conditions.

Carroll et al. (2016) document that CO_2-bearing brine attacks Portland cement through carbonation reactions that progressively degrade the cement matrix. Gholami et al. (2021) identify deficient cement installations as a likely cause of CO_2 migration from the near-wellbore region and document multiple leakage pathways: through the cement matrix, along the casing-cement interface, and through the annular space between cement and formation rock. Fentaw et al. (2024) review the geochemical interactions relevant to well integrity in CO_2 storage and note that Portland cement is chemically incompatible with CO_2-saturated fluids. Sun et al. (2023) review corrosion mechanisms for steel under CO_2 storage conditions and note that the kinetics,

particularly under supercritical conditions and in high-chloride brines, remain incompletely characterized and poorly understood.

The reason CO_2-resistant materials are needed at all depths is that CO_2 does not remain confined to the injection interval within the wellbore, and, because it is buoyant relative to brine, it can migrate upward along the well, contacting cement and casing at every depth between the injection zone and the surface. Tian et al. (2026) additionally show that seismic loading can compromise wellbore integrity, meaning wells face both chemical and mechanical degradation. If conventional materials are used above the injection zone on the assumption that CO_2 will remain below, and that assumption proves wrong, the upper sections become degradation pathways to shallower formations and potentially to USDWs. At Decatur, monitoring wells built under modern Class VI requirements developed corrosion leaks within a few years (Snider and Lefebvre, 2024).

I support amendments requiring CO_2-resistant cement and casing at all depths in zones that may encounter the plume, material compatibility recertification after an initial two years and every four years thereafter, and tying the project lifetime to the duration of CO_2 in supercritical phase so that material performance obligations persist as long as the corrosive exposure does.

Q: Dr. Harvey, can you explain the relevant differences between Class II and Class VI wells?

A: The central difference is what the well is designed to contain and for how long. Class II wells serve hydrocarbon production, either by injecting CO_2 to enhance recovery (Class II-R) or by disposing of produced water and oilfield brines (Class II-D). Class VI wells are designed for permanent storage of CO_2. The regulatory requirements for each class reflect these different purposes, and the gap between them is substantial.

The two Class II subtypes present distinct conversion risks. A Class II-R well injects into a reservoir whose caprock has at least demonstrated the capacity to retain a buoyant fluid, as evidenced by the historical presence of trapped hydrocarbons. Furthermore, depleted oil reservoirs are typically under pressured because of the historical extraction of oil. This history reduces uncertainty about seal competence but does not eliminate it: the seal has never been exposed to the buoyancy, pressure, or geochemistry of CO_2 storage.

A Class II-D well lacks even this baseline. The caprock overlying a Class II-D disposal interval has never been tested against an upward-migrating buoyant phase. These wells were sited for injectivity and operational convenience, not long-term CO_2 containment. Converting a Class II-D well to CO_2 service fundamentally reverses the buoyancy regime: there is now a gravitationally force pushing upward on the caprock.

Neither Class II subtype requires the pressure-based AoR delineation, multi-project interference modeling, or corrective action obligations that Class VI permits demand. As injection volumes scale up, the pressure footprint extends well beyond the CO_2 plume itself (Wang et al., 2025), creating far-field risks that Class II evaluations were not designed to assess.

I support amendments requiring Class II operators to apply for Class VI permits when the primary purpose is long-term storage or when there is an increased risk to USDWs, rather than requiring both conditions simultaneously. I also support defining quantitative risk factors, including quantitative injection rate thresholds, that trigger the conversion requirement.

Q. Dr. Harvey, can you explain why rigorous statistical methods are necessary for groundwater monitoring around Class VI wells?

A. Groundwater monitoring is the primary means by which a regulator detects whether injection is affecting overlying drinking water aquifers. A monitoring program is only as reliable as the statistical framework used to interpret its data.

The challenge is distinguishing a real contamination signal from natural variability in groundwater chemistry. Aquifer geochemistry may fluctuate due to pumping patterns, natural heterogeneity, and measurement error. A single elevated reading at a monitoring well could reflect contamination from CO_2-displaced brine or it could reflect normal variation. Standard practice is to collect baseline data over a period before injection begins, during which the temporal variation in the key characteristics of the systems to be monitored can be statistically characterized. This way, operators can identify deviations that fall outside the statistical norm. The statistical framework determines how that distinction is made: what test is applied, what significance level is used, and how false-positive and false-negative rates are balanced.

The regulatory precedent is the RCRA groundwater monitoring framework at 40 CFR 264.97, which governs monitoring around hazardous waste facilities. That framework requires the operator to specify in advance statistical methods, data to be evaluated, the significance level, and the acceptable false-positive rate. The EPA Unified Guidance (2009) provides detailed methodology for implementing these requirements and documents why pre-specification is essential: it prevents the retroactive selection of methods that minimize the appearance of contamination. CO_2 storage presents monitoring challenges at least as complex as other types of hazardous waste disposal: the contaminant source is larger, the timescales are longer, and the

subsurface heterogeneity is at least as great. The monitoring framework should be at least as rigorous.

I support amendments requiring that groundwater monitoring for Class VI wells meet or exceed the statistical rigor of 40 CFR 264.97, that operators pre-specify the data, statistical tests, and significance levels in the permit, and that the monitoring network design be evaluated against a quantitative detection probability standard.

Confidentiality of Information
(19.15.42.8.B(2)(c) NMAC)

Q: Dr. Harvey, why do you support the proposed amendment to exempt safety-relevant data from CBI protection, as shown below at 19.15.42.8.B(2)(c) NMAC[2]?

19.15.42.8.B(2) Claims of confidentiality for the following information will be denied:

…

(c) Information already in the public record.

A: When constructing a permit application, operators will necessarily rely on information that is already in the public record to build a safety case. Confidential business information claims on information already in the public record undermine the right of New Mexicans to evaluate key, public information that underpins the basis of a permit that may irreversibly affect their water resources. Information already in the public record often includes but is not limited to earthquake data, well locations and well completion reports, geologic stratigraphic sections, DFIT tests from existing wells, and topographic maps of the surface and geologic layers. The rights of New Mexicans should not be subordinated to claims of commercial sensitivity over geological and other relevant data already in the public domain.

[2] The proposed rules have two sections labeled 19.15.42.8 NMAC. This provision is located within the section entitled "General Provisions."

Transitioning from Class II to Class VI
(19.15.42.8.F NMAC)

Q: Dr. Harvey, please explain why you support differentiated handling of Class II-D conversions and Class II-R conversions at 19.15.42.8.F NMAC[3], as shown below?

> **19.15.42.8.F(1)** Owners or operators that are injecting carbon dioxide for the primary purpose of long-term storage into an oil and gas reservoir or for which there is an increased risk to USDWs compared to Class II operations must apply for and obtain a Class VI geologic sequestration permit ~~when there is an increased risk to USDWs compared to Class II operations~~. In determining if there is an increased risk to USDWs, the owner or operator must consider the factors specified within this section.
>
> **19.15.42.8.F(2)** The director shall determine when there is an increased risk to USDWs compared to Class II operations and a Class VI permit is required. In order to make this determination the Director must consider the following:
>
> …
>
> **(f)** integrity of the caprock seal for long-term containment;

A: Class II-D disposal wells and Class II-R enhanced-oil-recovery wells present fundamentally different risks for Class VI conversion, yet the current regulatory framework does not differentiate between them.

A Class II-R well injects into a hydrocarbon reservoir whose caprock has at least demonstrated the capacity to retain a buoyant fluid phase, as evidenced by the historical presence of trapped hydrocarbons. That geological history reduces uncertainty regarding seal competence but does not eliminate it. A caprock that successfully retained hydrocarbons demonstrates that it functioned as an effective geologic seal under the pressure, fluid composition, and multiphase flow conditions associated with the historical hydrocarbon accumulation. Injection of large volumes of supercritical CO_2 introduces a different fluid system characterized by different density, viscosity, compressibility, wettability, solubility, and geochemical reactivity. Large-volume injection of CO_2 and impose buoyancy forces and elevates pore pressures substantially

[3] The proposed rules have two sections labeled 19.15.42.8 NMAC. This provision is located within the section entitled "General Program Requirements."

above the historical trap pressure, imposing mechanical stresses on a seal whose integrity has only been demonstrated under the original pressure regime. Consequently, historical hydrocarbon trapping provides evidence of seal competence but does not establish that the seal will be effective under long-term CO_2 storage conditions. Even for Class II-R conversions, therefore, the relevant question is not whether a competent caprock exists, but whether that caprock can maintain its sealing capacity under fluid regimes, pressures, and upward boutancy forces to which it has never been exposed.

Class II-D wells do not provide this baseline demonstration of ability to contain a buoyant fluid. The fluids typically disposed of through Class II-D wells — produced water and other oilfield brines — may be denser than or neutrally buoyant relative to native formation fluids; accordingly, they migrate downward or spread laterally rather than exerting upward pressure on the confining zone. Class II-D wells were sited on the basis of injectivity and operational convenience rather than long-term containment integrity. Although the Class II-D permit requires the operator to demonstrate that injected fluids will remain within the target formation and the caprock's capacity to resist upward fluid migration is not part of the regulatory evaluation. Conversion to Class VI service fundamentally reverses this buoyancy regime. If the overlying caprock is fractured, faulted, or mineralogically reactive to carbonic acid, repurposing the well for CO_2 injection without comprehensive site characterization introduces a potential migration pathway for supercritical CO_2 or displaced brine into overlying USDWs, which is a risk that was neither assessed nor required to be assessed under the original Class II-D authorization.

Definitions
(19.15.43.9.B NMAC)

Q: Dr. Harvey, why do you support tying post-injection site care to plume stabilization at 19.15.43.9.B, as shown below?

> 19.15.43.9.B(10) "**Plume stabilization**" mean the state when the carbon dioxide stream that has been injected subsurface essentially no longer expands vertically or horizontally, as demonstrated by a minimum of five consecutive years of monitoring data.
>
> ~~(9)~~(11) "**Post-injection site care**" means appropriate monitoring and other actions (including corrective action) needed following cessation of injection to ensure plume stabilization has occurred and that USDWs are not endangered, as required under Subsection N of 19.15.43.9 NMAC.

A: The CO_2 plume does not immediately stop moving after injection stops. Buoyancy forces continue to drive supercritical CO_2 upward against the caprock, residual trapping gradually immobilizes portions of the plume, and dissolution into formation brine slowly reduces the mobile CO_2 mass. The pressure field also continues to evolve as overpressure dissipates outward. The proposed definition of plume stabilization as the point at which the injected CO_2 stream essentially no longer expands vertically or horizontally captures the physical reality that containment cannot be confirmed at the moment injection stops.

It is important to note in this context that plume stabilization does not correspond to the cessation of risk to drinking water resources. Pawar et al. (2020) show that plume migration continues during the post-injection phase and find that the overpressure area and the CO_2 plume area can differ significantly, with overpressure remaining above critical levels for a considerable period after injection stops. Bandilla et al. (2012) reach a similar conclusion at regional scale, showing that pressure dissipation occurs on different timescales than plume stabilization, meaning that even after the plume stops expanding, the pressure field may still be evolving and driving brine displacement. These are reasons that the PISC period must extend long beyond plume stabilization occurs.

Required Class VI Permit Information
(19.15.43.9.C NMAC)

Q: Dr. Harvey, what are the proposed changes at 19.15.43.9.C(1)(c)?

A: The proposed changes at 19.15.43.9.C(1)(c) are:

> **19.15.43.9.C(1)(c)** Information on the geologic structure and hydrogeologic properties of the proposed storage site and overlying formations, including:
>
> …
>
> **(ii)** the location, orientation, and properties of known or suspected faults and fractures that may transect the confining zone(s) in the area of review and a determination that they would not interfere with containment under anticipated changes in pressure associated with injection;
>
> …
>
> **(v)** information on the seismic history including the presence and depth of seismic sources and a determination that the seismicity would not interfere with containment under anticipated changes in pressure associated with injection;

Q: Dr. Harvey, why do you support requiring dynamic fault stability analysis, as specified in these changes?

A: Faults near an injection site present two distinct hazards: they are potential migration pathways through which CO_2 or displaced brine can bypass confining zones and reach overlying USDWs, and they are potential sources of induced seismicity that can compromise the mechanical integrity of wellbores and surface infrastructure. The current regulatory framework addresses these risks through a qualitative "seismic history" that, in practice, amounts to placement of a regional seismicity map in the permit narrative. That approach provides no information about how specific faults at a specific site will respond to the sustained pore-pressure increases that large-volume CO_2 injection produces.

EPA's Site Characterization Guidance acknowledges this gap.[4] Section 2.3.7 states that if seismic hazard maps "indicate a substantial likelihood of seismic activity, other required

[4] *Geologic Sequestration of Carbon Dioxide, Underground Injection Control (UIC) Program Class VI Well Site Characterization Guidance*, United States Environmental Protection Agency (May 2013), https://www.epa.gov/sites/default/files/2015-07/documents/epa816r13004.pdf.

geologic information, such as geomechanical data, depth to confining zones, and fault stability analysis may be needed to demonstrate that seismic activity will not compromise subsurface containment."[5] In the Appendix, EPA cites Rutqvist et al. (2007) as concluding that numerical methods for analyzing geomechanical fault slip "provided a more accurate estimation of the maximum sustainable carbon dioxide injection pressure than the conventional analytical method because the numerical models can better account for the spatial evolution of both in situ stresses and fluid pressure."[6] This amendment makes mandatory what EPA's cited research identifies as the better approach.

The inadequacy of a static, regional assessment follows from the physics of fault reactivation. Pre-existing faults throughout continental interiors are commonly critically stressed, such that pore-pressure increases can reduce effective normal stress sufficiently to induce slip (Zoback and Gorelick, 2012). Because injection-induced pressure changes propagate through the formation over distances that extend well beyond the CO_2 plume, faults that appear remote from the injection well on a map may nonetheless fall within the pressure footprint and be driven toward failure (Langenbruch and Zoback, 2016; Langenbruch et al., 2018). Whether a given fault reactivates, and whether reactivation produces a conductive fracture pathway or a damaging seismic event, depends on site-specific properties: the local stress field, fault orientation and frictional characteristics, proximity to crystalline basement, and the magnitude and rate of pressure change (Rutqvist et al., 2016). None of these parameters can be evaluated from a regional seismicity catalog.

Bukar et al. (2025) document direct field evidence from the Decatur CO_2 storage project that injected CO_2 migrated along a fault and emerged into overlying permeable formations,

[5] EPA, 2013b, §2.3.7.
[6] EPA, 2013b, Appendix A.

which is precisely the containment failure that the AoR framework is designed to prevent. Infrastructure is also at risk: Tian et al. (2026) demonstrate that seismic loading from induced events can degrade wellbore cement, creating secondary leakage pathways that compound the original fault-related migration.

Dynamic fault stability analysis, which entails quantitative modeling of how identified faults respond to projected injection-induced pressure evolution over the life of the project, addresses each of these gaps. It requires the operator to characterize the in-situ stress state, identify and map faults within the pressure footprint, and evaluate whether projected pressure changes are sufficient to bring those faults to failure under site-specific conditions. Requiring this analysis as a permit condition ensures that fault-related risks are evaluated with the same quantitative rigor applied to plume migration and pressure-front delineation.

This analysis must be grounded in site-specific data (such as in situ stress measurements, fault orientation and frictional properties measured at or near the fault, and pore pressure data) from the formation in question. Analog data from other formations or other basins are not acceptable substitutes. Williams-Stroud et al. (2020) demonstrate at the Decatur CO_2 storage project that reservoir response to fluid pressure changes varied significantly between two injection wells in the same formation at the same site, confirming that fault and reservoir behavior at one location cannot be assumed predictive of behavior at another. Several Class VI applications submitted to EPA have included only static fault assessments — an approach equivalent to evaluating a dam's safety without considering what happens when the reservoir behind it fills.

Area of Review and Corrective Action
(19.15.41.7.A(4), 19.15.41.8.E(8), 19.15.42.7.A(3), 19.15.43.9.E, 19.15.43.9.J(4) NMAC)

Q: Dr. Harvey, could you please outline the reasons why you support the mandating of automatic AoR/CAP re-evaluation upon the exceedance of pre-specified thresholds in monitoring data and the discovery of new artificial penetrations within the AoR at 19.15.43.9.E(2)(b)(ii), as shown below?

> **19.15.43.9.E(2)**… the owner or operator must submit an area of review and corrective action plan that includes the following information:
>
> …
>
> **(b)** A description of:
>
> …
>
> **(ii)** The monitoring and operational conditions that would warrant a reevaluation of the area of review prior to the next scheduled reevaluation as determined by the minimum fixed frequency established in item (i) of Subparagraph (b) of Paragraph (2) of this Subsection, including pre-specified, well-specific exceedance thresholds in pressure monitoring data and geochemical monitoring data and the discovery of a previously unidentified artificial penetration;

A: The Area of Review (AoR) is derived from a reservoir simulation model. That model predicts how pressure will propagate, where CO_2 will migrate, and at what rates. Monitoring data such as pressure readings and geochemical measurements provide a test of the model's predictions against observed subsurface behavior. If a pre-specified monitoring threshold is exceeded in any monitoring well, it means the model's predictions fail and that any product derived from the model, such as the AoR, is no longer dependable. The appropriate response is to recalibrate the model to match the observed data and re-delineate the AoR on the basis of the updated predictions. Making this re-evaluation automatic upon threshold exceedance removes the discretion to continue operating under an AoR that the operator's own monitoring data have invalidated. A model that cannot reproduce the data it was designed to predict has no basis for predicting the boundaries within which the public is supposed to be protected.

If a previously unknown well is discovered within the AoR after the permit has been issued, that well could be a path for pressure-driven brine or CO_2 to reach a drinking water aquifer, and neither the corrective action plan nor the monitoring network was designed to address it. Adding this to New Mexico's regulations is warranted by the fact that well inventories in mature basins are systematically incomplete. Gasda et al. (2004) show that in well-dense basins, hundreds of wells may penetrate the injection zone, and information on many of them is unavailable. Boutot et al. (2022) found that the documented orphaned well inventory in the United States grew by over 50% in just seven months through database updates and field inspections, showing that well discovery is an ongoing process. Arbad et al. (2024) found that within a study AoR in the Illinois Basin, the majority of well reports were handwritten and many were incomplete. Any framework that treats the initial well inventory as final is not defensible. Discovery of a new artificial penetration within the AoR is material new information that changes the project's risks and must trigger reassessment.

Q: Dr. Harvey, please explain your support for independent third-party verification of plume modeling and AoR delineation at 19.15.43.9.E(2)(c) and 19.15.43.9.E(3)(e) NMAC, as shown below?

> **19.15.43.9.E(2)**… the owner or operator must submit an area of review and corrective action plan that includes the following information:
>
> …
>
> **(c)** Findings of independent, certified third-party verification of the modeling ensemble used to delineate the area of review.
>
> **19.15.43.9.E(3)** Using a qualified professional expert, owners ~~Owners~~ or operators of Class VI wells must perform the following actions to delineate the area of review and identify all wells that require corrective action:
>
> …
>
> **(e)** Use independent, certified third-party verification of modeling ensemble.

A: The AoR model is a foundational component in the Class VI framework. The AoR model determines which drinking water aquifers receive regulatory protection and which do not; it determines which faults are critically assessed for stability; it determines which wells require corrective action. If the only people who have examined the model are the people the operator paid to build it, the state is accepting a safety determination it cannot independently evaluate. This is not a reflection on any individual operator's integrity; it reflects the structural reality that the entity submitting the model has an economic interest in the outcome.

The delineation of the AoR requires technically specialized skills requiring deep expertise in both numerical methods and site-specific geoscience. The process involves substantial professional judgment at every stage, and the scientific literature shows that these choices affect results in ways that can shift the AoR boundary by kilometers. Demyanov et al. (2019) show that geological scenario selection, which happens before a single simulation is run, introduces uncertainty that propagates through every prediction. Arnold et al. (2019) demonstrate that the geological prior assumptions embedded in a model can produce history matches that appear acceptable but yield unreliable predictions if those priors are not geologically plausible. The bias that Arnold et al. identify is a form of bias that even the experienced modeler (who chooses the priors) is unable to identify in their own work, because the model's apparent good fit confirms rather than challenges the assumptions. Independent review is the institutional mechanism for catching it. Independent technical review ensures that poor priors or optimistic assumptions can be identified before injection begins, not after drinking water has been contaminated.

Q: Dr. Harvey, please explain your support for the inclusion of an independent third-party verification of plume modeling and AoR delineation in materials made available to the public for comment at 19.15.41.8.E(8), as shown below?

> **19.15.41.8.E(8)** In addition to the general public notice described in Paragraph (5) of this subsection, all persons identified in Subparagraph (a) of Paragraph (5) of this subsection shall be mailed a copy of the fact sheet, the permit application (if any), inclusive of the third-party verification of the modeling ensemble, and the draft permit (if any).

A: I further endorse that the state of New Mexico make the verification findings available for public comment before permit issuance. It is important that this requirement be codified in the regulations themselves: for example, most if not all existing Class VI applications to the United States Environmental Protection Agency (e.g., Marquis CCS in Illinois) have not made the model evaluation reasoning part of the record available for public comment, requiring instead that the public know how to request specific administrative documents and be able to do so within a very limited time period during which Public Comment is open.

Q: Dr. Harvey, what are the proposed amendments relating to delineation of the AoR and identification of wells requiring corrective action at 19.15.43.9.E(3)(a) NMAC?

A: The proposed changes at 19.15.43.9.E(3)(a) NMAC are:

> **19.15.43.9.E(3)** Using a qualified professional expert, owners ~~Owners~~ or operators of Class VI wells must perform the following actions to delineate the area of review and identify all wells that require corrective action:
>
> > **(a)** Predict, using existing site characterization, monitoring and operational data, and computational, peer-reviewed or commercially-available modeling, the projected lateral and vertical migration of the carbon dioxide plume ~~and formation fluids in the subsurface from the commencement of injection activities~~ until the plume movement ceases~~, until pressure differentials sufficient to cause the movement of injected fluids or formation fluids into a USDW are no longer present, or until the end of a fixed time period as determined by the Director~~, calculate the area over which induced pressure differentials could drive movement of formation fluids or injected fluids into a USDW over the maximum duration of injection, and define the AoR as the union of these two areas. The model must:

Q: What is the basis for requiring that flow model development is conducted by a qualified professional expert?

A: The AoR model determines which drinking water aquifers the operator must protect, and the modeling choices involved are complex, subjective, and consequential enough that unqualified practitioners will make errors that put USDWs at risk. Celia and Nordbotten (2009) note that the mathematical description of CO_2 storage systems is inherently complex, requiring simplifying assumptions whose appropriateness depends on specialized judgment. Oliver and Chen (2011) show that reservoir model calibration is ill-posed, meaning that distinguishing a reliable fit from a misleading one requires deep expertise in both numerical methods and site-specific geoscience. Rudolph and Goulding (2017), analyzing over 500 ExxonMobil wildcats drilled over two decades, found that even highly experienced geoscientists with decades of proprietary data made predictions about reservoirs that contained considerable uncertainty. In Class VI applications submitted to the United States Environmental Protection Agency, it is often not clear whether a trained professional built the geologic model and associated reservoir simulation framework (see, for example, Pratt Zero Carbon, LLC, Class VI Permit Application, Pratt Energy CCUS#1 (PECCUS-1), UIC Permit No. KSS151570001, EPA Docket No. EPA-R07-OW-2026-1585). A qualified-professional requirement analogous to existing EPA standards for groundwater monitoring at CCR facilities ensures that the work on which drinking water protection depends meets a defensible professional standard.

Q: Why do you support the proposed amendment requiring operators to use peer-reviewed or commercially-available computational code?

A: The major elements of a Class VI permit — the area of review, the predicted plume footprint, the post-injection monitoring plan — rests on the output of reservoir simulation

models. The predictions can only be as reliable as the software that produces them. Without peer review or a model developed to a commercially available standard, neither the state nor the public can determine whether the code correctly implements the physics it claims to represent, and without full disclosure of the code's assumptions, the state cannot evaluate whether the model is appropriate for the site.

The choice of simulation code and method is a substantive scientific decision, not an implementation detail. Cavanagh and Haszeldine (2014) report that standard Darcy flow simulations failed to match the observed CO_2 plume geometry at Sleipner, requiring an entirely different modeling approach (capillary flow modeling with invasion percolation physics) to reproduce the plume's behavior. Nilsen et al. (2011) compare two fundamentally different simulation approaches (vertically integrated and full three-dimensional) applied to the same Sleipner site and show that they produce different predictions, with the appropriate choice depending on site-specific physical conditions. Cusini et al. (2019) find that the widely used Todd-Longstaff upscaling method, even after being calibrated against high-resolution reference simulations, was highly sensitive to changes in simulation parameters, meaning that a calibrated model may lose validity when conditions change, as they inevitably do during a decades-long injection project.

The same sensitivity applies to the constitutive relationships embedded in every simulation. Moodie et al. (2021) show that the choice of relative permeability curve — one of the fundamental constitutive relationships governing multiphase flow — significantly changes predictions of CO_2 phase distribution, trapping efficiency, and phase behavior, even when all other model parameters remain identical. Celia and Nordbotten (2009) emphasize that CO_2 storage modeling necessarily involves simplifying assumptions, and that the appropriateness of

those assumptions is influenced by the geological setting. An assumption that is valid for one site may be invalid for another, but a regulator who cannot see the assumptions cannot make that determination.

Requiring the modeler to reproduce documented test cases before permit submission serves a distinct function: it ensures that the person running the code for a specific permit understands its behavior and limitations under conditions relevant to the proposed site. Requiring full disclosure of code assumptions, governing equations, equations of state, and constitutive relationships ensures that the state can evaluate whether the model is appropriate. The current rule treats AoR modeling as a black box: the operator submits predictions, but the reasoning behind them is opaque. A regulator reviewing a conclusion without access to the reasoning behind it cannot perform meaningful oversight.

EPA's AoR guidance already recommends each element of this amendment. Section 3.3.3.1 recommends "a code be used that includes routines for the relevant physical processes at the site based on peer-reviewed theory and equations." On proprietary codes, Section 2.6 states that operators "are encouraged to clearly disclose to the UIC Program Director the code assumptions and, if necessary, governing equations and equations of state with the permit application" (EPA, 2013a, §2.6). EPA thus already recommends peer-reviewed code and assumption disclosure: these amendments convert these recommendations to requirements.

Q: Dr. Harvey, could you please explain why the definition of the AoR in the underground injection control program criteria and standards section, based on pressure, is necessary?

A. If the AoR is drawn around the CO_2 plume alone, it may exclude legacy wells, faults, and drinking water supply within a much larger pressure-affected zone outside the regulatory

perimeter. In most cases, the pressure front extends far beyond the plume itself, with pressure propagation reaching 100 km or more while plumes extend ~10 km (Birkholzer & Zhou, 2009). The zone of increased pressure may be very large in regions with more than one injection site (Wang et al., 2025). Within the zone of increased pressure, elevated formation pressure drives native brine upward through old wells and fractures into overlying drinking water aquifers (Tsang et al., 2008). White et al. (2020) demonstrate that at one of three studied CCS sites, the pressure-defined AoR was approximately 4 times the CO_2 plume footprint, confirming that a plume-only AoR can leave most of the pressure-affected zone outside the regulatory perimeter.

To take the precautionary approach to protecting New Mexico's water resources, the AoR needs to be delineated such that it is at least as large as the maximum extent of the modeled zone of increased pressure and the modeled CO_2-plume extent. EPA's AoR guidance already takes this position. In Section 3.4, the Agency states, "EPA recommends that the AoR encompass the maximum extent of the separate-phase plume or pressure front over the lifetime of the project and entire timeframe of the model simulations." This regulatory language makes the recommendation of EPA a requirement.

Q: Dr. Harvey, what is the basis for the proposed amendments to 19.15.41.7.A(4) and 19.15.42.7.A(3) NMAC, relating to the definition of the AoR, as shown below?

> **19.15.41.7.A(4) "Area of review"** means the area surrounding an injection well described according to the criteria set forth in § 40 CFR 146.06 ~~or in the case of an area permit, the project area plus a circumscribing area the width of which is either one-quarter of a mile or a number calculated according to the criteria set forth in § 40 CFR 146.06~~.
>
> **19.15.42.7.A(3) "Area of review"** means the area surrounding an injection well described according to the criteria set forth in § 40 CFR 146.06 ~~or in the case of an area permit, the project area plus a circumscribing area the width of which is either ¼ of a mile or a number calculated according to the criteria set forth in Section 40 CFR 146.06~~.

A: The rules proposed by the Division expressly prohibit Area Permits at 19.15.42.10.C NMAC. Accordingly, the reference to the calculation of the AoR for area permits here can be removed.

Q: What is the basis for the proposed amendments to 19.15.43.9.E(3)(a) NMAC, relating to a modeling ensemble approach, as shown below?

> **19.15.43.9.E(3)(a)(i)** Use an ensemble approach that considers the full range of realistic variation in and interaction among key parameters, including permeability-field parameters, kv/kh ratio, porosity, and relative permeability curves and hysteresis;

A: A single deterministic model run, which is what most Class VI applications currently use, produces one prediction of where pressure and CO_2 will go with no indication of how wrong that prediction might be. If the single run underestimates the AoR, then legacy wells, faults, and drinking water aquifers within the actual area of influence are left unprotected. The subsurface properties governing CO_2 migration are deeply uncertain: permeability varies over an order of magnitude across short distances (Ni et al., 2025), relative permeability curves substantially change predicted plume behavior (Moodie et al., 2021), and caprock geometry affects where CO_2 accumulates. Oliver and Chen (2011) show that reservoir model calibration is ill-posed, and Subbey et al. (2004) confirm that many different models can match available data while predicting very different outcomes. Pawar et al. (2020) demonstrate that realistic uncertainty bounds require simulations across multiple, equally likely realizations. The literature supporting this point is extensive and consistent: Saló-Salgado et al. (2024), Bandilla et al. (2012), Cremon et al. (2020), Arnold et al. (2019), Demyanov et al. (2019), Reynolds et al. (2018), Chen et al. (2018), Crain et al. (2024), Burton-Kelly et al. (2025), Hoffman and Alessio (2017), and Cusini et al. (2019). Protecting drinking water requires knowing the range of plausible outcomes, not just one.

EPA's AoR guidance takes a step toward this requirement but stops short. Section 3.3.4 recommends "sensitivity analyses as the principal evaluation tool for characterizing the [most and least important] sources of error in computational models" and recommends that "maximum-risk scenario simulations can be conducted... perturbation predictions that account for uncertainty" (EPA, 2013a, §3.3.4). The amendment requires what the guidance's own logic implies: if uncertainty in individual parameters matters enough to warrant sensitivity analysis, the compounding of those uncertainties matters enough to warrant ensemble simulation.

A two-level full factorial analysis is one straightforward method that would satisfy this requirement. To employ a full factorial analysis, the operator identifies the key uncertain parameters in the reservoir model (e.g., the topography of the bottom surface of the caprock, parameters shaping the formation permeability field, relative permeability curve shape, caprock thickness, the ratio of vertical to horizontal permeability, etc.) and assigns each a defensible high and low bound based on site characterization data. The model is then run for every combination of these high and low values. For five parameters, this produces $2^5 = 32$ simulations; for seven, 128.

This approach captures not only the effect of each parameter individually but also their interactions. The computational burden is modest: a minor ensemble of reservoir simulations is well within the capacity of any operator proposing a commercial-scale injection project. Such a method is systematic, reproducible, and auditable by the regulator. More sophisticated ensemble methods exist, but a full factorial design sets a defensible minimum floor: the operator must demonstrate that the model is robust across the plausible range of subsurface conditions, not merely consistent with one set of assumptions.

Ideally, the potential zone of increased pressure and the potential area of CO_2 plume dispersion can be delineated from a union of the zones of increased pressure and CO_2 plumes in each of the ensemble members: that is, for each, the operative boundary for protecting New Mexico's drinking water becomes the outermost boundary across the full set of outcomes.

Q: Dr. Harvey, what is the basis for the amendment at 19.15.43.9.E(3)(a)(ii) NMAC requiring the operator to install at least three of the monitoring wells in regions where modeling uncertainty is greatest, as shown below?

> **19.15.43.9.E(3)(a)~~(i)~~(ii)** Be based on detailed geologic data collected from at least three wells to characterize the injection zone(s), confining zone(s) and any additional zones; and anticipated operating data, including injection pressures, rates, and total volumes over the proposed life of the geologic sequestration project;

A. A monitoring well placed where the operator has high confidence of plume advancement can provide support for the use of the existing reservoir model (as outlined previously); however, this is not the only way in which monitoring wells can provide value. Given the uncertainty inherent to subsurface geologic systems, a well that is placed where uncertainty in subsurface characteristics is greatest can provide early evidence to support or disprove a given hypothesis about subsurface geology and likely plume evolution. Better understanding of the subsurface ensures a higher likelihood of protecting USDWs.

The operational record illustrates why this matters. Eiken et al. (2011) report that at Sleipner, In Salah, and Snøhvit, monitoring revealed geological controls on plume behavior that pre-injection characterization had not identified, and that the monitoring data proved as valuable for improving the understanding of the reservoir as for tracking the plume itself. Methods exist for translating this principle into practice. Hoffman and Alessio (2017) use probabilistic plume mapping to characterize the range of plausible plume paths and identify areas of key monitoring concern. Chen et al. (2018) find that well placement significantly affects the degree to which

monitoring data reduce uncertainty in CO_2 leakage estimates, with one location in their study yielding 24% more uncertainty reduction than another. Crain et al. (2024) reach a similar conclusion using a framework that integrates monitoring well optimization with ensemble-based history matching: data from optimally located wells yield substantially greater reduction in uncertainty about plume extent than data from heuristically placed wells, because the data are collected where they most effectively discriminate among competing geological models.

Q: Dr. Harvey, could you please explain why the definition of the AoR should be made as the maximum area between potential AoR boundaries, as shown below at 19.15.43.9.E(3)(a)(iii) NMAC?

> **19.15.43.9.E(3)(a)(iii)** Calculate the project AoR as the union of all potential AoRs computed using pressure-driven methods, the areal CO_2 plume extent, and a simple scalar factor for estimating distance of pressure front based on maximum plume extent;

A: Because the properties of the subsurface are unknown to any degree of certainty, no single estimation method can claim definitive accuracy for a geologically complex subsurface. If a single method underestimates the AoR, legacy wells beyond the project's AoR boundary go unevaluated and pressure-driven brine displacement into USDWs goes unmonitored. Birkholzer and Zhou (2009) explicitly warn against a one-size-fits-all approach, noting that the required characterization area depends on detailed basin-scale conditions and vulnerabilities. Bandilla et al. (2012) show that differences in geological representation substantially change simulated plume extent.

A straightforward way to manage this unavoidable uncertainty when protecting New Mexico's resources is to define the project's AoR as the union of the set of all candidate AoRs computed from all model simulations, effectively defined radially as the maximum extent of any candidate AoR computed with any method. This includes the set of AoRs corresponding to each

of simulations making up the ensemble of potentially realistic reservoir models; it includes all candidate AoRs computed as the boundary of the CO_2 plume, as simulated with each of the ensemble models. This approach is protective against unavoidable uncertainty. When the consequence of under-sizing the AoR is irreversible contamination of a drinking water aquifer, the conservative estimate is the only responsible one.

Q: Dr. Harvey, on what basis do you support regulations requiring CO_2 plume simulation to include reactive transport modeling that accounts for the geochemical reactions/lithology of the target reservoir and caprock, as shown below at 19.15.43.9.E(3)(a)(v) NMAC?

> **19.15.43.9.E(3)(a)(v)** Evaluate reactive transport to account for the geochemical reactions and lithology of the target reservoir and caprocks;

A: In certain rock types, particularly carbonate reservoirs, omitting geochemical reactions from the model will produce simulations that are wrong about where CO_2 will go and how the confining formations will perform, because such reactions change the rock's porosity, permeability, and mechanical strength over time. Ilgen et al. (2018) show that CO_2-brine-shale interactions can weaken caprock sealing capacity through mineral dissolution and pore structure changes, a process that a multiphase-flow-only model ignores entirely. Vilarrasa et al. (2019) identify geochemical effects as a triggering mechanism for induced seismicity in carbonate-containing formations. Gholami et al. (2021) report that deficient cementing of wellbores is a likely cause of CO_2 migration into overlying formations. Cheng et al. (2023) conclude that coupled thermal-hydraulic-mechanical-chemical processes must be modeled together for reliable predictions. The EPA's AoR guidance acknowledges the need for geochemical considerations (EPA, 2013). The EPA Site Characterization Guidance goes further, explicitly discussing reactive transport modeling as a tool for evaluating how “reactions (e.g., loss of carbonates,

precipitation of carbonates, long-term dissolution of silicates) can change permeability, release undesirable elements, alter injectivity, and affect ultimate storage capacity" (EPA, 2013b, §2.3.9). However, the guidance frames this important capability as optional: "The owner or operator may choose to conduct reactive transport modeling to account for any significant effects of geochemistry while delineating the AoR" (EPA, 2013b, §2.3.9). I support this regulation because it codifies an important capability.

In formations where carbonate minerals are present in the caprock or reservoir, the geochemical effects that reactive transport modeling captures are physical realities that will occur whether or not the model accounts for them. Making the modeling optional in such formations is equivalent to allowing the operator to ignore a known degradation mechanism. Choi et al. (2021) demonstrate that shale specimens exposed to both supercritical CO_2 and brine show significant mechanical weakening, confirming that in formations where CO_2-saturated brine contacts carbonate-bearing caprock, a model that omits geochemical reactions will overestimate caprock integrity.

Q: Dr. Harvey, could you please justify your support for explicit regulatory delineation of an Intensive Correction Action Area tied to the anticipated lateral extent of the CO_2 plume itself, as shown below at 19.15.43.9.B(9) and 19.15.43.9.E(3)(a)(v) NMAC??

> **19.15.43.9.B(9) "Intensive Corrective Action Area**" means the area into which brine with supercritical carbon dioxide will potentially intrude, defined radially from the injection well location as the maximum plume boundary extent across all model simulations, with an additional buffer of half the distance of the maximum plume boundary extent.
>
> **19.15.43.9.E(3)(a)(vi)** Identify the Intensive Corrective Action Area

A: CO_2 injection creates two qualitatively different zones of threat to drinking water, and the regulations must address both. In the zone of increased pressure caused by injection of CO_2,

elevated pressure can push native brine into overlying aquifers through old wells and faults. In the zone that may come into contact with the CO_2 plume, CO_2 also forms carbonic acid that attacks the cement and steel in wells it contacts, progressively converting adequately plugged wells into leaking conduits. The zone that may come into contact with the CO_2 plume requires more intensive corrective action specifically because of the geochemical degradation that CO_2 imposes: conventional Portland cement is degraded by reacting with CO_2-bearing brine through carbonation processes that, in the presence of pre-existing defects such as fractures, microannuli, or interface gaps, can either seal or widen leakage pathways depending on flow conditions (Carroll et al., 2016), which is an outcome that cannot be predicted without site-specific testing; steel casing corrodes through mechanisms not yet fully characterized (Sun et al., 2023). These degradation processes are absent in the outer pressure zone where no CO_2 is present. EPA's own Well Testing and Monitoring Guidance acknowledges that Class VI wells face a "more corrosive bottomhole environment" than other injection wells, and that the mandated monitoring methods have recognized limitations: the guidance cites a field case in which "extensive corrosion caused joints to collapse although coupons at the wellhead of the same well indicated minimal corrosion rates" (Smith and Pakalapati, 2004, cited in EPA, 2013c, §3.4.1). A monitoring regime that EPA's own guidance acknowledges can miss the failures it is designed to detect is not a substitute for requiring CO_2-resistant materials in the first place.

The 50% buffer is warranted because multiphase-flow simulation is notoriously uncertain, and ensemble modeling consistently shows substantial uncertainty in plume boundary predictions (Hoffman & Alessio, 2017; Onishi et al. 2019). Furthermore, we know that the true migration of multiphase flow in the subsurface is dominated by flow through channels and zones of high permeability. Without a buffer, an undersized Intensive Corrective Action Area is

possible, which would imply that wells within the actual plume zone but outside the regulatory boundary receive no CO_2-specific corrective action until their materials have already begun to degrade (Hoffman & Alessio, 2017).

Q: Dr. Harvey, why do you support requiring 3D seismic characterization of the full AOR, as shown below at 19.15.43.9.E(3)(a)(vii)?

> **19.15.43.9.E(3)(a)~~(iii)~~(vii)** Consider potential migration through faults, fractures, and artificial penetrations, using 3D seismic characterization; and

A: Faults within the AoR are the pathways through which CO_2 and brine can migrate from the injection zone to overlying drinking water aquifers, and induced seismicity on those faults can damage wellbore infrastructure. You cannot evaluate a fault you have not found, and 3D seismic is the only available technology with the coverage and resolution to systematically map faults across the full AoR. Furthermore, faults can only be properly identified on 3D seismic with individuals who have extensive geophysical interpretation training. Williams-Stroud et al. (2020) show that even with 3D seismic, identifying faults with small vertical offsets is challenging, underscoring that comprehensive coverage is the minimum standard. Making 3D seismic optional is equivalent to making fault identification optional.

EPA's Site Characterization Guidance supports this conclusion. Section 2.3.2 states that "EPA strongly encourages the use of seismic data when evaluating structures at a GS site and emphasizes the usefulness of 3D seismic data or a grid of 2D seismic profiles," and notes that "If geology is complex, especially around the point of injection, and greater detail is needed, 3D data are superior" (EPA, 2013b, §2.3.10.1). EPA further recommends that owners or operators "clearly indicate whether faulting is likely to enhance the project site by providing a trap, or potentially compromise the confining zone." However, the guidance frames 3D seismic as a recommendation, not a requirement, leaving operators free to submit permit applications with

only 2D data or no seismic data at all. The tool that EPA itself identifies as superior for fault detection should not be optional.

Q: Dr. Harvey, why should a Class VI project account for other operational or historic injection projects, as shown below at 19.15.43.9.E(3)(a)(viii) NMAC?

> **19.15.43.9.E(3)(a)(viii)** Consider pressure and chemical interactions with all other operational or historic injection projects within a ten-mile radius.

A: When multiple wells inject into the same formation, their individual pressure fields combine, pushing the total area of elevated pressure beyond what any individual well's model would predict, and with it, the area where drinking water aquifers are at risk. If each well is modeled independently, the resulting AoRs are undersized. Birkholzer and Zhou (2009), modeling 20 injection sites in the Illinois Basin, found that cumulative pressure buildup extended across much of the basin, with significant well-to-well interference. Wang et al. (2025) confirmed this with multiple Gulf Coast CCS projects: individually calculated AoRs merged into combined pressure footprints that encompassed large numbers of legacy wells. The EPA's AoR guidance acknowledges the need to account for inter-well effects (EPA, 2013). Prohibiting after-the-fact project expansions outside the unified framework prevents the incremental accumulation of unmodeled pressure effects. EPA's AoR guidance already envisions this. Section 3.4 states that "EPA recommends that the AoR delineation boundaries for the cumulative GS project be based on modeling that accounts for the anticipated injection rates from all planned Class VI injection wells." (EPA, 2013a, §3.4). This amendment makes that recommendation mandatory.

Q: How would this provision also account for potential interactions between Class I and Class VI wells?

A: Class I hazardous waste injection wells and Class VI CO_2 storage wells frequently target the same types of deep saline formations. Both programs inject large fluid volumes into confined

geologic intervals and depend on the same physical containment mechanisms: caprock seal integrity, well integrity, and stable pressure conditions. Tsang et al. (2008) systematically compare the hydrologic issues across nine technical areas — including well integrity, abandoned well problems, buoyancy, multiphase flow, and caprock effectiveness — and conclude that CO_2 injection involves more complex hydrologic processes than liquid waste injection. This means that introducing a Class VI project into a formation that already hosts a Class I hazardous waste plume does not merely add a second injection program; it superimposes a more complex and more disruptive set of subsurface processes onto an existing containment system that was not designed for those conditions.

The concern is pressure interaction. As I described in my earlier testimony on the two zones of concern, CO_2 injection generates pressure perturbations that propagate far beyond the CO_2 plume itself. Wang et al. (2025) demonstrate that when multiple injection projects target the same formation, their individual pressure fields combine and merge, creating cumulative pressure footprints that exceed what any single project would produce in isolation. This pressure interference is not limited to interactions among Class VI wells. Any injection operation in hydraulic communication with the Class VI injection zone — including Class I hazardous waste disposal wells — will experience the same pressure superposition. A Class I facility whose permit was issued under pressure conditions that existed before CO_2 injection began may find that the safety margins embedded in its containment analysis are no longer valid once a nearby Class VI project alters the regional pressure field.

The geochemical dimension compounds the pressure concern. If the CO_2 plume or CO_2-saturated brine migrates far enough to interact with a hazardous waste plume, it introduces carbonic acid into a geochemical system the Class I permit never evaluated for those conditions.

The confining formations and wellbore materials that contain the hazardous waste plume were selected and evaluated for the geochemistry of the waste stream, not for the acidified conditions that supercritical CO_2 mixed with brine creates. If CO_2-induced acidification degrades the seal or well materials that were relied upon in the Class I permit, the result is not a release of CO_2 or displaced brine — it is a potential release of hazardous waste into formations that overlie the injection zone, including USDWs.

The regulatory gap is straightforward. Under the current framework, Class I and Class VI permits are issued independently, under separate regulatory programs, often by different agencies. Nothing in either program requires the Class I operator to evaluate whether its containment analysis remains valid under the pressure and geochemical conditions that a nearby Class VI project will create, and nothing in the Class VI program requires the CO_2 operator to model the consequences of its pressure footprint reaching a hazardous waste plume. Each permit is issued as if the other program does not exist.

The consequences of a failure involving hazardous waste are categorically different from those involving displaced brine. If pressure-driven brine migrates upward through a compromised well, the contamination may be remediable over time. If hazardous waste — which by definition poses risks to human health and the environment at any concentration — migrates through the same pathway, the contamination may be permanent and the health consequences severe.

The Marquis Carbon Injection project in Putnam County, Illinois illustrates why this concern is not hypothetical. EPA permitted Marquis in April 2026 to inject up to 1.5 million metric tons of CO_2 per year into the Mt. Simon Sandstone. In the same town of Hennepin, a Class I hazardous waste injection well operated by ArcelorMittal, Hennepin Works, for several

decades injected RCRA-regulated spent steel pickle liquor — a corrosive, heavy-metal-laden hazardous waste classified under waste code K062 — into the same formation. The Class I well's no-migration demonstration, was predicated on analysis conducted under the geochemical and pressure conditions that existed before any CO_2 injection was contemplated. That analysis assumed no induced seismicity, native brine geochemistry with no CO_2-driven acidification, and a pressure regime unperturbed by large-scale injection into the same formation. Every one of those assumptions may be invalidated by the Class VI project, yet nothing in either regulatory program requires anyone to reassess whether the hazardous waste containment analysis remains valid under the altered conditions. If the CO_2-induced pressure front reaches the hazardous waste plume and alters flow paths, or if CO_2-acidified brine degrades the confining zone or wellbore materials that the Class I permit relied upon, the result is a potential release of hazardous waste into overlying formations and USDWs. New Mexico should not replicate this regulatory gap.

I therefore support the amendment to require operators to consider pressure and chemical interactions with all other operational or historic injection projects within a ten-mile radius in part because this will help protect New Mexico's drinking water resources from unintended interaction between Class I and Class VI plumes.[7]

Q: Dr. Harvey, could you please outline the reasoning behind your support of using specific predictions at key monitoring wells to help ensure that the CO_2 plume model is sufficiently accurate in its representation of plume evolution, as shown below at 19.15.43.9.E(3) NMAC?

> **19.15.43.9.E(3)** Using a qualified professional expert, owners ~~Owners~~ or operators of Class VI wells must perform the following actions to delineate the area of review and identify all wells that require corrective action:

[7] For further information on this subject, see U.S. EPA Region 5, "Proposal to Reissue an Exemption to ArcelorMittal — Hennepin Works for the Continued Injection of Hazardous Waste Subject to the Land Disposal Restrictions" (2008).

…

(b) Confirm the model's validity by placement of a monitoring well where plume is modeled to be after one year of commencement of injection.

A: Without direct observational evidence that the CO_2 plume is going where the model says it should, the entire permit safety framework rests on an uncertain and untested hypothesis. If the plume migrates in an unexpected direction or at an unexpected rate, it may encounter legacy wells, faults, or confining-zone weaknesses that the corrective action plan did not address, and the consequence is undetected migration toward a drinking water aquifer. At every saline-aquifer CCS site with published data, pre-injection models were wrong about plume behavior: at Sleipner, geological features discovered only during injection controlled plume development (Eiken et al., 2011); at Decatur, CO_2 migrated along a fault and re-emerged in overlying permeable formations (Bukar et al., 2025); at Snøhvit, after pressure analysis and rock mechanical investigation revealed that the original reservoir could not sustain the required injection rate, it was abandoned (Hansen et al., 2013). Cavanagh and Haszeldine (2014) are one of many groups of researchers who have shown that standard simulation approaches can fail to reproduce observed plume geometry: in the interest of protecting New Mexico's drinking water resources, a scientifically rigorous approach of testing model performance is warranted.

This amendment converts the plume model from an unverifiable assertion into a testable, falsifiable prediction. If an operator cannot predict CO_2 arrival at a location chosen for maximum confidence, the operator's claims about which aquifers are safe and which faults are beyond the pressure front lack credibility. Every CCS site with published data has shown that pre-injection models fail to capture actual plume behavior (Eiken et al., 2011; Hansen et al., 2013; Bukar et al., 2025). Requiring cessation upon prediction failure is proportional to the risk posed: a model that fails its first real-world test can no longer be trusted to identify risks to drinking water.

Q: Dr. Harvey, what are the proposed amendments at 19.15.43.9.E(3) NMAC?

A: The proposed amendments at 19.15.43.9.E(3) NMAC are:

> **19.15.43.9.E(3)~~(b)~~(c)** Using ~~methods approved by the director~~ state oil and gas, water, and geological agency databases, county records, and private well-databases, identify all penetrations, including active and abandoned wells and underground mines, in the area of review that may penetrate the confining zone(s). When plugging records are incomplete, use field testing to identify all penetrations. Provide a ~~description~~ record of each well's type, construction, date drilled, location, depth, record of plugging and/or completion, and any additional information the director may require.

Q: Could you please explain why you recommend that New Mexico adopt regulation to require Class VI applicants to document a detailed search for artificial penetrations?

A: Every missed well within the AoR is a potential unmonitored, unevaluated conduit through which injection-driven pressure can push contaminated brine into a drinking water aquifer. Relying on a single database will miss wells. Gasda et al. (2004) show that in mature basins, hundreds of wells may penetrate the injection zone within an AoR, and information on many of those wells is absent from any one source. Arbad et al. (2024) found that constructing a well inventory for a single AoR in the Illinois Basin required compiling data from over 550 individual well documents, many of which were handwritten, that they obtained from the state geological survey, and that even this effort left records incomplete for a substantial fraction of the wells evaluated. Boutot et al. (2022) report that the known orphaned well inventory nationally represents only 2–3% of all estimated abandoned wells, with critical attributes like depth and plugging status missing for most. Jahan et al. (2025) estimate hundreds of thousands of unplugged non-producing and undocumented orphan wells in Pennsylvania and Oklahoma alone, with field surveys confirming at least two undocumented wells for every documented one.

EPA's AoR guidance describes the scope of the problem and the multi-source approach needed to address it. Section 4.2 notes that wells “constructed prior to [early 1900s regulations]...

may not have been documented in state databases" and that "owners or operators may have gone bankrupt and [abandoned] their wells or used substandard materials" (EPA, 2013a, §4.2). The guidance identifies state databases, county records, and private databases as necessary sources and acknowledges that "detecting abandoned wells can be very challenging" (EPA, 2013a, §4.2). This amendment codifies the multi-source search that the guidance already describes as necessary.

Q: Similarly, would you explain the basis for the requirement that operators field test all abandoned wells without complete plugging records?

A: A well for which no plugging records exist may be completely open to the injection zone, completely sealed, or anything in between, and the only way to know is to go look at the well in question. Without field testing, the operator is guessing about whether a well that may directly connect a pressurized injection formation to a drinking water aquifer poses a leakage risk. A wrong guess leads to contamination that cannot be undone. Arbad et al. (2024) found that many wells within their study AoR lacked the cement bond logs and sustained casing pressure data needed to evaluate well integrity directly, requiring the authors to rely on indirect indicators such as well construction details and plugging reports to categorize risk. The EPA's AoR guidance specifically discusses field testing for wells with incomplete records. EPA's own AoR guidance provides a detailed decision tree for this evaluation. Section 4.3.2 states that wells whose plugging "cannot be proven adequate" through records review "must be evaluated by field [testing]" and that "if the integrity of the bottom plug or cement is in question, and records cannot prove that the plugging is adequate, of the hole cannot prove that the plugging is adequate, EPA recommends that the surface plug and possibly additional plugs down-hole be drilled out and tests conducted to determine the adequacy of the abandonment" (EPA, 2013a,

§4.3.2). This amendment codifies field testing into New Mexico's regulations rather leaving the decision with regard to the need for field testing to operator discretion.

Boutot et al. (2022) and Jahan et al. (2025) report that the majority of abandoned wells nationally have incomplete records. Kim et al. (2024) compile a dataset of aerial imagery to support automated detection of orphaned wells, reflecting the difficulty of identifying such wells through visual inspection alone. The *Pabst v. Peoples Gas* case illustrates the consequences of assuming integrity rather than verifying it.

Q: What are the proposed amendments to 19.15.43.9.E(4) NMAC, which relate to corrective action on wells within the AoR?

A: The proposed amendments to 19.15.43.9.E(4) NMAC are:

> **19.15.43.9.E(4)** Owners or operators of Class VI wells must perform corrective action on all wells in the area of review that are determined to need corrective action or breach any layer of the confining layer, or that are located in the Intensive Corrective Action Area, using methods designed to prevent the movement of fluid into or between USDWs, including use of materials compatible with the carbon dioxide stream and re-plugging with carbon dioxide resistant cement at all depths~~, where appropriate.~~

Q: What is the basis for the requirement that corrective action be taken on wells determined to breach any layer of the confining layer or are located in the Intensive Corrective Action Area, in addition to other wells determined to need corrective action?

A: Wells that breach any depth of the confining layer weaken that layer. Furthermore, there is uncertainty in the depths of the boundaries of different layers across an AoR: tops and bases of formations have topography and that topography is not exactly known without direct observation. Finally, in many shaley formations, some portions of the formation are more permeable than others: the precautionary principle dictates that a well penetrating any depth of the confining layer should be treated as a potential leakage pathway.

Any well within the ICAA has the potential to come into contact with the CO_2 plume, and we know that supercritical CO_2 in brine is a corrosive environment for the standard materials (carbon steel and Portland cement) used to construct and plug the vast majority of abandoned wells in New Mexico's mature basins. Within the ICAA, where CO_2-bearing brine will plausibly be present, every conventionally plugged well is therefore a potentially latent pathway for contamination of overlying drinking water aquifers, one that may not fail immediately but will fail eventually as the cement degrades over the years to decades that CO_2 remains in supercritical form. Protection of drinking water resources requires that we ensure that all wells that may come into contact with the CO_2 plume (i.e., wells in the ICAA) are able to withstand that corrosive environment through time. The default assumption must be that conventional plugs are inadequate for CO_2 service unless the operator can prove otherwise with contemporaneous documentation. The alternative, assuming adequacy and discovering the error after contamination, is irreversible. Supercritical CO_2 is buoyant and will migrate upward along the wellbore, contacting cement and casing at every depth from the injection zone to the surface. If conventional materials are used above the injection zone on the assumption that CO_2 will remain below, and that assumption proves wrong, the upper well sections become degradation pathways to drinking water aquifers.

Q: What is the basis for the requirement that owners or operators use CO_2-resistant materials in all components of well plugging used and at all depths?

A: CO_2-resistant cement and corrosion-resistant steel alloys are not perfect materials. Sun et al. (2023) review the corrosion literature and conclude that degradation mechanisms for steel under supercritical CO_2 conditions, particularly in high-chloride brines, remain incompletely characterized scientifically. No material can be guaranteed to perform indefinitely at reservoir

conditions over the centuries-to-millennia timescales relevant to CO_2 storage. Yet CO_2-resistant materials are the best available technology, and the standard alternatives — conventional Portland cement and carbon steel — are known to degrade with exposure to CO_2 mixed in brine. Carroll et al. (2016) show that when CO_2-bearing brine contacts conventional wellbore cement through pre-existing flow pathways such as fractures, microannuli, or interface gaps, carbonation reactions may either seal or widen the pathway depending on conditions that cannot be predicted in advance. Conventional materials do not merely carry a risk of failure; they carry a certainty of degradation whose rate and consequences are uncertain.

Plugging a well with CO_2-resistant materials at only select intervals does not address this problem. Supercritical CO_2 is buoyant and will migrate along the wellbore, contacting cement and casing at every depth from the injection zone upward. Any conventional interval it reaches becomes the failure point. Partial protection relocates the vulnerability rather than eliminating it. The cost difference between CO_2-resistant and conventional materials for well plugging is modest relative to the overall cost of a commercial-scale CO_2 storage project and is dwarfed by the magnitude of the 45Q tax credits that operators are expected to receive from the federal government. A potential consequence of using inadequate materials — degradation of a wellbore that serves as a direct conduit between a pressurized injection formation and a drinking water aquifer — is irreversible contamination. Permitting operators to use materials known to be incompatible with the injected fluid in order to reduce plugging costs is not a defensible basis for New Mexico's drinking water protection framework. CO_2-resistant materials throughout the full wellbore within the ICAA represent the minimum standard consistent with the state's obligation to protect underground sources of drinking water.

Q: Dr. Harvey, what are the proposed amendments to 19.15.43.9.E(5) NMAC?

A: The proposed amendments to 19.15.43.9.E(5) NMAC are:

> **19.15.43.9.E(5)** An initial AoR reevaluation shall occur no later than two years following the commencement of injection operations, or if the owners or operators fail to confirm the model's validity as specified in Subparagraph (b) of Paragraph (3) of Subsection E of 19.15.43.9 NMAC, the difference between the measured and modeled increases in pressure exceeds either 20 percent of the modeled increase in pressure or 50 kilopascals, the plume is detected in a monitoring well the plume was not expected to reach or more than one month earlier than expected, a seismic event greater than or equal to moment magnitude 2.0 occurs within the modeled pressure footprint, a pressure fall-off test results yielding formation properties materially inconsistent with model-assumed values, injection commences by another operator in the same formation or a hydraulically connected zone within the pressure footprint, or the owner, operator, or regulator discovers a previously unidentified well, fault, or fracture within the AoR. This early reevaluation must be used to confirm the accuracy and reliability of predictive modeling results submitted as part of the original permit application. Upon demonstration to the director, in accordance with Subparagraph (d) of Paragraph (5) of Subsection E of 19.15.43.9 NMAC, that the predictive modeling appropriately represents site conditions, AoR reevaluation frequency may be reduced to a minimum of once every four years. When conducting an AoR reevaluation an owner or operator must:

Q: What is the basis for the requirement that the AoR reevaluation occur if the pressure increase does not conform to modeled expectations?

A: The AoR is derived from a reservoir simulation model that predicts where pressure will propagate and at what magnitude. Every regulatory decision that flows from the AoR depends on those pressure-increase predictions being correct. If observed pressure increase in the formation over baseline pressure departs from the model's predicted increase, the model is not consistent with the subsurface it was supposed to represent, and the AoR it produced is no longer defensible. The appropriate response is to recalibrate the model to match the observed data and re-delineate the AoR.

Pressure is the mechanism by which CO_2 injection endangers drinking water beyond the plume itself (Birkholzer and Zhou, 2009), and Ranaee et al. (2022) demonstrate it is the binding constraint on safe storage capacity. If the model underestimates pressure propagation, the AoR is

undersized and legacy wells, faults, and aquifers within the actual pressure footprint go unevaluated. The amendment establishes two tiers for lack of conformance in simulated pressure increases. A 20 percent deviation triggers immediate reevaluation. A 50 kilopascal increase does the same because it indicates a systematic model error: the model is consistently wrong about how pressure propagates. Either condition indicates the model generating the pressure field (and the AoR that depends on its multiple simulations) must be re-evaluated and modified to better conform with real-world data.

Q: What is the basis for the requirement that the AoR reevaluation occur if plume is detected in a monitoring well the plume was not expected to reach or more than one month earlier than expected?

A: The basis for this response is explained in response to the proposed amendments at 19.15.43.9.E(3)(b) NMAC.

Q: What is the basis for the requirement that the AoR reevaluation occur if a seismic event greater than or equal to moment magnitude 2.0 occurs within the modeled pressure footprint?

A: The basis for this response is explained in response to the proposed amendments at 19.15.43.9.C(1)(c) NMAC and 19.15.43.9.O(4) NMAC.

Q: What is the basis for the requirement that the AoR reevaluation occur if a pressure fall-off test results yielding formation properties materially inconsistent with model-assumed values?

A: The basis for this response is explained in response to the proposed amendments at 19.15.43.9.K(6) NMAC.

Q: What is the basis for the requirement that the AoR reevaluation occur if injection commences by another operator in the same formation or a hydraulically connected zone within the pressure footprint?

A: The basis for this response is explained in response to the proposed amendments at 19.15.43.9.E(3)(a)(viii) NMAC.

Q: What is the basis for the requirement that the AoR reevaluation occur if the owner or operator discovers a previously unidentified well, fault, or fracture within the AoR?

A: The basis for this response is explained in response to the proposed amendments at 19.15.43.9.E(2)(b)(ii).

Injection Well Construction Requirements (19.15.43.9.G NMAC)

Q: Dr. Harvey, what are the proposed amendments at 19.15.43.9.G NMAC, as shown below?

A: The proposed changes are:

> **19.15.43.G(1) General.** The owner or operator must ensure that all Class VI and monitoring wells are constructed and completed to:
>
> **19.15.43.G(2)(a)** Casing and cement or other materials used in the construction of each Class VI well and monitoring wells must have sufficient structural strength and be designed for the life of the geologic sequestration project. All well materials must be compatible with fluids with which the materials may be expected to come into contact and must meet or exceed standards developed for such materials by the American Petroleum Institute, ASTM International, or comparable standards acceptable to the director. The casing and cementing program must be designed to prevent the movement of fluids into or between USDWs. In order to allow the Director to determine and specify casing and cementing requirements, the owner or operator must provide the following information:
>
> **19.15.43.G(2)(b)** Surface casing for all Class VI wells and monitoring wells shall be set and cemented through the base of the deepest known USDW and must extend into an underlying confining unit, such as a competent shale formation. The casing must be cemented with a volume sufficient to achieve full cement return from the casing shoe to the surface.

19.15.43.G(3)(a) Tubing and packer materials used in the construction of each Class VI well and monitoring wells must be compatible with fluids with which the materials may be expected to come into contact across all zones for all depths and must meet or exceed standards developed for such materials by the American Petroleum Institute, ASTM International, or comparable standards acceptable to the director.

Q: What is the basis for these changes?

A: Monitoring wells are definitionally either expected to come into contact with the CO_2 plume or have the possibility of coming into contact with the CO_2 plume. For this reason alone, they should be constructed throughout the wellbore with materials that have the best chance of withstanding the corrosive environment presented by contact with supercritical CO_2 dissolved in brine.

Testing and Monitoring Requirements
(19.15.43.9.K NMAC)

Q: Dr. Harvey, what motivates your support of the proposed amendment to ensure groundwater monitoring approaches the rigor of RCRA, as shown below at 19.15.43.9.K NMAC?

19.15.43.9.K Testing and monitoring requirements. The owner or operator of a Class VI well must prepare, maintain, and comply with a testing and monitoring plan to verify that the geologic sequestration project is operating as permitted and is not endangering USDWs. The requirement to maintain and implement an approved plan is directly enforceable regardless of whether the requirement is a condition of the permit. The testing and monitoring plan must be submitted with the permit application, for director approval, and must include a description of how the owner or operator will meet the requirements of this section, including accessing sites for all necessary monitoring and testing during the life of the project and the specific statistical test to be used for groundwater monitoring before collecting data. The statistical test for groundwater monitoring must include the number and kinds of samples collected to establish background appropriate for the form of statistical test employed, a sample size as large as necessary to ensure with reasonable confidence that a contaminant release to ground water from a facility will be detected, a statistical method appropriate for the distribution of chemical parameters or hazardous constituents, an accounting for data below the limit of detection with one more statistical procedures that are protective of human health and the environment, inclusion of procedures to control or correct for seasonal and spatial variability as well as temporal correlation in the data, and a determination of an

appropriate sampling procedure and interval for each hazardous constituent listed in the facility permit. It must also include a summary of community engagement activities conducted to develop a plan that addresses project-related risks. Testing and monitoring associated with geologic sequestration projects must, at a minimum, include:

A: The current Class VI rule requires a groundwater monitoring plan but does not require that the plan specify how contamination will be statistically determined. At the rule level, the operator is not required to specify what constitutes a detection, what statistical test is applied, what significance level is used, or how many background samples are needed. These choices are left to the regulator's case-by-case approval of plan language that may be qualitative rather than quantitative. The result is that two Class VI permits could use entirely different statistical approaches—or no formal statistical approach at all—and both would be in compliance.

RCRA's 40 CFR 264.97, developed over decades of hazardous waste monitoring, requires the operator to specify before the permit issues the complete quantitative framework: the statistical method, the significance level, the background dataset, and the performance standards including minimum Type I (false positive) error rates. The purpose is to ensure that whether contamination has occurred is determined by applying pre-registered methods to the data, not by a discretionary judgment made after the data are in hand. Yenigül et al. (2005) find that even the widely applied minimum of three downgradient monitoring wells achieves only 26% detection probability under favorable conditions, which is a number that can only be evaluated, and improved, if the statistical framework is defined in advance.

CO_2 storage presents groundwater monitoring challenges at least as demanding as hazardous waste disposal. Tsang et al. (2008) conclude that CO_2 injection involves more complex hydrologic processes than liquid waste injection, including multiphase flow, stronger buoyancy effects, and larger pressure footprints. The contaminant source is larger, the timescales are longer, and the subsurface heterogeneity is comparable. If EPA determined that hazardous

waste facilities require pre-specified statistical rigor to protect groundwater, there is no scientific basis for requiring less of CO_2 storage facilities that pose comparable or greater risks to the same aquifers.

Q: Dr. Harvey, what are the proposed changes at 19.15.43.9.K(4)(b) NMAC?

A: The proposed changes at 19.15.43.9.K(4)(b) NMAC are:

> **19.15.43.9.K(4)(b)** the monitoring frequency and spatial distribution of no fewer than four monitoring wells based on baseline geochemical data that has been collected under Subparagraph (f) of ~~Pararaph~~ Paragraph (1) of Subsection C of 19.15.43.9 NMAC, ~~and~~ on any modeling results in the area of review evaluation required by Paragraph (3) of Subsection E of 19.15.43.9 NMAC, a maximum-risk scenario simulation, and two simulations in which computational model grid spacing is increased and decreased by a factor of two. The monitoring plan must describe how the proposed monitoring will yield useful information on the area of review delineation and/or compliance with standards under Section 40 CFR 144.12.

Q: Why do you support the inclusion of a minimum number of site-specific data locations in regulations?

A: Several Class VI applications have relied on data from a single well or on analog data from distant formations, an approach that provides no basis for evaluating whether the characterization represents the geology through which CO_2 will migrate. The subsurface properties that control CO_2 flow vary over short distances and cannot be inferred from measurements made elsewhere. Ni et al. (2025) show that the capillary heterogeneity governing vertical CO_2 migration is formation-specific and scale-dependent; so a measurement at one location cannot be assumed representative of the formation as a whole. Reynolds et al. (2018) find that small-scale rock heterogeneity has a major impact on multiphase flow properties, and that models ignoring heterogeneity at the relevant scale risk significant errors. Moodie et al. (2021) show that without site-specific laboratory measurements of relative permeability, this

constitutive relationship becomes a dominant source of model uncertainty. A model built on insufficient data will define an AoR that does not reflect the actual subsurface.

EPA's Site Characterization Guidance recognizes the problem but does not identify a solution. The guidance states that "sufficient representative data will be needed from within the AoR" and that "heterogeneous formations would warrant more closely spaced core samples than uniform formations" (EPA, 2013b, §2.3.5.1). For core analyses, the guidance notes that "the optimal number of samples to analyze will vary by site, but representative samples should be chosen from cores and core sections with different lithologies and characteristics" (EPA, 2013b, §4.2). The guidance further requires the owner or operator to demonstrate "a sufficient number of samples have been analyzed to provide an indication of variability in mineralogy" (EPA, 2013b, §2.3.4). These are the right principles, but the guidance specifies no minimum, leaving data density to operator discretion despite acknowledging that heterogeneous formations need more data. A regulation that requires "sufficient" data without defining a minimum is a regulation that cannot be enforced. I therefore support a defined minimum as specified in the regulation.

Q: Why do you support ensuring that the network monitoring design accounts for detection of maximum-risk scenario simulations?

A. The scenarios most likely to damage USDWs are precisely the ones the model underestimates or misses: migration along an undetected fault, flow through a legacy wellbore the inventory missed, or pressure-driven brine displacement at the AoR periphery. If monitoring wells are clustered near the expected plume center, the first evidence of these departures may be contaminated drinking water rather than an actionable early warning. The operational record supports this view. Eiken et al. (2011) report that at every major saline-aquifer CCS site they

reviewed, monitoring revealed geological controls on plume behavior that pre-injection characterization had not identified.

Detection probability is highly sensitive to where wells are placed. Sarris et al. (2022) show that the same number of monitoring wells can achieve anywhere from 12% to 96% detection probability depending on placement relative to the contamination source. Yenigül et al. (2005) find that a three-well network achieves at most 26% detection probability even under the most favorable conditions. These results mean that a network optimized for the expected case can be nearly blind to the worst case. Chen et al. (2018), Crain et al. (2024), and Yonkofski et al. (2016) provide methods for optimizing well placement against the full range of simulated scenarios rather than a single expected trajectory. The amendment requires that well placement consider and optimize for detection of the maximum-risk simulations, because those are the scenarios in which early detection matters most and monitoring failure is most consequential.

Q: Dr. Harvey, why do you support the requirement to run additional simulations of the CO_2 plume in which grid spacing is increased and decreased by a factor of two?

Model grid spacing is a well-known source of uncertainty in models of fluid flow in the subsurface (e.g., Helmig, 1997). Given the critical role that the reservoir simulation of the CO_2 plume is playing in protection the water resources of New Mexico, it is important for both the operator and the regulator to understand the extent to which this well-known source of uncertainty alters simulated plume results.

Q: Dr. Harvey, why do you support the mandating of complete DFIT tests that rely on site-specific data only, as shown below at 19.15.43.9.K(6) NMAC?

> **19.15.43.9.K(6)** a pressure fall-off test based on site-specific data and run to completion at least once every five years unless more frequent testing is required by the Director based on site-specific information.

A: DFIT tests measure the fracture closure pressure, formation permeability, and reservoir characteristics that directly control whether injection will exceed the geomechanical limits of the confining layer, the geological barrier between the injection zone and overlying drinking water aquifers. Truncating the test before completion deprives the operator of the data needed to set a safe maximum injection pressure and increases the risk of fracturing the caprock. Substituting analog data from another formation introduces unacceptable uncertainty in the parameter that governs whether containment will hold, because subsurface properties are formation-specific and scale-dependent. Hansen et al. (2013) report that at Snøhvit, detailed fall-off pressure interpretation was essential for discovering that injection pressures were approaching fracture limits, preventing a containment failure. Properly constraining injection pressure is essential to project safety: White et al. (2014) conclude that at In Salah, the most likely explanation for observed pressure, seismic, and surface deformation data is that injection induced hydraulic fracturing of the lower portion of the caprock.

Q: Dr. Harvey, could you please explain why this continuous pressure monitoring at all monitoring wells is important to the protection of New Mexico drinking water resources, as shown below at 19.15.43.9.K(7) NMAC?

> **19.15.43.9.K(7)** Testing and continuous monitoring to track the extent of the carbon dioxide plume and the presence or absence of elevated pressure (e.g., the pressure front) and identification of excess pressure by calculating the absolute and excess pressure divided by hydrostatic pressure, by using:

A: Elevated formation pressure is the primary mechanism by which CO_2 injection can contaminate drinking water aquifers beyond the CO_2 plume itself. Injection-driven pressure increases push native brine upward through conduction pathways into overlying aquifers, and these pressure effects can propagate 100 km or more from the injection site (Birkholzer and Zhou, 2009). Pressure buildup is the binding constraint on safe storage capacity (Ranaee et al.,

2022). If the actual pressure response exceeds what the model predicted, drinking water aquifers far from the wellhead may be at risk.

Continuous pressure monitoring, even when not approaching a threshold, is the key measurement for testing and calibrating models. The operational record demonstrates the value of pressure data for catching developing problems. At Snøhvit, downhole pressure measurement and detailed fall-off pressure interpretation revealed that injection pressures were approaching rock fracture limits; the reservoir model was updated and the operator abandoned the original injection reservoir before those limits were exceeded (Hansen et al., 2013). At In Salah, monitoring observations indicated that pressure and probably CO_2 had migrated upward into the lower caprock, and subsequent analysis concluded that injection had likely induced hydraulic fractures there (White et al., 2014). In both cases, pressure data were an essential component of the monitoring evidence that identified developing threats to containment.

Continuous rather than periodic monitoring is warranted because the Hansen and White examples both involved pressure behavior that evolved over the course of active injection. A gauge that records only at scheduled intervals may capture the trend, but it cannot identify the timing of discrete pressure events — such as communication with a fault or a legacy wellbore — with the resolution needed to trigger an operational response before the event progresses. Monitoring at all wells rather than at the injection well alone is warranted because Birkholzer and Zhou (2009) show that the pressure footprint extends far beyond the injection point. A pressure anomaly developing at a legacy well or fault near the AoR boundary will not register at the injection well; detecting it requires a sensor near that location. Requiring continuous pressure monitoring at all monitoring wells matches the spatial and temporal coverage of the monitoring network to the spatial and temporal extent of the pressure risk.

Q: Dr. Harvey, why do you support mandatory surface air monitoring, as shown below at 19.15.43.9.K(9) NMAC?

> **19.15.43.9.K(9)** ~~the director may require~~ surface air monitoring is required to detect movement of carbon dioxide that could endanger a USDW, including in oil and gas fields or other areas with a high density of legacy wellbores.

A: Surface air monitoring provides a detection method independent of the subsurface well network that can catch CO_2 releases bypassing monitoring wells entirely, particularly leaks through failed legacy wells or unknown penetrations that vent directly to the surface. In areas with high legacy-well density, the ability to predict which specific well plug will fail is limited even with the best available models. A failed wellbore venting to the surface may be detectable by atmospheric sensors before the subsurface network registers the event. Pan and Oldenburg (2020) identify wellbore integrity failure as among the most consequential leakage scenarios. Surface air monitoring is technically well-established, relatively inexpensive compared to subsurface well installation, and covers the surface expression of leakage pathways that subsurface point measurements cannot reach.

Q: Dr. Harvey, what is the basis for a requirement that the owner or operator fund the State of New Mexico's purchase of distributed acoustic network sensors to monitor project seismic activity, as shown below at 19.15.43.9.K(10)(b) NMAC?

> **19.15.43.9.K(10)(b)** The owner or operator shall purchase a state owned, distributed acoustic network of seismic sensors, the resulting data of which shall be owned by the state.

A: The case for a state-owned, state-staffed seismic monitoring network rests on three findings from the peer-reviewed literature: induced seismicity from deep-well injection is not a speculative risk but a documented outcome; detecting and characterizing it in real time requires purpose-built monitoring infrastructure that did not previously exist in most jurisdictions; and an

operator-owned and operator-reported monitoring system creates a structural conflict of interest that undermines the system's protective function.

Regarding the first point, Zoback and Hennings (2025) report that every documented case of large-scale fluid injection into deep saline aquifers in hydrologic communication with crystalline basement has caused significant induced seismicity — triggering earthquakes as large as magnitude 5.8 and more than 200 $M \geq 4.0$ earthquakes that were widely felt in Oklahoma and Texas alone. CO_2 injection into deep saline aquifers is a physically analogous process. Zoback and Gorelick (2012) find that even small to moderate earthquakes threaten the seal integrity of CO_2 repositories. At ADM's Decatur CCS project in Illinois, injection in the first well (CCS1) produced sustained induced seismicity linked to pressure migration into crystalline basement through zones where a low-permeability basal formation was thin or absent. When the second well (CCS2) was brought online, its injection interval was set approximately 50 meters shallower and above a mudstone baffle — a decision informed by the seismicity experience at CCS1 — and the induced seismicity rate dropped markedly. Ongoing passive seismic monitoring continues to show earthquake activity on subsurface faults near the injection sites (Williams-Stroud et al., 2020). The question is not whether induced seismicity will occur at a New Mexico Class VI project but whether the state will have the capacity to detect, characterize, and respond to it independently when it does.

Effective seismic monitoring for induced seismicity requires a dense, spatially distributed sensor network capable of detecting small-magnitude events, locating them accurately in three dimensions, and measuring ground motion at relevant locations in real time. Langenbruch et al. (2018) demonstrate that physics-based seismic hazard forecasting (which is the kind needed to inform site-specific operational decisions) depends on spatially resolved monitoring data that

captures both the locations and the pressure-rate drivers of induced events. Without a dense network, small precursory events that signal escalating hazard go undetected, and the spatial resolution needed to associate seismicity with specific faults or injection operations is unavailable. The monitoring infrastructure is the mechanism by which the framework's safety thresholds are enforced.

State ownership of that infrastructure addresses a problem that operator ownership cannot. An operator who owns the seismic network, processes the data, and reports the results to the regulator is in the position of grading its own examination. The operator has an economic interest in continued injection and a corresponding disincentive to detect, characterize, or report events that could trigger a mandatory operational pause. A state-owned network eliminates this intermediary. The state receives the seismic data directly, processes it with its own staff, and evaluates whether a threshold has been exceeded without relying on the operator's characterization of the event. Because the operator's injection activity creates the seismic hazard, the operator — not New Mexico's taxpayers — should bear the cost of the infrastructure needed to monitor it.

Q: Dr. Harvey, what is the basis for the proposed amendments at 19.15.43.9.K(10)(d) NMAC, relating to the seismic threshold metric, as shown below?

> **19.15.43.9.K(10)(d)** The seismic threshold metric must use Peak Ground Velocity or Peak Ground Acceleration.

A: What damages wellbore cement, shears casing, and opens fracture pathways through which CO_2 can reach a drinking water aquifer is ground motion at the wellbore, not energy released at the earthquake's source. The same magnitude earthquake can produce vastly different ground shaking depending on depth, distance, and local geology: a magnitude 3.0 event directly beneath a wellbore at shallow depth can cause more damage than a magnitude 4.0 event 20 km

away, yet a magnitude-based threshold would trigger a response to the latter and not the former. Bommer et al. (2006) recognized this in developing a Peak Ground Velocity ("PGV")-based traffic light protocol for managing induced seismicity at an injection site, noting that the relationship between ground motion and damage potential is much better defined in terms of ground-motion characteristics than source magnitude alone. The USGS ShakeMap system[8] is based on this same idea: it takes earthquake magnitude, location, and depth as inputs and translates them into spatially resolved maps of peak ground acceleration and peak ground velocity, precisely because magnitude alone does not determine the shaking — and therefore the damage potential — at any given location (Worden et al., 2020).

Tian et al. (2026) demonstrate the physical basis for this approach through finite element modeling: formation displacement at the wellbore directly controls the stress concentration, tensile cracking, and interfacial separation that led to cement sheath failure — and formation displacement at any given wellbore depends on how much the ground moves there, not on how much energy the earthquake released at its source. Zoback and Gorelick (2012) note that even small earthquakes can threaten seal integrity, which underscores why a threshold set at a single magnitude value provides a false sense of security if it does not account for proximity and site conditions. Langenbruch et al. (2018) demonstrate that physics-based, spatially resolved seismic hazard assessment is feasible, providing the methodological foundation for site-specific threshold calibration. Switching to PGV or Peak Ground Acceleration calibrates the threshold to the actual risk of damage to the infrastructure protecting drinking water, rather than to a source-energy metric that tells you nothing about conditions at the wellbore.

[8] *ShakeMap*, USGS, https://earthquake.usgs.gov/data/shakemap/.

Q: Dr. Harvey, what motivates your support for requiring periodic material-compatibility re-certification of monitoring well construction against current CO_2-corrosion knowledge, as shown below at 19.15.43.9.K(12) NMAC?

> **19.15.43.9.K(12)** The owner or operator shall periodically review the testing and monitoring plan to incorporate monitoring data collected under this Part, operational data collected under Subsection I of 19.15.43.9 NMAC, ~~and~~ the most recent area of review reevaluation performed under Paragraph (5) of Subsection E of 19.15.43.9 NMAC, and new EPA standards regarding material compatibility for well infrastructure. An initial review of the testing and monitoring plan shall occur two years after injection begins, and at no time may exceed four years. Based on this review, the owner or operator shall submit an amended testing and monitoring plan or demonstrate to the director that no amendment to the testing and monitoring plan is needed. Any amendments to the testing and monitoring plan must be approved by the director, must be incorporated into the permit, and are subject to the permit modification requirements at Subsection H of 19.15.42.11 NMAC or Subsection J of 19.15.42.11 NMAC, as appropriate. Amended plans or demonstrations shall be submitted to the director as follows:

A: Because CO_2 injection into saline aquifers remains experimental, the science of material behavior under CO_2 storage conditions is still evolving: corrosion mechanisms under supercritical conditions are not yet fully characterized (Sun et al., 2023), degradation rates depend on site-specific conditions not always known at construction time (Carroll et al., 2016), and new failure modes continue to be identified as the research base grows (Ilgen et al., 2018). A monitoring well-built to specifications considered adequate a couple of ago may not meet current understanding of CO_2-corrosion risk, and a well that is itself degrading cannot reliably monitor whether drinking water aquifers are being contaminated. Gholami et al. (2021) identify multiple pathways through which CO_2 can compromise well integrity. Periodic recertification against current knowledge prevents the monitoring infrastructure on which drinking water protection depends from being grandfathered under specifications that advancing science may have rendered inadequate.

Reporting Requirements
(19.15.43.9.L(2) NMAC)

Q: Dr. Harvey, why do you support mandatory reporting of all gauge malfunctions and instrumentation failures to EPA, as shown below at 19.15.43.9.L(2) NMAC?

> **19.15.43.9.L Reporting requirements.** The owner or operator must, at a minimum, provide, as specified in Paragraph (5) of this Subsection, the following reports to the director and the EPA, for each permitted Class VI well:
>
> …
>
> **(2)** Report, within 30 days, the results of:
>
> **(a)** periodic tests of mechanical integrity;
>
> **(b)** gauge malfunction or instrumentation failure;
>
> **~~(b)~~(c)** any well workover; and,
>
> **~~(c)~~(d)** any other test of the injection well conducted by the permittee if required by the director.

A: For regulatory agencies to have confidence that monitoring data are complete and accurate, they must know when data are missing, suspect, or interpolated across gaps. Even a momentary instrumentation failure can coincide with a transient pressure excursion, a seismic event, or anomalous geochemistry whose significance would only become apparent in retrospect. Without mandatory reporting, the monitoring record presented to the regulator appears complete when it is not, and compliance determinations are made on data whose reliability is unknown. This is a data-integrity measure with negligible compliance cost relative to the value of the information it preserves.

Post Injection Site Care and Site Closure
(19.15.43.9.N(3) NMAC)

Q: Dr. Harvey, why do you support the elimination of pre-injection-cessation PISC-shortening petitions and a demonstration of at least five years of rigorously defined plume stabilization before such petitions are approved, as shown below at 19.15.43.9.N(3) NMAC?

> **19.15.43.9.N(3) Demonstration of alternative post-injection site care timeframe.** The director may approve, in consultation with EPA, an alternative

post-injection site care timeframe other than the 50 year default, if an owner or operator can demonstrate ~~during the permitting process~~ after injection operations cease that an alternative post-injection site care timeframe is appropriate and ensures non-endangerment of USDWs. The demonstration must be based on significant, site-specific data and information including all data and information collected pursuant to Subsections C and D of 19.15.43.9, and must contain substantial evidence that the geologic sequestration project will no longer pose a risk of endangerment to USDWs at the end of the alternative post-injection site care timeframe.

A: Allowing an operator to petition for shortened post-injection monitoring before injection has begun, or while it is ongoing, allows the most consequential long-term drinking water protection decision to rest on model predictions that have never been tested against operational data. The scientific record shows those predictions are unreliable precisely when they matter most. Saló-Salgado et al. (2024) show that even CO_2 plume models calibrated against detailed local measurements accumulate increasing errors with time — meaning that pre-injection predictions of post-injection behavior, which lack the benefit of any operational calibration, are the least reliable forecasts a model can produce. Pawar et al. (2020) find that the CO_2 plume continues migrating after injection ceases, with overpressure remaining above critical levels for extended periods, and that leakage risks depend on where the moving plume intersects specific features such as legacy wellbores — intersections that cannot be evaluated until the plume's actual trajectory is known from monitoring. The Sleipner monitoring record confirms this general problem at field scale: plume behavior there was dominated by geological features that could not be predicted from pre-injection characterization and were revealed only through sustained time-lapse observation (Eiken et al., 2011). Burton-Kelly et al. (2025) reach the same conclusion from the regulatory side, finding that plume stabilization must ultimately be demonstrated through post-injection monitoring data, not assumed from model predictions that, as the authors note, "will vary according to the geologic model used" and have not been history-matched to field data. Only after injection ceases and a body of operational evidence has

accumulated can a shortened PISC petition be evaluated on a basis that actually protects drinking water.

Restricting the timing of PISC petitions is insufficient, however, if the standard the petition must meet is left vague. Plume stabilization — the point at which the CO_2 plume has essentially ceased migrating — is the condition under which it becomes reasonable to reduce monitoring, because a plume that has stopped moving is no longer encountering new potential pathways to drinking water aquifers. Without a rigorous, multi-metric definition, an operator can characterize a pause in migration as stabilization, secure reduced oversight, and then face resumed plume movement that goes undetected because monitoring has been scaled back. Pawar et al. (2020) show why a single metric is insufficient: after injection ceases, the CO_2 plume's areal footprint can appear stable while its centroid continues to move and its shape continues to evolve. If only areal footprint is monitored, the plume can appear stable by that measure while other metrics show continued migration. Burton-Kelly et al. (2025) address this by developing a technical approach that defines stabilization through the rate of change of the plume's geographic footprint over time. Their case study demonstrates that stabilization is a gradual process, not a discrete event: even after their stabilization criterion was met, the plume continued to evolve slowly. Requiring five consecutive years of demonstrated stability across such metrics provides an evidentiary standard high enough to distinguish genuine stabilization from temporary equilibrium, seasonal variation, or sensor drift. Drinking water protection obligations should not be reduced until this standard is met with observed data.

Emergency Response
(19.15.43.9.O NMAC)

Q: Dr. Harvey, on what basis do you support the mandating of at least one employee on premises or on call with the authority to carry out the site's emergency response plan, as shown below at 19.15.43.9.O(3) NMAC?

> 19.15.43.9.O**(3)** The owner or operator must have at least one employee on the premises or otherwise available at all times with the authority to carry out the emergency and remedial response plan.

A: CO_2 injection is a continuous, high-pressure operation involving extreme compression of a toxic gas that is heavier than air at ground surface. The emergencies that CO_2 injection operations can produce (wellbore blowouts, pipeline ruptures, evidence of fluid migration into a USDW, sudden pressure anomalies, seismic events) do not confine themselves to business hours. If no one with the authority to execute the emergency response plan is available when an event occurs, the plan is a document, not a safeguard, and the delay between detection and response can be the difference between a contained incident and irreversible contamination of a drinking water aquifer. Analogous requirements under RCRA for hazardous waste facilities reflect the well-established principle that high-consequence facilities require continuously available authorized personnel. This is the operational requirement without which every other emergency response provision is hollow.

Q. Dr. Harvey, what are the proposed amendments at 19.15.43.9.O(4) NMAC?

A: The proposed amendments are as follows:

> 19.15.43.9.O.~~(3)~~**(4)** If the owner or operator obtains evidence that the injected carbon dioxide stream and associated pressure front may cause an endangerment to a USDW, a significant seismic event has occurred, a statistically significant geochemical change is detected above the confining zone, a release of carbon dioxide is detected by surface air monitoring, fluid has migrated into an unauthorized zone, or a gauge has malfunctioned for longer than one week, the owner or operator must:
>
> **(a)** immediately cease injection;

(b) take all steps reasonably necessary to identify and characterize any release, migration, or malfunction;
(c) notify the director within 24 hours; and
(d) implement the emergency and remedial response plan approved by the director.

Q: Dr. Harvey, why do you support the definition of an operational pause threshold following a seismic event?

A: An earthquake induced by CO_2 injection can damage the wells and cement seals that prevent CO_2 and brine from reaching drinking water aquifers, and once a fault has been opened as a fluid-transmission pathway, the contamination risk is immediate and irreversible. White et al. (2014) report that at In Salah, monitoring data revealed unexpected pressure and probable CO_2 migration into the lower caprock; injection was halted in 2011. Notably, that outcome was a discretionary operational decision, not a response compelled by any pre-specified regulatory trigger. Without a pre-specified numeric threshold, the decision to pause injection becomes a judgment call made under economic pressure at the worst possible moment.

Zoback and Gorelick (2012) find that even small to moderate earthquakes can threaten seal integrity. Tian et al. (2026) show through finite element analysis that seismic loading produces stress concentrations in cement sheaths that cause cracking and interfacial separation. Langenbruch et al. (2018) show that seismic hazard persists even after injection rate reductions, because pressure at seismogenic depth continues increasing, meaning continued injection after an event compounds the risk.

Q: Why do you support a requirement that injection immediately cease upon evidence of a statistically significant geochemical change above the confining zone?

A: A statistically significant geochemical change above the confining zone is direct evidence consistent with the case that the containment system is not performing as predicted.

The confining zone exists to prevent upward migration of CO_2 and displaced brine; a statistically significant geochemical signal above it is consistent with fluids breaching or bypassing the seal through a pathway that was either undetected or underestimated. Continued injection in this circumstance increases formation pressure and drives additional fluid through whatever pathway produced the signal. The rational response is to remove the driving force — injection pressure — immediately, before the pathway widens or additional formations are affected and while the operator does work to establish whether the seal has indeed been breached or bypassed. This is a response to observed evidence of containment failure. A statistically significant threshold, rigorously defined ahead of permit issuance, ensures that the response is not triggered by instrument noise or natural variability, because the statistical test and significance level were defined in the permit before injection began. Once that threshold is crossed, the question of whether to act has already been answered. Allowing injection to continue while the threat is more fully assessed risks compounding the very problem the monitoring system was designed to detect.

Q: Why do you support a requirement that injection immediately cease upon evidence of a release of carbon dioxide detected by surface air monitoring?

A: The basis for this response is explained in response to the proposed amendments at 19.15.43.9.K(9).

Q: Why do you support a requirement that injection immediately cease upon evidence of unauthorized fluid migration?

A: Evidence that CO_2 or displaced brine has entered an unauthorized zone means the containment system has failed, and continued injection will only drive more fluid through the breach. Once CO_2-mobilized metals or displaced brine have entered a USDW, the contamination

cannot be reversed on any human timescale. Allowing discretionary resumption before remediation is complete creates a structural incentive to characterize the problem as minor and resume revenue-generating injection rather than close the pathway. At In Salah, monitoring provided evidence of unexpected fluid migration into the caprock; injection was stopped in 2011 (White et al., 2014). No pre-specified regulatory threshold compelled that response. A different operator under different financial pressures might not have made the same decision. The *Pabst v. Peoples Gas* case shows what happens when response to migration evidence is inadequate. I support this amendment because it removes the discretion that makes delayed response legally possible.

Q: Dr. Harvey, why do you endorse a required shutdown when gauges malfunction for longer than 1 week?

A: The pressure and geochemical gauges at a CO_2 injection facility are the only real-time indicators of whether injection is proceeding safely. Hansen et al. (2013) demonstrate at Snøhvit that down-hole continuous pressure data were essential for discovering that injection pressures were approaching fracture limits, enabling the operator to act before those limits were exceeded. When such gauges are not working, the operator is injecting blind. Leaving the decision of when to restore instruments to operator discretion creates an economic incentive to continue injection during data gaps rather than incur the cost of a shutdown. The *Pabst v. Peoples Gas* case illustrates the consequences of operating without adequate monitoring: failure to detect well corrosion at an underground gas storage facility allegedly led to contamination of parts of the Mahomet Aquifer, a drinking water source for over half a million people. A one-week threshold provides reasonable time for equipment repair while preventing the indefinite accumulation of

unmonitored injection during which developing problems that threaten drinking water go undetected (*Pabst v. Peoples Gas*, 2022).

This concludes my testimony, which is accurate to the best of my knowledge.

_/s/Charles Harvey_____ _June 29, 2026_____

Charles Harvey Date

List of References

40 CFR 264.97 General Ground-Water Monitoring Requirements (2026).

Arbad, N., Watson, M., Heinze, L., & Emadi, H. (2024). Qualitative risk assessment of legacy wells based on publicly available data for class VI well permit applications—Illinois basin case study. *International Journal of Greenhouse Gas Control*, *133*, 104106. https://doi.org/10.1016/j.ijggc.2024.104106

Arnold, D., Demyanov, V., Rojas, T., & Christie, M. (2019). Uncertainty Quantification in Reservoir Prediction: Part 1—Model Realism in History Matching Using Geological Prior Definitions. *Mathematical Geosciences*, *51*(2), 209–240. https://doi.org/10.1007/s11004-018-9774-6

Bandilla, K. W., Celia, M. A., Elliot, T. R., Person, M., Ellett, K. M., Rupp, J. A., Gable, C., & Zhang, Y. (2012). Modeling carbon sequestration in the Illinois Basin using a vertically-integrated approach. *Computing and Visualization in Science*, *15*(1), 39–51. https://doi.org/10.1007/s00791-013-0195-2

Birkholzer, J. T., & Zhou, Q. (2009). Basin-scale hydrogeologic impacts of CO_2 storage: Capacity and regulatory implications. *International Journal of Greenhouse Gas Control*, *3*(6), 745–756. https://doi.org/10.1016/j.ijggc.2009.07.002

Bommer, J. J., Oates, S., Cepeda, J. M., Lindholm, C., Bird, J., Torres, R., Marroquín, G., & Rivas, J. (2006). Control of hazard due to seismicity induced by a hot fractured rock geothermal project. *Engineering Geology*, *83*(4), 287–306. https://doi.org/10.1016/j.enggeo.2005.11.002

Boutot, J., Peltz, A. S., McVay, R., & Kang, M. (2022). Documented Orphaned Oil and Gas Wells Across the United States. *Environmental Science & Technology*, *56*(20), 14228–14236. https://doi.org/10.1021/acs.est.2c03268

Bukar, I., Bell, R., Muggeridge, A. H., & Krevor, S. (2025). Carbon Dioxide Migration Along Faults at the Illinois Basin—Decatur Project Revealed Using Time Shift Analysis of Seismic Monitoring Data. *Geophysical Research Letters*, *52*(2), e2024GL110049. https://doi.org/10.1029/2024GL110049

Burton-Kelly, M. E., Hunt, J. E., Dotzenrod, N. W., Templeton, J. A., Regorrah, J. G., Dalkhaa, C., Livers-Douglas, A. J., Peck, W. D., Connors, K. C., & Azzolina, N. A. (2025). Quantifying CO_2 plume stabilization at carbon storage projects, North Dakota, USA. *International Journal of Greenhouse Gas Control*, *146*, 104456. https://doi.org/10.1016/j.ijggc.2025.104456

Carroll, S., Carey, J. W., Dzombak, D., Huerta, N. J., Li, L., Richard, T., Um, W., Walsh, S. D. C., & Zhang, L. (2016). Review: Role of chemistry, mechanics, and transport on well integrity in CO_2 storage environments. *International Journal of Greenhouse Gas Control*, *49*, 149–160. https://doi.org/10.1016/j.ijggc.2016.01.010

Cavanagh, A. J., & Haszeldine, R. S. (2014). The Sleipner storage site: Capillary flow modeling of a layered CO_2 plume requires fractured shale barriers within the Utsira Formation. *International Journal of Greenhouse Gas Control*, *21*, 101–112. https://doi.org/10.1016/j.ijggc.2013.11.017

Celia, M. A., & Nordbotten, J. M. (2009). Practical Modeling Approaches for Geological Storage of Carbon Dioxide. *Groundwater*, *47*(5), 627–638. https://doi.org/10.1111/j.1745-6584.2009.00590.x

Chen, B., Harp, D. R., Lin, Y., Keating, E. H., & Pawar, R. J. (2018). Geologic CO_2 sequestration monitoring design: A machine learning and uncertainty quantification based approach. *Applied Energy*, *225*, 332–345. https://doi.org/10.1016/j.apenergy.2018.05.044

Cheng, Y., Liu, W., Xu, T., Zhang, Y., Zhang, X., Xing, Y., Feng, B., & Xia, Y. (2023). Seismicity induced by geological CO_2 storage: A review. *Earth-Science Reviews*, *239*, 104369. https://doi.org/10.1016/j.earscirev.2023.104369

Chiyonobu, S., Nakajima, T., Zhang, Y., Tsuji, T., & Xue, Z. (2013). Effect of Reservoir Heterogeneity of Haizume Formation, Nagaoka Pilot Site, Based on High-resolution Sedimentological Analysis. *Energy Procedia*, *37*, 3546–3553. https://doi.org/10.1016/j.egypro.2013.06.247

Choi, C.-S., Kim, J., & Song, J.-J. (2021). Analysis of shale property changes after geochemical interaction under CO_2 sequestration conditions. *Energy*, *214*, 118933. https://doi.org/10.1016/j.energy.2020.118933

Crain, D. M., Benson, S. M., Saltzer, S. D., & Durlofsky, L. J. (2024). An integrated framework for optimal monitoring and history matching in CO_2 storage projects. *Computational Geosciences*, *28*(2), 211–225. https://doi.org/10.1007/s10596-023-10216-3

Cremon, M. A., Christie, M. A., & Gerritsen, M. G. (2020). Monte Carlo simulation for uncertainty quantification in reservoir simulation: A convergence study. *Journal of Petroleum Science and Engineering*, *190*, 107094. https://doi.org/10.1016/j.petrol.2020.107094

Cusini, M., Gielisse, R., Groot, H., Van Kruijsdijk, C., & Hajibeygi, H. (2019). Incomplete mixing in porous media: Todd-Longstaff upscaling approach versus a dynamic local grid refinement method. *Computational Geosciences*, *23*(2), 373–397. https://doi.org/10.1007/s10596-018-9802-0

De Andrade, J., & Sangesland, S. (2016). Cement Sheath Failure Mechanisms: Numerical Estimates to Design for Long-Term Well Integrity. *Journal of Petroleum Science and Engineering*, *147*, 682–698. https://doi.org/10.1016/j.petrol.2016.08.032

Demyanov, V., Arnold, D., Rojas, T., & Christie, M. (2019). Uncertainty Quantification in Reservoir Prediction: Part 2—Handling Uncertainty in the Geological Scenario. *Mathematical Geosciences*, *51*(2), 241–264. https://doi.org/10.1007/s11004-018-9755-9

Eiken, O., Ringrose, P., Hermanrud, C., Nazarian, B., Torp, T. A., & Høier, L. (2011). Lessons learned from 14 years of CCS operations: Sleipner, In Salah and Snøhvit. *Energy Procedia*, *4*, 5541–5548. https://doi.org/10.1016/j.egypro.2011.02.541

Fentaw, J. W., Emadi, H., Hussain, A., Fernandez, D. M., & Thiyagarajan, S. R. (2024). Geochemistry in Geological CO_2 Sequestration: A Comprehensive Review. *Energies*, *17*(19), 5000. https://doi.org/10.3390/en17195000

Freeman, C., Dhawan, R., Blanke, H., & Hopkins, J. (2025). Quest carbon capture and storage – 4D seismic monitoring and geologic controls on plume migration. *SSRN Electronic Journal*. https://doi.org/10.2139/ssrn.5066124

Gasda, S. E., Bachu, S., & Celia, M. A. (2004). Spatial characterization of the location of potentially leaky wells penetrating a deep saline aquifer in a mature sedimentary basin. *Environmental Geology*, *46*(6–7), 707–720. https://doi.org/10.1007/s00254-004-1073-5

Gholami, R., Raza, A., & Iglauer, S. (2021). Leakage risk assessment of a CO_2 storage site: A review. *Earth-Science Reviews*, *223*, 103849. https://doi.org/10.1016/j.earscirev.2021.103849

Global CCS Institute. (2025). *Global status of CCS 2025: Staying the course*. Global CCS Institute. https://www.globalccsinstitute.com/wp-content/uploads/2025/10/Global-Status-of-CCS-2025-report-9-October.pdf.

Hansen, O., Gilding, D., Nazarian, B., Osdal, B., Ringrose, P., Kristoffersen, J.-B., Eiken, O., & Hansen, H. (2013). Snøhvit: The History of Injecting and Storing 1 Mt CO_2 in the Fluvial Tubåen Fm. *Energy Procedia*, *37*, 3565–3573. https://doi.org/10.1016/j.egypro.2013.06.249

Helmig, R. (1997). *Multiphase flow and transport processes in the subsurface: a contribution to the modeling of hydrosystems* (Vol. 1). Berlin: Springer.

Hoffman, N., & Alessio, L. (2017). Probabilistic Approach to CO_2 Plume Mapping for Prospective Storage Sites: The CarbonNet Experience. *Energy Procedia*, *114*, 4444–4476. https://doi.org/10.1016/j.egypro.2017.03.1604

Ilgen, A. G., Aman, M., Espinoza, D. N., Rodriguez, M. A., Griego, J. M., Dewers, T. A., Feldman, J. D., Stewart, T. A., Choens, R. C., & Wilson, J. (2018). Shale-brine-CO_2 interactions and the long-term stability of carbonate-rich shale caprock. *International Journal of Greenhouse Gas Control*, *78*, 244–253. https://doi.org/10.1016/j.ijggc.2018.07.002

Ismail, I., & Gaganis, V. (2023). Carbon Capture, Utilization, and Storage in Saline Aquifers: Subsurface Policies, Development Plans, Well Control Strategies and Optimization Approaches—A Review. *Clean Technologies*, *5*(2), 609–637. https://doi.org/10.3390/cleantechnol5020031

Jahan, I., Mehana, M., Kang, M., Boutot, J., Govert, A., O'Malley, D., & Viswanathan, H. S. (2025). Data-driven estimates of undocumented orphan oil and gas wells with implications to the environment. *Science of The Total Environment*, *967*, 178746. https://doi.org/10.1016/j.scitotenv.2025.178746

Kim, A., Kadeethum, T., Downs, C., Viswanathan, H. S., & O'Malley, D. (2024). Aerial imagery dataset of lost oil wells. *Scientific Data*, *11*(1), 1005. https://doi.org/10.1038/s41597-024-03820-0

Langenbruch, C., Weingarten, M., & Zoback, M. D. (2018). Physics-based forecasting of man-made earthquake hazards in Oklahoma and Kansas. *Nature Communications*, *9*(1), 3946. https://doi.org/10.1038/s41467-018-06167-4

Langenbruch, C., & Zoback, M. D. (2016). How will induced seismicity in Oklahoma respond to decreased saltwater injection rates? *Science Advances*, *2*(11), e1601542. https://doi.org/10.1126/sciadv.1601542

Møll Nilsen, H., Herrera, P. A., Ashraf, M., Ligaarden, I., Iding, M., Hermanrud, C., Lie, K.-A., Nordbotten, J. M., Dahle, H. K., & Keilegavlen, E. (2011). Field-case simulation of CO_2 -plume migration using vertical-equilibrium models. *Energy Procedia*, *4*, 3801–3808. https://doi.org/10.1016/j.egypro.2011.02.315

Moodie, N., Ampomah, W., Jia, W., & McPherson, B. (2021). Relative Permeability: A Critical Parameter in Numerical Simulations of Multiphase Flow in Porous Media. *Energies*, *14*(9), 2370. https://doi.org/10.3390/en14092370

Ni, H., Li, B., Darraj, N., Ren, B., Harris, C., Krishnamurthy, P. G., Bukar, I., Berg, S., Snippe, J., Ringrose, P., Meckel, T. A., Krevor, S., & Benson, S. (2025). The impact of capillary heterogeneity on CO_2 flow and trapping across scales. *Earth-Science Reviews*, *270*, 105257. https://doi.org/10.1016/j.earscirev.2025.105257

Oliver, D. S., & Chen, Y. (2011). Recent progress on reservoir history matching: A review. *Computational Geosciences*, *15*(1), 185–221. https://doi.org/10.1007/s10596-010-9194-2

Onishi, T., Nguyen, M. C., Carey, J. W., Will, B., Zaluski, W., Bowen, D. W., Devault, B. C., Duguid, A., Zhou, Q., Fairweather, S. H., Spangler, L. H., & Stauffer, P. H. (2019). Potential CO_2 and brine leakage through wellbore pathways for geologic CO_2 sequestration using the National Risk Assessment Partnership tools: Application to the Big Sky Regional Partnership. *International Journal of Greenhouse Gas Control*, *81*, 44–65. https://doi.org/10.1016/j.ijggc.2018.12.002

Pabst v. The Peoples Gas Light and Coke Company et Al. (2022).

Pan, L., & Oldenburg, C. M. (2020). Mechanistic modeling of CO_2 well leakage in a generic abandoned well through a bridge plug cement-casing gap. *International Journal of Greenhouse Gas Control*, *97*, 103025. https://doi.org/10.1016/j.ijggc.2020.103025

Pawar, R. J., Chu, S., Makedonska, N., Onishi, T., & Harp, D. (2020). Assessment of relationship between post-injection plume migration and leakage risks at geologic CO_2 storage sites. *International Journal of Greenhouse Gas Control*, *101*, 103138. https://doi.org/10.1016/j.ijggc.2020.103138

Ranaee, E., Khattar, R., Inzoli, F., Blunt, M. J., & Guadagnini, A. (2022). Assessment and uncertainty quantification of onshore geological CO_2 storage capacity in China. *International Journal of Greenhouse Gas Control*, *121*, 103804. https://doi.org/10.1016/j.ijggc.2022.103804

Reynolds, C. A., Blunt, M. J., & Krevor, S. (2018). Multiphase Flow Characteristics of Heterogeneous Rocks From CO_2 Storage Reservoirs in the United Kingdom. *Water Resources Research*, *54*(2), 729–745. https://doi.org/10.1002/2017WR021651

Rudolph, K. W., & Goulding, F. J. (2017). Benchmarking exploration predictions and performance using 20+ yr of drilling results: One company's experience. *AAPG Bulletin*, *101*(2), 161–176. https://doi.org/10.1306/06281616060

Rutqvist, J., Rinaldi, A. P., Cappa, F., Jeanne, P., Mazzoldi, A., Urpi, L., Guglielmi, Y., & Vilarrasa, V. (2016). Fault activation and induced seismicity in geological carbon storage – Lessons learned from recent modeling studies. *Journal of Rock Mechanics and Geotechnical Engineering*, *8*(6), 789–804. https://doi.org/10.1016/j.jrmge.2016.09.001

Saló-Salgado, L., Haugen, M., Eikehaug, K., Fernø, M., Nordbotten, J. M., & Juanes, R. (2024). Direct Comparison of Numerical Simulations and Experiments of CO_2 Injection and Migration in Geologic Media: Value of Local Data and Forecasting Capability. *Transport in Porous Media*, *151*(5), 1199–1240. https://doi.org/10.1007/s11242-023-01972-y

Sarris, T. S., Kenny, A., Scott, D. M., & Close, M. E. (2022). Aquifer heterogeneity controls to quality monitoring network performance for the protection of groundwater production wells. *Water Research*, *218*, 118485. https://doi.org/10.1016/j.watres.2022.118485

Senel, O., & Chugunov, N. (2013). CO_2 Injection in a Saline Formation: Pre-Injection Reservoir Modeling and Uncertainty Analysis for Illinois Basin – Decatur Project. *Energy Procedia*, *37*, 4598–4611. https://doi.org/10.1016/j.egypro.2013.06.368

Snider, A., & Lefebvre, B. (2024, September 13). Carbon storage projects hit a hurdle: Corroding Steel. *E&E News by POLITICO*. Accessed at https://www.commerce.alaska.gov/web/Portals/18/pub/CCUS/Public%20Scoping%20Comments/2024-11-07/References%20for%20Center%20for%20Biological%20Diversity%20Comment/Snid

er%20and%20Lefebvre_Carbon%20storage%20projects%20hit%20a%20hurdle_EandE.pdf

Subbey, S., Christie, M., & Sambridge, M. (2004). Prediction under uncertainty in reservoir modeling. *Journal of Petroleum Science and Engineering*, *44*(1–2), 143–153. https://doi.org/10.1016/j.petrol.2004.02.011

Sun, H., Wang, H., Zeng, Y., & Liu, J. (2023). Corrosion challenges in supercritical CO2 transportation, storage, and utilization—a review. *Renewable and Sustainable Energy Reviews*, *179*, 113292.

Tian, C., Meng, H., Wu, J., Bai, K., Zhao, K., & Zheng, S. (2026). Mechanical integrity of cement sheath barriers in deepwater wells under earthquake-induced fault slip: A three-dimensional finite-element study for offshore geohazard conditions. *Ocean Engineering*, *362*, 126251. https://doi.org/10.1016/j.oceaneng.2026.126251

Tsang, C.-F., Birkholzer, J., & Rutqvist, J. (2008). A comparative review of hydrologic issues involved in geologic storage of CO_2 and injection disposal of liquid waste. *Environmental Geology*, *54*(8), 1723–1737. https://doi.org/10.1007/s00254-007-0949-6

Tuczyński, T., & Stopa, J. (2023). Uncertainty Quantification in Reservoir Simulation Using Modern Data Assimilation Algorithm. *Energies*, *16*(3), 1153. https://doi.org/10.3390/en16031153

U.S. Environmental Protection Agency. (2009). *Statistical Analysis of Groundwater Monitoring Data at RCRA Facilities: Unified Guidance* (EPA 530-R-09-007). U.S. EPA Office of Resource Conservation and Recovery.

U.S. Environmental Protection Agency. (2013a). *UIC Program Class VI Well Area of Review Evaluation and Corrective Action Guidance* (EPA 816-R-13-005). U.S. EPA Office of Water.

U.S. Environmental Protection Agency. (2013b). *UIC Program Class VI Well Site Characterization Guidance* (EPA 816-R-13-004). U.S. EPA Office of Water.

U.S. Environmental Protection Agency. (2013c). *UIC Program Class VI Well Testing and Monitoring Guidance* (EPA 816-R-13-001). U.S. EPA Office of Water.

Vilarrasa, V., Carrera, J., Olivella, S., Rutqvist, J., & Laloui, L. (2019). Induced seismicity in geologic carbon storage. *Solid Earth*, *10*(3), 871–892. https://doi.org/10.5194/se-10-871-2019

Wang, H., & Sharma, M. M. (2017). New variable compliance method for estimating in-situ stress and leak-off from DFIT data. *SPE Annual Technical Conference and Exhibition?*, D011S006R008. https://arxiv.org/pdf/1710.06464

Wang, Z., Hosseini, S. A., & Bump, A. P. (2025). Hub scale subsurface fluid injection of GCS and SWD wells: Implications on inter-project interferences and regional pressure buildup. *International Journal of Greenhouse Gas Control*, *147*, 104477. https://doi.org/10.1016/j.ijggc.2025.104477

White, J. A., Chiaramonte, L., Ezzedine, S., Foxall, W., Hao, Y., Ramirez, A., & McNab, W. (2014). Geomechanical behavior of the reservoir and caprock system at the In Salah CO_2 storage project. *Proceedings of the National Academy of Sciences*, *111*(24), 8747–8752. https://doi.org/10.1073/pnas.1316465111

White, J. C., Williams, G. A., & Chadwick, R. A. (2013). Thin Layer Detectability in a Growing CO_2 Plume: Testing the Limits of Time-lapse Seismic Resolution. *Energy Procedia*, *37*, 4356–4365. https://doi.org/10.1016/j.egypro.2013.06.338

White, S., Carroll, S., Chu, S., Bacon, D., Pawar, R., Cumming, L., Hawkins, J., Kelley, M., Demirkanli, I., Middleton, R., Sminchak, J., & Pasumarti, A. (2020). A risk-based approach to evaluating the Area of Review and leakage risks at CO_2 storage sites. *International Journal of Greenhouse Gas Control*, *93*, 102884. https://doi.org/10.1016/j.ijggc.2019.102884

Williams-Stroud, S., Bauer, R., Leetaru, H., Oye, V., Stanek, F., Greenberg, S., & Langet, N. (2020). Analysis of Microseismicity and Reactivated Fault Size to Assess the Potential for Felt Events by CO_2 Injection in the Illinois Basin. *Bulletin of the Seismological Society of America*, *110*(5), 2188–2204. https://doi.org/10.1785/0120200112

Wilson, P., Feitz, A., Jenkins, C., Berko, H., Loh, Z., Luhar, A., Hibberd, M., Spencer, D., & Etheridge, D. (2014). Sensitivity of CO_2 leak detection using a single atmospheric station. *Energy Procedia*, *63*, 3907–3914. https://doi.org/10.1016/j.egypro.2014.11.420

Worden, C. B., Thompson, E. M., Hearne, M., & Wald, D. J. (2020). *ShakeMap manual online: Technical manual, user's guide, and software guide*. U.S. Geological Survey. https://doi.org/10.5066/F7D21VPQ

Xiao, T., Chen, T., Ma, Z., Tian, H., Meguerdijian, S., Chen, B., Pawar, R., Huang, L., Xu, T., Cather, M., & McPherson, B. (2024). A review of risk and uncertainty assessment for geologic carbon storage. *Renewable and Sustainable Energy Reviews*, *189*, 113945. https://doi.org/10.1016/j.rser.2023.113945

Yenigül, N. B., Elfeki, A. M. M., Gehrels, J. C., Van Den Akker, C., Hensbergen, A. T., & Dekking, F. M. (2005). Reliability assessment of groundwater monitoring networks at landfill sites. *Journal of Hydrology*, *308*(1–4), 1–17. https://doi.org/10.1016/j.jhydrol.2004.10.017

Yonkofski, C. M. R., Gastelum, J. A., Porter, E. A., Rodriguez, L. R., Bacon, D. H., & Brown, C. F. (2016). An optimization approach to design monitoring schemes for CO_2 leakage detection. *International Journal of Greenhouse Gas Control*, *47*, 233–239. https://doi.org/10.1016/j.ijggc.2016.01.040

Zoback, M. D., & Gorelick, S. M. (2012). Earthquake triggering and large-scale geologic storage of carbon dioxide. *Proceedings of the National Academy of Sciences*, *109*(26), 10164–10168. https://doi.org/10.1073/pnas.1202473109

Zoback, M. D., & Hennings, P. (2025). Implications of earthquakes triggered by massive injection of produced water in saline aquifers for large-scale geologic storage of CO_2. *International Journal of Greenhouse Gas Control*, *146*, 104447. https://doi.org/10.1016/j.ijggc.2025.104447

EXHIBIT 6

Check for updates

Geophysical Research Letters

RESEARCH LETTER
10.1029/2024GL110049

Carbon Dioxide Migration Along Faults at the Illinois Basin—Decatur Project Revealed Using Time Shift Analysis of Seismic Monitoring Data

I. Bukar[1], R. Bell[1], A. H. Muggeridge[1], and S. Krevor[1]

[1]Department of Earth Science and Engineering, Imperial College London, Royal School of Mines, London, UK

Key Points:

- 4D seismic time shift attributes reveal previously unidentified CO_2 migration behavior where traditional amplitude attributes could not
- The CO_2 migrates from the injection interval, upwards along permeable faults and re-emerges in overlying permeable reservoir units
- This behavior has been previously theorized but not yet directly observed from a CO_2 storage site

Supporting Information:

Supporting Information may be found in the online version of this article.

Correspondence to:

I. Bukar,
i.bukar21@imperial.ac.uk

Citation:

Bukar, I., Bell, R., Muggeridge, A. H., & Krevor, S. (2025). Carbon dioxide migration along faults at the Illinois Basin—Decatur Project revealed using time shift analysis of seismic monitoring data. *Geophysical Research Letters*, *52*, e2024GL110049. https://doi.org/10.1029/2024GL110049

Received 10 MAY 2024
Accepted 18 DEC 2024

Author Contributions:

Conceptualization: I. Bukar, R. Bell, A. H. Muggeridge, S. Krevor
Formal analysis: I. Bukar
Funding acquisition: I. Bukar
Investigation: I. Bukar
Methodology: I. Bukar, R. Bell, A. H. Muggeridge, S. Krevor
Project administration: S. Krevor
Resources: S. Krevor
Supervision: R. Bell, A. H. Muggeridge
Validation: I. Bukar, R. Bell, A. H. Muggeridge, S. Krevor
Writing – original draft: I. Bukar
Writing – review & editing: R. Bell, A. H. Muggeridge, S. Krevor

© 2025. The Author(s).
This is an open access article under the terms of the Creative Commons Attribution License, which permits use, distribution and reproduction in any medium, provided the original work is properly cited.

Abstract Large scale geological storage of CO_2 is being deployed worldwide to reduce greenhouse gas emissions to the atmosphere. Previous modeling studies have investigated the potential for CO_2 migration along faults. We observe such migration at a commercial-scale, demonstration CO_2 storage project, including subsequent emergence of the CO_2 into overlying permeable layers. Previous attempts at interpreting the time-lapse seismic data using amplitude attributes were hindered by noise from the limited survey repeatability combined with a weak signal due to the stiffness of the rock. Here we apply an alternative interpretation of the seismic data using time shift attributes, resulting in clear plume anomalies. In addition to migrating up the fault, we observe the plume diverted by the start of injection at a neighboring project. This work provides field observations of theorized plume behaviors and demonstrates an alternative approach to overcome challenges in interpreting seismic monitoring data for geological CO_2 storage.

Plain Language Summary Large scale deployment of carbon dioxide storage in the pores of underground rocks is underway around the world to reduce greenhouse gas emissions to the atmosphere. It has since been theorized that sequestered carbon dioxide could migrate up faults or cracks within these underground rocks. However, this has not yet been directly observed until now. In this study, we have identified such migration at a commercial-scale demonstration project, where the sequestered carbon dioxide flows from the region of the rock it was injected into, up through these cracks and later emerges in shallower permeable regions of the rock. Previous interpretations of the data collected for monitoring this process was based on a standard analysis technique, however, a number of contributing factors including properties of the rock and data quality rendered this approach ineffective. We have successfully interpreted the carbon dioxide plumes using an alternative approach by measuring different attributes of the data. Through this work, we have provided field observations of previously theorized behaviors of carbon dioxide sequestered in underground rocks and demonstrated the effectiveness of an alternative approach to overcome challenges in the interpretation of data used for monitoring these plumes.

1. Introduction

Carbon capture and geological storage is being scaled up worldwide to achieve net zero carbon emissions by 2050 (Krevor et al., 2023; Portner et al., 2022). Monitoring CO_2 storage through time-lapse seismic techniques has provided observations of the flow and trapping behavior of the injected CO_2 at storage projects around the world (Furre et al., 2017; Hansen et al., 2013; Ivandic et al., 2015; Roach & White, 2018). The observations have revealed fluid dynamics which are more complex and dynamic than analogous subsurface fluids systems due to the properties of CO_2 as a supercritical fluid at reservoir conditions (Cavanagh & Haszeldine, 2014; Ringrose et al., 2022).

Of particular interest is the potential for CO_2 to move buoyantly upwards from a target reservoir through leakage pathways such as a fault or wellbore. This has been investigated using geological analogs, and theoretical and numerical modeling (Flemisch et al., 2024; Gasda et al., 2004; Gilmore et al., 2022; Miocic et al., 2016; Nordbotten et al., 2009). Models show that complex dynamics emerge depending on the permeabilities of fault zones relative to reservoir units, and CO_2 migration up leakage pathways can in some instances be entirely mitigated by trapping as the plume emerges in overlying permeable strata (Han et al., 2019; Yang et al., 2018).

Despite their importance, there are no engineered settings in which the movement of CO_2 along faults has been observed. CO_2 escape from natural subsurface accumulations has been inferred to occur through faults based on

Received by OCD: 6/29/2026

Geophysical Research Letters

10.1029/2024GL110049

19448007, 2025, 2, Downloaded from https://agupubs.onlinelibrary.wiley.com/doi/10.1029/2024GL110049, Wiley Online Library on [16/06/2026]. See the Terms and Conditions (https://onlinelibrary.wiley.com/terms-and-conditions) on Wiley Online Library for rules of use; OA articles are governed by the applicable Creative Commons License

geochemical and isotope measurements of carbonate deposits and travertine veins (Dockrill & Shipton, 2010; Jung et al., 2014; Kampman et al., 2012; Miocic et al., 2016; Shipton et al., 2004). Natural hydrocarbon gas leakage has also been inferred from seismic observations of gas chimneys and associated pockmark clusters on the seafloor (e.g., Gay et al., 2007; Roelofse et al., 2020).

Time-lapse seismic surveys are the industry standard for monitoring the plume dynamics, however, their acquisition and processing must be performed in a way that maximizes repeatability, which can be affected by factors such as seasonal variations and differences in acquisition geometry (Bakulin et al., 2007; Johnston, 2013; Landro, 1999; Lumley, 2001; Meunier et al., 2001). In addition, in general, land seismic surveys can suffer from significantly more noise than marine seismic surveys. This is mainly due to scattering by the near-surface layer and the partitioning of energy at the near surface between signal and noise such as ground roll (Al-Jabri & Urosevic, 2010; Pevzner et al., 2011; Stork, 2020).

In this work, we find evidence of CO_2 preferentially migrating up faults during injection at the onshore Illinois Basin—Decatur Project CO_2 storage site using post-stack time shift analysis of time-lapse 3D (i.e., 4D) vertical seismic profile (VSP) surveys. The initial interpretation approach for the 4D data was based on amplitude difference (Coueslan et al., 2014) and normalized RMS attributes (Bauer et al., 2019), but observations of the CO_2 plume were ambiguous (Coueslan et al., 2013). During the post-injection phase, well logs detected an isolated finger of CO_2 in the injection well in a shallower zone than the injection interval (Zaluski & Lee, 2021), the origins of which could not be ascertained previously. The application of an amplitude-agnostic time shift analysis reported here, reveals clear, qualitative images of growing CO_2 plumes in shallower intervals of the storage reservoir that arrived by migration up previously identified faults.

2. Data and Methods

2.1. The Illinois Basin—Decatur Project

The Illinois Basin - Decatur Project (IBDP) was a commercial-scale demonstration CO_2 sequestration project in Decatur, Illinois, USA, which stored 1 Mt of CO_2 over three years from 2011 to 2014. The CO_2 was injected into the Mt. Simon Sandstone at a depth of about 2,100 m. The project has an injection well (CCS1) and a monitoring well (VW1). Nearby wells CCS2, VW2 are the injection and monitoring wells for a secondary commercial project, the Illinois Industrial Carbon Capture and Storage (IL-ICCS) project. The monitoring and site characterization data from both projects have been made publicly available and provide a comprehensive data set suitable for studying the complex behavior of CO_2 plumes in the field.

2.2. Geologic Setting

The Mt. Simon sandstone is a Cambrian-age saline aquifer and is one of the major CO_2 sequestration resources in the United States. It is over 450 m thick at the Decatur site. Leetaru and Freiburg (2014) and Freiburg et al. (2014) provide a detailed depositional and diagenetic characterization of the Mt. Simon sandstone at Decatur. It is unconformably overlain by the Eau Claire Formation, which is a predominantly shale formation over 90 m thick at the Decatur site and serves as the primary caprock for the storage unit. The Mt. Simon Sandstone is subdivided into Upper, Middle and Lower units.

The most significant controls on reservoir quality in the Mt. Simon sandstone are diagenetic, with quartz cementation the most common feature. The Middle Mt. Simon is commonly referred to as the tight zone, comprising Mt. Simon C and D. The best reservoir quality occurs in the lower Mt. Simon formation, comprising units A and B, with porosities of up to 28% and permeabilities of up to 1,000 mD in Unit A, and an average porosity and permeability of 22% and 200 mD. Within this unit, there is significant variation is reservoir quality. Unit A is the injection interval for the project. Several faults were interpreted by Williams-Stroud et al. (2020) to transect the middle and lower units of the Mt. Simon sandstone with some of them extending down into the Precambrian basement. Williams-Stroud et al. (2020) interpret the fault lengths to range from approximately 250–1,000 m, and that some of them may comprise multiple intersecting fault planes or smaller faults.

2.3. Monitoring Data

The monitoring data set at the IBDP site comprises in-well and geophysical monitoring data including time-lapse 3D VSP surveys. Repeat saturation logs recorded CO_2 saturation profiles periodically in wells CCS1 and VW1,

Received by OCD: 6/29/2026

Geophysical Research Letters

10.1029/2024GL110049

19448007, 2025, 2, Downloaded from https://agupubs.onlinelibrary.wiley.com/doi/10.1029/2024GL110049, Wiley Online Library on [16/06/2026]. See the Terms and Conditions (https://onlinelibrary.wiley.com/terms-and-conditions) on Wiley Online Library for rules of use; OA articles are governed by the applicable Creative Commons License

an uncommon feature in such projects. Time-lapse 3D VSP surveying was chosen as the main geophysical monitoring technique to observe the CO_2 plume development over time. These surveys were acquired using surface vibrator sources with 3-component geophones permanently installed in a shallow geophysical monitoring well GM1 located 60 m northwest of the injection well. A monitor survey was acquired each year from 2012 to 2015 (M1–M4), with a baseline survey acquired in 2011 (B2) being the reference pre-injection survey. At the time of the M1, M2, M3 and M4 surveys, 74 kt, 433 kt, 730 kt and 1 Mt of CO_2 had been injected, respectively. Analysis and interpretation of these time-lapse VSP data is the main focus of this work. The survey dates, near-surface conditions during acquisition and injected CO_2 mass are reported by Coueslan et al. (2013) and provided in the Supporting Information S1. We use the migrated stacks, taken from the public repository (ISGS, 2021b) as inputs to our analysis. Details of the co-processing of that data are provided in the time-lapse 3D VSP processing reports (Schlumberger Petrotechnical Services, 2015).

2.4. Time Shift Analysis: An Amplitude-Agnostic Approach

Previous investigations at the IBDP used amplitude attributes including NRMS and amplitude difference to analyze the time-lapse seismic monitoring data. Coueslan et al. (2013) presented NRMS extracted over a zone containing the injection interval (1,980–2,195 m) and a shallow zone covering the Middle and Upper Mt. Simon and the Eau Claire Shale primary seal (1,524–1,980 m). While the strongest NRMS anomalies occur in the injection zone, there are still anomalies in the shallow zone. They also showed an amplitude difference section where differences can be observed outside the injection interval window (Coueslan et al., 2013). Questions remained as to whether these differences were due to potential fluid movement within the entire Mt. Simon sandstone, outside the injection interval, or artifacts due to noise and repeatability. We performed an analysis of time shifts in an attempt to answer these questions.

Time shift attributes of 4D seismic data have been used successfully to monitor fluid movement in oil and gas reservoirs (Benguigui et al., 2012; Falahat et al., 2011; Santos et al., 2016) and to support amplitude interpretation at CO_2 storage sites (Arts et al., 2004; Chadwick et al., 2004, 2005; Furre et al., 2015; Grude et al., 2013). Time shifts are induced when there are changes in fluid content or stress that cause compaction or extension in the reservoir or the overburden. For instance, a decrease in velocity in the reservoir due to CO_2 replacing brine results in an increase in two-way travel time of the seismic wave, which manifests as a stretched monitor trace when compared to the baseline trace. Landrø and Stammeijer (2004) define the relative change in travel time for a normal-incidence elastic wave due to changes in subsurface layer thicknesses (physical strain) and velocity as $\frac{\Delta t}{t} = \frac{\Delta z}{z} - \frac{\Delta v}{v}$, where $\frac{\Delta t}{t}$ is the relative time shift or time strain, $\frac{\Delta z}{z}$ is the vertical physical strain, and $\frac{\Delta v}{v}$ is the relative velocity change. $\frac{\Delta v}{v}$ depends on rock physics properties such as rock space stiffness and, where fluid replacement is involved, the elastic properties of the fluids and the magnitude of the saturation change.

There are a number of time shift algorithms ranging from the commonly used and simpler cross-correlation based methods to sophisticated waveform inversion approaches. A review of these various time shift estimation algorithms can be found in MacBeth et al. (2020). Signal processing algorithms in general typically depend on the magnitudes of amplitudes of signals to determine the correlation or misalignment between two signals. However, this can lead to erroneous results when the magnitudes of time-lapse amplitude difference change due to poor survey repeatability. Landrø et al. (2001) found that when time shifts are estimated by manually picking displaced well-defined events or features, time shift magnitudes are more accurate than when using a cross-correlation approach.

We implement a time shift algorithm using an approach that avoids any dependency on amplitude magnitudes. Our implementation is based on matching common features—peaks and troughs—between the baseline and monitor traces in search of a time strain. The implementation of this approach, termed feature-based warping, is performed in a similar way to the implementation of the Dynamic Time Warping algorithm (Hale, 2013), albeit focused purely on warping the monitor trace to match the baseline based on common features. In this approach, dynamic programming is employed to find an optimum path through a cost matrix. The objective is to align common features between two seismic traces by minimizing the positional dissimilarity between these features. The dissimilarity error is a cost function defined as:

$$e_{\text{feature}}[i,q] = d\Big(f_{\text{feature}}[i],\ g_{\text{feature}}[i+l]\Big) \tag{1}$$

Geophysical Research Letters 10.1029/2024GL110049

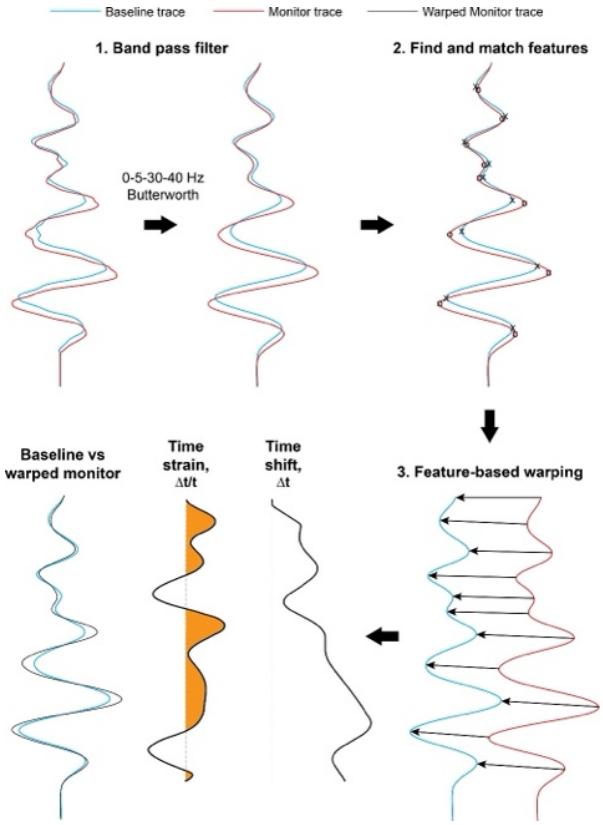


Figure 1. A schematic of the feature-based time shift analysis workflow employed in this study.

where $f_{\text{feature}}[i]$ and $g_{\text{feature}}[i+l]$ are the positions in two-way time (or samples) of corresponding key features in the baseline and monitor traces, respectively, and $d\left(f_{\text{feature}}[i], g_{\text{feature}}[i+l]\right)$ is a measure of the distance between the features when aligned. The cost function is used to populate a cost matrix, with points of aligned corresponding features assigned zero cost thereby serving as waypoints which the optimum warping path is encouraged to pass through. The warping path is then optimized to minimize the cumulative distance along the entire path. As a pre-processing step, band pass filtering is employed to smooth out any spurious features. The workflow is summarized in Figure 1. The key feature of this warping approach is that it is guided entirely by the spatial relationships between corresponding features in the traces, without any consideration of the magnitudes of the amplitudes of these features.

We performed time-lapse seismic forward modeling at the monitoring well location to demonstrate our approach to time shift analysis. We used an elastic property model derived from well log data from VW1 (see Figure 2a). We convolved a wavelet extracted from the 4D VSP data over the Mt. Simon with the elastic property model using a full waveform approach, yielding a baseline scenario. For a monitor scenario, we used the repeat saturation log data from VW1 to simulate CO_2 saturation as observed in the wells at the time of the time-lapse surveys. Changing ground conditions as in the real surveys were also simulated. The full workflow followed to generate the time-lapse synthetics is described in the Supporting Information S1.

With the time-lapse synthetics generated, we proceeded to extract time shifts using the feature-based warping approach. The resulting time shifts were converted into relative time shift or time strain. Band pass filtering using a zero phase Butterworth filter at different frequencies was used to smooth out the traces prior to time shift estimation. We ensured to check that the time shifts persist even as the traces were filtered to progressively lower frequencies, with the trade-off being an expected progressive loss of resolution. We then extracted time shifts in a similar approach from full stacks of the real time-lapse VSP surveys, with each of the four monitor surveys analyzed relative to the baseline (B2) survey. Time shifts were extracted starting from 870 ms (or about 1,500 m), because data folds are minimal in shallower intervals due to VSP geometry constraints. The extracted time shifts were then converted to time strain.

3. Results and Discussion

3.1. CO_2 Plume Interpretation From Time Strain

We begin by comparing the time strains from the synthetic seismic models generated at the location of VW1 with those obtained from the real time-lapse VSP data. Figure 2a shows a cross section through the computed time strain volume for Monitor 2 relative to the baseline. The cross-section intersects injection well CCS1 and monitoring well VW1. Zones of positive time strain (red) correspond to zones with CO_2 saturation. Time strain from time-lapse synthetics is shown at the location of VW1; note the excellent correlation with the real time strain volume. An amplitude difference analysis was also attempted on the synthetic time-lapse data. The combination of a stiff rock frame leading to subtle time-lapse effects together with simulated imperfect repeatability yielded an amplitude difference that is unclear. This is similar to the amplitude difference for the real VSP data (see Figure S3 in Supporting Information S1). This analysis confirms that time shift analysis can yield clear plume anomalies in such scenarios where amplitude attributes are unable to.

We identify CO_2 plumes in four zones or layers as illustrated in Figure 2a. The deepest detected plume corresponds to CO_2 accumulations in Mt. Simon Unit A, the lower unit of which is the injection interval. Because the approach employed in this study is to measure time shifts from feature to feature, the seismic frequency dictates the vertical resolution of any CO_2 plumes that can be identified through this approach. The limit of resolution in

19448007, 2025, 2, Downloaded from https://agupubs.onlinelibrary.wiley.com/doi/10.1029/2024GL110049, Wiley Online Library on [16/06/2026]. See the Terms and Conditions (https://onlinelibrary.wiley.com/terms-and-conditions) on Wiley Online Library for rules of use; OA articles are governed by the applicable Creative Commons License

Received by OCD: 6/29/2026

Geophysical Research Letters

10.1029/2024GL110049

19448007, 2025, 2, Downloaded from https://agupubs.onlinelibrary.wiley.com/doi/10.1029/2024GL110049, Wiley Online Library on [16/06/2026]. See the Terms and Conditions (https://onlinelibrary.wiley.com/terms-and-conditions) on Wiley Online Library for rules of use; OA articles are governed by the applicable Creative Commons License

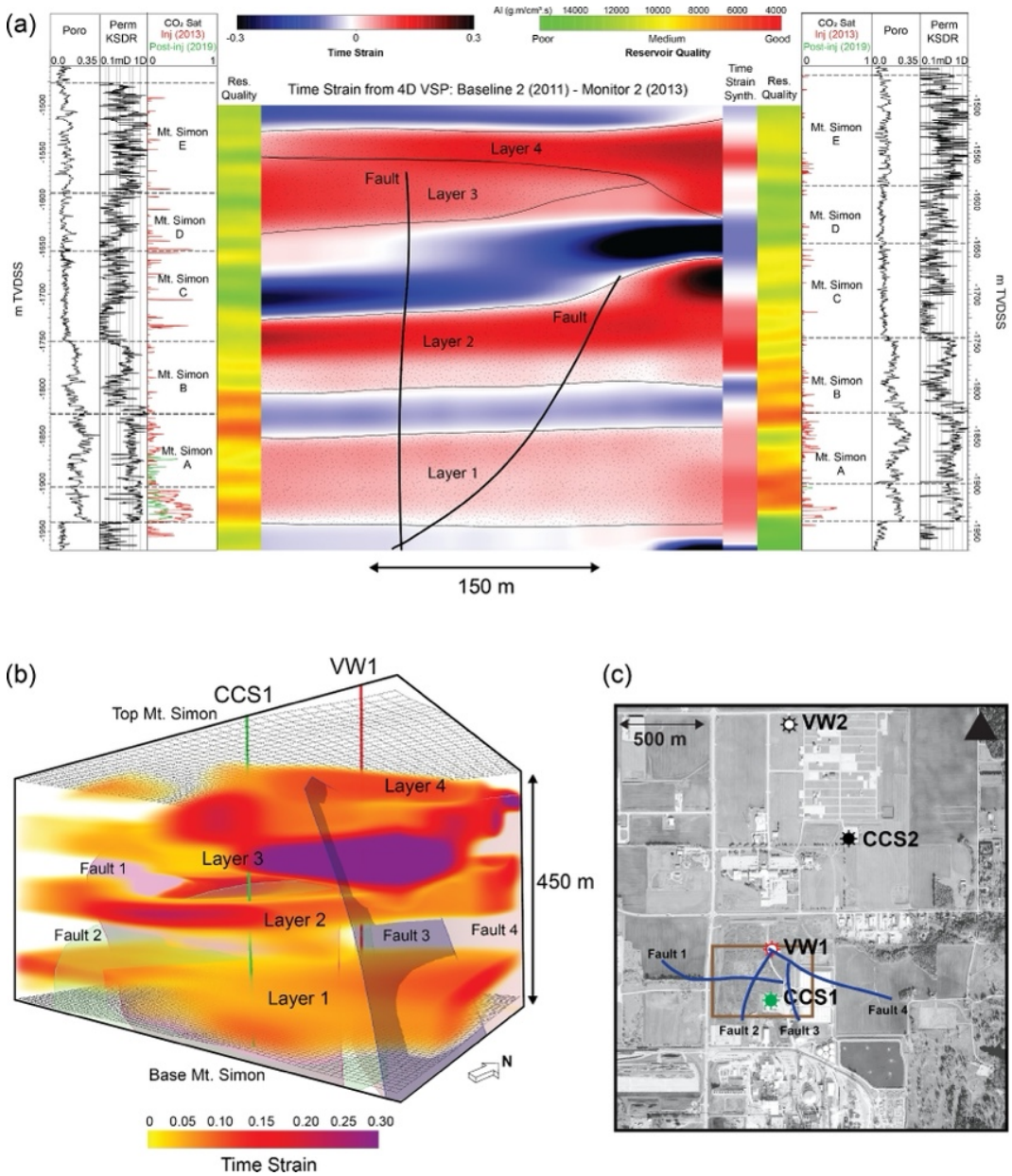


Figure 2. (a) A cross section through the computed time strain volume for Monitor 2 relative to the baseline. The cross section intersects injection well CCS1 and monitoring well VW1. Zones of positive time strain (red) correspond to zones with CO_2 saturation. Porosity logs are shown alongside permeability logs computed from Nuclear Magnetic Resonance log. Repeat saturation logs from during injection and post-injection are shown at both well locations. Time strain from time-lapse synthetics is shown at the location of VW1. (b) A 3D view of time strain from Monitor 2 relative to the baseline. Only positive time strains are shown. (c) A base map showing the locations of all deep wells at the site, the 4D vertical seismic profile coverage area (brown box) and major faults within the coverage.

this approach is therefore generally λ/2, where λ is the seismic wavelength (~100 m for the filtered VSP data in the Mt. Simon). The implication is that any time strains measured resulting from CO_2 saturation in any distribution within these intervals would appear as a single amalgamated zone or layer with a thickness on the order of ~50 m. A comparison of the CO_2 saturation distribution at the wells from the repeat saturation logs and the resulting time strain volume illustrates this (Figure 2a). Figure 2b shows a 3D view of time strain from Monitor 2

Received by OCD: 6/29/2026

Geophysical Research Letters

10.1029/2024GL110049

19448007, 2025, 2, Downloaded from https://agupubs.onlinelibrary.wiley.com/doi/10.1029/2024GL110049, Wiley Online Library on [16/06/2026]. See the Terms and Conditions (https://onlinelibrary.wiley.com/terms-and-conditions) on Wiley Online Library for rules of use; OA articles are governed by the applicable Creative Commons License

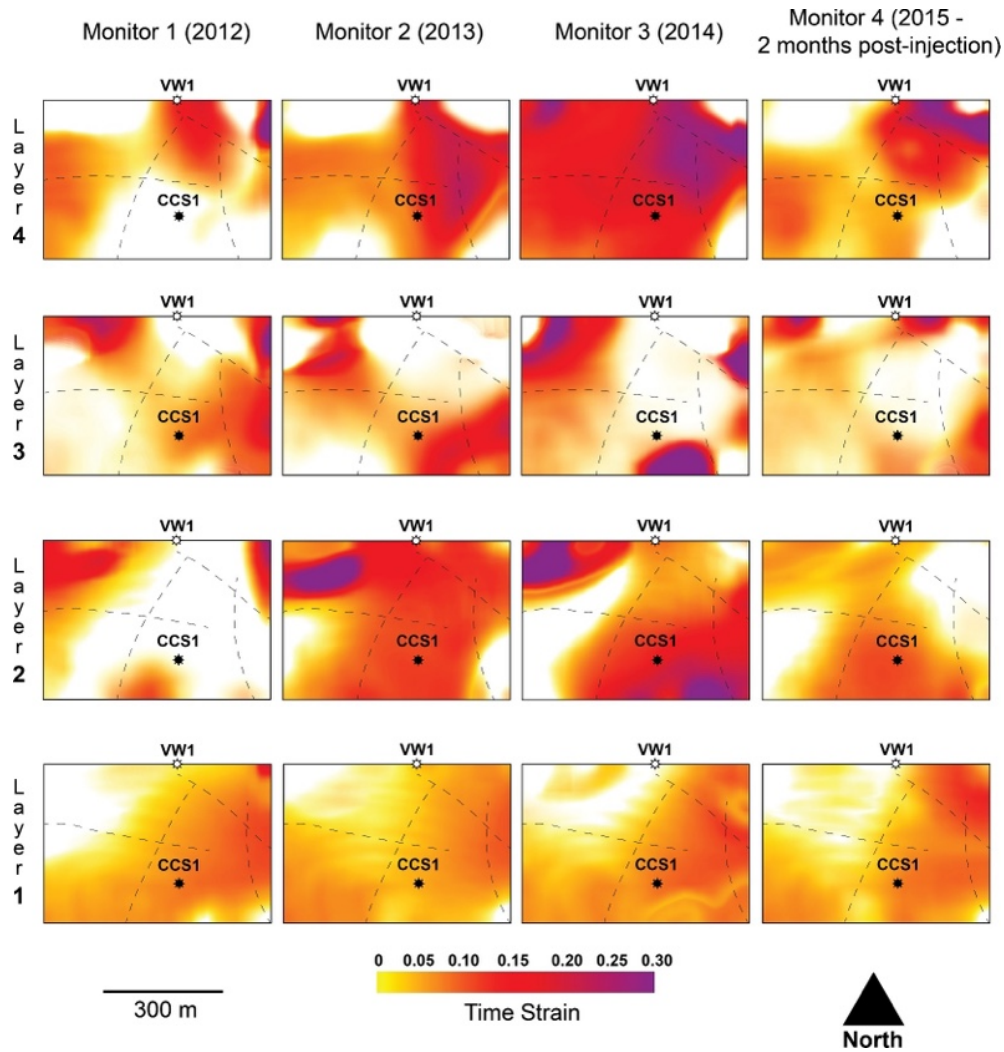


Figure 3. Map views of time strain for all four identified layers across all four monitors (M1–M4) relative to the baseline (B2). Note the excellent consistency for each of the layers from monitor to monitor, which also illustrate the plume development over time. The dashed lines show faults that had been previously mapped.

relative to the baseline. Only positive time strains are shown. Figure 2c shows a base map of the site, showing the locations of all deep wells at the site, the 4D VSP coverage area (brown box) and major interpreted faults within the coverage.

3.2. Plume Development, Capillary Barriers and Rapid Fault Zone Migration of CO_2 Within the Mt. Simon

Having established the presence of CO_2 across the Mt. Simon from time strain, we analyzed the evolution of the CO_2 plume over time. Figure 3 shows the development of the features associated with the four identified plume layers over time from 2012 to 2015. We interpret these features as reflecting the flow of CO_2 and associated pressure changes. There is a clear pattern of growth of the plume-related features. Some of the plume anomalies, particularly those in the Upper Mt. Simon (Layer 4) appear around the previously interpreted faults from Williams-Stroud et al. (2020); we interpret these as feeders allowing the injected CO_2 to migrate into overlying layers. This is more clearly shown in three dimensions in Figure 2b. Note that there are a number of particularly high time strain regions (purple colors), which are overemphasized likely due to phase rotations between surveys.

Received by OCD: 6/29/2026

Geophysical Research Letters

10.1029/2024GL110049

19448007, 2025, 2, Downloaded from https://agupubs.onlinelibrary.wiley.com/doi/10.1029/2024GL110049, Wiley Online Library on [16/06/2026]. See the Terms and Conditions (https://onlinelibrary.wiley.com/terms-and-conditions) on Wiley Online Library for rules of use; OA articles are governed by the applicable Creative Commons License

The occurrence of these presumed phase rotations only in the monitor surveys suggests that they are induced as a result of saturation or pressure changes or a combination of both. Although these areas of high time strain provide qualitative information on the location of CO_2 plumes, we are unable to quantify the amounts of CO_2 in these accumulations due to multiple sources of uncertainty. These include poor resolution of the thicknesses of the layers of CO_2, with the saturation distribution more in the form of multiple thin layers (as observed in the saturation logs in both wells) rather than thick, uniformly filled layers. Another factor is the lack of information about the fluid mixing type or velocity-saturation relationship, which is required to convert velocity changes to saturation. Potential errors in time shift estimation could also hinder accurate quantitative estimates of CO_2, as even small errors in time shift would magnify when converted to time strain or relative velocity change (MacBeth & Izadian, 2023). Nevertheless, the increasing intensity of time strain observed over time even in a qualitative sense represents either growing thicknesses of the CO_2 layers or increasing saturation or both. Either way, it is consistent with a growing mass of CO_2.

It is noteworthy that at the time of the first monitor, there is already a plume observed in the shallowest layer, in the Upper Mt. Simon (Figure 3, top left panel). This is evidence that CO_2 must have migrated rapidly from the injection interval up the faults to the Upper Mt. Simon, covering a vertical distance of about 350 m in 4 months or less. This puts the vertical migration speed at 3 m per day at least, consistent with an along fault permeability of $>10^{-14}$ m^2. For a purely buoyancy driven flow, this is within the bounds of reported along-fault permeabilities (Nicol et al., 2017). The flow behavior of the plumes appears to be controlled by reservoir quality. As can be observed from the porosity and permeability logs in both wells (Figure 2a), there is insufficient reservoir quality for CO_2 to migrate directly upwards from the injection interval except when there is a conductive fault. In other words, there are capillary barriers, which we define as zones with low porosities and permeabilities and high capillary entry pressures. This vertical reservoir quality heterogeneity is also indicated by the acoustic impedance inversion volume from inversion of 3D seismic data (Figure 2a). This is because the primary control on reservoir quality in the Mt. Simon is quartz cementation (Freiburg et al., 2014). Cementation increases the bulk density and stiffens the rock frame, both of which result in higher P-wave velocities. This results in higher acoustic impedance which is a product of density and P-wave velocity. Given the absence of high-quality pathways for CO_2 to migrate up the Mt. Simon, faults therefore provide the only plausible pathways for such migration. Specifically, the damaged zone around the fault core typically comprises a network of fractures with high permeabilities and very low capillary entry pressures would provide high velocity pathways for CO_2 migration.

The emergence of CO_2 in shallower reservoir zones could mitigate leakage further up conductive faults as the amount of CO_2 that continues to migrate upwards is progressively reduced with each high-quality zone encountered. Intra-reservoir conductive faults that do not traverse the seal would merely serve to provide access to other good quality zones of the reservoir, as has been shown through modeling (Yang et al., 2018; Zhang et al., 2024). This appears to be the case at Decatur; the fault provides flow pathways to overlying good quality zones and stringers in the Mt. Simon formation, which the injected CO_2 is otherwise unable to access due to lower quality intervening layers or capillary barriers.

3.3. Origins of Late CO_2 Arrival at Injection Well Post-Injection

Repeat saturation logs in the injection well detected the arrival of an isolated finger of CO_2 in the upper unit of the Mt. Simon A formation (above the injection interval) during the post-injection period of the project in May 2018. This finger had increased in CO_2 saturation from about 30% in May 2018 to about 40% in March 2019 (Figure 2a). The saturation logging report (Swager, 2019) suggested the CO_2 could have originated from the IL-ICCS project located about 1,100 m north of well CCS1. The injection well at this secondary project, well CCS2, had been injecting into the upper unit of the Mt. Simon A formation for 13 months at the time of first detection. A simplified mass balance analysis (see Supporting Information S1) shows it is highly unlikely that enough CO_2 had been injected in well CCS2 to have reached well CCS1 at the time of detection. In addition, the injected CO_2 would have had to flow downdip from the injection interval in CCS2 to arrive where the detection was made in CCS1. We provide this analysis in Supporting Information S1.

We present an alternative hypothesis (Figure 4) based on interpreted fault zone migration, pressure data (Figure S5 in Supporting Information S1) and saturation logging data (Figure 2a). We propose that the CO_2 instead originated from CCS1—the same well it was detected in—but from the underlying injection interval. The CO_2 traveled vertically through a fault under buoyancy, bypassing tight zones, and emerged and pooled in the upper

Received by OCD: 6/29/2026

Geophysical Research Letters

10.1029/2024GL110049

19448007, 2025, 2, Downloaded from https://agupubs.onlinelibrary.wiley.com/doi/10.1029/2024GL110049, Wiley Online Library on [16/06/2026]. See the Terms and Conditions (https://onlinelibrary.wiley.com/terms-and-conditions) on Wiley Online Library for rules of use; OA articles are governed by the applicable Creative Commons License

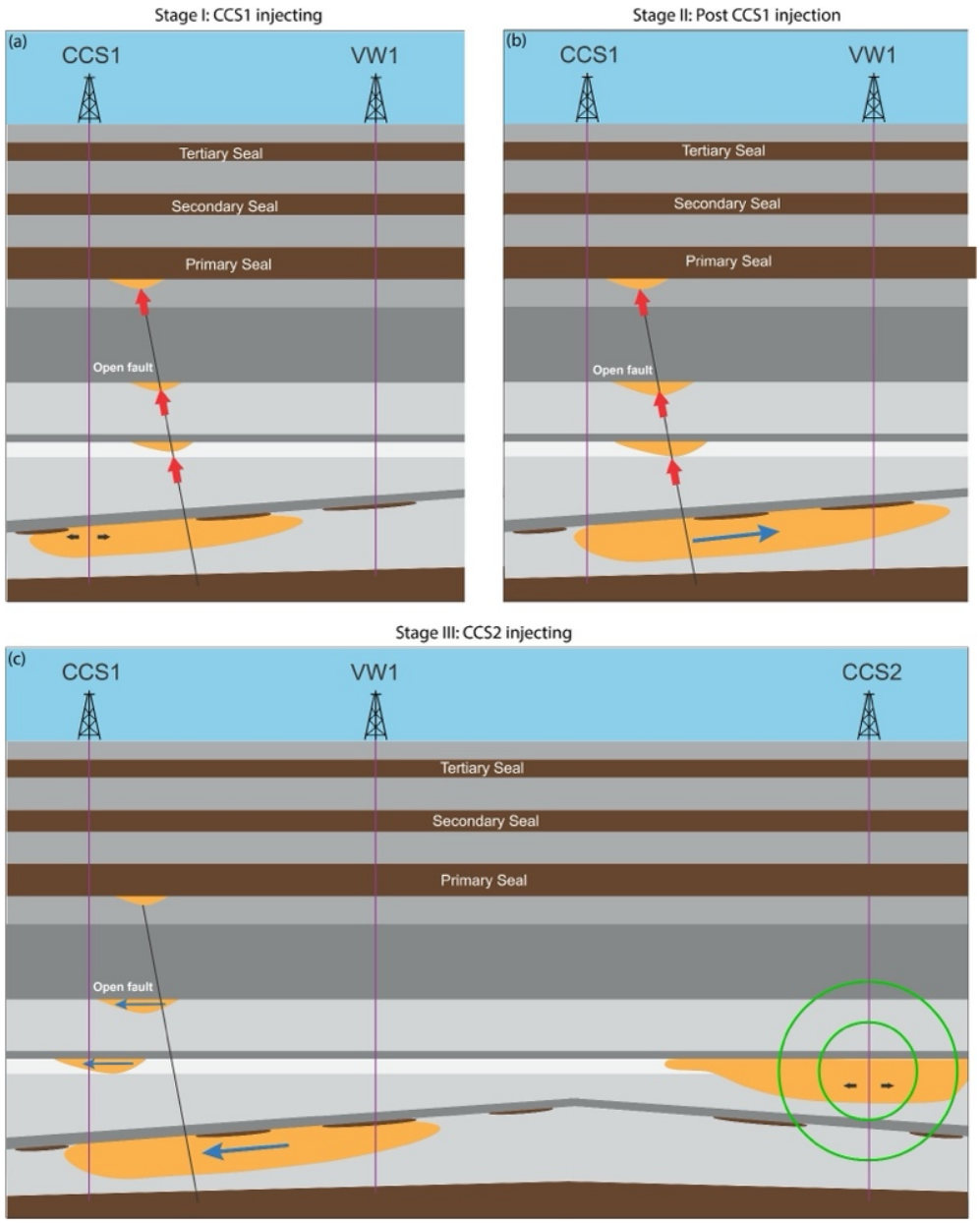


Figure 4. A conceptual schematic summarizing the overall plume behavior during (a) CCS injection, (b) post CCS1 injection, and (c) CCS2 injection. Reservoir quality is indicated in grayscale with darker tones representing tight zones. Green circles represent pressure waves from active injection at CCS2 well.

unit of Mt. Simon A. Once injection began in well CCS2 at the nearby IL-ICCS project, the resulting pressure gradient caused this accumulation to flow across the face of CCS1, resulting in this new detection. We argue this given that bottomhole pressure data shows good pressure communication between wells CCS1 and CCS2 and a significant pressure response in CCS1 from injection in CCS2 (Figure S5 in Supporting Information S1). Our interpretation of the overall CO_2 migration behavior at Decatur including this hypothesis is summarized in Figure 4.

Received by OCD: 6/29/2026

Geophysical Research Letters

10.1029/2024GL110049

19448007, 2025, 2, Downloaded from https://agupubs.onlinelibrary.wiley.com/doi/10.1029/2024GL110049, Wiley Online Library on [16/06/2026]. See the Terms and Conditions (https://onlinelibrary.wiley.com/terms-and-conditions) on Wiley Online Library for rules of use; OA articles are governed by the applicable Creative Commons License

4. Conclusion

We have analyzed data from time-lapse seismic surveys at the Illinois Basin—Decatur Project and interpret that the CO_2 plume migrated along major faults very soon after injection began, entering upper units of the reservoir and moving laterally in response to injection at a neighboring site. These observations emphasize the importance of considering faults as potential flow pathways as well as the impact of pressure from neighboring injection sites on plume dynamics. They also demonstrate the impact that robust and reliable seismic images of the plume will have on the identification of such plume dynamics. This work underscores the need for the identification of faults within potential reservoirs for CO_2 storage and modeling of their potential influence on plume dynamic behavior. These behaviors and their impacts have been previously theorized, and the observations provided from an industry scale geological CO_2 storage site provides important validation of these theories and data from which future projects may be designed.

This interpretation was not possible using a conventional analysis of amplitude attributes. The factors which hindered a more straightforward amplitude-based analysis, mainly changing near surface conditions and a stiff rock frame, may occur commonly in projects, especially in onshore settings. The much clearer picture of CO_2 plume anomalies provided by time shifts, exhibited in both synthetic and real data demonstrate the potential of mitigating challenges with analysis and interpretation of time-lapse seismic monitoring data in difficult environments.

Data Availability Statement

The original data set and reports used in this study were made publicly available by the National Energy Technology Laboratory through the Energy Data eXchange (ISGS, 2021a, 2021b). Bukar (2024) provides the processed data and code used in this study. The codes are also accessible at https://github.com/ImperialCollegeLondon/feature-based-warping.

Acknowledgments
The authors wish to acknowledge support from SLB, Halliburton and Ikon Science for academic licenses for software packages. We thank the Petroleum Technology Development Fund for providing the funding for this research.

References

Al-Jabri, Y., & Urosevic, M. (2010). Assessing the repeatability of reflection seismic data in the presence of complex near-surface conditions CO2CRC Otway Project, Victoria, Australia. *Exploration Geophysics*, *41*(1), 24–30. https://doi.org/10.1071/eg09010

Arts, R., Eiken, O., Chadwick, A., Zweigel, P., Van der Meer, L., & Zinszner, B. (2004). Monitoring of CO_2 injected at Sleipner using time-lapse seismic data. *Energy*, *29*(9–10), 1383–1392. https://doi.org/10.1016/j.energy.2004.03.072

Bakulin, A., Lopez, J., Herhold, I. S., & Mateeva, A. (2007). Onshore monitoring with virtual-source seismic in horizontal wells: Challenges and solutions. In *SEG Technical Program Expanded Abstracts 2007* (pp. 2893–2897). Society of Exploration Geophysicists. https://doi.org/10.1190/1.2793067

Bauer, R., Will, R., Greenberg, S. E., & Whittaker, S. G. (2019). Illinois basin–Decatur project. In *Geophysics and geosequestration* (pp. 339–369). Cambridge University Press. https://doi.org/10.1017/9781316480724.020

Benguigui, A., Roberts, G., & Shaw-Champion, M. (2012). Time-lapse 2D seismic steam-flood monitoring-a case study from offshore republic of Congo, the Emeraude field. In *74th EAGE Conference and Exhibition incorporating EUROPEC 2012*. cp–293. https://doi.org/10.3997/2214-4609.20148837

Brie, A., Pampuri, F., Marsala, A., & Meazza, O. (1995). Shear sonic interpretation in gas-bearing sands. In *SPE Annual Technical Conference and Exhibition*. SPE–30595. https://doi.org/10.2118/30595-MS

Bukar, I. (2024). ImperialCollegeLondon/feature-based-warping: v1.0 [Dataset]. *Zenodo*. https://doi.org/10.5281/ZENODO.14556854

Cavanagh, A. J., & Haszeldine, S. (2014). The Sleipner storage site: Capillary flow modeling of a layered CO_2 plume requires fractured shale barriers within the Utsira Formation. *International Journal of Greenhouse Gas Control*, *21*, 101–112. https://doi.org/10.1016/j.ijggc.2013.11.017

Chadwick, R., Arts, R., & Eiken, O. (2005). 4D seismic quantification of a growing CO_2 plume at Sleipner, North Sea. *Geological Society, London, Petroleum Geology Conference series*, *6*(1), 1385–1399. https://doi.org/10.1144/0061385

Chadwick, R., Arts, R., Eiken, O., Kirby, G., Lindeberg, E., & Zweigel, P. (2004). 4D seismic imaging of an injected CO_2 plume at the Sleipner Field, Central North Sea. *Geological Society, London, Memoirs*, *29*(1), 311–320. https://doi.org/10.1144/gsl.mem.2004.029.01.29

Coueslan, M. L., Ali, S., Campbell, A., Nutt, W., Leaney, W., Finley, R., & Greenberg, S. (2013). Monitoring CO_2 injection for carbon capture and storage using time-lapse 3D VSPs. *The Leading Edge*, *32*(10), 1268–1276. https://doi.org/10.1190/tle32101268.1

Coueslan, M. L., Butsch, R., Will, R., & Locke, R. A., II. (2014). Integrated reservoir monitoring at the Illinois Basin–Decatur Project. *Energy Procedia*, *63*, 2836–2847. https://doi.org/10.1016/j.egypro.2014.11.306

Coueslan, M. L., Leetaru, H. E., Brice, T., Leaney, W. S., & McBride, J. H. (2009). Designing a seismic program for an industrial CCS site: Trials and tribulations. *Energy Procedia*, *1*(1), 2193–2200. https://doi.org/10.1016/j.egypro.2009.01.285

Dockrill, B., & Shipton, Z. K. (2010). Structural controls on leakage from a natural CO_2 geologic storage site: Central Utah, USA. *Journal of Structural Geology*, *32*(11), 1768–1782. https://doi.org/10.1016/j.jsg.2010.01.007

Falahat, R., Shams, A., & MacBeth, C. (2011). Towards quantitative evaluation of gas injection using time-lapse seismic data. *Geophysical Prospecting*, *59*(2), 310–322. https://doi.org/10.1111/j.1365-2478.2010.00925.x

Flemisch, B., Nordbotten, J. M., Fernø, M., Juanes, R., Both, J. W., Class, H., et al. (2024). The FluidFlower validation benchmark study for the storage of CO_2. *Transport in Porous Media*, *151*(5), 865–912. https://doi.org/10.1007/s11242-023-01977-7

Received by OCD: 6/29/2026

Geophysical Research Letters 10.1029/2024GL110049

Freiburg, J., Morse, D. G., Leetaru, H. E., Hoss, R. P., & Yan, Q. (2014). A depositional and diagenetic characterization of the Mt. Simon sandstone at the Illinois Basin-Decatur Project carbon capture and storage site, Decatur, Illinois, USA. [Publisher: Illinois State Geological Survey, Prairie Research Institute, University of Illinois Urbana-Champaign]. https://hdl.handle.net/2142/55338

Furre, A.-K., Eiken, O., Alnes, H., Vevatne, J. N., & Kiær, A. F. (2017). 20 years of monitoring CO_2-injection at Sleipner. *Energy Procedia*, *114*, 3916–3926. https://doi.org/10.1016/j.egypro.2017.03.1523

Furre, A.-K., Kiær, A., & Eiken, O. (2015). CO_2-induced seismic time shifts at Sleipner. *Interpretation*, *3*(3), SS23–SS35. https://doi.org/10.1190/INT-2014-0225.1

Gasda, S. E., Bachu, S., & Celia, M. A. (2004). Spatial characterization of the location of potentially leaky wells penetrating a deep saline aquifer in a mature sedimentary basin. *Environmental Geology*, *46*(6–7), 707–720. https://doi.org/10.1007/s00254-004-1073-5

Gassmann, F. (1951). U¨ber die elastizit¨at por¨oser medien: Vierteljahrss-chrift der Naturforschenden Gesellschaft in Zurich (Vol. *96*). Retrieved from https://cir.nii.ac.jp/crid/1570291224657132800

Gay, A., Lopez, M., Berndt, C., & Séranne, M. (2007). Geological controls on focused fluid flow associated with seafloor seeps in the Lower Congo Basin. *Marine and Petroleum Geology*, *244*(1–4), 68–92. https://doi.org/10.1016/j.margeo.2007.06.003

Gilmore, K. A., Sahu, C. K., Benham, G. P., Neufeld, J. A., & Bickle, M. J. (2022). Leakage dynamics of fault zones: Experimental and analytical study with application to CO_2 storage. *Journal of Fluid Mechanics*, *931*, A31. https://doi.org/10.1017/jfm.2021.970

Grude, S., Landrø, M., & Osdal, B. (2013). Time-lapse pressure–saturation discrimination for CO_2 storage at the Snøhvit field. *International Journal of Greenhouse Gas Control*, *19*, 369–378. https://doi.org/10.1016/j.ijggc.2013.09.014

Hale, D. (2013). Dynamic warping of seismic images. *Geophysics*, *78*(2), S105–S115. https://doi.org/10.1190/geo2012-0327.1

Han, D., & Batzle, M. (2014). *FLAG fluid calculator*. University of Houston Fluids/DHI Consortium.

Han, G., Han, W. S., Kim, K. Y., Park, J. G., Piao, J., & Yun, T. K. (2019). Roles of fault structures and regional formations on CO_2 migration and distribution in shallow saline aquifer in Green River, Utah. *Journal of Hydrology*, *570*, 786–801. https://doi.org/10.1016/j.jhydrol.2019.01.027

Hansen, O., Gilding, D., Nazarian, B., Osdal, B., Ringrose, P., Kristoffersen, J.-B., et al. (2013). Snøhvit: The history of injecting and storing 1 mt CO_2 in the fluvial tub¨aen fm. *Energy Procedia*, *37*, 3565–3573. https://doi.org/10.1016/j.egypro.2013.06.249

Illinois State Geological Survey (ISGS). (2021a). Illinois Basin - Decatur Project (IBDP) geological models, July 7, 2021. Midwest Geological Sequestration Consortium (MGSC) Phase III data sets [Dataset]. DOE Cooperative Agreement No. DE-FC26-05NT42588. https://doi.org/10.18141/1854141

Illinois State Geological Survey (ISGS). (2021b). Illinois Basin - Decatur Project (IBDP) seismic data, July 7, 2021. Midwest Geological Sequestration Consortium (MGSC) phase III data sets [Dataset]. DOE Cooperative Agreement No. DE-FC26-05NT42588. https://doi.org/10.18141/1854142

Ivandic, M., Juhlin, C., Lueth, S., Bergmann, P., Kashubin, A., Sopher, D., et al. (2015). Geophysical monitoring at the Ketzin pilot site for CO_2 storage: New insights into the plume evolution. *International Journal of Greenhouse Gas Control*, *32*, 90–105. https://doi.org/10.1016/j.ijggc.2014.10.015

Johnston, D. H. (2013). *Practical applications of time-lapse seismic data*. Society of Exploration Geophysicists. https://doi.org/10.1190/1.9781560803126

Jung, N.-H., Han, W. S., Watson, Z., Graham, J. P., & Kim, K.-Y. (2014). Fault-controlled CO_2 leakage from natural reservoirs in the Colorado Plateau, east-central Utah. *Earth and Planetary Science Letters*, *403*, 358–367. https://doi.org/10.1016/j.epsl.2014.07.012

Kampman, N., Burnside, N. M., Shipton, Z. K., Chapman, H. J., Nicholl, J. A., Ellam, R. M., & Bickle, M. J. (2012). Pulses of carbon dioxide emissions from intracrustal faults following climatic warming. *Nature Geoscience*, *5*, 352–358. https://doi.org/10.1038/ngeo1451

Krevor, S., de Coninck, H., Gasda, S. E., Ghaleigh, N. S., de Gooyert, V., Hajibeygi, H., et al. (2023). Subsurface carbon dioxide and hydrogen storage for a sustainable energy future. *Nature Reviews Earth & Environment*, *4*(2), 1–17. https://doi.org/10.1038/s43017-022-00376-8

Landrø, M. (1999). Repeatability issues of 3-D VSP data. *Geophysics*, *64*(6), 1673–1679. https://doi.org/10.1190/1.1444671

Landrø, M., Digranes, P., & Strønen, L. K. (2001). Mapping reservoir pressure and saturation changes using seismic methods-possibilities and limitations. *First Break*, *19*(12). https://doi.org/10.1046/j.1365-2397.2001.00226.x

Landrø, M., & Stammeijer, J. (2004). Quantitative estimation of compaction and velocity changes using 4D impedance and traveltime changes. *Geophysics*, *69*(4), 949–957. https://doi.org/10.1190/1.1778238

Leetaru, H., & Freiburg, J. T. (2014). Litho-facies and reservoir characterization of the Mt Simon Sandstone at the Illinois Basin–Decatur Project. *Greenhouse Gases: Science and Technology*, *4*(5), 580–595. https://doi.org/10.1002/ghg.1453

Lumley, D. E. (2001). Time-lapse seismic reservoir monitoring. *Geophysics*, *66*(1), 50–53. https://doi.org/10.1190/1.1444921

MacBeth, C., Amini, H., & Izadian, S. (2020). Methods of measurement for 4D seismic post-stack time shifts. *Geophysical Prospecting*, *68*(9), 2637–2664. https://doi.org/10.1111/1365-2478.13022

MacBeth, C., & Izadian, S. (2023). A review and analysis of errors in post-stack time-shift interpretation. *Geophysical Prospecting*, *71*(8), 1497–1522. https://doi.org/10.1111/1365-2478.13391

MacBeth, C., Mangriotis, M.-D., & Amini, H. (2019). Post-stack 4D seismic time-shifts: Interpretation and evaluation. *Geophysical Prospecting*, *67*(1), 3–31. https://doi.org/10.1111/1365-2478.12688

Meunier, J., Huguet, F., & Meynier, P. (2001). Reservoir monitoring using permanent sources and vertical receiver antennae: The Céré-la-Ronde case study. *The Leading Edge*, *20*(6), 622–629. https://doi.org/10.1190/1.1439008

Miocic, J. M., Gilfillan, S. M., Roberts, J. J., Edlmann, K., McDermott, C. I., & Haszeldine, R. S. (2016). Controls on CO_2 storage security in natural reservoirs and implications for CO_2 storage site selection. *International Journal of Greenhouse Gas Control*, *51*, 118–125. https://doi.org/10.1016/j.ijggc.2016.05.019

Nicol, A., Seebeck, H., Field, B., McNamara, D., Childs, C., Craig, J., & Rolland, A. (2017). Fault permeability and CO_2 storage. *Energy Procedia*, *114*, 3229–3236. https://doi.org/10.1016/j.egypro.2017.03.1454

Nordbotten, J. M., Kavetski, D., Celia, M. A., & Bachu, S. (2009). Model for CO_2 leakage including multiple geological layers and multiple leaky wells. *Environmental Science & Technology*, *43*(3), 743–749. https://doi.org/10.1021/es801135v

Onishi, T., Nguyen, M. C., Carey, J. W., Will, B., Zaluski, W., Bowen, D. W., et al. (2019). Potential CO_2 and brine leakage through wellbore pathways for geologic CO_2 sequestration using the national risk assessment partnership tools: Application to the big sky regional partnership. *International Journal of Greenhouse Gas Control*, *81*, 44–65. https://doi.org/10.1016/j.ijggc.2018.12.002

Pevzner, R., Shulakova, V., Kepic, A., & Urosevic, M. (2011). Repeatability analysis of land time-lapse seismic data: CO2CRC Otway pilot project case study. *Geophysical Prospecting*, *59*(1), 66–77. https://doi.org/10.1111/j.1365-2478.2010.00907.x

P¨ortner, H., Roberts, D. C., Poloczanska, E., Mintenbeck, K., Tignor, M., Alegria, A., et al. (2022). *IPCC, 2022: Summary for policymakers*. Cambridge University Pres. https://doi.org/10.1017/9781009325844.001

Ringrose, P., Andrews, J., Zweigel, P., Furre, A.-K., Hern, B., & Nazarian, B. (2022). Why ccs is not like reverse gas engineering. *First Break*, *40*(10), 85–91. https://doi.org/10.3997/1365-2397.fb2022088

19448007, 2025, 2, Downloaded from https://agupubs.onlinelibrary.wiley.com/doi/10.1029/2024GL110049, Wiley Online Library on [16/06/2026]. See the Terms and Conditions (https://onlinelibrary.wiley.com/terms-and-conditions) on Wiley Online Library for rules of use; OA articles are governed by the applicable Creative Commons License

Received by OCD: 6/29/2026

Geophysical Research Letters

10.1029/2024GL110049

Roach, L. A., & White, D. (2018). Evolution of a deep CO_2 plume from time-lapse seismic imaging at the Aquistore storage site, Saskatchewan, Canada. *International Journal of Greenhouse Gas Control*, *74*, 79–86. https://doi.org/10.1016/j.ijggc.2018.04.025

Roelofse, C., Alves, M. T., & Gafeira, J. (2020). Structural controls on shallow fluid flow and associated pockmark fields in the East Breaks area, northern Gulf of Mexico. *Marine and Petroleum Geology*, *112*, 104074. https://doi.org/10.1016/j.marpetgeo.2019.104074

Santos, J. M., Davolio, A., MacBeth, C., & Schiozer, D. J. (2016). 4D seismic interpretation of the Norne Field-a semi-quantitative approach [Issue: 1]. In *78th EAGE Conference and Exhibition 2016* (Vol. 2016, pp. 1–5). https://doi.org/10.3997/2214-4609.201601313

Schlumberger Petrotechnical Services (2015). Time-lapse 3D VSP processing report, Illinois state geological survey Illinois Basin – Decatur project geophysical monitoring well #1, September 2015, 3D VSP Processing (tech. rep.).

Shipton, Z. K., Evans, J. P., Kirschner, D., Kolesar, P. T., Williams, A. P., & Heath, J. (2004). Analysis of CO_2 leakage through 'low-permeability' faults from natural reservoirs in the Colorado Plateau, east-central Utah. In S. J. Baines & R. H. Worden (Eds.), *Geological storage of carbon dioxide*. Geological Society, London, Special Publications (Vol. 233(1), pp. 43–58). https://doi.org/10.1144/GSL.SP.2004.233.01.05

Stork, C. (2020). How does the thin near surface of the earth produce 10–100 times more noise on land seismic data than on marine data? *First Break*, *38*(8), 67–75. https://doi.org/10.3997/1365-2397.fb2020062

Swager, L. (2019). ADM CCS1 injection well mechanical integrity report March 2019 pulsed neutron eXtreme (tech. rep.).

Williams-Stroud, S., Bauer, R., Leetaru, H., Oye, V., Stanek, F., Greenberg, S., & Langet, N. (2020). Analysis of microseismicity and reactivated fault size to assess the potential for felt events by CO_2 injection in the Illinois Basin. *Bulletin of the Seismological Society of America*, *110*(5), 2188–2204. https://doi.org/10.1785/0120200112

Yang, Z., Xu, T., Wang, F., Yang, Y., Li, X., & Zhao, N. (2018). Impact of inner reservoir faults on migration and storage of injected CO_2. *International Journal of Greenhouse Gas Control*, *72*, 14–25. https://doi.org/10.1016/j.ijggc.2018.03.006

Zaluski, W., & Lee, S.-Y. (2021). 2020 IBDP final static geological model development and dynamic modelling (tech. rep.).

Zhang, L., Yang, Q., Zhang, S., Shan, L., Jiang, Q., & Sun, M. (2024). Enhanced CO_2 storage efficiency due to the impact of faults on CO_2 migration in an interbedded saline aquifer. *International Journal of Greenhouse Gas Control*, *133*, 104104. https://doi.org/10.1016/j.ijggc.2024.1

19448007, 2025, 2, Downloaded from https://agupubs.onlinelibrary.wiley.com/doi/10.1029/2024GL110049, Wiley Online Library on [16/06/2026]. See the Terms and Conditions (https://onlinelibrary.wiley.com/terms-and-conditions) on Wiley Online Library for rules of use; OA articles are governed by the applicable Creative Commons License

EXHIBIT 7

Received by OCD: 6/29/2026

International Journal of Greenhouse Gas Control 146 (2025) 104456

Contents lists available at ScienceDirect

International Journal of Greenhouse Gas Control

journal homepage: www.elsevier.com/locate/ijggc

Quantifying CO_2 plume stabilization at carbon storage projects, North Dakota, USA

Matthew E. Burton-Kelly *, John E. Hunt, Neil W. Dotzenrod, John A. Templeton, Joshua G. Regorrah, Chantsalmaa Dalkhaa, Amanda J. Livers-Douglas, Wesley D. Peck, Kevin C. Connors, Nicholas A. Azzolina

Energy & Environmental Research Center, University of North Dakota, 15 North 23rd Street, Stop 9018, Grand Forks, ND 58202-9018, USA

ARTICLE INFO

Keywords:
CO_2 plume stability
CCS
Site closure requirements
Regulatory compliance
Post-injection site care
Plume monitoring

ABSTRACT

This study presents an approach for quantifying when injected carbon dioxide (CO_2) stabilizes pursuant to carbon capture and storage (CCS) project permitting and site closure requirements. The distribution of mobile-phase CO_2 (CO_2 plume) will evolve within the storage reservoir during and after injection through both physical and chemical trapping mechanisms. CCS policies generally agree that the CO_2 plume's migratory behavior in post-injection should demonstrate nonendangerment to the environment but do not provide specific guidance on how to meet the definition of plume stabilization, generating some uncertainty for operators. Plume stability herein means the CO_2 plume 1) changes size minimally and predictably in the storage reservoir such that it will not cross key boundaries identified in the permit and 2) does not pose a threat to human health, underground sources of drinking water (USDWs), and the environment because of lateral migration to areas where leakage pathways may exist. Published literature on plume metrics was reviewed to determine which metric(s) may be most appropriate for determining CO_2 plume stability. A technical approach that defines plume stabilization by estimating the rate of change in the geographic footprint of the CO_2 plume with respect to time was developed and illustrated using a case study from North Dakota, USA, as a proposed solution for CCS operators to apply at the project permitting stage. Any prospective CCS operator may benefit from using the same approach to inform the selection of pore space lease and monitoring areas and develop post-injection site care plans.

1. Introduction

Carbon capture and storage (CCS) is a process during which carbon dioxide (CO_2) is captured and injected underground into a geologic reservoir (storage reservoir, storage unit, or injection interval) for permanent storage. Injection wells are used to push compressed CO_2 into the target storage reservoir at a higher pressure than the initial reservoir pressure, displacing native reservoir fluids. Minor amounts of other constituents may be included in the injectate, but for simplicity, the entire stream will be referred to hereafter as CO_2. The three-dimensional (3D) distribution of injected mobile-phase CO_2 in the subsurface is called the CO_2 plume. During and after CO_2 injection operations, the CO_2 plume is expected to migrate within the storage reservoir in both vertical and lateral directions. CCS operators within the United States must track the CO_2 plume to provide assurance that the injected CO_2 is contained within the vertical injection interval and appropriate geographic boundaries permitted throughout the injection and post-injection site care (PISC) periods. Within the United States, before appropriate regulatory agencies approve a storage site for closure, operators must demonstrate that the CO_2 plume has stabilized (hereafter, plume stability or plume stabilization). The predicted date of stabilization and areal extent (footprint) of the stabilized plume are therefore required elements of storage permit applications.

The University of North Dakota Energy & Environmental Research Center (EERC) has established a technical approach for predicting plume stabilization that has been used in several permit applications approved by the North Dakota Industrial Commission (NDIC) Department of Mineral Resources (DMR), which has been granted primacy authority for regulating Class VI wells in North Dakota (Table 1; North Dakota Department of Mineral Resources, 2025). The approach uses numerical simulation (before the end of injection) and envisions incorporating monitoring data (after the end of injection) to demonstrate plume

* Corresponding author.
E-mail address: mburtonkelly@undeerc.org (M.E. Burton-Kelly).

https://doi.org/10.1016/j.ijggc.2025.104456
Received 30 April 2025; Received in revised form 8 August 2025; Accepted 17 August 2025
Available online 22 August 2025
1750-5836/© 2025 The Authors. Published by Elsevier Ltd. This is an open access article under the CC BY-NC-ND license (http://creativecommons.org/licenses/by-nc-nd/4.0/).

Received by OCD: 6/29/2026

Table 1
Permitted Broom Creek Formation CO_2 storage projects in North Dakota, USA.

Operator	Project	Project ID	DMR Case ID*	Injectors	Status
Red Trail Energy LLC	Red Trail Richardton Ethanol Broom Creek Storage Facility #1	RTE	28848	One	Operating
Minnkota Power Cooperative, Inc. (Milton R. Young Station)	Minnkota Center MRYS Broom Creek Storage Facility #1	MRYS	29029	Two (twin)	Permitted
Dakota Gasification Company	DGC Beulah Broom Creek Storage Facility #1	DGC	29450	Six (separate)	Operating
Blue Flint Sequester Company, LLC	Blue Flint Underwood Broom Creek Storage Facility #1	BF	29888	One	Operating
DCC West Project LLC	DCC West Center Broom Creek Storage #1	DCCW	30122	Two (twin)	Permitted
Summit Carbon Storage #1, LLC	TB Leingang Broom Creek Storage Facility	SCS1	30869	Two (twin)	Permitted
Summit Carbon Storage #2, LLC	BK Fischer Broom Creek Storage Facility	SCS2	30873	Two (twin)	Permitted
Summit Carbon Storage #3, LLC	KJ Hintz Broom Creek Storage Facility	SCS3	30877	Two (twin)	Permitted

* Storage facility permit (SFP) applications are referenced by case ID on the North Dakota DMR website.

stability.

This study provides a definition of CO_2 plume stability compliant across multiple CCS policies and frameworks applicable within the United States. A numerical simulation case study of this technical approach for plume stabilization is presented using a North Dakota, USA, example. The case study assumes an injection scenario of >1 Mt of CO_2 annually for 20 years at a single well location into a regionally extensive and shallowly dipping (<1°) aeolian sandstone and saline aquifer in the Williston Basin.

In addition to the simulation case study that demonstrates the technical plume stabilization approach, descriptive statistics from simulated stabilized plumes at permitted projects in North Dakota are also shared and discussed. These are provided both as a dataset against which future North Dakota projects targeting the same formation can be compared and an example of a dataset that can be generated from CO_2 storage simulations in other formations or depositional basins.

Regorrah et al. (2023) reviewed the UIC CO_2 injection well (Class VI) permitting program and Greenhouse Gas Reporting Program Subpart RR requirements as regulated by the U.S. Environmental Protection Agency (EPA) and U.S. states with Class VI primacy; low-carbon fuel incentive programs in California, USA; and CCS regulatory frameworks established by the provincial Government of Alberta, Canada, and the European Parliament. Each CCS policy was reviewed to identify guidance or regulatory definitions associated with plume stability. Table 2 summarizes the CCS policy review.

Table 2
Summary of Plume Stability Rules and Guidance from CCS Policies from Regorrah et al. (2023).

Regulatory Body	Policy	Reference	Guidance/Rule
EPA	Title 40 Code of Federal Regulations	§ 146.93(b)	"The owner or operator shall monitor the site following the cessation of injection to show the position of the carbon dioxide plume and pressure front and demonstrate that USDWs are not being endangered."
North Dakota, USA	North Dakota Century Code	§ 38–22–17 (5)(d)	Show that the injected CO_2 plume "has become stable, or that the plume is "essentially stationary or, if it is migrating or may migrate, that any migration will be unlikely to cross the storage reservoir boundary."
Wyoming, USA	Wyoming Code of Regulations	§ 24–2(hh)	Show that the injected CO_2 plume "essentially no longer expands vertically or horizontally and poses no threat to USDWs, human health, safety, or the environment, as demonstrated by a minimum of three consecutive years of monitoring data."
Louisiana, USA	Louisiana Administrative Code	43:XVII, Chapter 6, § 633.A.2	"The owner or operator shall monitor the site following the cessation of injection to show the position of the carbon dioxide plume and pressure front and demonstrate that USDWs are not being endangered."
California, USA	Low-Carbon Fuel Standard CCS Protocol	Chapter A Section (2)(a)(85)	Show that the injected CO_2 plume's "migration and pressure changes are small and predictable, such that the measured rate of plume migration has a high certainty of no CO_2 leakage over a 100-year period."
Government of Alberta, Canada	CCS Statutes Amendment Act of 2010	§ 14–9.120 (3)(f)	Show that the injected CO_2 plume is "behaving in a stable and predictable manner, with no significant risk of future leakage."
European Parliament	European Union Directive 2009/31/EC	Chapter 1, Article 18(2)	Demonstrate "conformity of the actual behavior of the injected CO_2 plume with the modeled behavior; the absence of detectable leakage; and that the storage site is evolving toward a situation of long-term stability."

Received by OCD: 6/29/2026

The study identified two key elements in each policy relative to plume stability: 1) containment of the injected CO_2 in three dimensions to protect human health and the environment from deleterious effects that would be caused by leakage of brine or injected CO_2 and 2) demonstration of a near-stationary geographic position of the CO_2 plume, not only to provide supporting evidence of containment but to uphold contractual and permitting agreements between the storage operator and other entities.

1.1. CCS policy review

The policy language around CO_2 plume stabilization varies according to the regulatory framework under which each policy was developed. For example, EPA focuses on nonendangerment to underground sources of drinking water (USDWs), as the Class VI rule is under the Safe Water Drinking Act. Other policies, such as those from California, the European Parliament, and the Government of Alberta, focus more broadly on eliminating the risk of leakage of any fluids from the injection interval, regardless of where fluids may accumulate after leakage. In North Dakota, the risk of the plume being unlikely to cross a project's permit boundary (e.g., pore space lease area) is discussed. The minimum period required for post-injection monitoring and site closure also varies among policies. The California Air Resources Board (CARB) requires the demonstration of plume stability no sooner than 15 years after injection ceases, while the Wyoming Department of Environmental Quality (DEQ) requires demonstration of three consecutive years of plume stability and 20 years minimum of post-injection monitoring before the site can be closed. In contrast, EPA and NDIC do not establish minimum requirements for the timing associated with demonstrating plume stability; however NDIC requires a minimum of 10 years before a certificate of project completion may be issued, while EPA recommends a 50-year PISC period but gives operators an opportunity to specify an alternative timeframe. Additional details on these policies can be found in Regorrah et al. (2023).

The policy frameworks reviewed in this paper share commonalities, which lay the groundwork for recommending an approach to demonstrate plume stabilization. Because monitoring data are required for any CCS project and key differences exist between policy frameworks, the technical approach presented in this study should be supplemented with appropriate monitoring data (e.g., time-lapse seismic) at a frequency and duration specific to the CCS project.

1.2. Definition of CO_2 plume stability

1.2.1. Plume identification

Few commercial-scale CCS projects have operated for long enough to observe CO_2 plume extents throughout operational and post-injection phases, so plume evolution and stabilization studies have relied on geologic modeling and numerical reservoir simulations that can incorporate each type of trapping mechanism and multiple phases of CO_2 (Zapata et al., 2020). The results from the simulated injection of CO_2 represent the "truth" against which plume evolution and stability can be characterized. During operation, the true distribution of CO_2 within the storage unit is unknown but can be approximated using indirect monitoring technology. Accuracy and precision of plume identification according to each monitoring technology must be balanced against deployment cost (Jenkins et al., 2024).

At one extreme, a closely spaced grid of wells within the expected plume footprint with continuous (e.g., distributed temperature and pressure sensors; Azzolina et al., 2018) or scheduled (e.g., spinner logs; Jiang et al., 2017) monitoring techniques would provide a high-confidence estimate of CO_2 plume evolution but would be prohibitively expensive. At the other extreme, operations data and simulations alone would provide much lower confidence. Although multiple capable monitoring options exist, industry and regulators have generally converged on using single monitoring wells and time-lapse (repeated) seismic surveys to estimate CO_2 plume evolution. This approach has shown relatively low comparative cost and minimal effects to surface activities (e.g., Chadwick and Noy, 2015; Burnison et al., 2017a,b; Pevzner et al., 2017; Barajas-Olalde et al., 2019; Dance et al., 2019; Saleh and Zhang, 2024). The standard practice is to acquire a baseline (pre-injection) seismic survey followed by subsequent repeat surveys during the operational and post-injection phases. Post-injection surveys without a baseline comparison can also estimate CO_2 plume extent but with lower confidence than pre-injection/post-injection comparison. When the seismic datasets are compared with one another, changes in the seismic response due to changes in CO_2 saturation in the storage reservoir are used to infer the extent of the CO_2 plume. Time-lapse seismic can provide a measure of changes in the storage unit during operations at relatively high spatial (geographic footprint) accuracy but low vertical precision. Time-lapse seismic has been documented to detect CO_2 gas/supercritical saturations down to about 5 % in good-porosity (20–30 %) reservoir rock, but CO_2 concentration differences within the plume may be difficult or impossible to detect (Whittaker et al., 2004; White et al., 2014; Roach et al., 2014, 2017).

Although simulation studies can subdivide and quantify injected CO_2 into multiple physical phases, the simulation results reported herein were prepared to conform with future time-lapse seismic monitoring. The CO_2 plumes described are represented by the presence of CO_2 in concentrations high enough to exhibit a difference in seismic properties. In the case study provided, a simulated gas saturation of 5 % or greater is defined as part of the CO_2 plume, where "gas saturation" is defined by density and includes both gas and supercritical mobile CO_2 phases but not CO_2 dissolved in formation brine (aqueous phase).

Geologic model grid resolution of simulation cases is important to consider, even when using a non-zero threshold for plume identification. Harp et al. (2019) used a 50 × 50-m grid, which resulted in a potential spatial resolution of 0.003 km^2 per time step. For a grid with 300 × 300-m cells, the resolution is only 0.09 km^2, meaning that the plume location in the latter grid is known with less precision.

Potential vertical flow through overlying seals is ignored for this study, except in the sense that a CO_2 plume migrating laterally may intersect with a potential vertical leakage pathway (e.g., legacy oil and gas well or fault).

1.2.2. Plume evolution

CO_2 plume evolution during and after the injection period can be quantified using simple metrics to define the size, shape, and location of the plume with limited parameters. For example, Doughty (2010) defined stabilization as "occurring when two successive snapshots show no advance of the leading edge of the plume." Zeidouni et al. (2016) discuss the distance of the geographic plume center from the injection well as a metric for plume dispersion in a dipping reservoir to compare different residual trapping scenarios. Chadwick and Noy (2015) defined performance metrics that could be used to describe plume migration and "conformance" with simulations but did not apply these metrics to stabilization. More recent work has attempted to distinguish "concordance" (degree to which simulation results match monitoring data), "performance" (degree to which storage complex behavior matches project requirements), and "conformance" (concordance plus performance); these terms will be used as such herein (Oldenburg et al., 2018; Harp et al., 2019b; Ennis-King and Jackson, 2020). Manceau and Rohmer (2016) also focused on tracking plume migration rather than stabilization and weighted the geographic plume center by mass of mobile CO_2 and proposed metrics to track the total mass of mobile CO_2 and the area of mobile CO_2 in contact with the upper seal.

Harp et al. (2019) developed three plume migration metrics based on spatial moment analysis: 1) change in footprint area (A) of the CO_2 plume with time (t) (dA/dt), 2) mobility of the CO_2 plume – defined as the effective centroid velocity in the x- and y-directions of the CO_2 plume, and 3) spreading of the CO_2 plume – defined as the effective longitudinal dispersion coefficient along the primary and secondary

Received by OCD: 6/29/2026

axes of the CO_2 plume. "Effective" here refers to the derivation of metrics according to CO_2 plume distributions that have been projected from 3D to 2D, therefore ignoring any vertical migration component. Harp et al. (2019) showed that these metrics can describe CO_2 plume evolution in both flat and dipping (4 degrees) storage reservoirs and for reservoirs with both homogeneous and heterogeneous permeability distributions as simulated in grids with high resolution (50 × 50-m grid cells) and tracking CO_2 concentration above 0 % gas saturation. Other recent work follows these proposed metrics (e.g., Pawar et al., 2020, and Fan et al., 2023, for CO_2 and Kumbhat and Ebigbo, 2024, for hydrogen).

1.2.3. Plume stability

Based on the CCS policy review above derived from Regorrah et al. (2023), this study defines plume stability as follows: 1) the CO_2 plume footprint changes size minimally and predictably in the storage reservoir such that it will not cross key boundaries identified in the permit (e.g., the "storage reservoir boundary" of North Dakota) and 2) the CO_2 plume does not pose a threat to human health, USDWs, and the environment because of lateral migration to areas where vertical leakage pathways may exist. The definition generally follows the first metric presented by Harp et al. (2019). The precision of such a definition depends on measurement resolution; for simulation studies, grid cells may show very small changes in CO_2 saturation over short vertical and horizontal distances, but time-lapse seismic may only show a non-zero minimum saturation over the storage unit thickness. For example, regions of the CO_2 plume with 10–20 % CO_2 gas saturation may be indistinguishable from regions of the CO_2 plume with 20–40 % CO_2 gas saturation.

The recommended technical approach presented herein uses the derivative of area (dA/dt) metric presented in Harp et al. (2019) because all policy frameworks require operators to track the CO_2 plume over time to demonstrate plume stabilization. The simulation-based approach identifies the point in time ($t_{critical}$) when the CO_2 plume's rate of areal expansion (the derivative of the area with respect to time [dA/dt]) slows significantly in the postinjection period, permanently drops below a threshold ($dA/dt_{critical}$), and approaches a horizontal asymptote.

The change in plume footprint area over time (dA/dt) metric was selected because tracking the CO_2 plume (as required under CCS policies) in terms of a rate of areal change is ideal for demonstrating concordance between predictions from numerical simulations and time-lapse geophysics-based monitoring results (e.g., Chadwick and Noy, 2015; Ennis-King and Jackson, 2020).

The definition of plume stability used herein is compatible with the descriptions of the plume stability metrics used in successful North Dakota SFP applications through 2024. Predicted plume stability (date and areal extent) is necessary for permits to be accepted, but monitoring data will need to be used to demonstrate plume stability before site closure. It is possible that regulatory rules and interpretations will change during a project; however, the methods presented below for predicting plume stabilization are currently accepted and result in the best estimation of predicted plume stability using available data in the current regulatory environment.

1.3. Permitted storage projects

In addition to this case study's calculated plume stability metrics, stabilized plume statistics were gathered from completed North Dakota SFP applications to investigate descriptive relationships that may be useful for informing other CCS projects in the permitting phase. Dozens of CCS projects are either planned or operating worldwide (e.g., International Energy Agency, 2024; National Energy Technology Laboratory, 2025; Clean Air Task Force, 2025; KED Interests, 2025). This study examines data from two operating and six permitted storage projects in the Broom Creek Formation, Williston Basin, North Dakota, USA (Table 1, Fig. 1). The complete SFP applications and associated orders are available online from the North Dakota Department of Mineral Resources (2025) under each case ID. Each SFP application includes detailed information about the geological characterization data, modeling, and predictive simulation results that support the proposed CCS operations.

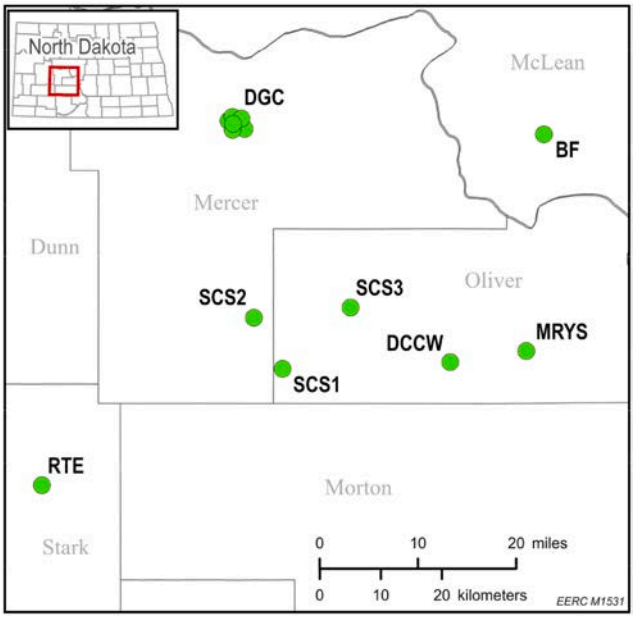


Fig. 1. Map showing the locations (well pads) of three operating (RTE, DGC, and BF) and five permitted storage projects in the Broom Creek Formation, Williston Basin, North Dakota, USA. RTE and BF each use one injector, while MRYS, DCCW, SCS1, SCS2, and SCS3 each use two wells in a twinned configuration where they deviate slightly from a single surface well pad. DGC coordinates six injectors on separate pads.

Each permitted project in Table 1 represents one or more injection wells, depending on the operator and the proposed injection scenario. RTE and BF each use one injector, while MRYS, DCCW, SCS1, SCS2, and SCS3 each use two wells in a twinned configuration where they deviate slightly from a single surface well pad. DGC coordinates six injectors on separate pads over ~9 km^2 for a single storage facility area (SFA) and area of review (AOR). In contrast to other permits, SCS1, SCS2, and SCS3 represent sites part of a much larger project with coordinated injection into wells spaced 9–16 km apart under separate permits with individual SFAs and AORs. Simulations reported in the DCCW SFP incorporated planned injection at MRYS but not vice versa; therefore the sites are discussed separately herein.

The Broom Creek Formation is the target injection interval and is dominated by an aeolian sandstone reservoir lithofacies and associated dolostone and anhydrite deposits that act as baffles. The upper confining zone comprises one or more of the combined siltstones of the Opeche, Minnekahta, Spearfish, and Piper Formations. The primarily dolostone Amsden Formation is the lower confining zone. Model and simulation values for average thickness, average gross porosity, and total mass of injected CO_2 were taken from each SFP application (Table 3). The predicted stabilized CO_2 plume area was calculated from plume maps in SFP applications. Average values for net porosity (reservoir rock types only) and gross permeability (across all rock types) were not available for all projects and were not included. All projects simulated 20 years of injection followed by multiple decades post-injection to assess CO_2 plume stabilization and return toward initial pressure equilibrium. Simulated CO_2 injection for each project was rate-limited according to project goals and to keep the storage unit below the fracture pressure. SFP application maps of the structure at the top of the storage unit show less than one degree of dip to the west or northwest for all projects.

Received by OCD: 6/29/2026

Table 3
Parameters from permitted Broom Creek Formation storage projects in North Dakota, USA.

Project	Average Storage Unit Gross Thickness, m	Average Storage Unit Gross Porosity, %	Total CO_2 Injected, Mt	Stabilized CO_2 Plume Area, km^2	Normalized Stabilized CO_2 Plume Area, km^2/Mt
RTE	95.4	23.0	4.00	5.73	1.59
MRYS	75.9	13.0	76.64	76.40	1.00
DGC	75.6	14.5	25.60	30.13	1.18
BF	31.4	22.6	4.00	8.73	2.18
DCCW	85.3	14.2	122.90	92.12	0.75
SCS1*	85.3	21.3	124.40	81.70	0.66
SCS2*	85.3	21.3	98.30	73.70	0.75
SCS3*	85.3	21.3	129.70	89.00	0.69

*Summit Carbon Storage, LLC (SCS) SFP applications share the same geologic model.

2. Methods

2.1. Case study geologic model and numerical simulation

The geologic model, built in SLB's Petrel software, is approximately 37 × 37 km (1369 km^2), which provided sufficient areal extent to capture the CO_2 plume throughout the operational and post-injection phases and to eliminate potential pressure effects near the lateral boundaries of the model. Grid cells were 305 × 305 m, and average thickness varies from 1.5 to 2 m according to experimental variograms. The upper surface of the reservoir includes a small amount of relief, but there is no large structural closure in the model. Interpreted lithofacies, porosity, and permeability were distributed as grid properties in the model based on regional core measurements, well logs, horizontal variograms constrained by 3D seismic data, and vertical variograms from well logs within the model area (see referenced DMR cases in Table 1). This model was also described by Regorrah et al. (2023) and Hunt et al. (2024).

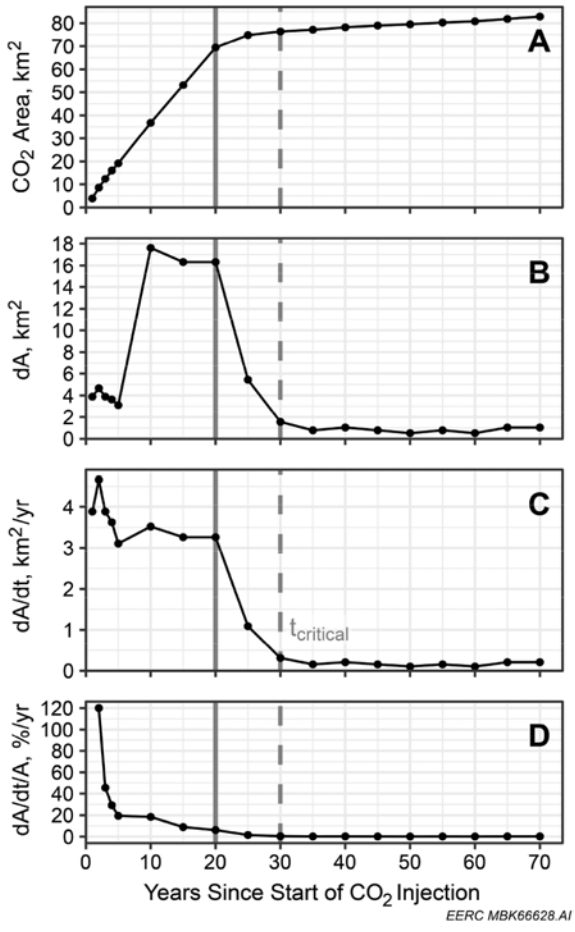


Fig. 2. Case study time-series plots showing years since the start of CO_2 injection on the x-axis and A) simulated CO_2 plume area, B) change in area (dA), C) rate of area change (dA/dt), and D) relative rate of area change (%/yr) (modified from Regorrah et al., 2023, and Hunt et al., 2024). Injection begins at the beginning of year 0 and ends at the end of year 20 (solid vertical line). The post-injection time frame goes from year 20 to year 70. Plume stabilization is identified at year 30 (dashed vertical line).

Because the storage unit approaches zero thickness (pinches out) tens to hundreds of kilometers beyond the modeled area, boundary conditions along the northern and eastern extents of the geologic model were defined as partially closed. The western and southern boundaries were defined as open. The upper and bottom boundaries of the model are defined as closed to represent the relatively low-porosity and low-permeability lithofacies of the upper and lower confining zones. Multiphase fluid flow numerical simulations were performed in Computer Modelling Group's GEM software. The simulated CO_2 injection scenario was 77 Mt into the Broom Creek Formation through two deviated injection wells on the same pad over a 20-year injection period, followed by a 50-year post-injection period. Local grid refinement down to 61 × 61 m was used around the injection wells. The minimum 50-year post-injection simulation period was chosen based on the EPA ruling provided under Title 40 Code of Federal Regulations § 146.93.

Gas saturation, representing the gas-phase or supercritical CO_2 plume present in the injection interval, was exported annually for the first 5 years and every 5 years until the 70th year after the beginning of injection. A 5-year time step was used to correspond with CCS policies that require operators to regularly review the permit (e.g., North Dakota Administrative Code Chapter 43–05–01–05.1.1[b][1] and Wyoming Code Rule § 24-14[b][xii]) and is considered a reasonable period between seismic surveys.

Plume stability predictions from numerical simulation will vary according to the geologic model used. The effects of geological uncertainty on plume stability were not assessed for this case study, but a range of values for the same plume stabilization metric could be quantified by simulating multiple model realizations based on the same input data. Plume stability uncertainty is expected to reduce as simulation models are history matched to operations and monitoring data and concordance is increased over time (Lüth et al., 2015; Jenkins et al., 2024).

2.2. Plume stabilization metrics

Harp et al. (2019) define and Pawar et al. (2020) apply a moment-based metric to describe the area of a CO_2 plume. In practice, on a simulation grid, the plume area is defined by the number of grid columns that include CO_2 in any layer. CO_2 plume grid properties were generated by discarding cells with gas saturation values below 5 % at various time steps. Any grid column with at least one cell > 5 % CO_2 gas saturation is considered within the plume. Variability in CO_2 concentration above the threshold is not accounted for. Area calculations were performed using a binary indication of the CO_2 plume boundary (i.e., individual grid cells in the model are either inside or outside the CO_2 plume).

Four metrics are calculated for each plume area time step: area (A, km^2), change in area (dA, km^2), rate of change in area over time (dA/dt, km^2/yr), and relative rate of change in area (dA/dt/A × 100, %/yr). The time after which the CO_2 plume is stabilized is identified as $t_{critical}$, and the metric values below which stabilization has occurred are identified as $dA/dt_{critical}$ and $dA/dt/A_{critical}$.

Received by OCD: 6/29/2026

Table 4
Case study summary of CO_2 plume simulations for years 1 through 70.

Simulation Year	Years Since Injection Start	CO_2 Plume Area, A, km^2	Area Change, dA, km^2	Area Change Rate, dA/dt, km^2/yr	Relative Area Change, dA/dt/A, %/yr
2023	1	3.9	3.9	3.9	–
2024	2	8.5	4.7	4.7	120.0
2025	3	12.4	3.9	3.9	45.5
2026	4	16.1	3.6	3.6	29.2
2027	5	19.2	3.1	3.1	19.4
2032	10	36.8	17.6	3.5	18.4
2037	15	53.1	16.3	3.3	8.9
2042*	20	69.4	16.3	3.3	6.1
2047	25	74.9	5.4	1.1	1.6
2052**	30	76.4	1.6	0.3	0.4
2057	35	77.2	0.8	0.2	0.2
2062	40	78.2	1.0	0.2	0.3
2067	45	79.0	0.8	0.2	0.2
2072	50	79.5	0.5	0.1	0.1
2077	55	80.3	0.8	0.2	0.2
2082	60	80.8	0.5	0.1	0.1
2087	65	81.8	1.0	0.2	0.3
2092	70	82.9	1.0	0.2	0.3

*End of injection.
** CO_2 plume stabilization.

2.3. Stabilized plume area normalization

Successful Broom Creek Formation SFP applications in North Dakota (Table 1) have not (thus far) included multiple simulation time step snapshots of plume evolution as used in the plume stabilization metric case study above. All Broom Creek Formation permits have included at least one map of the stabilized plume from which an area can be calculated. The target total CO_2 injection for these permits is between 3.6 and 129.7 Mt per permit (between 3.6 and 352.4 Mt per multi-permit coordinated project) into the Broom Creek Formation (Table 3). To simplify the comparison of stabilized plume area among projects, a normalization metric was developed (Eq. (1)).

$$SPA_{norm} = \frac{SPA}{M_{total}} \quad (1)$$

where SPA is the stabilized plume area (km^2), M_{total} is the injected CO_2 mass (Mt), and SPA_{norm} is the normalized stabilized plume area (km^2/Mt). This form of area divided by mass, rather than mass divided by area (c.f. Ulfah et al., 2022), was chosen to address stabilized plume area rather than stabilized plume areal storage efficiency (Bachu, 2015; Zapata et al., 2020).

3. Results and discussion

3.1. Case study plume stabilization

Determination of the plume stabilization date for this case study was identified by calculating and plotting dA/dt over time and identifying the date ($t_{critical}$) after which dA/dt slows substantially, permanently drops below a threshold, and approaches a horizontal asymptote (Fig. 2, Table 4).

Table 4 and Fig. 2 summarize model time steps from years 1 through 70 as the CO_2 plume area (A, km^2), the difference in CO_2 plume area (dA, km^2) between subsequent time steps, the change in area per year or derivative of area with respect to time (dA/dt, km^2/yr), and the relative

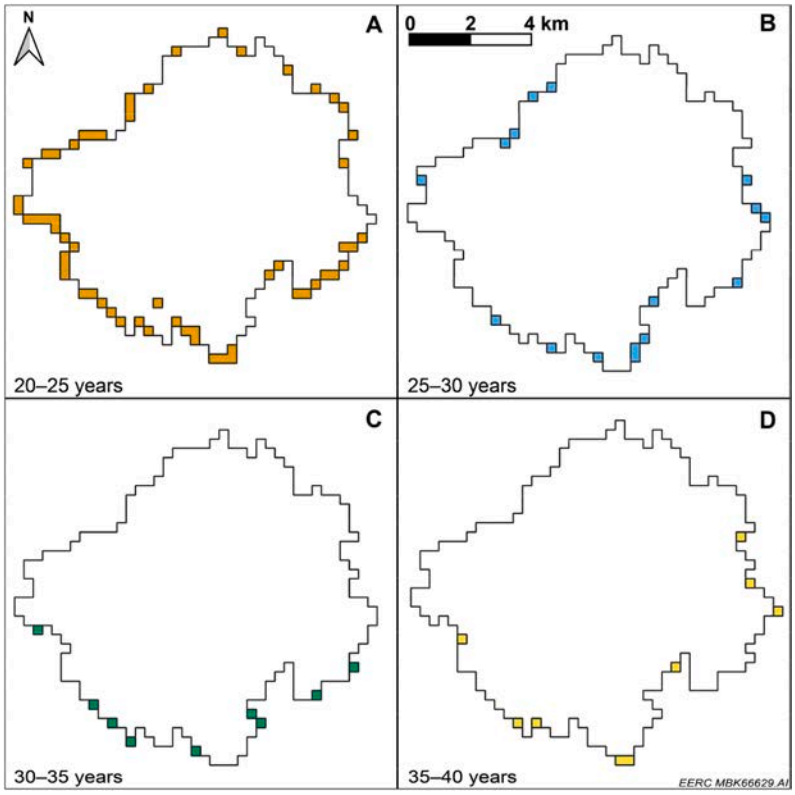


Fig. 3. Case study simulated change in CO_2 plume area between successive 5-year time steps as measured from the start of injection (modified from Regorrah et al., 2023, and Hunt et al., 2024). Injection ended after 20 years. Maps show an empty polygon for the first time step, and shaded areas show additional cells identified as belonging to the CO_2 plume for the second time step. All comparisons show growth (new plume areas); once CO_2 gas saturation increased above 5 % in each grid cell, it remained above that threshold. For example, Panel A from 20 to 25 years shows the change in the CO_2 plume (orange grid cells) between year 20 and year 25 since the start of injection.

Received by OCD: 6/29/2026

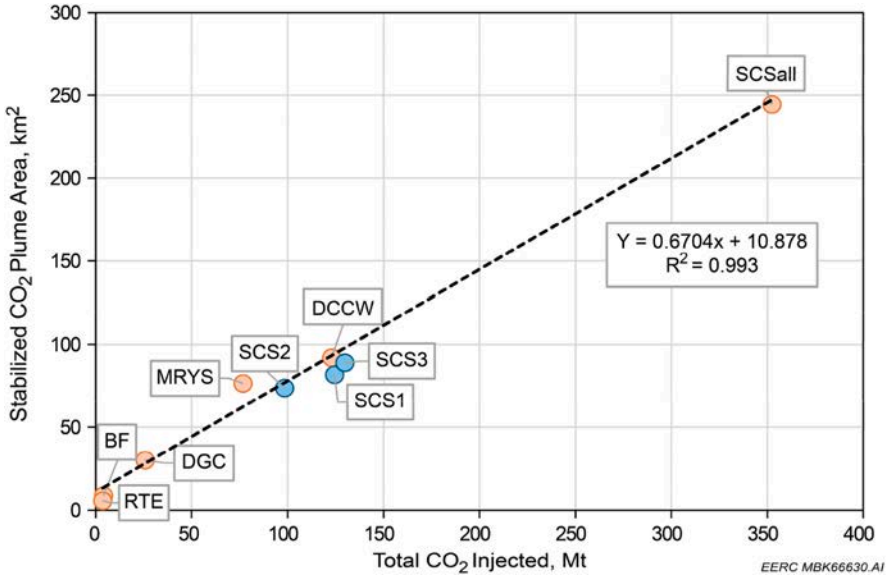


Fig. 4. Relationship between total injected CO_2 mass and stabilized CO_2 plume area for permitted projects in North Dakota. The three SCS sites are plotted individually (SCS1, 2, and 3) and combined into a single coordinated project (SCSall). The least squares linear regression line incorporates individual projects and SCSall, not the individual SCS sites.

rate of change in area (dA/dt/A, %/yr). At the end of year 1, the CO_2 plume area was

3.9 km^2; therefore, dA/dt between year 1 and year 0 (prior to CO_2 injection) was 3.9 km^2. Similarly, at the end of year 2, the CO_2 plume area was 8.5 km^2 and dA between year 2 and year 1 was (8.5 – 3.9 km^2) = 4.7 km^2. The derivative of area with respect to time at the end of year 2 was the change in area (dA = 4.7 km^2) divided by the difference in time (dt) (1 year). Two time step intervals from the simulation results are included in this case study: years 1–5 increment by 1 year and years 6–70 increment in 5-year time steps. As a result, Fig. 2B indicates a rapid increase in plume size from year 5 to year 10 because the change in plume size is not normalized to year as in Figs. 2C and 2D.

The CO_2 plume area increases rapidly during the operational phase (years 1–20) from zero to approximately 69.4 km^2. The rate of expansion of the CO_2 plume area, then begins to slow and approach a horizontal asymptote after year 20. At year 30 (10 years into the post-injection phase), dA/dt is approximately 0.3 km^2/yr, dA/dt/A is approximately 0.4 %/yr, and both remain consistently low through the end of the simulation. Year 30 was chosen as the stabilization date ($t_{critical}$), with a more apparent inflection point in Fig. 2C than 2D. There is a possibility that $t_{critical}$ may occur between year 25 and year 30, which could be determined if more time steps were captured. The absolute value of A and dA will vary among injection projects of different sizes, but the asymptotic character of both dA/dt and dA/dt/A is expected to persist once the plume stabilizes.

Following year 30, subtle changes occur along the CO_2 plume boundary throughout the life of the simulation (Fig. 3). Beyond $t_{critical}$, however, the CO_2 plume can be considered to have ceased migration, as any additional movement is anticipated to be insignificant relative to the CO_2 plume's areal extent at $t_{critical}$. Within the plume, the pressure and CO_2 saturation gradients also change as the reservoir slowly equilibrates post-injection (Harp et al., 2019), but monitoring results from operational projects will have a much lower resolution than in this case study simulation.

3.2. Predicted stabilized plume comparisons among permitted projects

Predicted simulated stabilized plume areas (Table 4) from permitted North Dakota Broom Creek Formation CO_2 storage project sites vary from 5.7 to 92.1 km^2 (mean 57.2, SD 36.3 km^2) according to the amount of CO_2 injected per site, ranging from 3.6 to 129.7 Mt (mean 73.14, SD 54.54 Mt). The SCS sites are a special case because although they have separate permits, the model supporting each permit incorporated injection from all three sites (Table 1), which are spaced 9–16 km apart. The combined total SCS CO_2 injection and plume area are more than twice those of the next-largest single-site project (DCCW).

3.2.1. Area-to-mass relationship

A strong linear relationship exists between the stabilized plume area and the total CO_2 injected (area-to-mass relationship) (Fig. 4). Fig. 4 plots the three SCS sites individually (SCS1, SCS2, and SCS3) and combined into a single coordinated project (SCSall). The least squares linear regression line incorporates individual projects and SCSall, not the individual SCS sites. However, the SCS1, SCS2, and SCS3 area-to-mass relationship follows the same linear relationship as the individual permits. Different model forms besides linear regressions are possible for various subsets of the data; however, the linear relationship explains a significant portion of the variation ($R^2 = 0.993$) in the area-to-mass relationship. This is partially attributable to the fact that all these projects targeted the Broom Creek Formation in North Dakota; thus geological properties like porosity and permeability or factors like pressure and temperature that affect CO_2 properties were likely more homogeneous for this dataset than would be encountered in a broader national dataset.

3.2.2. Normalized area-to-mass relationship

Normalized stabilized plume area (SPA_{norm}) values (Eq. (1)) range from 0.66 to

2.18 km^2/Mt (mean 1.10, SD 0.54 km^2/Mt) (Table 4). A power law relationship exists between the total CO_2 injected and the normalized stabilized plume area (Fig. 5).[1] A greater total CO_2 injected results in a smaller SPA_{norm}. Most of the variability in the SPA_{norm} distribution comes from the smallest projects (BF, RTE, DGC), which inject <50 Mt

[1] A plot of Y = 1/X, or X^{-1}, will be a hyperbola and is a special case of the power law relationship of $Y = kX^n$, where $k = 1$ and $n = -1$. However, the fitted power law equation provides additional information about the relationship between the total CO_2 injected (Mt CO_2) and the normalized stabilized plume area (km^2/Mt CO_2).

Received by OCD: 6/29/2026

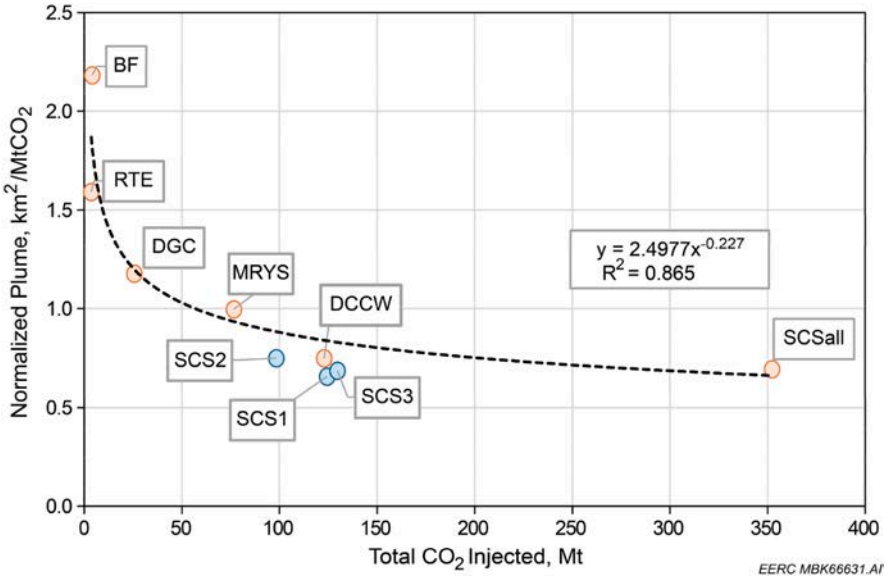


Fig. 5. Relationship between total injected CO_2 mass and normalized stabilized CO_2 plume area for permitted projects in North Dakota. The three SCS sites are plotted individually (SCS1, 2, and 3) and combined into a single coordinated project (SCSall). The power law regression line incorporates individual projects and SCSall, not the individual SCS sites.

over 20 years, <2.5 Mtpa. At these smaller project scales, the CO_2 plume takes up more area per Mt of injected CO_2 than at larger projects, which may indicate lower storage efficiency.

Specific reasons for deviations from the fitted regression curves in Figs. 4 and 5 are unclear. Although the Broom Creek Formation is a high-quality storage unit, it contains internal heterogeneity that contributes to the shape of each simulated CO_2 plume, as the geologic models developed for each site included log and core data and incorporated variability into the model domain. Additionally, pressure interaction among coordinated SCS sites or uneven pressure buildup in sites near the edge of the formation can influence CO_2 distribution during and after injection. For example, the edge of the Broom Creek Formation is contained within the simulation model for BF, which affects pressure distribution more than other projects that are farther from the formation edge. Other site properties like storage unit thickness, porosity, and permeability did not significantly improve the goodness of fit.

The predictive relationships shown in Figs. 4 and 5 have implications for future geologic models, injection simulations, and monitoring. Each simulation model was developed in collaboration with the EERC by different personnel, using site-specific characterization and modeling techniques and the best available data. SFP applications were approved between 2021 and 2024, but injection has only started at three locations (RTE, DGC, and BF). The simulations represent forward-modeling predictions that have not been history-matched to field data. Post-injection seismic surveys have not yet been collected for the Broom Creek Formation projects, but measurable differences from the simulations are expected due to intrinsic uncertainty in the subsurface. As injections continue and new sites come online, operational data and time-lapse seismic will be used to refine simulation models and test the predictive relationships shown in the SFP application simulations.

4. Conclusions

CCS regulatory policies and frameworks evaluated by Regorrah et al. (2023) require the prediction and demonstration of plume stability at permitting and sometime following the injection phase of a CCS project. The EERC has developed a technical approach to predict and demonstrate plume stability for potential CCS projects, which has been used (thus far) as an input to permit several Class VI storage applications in North Dakota, USA. Plume stability means 1) the CO_2 plume footprint changes size minimally and predictably in the storage reservoir such that it will not cross key boundaries identified in the permit (e.g., the "storage reservoir boundary" of North Dakota) and 2) the CO_2 plume does not pose a threat to human health, USDWs, and the environment because of lateral migration to areas where leakage pathways may exist. A recommended best practice during injection and in the post-injection phase prior to site closure is to incorporate monitoring data (e.g., time-lapse seismic) to show concordance with predictions from the presented methodology.

It is crucial to demonstrate plume stabilization with post-injection monitoring data. Some CCS policies (e.g., California's CCS Protocol) also recommend using risk assessment to show how the risk profile of CO_2 plume migration has decreased as part of the demonstration. Commercial-ready methods for tracking CO_2 plumes indirectly include performing geophysical surveys, such as time-lapse seismic and saturation logging.

Prospective operators may use the presented plume stabilization approach to inform selection of the pore space lease and monitoring areas that best meet the goals of the CCS project and ensure the regulatory definition of plume stability is met. The authors acknowledge that the appropriate regulatory authority has final power to determine whether an operator has satisfactorily demonstrated plume stability, but the approach provides operators and regulators with a first-pass opportunity to come to an agreed upon interpretation of the requirements. Determining plume stability as part of the initial permitting process may also help inform post-injection monitoring activities and timing and derive total cost as an input into the financial assurance needed to permit the project.

Results from the case study Broom Creek Formation project show that the rate of change in the plume area (dA/dt) can be an effective measure of plume stability from a regulatory standpoint because this metric is normalized to the simulation timesteps used and shows a steep decrease at the end of injection followed by consistent low values after $t_{critical}$. Percent rate of change (dA/dt/A) may also be a useful metric, although it may be difficult to establish a threshold low value that would be consistent across projects. Without a structural or stratigraphic closure to prevent lateral CO_2 migration, the case study simulation shows that the plume will continue to evolve, albeit slowly, even after the stabilization date of $t_{critical}$.

Although CO_2 injection simulation models are informative, they may

Received by OCD: 6/29/2026

present higher resolution and certainty of CO_2 plume metrics than what can be measured with current monitoring technologies like time-lapse seismic. To improve potential concordance, the examples provided in this study attempt to align simulation results with expected results from monitoring techniques, including time-lapse seismic, by using fairly large grid cells and ignoring CO_2 gas saturation values below 5 %. Multiple geologic and simulation model realizations may be used to understand the effects of uncertainty on stabilized plume area (larger or smaller than a base case) and stabilization date (earlier or later than a base case). Effectively communicating plume stabilization uncertainties may require discussion with regulators before storage permits are accepted or approved. Concordance among realizations and monitoring data is expected to increase as models are history-matched to injection and monitoring data.

Predicted stabilized CO_2 footprints from North Dakota SFP applications can be used to derive simple (absolute) and normalized (relative to total CO_2 injection) relationships with total CO_2 injection for the Broom Creek Formation. These relationships can be used to estimate the stabilized plume area according to total injection volume in support of project planning in this formation in North Dakota. Similar relationships should be able to be derived from numerical simulation for other North Dakota formations or formations in other depositional basins.

Funding sources

Support for this study was provided by the U.S. Department of Energy (Award No DE-FE0032331 and DE-FE0032371) and the Plains CO_2 Reduction (PCOR) Partnership through the U.S. Department of Energy National Technology Laboratory (Award No DE-FE0031838) and North Dakota Industrial Commission (Contract Nos FY20-XCI-226 and G-050-96).

CRediT authorship contribution statement

Matthew E. Burton-Kelly: Writing – original draft, Supervision, Methodology, Formal analysis. **John E. Hunt:** Writing – review & editing, Writing – original draft, Conceptualization. **Neil W. Dotzenrod:** Writing – original draft, Methodology, Investigation, Conceptualization. **John A. Templeton:** Methodology, Investigation, Conceptualization. **Joshua G. Regorrah:** Writing – original draft, Methodology, Conceptualization. **Chantsalmaa Dalkhaa:** Writing – original draft, Methodology, Conceptualization. **Amanda J. Livers-Douglas:** Writing – original draft, Project administration, Conceptualization. **Wesley D. Peck:** Project administration, Funding acquisition, Conceptualization. **Kevin C. Connors:** Project administration, Funding acquisition, Conceptualization. **Nicholas A. Azzolina:** Writing – review & editing, Methodology, Investigation, Formal analysis, Data curation, Conceptualization.

Declaration of competing interest

The authors declare that they have no known competing financial interests or personal relationships that could have appeared to influence the work reported in this paper.

Data availability

Data will be made available on request.

References

Azzolina, N.A., Torres, J.A., Chimote, S., Pekot, L.J., Burton-Kelly, M.E., Dotzenrod, N. W., Bosshart, N.W., Dalkhaa, C., Ayash, S.C., Li, C., Nakles, D.V., Gorecki, C.D., Vettleson, H.M., 2018. Development of Intelligent Monitoring System (IMS) Modules For the Aquistore CO_2 Storage Project. United States.

Bachu, S., 2015. Review of CO_2 storage efficiency in deep saline aquifers. Int. J. Greenh. Gas Control 40, 188–202.

Barajas-Olalde, C., Haffinger, P., Gisolf, D., Zhang, M., Droujinina, A., Doulgeris, P., Khatibi, S., Jin, L., Burnison, S.A., Hamling, J.A., Gorecki, C.D., 2019. Simultaneous time-lapse WEB-AVO inversion for seismic reservoir monitoring—application to CO_2 enhanced oil recovery at the Bell Creek oil field; in SEG Technical Program Expanded Abstracts Society of Exploration Geophysicists. In: SEG Technical Program Expanded Abstracts, pp. 564–568.

Burnison, S.A., Livers, A.J., Hamling, J.A., Salako, O., Gorecki, C.D., 2017a. Design and implementation of a scalable, automated, semi-permanent seismic array for detecting CO_2 extent during geologic CO_2 injection. Energy Procedia 114, 3879–3888.

Burnison, S.A., Bosshart, N.W., Salako, O., Reed, S., Hamling, J.A., Gorecki, C.D., 2017b. 4-D seismic monitoring of injected CO_2 enhances geological interpretation, reservoir simulation, and production operations. Energy Procedia 114, 2748–2759.

Chadwick, R.A., Noy, D.J., 2015. Underground CO_2 storage: demonstrating regulatory conformance by convergence of history-matched modeled and observed CO_2 plume behavior using Sleipner time-lapse seismics. Greenh. Gas Sci. Technol. 5, 305–322.

Clean Air Task Force, 2025. US Carbon Capture Activity and Project Map. www.catf.us/ccsmapus/ (Accessed March 2025).

Dance, T., LaForce, T., Glubokovskikh, S., Ennis-King, J., Pevzner, R., 2019. Illuminating the geology: post-injection reservoir characterisation of the CO_2CRC Otway site. Int. J. Greenh. Gas Control 86, 146–157. https://doi.org/10.1016/j.ijggc.2019.05.004.

Doughty, C., 2010. Investigation of CO_2 plume behavior for a large-scale pilot test of geologic carbon storage in a saline formation. Transp. Porous Media 82, 49–76.

Ennis-King, J., Jackson, S., 2020. Plume Stabilisation in the CO2CRC Otway Stage 2C Project CO2CRC Limited. CO2CRC Publication Number RPT20-6230, Melbourne, Australia.

Fan, M., Lu, D., Liu, S., 2023. A deep learning-based direct forecasting of CO_2 plume migration. Geoenergy Sci. Eng. 221, 211363.

Harp, D., Onishi, T., Chu, S., Chen, B., Pawar, R., 2019. Development of quantitative metrics of plume migration at geologic CO_2 storage sites. Greenh. Gas Sci. Technol. 9, 687–702. https://doi.org/10.1002/ghg.

Harp, D.R., Oldenburg, C.M., Pawar, R., 2019b. A metric for evaluating conformance robustness during geologic CO_2 sequestration operations. Int. J. Greenh. Gas Control 85, 100–108. https://doi.org/10.1016/j.ijggc.2019.03.023.

Hunt, J., Dotzenrod, N., Templeton, J., Regorrah, J., Connors, K., 2024. Demonstration of plume stability for carbon storage projects (December 18, 2024). In: Proceedings of the 17th Greenhouse Gas Control Technologies Conference (GHGT-17) 20–24 October 2024. https://doi.org/10.2139/ssrn.5064536.

International Energy Agency, 2024. CCUS Projects Explorer. www.iea.org/data-and-statistics/data-tools/ccus-projects-explorer (Accessed March 2025).

Jenkins, C., Barraclough, P., Correa, J., Dance, T., Dodds, K., Ennis-King, J., Freifeld, B., Glubokovskikh, S., Green, C., Gunning, J., Gurevich, B., Isaenkov, R., Jackson, S.J., Paterson, L., Pevzner, R., Popik, D., Popik, S., Shulakova, V., Tertyshnikov, K., Shashkin, P., Sidenko, E., Singh, R., Watson, M., Wilkins, A., Wood, T., Yavuz, S., Yurikov, A., Zhang, Y., Raab, M., 2024. Field tests of geological storage of CO_2 at the Otway International Test Centre, Australia: trapping and monitoring the migrating plumes. Geoenergy 2. https://doi.org/10.1144/geoenergy2023-035 geoenergy2023-035**[1]. https://pubs.geoscienceworld.org/gsl/geoenergy/article/2/1/geoenergy2023-035/637041/Field-tests-of-geological-storage-of-CO2-at-the.

Jiang, T., Pekot, L.J., Jin, L., Peck, W.D., Gorecki, C.D., Worth, K., 2017. Numerical modeling of the Aquistore CO_2 storage project. Energy Procedia 114, 4886–4895.

KED Interests, LLC, 2025. CCUS Project Databases. www.ccus.com/projects/ (Accessed March 2025).

Kumbhat, D.S., Ebigbo, A., 2024. Effect of relative permeability hysteresis on plume dynamics, wellbore flow regime, and storage efficiency in underground hydrogen storage. Int. J. Hydrog. Energy.

Lüth, S., Ivanova, A., Kempka, T., 2015. Conformity assessment of monitoring and simulation of CO_2 storage: a case study from the Ketzin pilot site. Int. J. Greenh. Gas Control 42, 329–339. https://doi.org/10.1016/j.ijggc.2015.08.005.

Manceau, J.C., Rohmer, J., 2016. Post-injection trapping of mobile CO_2 in deep aquifers: assessing the importance of model and parameter uncertainties. Comput. Geosci. 20, 1251–1267.

National Energy Technology Laboratory, 2025. Carbon Capture and Storage Database. https://netl.doe.gov/carbon-management/carbon-storage/worldwide-ccs-database (Accessed March 2025).

North Dakota Department of Mineral Resources, 2025. Class VI – Geologic Sequestration Wells. www.dmr.nd.gov/dmr/oilgas/ClassVI (Accessed March 2025).

Oldenburg, C.M., 2018. Are we all in concordance with the meaning of the word conformance, and is our definition in conformity with standard definitions? Greenh. Gas Sci. Technol. 8, 210–214. https://doi.org/10.1002/ghg.1773.

Pawar, R.J., Chu, S., Makedonska, N., Onishi, T., Harp, D., 2020. Assessment of relationship between post-injection plume migration and leakage risks at geologic CO_2 storage sites. Int. J. Greenh. Gas Control 101, 103138.

Pevzner, R., Urosevic, M., Popik, D., Shulakova, V., Tertyshnikov, K., Caspari, E., Correa, J., Dance, T., Kepic, A., Glubokovskikh, S., Ziramov, S., Gurevich, B., Singh, R., Raab, M., Watson, M., Daley, T., Robertson, M., Freifeld, B., 2017. 4D surface seismic tracks small supercritical CO_2 injection into the subsurface: CO_2CRC Otway project. Int. J. Greenh. Gas Control 63, 150. –15.

Regorrah, J.G., Hunt, J.E., Templeton, J.A., Dotzenrod, N.W., Azzolina, N.A., Dalkhaa, C., Peck, W.D., Livers-Douglas, A.J., Connors, K.C., 2023. A Quantitative Approach for Demonstrating Plume Stabilization Under CCS Policy Frameworks. Plains CO2 Reduction (PCOR) Partnership White Paper, 2023-EERC-05-03.

Roach, L.A.N., White, D.J., Roberts, B., 2014. Assessment of 4D seismic repeatability and CO_2 detection limits using a sparse land array at the Aquistore CO_2 storage site. Geophysics 80, WA1–WA13. https://doi.org/10.1190/GEO2014-0201.1.

Received by OCD: 6/29/2026

Roach, L.A.N., White, D.J., Roberts, B., Angus, D., 2017. Initial 4D seismic results after CO_2 injection start-up at the Aquistore storage site. Geophysics 82, B95–B107. https://doi.org/10.1190/geo2016-0488.1.

Saleh, W.B., Zhang, B., 2024. Uncertainty quantification through the assimilation of CO_2 plume size from 4D seismic survey. In: SPE Canadian Energy Technology Conference and Exhibition D011S015R003.

Ulfah, M., Hosseini, S., Hovorka, S., Bump, A., Bakhshian, S., Dunlap, D., 2022. Assessing impacts on pressure stabilization and leasing acreage for CO_2 storage utilizing oil migration concepts. Int. J. Greenh. Gas Control 115, 103612.

White, D.J., Roach, L.A.N., Roberts, B., Daley, T.M., 2014. Initial results from seismic monitoring at the Aquistore CO_2 storage site, Saskatchewan, Canada. Energy Procedia 63, 4418–4423.

Whittaker, S., White, D., Law, D., Chalaturnyk, 2004. IEA GHG Weyburn CO_2 monitoring and storage project summary report, 2000–2004. In: Wilson, M., Monea, M. (Eds.), Proceedings of the 7th International Conference on Greenhouse Gas Control Technologies: September 5–9, 2004. Vancouver, Canada, III.

Zapata, Y., Kristensen, M.R., Huerta, N., Brown, C., Kabir, C.S., Reza, Z., 2020. CO_2 geological storage: critical insights on plume dynamics and storage efficiency during long-term injection and post-injection periods. J. Natural Gas Sci. Eng. 83, 103542.

Zeidouni, M., Hovorka, S.D., Shi, K., 2016. Tracer test to constrain CO_2 residual trapping and plume evolution. Environ. Earth Sci. 75, 1451.

EXHIBIT 8

Received by OCD: 6/29/2026

International Journal of Greenhouse Gas Control 49 (2016) 149–160

Contents lists available at ScienceDirect

International Journal of Greenhouse Gas Control

journal homepage: www.elsevier.com/locate/ijggc

Review: Role of chemistry, mechanics, and transport on well integrity in CO_2 storage environments

Susan Carroll[a,*], J. William Carey[b], David Dzombak[c], Nicolas J. Huerta[d], Li Li[e], Tom Richard[e], Wooyong Um[f], Stuart D.C. Walsh[a], Liwei Zhang[g]

[a] Lawrence Livermore National Laboratory, Livermore, CA 94550, United States
[b] Los Alamos National Laboratory, Los Alamos, NM 87545, United States
[c] Carnegie Mellon University, Pittsburgh, PA 15213, United States
[d] National Energy Technology Laboratory, Albany, OR 97322, United States
[e] The Pennsylvania State University, University Park, PA 16802, United States
[f] Pacific Northwest National Laboratory, Richland, WA 99354, United States
[g] National Energy Technology Laboratory, Pittsburgh, PA 15236, United States

ARTICLE INFO

Article history:
Received 2 July 2015
Accepted 11 January 2016
Available online 22 March 2016

Keywords:
Well integrity
Reactive transport
Mechanical deformation

ABSTRACT

Among the various risks associated with CO_2 storage in deep geologic formations, wells are important potential pathways for fluid leaks and groundwater contamination. Injection of CO_2 will perturb the storage reservoir and any wells that penetrate the CO_2 or pressure footprints are potential pathways for leakage of CO_2 and/or reservoir brine. Well leakage is of particular concern for regions with a long history of oil and gas exploration because they are top candidates for geologic CO_2 storage sites. This review explores in detail the ability of wells to retain their integrity against leakage with careful examination of the coupled physical and chemical processes involved. Understanding time-dependent leakage is complicated by the changes in fluid flow, solute transport, chemical reactions, and mechanical stresses over decade or longer time frames for site operations and monitoring.

Almost all studies of the potential for well leakage have been laboratory based, as there are limited data on field-scale leakage. Laboratory experiments show that CO_2 and CO_2-saturated brine still react with cement and casing when leakage occurs by diffusion only. The rate of degradation, however, is transport-limited and alteration of cement and casing properties is low. When a leakage path is already present due to cement shrinkage or fracturing, gaps along interfaces (e.g. casing/cement or cement/rock), or casing failures, chemical and mechanical alteration have the potential to decrease or increase leakage risks. Laboratory experiments and numerical simulations have shown that mineral precipitation or closure of strain-induced fractures can seal a leak pathway over time or conversely open pathways depending on flow-rate, chemistry, and the stress state. Experiments with steel/cement and cement/rock interfaces have indicated that protective mechanisms such as metal passivation, chemical alteration, mechanical deformation, and pore clogging can also help mitigate leakage. The specific rate and nature of alteration depend on the cement, brine, and injected fluid compositions. For example, the presence of co-injected gases (e.g. O_2, H_2S, and SO_2) and pozzolan amendments (fly ash) to cement influences the rate and the nature of cement reactions. A more complete understanding of the coupled physical–chemical mechanisms involved with sealing and opening of leakage pathways is needed.

An important challenge is to take empirically based chemical, mechanical, and transport models reviewed here and assess leakage risk for carbon storage at the field scale. Field observations that accompany laboratory and modeling studies are critical to validating understanding of leakage risk. Long-term risk at the field scale is an area of active research made difficult by the large variability of material types (cement, geologic material, casing), field conditions (pressure, temperature, gradient in potential, residence time), and leaking fluid composition (CO_2, co-injected gases, brine). Of particular interest are the circumstances when sealing and other protective mechanisms are likely to be effective, when they are likely to fail, and the zone of uncertainty between these two extremes.

© 2016 The Authors. Published by Elsevier Ltd. This is an open access article under the CC BY-NC-ND license (http://creativecommons.org/licenses/by-nc-nd/4.0/).

* Corresponding author.
E-mail addresses: carroll6@llnl.gov (S. Carroll), bcarey@lanl.gov (J.W. Carey), dzombak@cmu.edu (D. Dzombak), Nicolas.Huerta@NETL.gov (N.J. Huerta), lili@eme.psu.edu (L. Li), trichard@psu.edu (T. Richard), wooyong.um@pnnl.gov (W. Um), walsh24@llnl.gov (S.D.C. Walsh), ziwe88@gmail.com (L. Zhang).

http://dx.doi.org/10.1016/j.ijggc.2016.01.010
1750-5836/© 2016 The Authors. Published by Elsevier Ltd. This is an open access article under the CC BY-NC-ND license (http://creativecommons.org/licenses/by-nc-nd/4.0/).

Received by OCD: 6/29/2026

1. Introduction

The goal of any CO_2 storage project is to retain 99% of the injected CO_2 in the target reservoir for 100s of years with a maximum CO_2 surface leakage rate of 0.01–0.1% of CO_2 inventory per year (Hepple and Benson, 2005; NETL, 2011). Wells at storage sites can threaten this goal, as they represent a direct connection between the CO_2 storage reservoir and the atmosphere, as well as underground sources of drinking water (Gasda et al., 2004; Metz et al., 2005; Viswanathan et al., 2008; Carroll et al., 2014). These wells penetrate protective geologic formations such as caprock and were originally constructed to produce or inject large volumes of fluids from or into the subsurface. The long-term integrity of wells is of particular concern because of the potential for CO_2 (as a free phase or dissolved in formation brine) to react with and degrade the materials used in well construction. Wells in sequestration projects are generally planned, drilled, and completed following best practices, using best available materials, and following government regulations that were developed to address most of the common problems discussed above. As a result, modern wells have a much higher likelihood for well integrity. However, in many areas that are prime candidates for CO_2 storage there are legacy wells that were drilled when regulations were less restrictive, often using methods or materials that are now outdated (Gasda et al., 2004; Watson and Bachu, 2008; Nicot, 2009).

Well integrity can be compromised by defective well completion or as a result of chemical and mechanical stresses that damage the well during the operation or abandonment phases. Possible principle leakage paths are illustrated in Fig. 1 (Viswanathan et al., 2008). Key problems in poor completions include: thread leaks between casing joints, possibly accounting for 90% of all tubular failures (#5; Schwind et al., 2001); inadequate or incomplete cement placement or incomplete cement coverage especially in non-vertical wells (#2, #9); poor cement quality (i.e. high permeability cements; #8); development of mud or gas channels in the cement (#11); failure to adequately remove filter-cake from the borehole and other problems associated with a poor bond between casing/cement and cement/formation (#7, #12); and formation damage during drilling (#6).

Post-completion problems may be caused by thermal stresses induced by production or injection of fluids; mechanical stresses due to changes in pressure inside tubing or within the injection/production reservoir as well as due to tectonic stresses; and chemical stresses due to fluids and gases within or surrounding the well attacking cement or steel. Potential post-completion leakage pathways include: casing and tubular corrosion which has large financial impacts across all of the oil and gas sector and can allow communication of fluids inside and outside the well (#1; Brondel et al., 1994); fractured cement (#10); dissolution-induced cement defects (#9); formation of microannuli at the casing/cement or cement/formation interfaces (#7, #12); and chemical degradation of the cement resulting in elevated permeability (#8). If fluids migrate past the cement barriers, then flow may occur via open-hole flow within the casing (#4) or by external annulus flow (#3). If fluids escape the multiple barriers in the well system and migrate through the external annulus, they still must have access to permeable formations or the atmosphere in order to impact the environment.

The proportion of well integrity problems arising during the completion stage, as opposed to the operational or abandonment phases, has not been formally investigated. A common hypothesis from field experience is that most problems originate because of poor completion and inadequate cement coverage creating leakage pathways or leaving the well more susceptible to subsequent mechanical, thermal or chemical stresses.

In this review we evaluate the evolution of leakage risk over time as a consequence of chemical, mechanical, and transport processes. Because CO_2 must be stored for long periods of time to mitigate climate change, relevant time scales range from seconds and days for stresses associated with well completion and operations, to decades and centuries for processes associated with corrosion, dissolution and precipitation. Of particular interest to the carbon storage community is the ability of potential wellbore leakage pathways to seal in the highly reactive system involving

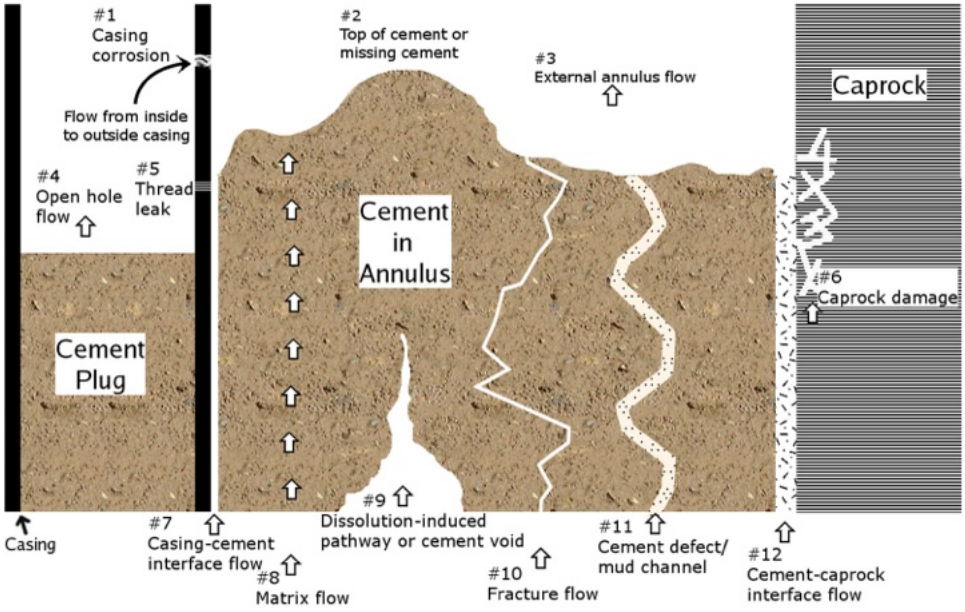


Fig. 1. Schematic diagram of an abandoned well showing principle leakage pathways. Note that cement plugs can have many of the same problems as cement in the annulus. These pathways may originate during well completion activities or as a result of stresses occurring during the life of the well. Pathways are not drawn to scale; the plug may have a 10 cm diameter while the cement annulus will be closer to 2 cm.
Modified from Viswanathan et al. (2008).

Received by OCD: 6/29/2026

carbon steel casings, alkaline Portland cement, and CO_2-rich, acidic brines. This work highlights significant advances on the evolution of well integrity since the review of Zhang and Bachu (2011) and expands upon the geochemistry-focused review of Carey (2013). This review was developed as part of DOE's National Risk Assessment Partnership (Pawar et al., 2014) and includes work conducted by members of the partnership as well as important contributions made throughout the CO_2 sequestration community.

2. Key processes controlling leak path evolution

Quantifying the behavior of well leakage over time requires understanding the coupling of leak path geometry, geochemical reactions, geomechanics, and advective and diffusive transport processes at conditions and time scales relevant to geologic carbon storage. Over the past decade researchers used both laboratory experiments (static and flow-through experiments) and numerical modeling to understand the complex relationship between well materials and the reactive fluids in geologic carbon storage systems. Coupled processes are critical to understanding well integrity as it is the physical-chemical interactions with materials and at interfaces that allow fluid flow. Below we identify the major chemical and mechanical alteration processes important to well integrity (Section 2.1) and coupled chemical, mechanical, and transport processes that lend themselves to sealing or opening of leakage pathways (Section 2.2).

2.1. Fundamental reaction mechanisms

2.1.1. Cement alteration

Most studies on chemical interactions of CO_2 and brine with well materials have focused on ordinary Portland cements. These cements are commonly used in well completions and abandonment and are known to be reactive in geologic CO_2 storage environments (Carey et al., 2007; Duguid and Scherer, 2010; Huerta et al., 2013; Kutchko et al., 2009, 2008, 2007; Mason et al., 2013; Scherer et al., 2011; Walsh et al., 2014a,b). Collectively, these studies confirm that reactions between Ca-containing solid phases, especially portlandite, and CO_2-saturated brine are so fast that cement alteration is limited by the diffusion of reactants and products, which results in a series of reaction fronts that divide the cement into distinct zones (Carey et al., 2007; Kutchko et al., 2009, 2008, 2007; Mason et al., 2013; Walsh et al., 2014a; Zhang et al., 2015). The zones consist of unaltered cement, a zone depleted in portlandite, a calcium carbonate zone, and a residual amorphous silicate zone, presented in the order from inner unreacted cement to the cement–brine interface in Fig. 2.

Despite the complex nature of cement, typically only a few mineral phases and associated chemical reactions suffice to model cement alteration (Table 1). Aqueous complexation reactions include CO_2 dissolution into the brine and the formation of a weak acidic solution rich in dissolved carbonate species. The dissolution of CO_2 lowers the pH and dissolves many cement phases, including portlandite (CH),

$$Ca(OH)_2 + 2H^+ \leftrightarrow Ca^{2+} + 2H_2O \quad (1)$$

calcium silicate hydrate (C-S-H, composition varies),

$$Ca_{1.2}SiO_{3.2}{\cdot}2.06H_2O + 2.4H^+ \leftrightarrow 1.2Ca^{2+} + SiO_2 + 3.26H_2O \quad (2)$$

monosulfate (AFm),

$$Ca_4Al_2O_6(SO_4){\cdot}12H_2O + 12H^+ \leftrightarrow 4Ca^{2+} + 2Al^{3+} + SO_4^{2-} + 18H_2O \quad (3)$$

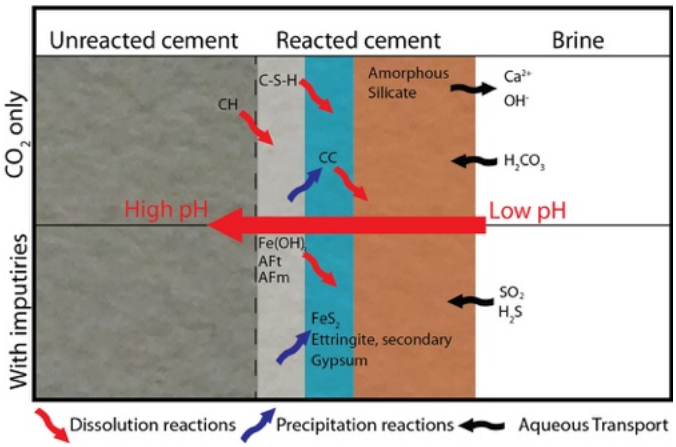


Fig. 2. Schematic of interaction between well cement and CO_2 with and without H_2S/SO_2 impurities, where the phases are described in Table 1 and the reactions are described in the text. The alteration products noted in the CO_2 only gas stream also occur when impurities are present. (Kutchko et al., 2007, 2011; Mason et al., 2013; Zhang et al., 2013).

Table 1
Primary cement phases in ordinary Portland cement and secondary alteration products when cement is reacted with CO_2, H_2S, and SO_2 saturated brines.

Phase	Formula	Notes
Primary phases		
Portlandite (CH)	$Ca(OH)_2$	
Calcium-silicate-hydrate (C-S-H)	$Ca_xSiO_{2+x}{\cdot}xH_2O$	Idealized formula, $x = 1.7$
Monosulfate (AFm)	$Ca_4Al_2(OH)_{12}SO_4{\cdot}6H_2O$ $Ca_4Fe_2(OH)_{12}SO_4{\cdot}6H_2O$	Variable composition between the Al_2O_3 and Fe_2O_3 end members
Trisulfate (AFt)	$Ca_6Al_2(OH)_{12}(SO_4)_3{\cdot}26H_2O$ $Ca_6Fe_2(OH)_{12}(SO_4)_3{\cdot}26H_2O$	Variable composition between the Al_2O_3 and Fe_2O_3 end members. Ettringite is the Al_2O_3 end member
Katoite	$Ca_3Al_2(OH)_{12}$	
Gypsum	$CaSO_4{\cdot}2H_2O$	
Secondary alteration products		
Calcium carbonate (CC)	$CaCO_3$	Calcite, aragonite, and vaterite
Decalcified C-S-H	$Ca_{x-y}SiO_{2+x-y}{\cdot}(x-y)H_2O$	
Friedel's salt	$Ca_4Al_2(OH)_{12}Cl_2{\cdot}6H_2O$	
Ettringite	$Ca_6Al_2(OH)_{12}(SO_4)_3{\cdot}26H_2O$	From H_2S and SO_2 impurities
Gypsum	$CaSO_4{\cdot}2H_2O$	
Amorphous silicate	SiO_2 or $Ca_xNa_{1-2x}Al_ySi_{6-y}O_{12}{\cdot}nH_2O$	Outer layer has been modeled as amorphous silica and as amorphous silicate with a zeolite-like structure
Amorphous alumina	$Al(OH)_3$	
Amorphous iron hydroxide	$Fe(OH)_3$	
Brucite	$Mg(OH)_2$	
Pyrite	FeS_2	
Amorphous iron sulfide	FeS	

Received by OCD: 6/29/2026

trisulfate (Aft),

$$Ca_6Al_2(SO_4)_3(OH)_{12}\cdot 26H_2O + 12H^+ \leftrightarrow 6Ca^{2+} + 2Al^{3+} + 3SO_4^{2-} + 38H_2O \quad (4)$$

and katoite

$$Ca_3Al_2(OH)_{12} + 12H^+ \leftrightarrow 3Ca^{2+} + 2Al^{3+} + 12H_2O \quad (5)$$

Monosulfates and trisulfates have variable compositions between their aluminum and iron endmembers. The dissolution rates for portlandite are typically faster than C-S-H by as much as four orders of magnitude (Baur et al., 2004; Galíí et al., 2001; Marty et al., 2009). Faster portlandite dissolution rates are responsible for the development of the portlandite depleted zone (Carey and Lichtner, 2007; Mason et al., 2013). The calcium carbonate zone forms as dissolved calcium from the cement minerals diffuses away from the unaltered cement and carbonic acid diffuses toward the portlandite depleted zone, leading to the precipitation of calcite or a mixture of calcite, aragonite and vaterite (CC).

$$CaCO_3 \leftrightarrow Ca^{2+} + CO_3^{2-} \quad (6)$$

The residual amorphous silicate zone, located at the cement interface where the fluids are the most acidic, is a by-product of restructuring of calcium-free C-S-H phases with dissolved sodium and aluminum to form an amorphous aluminosilicate (identified as having a zeolite structure similar to mordenite in the work of Mason et al., 2013). Cement alteration can be modeled by explicitly accounting for chemical reactions among the phases in Table 1 (Carey and Lichtner, 2007; Marty et al., 2009; Wolery et al., 1990; Zhang et al., 2013) or as a series of moving chemical fronts controlled by portlandite and calcium carbonate solubility (Kutchko et al., 2007; Walsh et al., 2014a). Cement alteration is initially fast and slows down at later times. The extent of alteration and the relative width of the layers depend on the duration, the specific reaction conditions, and the initial cement composition. The initial cement properties, in particular the ratio of the initial portlandite content to porosity, determine the evolution of cement properties. Portlandite-rich cement results in localized "sharp" reactive diffusive fronts characterized by calcite precipitation, leading to significant porosity reduction, which eventually clogs the pore space and prevents further acid penetration (Brunet et al., 2013).

2.1.2. O_2, H_2S, and SO_2 impurities in the CO_2 stream

The chemical alteration model for cement requires some modification to account for the effect of O_2, H_2S, and SO_2 impurities in the injected CO_2 captured from power plant exhaust and other industrial sources. The presence of O_2 in the injected CO_2 stream is not expected to result in different reaction pathways. We note that cement phases are already present in their oxidized forms of Fe^{3+} and SO_4^{2-}.

In contrast to O_2, H_2S and SO_2 impurities modify the redox potential and drive a second set of alteration reactions. Kutchko et al. (2011) observed that cement exposed to a mixture of CO_2 and H_2S underwent a sequence of oxidation–reduction and sulfidation reactions in addition to the alteration zones observed when cement is in contact with brines saturated with only CO_2 (Fig. 2). When the brine is saturated with both H_2S and CO_2, the resulting carbonation zone contains secondary ettringite and unidentified particles rich in iron and sulfur, as well as pyrite in the outer rim of the carbonation zone. The formation of ettringite is attributed to a two-step reaction (Kutchko et al., 2011; Zhang et al., 2013). In the first step, H_2S is oxidized by the dissolution of Fe^{3+} bearing minerals in the cement to form SO_4^{2-}. The equation below uses iron hydroxide as a proxy for any Fe^{3+} bearing minerals in the cement:

$$8Fe(OH)3 + HS^- \leftrightarrow 8Fe^{2+} + SO_4^{2-} + 5H_2O + 15OH^- \quad (7)$$

In the second step, SO_4^{2-} reacts with $Al(OH)_4^-$ from the dissolution of Al-bearing minerals to produce ettringite (Eq. (4)). The formation of pyrite is attributed to a direct reaction between H_2S and Fe^{2+} from the reduction of Fe-bearing minerals in cement.

$$Fe^{2+} + HS^- \leftrightarrow FeS + H^+ \quad (8)$$

$$FeS + H2S \leftrightarrow FeS_2 + H_2 \quad (9)$$

Kutchko et al. (2011) concluded that the Fe^{3+}-containing phases are the key for cement–H_2S reactions.

The dominance of the sulfidation reactions may also depend on the amount of H_2S. Studies with abundant H_2S (e.g. 66 mol% in Jacquemet et al., 2008) observed iron reduction in the cement minerals to form sulfides (Jacquemet et al., 2012, 2008; Kutchko et al., 2011). In contrast, studies with much lower concentrations of H_2S yielded cement alteration rates and products similar to those observed in the experiments with 100% CO_2.

The alteration products generated by reacting well cement and a mixture of CO_2 and SO_2 are similar to those between cement and CO_2 and H_2S. Dissolved CO_2 reacts with portlandite and C-S-H to produce $CaCO_3$ precipitates such as calcite, aragonite, and vaterite, while SO_2 is oxidized by either O_2 or Fe^{3+}containing phases to form SO_4^{2-}. Dissolved SO_4^{2-} then reacts with Ca^{2+} and various Al and Fe-bearing minerals to form ettringite and gypsum.

2.1.3. Pozzolan additives

Additives are commonly combined with the ordinary Portland cement to reduce slurry density, improve acidity resistance, and reduce costs in oil and gas operations (Lyons, 1996; Neville, 2004; Sideris et al., 2006; Türkel et al., 2007). Pozzolan is a generic term for reactive additives, such as fly ash, volcanic glass/ash, silica flour, and ground blast furnace slag. Fly-ash is one of the most common additives in oil and gas well cement formulations and can comprise up to 75% of the cement volume (API, 2011, 1997; Kutchko et al., 2009; Lyons, 1996; Massazza, 1993; Nelson and Guillot, 2006; Neville, 2004; Sideris et al., 2006; Türkel et al., 2007). The chemical reactions for a fly ash-amended cement are identical to those outlined in Fig. 2 (with the exception of reduced portlandite content in the cement), because mixing fly ash, which contains amorphous aluminosilicate, crystalline and amorphous SiO_2, small amounts of lime (CaO), and hematite (Fe2O3) (Papadakis, 1999; Shehata et al., 1999) with neat cement converts the portlandite and gypsum in the neat cement into C-S-H, mono- and tri-sulfate phases during the hydration process (Papadakis, 1999).

Pozzolan-amended cement allows faster penetration of CO_2 than neat cement under typical CO_2 sequestration conditions with very high dissolved CO_2 concentrations. Carbonation depth was measured to be 20 times higher than neat cement after 9 days exposure to CO_2-saturated brine for cement with 35 vol% pozzolan and 65 vol% class H cement (Kutchko et al., 2009, 2008). Further, the neat cement showed progressively slower rates of penetration in time, possibly due to the precipitation of calcium carbonate. The cause of fast CO_2 penetration in pozzolan-amended cement is not clear. A possible explanation is that combined higher porosity and lower portlandite content for calcite precipitation leads to faster diffusion and a more permeable carbonate zone and therefore a higher penetration/alteration depth (Fig. 6 in Brunet et al., 2013). Despite the extent of alteration, the altered pozzolan cements maintained a good hydraulic barrier with permeability values well below the American Petroleum Institute recommended maximum value of 200 μD (Kutchko et al., 2009).

Impurities in the CO_2 stream further alter pozzolan-amended cements. In one study, H_2S penetrated the cement more rapidly than CO_2, but the resulting reaction products impeded further penetration of CO_2 (Kutchko et al., 2011). Two other studies found that the H_2S impurity altered the cement chemistry considerably

Received by OCD: 6/29/2026

farther into the cement than CO_2 alone, and resulted in significant alteration of the surface region of the cement (Zhang et al., 2015), including porosity (Zhang et al., 2013).

2.1.4. Steel corrosion

Steel casing (i.e. pipe) is the third component of the steel–cement–caprock system that determines well integrity. The steel casing must have adequate strength to contain the fluids within the well and to resist external stresses. Although casing rupture does occur, the most common problems are associated with leaking pipe connections and corrosion of steel. The steel used in most wells is low-cost, low-carbon steel that is not corrosion resistant. The near surface environment is particularly problematic, as the greater availability of oxygen can cause surface and conductor casing to rapidly deteriorate without adequate cement protection (Fig. 1, #1) (Talabani et al., 2000). For steel casing, factors that can exacerbate corrosion problems include sand (introduced during hydraulic fracturing or during production of poorly lithified reservoirs, resulting in metal erosion), the presence of oxygen, hydrogen evolution (which can cause embrittlement), chloride and sulfate-rich formation waters, acids used to stimulate the formation, in situ H_2S and CO_2, and the higher temperature and pressure that occur at drilling depths (Rahman and Chilingarian, 1995; Talabani et al., 2000).

Choi et al. (2013) recently reviewed casing corrosion issues specifically relevant to CO_2 sequestration. CO_2 transforms the oxygen-free subsurface to a highly corrosive environment primarily because of carbonic acid (Han et al., 2011a; Nešić, 2007). The key half-cell reaction is:

$$2H_2CO_3 + 2e^- \rightarrow H_2 + 2HCO_3^- \quad (10)$$

which is balanced by the dissolution of iron:

$$Fe_{(s)} + 2e^- \rightarrow Fe^{2+} \quad (11)$$

Corrosion can be rapid and destructive because it allows fluids to communicate between the inside and outside of the well. Uniform corrosion rates of bare metal can reach tens of mm/year for unpassivated low-carbon steel in the presence of high-pressure CO_2 (Han et al., 2011a). Fortunately, cement carbonation appears to passivate and protect the steel surface, despite its more acidic pH. Han et al. (2011b) reported reductions in corrosion rates by a factor of 20 due to formation of iron carbonate scale on the steel casing. These reduced corrosion rates still have a potential impact on well integrity, because CO_2 storage wells need to operate for decades and to protect against leaks for centuries. We currently lack a good basis for predicting the impact of corrosion rates on well integrity in the presence of passivating iron carbonate scales.

In addition to these general reactions that are expected to cause relatively uniform corrosion over large areas, there will also be localized CO_2-induced corrosion rates (Kermani and Morshed, 2003). These effects can be more rapid and penetrating than uniform corrosion. Factors that exacerbate localized corrosion include stress-induced defects, incomplete passivation layers, mechanical damage to passivated surfaces, and some dissolved chemical species such as acetic acid or H_2S (Kermani and Morshed, 2003).

Corrosion of low-carbon steel can be prevented through the use of corrosion inhibitors or cathodic protection among other measures. However, one of the most important methods for protecting against corrosion of external casing is an adequate coverage with cement, particularly on the surface casing in the subsurface across formations with problematic fluids (Choi et al., 2013; Rahman and Chilingarian, 1995; Talabani et al., 2000).

2.2. Geomechanical factors

The stresses acting on a well are an important factor influencing the risk of a leakage event. Wellbore stresses will change over time, as a result of shifts in pressure due to pumping or leakage, fluctuations in subsurface temperature (also potentially a byproduct of injection or leakage), or due to natural variations in subsurface conditions (tectonic stresses and seismicity). These changes can directly affect the permeability of any of the previously discussed well leakage pathways through several mechanisms. Variations in the normal stress on a fracture have a non-linear effect on fracture transmissivity related to the surface roughness (Bandis et al., 1983; Barton et al., 1985), while shear motion will induce preferential flow pathways that depend on the direction and extent of the relative displacement between the two fracture surfaces (Detwiler and Morris, 2014). Likewise, multicomponent and multiphase flow along fractures are also strongly influenced by changes in stress on the well, due to the coupling between the effective stress and the aperture distribution (Walsh and Carroll, 2013), and this effect varies with the relative permeabilities of the component fluids. In the event of CO_2 leakage, these complexities interact with chemical reactions that occur between cement, steel, rock and carbonated brine. The chemical alteration within the reaction zones changes the mechanical properties of the fracture interface, potentially resulting in collapse of the fracture aperture (Walsh et al., 2014a,b). Due to the interplay between these different processes, the coupled effects of mechanics, chemistry and flow should be incorporated into an assessment of wellbore leakage.

There are a multitude of processes throughout a well's construction and use that contribute to its stress state. As a well is drilled, subsurface stress is concentrated in the surrounding formation – the forces previously born by the excavated rock are redistributed to the intact material around the hole. While analytical expressions can be found to describe the resulting stress distribution (e.g. Bradley, 1979; Peška and Zoback, 1995), in reality, the stress state around the well is more complex: a product of a dynamic layered environment consisting of the well casing, the surrounding well cement, drilling fluid filter cake (if present) and a zone of damaged rock from the drilling process, within the larger (largely undamaged) far-field formation (e.g. Gray et al., 2009; Nygaard et al., 2014).

After the hole is drilled and the well casing inserted, well cement is introduced in the annulus between the casing and the formation. Pouring and setting of cement occurs in a far-from-pristine environment. In particular, the drilling fluid used to create the borehole, along with any subsurface liquids and gases, can produce fluid channels that decrease the bonding strength between the cement and the casing and the formation and may be the source of preferential flow pathways (Agbasimalo and Radonjic, 2012; Agbasimalo, 2012; Randhol, 2008). Mixing between these liquids and the well cement negatively impacts the cement's mechanical properties (El-Sayed, 1995).

As the cement cures, it undergoes a two stage process of hardening (conversion of the liquid cement into a solid body) and shrinkage (a reduction in volume upon curing of the solid cement) (Gray et al., 2009; Randhol, 2008; Ravi et al., 2002). Hardening has little effect on the stress of the cement (as the cement is generally considered to remain under hydrostatic stress throughout), though it will affect cement rheology. Shrinkage, however, results in a change in the cement's stress state, which can potentially lead to plastic deformation of not only the cement, but also the casing and formation, or debonding at either the casing or formation interfaces (Ravi et al., 2002). In addition, the casing may not be located in the center of the borehole, and thus shrinkage can result in an uneven distribution of stress in the cemented annulus (Gray et al., 2009). In time, the surrounding rock can creep toward the borehole,

Received by OCD: 6/29/2026

gradually applying far-field stresses to the cement. These diverse processes create a range of possible stress conditions for cement that include hydrostatic, completely detached from the rock formation, and in stress-continuity with the rock formation.

Over it's lifetime, a well is subjected to variations in pressure induced by processes internal to the well (resulting from stimulation processes, mechanical testing, and injection and production), by changes in the formation (again due to injection or production from either the well itself or an adjacent source), and by natural fluctuations (e.g. tidal variations). The well is also subject to thermal stresses that accompany fluid flow during injection and production. For example, Thiercelin et al. (2007) calculate stresses induced in cement for a number of these processes. Thermal stresses are particularly important when supercritical CO_2 is injected into the subsurface (Nygaard et al., 2014), and most notably if injection follows a cyclic pattern causing fluctuations in the thermal field and associated stresses (De Andrade et al., 2014). Cyclic stresses may encourage growth of fractures within the well cement or result in debonding between the cement and formation (De Andrade et al., 2014; Heathman and Beck, 2006; Shen and Pye, 1989). Fluctuations in stress also play a role in determining the active flow pathways due to the coupling between applied stress and fracture permeability.

2.3. Impact of coupled chemical, mechanical, and transport processes on well integrity

Field observations show that CO_2 has migrated over substantial distances along sections of the wellbore above a CO_2-containing reservoir. Crow et al. (2010) observed carbonation of cement more than 60 m above a natural CO_2 reservoir adjacent to shale. Similarly, Carey et al. (2007) found evidence of CO_2 migration 3 m above a CO_2-enhanced oil recovery reservoir along the interface between cement and caprock. They also saw unusual silica-carbonate bands within the shale-fragment zone indicating mobilization and deposition of silica (Fig. 6 in Carey et al., 2007). In both of these studies, the amount of migrating CO_2 was not possible to quantify. The cement barriers remained intact and the observed carbonate precipitates in void spaces suggests the leakage path was sealed during the operation of the site. The field observations in the two studies cited suggest a barrier failure, but as emphasized by King and King (2013), the failure of a single barrier does not necessitate leakage to the atmosphere. Neither study observed evidence of CO_2 migration to the surface or sustained casing pressure indicative of a breach of the well annuli. Combined with observations from experiments and numerical simulations described below, these findings suggest that under some circumstances coupled processes can help limit leakage.

In this section we draw on a variety of laboratory experiments as well as numerical simulations that characterize how coupled flow, geochemical reactions and mechanical alteration change permeability of fractures within the cement and at the cement–caprock and cement–steel interfaces. Collectively the studies described below find a reduction of fracture permeability due to swelling of the amorphous silica layer, precipitation of carbonate minerals and/or concurrent chemical alteration and deformation of the cement asperities that allow fluid flow. Instances of sustained or increasing permeability were attributed to large initial fracture apertures or high fluid flow rates that promote dissolution-dominated environments.

2.3.1. Coupled chemistry and diffusion

Good quality cement that is well bonded to casing and formation rock provides a barrier that permits transport of CO_2 only by diffusion or by very slow flow that is effectively diffusion-like in character. In addition, capillary entry pressures in good quality cement will prevent the supercritical CO_2 phase from entering the cement further limiting any flow processes to CO_2-saturated brine (Carey and Lichtner, 2011). The rate of progress of chemical alteration of cement under diffusive CO_2-saturated brine transport (leakage pathway #8 in Fig. 1) is insufficient to pose a threat to well integrity. This conclusion is based on the slow rates of diffusive transport, the tens of meters of transport distance in wellbore cement, and the fact that the thickness of diffusion-controlled alteration zones shown in Fig. 2 is limited by the growth of a dense carbonate zone in neat cements serves as a barrier to further cement degradation (Kutchko et al., 2007, 2008; Matteo and Scherer, 2012). Kutchko et al. (2008) estimated a penetration depth of only about 1 mm after contacting the CO_2-saturated brine for 20–30 years. Simulations conducted under the same diffusion controlled conditions suggest that higher amounts of portlandite and lower initial porosity further limit cement degradation (alteration zones varied between 0.5 and 6 mm after 200 days of exposure to CO_2-saturated brine, Brunet et al., 2013). While pozzolan-bearing cements carbonate at faster rates than neat cements (Kutchko et al., 2009; Crow et al., 2010), these cements maintain relatively low permeability and thus the mass flow rate is effectively limited to low values.

2.3.2. Coupled chemistry and flow

Flow of CO_2 and CO_2-saturated brine can occur where a leakage pathway exists due to a poor completion or due to mechanical damage (leakage pathways #7, #10, #11, and #12 in Fig. 1). Under fluid flow conditions, fresh reactants (H^+, H_2CO_3, etc.) are continuously supplied while reaction products including calcium and carbonate species are removed. In this environment, the residence time or the time scale over which the CO_2 is in contact with cement, determines the relative rates of cement dissolution compared with precipitation or other processes that reduce pore space and permeability to seal the fracture pathway. Thus, the combination of fluid residence time and aperture width can cause wellbore cement pathways to seal or open as a consequence of chemical reaction. The relative magnitude of the two competing processes ultimately controls the cement properties and long-term leakage potential.

A summary of experimental studies of the permeability evolution of fractured wellbore components using flow-through systems is shown in Table 2. Most of the experiments involved flow through pre-fractured cement samples. Some studies used HCl solutions as a surrogate for the acidic CO_2–brine system and conditions ranged from ambient conditions to pressure and temperatures above the supercritical point of CO_2. The majority of studies observed a drop in permeability with time. Two studies (Luquot et al., 2013; Huerta et al., 2015) showed an increase in permeability under conditions associated with larger apertures and higher flow rates, while decreases in permeability were associated with smaller apertures and lower flow rates. These results are consistent with the concept that permeability evolution is governed by a competition between advection of acidic solution and precipitation of supersaturated solutions (see below). The studies attributed permeability reduction to a variety of effects including relative permeability (due to exsolution of CO_2 along the length of the core), precipitation of carbonate, and swelling of the amorphous silica residue that remains after cement reaction with the acidic solution.

A similar set of studies examined the permeability evolution of the cement–rock interface (Table 2). Permeability decreases were found in two studies and attributed to several mechanisms including relative permeability effects, fines migration, reprecipitation of cement phases, silica gel swelling, and mechanical closure of the aperture under confining stress. A permeability increase was found in an experimental setup that included large fracture apertures (Cao et al., 2013), which is consistent with the Luquot et al. (2013) observations on aperture/flow control of permeability evolution. A fourth study (Walsh et al., 2014a,b) found both an increase and decrease in permeability depending on the initial fracture geometry.

Received by OCD: 6/29/2026

Table 2
Summary of experimental studies that evaluate permeability evolution of wellbore systems for CO_2 and brine leakage.

Fractured cement experiments				
Bachu and Bennion (2009)	$scCO_2$	Hi PT	Permeability drop	Relative permeability effects
Wigand et al. (2009)	$scCO_2$	Hi PT	n/a	Carbonate precipitation
Yalcinkaya et al. (2011)	CO_2	Unclear	n/a	Widening of apertures
Liteanu and Spiers (2011)	$scCO_2$	Hi PT	Permeability drop	Carbonate precipitation
Huerta et al. (2013)	HCl	Ambient*	Permeability drop	Carbonate precipitation
Luquot et al. (2013)	$scCO_2$	Hi PT	Permeability drop and rise	Carbonate and silica gel precipitation
Abdoulghafour et al. (2013)	$scCO_2$	Hi PT	Permeability drop	Silica gel precipitation
Wenning et al. (2013)	HCl	Ambient	n/a	Modified fracture geometry
Huerta et al. (2015)	CO_2	Hi P	Permeability drop	Silica gel and carbonate precipitation
Cao et al. (2016)	CO_2	Mod. P	Permeability drop	Carbonate precipitation
Cement–rock interface experiments				
Newell and Carey (2013)	$scCO_2$	Hi PT	Permeability drop	Relative permeability, fines migration and cement precipitation
Cao et al. (2013)	CO_2	Mod PT	Permeability rise	Aperture widening
Mason et al. (2013) and Walsh et al. (2013)	CO_2(aq)	Hi PT	Permeability drop	Chemical alteration and mechanical deformation; and possible silica gel swelling
Walsh et al. (2014a,b)	CO_2(aq)	Hi PT	Permeability drop and rise	Chemical alteration and mechanical deformation

In order to investigate the relationship of permeability, aperture and flow rate observed in experiments, Brunet et al. (2016) developed a reactive transport model calibrated against the experiments of Huerta et al. (2015). The model calculates change in fracture permeability as a consequence of diffusion and dispersion when CO_2-saturated water reacts with cement. The authors conducted 250 simulations with aperture width ranging from 6 to 90 μm, initial flow rates from 0.0015 to 0.130 ml/min, and fracture length from 109.6 to 328.7 mm. Each fracture was exposed to CO_2-enriched water for more than 100 days. The results suggest that the long-term permeability of the fracture depends on both the initial fluid residence time (i.e., the fluid flow rate) and aperture width (Fig. 3). There is a clear division between fracture sealing and opening conditions. The fracture has a tendency to fill with calcite for residence times above the threshold and remain open when the residence times are below the threshold. A narrow transition zone is observed around the threshold, where both fracture sealing or opening behavior occurs and the permeability changes are sensitive to specific conditions.

The simulated relationship for the critical aperture is consistent with experimental observations of Huerta et al. (2015; Fig. 4). For some simulated cases with initial residence times below the critical threshold, carbonate minerals precipitate at some point, however at an insufficient amount to clog the fracture or are dissolved by continued acidity, leading to no change or increased fracture permeability. Similarly, Luquot et al. (2013) observed and concluded that longer fractures and smaller apertures (longer residence time) tend to seal while fractures tend to open in flow regimes with shorter path lengths and/or larger apertures.

Although the critical threshold parameter is based on data from fractured cement, it is also consistent with observations for CO_2 interactions at cement/rock interfaces. For example, Newell and Carey (2013) observed self-sealing behavior in a composite cement/siltstone core using a brine flow rate of 0.25 ml/min

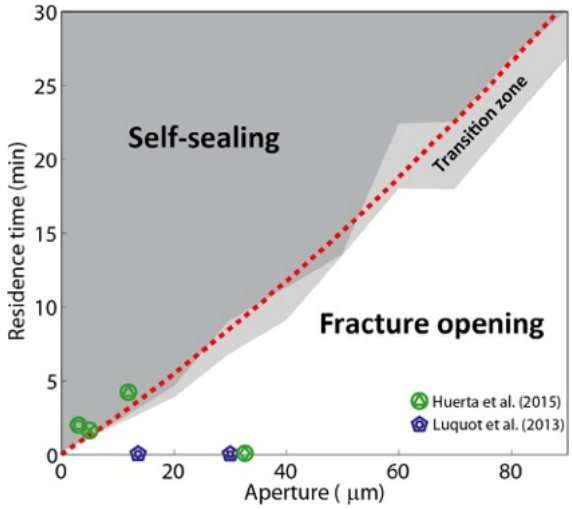


Fig. 3. Illustration of the critical threshold between fluid residence time and initial fracture aperture on the ability of CO_2–H_2O–Ca reactions to seal or open fracture pathways within cement–cement interfaces based on numerical simulations. The green and blue symbols represent the initial aperture and residence time of experiments from Huerta et al. (2015) and Luquot et al. (2013), respectively (Brunet et al., 2016). (For interpretation of the references to color in figure legend, the reader is referred to the web version of the article.)

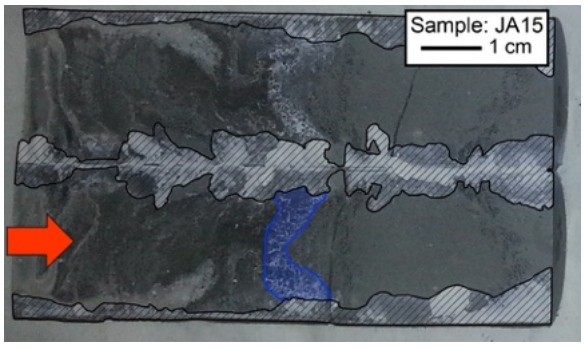


Fig. 4. Open core showing the cement fracture surface after reaction with CO_2-rich brine (modified from Huerta et al., 2015). Red arrow indicates flow direction. Hatched sections denote no-flow regions where caulk was used to seal the outer boundary of the core prior to reaction. Downstream calcium carbonate precipitated and is inferred to be the mechanism for sealing the conductive pathway. Carbonate zones are shown on both fracture surfaces, but only highlighted in blue on one side of the fracture. (For interpretation of the references to color in figure legend, the reader is referred to the web version of the article.)

Received by OCD: 6/29/2026

and a CO_2 flow rate of 0.08 ml/min. Although the alteration zone extended 5 mm into the cement, the effective brine permeability decreased from ~200 to 90 mD due to the transition to two-phase flow and then further declined to 35 mD. The permeability drop is not attributed to carbonation of cement but rather to the migration and precipitation of alteration products derived from cement within the defect. Cao et al. (2016) observed a permeability increase of 3 times in a composite cement/sandstone core using a CO_2-saturated brine flow rate of 0.5 ml/min. The permeability increase was attributed to the cement dissolution/degradation at the cement–sandstone interface. At a much higher flow rate of 2 ml/min, Cao et al. (2013) observed a permeability increase of 8 times within 8 days during a flow experiment with a composite cement/sandstone core with a large defect void at the cement–sandstone interface that served as the major conductive flow path. Both the high flow rates and large void (similar to large aperture size) contribute to the observed permeability increase.

Fig. 3 implies that for fractured cement with hydraulic aperture size of 90 μm or less, sealing can be observed when critical residence time is 30 min or longer. This short residence time indicates that in geological CO_2 storage systems, where cemented intervals are 10s of meters in length, the residence time is likely to be long (assuming there is not a large fracture). Thus, fracture sealing may be more common than fracture opening. This might also explain the lack of observations of CO_2 at the surface in field sites showing cement carbonation at depth (Carey et al., 2007; Crow et al., 2010).

The critical aperture threshold is a useful metric to better define wellbore risk over time, however it does not consider the role of other factors identified in experiments such as portlandite or fly ash content or mechanical deformation of the altered cement. In addition to carbonate mineral precipitation in fracture pathways, it is possible that swelling of the amorphous silicate layer may also contribute to the reduction in fracture permeability (Walsh et al., 2013; Abdoulghafour et al., 2013; Huerta et al., 2015). This mechanism was called on to explain decreases in fracture permeability, because the increased volume associated with the calcium carbonate alteration zone was not sufficient to counteract the overall increase in porosity caused by cement dissolution.

2.3.3. Coupled chemistry, mechanics and flow

Chemical and mechanical alterations are tightly coupled and represent an active area of research. Chemical alteration has the potential to change the local stress and aperture fields within the cement as was observed when calcium carbonate precipitated in fractures of cement/basalt samples exposed to CO_2-saturated groundwater and wet supercritical-CO_2 (Jung and Um, 2013; Jung et al., 2013). Carbonate precipitation caused some fractures to open as a result of crystallization-induced pressure, as well as isolating other cement fractures (also see Wigand et al., 2009). Combined fracture opening and isolation consequently reduced the permeability by an order of magnitude (Jung et al., 2014; Um et al., 2014).

The mechanical factors affecting flow along cement interfaces are further complicated by the structural changes induced by reactions with CO_2-saturated brine. Reactions between carbonic acid and cement are often accompanied by an increase in porosity (Kutchko et al., 2007; Rimmelé et al., 2008). While this increased porosity would normally be indicative of enhanced permeability, decreased permeability can be induced by changes in the mechanical properties of the altered zones, by weakening asperities that maintain contact between cement and rock in the fracture (Walsh et al., 2014a,b). Nano-indentation measurements of the reaction layers reveal that both the amorphous and depleted regions have lower elastic moduli and hardness than the unreacted cement (Kutchko et al., 2009; Mason et al., 2013; Walsh et al., 2014a). Zhang et al. (2013) found that acid gas impurities had a similar impact on the mechanical properties of the cement alteration zone. These findings are also consistent with the effects caused of calcium leaching from cements exposed to uncarbonated brines (Constantinides and Ulm, 2004; Ulm et al., 2003). These results illustrate several ways that well integrity and risk of CO_2 leakage are controlled by coupled geomechanical and geochemical alterations of well materials.

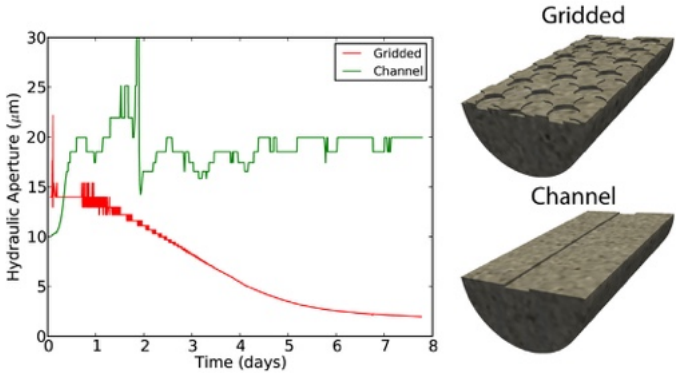


Fig. 5. Hydraulic aperture as a function of time in samples of mated cement/caprock half cores with distinct flow-path geometries.
Modified from Walsh et al. (2014b).

The extent to which reaction-induced changes in structural properties affect transmissivity depends upon the interface geometry (Walsh et al., 2014b). To illustrate this, Fig. 5 compares results from core-flow reaction experiments performed under confining stress representative of subsurface conditions. During the experiment, carbonated brine was introduced into a core consisting of half-cement and half-caprock samples. The contacting surfaces were imprinted with two distinct geometries: a single flow channel and a grid of circular apertures. The hydraulic aperture increased over time in the channel sample, whereas a consistent decrease in aperture was observed for the gridded sample. The difference in behavior is explained by the manner in which the reaction fronts affect the contact between the sample half-cores. In the gridded sample the reactions fronts removed significant amounts of portlandite and CSH from the asperities maintaining the fracture, resulting in weakened mechanical properties that allowed the asperities to deform. This deformation results in an overall decrease in the hydraulic aperture despite an increase in the cement porosity. Conversely, in the channel sample, although the reaction fronts decreased the contact area between the two half cores, sufficient unreacted cement remained at the contact to support the stress on the fracture. In this case, the permeability is increased slightly due to the increased porosity.

Walsh et al. (2014b) developed a coupled chemical–mechanical–transport model that ties the extent of deformation of the cement asperities to chemical alteration of the cements. Although empirical in nature, the model could be used to refine the relationship between residence time, chemical alteration, mechanical deformation and the ability of flow pathways in the cement to seal or open. Briefly, the model captures the response of the fracture with a set of simple models representing the inelastic deformation of the unreacted cement and each alteration layer. The relative contributions of each layer to the effective stress change as the relative contact areas of the reaction zones evolve, which in turn influences the mechanical and hydraulic apertures of the fracture. The contact areas and depth of the alteration zones are modeled using an idealized representation of the cement chemistry in which portlandite, calcite, and zeolite equilibrium conditions are enforced as a series of discrete reaction fronts. The equilibrium conditions are coupled by diffusive transport between the fronts, which also determines the rate of front propagation.

Received by OCD: 6/29/2026

2.3.4. Coupled casing corrosion and flow

There has been relatively little work on the geochemical and hydrologic behavior of the casing/cement interface (leakage pathway #2 in Fig. 1). In the absence of a defect at this interface, the cement protects steel from corrosion due to high-pH pore fluids that create a protective iron-oxide coating. Well integrity risks at the cement/casing interface are considered separately from the evolution of the permeability along fractures within the cement and along cement/caprock interface, because the consequences of chemical reactivity of the steel casing allow for the development of flow paths that are distinct from the cement/caprock aperture controlled processes discussed above.

In wells with casing made of corrosion-resistant alloy, the chief concern for this interface would be the possible dissolution of cement. However, at present there are no studies that have directly examined this system. Carey et al. (2010) examined the more common situation (particularly in non-CO_2-specific wells) in which there was a microannulus between low-carbon steel and cement. They found that steel was far more reactive than cement during flow of a mixture of CO_2–brine at sequestration conditions (Fig. 6). The steel showed evidence of extensive corrosion reactions that were limited to some extent by deposition of an iron carbonate. Cement, on the other hand, showed evidence only of diffusion of CO_2 and carbonation of cement. The cement did not erode or noticeably dissolve. Although this study indicates that the more vulnerable component of the interface system is steel, permeability gradually decreased with time, which was attributed to the accumulation of iron carbonate deposits within the interface. The long-term fate of steel in this situation is unknown. It is possible that the iron carbonate scale may provide lasting protection; it is also possible that corrosion may eventually penetrate through the steel wall, allowing communication between the interface and the well interior.

An important research question is whether carbonated cement can protect steel from corrosion. If there is flow of CO_2-saturated brine, either migrating along the cement/caprock interface (#12) through fractures in the cement (#8) or other mechanisms shown in Fig. 1, it could carbonate the cement that is in contact with the steel. In a field sample, Carey et al. (2007) found evidence of CO_2 leakage along the casing/cement interface in the form a carbonate rind attached to the cement surface adjacent to casing. The casing was not damaged, because the well was under cathodic protection. The origin of the CO_2 creating this deposit is unknown, but may have been derived by leakage through joints in the casing. A limited number of experiments show that casing corrosion rates are less than they would in the absence of carbonated cement (Han et al., 2012). On this topic, as for many questions related to wellbore integrity and risk, there is still much to learn through combinations of theoretical, experimental, computational and field research.

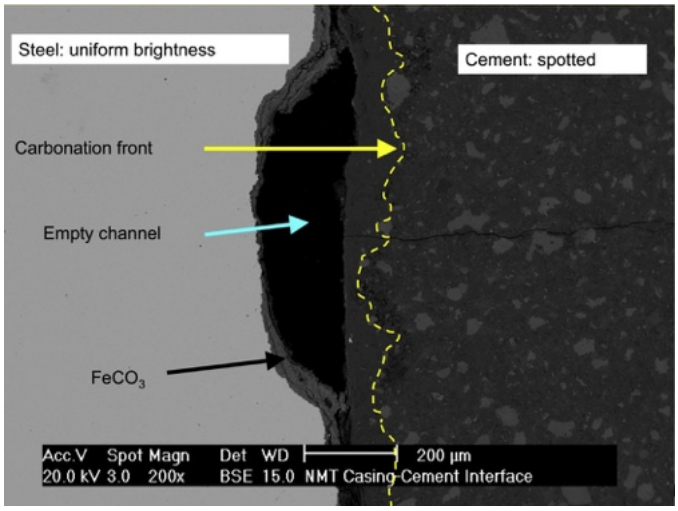


Fig. 6. Back-scattered electron micrograph of the interface between steel (solid white material left) and Portland cement (spotted material right). The experiment involved flow of a mixture of supercritical CO_2-brine through notches cut into the steel. The steel corroded forming iron carbonate deposits while the cement carbonated without a significant loss of material.
Modified from Carey et al. (2010).

3. Conclusions

This review summarizes recent research outcomes that have significantly advanced understanding of the basic science, causes, and impacts associated with well leakage. Wellbores and their immediate environments are chemically and mechanically complex, and represent an important leakage risk for CO_2 storage systems.

Important progress has been made in understanding the chemical alteration of cement, especially the ordinary Portland cements that are most commonly used for wellbore completions and abandonment. Although cement is a complex material, typically a relatively small number of reactions suffice to model these systems, and most thermodynamic parameters of the reactions are well defined. Kinetics has been measured for some reactions of interest, but empirical determination of rate expressions are needed for most. Both experimental and theoretical considerations have confirmed that cement alteration is limited by the diffusion of reactants and products, and that these processes result in discrete reaction fronts and defined alteration zones. Pozzolan (fly ash) amendments can accelerate these diffusion rates, but in experimental systems the effective permeability remained low and within the range of current standards. Additional reactions must be considered to account for H_2S and SO_2 impurities in the injected CO_2, but these are also chemically tractable. Changes in oxidation, redox-potential and sulfidation reactions associated with these impurities can affect dissolution and precipitation rates and cement mineralogy, but these effects are concentration dependent, and at low concentrations permeability and performance are expected to be similar to those observed with pure CO_2.

Carbon steel, as used in most oil and gas wells, is highly susceptible to corrosion by CO_2-bearing fluids. In the presence of high pressure CO_2 and the resulting carbonic acid, low-carbon steel can erode at rates of millimeters per year. However, if there is good contact between steel and cement, the high pH of cement passivates and protects steel. Passivation may also be crucial where CO_2 manages to migrate along the cement–steel interface, because iron carbonate precipitation provides additional protection against corrosion, reducing rates of corrosion by more than an order of magnitude in some circumstances. Thus the presence of cement is a minimum requirement for demonstrating that steel in existing wells will not be damaged by injected CO_2. Less well understood is whether carbonated cement can provide protection to steel casing. In this situation, the high pH environment of unreacted cement is lost but the potential to provide a barrier to flow of corrosion reactants and an environment for carbonate precipitation persists. However, even this level of protection may not be adequate to maintain wellbore integrity for the decades and even centuries that may be required of CO_2 storage systems.

We are still in the early stages of understanding how chemical alteration affects the physical properties of wellbore cement. Evidence suggests that well permeability can decrease when

Received by OCD: 6/29/2026

reacting with CO_2 rich brines, thereby lowering the risk of leakage in abandoned wells. Geochemical and geomechanical interactions between well cements and supercritical CO_2 or CO_2-saturated brine can in some circumstances promote sealing and closure of leak paths. Studies have investigated different interface materials (e.g. cement-to-cement or cement-to-rock) and geometries, the role of oxygen and acids, and the impacts of driving force and residence time. CO_2-promoted sealing is a function of portlandite abundance and cement porosity, as well as flow rates and residence time along the leakage path. Similar phenomena were observed at the cement–rock interface under CO_2 storage conditions. These protective processes were observed under both diffusion dominated and convection dominated flow regimes, and with a range of expected pressures and fluid chemistries. A more complete understanding of the mechanisms and limitations of this self-sealing phenomenon is important in several respects. In areas where good wellbore records exist and the well materials and construction are well characterized, it may reduce the need to recomplete all the wells in the area of review. And in cases where there may be unknown or uncharacterized wells, CO_2-promoted sealing may provide an additional measure of protection from wellbore leakage risks.

At present we have a relatively poor understanding of the role of stress in the wellbore environment. In addition to geomechanical stress associated with well construction and surrounding geological formations, there will be additional thermal stress from the injection of cold CO_2 whose effects on wellbore integrity remain largely unknown. Similarly, it will be important to define the pressures that will result in damaging interface bonds in the well. The cumulative stresses at well interfaces are likely to have important effects on some of the mechanisms previously discussed. Any separation of cement from steel will cause discontinuities in cement-induced passivation, and can introduce larger diameter pores and flow paths that can reduce or reverse the self-sealing effects.

Computational tools to simulate and predict these effects are under development within a framework to quantify and integrate wellbore leakage risks. Reactive transport models have been developed that tie the extent of reaction to mechanical alteration, and that account for the precipitation of fracture filling minerals (e.g. Huerta et al., 2014; Walsh et al., 2014b). To scale these models to full wellbore systems several challenges must be addressed, paramount among them the computational effort required. Although chemical reactions, CO_2 and brine diffusion, dissolution and precipitation occur at scales of microns and smaller, the wellbores and potential leakage pathways are on the order of 1000 m. Process complexity must also be addressed, including chemical kinetic and equilibrium reactions, diffusion and advective transport, thermal and mechanical stress and mechanical deformation. To fully capture these processes, including interactions with reservoirs, caprock, and overlying aquifers, is computationally prohibitive with high fidelity full physics and chemistry models. The National Risk Assessment Partnership for CO_2 storage (Pawar et al., 2014) has developed reduced order models for wellbore systems and each of these interacting components, coupled within an integrated assessment framework (Jordan et al., 2015; Harp et al., 2016). However, to date these models do not consider changes in wellbore permeability due to chemical, mechanical and transport processes.

To advance understanding of and models for risk of wellbore leakage at CO_2 geological storage sites, it is important that carefully designed field research be conducted at demonstration-scale projects. Direct observations from field site characterization and monitoring campaigns will be needed to develop further, test and validate the complex, integrated models needed to assess risk of wellbore leakage.

Acknowledgements

This work was completed as part of National Risk Assessment Partnership (NRAP) project. Support for this project came from the DOE Office of Fossil Energy's Crosscutting Research program. The authors wish to acknowledge Robert Romanosky (NETL Strategic Center for Coal) and Regis Conrad (DOE Office of Fossil Energy) for programmatic guidance, direction, and support.

The authors would like to acknowledge Brian Strazisar, Preston Jordan, and David Nakles for their contributions early on in the development of this manuscript, and Brian Tost for help with the reference list.

This work was prepared in part by LLNL under contract DE-AC52-07NA27344 and has been reviewed and released (LLNL-JRNL-681465).

References

Abdoulghafour, H., Luquot, L., Gouze, P., 2013. Characterization of the mechanisms controlling the permeability changes of fractured cements flowed through by CO_2-rich brine. Environ. Sci. Technol. 47, 10332–10338, http://dx.doi.org/10.1021/es401317c.

Agbasimalo, N., Radonjic, M., 2012. Experimental Study of Portland Cement/Rock Interface in Relation to Wellbore Stability for Carbon Capture and Storage (CCS). American Rock Mechanics Association, ARMA.

Agbasimalo, N.C., 2012. Experimental Study of the Effect of Drilling Fluid Contamination on the Integrity of Cement-Formation Interface (Masters). Louisiana State University.

API, 2011. ANSI/API 10A: Specification for Cements and Materials for Well Cementing.

API, 1997. Recommended Practice for Testing Well Cements 10B.

Bachu, Stefan, Bennion, D.B., 2009. Experimental assessment of brine and/or CO_2 leakage through well cements at reservoir conditions. Int. J. Greenh. Gas Control 3 (July (4)), 494–501, http://dx.doi.org/10.1016/j.ijggc.200811.002.

Bandis, S.C., Lumsden, A.C., Barton, N.R., 1983. Fundamentals of rock joint deformation. Int. J. Rock Mech. Min. Sci. Geomech. Abstr. 20, 249–268.

Barton, N., Bandis, S., Bakhtar, K., 1985. Strength, deformation and conductivity coupling of rock joints. Int. J. Rock Mech. Min. Sci. Geomech. Abstr. 22, 121–140.

Baur, I., Keller, P., Mavrocordatos, D., Wehrli, B., Johnson, C.A., 2004. Dissolution–precipitation behaviour of ettringite, monosulfate, and calcium silicate hydrate. Cem. Concr. Res. 34, 341–348, http://dx.doi.org/10.1016/j.cemconres.2003.08.016.

Bradley, W.B., 1979. Failure of inclined boreholes. J. Energy Resour. Technol. 101, 232–239, http://dx.doi.org/10.1115/1.3446925.

Brondel, D., Edwards, R., Hayman, A., Hill, A., Mehta, S., Semerad, T., 1994. Corrosion in the oil industry. Oilfield Rev.

Brunet, J.-P.L., Li, L., Karpyn, Z.T., Huerta, N.J., 2016. Cement fracture opening or self-sealing: critical residence time unifies diverging observations under geological carbon sequestration conditions. Int. J. Greenh. Gas Control., http://dx.doi.org/10.1016/j.ijggc.2016.01.024.

Brunet, J.-P.L., Li, L., Karpyn, Z.T., Kutchko, B.G., Strazisar, B., Bromhal, G., 2013. Dynamic evolution of cement composition and transport properties under conditions relevant to geological carbon sequestration. Energy Fuels 27, 4208–4220, http://dx.doi.org/10.1021/ef302023v.

Cao, P., Karpyn, Z.T., Li, L., 2013. Dynamic alterations in wellbore cement integrity due to geochemical reactions in CO_2-rich environments. Water Resour. Res. 49, 4465–4475, http://dx.doi.org/10.1002/wrcr.20340.

Cao, P., Karpyn, Z.T., Li, L., 2016. The role of host rock properties in determining potential CO_2 migration pathways. Int. J. Greenh. Gas Control. 45, 18–26, http://dx.doi.org/10.1016/J.Ijggc.2015.12.002.

Carey, J.W., 2013. Geochemistry of wellbore integrity in CO_2 sequestration: Portland cement–steel–brine–CO_2 interactions. In: DePaolo, D.J., Cole, D., Navrotsky, A., Bourg, I. (Eds.), Geochemistry of Geologic CO_2 Sequestration: Reviews in Mineralogy and Geochemistry. Mineralogical Society of America, Washington, DC, pp. 505–539.

Carey, J.W., Lichtner, P.C., 2011. Computational studies of two-phase cement–CO_2–brine interaction in wellbore environment. SPE J. 16, 940–948.

Carey, J.W., Lichtner, P.C., 2007. Calcium silicate hydrate (C-S-H) solid solution model applied to cement degradation using the continuum reactive transport model FLOTRAN. In: Mobasher, B., Skalny, J. (Eds.), Transport Properties and Concrete Quality: Materials Science of Concrete, Special Volume. American Ceramic Society; John Wiley & Sons, Inc., pp. 73–106.

Carey, J.W., Wigand, M., Chipera, S.J., WoldeGabriel, G., Pawar, R., Lichtner, P.C., Wehner, S.C., Raines, M.A., Guthrie Jr., G.D., 2007. Analysis and performance of oil well cement with 30 years of CO_2 exposure from the SACROC Unit, West Texas, USA. Int. J. Greenh. Gas Control 1, 75–85, http://dx.doi.org/10.1016/S1750-5836(06)00004-1.

Carey, W., Svec, R., Grigg, R., Zhang, J., Crow, W., 2010. Experimental investigation of wellbore integrity and CO_2–brine flow along the casing–cement microannulus. Int. J. Greenh. Gas Control 4, 272–282, http://dx.doi.org/10.1016/j.ijggc.2009.09.018.

Received by OCD: 6/29/2026

Carroll, S.A., Keating, E., Mansoor, K., Dai, Z., Sun, Y., Trainor-Guitton, W., Brown, C., Bacon, D., 2014. Key factors for determining groundwater impacts due to leakage from geologic carbon sequestration reservoirs. Int. J. Greenh. Gas Control 29, 153–168, http://dx.doi.org/10.1016/j.ijggc.2014.07.007.

Choi, Y.-S., Young, D., Nešić, S., Gray, L.G.S., 2013. Wellbore integrity and corrosion of carbon steel in CO_2 geologic storage environments: a literature review. Int. J. Greenh. Gas Control 16 (Suppl. 1), S70–S77, http://dx.doi.org/10.1016/j.ijggc.2012.12.028, The IEAGHG Weyburn–Midale CO_2 Monitoring and Storage Project.

Constantinides, G., Ulm, F.-J., 2004. The effect of two types of C-S-H on the elasticity of cement-based materials: results from nanoindentation and micromechanical modeling. Cem. Concr. Res. 34, 67–80, http://dx.doi.org/10.1016/S0008-8846(03)00230-8.

Crow, W., Carey, J.W., Gasda, S., Brian Williams, D., Celia, M., 2010. Wellbore integrity analysis of a natural CO_2 producer. Int. J. Greenh. Gas Control 4, 186–197, http://dx.doi.org/10.1016/j.ijggc.2009.10.010.

De Andrade, J., Torsaeter, M., Todorovic, N., Opedal, N., Stroisz, A., Vralstad, T., 2014. Influence of casing centralization on cement sheath integrity during thermal cycling. In: Presented at the IADC/SPE Drilling Conference and Exhibition, Society of Petroleum Engineers.

Detwiler, R.L., Morris, J.P., 2014. Transmissivity anisotropy in rough-walled fractures: the combined influence of shear offset and normal deformation. In: Presented at the In 48th US Rock Mechanics/Geomechanics Symposium, American Rock Mechanics Association.

Duguid, A., Scherer, G.W., 2010. Degradation of oilwell cement due to exposure to carbonated brine. Int. J. Greenh. Gas Technol. 4, 546–560.

El-Sayed, A.A.H., 1995. Effect of drilling muds contamination on cement slurry properties. In: Presented at the Fourth Saudi Engineering Conference, pp. 287–295.

Galí, S., Ayora, C., Alfonso, P., Tauler, E., Labrador, M., 2001. Kinetics of dolomite–portlandite reaction: application to portland cement concrete. Cem. Concr. Res. 31, 933–939, http://dx.doi.org/10.1016/S0008-8846(01)00499-9.

Gasda, S.E., Bachu, S., Celia, M.A., 2004. Spatial characterization of the location of potentially leaky wells penetrating a deep saline aquifer in a mature sedimentary basin. Environ. Geol. 46, 707–720, http://dx.doi.org/10.1007/s00254-004-1073-5.

Gray, K.E., Podnos, E., Becker, E., 2009. Finite-element studies of near-wellbore region during cementing operations: Part I. SPE Dril. Complet., 127–136, http://dx.doi.org/10.2118/106998-PA.

Han, J., Carey, J.W., Zhang, J., 2012. Degradation of cement–steel composite at bonded steel-cement interfaces in supercritical CO_2 saturated brines simulating wellbore systems. In: Presented at the NACE International – Corrosion Conference and Expo 2012, pp. 151–179.

Han, J., Carey, J.W., Zhang, J., 2011a. A coupled electrochemical–geochemical model of corrosion for mild steel in high-pressure CO_2–saline environments. Int. J. Greenh. Gas Control 5, 777–787.

Han, J., Carey, J.W., Zhang, J., 2011b. Effect of debonded interfaces on corrosion of mild steel composites in supercritical CO_2-saturated brines. In: Presented at the NACE Annual Conference, Dallas, Texas, p. 14.

Harp, D.R., Pawar, R., Carey, J.W., Gable, C.W., 2016. Development of reduced order models of transient wellbore leakage at geologic carbon sequestration sites. Int. J. Greenh. Gas Control, http://dx.doi.org/10.1016/j.ijggc.2015.12.001.

Heathman, J., Beck, F., 2006. Finite element analysis couples casing and cement designs for HT/HP wells in East Texas. Soc. Pet. Eng., http://dx.doi.org/10.2118/98869-MS.

Hepple, R.P., Benson, S.M., 2005. Geologic storage of carbon dioxide as a climate change mitigation strategy: performance requirements and the implications of surface seepage. Environ. Geol. 47, 576–585.

Huerta, N.J., Hesse, M.A., Bryant, S.L., Strazisar, B.R., Lopano, C., 2015. Reactive transport of CO_2-saturated water in a cement fracture: application to wellbore leakage during geologic CO_2 storage. Int. J. Greenh. Gas Control., http://dx.doi.org/10.1016/j.ijggc.2015.02.006.

Huerta, N.J., Strazisar, B.R., Bryant, S.L., Hesse, M.A., 2014. Time-dependent fluid migration from a storage formation via leaky wells. Energy Procedia. In: 12th International Conference on Greenhouse Gas Control Technologies, GHGT-12 63, pp. 5724–5736, http://dx.doi.org/10.1016/j.egypro.2014.11.605.

Huerta, N.J., Hesse, M.A., Bryant, S.L., Strazisar, B.R., Lopano, C.L., 2013. Experimental evidence for self-limiting reactive flow through a fractured cement core: implications for time-dependent wellbore leakage. Environ. Sci. Technol. 47, 269–275, http://dx.doi.org/10.1021/es3013003.

Jacquemet, N., Pironon, J., Lagneau, V., Saint-Marc, J., 2012. Armouring of well cement in H_2S–CO_2 saturated brine by calcite coating – experiments and numerical modelling. Appl. Geochem. 27, 782–795, http://dx.doi.org/10.1016/j.apgeochem.2011.12.004.

Jacquemet, N., Pironon, J., Saint-Marc, J., 2008. Mineralogical changes of a well cement in various H_2S-CO_2(-brine) fluids at high pressure and temperature. Environ. Sci. Technol. 42, 282–288, http://dx.doi.org/10.1021/es070853s.

Jordan, A.B., Stauffer, P.H., Harp, D., Carey, J.W., Pawar, R.J., 2015. A response surface model to predict CO_2 and brine leakage along cemented wellbores. Int. J. Greenh. Gas Control 33, 27–39, http://dx.doi.org/10.1016/j.ijggc.2014.12.002.

Jung, H.B., Jansik, D., Um, W., 2013. Imaging wellbore cement degradation by carbon dioxide under geologic sequestration conditions using X-ray computed microtomography. Environ. Sci. Technol. 47, 283–289, http://dx.doi.org/10.1021/es3012707.

Jung, H.B., Kabilan, S., Carson, J.P., Kuprat, A.P., Um, W., Martin, P., Dahl, M., Kafentzis, T., Varga, T., Stephens, S., Arey, B., Carroll, K.C., Bonneville, A., Fernandez, C.A., 2014. Wellbore cement fracture evolution at the cement–basalt caprock interface during geologic carbon sequestration. Appl. Geochem. 47, 1–16, http://dx.doi.org/10.1016/j.apgeochem.2014.04.010.

Jung, H.B., Um, W., 2013. Experimental study of potential wellbore cement carbonation by various phases of carbon dioxide during geologic carbon sequestration. Appl. Geochem. 35, 161–172, http://dx.doi.org/10.1016/j.apgeochem.2013.04.007.

Kermani, M.B., Morshed, A., 2003. Carbon dioxide corrosion in oil and gas production—a compendium. Corrosion 59, 25.

King, G.E., King, D.E., 2013. Environmental risk arising from well construction failure: differences between barrier failure and well failure, and estimates of failure frequency across common well types, locations and well age. In: Society of Petroleum Engineers, SPE, http://dx.doi.org/10.2118/166142-MS.

Kutchko, B.G., Strazisar, B.R., Dzombak, D.A., Lowry, G.V., Thaulow, N., 2007. Degradation of well cement by CO_2 under geologic sequestration conditions. Environ. Sci. Technol. 41, 4787–4792, http://dx.doi.org/10.1021/es062828c.

Kutchko, B.G., Strazisar, B.R., Hawthorne, S.B., Lopano, C.L., Miller, D.J., Hakala, J.A., Guthrie, G.D., 2011. H_2S–CO_2 reaction with hydrated class H well cement: acid–gas injection and CO_2 co-sequestration. Int. J. Greenh. Gas Control 5, 880–888, http://dx.doi.org/10.1016/j.ijggc.2011.02.008.

Kutchko, B.G., Strazisar, B.R., Huerta, N., Lowry, G.V., Dzombak, D.A., Thaulow, N., 2009. CO_2 reaction with hydrated class H well cement under geologic sequestration conditions: effects of flyash admixtures. Environ. Sci. Technol. 43, 3947–3952, http://dx.doi.org/10.1021/es803007e.

Kutchko, B.G., Strazisar, B.R., Lowry, G.V., Dzombak, D.A., Thaulow, N., 2008. Rate of CO_2 attack on hydrated class H well cement under geologic sequestration conditions. Environ. Sci. Technol. 42, 6237–6242, http://dx.doi.org/10.1021/es800049r.

Liteanu, E., Spiers, C.J., 2011. Fracture healing and transport properties of wellbore cement in the presence of supercritical CO_2. Chem. Geol. 281 (February (3–4)), 195–210, http://dx.doi.org/10.1016/j.chemgeo.2010.12.008.

Luquot, L., Abdoulghafour, H., Gouze, P., 2013. Hydro-dynamically controlled alteration of fractured Portland cements flowed by CO_2-rich brine. Int. J. Greenh. Gas Control 16, 167–179, http://dx.doi.org/10.1016/j.ijggc.2013.04.002.

Lyons, W.C. (Ed.), 1996. Standard Handbook of Petroleum and Natural Gas Engineering, vol. 1. Gulf Publishing Company, Houston, TX.

Marty, N.C., Tournassat, C., Burnol, A., Giffaut, E.C., 2009. Influence of reaction kinetics and mesh refinement on the numerical modeling of concrete/clay interactions. J. Hydrol. 364, 58–72.

Mason, H.E., Du Frane, W.L., Walsh, S.D.C., Dai, Z., Charnvanichborikarn, S., Carroll, S.A., 2013. Chemical and mechanical properties of wellbore cement altered by CO_2-rich brine using a multianalytical approach. Environ. Sci. Technol. 47, 1745–1752, http://dx.doi.org/10.1021/es3039906.

Massazza, F., 1993. Pozzolanic cements. Cem. Concr. Compos. Spec. Issue Compos. Cem. 15, 185–214, http://dx.doi.org/10.1016/0958-9465(93)90023-3.

Matteo, E.N., Scherer, G.W., 2012. Experimental study of the diffusion-controlled acid degradation of class H Portland cement. Int. J. Greenh. Gas Control 7, 181–191.

Metz, Bert, Ogunlade Davidson, Heleen de Coninck, Manuela Loos, Leo Meyer (Eds.), 2005. IPCC Special Report on Carbon Dioxide Capture and Storage. Cambridge University Press http://www.ipcc.ch/publications_and_data/publications_and_data_reports.shtml#2.

Nelson, E.B., Guillot, D. (Eds.), 2006. Well Cementing. , 2nd ed. Schlumberger, Developments in Petroleum Science.

Nešić, S., 2007. Key issues related to modelling of internal corrosion of oil and gas pipelines – a review. Corros. Sci. 49, 4308–4338, http://dx.doi.org/10.1016/j.corsci.2007.06.006.

NETL., 2011. Carbon Sequestration Program: Technology Program Plan – Enhancing the Success of Carbon Capture and Storage Technologies, Applied Research and Development from Lab- to Large-Field Scale. National Energy Technology Laboratory, Morgantown.

Neville, A.M., 2004. Properties of Concrete, 4th ed. John Wiley and Sons, New York, NY.

Newell, D.L., Carey, J.W., 2013. Experimental evaluation of wellbore integrity along the cement–rock boundary. Environ. Sci. Technol. 47, 276–282, http://dx.doi.org/10.1021/es3011404.

Nicot, J.-P., 2009. A survey of oil and gas wells in the Texas Gulf Coast, USA, and implications for geological sequestration of CO_2. Environ. Geol. 57, 1625–1638, http://dx.doi.org/10.1007/s00254-008-1444-4.

Nygaard, R., Salehi, S., Lavoie, R., 2014. Effect of dynamic loading on wellbore leakage for the Wabamum Area CO_2 Sequestration Project. J. Can. Pet. Technol. 53, 69–82, http://dx.doi.org/10.2118/146640-PA.

Pawar, R., Bromhal, G., Carroll, S., Chu, S., Dilmore, R., Gastelum, J., Oldenburg, C., Stauffer, P., Zhang, Y., Guthrie, G., 2014. Quantification of key long-term risks at CO_2 sequestration sites: latest results from US DOE's National Risk Assessment Partnership (NRAP) project. Energy Procedia 63, 4816–4823.

Papadakis, V.G., 1999. Effect of fly ash on Portland cement systems: Part I. Low-calcium fly ash. Cem. Concr. Res. 29, 1727–1736, http://dx.doi.org/10.1016/S0008-8846(99)00153-2.

Peška, P., Zoback, M.D., 1995. Compressive and tensile failure of inclined well bores and determination of in situ stress and rock strength. J. Geophys. Res. Solid Earth 100, 12791–12811, http://dx.doi.org/10.1029/95JB00319.

Rahman, S.S., Chilingarian, G.V., 1995. Casing Design Theory and Practice. Elsevier.

Received by OCD: 6/29/2026

Randhol, P., Carlsen, I.M., 2008. Assessment of sustained well integrity on the Norwegian Continental shelf. In: 4th Annual IEA Greenhouse Gas R&D Programme Wellbore Integrity Network Meeting, Paris, France, March 17–18th.

Ravi, K., Bosma, M., Gastebled, O., 2002. Safe and economic gas wells through cement design for life of the well. Soc. Pet. Eng., http://dx.doi.org/10.2118/75700-MS.

Rimmelé, G., Barlet-Gouédard, V., Porcherie, O., Goffé, B., Brunet, F., 2008. Heterogeneous porosity distribution in Portland cement exposed to CO_2-rich fluids. Cem. Concr. Res. 38, 1038–1048, http://dx.doi.org/10.1016/j.cemconres.2008.03.022.

Scherer, G.W., Kutchko, B.G., Thaulow, N., Duguid, A., Mook, B., 2011. Characterization of cement from a well at Teapot Dome Oil Field: implications for geological sequestration. Int. J. Greenh. Gas Control 5, 115–124, http://dx.doi.org/10.1016/j.ijggc.2010.06.010.

Schwind, B.E., Payne, M.L., Otten, G.K., Pattillo, P.D., 2001. Development of leak resistance in industry standard OCTG connections using finite element analysis and full scale testing. In: Offshore Technology Conference, OTC, http://dx.doi.org/10.4043/13050-MS.

Shehata, M.H., Thomas, M.D.A., Bleszynski, R.F., 1999. The effects of fly ash composition on the chemistry of pore solution in hydrated cement pastes. Cem. Concr. Res. 29, 1915–1920, http://dx.doi.org/10.1016/S0008-8846(99)00190-8.

Shen, J.C., Pye, D.S., 1989. Effects of CO_2 attack on cement in high-temperature applications. Soc. Pet. Eng., http://dx.doi.org/10.2118/18618-MS.

Sideris, K.K., Savva, A.E., Papayianni, J., 2006. Sulfate resistance and carbonation of plain and blended cements. Cem. Concr. Compos. 28, 47–56, http://dx.doi.org/10.1016/j.cemconcomp.2005.09.001.

Talabani, S., Atlas, B., Al-Khatiri, M.B., Islam, M.R., 2000. An alternate approach to downhole corrosion mitigation. J. Pet. Sci. Eng. 26, 41–48, http://dx.doi.org/10.1016/S0920-4105(00)00019-X.

Thiercelin, M., Dargaud, B., Baret, J., Rodriguez, W., 1997. Cement design based on cement mechanical response. In: Proceedings of the 1997 SPE Annual Technical Conference and Exhibition. Pi, 19971005–19971008, San Antonio, TX, USA, pp. 337–348.

Türkel, S., Felekoğlu, B., Dulluç, S., 2007. Influence of various acids on the physico-mechanical properties of pozzolanic cement mortars. Sadhana 32, 683–691, http://dx.doi.org/10.1007/s12046-007-0048-0.

Ulm, F.-J., Lemarchand, E., Heukamp, F.H., 2003. Elements of chemomechanics of calcium leaching of cement-based materials at different scales. Eng. Fract. Mech. 70, 871–889, http://dx.doi.org/10.1016/S0013-7944(02)00155-8.

Um, W., Jung, H.B., Suh, D.M., Fernandez, C.A., 2014. Geochemical and Geomechanical Effects on Wellbore Cement Fractures: Data Information for Wellbore Reduced Order Model (PNNL-23148). Pacific Northwest National Laboratory.

Viswanathan, H.S., Pawar, R.J., Stauffer, P.H., Kaszuba, J.P., Carey, J.W., Olsen, S.C., Keating, G.N., Kavetski, D., Guthrie, G.D., 2008. Development of a hybrid process and system model for the assessment of wellbore leakage at a geologic CO_2 sequestration site. Environ. Sci. Technol. 42, 7280–7286, http://dx.doi.org/10.1021/es800417x.

Walsh, S.D.C., Carroll, S., 2013. Fracture-scale model of immiscible fluid flow. Phys. Rev. E 87, 013012, http://dx.doi.org/10.1103/PhysRevE.87.013012.

Walsh, S.D.C., Frane, W.L.D., Mason, H.E., Carroll, S.A., 2013. Permeability of wellbore-cement fractures following degradation by carbonated brine. Rock Mech. Rock Eng. 46, 455–464, http://dx.doi.org/10.1007/s00603-012-0336-9.

Walsh, S.D.C., Mason, H.E., Du Frane, W.L., Carroll, S.A., 2014a. Experimental calibration of a numerical model describing the alteration of cement/caprock interfaces by carbonated brine. Int. J. Greenh. Gas Control 22, 176–188, http://dx.doi.org/10.1016/j.ijggc.2014.01.004.

Walsh, S.D.C., Mason, H.E., Du Frane, W.L., Carroll, S.A., 2014b. Mechanical and hydraulic coupling in cement–caprock interfaces exposed to carbonated brine. Int. J. Greenh. Gas Control 25, 109–120, http://dx.doi.org/10.1016/j.ijggc.2014.04.001.

Watson, T., Bachu, S., 2008. Identification of wells with high CO_2-leakage potential in mature oil fields developed for CO_2-enhanced oil recovery. Soc. Pet. Eng., http://dx.doi.org/10.2118/112924-MS.

Wenning, Q.C., Huerta, N.J., Hesse, M.A., Bryant, S.L., 2013. Reactive flow channelization in fractured cement-implications for wellbore integrity. Energy Procedia 37, 5773–5780, http://dx.doi.org/10.1016/j.egypro.2013.06.500.

Wigand, M., Kaszuba, J.P., Carey, J.W., Hollis, W.K., 2009. Geochemical effects of CO_2 sequestration on fractured wellbore cement at the cement/caprock interface. Chem. Geol. 265, 122–133.

Wolery, T.J., Jackson, K.J., Bourcier, W.L., Bruton, C.J., Viani, B.E., Knauss, K.G., Delany, J.M., 1990. Current status of the EQ3/6 Software package for geochemical modeling. ACS Symp. Ser. 416, 104–116.

Yalcinkaya, T., Radonjic, M., Willson, C.S., Bachu, S., 2011. Experimental study on a single cement-fracture using CO_2 rich brine. Energy Procedia 4, 5335–5342.

Zhang, L., Dzombak, D.A., Kutchko, B.G., 2015. Wellbore cement integrity under geologic carbon sequestration conditions. In: Morreale, B., Shi, F. (Eds.), Novel Materials for CO_2 Mitigation Technology. Elsevier, United States of America.

Zhang, L., Dzombak, D.A., Nakles, D.V., Brunet, J.-P.L., Li, L., 2013. Reactive transport modeling of interactions between acid gas ($CO_2 + H_2S$) and pozzolan-amended wellbore cement under geologic carbon sequestration conditions. Energy Fuels 27, 6921–6937, http://dx.doi.org/10.1021/ef401749x.

Zhang, M., Bachu, S., 2011. Review of integrity of existing wells in relation to CO_2 geological storage: what do we know? Int. J. Greenh. Gas Control 5, 826–840, http://dx.doi.org/10.1016/j.ijggc.2010.11.006.

EXHIBIT 9

Received by OCD: 6/29/2026

International Journal of Greenhouse Gas Control 21 (2014) 101–112

Contents lists available at ScienceDirect

International Journal of Greenhouse Gas Control

journal homepage: www.elsevier.com/locate/ijggc

The Sleipner storage site: Capillary flow modeling of a layered CO_2 plume requires fractured shale barriers within the Utsira Formation

Andrew J. Cavanagh [a,b,*], R. Stuart Haszeldine [a]

[a] SCCS, School of GeoSciences, University of Edinburgh, Edinburgh EH9 3JW, Scotland, UK
[b] Halliburton, Ottawa, Ontario K1Y 1B4, Canada

ARTICLE INFO

Article history:
Received 4 September 2012
Received in revised form
20 November 2013
Accepted 21 November 2013
Available online 22 January 2014

Keywords:
Saline aquifer storage
CO_2 sequestration
Invasion percolation model
Mass balance calibration
Ice sheet loading
Caprock seal integrity

ABSTRACT

To prevent ocean acidification and mitigate greenhouse gas emissions, it is necessary to capture and store carbon dioxide. The Sleipner storage site, offshore Norway, is the world's first and largest engineered waste repository for a greenhouse gas. CO_2 is separated from the Sleipner gas condensate field and stored in the pore space of the Utsira Formation, a saline aquifer approximately 1 km below the surface and 200 km from the coast. Statoil, the field operator, has injected almost 1 Mt/yr of captured CO_2 into the storage site since 1996. The buoyant CO_2 plume ascended rapidly through eight thin shale barriers within the aquifer to reach the top seal in less than three years. The plume's progress has been monitored by eight seismic surveys, as well as gravimetric and electromagnetic monitoring, which record the spreading of nine thin CO_2 layers. This paper presents a capillary flow model using invasion percolation physics that accurately matches the plume's geometry. The approach differs from standard Darcy flow simulations, which fail to match the plume geometry. The calibrated capillary flow simulation indicates that a mass balance for the plume is likely, but can only replicate the plume geometry if the thin intra-formational shale barriers are fractured. The model enables an estimate of the shale barrier behavior and caprock performance. The fractures are very unlikely to have been caused by CO_2 injection given the confining stress of the rock and weak overpressure of the plume, and so fracturing must pre-date injection. A novel mechanism is suggested: the deglaciation of regional ice sheets that have rapidly and repeatedly unloaded approximately 1 km of ice. The induced transient pore pressures are sufficient to hydro-fracture thin shales. The fractures enable fast CO_2 ascent, resulting in a multi-layered plume. Shallow CO_2 storage sites in the Northern North Sea and other regions that have been loaded by Quaternary ice sheets are likely to behave in a similar manner.

© 2014 The Authors. Published by Elsevier Ltd. Open access under CC BY license.

1. Introduction

Climate change and ocean acidification are driven by high rates of CO_2 emission to the atmosphere. One contribution to the mitigation of CO_2 emissions is carbon capture and storage, CCS (Lovell, 2011). This is proposed by the G8 and the International Energy Agency as an essential technology for lowering greenhouse gas emissions. CCS reduces the emission of CO_2 at a power station, or other large industrial sources such as oil and gas fields. This captured CO_2 is compressed, transported by pipeline, and injected for storage into porous rock formations deep below the land or sea surface. Large-scale sites have been demonstrating engineered CO_2 storage technology for nearly two decades. At the Sleipner field, CO_2 is produced with natural gas and condensate, separated from the production stream, and compressed. The supercritical CO_2 is then injected into the Utsira Formation, offshore Norway. This is the longest running carbon capture and storage experiment in the world, with more than 14 Mt of supercritical CO_2 injected during the period 1996–2013. The injection schedule is intended to remain at around 0.9 Mt/yr until around 2020, separating and storing CO_2 from the West Sleipner gas-condensate field to prevent climate change. This is incentivized by the Norwegian state tax on offshore petroleum industry emissions, commencing in 1991 at NOK 210 and increasing to NOK 410 in 2013, equivalent to about $65 per tonne of CO_2.

The storage site, a saline formation and sandstone aquifer, is 800 m below sea level (mbsl). This is considered to be a shallow depth setting for a storage environment (Chadwick et al., 2008) as the pressure and temperature conditions are likely to be close to the critical point above which CO_2 becomes a more buoyant

* Corresponding author. Current address: Statoil Research Centre, Trondheim 7053, Norway.
E-mail address: acava@statoil.com (A.J. Cavanagh).

1750-5836 © 2014 The Authors. Published by Elsevier Ltd. Open access under CC BY license.
http://dx.doi.org/10.1016/j.ijggc.2013.11.017

Received by OCD: 6/29/2026

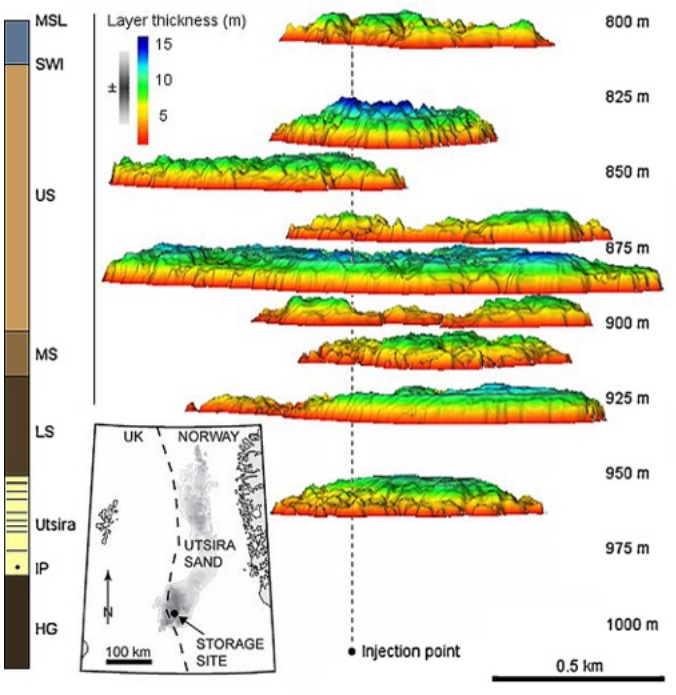


Fig. 1. The Sleipner plume profile, viewed from the southeast, circa July 2002. The figure shows the distribution of injected CO_2 after 5 Mt of injected CO_2 (Bickle et al., 2007). The nine plume layers are well defined aerially, having ponded beneath intra-formational shales within the Utsira Sand. The uncertainty relating to layer thickness is high. The ninth layer first appeared in 1999, indicating that the CO_2 has migrated approximately 220 m vertically from the injection point (IP) at 1012 mbsl in 3 years. The left panel is a regional stratigraphic column: MSL, Mean Sea Level; SWI, Sediment Water Interface; The Nordland Group extends from the caprock to seafloor, and is subdivided into three seals: US, Upper Seal (Pleistocene); MS, Middle Seal (Upper Pliocene); LS, Lower Seal (Upper Pliocene); Utsira, storage site (Middle Miocene–Early Pliocene); HG, Hordland Group (Early Miocene).

gas phase. The overlying Nordland Group, which extends from the top of the Utsira Formation to the seafloor, is predominantly shale (Fig. 1), and is expected to provide a caprock with a high threshold pressure, sufficient to seal the site and prevent leakage of the buoyant CO_2 fluid over several millennia, i.e. the timescale required to offset climate change (Lindeberg and Bergmo, 2003). Saline formations worldwide are considered to be candidates for carbon sequestration because of their suitable depths, large storage volumes, and common occurrence. However, one of the critical uncertainties for saline formation storage is the ability of the caprock (primary seal), and the overlying containment geology (secondary seals), to retain buoyant CO_2 without leakage. The fluid flow processes currently occurring in the Sleipner storage site provide a crucial exemplar for saline formation storage projects worldwide.

Published interpretations of a series of seismic reflection surveys show that, by 1999, the Sleipner CO_2 plume had ascended more than 200 m vertically within the Utsira Formation from the injection point (1012 mbsl) to the caprock (800 mbsl). The plume has encountered and breached eight shale barriers within the storage site: seven thin shales that are approximately 1–2 m thick, and an uppermost thick shale that is 6–7 m thick and geologically similar to the primary seal (Gregersen and Johannessen, 2001; Zweigel et al., 2004). These shale barriers result in 10–20 m thick CO_2 layers that are vertically stacked and extend laterally for hundreds of meters. Biennial monitoring of the plume behavior and the resultant six seismic reflection surveys make this experiment ideally suited to numerical modeling studies (Hamborg et al., 2003; Zweigel et al., 2004; Hellevang, 2006). The areal distribution of CO_2 stored within the storage site has been precisely mapped from the seismic surveys (Chadwick et al., 2006; Bickle et al., 2007). However, no published dynamic model to date has accurately replicated the layered morphology of the plume or flow behavior, and three significant aspects of the plume are poorly understood, as outlined below.

Fundamental aspects of the CO_2 plume layering are examined by constructing a mass-balanced flow model to test the physical containment processes through iterative numerical simulation. The simulations are calibrated to published observations. Capillary flow, not Darcy flow, is applied to obtain a good match with observations. It is essential for the calibration that the shale barriers within the Utsira Formation have high vertical permeabilities. This implies that the shales may be fractured. A novel mechanism is proposed to account for fracturing prior to CO_2 injection: transient fluid overpressure during rapid deglaciation.

2. Unexplained aspects of the plume

Firstly, there is a significant uncertainty concerning mass-balance estimates for the plume. To illustrate this, consider estimates for the uppermost layer alone, circa July 2002, equivalent to 5 Mt injected, bearing in mind that the uppermost layer is the best constrained portion of the plume with respect to observational data (Chadwick et al., 2008). The CO_2 volume in this layer is estimated to be approximately 110–165 thousand cubic meters (Chadwick et al., 2009). Assuming an upper layer density of 426 kg/m^3 (after Bickle et al., 2007), this is equivalent to a mass of 0.05–0.07 Mt. Although Chadwick and co-workers (2009) favor the upper end of this range, 0.07 Mt is considerably less than estimates of 0.11 Mt (Bickle et al., 2007) and 0.16 Mt (Singh et al., 2010). This wide disparity in outcomes stems partly from (a) uncertainty concerning the plume temperature profile (Fig. 2a), with Singh and co-workers (2010) assuming a much colder plume with an uppermost layer density of 760 kg/m^3; and (b) poorly constrained assumptions regarding layer thickness (Fig. 2b), which are unresolvable at less than 15 m thick given the seismic resolution (Arts et al., 2004). This uncertainty is further compounded by poorly constrained gas saturations for the plume layers. All three aspects are discussed further below.

Secondly, despite the layer thickness uncertainty, the plume morphology indicates that column heights for trapped CO_2 are unexpectedly low. The only published laboratory measurements for the caprock threshold pressure (Springer and Lindgren, 2006; Harrington et al., 2009), from a cored production well, 15/9A-11, close to the storage site, suggest a range of 1.6–1.9 MPa, i.e. the fluid pressure necessary for CO_2 to break through a low permeability rock. If this range is applicable to the shale barriers within the Utsira Formation, such a scenario would result in CO_2 column heights of hundreds of meters (Springer and Lindgren, 2006). However, estimated column heights for the layered plume consistently fall within the range 7–14 m (Chadwick et al., 2005, 2006; Bickle et al., 2007). These thin layers occur beneath all three-barrier types: (a) the 1–2 m thin shales within the formation; (b) the uppermost 7 m thick shale barrier; and (c) the much thicker Nordland Group shale caprock that forms the primary seal.

Thirdly, the plume flow behavior is not indicative of sealing shale barriers punctuated by faults, holes or penetrated by a high permeability chimney or sand injectite (Zweigel et al., 2004), and the means of CO_2 ascent is poorly understood. The plume initially ascended 200 m vertically through the eight shale barriers in less than three years (Chadwick et al., 2006), resulting in a 'pancake stack' of layers. If the laterally extensive shales had acted as seals, preventing the vertical migration of CO_2, the plume would have taken much longer to breakthrough, and its behavior would have been more akin to a 'zig-zag' distribution with lateral offsets,

Received by OCD: 6/29/2026

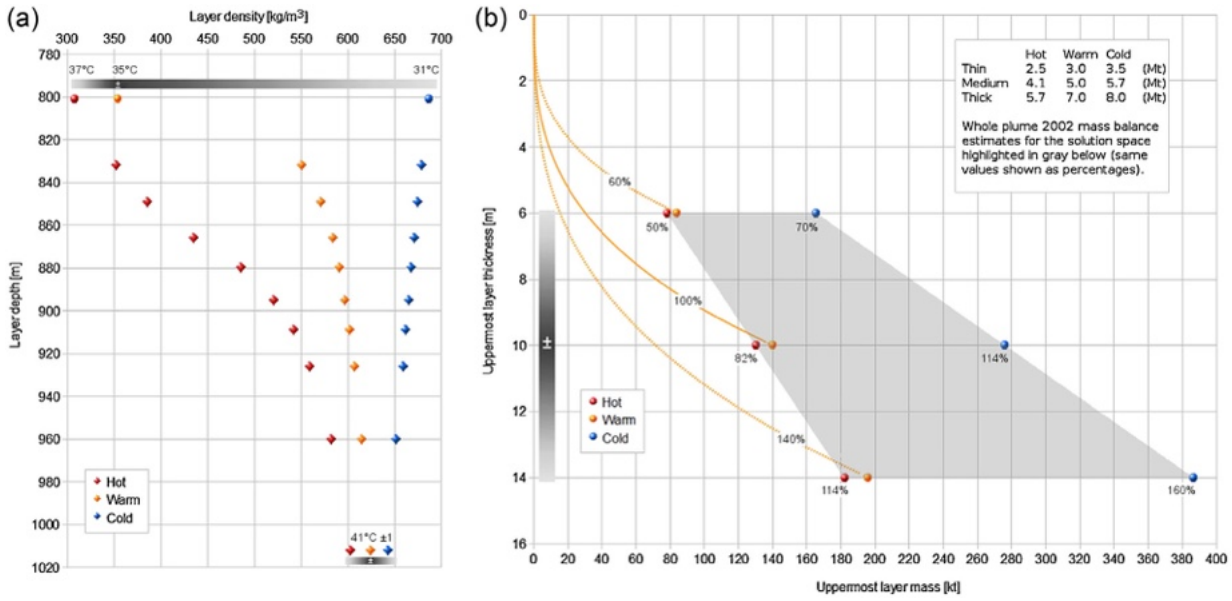


Fig. 2. Mass balance uncertainty related to plume density and layer thickness assumptions: (a) layer density variations assuming linear geothermal gradients and the common range of uncertainty associated with the plume temperature profile; (b) layer thickness versus mass for the uppermost CO_2 layer, and related mass-balance estimates for the whole plume circa July 2002 (equivalent to 5 Mt injected). The sensitivity of mass estimate for a single layer with respect to layer thickness is apparent (orange curves). A 10 m thick layer shows a mass variation of ±40% (80–200 kt), for a 35 °C scenario, and a thickness uncertainty of ±4 m. As the trap fills, the volume and related mass increases rapidly. For gas layers with a fixed aerial footprint but uncertain thickness, it can be shown that the uncertainty in volume is equivalent to the error on thickness. Compounding this with density uncertainty, the solution space for a 5 Mt mass balance (gray trapezoid) varies from 50% (thin, warm layers) to 160% (thick, cool layers).

resulting from the CO_2 tracking along the base of a barrier until encountering a hole through which to escape up to the next barrier, and then repeating this behavior.

2.1. Mass balance estimates

Addressing the mass balance question first, available areal mapping of the plume layers derived from time-lapse seismic reflection survey images (Bickle et al., 2007) are combined with layer-thickness estimates (Chadwick et al., 2009) to build a three-dimensional representation of the CO_2 plume (Fig. 1). The approach assumes a flat gas–water contact for the plume layers, which implies that each layer has backfilled the trap as a gravitationally ponding fluid. The model provides an insight into the volumetric relationship between layer thickness and mass balance (Fig. 2). Recent published estimates of volume and mass balance appear to have been primarily hampered by uncertainty in layer thickness and plume density (Fig. 2). For the uppermost layer, circa 2002, thickness estimates vary from 4 to 7 m (Chadwick et al., 2005; Bickle et al., 2007). The CO_2 layers circa 2006 have recently been estimated as 10 m thick (Lippard et al., 2008; Chadwick et al., 2009). Both these estimates are thinner than the limit of phenomena resolvable by conventional seismic reflection surveys at this depth (Arts et al., 2004; Chadwick et al., 2006). A case has been made for amplitude tuning of the Sleipner seismic to produce greater precision (Chadwick et al., 2006); however, the sensitivity of this seismic interpretation technique is such that the amplitude does not discriminate between layers more than 4 m thick and less than 15 m thick. Furthermore, the thin shale barriers within the aquifer are unresolvable on the baseline 1994 seismic (Arts et al., 2004) making tuning even more difficult. Published estimates of the CO_2 volume in the top layer (110,000 m^3 from amplitude analysis, and 165,000 m^3 from structure) differ by 150% for the same seismic survey (Chadwick et al., 2009). Although structure estimates are considered to be more reliable than amplitude (Chadwick et al., 2008), there is no method to discriminate between them.

An additional uncertainty arises from saturation profiling, which discerns between pores filled with brine and pores filled with CO_2 above a poorly constrained level of saturation (Arts et al., 2004). It follows from the commonly used Gassmann equation (Gassmann, 1951) that: (a) very low saturations of less than a few percent are undetectable; (b) a strong correlation emerges as the gas saturation increases from a few percent to around thirty percent; and (c) for saturations much above thirty percent, it is difficult to distinguish between moderate and high saturations. It follows that the 80% gas saturation that is commonly assumed for the Sleipner plume, while reasonable (Chadwick et al., 2005; Bickle et al., 2007), remains uncertain (Lumley, 2008). If the 80% assumption represents a reasonable upper limit to the mean saturation for the plume, the lower limit could be as low as 40%, halving mass balance estimates premised on the widely assumed high-saturation value.

Finally, the liminal pressure and temperature conditions of the plume with respect to the critical point of CO_2 (31 °C and 7.4 MPa) compound the uncertainty. The ambient temperature at the injection depth is reasonably well constrained at 41 ± 1 °C (Bickle et al., 2007); however, the temperature at the top of the plume is much more poorly constrained at around 34 ± 3 °C (Singh et al., 2010). This results in a potential density range for CO_2 in the uppermost layer of 300–700 kg/m^3; a mid-range scenario is assumed, with a temperature of 35 °C at the caprock and a linear geothermal gradient to the injection depth at 41 °C for the flow simulations that follow (orange diamonds, Fig. 2a). However, a brief consideration of different thickness and density scenarios (assuming 80% saturation) with respect to the solution space for mass balance (gray area, Fig. 2b) suggests that a cold high-density plume requires an upper layer that is at least 8–9 m thick, circa July 2002 and 5 Mt injected; while a hot low-density plume exceeds a mass balance with layers that are greater than 13 m thick. The uppermost layer thickness necessary for a mass balance, circa July 2002 and 5 Mt injected, lies in the range 8–13 m.

Consequently, these compounded uncertainties in mass balance (layer thickness, gas saturation and gas density) are highly sensitive to small changes in assumptions that are unresolvable by remote

Received by OCD: 6/29/2026

geophysical monitoring given the broadly constrained fields of pressure, temperature and saturation. Although an accurate mass balance estimate would be desirable to confirm site integrity with respect to the present-day caprock behavior, this aspect of Sleipner is likely to remain elusive due to the uncertainties inherent in remote geophysical monitoring of gas plumes.

3. Modeling methodology

To better understand the mass balance, spatial distribution and flow behavior of the plume, a numerical flow model of the storage site is constructed. This three-dimensional model consists of a geological framework of nine alternating intervals of sandstone and shale that extends from the base of the Utsira Formation below the injection point to the primary seal above the storage site. Published morphology maps for each CO_2 layer (Bickle et al., 2007) are used as the topography for the base of each shale barrier, assuming a flat gas–water contact for the layers. This implies that the CO_2 is ponding, and the layers are close to equilibrium with respect to any Darcy flow dynamics (Cavanagh, 2013). The flow of CO_2 within the storage site is then simulated with an invasion percolation simulator (Permedia, 2012), assuming percolation as a function of CO_2 capillary pressure and shale threshold pressure. This approach examines capillary flow in a deep saline formation that is segmented by thin laterally extensive horizontal shale layers. Scenarios are tested for resemblance to the plume morphology and then quantified for CO_2 in place to arrive at the best mass balance scenario for the simulated plume with respect to the known injected volume.

3.1. Conceptual model

The conceptual model for the simulation is a plume of vertically stacked buoyant CO_2 layers that are trapped in the sandstone intervals as thin but highly saturated layers, breaking through the shale barriers as a result of percolation. Percolation occurs when the threshold pressure of the shale barrier is exceeded by the buoyant gas capillary pressure of the trapped CO_2 layer (Boettcher et al., 2002; Carruthers, 2003). The 3D model is calibrated by adjusting the breakthrough threshold pressures of the shales to match published estimates of layer thickness (column heights underlying shale barriers) and the areal distribution for trapped CO_2 derived from 4D seismic.

The Sleipner plume is likely to ascend as a result of gravity segregation (Singh et al., 2010), given the strong density contrast between the brine and CO_2, and the high permeability of the Utsira Formation sandstones. However, the crucial distinction between our model and other approaches is our assumption concerning the dominant physics of the flow process. The buoyant separate phase behavior of CO_2 in the formation not only promotes gravity segregation, but also results in strong capillary forces at the interface between the ascending gas (non-wetting fluid) and the brine (wetting fluid) in the pore throats of the geological media, which manifest as threshold pressures for the sandstones and shales. This is quite distinct from other modeling approaches that assume a Darcy flow regime, where the plume behavior is primarily a function of the interplay between viscosity, pressure gradients, and permeability. If capillary forces dominate over viscous forces, the plume will ascend and backfill beneath flow barriers, manifesting a sensitivity to the topography at the base of each shale barrier (Cavanagh, 2013). Given the known correlation in shape between the upper layers and the basal topography of the caprock and underlying thick shale, it is proposed that the flow behavior may be best characterized as a gravity-dominated percolation phenomenon, as explained below.

3.2. Choice of simulator

Previous attempts to model the distribution of CO_2 within the Utsira Formation have used fluid flow software based on Darcy flow physics. To obtain multiple layers of CO_2, these have either imposed a discrete vertical pathway to by-pass the thin shales within the Formation (Chadwick et al., 2006; Hermanrud et al., 2009, 2010) or assumed a convenient vertical juxtaposition of pre-existing holes (erosional or otherwise) for the eight intra-formational shale barriers. These simulations fail to quantitatively or qualitatively reproduce the multi-layered CO_2 plume. To quote Chadwick et al. (2006) '*observed fluxes derived from the seismic data, do not match the flow simulation*'. In this approach, a flow simulator based on a different flow physics is used, and a different workflow undertaken to achieve a very good match and calibrated mass balance.

Permedia Migration is a multi-phase invasion percolation simulator. The simulator uses capillary threshold pressures and fluid density descriptions for oil, gas and CO_2. Assuming a flow domain dominated by capillary and gravity forces, invasion percolation describes the behavior of an immiscible fluid (CO_2) that is migrating, or percolating into, a porous medium (sandstones and shales). Commonly known as drainage within petroleum systems modeling, as distinct from imbibition, the buoyant phase displaces the original pore fluid (brine). Invasion percolation is commonly applied to slow moving immiscible fluids in geological flow systems. Below a critical flux velocity threshold, such flow systems tend to self-organize into discrete migration pathways and pooling traps (de Gennes et al., 2004). Percolation theory has been successfully applied to the invasion of non-wetting fluids such as oil and gas into water-wet porous geological media when studying regional hydrocarbon migration and local hydrocarbon field charge processes (Carruthers and Ringrose, 1998; Boettcher et al., 2002; Glass and Yarrington, 2003). The approach is valid at low flux rates, as the viscosity contribution to flow is negligible and the viscous-dominated Darcy flow approximation breaks down. Under capillary-dominated conditions the immiscible fluid is either migrating along a pathway at a low critical saturation or, is backfilling and flooding a trap at a higher saturation not exceeding the maximum gas saturation for the porous medium (Cavanagh and Rostron, 2013).

The model presented here differs significantly from earlier conceptual models of the storage site (e.g. Hellevang, 2006; Chadwick et al., 2008; Hermanrud et al., 2009, 2010) where researchers have assumed Darcy flow along a pressure gradient via holes in the shale barriers. This study assumes that the thin shales represent laterally continuous barriers to flow. While a Darcy flow model requires a rising cascade of fluid through the sandstone and around the shales, via holes or breaks in the shale succession, the approach presented here suggests a simpler hypothesis: the vertical stacking of kilometer-wide and meter-thick CO_2 layers that are the result of buoyant gas percolating through the vertical heterogeneity of sandstones and shales found in the Utsira Formation, in a similar manner to hydrocarbon migration and trap charge in petroleum systems, as appropriate for two-phase flow with a low capillary number (England et al., 1987). The capillary flow and ponding hypothesis does not require the unlikely geological coincidence of nine vertically aligned holes in the shales through which fluid cascades within the storage site.

3.3. Sleipner capillary number

An invasion percolation simulation assumes a dominance of capillary and gravity forces over viscous forces. The interplay of forces (viscous, capillary and gravity) in reservoir models is commonly defined using scaling-group theory (Ringrose et al., 1993; Li and Lake, 1995), with the commonly accepted limiting condition

Received by OCD: 6/29/2026

Table 1
A capillary number estimate for the Sleipner injection rate. *Ca*, capillary number; μ, viscosity of formation water; γ, interfacial tension between CO_2 and brine; *M*, mass per unit time; *Q*, volume per unit time; *q*, flux, volume per unit area per unit time; the calculation assumes an injection density of 630 kg/m^3, a perforation length of 50 m, an ascent width from the well of 1 m, a porosity of 0.36 and a near-well gas saturation of 80%. The boundary condition for capillary flow is 10^{-4} (England et al., 1987).

Capillary number	Injection rate	Near-well capillary number
$Ca = \mu q/\gamma$	$M \sim 1$ Mt/yr	$Ca = 0.0007 \times 0.0035/0.027$
$\mu \sim 0.7$mPa s	$Q \sim 0.05$ m^3/s	$Ca = 9 \times 10^{-5}$
$\gamma \sim 27$ mN/m	$q \sim 3.5$ mm/s	$Ca \sim 1 \times 10^{-4}$

for invasion percolation being that the capillary force must exceed the viscous force by a ratio of ten thousand-to-one. In other words, the capillary number, Ca, is less than 10^{-4}:

$$\text{Capillary number}, Ca = \frac{\mu q}{\gamma} \quad (1)$$

where, *Ca*, the capillary number for a given flow regime; μ, the viscosity of the more viscous fluid in a two-phase system; *q*, the volumetric flux; γ, the interfacial tension between the invading phase and resident phase.

Under these conditions, invasion percolation is a reasonable approximation for the flow physics. For example hydrocarbon migration typically has a capillary number of 10^{-10}–10^{-14} (England et al., 1987). If the capillary number is less than 10^{-4}, flow modeling lends itself to fast invasion percolation simulations which yield high-resolution numerical solutions (Carruthers, 2003). With respect to the Sleipner CO_2 plume, the viscosity of the brine (0.7–0.8 mPas) and interfacial tension between the brine and CO_2 (25–27 mN/m) have been estimated (Singh et al., 2010). Therefore, the limiting migration rate ($Ca \sim 10^{-4}$) for the storage site can be calculated as 3–4 mm/s. This fits well with observations, as the Sleipner CO_2 plume flux is reasonably well constrained both vertically and horizontally: (a) the plume reached the caprock in 1999, approximately 3 years after injection began from the well 210 m below – an observed ascent rate of about 70 m/yr or 2 μm/s; (b) the plume has spread laterally beneath the caprock, and is about 0.5 km wide (E–W) and 3 km long (N–S) after a decade – an observed lateral flux rate of less than 300 m/yr or 10 μm/s.

It follows that the capillary number for the plume ($Ca < 10^{-7}$) is much lower than the necessary limit for a viscous-dominated Darcy flow simulation. The CO_2 ascent and lateral spreading is very likely to be dominated by buoyancy and capillary forces, and therefore highly sensitive to contrasts in formation and shale threshold pressure (Table 1). Given these flow rate indications, it makes sense, a priori, to model the plume distribution with an invasion percolation simulator.

The Young–Laplace equation describes the governing physics: a capillary pressure occurs at an interface between two immiscible fluids such as CO_2 and brine. This equation, named after the Enlightenment scientists who discovered the principles of capillary action (Young, 1805; Laplace, 1806), is commonly used for multi-phase migration models. The pressure is a result of the tension of the surface that forms at the interface between the two fluids. A popular expression of the Young–Laplace equation (Eq. (2a)) relates the gravitationally stable column height of an oil or gas trap, and related capillary pressure, to the threshold pressure of the rock at which breakthrough occurs (Hobson, 1954). By exchanging the capillary pressure term with the density difference between the two fluids, the column height of the buoyant fluid can be determined (Eqs. (2b) and (2c)):

$$\text{Threshold pressure}, Pth = \frac{2\gamma \cos\theta}{r} \quad (2a)$$

$$\text{Capillary pressure}, Pc = \Delta\rho g h \quad (2b)$$

$$\text{Breakthrough condition}, \Delta\rho g h = \frac{2\gamma \cos\theta}{r} \quad (2c)$$

Where *Pth* is the threshold pressure of the rock at which breakthrough occurs; γ, the interfacial tension between the invading phase and resident phase; θ, the wetting angle between the invading phase and the rock (a low angle results in a high threshold pressure as the cosine value approaches unity); *r*, the representative pore throat radius for the rock. *Pc*, the capillary pressure of the invading phase at the interface; $\Delta\rho$, the density difference between the two phases; *g*, standard gravity; *h*, the column height of the invading phase.

If the capillary pressure does not exceed the threshold pressure, the fluid will pool beneath the shale and back-fill the shale topography until a spill-point is reached. The CO_2 will then migrate laterally until trapped again. However, if the capillary pressure at the top of the CO_2 pool does exceed the shale threshold pressure, the pool will breach the seal and migrate vertically until the next shale is reached and trapping occurs again, resulting in a vertical stack of pools. Hence, the conceptual model is that this pattern of pooling, breaching and lateral spill will match the observed plume distribution.

4. Plume model

The properties of the shale and sandstone intervals are constrained by the geological framework of the Utsira Formation and present-day observations from the Sleipner storage site. The Utsira Formation is internally segmented by laterally extensive horizontal shales, approximately 1–2 m thick, acting as barriers (Isaksen and Tonstad, 1989). Approximately 20 m beneath the caprock of the Lower Seal, the shallowest shale barrier (7 m thick shale) is thought to be lithologically identical to the caprock (Gregersen and Johannessen, 2001). Reviews of the reservoir geology indicate that this 7 m thick shale merges laterally with the Lower Seal, which is considered to be an effective primary seal (Arts et al., 2000; Chadwick et al., 2004). As such, above the storage site and interlayering with it as the 7 m thick shale, are the Lower Seal shales of the Nordland Group. This is overlain by the Middle Seal, bounded at the top and base by regional unconformities (Gregersen and Johannessen, 2001; Gregersen and Johannessen, 2007). The upper unconformity provides important evidence of ice sheet erosion and exhumation during the Pleistocene. The shallower Pleistocene shales are referred to as the Upper Seal (Fig. 1). The primary seal and overburden stratigraphy have considerably more complexity and heterogeneity when considered in detail (Nicoll et al., 2012), with numerous shallow sands, chimney structures and sub-glacial relict features. However, a simple first approximation is suitable for this study.

4.1. Geocellular model design

The 3D profile of the plume (Fig. 1) is used to build a three-dimensional model of the storage site. The geometry of each CO_2 layer and the associated shale barrier topographies are derived from published images of the CO_2 layering (Bickle et al., 2007; Chadwick et al., 2008). The nine layers define the cross-sectional relief of the shale barriers above the CO_2. The thin shale barriers that trap the first seven layers are assumed to be 1–2 m thick; the thick shale overlying layer 8 is assumed to be 7 m thick. The modeled shales are assumed to be petrologically similar to the Lower Seal shale, conforming to petrophysical data from the sampled well, 15/9A-11 (Gregersen and Johannessen, 2001). The model Utsira

Received by OCD: 6/29/2026

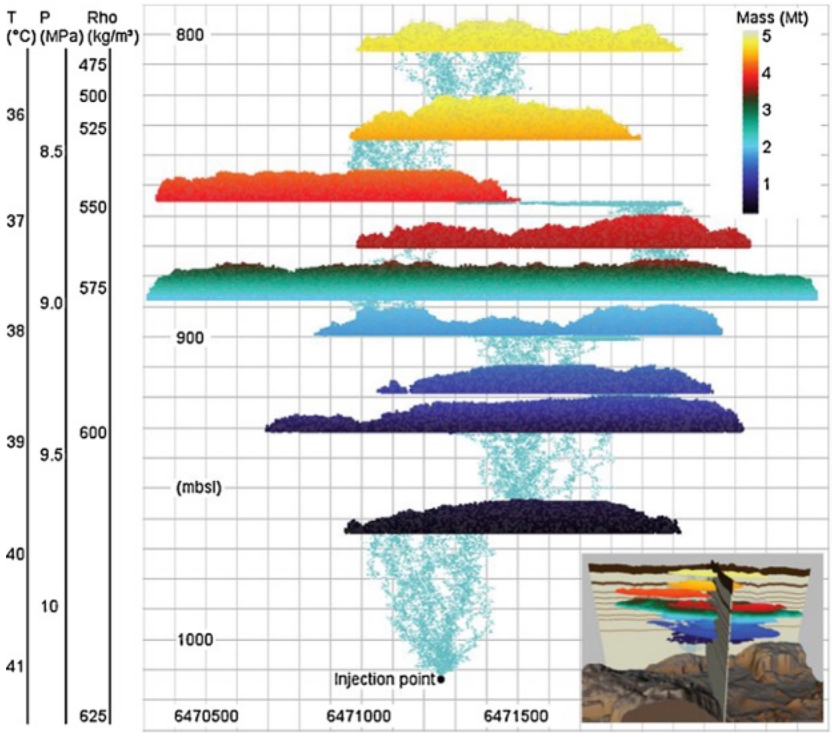


Fig. 3. A calibrated simulation for the Sleipner storage site. The model, viewed from the east, shows the simulated plume within the model context of sandstones separated by thin intra-formational shales and capped by the thick caprock shale (model dimensions: 2 km × 3 km × 0.24 km; element dimensions: 5 m × 5 m × 0.5 m; element count: 115 million). The profile shows the calibrated layer thicknesses (range: 9–14.5 m, mean: 11 m) that result in a 99% mass balance for 5 Mt of CO_2 (vertical color bar, equivalent to the total CO_2 injected circa July 2002). Light blue lines linking the layers are CO_2 migration pathways. Vertical axes show the reservoir temperature (T), hydrostatic pressure (P), and CO_2 density (Rho). Replication of the plume profile requires extremely low threshold pressures for the eight intra-formational shale barriers and caprock. An important feature is that the layer thicknesses indicate threshold pressures about 100× less than normal mudrock at this depth, and so imply that permeable micro-fractures exist. Precise model parameters required to replicate the plume morphology are documented in the appendix.

sandstone conforms to petrophysical data, i.e. clean, well-sorted and poorly cemented (Hellevang, 2006).

4.2. Numerical simulation

The simulation releases CO_2 at the known perforation interval of the injection well, close to the base of the model, and calculates the percolation pathway and resultant accumulations for the ascent of a discrete supercritical phase of CO_2. The simulation assumes a buoyant gravity-driven flow dominated by capillary forces. The depth range of the storage site is close to the phase boundary conditions for supercritical CO_2. This results in significant fluid density changes with ascent (Bickle et al., 2007). These density variations are estimated from a commonly used equation of state for CO_2 (Duan and Sun, 2003) assuming hydrostatic pressure and geothermal temperature profiles for the storage site (Table 2). The output of the model is a plume distribution of CO_2 with respect to the geological framework (Fig. 3) and a numerical estimate of the associated masses for each CO_2 layer and threshold pressures for each shale barrier (Table 2). While the layer distributions are known and stable in the model, the multiple migration pathways and breakthrough points for vertical migration (Fig. 3) only represent equivalent simulation pathways and potential breach locations for a given barrier at its shallowest expression. These are not expected to be better than an accurate approximation of the breach locations, as ascending migration paths in the actual storage site are likely to be sensitive to local heterogeneities in the shale barriers and sandstone formation. However, multiple realisations of the simulation confirm the robust and stable outcome of stacked CO_2 layers that insensitive to variations in the precise position of CO_2 breakthrough.

4.3. Results for two simulation scenarios

Two scenarios with identical geometry were tested by varying the threshold pressure of the shales within Utsira Formation: the first, a base case, assumed that the threshold pressure of approximately 1.6–1.9 MPa measured in core recovered from Lower Seal shales (Springer and Lindgren, 2006) is applicable to all shale barriers within the model. The threshold pressures are assigned to the shales as a global mean value i.e. a single shale barrier has a uniform mean threshold pressure of 1.75 MPa (three-sigma standard deviation of ±0.15 MPa, equivalent to approximately ±8.5%, assuming a normal distribution). This base case model failed to match the observed CO_2 distribution, as the high threshold pressures for the shales resulted in a 'zig-zag' pattern of predominantly laterally spilling migration. The simulation ultimately failed to reach the caprock, as the CO_2 backfilled beneath the 7 m thick shale without breaching, resulting in a final column height of hundreds of meters and total saturation of the reservoir. This scenario is totally unlike the Sleipner plume seismic observations, and is rejected.

The second scenario is unchanged from the base case with the exception of reduced threshold pressures for the shales within the storage site. The threshold pressure was gradually reduced by iterative experimentation until the simulation exhibited thin CO_2 layers similar to those observed in the seismic monitoring. The normal distribution range for the lower threshold pressures remained as ±8.5% of the mean assigned to a given shale barrier. This second scenario provides an excellent match with the observed phenomena i.e. a vertical 'pancake stack' of layers approximately 7–11 m thick (Figs. 1 and 3). The barrier geometry is prescribed by the observed geometry of the CO_2 layers, and so the morphology of the simulated layers is forced, given the derivation of shale layer topography from

Received by OCD: 6/29/2026

Table 2
The model output indicates a 99% mass balance for Sleipner (5 Mt circa July 2002) calculated from CO_2 volume and density (density values are based on pressure and temperature at mean depth). Volume is critically sensitive to layer thickness and gas density. This model assumes a mid-range temperature profile. Warmer models require slightly thicker layers to account for a mass balance. Colder models require slightly thinner layers. Threshold pressure and fracture estimates are dependent on layer thickness and CO_2 density. Final column, *M*/*S*: mean (thickness, pressure, fracture width) or sum (mass balance).

Plume layer	Units	L1	L2	L3	L4	L5	L6	L7	L8	L9	*M*/*S*
Crest depth	(mbsl)	955	920	905	890	875	860	845	825	795	–
Mean depth	(mbsl)	960	926	909	895	880	866	849	832	801	–
Layer thickness	(m)	10.5	12	9	9.5	13	10.5	10	14.5	10	11
Volume	(10^6 m^3)	2.78	4.29	2.51	1.18	10.4	1.29	2.60	3.34	1.40	–
Pressure	(MPa)	9.71	9.37	9.20	9.06	8.91	8.77	8.60	8.43	8.12	–
Temperature	(°C)	39.5	38.6	38.1	37.7	37.3	36.9	36.4	35.9	35.0	–
Density	(kg/m^3)	616	606	602	597	589	582	571	551	355	–
Mass balance	(Mt)	0.49	0.75	0.44	0.20	1.76	0.22	0.43	0.53	0.14	4.96
Mass balance	(%)	0.10	0.15	0.09	0.04	0.35	0.04	0.09	0.11	0.03	0.99
Modeled *Pth*	(kPa)	42	49	38	40	56	46	45	68	54	49
Fracture width	(μm)	2.6	2.2	2.8	2.7	1.9	2.3	2.4	1.6	2.0	2.3

the 4D seismic. However, the significance of the result lies in the replication of the stacked plume layering, and an estimate of CO_2 layer thicknesses that results in a reasonable match to observations and a plausible mass balance (Fig. 3 and Table 2).

It is notable that the model breakthrough pressure is surprisingly low in the calibrated match to the observed Sleipner plume. The simulation enables the inference of permeability and threshold pressures for the shales at the kilometer scale of the entire Sleipner storage site which are difficult or impossible to measure directly. The inferred threshold pressures required to achieve a thinly layered plume trapped by intra-formational shales are two orders of magnitude lower than the laboratory values measured on the caprock at well 15/9A-11. This is an important outcome of the model.

5. The mode of CO_2 ascent

Given the model results, the mode of CO_2 ascent within the storage site deserves further scrutiny. The favored scenario of thin, and stacked, CO_2 layering with low intra-formational shale threshold pressures raises an obvious concern: if the assumptions hold regarding the similarity of the 7 m thick shale to the Lower Seal, and the unbroken lateral continuity of the shale barriers, then the breakthrough condition for CO_2 at the caprock may be as low as 50 kPa (Table 2). Such an extremely low threshold pressure for shales can only occur in fractured rocks. It is therefore inferred that a network of micro-fractures span the shale barriers within the Utsira Formation, allowing the plume to ascend vertically, leaving a stack of thin CO_2 layers. The significance of this finding with respect to the integrity of the caprock and Nordland Group shales is discussed below.

5.1. Inferred fracture networks for shale barriers

The width of the inferred micro-fractures can be characterized to a first approximation by a modified form of the Young–Laplace equation (Pankow and Cherry, 1996). In this modification for a fractured shale, the fracture half-width substitutes for pore throat radius, and the seal is breached when the capillary pressure of the CO_2 layer, *Pc* (Eq. (2b)), exceeds the threshold pressure of a fracture, *Pf*, equivalent to the product of the interfacial tension, γ, and cosine of the wetting angle, θ, divided by the fracture half-width, f (Eq. (3)). The calibrated invasion percolation simulation (Fig. 3) enables the fracture width to be estimated as a function of the height of column retained beneath the shales. This indicates a fracture width of approximately 2 μm (Table 2). Micron-thick fractures commonly occur in shales, and are physically observed in physical shale specimens as pale gossamer-like threads that appear on the faces of rock samples indicating cement-filled fractures, or salts drying out from fluids in open fractures.

$$\text{Fracture threshold pressure, } Pf = \frac{2\gamma \cos\theta}{f} \quad (3)$$

where, P_f, threshold pressure of the fracture; γ, interfacial tension; θ, wetting angle; f, the half-width of the representative fracture aperture.

The micro-fracture explanation for low threshold pressures raises a number of questions: what is the vertical extent of the inferred fractures? And, do these connect to form fracture networks that span the shale barriers? What are the origins of the fractures? And, is the integrity of the caprock compromised? Firstly, it is apparent that the 7 m thick shale within the Utsira Formation transmits CO_2. It follows that this span is the minimum limit for a connected network of percolating fractures within the storage site. It is unclear if such a percolation bridge might affect the much thicker Lower Seal. No observational evidence to date indicates that CO_2 has penetrated the caprock. Given the very thin layers of CO_2 (10–15 m column heights with correspondingly low capillary pressures), a caprock breach would require a pre-existing fracture network. The evidence from a neighboring shale caprock, albeit older, more compacted and buried to 4 km (the seal for the nearby Miller oilfield), shows that CO_2 penetration of an unfractured caprock is very slow, taking approximately 70 Ma to diffuse 10 m into the caprock (Lu et al., 2009). However, the maximum limit of fracture connectivity at the Sleipner caprock, or through the Lower Seal remains unknown. In addition to potential fracture networks, paleo-gas chimneys and glacial tunnel valleys with the Nordland Group shales may provide physical routes for the rapid vertical escape of CO_2, though these are not thought to intersect the present CO_2 plume footprint or expected future distribution beneath the caprock (Zweigel et al., 2004; Nicoll et al., 2012).

Concerning the origin of the micro-fractures, CO_2 injection is an unlikely fracture mechanism for the breaching of thick or thin shales. A low capillary pressure of around 50 kPa, associated with the buoyancy of a 10–15 m CO_2 column, may be high enough to allow CO_2 to percolate through an existing fracture network for 1–7 m thick shale barriers. However, the fracturing of shales as a consequence of such small pressure changes within the Utsira Formation is highly unlikely. By analogy, micro-fractures in overpressured hydrocarbon fields occur when the pore pressures exceed around 80% of the lithostatic pressure, typically equivalent to multi-MPa changes (Aplin et al., 2000). The Sleipner storage site is not significantly stressed or overpressured at the present day (Wei et al., 1990); the pore fluids are effectively at hydrostatic pressure; and so for Sleipner, the fluid pressure increase

Received by OCD: 6/29/2026

necessary to fracture an intact seal (about 10 MPa) is highly unlikely. It is therefore inferred that the shales have been fractured prior to CO_2 injection.

5.2. Ice sheet unloading as a mechanism for fracturing

Previous studies have put forward a number of ideas to explain the rapid vertical migration of CO_2 within the Utsira Formation, as neatly summarized by Chadwick et al. (2009). The gamut ranges from small faults and natural holes in the intra-formational shale barriers, to geomechanically induced chimneys, sand injectites and changes in the wetting characteristics of shales exposed to CO_2. However, these scenarios are hypothetical and frequently driven by model design, in terms of creating suitable pathways for simulating flow. The lack of sampling and direct observations from within the Utsira Formation has done little to narrow the field of possibilities. The modeling presented in this paper implies fracturing prior to CO_2 injection, as outlined above. As a consequence, a plausible pre-injection fracturing mechanism is sought, given the geological history and context of the storage site. The following hypothesis further adds to the various competing ideas concerning the flow properties of the Utsira Formation, and the shale barriers in particular; and in common with those ideas, shares a lack of direct evidence from the storage site itself. However, there are a number of supporting regional indications, presented below, and the simplicity of the model, in itself, is encouraging.

The Sleipner storage site location lies within the Pleistocene ice sheet domain of NW Europe (Boulton and Hagdorn, 2006). An erosional unconformity at the Pliocene/Pleistocene boundary between the Middle Seal and Lower Seal of the Nordland Group shales indicates that ice was in contact with the seabed, scouring and eroding the underlying sediments. Additional unconformities within the Middle Seal and Upper Seal indicate several similar events (Nicoll, 2012). The youngest ice sheet (Late Devensian) has left well-preserved sediments to record its position and demise; reconstructions of ice sheet thickness over the British Isles and Southern Norway during this final stage indicate that the ice was around 1000 m thick and grounded over the Sleipner area of the Northern North Sea (Boulton and Hagdorn, 2006). Similar grounded ice sheets probably occurred during several glaciations over the last 1 Ma from marine isotope stage MIS 12 onwards. Considering the effect of ice on fluid pressure and stress on the underlying shale, the following scenario is hypothesized:

The gradual increase of ice sheet thickness during prograde glaciation produces a slow transient additional overburden load. This load is transferred to the sediments below the ice sheet if it is grounded rather than floating. The youngest grounded ice sheet (Late Devensian, MIS 2) can be precisely mapped; the MIS 2 ice sheet formed as a confluence of the British and Fennoscandian ice sheets, flowing to the north-west, and ultimately reaching the continental margin (Bradwell et al., 2008; Davison, 2012). The preservation of relict landform features indicates that, during deglaciation, the ice melted very rapidly, possibly catastrophically, within hundreds of years at 24 ka, coincident with a global sea-level change (Bradwell et al., 2008). It is possible that the sea level rise transgressed beneath the grounded ice, causing it to float off the seabed; at which point the overburden pressure is removed instantaneously (Davidson, 2005; Bradwell et al., 2008). The significance of this deglaciation event is the possibility of unusually rapid and transient pore pressure changes within shales that may have exceeded the geomechanical limit, fracturing the shales (Cavanagh et al., 2006).

Pressure fluctuations associated with deglaciation are distinct from more commonly encountered subsurface overpressure regimes in that both the hydrostatic and lithostatic baseline pressures are offset to higher values by loading from a grounded ice sheet (Fig. 4). Gradients remain the same but a change in the baseline pressure occurs which is dependent on ice sheet thickness. Hypothetically, the loading of the Nordland Group shales by a 1000 m thick ice sheet (gray upper layer, Fig. 4) would cause both hydrostatic and lithostatic values to increase by about 10 MPa during a glacial stage lasting several tens of millennia (Fig. 4). This affects a pore pressure increase within the Utsira Formation from 7 MPa (700 m depth) to a new equilibrium beneath the ice of 16 MPa (1700 m depth, including ice sheet). The new hydrostatic pressure gradient (gray lines, Fig. 4) starts near the top of the ice sheet; the new lithostatic gradient runs from the base of the ice sheet. The maximum ice load does not need to be located directly above the Utsira Formation as, for a hydraulically connected aquifer, a lateral transmission of pressure will occur for tens of kilometers. During deglaciation the ice melts rapidly, and both the lithostatic and hydrostatic equilibrium lines return geologically instantaneously to their normal positions (black lines, Fig. 4). Since pore fluids in the deep subsurface cannot flow instantaneously to re-equilibrate

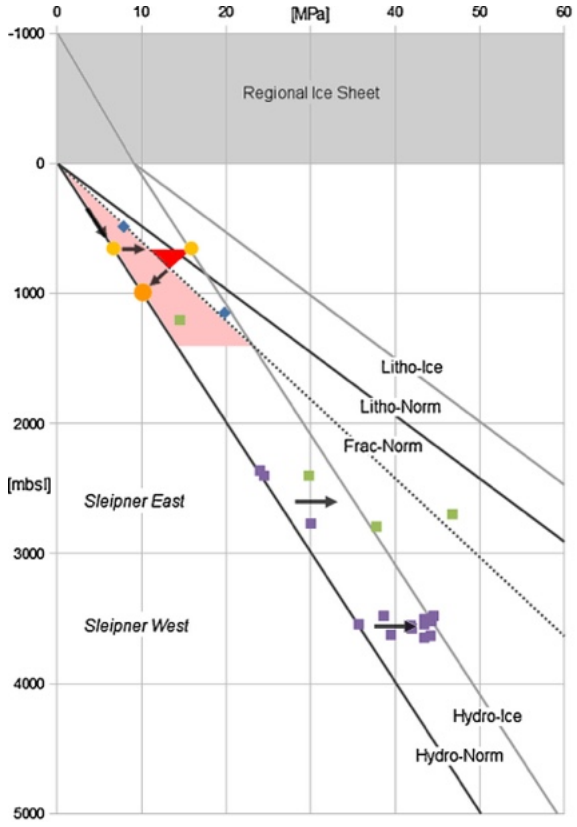


Fig. 4. A model for ice-loaded and ice-free pressure regimes in the Utsira region. In this scenario, assuming very rapid melting of a 1000 m thick ice sheet (shaded top layer), the Sleipner storage site is shallow enough for pore pressures to have exceeded the ice-free fracture gradient (dashed line). This potentially results in hydraulic micro-fracturing of the shale barriers, as the high pore pressures associated with the ice sheet load fail to dissipate rapidly from the low permeability shales, leaving the shale barriers above the fracture gradient (red triangular zone at around 800 m depth); arrows indicate the inferred formation pressure evolution (yellow circles) to the present-day hydrostatic state (larger orange circle). The Sleipner gas fields are much deeper than the fracture-critical zone of glacial overpressure (pink shaded area, from sea level to 1400 m), and are likely to have preserved recent ice-related perturbations in reservoir pressure. Both fields report several megapascals of overpressure, similar to that predicted for the ice sheet loading (pore pressure offset arrows at 2600 and 3600 mbsl); reported hydrocarbon overpressure data (light green and dark purple squares) after Wei et al. (1990) and NPD (2013); normal hydrostatic and lithostatic gradients, assuming pore water and bulk rock densities of 1020 and 2100 kg/m^3, respectively (Pillitteri et al., 2003; Zweigel et al., 2004;): fracture gradient assumed to be 80% of lithostatic, based on leak-off tests (blue diamonds) after Nicoll (2012). Ice-related gradients assume an ice density of 920 kg/m^3 (Shumsky, 1959).

Received by OCD: 6/29/2026

the rock, this rapid deglaciation leaves the pore fluids isolated at, or above the re-established normal fracture gradient. While the highly permeable Utsira Formation is free to flow and equilibrate rapidly, the much lower permeability shales are not. The shale pore pressure collides with the fracture gradient, at about 80% of lithostatic pressure, creating a zone of hydraulic fracturing potential (red triangle, Fig. 4). The thickness and strength of the overburden for any given stage is highly uncertain, hence the dashed line (fracture gradient, Fig. 4), which is conservatively estimated from present day leak-off test data (Nicoll, 2012). This mechanism suggests that, within this zone of fracturing potential, the shales of the Utsira Formation pervasively micro-fractured perpendicular to geological bedding, enabling rapid porewater escape during deglaciation. This fracturing is now responsible for the rapid migration of CO_2 within the storage site. Five independent lines of evidence are considered to support this hypothesis:

Firstly, reservoirs in the much deeper Sleipner hydrocarbon fields, both East and West, appear to be overpressured by about 10 MPa (Wei et al., 1990; NPD, 2013). Secondly, a phenomenon known as the 'Oligocene-Miocene bump' appears to record a regional occurrence of 5–10 MPa overpressure at about 1.3–1.5 km depth in the Northern North Sea (Vik et al., 1998). There is no diagenetic reaction or hydrocarbon charge effect to explain such an overpressure. This suggests that both pressure phenomena are relicts from regional deglaciation events.

Thirdly, seismic data for the Sleipner storage site locale display a number of discrete anomalies (pock marks, soft kicks, small chimney features) where sediment layering is disrupted, indicative of vertical gas migration in the Nordland Group shales (Zweigel, 2000; Nicoll et al., 2012). It is proposed that these shallow gas indications are relicts of natural gas leakage from the Utsira Formation during depressurization. Fourthly, observations of thirty nine deeper hydrocarbon fields across the North Sea show that thermogenic gas and condensates have leaked through caprocks to form diffuse zones hundreds of meters thick above the hydrocarbon reservoirs (Aplin et al., 2006). These seismic chimneys suggest that the leakage may be a regional manifestation of vertical micro-fractures created by the same transient depressurization phenomenon associated with ice sheet unloading.

Finally, tectonophysical modeling of lithospheric flexure in response to the elastic deformation of the crust during glaciation and deglaciation (Grollimund and Zoback, 2000) indicates that the Sleipner region is currently in a state of horizontal extensional stress (5–15 MPa at 2–3 km depth) as a consequence of ice sheet unloading. Grollimund and Zoback suggest an explanation that is sympathetic to the hypothesis proposed here, i.e. the present-day unstressed hydrostatic pore pressure regime results from fracturing and pore fluid leakage: '*The stress decrease due to deglaciation might have brought horizontal compressional* stress *down to the existing pore pressure at the time when the stress decrease took place and parts of the fluids leaked away, leading to a pore pressure reduction*' (Grollimund and Zoback, 2000).

A recent, more detailed, analysis by Grollimund and Zoback (2003) includes the influence of ice sheet loading from 1 Ma onwards, and a history of recent ice sheet melting events, with similar results. They determine that the common and widely observed indications of vertical fluid leakage from oil and gas fields within the region via faults or fractures is unlikely during glacial stages, but much more likely during regional deglaciations, with particular emphasis on events at 60 ka and 15 ka. It seems reasonable that these regional findings for paleo-stress, pore pressure, and fluid flow also apply to the Sleipner storage site.

This combination of present-day overpressure observations, local vertical natural gas migration features and regional indications of pore pressure fluctuations associated with ice sheet-related lithospheric stress changes affirm the possibility of our inferred process for fracturing the Utsira Formation shales, both with respect to mechanism and magnitude.

6. Discussion

Successive seismic reflection surveys of the Sleipner CO_2 storage site have shown by observation that the plume of injected CO_2 at the Sleipner storage site has a geometry which reveals partial trapping beneath thin shales within the Utsira Formation. The flow modeling approach and analysis presented here suggest that the shale barriers have uncharacteristically low threshold pressures, enabling the rapid vertical migration of injected CO_2 within the storage site. The inferred threshold of around 50 kPa is much lower than the observed value of approximately 1.75 MPa from core measurements by Springer and Lindgren (2006) and Harrington et al. (2009). However, it should be noted that standard methodologies for core sampling and threshold pressure measurements specifically avoid fractured samples, assuming such fractures to be indicative of drilling damage. As such, the influence of natural fracture networks on bulk shale threshold pressures is likely to be under-represented, if considered at all. The model results indicate that a definitive mass balance for the plume is difficult to ascertain given the inherent uncertainties in the data. However, a mid-range temperature profile and reasonable layer thickness estimate indicates that a mass balance for the plume is certainly possible.

The modeled low shale barrier threshold pressures are potentially indicative of fracturing. However, the current pressure regime is extremely unlikely to cause fracturing, and so it is inferred that the shales may have been pervasively fractured in the past. A fracturing process consistent with the geological history of the region is that the shale barriers have undergone a transient pulse of fluid overpressure sufficient to fracture the rock. Such a pressure history could be a consequence of the rapid unloading of hundreds of meters of ice from the overburden during a deglaciation. A transient ice sheet load equivalent to 10 MPa of overpressure could have been removed rapidly by melting, or instantly by a sea level rise and the flotation of an ice sheet grounded on the seabed, during a typical ablation timespan of less than a few thousand years. At the shallow burial depth of these shales, 10 MPa is sufficient to exceed the tensional rock strength and cause pervasive hydraulic fracturing. This may have happened as a consequence of one or more regional ice sheet excursions into the basin. While the strength and thickness of the overburden at any given ice collapse is unknown, a conservative approximation for the fracture gradient, based on present-day leak-off tests (Nicoll, 2012), suggests that such an event is plausible.

Two rival processes are acting on today's CO_2 storage performance at this site. The first process, favoring retention, is the spreading and dispersal of the injected CO_2. For this process, weak shale barriers within the storage formation are beneficial. These encourage the development of many thin layers of injected CO_2, rather than one thick plume. This maximizes the surface area contact of CO_2 to porewater within the formation while decreasing the column height acting on the caprock and minimizing the lateral spread of CO_2. An increased surface area promotes the dissolution of CO_2 in brine (Gilfillan et al., 2009), which results in permanent sequestration, as the slightly increased brine density causes the dissolved CO_2 to descend away from the upper barrier surface (Arts et al., 2008). Solubility trapping is desirable as it eliminates the need to physically retain a lower density buoyant fluid; sequestration of CO_2 by growth into new minerals is likely to be too slow in nature to effect trapping over the required timescale of hundreds-to-thousands of years (Wilkinson et al., 2011).

The second process, opposing retention, is the vertical flow of CO_2 which may be mediated by existing micro-fracture networks

Received by OCD: 6/29/2026

that span the shale barriers. This may be disadvantageous to CO_2 storage for two reasons: firstly, because the CO_2 is only partially spread laterally beneath the shale barriers, potentially resulting in a focused vertical flow path; secondly, because CO_2 could potentially break through the caprock seal. Evidence from Sleipner indicates that the fracturing affects all the internal shale barriers including the uppermost 7 m thick shale. This thick shale is geologically considered to be part of the overlying Lower Seal (Gregersen and Johannessen, 2001; Eidvin et al., 2013). Fracturing of the Lower Seal would be of particular concern, as the caprock acts as the primary seal for storage site. The question arises, has the caprock been fractured by the same deglaciation mechanism? And if so, do the observed chimney-like structures in the secondary seal within the vicinity of the storage site (Nicoll et al., 2012) contain vertical fracture networks that compromise the seal integrity? As yet, a percolation network of connected fractures through the much thicker shale sequences of the overburden has not been proven. Evidence against such a fracture network is the continued lateral migration of the uppermost CO_2 plume at about 1 m per day to the north (Chadwick et al., 2008), and the lack of seismic velocity changes observed in the caprock above the storage site, and within the Middle Seal, on successive 4D seismic surveys (StatoilHydro, 2009; Chadwick et al., 2009). This is encouraging, as even small amounts of CO_2 gas added to the Lower Seal would result in a strong seismic reflection signal, given the strong density contrast between brine and gas for the pressure and temperature conditions of the overburden. These are reasonable grounds to assert that the caprock is a functioning seal that is significantly thicker than the underlying shales. If CO_2 were to seep into the Lower Seal, then predictions of observable phenomena to be expected would include:

(a) Stabilization or shrinkage of the upper plume layer on a timescale of years rather than decades, due to the seepage of CO_2 via fractures rather than dissolution into the underlying formation.
(b) Observable brightening and extending of seismic anomalies for the existing bright spots of natural gas pockets above and within the Lower Seal; 'lighting up' of existing seismic chimneys.
(c) New 'soft kick' seismic anomalies appearing in the overburden as a consequence of gaseous CO_2 ascending through microfractures and charging shallow sand bodies within the near future.
(d) Ultimately, some form of surface expression at the sea floor, including pockmarking, seawater geochemical changes, bubble trains, and possibly behavioral changes in bottom-dwelling fauna.

While none of these are apparent, or inferred at present (Pedersen et al., 2012), future monitoring of the Sleipner storage site could be directed toward testing such possibilities. Note that a significant increase in fluid pressure for aquifers and sand bodies above Utsira, a commonly cited detection criteria, is not expected due to the buoyant capillary-dominated nature of the flow and associated weak pressure differentials.

Processes occurring in this storage site are relevant for all areas of the North Sea affected by regional ice sheets. The hydraulic fracturing of thin, shallow shale intervals during deglaciation could be a widespread feature beneath continental ice sheets. Similar processes may be expected to affect all northern hemisphere regions exposed to thick regional ice sheets in the past million years. Consequently, shales shallower than about 1.5 km may be less effective primary seals than anticipated, but vertical stacking of multiple thin CO_2 layers within storage formations is advantageous, as is the distribution of further CO_2 layers beneath secondary seals within the storage complex, increasing the contact area with porewater and enhancing dissolution trapping. Dissolution uses more of the reservoir pore volume efficiently, and potentially increases site capacity relative to regional estimates of storage efficiency. However, a lack of understanding with respect to flow processes in the overburden will likely lead to conservative estimates of the secondary sealing potential and an underestimation of the important contribution of the overlying stratigraphy to the performance of a storage site. At the present time, in our opinion, the evidence from the very extensively analyzed geophysical data for Sleipner is compatible with retention of CO_2.

7. Conclusions

The Sleipner CO_2 storage site is an iconic carbon sequestration project and extraordinary fluid flow experiment in terms of the setting, nature and volume of fluid injected. This paper has documented a numerical modeling approach that results in a plausible CO_2 distribution and mass balance estimate. Data acquisition and monitoring at Sleipner has been via remote geophysical sensing, primarily 4D seismic. As a consequence, a number of quite large uncertainties remain with respect to the observed plume distribution. The paper demonstrates the sensitivity of mass balance estimates associated with a poorly constrained temperature profile close to the critical point of CO_2, and poorly constrained thickness estimates of the multiple thin layers that characterize the plume.

With respect to simulations, it is noted that previous attempts to numerically model the plume have used software governed by Darcy flow physics, and achieved poor results. This paper presents an alternative approach that leads to a successful 3D simulation of the injected plume distribution using a model based on capillary flow and percolation physics. The paper carefully documents the modeling approach and justification for this unusual but effective method. The modeling indicates that the multiple layers of thin CO_2 are likely a consequence of unexpectedly low threshold pressures for vertical migration through the shale barriers within the Utsira Formation. The estimated threshold pressures for CO_2, at around 50 kPa, are approximately 35-fold less than that measured on a sample of the caprock shale from well 15/9A-11, close to the site, at approximately 1.75 MPa. This difference is most plausibly explained by microfracturing of the shale barriers, but CO_2 injection at Sleipner is not considered to be a likely cause of fracturing.

It is postulated that the fracturing occurred long before CO_2 injection commenced, as a result of rapid pore pressure fluctuations associated with the collapse of thick ice sheets during multiple episodes of deglaciation in the region over the last million years. A number of independent observations are considered to support this hypothesis. Concerning seal integrity, the caprock and overlying Nordland Group shales of the Lower Seal may have also been fractured during deglaciation. However, it is noted that there is no evidence of CO_2 leaking, possibly as a result of a different caprock response to CO_2 retention, which is notably thicker than the thin shale barriers within the storage site. It is inferred that similar fracture networks within the primary seal are potentially only proximal to the formation, and may have limited percolation connectivity, preventing vertical migration through the overburden.

Acknowledgements

AJC was funded by the Scottish Funding Council. RSH was funded by the UK Energy Research Center, NERC, Scottish Power, and EPSRC (EP/F034520/1 and EP/K000446/1). We wish to thank Permedia for a license to use their software. We are also grateful to the Norwegian Petroleum Directorate archives for open-access. Much thanks to Grant Nicoll and Mark Wilkinson, University of Edinburgh, for helpful discussions. We sincerely appreciate the editorial work of

Received by OCD: 6/29/2026

Stefan Bachu, and constructive comments from the two anonymous reviewers.

Appendix.

Surface datum is mean sea level. All measurements are in SI units unless stated otherwise. Geothermal gradient assumed linear between 41 °C at 1012 m (Bickle et al., 2007) and 35 °C at 800 m (Singh et al., 2010). Hydrostatic gradient, $Pz = Pa + \rho gz$, the standard formulation (atmospheric pressure, 101.3 kPa; gravitational constant, 9.81 kg/m^3). Pore water density, 1020 kg/m^3, assumed constant. CO_2 interfacial tension, 27 mN/m and CO_2-pore water contact angle, 140°, assumed constant given reservoir temperature and pressure gradients, after published data (Shah et al., 2008; Bachu and Bennion, 2009). CO_2 density 377–625 kg/m^3, from crest to injection point, calculated from Permedia PVT solver, based on a published equation of state (Huang et al., 1985). Sandstone porosity, 0.36 ± 0.04 below the caprock. Sandstone porosity, 0.34 ± 0.04 at the base of the formation. Sandstone permeability assumed to be 1–5 darcy, after published data (Singh et al., 2010). Sandstone threshold pressure ~10–20 kPa (Sorkhabi and Tsuji, 2005). Sandstone CO_2 saturation 0.80 (after a published Scw value of 0.2 (Bickle et al., 2007). Shale porosity, 0.30 ± 0.02 assumed given depth.

References

Aplin, A.C., Fleet, A.J., Macquaker, J.H.S., 2000. Muds and shales: physical and fluid-flow properties. Geological Society, London, Special Publications 158, 200 pp.

Aplin, A.C., Kuncho, D.K., Larter, S.R., 2006. Dynamic analysis of imperfect seals. In: Proceedings of the AAPG International Conference and Exhibition, Perth, Australia, November 5–8.

Arts, R.J., Zweigel, P., Lothe, A.E., 2000. Reservoir geology of the Utsira Sand in the Southern Viking Graben area – a site for potential CO_2 storage. In: 62nd EAGE Meeting, Glasgow B20, pp. 1–4.

Arts, R., Eiken, O., Chadwick, A., Zweigel, P., van der Meer, L.G.H., Zinszner, B., 2004. Monitoring of CO_2 injected at Sleipner using time-lapse seismic data. Energy 29, 1383–1392.

Arts, R., Chadwick, A., Eiken, O., Thibeau, S., Nooner, S., 2008. Ten years' experience of monitoring CO_2 injection in the Utsira Sand at Sleipner (offshore Norway). First Break 26, 65–72.

Bachu, S., Bennion, D.B., 2009. Interfacial tension between CO_2, freshwater and brine in the range of pressure from 2 to 27 MPa, temperature from 20 to 125 °C, and water salinity from 0 to 334,000 mg/L. Journal of Chemical Engineering and Data 54, 765–775.

Bickle, M., Chadwick, R.A., Huppert, H.E., Hallworth, M., Lyle, S., 2007. Modelling CO_2 accumulation at Sleipner: implications for underground carbon storage. Earth and Planetary Science Letters 255, 164–176.

Boettcher, S.S., Barboza, S.A., Symington, W.A., Maliassov, S., Bunney, J., 2002. Calibration and application of Permedia for modelling secondary hydrocarbon migration. In: AAPG Hedberg Research Conference, Australia, December 1–5.

Boulton, G., Hagdorn, M., 2006. Glaciology of the British Isles Ice Sheet during the last glacial cycle: form, flow, streams and lobes. Quaternary Science Reviews 25, 3359–3390.

Bradwell, T., Stoker, M.S., Golledge, N.R., Wilson, C.K., Merritt, J.W., Long, D., Everest, J.D., Hestvik, O.B., Stevenson, A.G., Hubbard, A.L., Finlayson, A.G., Mathers, H.E., 2008. The northern sector of the last British Ice Sheet: maximum extent and demise. Earth Science Reviews 88, 207–226.

Carruthers, D.J., 2003. Modeling of secondary petroleum migration using invasion percolation techniques. In: Düppenbecker, S., Marzi, R. (Eds.), Multidimensional Basin Modeling, AAPG Datapages Discovery Series 7. , pp. 21–37.

Carruthers, D.J., Ringrose, P.S., 1998. Secondary oil migration: oil-rock contact volumes, flow behaviour and rates. Geological Society, London, Special Publications 144, 205–220.

Cavanagh, A.J., 2013. Benchmark calibration and prediction of the Sleipner CO_2 plume from 2006 to 2012. Energy Procedia 37, 3529–3545.

Cavanagh, A.J., di Primio, R., Scheck-Wenderoth, M., Horsfield, B., 2006. Severity and timing of Cenozoic exhumation in the SW Barents Sea. Journal of the Geological Society 163, 761–774.

Cavanagh, A.J., Rostron, B., 2013. High-resolution simulations of migration pathways and related potential well risk at the IEAGHG Weyburn-Midale CO_2 storage project. International Journal of Greenhouse Gas Control 16, S15–S24.

Chadwick, R.A., Zweigel, P., Gregersen, U., Kirbya, G.A., Holloway, S., Johannessen, P.N., 2004. Geological reservoir characterization of a CO_2 storage site: the Utsira Sand, Sleipner, Northern North Sea. Energy 29, 1371–1381.

Chadwick, R.A., Arts, R., Eiken, O., 2005. 4D seismic quantification of a growing CO_2 plume at Sleipner North Sea. In: Dore, A.G., Vining, B.A. (Eds.), Petroleum Geology: North-West Europe and Global Perspectives – Proceedings of the 6th Petroleum Geology Conference. Geological Society, London, 1385–1399.

Chadwick, R.A., Noy, D., Lindeberg, E., Arts, R., Eiken, O., Williams, G., 2006. Calibrating reservoir performance with time-lapse seismic monitoring and flow simulations of the Sleipner CO_2 plume. In: GHGT-8: 8th International Conference on Greenhouse Gas Control Technologies, Trondheim, Norway, June 19–22, 2006. Elsevier, Oxford, pp. 1–6.

Chadwick, R.A., Arts, R., Bernstone, C., May, F., Thibeau, S., Zweigel, P., 2008. Best practice for the storage of CO_2 in saline aquifers – observations and guidelines from the SACS and CO_2STORE projects. British Geological Survey Occasional Publication 14, 1–267.

Chadwick, R.A., Noy, D., Arts, R., Eiken, O., 2009. Latest time-lapse seismic data from Sleipner yield new insights into CO_2 plume development. GHGT-9 Proceedings. Energy Procedia 1, 2103–2110.

de Gennes, P.-G., Brochard-Wyart, F., Quéré, D., 2004. Capillarity and Wetting Phenomena: Drops, Bubbles, Pearls, Waves. Springer, New York, 289 pp.

Davidson, J.K., 2005. Impact of glacially induced stress changes on fault-seal integrity offshore Norway: discussion. AAPG Bulletin 89, 271–274.

Davison, S., 2012. Reconstructing the Last Pleistocene (Late Devensian) Glaciation on the Continental Margin of Northwest Britain. Ph.D. Thesis, University of Edinburgh, 321 pp.

Duan, Z., Sun, R., 2003. An improved model calculating CO_2 solubility in pure water and aqueous NaCl solutions from 273 to 533 K and from 0 to 2000 bar. Chemical Geology 193, 257–271.

England, W.A., Mackenzie, A.S., Mann, D.M., Quigley, T.M., 1987. The movement and entrapment of petroleum fluids in the subsurface. Journal of the Geological Society 144, 327–347.

Eidvin, T., Riis, F., Rasmussen, E.S., Rundberg, Y., 2013. Investigation of oligocene to lower pliocene deposits in the Nordic offshore area and onshore. Denmark. Norwegian Petroleum Directorate, NPD Bulletin 10, 59 pp.

Gassmann, F., 1951. Uber die elastizitat poroser median. Vierteljahrsschrift der Naturforschenden Gesellschaft in Zürich 96, 1–23.

Gilfillan, S.M.V., Lollar, B.S., Holland, G., Blagburn, D., Stevens, S., Schoell, M., Cassidy, M., Ding, Z., Zhou, Z., Lacrampe-Couloume, G., Ballentine, C.J., 2009. Solubility trapping in formation water as dominant CO_2 sink in natural gas fields. Nature 458, 614–618.

Glass, R.J., Yarrington, L., 2003. Mechanistic modelling of fingering, nonmonotonicity, fragmentation, and pulsation within gravity/buoyant destabilized two-phase/unsaturated flow. Water Resources Research 39, 1058.

Gregersen, U., Johannessen, P.N., 2001. The Neogene Utsira Sand and its seal in the Viking Graben area, North Sea Saline Aquifer CO_2 Storage (SACS) project, Phase 2 Task 1.7 Geology. Geological Survey of Denmark and Greenland Report 2001/100, pp. 1–2.

Gregersen, U., Johannessen, P.N., 2007. Distribution of the Neogene Utsira Sand and Hutton Sand, and the succeeding deposits in the Viking Graben area. North Sea, Marine and Petroleum Geology 24, 591–606.

Grollimund, B., Zoback, M.D., 2000. Post glacial lithospheric flexure and induced stresses and pore pressure changes in the northern North Sea. Tectonophysics 327, 61–68.

Grollimund, B., Zoback, M.D., 2003. Impact of glacially induced stress changes on fault-seal integrity offshore Norway. AAPG Bulletin 87, 493–506.

Hamborg, M., Kirby, G.A., Lothe, A.E., Zweigel, P., 2003. Seismic mapping and simulation of CO_2 migration in the upper Utsira sand wedge east of the Sleipner injection site. SINTEF Report 33.5324.00/03/03, 42 pp.

Harrington, J.F., Noy, D.J., Horseman, S.T., Birchall, D.J., Chadwick, R.A., 2009. Laboratory study of gas and water flow in the Nordland Shale, Sleipner, North Sea. In: Grobe, M., Pashin, J., Dodge, R. (Eds.), Carbon Dioxide Sequestration in Geological Media. State of the Science: AAPG Studies in Geology, Special Publication of the American Association of Petroleum Geologists 59, 521–543.

Hellevang, H., 2006. Interactions between CO_2, saline water and minerals during geological storage of CO_2. Ph.D. Thesis, University of Bergen, 38 pp.

Hermanrud, C., Andresen, T., Eiken, O., Hansen, H., Janbu, A., Lippard, J., Bolås, H.N., Simmenes, T.H., Teige, G.M.G., Østmo, S., 2009. Storage of CO_2 in saline aquifers-Lessons learned from 10 years of injection into the Utsira Formation in the Sleipner area. Energy Procedia 1, 1997–2204.

Hermanrud, C., Teige, G.M.G., Iding, M., Eiken, O., Rennan, L., Ømo, S., 2010. Differences between flow of injected CO_2 and hydrocarbon migration. Petroleum Geology Conference Series 7, 183–1188.

Hobson, D.G., 1954. Some Fundamentals of Petroleum Geology. Oxford University Press, London, 139 pp.

Huang, F.H., Li, M.H., Lloyd, L.L., Starling, K.E., Chung, F.T.H., 1985. An accurate equation of state for carbon dioxide. Journal of Chemical Engineering of Japan 6, 490–496.

Isaksen, D., Tonstad, K., 1989. A revised cretaceous and tertiary lithostratigraphic nomenclature for the Norwegian North Sea. Norwegian Petroleum Directorate, NPD Bulletin 5, 60 pp.

Laplace, P.S., 1806. Traité de Mécanique Céleste; Supplément au dixième livre, Sur l'Action Capillaire. Courcier, Paris, 349 pp.

Li, D., Lake, L.W., 1995. Scaling fluid flow through heterogeneous permeable media. SPE Advanced Technology Series 3, 188–197.

Lindeberg, E., Bergmo, P., 2003. The long-term fate of CO_2 injected into an aquifer. In: Gale, J., Kaya, Y. (Eds.), Proceedings of the 6th International Conference on Greenhouse Gas Control Technologies (GHGT-6), Kyoto, Japan, October 1–4, 2002. Pergamon 1, 489–494.

Received by OCD: 6/29/2026

Lippard, J., Cavanagh, A.J., Kennedy, D., Hermanrud, C., 2008. Modelling of CO_2 injection and seismic data analysis in the Utsira formation. In: 33rd International Geological Congress, Oslo, Norway, August 6–14.

Lovell, B., 2011. Challenged by Carbon: The Oil Industry and Climate Change. Department of Earth Sciences, University of Cambridge, 211 pp.

Lumley, D.E., 2008. Introduction to uncertainty: data and parameters. Presented at the SEG Workshop: Uncertainty analysis in geophysical imaging, estimation and inverse problems. Las Vegas, 13 November.

Lu, J., Wilkinson, M., Haszeldine, R.S., Fallick, A.E., 2009. Long-term performance of a mudrock seal in natural CO_2 storage. Geology 37, 35–38.

Nicoll, G.D., 2012. Evaluation of the Nordland Group overburden as an effective seal for the Sleipner CO_2 storage site (offshore Norway) using analytical and stochastic modelling techniques. Ph.D. Thesis, University of Edinburgh, 363 pp.

Nicoll, G.D., Cavanagh, A.J., Geiger, S., Haszeldine, R.S., 2012. Overburden architecture and palaeo-fluid migration indicators above the Sleipner CO_2 storage site. Proceedings of the National Academy of Sciences (in preparation) – from Nicoll Ph.D. Thesis, University of Edinburgh.

NPD, 2013. Norwegian Petroleum Directorate Fact-Pages, Fields, Sleipner Øst and Vest, available at: http://factpages.npd.no/factpages/default.aspx (accessed 05.11.13).

Pankow, J.F., Cherry, J.A., 1996. Dense Chlorinated Solvents and Other DNAPL in Groundwater: History, Behavior, and Remediation. Waterloo Press, Portland, Oregon, 525 pp.

Pedersen, R.B., Reigstad, L.J., Baumberger, T., 2012. ECO2 Cruise Report GS12A - Scientific cruise to the Sleipner area in the North Sea; R/V G.O. Sars Expedition No. 2012108/CGB2012, June 22th–30th 2012, Bergen, Norway - Bergen, Norway Centre for Geobiology, University of Bergen, Bergen, Norway, 28 pp.

Permedia, 2012. Migration Software, Version 5.1. Halliburton, Ottawa, Ontario.

Pillitteri, A., Cerasi, P., Stavrum, J., Zweigel, P., Bøe, R., 2003. Rock mechanical tests of shale samples from the cap rock of the Utsira Sand in well 15/9A-11 – a contribution to the Saline Aquifer CO_2 Storage (SACS) project. Sintef Petroleum Research Report 33.5324.00/06/03.

Ringrose, P.R., Sorbie, K.S., Corbett, P.W.M., Jensen, J.L., 1993. Immiscible flow behaviour in laminated and cross-bedded sandstones. Journal of Petroleum Science and Engineering 9, 103–124.

Shah, V., Broseta, D., Mouronval, G., 2008. Capillary alteration of caprocks by acid gases. Society of Petroleum Engineers SPE-113353, 1–11.

Shumsky, P.A., 1959. Density of glacier ice. Journal of Glaciology 3, 568–573.

Singh, V., Cavanagh, A., Hansen, H., Nazarian, B., Iding, M., Ringrose, P., 2010. Reservoir modeling of CO_2 plume behavior calibrated against monitoring data from Sleipner, Norway. Society of Petroleum Engineers SPE-134891, 1–18.

Sorkhabi, R., Tsuji, Y., 2005. The place of faults in petroleum traps. In: Sorkhabi, R., Tsuji, Y. (Eds.), Faults, fluid flow, and petroleum traps. American Association of Petroleum Geologists Memoir 85, 1–31.

Springer, N., Lindgren, H.,2006. Caprock properties of the Nordland Shale recovered from the 15/9-A11 well, the Sleipner area. In: Greenhouse Gas Technology Conference 2006 (GHGT-8) Proceedings. Elsevier Science Ltd., Oxford, pp. 1–6.

StatoilHydro, 2009. Greenhouse store staying sealed, available at: http://www.statoil.com/en/NewsAndMedia/News/2009/Pages/03MarSleipner.aspx (published 05.03.09; accessed 05.11.13).

Vik, E., Løseth, H., Wensaas, L., 1998. Porepressures and indications of vertical fluid flow in the northern North Sea, Norwegian continental shelf. In: Mitchell, A., Grauls, D. (Eds.), Overpressures in petroleum exploration. Bulletin Centre Recherche Elf Exploration and Production Memoir 22, 117–122.

Wei, Z.P., Hermanrud, C., Lerche, I., 1990. Numerical basin modelling of the Sleipner field, North Sea. Terra Nova 2, 31–42.

Wilkinson, M., Haszeldine, R.S., Fallick, A.E., Odling, N., Stoker, S.J., Gatliff, R.W., 2011. CO_2–mineral reaction in a natural analogue for CO_2 storage – implications for modeling. Journal of Sedimentary Research 79, 486–494.

Young, T., 1805. Essay on the cohesion of fluids. Philosophical Transactions of the Royal Society 95, 65–87.

Zweigel, P., 2000. Seismic anomaly maps in the Neogene, Sleipner area. SINTEF Report, Project IK23430000, 9 pp.

Zweigel, P., Arts, R., Lothe, A.E., Lindeberg, E.B.G., 2004. Reservoir geology of the Utsira Formation at the first industrial-scale underground CO_2 storage site (Sleipner area, North Sea). In: Baines, S.J., Worden, R.H. (Eds.), Geological Storage of Carbon Dioxide. Geological Society, London, Special Publications, 233, pp. 165–180.

EXHIBIT 10

Received by OCD: 6/29/2026

Applied Energy 225 (2018) 332–345

Contents lists available at ScienceDirect

Applied Energy

journal homepage: www.elsevier.com/locate/apenergy

Geologic CO_2 sequestration monitoring design: A machine learning and uncertainty quantification based approach

Bailian Chen*, Dylan R. Harp, Youzuo Lin, Elizabeth H. Keating, Rajesh J. Pawar

Earth and Environmental Sciences Division, Los Alamos National Laboratory, Los Alamos, NM 87544, United States

HIGHLIGHTS

- Filtering-based data assimilation method is developed to perform monitoring design.
- Machine learning is used to reduce computational cost of data assimilation process.
- Uncertainty reduction is chosen as the metric to quantify the VOI of monitoring data.

ARTICLE INFO

Keywords:
Geologic carbon sequestration
Monitoring design
Machine learning
Reduced order model
Data assimilation
Uncertainty reduction

ABSTRACT

Monitoring is a crucial aspect of geologic carbon dioxide (CO_2) sequestration risk management. Effective monitoring is critical to ensure CO_2 is safely and permanently stored throughout the life-cycle of a geologic CO_2 sequestration project. Effective monitoring involves deciding: (i) where is the optimal location to place the monitoring well(s), and (ii) what type of data (pressure, temperature, CO_2 saturation, etc.) should be measured taking into consideration the uncertainties at geologic sequestration sites. We have developed a filtering-based data assimilation procedure to design effective monitoring approaches. To reduce the computational cost of the filtering-based data assimilation process, a machine-learning algorithm: Multivariate Adaptive Regression Splines is used to derive computationally efficient reduced order models from results of full-physics numerical simulations of CO_2 injection in saline aquifer and subsequent multi-phase fluid flow. We use example scenarios of CO_2 leakage through legacy wellbore and demonstrate a monitoring strategy can be selected with the aim of reducing uncertainty in metrics related to CO_2 leakage. We demonstrate the proposed framework with two synthetic examples: a simple validation case and a more complicated case including multiple monitoring wells. The examples demonstrate that the proposed approach can be effective in developing monitoring approaches that take into consideration uncertainties.

1. Introduction

Geologic CO_2 sequestration (GCS) is being considered as an important technology to reduce anthropogenic greenhouse gas emissions to the atmosphere [1–9]. Many potential reservoirs have been proposed to store anthropogenic CO_2 emissions, such as depleted oil or gas reservoirs, coal beds, deep oceans and deep saline formations [10–13]. The isolation of CO_2 from the environment is imperative for a GCS project not only for the project to successfully store CO_2, but also due to the fact that CO_2 leakage is a threat to the environment, the groundwater resources and human health [14–16]. CO_2 leakage may occur through improperly plugged and abandoned wellbores or through natural fractures or faults [1,17–19]. Given that depleted oil or gas reservoirs with significant numbers of abandoned wellbores are attractive locations for GCS [10,20–27], potential leakage through abandoned wellbores becomes a primary concern.

To ensure that large-scale GCS is safe and effective, a risk management strategy is generally used to minimize and mitigate risks during CO_2 injection and post-injection periods of a storage site [28–30]. Monitoring is an essential aspect of GCS risk management. To effectively monitor for CO_2 leakage, several monitoring technologies have been developed, including near-surface measurements of soil CO_2 flux and tracer [31,32], pressure monitoring [33–35], shallow groundwater chemistry monitoring [36,37], and micro-seismic and cross-well seismic survey [32,38]. A few studies have been conducted to evaluate the performance of different monitoring strategies or perform monitoring optimization for CO_2 storage sites. Next, we provide a discussion of some of the most relevant work in order to put the methodology introduced in this paper in context.

* Corresponding author.
E-mail address: chenbailian719@gmail.com (B. Chen).

https://doi.org/10.1016/j.apenergy.2018.05.044
Received 20 December 2017; Received in revised form 6 May 2018; Accepted 7 May 2018
Available online 15 May 2018
0306-2619/ Published by Elsevier Ltd.

Received by OCD: 6/29/2026

Nomenclature

Symbols

d_i	ith individual data point that would be obtained if the monitoring design were implemented
$\widetilde{d}^j$	jth data vector corresponding to each $\widetilde{m}^j$
$\widehat{d}^k$	kth data vector corresponding to each $\widehat{m}^k$
D	data that would be measured for a particular monitoring program
D^j	jth realization of D
e^j	jth realization of the vector of measurement errors
E_d	expectation with respect to all realizations of D
l_d	number of data realizations
l_{mc}	number of Monte Carlo samples
m	uncertain input parameter
$\widetilde{m}^j$	jth model realization generated from prior probability density function of m
$\widehat{m}^k$	kth Monte Carlo sample
M_c	cumulative CO_2 leakage
n_d	number of data points in the data vector D
$O(m)$	ROM vector for data
$P(M_c)$	prior probability density function of M_c
$P(M_c\|D^j)$	posterior probability density function of M_c
P_{10}	10th percentile
P_{90}	90th percentile
P_{acc}	acceptance probability
U	amount of uncertainty
U_R	uncertainty reduction
τ	threshold for maximum absolute error

Acronyms

AZMI	above zone monitoring intervals
BIPP	binary integer programming problem
EnKF	ensemble Kalman Filter
ES-MDA	ensemble smoother with multiple data assimilation
FEHM	Finite Element Heat and Mass transfer
GCS	Geologic Carbon Sequestration
LHS	Latin Hypercube Sampling
MAE	maximum absolute error
MARS	Multivariate Adaptive Regression Splines
MCMC	Markov chain Monte Carlo
PCKF	probabilistic collocation based Kalman Filter
PDF	probability density function
ROMS	reduced-order-models
VOI	value of information

Yang et al. [39] provided a probabilistic method for predicting the performance of different monitoring networks at GCS sites. The objective of their method is to estimate the probability that a monitoring network will detect CO_2 leakage. Yang et al. [40] developed a risk-based monitoring assessment methodology, which was an extended work of Yang et al. [39], to incorporate background data for monitoring design. In this method, the detection probability defined as the probability that a measured signal will be above the preselected threshold at the monitoring location is first calculated, and then the detection probability is used to estimate the monitoring well density and response time for both known and unknown wellbore leakage locations.

Seto and McRae [41] presented a model-based framework for integrated monitoring design that can provide a quantitative understanding of the trade-offs between operational costs and risks in potential monitoring strategies. In addition, the challenges, risks and design considerations of large scale CO_2 storage were comprehensively reviewed and discussed in their work. In the work of Seto and McRae [42], a method for CO_2 detection based on a Bayesian model selection framework was introduced and applied to distinguish whether detected CO_2 is from a leak or from background fluctuations. The limits of different monitoring technologies, the challenges of leak detection and what are acceptable rates of leakage were thoroughly investigated in their research.

Sun et al. [43] proposed an approach to optimize monitoring networks under geological uncertainty. A binary integer programming problem (BIPP) formulated in their work was demonstrated for effectively selecting optimal monitoring locations in both homogeneous and heterogeneous formations. However, the proposed method requires running a forward full-scale model many times for different design options, which makes the BIPP computationally demanding. Sun et al. [43] suggested that a reduced order model or surrogate model can be used to speed up the BIPP optimization process. Cameron [44] demonstrated an approach to optimize sensor locations for CO_2 plume monitoring at a GCS site under geological uncertainty by minimizing the expected prediction error of the CO_2 plume size.

Dai et al. [45] proposed a data-worth analysis approach using probabilistic collocation based Kalman Filter (PCKF) to optimize the surveillance operation in a GCS project. In this approach, surrogate models are developed using polynomial chaos expansion to replace the original flow models. Thereafter, the expected variance reduction of field cumulative CO_2 leakage is assessed via data-worth analysis. An optimal monitoring operation scheme is selected by comparing the value of data-worth for different monitoring strategies. Dai et al. [46] applied the data-worth analysis and PCKF based approach to quantify the uncertainty reduction associated with the characterization of a migrating contaminant plume for different monitoring networks in groundwater systems.

Chen et al. [47] proposed an approach based on the Markov chain Monte Carlo (MCMC) method and reduced order models (ROMs) to quantify the uncertainty reduction of different pilot designs in an oil field. Note that a pilot refers to small-scale test and data collection operations prior to a full field development. In the proposed method, multiple realizations of monitoring data from a pilot test are generated, and probabilistic history matching (data assimilation) based on an MCMC method is performed for each data realization to obtain the corresponding posterior distribution. Though the MCMC based history matching is accomplished with the help of ROMs, the computational demand is still high due to the fact that for each data realization, MCMC often takes hundreds of thousands of runs to converge [48–50]. As mentioned in the work of Chen et al. [47], one limitation of their proposed framework is that with the increase of the uncertain model parameters, it would be difficult for the Markov chain to converge to the target distribution.

In this work, we build off the previously mentioned monitoring design algorithms to capture full physics simulations in a computationally efficient manner by using reduced order models and determine the optimal monitoring design for GCS sites based on many potential leakage scenarios that could occur. To quantify the uncertainty reduction, instead of using an MCMC method as in the work of Chen et al. [47], we apply a filtering based data assimilation method [51] in this study, which overcomes the convergence issue inherent in the MCMC method. In addition, a popular machine learning technique, Multivariate Adaptive Regression Splines (MARS) [52], is used to construct the ROMs or proxy models to reduce the computational cost when the filtering based data assimilation method is applied.

Received by OCD: 6/29/2026

2. Methodology

2.1. Uncertainty quantification

In this study, the goal of monitoring design is to evaluate the value of data, where the value of data is quantified by the amount of uncertainty that is reduced in one of the metrics for CO_2 leakage risk assessment, cumulative CO_2 leakage. The cumulative CO_2 leakage over a specified time period is designated as the objective function here and denoted as M_c. The prior probability density function (PDF) of M_c is denoted as $P(M_c)$. Note that "prior" refers to a probability distribution before a monitoring program is implemented. The distribution of potential monitoring data that could be measured for a particular monitoring program and leakage scenario is denoted by D; that is, $D = [d_1,d_2,\cdots,d_{n_d}]$, where $d_i,i = 1,2,\cdots,n_d$ are the individual monitoring data points that would be obtained if the monitoring design were implemented given a particular leakage scenario and n_d is the number of monitoring data points in D. Here, d_i represents the ith monthly pressure, CO_2 saturation, or temperature values at a monitoring well. We denote D^j to be the jth realization from D. For each D^j, a posterior PDF of M_c denoted by $P(M_c|D^j)$ can be calculated by an ensemble-based history matching or data assimilation procedure, where $P(M_c|D^j)$ is the probability that the cumulative CO_2 leakage is M_c given that the data are D^j.

In conventional history-matching, D would represent the actual measurements and the simulation model(s) would be calibrated so that they match or honor these measurements [53–56]. In this study, D corresponds to a potential monitoring dataset from a distribution of potential monitoring datasets that are all considered equally based on available information. The objective of monitoring optimization is to quantify the value of information (VOI) estimated from a distribution of potential monitoring datasets. Quantifying the VOI of a distribution of potential monitoring data sets allows one to choose a CO_2 monitoring design that will perform well for a distribution of potential leakage scenarios.

As illustrated in the work of Chen et al. [47], the VOI of monitoring data, similar to the concept of data-worth [45], can be quantified by the uncertainty reduction in an objective function. In this study, uncertainty reduction is also applied to quantify the VOI of potential monitoring data. We denote the amount of uncertainty in a cumulative CO_2 leakage distribution $P(M_c)$ as $U(P(M_c))$, which, as in Le and Reynolds [57], is defined as

$$U(P(M_c)) = P_{90}(P(M_c)) - P_{10}(P(M_c)), \tag{1}$$

where $P_{10}(P(M_c))$ and $P_{90}(P(M_c))$, respectively, are the 10th and 90th percentiles of the distribution $P(M_c)$. Note that in our approach, we don't expect that the distribution of cumulative CO_2 leakage, $P(M_c)$, is measured in field practices, but simulated in groundwater flow models. The distribution of cumulative CO_2 leakage is due to the uncertainty in the model parameters which lead to the monitoring data realizations D^j. Selecting a monitoring design that reduces the uncertainty in M_c ensures that the monitoring design will function effectively under many potential leakage scenarios. The expected posterior uncertainty in M_c given D is given by

$$E_d(U(P(M_c|D))) = \frac{1}{l_d}\sum_{j=1}^{l_d} U(P(M_c|D^j)), \tag{2}$$

where E_d represents the expectation with respect to all realizations of D, and l_d is the number of data realizations. The expected uncertainty reduction, U_R, due to data acquisition from a potential CO_2 monitoring operation, is defined as the difference between the prior uncertainty and the expected posterior uncertainty in the cumulative CO_2 leakage, which is given by

$$U_R = U(P(M_c)) - E_d(U(P(M_c|D))). \tag{3}$$

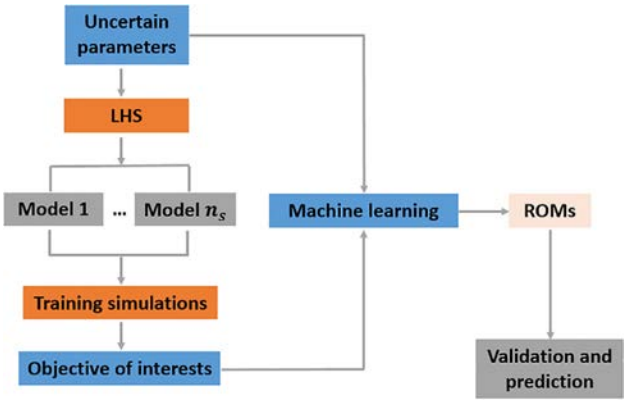


Fig. 1. Workflow diagram for ROM development.

The uncertainty reduction, U_R, quantifies the effectiveness of a particular monitoring design. The higher reduction in uncertainty in the cumulative CO_2 leakage, the higher the VOI contained in the monitoring data that would be obtained from the monitoring design.

2.2. Reduced order model development

To make the filtering approach computationally feasible, reduced order models (ROM) are developed in this study. The workflow for the ROM development is presented in Fig. 1. In this section, we give a brief summary of the main steps of this workflow.

Step 1: *Perform experimental design:* Staring from a set of uncertain parameters, we generate n_s training samples using Latin Hypercube Sampling (LHS) [58]. In this study, the uncertain parameters include the permeability multiplier of the storage reservoir and the permeabilities of all potentially leaky pathways.
Step 2: *Perform training simulations:* A numerical simulation of CO_2 injection and subsequent migration is performed with each of the n_s training samples. The Finite Element Heat and Mass transfer code (FEHM simulator) [59] is used to perform the simulations.
Step 3: *Collect inputs and outputs from the training simulations:* For each simulation, the uncertain parameters, monitoring datasets, and cumulative CO_2 leakage are collected. Note that in Fig. 1, the uncertain parameters are the inputs and the objectives of interest are the outputs from training simulations. For the purposes of ROM building, the objectives of interest can be cumulative CO_2 leakage and different monitoring data.
Step 4: *Generate ROMs for the objectives of interest:* A reduced order model can be used to approximate relations between training simulation input parameters and outputs. Note that we build one ROM for each objective of interest. The objectives of interest include cumulative CO_2 leakage (M_c) and simulated monitoring data (D) at specified times. A Multivariate Adaptive Regression Splines (MARS) algorithm [52], which has been successfully applied to the ROM development in GCS related research [60,18,61], is implemented to build the ROMs.
Step 5: *Validate the fidelity of ROMs to numerical simulator:* In this study, the fidelity of the ROMs to the numerical simulation results is tested with 10-fold cross-validation ([64]). Note that the cross-validation does not check whether the ROMs can predict the cases that it is trained with, but it can predict the cases that were not used for training. The validated ROMs can be used for further prediction instead of computationally intensive numerical simulations.

2.3. Workflow for monitoring design

In this section, a filtering and ROM based workflow for CO_2

monitoring design is presented. The flow diagram is shown in Fig. 2. The main steps of this workflow are summarized below.

Step 1. *Develop ROMs for the objective function, M_c, and predicted monitoring data, D:* The details of the ROM development were presented in the previous section. Note that we build one ROM for each monitoring data point in each data vector D^j). The vector of ROM simulated monitoring data is denoted as $O(m) = [O_1(m),\cdots,O_{n_d}(m)]^T$, where m denotes the vector of uncertain input parameters. The ROMs can then be used to replace the FEHM simulator to predict the objectives of interest for new input parameters that are not in the training ensemble.

Step 2. *Generate plausible realizations of the monitoring data, D:* First, l_d realizations are sampled from the prior PDF of m, and are denoted by $\widetilde{m}^j, j = 1,2,\cdots,l_d$. Then the monitoring data $\widetilde{d}^j_{\text{obs}}$ corresponding to each $\widetilde{m}^j$ is generated by the following equation;

$$\widetilde{d}^j_{\text{obs}} = O(\widetilde{m}^j) + e^j, \tag{4}$$

where $O(\widetilde{m}^j)$ is calculated from the ROMs for the n_d predicted monitoring data points, i.e., $O(\widetilde{m}^j) = [O_1(\widetilde{m}^j),\cdots,O_{n_d}(\widetilde{m}^j)]^T$ and the vector e denotes a realization of the vector of measurement errors. Note that the elements of e follow a Gaussian distribution.

Step 3. *Generate Monte Carlo samples and calculate the prior uncertainty:* A large number of Monte Carlo samples $\widehat{m}^k, k = 1,2,\cdots,l_{mc}$ are generated from the prior distribution of m, and these Monte Carlo samples are used to construct the prior distribution. Then, the amount of uncertainty in the prior distribution of m can be calculated using Eq. (1).

Step 4. *Filter the Monte Carlo samples and compute the expected posterior uncertainty:* We use the filtering method [51] to construct a posterior distribution of m conditional to each $\widetilde{d}^j_{\text{obs}}, j = 1,2,\cdots,l_d$. The filtering method (or rejection sampling) with ROMs is performed as follows. First, using the Monte Carlo samples, $\widehat{m}^k$ generated in Step 3, we simulate the corresponding monitoring data $\widehat{d}^k$ using the ROMs constructed in Step 1, i.e., $\widehat{d}^k = O(\widehat{m}^k)$. The data vector $\widehat{d}^k$ can be expressed as $\widehat{d}^k = [\widehat{d}^k_1,\widehat{d}^k_2,\cdots,\widehat{d}^k_{n_d}]$ and represents a realization from the distribution of potential monitoring datasets that capture the many potential leakage scenarios that may occur given the uncertainty in the input parameters. We define the data assimilation error of the Monte Carlo samples, $\widehat{m}^k$, as the maximum absolute error (MAE), which is expressed as

$$\text{MAE}(\widehat{d}^k, d^j_{\text{obs}}) = \max_{1\le i\le n_d} \left|\widehat{d}^k_i - \widetilde{d}^j_{\text{obs},i}\right|. \tag{5}$$

$\widehat{m}^k$ is accepted as a legitimate realization of the posterior distribution according to the following acceptance probability:

$$P_{acc}(\widehat{m}^k) = \begin{cases} 1, & \text{if MAE} < \tau \\ 0, & \text{otherwise} \end{cases}. \tag{6}$$

This means the Monte Carlo sample $\widehat{m}^k$ will be accepted only if the corresponding MAE is smaller than the threshold τ. The threshold τ should be chosen based on engineering judgment that takes into consideration the measurement error and the modeling error. In other words, $\widehat{m}^k$ is accepted if it is deemed sufficiently consistent with the monitoring data realization. The acceptance probability in Eq. (6) is evaluated for all the Monte Carlo samples, and the accepted cases constitute the posterior distribution of m conditional to monitoring data realization $\widetilde{d}^j_{\text{obs}}$. This procedure is repeated for all the data realizations so that l_d posterior distributions of m are obtained. We compute the amount of uncertainty for each posterior distribution of m using Eq. (1) and then calculate the expected posterior uncertainty using Eq. (2).

Step 5. *Calculate the expected amount of uncertainty reduction U_R:* The expected uncertainty reduction U_R is calculated by comparing the uncertainty of the prior distribution and the expectation of the uncertainty for the posterior distributions of the cumulative CO_2 leakage using Eq. (3).

With this workflow, the expected uncertainty reduction in the cumulative CO_2 leakage for each of the potential monitoring operations can be computed, and the optimal monitoring design can be determined based on choosing the monitoring design that reduces the uncertainty in the simulated amount of CO_2 leakage.

3. Model description

To validate the introduced workflow for CO_2 monitoring design, we consider a synthetic GCS model consisting of a heterogeneous storage reservoir, a homogeneous caprock layer and a homogeneous aquifer. Fig. 3 presents the schematic of the base model. The thicknesses of the reservoir, caprock layer and aquifer are all 30 m. The model is 1000 m wide in the horizontal dimensions. The depth from the top of the model to the ground surface is 1000 m. It has a CO_2 injection well located in the center of the reservoir and multiple potentially leaky pathways in the caprock. CO_2 injected into the storage reservoir can potentially leak to the aquifer through the leaky pathways in the caprock layer. Note that only one leak location is shown in Fig. 3 while we have considered scenarios with multiple leak points. We consider a homogeneous permeability distribution for both the caprock layer and the aquifer with the permeability equal to 1×10^{-19} and 1×10^{-13} m^2, respectively. Note 10^{-15} m^2 is approximately equal to 1 mD. The heterogeneous permeability distribution for the storage reservoir of the base model is generated assuming a spherical anisotropic variogram model [62] with a major correlation length of 680 m and a minor correlation length of 280 m. The direction of maximum spatial correlation continuity is equal to 45 degrees measured from the positive x-axis. The mean of the permeability field of the reservoir is 1×10^{-13} m^2. We assume that the storage reservoir permeability is uncertain. To represent the uncertainty in reservoir permeability, we use a permeability multiplier to multiply the base permeability distribution described earlier. The value of the permeability multiplier is varied randomly to generate multiple realizations of permeability distributions. The lower and upper bounds for the multiplier are shown in Table 1. The other uncertain parameters we consider are the permeabilities of the potentially leaky pathways.

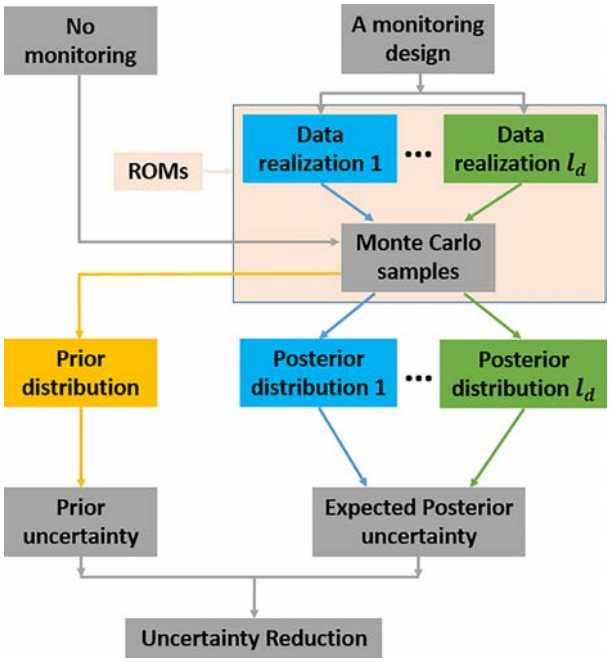


Fig. 2. Filtering and ROMs based workflow for CO_2 monitoring design.

Received by OCD: 6/29/2026

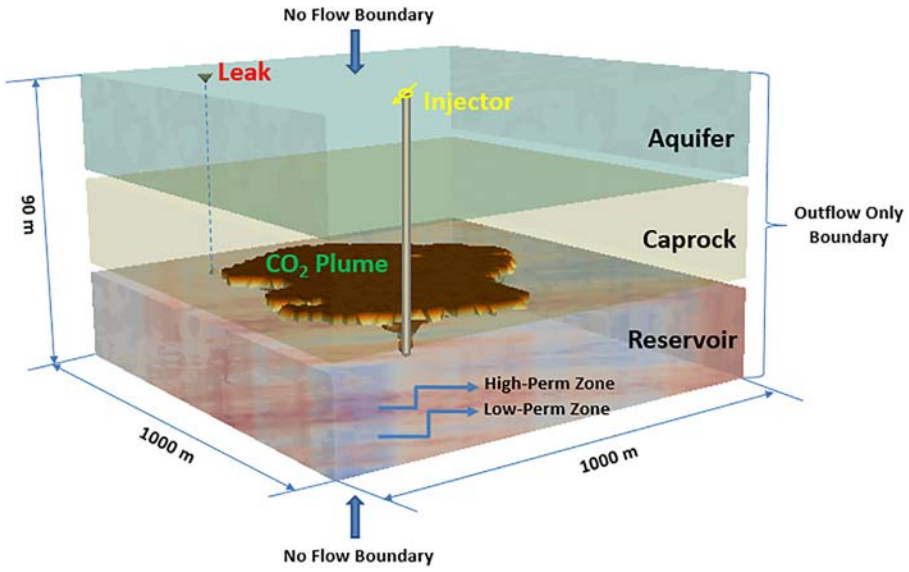


Fig. 3. Schematic of the model, in which storage reservoir and aquifer are separated by caprock. A CO_2 injection well is located in the center of the storage reservoir. The vertical axis is exaggerated 7 times.

Table 1
Uncertain parameters and their lower and upper bounds.

Uncertain parameters	Lower bound	Upper bound	Unit
Reservoir permeability multiplier	0.5	2	–
Permeability of leaky pathway(s)	−19	−14	$\log_{10}$ [m^2]
	(0.0001)	(10)	mD

The values of these are assumed to vary between the lower and upper bounds listed in Table 1.

The numerical mesh for the reservoir simulation model were generated using a grid generation toolkit LaGriT (http://lagrit.lanl.gov) [63]. The numerical mesh has 51 nodes in both x and y directions and 31 nodes in the z direction. The distance between two nodes in x and y directions is 20 m, and the distance between two nodes in z direction is 3 m. The number of nodes used for reservoir, cap rock and aquifer, respectively, is 26010, 26010 and 28611. The total number of nodes for simulation is 80631. 3D multi-phase simulations are performed by the Finite Element Heat and Mass transfer code (FEHM simulator) [59]. The sides of the reservoir, caprock layer and aquifer are Dirichlet boundaries allowing outflow of CO_2 and water at pressures above hydrostatic. Inflow is not allowed at these boundaries. The top and bottom of the model are no-flow boundaries. The model is initialized to a geothermal gradient of 0.03 °C/m with a temperature of 20 °C along the top. Pressures are initialized to a gradient of 9.81×10^{-3} MPa/m with a pressure of 0.2 MPa along the top. In this study, we consider a five-year CO_2 injection period with the injection rate equal to 0.1 million tons/year.

4. Results and analysis

4.1. Workflow validation

We validate the workflow for CO_2 monitoring design using a simple example. Fig. 4 shows the log-permeability distribution for the base model, the three potentially leaky locations (in yellow) and two optional locations (M1 and M2) for a single monitoring well design. All the monitoring data in this study are collected in the aquifer, similar to monitoring at the above zone monitoring intervals (AZMI) in the work of Sun et al. [43]. In this example, the monitoring data used is pressure. The monitoring frequency is once per month for the duration of 5 years, resulting in 60 monitoring data points. The objective function, M_c, is cumulative CO_2 leakage at the end of 5 years. In the model, we set up three material zones corresponding to three formations (i.e., Reservoir, Caprock and Aquifer). The cumulative CO_2 in different material zones can be output from the simulator FEHM. The cumulative CO_2 leakage is computed by summing up the CO_2 mass of in the aquifer and caprock. Note that our approach for monitoring design is based on quantifying the uncertainty reduction by monitoring pressure, temperature and/or CO_2 saturation at potential monitoring well(s). The pressure, temperature and saturation for a certain location (corresponding to a node in the simulator) at a particular time can also be computed in the simulator.

The data assimilation error tolerance, τ from Eq. (6), for pressure data is set equal to 0.002 MPa. Note that the choice of τ is site and case specific and should be based on engineering judgment that takes into consideration the measurement and modeling error.

Four uncertain model parameters are considered: the permeability multiplier for storage reservoir and the three permeability values for

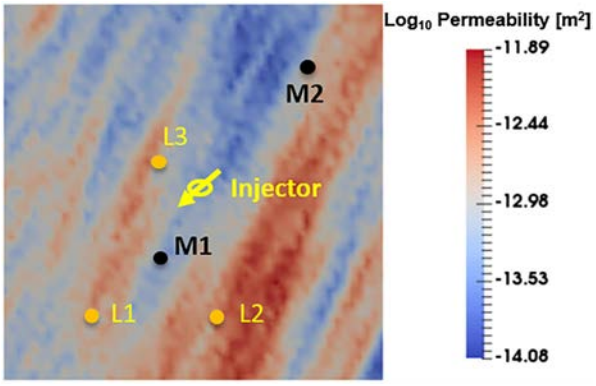


Fig. 4. Log-permeability distribution for the base model and the locations of potential leakages, potential monitoring wells and injector. The unit for permeability is $\log_{10}$ [m^2]. The darkest blue color corresponds to the lowest permeability, while the darkest red color corresponds to the highest permeability. Yellow dots indicate the potentially leaky points; black dots indicate the potential monitoring location(s); yellow circle with an arrow indicates the injector. (For interpretation of the references to color in this figure legend, the reader is referred to the web version of this article.)

Received by OCD: 6/29/2026

the three potentially leaky pathways. The lower and upper bounds for these uncertain parameters can be found in Table 1. We first run 500 training simulations generated by LHS sampling with the four uncertain parameters. It takes about 22 min for each simulation. In this study, 8 simulations are run concurrently. It takes around 23 h to finish all 500 training simulations.

Here, we choose one simulation from 500 training simulations to show when leakage occurs. The values of different parameters for the chosen model are shown in Table 2. Fig. 5 shows the cumulative CO_2 leakage over time computed from one chosen training simulation. It can be seen from Fig. 5 that CO_2 leakage happens after about 210 days' CO_2 injection. The leaked CO_2 saturation distribution at the top of the aquifer is shown in Fig. 6. We can see that the CO_2 is leaked through the potentially leaky pathway (L3) which is 141.4 m away from the injector, while no CO_2 leakage is observed within the 5 years' CO_2 injection at the potentially leaky pathways (L1 & L2). It should be noted that the permeability of L3 is higher than that of L1 and L2 for this specific example.

Based on the training simulations, ROMs for the monitoring data and the cumulative CO_2 leakage are constructed using MARS. Fig. 7 shows the quality of the ROMs tested by 10-fold cross validation [64]. Fig. 7(a) and (b), respectively, show the quality of ROMs from the cross validation for the cumulative CO_2 leakage and for an example data point pressure at M1 at year two. The correlation coefficients between the true values from simulations and the ROM predictions for the objective function and monitoring data point at year two, respectively, are 0.996 and 0.995, which indicates that the fidelity of the ROMs to the numerical simulations is high in this case and also in the other ROMs which are not shown here.

For the example introduced above, it is obvious that monitoring at M1 would obtain more information (i.e., higher uncertainty reduction in objective function) than monitoring at M2 since M1 is much closer to the potentially leaky points than M2; that is, simple intuition indicates that monitoring at M1 is a better choice than monitoring at M2. The purpose of this simple example is to demonstrate that our proposed workflow can successfully capture this intuitive result.

With the proposed workflow, the expected uncertainty reduction of the cumulative CO_2 leakage can be computed for the two monitoring data sets, one obtained from M1 and the other one obtained from M2. For each data set, 200 plausible realizations of monitoring data are generated following Step 2 described in Section 2.3. Fig. 8 shows one plausible monitoring data realization obtained from potential monitoring locations M1 and M2. It can be seen that the monitoring data predicted by ROM matches well with the simulation results. To calculate the expected uncertainty reduction using Eq. (3), the prior uncertainty $U(P(M_c))$ and posterior uncertainty $U(P(M_c|D^j))$ corresponding to each plausible monitoring data realization D^j should be computed. Fig. 9 shows how these values, i.e., the prior and posterior uncertainties, are obtained. For simplicity, only one posterior CDF (obtained from specific data realization used for this example) for each potential monitoring location is shown in Fig. 9. In Fig. 9, the difference between the 10th and 90th percentiles of a cumulative density function (CDF) is the amount of uncertainty in a distribution. $U(P(M_c))$ denotes the amount of uncertainty in a cumulative CO_2 leakage distribution $P(M_c)$, i.e., prior uncertainty; $U(P(M_c|D^j))$ denotes the amount of uncertainty in $P(M_c)$ conditional to plausible monitoring data realization D^j, i.e., one posterior uncertainty. 200 plausible data realizations generate 200 posterior CDFs which produce 200 posterior uncertainties corresponding to each data realization. The expected posterior uncertainty which is the average value of the 200 posterior uncertainties can then be computed by Eq. (2).

With the computed prior and expected posterior uncertainties, the uncertainty reduction is calculated by Eq. (3). Fig. 10 shows the uncertainty reduction at the end of five years given the distribution of potential monitoring data sets that may be obtained at M1 and M2. In Fig. 10, the red[1] diamond indicates the prior uncertainty which is equal to 39.24 thousand tons for this example; the blue dash line indicates the expected posterior uncertainty which is the average value of the 200 posterior uncertainties corresponding to each data realization. It can be

[1] For interpretation of color in Fig. 10, the reader is referred to the web version of this article.

Table 2
The parameters for one chosen model from 500 training models.

Parameters	Value
CO_2 injection rate	3.17 kg/s
Thickness of caprock layer	30 m
Permeability of 1st potentially leaky pathway	2.19×10^{-17} m^2 (0.0219 mD)
Permeability of 2nd potentially leaky pathway	3.37×10^{-17} m^2 (0.0337 mD)
Permeability of 3rd potentially leaky pathway	2.97×10^{-16} m^2 (0.297 mD)
Distance between injector and 1st potentially leaky pathway	424.3 m
Distance between injector and 2nd potentially leaky pathway	360.6 m
Distance between injector and 3rd potentially leaky pathway	141.4 m
Permeability for aquifer layer	1×10^{-13} m^2 (100 mD)
Permeability for caprock layer	1×10^{-19} m^2 (0.0001 mD)
Reservoir permeability multiplier	1.88

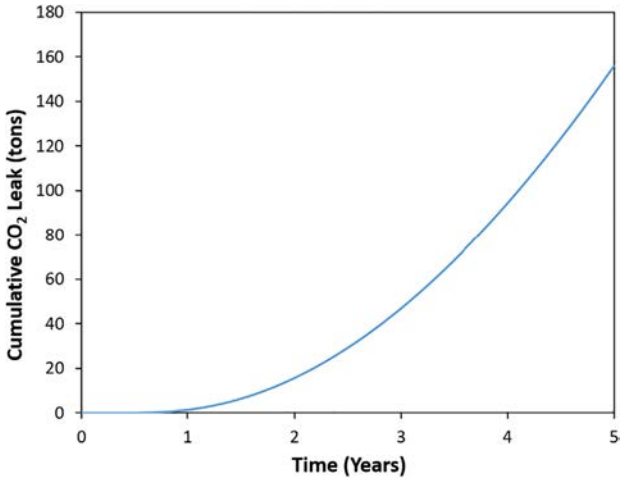


Fig. 5. Cumulative CO_2 leakage over time computed from one chosen training simulation.

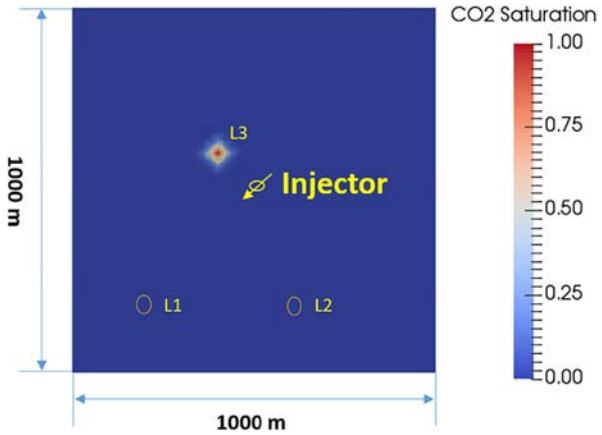
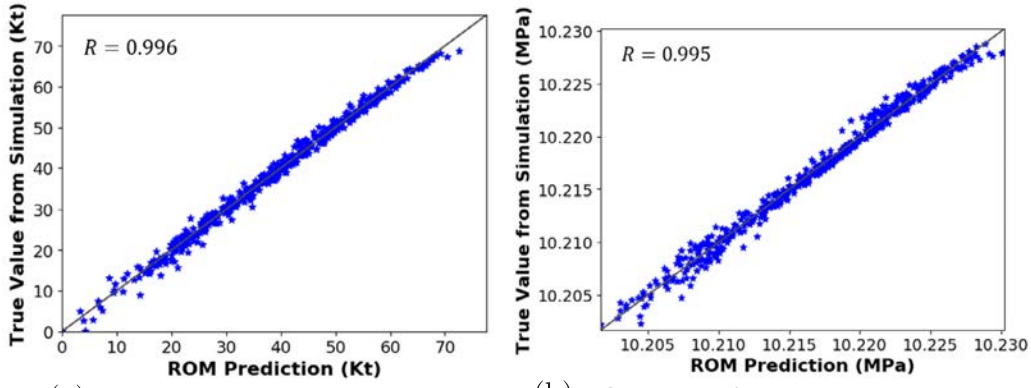


Fig. 6. Plan view (top of the aquifer) of CO_2 leakage at the end of five years based on the chosen training simulation. Yellow circles indicate the potentially leaky locations. Unit for CO_2 saturation is fraction. (For interpretation of the references to color in this figure legend, the reader is referred to the web version of this article.)



(a) ROM quality for objective function (b) ROM quality for pressure at year two, M1

Fig. 7. Quality of the ROMs tested by 10-fold cross validation. R indicates the correlation coefficient between the true values from simulations and the ROM predictions for the objective function.

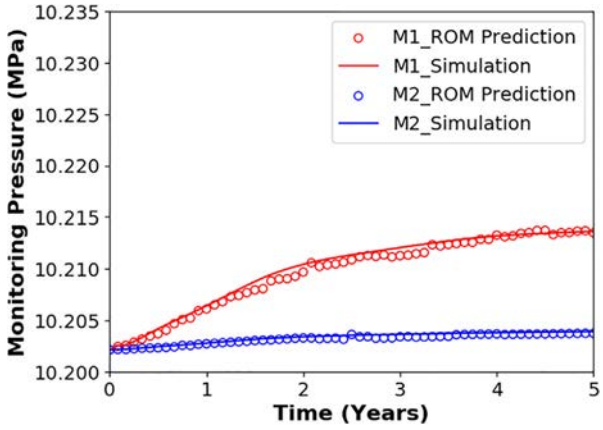


Fig. 8. One plausible monitoring data realization obtained from potential monitoring locations M1 and M2.

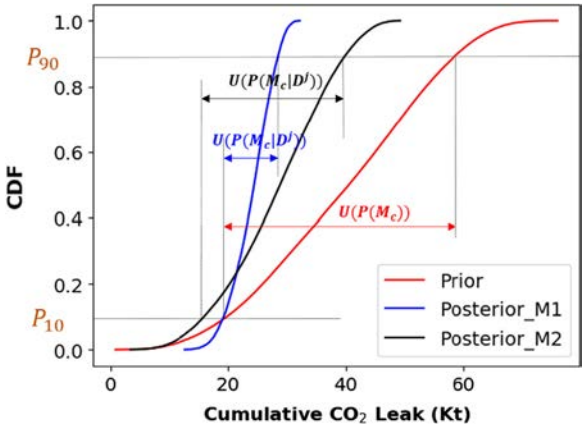


Fig. 9. CDF of cumulative CO_2 leakage for the prior distribution and posterior distributions conditional to plausible monitoring data D^j obtained from potential monitoring locations M1 and M2.

seen that monitoring at location M1 gives much higher uncertainty reduction than M2. Higher uncertainty reduction of the objective function indicates greater VOI in the monitoring data set to be obtained from location M1, thereby demonstrating our assertion. Through this example, we can see that our proposed workflow can be effectively used to determine the optimal CO_2 monitoring design from a set of alternative monitoring designs.

The evolution of the expected posterior uncertainty in the cumulative CO_2 leakage over time can be evaluated to understand the VOI of the monitoring data over time. Fig. 11 shows the expected posterior uncertainty in cumulative CO_2 leakage over time for two monitoring data sets obtained from monitoring locations M1 and M2, respectively. It can be observed that the pressure data set obtained from M1 is expected to reduce the uncertainty more than the pressure data obtained from M2 within the first 1 year. This is due to the fact that we can observe more significant pressure changes at the monitoring location M1 than M2 at year one as can be seen in Fig. 12. Almost no uncertainty can be reduced with the pressure data obtained from monitoring location M2 after 2 years, this is because significant pressure changes do not occur after 2 years at M2 for all the possible pressure realizations; see Fig. 12(b).

Sensitivity analysis is performed using Pearson correlation [65]. The plot in Fig. 13 shows the correlation coefficients between the four uncertain model parameters and the maximum pressure data in each pressure data realization as shown in Fig. 12. Recall that the four uncertain model parameters are the permeabilities of the three potentially leaky pathways (K_L1, K_L2 and K_L3) and the reservoir permeability multiplier (K_Reservoir). It can be observed from Fig. 13 that the pressure data have positive sensitivity to the permeabilities of the three potentially leaky pathways; that is to say the higher the permeability of the potentially leaky pathways, the higher the pressure that could be measured at locations M1 or M2. Moreover, the pressure data are most sensitive to the permeability of the third potentially leaky pathway (L3), due to the fact that the third potentially leaky pathway is closer to the injector than the other two potentially leaky pathways (see Fig. 4). It can also be seen from Fig. 13 that the pressure data have negative sensitivity to the reservoir permeability multiplier (K_Reservoir). This is because the higher the permeability of the reservoir, the faster the CO_2 migrates towards to the boundaries of the storage site, which results in less CO_2 leaking through the potentially leaky pathways and the strength of pressure signals will be reduced accordingly. We can also observe from Fig. 13 that the pressure data monitored at M1 are about twice as sensitive to the permeability of the first potentially leaky pathways (L1) than the pressure data monitored at M2. This is due to the fact that M1 is much closer to L1 than M2 (see Fig. 4).

Fig. 14 shows box plot of the samples remaining after the filtering approach for each monitoring data realization (200 realizations in total) of the pressure data obtained from monitoring locations M1 and M2. It can be seen from Fig. 14 that for any monitoring data realization, the number of remaining samples to construct the posterior distribution is over 1800, which is greater than the minimum required samples (30 samples) to construct a PDF to calculate P90 and P10 [47].

Fig. 15 shows the histograms for the posterior distributions of the objective function obtained from data realizations 1 and 100 as well as

Received by OCD: 6/29/2026

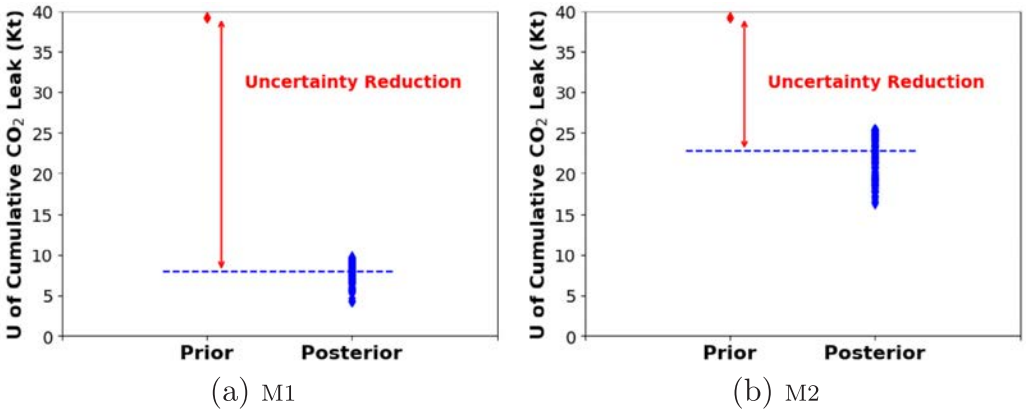


Fig. 10. The U value (uncertainty) of the prior and posterior distributions for the objective function.

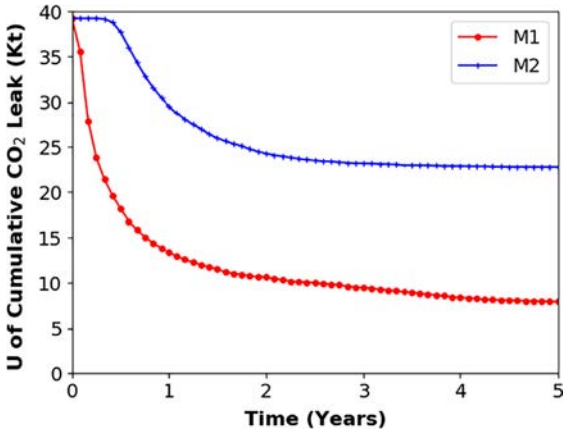


Fig. 11. Expected posterior uncertainty in objective function over time.

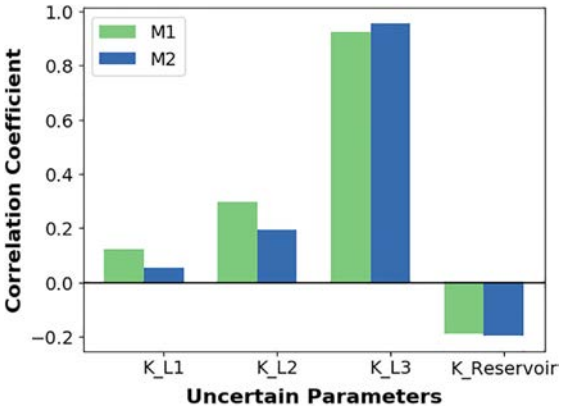


Fig. 13. Correlation coefficients between the uncertain model parameters and the maximum pressure data to be monitored.

the histogram for the prior distribution of the objective function. Note that the prior distribution of the objective function is generated by using the Latin hypercube sampling of the uncertain input parameters with uniform distributions and calculating the cumulative CO_2 leakage using the ROMs. We can observe from Fig. 15 that the variances of the posterior distributions calculated from data realizations 1 and 100 as well as the variances of the posterior distributions calculated from other data realizations which are not shown here are significantly decreased compared to the variance of prior distribution, and the variances of posterior distributions for M1 are much smaller than those for M2, which results in significantly higher uncertainty reduction in cumulative CO_2 leakage for M1 than for M2.

4.2. *Effect of measurement type and location in vertical direction*

Next, we will investigate the effect of different types of measurements (i.e., pressure, CO_2 saturation and temperature) as well as the monitoring location on the uncertainty reduction in the cumulative CO_2 leakage. We explore two different monitoring locations in the vertical direction at M1. The data measurement frequency is still once per month for five years. The data assimilation error tolerances, τ, for pressure, CO_2 saturation and temperature, respectively, are 0.002 MPa, 0.05 and 0.002 °C. All the other parameters that are mentioned here are the same as those in the first case.

Fig. 16 shows the expected posterior uncertainty in the objective

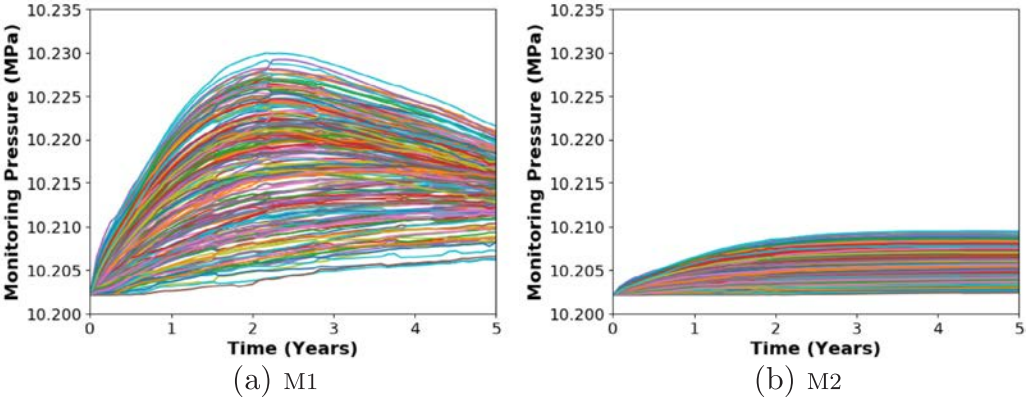


Fig. 12. Pressure for different data realizations obtained from monitoring locations M1 and M2.

Received by OCD: 6/29/2026

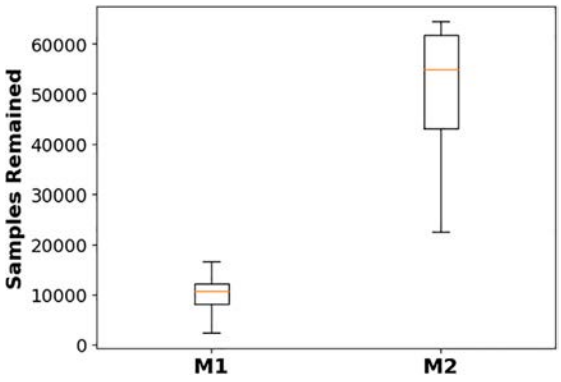


Fig. 14. Samples remaining after the filtering approach. The number of prior samples is 100,000.

function changing over time for different type of measurements and different vertical monitoring locations (at the bottom or top of the aquifer). The values of uncertainty reduction for different monitoring designs are recorded in Table 3. From Fig. 16 and Table 3, it can be observed that pressures (P) observations lead to higher uncertainty reduction compared to CO_2 saturation (S) and temperature (T). Additionally, pressure observations measured at the bottom of the aquifer give slightly higher uncertainty reduction than those measured at the top of the aquifer. It can also be observed that CO_2 observations measured at the bottom of the aquifer do not lead to any reduction in uncertainty. This is due to the fact that because of the buoyancy, CO_2 primarily pools towards the top of the aquifer which results in very little to no CO_2 saturation observed at the bottom of the aquifer; see Fig. 17(c). Since no CO_2 is observed during the first year at the monitoring location (see Fig. 17(d)), no uncertainty reduction is observed at the beginning of the first year; see Fig. 16(d). However, after one year, CO_2 saturation at the monitoring location starts changing, which leads to significant uncertainty reduction. It is important to note that the lag of the uncertainty reduction with CO_2 saturation data set compared to the uncertainty reduction with pressure data set is due to the fact that pressure signals travel much faster than the signals for CO_2 saturation in porous media. From Fig. 17(e), we cannot observe any significant temperature change over time, resulting in no uncertainty reduction when the temperature data were measured at the bottom of the aquifer. However, in Fig. 17(f), we can observe the temperature change due to the leaked CO_2 accumulated at the top of the aquifer, but the difference in the temperature for different realizations at a particular time is negligible for the first two and half years (i.e., the temperature data are not sensitive to the uncertain parameters for the first two and half years), which results in no uncertainty reduction in the first two and half years. After two and half years, the temperature data measured at the top of aquifer do result in a small amount of uncertainty reduction.

We also computed the effect of joint measurements of multiple types of data on reduction in uncertainty. The results are summarized in Table 3. A combination of pressure and CO_2 saturation data sets leads to a slightly higher uncertainty reduction (1.09 thousand tons) than that due to pressure data set alone. On the other hand, combined measurement of pressure and temperature data sets leads to only 0.17 thousand tons higher uncertainty reduction compared to the pressure data set alone. Furthermore, only 0.01 thousand tons more uncertainty can be reduced by adding the temperature data set to the combined pressure and CO_2 saturation data sets. The above analysis indicates that one can benefit more from monitoring both pressure and CO_2 saturation data than monitoring only pressure data. However, monitoring pressure, CO_2 saturation, and temperature data sets together will not add any VOI. The prior and expected posterior uncertainties for different types of monitoring strategies (monitoring at the top of the aquifer) are presented in Fig. 18, which clearly shows the distributions for posterior uncertainties computed from different type of monitoring strategies.

4.3. Effect of the number of monitoring wells

To investigate the effect of the number of monitoring wells on the decision of monitoring strategy, we develop a second example as shown in Fig. 19. More potentially leaky points (6 leaky points) are considered in this example than those in the first example. 500 training samples are generated by LHS sampling with the seven uncertain parameters, i.e., 6 uncertain parameters for the permeability of 6 potentially leaky points and one uncertain parameter for the reservoir permeability multiplier. All the training samples are simulated by the FEHM simulator. The type of data to be measured is pressure. All the other parameters for the example set-up that are not mentioned here are the same as described in the first example.

Based on the inputs and outputs of training simulations, we build the ROMs for both objective function (cumulative CO_2 leakage) and the 60 data measurements. Fig. 20 shows the quality of the ROMs tested by 10-fold cross validation. The correlation coefficients between the simulated values and the ROMs predicted values for the objective function and the example monitoring data point at year one, respectively, are 0.995 and 0.994, which indicates the constructed ROMs as well as the other ROMs not shown here have high fidelity to the numerical simulations.

The specifications of the four schemes, according to the different number of the monitoring locations and the corresponding uncertainty reductions in the objective function, are listed in Table 4. The expected posterior uncertainty in the objective function over time for different schemes is shown in Fig. 21. From Table 4 and Fig. 21, it can be

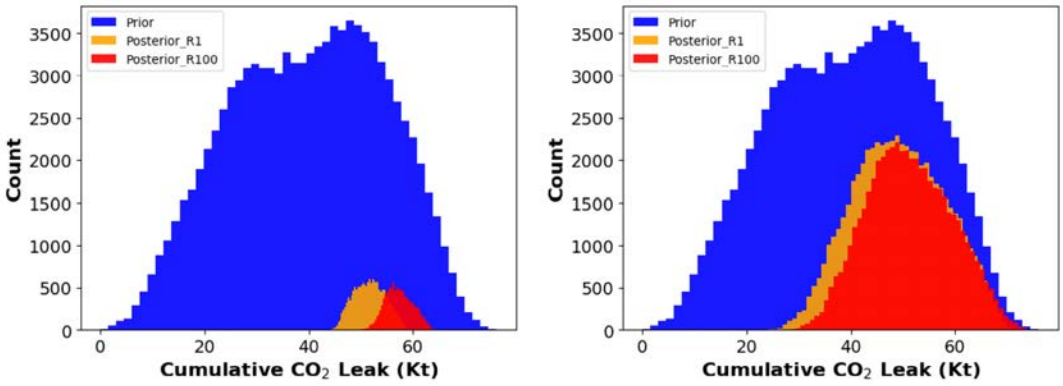


Fig. 15. The histograms for the posterior distributions obtained from the data realizations 1 and 100 as well as the histogram for the prior distribution.

Received by OCD: 6/29/2026

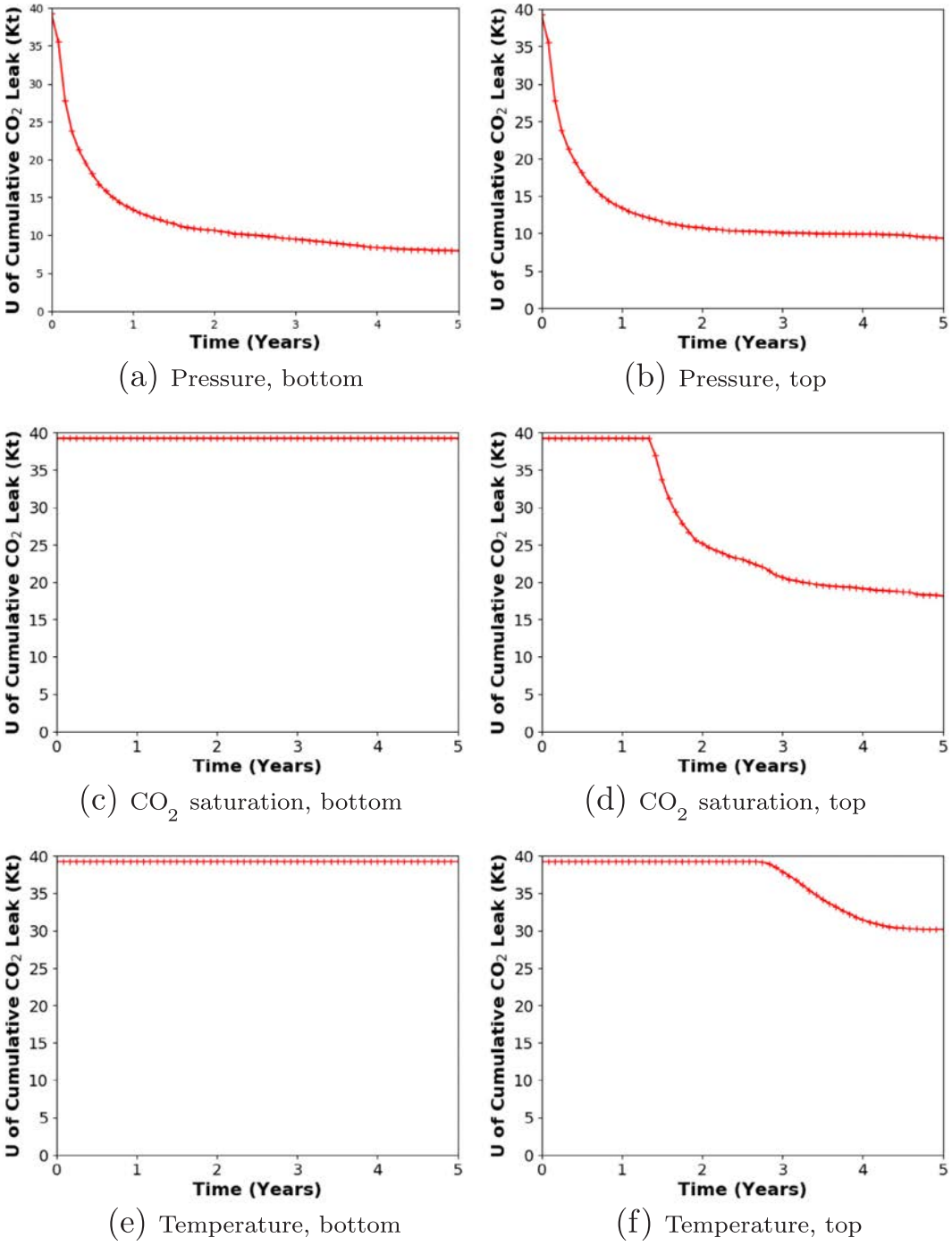


Fig. 16. Expected posterior uncertainty in objective function over time.

observed that measurements at M2 would give a 24.3% higher uncertainty reduction in cumulative CO_2 leakage than measurements at M1. A combination of the measurements at M1 and M2 would give a much higher uncertainty reduction than each individual measurement. For the scheme 4, addition of a third monitoring well at location M3 leads to only a slight increase in the uncertain reduction in the objective function. The result indicates that the additional costs of adding a third monitoring location M3 will not may not be justified given the insignificant effect on uncertainty reduction resulting from the data collected at that location.

5. Discussion

The high cost of performing monitoring operations often requires evaluating the potential value of monitoring data (e.g., the potential value of pressure, temperature and/or CO_2 saturation data) before the actual monitoring strategy takes place. The workflow proposed here can be used to select a monitoring design that is optimal under many potential leakage scenarios. Even though the examples used in our study demonstrated how monitoring data from a shallow aquifer can be used, the proposed workflow can be applied to monitoring data

Received by OCD: 6/29/2026

Table 3
Uncertainty reduction under different type of measurements at end of five years.

Measurement	Uncertainty reduction (Kt), top	Uncertainty reduction (Kt), bottom
P	29.88	31.29
S	21.10	0
T	9.05	0
P + S	30.97	\
P + T	30.05	\
S + T	21.40	\
P + S + T	30.98	\

collected at any location within the CO_2 storage complex ranging from storage reservoir to shallow aquifer to atmosphere. The potential value of monitoring data can be evaluated by the presented workflow.

At a CO_2 storage field operation, an optimal monitoring schedule based on the VOI approach described here can be used to collect monitoring data. The monitoring data can be assimilated to calibrate the uncertain field model(s) using the traditional history matching or data assimilation methods, such as ensemble Kalman filter (EnKF) [66] and ensemble smoother with multiple data assimilation (ES-MDA) [67] methods. The calibrated model(s) can subsequently be used to improve accuracy in predictions of the long-term fate of stored CO_2.

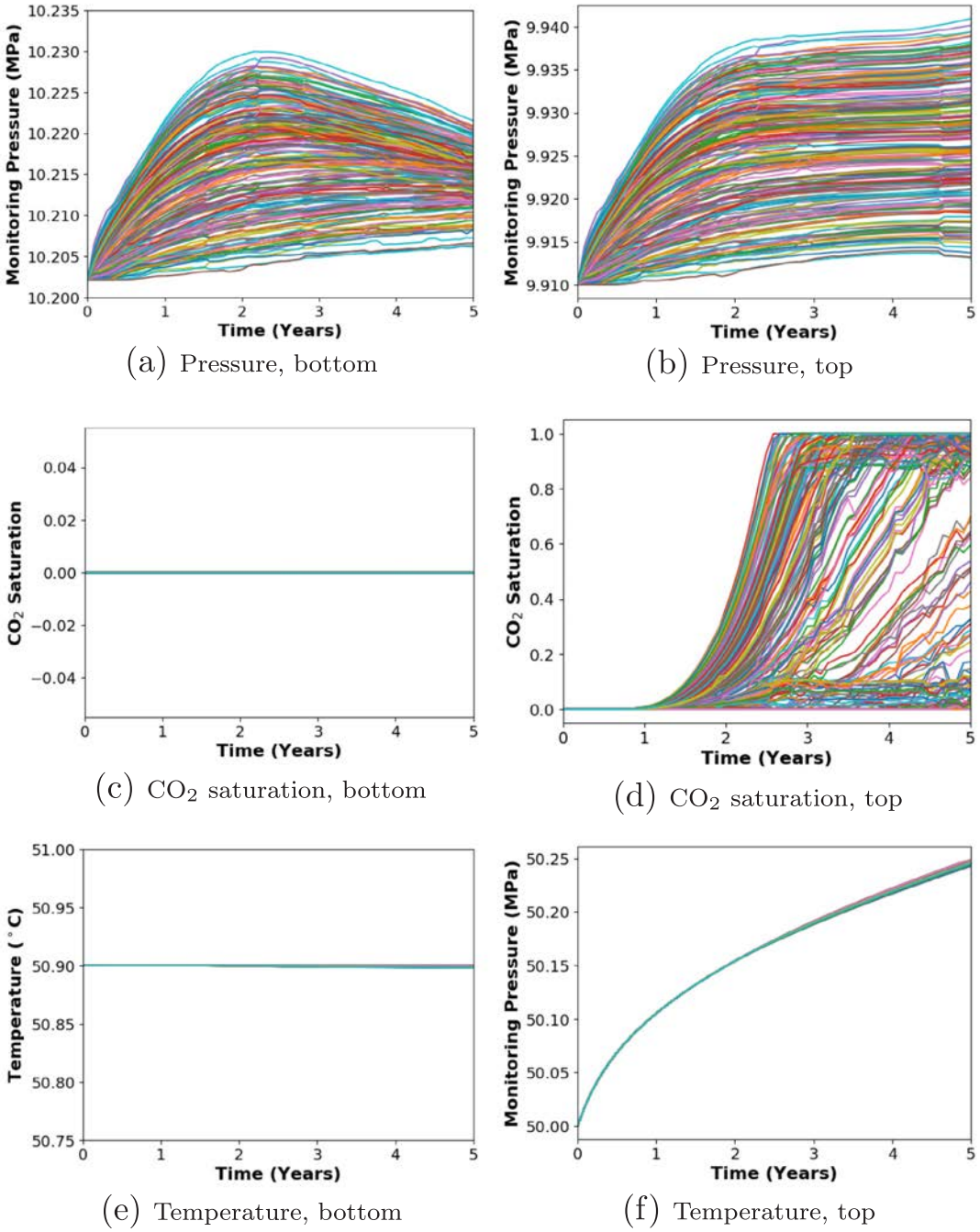


Fig. 17. Data realizations obtained from different measurements. Unit for CO_2 saturation is fraction.

Received by OCD: 6/29/2026

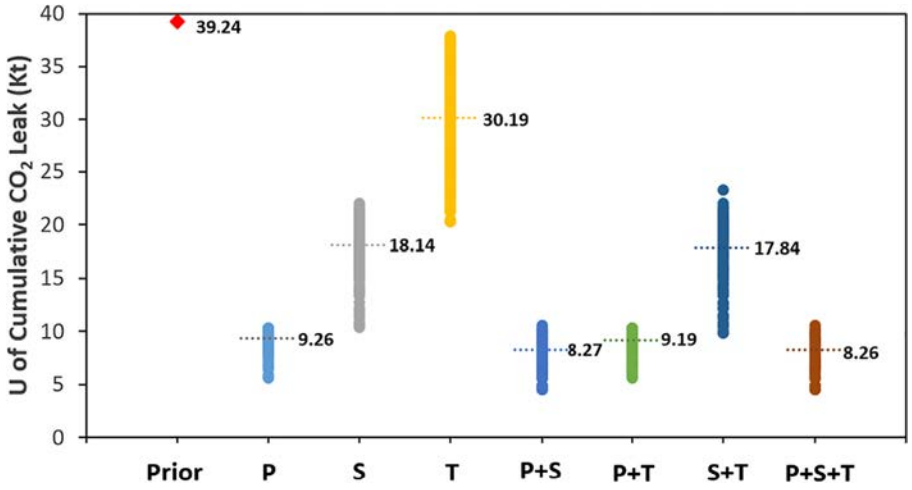


Fig. 18. The prior and posterior uncertainties for different types of monitoring strategies (monitoring at the top of the aquifer). The dash lines in this plot indicate the expected (average) posterior uncertainties for different monitoring strategies.

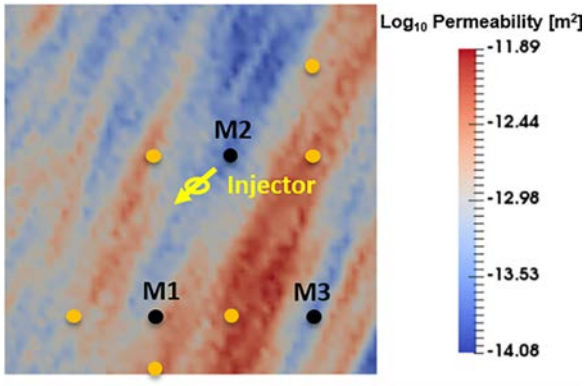
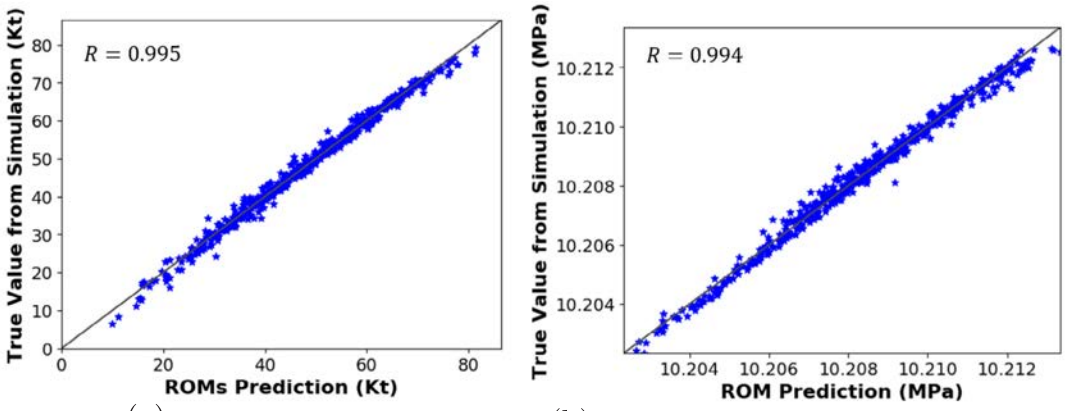


Fig. 19. Locations of potential leaky points, potential monitoring wells and injector, example 2. The darkest blue color corresponds to the lowest permeability, while the darkest red color corresponds to the highest permeability. The unit for permeability is log_{10} [m^2]. Yellow dots indicate potential leaky locations; black dots indicate potential monitoring well locations; yellow circle with an arrow indicates the injector. (For interpretation of the references to color in this figure legend, the reader is referred to the web version of this article.)

6. Conclusions

In this study, a workflow based on a machine learning technique and uncertainty quantification method is proposed for geologic CO_2 sequestration monitoring design. We use the uncertainty reduction in simulated cumulative CO_2 leakage as a metric to quantify the potential value of yet-to-be measured monitoring data. The following conclusions have been drawn from this research:

(1) The proposed workflow can generate reasonable values of uncertainty reduction in different risk metrics at CO_2 storage site including cumulative CO_2 leakage utilizing different monitoring designs and has been demonstrated using a synthetic CO_2 storage site.
(2) The effect of different types of measurements (pressure, CO_2 saturation and temperature) and the effect of monitoring locations (at the top or bottom of the aquifer) on the choice of monitoring design is investigated. It is observed that pressure data has more value of information than CO_2 saturation and temperature data, while the temperature data has the least value of information.
(3) Simultaneous use of multiple types of monitoring signals can reduce the uncertainty more than using a single type of signal though the relative benefits of utilizing different types of signals can vary.
(4) The incremental reduction in uncertainty in the cumulative CO_2 leakage may not increase proportional to the number of monitoring locations.



(a) ROM quality for obj (b) ROM quality for pressure at year one, M1

Fig. 20. Quality of the ROMs tested by 10-fold cross validation, example 2. *R* indicates the correlation coefficient between the true values from simulations and the ROM predictions for the objective function.

Received by OCD: 6/29/2026

Table 4
Uncertainty reduction under different type of measurements.

Scheme	Measurement locations	Uncertainty reduction (Kt)
1	M1	21.89
2	M2	27.22
3	M1 + M2	31.96
4	M1 + M2 + M3	32.01

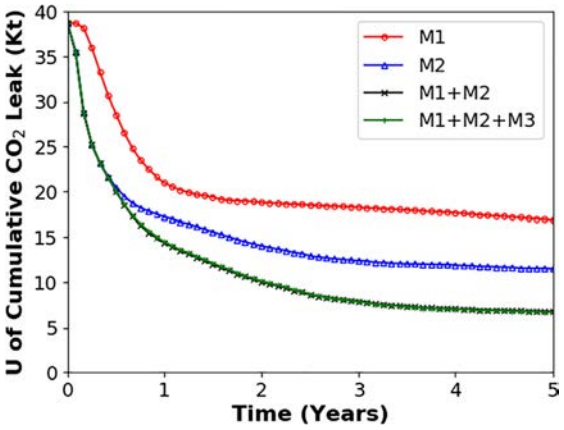


Fig. 21. Expected posterior uncertainty in objective function over time, example 2. The green curve almost overlaps with black curve. (For interpretation of the references to color in this figure legend, the reader is referred to the web version of this article.)

Acknowledgments

This work was funded by the US DOE's Fossil Energy Office through the National Risk Assessment Partnership (NRAP) managed by the National Energy Technology Laboratory (NETL). Numerical simulations were performed on Los Alamos National Laboratory clusters supported by the High Performance Computing Division.

References

[1] Metz B. Carbon dioxide capture and storage: special report of the intergovernmental panel on climate change. Cambridge University Press; 2005.
[2] Michael K, Golab A, Shulakova V, Ennis-King J, Allinson G, Sharma S, et al. Geological storage of CO_2 in saline aquifers—a review of the experience from existing storage operations. Int J Greenhouse Gas Control 2010;4(4):659–67.
[3] Sharma SS. Determinants of carbon dioxide emissions: empirical evidence from 69 countries. Appl Energy 2011;88(1):376–82.
[4] Viebahn P, Vallentin D, Höller S. Prospects of carbon capture and storage (CCS) in India's power sector—an integrated assessment. Appl Energy 2014;117:62–75.
[5] Viebahn P, Vallentin D, Höller S. Prospects of carbon capture and storage (CCS) in China's power sector—an integrated assessment. Appl Energy 2015;157:229–44.
[6] Zhou W, Wang T, Yu Y, Chen D, Zhu B. Scenario analysis of CO_2 emissions from China's civil aviation industry through 2030. Appl Energy 2016;175:100–8.
[7] Aminu MD, Nabavi SA, Rochelle CA, Manovic V. A review of developments in carbon dioxide storage. Appl Energy 2017;208:1389–419.
[8] Chen B, Harp D, Lin Y, Keating E, Pawar R. A machine-learning and filtering based data assimilation framework for geologic carbon sequestration monitoring optimization. In: AGU fall meeting abstracts; 2017a.
[9] Lin Y, Harp D, Chen B, Pawar R. Geologic carbon sequestration leakage detection: a physics-guided machine learning approach. In: AGU fall meeting abstracts; 2017.
[10] Dai Z, Middleton R, Viswanathan H, Fessenden-Rahn J, Bauman J, Pawar R, et al. An integrated framework for optimizing CO_2 sequestration and enhanced oil recovery. Environ Sci Technol Lett 2013;1(1):49–54.
[11] Zhao X, Liao X, He L. The evaluation methods for CO_2 storage in coal beds, in China. J Energy Inst 2016;89(3):389–99.
[12] Herzog H, Golomb D, Zemba S. Feasibility, modeling and economics of sequestering power plant CO_2 emissions in the deep ocean. Environ Prog Sustain Energy 1991;10(1):64–74.
[13] Shabani B, Vilcáez J. A fast and robust TOUGH2 module to simulate geological CO_2 storage in saline aquifers. Comput Geosci 2018;111:58–66.
[14] Benson SM, Myer L. Monitoring to ensure safe and effective geologic sequestration of carbon dioxide. In: Workshop on carbon dioxide capture and storage; 2003.
[15] Wilkin RT, DiGiulio DC. Geochemical impacts to groundwater from geologic carbon sequestration: controls on pH and inorganic carbon concentrations from reaction path and kinetic modeling. Environ Sci Technol 2010;44(12):4821–7.
[16] Keating E, Bacon D, Carroll S, Mansoor K, Sun Y, Zheng L, et al. Applicability of aquifer impact models to support decisions at CO_2 sequestration sites. Int J Greenhouse Gas Control 2016;52:319–30.
[17] Song J, Zhang D. Comprehensive review of caprock-sealing mechanisms for geologic carbon sequestration. Environ Sci Technol 2012;47(1):9–22.
[18] Harp DR, Pawar R, Carey JW, Gable CW. Reduced order models of transient CO_2 and brine leakage along abandoned wellbores from geologic carbon sequestration reservoirs. Int J Greenhouse Gas Control 2016;45:150–62.
[19] Jia B, Tsau J-S, Barati R. Role of molecular diffusion in heterogeneous, naturally fractured shale reservoirs during CO_2 huff-n-puff. J Petrol Sci Eng 2018;164:31–42.
[20] Godec M, Koperna G, Petrusak R, Oudinot A. Enhanced gas recovery and CO_2 storage in gas shales: a summary review of its status and potential. Energy Procedia 2014;63:5849–57.
[21] Tapia JFD, Lee J-Y, Ooi RE, Foo DC, Tan RR. Optimal CO_2 allocation and scheduling in enhanced oil recovery (EOR) operations. Appl Energy 2016;184:337–45.
[22] Ampomah W, Balch R, Cather M, Rose-Coss D, Dai Z, Heath J, et al. Evaluation of CO_2 storage mechanisms in CO_2 enhanced oil recovery sites: application to Morrow sandstone reservoir. Energy Fuels 2016;30(10):8545–55.
[23] Ampomah W, Balch R, Cather M, Will R, Gunda D, Dai Z, et al. Optimum design of CO_2 storage and oil recovery under geological uncertainty. Appl Energy 2017;195:80–92.
[24] Welkenhuysen K, Rupert J, Compernolle T, Ramirez A, Swennen R, Piessens K. Considering economic and geological uncertainty in the simulation of realistic investment decisions for CO_2-EOR projects in the North Sea. Appl Energy 2017;185:745–61.
[25] Francu J, Pereszlényi M, Riis F, Prokop O, Jurenka L, Hladík V, et al. 3D geological model of potential CO_2 storage: abandoned oil and gas field LBr-1in the Vienna Basin. Energy Procedia 2017;114:2772–80.
[26] Jin L, Hawthorne S, Sorensen J, Pekot L, Kurz B, Smith S, et al. Advancing CO_2 enhanced oil recovery and storage in unconventional oil play – experimental studies on Bakken shales. Appl Energy 2017;208:171–83.
[27] Chen B, Reynolds AC. CO_2 water-alternating-gas injection for enhanced oil recovery: optimal well controls and half-cycle lengths. Comput Chem Eng 2018;113:44–56.
[28] Pawar R, Bromhal G, Dilmore R, Foxall B, Jones E, Oldenburg C, et al. Quantification of risk profiles and impacts of uncertainties as part of US DOE's National Risk Assessment Partnership (NRAP). Energy Procedia 2013;37:4765–73.
[29] Pawar R, Bromhal G, Carroll S, Chu S, Dilmore R, Gastelum J, et al. Quantification of key long-term risks at CO_2 sequestration sites: latest results from US DOE's National Risk Assessment Partnership (NRAP) Project. Energy Procedia 2014;63:4816–23.
[30] Pawar RJ, Bromhal GS, Carey JW, Foxall W, Korre A, Ringrose PS, et al. Recent advances in risk assessment and risk management of geologic CO_2 storage. Int J Greenhouse Gas Control 2015;40:292–311.
[31] Yang Y-M, Small MJ, Ogretim EO, Gray DD, Wells AW, Bromhal GS, et al. A Bayesian belief network (BBN) for combining evidence from multiple CO_2 leak detection technologies. Greenhouse Gases: Sci Technol 2012;2(3):185–99.
[32] Ren B, Ren S, Zhang L, Chen G, Zhang H. Monitoring on CO_2 migration in a tight oil reservoir during CCS-EOR in Jilin Oilfield China. Energy 2016;98:108–21.
[33] Keating E, Dai Z, Dempsey D, Pawar R. Effective detection of CO_2 leakage: a comparison of groundwater sampling and pressure monitoring. Energy Procedia 2014;63:4163–71.
[34] Wang Z, Small MJ. A Bayesian approach to CO_2 leakage detection at saline sequestration sites using pressure measurements. Int J Greenhouse Gas Control 2014;30:188–96.
[35] Azzolina NA, Small MJ, Nakles DV, Bromhal GS. Effectiveness of subsurface pressure monitoring for brine leakage detection in an uncertain CO_2 sequestration system. Stochast Environ Res Risk Assess 2014;28(4):895–909.
[36] Dai Z, Keating E, Bacon D, Viswanathan H, Stauffer P, Jordan A, et al. Probabilistic evaluation of shallow groundwater resources at a hypothetical carbon sequestration site. Sci Rep 2014;4:4006.
[37] Yang C, Hovorka SD, Treviño RH, Delgado-Alonso J. Integrated framework for assessing impacts of CO_2 leakage on groundwater quality and monitoring-network efficiency: case study at a CO_2 enhanced oil recovery site. Environ Sci Technol 2015;49(14):8887–98.
[38] Zhang L, Ren B, Huang H, Li Y, Ren S, Chen G, et al. CO_2 EOR and storage in Jilin oilfield China: monitoring program and preliminary results. J Petrol Sci Eng 2015;125:1–12.
[39] Yang Y-M, Small MJ, Ogretim EO, Gray DD, Bromhal GS, Strazisar BR, et al. Probabilistic design of a near-surface CO_2 leak detection system. Environ Sci Technol 2011;45(15):6380–7.
[40] Yang Y-M, Dilmore R, Mansoor K, Carroll S, Bromhal G, Small M. Risk-based monitoring network design for geologic carbon storage sites. In: 13th International conference on greenhouse gas control technologies, 14–18 November, Lausanne, Switzerland; 2016.
[41] Seto C, McRae G. Reducing risk in basin scale CO_2 sequestration: a framework for integrated monitoring design. Environ Sci Technol 2011;45(3):845–59.
[42] Seto C, McRae G. Reducing risk in basin scale sequestration: a Bayesian model selection framework for improving detection. Energy Procedia 2011;4:4199–206.
[43] Sun AY, Nicot J-P, Zhang X. Optimal design of pressure-based, leakage detection monitoring networks for geologic carbon sequestration repositories. Int J Greenhouse Gas Control 2013;19:251–61.
[44] Cameron D. Optimization and monitoring of geological carbon storage operations [Ph.D. thesis]. Stanford (California, USA): Stanford University; 2013.

Received by OCD: 6/29/2026

[45] Dai C, Li H, Zhang D, Xue L. Efficient data-worth analysis for the selection of surveillance operation in a geologic CO_2 sequestration system. Greenhouse Gases: Sci Technol 2015;5(5):513–29.
[46] Dai C, Xue L, Zhang D, Guadagnini A. Data-worth analysis through probabilistic collocation-based Ensemble Kalman Filter. J Hydrol 2016;540:488–503.
[47] Chen B, He J, Wen X, Chen W, Reynolds A. Uncertainty quantification and value of information assessment using proxies and Markov chain Monte Carlo method for a pilot project. J Petrol Sci Eng 2017;157:328–39.
[48] Liu N, Oliver DS, et al. Evaluation of Monte Carlo methods for assessing uncertainty. SPE J 2003;8(02):188–95.
[49] Emerick AA, Reynolds AC, et al. Combining the ensemble Kalman filter with Markov-Chain Monte Carlo for improved history matching and uncertainty characterization. SPE J 2012;17(02):418–40.
[50] Chen B, He J, Wen X, Chen W, Reynolds A. Pilot design analysis using proxies and Markov chain Monte Carlo method. In: ECMOR XV-15th European conference on the mathematics of oil recovery; 2016.
[51] Caers J. Modeling uncertainty in the earth sciences. John Wiley & Sons; 2011.
[52] Friedman JH. Multivariate adaptive regression splines. Ann Stat 1991:1–67.
[53] Oliver DS, Reynolds AC, Liu N. Inverse theory for petroleum reservoir characterization and history matching. Cambridge University Press; 2008.
[54] Zhang K, Zhang X, Zhang L, Li L, Sun H, Huang Z, et al. Assisted history matching for the inversion of fractures based on discrete fracture-matrix model with different combinations of inversion parameters. Comput Geosci 2017;21(5–6):1365–83.
[55] Zhang K, Ma X, Li Y, Wu H, Cui C, Zhang X, et al. Parameter prediction of hydraulic fracture for tight reservoir based on micro-seismic and history matching. Fractals 2018:1840009.
[56] Guo Z, Reynolds AC, Zhao H, et al. A physics-based data-driven model for history matching, prediction, and characterization of waterflooding performance. SPE J 2018;23(02):367–95.
[57] Le DH, Reynolds AC. Optimal choice of a surveillance operation using information theory. Comput Geosci 2014;18(3–4):505–18.
[58] Iman RL. Latin hypercube sampling. Wiley Online Library; 2008.
[59] Zyvoloski G. FEHM: a control volume finite element code for simulating subsurface multi-phase multi-fluid heat and mass transfer. Los Alamos unclassified Report LA-UR-07-3359.
[60] Jordan AB, Stauffer PH, Harp D, Carey JW, Pawar RJ. A response surface model to predict CO_2 and brine leakage along cemented wellbores. Int J Greenhouse Gas Control 2015;33:27–39.
[61] Keating EH, Harp DH, Dai Z, Pawar RJ. Reduced order models for assessing CO_2 impacts in shallow unconfined aquifers. Int J Greenhouse Gas Control 2016;46:187–96.
[62] Chen B, Reynolds AC. Optimal control of ICV's and well operating conditions for the water-alternating-gas injection process. J Petrol Sci Eng 2017;149:623–40.
[63] George D, Kuprat A, Carlson N, Gable C. LaGriT - Los Alamos Grid Toolbox. < http://lagrit.lanl.gov/ > .
[64] Geisser S. Predictive inference vol. 55. CRC Press; 1993.
[65] Pearson K. Note on regression and inheritance in the case of two parents. Proc Roy Soc Lond 1895;58:240–2.
[66] Evensen G. Data assimilation: the ensemble Kalman filter. Springer Science & Business Media; 2009.
[67] Emerick AA, Reynolds AC. Ensemble smoother with multiple data assimilation. Comput Geosci 2013;55:3–15.

EXHIBIT 11

Received by OCD: 6/29/2026

Energy 214 (2021) 118933

Contents lists available at ScienceDirect

Energy

journal homepage: www.elsevier.com/locate/energy

Analysis of shale property changes after geochemical interaction under CO_2 sequestration conditions

Chae-Soon Choi [a], Jineon Kim [b], Jae-Joon Song [c, *]

[a] Radioactive Waste Disposal Research Division, Korea Atomic Energy Research Institute, Daejeon, 34057, Republic of Korea
[b] Department of Energy Resources Engineering, Seoul National University, Seoul, 08826, Republic of Korea
[c] Department of Energy Resources Engineering, Research Institute of Energy and Resources, Seoul National University, Seoul, 08826, Republic of Korea

ARTICLE INFO

Article history:
Received 12 July 2020
Received in revised form
18 September 2020
Accepted 22 September 2020
Available online 2 October 2020

Keywords:
Hale
Supercritical CO_2
Brine saturation
Chemical interaction
Property changes

ABSTRACT

This study implements a supercritical CO_2 ($scCO_2$) sequestration environment in a laboratory and investigates the geochemical effects of $scCO_2$ on the properties of rock specimens. Shale specimens constituting caprock were kept in a laboratory reactor chamber with $scCO_2$ for 63 days. Chemical interaction between rock surface and the $scCO_2$ was then induced, and the changes in the properties were inspected before and after the reaction through various tests. The non-destructive tests comprised measurement of elastic wave velocity, shore hardness followed by investigation using the inductively coupled plasma mass spectrometer, and scanning probe microscope. The destructive tests include uniaxial compressive strength, Brazilian tensile strength, and X-ray fluorescence tests. Results show that mechanical properties are significantly weakened when shale specimens are exposed to both $scCO_2$ and brine. The specimens reacting with only $scCO_2$ induced a self-healing effect by precipitation of secondary sediments, becoming a more intact rock with increased strength and elastic modulus. The results denote that the geochemical alteration of shale occurs in a short time and are highly dependent on the reaction conditions. These results provide fundamental information for the stability of CO_2 storage sites regarding the physical and chemical reactions between rocks under geological sequestration conditions.

© 2020 Elsevier Ltd. All rights reserved.

1. Introduction

Most of the ongoing CO_2 underground storage projects in the world are being conducted by applying technologies such as enhanced oil recovery to oil and gas fields (Fig. 1 [1]). Other than the oil and gas fields, the CO_2 underground storage technology is also being extended to deep saline formation since it has an expected storage capacity up to 10 times higher than that of the oil and gas fields (Table 1 [2]). To further utilize the high storage capacity of saline formations, the mechanism of CO_2 sequestration in a saline aquifer environment must be understood and studied. When CO_2 is injected into a saline formation, reservoir rocks may undergo a direct geochemical interaction with the injected CO_2, but it can also come into highly active reactions with acidified brine as CO_2 progressively dissolves [3–5]. Changes in micro-cracks and pore structure of some minerals by geochemical weathering processes could lead to physical and mechanical property changes such as porosity and rock strength. Several studies have reported that the changes in the properties could occur in a relatively short period and are affected by variables such as NaCl concentrations and CO_2 phases with temperature and pressure [6–8].

Therefore, it is necessary to conduct laboratory experiments on the changes in the physical properties of rocks by considering the saline aquifer environment to predict the short- and long-term stability. Given this, studies on various geochemical reactions have been extensively executed, and most of the studies were conducted on reservoir rocks such as sandstone, carbonate, or coal bed [9–11].

In this laboratory, CO_2 injection tests using various types of sandstone were conducted to simulate the reservoir environment in which CO_2 is injected (Fig. 2a), and CO_2 flow behavior was analyzed [12,13]. However, studies on the geochemical reaction of impermeable caprocks existing on top of reservoir rocks have been insufficient [14,15]. Changes in the rock surface due to geochemical weathering can be concentrated on the lower surface of the caprock when the fluid rises because of buoyancy (Fig. 2). Given this, several representative experimental studies simulated a storage environment to induce a geochemical reaction and thus investigate the

* Corresponding author.
E-mail address: songjj@snu.ac.kr (J.-J. Song).

https://doi.org/10.1016/j.energy.2020.118933
0360-5442/© 2020 Elsevier Ltd. All rights reserved.

Received by OCD: 6/29/2026



Fig. 1. Global map of development and deployment for carbon capture and storage projects modified from the Global status report of CCS 2019 [1]. In 2019, the number of large-scale projects increased to 51. The projects marked in red show that the storage type is enhanced oil recovery, and the other projects marked in blue use a saline aquifer for storage (Mtpa: million metric tons per annum). (For interpretation of the references to color in this figure legend, the reader is referred to the Web version of this article.)

Table 1
Estimation of storage capacity for the geological sequestration according to the target formation [2].

Geological formation	Estimated storage capacity ($GtCO_2$)	
	Minimum	Maximum
Oil and gas formation	675	900
Coal bed seams (ECBM[a])	3–15	200
Deep saline aquifer	1000	10,000

[a] Enhanced coal bed methane.

mechanical property changes of the shale. Research using batch systems with high-pressure reaction cells analyzed the changes in chemical compositions according to reaction time or CO_2 phases and examined changes in the physical structure, such as porosity and pore skeleton which influences the mechanical properties. Ao et al. [16] conducted periodic imbibition tests of supercritical CO_2 ($scCO_2$) and shale for 120 h. Specific surface and induced deformation of shale according to adsorption and fluid pressure were measured. Consequently, the porosity and average pore size increased with the decrease in specific surfaces. The mineral content of the shale decreased after $scCO_2$ treatment, decreasing tensile, triaxial compressive strength, and elastic modulus. Similarly, Lye et al. [17] and Lu et al. [18] considered the effect of CO_2 phase change on micro-crack or pore structures and the accompanying mechanical property changes using the uniaxial compression test with an acoustic emission technique and scanning electron microscope test. In common, the effect of $scCO_2$ was more significant than that of gaseous or subcritical CO_2 because it generates macro-pores.

The increase in CO_2 saturation time weakens the uniaxial compressive strength and elastic modulus with change of deformation behavior from brittle to ductile. A large-energy acoustic emission event is frequented after CO_2 saturation, indicating that an increase in the volume proportion of larger macro-pores results in more likely discharge of large-energy acoustic emissions. Considering the anisotropy of shale, Feng et al. [19] prepared shale specimens for Brazilian tensile strength tests by considering the angles of various bedding planes and implemented the $scCO_2$ immersion environment. They observed a decrease of approximately 20%–50% in Brazilian splitting strength, splitting modulus, and absorbed energy. The above studies reported that chemical interactions between various substances of shale and a $scCO_2$ imbibition environment can modify the pore structure. Pores and micro-cracks were produced in the shale, gradually intensifying as adsorption time increases. These damaged fissures connected and eventually formed micro-fragmentation, deteriorating the mechanical properties. However, these studies were subjected to low-clay shale with a large content of quartz (50% or more), which is reported to have relatively low chemical reactivity. Furthermore, each study has a significantly different reaction environment, such as temperature and saturation conditions with brine or water. Therefore, generalizing the results of strength degradation for shale that could contain various minerals in some cases with various reaction conditions was challenging.

The present study devised a CO_2 sequestration environment of a saline aquifer reaction system in a laboratory to induce a geochemical interaction between the surface of a clay-rich shale and $scCO_2$ by referring to reaction methods of previous studies. The temperature and pressure of the batch system with the reaction chamber were adjusted to realize a supercritical environment. Then, shale specimens were inserted into the reactor chamber, inducing a geochemical change on the rock surface for approximately 63 days (Fig. 2b). The chamber simulated predefined reaction conditions consisting of two cases. The first is when only $scCO_2$ is present, and the second is when $scCO_2$ and brine coexist. After the reaction under both conditions, the changes and differences in the properties of shale were examined.

Received by OCD: 6/29/2026

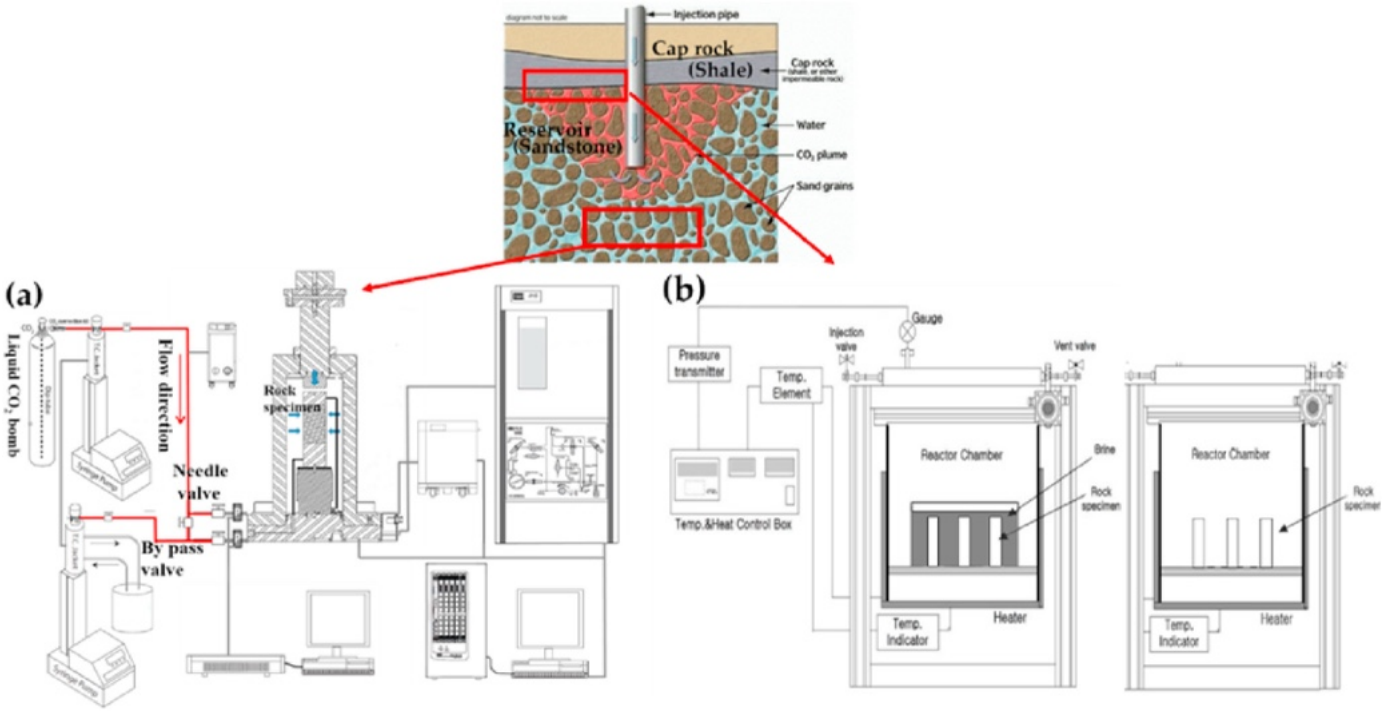


Fig. 2. Classification of laboratory experiments considering a sequestration mechanism (a) $scCO_2$ injection system into the porous rock-like sandstone (already constructed in this laboratory [12,13]) (b) Rock surface reaction system between $scCO_2$ and non-permeable rock-like shale (newly reconstructed for the present study).

2. Rock and test methods

2.1. Shale specimen and demonstration of geological sequestration conditions

Shale mostly consists of clay minerals with a particle size smaller than 60 μm and fine-grained quartz, feldspar, and carbonate minerals [20]. Porosity and permeability are 1%–12% and 10^{-22}–10^{-19} m^2, respectively [21,22]. The mineralogical characteristics of the geological layers that exist as caprocks in typical carbon dioxide underground reservoirs in the world are shown in Table 2. The dominant components are clay minerals composed of crystallized layered silicate minerals in the form of plate-type particles smaller than 10 μm [23]. In the present study, core-shaped specimens from a promising site for CO_2 underground storage in South Korea could not be obtained (i.e., the Pohang Basin); therefore, a clay-rich shale specimen was selected referring to the characteristics of the caprock in other countries.

The heterogeneous shale was taken from an outcrop in Boryeong, Chungcheongnam-do, Korea. All the cylindrical core specimens were prepared with the core axis perpendicular to the bedding plane, with dimensions of 38 mm in diameter and 70 mm in length. The contained minerals were analyzed using X-ray diffraction analysis (XRD), and the results are shown in Table 3. The

Table 2
Dominant minerals of caprocks at global carbon storage sites (adapted from Kim et al. [25]).

Site	Clay mineral	Other minerals	Reservoir depth (m)	Porosity (%)
Krechba, Algeria	Muscovite–illite 20%–50% Chlorite 4%–20% Kaolinite 4%–8%	Siderite ~15%	1850	1.8–11.3
Sleipner, Norway	Mica–illite ~25% Kaolinite 14%–18% Smectite 3%–9% Chlorite 1%–4%	Calcite 1%–3% Siderite 2%	750	35
Frio, USA	Illite–smectite ~45% Illite ~10% Kaolinite 13% Chlorite ~3%	Calcite (trace)	1450	8–10
SACROC, USA	Illite–smectite 62%	Calcite 2.5% Dolomite 2% Halite 0.1%	2000	1.3
Kenzin, Germany	Illite 42%–74% Chlorite 1%–3%	Dolomite 4%–35%	600	10
Carnarvon, Australia	Illite–smectite 25%–30% Illite 15%–20% Kaolinite 15% Chlorite 5%	Siderite 1%–4%	1100	21

Received by OCD: 6/29/2026

Table 3
Min eral components and basic properties of shale specimens.

Mineral composition ratio (%)			Property	
Muscovite	Quartz	Chlorite	Specific weight (g/cm^3)	Effective porosity (%)
47.1	39.3	13.6	2.7	3.9

shale matrix comprised muscovite and quartz with a small amount of chlorite, which was reported as sensitively alterative with CO_2 [6]. Muscovite and chlorite are typical clay minerals and similar to illite because of their structural sheets and chemical composition. As confirmed in Table 2, the selected shale specimen has similar characteristics with caprock of CO_2 sequestration formation around the world. A high-temperature and pressure reactor that can maintain a targeted in situ condition for long periods was used to implement the supercritical condition of CO_2. Previous laboratory studies used a small-capacity reactor to subject small-sized cuboid rock samples or rock powders to geochemical reactions with $scCO_2$, whereas the present study features the reaction of large numbers of specimens and large-sized rock core samples by using large-capacity reactors ([24] see Fig. 3a for a reactor with a capacity of 30 L).

By reacting large-sized core specimens, destructive compression tests can be conducted to analyze mechanical property changes, such as compressive and tensile strength, that could occur after a geochemical reaction. The suitable size of the test specimen is calculated according to ASTM specifications [26]. As mentioned in Section 1, to understand the effect of the presence or absence of brine by considering the actual site conditions, the reaction was conducted for 63 days by dividing the samples into shale−$scCO_2$ alone (after Case C) and shale−$scCO_2$−brine (after Case BC). Demo brine was prepared by dissolving sodium chloride to distilled water. The concentration of the demo brine was 1 M (5.84% of the percentage concentration) which is a relatively high concentrations; therefore, it can be included in briny water [27]. Demo brine would simulate the deep saline formation by considering an increase in the NaCl concentration in the pore fluid as the depth of the reservoir increases. The dissolved element in the demo brine solution was calculated by an inductively coupled plasma mass spectrometer (ICP-MS) test.

The results of the element concentration contained in the actual or demo brine reported in other studies are compared in Table 4. Because distilled water was used as a solution, almost no components other than sodium were detected compared with seawater. Although in situ brine may have other minor element concentrations, we focused on sodium concentrations to generalize in situ brine since minor element compositions can vary largely for different sites. Such generalization also enables clear comparison of the changes in the properties of shale according to the presence and absence of brine and CO2. The Case BC test was conducted, as suggested by Shao et al. [8]. After saturating the shale specimens with demo brine and placing the saturation vessel in the reactor chamber, target pressure and temperature conditions (10 MPa/50 °C) were applied by injecting and regulating $scCO_2$ pressure with increasing temperature. The supercritical state inside the chamber was kept constant during the periodic reaction. The target temperature and pressure condition were adapted to simulate the depth of a deep saline reservoir of approximately 1800−2000 m according to the geothermal and overburden pressure gradient [28].

Fig. 3b shows a rock specimen and a demo-brine saturation vessel placed inside the reactor chamber. In both Cases C and BC, three rock core specimens were reacted, respectively, and the results of each physical test were investigated for reliable interpretation. Besides these core specimens, as shown in Fig. 3b, a rock slab specimen of 20 mm wide was simultaneously reacted to analyze a change in the roughness of the rock surface using a scanning probe microscope (SPM) test. The slab specimens were smoothed through a polishing process before the reaction test, and one slab was subjected to each condition. The non-destructive tests, including the SPM test, comprised the seismic velocity and shore hardness test. The test specimen was periodically removed from the reactor to analyze the property changes according to the reaction time.

Fig. 4 shows a series of tests and processes for each periodic reaction cycle. After the reaction process, the retrieved specimens exist in different states; Case C is in a non-wetting, and Case BC is in a wetting conditions. It has been reported that the difference in physical properties significantly.

Depends on the wetting or non-wetting state. Moisture conditions could reduce the strength of rock mass because of the reduction in fracture energy, stiffness, and the frictional force between rock grains [7,10]. To estimate the property changes solely due to geochemical alterations, the same test conditions must be

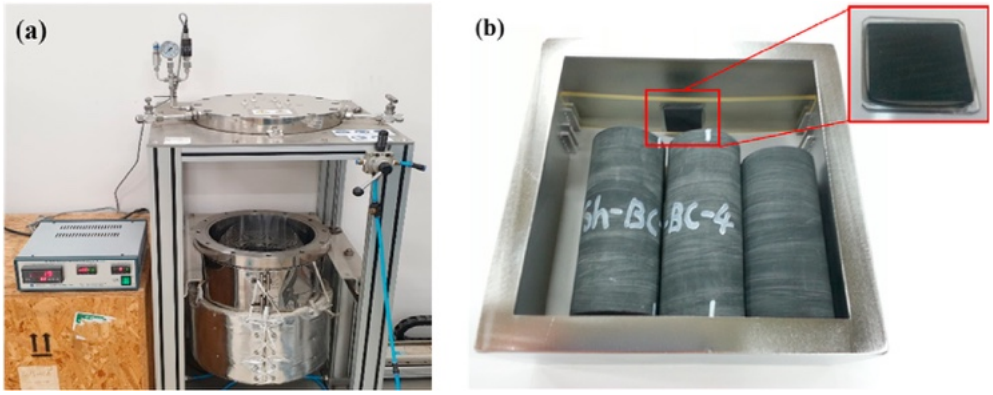


Fig. 3. Experimental equipment for realizing the carbon sequestration environment: (a) Large-capacity reactor with $scCO_2$ and large-sized shale specimen. (b) Container for reaction condition between shale and brine.

Received by OCD: 6/29/2026

Table 4
Components of demo brine used in the present study and other studies.

Ion (mg/L)	Demo brine (in the present study)	Demo brine [29]	Demo brine [25]	Seawater [29]
Na	22,278	19,872	21,410	11,020
Ca	2.21	6500	ND	422
Mg	0.65	54	ND	1322
K	0.09	500	ND	408

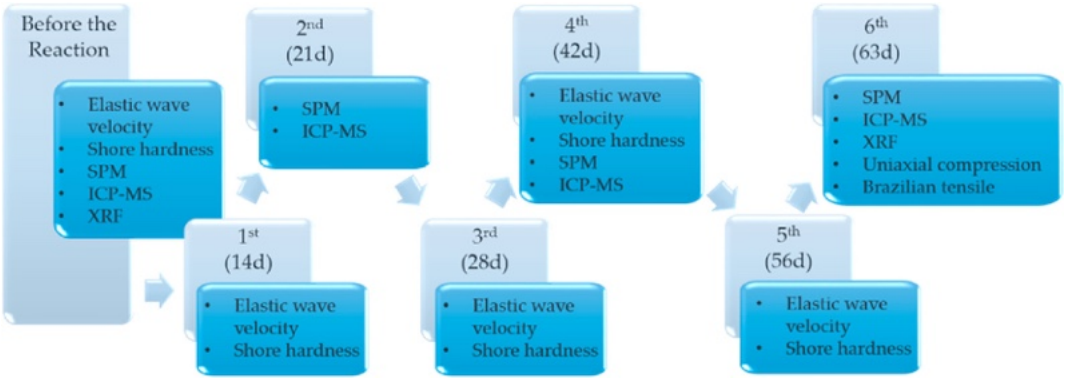


Fig. 4. Process and type of non-destructive and destructive tests according to the reaction cycle.

assigned to the retrieved specimen from each reaction condition. Therefore, the Case BC specimens were initially vacuum-dried for 24 h to remove surface moisture and entrapped fluid, and each property analysis was conducted according to the test process.

2.2. Tests for analysis of property changes

Four non-destructive tests are shown in Fig. 4. First, P-wave and S-wave velocity were measured using an instrument to calculate the travel time of ultrasonic waves through the dried core specimen (Sonic Viewer-SX, OYO Corp.). Shore hardness with D-type is suitable for semi-rigid material, such as rock, and the average value and frequency of the hardness value were estimated by 20 measurements of the shale surface for each specimen. ICP-MS (Varian 820-MS, Varian Inc.) was conducted only in Case BC because, due to the test characteristics, a liquid solution is necessary. A small amount of brine solution was obtained from the brine vessel, according to the reaction period. An SPM (SPA-400, Seiko Instrument) test was conducted to detect a change in the roughness of the slab specimen. The SPM test scans the surface of a sample and images the surface through the measured displacement of the cantilever that moves up and down over the uneven height of the surface. The displacement values in the z direction are measured with nano-meter units. The surface roughness value in the pre-designated region can be obtained as a root-mean-square (RMS) value or mean value (R_a). The specified area (approximately 0.04 mm $\times$ 0.04 mm) was analyzed with the same x and y coordinated values before the reaction process.

The retrieved slab from the reactor chamber for each reaction cycle was first washed with distilled water, and the roughness in the designated area was measured using the SPM test. The surface of the shale slab was extracted using two-dimensional profile data and three-dimensional imaging. Through such surface data, changes in roughness that could be attributed to dissolution and precipitation were investigated quantitatively. Each non-destructive test equipment is shown in Fig. 5a. Compressive and

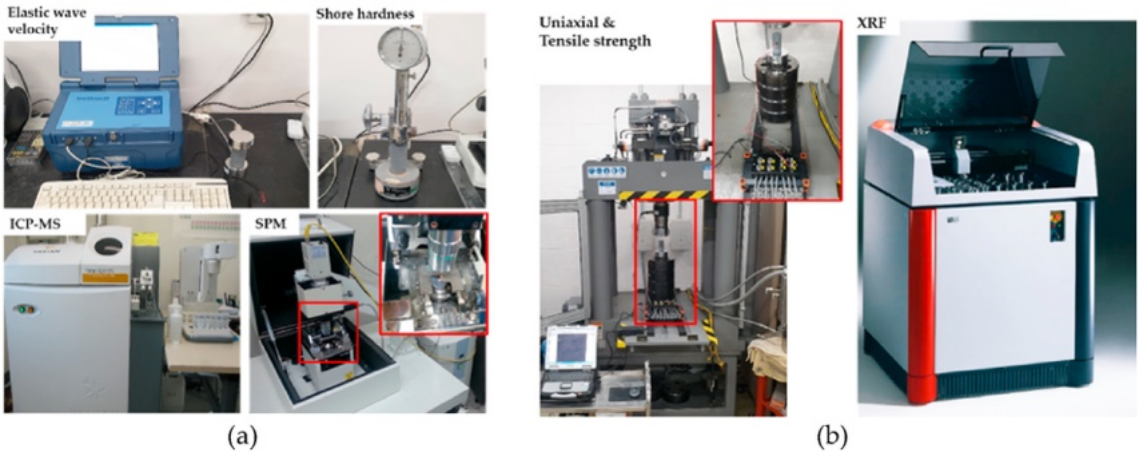


Fig. 5. Test equipment for (a) non-destructive tests and (b) destructive tests.

Table 5
Results of non-destructive test by duration time of each reaction condition.

Time (days)	pH of Case BC	Av. elastic wave velocity (km/s)				Av. shore hardness (20 points for each specimen)					
		Case C		Case BC		Case C			Case BC		
		Av. P	Av. S	Av. P	Av. S	No.1	No.2	No.3	No.1	No.2	No.3
0	8.1	3.79	2.20	3.25	1.94	48	49	49	47	47	48
14	6.2	3.79	2.20	2.94	1.88	49	52	49	47	48	48
28	3.7	3.8	2.22	2.77	1.85	51	53	52	44	45	47
42	3.6	3.87	2.25	2.72	1.82	53	53	52	44	44	46
56	3.6	3.9	2.30	2.65	1.52	54	55	53	42	41	45

tensile strengths were derived by conducting destructive tests using shale specimens that did not react and those that completed the reaction for 63 days.

The tests were conducted on an MTS rock test system (model 819, MTS Corp.; Fig. 5b), and the loading and displacement were recorded using a data acquisition system (DEWE 43 V, DEWE soft LTD.). The volume strain curve was plotted using the stress–strain data to compare and examine the deformation behavior. Based on the stress–volume strain curve, a linear elastic deformation stage was derived, and the tangential elastic modulus and Poisson's ratio in that stage were calculated to examine the changes in the physical properties before and after the reaction. An X-ray fluorescence (XRF, S4 Pioneer, Bruker AXS) test was conducted by preparing a powder sample using the fragments of destructive test pieces. Through the XRF test, the changes in oxide contents before and after the reaction could be examined.

3. Results

3.1. Non-destructive test

The results of seismic wave velocity and shore hardness of reacted specimens are shown in Table 5. The specimens of Case C showed a slight increase in P-wave velocity; however, in Case BC, the decrease in seismic velocity was evident. The P-wave and S-wave show a decreased rate of approximately 2%–10% for each 14 day reaction cycle, compared with the non-reacted specimens. Finally, the P-wave and S-wave decreased by 0.6 and 0.4 km/s, respectively. The tendency of the change in shore hardness was similar to that of the seismic velocity. The three shale specimens which reacted only with $scCO_2$ showed increasing hardness values as reaction time passes. Conversely, all specimens of Case BC decreased in hardness values. Fig. 6a and b are graphs of each test result. It was confirmed that both seismic velocity and shore hardness exhibit different trends depending on the presence or

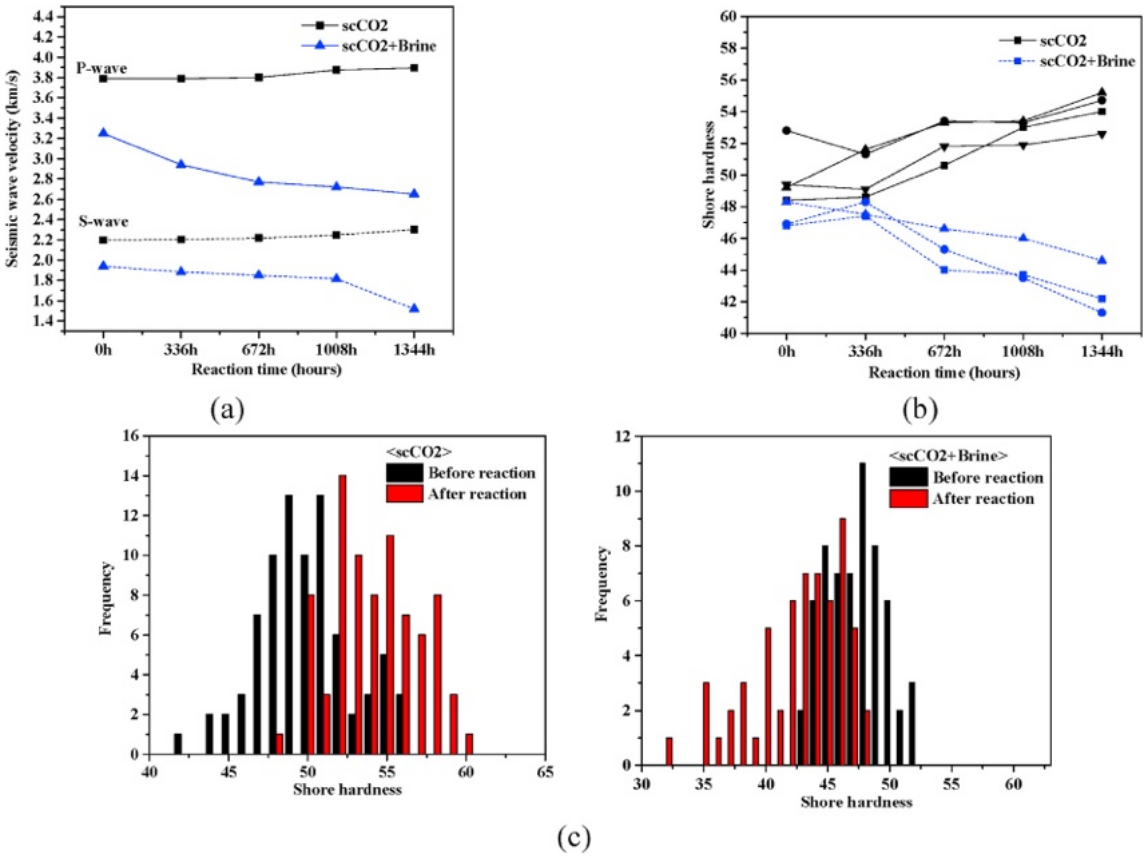


Fig. 6. Changes in elastic wave velocity and shore hardness value for each reaction conditions: (a) elastic wave velocity, (b) shore hardness, and (c) frequency changes of shore hardness before and after the reaction.

Received by OCD: 6/29/2026

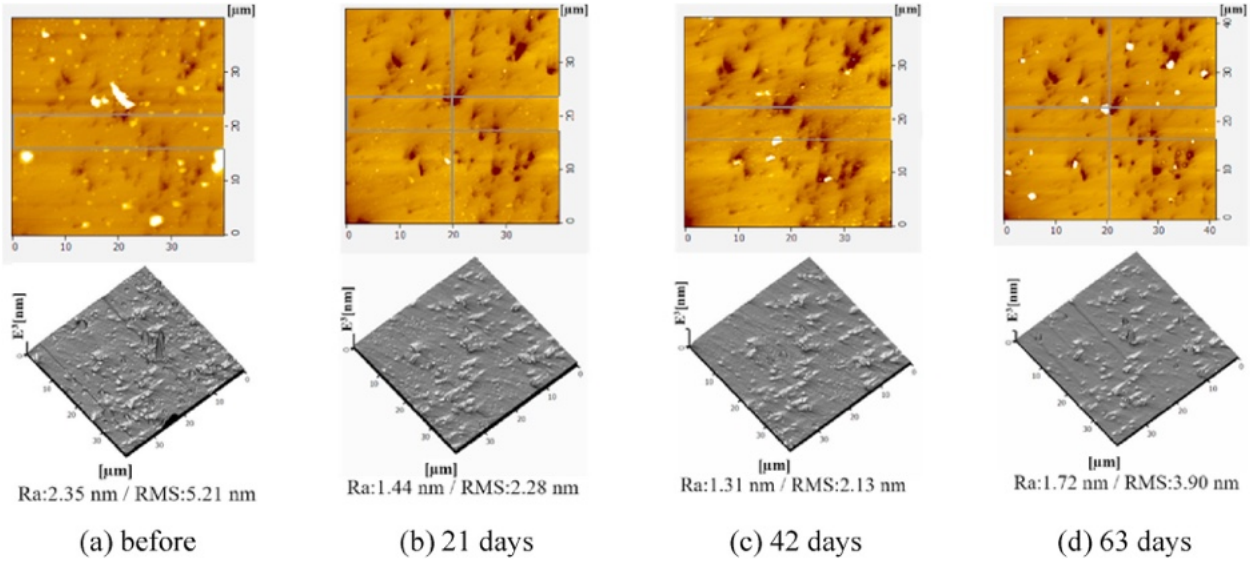


Fig. 7. The SPM test results of reacted slab with $scCO_2$.

absence of brine. Specially, it is notable how the trend of shore hardness is completely opposite in each case.

Fig. 6c shows the result of analyzing the frequency of hardness values, given that the shore hardness test was conducted 20 times. When only $scCO_2$ was reacted, the number of times of measurement of significant hardness values increased. By contrast, in Case BC, the bar graph moves to the left, showing an increase in the small hardness value. This aspect of changes can be explained by the geochemical effects of $scCO_2$ and brine. For Case BC (Table 5), when $scCO_2$ and brine coexist, the pH of CO_2-dissolved brine decreases from 8.1 to 3.6 forming oxidized brine In such environment, the dissolution and weathering process of shale will occur, inducing phenomena such as the growth of micro-cracks and ultimately weakening the mechanically properties of shale.

However, when only $scCO_2$ is present, shale could be affected by self-healing effects, such as cracking closures caused by secondary oxides or sediment precipitation, as reported in several studies [30,31]. The precipitation and dissolution of the shale surface was further analyzed through the SPM test.

Three-dimensional images of shale slab surfaces and reconstructed domains are shown in Figs. 7 and 8. The average and RMS roughness values for each condition are also shown. The slab specimen that only reacted with $scCO_2$ slightly decreases in roughness as the reaction progressed and then increases after 40 days of reaction. However, the shale slab that reacted with brine and $scCO_2$ shows significantly increased roughness values which can be attributed to weathering effect during reaction. Both the roughness value and two-dimensional surface image denoted these alterations. The white part of the image shows irregularities with a high *z* axis height. The slabs used for both reactions had some irregularities before the reaction. Particularly, the slab surface of Case C had large irregularities which are reflected in the surface's initial

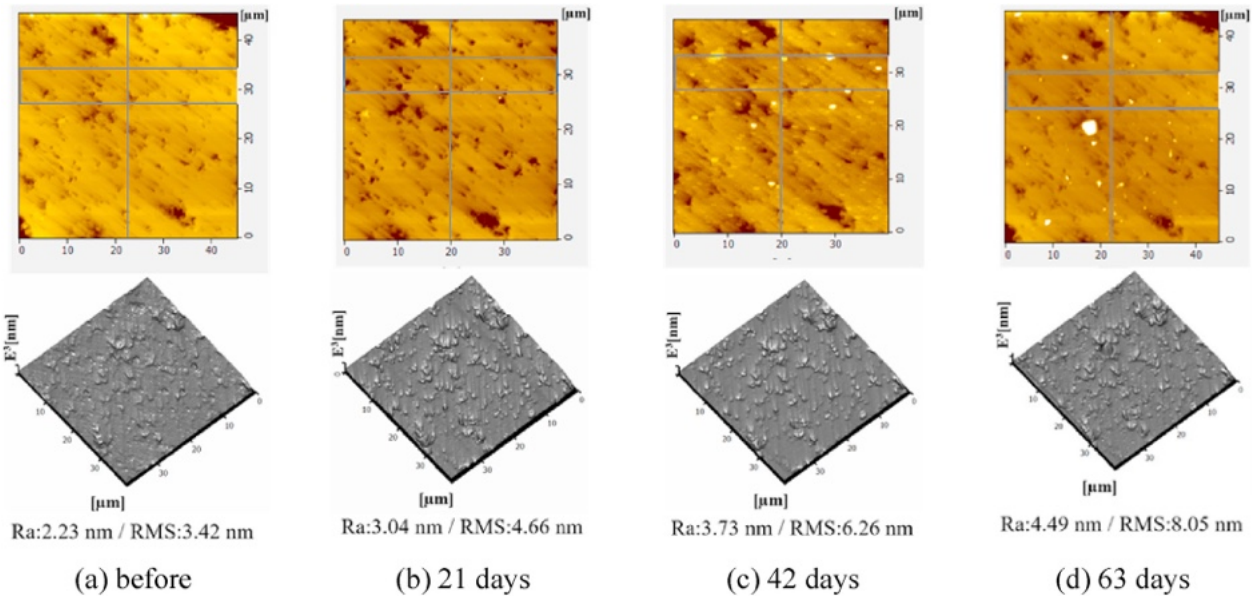


Fig. 8. The SPM test results of reacted slab with $scCO_2$ and brine.

Received by OCD: 6/29/2026

Table 6
ICP-MS and XRF test results.

Element	ICP-MS test (mg/L)				Oxide	XRF test (%)			
	Case BC					Case C		Case BC	
	Before	21 days	42 days	63 days		Before	After 63 days	Before	After63 days
Ca	2.21	43.97	60.87	80.34	SiO_2	68.1	69.0	68.1	56.6
Mg	0.65	26.13	42.11	59.60	Al_2O_3	36.6	37.1	36.6	19.2
Si	ND	27.0	29.72	36.80	Fe_2O_3	4.95	4.04	4.95	0.95
K	0.09	0.30	59.02	69.14	K_2O	4.51	4.45	4.51	3.51
Fe	ND	115.23	169.06	269.6	MgO	0.59	1.51	0.59	0.15
Al	ND	29.39	36.69	44.10	CaO	0.51	0.55	0.51	0.15

roughness value. As the reaction progressed, large irregularities were dissolved, and the roughness was significantly reduced. Excessive dissolution may increase the surface roughness, but considering the result of decreased roughness, the effect of sediments from secondary precipitation seem to be more dominant. The increase in the sediments can be inferred by the white spots in the image. The slab that reacted with brine and $scCO_2$, on the other hand, shows growing black parts in its surface image which indicate excessive dissolution. Meanwhile, some areas of the surface also indicated increase of sediments compared with its initial surface status. These weathering processes, representing the dissolution and precipitation phenomena, were examined through a geochemical analysis of the dissolved ion components in the brine and oxide composition in shale powder specimen after the final reaction cycle.

Table 6 shows the results. As mentioned in Section 2.2, only Case BC was subjected to the ICP-MS test. The results confirm that the ionic content in the brine increases as the reaction progresses by dissolving the oxide components, such as Si, Al, Fe, K, Mg, and Ca, in muscovite [$(K(OH, F)_2Al_3Si_3O_{10})$] and chlorite [$(Mg, Fe, Al)_{12}(Si, Al)_8O_{20}(OH)_2$] contained in the shale. The dissolution of Fe in chlorite is evident, as in studies [6].

These results are consistent with the XRF test results which clearly show the decrease of the oxide composition in Case BC. In Case C, the change of oxide composition was not obvious. The amount of SiO_2, Al_2O_3, and MgO slightly increased which can be considered as the effect of adsorption of CO_2 on the surface of muscovite, as reported in Ref. [31]. Overall, in Case C, it can be inferred that the degree of dissolution and precipitation is similar; although when compared, precipitation seems to be marginally dominant. These results from the ICP-MS and XRF test confirm that the geochemical response of shale is much significant when brine coexists with scCO2 and, consequently, that physical properties of shale can be significantly affected in such environment. However, because of the limitations of laboratory experiments, the reaction time of shale and CO_2 was short compared with the real time required for the mineralogical alteration that could occur in the in situ reservoir formation. Therefore, the reaction time may have been insufficient for the detection of secondary mineral precipitation. Nevertheless, the results of the present study is still is meaningful since the analysis of ions and oxides confirms that geochemical changes in a CO_2 sequestration environment can take place in a relatively short period, and the aspect and degree of these changes are highly dependent on the presence of saline water.

3.2. Destructive test

The results of the uniaxial compression tests for each condition are presented in this section. As shown in Fig. 9, the stress–strain curve and corresponding volumetric strain curve are obtained from the compression tests. Based on the volumetric strain curve, the crack propagation process can be divided into a crack closing stage, elastic deformation stage, stable crack growth stage, and unstable crack growth stage. The elastic modulus was obtained from the tangent slope of the axial stress–strain curve corresponding to the linear elastic deformation stage. The Poisson's ratio was analyzed by the axial and lateral strain at the same stage. The uniaxial compressive strength and tensile strength were also measured. The obtained test results for each reaction condition are organized and presented in Table 7. In the specimens of Case C, the compressive strength increased by approximately 10%, and the specimens of Case BC showed a significant decrease in compressive

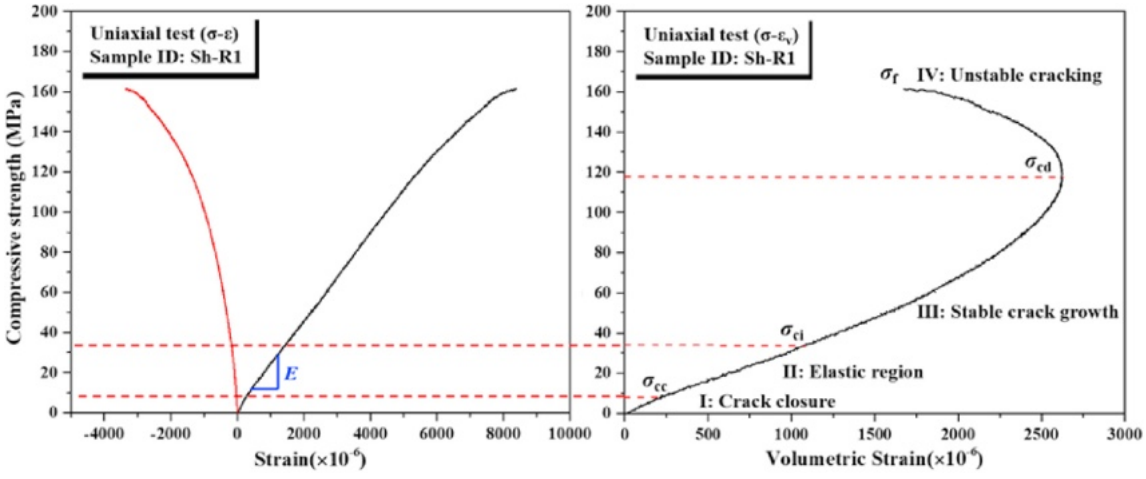


Fig. 9. Volumetric strain curve showing the stages of crack development and elastic region.

Received by OCD: 6/29/2026

Table 7
Mechanical properties measured by the destructive test.

Reaction condition	Compression strength (MPa)	Elastic modulus (GPa)	Poisson's ratio	Tensile strength (MPa)
Case R	161.4	21.5	0.142	13.5
	162.9	27.7	0.147	16.3
	179.3	24.5	0.150	
	171.4	25.1	0.143	
	180.0	22.5	0.138	
Mean (St. Dev)	171.0 (7.8)	24.2 (2.1)	0.144 (0.004)	14.9 (1.4)
Case C	196.8	31.4	0.127	19.5
	189.4	28.2	0.128	20.0
	184.6	28.4	0.137	
Mean (St. Dev)	190.3 (5.0)	29.4 (1.5)	0.131 (0.004)	19.7 (0.3)
Case BC	111.4	13.9	0.096	7.8
	122.1	13.1	0.091	10.5
	112.0	10.1	0.106	
Mean (St. Dev)	115.2 (4.9)	12.4 (1.6)	0.098 (0.006)	9.2 (1.4)

strength of more than 30%. The tensile strength of Cases C and BC specimens each increased and decreased by approximately 5 MPa, respectively. As in the strength change, the elastic modulus also increased by approximately 20% for Case C and decreased more than 50% for Case BC. These results are consistent with the non-destructive test results described in Section 3.1. The test specimen that reacted only with $scCO_2$ showed enhancements in mechanical properties which can be attributed to crack closure from the formation of secondary sediments. The specimens that reacted with CO_2-dissolved acidified brine showed degradation of mechanical properties which can be explained by weathering phenomena such as growth of micro-cracks.

The volumetric strain of the non-reacted test specimens and the reacted specimens were plotted simultaneously to compare and analyze the deformation behavior in detail. The stress–volume strain curve is more specific than the stress–strain for analyzing the generation and propagation of micro-cracks and the deformation behavior of the rock [32].

As shown in Fig. 10, for each reaction condition, the profile of the volumetric strain curve was significantly different. The specimens of Case C generally had a smaller volumetric deformation, whereas the specimens of Case BC had a larger volumetric deformation than those not reacted. These trends in volumetric strain, with the changes in strength and elastic modulus, further confirm the intact rock-like behavior of the test specimens of Case C. For the test specimens of Case BC, large volumetric deformation accompanies the decrease in strength and elastic modulus, indicating severally weakened mechanical performance. It is notable that, in Case BC, the volumetric strain increases while Poisson's ratio decreases. This indicates that while both axial and lateral strains increase in Case BC, the axial strain is increased more than the lateral strain. Meanwhile, the simultaneous decrease in volumetric strain and Poisson's ratio of Case C indicates decreased lateral strain in Case C. The above results and analysis emphasize the need for examining the mechanical stability of the caprock, especially the lower part, when brine and CO_2 coexist.

4. Discussion

4.1. Quantitative analysis of dissolution and precipitation

The surface profiles of the slab specimen were extracted through SPM test, and analyzed for quantitatively estimating regional size of the dissolution and precipitation after the final reaction. The change in roughness in the z axis direction, measured along a specific detection line on the slab, is shown in Fig. 11. The black line shows the profile before the reaction, and the red line shows the changes in the roughness profile after the reaction. The profile after the end of the final reaction is only compared, since it represents the overall profile change during the reaction. The weathering areas

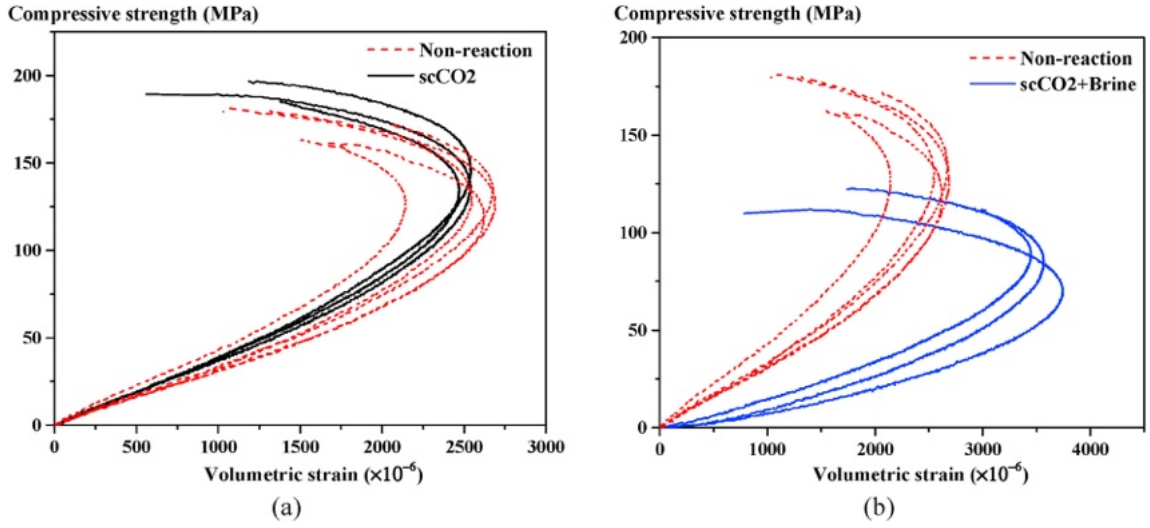


Fig. 10. Volumetric strain curve difference according to the reaction condition.

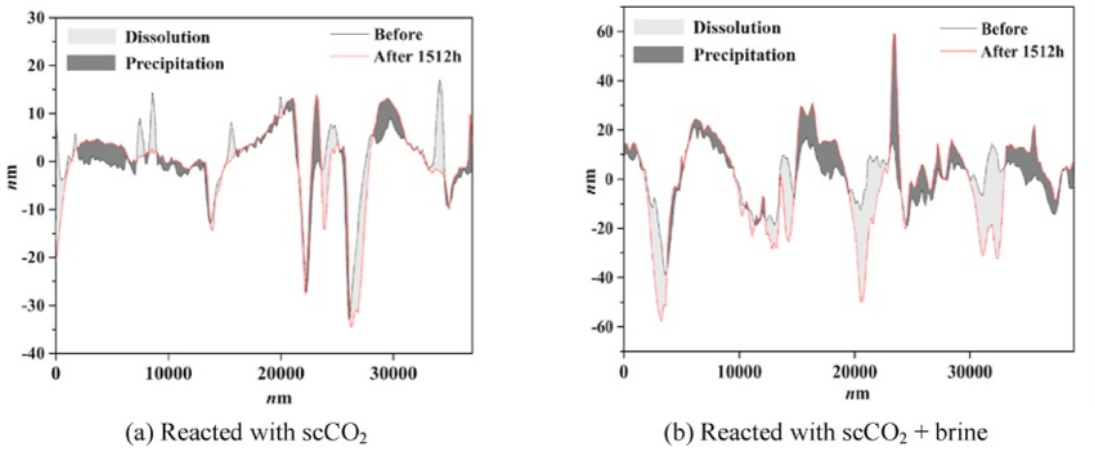


Fig. 11. Changes in profile of slab specimen before and after the reaction.

are estimated by analyzing the height difference between the profiles. The different colors in Fig. 11 display the corresponding areas; the light grey areas and the dark grey areas indicate the dissolution and precipitation areas, respectively. The area of the marked areas are quantitatively calculated and compared. First, for the slab which reacted with CO_2 only, the dissolution and precipitation regions were approximately 0.718 and 0.720 μm^2, respectively. The degree of alteration by geochemical interaction seems to be similar. However, the slab of Case BC shows significant geochemical reactivity compared with Case C, with a dissolution and precipitation area of 2.142 and 1.869 μm^2, respectively. Particularly, the dissolution is more critical than the sedimentation, resulting in a large amount of geochemical weathering. These results are reasonable and consistent with the non-destructive and destructive test results mentioned earlier.

Studies have reported the dissolution and precipitation path of muscovite and chlorite in shale when shale reacts with brine or brine with CO_2. The following mechanisms present the general dissolution of muscovite and chlorite [6,25,33]:

Muscovite: $KAl_3Si_3O_{10}(OH)_2 + 12H_2O \leftrightarrow K^+ + 3Al(OH)_4^- + 2H_4SiO_4 + 2H^+$.

Chlorite: $(Mg, Fe, Al)_{12}(Si, Al)_8O_{20}(OH)_2 + 10H^+ \leftrightarrow 12(Mg^{2+}, Fe^{2+}, Al^{3+}) + 8Al^{3+} + 8SiO_2 + 6H_2O$.

When CO_2 and calcium ions are present, the dissolution of muscovite can result in the simultaneous precipitation of kaolinite and carbonate:

$2KAl_3Si_3O_{10}(OH)_2$ [muscovite] $+ 4H_2O + CO_2 + Ca^{2+} \leftrightarrow 2\ K^+ + 3Si_2Al_2O_5(OH)_4$ [kaolinite] $+ CaCO_3$ [calcite].

A different mechanism can be considered when the shale mineral composition contains muscovite and quartz, similar to the shale specimens in the present study. When these two minerals are dissolved simultaneously in saline water and reacted with ions such as aluminum and magnesium, illite sediments can be formed as follows:

$3KAl_3Si_3O_{10}(OH)_2 + 8.5SiO_2 + 2.5Al^{3+} + 1.25Mg^{2+} + 7H_2O \leftrightarrow 5K_{0.6}Mg_{0.25}Al_{2.3}Si_{3.5}O_{10}(OH)_2$ [illite] $+ 10H^+$.

Similarly, when chlorite reacts with dissolved CO_2 in brine, it forms kaolinite and carbonate magnesium:

$Mg_5Al_2Si_3O10(OH)_8 + 5CO_2 \leftrightarrow MgCO_3 + Al_2Si_2O_5(OH)_4$ [kaolinite] $+ SiO_2 + 2H_2O$.

As such, the surface of the shale is weathered by the reaction with acidified brine or CO_2. In this process, the exposed mineral components interaction with the dissolved ions in the brine and form secondary sediments. In the specimens of Case BC, the above various weathering mechanisms given above could explain the SPM test results that showed increase in roughness and area of dissolution and precipitation. Similarly, the increase in the cation concentration observed in the ICP-MS test results could also be explained. However, an accurate specification of the type and degree of reaction is challenging because the reaction is composed of simultaneous dissolution or precipitation phenomena of various minerals. Also, considering Case C, analysis of the ion contents through the ICP-MS test was not possible due to the absence of a solvent, brine. A XRF test was conducted on Case C, but the changes of the oxides in the shale specimens were minor and consequently it was difficult to give detailed explanations about the geochemical reactions.

However, the analysis of the present study is meaningful since the regional size of the weathering reactions are revealed and quantified by the SPM tests. In addition locations of precipitation and dissolution were also visualized and compared. The local distribution of these phenomena should be closely related to the distribution of minerals on the surface of the shale specimen. To increase the roughness, the dissolution and precipitation must occur in the ravine and ridge of roughness, respectively. To reduce the roughness, the contrary would be required.

The detailed profile changes of Case BC, in Fig. 11, show how the roughness is increased; the ridges of the roughness become taller by precipitation, while the ravines become deeper in general by dissolution. To accurately examine the changes in surface minerals, it is necessary to conduct spectroscopy tests such as electron dispersive X-ray spectroscopy and XPS. In this study such tests were not conducted, but results of other studies that have analyzed changes in surface minerals and specific surface area through spectroscopy tests referred to the simultaneous mechanisms and imbalances in the occurrences of deposits and solubility of minerals [34,35]. These studies presented significantly different dissolution process for different experiment condition and mineralogical specimens. Some authors emphasized that the reactive surface area is not constant during reaction because of its dependence to the stability of the secondary mineral sediments. Furthermore, they also emphasized that the grain size distribution and the presence of minerals with high reactivity should be considered. Many studies recognized that quantifying the reactive surface area in a heterogeneous state involving simultaneous dissolution and precipitation of several minerals is extremely challenging. For example it is generally reported that the dissolution rate of calcite is several orders of magnitude higher than that of silicate minerals. There also

Received by OCD: 6/29/2026

Table 8
The normalized relationship between crack growth threshold and peak stress.

Reaction condition Threshold parameter		Case R	Case C	Case BC
Crack closed, σ_{cc}	Stress (MPa)	8.8 (0.5)	13.6 (1.0)	5.4 (1.3)
	Normalized ratio	$0.051\sigma_f$	$0.071\sigma_f$	$0.047\sigma_f$
Crack initiation, σ_{ci}	Stress (MPa)	38.8 (5.2)	52.0 (1.5)	22.0 (3.5)
	Normalized ratio	$0.228\sigma_f$	$0.273\sigma_f$	$0.191\sigma_f$
Crack damage, σ_{cd}	Stress (MPa)	127.5 (5.2)	138.6 (5.6)	83.1 (8.3)
	Normalized ratio	$0.747\sigma_f$	$0.728\sigma_f$	$0.722\sigma_f$
Peak strength, σ_f	Stress (MPa)	171.0 (7.8)	190.3 (5.0)	115.2 (4.9)
	Normalized ratio	$1.00\sigma_f$	$1.00\sigma_f$	$1.00\sigma_f$

have been cases where the reactivity of phyllosilicate, such as illite and muscovite in shale, has been intensively examined.

As reported by Wan et al. [31], muscovite, having a layered structure similar to that of illite, has a large surface adsorption rate of CO_2 and a relatively small bulk interlayer expansion than illite. Therefore, it has the advantage of capturing CO_2 more stable than other clay minerals. The sedimentation in the specimen of Case C observed in the SPM test can be interpreted by these mechanisms. In the scope of CO_2 geological sequestration research, several studies have correlated geochemical weathering with the mechanical properties of shale by considering various reservoir environments. The following section provides a detailed analysis of the changes in mechanical properties caused by geochemical weathering regarding the results obtained in this study.

4.2. Determination of damage threshold at different stress levels

As shown in Fig. 9 of Section 3.2, based on the stress-volume strain curve, the strain increment process was analyzed in detail by dividing the process into the crack closing, crack initiation, and crack damage stages. First, stresses were expressed as a percentage of the maximum failure stress to compare the stress level in each stage. Table 8 shows the mean value and standard deviation (in parentheses) for each reaction condition. The crack closure stress and the crack initiation stress were bot the highest in Case C, showing values higher than that of Case R. The peak strength of Case C was also about 19 MPa higher than the strength of Case R. The lowest crack closure stress and crack initiation stress, on the other hand, were both observed in Case BC. The crack initiation stress in Case BC was less than 20% of the maximum load. This implies an important fact that, when shale is reacted with CO_2-dissolved brine, a stress level of only 20% of the maximum load (which also corresponds to 13% of the non-reacted shale peak strength) can induce cracks and when such stress levels are maintained the induced cracks will continue to propagate, possibly resulting in failure within a certain time. Such behavior is reflected in the crack damage stress which is generally considered for the long-term strength of rock. Although the normalized ratios of crack damage stress are similar between the specimens, the absolute magnitude is significantly small for Case BC. When considering the peak strength, Case BC also shows the lowest value, 115 MPa, which corresponds to a decrease in strength of approximately 50 MPa.

The plotting bar in Fig. 12 compares the induced axial and lateral strain at each stage of the crack development process which are shown in Fig. 9. First, in the initial crack closure stage, the largest axial strain occurred in Case BC with the axial strain of Case C being slightly smaller than that of Case R. However, these strain increment were insignificant in magnitude when compared with the strain induced during and after the stable crack growth stage. Particularly, the lateral strain of all cases which occurred before crack growth were only 4%–6% of the total lateral strain. The vast majority of axial and lateral deformation occurred during and after crack growth, as depicted in the axial strain of the specimens of Case BC (black bars in the graph) which shows the largest deformation in the crack growth stage.

The cumulative value of the strain rate that was induced in each stage is also shown as a solid line. As mentioned in Section 3.2, the ultimate amount of strain that occurs before failure can be compared between non-reacted and reacted specimens. The specimens that reacted with CO_2-dissovled brine, Case BC, showed an increase in axial and lateral strain by approximately 25% and 13%, respectively. In contrast, the specimens that reacted with CO_2 only, Case C, showed a decrease of axial strain by approximately 6% and the lateral strain was similar to that of non-reacted specimens. This trend illustrates how the mechanical properties of shale are deteriorated when reacted with CO_2-dissolved brine, whereas it becomes more intact when reacted with only CO_2.

There are various interpretations for such contradictory results. First, many studies have reported that when $scCO_2$ and brine coexist, chemical reactions such as dissolution occur in pore

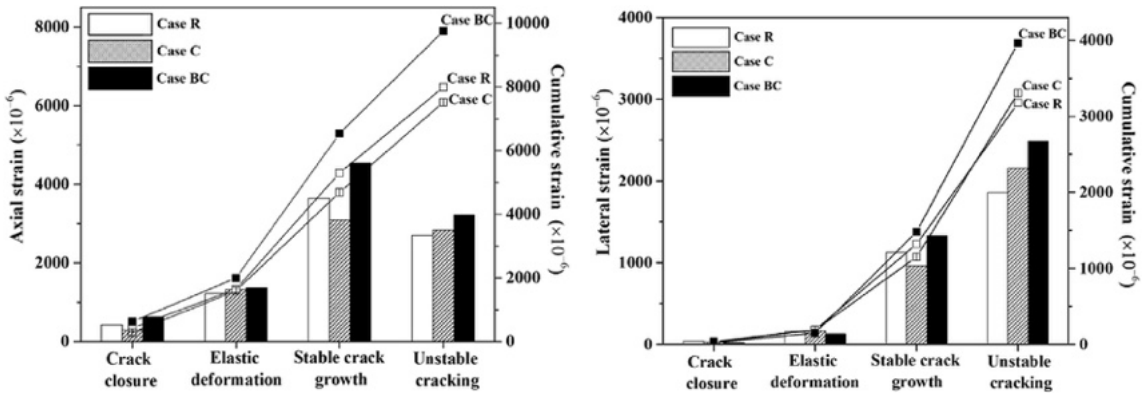


Fig. 12. Degree of strain in each stage of crack development.

Received by OCD: 6/29/2026

structures due to acidified brine and the contact force between rock grains or discontinuities is weakened which eventually affects the mechanical properties of shale [30,36,37]. The enhancement of mechanical properties when shale reacts solely with $scCO_2$, on the other hand, can be attributed to the self-sealing effect and compression effect of the pressure of $scCO_2$. Cerasi et al. [30] and Balashov et al. [38] reported the self-seal effect and slight enhancement of creep deformation in shale after imbibition with $scCO_2$. Especially, the results implied that shale with a higher Ca, Mg, and Fe ions (e.g., more chlorite or smectite) content will be more likely benefit form self-seal effect after CO_2 injection than other shale formations. Since the shale specimen of the present study also contained chlorite which consisted about 14% of the shale, it is likely for the specimen to have experienced the self-seal effect, especially by adsorption of $scCO_2$ through Ca or Fe. Another possible reason for the enhancement of mechanical properties is compression effect due to the high-pressure $scCO_2$. Yin et al. [39] examined the mechanical properties of shale after an absorption test of CO_2 while increasing the saturation pressure to 4, 6, 8, 12, and 16 MPa. The results showed a decrease in mechanical properties up to the saturation pressure of 12 MPa, yielding minimum values at 12 MPa. However, from 12 MPa to 16 MPa, the properties inversely increased which was explained by the effect of high CO_2 pressure consolidating shale into a more intact rock. Although the present study's $scCO_2$ compression pressure is 10 MPa, such compression effect could be considered as a factor for explaining the observed enhancement of mechanical properties.

This study and also previous studies have conducted thorough investigation about the correlation between geochemical and mechanical changes of shale, but they could not quantitatively identify which oxides form or dissolves in the reaction and how it leads to specific changes in mechanical properties. For precise interpretation, research and novel techniques are required in order to quantitatively analyze the geochemical reaction which consists of complex processes, as described in Section 4.1. Furthermore, a careful coupling analysis should be conducted on the formation mechanism of secondary sediments and the simultaneous change in mechanical properties, since interactions would exist between micro structure changes such as the amount of micro-pores or cracks and geochemical reactions.

5. Conclusion

In the present study, a method is devised to implement a $scCO_2$ sequestration environment on a laboratory scale and investigate the geochemical effects of $scCO_2$ on the properties of rock specimens. During a 63 day periodic reaction, shale specimens were reacted with predefined conditions of $scCO_2$ only (Case C) or $scCO_2$ and brine coexisting (Case BC) environment. Changes in the properties were inspected according to the reaction time through non-destructive and destructive tests. The results of these tests showed opposing changes in shale properties for different reaction conditions. The main results for each test are discussed below.

- The results confirmed that the seismic velocity and the shore hardness have similar tendencies of change along the reaction time and that the changes in the shore hardness value and P-wave velocity were remarkably opposite depending on the presence or absence of brine. In Case BC, the shore hardness decreased while the P-wave velocity also decreased by 0.6 km/s. Conversely, in Case C, the hardness increased with a slight increase in P-wave velocity.
- The SPM test allowed the researchers to analyze the precipitation and dissolution of the shale surface both visually and quantitatively. The shale slab of Case BC showed significantly increased roughness values along the reaction time. However, Case C showed a slightly decreased as the reaction time progressed and then increased by secondary sediments. The changes in the surface profile of slab specimens were extracted along a specific detection line to quantitatively analyze the area of weathering. The dissolution and precipitation regions occurred at approximately 0.718 and 0.720 μm^2 in Case C. However, the slab of Case BC showed significant geochemical reactivity compared with Case C, with dissolution and precipitation area of 2.142 and 1.869 μm^2, respectively.
- These weathering processes, the dissolution and precipitation on the shale surface, were further investigated by inspecting the dissolved ion components in brine and oxide compositions in shale powder specimens. The ionic content in the brine increased as the reaction progressed by dissolving the oxide components such as Si, Al, Fe, K, Mg, and Ca in muscovite and chlorite which were contained in the shale. The dissolution of Fe in chlorite was especially visible in the $scCO_2$ and brine coexisting environment.
- To investigate mechanical property changes, uniaxial compression test and Brazilian tests were conducted. The compressive strength of Case C specimens increased by approximately 10%, and Case BC showed a significant decrease of more than 30%. The tensile strength of Case C and Case BC increased and decreased by approximately 5 MPa, respectively. Similar to the change in strength, the elastic modulus also increased by approximately 20% for Case C, and the Case BC specimens decreased by more than 50%. These results can be considered consistent with the non-destructive test results. It was confirmed that the test specimens that reacted with $scCO_2$ gradually showed brittle behavior with its increase in the mechanical strength. However, the specimens that reacted with $scCO_2$ and brine showed a great decrease in strength and elastic modulus with a large volumetric strain. The cumulative value of the strain until failure could be compared with the non-reacted specimens. The axial and lateral strain of Case BC increased by approximately 25% and 13%, respectively, and Case C showed a decrease of axial strain of approximately 6%. Therefore, it was concluded that the mechanical properties deteriorated in Case BC. Further analysis was conducted by investigating the strain increment process according to the crack closing, crack initiation, and crack damage stages, which were determined by the stress-volume strain curve.

These results revealed that if CO_2 and brine existed simultaneously and responded to the shale surface, the geochemical response could significantly affect the physical properties of the shale compared with the environment in which only CO_2 existed. The mechanical and geochemical analysis of this study explains that when brine coexists with CO_2, dissolution becomes more dominant than precipitation which ultimately results in the weakening of mechanical properties. Based on these results, regarding CO_2 sequestration in deep saline formations, the present study emphasizes the need to examine the mechanical stability of the lower part of the caprock where brine and CO_2 coexist. To reveal the precise mechanism of the geochemical and mechanical changes in shale, further research is required on quantifying the underlying chemical reactions and its coupled interactions with mechanical properties such as the extent of crack closure or damage.

Credit author statement

Chae-Soon Choi: Conceptualization, Methodology, Data curation, Visualization, Writing - original draft Jineon Kim: Data curation, Visualization, Validation, Writing - review & editing Jae-Joon

Received by OCD: 6/29/2026

Song: Supervision, Writing - review & editing.

Declaration of competing interest

The authors declare that they have no known competing financial interests or personal relationships that could have appeared to influence the work reported in this paper.

Acknowledgments

This work was supported by a grant from the Human Resources Development program of the Korea Institute of Energy Technology Evaluation and Planning (KETEP), funded by the Ministry of Trade, Industry, and Energy of the Korea Government (No. 20204010600250).

This work was supported by the National Research Foundation of Korea (NRF) funded by the Ministry of Science and ICT (MSIT) of the Korea Government (No. NRF-2019R1F1A1060064).

References

[1] Global CCS Institute. Global status report of CCS 2019. Australia: Docklands; 2019.
[2] IPCC. IPCC special report on carbon dioxide capture and storage. US: Cambridge University Press; 2005.
[3] Bachu S, Gunter WD, Perkins EH. Aquifer disposal of CO_2-hydrodynamic and mineral trapping. Energy Convers Manag 1995;35(4):269–79.
[4] Park ED, Wang SK, Kin SO, Lee MH. The effects of the carbon dioxide stored in geological formations on the mineralogical and geochemical alterations of phyllosilicate minerals. J Geol Soc Korea 2014;50(2):231–40.
[5] Potdar RS, Vishal V. Trapping mechanism of CO_2 storage in deep saline aquifers: brief review. Geologic carbon sequestration: understanding reservoir behavior. Switzerland: Springer; 2016.
[6] Ko MJ, Kang HM, Wang SK, Lee MH. The weathering process of olivine and chlorite reacted with the supercritical CO_2 on the sequestration condition. J Geol Soc Korea 2011;47(6):635–45.
[7] Sampath KHSM, Perera MSA, Li DY, Ranjith PG, Matthai SK. Evaluation of the mechanical behavior of brine+CO_2 saturated brown coal under mono-cyclic uni-axial compression. Eng Geol 2019;263(20):105312.
[8] Shao H, Ray JR, Jun YS. Effects of organic ligands on supercritical CO_2-induced phlogopite dissolution and secondary mineral formation. Chem Geol 2011;290(3–4):121–32.
[9] Izgec O, Demiral B, Bertinm H, Akin S. CO_2 injection into saline carbonate aquifer formations I: laboratory investigation. Transport Porous Media 2008;72(1):1–24.
[10] Sampath KHSM, Perera MSA, Elsworth D, Ranjith PG, Matthai SK, Rathnaweera T. Experimental investigation on the mechanical behavior of Victorian brown coal under brine saturation. Energy Fuel 2018;32(5):5799–811.
[11] Shukla R, Ranjith PG, Choi SK, Haque A, Yellishetty M, Hong L. Mechanical behaviour of reservoir rock under brine saturation. Rock Mech Rock Eng 2013;46(1):83–93.
[12] Choi CS, Cheon DS, Song JJ. Effect of pore and confining pressure on the supercritical CO_2 permeability of sandstone: implications for the effective pressure law. J Geophys Res: Solid Earth 2017;122(8):6231–46.
[13] Choi CS, Song JJ. Estimation of the non-Darcy coefficient using supercritical CO_2 and various sandstones. J Geophys Res: Solid Earth 2019;124(1):442–55.
[14] Faye L, Peng L, Graig G, Sheila WH, Yee S, Helge H, Chen Z. CO_2-brine-caprock interaction: reactivity experiments on Eau Claire shale and a review of relevant literature. Int J Greenh Gas Con 2012;7:153–67.
[15] Park JY, Lee MH, Wang SK. Study on the geochemical weathering process of sandstones and mudstones in Pohang basin at CO_2 storage condition. Econ Environ Geol 2013;46(3):221–34.
[16] Ao X, Lu Y, Tang J, Chen Y, Li H. Investigation on the physics structure and chemical properties of the shale treated by supercritical CO_2. J CO_2 Util 2017;20:274–81.
[17] Lyu Q, Long X, Ranjith PG, Tan J, Kang Y, Wang Z. Experimental investigation on the mechanical properties of a low-clay shale with different adsorption times in sub-/super-critical CO_2. Energy 2018;147:1288–98.
[18] Lu Y, Chen X, Tang J, Li H, Zhou L, Han S, Ge Z, Xia B, Shen H, Zhang J. Relationship between pore structure and mechanical properties of shale on supercritical carbon dioxide saturation. Energy 2019;172:270–85.
[19] Feng G, Kang Y, Sun ZD, Wang XC, Hu YQ. Effects of supercritical CO_2 adsorption on the mechanical characteristics and failure mechanisms of shale. Energy 2019;173:870–82.
[20] Gueguen Y, Palciauskas V. Introduction to the physics of rocks. US: Princeton University Press; 1994.
[21] Armitage PJ, Worden RH, Faulkner DR, Aplin AC, Iliffe J. Diagenetic and sedimentary controls on porosity in lower carboniferous fine-grained lithologies, Krechba field, Algeria: a petrological study of a caprock to a carbon capture site. Mar Petrol Geol 2010;27(7):395–1410.
[22] Watson MN, Daniel RF, Tingate PR, GibsonPoole CM. CO_2 related seal capacity enhancement in mudstones: evidence from the pine lodge natural CO_2 accumulation, Otway basin, Australia. Proceedings of the 7th international conference on greenhouse gas control technologies 2005;2(2):2313–6.
[23] Mitchell JK, Soga K. Fundamentals of soil behavior. US: John Wiley & Sons; 1976.
[24] Zhang X, Wei B, Shang J, Gao K, Pu W, Xu X, Wood C, Sun L. Alterations of geochemical properties of a tight sandstone reservoir caused by supercritical CO_2-brine-rock interactions in CO_2-EOR and geosequestration. J CO_2 Util 2018;28:408–18.
[25] Kim SO, Wang S, Lee M. Geochemical reactive experimental and modeling studies on caprock in the Pohang basin. Econ Environ Geol 2016;49(5):371–80.
[26] ASTM D. 2938. Standard test method for unconfined compressive strength of intact rock core specimens. West Conshohocken, PA: ASTM International; 2019.
[27] Panagopoulos A, Haralambous KJ, Loizidou M. Desalination brine disposal methods and treatment technologies-A review. Sci Total Environ 2019;693(25):133545.
[28] Vugrinovich R. Subsurface temperatures and surface heat flow in the Michigan basin and their relationships to regional subsurface fluid movement. Mar Petrol Geol 1989;6(1):60–70.
[29] Wang L, Kan AT, Zhang Z, Yan F, Liu Y, Dai Z, Tomson MB. Field method for determination of bicarbonate alkalinity. In: Proceedings. The SPE international oilfield scale conference and exhibition. Scotlan.: Aberdeen; 2014.
[30] Cerasi P, Lund E, Kleiven ML, Stroisz A, Pradhan S, Kjoller C, Frykman P, Fjaer E. Shale creep as leakage healing mechanism in CO_2 sequestration. Energy Procedia 2017;114:3096–112.
[31] Wan J, Tokunaga TK, Ashby PD, Kim Y, Voltolini M, Gilbert B, DePaolo DJ. Supercritical CO_2 uptake by nonswelling phyllosilicates. Proc Natl Acad Sci USA 2018;115(5):873–8.
[32] Heo JS. Measurement of acoustic emission and the characteristics of deformation and fracturing of rock under triaxial compression. Ph.D paper; 2001.
[33] Audigane P, Lions J, Gaus I, Robelin C, Durst P, Meer BVD, Geel K, Oldenburg CM, Xu T. Geochemical modeling of CO_2 injection into a methane gas reservoir at the K12-B field, North Sea. AAPG Stud Geol 2009;59:499–519.
[34] Beckingham LE, Mitnick EH, Steefel CI, Zhang S, Voltolini M, Swift AM, Yang L, Cole DR, Sheets JM, Ajo-Franklin JB, DePaolo DJ, Mito S, Xue Z. Evaluation of mineral reactive surface area estimates for prediction of reactivity of a multi-mineral sediment. Geochem Cosmochim Acta 2016;188:310–29.
[35] Scislewski A, Zuddas P. Estimation of reactive mineral surface area during water-rock interaction using fluid chemical data. Geochem Cosmochim Acta 2010;74(24):6996–7007.
[36] Lin Y, Zhou K, Gao R, Li J, Zhang J. Influence of chemical corrosion on pore structure and mechanical properties of sandstone. Geofluids 2019;15.
[37] Jayasekara DW, Ranjith PG, Wanniarachchi WAM, Rathnaweera TD, Chaudhuri A. Effect of salinity on supercritical CO_2 permeability of caprock in deep saline aquifers: an experimental study. Energy 2020;191:116486.
[38] Balashov VN, Guthrie GD, Lopano CL, Hakala JA, Brantley SL. Reaction and diffusion at the reservoir/shale interface during CO_2 storage: impact of geochemical kinetics. Appl Geochem 2015;61:119–31.
[39] Yin H, Zhou J, Xian X, Jiang Y, Lu Z, Tan J, Liu G. Experimental study of the effects of sub- and super-critical CO_2 saturation on the mechanical characteristics of organic-rich shales. Energy 2017;132:84–95.

EXHIBIT 12

Computational Geosciences (2024) 28:211–225
https://doi.org/10.1007/s10596-023-10216-3

ORIGINAL PAPER

An integrated framework for optimal monitoring and history matching in CO_2 storage projects

Dylan M. Crain[1] · Sally M. Benson[1] · Sarah D. Saltzer[1] · Louis J. Durlofsky[1]

Received: 17 November 2022 / Accepted: 20 April 2023 / Published online: 23 July 2023
© The Author(s), under exclusive licence to Springer Nature Switzerland AG 2023

Abstract
Monitoring is an important component of geological carbon storage operations because it provides data that can be used to estimate key quantities such as CO_2 plume location. The design of the monitoring strategy is complicated, however, because the monitoring plan must be established prior to the availability of extensive flow data. In this work, we present and apply a framework that integrates monitoring well optimization and (subsequent) history matching. The monitoring well optimization entails finding the locations of monitoring wells such that, with the data acquired at those locations, the expected uncertainty reduction in a particular flow quantity is maximized. This optimization requires the simulation of a large set of prior models, though these simulations need only be performed once for a given injection scenario. Once the monitoring wells are in place and CO_2 injection begins, history matching is performed using the monitoring data. This is accomplished here using an ensemble smoother with multiple data assimilation. The overall framework is applied to variogram-based geomodels that are representative of an actual storage project under development in the USA. Two injection scenarios are considered with two different (synthetic) 'true' models, which provide the observed data. History matched models are constructed using data from both optimally located and heuristically placed monitoring wells. Posterior uncertainty, evaluated in terms of the cumulative distribution function for a metric related to plume extent over the ensemble of history matched models, is shown to be minimized through use of optimized monitoring wells. These results demonstrate the importance of optimizing the monitoring plan, and the degree of uncertainty reduction that can be realistically achieved.

Keywords Carbon capture and Storage · Monitoring well · Optimization · Reservoir simulation · Data assimilation

1 Introduction

Subsurface storage of CO_2 in deep saline aquifers represents a promising strategy for achieving large reductions in greenhouse gas emissions to the atmosphere. Monitoring is an essential aspect of any storage operation, as it can identify leakage and provide information on the location of the CO_2 plume. Although monitoring is conducted over many decades, an initial monitoring plan must be defined when CO_2 injection begins. This poses challenges because the storage aquifer geology is highly uncertain at this point, yet monitoring well locations and types must nonetheless be in place.

In this paper, we describe an overall strategy for determining the 'optimal' locations of monitoring wells and for history matching using pressure and saturation data as they are collected during CO_2 injection. The monitoring well optimization is accomplished using the general approach described in [21]. This procedure requires simulation of an ensemble of prior geological realizations. Monitoring well locations are then determined such that the expected uncertainty reduction is maximized (under Gaussian assumptions on the data). Once CO_2 injection is underway, the monitoring wells provide pressure and saturation data. History matching using these observed data is accomplished through use of an ensemble smoother with multiple data assimilation, ES-MDA [7]. Our procedures are demonstrated on models

✉ Dylan M. Crain
cooper96@stanford.edu

Sally M. Benson
smbenson@stanford.edu

Sarah D. Saltzer
sarah.saltzer@stanford.edu

Louis J. Durlofsky
lou@stanford.edu

[1] Department of Energy Science and Engineering, Stanford University, 94305 Stanford, CA, USA

corresponding to an actual sequestration project now being planned for the Illinois basin in the USA.

Many previous investigations have addressed monitoring and history matching for CO_2 storage operations. Here we discuss studies that are most relevant to our work. History matching using multilevel pressure time-series data was performed for a carbon sequestration pilot project in Illinois, USA [20]. The history matching process was heuristic, though the results demonstrated the utility of assimilating multilevel pressure data. Geophysical data from electromagnetic and seismic surveys, as well as satellite images, have also been used for history matching in carbon sequestration [1, 16, 23]. According to [9, 13], well-based pressure and saturation measurements, along with seismic surveys, provide the most informative data in practice.

Recent studies involving data assimilation have often applied some type of ensemble-based history matching. ES-MDA, in particular, has been widely used in CO_2 storage studies [2, 6, 22]. ES-MDA is more expensive than some other ensemble-based methods because the data assimilation computations are repeated several times (there are typically 4–10 assimilation steps). For this reason, recent work has focused on reducing computational cost by modifying the algorithm [6, 10, 22] or by using surrogate flow models to approximate expensive forward flow simulations [12, 14, 16, 23, 24].

There has also been a substantial amount of work on determining monitoring plans for CO_2 storage projects. Monitoring wells can be used for different objectives, including detecting leakage and identifying the plume location. Although our interest here is in minimizing uncertainty in the plume location, existing work in both areas is relevant to our investigation. In several previous studies, monitoring well locations and sensor types were specified heuristically, and the post-history matching uncertainty reduction for each scenario was assessed [4, 5, 14, 25]. This procedure can be iterated manually to achieve further reduction in expected posterior uncertainty. Optimal experimental design has also been applied in this setting [11, 26]. Particle swarm optimization (PSO) was used in [3] to find the optimum monitoring well locations that minimized the uncertainty in a particular metric. However, in order to reduce computational costs, samples were drawn from a set of prior results instead of being generated through history matching. A more formal approach was presented in [21], where monitoring wells were placed such that a metric quantifying posterior uncertainty was minimized.

In this work, we combine ideas from some of the studies noted above to define an overall monitoring and history matching framework. The locations of a predefined number and type of monitoring wells are optimized using a variant of the procedure presented in [21]. This requires the simulation of an ensemble of prior models intended to capture the range of prior geological uncertainty. Then, under the assumption of Gaussian prior and posterior flow statistics, the optimal monitoring well locations can be determined without conducting additional simulations. The objective of the monitoring well optimization is to maximize the degree of uncertainty reduction in a quantity related to plume location. Once the storage project is in operation, history matching (ES-MDA) is performed using pressure and saturation measurements from the monitoring wells. The framework is applied to models based on those for a storage operation being planned for Illinois, USA [17]. The performance of the methodology will be demonstrated for different synthetic 'true' models and different injection strategies.

This paper proceeds as follows. In Section 2, we describe the computational approaches for monitoring well optimization and history matching. Next, in Section 3, the aquifer model used in this study is presented. Numerical results are then provided for several cases, and the reduction in uncertainty achieved using optimized monitoring well locations is compared to that using heuristic designs. Finally, in Section 4, we summarize our findings and give suggestions for future work in this area.

2 Optimization of monitoring well locations and history matching procedure

Our goal in this study is to maximize uncertainty reduction in carbon storage operations by applying history matching using data from monitoring wells. The amount of uncertainty reduction that can be achieved is dependent on the number of monitoring wells, their locations, and the type of data they provide. A key challenge in this setting is that the permitting procedure requires a monitoring plan to be established before any CO_2 is injected, and thus before any flow data are collected. This means that one or more monitoring well locations must be determined based only on a prior understanding of the subsurface geology.

The workflow applied here is illustrated in Fig. 1. This framework involves two steps – monitoring well optimization and history matching. We assume that all monitoring wells are drilled prior to injection. Thus the two steps, which will now be described, are sequential. The procedure could be modified to include the addition of monitoring wells during the injection stage, but this is not considered here.

2.1 Monitoring well location optimization

In this work, the monitoring scheme is optimized using a modified version of the strategy described in Sun and Durlofsky [21]. In that study, a data-space inversion procedure was applied, and the goal was to provide posterior data predictions, e.g., CO_2 plume location at a particular time. Here our

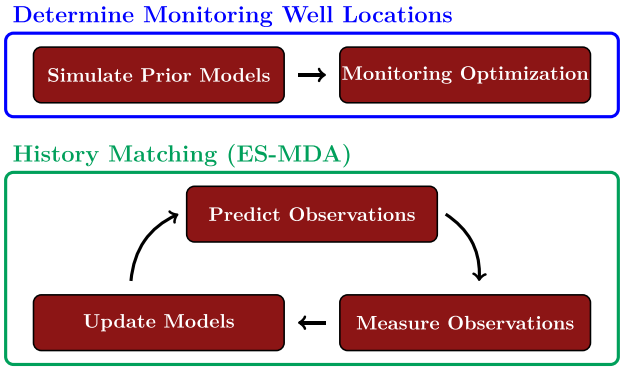


Fig. 1 Workflow for CO_2 monitoring and history matching. Monitoring well locations are determined in the first step, and history matching is then performed as CO_2 is injected over time

goal is to construct posterior (history matched) geomodels. The monitoring well optimization step, however, is essentially the same regardless of whether the history matching entails a data-space or a model-based procedure.

The vector containing the uncertain aquifer model parameters is represented by $\mathbf{m} \in \mathbb{R}^{N_m \times 1}$. Here $N_m = 2N_b$, where N_b is the number of grid blocks in the geomodel. The two geological parameters in each grid block correspond to porosity and permeability. Only a single value is required for permeability because we set $k_x = k_y$ and take $k_z = \alpha k_x$, where α is a specified parameter (here k_x, k_y, and k_z denote directional permeabilities). The aquifer models in this work are based on those in Okwen et al. [17], in which porosity and permeability are uncorrelated. Thus, we do not prescribe any correlation between these two sets of parameters in the models used here.

The forward simulation model is represented as

$$\mathbf{d}_f = \mathbf{g}(\mathbf{m}), \tag{1}$$

where $\mathbf{g}$ denotes the flow simulation and $\mathbf{d}_f \in \mathbb{R}^{N_f \times 1}$ represents simulation results. Our intent is to determine the optimal monitoring well locations such that, at a prescribed (future) time, the uncertainty reduction in a quantity of interest (QoI) will be maximized. For specificity, here this QoI is a measure of the plume extent after 20 years of CO_2 injection. Data up to this time are referred to as 'historical' data (even though no data have yet been collected) and are denoted by $\mathbf{d}_h \in \mathbb{R}^{N_h \times 1}$, where N_h is the number of observations. Data corresponding to the QoI are denoted $\mathbf{d}_p \in \mathbb{R}^{N_p \times 1}$, where N_p is the number of QoI. The data vector $\mathbf{d}_f$ can be viewed as a concatenation of these two sets of data, i.e., $\mathbf{d}_f = [\mathbf{d}_h^T, \mathbf{d}_p^T]^T$.

We proceed by first simulating a set of N_r prior geological models, intended to represent our prior knowledge of the subsurface. In this study we set $N_r = 350$. This will provide a large set of prior data vectors – specifically, $(\mathbf{d}_f)_i$, $i = 1, \ldots, N_r$, each of which is comprised of $(\mathbf{d}_h)_i$ and $(\mathbf{d}_p)_i$, $i = 1, \ldots, N_r$. The goal of the first-stage optimization is to determine the monitoring well locations such that the measured data, when used for history matching, minimize an appropriate metric over the set of prior models.

Monitoring wells are assumed to extend vertically through the entire storage aquifer, with areal locations defined by their (i, j) locations on the simulation grid. Monitoring wells can contain multiple transducers, each of which provides pressure data, along their length. We denote the number of pressure transducers on each well by N_t, and treat each transducer as if it is located in the center of the grid block. Each monitoring well is thus defined by $2 + N_t$ design variables (i and j areal locations and N_t vertical locations). The full set of N_w monitoring wells is denoted by $\mathbf{y} \in \mathbb{N}^{N_y \times 1}$, where $N_y = N_w \times (2 + N_t)$.

In our setup, the goal is to maximize uncertainty reduction in a plume-location metric after 20 years of injection. We assume that pressure data are measured every 3 months at the pressure transducer locations, and that CO_2 saturation is measured along the monitoring well once per year. This is accomplished in practice using a saturation logging tool [8].

The actual observations will contain error due to imprecision in the measurements, along with model error, though the latter may be difficult to quantify. We denote the observed data as $\mathbf{d}_{obs} \in \mathbb{R}^{N_h \times 1}$, with $\boldsymbol{\epsilon} \in \mathbb{R}^{N_h \times 1}$ the measurement error. Here $\boldsymbol{\epsilon}$ is assumed to be normally distributed with mean $\mathbf{0}$ and covariance $C_D \in \mathbb{R}^{N_h \times N_h}$.

Strandli et al. [20] cited a pressure measurement error of about 1 kPa (0.001 MPa), while Sun and Durlofsky [21] applied a pressure error of 0.1 MPa, which includes some amount of model error. The latter study used a saturation error of 0.02. Here we use a pressure error of 10.34 kPa (1.5 psi), which is between those used in [20] and [21], and a saturation error of 0.02, as in [21]. The model error contribution could be adjusted in cases where this component can be accurately quantified.

The $\mathbf{d}_p$ portion of $\mathbf{d}_f$ in our case corresponds to a scalar QoI, which will be used in the monitoring well optimization problem (note the QoI must be a scalar quantity in our optimization framework). Here this quantity is the volume of CO_2 beyond a given target region after 20 years of injection. The target region here is taken to be a volume corresponding to $n \times n \times n_p$ blocks around the injection well(s). Here $n = 5$ or 7, and n_p is the number of layers in which the well is perforated. Further details (and illustrations) will be provided in Section 3.

This QoI, now denoted by J, is given by

$$J = \sum_{i \notin \mathrm{TR}} v_i \phi_i S_i, \tag{2}$$

where i denotes a grid block, the sum is over all blocks outside the target region (TR), v_i is the bulk volume of cell i, ϕ_i

is the porosity of cell i, and S_i is the CO_2 saturation in cell i. The goal of the monitoring well optimization is to locate the monitoring wells such that the expected variance in J (over the set of N_r realizations), conditioned to the measurement data, is minimized. This acts to increase our knowledge regarding the plume extent after the 20-year time frame.

The optimization problem can be expressed as

$$\mathbf{y}_{\text{opt}} = \arg\min_{\mathbf{y}} \left[\int \int \sigma^2_{J|d_{obs}(m,y,\epsilon)} p(\mathbf{m}) p(\boldsymbol{\epsilon}) d\mathbf{m} d\boldsymbol{\epsilon} \right], \quad (3)$$

where $\mathbf{y}_{\text{opt}}$ denotes the optimum monitoring locations and $\sigma^2_{J|d_{obs}(m,y,\epsilon)}$ is the posterior variance of J, given measured data $\mathbf{d}_{obs}(\mathbf{m}, \mathbf{y}, \boldsymbol{\epsilon})$. Assuming that multivariate Gaussian statistics are preserved in the data space, Sun and Durlofsky [21] showed that the integral in Eq. 3 can be expressed as

$$\int \int \sigma^2_{J|d_{obs}(m,y,\epsilon)} p(\mathbf{m}) p(\boldsymbol{\epsilon}) d\mathbf{m} d\boldsymbol{\epsilon} = \sigma^2_{JJ} - C_{Jd_h}(C_{d_h d_h} + C_D)^{-1} C_{d_h J}, \quad (4)$$

where the covariances are determined from the simulation results over the N_r prior models. The specific computations are

$$\sigma^2_{JJ} = \frac{1}{N_r - 1} \sum_{i=1}^{N_r} (J_i - \mu_J)^2, \quad (5)$$

$$C_{Jd_h} = C^T_{d_h J} = \frac{1}{N_r - 1} \sum_{i=1}^{N_r} (J_i - \mu_J) \left[(\mathbf{d}_h)_i - \boldsymbol{\mu}_{d_h} \right], \quad (6)$$

$$C_{d_h d_h} = \frac{1}{N_r - 1} \sum_{i=1}^{N_r} \left[(\mathbf{d}_h)_i - \boldsymbol{\mu}_{d_h} \right] \left[(\mathbf{d}_h)_i - \boldsymbol{\mu}_{d_h} \right]^T, \quad (7)$$

where J_i and $(\mathbf{d}_h)_i$ represent the simulated QoI value and monitoring well data (at locations defined by $\mathbf{y}$) for prior model i. Furthermore, μ_J and $\boldsymbol{\mu}_{d_h}$ denote the prior means over the N_r models in the ensemble.

Combining Eqs. 3 and 4 gives

$$\mathbf{y}_{\text{opt}} = \arg\min_{\mathbf{y}} \left[\sigma^2_{JJ} - C_{Jd_h}(C_{d_h d_h} + C_D)^{-1} C_{d_h J} \right]. \quad (8)$$

The covariance terms depend on the monitoring well locations $\mathbf{y}$, but the variance σ^2_{JJ} does not depend on $\mathbf{y}$ because the QoI values for the prior models are not affected by the monitoring plan. This allows the optimization problem to be rewritten as

$$\mathbf{y}_{\text{opt}} = \arg\min_{\mathbf{y}} \left[1 - \frac{C_{Jd_h}(C_{d_h d_h} + C_D)^{-1} C_{d_h J}}{\sigma^2_{JJ}} \right], \quad (9)$$

where the entire fractional term can be interpreted as a measure of expected uncertainty reduction in J given the data measured at the monitoring well locations defined by $\mathbf{y}$. As discussed in [21], this overall approach is still applicable (though more approximate) in cases where the flow statistics are non-Gaussian.

The optimization problem given in Eq. 9 is solved using a genetic algorithm formulated in a Python environment. The optimization requires only prior simulation data. This means that, once the N_r prior realizations are simulated, no additional flow computations need be performed for the design of the monitoring strategy.

2.2 History matching procedure

We now describe the approach used for history matching. The observed data considered in the history matching step are those measured by the (optimized) monitoring wells. In this work, the 'true' data derive from a selected synthetic 'true' model that is consistent with the prior ensemble (but it is not one of the N_r models used for monitoring well optimization). Ensemble smoothing with multiple data assimilation (ES-MDA), introduced by Emerick & Reynolds [7], is applied. Specialized treatments such as localization are not used in this work.

In ES-MDA, at each of the N_a data assimilation steps, we apply

$$\mathbf{m}_i^{k+1} = \mathbf{m}_i^k + C^k_{md_h}(C^k_{d_h d_h} + \alpha_k C_D)^{-1} \left[\mathbf{d}^k_{pert,i} - \mathbf{d}^k_{h,i} \right], \quad (10)$$

for $i = 1, \ldots, N_r$ and $k = 1, \ldots, N_a$. Here $\mathbf{m}_i^{k+1}$ represents updated geomodel i ($\mathbf{m}_i^k$ is the model at the previous assimilation step), $\mathbf{d}^k_{h,i}$ contains the simulation results for model i at step k, and the covariance matrices $C^k_{md_h}$ and $C^k_{d_h d_h}$ are computed at each step. The vector $\mathbf{d}^k_{pert,i}$ denotes (perturbed) observation data, sampled from $\mathbf{d}^k_{pert,i} = \mathbf{d}_{obs} + \sqrt{\alpha_k} C_D^{1/2} \mathbf{z}^k_{d,i}$, where α_k is the ES-MDA inflation parameter, C_D is the data covariance, and $\mathbf{z}^k_{d,i} \sim \mathcal{N}(\mathbf{0}, I)$. In this work, we set $N_a = 4$ and $\alpha_k = 4$ at all assimilation steps.

The ES-MDA procedure requires a total of $N_r \times N_a$ simulation runs. Thus the computational demands for this step are substantial. The final set of history matched models, $\mathbf{m}_i$, $i = 1, \ldots, N_r$, generated after assimilation step 4, are used to provide predictions for any QoI. They can also be applied to evaluate or optimize storage aquifer performance under new conditions (e.g., increased injection rates, the introduction of additional injection wells).

3 Computational results

In this section, we first present the aquifer model and problem setup. The workflow described in Section 2 is then applied to two different injection scenarios. For each scenario, two different true models are considered. The first scenario (Section 3.2) involves a single injection well, while the second scenario (Section 3.3) involves two injection wells, with the second well starting injection 5 years after the first well.

3.1 Aquifer model

The models and problem setup in this work are based on the study by Okwen et al. [17]. That work entailed a feasibility assessment for a carbon storage project in central Illinois, USA, with CO_2 injected into the Mt. Simon formation. Aspects of the problem specification have been modified in this work, including the injection well location, injection rate, and simulation time frame. In our model the storage aquifer extends 16.15 km × 16.46 km areally. It is 1.14 km thick, with this thickness including the confining shale layer. The models are represented on a 40 × 40 × 40 grid, with cells of dimension 403.9 m × 411.5 m × 28.6 m. The size of the grid blocks and the level of resolution in these models are certainly less than ideal. In particular, the grid is too coarse to resolve detailed CO_2 plume evolution or complex multiphase flow physics. This is not a major concern here since our goal is to illustrate the overall methodology. In a practical application, it would be appropriate to introduce grid refinement, particularly in the region around the injection and monitoring wells. In addition, the incorporation of properly upscaled geomodels, and/or error models developed to correct for unresolved physics, would be useful.

The models contain six geological layers (one of these is the confining shale layer) and are constructed through Cartesian 'mappings' of more complex models defined on irregular grids. The topological structure of the layers defined in [17] is preserved in the mapping, though this treatment requires cells above the shale and below geological layer 6 to be deactivated. A geological realization of the system (geostatistical parameters are given below) is shown in Fig. 2. The zero-valued regions in this figure represent the inactive cells.

The initial pressure of the aquifer is 20.07 MPa at a depth of 1750 m. We specify a maximum bottom-hole pressure (BHP) for the injectors of 27.63 MPa. According to [17], the Environmental Protection Agency (EPA) stipulates that the maximum BHP of a Class VI injection well can be at most 90% of the formation fracture pressure. At the target injection depth of 1750 m for the Mt. Simon formation, this criterion corresponds to a maximum BHP of 29.14 MPa. Thus our specified maximum of 27.63 MPa is well within the acceptable range. Consistent with [17], no additional aquifer support is introduced into the models. The highest

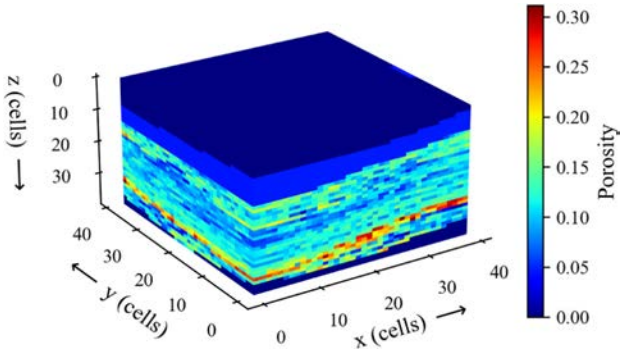


Fig. 2 Porosity field for a prior realization. The region above the confining shale layer is inactive. Vertical exaggeration applied

BHP actually reached (in all runs) remained below the specified maximum, indicating the pore volume of the models is sufficiently large for the volume of CO_2 injected.

The system is isothermal (with a temperature of 50.3°C) and initially contains only brine, of density 1150 kg/m^3. Simulations are performed using Eclipse [19] with the CO2STORE option. This simulator has preset models for the mutual solubility and fluid properties of CO_2 and brine. The gas-water relative permeability curves, which correspond to one of the scenarios considered by Okwen et al. [17], are shown in Fig. 3.

Permeability and porosity in all layers of the model, except for the confining shale layer, are taken to be uncertain. For the shale layer (layer 1), we specify a constant permeability of 0.045 md and a constant porosity of 0.046. Porosity and log-permeability realizations for the other five layers are generated through application of Gaussian sequential simulation. Realizations are constructed independently for each geological layer using the SGeMS toolbox [18]. The geological layers are then stacked to create the full realization. We proceed in this manner because the layers are geologically distinct and are characterized by different statistical distributions.

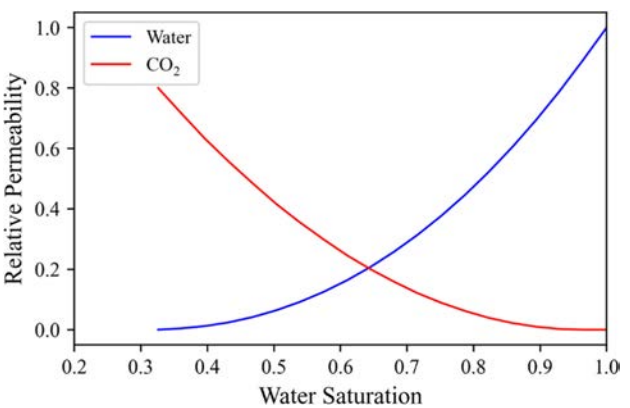


Fig. 3 Relative permeability curves for CO_2 and brine

The mean (μ) and standard deviation (σ) for the log-permeability and porosity in each layer are provided in Table 1. The models are all generated using an ellipsoid-shaped exponential variogram model. The correlation lengths in the x, y, and z-directions (l_x, l_y, l_z) for each layer are also given in Table 1. Consistent with the actual modeling of this formation, we specify $k_x = k_y$ and $k_z = 0.12k_x$ for all cells. A total of $N_r = 350$ prior geological models are constructed. Two prior realizations are shown in Fig. 4 ($\log_e k_x$ for x-z cross sections is displayed).

The geomodels are not conditioned to hard data at the well locations. Although it would be appropriate to introduce this conditioning in practice (after accounting for the difference in scale between the hard data and the grid blocks), it is somewhat involved to do this within the context of this study. This is because we will consider several different monitoring well configurations, which means the conditioning would be different in each case. This would complicate both the workflow and the comparisons between the different monitoring well strategies.

3.2 Injection scenario 1

In the first injection scenario, we consider a single vertical well, located in the center of the model. This well injects at a rate of 2.0 Mt/yr of CO_2 over a 20-year period. The injection well is perforated in the two lowermost cells in geological layer 4, in the two cells in geological layer 5, and in the uppermost cell of layer 6. As noted earlier, in all simulation runs (for prior and posterior realizations and true models), the injection-well BHP never exceeds the maximum allowable value of 27.63 MPa, indicating that pressure buildup remains within an acceptable range.

Any number of wells can be considered for monitoring, though economic considerations will limit their number in practice. Here we consider two vertical monitoring wells. These wells are assumed to measure saturation at every cell along their depth once per year, as well as pressure at three depths every 3 months. The optimization variables thus include, for each well, an x (i) location, a y (j) location, and three vertical (k) pressure transducer locations (thus $N_y = 10$).

The QoI J, for which we seek to minimize posterior uncertainty, is the CO_2 volume beyond the cells forming a $7 \times 7 \times 5$ target region centered around the injection well perforations. In qualitative terms, we wish to find the monitoring well locations that best quantify (after history matching) the volume of CO_2 that is outside this region after 20 years of injection. The target region is shown in gray in Fig. 5. To compute the objective function, we apply Eq. 2 for each realization. The goal of the monitoring well optimization is to minimize the variance of J over all N_r realizations.

A genetic algorithm, with a population of 100 individuals, is used for the optimization defined in Eq. 9. The optimization proceeds for 150 generations (iterations). The resulting optimum locations for the two monitoring wells are shown in Fig. 5 (the injection well location is also displayed). The optimization leads to a remaining variance of 0.0709. This value corresponds to the argument of Eq. 9 evaluated for the optimal monitoring well configuration. Note that the monitoring wells are located in blocks adjacent to the injector. The pressure transducers are placed above and below the injector perforations.

We will compare the performance of the optimal monitoring scheme shown in Fig. 5 to that of other (heuristic) monitoring well configurations. Three such qualitative configurations are considered. These cases are displayed in Fig. 6 along with the injection well and optimal monitoring well locations.

In Case 1, the monitoring wells are placed where the variance in the prior results is a maximum. Here variance is computed in both saturation and pressure for each cell at each time step, over all $N_r = 350$ prior simulation runs. The normalized pressure and saturation variances are combined with equal weighting. The (i, j) locations for the monitoring wells, along with the corresponding depths for the pressure transducers, are then determined such that the variance is maximized. In the case of two or more monitoring wells, this procedure is repeated to find the next (i, j) location and corresponding depths. Note that this approach, although quantitative in character, does not account for the specific QoI (J). In Cases 2 and 3, the monitoring wells are located just outside the target region, in different configurations. For these cases, the pressure transducer depths are taken to be the same as in the optimal configuration.

We can directly evaluate the argument of Eq. 9 for each of the three heuristic cases. The remaining variance is, for Cases 1–3, 0.0784, 0.6912, 0.6508, respectively. These values are all greater than that for the optimum configuration (0.0709), though Case 1 (based on prior variance) is comparable to the optimum. We might thus expect this configuration

Table 1 Geostatistical parameters for each geological layer

Layer	μ_ϕ	σ_ϕ	$\mu_{\log k}$	$\sigma_{\log k}$	l_x	l_y	l_z
2	0.117	0.039	2.223	2.332	24	24	4
3	0.096	0.018	1.061	2.631	21	22	3
4	0.102	0.016	1.690	1.173	29	30	4
5	0.215	0.040	4.641	1.994	26	23	1
6	0.123	0.043	2.540	2.667	25	24	2

Layer 1 (shale layer) is not shown because these properties do not vary. Log properties are $\log_e k_x$ in md. Correlation lengths are in number of grid blocks in the corresponding direction. Mean values for each layer are from [17]

Received by OCD: 6/29/2026

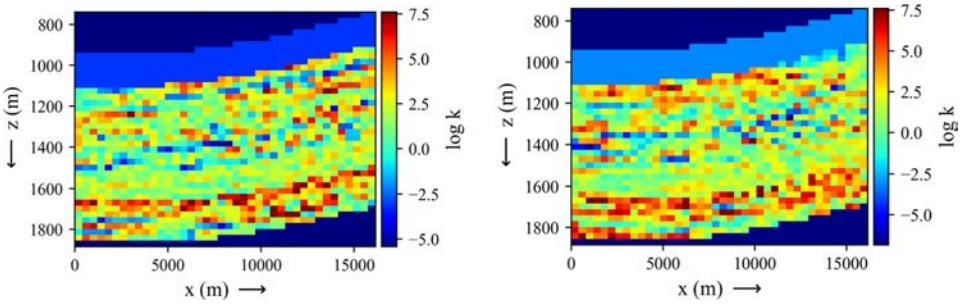


Fig. 4 Two prior realizations of log-permeability for x-z cross sections

(a) Realization 2

(b) Realization 214

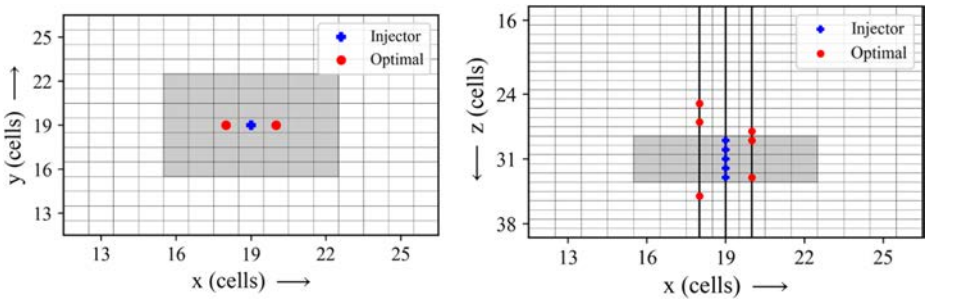


Fig. 5 Optimal monitoring well configuration. Injection well location and perforations also shown (injection scenario 1). Gray shaded blocks indicate target region

(a) Top view of optimum monitoring wells

(b) Cross-sectional view of optimum monitoring wells

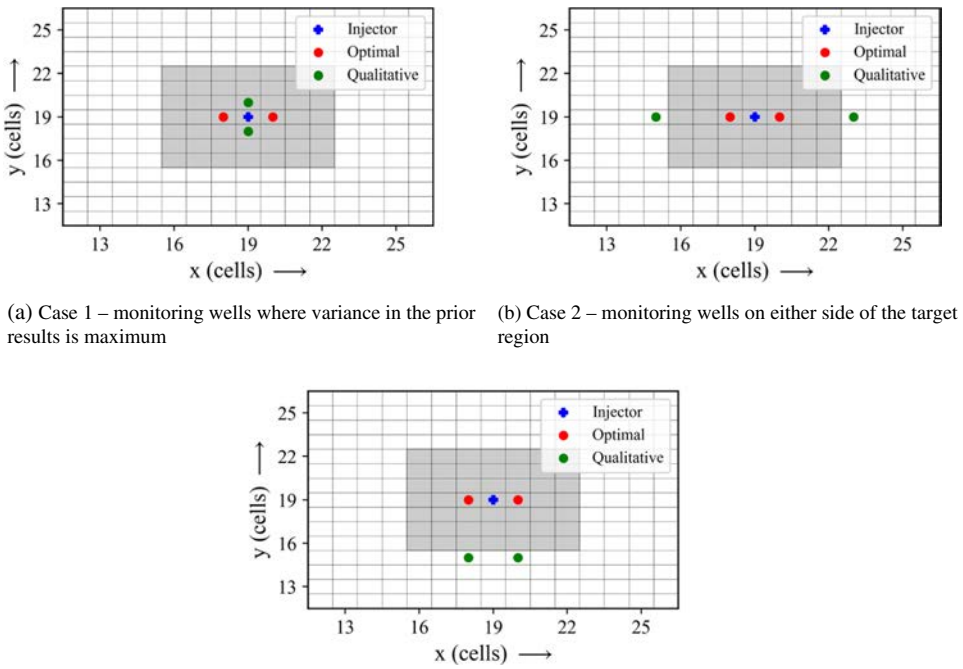


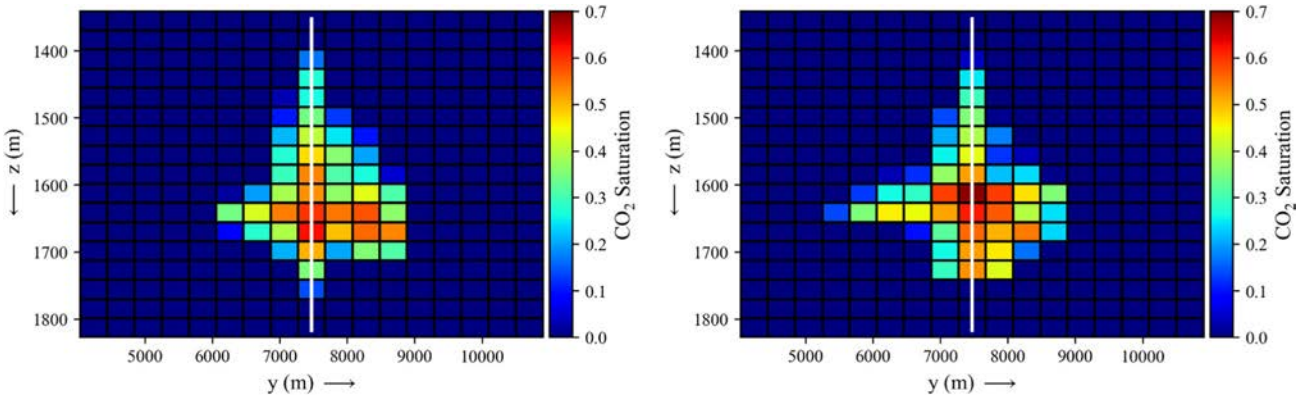
Fig. 6 Monitoring well locations for various qualitative (heuristic) schemes. Optimal configuration and injection well also shown (injection scenario 1). Gray shaded blocks indicate target region

(a) Case 1 – monitoring wells where variance in the prior results is maximum

(b) Case 2 – monitoring wells on either side of the target region

(c) Case 3 – monitoring wells near one another outside the target region

Received by OCD: 6/29/2026



(a) True model 1 (b) True model 2

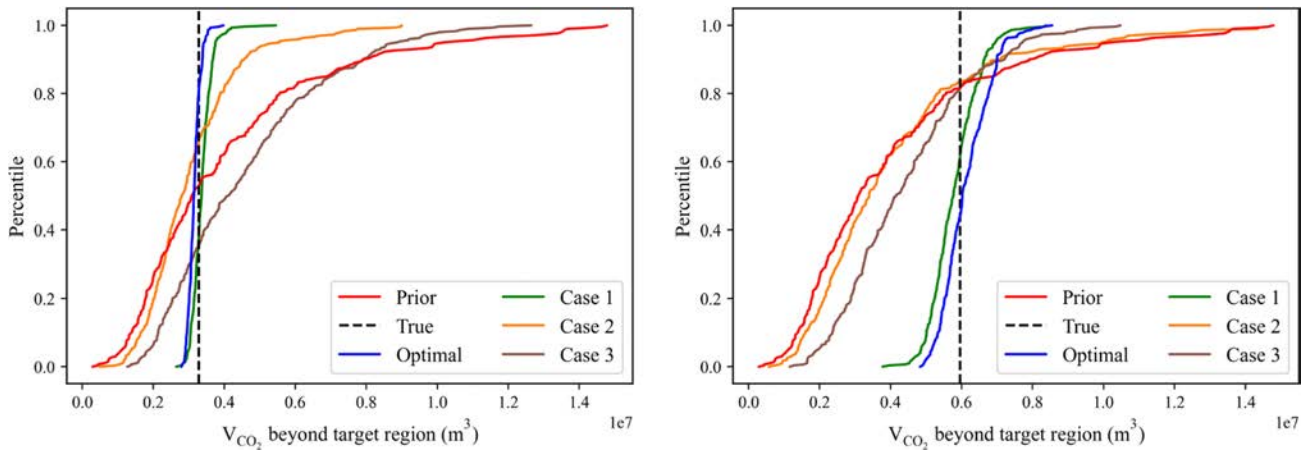
Fig. 7 Cross-sectional view of CO_2 plume (along $x = 19$) after 20 years of injection for both true models (injection scenario 1). White line indicates the injection well

to perform better than the other two cases in terms of the uncertainty reduction achieved via history matching.

We now apply history matching using the data provided by the monitoring wells over the 20-year injection period. As this study involves synthetic models, the data here derive from the simulation of a 'true' model. This model is a new geological realization that is consistent with the prior ensemble but was not included in the monitoring well optimization. We will consider two such true models (in turn).

ES-MDA is applied (separately) using data from the optimal monitoring scheme and from each of the three heuristic monitoring scenarios. A cross-sectional y-z view (through $x = 19$, where x here refers to the grid index) of the CO_2 plume for true model 1, after 20 years of injection, is shown in Fig. 7a. Note that this cross-section contains the injector, which is indicated in the figure.

After performing history matching using observed data from true model 1, the volume of CO_2 beyond the target region for each of the 350 posterior models is computed. Empirical cumulative distribution functions (CDFs) for this quantity, computed over the 350 posterior models for each monitoring scheme, are shown in Fig. 8a. The dashed vertical line (at a J value of 3.27×10^6 m^3) indicates the true-model result. The red curve depicts the prior CDF (before any data assimilation is performed). The blue curve shows the posterior CDF for the optimal monitoring well configuration, and the other curves correspond to the qualitative monitoring scenarios.



(a) True model 1 (b) True model 2

Fig. 8 CDFs for CO_2 volume beyond the target region (J). The red curve is the prior, blue curve is the posterior for the optimal monitoring scheme, and the other solid curves are posteriors for heuristic monitoring schemes. The vertical dashed line is the J value for the corresponding true model (injection scenario 1)

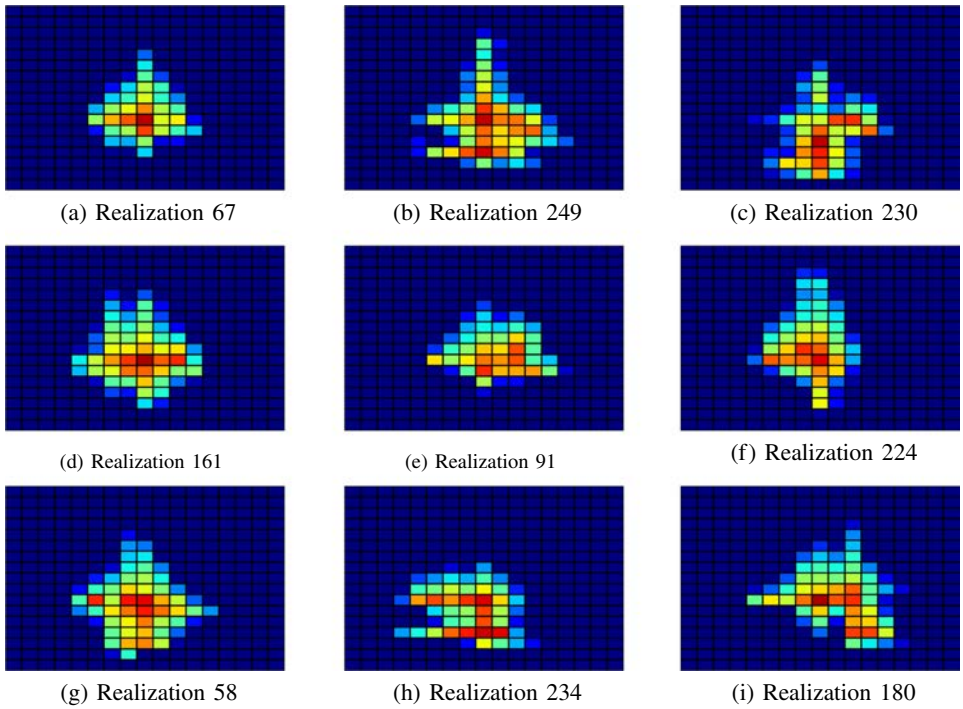


Fig. 9 CO_2 plumes in $x = 19$ cross-section after 20 years of injection for nine randomly chosen prior realizations (injection scenario 1)

(a) Realization 67 (b) Realization 249 (c) Realization 230

(d) Realization 161 (e) Realization 91 (f) Realization 224

(g) Realization 58 (h) Realization 234 (i) Realization 180

In this figure, the width of each CDF corresponds to the degree of uncertainty in J. The prior is very broad, indicating high initial uncertainty. We see that the blue curve, which depicts the CDF for the posterior of J after history matching using data from the optimum monitoring well configuration, is relatively narrow and is centered around the true result. This is precisely as desired, and indicates that the history matching has successfully reduced uncertainty in the quantity of interest (J). In Fig. 8a we also see that the heuristic scheme based on prior variance (Case 1) leads to a posterior CDF that is close to that for the optimum configuration. The other cases provide less uncertainty reduction. This illustrates the strong

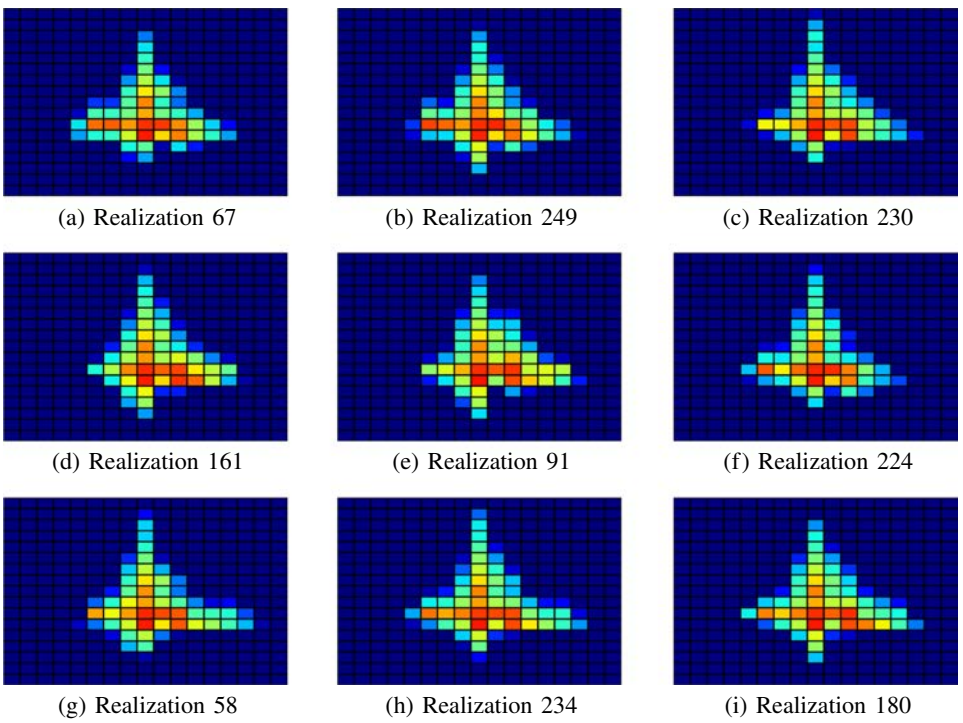


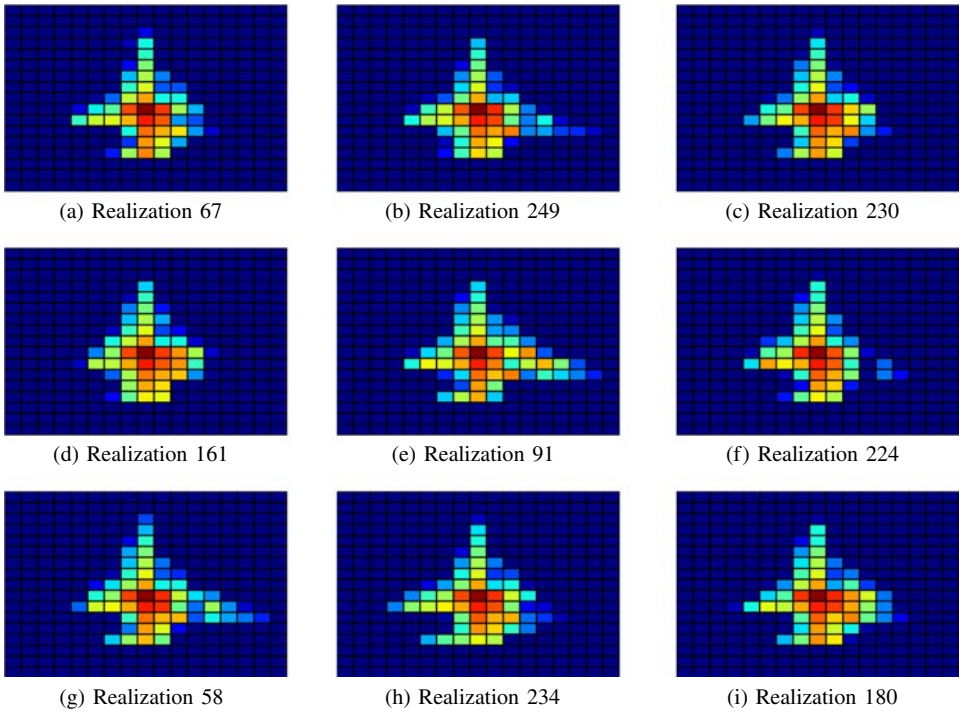
Fig. 10 CO_2 plumes in $x = 19$ cross-section after 20 years of injection for nine posterior realizations. Observed data are from the optimum monitoring well configuration (true model 1, injection scenario 1)

(a) Realization 67 (b) Realization 249 (c) Realization 230

(d) Realization 161 (e) Realization 91 (f) Realization 224

(g) Realization 58 (h) Realization 234 (i) Realization 180

Received by OCD: 6/29/2026



(a) Realization 67 (b) Realization 249 (c) Realization 230

(d) Realization 161 (e) Realization 91 (f) Realization 224

(g) Realization 58 (h) Realization 234 (i) Realization 180

Fig. 11 CO_2 plumes in $x = 19$ cross-section after 20 years of injection for nine posterior realizations. Observed data are from the optimum monitoring well configuration (true model 2, injection scenario 1)

effect that the locations of the monitoring wells have on the quality of posterior predictions.

We next consider prior and posterior simulation results for CO_2 plume location. This is an essential quantity in any data assimilation workflow in a CCUS setting. Figure 9 displays the CO_2 plume saturations after 20 years of injection for nine randomly selected prior realizations. These figures again correspond to cross-sections through $x = 19$, as in Fig. 7a.There is clear variability in the shape and extent (vertical and lateral) of these plumes, consistent with the broad prior CDF in Fig. 8a. Plumes corresponding to posterior models are shown in Fig. 10. These plumes are clearly more consistent in size and shape than those in Fig. 9. More importantly, they are visually similar to the true-model plume shown in Fig. 7a.

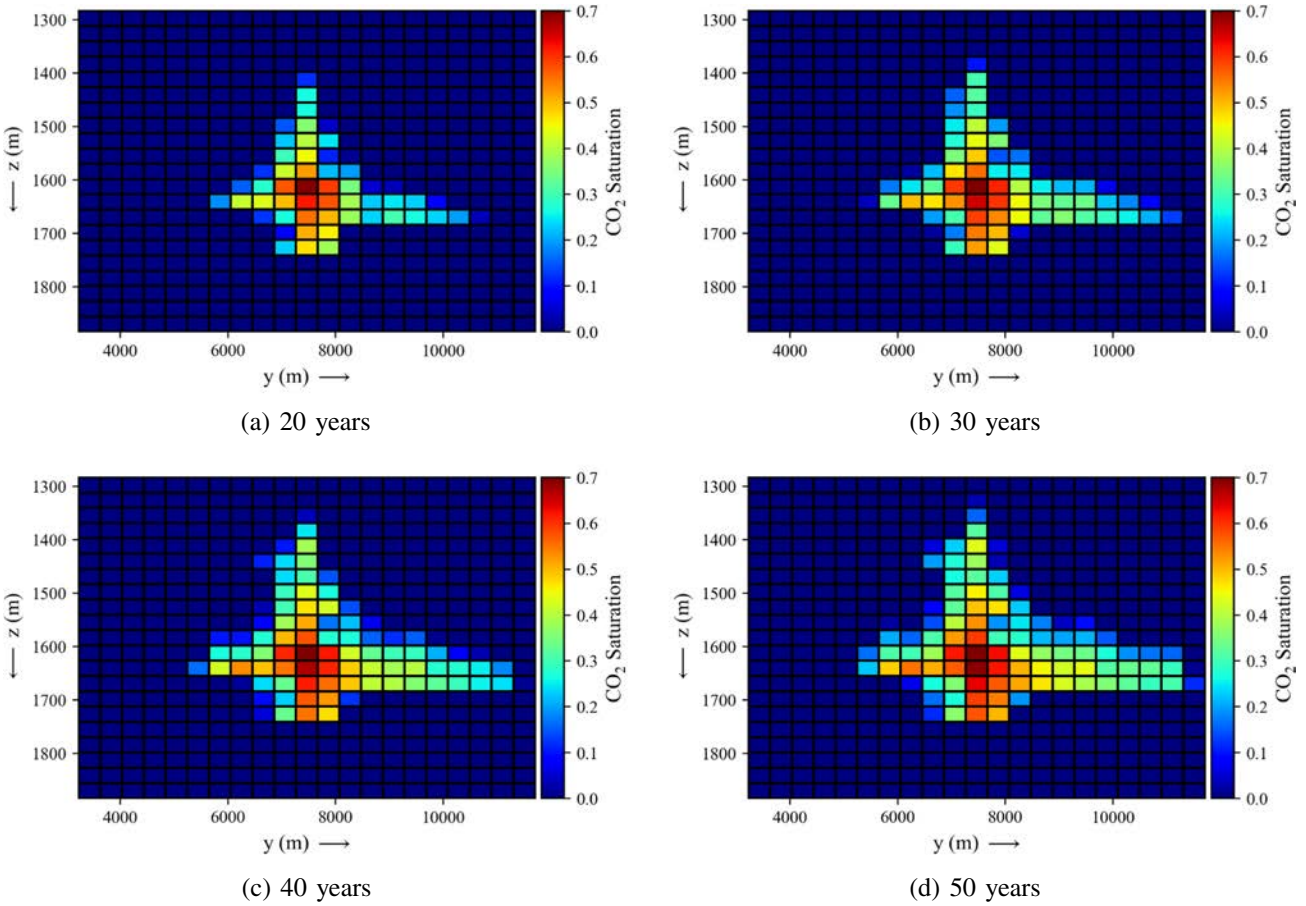
We now present posterior results for a different true model. Note that the monitoring well optimization and associated simulations do not need to be repeated, as these involve only prior models and no observed data. The CO_2 plume saturation for true model 2 is shown in Fig. 7b. The prior and posterior CDFs for this case are presented in Fig. 8b. Note that the true J value is now larger than it was for true model 1 (here it corresponds to the 81st percentile on the prior CDF compared to the 52nd percentile for true model 1). For this true model, the optimal monitoring well configuration clearly provides the most uncertainty reduction. Of the heuristic monitoring schemes, Case 1 again performs the best. The CO_2 plumes for the posterior models, for the optimal monitoring well scenario, are shown in Fig. 11. These plumes again resemble the true-model result (Fig. 7b) and they display less variation than the plumes corresponding to prior realizations shown in Fig. 9.

The application of ES-MDA provides an ensemble ($N_r = 350$) of posterior geomodels and corresponding simulation results. These results can be used to provide possible future plume migration scenarios conditioned to the data measured at the monitoring wells. As an example, time-evolution results for a particular posterior realization from the true model 2 example, with data collected at optimally located monitoring wells, are displayed in Fig. 12. In this case, we continue injecting CO_2 for an additional 30 years. The saturation field is again for the $x = 19$ cross-section.

From the full history matched ensemble we can compute, e.g., average behavior, the expected lateral extent of the plume, the probability that the plume will migrate a specific distance in a particular direction at a given time, etc. Thus these results can be very useful for aquifer management and risk assessment.

3.3 Injection scenario 2

We now consider a second injection scenario. A more limited set of results will be presented for this scenario than for injection scenario 1, as the goal here is to illustrate the

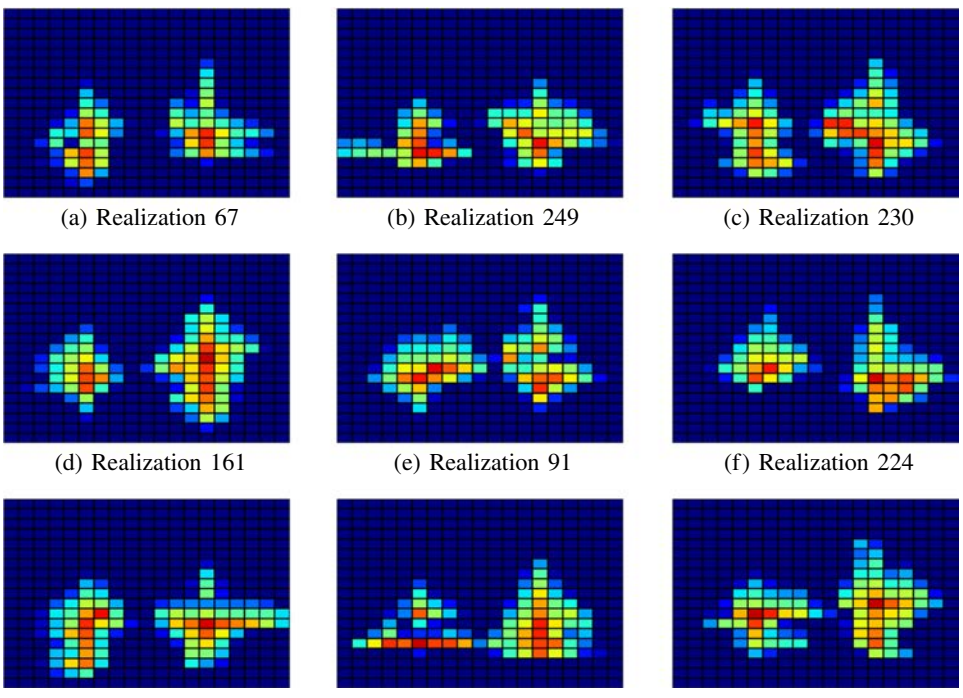


(a) 20 years (b) 30 years

(c) 40 years (d) 50 years

Fig. 12 CO_2 plumes in $x = 19$ cross-section for posterior realization 42 at later times. CO_2 is injected in this case for 50 years. Observed data are from the optimum monitoring well configuration (true model 2, injection scenario 1)

Fig. 13 CO_2 plumes in $x = 19$ cross-section after 20 years of injection for nine randomly chosen prior realizations (injection scenario 2)



(a) Realization 67 (b) Realization 249 (c) Realization 230

(d) Realization 161 (e) Realization 91 (f) Realization 224

(g) Realization 58 (h) Realization 234 (i) Realization 180

Received by OCD: 6/29/2026

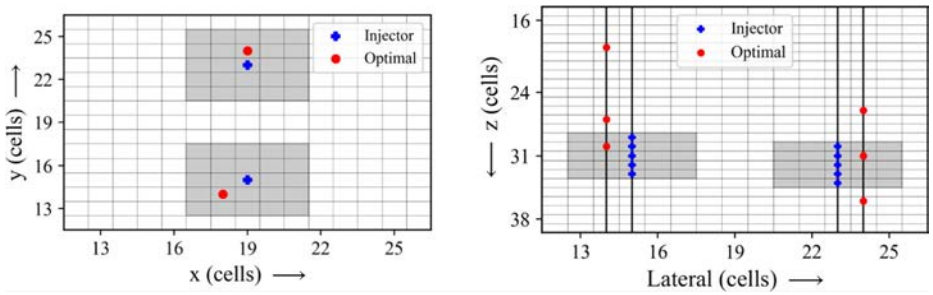


Fig. 14 Optimal monitoring well configuration. Injection well location and perforations also shown (injection scenario 2). Gray shaded blocks indicate target region

(a) Top view of optimum monitoring wells

(b) Conceptual cross-sectional view of optimum monitoring wells

applicability of the framework in a range of settings. This scenario involves two vertical injection wells, with both wells injecting 2.0 Mt CO_2/yr. The first injector operates at this rate for the full 20-year period, while the second begins injection after 5 years. The maximum injection-well BHP is specified as 27.63 MPa for each well (this is the same value used in injection scenario 1).

We again consider a strategy with two vertical monitoring wells, each with three pressure transducers. Pressure data at each transducer are collected every three months and saturation data are measured once per year along the well (at each grid block). The objective function, J, is analogous to that used for injection scenario 1. In this case it is defined as the CO_2 volume beyond $n \times n \times n_p$ regions around the perforated portion of each injector. Here we set $n = 5$. The target region now entails all gray-shaded blocks in Fig. 13.

The prior flow simulations must be rerun, as the injector locations and rate schedules are different in this scenario. The setup is otherwise identical to that described in Section 3.2. Prior flow simulation results for nine realizations are shown in Fig. 13. The two separate plumes for this case are clearly evident. The monitoring optimization is also rerun, again with the same specifications as were used previously.

The optimized monitoring well locations, along with the injection wells, are displayed in Fig. 14. The monitoring wells are placed close to each of the injectors. In injection scenario 1, the optimal monitoring wells were aligned with the y-axis (Fig. 5a), which allowed for direct visualization of the pressure transducer depths (Fig. 5b). However, for this injection scenario, the monitoring wells are not aligned along either the x or y axis (as is evident in Fig. 14a). Therefore, in order to display the pressure transducers, we plot them in Fig. 14b along a 'conceptual' cross section that runs through both injectors and both monitoring wells. For this optimized plan, the remaining variance corresponding to the argument in Eq. 9 is 0.2351. Note that this value is larger than in injection scenario 1 (where it was 0.0709), which is

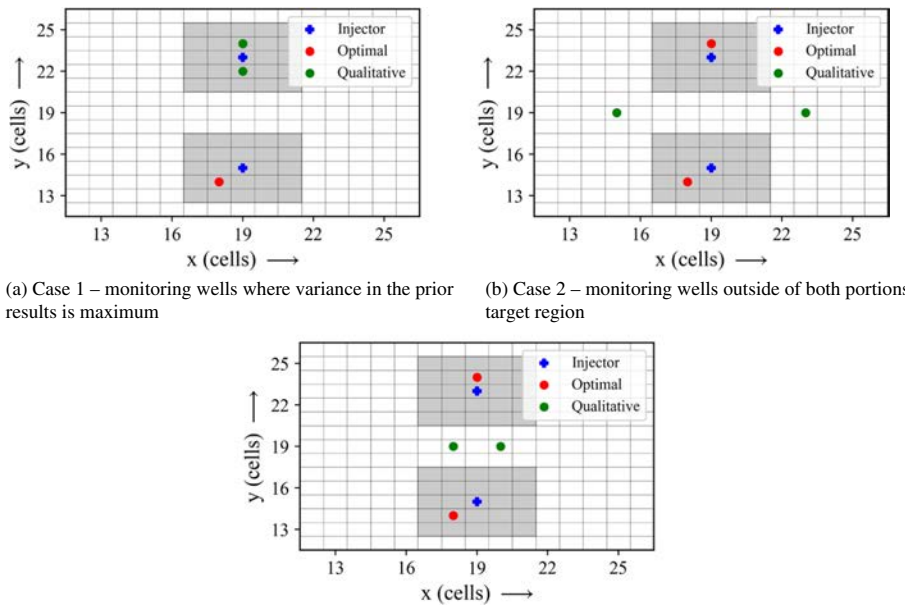
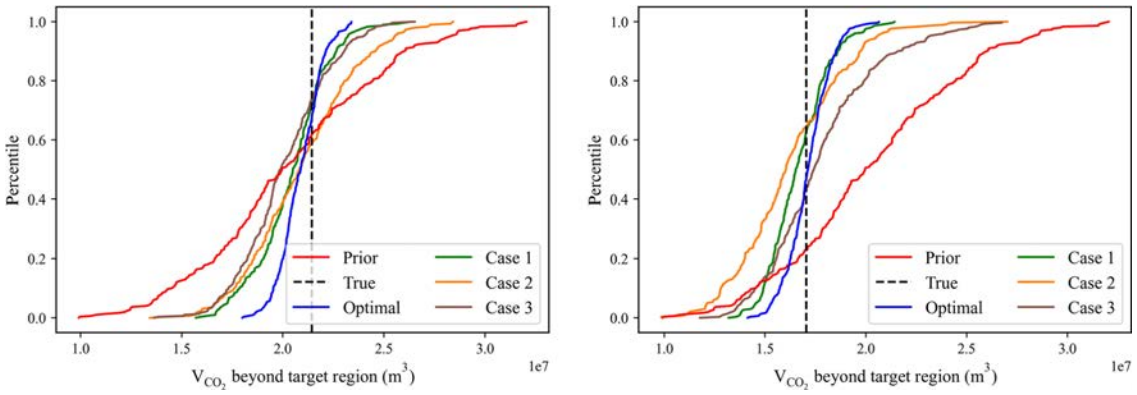


Fig. 15 Monitoring well locations for various qualitative (heuristic) schemes. Optimal configuration and injection wells also shown (injection scenario 2). Gray shaded blocks indicate target region

(a) Case 1 – monitoring wells where variance in the prior results is maximum

(b) Case 2 – monitoring wells outside of both portions of the target region

(c) Case 3 – monitoring wells between the two portions of the target region



(a) True model 1 (b) True model 2

Fig. 16 CDFs for CO_2 volume beyond the target region (J). The red curve is the prior, blue curve is the posterior for the optimal monitoring scheme, and the other solid curves are posteriors for heuristic monitoring schemes. The vertical dashed line is the J value for the corresponding true model (injection scenario 2)

likely due to the added complexity from having two injection wells rather than one.

Three heuristic monitoring plans are again considered. These are shown, along with the injection wells and optimal monitoring well locations, in Fig. 15. Case 1 again corresponds to placing monitoring wells where the variance in the prior results is the largest. In this case the monitoring wells are both positioned near one injection well (the well that begins injecting at the start of the operation).

For Cases 2 and 3, the x-y locations for the monitoring wells are shifted relative to the optimum, but the vertical locations of the pressure transducers are the same as in the optimum strategy. The remaining variance (from Eq. 9) for Case 1 is 0.3512, which is further from the optimal value than in injection scenario 1. For Cases 2 and 3, the remaining variance is larger, 0.6128 and 0.5023, respectively.

We now present posterior results for the same two true models as were used in Section 3.2. For each true model and monitoring scheme, ES-MDA is applied with data collected over the 20-year period. Results for the different monitoring schemes are shown in Fig. 16. The curves are as described earlier, and the dashed line denotes the true value. Note that the J values are consistently larger here than in injection scenario 1. This is due to the additional 2.0 Mt CO_2/yr injected into the system (starting after 5 years), and also to the smaller target region around each injector (5×5 areally versus 7×7).

For true model 1 (Fig. 16a), all of the monitoring schemes achieve a reasonable degree of uncertainty reduction, though the optimal scheme clearly provides the most narrow posterior CDF. There is more difference between the optimal scheme and Case 1 for this injection scenario than for injection scenario 1 (compare Figs. 16a and 8a). For true model 2 (Fig. 16b), the optimal strategy again outperforms the other monitoring schemes. The Case 1 posterior CDF is close to the optimal, while the other two heuristic strategies show larger differences. Note that true model 2 corresponds to a lower percentile on the prior CDF for J than true model 1 for this injection scenario. This is in contrast to injection scenario 1 (Fig. 8).

3.4 Comparison of posterior variance assessments

As discussed in Section 2.1, the monitoring optimization strategy used in this study is strictly applicable when the simulated flow data follow multi-Gaussian distributions. The data for complex, nonlinear multiphase flow systems do not, however, follow this distribution, even if the input geomod-

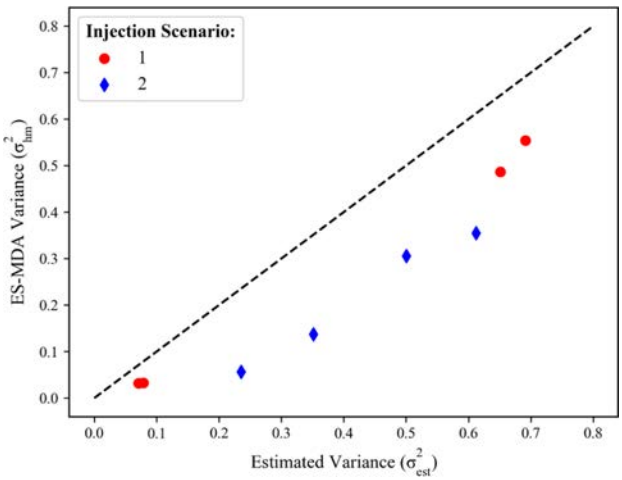


Fig. 17 Cross-plot of posterior variance in J in the history matched models versus estimated posterior variance in J under Gaussian-data assumption, for both injection scenarios and all monitoring schemes. The σ^2_{hm} results are averages over true models 1 and 2. The 45° line is also shown

els are themselves multi-Gaussian. Thus, it is of interest to compare the actual uncertainty reduction achieved through ES-MDA-based history matching to that estimated from the argument of Eq. 9. This assessment can be performed for the various monitoring schemes and injection scenarios. One caveat is that Eq. 9 provides an estimate over all possible true models (assuming the prior ensemble is representative), while the history matching results in this study involve only two different true models.

In Fig. 17, we present a cross-plot between the estimated posterior variance in J (from Eq. 9), denoted σ^2_{est}, and the posterior variance in J actually observed in the history matched models, denoted σ^2_{hm}. Here σ^2_{hm} is the average of the results for true models 1 and 2. Results are displayed for all monitoring schemes with both injection scenarios. Two notable features are evident. First, the trend/ordering is consistent between the two sets of results. This suggests that different monitoring strategies can be (at least approximately) ranked by evaluating σ^2_{est}, which is useful because the computation of σ^2_{est} requires only prior-model simulations (not history matching). The second observation is that the history matched results consistently lie below the 45° line. This is consistent with theory, since the Gaussian estimate is known to provide an upper bound for posterior variance in cases where the data are non-Gaussian [21]. It is also possible that some of this discrepancy is due to the under-estimation of posterior uncertainty by ES-MDA. This effect, particularly in the absence of localization, has been discussed in previous studies (e.g., [15]) and may be occurring in our results. A full understanding of the shift evident in Fig. 17 will, however, require further investigation.

4 Concluding remarks

In this study, we presented a framework for optimally monitoring and history matching a CO_2 storage project. The workflow involves the determination of the optimal monitoring well locations based on simulations of prior realizations, followed by the application of history matching as data are collected. The monitoring well optimization step is essentially that presented in [21], though history matching here is performed in a model-based (rather than data-space) setting using ES-MDA. The framework was applied to a system representative of a CO_2 storage project under study for the Mt. Simon formation in Illinois, USA. An efficient remapping algorithm was used to represent the underlying unstructured model on a coarser Cartesian grid.

Results were presented for two different injection scenarios and two true models. In the first injection scenario, a single well operated for a 20-year period, while the second scenario involved two CO_2 injectors. The true models in each case were consistent with the prior ensemble and provided the (synthetic) observations used for data assimilation. History matching using data from optimally located monitoring wells was shown to provide more uncertainty reduction than was achieved using heuristic monitoring plans, though the advantage was relatively slight in some cases.

In contrast to the data-space approach in [21], the workflow here provides an ensemble of posterior models. These can be used to assess average or outlier plume evolution scenarios, analyze commonalities and differences in history matched geomodels, etc.

There are many directions that should be pursued in future work in this area. The models in this study were defined on 40 × 40 × 40 grids. Models of these dimensions are too coarse to resolve detailed CO_2 saturation distributions, so higher grid resolution will be required in practice. This could be achieved through use of locally refined models, with high resolution near injection and monitoring wells. Error modeling procedures, in which errors due to grid resolution are quantified based on simulation results from selected pairs of fine and coarse-scale models, could also be effective. The use of deep-learning-based surrogate models, such as those described in [23, 24], should also be considered. The impact of additional monitoring wells, and/or the effect of measuring data more frequently, should be studied. This could be treated in a multiobjective optimization setting where the objectives are to maximize uncertainty reduction while minimizing monitoring cost. Other data types, particularly geophysical measurements, could be included in the history matching step. Additional physics, such as geomechanical effects, can be incorporated into the overall workflow. Finally, the methodology should be generalized to optimize new monitoring wells placed after the start of CO_2 injection.

Acknowledgements We thank Oleg Volkov for his assistance with computational resources, Su Jiang for providing ES-MDA code, David Cameron for useful discussions, Steven Whittaker for project management, Roland Okwen and Yang Fang for assistance with the geomodels and simulations, and Nathan Grigsby for geological data. We also acknowledge the Stanford Center for Computational Earth & Environmental Science for providing the computational resources used in this study.

Funding This work was funded by the U.S. Department of Energy under project DE-FE0031892. Additional support was provided by the Stanford Center for Carbon Storage and Stanford Smart Fields Consortium.

Declarations

Conflicts of interest The authors declare that they have no known competing financial interests or personal relationships that could have appeared to influence the work reported in this paper

Received by OCD: 6/29/2026

References

1. Ayani, M., Grana, D., Liu, M.: Stochastic inversion method of time-lapse controlled source electromagnetic data for CO_2 plume monitoring. Int. J. Greenhouse Gas Control **100**, 103098 (2020)
2. Barros, E., Leeuwenburgh, O., Szklarz, S.: Quantitative assessment of monitoring strategies for conformance verification of CO_2 storage projects. Int. J. Greenhouse Gas Control **110**, 103403 (2021)
3. Cameron, D.A., Durlofsky, L.J.: Optimization and data assimilation for geological carbon storage. Computational models for CO_2 sequestration and compressed air energy storage, R. Al-Khoury and J. Bundschuh, eds., Taylor & Francis Group/CRC Press pp. 357–388 (2014)
4. Cameron, D.A., Durlofsky, L.J., Benson, S.M.: Use of above-zone pressure data to locate and quantify leaks during carbon storage operations. Int. J. Greenhouse Gas Control **52**, 32–43 (2016)
5. Chen, B., Harp, D.R., Lin, Y., Keating, E.H., Pawar, R.J.: Geologic CO_2 sequestration monitoring design: a machine learning and uncertainty quantification based approach. Appl. Energy **225**, 332–345 (2018)
6. Chen, B., Harp, D.R., Lu, Z., Pawar, R.J.: Reducing uncertainty in geologic CO_2 sequestration risk assessment by assimilating monitoring data. Int. J. Greenhouse Gas Control **94**, 102926 (2020)
7. Emerick, A.A., Reynolds, A.C.: Ensemble smoother with multiple data assimilation. Comput. Geosci. **55**, 3–15 (2013)
8. Finley, R.J., Frailey, S.M., Leetaru, H.E., Senel, O., Couëslan, M.L., Scott, M.: Early operational experience at a one-million tonne CCS demonstration project, Decatur, Illinois, USA. Energy Proced. **37**, 6149–6155 (2013)
9. Furre, A.K., Eiken, O., Alnes, H., Vevatne, J.N., Kiær, A.F.: 20 years of monitoring CO_2-injection at Sleipner. Energy Proced. **114**, 3916–3926 (2017)
10. González-Nicolás, A., Baù, D., Alzraiee, A.: Detection of potential leakage pathways from geological carbon storage by fluid pressure data assimilation. Adv. Water Resources **86**, 366–384 (2015)
11. González-Nicolás, A., Cihan, A., Petrusak, R., Zhou, Q., Trautz, R., Riestenberg, D., Godec, M., Birkholzer, J.T.: Pressure management via brine extraction in geological CO_2 storage: adaptive optimization strategies under poorly characterized reservoir conditions. Int. J. Greenhouse Gas Control **83**, 176–185 (2019)
12. He, X., Zhu, W., Santoso, R., Alsinan, M., Kwak, H., Hoteit, H.: CO_2 leakage rate forecasting using optimized deep learning. In: SPE Annual Technical Conference and Exhibition. OnePetro (2021)
13. Jenkins, C.: The state of the art in monitoring and verification: an update five years on. Int. J. Greenhouse Gas Control **100**, 103118 (2020)
14. Jeong, H., Sun, A.Y., Zhang, X.: Cost-optimal design of pressure-based monitoring networks for carbon sequestration projects, with consideration of geological uncertainty. Int. J. Greenhouse Gas Control **71**, 278–292 (2018)
15. Lacerda, J.M., Emerick, A.A., Pires, A.P.: Using a machine learning proxy for localization in ensemble data assimilation. Computat. Geosci. **25**, 931–944 (2021)
16. Liu, M., Grana, D.: Petrophysical characterization of deep saline aquifers for CO_2 storage using ensemble smoother and deep convolutional autoencoder. Adv. Water Resources **142**, 103634 (2020)
17. Okwen, R., Babrinde, O., Taft, K.: Storage complex modeling for CarbonSAFE Illinois – Macon county. Tech. Rep., Univ. of Illinois at Urbana-Champaign, IL (United States) (2022)
18. Remy, N., Boucher, A., Wu, J.: Applied geostatistics with SGeMS: a User's guide. Cambridge University Press (2009)
19. Schlumberger: Eclipse reference manual, 2017.2 edn. (2017)
20. Strandli, C.W., Mehnert, E., Benson, S.M.: CO_2 plume tracking and history matching using multilevel pressure monitoring at the Illinois Basin-Decatur project. Energy Proc. **63**, 4473–4484 (2014)
21. Sun, W., Durlofsky, L.J.: Data-space approaches for uncertainty quantification of CO_2 plume location in geological carbon storage. Adv. Water Resources **123**, 234–255 (2019)
22. Tadjer, A., Bratvold, R.B.: Managing uncertainty in geological CO_2 storage using Bayesian evidential learning. Energies **14**(6), 1557 (2021)
23. Tang, M., Ju, X., Durlofsky, L.J.: Deep-learning-based coupled flow-geomechanics surrogate model for CO_2 sequestration. Int. J. Greenhouse Gas Control **118**, 103692 (2022)
24. Wen, G., Hay, C., Benson, S.M.: CCSNet: a deep learning modeling suite for CO_2 storage. Adv. Water Resources **155**, 104009 (2021)
25. Yang, Y.M., Dilmore, R., Mansoor, K., Carroll, S., Bromhal, G., Small, M.: Risk-based monitoring network design for geologic carbon storage sites. Energy Proc. **114**, 4345–4356 (2017)
26. Yang, Y.M., Dilmore, R.M., Bromhal, G.S., Small, M.J.: Toward an adaptive monitoring design for leakage risk - closing the loop of monitoring and modeling. Int. J. Greenhouse Gas Control **76**, 125–141 (2018)
27. Zou, A., Durlofsky, L.J.: Integrated framework for optimization of horizontal/deviated well placement and control for geological CO_2 storage. In: SPE Reservoir Simulation Conference. OnePetro (2023)

Publisher's Note Springer Nature remains neutral with regard to jurisdictional claims in published maps and institutional affiliations.

Springer Nature or its licensor (e.g. a society or other partner) holds exclusive rights to this article under a publishing agreement with the author(s) or other rightsholder(s); author self-archiving of the accepted manuscript version of this article is solely governed by the terms of such publishing agreement and applicable law.

EXHIBIT 13

Received by OCD: 6/29/2026

Earth-Science Reviews 223 (2021) 103849

Contents lists available at ScienceDirect

Earth-Science Reviews

journal homepage: www.elsevier.com/locate/earscirev

Leakage risk assessment of a CO_2 storage site: A review

Raoof Gholami [a], Arshad Raza [b,*], Stefan Iglauer [c]

[a] Department of Energy Resources, University of Stavanger, Norway
[b] Department of Petroleum Engineering, King Fahd University of Petroleum and Minerals, Saudi Arabia
[c] Edith Cowan University, School of Engineering, Australia

ARTICLE INFO

Keywords:
Risk assessment
Leakage
CO_2 storage
Interactions
Uncertainty

ABSTRACT

Carbon Capture and Storage (CCS) has been widely recognized as an effective strategy that may significantly contribute to achieving the net zero emission target by 2050. There are currently more than 50 CCS injection and pilot sites around the globe that may require a long-term integrity assessment to avoid leakages or contamination of subsurface resources. The major concern here is the complex interactions of CO_2 with rocks and other sealing materials (cement) that can be accelerated by pressure and temperature conditions. In this paper, we review different mechanisms that may lead to the generation of leakage paths in CO_2 geological sites and attempt to provide a risk assessment scheme that may improve the safety of injection and storage operations. It seems that the results reported from the laboratory experiments are still inconclusive and not comparable with the field observations. This could be due to the limited duration of the tests conducted, complexity of mechanisms involved and the slow reaction rates of many chemical processes in a CO_2 storage site. Geochemical reactions, pressure and temperature are the main parameters that can potentially induce leakages from different geological sites, but a poor cement job is perhaps the main reason behind the leakage of CO_2 from the near wellbore region during injection and storage.

1. Introduction

Climate change is taking place and has been largely documented by the rise of temperature, melting of the glaciers, bushfires and many other growing catastrophes (IPCC, 2007). It is argued that these changes in the climate are induced by the significant release of greenhouse gases (carbon dioxide, methane, nitrous oxide, etc.) to the atmosphere since the industrial revolution (IPCC, 2007). To address this issue, carbon capture and storage (CCS) has been proposed and soon widely accepted as an effective technology to reduce the greenhouse gas emission (Liebscher et al., 2013; Underschultz et al., 2011; Zhu et al., 2015a). In the CCS, CO_2 is captured from large emission sources (e.g., cement and iron industry), transported through the pipelines and disposed into deep geological sites such as saline aquifers, depleted hydrocarbon reservoirs and coal bed seams (Iglauer, 2018). Here, aquifers are one of the attractive options with a large storage capacity, but require new wells, reservoir integrity assessment, and technical viability analysis. Depleted hydrocarbon reservoirs are also a good option for CO_2 storage given their available infrastructure and proven capacity, but the integrity of old wells and potential leakages from the caprock or fault seals have been addressed as the major concerns (Raza and Gholami, 2019). Coal beds and perhaps shale gas reservoirs have been considered lately as potential storage sites given their favourable geochemical trapping potentials and adsorption capacity, but they still suffer from technical viability and limited capacity (Herzog et al., 1997).

Technically speaking, a geologic formation chosen for a CCS project must be evaluated for: 1) capacity (i.e., total usable storage volume of a site), 2) injectivity (i.e., ease of fluids flow through the pore throats), 3) trapping mechanisms (i.e., CO_2 can be trapped during plume migration) and 4) confinement (i.e., capability to contain CO_2 in the site) (IPCC, 2005). Upon injection, four trapping mechanisms cease the migration of CO_2 plume which include: 1) structural trapping where a tight seal caprock stops the migration of CO_2 (Iglauer, 2017), 2) residual trapping where the plume of CO_2 is immobilized by the capillary force in the pore structure (Iglauer et al., 2011), 3) dissolution trapping where CO_2 mixes with brine over time (Iglauer, 2011) through convection, and 4) mineral trapping where CO_2 chemically interacts with rocks leading to mineral transformation/precipitation (Bachu et al., 1994). These trapping mechanisms act on different timescales as shown in Fig. 1. For instance, the structural and capillary trappings will be active at the early stages for

* Corresponding author.
E-mail address: arshad.raza@kfupm.edu.sa (A. Raza).

https://doi.org/10.1016/j.earscirev.2021.103849
Received 22 June 2021; Received in revised form 22 October 2021; Accepted 31 October 2021
Available online 3 November 2021
0012-8252/© 2021 Elsevier B.V. All rights reserved.

Received by OCD: 6/29/2026

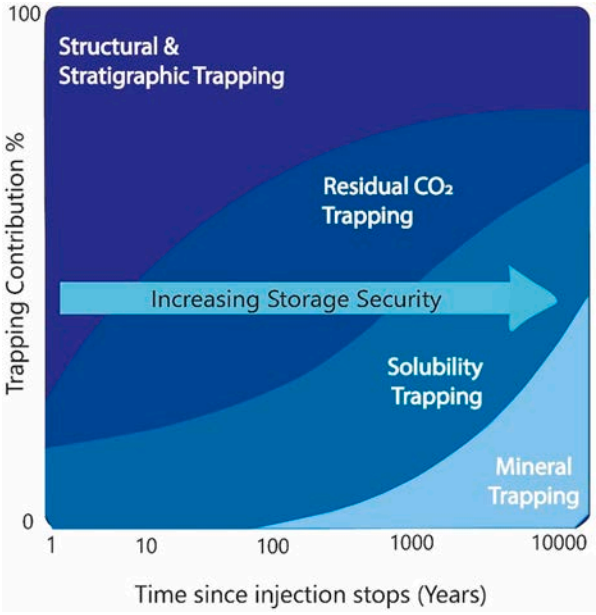


Fig. 1. Contribution of trapping mechanisms in a CO_2 storage site at different time scales.
Modified after (IPCC, 2005).

hundred years while the mineral and dissolution trappings will take place very slowly in a long term (Iglauer, 2017). These trapping are the main mechanisms in a geological site that can control the migration of free CO_2. Thus, if they can be understood and enhanced, the risk of leakage during or after injection can be significantly decreased.

1.1. Risks assessment of CO_2 storage sites

Leakage of CO_2 from the storage sites is the major risk associated with a CCS project (Deel et al., 2007). According to the risk profile shown in Fig. 2, the risk of leakage from a storage site is very high when a reservoir/field is gone through injection for the first time (Benson, 2007). This is mainly because of geological complexity and lack of sufficient data to fully understand the consequences of CO_2 injection in a geological site. However, the experience and knowledge gained from the first injection can help to have a safer injection in the same reservoir/field over time. Therefore, a good risk assessment method is vital, particularly at the early stage of carbon storage, to ensure the safety and security of a storage site based on a proper site selection, characterization and decision-making analysis (Li and Liu, 2016). International

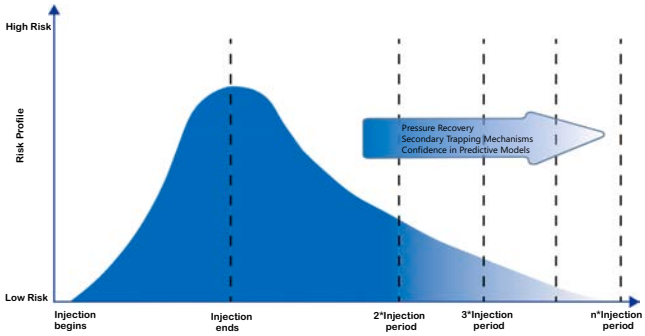


Fig. 2. Conceptual risk profile of CO_2 storage in geological porous media (Benson, 2007). The first injection is always associated with a huge risk due to the presence of many uncertain parameters. However, the experience gained from the 1st attempt can help to have a safer injection in the 2nd or 3rd attempts.

Energy Agency (IEA) has proposed a risk assessment, management, and communication framework for CO_2 storage projects, as shown in Fig. 3 (Korre and Durucan, 2009). According to this framework, a good understanding of potential risks and problem formulation through proper communication and consultation is the first step to reduce the risk of CO_2 storage. Once the risks involved are formulated and understood, they can be reduced through a detailed storage site characterizations and assessment of uncertain/unknown parameters. This can then be followed by planning, strategies, and monitoring approaches to improve the safety of the entire operation.

There have several studies attempting to develop different risks assessment methods and guidelines for CO_2 storage site assessments. For instance, ATLANTIC (2007) presented a CO_2 storage life cycle risk management framework to ensure the permanent containment of injected CO_2 without any information on how parameters in each stage must be evaluated. They proposed six stages for a proper risk assessment including: i) problem formulation (critical scoping step), ii) site selection and characterization (collection and analysing data), iii) exposure assessment (characterization and movement of CO_2 plume), iv) effective assessment (assembly of information to describe the response of receptors), v) risk characterization (integration of data to estimate the likely impact) and vi) risk management (monitoring, mitigation and remediation measures). Tucker and Holley (2013) considered the Goldeneye CO_2 storage site and employed the Bow-tie risk assessment methodology for the containment risk assessment. They showed that the risk of containment breach is practically very low. The bowtie method builds a bowtie diagram to provide a qualitative risk assessment of the storage medium, but major CO_2 interaction and caprock leakage are not evaluated there. Wilday et al. (2011) provided an outline for the identification of risks during capture, transport, injection, and storage by the bow-tie techniques, modified risk matrix approaches and the life cycle analysis approaches. He et al. (2011) reviewed different methodologies with particular emphasis on the Bayesian network (BN) for the risk assessment involved in the storage of CO_2. They recommended the BN

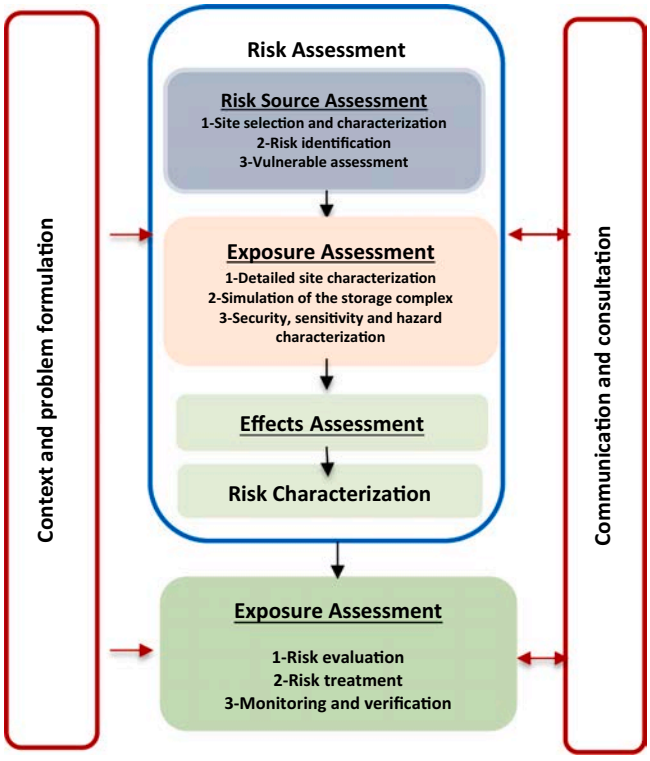


Fig. 3. IEA GHG recommended risk assessment, management and communication framework for CO_2 storage sites (Korre and Durucan, 2009).

Received by OCD: 6/29/2026

method as a powerful tool for the decision making and risk management of the storage sites. Govindan et al. (2014) performed a risk assessment by numerical modelling for the post-closure period at the Ketzin pilot site in Germany and demonstrated the results in terms of probability maps of the CO_2 plume distribution in the reservoir at different time scales. They reported that the risk of leakage is very high but the solubility of CO_2 in brine may reduce the leakage risks more than the capillary trapping. Li and Liu (2016) presented a detailed review on the environment, health and safety risks involved in a CO_2 storage operation at different stages. Ringrose et al. (2017) presented ranking and risking alternatives for CO_2 storage in three storage sites (i.e., Heimdal gas field, Smeaheia and Utsira South) in Norway. They reported that these sites are suitable from a geological and reservoir engineering point of view. However, the Utsira site had a high leakage risk from the injection well while the depleted Heimdal gas field was not economically feasible. Smeaheia, on the other hand, appears to be a feasible site from the operational and geological point of view. Alcalde et al. (2018) proposed a numerical program to evaluate CO_2 storage integrity and leakage over 10,000 years. They reported that a moderate well density has a 50% probability that leakage remains below 0.0008% per year, with at least 98% of the injected CO_2 retained in the subsurface over 10,000 years. Larkin et al. (2019) provided a collection of risk assessment and management frameworks to assess carbon storage projects but did not cover different aspects of leakages. Xiao et al. (2020) considered the response surface methodology (RSM) to assess the associated risks of CO_2 and brine leakage from a large-scale CO_2-enhanced oil recovery (CO_2-EOR) and storage field. They reported arsenic and selenium traces that were adsorbed on clay minerals and suggested pH as an indicator for an early detection of leakage.

In view of the above studies, it appears that any risk assessment frameworks require identification of potential risk scenarios based on qualitative and quantitative techniques including CO_2-FEP (Feature, Event, and Process) (Cherkaoui and Lopez, 2009), Certification Framework (Oldenburg et al., 2009), RISQUE (Risk Identification and Strategy using Quantitative Evaluation) or any other practically proven approaches. These techniques, once employed wisely, will be able to determine the likelihood of potential leakages and help to design a prevention/mitigation plan in a timely manner.

In the following section, different mechanisms and parameters involved in the creation of leakage paths in a geological storage site are presented and a preliminary assessment strategy is advised to reduce the risk of the operation. The aim here is to identify key uncertainties that need to be addressed and reduced when it comes to a storage operation.

2. Leakages and mechanisms

Given the studies carried out so far and the CCS projects implemented worldwide, it seems that the leakage can happen in short- or long-term during injection and storage. Sandstone and carbonate reservoirs are often considered as the best geological sites given their favourable petrophysical properties, sealing integrity and trapping mechanisms (Gaus, 2010). However, geochemical interactions posed by CO_2 in these storages site may induce leakage paths during injection/storage once combined with the variation of geomechanical parameters, pressure, and temperature (Espinoza et al., 2011; Raza et al., 2016a). These concepts are further discussed in this section.

2.1. Geochemical interactions

Upon injection, the primary mechanisms that may have impacts on the migration of CO_2 plume include: i) pressure gradient and natural hydraulic gradient, ii) buoyancy due to the density differences between CO_2 and formation fluids, iii) phase trapping and diffusion, iv) dispersion and fingering due to the reservoir heterogeneities and mobility contrast between CO_2 and formation fluids, v) CO_2 solubility into the resident fluid, vi) adsorption of CO_2 by the organic materials and vii) mineralization or mineral transformations (Solomon, 2006).

Given the pressure and temperature of a storage site, CO_2 appears as a supercritical fluid at the depths greater than 800 m (i.e., temperature becomes 304 K and the pressure is greater than 7.38 MPa) (Bachu, 2001). On these occasions, the bulk compressibility of CO_2 becomes higher than water while its viscosity reduces by 10 times (Espinoza et al., 2011). Thus, soon after the injection, as the plume migrates away from the wellbore (viscous force disappears), buoyancy force pushes CO_2 upward until it is immobilized by the capillary or structural (faults and caprock) traps. CO_2 can also be dissolved in formation water depending on the pressure, temperature, and the salinity level. This eliminates the buoyant force and the dense brine sinks at the bottom of a storage site due to the phenomenon commonly known as the solubility trapping. Fraction of the aqueous carbon dioxide mixes with water to generate carbonic acid and decrease the level of pH to 5 (Iglauer, 2011; Solomon, 2006). Water saturated CO_2 is slightly denser than water, promotes gravity-driven flow and can be adsorbed onto the organic surfaces of shale and coal. Viscous fingering may also occur, under these circumstances, due to the differences between the viscosity of wet/dry CO_2 and water. The acidic environment posed by the dissolution of CO_2 into the formation brine can result in a significant ion exchange and induce geochemical interactions that may either dissolve certain minerals (carbonates, feldspar, kaolinite, calcite, chlorite, and barite) or pose clay precipitation. These geochemical reactions often have different rates depending on the pH, pressure, temperature (Pokrovsky et al., 2005), mineral composition of rocks (Espinoza et al., 2011), level of anisotropy (De Silva et al., 2015). For instance, silicates with less reaction rate provides more dissolved cations than carbonates (Gunter et al., 2000). These geochemical reactions, once combined with pressure due to continues injection, can decrease the capillary entry pressure and initiate leakage paths through the caprock or faults. Table 1 gives a summary of the geochemical reactions induced by the injection of CO_2 into a storage site with different mineral dominations.

It should be recalled that the above geochemical interactions may or may not occur in the presence of impurities (e.g., methane, SO_x and NO_x). It is obvious that decreasing the purity of CO_2 stream can remarkably reduce the cost and complexity of capturing processes, but impurities can change the phase behaviour of CO_2 and cause unknown/unpredictable geochemical reactions during injection and storage (IEAGHG, 2011). Given the risks and uncertainties involved, there have not been any large-scale impure CO_2 storage projects around the globe so far.

2.1.1. CO_2-rock interactions

Porosity and permeability of rocks play an important role in the success of a CO_2 storage operation, particularly at the early injection stage. These properties must be well understood and evaluated as they may change by the variation of pressure, temperature, pH and mineral transformation (Rosenbrand et al., 2014). Apart from these physical factors, CO_2–water–rock interactions can shift a rock-dominated reaction system to a fluid-dominated system controlled by the reduction of pH due to the dissolution of CO_2 into the formation brine. These chemical reactions may enlarge the pore spaces (Hemme and van Berk, 2017), reduce the strength of reservoir rocks (Emberley et al., 2004) and caprock (Li et al., 2019), or cause unforeseen pressure to build up during injection (Seyyedi et al., 2020). In a long-term, these geochemical activities may induce reservoir compaction and wellbore integrity issues (Espinoza et al., 2011), particularly in carbonates even at a low temperature condition (Vilarrasa and Rutqvist, 2017). These interactions are the important processes that must be understood to ensure the long-term integrity of the storage sites (Gaus, 2010). Table 1 gives a summary of geochemical reactions taking place in a CO_2 storage site.

Along with the dissolution, salt precipitation takes place when water evaporation increases the concentration of salt in an under-saturated aquifer. Consequently, salt concentration under the thermodynamic state of a given reservoir exceeds its solubility limit and, as such, the

Received by OCD: 6/29/2026

Table 1
Geochemical reactions induced by CO_2 injection in rocks with different minerals.

Primary mineral	Reaction	Reaction rate[a]	Secondary mineral
Dissolution reactions			
	$CO_2(g) \rightarrow CO_2(aq)$ $CO_2(g) + H_2O(l) \rightleftharpoons H_2CO_3(aq)$ $H_2CO_3(aq) \rightleftharpoons H^+(aq) + HCO_3^-(aq)$ $HCO^-_3(aq) \rightleftharpoons H^+(aq) + CO_3^{2-}(aq)$		
Silicates[a]	$SiO_{2(s)} + 2H_2O \rightleftharpoons H_4SiO_4 \rightleftharpoons H^+ + H_3SiO_4^- \rightleftharpoons H^+ + H_2SiO_4^{2-}$	1.26×10^{-14} mol. m^{-2} s^{-1}	Solubility of quartz does not change with concentration of dissolved CO_2.
Kaolinite[b]	$Al_2Si_2O_5(OH)_4(s) + 6H^+(aq) \rightarrow 5H_2O + 2SiO_2(aq) + 2Al^{3+}(aq)$	10^{-14}-to-10^{-15} mol. m^{-2} s^{-1}	Complete Dissolution
Arnorthite[b]	$CaAl_2Si_2O_8(s) + CO_2(g) + 2H_2O(l) \rightarrow CaCO_3(s) + Al_2Si_2O_5(OH)_4(s)$	1.2×10^{-5} mol.m^{-2} s^{-1}	Calcite, kaolinite
Illite[b]	Illite $+8H^+(aq) \rightarrow 5H_2O(l) + 0.6\ K^+(aq) + 0.25\ Mg^{2+}(aq) + 3.5SiO_2(aq) + 2.3Al^{3+}(aq)$	–	Complete Dissolution
Labradorite (2)	$Ca_{0.6}Na_{0.4}Al_{1.6}Si_{2.4}O_8 + 5.4H^+(aq) + CO_2(aq) \rightarrow 0.6Ca^{2+}(aq) + HCO3^-(aq) + 2.2H_2O(l) + 0.4Na^+(aq) + 1.6Al^{3+} + 2.4SiO_2(aq)$	–	Complete Dissolution
Albite (2)	$NaAlSi_3O_8(s) + CO_2(g) + H_2O(l) \rightarrow NaAl(CO_3)(OH)_2(s) + 3SiO_2(s)$	–	Dawsonite, quartz
K-feldspar (2)	$KAlSi_3O_8(s) + Na^+(aq) + CO_2(g) + 2H_2O(l) \rightarrow NaAl(CO_3)(OH)_2(s) + 3SiO_2(s) + K^+(aq)$	–	Dawsonite, quartz
Calcite[b]	$CaCO_3(s) + H^+(aq) \rightarrow Ca^{2+}(aq) + HCO^-3\ (aq)$, *at high PH values only*	$1.6\text{-to-}3.2 \times 10^{-5}$ mol.m^{-2} s^{-1}	Complete Dissolution
Glauconite[b]	Glauconite $+14H^+(aq) \rightarrow 1.5\ K^+(aq) + 2.5Fe^{3+}(aq) + 0.5Fe^{2+}(aq) + Mg^{2+}(aq) + 1.0Al^{3+}(aq) + 7.5SiO_2(aq) + 9H_2O(l)$		Quartz
Annite[b]	annite $+3CO_2 \rightleftharpoons$ 3siderite + K-feldspar		Siderite, K-feldspar
Chlorite[b]	Chlorite $+20H^+(aq) \rightarrow 5Fe^{2+}(aq) + 5\ Mg^{2+}(aq) + 4Al(OH)_3(aq) + 6H_4SiO_4(aq)$		Aluminium hydroxide
Dolomite[b]	$CaMg(CO_3)_2(s) + 2H^+(aq) + Mg_{2+}(aq) + HCO^-3\ (aq)$		Complete Dissolution
Muscovite[c]	$H_2O_{(l)} + CO_{2\ (aq)} \leftrightarrow H^+_{(aq)} + HCO^-_{3(aq)}$ (I) Muscovite to Kaolinite $2\ KAl_2(AlSi_3O_{10})(OH)_2$ $_{(muscovite)} + 3H_2O_{(l)} + 2H^+_{(aq)} \rightarrow 3Al_2Si_2O_5(OH)_4$ $_{(kaolinite)} + 2\ K^+_{(aq)}$ (2)		Kaolinite
Precipitation reactions[b]			
	$Ca^{2+}(aq) + CO_3^{2-}(aq) \rightarrow CaCO_3(s)$		Calcite
	$Fe^{2+}(aq) + CO_3^{2-}(aq) \rightarrow FeCO_3(s)$		Siderite
	$Mg^{2+}(aq) + CO_3^{2-}(aq) \rightarrow MgCO_3(s)$		Magnesite
	$Ca_{2+}(aq) + SO_{42-}(aq) \rightarrow CaSO_4(s)$		Anhydrite
	$K^+(aq) + 3Al^{3+}(aq) + 2SO_4^{2-}(aq) + 6H_2O(l) \rightarrow KAl_3(SO_4)_2(OH)_6(s) + 6H^+(aq)$		Alunite
	$Ca^{2+}(aq) + Mg^{2+}(aq) + 2HCO_3^-(aq) \rightarrow CaMg(CO_3)_2(s) + 2H^+(aq)$		Dolomite

[a] Espinoza et al. (2011).
[b] De Silva et al. (2015).
[c] Mangini (2015).

excess salt precipitation occurs (salting-out) which can block the pore throats and reduce the injectivity (Cinar and Riaz, 2014; Hurter et al., 2007). This phenomenon was experienced in the early stages of injection at the Snøhvit site in Norway. Secondary mineral (silicate or carbonate) precipitations that may take place, under these circumstances, due to the changes in the thermodynamic of the system, can seal the fracture and help to improve the integrity of a storage site, although they may also close the pore throats and cause injectivity issues (Miri and Hellevang, 2016; Shukla et al., 2010).

Capillary drying salt might also massively precipitate under certain thermophysical conditions during CO_2 injection when the rate of evaporation in the beginning is significantly larger than the capillary backflow. This evaporation regime occurs when the injection rate is higher than a critical limit (Miri and Hellevang, 2016). In fact, there is a critical velocity above which local salt accumulation occurs, which reduces the injectiivity and/or increases the rate of pressure build up. This pressure can reach the fracture initiation pressure and the leakage path will be induced in the caprock or faulting seals. A practical approach to mitigate this issue is to apply freshwater treatment either after the clogging to dissolve the precipitated salt or pre-flushing before CO_2 injection to decrease the salinity of the near wellbore brine (Miri and Hellevang, 2016).

Changes in the petrophysical and geomechanical properties of reservoirs due to CO_2-rock-fluid interaction has been reported in several studies conducted on sandstone. For instance, Shiraki and Dunn (2000) checked the effect of chemical reactions on the anhydrite content of sandstone using a series of experimental tests. The result obtained showed that the relative permeability of CO_2 decreases due to the precipitation of kaolinite and anhydrite. Rochelle et al. (2002) focused on the evaluation of reservoir chemistry in sandstone where CO_2 was injected, and significant chemical changes were reported during the first 8 days due to the dissolution of calcite in the rock cement (Rochelle et al., 2002). Rimmelé et al. (2010) reported an increase in the porosity and permeability of sandstone without any significant changes in the mineral structure due to clay transportation (fine migration) induced by CO_2 (Rimmelé et al., 2010). Hangx et al. (2010) found no remarkable impacts on the sandstone properties after CO_2 flooding. Hangx et al. (2013) experimentally assessed the mechanical properties of sandstone due to the geochemical activities of CO_2. They reported calcite dissolution without any remarkable change in the geomechanical characteristics of sandstone. Marbler et al. (2013) carried out a study on sandstone to evaluate the effect of CO_2 injection and found a significant reduction in the geomechanical properties of the rock, particularly strength, internal friction angle and cohesion. They attributed these changes to the weakening of the bond between minerals and cement where removal of feldspar, carbonate dissolution and formation of week minerals such as kaolinite were observed. Campos et al. (2015) considered a two-month CO_2 injection in sandstone and found remarkable changes in the porous system of the Utrillas sandstone (Campos et al., 2015). Huq et al. (2015) conducted experimental and numerical modelling to study the behaviour of storage sites upon CO_2 injection and found that calcite dissolutions in sandstone can change the permeability. Ghafoori et al. (2017) initiated geochemical modelling based on the salt precipitation in sandstone and carbonates during CO_2 injection. They showed that in a sandstone aquifer, chemical equilibrium is established

Received by OCD: 6/29/2026

in the long term (more than 100 years), but it can occur in carbonates in less than a day. Ma et al. (2020) studied the CO_2–water–rock interactions based on the aluminosilicate (clay) composition in sandstone where they found that mineral kinetics exert more influences on the CO_2–water–rock interactions in a deep burial environment (Ma et al., 2020).

There have also been numerous studies on the reservoir chemistry upon CO_2 injection in limestone. For example, Le Guen et al. (2007) used triaxial compression tests and reported that CO_2 pressure, and the rate of fluid-rock interactions are directly related to each other which may result in rock deformation and integrity loss. Izgec et al. (2008) highlighted minor changes in the permeability of limestone due to CO_2 injection at different injection rates. Gharbi et al. (2013) found wormholes and increase in the porosity and permeability of the limestone once CO_2 injected at different pressure and temperature conditions. Garcia-Rios et al. (2015) used CO_2-rich sulphate solutions in fractured limestone and observed a remarkable rock dissolution over time at 15 MPa and 60 °C. Zhang et al. (2016a, 2016b) conducted a study to experimentally assess the effect of $scCO_2$ on the geomechanical characteristics of limestone. They reported a significant rock dissolution and mechanical weakening that was induced due to the dissolution. Cui et al. (2017) performed an experimental study on the geochemical interactions induced in carbonates during CO_2 injection where calcite precipitation and dolomite dissolution were observed. Raza et al. (2020) investigated the impact of CO_2 storage in limestone at a low injection rate using different experimental methods. They reported wormholes, calcite dissolution and a remarkable decrease in the elastic and strength properties of the rock.

There are several studies focusing on the chemical alteration induced by CO_2 injection in in shales upon. For example, Olabode and Radonjic (2014) exposed shale samples to CO_2 in a reactor for 92 days and indicated that the petrophysical properties of shale caprock can be improved due to the exposure. Mouzakis et al. (2016) analysed shale samples from two caprock formations (Gothic and Marine) once exposed to CO_2 and found an increase in pore connectivity and total porosity in the Gothic Shale. It was observed that the pore connectivity can be decreased by the precipitation or hydration of clays. Hadian and Rezaee (2020) exposed several shale samples to $scCO_2$ in the presence of NaCl brine under reservoir conditions ($T = 60$ °C and $P = 2000$ psi) for 9 months. They emphasised on the mineralogical changes (dissolution of quartz, feldspars, kaolinite, and goethite together with the precipitation of muscovite and halite) that could increase the pore volume and reduce the capillary threshold pressure. Two recent studies on shales exposed to CO_2 showed a steady increase in shale-water contact angle and surface wettability alteration over time (Fatah et al., 2021a; Gholami et al., 2021), with trends that indicate additional exposure would lead to further increase of contact angle. Fatah et al. (2021b) also argued that the CO_2 adsorption capacity increases when huge amounts of oxygen-containing groups are present in the shale. This indicates the fact that exploration and production of hydrocarbon from shale formations using CO_2 as a fracturing fluid or mineral dissolver (huff-puff) can be beneficial from geological storage point of view. Table 2 gives a summary of studies carried out to evaluate the effect of CO_2 Injection on the chemistry of different reservoir rocks (Fatah et al., 2021b).

It should be recalled that the results reported in the above studies were obtained from a series of experiments that were only conducted for few weeks or months. Given the alteration and changes reported so far, further studies are required to evaluate the integrity of CO_2 storage sites for hundreds of years.

2.1.2. Demands for up scaling

Assessment methods used to evaluate the interaction of CO_2 with rocks are often divided into numerical modelling and experimental studies (core flooding and batch-soak reactors/autoclaves observations), although machine learning based methods have shown some promising results (Bertier et al., 2006; Rimmelé et al., 2010). In the batch soak reactor/autoclaves tests, the rock samples are exposed to CO_2 in the present of brine for several weeks or months at certain pressure and temperature conditions. The samples are then analysed for the dissolution reaction, mineral transformations, alteration of petrophysical properties and changes in the geomechanical parameters (De Silva et al., 2015). Computer modelling based methods, on the other hand, are used to see the effect of the geochemical interaction on the behaviour of reservoir and caprock in a long term (Ennis-King and Paterson, 2007; Raza et al., 2019; Varre et al., 2015). *TOUGHREACT* is a numerical simulation program commonly used for the chemically reactive non-isothermal flows of multiphase fluids in porous media (https://tough.lbl.gov). Here, geochemical reactions in a reservoir which is a function of CO_2 dissolution is evaluated by using the dissolution equilibrium constant, gas fugacity coefficient, and the partial pressure of CO_2 (Tambach et al., 2015). Ennis-King and Paterson (2007) performed a numerical modelling using the TOUGH-REACT codes to see the CO_2-rock interaction and convective mixing in sandstone upon storage. They reported a significant CO_2 dissolution due to the geochemical and convective mixing in the aquifer which could reduce the risk of CO_2 migration from the storage site. Mito et al. (2008) conducted a field-scale study on a sandstone aquifer and examined the fluid before and after CO_2 injection at different distances away from the injection well. They found evidence of CO_2 geochemical activities given the high fraction of HCO_3 and Ca, Mg, Fe, Al, and Si observed at the site of sampling in different time scales. Varre et al. (2015) used the computer modelling group (CMG) simulator to study a coupled multiphase fluid flow-geochemical-geomechanical process over a large-scale injection of CO_2 into an aquifer for 1000 years. Their results revealed that the geochemical processes cannot significantly change the porosity or induce compaction (subsidence).

Kim and Lee (2017) used artificial neural network (ANN), as a robust machine learning technique, to address the storage efficiency in a saline aquifer. They stated that the ANN is a robust technique to examine the feasibility of CO_2 sequestration (Kim and Lee, 2017). Ahmadi et al. (2016) and Le Van and Chon (2017) deployed ANN models to either predict the behaviour of CO_2 in a sequestration site or evaluate the performance of the reservoir during Enhanced Oil Recovery (EOR) operations. They highlighted the potential application of ANNs in the assessment of geological storage sites on the field scale. You et al. (2020) stated that an ANN expert system can propose a reliable technical and economic scheme for CO_2 storage or EOR projects. You et al. (2020b) developed a framework to integrate ANNs with multi-objective optimizers to discover the best strategy for CO_2-EOR and storage in the FWU field. Thanh et al. (2020) used ANN to evaluate the performance of CO_2 injection in a storage site from the Permian Basin. They argued that the ANN has an excellent prediction performance over the classical mathematical and statistical methods.

Despite the above studies, it does not seem that the experimental approaches, numerical methods, or machine learning based methods could really provide conclusive or reliable results. The experimental methods cannot be run for a very long time given the safety regulation and limitation of laboratory set-ups. Numerical simulation and machine learning based methods, on the other hand, perform analysis mostly based on the incomplete dataset obtained from the laboratory measurement and cannot be totally trusted. Field scale experiment and pilot tests can be a reasonable alternative to avoid many of these issues, particularly those raised by the short-term laboratory experiments. Having said that, the need for a suitable method(s) that can provide a relatively accurate prediction of CO_2 plume migration and interactions in a storage site has not been totally fulfilled.

2.2. Pressure and temperature

As stated earlier, carbonic acid is produced upon mixing of residual brine with CO_2 in a geological storage site. This acidic environment is the initial cause of mineral dissolution/precipitation and changes in the petrophysical and geomechanical characteristics of reservoir/seals

Received by OCD: 6/29/2026

Table 2
Studies carried out to evaluate the effect of CO_2 Injection on different reservoir rocks.

Reference	Approach	Exposure time and methods	Rock/medium	Conclusions
(Gunter et al., 1997)	Experimental	1 month –SEM, XRD, grain size analysis	Glauconitic sandstone	High salinity supports slow reaction in fast-reacting carbonate minerals
(Shiraki and Dunn, 2000)	Experimental and modelling	7 days –core flooding and Geo-chemical model PATHARC.94	Sandstone from Tensleep formation	Kaolinite block pore spaces and reduce permeability
(Xu et al., 2005)	Simulation	Conceptual model up to 100,000 years	Sandstone	Capability to store CO_2 volume approaches 90 kg/m^3 at 100,000 years
(Lagneau et al., 2005)	Simulation	Chemical modelling	Bunter sandstones/ Bunter Aquifer	Annite and feldspar minerals gets dissolved
(Bertier et al., 2006)	Experimental	8 months –experimental (SEM/EDS/EMPA element mappings)	Westphalian sandstones	Dissolution and precipitation of minerals observed with effect on permeability
(Wigand et al., 2008)	Experimental	62.3 days experimental	Bunter sandstone	Carbonate dissolution at early stage while feldspar and albite dissolution in the later stage
(Noiriel et al., 2009)	Experimental	15 h/Micro-computed tomography and chemical analysis	Limestone samples	Dissolution induced enhanced porosity, permeability and reactive surface.
(Sterpenich et al., 2009)	Experimental	1 month/Optical and electronic microscopy, mercury porosimeter, UPM	Oolitic limestone	Slight calcite dissolution and precipitation found
(Rimmelé et al., 2010)	Experimental	1 month experimental (SEM, XRD)	Adamswiller sandstone	CO_2-saturated water doesn't alter any rock characteristics but wet $SCCO_2$ does i.e., Permeability and porosity increased by 6–7% and by 4% times respectively.
(Hangx et al., 2010)	Experimental	6 days-core flooding and uniaxial compaction test	Sandstone/ Aquifer and Oil	During short term, not notable variation in rock geomechanical characteristics
(Zemke et al., 2010)	Experimental	Several months-Core flooding and NMR relaxation and mercury injection	Sandstone/aquifer	Porosity increments of porosity in several months
(De Lima et al., 2011)	Experimental	3–6 months experimental (SEM/TEM/XRD)	Sandstone/aquifer	Some fraction of illite and smectite mixed layer transformed into illite after three months
(Fischer et al., 2011)	Experimental	63 days- high-quality steel pressure vessels, optical microscopy, XRD, EMP and SEM	Sandstone/aquifer	Dissolution of calcium-rich plagioclase, K-feldspar and anhydrite along with slight changes in petrophysical characteristics for 63 days
(Evans et al., 2012)	Experimental	Core flooding, UPM, CT scan, UCT	Sandstones	Slight change of geomechanically properties of sandstone and effect on injectivity
(Marbler et al., 2012)	Experimental	2-4 weeks-Autoclave flow system with triaxial cell and reactor system	Sandstones	Reduced strength parameters, modified elastic deformation behaviour and changes of the effective porosity for 2–4 weeks
(Marbler et al., 2013)	Experimental	12–35 days experimental –Autoclave system (SEM)	Sandstones	Creation of micro-fractures with calcite dissolution
(Hangx et al., 2013)	Experimental	6 days-Triaxial Compression test and ultrasonic pulse measurement	Sandstones	Calcite-dissolution during 6 days
(Gharbi et al., 2013)	Experimental	–/Core flooding	Carbonate	Dissolution induced enhanced porosity, permeability
(Olabode and Radonjic, 2014)	Experimental	92 days/ Mercury intrusion analysis (MIP), fixed volume reactor	Pottsville Shale	Petrophysical properties of shale caprock can be altered by a factor of 2
(Kempka et al., 2014)	Simulation	>50 years-Coupled numerical simulation	Aquifer/ Sandstones	Effect on mechanical stability for 50 years
(Varre et al., 2015)	Simulation	25 years -injection 1000 years- monitoring CMG-GEM	Sandstones/ Aquifer	Slight change of porosity and geomechanical characteristics
(Hangx et al., 2015)	Experimental	Hours to days-X-ray Diffraction Analysis (XRD), polarised light, UV and cathodoluminescence microscopy, density, porosity and permeability, Rock strength triaxial tests, direct shear experiment	Sandstone/ Depleted oil reservoir	Minor effect on the petrophysical and geo-mechanical properties
(Huq et al., 2015)	Experimental/ Simulation	6 days - Autoclave flow system and Ion Chromatograph	Sandstone	Permeability increments due to dissolution of cement during 6 days
(Ott et al., 2015b)	Experimental/ Simulation	Core flood and CT scan	Sandstone/ Aquifer	Permeability reduction because of drying and salt precipitation processes
(Erickson et al., 2015)	Experimental	Some weeks-Autoclave flow system, SEM, triaxial compression tests	Sandstones/	Changes in compressive strength of rocks during some weeks
(Garcia-Rios et al., 2015)	Experimental	XRD, X-ray computed microtomography (XCMT), computed tomography, and aqueous chemistry, Core flooding	Fractured limestone	Flow rate increase accelerate dissolution
(Ott et al., 2015a)	Experimental	3–11 h/Unsteady-state core flood and CT scan	Estaillades limestone	Lower fluid-phase mobilities owing to high scale heterogeneity
(Mouzakis et al., 2016)	Experimental	45 days of fixed volume reactor	Gothic & Marine Shale	Changes in pore connectivity is mineralogical dependent
(Zhang et al., 2016a)	Experimental	–/Core flooding and routine core analysis, mechanical tests	Savonnières limestone	Decrease in rock strength and increase in petrophysical properties
(Zhang et al., 2016b)	Experimental	-/NMR-T2 response, porosity, computed tomography and mechanical tests	Savonnières limestone	A significant permeability increase was observed (up to 42.3% after injection), consistent with the wormhole formation
(Ghafoori et al., 2017)	Simulation	1000 years/MATLAB R2013a	Sandstone & Carbonates/ Aquifer	Mineral trapping capacity of carbonate aquifer is less than sandstone aquifer in the CO_2 storage process. Rock dissolution and mineral precipitation

(*continued on next page*)

Received by OCD: 6/29/2026

Table 2 (*continued*)

Reference	Approach	Exposure time and methods	Rock/medium	Conclusions
(Cui et al., 2017)	Experiment and Simulation	200 h / Geochemical apparatus, XRD/3D reactive transport simulation	Limestone and sandstone	
(Raza et al., 2020)	Experimental	-/Core Flooding, SEM, Routine core analysis (NMR), (UPM), (UCT)	Savonnières limestone	Change in petrophysical and geomechanically properties due to rock dissolution and mineral precipitation at low injection rate
(Hadian and Rezaee, 2020)	Experimental	9 months/XRD, NMR, LPNA, MICP, flooding	Shale	Mineralogical changes by dissolution of Quartz, feldspars, kaolinite, and goethite and muscovite, and halite were precipitated.
(Cui et al., 2021)	Simulation	–	Calcite, anorthite, and kaolinite	The geochemical reactions show litter change in reservoir porosity and permeability

NMR 5nuclear magnetic resonance; $scCO_2$ = supercritical CO_2; SEM, scanning electron microscope; T2 = relaxation time; UCT = unconfined compression tests; UPM = ultrasonic pulse measurements; XRD = X-Ray Diffraction; TED = transmission electron microscope; EMP = electron microprobe; CT = computerized tomography; LPNA = low-pressure nitrogen adsorption; MICP = Mercury injection capillary pressure.

(Emberley et al., 2004). The dissolution of CO_2 and transformation of minerals can be affected by pressure and temperature conditions because of their impact on the mass of minerals and the aqueous species involved in the equilibrium reactions. They can also accelerate the chemical reactions, develops fractures, or reactivate faults. However, the effect of pressure on the change of petrophysical properties is slightly stronger than temperature (Hemme and van Berk, 2017).

2.2.1. Pressure

During the injection, pressure builds up around the injection sites and fractures will be initiated once the injection pressure exceeds the minimum principal stress (Pan et al., 2016; Raza et al., 2016a; Rutqvist, 2012). In the long term, regional pressure changes the state of in-situ stresses and permanent geomechanical issues such as vertical uplift (Shi and Durucan, 2009; Tillner et al., 2014; Zhu et al., 2015b), fault reactivations (Ferronato et al., 2010; Miocic et al., 2019; Olden et al., 2012; Tillner et al., 2014; Zhu et al., 2015b) and caprock integrity can be observed (Goodarzi et al., 2011; Rutqvist et al., 2008). In saline aquifers, pressure build up can be more catastrophic since, unlike depleted reservoirs, aquifers are holding a hydrostatic pressure and may not have a huge pressure margin to play with. Thus, active CO_2 reservoir pressure management will be the key for a successful injection operation, particularly in aquifers (Buscheck et al., 2012).

U.S. regulatory standards limit the maximum injection pressure to the measured fracture propagation pressure of caprock (USEPA, 1994). Thus, to manage the injection process effectively, pore and fracture pressure of storage sites are evaluated based on the data obtained from direct measurements techniques such as Repeat Formation Testing (RFT) and Leak-Off Test (LOT) (Chopra and Huffman, 2006). Indirect estimation methods that work principally based on wireline logs or drilling data can also be considered once calibrated against the direct measurements. However, continues monitoring of the pressure during the injection and storage will still be required given the huge uncertainty of the estimated parameters and complexity of geological settings. Here, continues monitoring of pressure using a standard pressure transducer is suggested. This was already practiced at the pilot site of Ketzin (Germany) where pressure gauges were installed on the wellhead and at the end of the injection tube (Liebscher et al., 2013). Vilarrasa et al. (2013) recommended to use liquid CO_2 for injection given its high density that reduces the compression energy required to feed CO_2 into a reservoir. However, this will increase the chances of reaching the fracture pressure sooner than expected and may cause integrity concerns (Vilarrasa et al., 2013).

It is also crucial to analyse poorly oriented faults and fractures crossing the reservoir and caprock. These faults can act as a conduit for CO_2 leakage or can be reactivated causing significant leakages and induced seismicity. Identification of fracture direction or stress orientation on the field scale using shear wave velocity data (i.e., cross dipole sonic imager) or examining the borehole failure using image logs (e.g., FMI, FMS, UBI, CBIL) can be very useful under these circumstances.

Table 3
Different methods used to determine the magnitude and orientation of stresses on the field scale.

Parameter	Types of stress	Measurement technique	Estimation method
Reservoir pressure	P_{res}	▪ Drill-stem Test (DST) ▪ Repeat Formation Test	▪ Sonic Log ▪ Seismic Velocity ▪ Mud Weight Used
Stress magnitude	σ_v σ_H		▪ Density Log ▪ Wellbore Breakout
	σ_h	▪ Hydraulic Fracturing ▪ Leak-off (LOT) Test ▪ Formation Integrity Test	▪ Lost Circulation ▪ Drilling Induced Frac
Stress orientation	$\sigma_h$or σ_H	▪ Cross Dipole Sonic Imaging ▪ Mini-frac test ▪ Hydraulic Fracture Test ▪ Drilling Induced Fracs ▪ Breakout	▪ Fault Direction ▪ Natural Frac Direction

Modified after Aadnoy and Looyeh (2011).

Table 3 gives a summary of different direct or indirect methods used to determine the in-situ stresses and pore pressure on the field scale (Aadnoy and Looyeh, 2011).

2.2.2. Temperature

Temperature is an important parameter to consider when it comes to a storage site selection. This is mainly because dry supercritical CO_2 might be at a different temperature than the reservoir during injection and the exchange heat with surrounding rock may induce thermal stress, and fracture generation/growth (Goodarzi et al., 2013). These thermal shocks are induced because of cold CO_2 advection, the Joule-Thomson (JT) effect, endothermic water vaporization and exothermic CO_2 dissolution. Moreover, strong cooling can also be developed due to CO_2 expansion as the pressure may decrease because of leakage from faults, wellbore or caprock (Vilarrasa and Rutqvist, 2017). CO_2 can also be colder than the reservoir rock due to a lower injection temperature, particularly at a high flow rate (Paterson et al., 2010). Similar observation was made at Cranfield, Mississippi where CO_2 temperature was enhanced by 16 °C by decreasing the flow rate (Luo et al., 2013).

It should be recalled that heat exchange is generally limited, and adiabatic condition prevails until a thermal equilibrium is reached within hours or days (Lu and Connell, 2008). Before the equilibrium, the

Received by OCD: 6/29/2026

thermal stress not only affects the rock surrounding the injection well but the cold front progresses into the reservoir and induces thermal contraction by deformation (Jeanne et al., 2014; Vilarrasa et al., 2017) which may change the state of faults and fractures, increasing the chance of shear failure or induce seismicity (Rutqvist, 2012). Moreover, once the cold CO_2 migrates upward, the lower portion of caprock near the injection well will be cooled down and fracture instability can be induced if the reservoirs and caprock have different thermal expansion coefficients (Vilarrasa and Laloui, 2016). Table 4 gives a summary of studies carried out to evaluate CO_2 injection in the presence or absence of the thermal stress.

It can be safely said that temperature affects the dynamics of CO_2 storage due to the thermal conduction (transfer of thermal energy by direct contact) and convection (transfer of thermal energy by the movement of a liquid or gas) (Fu et al., 2021; Goodarzi et al., 2013; Salimzadeh et al., 2018). Reduction in the formation temperature during injection of cold CO_2 through thermal conduction and convection decreases the total stresses in the reservoir and possibly caprock, causing reduction in the fracture pressure, and injectivity. In a long term, deviatoric (differential) stress reduces due to the significant effect of the thermal stress on the horizontal stresses and the stability of the storage site is improved in a reverse faulting stress regime (Vilarrasa and Rutqvist, 2017). On the other hand, caprocks accumulate less deviatoric stress due to tectonic plate movements as they are typically softer than storage rocks (Hergert et al., 2015) and, as such the chance of fracture propagation into caprock is less likely. To mitigate the effect of thermal stresses on the caprock, injection intervals must be far from the caprock (Vilarrasa and Rutqvist, 2017). Gor et al. (2013) analysed changes in the stress due to the thermal effects and revealed that when CO_2 is injected at a temperature of 40 to 50 °C, the fracture pressure of the caprock reduces over time and fractures can be initiated at a lower pressure than expected. Moreover, differences in the temperature in the medium changes the friction angle and may increase the chance of shear failure in the faulting seals. Gor and Prévost (2013) modelled a fully coupled thermo-poromechanical process to simulate 10 years of continuous injection of CO_2 at different temperatures in the In-Salah storage site of Algeria. The study concluded that the tensile strength of the caprock reduces when CO_2 is injected at the temperature of 40–50 °C, inducing fractures with a length of 50 m within the first 10 years of injection. Fracturing near the wellbore may ease the injection due to the increase in permeability (Gor et al., 2013; Vilarrasa et al., 2017), but the effect of cooling on the long-term injectivity enhancement is limited to only pressurized storage sites (Vilarrasa et al., 2017). Salimzadeh et al. (2018) later found that thermo-poroelastic effects caused by the thermal stress upon CO_2 injection can increase the chance of fault reactivation and leakage in the long term. Therefore, it is essential to examine the maximum sustainable injection pressure together with the thermal stress effect to ensure the safety of a storage site.

In a storage site and a few meters around the injection well, hydrate formation and salt (scale) precipitation may also occur due to the temperature contrasts (Mathias et al., 2010), which may reduce the injectivity. Water vaporization may result in an extra temperature drop of 1 to 2 °C in the vicinity of the injection well. Exothermic CO_2 dissolution in the brine rises the temperature by 0.5 °C outside the water

Table 4
A summary of studies evaluating CO_2 injection in the presence or absence of thermal stress.

Reference	Approach	Thermal effects included	Medium/ simulation time	Objective	Conclusions
(Ju et al., 2021)	Coupled thermo-hydro-mechanical modelling	YES	Aquifer/3 years injection time	Fractures	A gradual decline in the pumping pressure can be used as a practical indicator of fracture growth during injection
(Fu et al., 2021)	Numerical modelling	YES	Gas/2000 days	Pressure build-up	Maintaining an open fracture in the reservoir requires a continuous increase of pressure which potentially exceeds the fracturing pressure of the caprock.
(Salimzadeh et al., 2018)	Numerical modelling	YES	Gas/160 yeas	Thermoporoelastic effects caused by cold CO_2 injection	Reservoir layer undergoes contractions, fault's aperture increases withing the reservoir and decreases within the caprock
(Zhang et al., 2015b)	Geomechanical–fluid flow modelling	NO	Aquifer/20 year	Reactivation of fault and uplift of ground surface	Observed ground uplift but no effect on fracture pressure
(Zhu et al., 2015b)	Geomechanical–fluid flow modelling	NO	Aquifer/ 10 years	Reservoir stresses	Maximum ground surface uplift of 1.49 mm!
(Bao et al., 2014)	Coupled thermal-hydro-mechanical model	YES	Aquifer	Zone failure	Potential failure zone was induced by the fluid injection and thermal effect, especially at the early stages of injection.
(Kim and Hosseini, 2014)	Analytical	YES	–	Reactivation of pre-existing fractures	Different stress regimes and corresponding models were proposed for the maximum pressure profiles
(Tillner et al., 2014)	Geomechanical–fluid flow modelling		Aquifer/ 40 years	-Leakage through fault - Reservoir stresses	Ground uplift and fault slip were observed during CO2 injection
(Shi et al., 2013)	Coupled geomechanical–fluid flow modelling	NO	Aquifer/5 years	Reservoir stresses	Observed ground uplift
(Lynch et al., 2013)	Geomechanical–fluid flow modelling	NO	depleted oil & gas/20 years	Stress path hysteresis	change in the stress path during depletion and injection
(Alonso et al., 2012)	Finite element model	NO	Aquifer/5.5-22 years	Potential leakage path	Deformation in brittle regions and new flow paths when the yield strength of rocks is exceeded
(Goodarzi et al., 2011)	Geomechanical modelling	YES	Aquifer/50 years	Fracture initiation	Fracture pressure limit is important to avoid caprock integrity
(Chiaramonte et al., 2011)	Stochastic 3D geomechanical modelling	NO	Oil reservoir/6 weeks	Role of minor faults and fault reactivation	No harm to faults and no cap-rock integrity
(Ferronato et al., 2010)	Geomechanical modelling	NO	Gas reservoir/ 22–150 years	Reservoir stresses Fault reactivation	New fractures and shear failures in the cap-rock
(Shi and Durucan, 2009)	Geomechanical–fluid flow modelling	NO	gas reservoir/40 years	Reservoir stresses	Compaction by depletion and uplift by injection in a strike-slip fault stress regime
(Rutqvist et al., 2007)	Geomechanical–fluid flow modelling	YES	Aquifer/2.5 years	fault-slip analysis	Maximum sustainable pressure dependent on reservoir structure and in-situ stress

Received by OCD: 6/29/2026

vaporization front (Han et al., 2010) which can help to monitor the CO_2 plume (Zhao and Cheng, 2015) by detecting the temperature variation of CO_2 in the observation well(s). It should be recalled that a high temperature condition can also accelerate the vertical CO_2 migration, CO_2 mobility and solubility trapping while reduces the residual trapping (Al-Khdheeawi et al., 2018). Thus, apart from the chemical interaction and pressure build up that must be considered in a geomechanical analysis (Hermanrud et al., 2013; Raza et al., 2015), the effect of thermal effects on the long-term integrity of geologic site must be fully understood (Gor and Prévost, 2013; Raza et al., 2019; Varre et al., 2015).

There are certain direct measurement tools such as fibre optic, distributed temperature sensing (DTS) cables, wireline-deployed instruments or point measurements (Nuñez-Lopez et al., 2014; Reinsch et al., 2013) that can be used for the continues monitoring of the changes in the temperature during or after injection. Wireline-deployed instruments record the variation of temperature as a function of depth while the DTS provides continuous temperature measurements over time along the cable. Similar practice was done at the pilot site of Ketzin, Germany where the bottom hole temperature was monitored by pressure/temperature gauges installed at the end of the injection tube for every 3 min with a temperature resolution of 0.1 °C (Liebscher et al., 2013).

3. Leakage paths

There are many pathways that may become a conduit for the migration and seepage of CO_2 from a storage site. In this section, these leakage scenarios are presented and discussed with details.

3.1. Wells

Active or abandoned wells in a storage site can be a potential leakage path for CO_2 (Zhang and Bachu, 2011). Drilling, production, and abandonment operation of the wells used for CO_2 storage have a drastic effect on the well integrity. Not to mentioned that CO_2 storage wells must act as a secure barrier against the leakage for centuries. Faulty construction and/or degradation (corrosion, micro-fractures, cement channelling, etc.) of wells can provide a migration pathway for CO_2.

Prior to CO_2 injection and during the operation and abandonment phases, well integrity can be affected by faulty well completion or chemical and mechanical stresses as shown in Fig. 4 (Viswanathan et al., 2008). There are many reasons behind this faulty completion including tabular failures due to the thread leaks between casing joints (Schwind et al., 2001), poor cementing job, placement of a highly permeable cement, failure to remove the mud cake and many other operational issues inducing poor bond among casing, cement, and formations. Thermal, mechanical, tectonic and chemical stresses can also raise the leakage risks by the corrosion of casing and tubular, fracturing the cement, cement dissolution and cement permeability enhancement (Carroll et al., 2016). A poor cement job is perhaps the most important reason behind the migration and leakage of CO_2 and external corrosion of casing (IEA, 2009).

Around abandoned wells, hydraulic aperture of rock-cement and casing-cement interfaces is affected during CO_2 injection by stress changes, deformation, and chemical degradation (Bachu and Bennion, 2009; Wigand et al., 2009). It is known that CO_2-rock interactions are capable of triggering leakage pathways through wells, caprock and reservoirs (Gaus, 2010). It should be recalled that the Portland cement (classes G and H) that is typically used during well completions and abandonment are highly sensitive to the acidic environment induced by CO_2 injection. Upon chemical interaction between Portlandite and CO_2-saturated brine, cement degradation is initiated by the production of calcium carbonate and residual amorphous silicates (Abid et al., 2015; Carey et al., 2007; Huerta et al., 2013; Zhang et al., 2015a). Zhang and Bachu (2011) provided a review on the well integrity in CO_2 storage sites and highlighted certain approaches that can determine the rate of cement carbonation. Laboratory experiments showed that the rate of carbonation is directly related to pressure, temperature, and flow rate, and indirectly related to the salinity. Moreover, cement water system without carbonate minerals revealed a larger carbonation rate than a system with carbonate water. The results obtained from the field scale analysis indicated that the interaction with CO_2 will take place over a long period of time and carbonation, or changes in porosity and permeability can be induced (Zhang and Bachu, 2011).

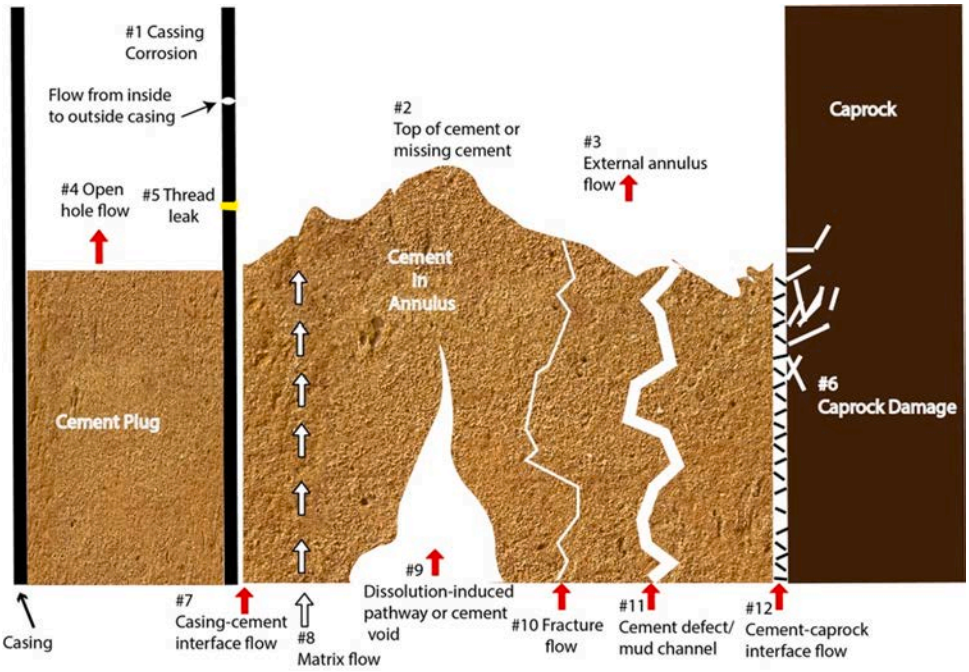


Fig. 4. A schematic view of an abandoned wells where the leakage pathways can be induced during or after CO_2 injection. Modified after Carroll et al. (2016).

Received by OCD: 6/29/2026

To enhance the cement integrity against the interaction with dry (supercritical) or wet (dissolved in brine) CO_2, several approaches have been proposed which include employing pozzolanic materials, decreasing the water to cement ratio, adding latex and dispersing nanomaterials (Abid et al., 2015; Tiong et al., 2020). However, many of these methods suffer from significant shortcomings. For instance, a large quantity of pozzolanic materials can significantly reduce the thickening time of the cement. Reducing the water to cement ratio, on the other hand, can increase the chance of inducing cracks in the cement. Non-Portland cement cannot resist against the interaction with $scCO_2$ for a long time and special additives may lose their integrity over time. Nanomaterials can improve the cement performance in CO_2 storage sites, but they are expensive and require operational cost justification (Tiong et al., 2020). According to Ringrose (2020), wellbore integrity in a CO_2 storage site can be maintained by a good cement placement and a standard Portland cement can provide a long-term hydraulic isolation. He argued that the cement interface with casing or formations is the likely path of fluid migration that must be carefully monitored (Ringrose, 2020).

It should be remembered that upon chemical degradation of the cement, corrosion of the casing will be induced and the chance of leakage from the storage site increases (IEA, 2009). This corrosion can be mitigated by a proper material selection, applying corrosion inhibitors, cathodic protection, or coating of the cement (Choi et al., 2013; Talabani et al., 2000), but the chance of degradation and leakage will always be there.

IEA Greenhouse Gas R&D Programme (IEA GHG) released a report on "Long Term Integrity of CO_2 Storage-Well Abandonment" where potential factors contributing to CO_2 leakage from an injection well have been analysed (IEA, 2009). These factors are categorized into parameters with no impacts (well age, well operational mode, completion interval, H_2S or CO_2 presence), minor impacts (casing depth, total depth, well density, topography) and major impacts (geographic area, wellbore deviation, well type, abandonment method, and uncemented casing/hole annulus) (IEA, 2009). According to this report, 98% of leakages are observed in abandoned cased wells, with a poor cement job. Table 5 gives a summary of the factors reported by IEA GHG with different impacts on the CO_2 leakage from wells used for the injection in a storage site.

Table 5
Summary of the factors with impacts on the leakages from an injection well (IEA, 2009).

Impact	Parameters	Description
No impact	Well age	Poor construction and materials of old wells cannot be supported by data!
	Operational mode	Different operational approaches (acid, solvent or water injection) do not appear to have a significant effect on the creation of leakage paths.
	Completion interval	The cement logs and other in-situ measurements verified that there is no connection between the depth of leaking gas and completion intervals.
	H_2S or CO_2 presence	Analysis of reservoirs with hydrogen sulphide and CO_2 is not complete to verify the casing corrosion and creation of leakage paths.
Minor Impact	Licensee	Different abandonment practices used by operators may not be effective.
	Surface casing depth	Depth of surface casing does not affect the leakage rate but may increase the probability of leakage.
	Well depth	Well depth increases the chance of gas migration due to the probability of having a poor cement job
	Well density	Leakage rates may increase in the regions with a significant number of wells due to well-to well crossflow.
	Topography	Leakage risks may increase in river valleys due to the elimination of overburden stress and reduction in the hydrostatic pressure
Major Impact	Geographic area	It seems that at certain regions, leakage has correlations with the geographic location, but this could not be supported by data.
	Wellbore deviation	Deviated wells usually encounter significant flow migration but may not have a significant effect on the leakage.
	Well Type	98% of leakages have been reported from cased abandoned wells while the remaining 2% are drilled and abandoned wells.
	Abandonment method	Cased and completed wells are often abandoned by bridge plugs capped with cement, particularly in Alberta. Around 10% of these bridge plugs will lose their integrity in centuries, allowing leakages.
	Oil prices and regulatory changes	Leakage has a good relationship with oil price. High satisfaction demand with restricted resources has a remarkable effect on the primary cement operations.
	Uncemented casing / hole annulus	It was found that low cement top is the common reasons behind the leakages and casing corrosion.

3.2. Storage site

3.2.1. Caprock and vertical migration

Free CO_2 can find its way out of a storage site due to the mechanisms explained earlier. Thus, it is important to ensure that CO_2 can be immobilized by the active trapping mechanisms in a storage site. During the injection, CO_2 migrates laterally away from the injection well (due to the viscous force) and then starts to migrate vertically towards the top of the reservoir because of the buoyancy force (see Fig. 5). In a long-term, CO_2 dissolves in the residual brine (dissolution trapping) and goes into a slow convection process (Green and Ennis-King, 2010). It also stops by the capillary trapping (water wet rocks) and mineral trapping. The rest of the dry supercritical CO_2, however, will continue its vertical migration and comes in contact with the caprock (the structural trap) (Nelson, 2005) where the geochemical interactions, pressure and temperature condition may trigger the leakage (Green and Ennis-King, 2010). In fact, stress perturbation by the pressure changes, together with the weakening posed by the geochemical interactions can develop new fractures, reactivate the existing fractures and increase the caprock permeability (Gheibi et al., 2017; Renard et al., 2012).

Factors affecting the vertical migration of CO_2 have been studied by many researchers. It has been reported that CO_2 solubility decreases the vertical migration but the rate of migration depends on the vertical permeability (Yu et al., 2019). The extent of the vertical flow has also a direct relationship with the injection rate where the horizontal migration would be larger at a lower injection rate. A medium with a CO_2 wet system promotes the vertical flow compared to a water-wet reservoir. Reservoir heterogeneity reduces the vertical migration and helps the lateral migration of CO_2 but it reduces the residual trapping (Al-Khdheeawi et al., 2017). Furthermore, temperature rise can decrease the sweeping efficiency of CO_2 and favours the vertical migration due to the increase in buoyancy (Bielinski et al., 2008). The flow velocity of the reservoir water can also affect the rate of CO_2 migration out of a geologic sink (Nelson, 2005). The convective mixing of CO_2 in brine is a function of reservoir rock and fluid characteristics (Singh and Islam, 2018). To halt the flow of buoyant CO_2 from a storage site, injection of CO_2 premixed with brine can be helpful, particularly in saline aquifers.

Time-lapse (4D) seismic data acquisition can be a useful tool to track the migration of CO_2 and characterise the flow dynamics of a reservoir over time (Li et al., 2016). Azuma et al. (2014) pointed out that if the quantitative relationship between the seismic attenuation and CO_2 saturation can be well established, seismic method can become the most reliable method of CO_2 monitoring (Azuma et al., 2014).

Received by OCD: 6/29/2026

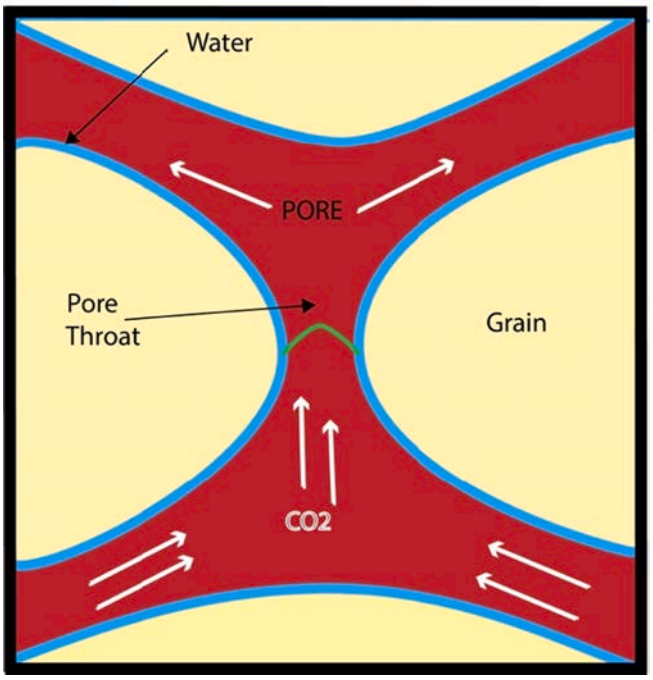


Fig. 5. Upward migration of CO_2 driven by the buoyancy pressure that is immobilized by the capillary traps (surface wettability) in porous media.

3.2.2. Faults

Faults are discontinuities in subsurface geologic formations that may act as a conduit or barrier depending on the type of rocks dominating the fault zone. Numerous processes are involved to induce a fault including plate motions, folding, gravitational sliding, volcanic intrusion, crustal unloading and fluid injection/withdrawal (Kaldi et al., 2013). It is typically assumed that faults are impermeable because of the shale gouge or clay smear but many faults are membrane or capillary seals (Yielding, 2015). For a membrane seal, leakage will start when the buoyancy pressure of injected CO_2 becomes larger than the capillary entry pressure of the rocks dominated in a fault zone. Once the leakage initiated, there will be two likely scenarios: 1) there is a permeable formation on the other side of a fault that will receive CO_2 and release the pressure from the fault's surface causing across-fault leakage, and 2) faults are juxtaposed against an impermeable formation, CO_2 will accumulate inside the fault surface and reactivation will be triggered once the maximum shear strength of the fault is reached (Umar et al., 2019).

The sealing capacity of a fault is affected by the pore-throat size and the surface wettability of rocks dominated in the fault zone as well as the interfacial tension between the fluids filling the pore throats of rocks in a fault zone (Daniel and Kaldi, 2008). Thus, a fault dominated by fine grained rocks such as shale with a strongly water wet system (e.g., dominated by quartz and feldspar) can be an impressive seal against the CO_2 migration (Iglauer et al., 2015). However, according to Gholami et al. (2021), the surface wettability of rocks can be altered over time due to the exposure to CO_2. Therefore, a comprehensive assessment of the seal capacity of a fault must be performed during and after injection.

The results obtained from a series of studies on the CO_2 pilot site in Wyoming (Chiaramonte et al., 2008), In-Salah, Algeria (Rutqvist et al., 2010), Otway, Australia (Vidal-Gilbert et al., 2010) and Ketzin, Germany (Ouellet et al., 2011) indicated that fault reactivation can be triggered during or after CO_2 injection depending on the injection pressure and changes in the capillary entry pressure. However, due to the uncertainty in the estimation of in-situ (and normal) stresses and presence of heterogeneity in geological formations, it is very difficult to estimate when exactly a fault may reactivate. A fully coupled modelling of geochemical alteration and geomechanical changes could be able to indicate the status of a fault during injection under these circumstances (Rutqvist, 2012). However, these coupled models may require complete understanding of CO_2 flow behaviour in the presence of fractures and dynamics of fractures once their critical stability limit is reached (Kaldi et al., 2013).

Microseismic data recording is one of the best monitoring approaches proposed so far to evaluate fault reactivation and induced seismicity (Maxwell, 2014). In this method, the energy released by the shear failure (deformations) of fractures is used to identify the moment magnitude of the event and the location of fractures. A decision can then be made if the fluid injection should be continued or stopped based on the traffic light system developed for the storage site (Walters et al., 2015). However, there are two major shortcomings when it comes to the microseismic method: 1) it can only identify triggered events (if large enough) and is unable to act as a warning system and 2) it does not reflect the entire perturbation energy induced by fault reactivation (Das and Zoback, 2013). It should be remembered that faults that are exposed to a high normal stress with the domination of phyllosilicates (clays) on their sliding interface are often considered as a safe seal for injection (Umar et al., 2019). According to Rutqvist et al. (2016) and Hirakawa and Ma (2016), these faults show a velocity strengthening behaviour due to the presence of clays and will go into a slow slip once their critical stability state is reached. This indicates the fact that many faults may not induce a detectable induced seismic event and may go into a slow creep once reactivated. Therefore, it is strongly advised to deploy fibre optic sensors in the injection borehole to measure the deformation (aseismic event) induced by fault reactivations.

3.2.3. Sealing potential

The capability of a caprock to confine CO_2 is controlled by many parameters ranging from capillary sealing pressure to lateral continuity, thickness, ductile/brittle behaviour and presence of fractures or faults (Vavra et al., 1992). Sealing potential is defined as the capacity of a caprock to maintain its strength against the migration of fluid during or after fluid injection (Kaldi and Atkinson, 1997). It should be recalled that the leakage through caprock can take place in two ways: i) through interconnected pore space and ii) through initiation of new factures or reactivation of preexisting fractures. Leakage through the interconnect pore space is evaluated based on the capillary entry pressure (Gaus, 2010). The factors controlling the capillary pressure, on these occasions, are pore throats size, CO_2-water interfacial tension and surface wettability of rock (see Fig. 6). Thus, the sealing capacity of caprocks increases

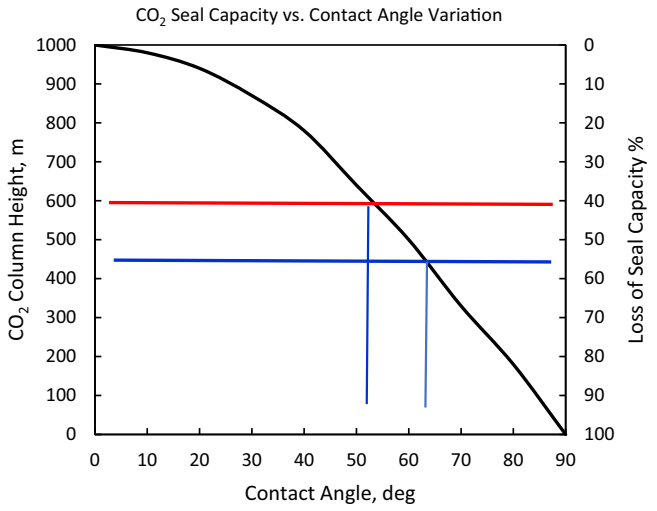


Fig. 6. Column height of CO_2 against the surface wettability variation measured by the contact angle.

Received by OCD: 6/29/2026

with the decrease of the pore throat size and increases of CO_2-water interfacial tension in a strongly water wet system (Schowalter, 1979). To determine the pore throat size of rocks, mercury injection based capillary pressure (MICP) test is often considered (Gaus, 2010; Schowalter, 1979). Surface Wettability, on the other hand, can be determined experimentally in laboratory using numerous experimental set-up such as the capillary rise methods (Washburn, 1921), spontaneous imbibition (Graham and Richardson, 1959), Amott and Amott-Harvey index approach (Anderson, 1986a), U.S. Bureau of Mines (USBM) method (Donaldson et al., 1969), and contact angle measurement (Anderson, 1986b; Iglauer et al., 2015). The Interfacial tension of a two-phase systems can be determined using the pendant (or rising) drop method as a well-established measurement approach (Chalbaud et al., 2009).

Leakage through initiation of new factures or reactivation of preexisting fractures is the second pathway for CO_2 migration from a storage site which is a function of caprock thickness, lateral extent, and mineral composition. Thickness of the caprock ensures an effective seal with a greater strength to hold free CO_2 from breaching. (Kaldi et al., 2013). On the other hand, caprocks are composed of fine grain rocks with low permeability (Bifani, 1986; Ketter, 1991). Ductile lithologies such as halite and organic shales are less likely to have conductive fractures while brittle caprocks have a high chance of fracture initiation and integrity failure. Here, rocks with carbonate content or siliciclastic composition often exhibit a brittle behaviour, with a high chance of fracturing (Stearns and Friedman, 1972). The Brittleness Index (BI) is often defined on these occasions as a measure of fracture growth. As a rule of thumb, rocks with a higher BI, will have a higher tendency to grow fractures while ductile rocks (often those with a huge amount of clay) has a significant sealing potential and will exhibit a plastic behaviour. Leak-off tests (LOT) data analysis together with a proper geomechanical assessment can help to determine the likelihood of fracture initiation and propagation in a caprock under different pressure and temperature conditions (Mildren et al., 2005). Fig. 7 shows the sealing behaviour of different rocks based on the compressibility and ductility factors.

4. Safety assessment of a CO_2 storage site

Given the complexity of geological storage sites, a risk management/assessment guideline is essential to ensure that CO_2 leakage can be minimized during and after injection. In this section, certain steps that need to be taken to assess the suitability of a geological medium for possible CO_2 storage are presented and possible management strategies are recommended. These steps are summarized into six phases and described in the following sections.

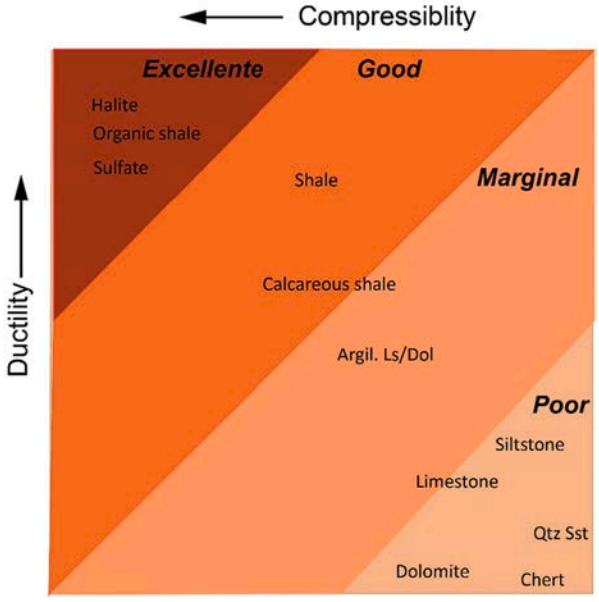


Fig. 7. Sealing behaviour of different rocks based on the compressibility and ductility factors (Kivior et al., 2002).

4.1. Phase 1-initial screening

Initial screening of different storage sites is done based on a series of criteria developed for the reservoir (Bachu, 2003; Bachu, 2010; Kovscek, 2002; Raza et al., 2016b), wellbore (IEA, 2009) and caprock selection (Kivior et al., 2002; Nakanishi and Lang, 2002). Table 6 summarises the initial screening criteria that can be used in this phase.

4.2. Phase 2-reservoir characterization

In this stage, reservoirs are characterized based on the key storage aspects including capacity, injectivity and trapping criteria (Raza and Gholami, 2019) through experimental (small scale) or numerical modelling (large scale) approaches. The following steps are recommended to be taken at this stage:

i. CO_2-reservoir rock interaction must be studied (Bertier et al., 2006; Rimmelé et al., 2010) through core flooding or any other reactive transport flow simulators. Given that these interactions are very slow, the laboratory measurements should be run for more than a few months to observe the potential changes that may take place in a long-term storage practice.
ii. Drilling activities and seismic survey data can provide vital information about the potential leakage pathways from the near wellbore or the reservoir itself. All available surveys (geological, geophysical, and drilling) together with the core and well logs must be used, if available, to assess the storage medium on the large scale.
iii. To avoid fracturing the caprock during or after injection, pore pressure, in-situ stresses, strength, and elastic properties of rocks must be determined with sufficient accuracy. Leak-Off Test (LOT) can be used to determine/calibrate the minimum principal stress while correlations can be considered to determine the elastic and strength properties of rocks using wireline logs data.
iv. To avoid leakages through faults and fractures, poorly oriented faults/fractures must be identified, and characterized for their geometry, size, and strength. The dynamics of faults and fractures (reactivation mechanisms) must be analysed, and potential of creep or dynamic rupture should be well quantified.
v. A reservoir model should be built to couple the geochemical interactions induced by CO_2 to geomechanical alterations such as changes in the state of in-situ stresses or reductions of the mechanical properties. This may help to understand the status of faults as the injection progresses.
vi. Reservoir injecitvity and capacity must be analysed by evaluating the trapping mechanisms, geochemical reactions and geomechanical changes in the short and long term. For injectivity, number and locations of wells, maximum sustainable injection pressure and CO_2-rock interaction are important. For the capacity and storage operational efficiency, trapping mechanisms, number and location of wells, water disposal, pressure relief wells, potential subsidence and fault reactivation must be analysed. Teletzke and Lu (2013) provided a series of recommendation for CO_2 storage site characterization that can be followed at this stage (Teletzke and Lu, 2013).

4.3. Phase 3- operational aspects

There are certain recommendations that should be taken into consideration when it comes to CO_2 injection:

Received by OCD: 6/29/2026

Table 6
A screening criterion for selection of global depleted gas reservoirs (Raza et al., 2016b).

Parameters	Positive indicators	Cautionary indicators	Indication of aspect
CO_2 source and total storage capacity	Total capacity of reservoir estimated to be much larger than the total amount produced from the CO_2 source	Total capacity of reservoir estimated to be similar or less than the total amount produced from the CO_2 source	Storage potential
Depth	>800 m	800 m > depth > 2000 m	Storage Capacity
CO_2 density	High	Low	Storage Capacity
Porosity	>20%	<10%	Storage Capacity Capillary trapping
Thickness (net)	> > 50 m	<20 m	Storage Capacity Injectivity
Permeability (near-wellbore)	>100 mD	10-100 mD	Injectivity
Well type	Horizontal well with or without hydraulic fracture/ vertical well with hydraulic fracture	Vertical well without hydraulic fracture	Injectivity
Type of minerals	Ca-, Mg-, or Fe-rich framework minerals such as (feldspars, clays, micas, and Fe-oxides	Fast reacting carbonates minerals	Injectivity/mineral trapping
Residual gas /water saturation	Less	High	Injectivity
Pore throat size distribution	Less heterogeneous	High heterogeneous	Injectivity and Trapping
Salinity	Low	High	Solubility trapping
Temperature	Low temperature gradient	High temperature gradient	Solubility trapping
Pressure	Under pressure	Overpressure	Solubility trapping
Gravity number	Less	High	Capillary trapping
Rock type	Quartz rich sandstones and carbonates	Highly stress sensitive carbonates	Capillary trapping
Rock wettability	Strong water wet	Less water wet or oil-wet	Capillary trapping
Interfacial tension	High	Low	Capillary trapping
Hydraulic integrity — Reservoir type	Reservoir without compaction/ aquifer support Have not experienced any injection in past Less faults and fractures	Reservoir with compaction/aquifer support Have experienced any injection in past More faults and fractures	Containment
Hydraulic integrity — Well location & condition	Good completion condition and away from faults & fractures	Poor completion and near to faults & fractures	Injectivity
Seal capacity – CO_2 column height	Capillary entry pressure much greater than buoyancy force of maximum produced CO_2 column height	Capillary entry pressure similar to buoyancy force of maximum produced CO_2 column height	Containment
Seal geometry - Lateral continuity	Un-faulted	Laterally variable faults	Containment
Seal geometry –Thickness	>100 m	<20 m	Containment
Hydraulic integrity: Seal	Presence of mineral and stress characterization data of seal	Absence of mineral and stress characterization data of seal	Containment
Distance between CO_2 emissions source and target medium	<300 km	>300 km	Transportation cost

i. CO_2 in a gas phase or with impurities (methane, nitrogen, and water) must be avoided as they pose potential corrosion, poor injectivity and leakage from wellbores or reservoirs. Liquid CO_2 (i.e., held in the temperature below −22 and pressure of 15 MPa) is the best option for transport and storage. Supercritical CO_2 can then be generated during injection in a reservoir located beneath 800 m (pressure of 7 MPa and temperature of 30 °C), providing a good compressibility, viscous force, and mobility.
ii. Injection of CO_2 may induce thermal shock and salt (scale) precipitation in the pore throats of a reservoir near the wellbore region (injection site). Freshwater treatment after clogging to dissolve the salt or pre-flushing before CO_2 injection to decrease the level of salinity near the wellbore region can be considered.
iii. After the stoppage of injection, fractions of CO_2 remain mobile and need to be stabilized to reduce the risk of leakage. Structural traps are the last line of defence against the CO_2 plume migrations. Continues monitoring of plume migration using time lapse seismic surveys or any other direct or indirect methods is recommended.
iv. Although there have been many studies on the degradation of the cement during injection or storage of CO_2, it is not still clear if the cement integrity can be maintained in the long term. Adding Pozzolanic materials, employing non-Portland cements, or considering nanomaterials could be some of the options to improve the cement integrity in CO_2 storage sites.

4.4. Phase 5- monitoring

During and after the injection, it is important to ensure that the injected CO_2 remains in the geologic sites and does not contaminate surface or subsurface resources (groundwater, soil, lakes, rivers) (De Lary et al., 2015; Deel et al., 2007). Thus, a proper monitoring system must be in place when pressure builds up and CO_2 plume starts to move due to physical, chemical, and mechanical changes.

There are several techniques that can be used as a monitoring system to ensure the integrity of a storage reservoir (Winthaegen et al., 2005) as summarized in Table 7. Generally, these monitoring techniques are divided into direct and indirect approaches. The direct measurements are often wellhead or downhole pressure and temperature gauges in the injection or observation wells. (Liebscher et al., 2013). Indirect methods, on the other hand, often include gravity, electro-magnetic and seismic (VSP, cross-borehole or surface reflection) geophysical techniques. Time lapse (4D) seismic reflection data is perhaps the most valuable tool for monitoring CO_2 plume migration. In this approach, changes in the poroelastic properties of rocks, such as fluid distribution, stress, and pressure changes during or after injection can be detected through the analysis of the seismic amplitude. Downhole logging tools such as cement bond logs can also be used to verify the wellbore integrity and monitor the condition of the cement behind the casing (Winthaegen et al., 2005).

4.5. Phase 6- remediation strategies

When it comes to CO_2 storage, potential leakage paths near the wellbore region and inside the storage sites that can be induced through thermal shock and geochemical-geomechanical interactions must be well understood. Currently, the poor cement sheath behind the casing in abandoned wells is recognized as the most likely leakage path when it comes to CO_2 storage sites (Abid et al., 2015). These wells should be recapped or repaired once the poor placement intervals are identified using the cement bond log. Leakages through faults or fractures, on the other hand, can be mitigated by reducing the injection pressure or

Received by OCD: 6/29/2026

Table 7
Summary of direct and indirect techniques used to monitor CO_2 storage sites (IPCC, 2005).

Measurement technique	Measurement parameters	Example applications
Tracers	1) Travel time. 2) Partitioning of CO_2 into brine or oil. 3) Identification of CO_2 sources	1) Tracing movement of CO_2 in the storage site 2) Quantifying the solubility trapping. 3) Tracing leakage
Water composition	1) CO_2, 3H CO_3^-, CO_3^2 2) Major ions 3) Trace elements 4) Salinity	1) Quantifying the solubility and mineral trapping 2) Quantifying CO_2-water-rock interactions 3) Detecting leakage into shallow groundwater aquifers
Subsurface pressure	1) Formation pressure 2) Annulus pressure 3) Groundwater aquifer pressure	1) Control of formation pressure below the fracture gradient 2) Wellbore and injection tube condition 3) Leakage detection from the storage formation
Well logs	1) Brine salinity 2) Sonic velocity 3) CO_2 saturation	1) Tracing CO_2 movement in and above the storage formation 2) Tracking the migration of brine into shallow aquifers 3) Calibrating seismic velocities for 3D seismic surveys
Time-lapse 3D seismic imaging	1) P-and S-wave velocities 2) Reflection horizons 3) Seismic amplitude attenuation	Tracing CO_2 movement in and above the storage formation
Vertical seismic profiling and cross wellbore seismic imaging	1) P- and S-wave velocities 2) Reflection horizons 3) Seismic amplitude attenuation	1) Detecting distribution of CO_2 in the storage formation 2) Detecting leakages through faults and fractures
Passive seismic monitoring	Location, magnitude, and source of seismic events	1) Development of micro fractures in the formation or caprock 2) CO_2 migration paths
Electrical and electromagnetic techniques	1) Formation conductivity. 2) Electromagnetic induction	1) Tracking movement of CO_2 in the storage formation 2) Detecting migration of brine into shallow aquifers
Time-lapse gravity measurements	Density changes caused by fluid displacements	1) Detecting CO_2 movement in or above the storage formation 2) CO_2 mass balance in the subsurface
Surface deformation	1) Tilting 2) Vertical/horizontal displacements	1) Detecting geomechanical changes 2) Identifying CO_2 migration pathways
Visible and infrared imaging from satellite or planes	Hyperspectral imaging of land surface	Detecting vegetative stress
Soil gas sampling	1) Soil gas composition. 2) Isotopic analysis of CO_2	1) Detecting elevated levels of CO_2. 2) Identifying the source of elevated gas in soil 3) Evaluating ecological impacts

plugging/sealing the leakage channels (ATLANTIC, 2007).

5. Discussion

Different mechanisms are involved in the creation of leakage paths in a CO_2 storage site. Upon injection, CO_2 is trapped by a variety of mechanisms including the phase trapping, dispersion, dissolution, adsorption, mineral transformations, and structural seals. However, plume migration in a reservoir cause stress perturbation due to the changes in pressure and temperature conditions. Once combined with the geochemical interactions, these changes can induce leakage pathways in a storage site. Careful geochemical analysis coupled with geomechanical modelling could be the best approach to identify these leakage pathways. However, experimental tests carried out in the laboratory can only be run for few months and may not really provide a deep insight into the interactions taking place in the long term. Numerical modelling could be a good option, on these occasions, but it requires inputs that are often obtained from those limited experimental studies. Thus, further studies are required to develop a suitable upscaling approach that can confirm the integrity of CO_2 storage sites in thousands of years.

In view of these complexities, continues and reliable monitoring techniques must be deployed during and after CO_2 injection to ensure the integrity of the storage sites. Equinor, as one of the pioneers of CO_2 storage in the North Sea considers three simultaneous monitoring system for CO_2 storage sites which include: i) surface monitoring for induced seismicity, ii) deploying fibre optic sensors in the borehole and iii) continues sampling of ground water above the storage sites. Given that the source and mechanisms of leakages have not been totally understood, deploying different monitoring systems simultaneously can be a great strategy.

Determination of CO_2 plume migration and distribution has always been challenging. Many mathematical and numerical approaches have been proposed to determine how CO_2 may spread in the reservoir over time during injection and storage, but limited success has been reported to the application of these methods once tested on the field scale. 4D (time lapse) seismic data has been the only reliable method so far that can determine how exactly CO_2 migrates in a storage site but the search for a cheaper and less complicated method has not been stopped.

Although different CO_2 leakage scenarios have been identified for a storage site, it appears that offshore storage sites are totally safe, once screened carefully based on many established geological and operational criteria. Zero Emission Platform (ZEP) (https://zeroemissionsplatform.eu/) released a report in 2019 on "CO_2 storage safety in the North Sea" and assessed different theoretical leakage scenarios based on the containment risk, their probability, impact, duration, and cost implications. It was found that high leakage rates to the sea floor are highly unlikely to occur and much of the CO_2 would be trapped or dissolved in overlying formation waters before reaching the seafloor. Thus, the chance of marine ecosystems destruction due to CO_2 leakage is extremely low.

6. Conclusions

There are different mechanises in a storage site that can trap CO_2 in a short- or long-term scales. However, there will still be a huge amount of free CO_2 that will interact with the wellbore materials (cement), caprock, reservoir and faults. Certain leakage paths can be generated due to the geochemical interactions enhanced by the pressure and temperature of a storage site. Laboratory measurements have been taken to understand these interactions, but they cannot often replicate the observations made on the field scale due either to limited duration of tests or poor understanding of complex interactions that may take place in a CO_2 storage site. It appears that pilot projects can shed more lights into the potential integrity problems of the storage sites than relying on the laboratory tests combined with numerical simulations.

Received by OCD: 6/29/2026

Declaration of Competing Interest

The authors declare that they have no conflict of interest.

References

Aadnoy, B., Looyeh, R., 2011. Petroleum Rock Mechanics: Drilling Operations and Well Design. Gulf Professional Publishing, USA.

Abid, K., Gholami, R., Choate, P., Nagaratnam, B.H., 2015. A review on cement degradation under CO_2-rich environment of sequestration projects. J. Nat. Gas Sci. Eng. 27, 1149–1157. Elsevier.

Ahmadi, M., Kashiwao, T., Rozyn, J., Bahadori, A., 2016. Accurate prediction of properties of carbon dioxide for carbon capture and sequestration operations. Pet. Sci. Technol. 34 (1), 97–103.

Alcalde, J., Flude, S., Wilkinson, M., Johnson, G., Edlmann, K., Bond, C.E., Scott, V., Gilfillan, S.M.V., Ogaya, X., Haszeldine, R.S., 2018. Estimating geological CO2 storage security to deliver on climate mitigation. Nat. Commun. 9 (1), 2201.

Al-Khdheeawi, E.A., Vialle, S., Barifcani, A., Sarmadivaleh, M., Iglauer, S., 2017. Impact of reservoir wettability and heterogeneity on CO2-plume migration and trapping capacity. Int. J. Greenhouse Gas Control 58, 142–158.

Al-Khdheeawi, E.A., Vialle, S., Barifcani, A., Sarmadivaleh, M., Iglauer, S., 2018. Effect of wettability heterogeneity and reservoir temperature on CO2 storage efficiency in deep saline aquifers. Int. J. Greenhouse Gas Control 68, 216–229.

Alonso, J., Navarro, V., Calvo, B., 2012. Flow path development in different CO_2 storage reservoir scenarios: a critical state approach. Eng. Geol. 127, 54–64.

Anderson, W., 1986a. Wettability literature survey-part 2: wettability measurement. J. Pet. Technol. 38 (11), 1246–1262.

Anderson, W.G., 1986b. Wettability literature survey-part 3: the effects of wettability on the electrical properties of porous media. J. Pet. Technol. 38 (12), 1,371–1,378.

ATLANTIC, N.-E, 2007. OSPAR Guidelines for Risk Assessment and Management of Storage of CO2 Streams in Geological Formations.

Azuma, H., Xue, Z., Matsuoka, T., 2014. Utilization of seismic attenuation in the monitoring of CO2 geological storage project. Energy Proc. 63, 4216–4223.

Bachu, S., 2001. Screening and Ranking of Hydrocarbon Reservoirs for CO_2 Storage in the Alberta Basin, Canada. US Department of Energy–National Energy Technology Laboratory, National Conference on Carbon Sequestration, pp. 1–11.

Bachu, S., 2003. Screening and ranking of sedimentary basins for sequestration of CO_2 in geological media in response to climate change. Environ. Geol. 44 (3), 277–289.

Bachu, S., 2010. 2 - Screening and selection criteria, and characterisation techniques for the geological sequestration of carbon dioxide (CO2). In: Maroto-Valer, M.M. (Ed.), Developments and Innovation in Carbon Dioxide (Co2) Capture and Storage Technology. Woodhead Publishing, pp. 27–56.

Bachu, S., Bennion, D.B., 2009. Experimental assessment of brine and/or CO2 leakage through well cements at reservoir conditions. Int. J. Greenhouse Gas Control 3 (4), 494–501.

Bachu, S., Gunter, W., Perkins, E., 1994. Aquifer disposal of CO_2: hydrodynamic and mineral trapping. Energy Convers. Manag. 35 (4), 269–279.

Bao, J., Xu, Z., Fang, Y., 2014. A coupled thermal-hydro-mechanical simulation for carbon dioxide sequestration. Environ. Geotech. 3 (5), 312–324.

Benson, S., 2007. Geological Storage of CO2: Analogues and Risk Management Presentation to Carbon Sequestration Leadership Forum-CSLF, 7 May 2007 (Pittsburgh PA).

Bertier, P., Swennen, R., Laenen, B., Lagrou, D., Dreesen, R., 2006. Experimental identification of CO2–water–rock interactions caused by sequestration of CO2 in Westphalian and Buntsandstein sandstones of the Campine Basin (NE-Belgium). J. Geochem. Explor. 89 (1–3), 10–14.

Bielinski, A., Kopp, A., Schütt, H., Class, H., 2008. Monitoring of CO2 plumes during storage in geological formations using temperature signals: numerical investigation. Int. J. Greenhouse Gas Control 2 (3), 319–328.

Bifani, R., 1986. Esmond gas complex. Geol. Soc. Lond., Spec. Publ. 23 (1), 209–221.

Buscheck, T.A., Friedmann, S.J., Sun, Y., Chen, M., Hao, Y., Wolery, T.J., Aines, R.D., 2012. Active CO_2 reservoir management for CO_2 capture utilization and storage: an approach to improve CO_2 storage capacity and to reduce risk. In: Carbon Management Technology Conference, 7-9 February, Orlando, Florida, USA. Carbon Management Technology Conference, pp. 1–18.

Campos, R., Barrios, I., Lillo, J., 2015. Experimental injection: study of physical changes in sandstone porous media using Hg porosimetry and 3D pore network models. Energy Rep. 1, 71–79.

Carey, J.W., Wigand, M., Chipera, S.J., WoldeGabriel, G., Pawar, R., Lichtner, P.C., Wehner, S.C., Raines, M.A., Guthrie Jr., G.D., 2007. Analysis and performance of oil well cement with 30 years of CO2 exposure from the SACROC Unit, West Texas, USA. Int. J. Greenhouse Gas Control 1 (1), 75–85.

Carroll, S., Carey, J.W., Dzombak, D., Huerta, N.J., Li, L., Richard, T., Um, W., Walsh, S. D.C., Zhang, L., 2016. Review: Role of chemistry, mechanics, and transport on well integrity in CO2 storage environments. Int. J. Greenhouse Gas Control 49, 149–160.

Chalbaud, C., Robin, M., Lombard, J.M., Martin, F., Egermann, P., Bertin, H., 2009. Interfacial tension measurements and wettability evaluation for geological CO_2 storage. Adv. Water Resour. 32 (1), 98–109.

Cherkaoui, A., Lopez, P., 2009. CO2 storage risk assessment: feasibility study of the systemic method MOSAR. In: WIT Transactions on The Built Environment, 108, pp. 173–184.

Chiaramonte, L., Zoback, M.D., Friedmann, J., Stamp, V., 2008. Seal integrity and feasibility of CO 2 sequestration in the Teapot Dome EOR pilot: geomechanical site characterization. Environ. Geol. 54 (8), 1667–1675.

Chiaramonte, L., Zoback, M., Friedmann, J., Stamp, V., Zahm, C., 2011. Fracture characterization and fluid flow simulation with geomechanical constraints for a CO_2–EOR and sequestration project Teapot Dome Oil Field, Wyoming, USA. Energy Proc. 4, 3973–3980.

Choi, Y.-S., Young, D., Nešić, S., Gray, L.G., 2013. Wellbore integrity and corrosion of carbon steel in CO2 geologic storage environments: a literature review. Int. J. Greenhouse Gas Control 16, S70–S77.

Chopra, S., Huffman, A.R., 2006. Velocity determination for pore-pressure prediction. Lead. Edge 25 (12), 1502–1515.

Cinar, Y., Riaz, A., 2014. Carbon dioxide sequestration in saline formations: part 2—review of multiphase flow modeling. J. Pet. Sci. Eng. 124, 381–398.

Cui, G., Zhang, L., Tan, C., Ren, S., Zhuang, Y., Enechukwu, C., 2017. Injection of supercritical CO2 for geothermal exploitation from sandstone and carbonate reservoirs: CO2–water–rock interactions and their effects. J. CO2 Util. 20, 113–128.

Cui, G., Zhu, L., Zhou, Q., Ren, S., Wang, J., 2021. Geochemical reactions and their effect on CO2 storage efficiency during the whole process of CO2 EOR and subsequent storage. Int. J. Greenhouse Gas Control 108, 103335.

Daniel, R., Kaldi, J., 2008. Evaluating seal capacity of caprocks and intraformational barriers for the geosequestration of CO_2. In: Eastern Australasian Basins Symposium (3rd: 2008: Sydney, Australia). Petroleum Exploration Society of Australia, pp. 475–484.

Das, I., Zoback, M.D., 2013. Long-period, long-duration seismic events during hydraulic stimulation of shale and tight-gas reservoirs—part 1: Waveform characteristics. Geophysics 78 (6), KS97–KS108.

De Lary, L., Manceau, J.C., Loschetter, A., Rohmer, J., Bouc, O., Gravaud, I., Chiaberge, C., Willaume, P., Yalamas, T., 2015. Quantitative risk assessment in the early stages of a CO2 geological storage project: implementation of a practical approach in an uncertain context. Greenhouse Gas. 5 (1), 50–63.

De Lima, V., Einloft, S., Ketzer, J.M., Jullien, M., Bildstein, O., Petronin, J.-C., 2011. CO2 Geological storage in saline aquifers: Paraná Basin caprock and reservoir chemical reactivity. Energy Proc. 4, 5377–5384.

De Silva, G.P.D., Ranjith, P.G., Perera, M.S.A., 2015. Geochemical aspects of CO_2 sequestration in deep saline aquifers: a review. Fuel 155, 128–143.

Deel, D., Mahajan, K., Mahoney, C.R., McIlvried, H.G., Srivastava, R.D., 2007. Risk assessment and management for long-term storage of CO2 in geologic formations-United States Department of Energy R&D. Syst. Cybernet. Inform. 5 (1), 79–84.

Donaldson, E.C., Thomas, R.D., Lorenz, P.B., 1969. Wettability determination and its effect on recovery efficiency. Soc. Pet. Eng. J. 9 (01), 13–20.

Emberley, S., Hutcheon, I., Shevalier, M., Durocher, K., Gunter, W., Perkins, E., 2004. Geochemical monitoring of fluid-rock interaction and CO2 storage at the Weyburn CO2-injection enhanced oil recovery site, Saskatchewan, Canada. Energy 29 (9–10), 1393–1401.

Ennis-King, J., Paterson, L., 2007. Coupling of geochemical reactions and convective mixing in the long-term geological storage of carbon dioxide. Int. J. Greenhouse Gas Control 1 (1), 86–93.

Erickson, K.P., Lempp, C., Pöllmann, H., 2015. Geochemical and geomechanical effects of $scCO_2$ and associated impurities on physical and petrophysical properties of Permotriassic Sandstones (Germany): an experimental approach. Environ. Earth Sci. 74 (6), 4719–4743.

Espinoza, D.N., Kim, S.H., Santamarina, J.C., 2011. CO_2 geological storage — geotechnical implications. KSCE J. Civ. Eng. 15 (4), 707–719.

Evans, B., Saeedi, A., Rasouli, V., Liu, K., Lebedev, M., 2012. Predicting CO_2 Injectivity Properties for Application at CCS Sites. Curtin University, Australia.

Fatah, A., Bennour, Z., Mahmud, H.B., Gholami, R., Hossain, M., 2021a. Surface wettability alteration of shales exposed to CO2: implication for long-term integrity of geological storage sites. Int. J. Greenhouse Gas Control 110, 103426.

Fatah, A., Mahmud, H.B., Bennour, Z., Hossain, M., Gholami, R., 2021b. Effect of supercritical CO2 treatment on physical properties and functional groups of shales. Fuel 303, 121310.

Ferronato, M., Gambolati, G., Janna, C., Teatini, P., 2010. Geomechanical issues of anthropogenic CO_2 sequestration in exploited gas fields. Energy Convers. Manag. 51 (10), 1918–1928.

Fischer, S., Zemke, K., Liebscher, A., Wandrey, M., 2011. Petrophysical and petrochemical effects of long-term CO_2 -exposure experiments on brine-saturated reservoir sandstone. Energy Procedia 4 (0), 4487–4494.

Fu, P., Ju, X., Huang, J., Settgast, R.R., Liu, F., Morris, J.P., 2021. Thermo-poroelastic responses of a pressure-driven fracture in a carbon storage reservoir and the implications for injectivity and caprock integrity. Int. J. Numer. Anal. Methods Geomech. 45 (6), 719–737.

Garcia-Rios, M., Luquot, L., Soler, J.M., Cama, J., 2015. Influence of the flow rate on dissolution and precipitation features during percolation of CO_2-rich sulfate solutions through fractured limestone samples. Chem. Geol. 414, 95–108.

Gaus, I., 2010. Role and impact of CO_2–rock interactions during CO_2 storage in sedimentary rocks. Int. J. Greenhouse Gas Control 4 (1), 73–89.

Ghafoori, M., Tabatabaei-Nejad, S.A., Khodapanah, E., 2017. Modeling rock-fluid interactions due to CO2 injection into sandstone and carbonate aquifer considering salt precipitation and chemical reactions. J. Nat. Gas Sci. Eng. 37, 523–538.

Gharbi, O., Bijeljic, B., Boek, E., Blunt, M.J., 2013. Changes in pore structure and connectivity induced by CO_2 injection in carbonates: a combined Pore-Scale approach. Energy Proc. 37, 5367–5378.

Gheibi, S., Holt, R.M., Vilarrasa, V., 2017. Effect of faults on stress path evolution during reservoir pressurization. Int. J. Greenhouse Gas Control 63, 412–430.

Gholami, R., Raza, A., Andersen, P., Escalona, A., Cardozo, N., Marín, D., Sarmadivaleh, M., 2021. Long-term integrity of shaly seals in CO2 geo-sequestration sites: an experimental study. Int. J. Greenhouse Gas Control 109, 103370.

Received by OCD: 6/29/2026

Goodarzi, S., Settari, A., Keith, D., 2011. Geomechanical modeling for CO_2 storage in wabamun lake area of Alberta, Canada. Energy Procedia 4, 3399–3406.
Goodarzi, S., Settari, A., Zoback, M., Keith, D.W., 2013. Thermal effects on shear fracturing and injectivity during CO 2 storage. In: ISRM International Conference for Effective and Sustainable Hydraulic Fracturing. International Society for Rock Mechanics and Rock Engineering.
Gor, G.Y., Prévost, J.H., 2013. Effect of CO2 injection temperature on caprock stability. Energy Proc. 37, 3727–3732.
Gor, G.Y., Elliot, T.R., Prévost, J.H., 2013. Effects of thermal stresses on caprock integrity during CO2 storage. Int. J. Greenhouse Gas Control 12, 300–309.
Govindan, R., Babaei, M., Korre, A., Shi, J.-Q., Durucan, S., Norden, B., Kempka, T., 2014. CO2 storage uncertainty and risk assessment for the post-closure period at the Ketzin pilot site in Germany. Energy Proc. 63, 4758–4765.
Graham, J., Richardson, J., 1959. Theory and application of imbibition phenomena in recovery of oil. J. Pet. Technol. 11 (02), 65–69.
Green, C.P., Ennis-King, J., 2010. Effect of vertical heterogeneity on long-term migration of CO 2 in saline formations. Transp. Porous Media 82 (1), 31–47.
Gunter, W., Wiwehar, B., Perkins, E., 1997. Aquifer disposal of CO 2-rich greenhouse gases: extension of the time scale of experiment for CO 2-sequestering reactions by geochemical modelling. Mineral. Petrol. 59 (1–2), 121–140.
Gunter, W.D., Perkins, E.H., Hutcheon, I., 2000. Aquifer disposal of acid gases: modelling of water–rock reactions for trapping of acid wastes. Appl. Geochem. 15 (8), 1085–1095.
Hadian, P., Rezaee, R., 2020. The effect of supercritical CO2 on Shaly Caprocks. Energies 13 (1), 149.
Han, W.S., Stillman, G.A., Lu, M., Lu, C., McPherson, B.J., Park, E., 2010. Evaluation of potential nonisothermal processes and heat transport during CO2 sequestration. J. Geophys. Res. 115 (B7).
Hangx, S., Spiers, C., Peach, C., 2010. Creep of simulated reservoir sands and coupled chemical-mechanical effects of CO_2 injection. J. Geophys. Res. 115 (B9), 1–23.
Hangx, S., van der Linden, A., Marcelis, F., Bauer, A., 2013. The effect of CO_2 on the mechanical properties of the captain sandstone: geological storage of CO_2 at the Goldeneye Field (UK). Int. J. Greenhouse Gas Control 19 (0), 609–619.
Hangx, S., Bakker, E., Bertier, P., Nover, G., Busch, A., 2015. Chemical–mechanical coupling observed for depleted oil reservoirs subjected to long-term CO_2-exposure – a case study of the Werkendam natural CO_2 analogue field. Earth Planet. Sci. Lett. 428, 230–242.
He, M., Luis, S., Rita, S., Ana, G., Euripedes, V., Zhang, N., 2011. Risk assessment of CO2 injection processes and storage in carboniferous formations: a review. J. Rock Mech. Geotech. Eng. 3 (1), 39–56.
Hemme, C., van Berk, W., 2017. Change in cap rock porosity triggered by pressure and temperature dependent CO2–water–rock interactions in CO2 storage systems. Petroleum 3 (1), 96–108.
Hergert, T., Heidbach, O., Reiter, K., Giger, S., Marschall, P., 2015. Stress field sensitivity analysis in a sedimentary sequence of the Alpine foreland, northern Switzerland. Solid Earth 6 (2), 533–552.
Hermanrud, C., Simmenes, T., Hansen, O.R., Eiken, O., Teige, G.M.G., Johansen, S., Bolaas, N., Marit, H., Hansen, H., 2013. Importance of pressure management in CO_2 storage. In: Offshore Technology Conference, 6-9 May, Houston, Texas, USA, pp. 1–4.
Herzog, H., Drake, E., Adams, E., 1997. CO_2 Capture, Reuse, and Storage Technologies for Mitigating Global Climate Change. A White Paper, pp. 1–70.
Hirakawa, E., Ma, S., 2016. Dynamic fault weakening and strengthening by gouge compaction and dilatancy in a fluid-saturated fault zone. J. Geophys. Res. 121 (8), 5988–6008.
Huerta, N.J., Hesse, M.A., Bryant, S.L., Strazisar, B.R., Lopano, C.L., 2013. Experimental evidence for self-limiting reactive flow through a fractured cement core: implications for time-dependent wellbore leakage. Environ. Sci. Technol. 47 (1), 269–275.
Huq, F., Haderlein, S.B., Cirpka, O.A., Nowak, M., Blum, P., Grathwohl, P., 2015. Flow-through experiments on water–rock interactions in a sandstone caused by CO_2 injection at pressures and temperatures mimicking reservoir conditions. Appl. Geochem. 58, 136–146.
Hurter, S., Berge, J.G., Labregere, D., 2007. Simulations for CO2 injection projects with compositional simulator. In: SPE Offshore Europe Oil and Gas Conference and Exhibition. Society of Petroleum Engineers.
IEA, 2009. Greenhouse Gas R&D Programme (IEA GHG), "Long Term Integrity of CO2 Storage – Well Abandonment".
IEAGHG, 2011. Caprock System for CO2 Geological Storage.
Iglauer, S., 2011. Dissolution trapping of carbon dioxide in reservoir formation brine-a carbon storage mechanism. Mass Transfer (Nakajima H), ijeka: InTech 2011.
Iglauer, S., 2017. CO2–water–rock wettability: variability, influencing factors, and implications for CO2 geostorage. Acc. Chem. Res. 50 (5), 1134–1142.
Iglauer, S., 2018. Optimum storage depths for structural CO2 trapping. Int. J. Greenhouse Gas Control 77, 82–87.
Iglauer, S., Paluszny, A., Pentland, C.H., Blunt, M.J., 2011. Residual CO_2 imaged with X-ray micro-tomography. Geophys. Res. Lett. 38 (21), 1–6.
Iglauer, S., Pentland, C.H., Busch, A., 2015. CO_2 wettability of seal and reservoir rocks and the implications for carbon geo-sequestration. Water Resour. Res. 51 (1), 729–774.
IPCC, 2005. IPCC special report on carbon dioxide capture and storage. In: Prepared by Working Group III of the Intergovernmental Panel on Climate Change, Cambridge, United Kingdom and New York, NY, USA.
IPCC, 2007. In: Metz, B., et al. (Eds.), Climate Change 2007: Mitigation of Climate Change: Contribution of Working III to the Fourth Assessment Report of the Intergovernmental Panel on Climate Change. Cambridge University Press, Cambridge, United Kingdom and New York, United States.
Izgec, O., Demiral, B., Bertin, H., Akin, S., 2008. CO_2 injection into saline carbonate aquifer formations I: laboratory investigation. Transp. Porous Media 72 (1), 1–24.
Jeanne, P., Rutqvist, J., Dobson, P.F., Walters, M., Hartline, C., Garcia, J., 2014. The impacts of mechanical stress transfers caused by hydromechanical and thermal processes on fault stability during hydraulic stimulation in a deep geothermal reservoir. Int. J. Rock Mech. Min. Sci. 72, 149–163.
Ju, X., Fu, P., Settegast, R., Morris, J., 2021. A Simple Method to Simulate Thermo-hydro-mechanical Processes in Leakoff-dominated 1 Hydraulic Fracturing With Application to Geological Carbon Storage 2.
Kaldi, J., Atkinson, C., 1997. Evaluating Seal Potential: Example From the Talang Akar Formation, Offshore Northwest Java, Indonesia. Memoirs-American Association Of Petroleum Geologists, pp. 85–102.
Kaldi, J., Daniel, R., Tenthorey, E., Michael, K., Schacht, U., Nicol, A., Underschultz, J., Backe, G., 2013. Containment of CO_2 in CCS: role of caprocks and faults. Energy Proc. 37 (0), 5403–5410.
Kempka, T., De Lucia, M., Kühn, M., 2014. Geomechanical integrity verification and mineral trapping quantification for the Ketzin CO_2 storage pilot site by coupled numerical simulations. Energy Proc. 63, 3330–3338.
Ketter, F., 1991. The Esmond, Forbes and Gordon Fields, Blocks 43/8a, 43/13a, 43/15a, 43/20a, UK North Sea. Geol. Soc. Lond. Mem. 14 (1), 425–432.
Kim, S., Hosseini, S.A., 2014. Geological CO_2 storage: incorporation of pore-pressure/stress coupling and thermal effects to determine maximum sustainable pressure limit. Energy Proc. 63, 3339–3346.
Kim, C., Lee, J., 2017. Experimental study on the variation of relative permeability due to clay minerals in low salinity water-flooding. J. Pet. Sci. Eng. 151, 292–304.
Kivior, T., Kaldi, J., Lang, S., 2002. Seal potential in cretaceous and late Jurassic rocks of the Vulcan sub-basin, North West Shelf Australia. APPEA J. 42 (1), 203–224.
Korre, A., Durucan, S., 2009. A Review of the International State of the Art in Risk Assessment Guidelines and Proposed Terminology for Use in CO2 Geological Storage. Imperial College London: IEA GHG R&D Programme.
Kovscek, A.R., 2002. Screening criteria for CO_2 storage in oil reservoirs. Pet. Sci. Technol. 20 (7–8), 841–866.
Lagneau, V., Pipart, A., Catalette, H., 2005. Reactive transportmodelling and long term behaviour of CO2 sequestration in saline aquifers. Oil Gas Sci. Technol. 60 (2), 231–247.
Larkin, P., Leiss, W., Krewski, D., 2019. Risk assessment and management frameworks for carbon capture and geological storage: a global perspective. Int. J. Risk Assess. Manag. 22 (3–4), 254–285.
Le Guen, Y., Renard, F., Hellmann, R., Brosse, E., Collombet, M., Tisserand, D., Gratier, J. P., 2007. Enhanced deformation of limestone and sandstone in the presence of high fluids. J. Geophys. Res. 112 (B5), 1–21.
Le Van, S., Chon, B.H., 2017. Effects of salinity and slug size in miscible CO2 water-alternating-gas core flooding experiments. J. Ind. Eng. Chem. 52, 99–107.
Li, Q., Liu, G., 2016. Risk assessment of the geological storage of CO 2: a review. Geol. Carbon Sequestr. 249–284.
Li, B., Liu, C., Lu, Q., Pang, S., 2016. Modeling CO2 vertical migration based on seismic frequency-dependent AVO responses. J. Geophys. Eng. 13 (2), 164–171.
Li, D., Ren, S., Rui, H., 2019. CO2 leakage behaviors in typical Caprock–Aquifer system during geological storage process. ACS Omega 4 (18), 17874–17879.
Liebscher, A., Möller, F., Bannach, A., Köhler, S., Wiebach, J., Schmidt-Hattenberger, C., Weiner, M., Pretschner, C., Ebert, K., Zemke, J., 2013. Injection operation and operational pressure–temperature monitoring at the CO2 storage pilot site Ketzin, Germany—design, results, recommendations. Int. J. Greenhouse Gas Control 15, 163–173.
Lu, M., Connell, L.D., 2008. Non-isothermal flow of carbon dioxide in injection wells during geological storage. Int. J. Greenhouse Gas control 2 (2), 248–258.
Luo, Z., Bryant, S., Meckel, T., 2013. Application of improved injection well temperature model to Cranfield measurements. Energy Proc. 37, 4128–4135.
Lynch, T., Fisher, Q., Angus, D., Lorinczi, P., 2013. Investigating stress path hysteresis in a CO_2 injection scenario using coupled geomechanical-fluid flow modelling. Energy Proc. 37, 3833–3841.
Ma, B., Cao, Y., Zhang, Y., Eriksson, K.A., 2020. Role of CO2-water-rock interactions and implications for CO2 sequestration in Eocene deeply buried sandstones in the Bonan Sag, eastern Bohai Bay Basin, China. Chem. Geol. 541, 119585.
Mangini, S.A., 2015. An Investigation of the Reactions of Supercritical CO 2 and Brine With the Berea Sandstone, Muscovite, and Iron Bearing Minerals. Montana State University-Bozeman, College of Letters & Science.
Marbler, H., Erickson, K.P., Schmidt, M., Lempp, C., Pöllmann, H., 2012. Geomechanical and geochemical effects on sandstones caused by the reaction with supercritical CO_2: an experimental approach to in situ conditions in deep geological reservoirs. Environ. Earth Sci. 69 (6), 1981–1998.
Marbler, H., Erickson, K.P., Schmidt, M., Lempp, C., Pöllmann, H., 2013. Geomechanical and geochemical effects on sandstones caused by the reaction with supercritical CO 2: an experimental approach to in situ conditions in deep geological reservoirs. Environ. Earth Sci. 69 (6), 1981–1998.
Mathias, S.A., Gluyas, J.G., Oldenburg, C.M., Tsang, C.-F., 2010. Analytical solution for Joule–Thomson cooling during CO2 geo-sequestration in depleted oil and gas reservoirs. Int. J. Greenhouse Gas Control 4 (5), 806–810.
Maxwell, S., 2014. Microseismic Imaging of Hydraulic Fracturing: Improved Engineering of Unconventional Shale Reservoirs. Society of Exploration Geophysicists.
Mildren, S.D., Hillis, R.R., Lyon, P.J., Meyer, J.J., Dewhurst, D.N., Boult, P.J., 2005. FAST: A New Technique for Geomechanical Assessment of the Risk of Reactivation-related Breach of Fault Seals.
Miocic, J.M., Johnson, G., Bond, C.E., 2019. Uncertainty in fault seal parameters: implications for CO2 column height retention and storage capacity in geological CO2 storage projects. Solid Earth 10 (3), 951–967.

Received by OCD: 6/29/2026

Miri, R., Hellevang, H., 2016. Salt precipitation during CO_2 storage—a review. Int. J. Greenhouse Gas Control 51, 136–147.
Mito, S., Xue, Z., Ohsumi, T., 2008. Case study of geochemical reactions at the Nagaoka CO2 injection site, Japan. Int. J. Greenhouse Gas Control 2 (3), 309–318.
Mouzakis, K.M., Navarre-Sitchler, A.K., Rother, G., Bañuelos, J.L., Wang, X., Kaszuba, J. P., Heath, J.E., Miller, Q.R., Alvarado, V., McCray, J.E., 2016. Experimental study of porosity changes in shale caprocks exposed to CO2-saturated brines I: evolution of mineralogy, pore connectivity, pore size distribution, and surface area. Environ. Eng. Sci. 33 (10), 725–735.
Nakanishi, T., Lang, S.C., 2002. Towards an efficient exploration frontier: constructing a portfolio of stratigraphic traps in fluvial-lacustrine successions, Cooper-Eromanga Basin. APPEA J. 42 (1), 131–150.
Nelson, C.R., 2005. Factors Affecting the Potential for CO2 Leakage From Geologic Sinks.
Noiriel, C., Luquot, L., Madé, B., Raimbault, L., Gouze, P., Van Der Lee, J., 2009. Changes in reactive surface area during limestone dissolution: an experimental and modelling study. Chem. Geol. 265 (1), 160–170.
Nuñez-Lopez, V., Muñoz-Torres, J., Zeidouni, M., 2014. Temperature monitoring using distributed temperature sensing (DTS) technology. Energy Proc. 63, 3984–3991.
Olabode, A., Radonjic, M., 2014. Shale caprock/acidic brine interaction in underground CO2 storage. J. Energy Resour. Technol. 136 (4).
Olden, P., Pickup, G., Jin, M., Mackay, E., Hamilton, S., Somerville, J., Todd, A., 2012. Use of rock mechanics laboratory data in geomechanical modelling to increase confidence in CO_2 geological storage. Int. J. Greenhouse Gas Control 11, 304–315.
Oldenburg, C.M., Bryant, S.L., Nicot, J.-P., 2009. Certification framework based on effective trapping for geologic carbon sequestration. Int. J. Greenhouse Gas Control 3 (4), 444–457.
Ott, H., Pentland, C.H., Oedai, S., 2015a. CO_2–brine displacement in heterogeneous carbonates. Int. J. Greenhouse Gas Control 33, 135–144.
Ott, H., Roels, S.M., de Kloe, K., 2015b. Salt precipitation due to supercritical gas injection: I. Capillary-driven flow in unimodal sandstone. Int. J. Greenhouse Gas Control 43, 247–255.
Ouellet, A., Bérard, T., Desroches, J., Frykman, P., Welsh, P., Minton, J., Pamukcu, Y., Hurter, S., Schmidt-Hattenberger, C., 2011. Reservoir geomechanics for assessing containment in CO_2 storage: a case study at Ketzin, Germany. Energy Proc. 4, 3298–3305.
Pan, P., Wu, Z., Feng, X., Yan, F., 2016. Geomechanical modeling of CO_2 geological storage: a review. J. Rock Mech. Geotech. Eng. 8 (6), 936–947.
Paterson, L., Ennis-King, J.P., Sharma, S., 2010. Observations of thermal and pressure transients in carbon dioxide wells. In: SPE Annual Technical Conference and Exhibition. Society of Petroleum Engineers.
Pokrovsky, O.S., Golubev, S.V., Schott, J., 2005. Dissolution kinetics of calcite, dolomite and magnesite at 25 °C and 0 to 50 atm pCO2. Chem. Geol. 217 (3), 239–255.
Raza, A., Gholami, R., 2019. Introduction to carbon dioxide capture and storage. In: Inamuddin, A.M. Asiri, Lichtfouse, E. (Eds.), Sustainable Agriculture Reviews 37: Carbon Sequestration Vol. 1 Introduction and Biochemical Methods. Springer International Publishing, Cham, pp. 1–11.
Raza, A., Rezaee, R., Gholami, R., Rasouli, V., Bing, C.H., Nagarajan, R., Hamid, M.A., 2015. Injectivity and quantification of capillary trapping for CO_2 storage: a review of influencing parameters. J. Nat. Gas Sci. Eng. 26, 510–517.
Raza, A., Gholami, R., Sarmadivaleh, M., Tarom, N., Rezaee, R., Bing, C.H., Nagarajan, R., Hamid, M.A., Elochukwu, H., 2016a. Integrity analysis of CO_2 storage sites concerning geochemical-geomechanical interactions in saline aquifers. J. Nat. Gas Sci. Eng. 36PA, 224–240.
Raza, A., Rezaee, R., Gholami, R., Bing, C.H., Nagarajan, R., Hamid, M.A., 2016b. A screening criterion for selection of suitable CO2 storage sites. J. Nat. Gas Sci. Eng. 28, 317–327.
Raza, A., Gholami, R., Rabiei, M., Rasouli, V., Rezaee, R., Fakhari, N., 2019. Impact of geochemical and geomechanical changes on CO2 sequestration potential in sandstone and limestone aquifers. Greenhouse Gas. 9 (5), 905–923.
Raza, A., Gholami, R., Sarmadivaleh, M., 2020. Feasibility of limestone reservoirs as a carbon dioxide storage site: an experimental study. AAPG Bull. 104 (1), 83–96.
Reinsch, T., Henninges, J., Ásmundsson, R., 2013. Thermal, mechanical and chemical influences on the performance of optical fibres for distributed temperature sensing in a hot geothermal well. Environ. Earth Sci. 70 (8), 3465–3480.
Renard, F., Mair, K., Gundersen, O., 2012. Surface roughness evolution on experimentally simulated faults. J. Struct. Geol. 45, 101–112.
Rimmelé, G., Barlet-Gouédard, V., Renard, F., 2010. Evolution of the petrophysical and mineralogical properties of two reservoir rocks under thermodynamic conditions relevant for CO2 geological storage at 3 km depth. Oil Gas Sci. Technol. 65 (4), 565–580.
Ringrose, P., 2020. CO 2 Storage Project Design, How to Store CO2 Underground: Insights From Early-mover CCS Projects. Springer, pp. 85–126.
Ringrose, P., Thorsen, R., Zweigel, P., Nazarian, B., Furre, A.-K., Paasch, B., Thompson, N., Karstad, P., 2017. Ranking and Risking Alternative CO2 Storage Sites Offshore Norway, Fourth Sustainable Earth Sciences Conference. European Association of Geoscientists & Engineers, pp. 1–5.
Rochelle, C., Bateman, K., Pearce, J., 2002. Geochemical interactions between supercritical CO_2 and the Utsira Formation: an experimental study. In: British Geological Survey Report CR/02/060: 57.
Rosenbrand, E., Haugwitz, C., Jacobsen, P.S.M., Kjøller, C., Fabricius, I.L., 2014. The effect of hot water injection on sandstone permeability. Geothermics 50, 155–166.
Rutqvist, J., 2012. The geomechanics of CO_2 storage in deep sedimentary formations. Geotech. Geol. Eng. 30 (3), 525–551.
Rutqvist, J., Birkholzer, J., Cappa, F., Tsang, C.F., 2007. Estimating maximum sustainable injection pressure during geological sequestration of CO_2 using coupled fluid flow and geomechanical fault-slip analysis. Energy Convers. Manag. 48 (6), 1798–1807.
Rutqvist, J., Birkholzer, J.T., Tsang, C.-F., 2008. Coupled reservoir–geomechanical analysis of the potential for tensile and shear failure associated with CO_2 injection in multilayered reservoir–caprock systems. Int. J. Rock Mech. Min. Sci. 45 (2), 132–143.
Rutqvist, J., Vasco, D.W., Myer, L., 2010. Coupled reservoir-geomechanical analysis of CO2 injection and ground deformations at In Salah, Algeria. Int. J. Greenhouse Gas Control 4 (2), 225–230.
Rutqvist, J., Rinaldi, A.P., Cappa, F., Jeanne, P., Mazzoldi, A., Urpi, L., Guglielmi, Y., Vilarrasa, V., 2016. Fault activation and induced seismicity in geological carbon storage–lessons learned from recent modeling studies. J. Rock Mech. Geotech. Eng. 8 (6), 789–804.
Salimzadeh, S., Paluszny, A., Zimmerman, R.W., 2018. Effect of cold CO2 injection on fracture apertures and growth. Int. J. Greenhouse Gas Control 74, 130–141.
Schowalter, T.T., 1979. Mechanics of secondary hydrocarbon migration and entrapment. AAPG Bull. 63 (5), 723–760.
Schwind, B., Payne, M., Otten, G., Pattillo, P., 2001. Development of leak resistance in industry standard OCTG connections using finite element analysis and full scale testing. In: Offshore Technology Conference.
Seyyedi, M., Mahmud, H.K.B., Verrall, M., Giwelli, A., Esteban, L., Ghasemiziarani, M., Clennell, B., 2020. Pore structure changes occur during CO2 injection into carbonate reservoirs. Sci. Rep. 10 (1), 3624.
Shi, J.-Q., Durucan, S., 2009. A coupled reservoir-geomechanical simulation study of CO_2 storage in a nearly depleted natural gas reservoir. Energy Proc. 1 (1), 3039–3046.
Shi, J.-Q., Smith, J., Durucan, S., Korre, A., 2013. A coupled reservoir simulation-geomechanical modelling study of the CO_2 injection-induced ground surface uplift observed at Krechba, in Salah. Energy Proc. 37, 3719–3726.
Shiraki, R., Dunn, T.L., 2000. Experimental study on water–rock interactions during CO2 flooding in the Tensleep Formation, Wyoming, USA. Appl. Geochem. 15 (3), 265–279.
Shukla, R., Ranjith, P., Haque, A., Choi, X., 2010. A review of studies on CO_2 sequestration and caprock integrity. Fuel 89 (10), 2651–2664.
Singh, H., Islam, A., 2018. Enhanced safety of geologic CO_2 storage with nanoparticles. Int. J. Heat Mass Transf. 121, 463–476.
Solomon, S., 2006. Criteria for Intermediate Storage of Carbon Dioxide in Geological Formations. The Bellona Foundation, Oslo, pp. 1–6.
Stearns, D.W., Friedman, M., 1972. Reservoirs in Fractured Rock: Geologic Exploration Methods.
Sterpenich, J., Sausse, J., Pironon, J., Géhin, A., Hubert, G., Perfetti, E. and Grgic, D., 2009. Experimental ageing of oolitic limestones under CO_2 storage conditions: petrographical and chemical evidence. Chem. Geol., 265(1–2): 99–112.
Talabani, S., Atlas, B., Al-Khatiri, M., Islam, M., 2000. An alternate approach to downhole corrosion mitigation. J. Pet. Sci. Eng. 26 (1–4), 41–48.
Tambach, T.J., Koenen, M., Wasch, L.J., van Bergen, F., 2015. Geochemical evaluation of CO_2 injection and containment in a depleted gas field. Int. J. Greenhouse Gas Control 32 (0), 61–80.
Teletzke, G.F., Lu, P., 2013. Guidelines for reservoir modeling of geologic CO2 storage. Energy Proc. 37, 3936–3944.
Thanh, H.V., Sugai, Y., Sasaki, K., 2020. Application of artificial neural network for predicting the performance of CO 2 enhanced oil recovery and storage in residual oil zones. Sci. Rep. 10 (1), 1–16.
Tillner, E., Shi, J.-Q., Bacci, G., Nielsen, C.M., Frykman, P., Dalhoff, F., Kempka, T., 2014. Coupled dynamic flow and geomechanical simulations for an integrated assessment of CO_2 storage impacts in a saline aquifer. Energy Proc. 63, 2879–2893.
Tiong, M., Gholami, R., Abid, K., Rahman, M.E., 2020. Nanomodification: an efficient method to improve cement integrity in CO2 storage sites. J. Nat. Gas Sci. Eng. 84, 103612.
Tucker, O., Holley, M., 2013. Containment Risk Management for CO2 Storage in the Goldeneye Depleted Gas Field, UK North Sea.
Umar, B.A., Gholami, R., Raza, A., Downey, W.S., Sarmadivaleh, M., Shah, A.A., Nayak, P., 2019. A study on the surface wettability of clastic rocks with potential application for CO2 storage sites. Nat. Resour. Res. 29 (3), 2051–2061.
Underschultz, J., Boreham, C., Dance, T., Stalker, L., Freifeld, B., Kirste, D., Ennis-King, J., 2011. CO_2 storage in a depleted gas field: an overview of the CO2CRC Otway Project and initial results. Int. J. Greenhouse Gas Control 5 (4), 922–932.
USEPA, 1994. Determination of Maximum Injection Pressure for Class I Wells. United States Environmental Protection Agency.
Varre, S.B.K., Siriwardane, H.J., Gondle, R.K., Bromhal, G.S., Chandrasekar, V., Sams, N., 2015. Influence of geochemical processes on the geomechanical response of the overburden due to CO_2 storage in saline aquifers. Int. J. Greenhouse Gas Control 42, 138–156.
Vavra, C.L., Kaldi, J.G., Sneider, R.M., 1992. Geological applications of capillary pressure: a review. AAPG Bull. 76 (6), 840–850.
Vidal-Gilbert, S., Tenthorey, E., Dewhurst, D., Ennis-King, J., Van Ruth, P., Hillis, R., 2010. Geomechanical analysis of the Naylor Field, Otway Basin, Australia: implications for CO_2 injection and storage. Int. J. Greenhouse Gas Control 4 (5), 827–839.
Vilarrasa, V., Laloui, L., 2016. Impacts of thermally induced stresses on fracture stability during geological storage of CO2. Energy Proc. 86, 411–419.
Vilarrasa, V., Rutqvist, J., 2017. Thermal effects on geologic carbon storage. Earth Sci. Rev. 165, 245–256.
Vilarrasa, V., Silva, O., Carrera, J., Olivella, S., 2013. Liquid CO2 injection for geological storage in deep saline aquifers. Int. J. Greenhouse Gas Control 14, 84–96.
Vilarrasa, V., Rinaldi, A.P., Rutqvist, J., 2017. Long-term thermal effects on injectivity evolution during CO2 storage. Int. J. Greenhouse Gas Control 64, 314–322.

Received by OCD: 6/29/2026

Viswanathan, H.S., Pawar, R.J., Stauffer, P.H., Kaszuba, J.P., Carey, J.W., Olsen, S.C., Keating, G.N., Kavetski, D., Guthrie, G.D., 2008. Development of a hybrid process and system model for the assessment of wellbore leakage at a geologic CO2 sequestration site. Environ. Sci. Technol. 42 (19), 7280–7286.

Walters, R.J., Zoback, M.D., Baker, J.W., Beroza, G.C., 2015. Characterizing and responding to seismic risk associated with earthquakes potentially triggered by fluid disposal and hydraulic fracturing. Seismol. Res. Lett. 86 (4), 1110–1118.

Washburn, E.W., 1921. The dynamics of capillary flow. Phys. Rev. 17 (3), 273.

Wigand, M., Carey, J., Schütt, H., Spangenberg, E., Erzinger, J., 2008. Geochemical effects of CO2 sequestration in sandstones under simulated in situ conditions of deep saline aquifers. Appl. Geochem. 23 (9), 2735–2745.

Wigand, M., Kaszuba, J.P., Carey, J.W., Hollis, W.K., 2009. Geochemical effects of CO2 sequestration on fractured wellbore cement at the cement/caprock interface. Chem. Geol. 265 (1–2), 122–133.

Wilday, J., Paltrinieri, N., Farret, R., Hebrard, J., Breedveld, L., 2011. Carbon capture and storage: a case study of emerging risk issues in the iNTeg-Risk project, 22. In: Hazards Symposium" Process Safety and Environmental Protection". ICHEME. NC, pp. 339–346.

Winthaegen, P., Arts, R., Schroot, B., 2005. Monitoring subsurface CO2 storage. Oil Gas Sci. Technol. 60 (3), 573–582.

Xiao, T., McPherson, B., Esser, R., Jia, W., Dai, Z., Chu, S., Pan, F., Viswanathan, H., 2020. Chemical impacts of potential CO2 and brine leakage on groundwater quality with quantitative risk assessment: a case study of the farnsworth unit. Energies 13 (24), 6574.

Xu, T., Apps, J.A., Pruess, K., 2005. Mineral sequestration of carbon dioxide in a sandstone–shale system. Chem. Geol. 217 (3–4), 295–318.

Yielding, G., 2015. Trapping of buoyant fluids in fault-bound structures. Geol. Soc. Lond., Spec. Publ. 421 (1), 29–39.

You, J., Ampomah, W., Sun, Q., 2020. Development and application of a machine learning based multi-objective optimization workflow for CO2-EOR projects. Fuel 264, 116758.

Yu, X., Ahmadinia, M., Shariatipour, S.M., Lawton, D., Osadetz, K., Saeedfar, A., 2019. Impact of Reservoir Permeability, Permeability Anisotropy and Designed Injection Rate on CO 2 Gas Behavior in the Shallow Saline Aquifer at the CaMI Field Research Station, Brooks, Alberta. Natural Resources Research, pp. 1–18.

Zemke, K., Liebscher, A., Wandrey, M., 2010. Petrophysical analysis to investigate the effects of carbon dioxide storage in a subsurface saline aquifer at Ketzin, Germany (CO2 SINK). Int. J. Greenhouse Gas Control 4 (6), 990–999.

Zhang, M., Bachu, S., 2011. Review of integrity of existing wells in relation to CO2 geological storage: what do we know? Int. J. Greenhouse Gas Control 5 (4), 826–840.

Zhang, L., Dzombak, D., Kutchko, B., 2015a. Wellbore cement integrity under geologic carbon sequestration conditions. Novel Mater. CO 2.

Zhang, Y., Langhi, L., Schaubs, P., Delle Piane, C., Dewhurst, D., Stalker, L., Michael, K., 2015b. Geomechanical stability of CO_2 containment at the South West Hub Western Australia: a coupled geomechanical–fluid flow modelling approach. Int. J. Greenhouse Gas Control 37, 12–23.

Zhang, Y., Lebedev, M., Sarmadivaleh, M., Barifcani, A., Iglauer, S., 2016a. Change in geomechanical properties of limestone due to supercritical CO_2 injection. In: SPE Asia Pacific Oil & Gas Conference and Exhibition. Society of Petroleum Engineers, 25–27 October, Perth, Australia, pp. 1–10.

Zhang, Y., Sarmadivaleh, M., Lebedev, M., Barifcani, A., Rezaee, R., Testamantia, N., Iglauer, S., 2016b. Geo-mechanical weakening of limestone due to supercritical CO_2 injection. In: Offshore Technology Conference, 22–25 March, Kuala Lumpur, Malaysia, pp. 1–8.

Zhao, R., Cheng, J., 2015. Non-isothermal modeling of CO 2 injection into saline aquifers at a low temperature. Environ. Earth Sci. 73 (9), 5307–5316.

Zhu, C., Zhang, G., Lu, P., Meng, L., Ji, X., 2015a. Benchmark modeling of the Sleipner CO2 plume: calibration to seismic data for the uppermost layer and model sensitivity analysis. Int. J. Greenhouse Gas Control. 3, 233–246.

Zhu, Q., Zuo, D., Zhang, S., Zhang, Y., Wang, Y., Wang, L., 2015b. Simulation of geomechanical responses of reservoirs induced by CO_2 multilayer injection in the Shenhua CCS project, China. Int. J. Greenhouse Gas Control 42, 405–414.

EXHIBIT 14

Received by OCD: 6/29/2026

An update to this article is included at the end

Science of the Total Environment 967 (2025) 178746

Contents lists available at ScienceDirect

Science of the Total Environment

journal homepage: www.elsevier.com/locate/scitotenv

Data-driven estimates of undocumented orphan oil and gas wells with implications to the environment

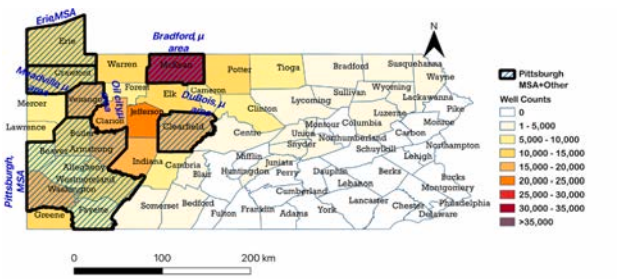
Ismot Jahan [a], Mohamed Mehana [a,*], Mary Kang [b], Jade Boutot [b], Andrew Govert [c], Dan O'Malley [a], Hari S. Viswanathan [a]

[a] Energy and Natural Resources Security Group (EES-16), Earth and Environmental Sciences Division, Los Alamos National Laboratory, Los Alamos, NM 87545, United States
[b] Department of Civil Engineering, McGill University, Montreal, Quebec H3A 0C3, Canada
[c] Methane Mitigation Technologies Division, Office of Fossil Energy Carbon Management, Department of Energy, United States

HIGHLIGHTS

- A novel workflow estimates number of wells drilled in a state through its lifetime.
- It estimates undocumented orphan and unplugged non-producing wells in PA and OK.
- The geospectral distribution of wells is crucial for prioritizing areas in future.
- Our estimated wells emit 14 times more methane than IOGCC's estimate for all states.

GRAPHICAL ABSTRACT



Spatial distribution of the estimated undocumented wells highlighting potential area for future analysis and surveys to seal these wells

ARTICLE INFO

Editor: Bo Gao

Keywords:
Orphan wells
Abandoned wells
Unplugged wells
Oil and gas
Methane
Environmental impacts
Health risks

ABSTRACT

The historical extraction of natural gas and oil in the United States (U.S.) has led to the drilling of millions of wells since the inception of the Drake oil well in Pennsylvania in 1859. A significant portion of these wells remain undocumented, posing potential risks to public health, safety, and the environment due to their unknown locations and conditions. To address this issue, we developed a methodology to estimate the number and spatial distribution of undocumented orphan wells (UOWs) at the state and county levels, leveraging publicly accessible historical well and production data. Applying this methodology to Pennsylvania and Oklahoma, we identified approximately 340,827 UOWs in Pennsylvania and 309,462 in Oklahoma, considering underreporting and enhanced oil recovery activities. We also highlight specific counties, such as Osage and Creek County in Oklahoma and McKean County in Pennsylvania, with over 30,000 UOWs in each county. We validated our results with proprietary databases (Pennsylvania Department of Environmental Protection (PA DEP) historical well and Enverus) and a previous aeromagnetic survey, which found at least two UOWs for every documented well in three large areas of western Pennsylvania. Our method could estimate UOWs nationwide, supporting the initiation of state and federal programs to mitigate health risks from these wells.

Synopsis

* Corresponding author.
E-mail address: mzm@lanl.gov (M. Mehana).

https://doi.org/10.1016/j.scitotenv.2025.178746
Received 1 June 2024; Received in revised form 11 December 2024; Accepted 3 February 2025
Available online 16 February 2025
0048-9697/© 2025 Elsevier B.V. All rights are reserved, including those for text and data mining, AI training, and similar technologies.

Received by OCD: 6/29/2026

Legacy wells cause severe environmental pollution and health risks to the U.S. This study proposes a workflow to locate these wells at the county level and mitigate those risks.

1. Introduction

American oil and gas exploration commenced in 1859, with the first well drilled in north-western Pennsylvania (Eno Petroleum, 2024). Over 170 years, the industry's growth reached 12 million barrels per day of crude oil and 120 billion standard cubic feet per day of natural gas by September 2022 (U.S. Energy Information Administration, 2023), which resulted in millions of non-producing oil and gas wells scattered across the United States (U.S.). Unplugged non-producing wells (UNpWs) are wells that are currently not producing oil or gas and are not plugged (or sealed, typically with cement). Some UNpWs are orphaned wells (OWs) with insolvent operators or no available responsible party (Grove and Merrill, 2022). The exact number of OWs is currently unknown, limiting our ability to plug and remediate them and assess their impacts. It is important to determine the number of UNpWs since they are currently unplugged and non-producing and potential OW candidates.

Two types of OWs exist documented orphan wells (DOWs) and undocumented orphan wells (UOWs). DOWs have government records confirming their existence, while UOWs lack such records, and need identification and/or further verification. Since UOWs have no paper trace, innovative technologies are required to locate and characterize them. According to the Interstate Oil and Gas Compact Commission (IOGCC), the number of UOWs across the U.S. is between 300,000–800,000 (Interstate Oil and Gas Compact Commission, 2021). However, the IOGCC number of UOWs is based on expert opinion and there remain no data-driven estimates of UOW numbers for the U.S. UOWs and UNpWs pose significant environmental (Kang et al., 2023; Schout et al., 2019) and health risks, including emissions of methane and other air pollutants (El Hachem and Kang, 2022; Williams et al., 2021; Riddick et al., 2024; Cooper et al., 2022; Gurevich et al., 1993), and release toxic substances like volatile organic compounds, hydrogen sulfide, benzene, and arsenic, posing threats to soil, water quality, thereby increasing health risks to nearby populations (Li et al., 2016; Lebel et al., 2020). Methane, the second-highest greenhouse gas emitter in the U.S. after CO_2, is considered a "short-lived climate forcer", exerting 80 times the warming effect of CO_2 over 20 years and oil and gas sector is one of the highest producers of methane (U.S. Environmental Protection Agency, 2022).

To address methane and other environmental issues associated with OWs, in 2022, the U.S. federal government allocated $4.7 billion through the Bipartisan Infrastructure Law (U.S. Department of Interior, 2022). The Consortium Advancing Technology for Assessment of Lost Oil & Gas (CATALOG) is formed by five Department of Energy (DOE) laboratories. It focuses on identifying the physical locations, methane emissions, wellbore integrity, and environmental impacts of OWs so that state and federal agencies can prioritize plugging and remediation of these wells (CATALOG, 2024).

In this study, we establish a workflow to estimate the number of UNpWs and UOWs at the state and county levels using historical well and production data. We highlighted its implication to the environment by estimating the methane emission for these wells and correlated that with a high number of patients due to air pollution. In the background section, we summarize the ongoing efforts of different organizations to identify OWs. Next, we briefly describe how boomtowns emerged, corresponding to drilling activities in Pennsylvania and Oklahoma. Because the role of rules and regulations highly impacted the reported number of drilled wells over time, we provide an overview in the Regulations Impacting Well Reporting. The Materials and Method section describes the data sources and methods used to estimate the number of UNpWs, UOWs, methane emissions from these wells, the impact on human health, and the Social Cost of Methane (SC-CH_4). The results and validation are described in the Result section. Our innovative method allows us to estimate UNpWs- and UOWs-per-county for Oklahoma and Pennsylvania with the impact on the environment and human health by combining historical well and production data, current state databases, and partial regional distribution of existing and historical wells. This workflow adapts to challenges associated with missing data, considering the influence of rules and regulations during different periods, which previous studies have not considered. An estimate of UNpWs and UOWs can also inform strategies for identifying physical locations. For example, aerial-based surveys for well finding are in active development and an efficient strategy (Raimi et al., 2021; de Smet et al., 2020; Saint-Vincent et al., 2021; Nikulin and de Smet, 2019), and the application of these technologies requires spatial distributions of UNpW and UOW similar to this paper.

2. Background

In the background analysis, we explain the various terminologies used by different agencies to identify DOWs and discuss the databases that estimate DOWs. This section also covers the temporal variation in DOW numbers. The boomtown analysis explores the history of oil and gas development in Pennsylvania and Oklahoma, which is crucial for understanding the missing well counts and determining the underreporting factor in our method. Additionally, we analyze past regulations that significantly impacted well-reporting in the regulation affecting the well reporting section.

2.1. Databases and temporal variation in DOW numbers

Different states use diverse terminology, such as "shut in," "deserted," "potentially deserted," "temporarily abandoned," "abandoned," "potential orphan," "orphan pending," "forfeited," and "unknown," making nationwide OWs identification complex. For some states, it is not possible to identify DOWs using databases and records and numbers of DOWs need to be requested directly from the states. Therefore, a state-by-state approach is needed for the compilation of DOWs.

There are different approaches to counting the number of OWs by state. For example, Boutot et al., 2022 only compiled DOWs with state records, including a few wells without detailed location information. On the other hand, estimates from the IOGCC are based on state surveys and can be based on expert opinion (Interstate Oil and Gas Compact Commission, 2021), especially for estimates made after the announcement of BIL funding (whitehouse.gov., 2021). Furthermore, there are states that did not participate in the IOGCC survey. Importantly, these OW counts are limited to DOWs and omit UOWs.

For DOWs, databases have been compiled from state and government-owned public databases, which provide well attributes like location and depth. A McGill University and Environment Defence Fund (EDF) study collected data from online state databases, revealing 81,857 DOWs in September 2021 and 123,318 DOWs in April 2022, signifying a nearly 50 % increase in six months (Boutot et al., 2022). The 123,318 DOWs, as of April 2022, constitute 3 % of all estimated abandoned wells (about 4 million) for 2022 in the U.S. (U.S. Environmental Protection Agency, 2022). Moreover, the IOGCC reported 92,198 DOWs as of Dec 31, 2020 and 131,227 DOWs as of Nov 15, 2021 (Interstate Oil and Gas Compact Commission, 2021). Overall, DOW numbers have varied and will continue to vary, with new wells being orphaned and plugged over time.

Received by OCD: 6/29/2026

2.2. History of oil and gas development (boomtown analysis)

A boomtown emerges when there is a sudden surge in oil and gas activities, leading to rapid population growth. Examining the historical evolution of oil and gas fields in a state offers insights into their development and production history, particularly in areas heavily impacted by past drilling activities. While unconventional reservoirs now dominate U.S. oil and gas production, boomtown counties often indicate regions where numerous OWs may be found due to past reliance on conventional extraction methods. With limited historical digital records and few regulations governing well documentation, determining the total number of wells drilled within a state is challenging. To address this, our workflow estimates historical well counts in Pennsylvania and Oklahoma by considering underreporting and enhanced recovery (ER) factors, estimated based on boomtown appearances and the evolution of laws and regulations. This context helps determine the best data source for estimating historical well numbers when multiple sources are available for a specific year within a state.

2.2.1. Pennsylvania

The initial well, also known as the "Drake Well", drilled in 1859 in Titusville, Pennsylvania, marked the beginning of the first U.S. oil boom (Smith, 2021). The Oil Creek area, approximately 90 miles north of Pittsburgh, including Venango and Crawford County along the Allegheny River, saw the onset of this historic boom (Smith, 2021). Following Drake's pioneering efforts, the region around Titusville and Venango County underwent a radical transformation for the next 90 years. It changed from a wooded wilderness to a landscape adorned with oil derricks and bustling boomtowns. "Pennsylvania crude" set the standard for oil quality throughout the 19th and 20th centuries (Pennsylvania Historical and Museum Commission, 1997). In 1860, Erie County in Pennsylvania revealed the state's first gas field along Lake Erie, where natural gas was abundant at depths ranging from 450 to 1200 ft (Erie's History and Memorabilia, 2015). Over the following 40 years, Pennsylvania's oil fields expanded, covering over 150 miles along Oil Creek and its tributaries in the Allegheny Valley, encompassing around 2000 mile^2, including Crawford, Butler, Clarion, and Armstrong County (Eby, 2009). In the first decade of oil production, Venango County dominated, while Erie County led in gas production (Pennsylvania Historical and Museum Commission, 1997). By 1870, Pennsylvania produced over 5.4 million barrels of oil annually, with gas production information unavailable (Pennsylvania Historical and Museum Commission, 1997). In 1860, oil was discovered in Cherry Grove, Warren County, centralizing around Tidioute, giving rise to boomtowns until 1882 (Miller, 1952). The Smith's Ferry Field in Beaver County saw wells drilled from 1860 to 1875, initially producing 25 barrels/day in 1910 (Armler, 1976). By the early 20th century, the Economy Oil Field in the same county peaked at 45,000 barrels/day in 1910 (Armler, 1976). These fields sustained significant oil production until the emergence of the Bradford Oil Field, altering Pennsylvania's production curve by millions of barrels.

The giant Bradford Oil Field, spanning 85,000 acres in McKean County, saw its first producing well drilled in 1864 (Harper, 2013). By 1880, the Bradford Oil District had 4000 wells generating 50,000 barrels/day (The McKean County Planning Comm, 1982). Alongside the main Bradford Field, additional fields like Burning Well, Windfall, Marvin, Creek, Guffy, Moody, Hollow, West Branch, and East Kinzua had opened by 1880 (The McKean County Planning Comm, 1982). The Kane area fields (Kane – 1881, Cooper – 1882) were developed shortly after that, reaching 11,200 producing wells by the end of 1881 (The McKean County Planning Comm, 1982). That year, Bradford Field achieved an all-time peak production of 23 million barrels of oil. By 1884, it became the most prolific oil field globally, producing 681 million barrels of crude oil in its lifetime (Armler, 1976).

Around 1869, the oil fervor in western Pennsylvania started to shift south to the lower oil region (Parker's Landing), encompassing Clarion, Armstrong, and Butler County (Greco, 2020). Subsequently, Butler County experienced significant production in the Thorn Creek Stream area, contributing 37 million barrels between 1870 and 1880 (History of Butler County Pennsylvania, 1895a). The county also boasts substantial gas reserves, producing since 1872, with some wells yielding up to 12 million cubic feet/day (History of Butler County Pennsylvania, 1895b) In 1878, exploration near Pittsburgh led to the Haymaker brothers discovering natural gas in Murrysville, 18 miles east of the city, with an estimated daily production of 30 million cubic feet, creating the iconic "Roaring Torch" flame and laying the groundwork for modern petroleum companies (Wells and Wells, 2015). Other nearby counties, including Indiana County, played a pivotal role, contributing to Pennsylvania's highest-ever annual oil output of 32 million barrels in 1891 (Wintermantel, 2012). By 1909, Indiana County became the second-largest producer in the state (Wintermantel, 2012). Washington County, another significant producer, discovered the Gantz and Gordon Sands in 1884, peaking at 20,000 barrels/day (Washington, 2020). The McDonald Oil Field, founded in 1890, set world-leading production levels in 1891–1892, yielding the highest oil production levels in the world (Wintermantel, 2012). Greene County has maintained oil and gas production since 1886, drilling over 1300 wells between 1890 and 1905 (Stone and Clapp, 1907). Elk County contributed to the Kane Field in 1885, situated at the corners of Elk, McKean, Forest, and Warren County (Pennsylvania Historical and Museum Commission, 1997). Mercer, Lawrence, Clearfield, Cameron, Clinton, Potter, Tioga, and Jefferson counties also witnessed gas discoveries between 1887 and 1920 (paroots, 1939). Although gas was produced in several counties, it was not significant compared to oil production in the past century (Stephens, 2016).

2.2.2. Oklahoma

Oklahoma has been a major oil producer for over a century. Between 1900 and 1935, it was ranked the top oil producer among U.S. states, producing over 906 million barrels of oil and ranked first in nine years (Franks, 2023). The first oil well was drilled in 1859 by Lewis Ross (Franks, 2023), but commercial production began in 1897 in Bartlesville-Dewey Field, Washington County, which produced >100,000 barrels of oil during its lifetime (Knight, 2016). Initial production was modest, such as the Red Fork Field in Tulsa County, yielding only 50 barrels/day in 1901 (Weaver, 2023a). However, the Cherokee Shallow Sands at the Alluwe Field (Nowata County) and Cleveland Field (Pawnee County) in 1904 drew nationwide attention (Weaver, 2023b). By the late 1920s–1930s, over one-third of Oklahoma's wells were in Nowata County (Craun, 2020). Rogers County discovered gas in Cherokee Sand in 1906, with wells producing from depths <1000 ft (Craun, 2020). In subsequent years, Oklahoma's ascent to the top U.S. oil producer occurred with significant discoveries in Creek, Osage, Okfuskee and neighbouring counties. Creek County hosts two of Oklahoma's major oil fields. The first significant oil play, Glenn Pool, discovered in 1905, spanned Tulsa and Creek Counties (Weaver, 2023c). It rapidly grew from 80 to 8000 acres in the first year, leading to a large-scale oil boom in the state (Weaver, 2023c). Glenn Pool's production reached 20 million barrels/year in 1907, surpassing 43 million barrels/year, making Oklahoma the global oil leader (Weaver, 2023c). Another major field, the Cushing-Drumright Oil Field, in Payne, Creek, and Lincoln County, began production in 1912, contributing 3 % to the world's oil by 1919, peaking at 310 thousand barrels/day in 1917 (Franks, 2023). Concurrently, the Osage oil discoveries in Bartlesville, Hominy, Fairfax, Grainola, Pawhuska, and Burbank areas, along with >36 Osage Oil Fields by 1930, solidified Tulsa as the "Oil Capital of the World" (Wells and Wells, 2014; Bass et al., 1941; Bone, 2023). Osage, Creek, Washington, Nowata, Pawnee, Lincoln, and Tulsa experienced intensive drilling due to these discoveries (Bass et al., 1941). Despite this, other counties also played a role in achieving Oklahoma's maximum historical production in subsequent years.

By 1911, Ponca City in Kay County emerged as a significant oil hub

Received by OCD: 6/29/2026

with 12 separate Oil fields (May, 2023). The Burbank Field, discovered in 1920, saw major operations by Conoco, Phillips, and Sinclair, producing over 31 million barrels in 1920 (May, 2023). The Tonkawa-Three Sand Field, active from 1920, consistently yielded 23 to 28 million barrels annually from 1923 to 1925 (Weaver, 2023d). Carter County played a vital role in Oklahoma's oil history, with Healdton Field starting production in 1913 and Hewitt Field in 1919, becoming among the state's most productive fields (Franks, 2023). In 1917, Garber Field in Garfield County opened and emerged as one of Oklahoma's largest producing areas, with oil and gas extracted from 11 intervals (Gish and Carr, 1929). These discoveries collectively contributed to Oklahoma reaching its peak annual production of 278 million barrels (762,000 bbls/day) in 1927 (Boyd, 2002).

Oklahoma was a leading oil and gas producer in the past, exemplified by the enduring Hugoton-Guymon Gas Field, which has been producing for over 100 years since its inception in 1920 (Carr and Sawin, 1996). Spanning Kansas, Oklahoma (Beaver and Texas County), and Texas, it remains one of the nation's largest natural gas discoveries (Carr and Sawin, 1996). In the 1920s, the Greater Seminole Field marked significant oil and gas discoveries, with five of the state's largest oil finds in 1926–27 located in parts of Pottawatomie, Okfuskee, Hughes, and Pontotoc County, yielding 150–200 million barrels of oil/year from July 1926 to September 1929 (Weaver, 2023e). Oklahoma City was followed by a colossal discovery in 1928, producing over 735 million barrels of oil and 2 trillion cubic feet of gas through 1969, ranking among the world's giant oil and gas fields (Mariner, 2020).

The provided tables (Table SI-1-2) offer information on oil fields, associated counties, and the initial production year for those counties in Pennsylvania and Oklahoma. Our boomtown analysis reveals that the Bradford Field in McKean County played a dominant role during peak production in Pennsylvania, with significant waterflooding wells drilled in the 1930s. In Oklahoma, Osage, Creek, and Okfuskee Counties boast multiple major oil fields and numerous smaller ones, likely correlating with higher numbers of UOWs in the spatial distribution section. This boomtown analysis is pivotal for providing context in evaluating the data sources per county from the multiple databases in the spectral analysis and adjusting underreporting factors to estimate total drilled wells.

2.3. Regulations impacting well reporting

Regulations impacting well-reporting and databases vary among states and have evolved with time. In the early years of oil and gas development, the legal concept of the “rule of capture” in Oklahoma and many other states, including Pennsylvania, encouraged extensive drilling to maximize production (Dancy and Dancy, 1986). This resulted in numerous wells drilled side by side in a common reservoir, contributing to the underreporting of well numbers until new regulations mandated well registration before drilling (Dancy and Dancy, 1986).

The plugging of legacy wells is tied to developing the modern petroleum industry and introducing effective well-cementing technology, which then became incorporated in regulations and led to well reporting. While the first attempt to use Portland cement for isolation was reported in 1903, the first proven cementing system for zonal isolation emerged in 1916 (King and Daniel, 2013). In Pennsylvania, the law for real estate purchaser protection, established in 1925 under 21 P.S. 351, stipulates that any interest in real estate not recorded is deemed invalid concerning a subsequent purchaser without notice of the interest or claim, which promoted to increase reporting of oil and gas wells in their property in Pennsylvania (Burnett, 2023). Standardization of plugging procedures and cement composition by the American Petroleum Institute occurred in 1952 (King and Daniel, 2013). In Pennsylvania, Act 225, the Gas Operations Well Drilling, Petroleum and Coal Mining Act, passed on November 30, 1955, and set drilling standards and mandated well registration from 1957 onwards (Carter et al., 2011).

Established in 1907, OCC initially focused on regulating monopolistic practices of railroads and telegraph lines in the newly formed state (Bass Law, 2023). While it plays a significant role in overseeing the oil and gas industry in Oklahoma, this was not its original mandate (Dancy and Dancy, 1986). In 1919, the Railroad Commission of Texas enacted the first well-spacing rule in the U.S. (Dancy and Dancy, 1986). The resolution of a Texas-Oklahoma boundary dispute in June 1924 improved reporting in shared oil and gas fields (Short, 1924). Oklahoma introduced well-density regulation in May 1929 through a city ordinance in Oklahoma City, which occurred later in 1931, restricting drilling to specific areas within city limits (Dancy and Dancy, 1986). The subsequent “Well Spacing Act” of 1935 empowered the Commission to create drilling and spacing units (Dancy and Dancy, 1986). To enforce this law, forced pooling was introduced in 1945 and a separate law was passed named “Senate Bill 190” in 1947, later codified as 52 O.S. Section 87.1 (Bass Law, 2023), which set limits on the number of wells and mandated drilling permits. Though the bill passed in 1947, the data from OCC does not specify the well type (oil, gas or dry) for each well before 1957 (Oklahoma Corporate Commission, 2010). Hence, a complete report of the well type and well locations was found for both states in 1957.

3. Methods

This study comprehensively examines well drilling activities in Pennsylvania and Oklahoma while considering past underreporting and the role of enhanced recovery (ER) wells to estimate the number of UNpWs and UOWs. Since we aim to identify UNpWs, we consider all oil and gas wells drilled, including dry and ER wells. We did not include storage, test, observation, and waste disposal wells due to data limitations for years before 1957. For years after 1957, we assume that these other well types are included in modern digital records. Here, we discuss the estimation of the numbers of UNpWs and UOWs and their spatial distribution, validate the results based on past studies and existing databases. Here, we outline several crucial assumptions and key data sources used in this methodology.

3.1. Key assumptions and data sources associated with methodology

In this section, we highlight the key assumptions and data sources underlying the methodology.

(a) Currently, there is no consistent data-driven method for estimating the number of UOWs applicable to all producing states across the U.S. Therefore, the goal of this research is to establish a straightforward workflow that can be uniformly applied to all oil and gas-producing states. This is a key responsibility of the CATALOG consortium and is essential for prioritizing and allocating DOE funding to various states.
(b) To develop our methodology, we rely on a study by Dilmore et al. (2015) for Pennsylvania, which uses well counts from Arnold and Kemnitzer (1931) as the primary source for annual well completion data from 1859 to 1929. This dataset includes over 160 K historical wells predating 1930, as listed in Table 1. Additionally, we use the spatial distribution of these wells to estimate spatial patterns for Pennsylvania.
(c) After developing the workflow in Pennsylvania, we implement it to estimate the number of UOWs in Oklahoma using drilled well counts from the Oklahoma Corporation Commission's 2010 annual report, which covers the period from 1904 to 2010 (Oklahoma Corporate Commission, 2010).
(d) A key component of this workflow for estimating the number of UOWs is the underreporting factor, which ranges from 1.3 to 2, and the waterflooding wells factor, which ranges from 1.5 to 2. These factors adjust well counts for specific time periods (Tables 1 and 2) based on the timeline of various rules and regulations (Section 2.3) and insights from reports by the

Received by OCD: 6/29/2026

Table 1
Estimated number of UNpWs and UOWs in Pennsylvania, including ER wells and potential historical underreporting.

Year(s)	Number	Source/laws on effect (regulations impacting well reporting)	Incl. ER wells		Underreporting	
			Factor 1	Number	Factor 2	Number
1859–1924	156,749	Arnold & Kemnitzer (no laws)	1	156,749	2	313,498
1925–1928	11,448	Arnold & Kemnitzer (real state purchaser protection under 21 P.S. 351)	2	22,896	1.3	29,765
1929	3600	Scaled for PA from Arnold & Kemnitzer data (real state purchaser protection under 21 P.S. 351)	2	7200	1.3	9300
1930–1937	28,253	Model 1919–1929 Arnold & Kemnitzer data (real state purchaser protection under 21 P.S. 351)	2	56,506	1.3	73,458
1938–1949	31,859	Model 1950–1959 PA DEP data (real state purchaser protection under 21 P.S. 351)	1	31,859	1.3	41,417
1950–1956	10,443	PA DEP (real state purchaser protection under 21 P.S. 351)	1	10,443	1.3	13,576
1957–2012	114,154	PA DEP (Act 225, mandatory reporting)	1	114,154	1	114,154
2013–2023	9790	PA DEP	1	9790	1	9790
TOTAL Well Drilled (1859–2023)	366,296			409,597		604,957
Active Wells (Dec 2023)	153,783	PA DEP		153,783		153,783
P&A (Dec 2023)	55,827	PA DEP		55,827		55,827
UNpWs	156,686			284,804		480,164
Total PADEP Drilled Well (Dec 2023)	264,130			264,130		264,130
Estimated UOWs	102,166			145,467		340,827
DOWs (Boutot et al., 2022)	18,513					

Table 2
Estimated number of UNpWs and UOWs in Oklahoma, including ER wells and potential historical underreporting.

Year(s)	Number	Source/laws on effect (regulations impacting well reporting)	Incl. ER wells		Underreporting	
			Factor 1	Number	Factor 2	Number
1891–1903	451	MILLS-BULLARD (1924) (no laws)	1	451	2	902
1904–1923	110,297	OCC-2010 report (no laws)	1	110,297	2	220,594
1924–1931	62,620	Model 1944–1953 OCC data) (TX-OK boundary dispute resolved)	1	62,620	1.8	112,716
1932–1943	58,889	Model 1944–1953 OCC data (OK City well density regulation)	1.5	88,334	1.3	114,834
1944–1946	7395	OCC (OK City well density regulation)	1.5	11,093	1.3	14,420
1947–1956	60,454	OCC (Senate Bill 190-mandatory reporting)	1.5	90,681	1	90,681
1957–2023	244,998	OCC	1	244,998	1	244,998
TOTAL Well Drilled (1891–2023)	545,104	Combined with Regression Analysis		608,473		799,145
Active Wells (Dec 2023)	156,427	OCC		156,427		156,427
P&A (Dec 2023)	257,757	OCC		257,757		257,757
UNpWs	130,920			194,289		384,961
OCC Well Database (Excluding Osage Wells - Dec 2023)	445,861			445,861		445,861
Osage Well Database (Dec 2023)	43,822			43,822		43,822
Total Well (OCC + Osage) (Dec 2023)	489,683			489,683		489,683
Estimated UOWs	55,421			118,790		309,462
DOWs (Boutot et al., 2022)	15,557					

Department of the Interior (Taliaferro and Logan, 1943) and multiple past studies (Harper, 2013; Kang et al., 2016; Mahmud et al., 2019; Pennsylvania Department of Environmental Protection, 2024b). Previous attempts (Dilmore et al., 2015; Kang et al., 2016) to estimate well counts in Pennsylvania did not adjust for rule effective dates, a unique feature of this workflow.

(e) For periods with unreliable historical data (1930–1937 and 1938–1949 in Pennsylvania) or conflicting trends between well production and wells drilled per year (1924–1943 in Oklahoma), we use production-drilling relationships from adjacent years, following the methodology of Kang et al. (2016), to fill these gaps. These production-drilling relationships are not used for any years outside these specified periods. It can be argued that wells typically continue producing at a declining rate over time, and current year production is influenced by wells drilled in previous years. Therefore, a predictive model based on year-over-year changes in production could more accurately estimate the number of wells drilled in a given year, which we plan to explore in future research.

(f) We understand that data is very limited before the 1950s, as there was no requirement to report wells in most states. Therefore, we assume that proportional under-reporting in historical data is consistent across all counties within a state.

(g) For validation, we use data from the PA DEP's mine map restoration projects, which includes over 30 K potential historic well locations but is limited to selected counties (Pennsylvania Department of Environmental Protection, 2024a). Additionally, we analyze well data from the Enverus database (Enverus, 2024). Since none of this data is used in the original estimation of UOWs, the validation dataset is completely independent.

In the following paragraphs, we provide further details on the estimation of the numbers of UNpWs and UOWs, their spatial distribution, and the validation of results based on past studies and existing databases.

(1) Estimation of the Numbers of UNpWs and UOWs: We provide a synthesis of historical and digital well records to reveal spatial trends in the number, location, and abandonment of wells in Pennsylvania and Oklahoma (Fig. 1), where 80 % of estimated UOWs are located according to the IOGCC (Interstate Oil and Gas Compact Commission, 2021).

Initially, data is collected from oil and gas regulatory agencies and historical reports, focusing on annual oil production and drilled well count. Gas production before 1957 is not considered due to its historical insignificance (<100–300 million cubic feet/year) compared to oil production in Pennsylvania and Oklahoma (U.S. Energy Information

Received by OCD: 6/29/2026

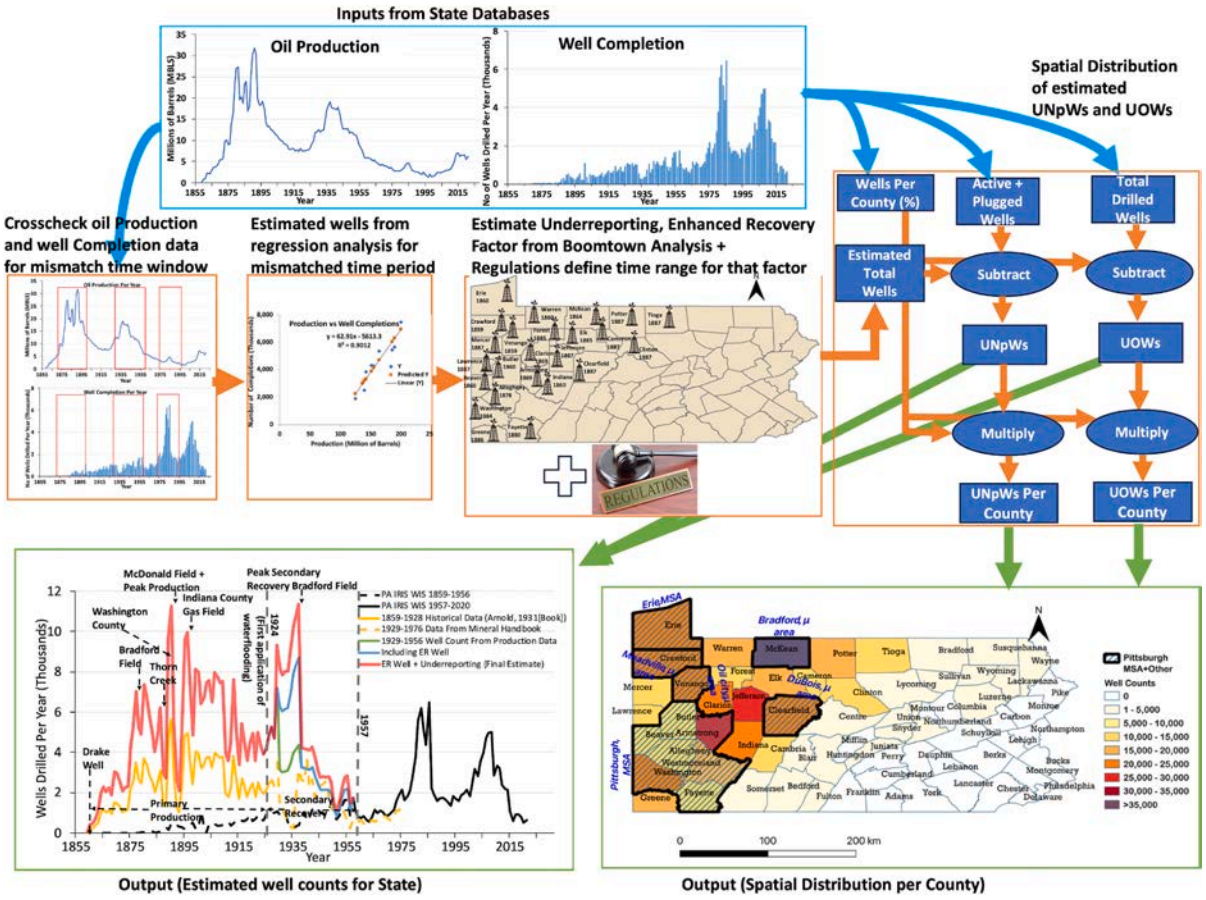


Fig. 1. Workflow for estimating a state's number of UNpWs and UOWs using historical and modern digital records. Different components of the workflow are identified with different colours where blue represents input data, green is the output and orange represent a process.

Administration, 2023). Additionally, the well type (i.e., oil and/or gas) is undefined in state records before 1957. We identify mismatches in drilled well count trends concerning production and use regression analysis to predict well counts for these years. Then, we estimate underreporting and ER well factors, considering the wells drilled in the boomtowns and the impact of laws and regulations over time. Regulations define distinct periods. Boomtown analysis elucidates the corresponding multiplying underreporting factors (2–1.3) for these periods and identifies relevant data sources for spatial analysis when multiple data sources are available for the same period. The mid-20th century marks significant changes in industry practices, regulations, and well-permitting requirements in the U.S., which guide our adjustment of drilled well counts, applying varying underreporting factors based in Pennsylvania (1859–1924, 1925–1957) and Oklahoma (1891–1923, 1924–1931, 1932–1946).

The annual well count is calculated by multiplying the underreporting and ER well factors with predicted wells from regression analysis in specific periods and from historical well records for the remaining periods (Table 1–2). The total annual well counts are summed over all years to determine a state's total drilled well count. For UNpW counts, we subtract active, intend-to-drill (terms like: "Operator reported not drilled", "Proposed but never materialized", "New Drill"), and plugged wells from estimated total drilled well counts. For UOW counts, we subtract all documented wells in state databases from our total drilled well counts. Hence, our estimated UOWs solely rely on historical well counts, regression analysis, underreporting, and ER factors.

(2) Spatial Distribution of UNpWs and UOWs: While existing IOGCC reports estimate UOWs in various states, such as Pennsylvania, Oklahoma, Texas, and California, they do not provide a localized spatial distribution of these wells below the state level. Here, we distribute our estimated UNpWs and UOWs to individual counties based on historical well-drilling per county. To enhance accuracy, boomtown information (Table SI-1-2) is employed when multiple datasets are available for a specific period and aid in determining the most reliable dataset for each county.

(3) Validation of Well Counts and Spatial Distribution of UNpWs and UOWs: We validate our spatial distributions and well counts in two different ways: (1) with a previous study (Sams et al., 2017) by National Energy Technology Laboratory (NETL) in Northern Pennsylvania for the overall count and (2) with existing database of PA DEP historical wells (Pennsylvania Department of Environmental Protection, 2024a) and Enverus (Enverus, 2024) database for spatial distribution.

4. Results

This section discusses the results from the processes mentioned in the method. Based on background studies, the first section provides detailed estimates of UNpWs and UOWs in Pennsylvania and Oklahoma. The following section distributes the total number of UNpWs and UOWs across different counties in these states with figures. Subsequent sections include figures and results that validate the total estimated well counts and their spatial distribution. Finally, the last two sections address the estimated methane emissions from UNpWs and UOWs and their impact on human health.

Received by OCD: 6/29/2026

4.1. Estimated number of UNpWs and UOWs

4.1.1. Pennsylvania

Incomplete records hinder the reconstruction of annual drilled wells for Pennsylvania before 1957 using state data alone. Following Dilmore et al. (2015), we use well counts from Arnold and Kemnitzer (1931) as a primary source for annual well completion information from 1859 to 1929. We have plotted the annual oil production and well completion data from the PA*IRIS/WIS digital data portal (PA Department of Environmental Protection, 2024b) and compared them to identify periods where the mismatched happened between the oil production and number of wells drilled each year. Three time periods for which the trend in oil production is not proportional to the trend in well completion numbers: (1) 1870–1900, (2) 1928–1958, and (3) 1970–1993 (Fig. 2).

The period (1859–1924, 1925–1957) for the underreporting factor is defined based on the laws impacting the reporting (discussed in the Regulations Impacting Well Reporting section), and the multiplication factor for these periods is determined from the historical analysis discussed here. During the first interval (1870–1900), oil production peaked at 32 million barrels in 1891 (Fig. 2a), while the well count was historically low (Fig. 2b). In this period, high oil production led to a significant number of wells drilled, suggesting substantial underreporting during this era, highlighted in the boomtown analysis. For instance, in the Bradford Field in 1881, over 7000 wells were drilled (Harper, 2013), but historical data (Arnold and Kemnitzer, 1931) reported only 3395 completed wells for the entire state. To address this underreporting, a multiplication factor of 2 (Table 1) is applied from 1859 to 1924.

Secondary oil production peaked in the second interval (1928–1958) (Fig. 2a), but well counts do not reflect it due to unreliable data sources. From 1930 to 1949, there was no reliable well count available, and thus, for these years, we have made estimates using oil production data and regression analysis. After 1929, there are records from sources like Oil Weekly Annual activity reports, Minerals Yearbooks, and Pennsylvania Division of Oil and Gas Annual Reports. Still, these records are often incomplete and poorly documented, lacking comprehensive state coverage and sometimes missing entire years of data (Dilmore et al., 2015). We have used a regression analysis model based on the previous or subsequent years' data to reconcile the mismatch in the oil production and the number of wells drilled trends. Following Kang's study (Kang et al., 2016), the interval is divided into 1930–1937 and 1938–1949. For 1930–1937, a linear relationship ($R^2 = 0.63$) between oil production and well numbers (Fig. 3a) was established using 1919–1929 data, estimating 28,253 wells (Kang et al., 2016). For 1938–1949, PA DEP (1950–1959) data predicted a linear relationship ($R^2 = 0.81$) (Fig. 3b), estimating 31,859 wells (Kang et al., 2016). The two regression models exhibit different slopes and intercepts due to the contrasting trends in production during their respective time windows: an increasing trend for the first regression model and a decreasing trend for the second one. Also, technological advancements in drilling and exploration contributed to increased production with fewer drilled wells during the second time interval (Fig. 3b). The adjustment of the underreporting factor to 1.3 during 1925–1956 is based on a comparison of well-drilling and oil production data (Fig. 2a) (1000–1800 wells are drilled per year between 1925 and 1956 compared to 200–800 wells in 1859–1924 despite the production is much lower than earlier time), reflecting over a 3-fold increase in reporting, leading to a reduction in the underreporting factor from 2 to 1.3.

Secondary recovery through waterflooding and ER wells started accidentally in Pithole, Pennsylvania, in 1865 (Mahmud et al., 2019). The first commercial waterflooding occurred in Bradford Field in 1924 and expanded to many fields in subsequent years (Mahmud et al., 2019). Data from 25 Bradford Field waterflooding projects showed ER wells to producing wells ratios ranging from 1.7 to 3.3, with a mean of 2.554 (Kang et al., 2016). However, the Bradford Field was heavily waterflooded in the early days compared to other fields in the vicinity (Harper, 2013). So, the estimated ER wells ratio of the entire state will be lower than the values of the Bradford Field. Given that waterflooding peaked between 1925 and 1937 (Fig. 4), and considering the Bradford Field's early emphasis, a factor of 2 (ER/producing wells = 1) is used to estimate the minimum number of waterflooding-associated wells for the entire state in that period (1925–1937). From 1938 onwards, no waterflooding factor was applied, as PA DEP data include ER wells (Pennsylvania Department of Environmental Protection, 2024b).

Adding ER wells and accounting for potential underreporting, we estimate the total number of wells drilled between 1859 and 2023 is 604,957 for Pennsylvania (Table 1, Fig. 4). We find UNpWs count is 480,164 and the number of UOWs is 340,827 (estimated well count (604,957) - PA DEP well database count (264,130)). Our estimate is conservative because we did not adjust for ER wells before 1924. The estimate of UOWs in Pennsylvania is in the range of IOGCC's UOWs of 100,000–560,000 (Interstate Oil and Gas Compact Commission, 2021).

4.1.2. Oklahoma

We use OCC data from the 2010 annual report for drilled well counts between 1904 and 2010 (Oklahoma Corporate Commission, 2010). As there is no year-by-year data in OCC reports from 1891 to 1903, we reference oil production and well completion numbers by year from Mills-Bullard published in 1924 (Mills-Bullard, 1924). We plotted the annual oil production and well completion data from the OCC portal (Oklahoma Corporate Commission, 2010) and compared them to identify periods where the mismatch happened between the oil production and the number of wells drilled each year. The period between 1924 and

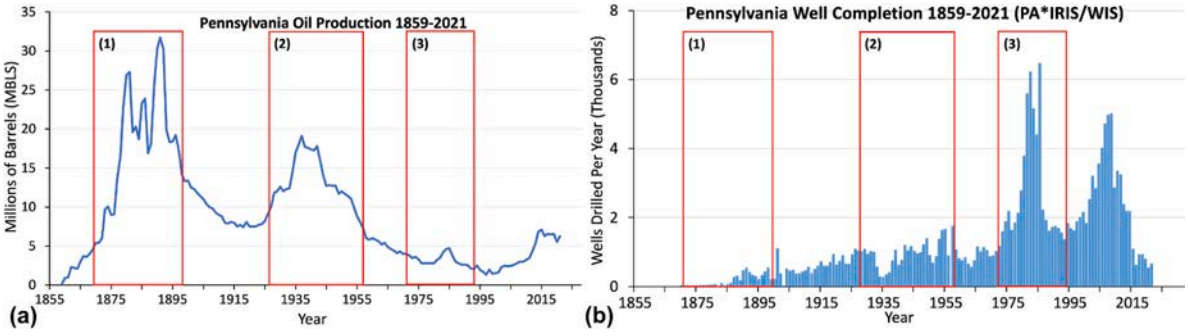


Fig. 2. (a) Oil production and (b) completed wells per year obtained from the PA*IRIS/WIS digital data portal (Pennsylvania Department of Environmental Protection, 2024b). The figures highlight three periods in red boxes: (1) 1870–1900, marked by a historical high in oil production but a historical low in well count; (2) 1928–1958, featuring a peak in secondary oil production, with an unreflective well count due to the absence of reliable digital data sources; and (3) 1970–1993, characterized by increased oil production but historically high well counts in digital records. Reconciling the mismatch between oil production and well counts in the first two intervals is necessary.

Received by OCD: 6/29/2026

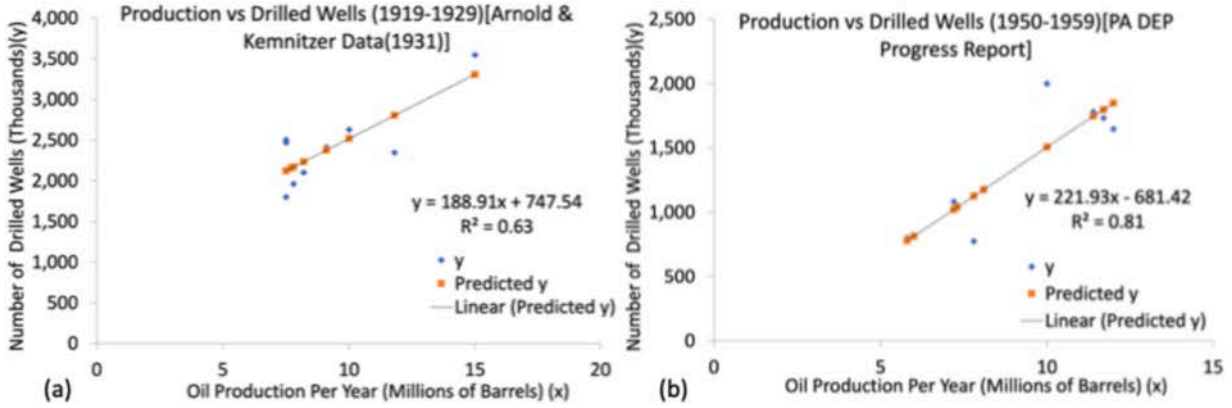


Fig. 3. Regression analysis for Pennsylvania oil production and well completion numbers from two historical sources (a) 1919–1929 and (b) 1950–1959 modified from Kang et al., 2016.

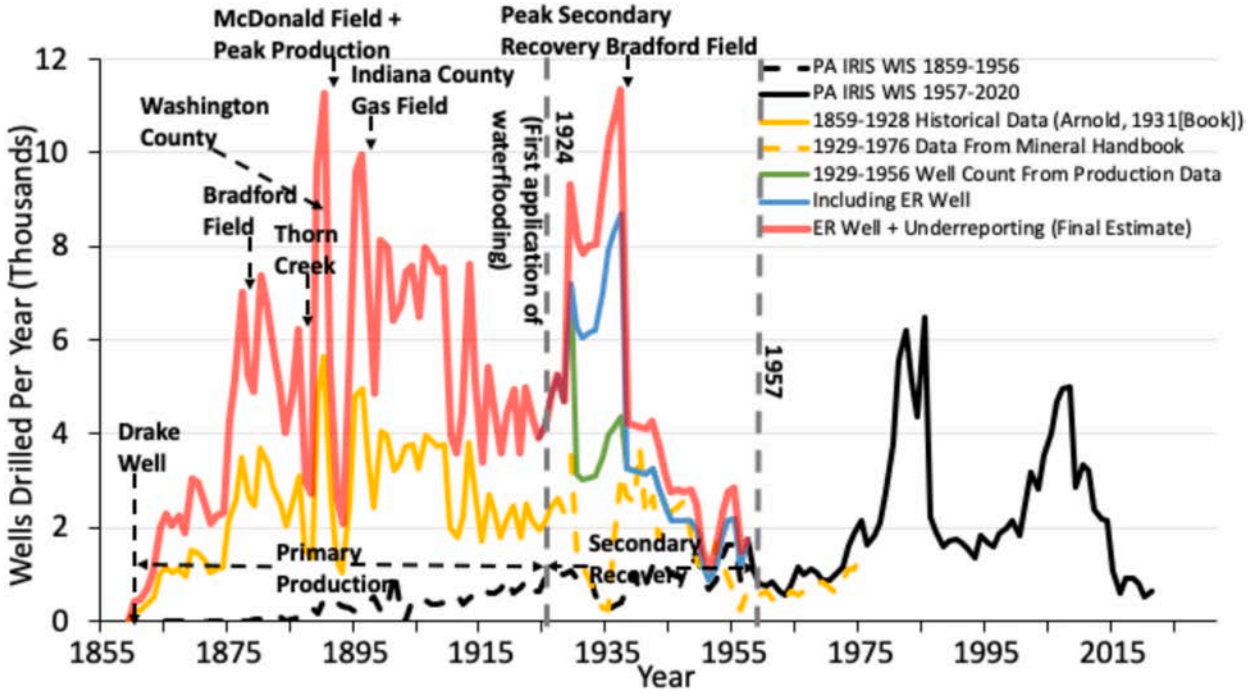


Fig. 4. Pennsylvania's yearly well drilling estimates, encompassing ER (waterflooding) wells (blue) and potential underreporting (red) from historical records, PA*IRIS/WIS digital data portal (Pennsylvania Department of Environmental Protection, 2024b) spanning 1859–2021 (solid and dotted black lines), and additional historical data (yellow and dotted yellow lines). The green curve illustrates well estimates derived from oil production using regression analysis. Noteworthy oil discoveries and historical events are indicated with black arrows.

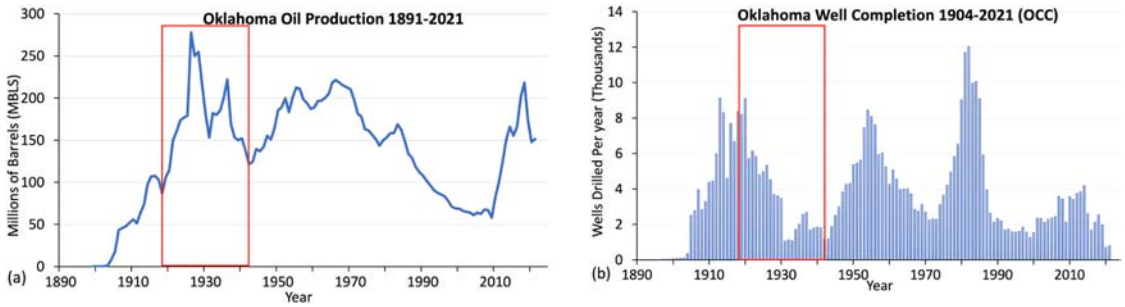


Fig. 5. (a) The oil production and (b) well completion per year from OCC summary report (Oklahoma Corporate Commission, 2010). In these two figures, the years between 1924 and 1943 are highlighted in red as the oil production is historically high, but the well count is historically low.

Received by OCD: 6/29/2026

1943 is non-consistent, with the trend in oil production not being proportional to the trend in well-completion numbers, and this needs to be readjusted. Oklahoma had the highest production of 278 million barrels of oil in 1927, but the drilled well count from the OCC dataset decreased when the production increased to a historical high (Fig. 5a). Discrepancies in well numbers between 1924 and 1943 are evident (red box in Fig. 5b), necessitating reconciliation with oil production using regression analysis. We have applied regression analysis to reconcile the discrepancies between the oil production and the number of wells drilled during this time. The OCC data indicated a linear relationship (R^2 = 0.90) between oil production and well numbers from adjacent years of 1944–1953 since the technologies for well drilling and production will be similar in the adjacent years, yielding an estimated count of 121,509 wells (Fig. 6).

After adjusting the well counts based on regression analysis, we factored in historical underreporting and the impact of waterflooding (enhanced recovery) wells by multiplying the counts with specific multiplication factors. We have defined the period (1891–1923, 1924–1931, 1932–1946) for the underreporting factor based on the laws impacting the reporting (discussed in the Regulations Impacting Well Reporting section) and the multiplication factors during these periods are defined from the following discussion. Early 20th-century regulations in Oklahoma lead to significant underreporting during 1891–1923, resulting in an underreporting factor of 2, aligning with Pennsylvania's approach. The 1924 resolution of the Texas-Oklahoma boundary dispute improved reporting, affecting 8 associated counties, but only 2 counties (Texas, Beaver) were major oil and gas producers among >30 other producing counties during that time. For this reason, an underreporting factor of 1.8 (20 % reduction from 2) is applied for 1924–1931. It was not mandatory to register an oil well until 1947 for Oklahoma, but one law came into effect only for Oklahoma City Boundary around 1931 (Dancy and Dancy, 1986). Hence, the underreporting largely happened in all other counties except Oklahoma City Boundary, which had at least 5 major oil and gas fields (Oklahoma City, Watonga-Chickasha, Sooner Trend, Cement, Stroud) (Boyd, 2002) and numerous small fields located during this time. Hence, a 1.3 (50 % reduction of 1.8) underreporting factor for 1932–1946, matching Pennsylvania's approach, is applied to address underestimation due to missing data and uncertainties.

Waterflooding initiation in Oklahoma, in the Chelsea oil field (Rogers County), dates back to 1931 (Phillipsfor, 2017). Our analysis paralleled Pennsylvania's approach in determining ER well numbers for Oklahoma. A 1943 Department of the Interior report explored waterflooding in the state, identifying 13,941 ER wells across 62 projects between 1935 and 1942, with a ratio of 1.1 ER wells per producing well (Taliaferro and Logan, 1943). This report indicates that Oklahoma's systematic floods exclusively use a “five-spot” well pattern, with a producing well at the center of a square. This layout ensures the number of producing wells nearly equals the number of water-flooded wells, as each water-flooded well serves adjacent patterns. The report also claims that 73 water-flooding projects started on July 1st, 1942 (Taliaferro and Logan, 1943). However, no further report was found about the waterflooding projects in 1932–1935 and 1943–1956. We have used a factor of 1.5 (ER/producing wells = 0.5 < the average value of 1.1 from the report) for ER wells between 1932 and 1956 (Table 2), since around 40–50 % of the production in the entire U.S. is related with this technique (U.S. Office of Fossil Energy and Carbon Management, 2024). From 1957, we directly used the well numbers from the OCC reports, which included dry wells. Considering ER wells and potential underreporting, our analysis suggests a minimum of 799,145 wells are drilled in Oklahoma between 1891 and 2023, exceeding OCC reports by ~300,000 (Oklahoma Corporate Commission, 2010). Based on our analysis, the number of UNpWs is 384,961. The estimated UOWs (Table 2) stand at 309,462, derived from the difference between the estimated well count (799,145) and the combined OCC and Osage well database count (489,683) (Table 2). Our UOW counts (309,462) are 3-times higher than the current IOGCC estimates of 105,907 UOWs (Interstate Oil and Gas Compact Commission, 2021). Notably, no prior studies for Oklahoma have estimated abandoned wells, UNpW, or UOW counts with historical data considering the impact of waterflooding wells and regulations. Our Oklahoma well estimate, incorporating historical and digital records, is conservative and aligns closely with major oil and gas field discoveries, evident in peak well counts during those events (Fig. 7).

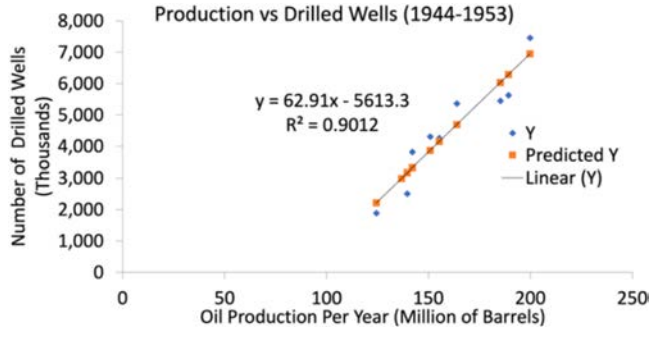


Fig. 6. Regression analysis for oil production and number of well completions per year for 1944–1953 from OCC (Oklahoma Corporate Commission, 2010).

4.2. Spatial distribution of UNpWs and UOWs

To establish a spatial well distribution, we examine various data sources (PA DEP (Spud Data Report/Wells drilled per county) (Pennsylvania Department of Environmental Protection, 2024c), Arnold & Kemnitzer (Arnold and Kemnitzer, 1931), Dilmore (Dilmore et al., 2015)) containing county names. Challenges arose due to incomplete attributes for wells before 1957 in the PA DEP (Pennsylvania Department of Environmental Protection, 2024b), database where entries for county name, drilled year, completion date, and spud date are generally empty or filled with placeholder values (like 1800). Moreover, there are only 3097 wells drilled before 1957 in the PA DEP (Spud Data Report/Wells drilled per county) database (Pennsylvania Department of Environmental Protection, 2024c), which is notably low compared to >200,000 wells during that period in PA DEP database (Pennsylvania Department of Environmental Protection, 2024b), and several boomtowns are entirely absent in this database. Arnold & Kemnitzer (Arnold and Kemnitzer, 1931) reported a higher number of wells per county than the PA DEP database, but they only contained wells before 1929, including wells from New York. Therefore, neither data source is suitable for reliable spatial distribution analysis. Dilmore's (Dilmore et al., 2015) wells-per-county data, which is a compilation of multiple historical data before 1957, is chosen for its close alignment with our boomtown analysis (cross-checked with the first production year in Table SI-1). For Oklahoma, we have used the wells-per-county from the OCC database (Oklahoma Corporate Commission, 2010) since it matches our findings from the boomtown analysis. The resulting map highlights counties with significant historical numbers of UNpWs and UOWs (Fig. 8) in Pennsylvania and Oklahoma.

From the Boomtown analysis, we know that the giant Bradford Field (McKean County) dominated the production during peak production times and a large number of waterflooding wells were drilled for secondary production in this field. In the spatial analysis (Fig. 8a-b, Table SI-3), McKean County stands out with an estimated 46,713 UNpWs, of which 33,158 are UOWs. Other Pennsylvania counties like Jefferson, Armstrong, Clarion, Washington, Venango, Erie, Clearfield, Crawford, Indiana, each have 20–28 thousand UNpWs, with 14–20 thousand being UOWs. Associated with these counties are three μSAs: Meadville (Crawford County), Oil City (Venango County), and DuBios (Clearfield County) with 82,670, 49,777 and 77,904 residents respectively (Pennsylvania Demographics, 2024). Pittsburgh MSA is the second largest in Pennsylvania, consisting of Fayette, Washington,

Received by OCD: 6/29/2026

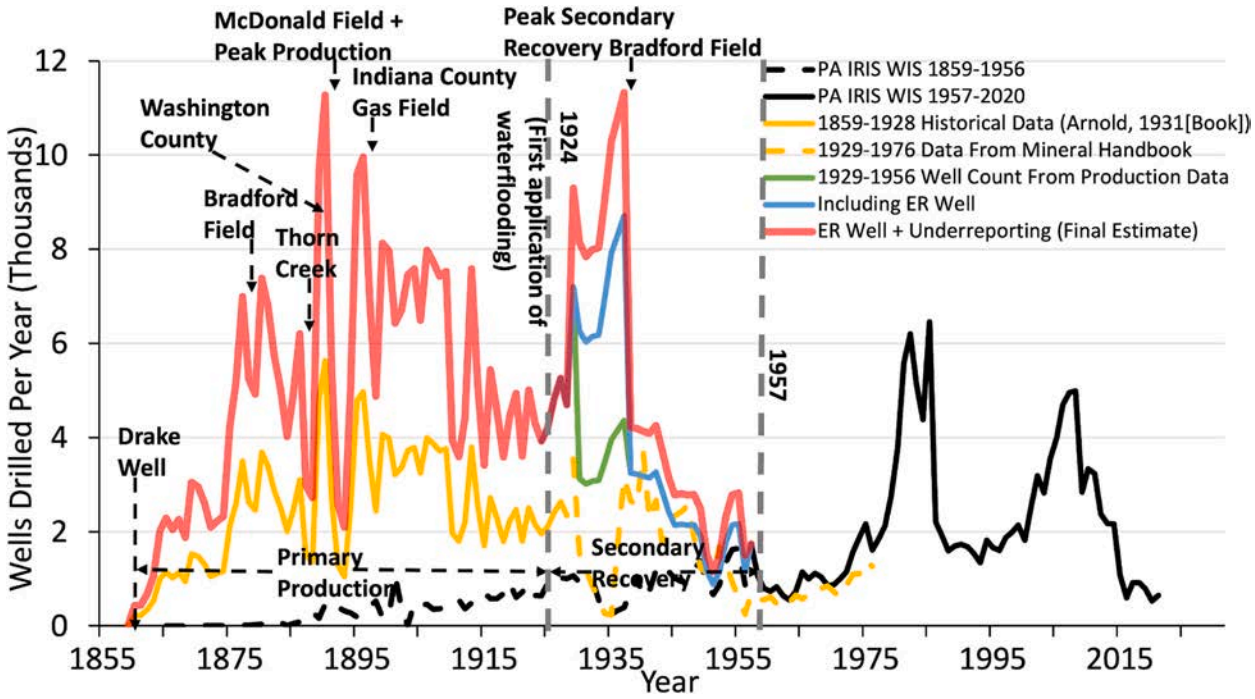


Fig. 7. The plot illustrates Oklahoma's estimated annual well completion, considering ER (waterflooding) wells and potential underreporting (blue and red lines, respectively). It includes historical data (yellow line), OCC data from 1904 to 2010 (black line), Enverus data for 2011–2023 (grey line), and a green curve representing well completions from oil production between 1924 and 1943. Major oil discoveries and historical events are marked with black arrows.

Westmoreland, Allegany, Armstrong, Beaver, and Butler County, with 2,349,172 current residents (Pennsylvania Demographics, 2024). Our estimate indicates 117,314 UNpWs in this region, of which 83,271 are UOWs. The Erie MSA, with 267,689 residents, has 20,895 UNpWs. Overall, over 2.5 million people in these MSAs live at a heightened risk of various exposures associated with oil and gas wells, including pollution and health issues like cancer and severe respiratory illnesses (Pianko, 2020).

Oklahoma's production history (1891–2023) saw widespread drilling activity (reflected in the list of counties and first production year in Table SI-2). Notably, 72 out of 77 counties in Oklahoma were actively producing oil in 2012 (Oklahoma Corporate Commission, 2010). Major historical oil and gas fields significantly influenced the number of UNpWs and UOWs in those counties (Fig. 8c-d, Table S4). From the boomtown analysis (Supporting Information), we know that Osage County not only had multiple major oil fields in the past decade but also had many smaller ones – 36 oil fields total. Creek County had two of the greatest oil fields (Glenn Pool, Cushing-Drumright) in Oklahoma's history. Osage and Creek County, with historically significant oil fields, lead in UNpW numbers in the spatial distribution (Fig. 8c-d). Creek County has 36,190 wells, while Osage County has 34,675 wells (Fig. 8c), with 34,293 and 30,873 of these being UOWs (Fig. 8d). Okmulgee County has 27,169 estimated UNpWs (25,953 UOWs). Moreover, all three counties are part of the Tulsa MSA, having 133,453 UNpWs; among those 123,670 wells are UOWs. This poses a health threat to the residents in the Tulsa MSA, the second largest MSA in Oklahoma state with more than one million current residents (Oklahoma Demographics, 2024). Counties like Stephens, Carter, Seminole, Nowata, and Washington each have 12–20 thousand UNpWs, mainly UOWs (Fig. 8d). Additionally, Duncan (Stephens County) and Ardmore (Carter & Love County) μSAs in Oklahoma also have 17–20 thousand UNpWs each.

4.3. Validation of the total estimated well count and spatial distributions of UNpWs and UOWs in Pennsylvania

In a NETL study (Sams et al., 2017), covering three large areas in western Pennsylvania, where wells were mostly spudded between 1860 and 1930, aeromagnetic surveys revealed at least 2 undocumented wells for every documented well, surpassing our UOWs estimate (340 K/264 K = 1.3). Since we have used a conservative approach to estimate the well counts, this data validates our estimation for Pennsylvania. The aeromagnetic and follow-up ground surveys at Hillman State Park, exhibited an even more concerning situation, with the survey uncovering 5 undocumented wells for every documented well (Sams et al., 2017). The state database recorded 33 wells in Hillman, while the aeromagnetic survey identified 160 well-type magnetic anomalies, likely corresponding to wells, surpassing an early Farm Line map's count of 192 wells on canvas (Sams et al., 2017).

To identify UOWs, the PA DEP is collaborating on mine map restoration projects, assembling potential well locations from collections like WPA, Ksheets, and Hsheets (Pennsylvania Department of Environmental Protection, 2024a). This dataset, containing over 30,000 potential historic well locations (Fig. 9), only covers selected counties like Greene, Washington, Beaver, Allegheny, Butler, Lawrence, Westmoreland, Indiana, Armstrong, Clarion, and Venango. However, the screening of some of these counties (Westmoreland, Indiana, Clarion, Jefferson, Lawrence, Beaver) is not completed, as observed in the plot (Fig. 9). We have also analysed well data from another database named Enverus (Enverus, 2024), which acquires well information from government and private companies. In the PA DEP (Pennsylvania Department of Environmental Protection, 2024b) database, most counties have significantly fewer wells compared to our estimate (Fig. 10) and the Enverus (Enverus, 2024) database, with historical well counties (Fig. 9) being an exception. Notably, after merging the historical well data with the PA DEP database, Allegheny County (Fig. 10) has more wells (15,177) than our estimate (12,221), and Butler County's well count (13,713) aligns closely with our estimate (14,792). Similarly, Warren County in the

Received by OCD: 6/29/2026

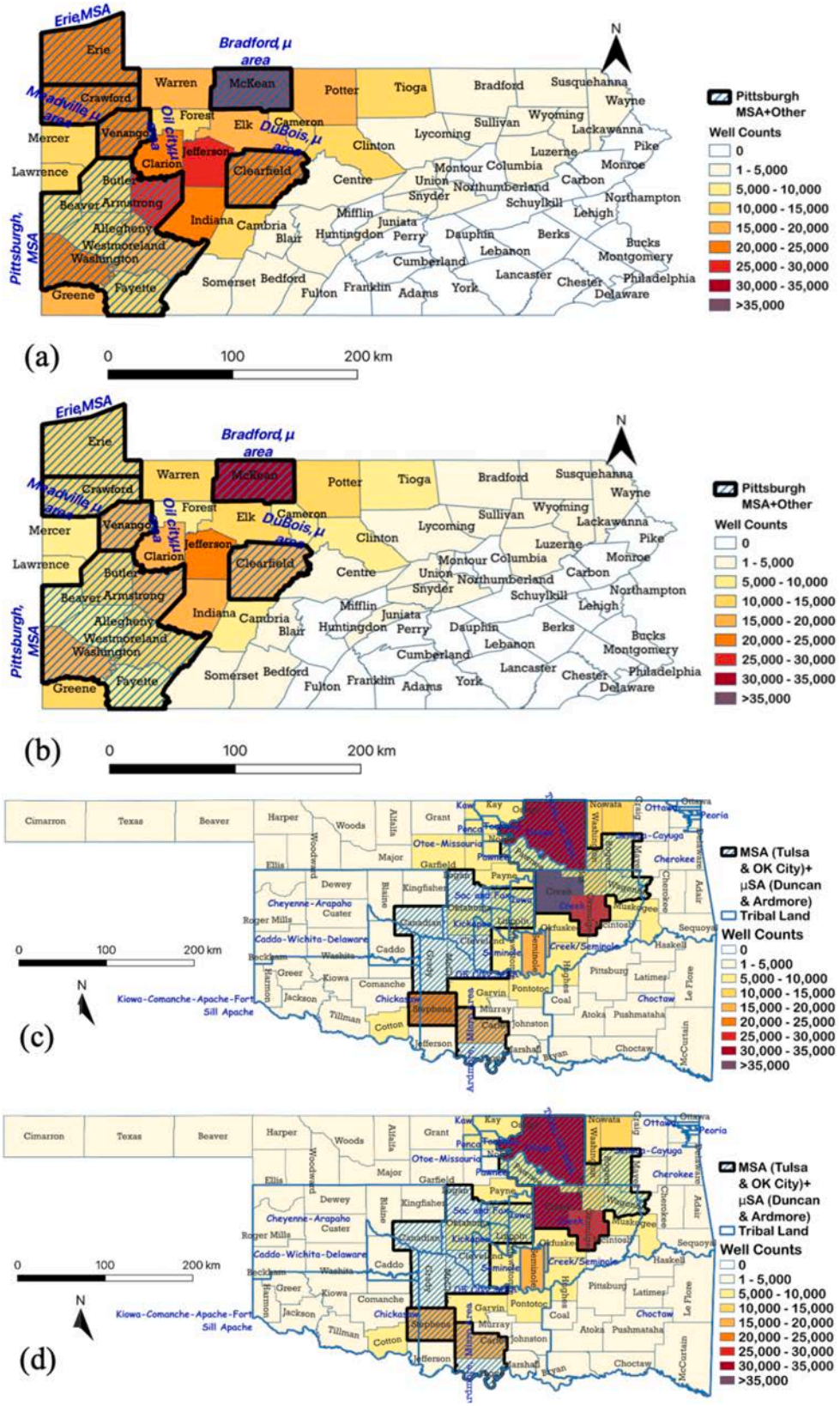


Fig. 8. The plot illustrates the contribution of (a) UNpWs and (b) UOWs in each county in Pennsylvania, with emphasis on Pittsburgh, Erie MSA, and four other Micropolitan Statistical Areas (μSAs) (Bradford, DuBois, Meadville, and Oil City) highlighted using black line patterns. Estimated (c) UNpWs and (d) UOWs per county in Oklahoma are depicted with tribal land boundaries in blue lines. Tulsa and Oklahoma City MSA, the major MSAs, and two μSAs (Duncan and Ardmore) are consistently highlighted in all plots using black line patterns.

Received by OCD: 6/29/2026

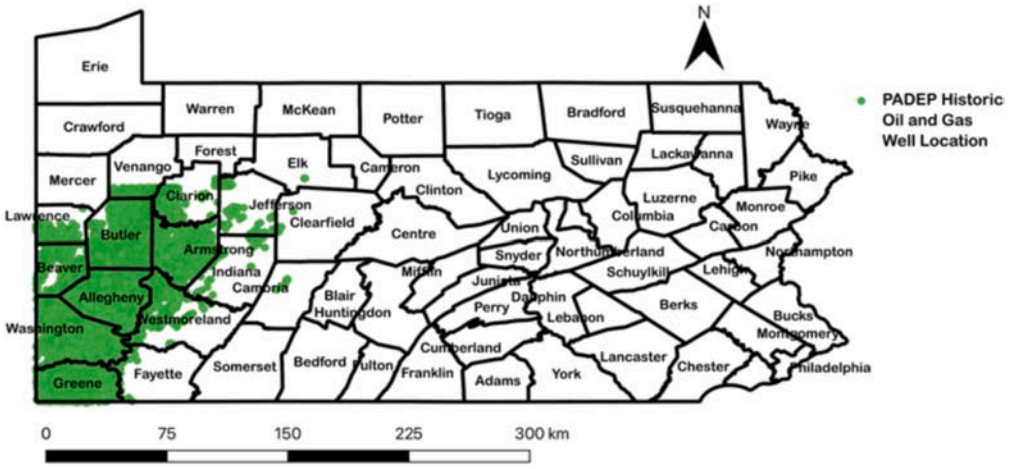


Fig. 9. Historical well location where only few counties are analysed using the mining maps.

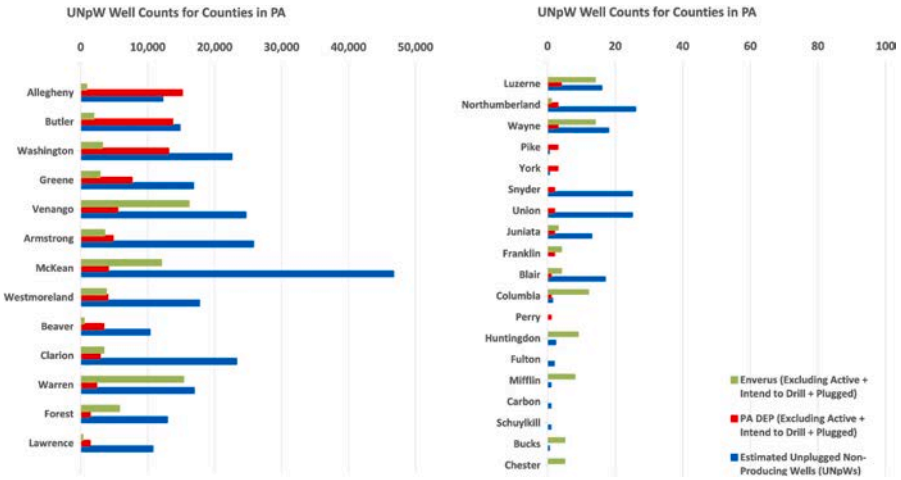


Fig. 10. Comparison of UNpWs with PA DEP (Pennsylvania Department of Environmental Protection, 2024b) and Enverus (Enverus, 2024) databases for all counties, where PA DEP has more wells (left chart) and fewer wells (right chart). Our estimated UNpWs are shown in blue, while PA DEP and Enverus databases are represented in red and green, respectively.

Enverus database (Enverus, 2024) has a well count (15,328) close to our estimated UNpWs (16,938). The Enverus database (Enverus, 2024) collects data from historically significant counties, such as Cherry Grove in Warren County, aligning well with our estimates. However, our study indicates underreporting in lower production counties compared to the Enverus (Enverus, 2024) and PA DEP database (Pennsylvania Department of Environmental Protection, 2024b), highlighting areas for future data collection. Counties with historical insignificant oil and gas exploration have low well counts in all three databases (Fig. 10 – bottom chart), which verifies our workflow.

5. Challenges and risks associated with unplugged abandoned wells and OWs

Abandoned and orphan oil and gas wells pose significant environmental, safety, and economic challenges, directly impacting housing prices and property development. Leaching into freshwater aquifers often results from old, leaking casings or cement, while surface contamination is caused by spills or fluids rising to the surface (Allison and Mandler, 2018). A study in Pennsylvania found that leaking wells are more likely to have residual casing left in the ground compared to non-leaking wells, exacerbating these risks (Pelepko, 2020). A 1988 U.S. Geological Survey study found that brine pollution from abandoned wells contaminated groundwater supplies for 50,000 people in Kentucky (Allison and Mandler, 2018). Similarly, a 2011 study documented 41 groundwater contamination incidents in Ohio and 30 in Texas caused by abandoned wells, unrelated to fracking (Kell, 2011). These risks are often compounded in regions where coal and oil and gas operations occur in close proximity, leading to additional hazards such as acid mine drainage or coal mine-influenced water (Boettner, 2021).

Unplugged or improperly plugged wells pose significant safety risks. In a 1985 incident in Los Angeles, a gas leak from an abandoned well caused a department store explosion, injuring two dozen people (Allison and Mandler, 2018). In one infamous example, migrating gas from an unplugged gas well caused a house to explode in McKean County, Pennsylvania, which further resulted in a lawsuit against the state (Schellhammer, 2013). The risk is heightened near active hydraulic fracturing operations, where increased underground pressure can cause abandoned wells to leak, a phenomenon called “communication.” Methane migration from new shale wells can bring gas to the surface, water wells, and homes, as seen in Tioga County, Pennsylvania, where a 30-ft geyser prompted evacuations of all residents in nearby community, and in Dayton, Pennsylvania, where methane led to the evacuation of a school and nearby homes (Detrow, 2012).

These safety and environmental risks also impact housing prices and economic development. Abandoned wells often reduce housing values,

making properties near such hazards more affordable but less desirable. This reduction in housing prices can attract lower-income individuals who may already face health vulnerabilities, further concentrating populations at higher risk of exposure to these hazards. A 2020 study by Mariya Shappo at the University of Illinois found that abandoned wells in Pennsylvania reduce house prices by an average of 11 %, or $15,000, a larger negative impact than active oil and gas wells (Shappo, 2020). Proper well restoration, however, can reverse these effects, with the benefits of plugging outweighing the costs. Similarly, a study by the University of Pittsburgh focused on Washington County, Pennsylvania, revealed that unplugged wells lower nearby property values by 12 % compared to properties near plugged wells (Harleman et al., 2020). This devaluation reduces the local tax base, with one school district losing at least $112 in annual revenue per student due to unplugged wells (Harleman et al., 2020).

In areas where residential, commercial, and educational infrastructure encroaches on former oil and gas fields, abandoned wells deter real estate investment, lower housing prices, and hinder economic development. Reduced housing values not only limit economic growth but also perpetuate social inequalities, as they attract vulnerable populations who prioritize affordability over safety. These findings highlight the urgent need for proper well plugging and restoration efforts to mitigate risks, protect public health, and support equitable community development. The results from this paper will play a crucial role in identifying localized areas with a high density of these wells.

6. Implications

Identifying and characterizing UNpWs and UOWs is crucial to mitigating methane emissions, water pollution, and health and safety hazards associated with OWs. The location (latitude/longitude) of UOWs is uncertain since there are no records of their existence, especially since little or no regulations existed before the 1950s to document oil and gas wells. However, this study has synthesized available digital records and historical data to refine the historical drilling activities from the past 150 years in Pennsylvania and Oklahoma.

Our workflow estimates the minimum number of UNpWs and UOWs from historical data and modern digital records for a particular state, which can be applied to other states. We demonstrated our workflow in Oklahoma and Pennsylvania. Combining these two states, >860 K UNpWs (480,164 in Pennsylvania and 384,961 in Oklahoma) have been estimated using this workflow, where >350 K (340,827 in Pennsylvania and 309,462 in Oklahoma) are UOWs. These estimates allow us to constrain budget/strategies using high-end technologies and advanced methods such as machine learning (Santos et al., 2023; Ciulla, 2023), drones (Guiltinan et al., 2023), satellites (Kadeethum et al., 2023), airplane surveys (Jahan et al., 2023). Additionally, the spatial distribution of OWs is beneficial in identifying regions with a high density of OWs so that these regions can be prioritized for future surveys using advanced identification techniques (Saint-Vincent et al., 2021; Kang et al., 2021; Gianoutsos et al., 2024). According to the IOGCC 2021 report, Pennsylvania has 67 % and Oklahoma contained only 13 % of all UOWs in the U.S. (Interstate Oil and Gas Compact Commission, 2021), which changed to 42 % (Pennsylvania) and 38 % (Oklahoma) after our estimate, suggesting a significant change in distribution. It also indicates that the IOGCC estimates are more off for Oklahoma than in Pennsylvania. If applied nationwide, this workflow may reveal a much higher estimated number of UOWs in states like West Virginia, Kansas, Missouri, Texas, Louisiana, and California, which currently have very low estimates of UOWs.

CRediT authorship contribution statement

Ismot Jahan: Writing – review & editing, Writing – original draft, Methodology, Investigation, Formal analysis, Data curation, Conceptualization. **Mohamed Mehana:** Writing – review & editing, Validation, Supervision, Resources, Project administration, Investigation, Funding acquisition, Conceptualization. **Mary Kang:** Writing – review & editing, Validation. **Jade Boutot:** Writing – review & editing. **Andrew Govert:** Validation. **Dan O'Malley:** Writing – review & editing. **Hari S. Viswanathan:** Writing – review & editing, Supervision, Resources, Project administration, Funding acquisition, Conceptualization.

Declaration of competing interest

The authors declare the following financial interests/personal relationships which may be considered as potential competing interests: Ismot Jahan reports financial support was provided by US Department of Energy. If there are other authors, they declare that they have no known competing financial interests or personal relationships that could have appeared to influence the work reported in this paper.

Acknowledgment

This work is supported by the Department of Energy (DOE) and Consortium Advancing Technology for Assessment of Lost Oil and Gas Wells (CATALOG).

Appendix A. Supplementary data

Additional information provides details on the methodology, data curation, and results of well estimation. Supplementary data to this article can be found online at https://doi.org/10.1016/j.scitotenv.2025.178746.

Data availability

The authors do not have permission to share data.

References

Allison, E., Mandler, B., 2018. "Abandoned Wells," Petroleum and the Environment, Part 7. American Geosciences Institute. https://www.americangeosciences.org/geoscience-currents/abandoned-wells (accessed 04 Dec 2024).

Armler, N.S., 1976. Oil in beaver county. Beaver County History Online 2 (2). https://www.bcpahistory.org/beavercounty/BeaverCountyTopical/Oil/OilInBeaverCountyM1976/OilinBCM1976.html (accessed 21 May 2024).

Arnold, R., Kemnitzer, W.J., 1931. Petroleum in the United States and possessions: a presentation and interpretation of the salient data of geology. In: Technology, and Economics of Petroleum in Each State and Possession Treated According to the Conventional Major Field Divisions. Harper & brothers.

Bass Law, 2023. Forced Pooling in Oklahoma, Bass Law. https://basslaw.net/forced-pooling-in-oklahoma/ (accessed 21 May 2024).

Bass, N.W., Dillard, W.R., Kennedy, L.E., Goodrich, H.B., 1941. Subsurface Geology and Oil and Gas Resources of Osage County, Oklahoma. U.S. Department of the Interior, Washington. Bulletin 900-I. https://pubs.usgs.gov/bul/0900i/report.pdf. (Accessed 21 May 2024).

Boettner, T., 2021. Repairing the Damage from Hazardeous Abandoned Oil & Gas Wells: A Federal Plan to Grow Jobs in the Ohio River Valley and Beyond. Ohio River Valley Institute. https://ohiorivervalleyinstitute.org/wp-content/uploads/2021/04/Repairing-the-Damage-from-Hazardous-AOG-Wells-Report.pdf. (Accessed 4 December 2024).

Bone, C., 2023. Osage Oil. The Encyclopedia of Oklahoma History and Culture. Oklahoma Historical Society, Oklahoma City, Oklahoma. https://www.okhistory.org/publications/enc/entry?entry=OS006 (accessed 21 May 2024).

Boutot, J., Peltz, A.S., McVay, R., Kang, M., 2022. Documented orphaned oil and gas wells across the United States. Environ. Sci. Technol. 56 (20), 14228–14236. https://doi.org/10.1021/acs.est.2c03268.

Boyd, D.T., 2002. Oklahoma Oil: Past, Present, and Future. Oklahoma Geology Notes. http://www.ogs.ou.edu/fossilfuels/pdf/OKOilNotesPDF.pdf.

Burnett, R.J., 2023. Pennsylvania Superior Court Rules that Oil and Gas Rights Did Not Transfer to Buyer. HoustonHarbaugh, The Oil and Gas Addendum. https://hh-law.com/blogs/oil-and-gas-addendum/pennsylvania-superior-court-rules-that-oil-and-gas-rights-did-not-transfer-to-buyer/ (accessed 21 May 2024).

Carr, T., Sawin, T.C., 1996. Hugoton Natural Gas Area of Kansas – History, Kansas Geological Survey. https://www.kgs.ku.edu/Publications/pic5/pic5_1.html. (Accessed 21 May 2024).

Carter, K.M., Harper, J.A., Schmid, K.W., Kostelnik, J., 2011. Unconventional natural gas resources in Pennsylvania: The backstory of the modern Marcellus Shale play. Environ. Geosci. 18 (4), 217–257. https://doi.org/10.1306/eg.09281111008.

Received by OCD: 6/29/2026

CATALOG, 2024. CATALOG - Consortium Advancing Technology for Assessment of Lost Oil & Gas Wells. https://catalog.energy.gov/ (accessed 21 May 2024).
Ciulla, F., 2023. Discovery of undocumented oil and gas wells using historical topographic maps. In: AGU Annual Meeting, The American Geophysical Union. https://doi.org/10.22541/essoar.170365263.33805026/v1.
Cooper, J., Dubey, L., Hawkes, A., 2022. Methane detection and quantification in the upstream oil and gas sector: the role of satellites in emissions detection, reconciling and reporting. Environ. Sci. Atmos. 2 (1), 9–23. https://doi.org/10.1039/d1ea00046b.
Craun, C., 2020. Development of Oil had a Great Impact on the Area. Nowata & the Oil Industry, Knowing Nowata issue.com. https://issuu.com/bartlesvillemonthly/docs/bmonthlyreducedsize_oct20/s/11082822 (accessed 21 May 2024).
Dancy, J.R., Dancy, V.A., 1986. Regulation of the Oil and Gas Industry by the Oklahoma Corporation Commission. Tulsa Law Review 21 (4). https://digitalcommons.law.utulsa.edu/cgi/viewcontent.cgi?article=1737&context=tlr.
Detrow, S., 2012. Perilous Pathways: How Abandoned Wells Can Contribute To Methane Migration Problems. STATEIMPACT PENNSYLVANIA. https://stateimpact.npr.org/pennsylvania/2012/10/09/perilous-pathways-how-drilling-near-an-abandoned-well-produced-a-methane-geyser/. (Accessed 4 December 2024).
Dilmore, R.M., Sams, J.I., Glosser, D., Carter, K.M., Bain, D.J., 2015. Spatial and temporal characteristics of historical oil and gas wells in Pennsylvania: implications for new shale gas resources. Environ. Sci. Technol. 49 (20), 12015–12023. https://doi.org/10.1021/acs.est.5b00820.
Eby, J., 2009. Oil Industry Originated 150 Years Ago in Pennsylvania. LeaderPublications. https://www.leaderpub.com/2009/03/05/oil-industry-originated-150-years-ago-in-pennsylvania/ (accessed 21 May 2024).
El Hachem, K., Kang, M., 2022. Methane and hydrogen sulfide emissions from abandoned, active, and marginally producing oil and gas wells in Ontario, Canada. Sci. Total Environ. 823, 153491. https://doi.org/10.1016/j.scitotenv.2022.153491.
Eno Petroleum, 2024. Early Oil in Pennsylvania. https://www.enopetroleum.com/earlyoilpennsylvania.html (accessed 20 May 2024).
Enverus, 2024. Enverus - Creating the Future of Energy Together. https://www.enverus.com/ (accessed 21 May 2024).
Erie's History and Memorabilia, 2015. Erie's Rush to Oil, Erie's History and Memorabilia, History of the City and County of Erie Pennsylvania. https://eriehistory.blogspot.com/2015/08/erie-rush-to-oil.html (accessed 21 May 2024).
Franks, K.A., 2023. Petroleum Industry, The Encyclopedia of Oklahoma History. Oklahoma Historical Society, Oklahoma City, Oklahoma. https://www.okhistory.org/publications/enc/entry.php?entry=PE023 (accessed 21 May 2024).
Gianoutsos, N.J., Haase, K.B., Birdwell, J.E., 2024. Geologic sources and well integrity impact methane emissions from orphaned and abandoned oil and gas wells. Sci. Total Environ. 912, 169584. https://doi.org/10.1016/j.scitotenv.2023.169584.
Gish, W.G., Carr, R.M., 1929. Garber Field, Garfield County, Oklahoma. In: Powers, S., Structure of Typical American Oil Fields, Volume I. American Association of Petroleum Geologists. https://doi.org/10.1306/SV3331.
Greco, I., 2020. Western PA's Black Gold in the late 1800s: the Rise and Fall of Two Oil Boom Towns. Former Western PA Oil Boom Towns, Petrolia and Parker City. https://formerwesternpaoilboomtowns.weebly.com/index.html (accessed 21 May 2024).
Grove, C.A., Merrill, M.D., 2022. United States Documented Unplugged Orphaned Oil and Gas Well Dataset: USGS Data Release. https://doi.org/10.5066/P91PJETI (accessed 09/11/2023).
Guiltinan, E.J., Milazzo, D., Coats, D.E., Lee, J., Follansbee, E.R., Dubey, M.K., Viswanathan, H.S., 2023. Undocumented orphan well detection in the four corners region. In: AGU Annual Meeting 2023. The American Geophysical Union.
Gurevich, A.E., Endres, B.L., Robertson, J.O., Chilingar, G.V., 1993. Gas migration from oil and gas fields and associated hazards. J. Pet. Sci. Eng. 9 (3), 223–238. https://doi.org/10.1016/0920-4105(93)90016-8.
Harleman, M., Weber, J., Berkowitz, D., 2020. Environmental hazards and local investment: a half-century of evidence from abandoned oil and gas wells. USAEE Working Paper No. 20-470. https://doi.org/10.2139/ssrn.3692098.
Harper, J.A., 2013. History and geology of the giant bradford oil field, Mckean County, PA and Cattaraugus County, NY. Oil-Industry History 2013 14 (01), 19–32. https://archives.datapages.com/data/phi/v14_2013/harper.html.
History of Butler County Pennsylvania, 1895a. History of Butler County Pennsylvania, 1895, Chapter 19 - The Butler Oil Field. https://sites.rootsweb.com/~pabutler/1895/95x19.htm (accessed 21 May 2024).
History of Butler County Pennsylvania, 1895b. History of Butler County Pennsylvania, 1895, Chapter 20 - The Butler Oil Field. https://sites.rootsweb.com/~pabutler/1895/95x20.htm (accessed 21 May 2024).
Interstate Oil and Gas Compact Commission, 2021. Idle and Orphan Oil and Gas Wells: State and Provincial Regulatory Strategies, 2021. https://iogcc.ok.gov/sites/g/files/gmc836/f/iogcc_idle_and_orphan_wells_2021_final_web.pdf (accessed 19 May 2024).
Jahan, I., Mehana, M., Ahmmed, B., Santos, J.E., O'Malley, D., Viswanathan, H., 2023. Deep learning models for methane emissions identification and quantification. In: SPE/AAPG/SEG Unconventional Resources Technology Conference, Denver, Colorado, USA. https://doi.org/10.15530/urtec-2023-3866049.
Kadeethum, T., Kim, A., O'Malley, D., Downs, C., 2023. Satellite data analysis for detecting (undocumented) oil and gas wells and improving model generalization with attention mechanisms. In: AGU Annual Meeting 2023. The American Geophysical Union.
Kang, M., Christian, S., Celia, M.A., Mauzerall, D.L., Bill, M., Miller, A.R., Chen, Y., Conrad, M.E., Darrah, T.H., Jackson, R.B., 2016. Identification and characterization of high methane-emitting abandoned oil and gas wells. Proc. Natl. Acad. Sci. 113 (48), 13636–13641. https://doi.org/10.1073/pnas.1605913113.
Kang, M., Brandt, A.R., Zheng, Z., Boutot, J., Yung, C., Peltz, A.S., Jackson, R.B., 2021. Orphaned oil and gas well stimulus—maximizing economic and environmental benefits. Elem. Sci. Anth. 9 (1). https://doi.org/10.1525/elementa.2020.20.00161.
Kang, M., Boutot, J., McVay, R.C., Roberts, K.A., Jasechko, S., Perrone, D., Wen, T., Lackey, G., Raimi, D., Digiulio, D.C., 2023. Environmental risks and opportunities of orphaned oil and gas wells in the United States. Environ. Res. Lett. 18 (7), 074012. https://doi.org/10.1088/1748-9326/acdae7.
Kell, S., 2011. State Oil and Gas Agency Groundwater Investigations and Their Role in Advancing Regulatory Reforms. A Two-state Review: Ohio and Texas Technical Report (Ground Water Protection Council). https://hero.epa.gov/hero/index.cfm/reference/details/reference_id/2215321. (Accessed 4 December 2024).
King, G.E., Daniel, E.K., 2013. Environmental risk arising from well-construction failure—differences between barrier and well failure, and estimates of failure frequency across common well types, locations, and well age. SPE Prod. & Oper. 28, 323–344. https://doi.org/10.2118/166142-PA.
Knight, G., 2016. A look back at one of the biggest oil and gas fields. Oklahomaminerals. https://www.oklahomaminerals.com/look-back-one-biggest-oil-gas-fields (accessed 21 May 2024).
Lebel, E.D., Lu, H.S., Vielstadte, L., Kang, M., Banner, P., Fischer, M.L., Jackson, R.B., 2020. Methane emissions from abandoned oil and gas wells in California. Environ. Sci. Technol. 54 (22), 14617–14626. https://doi.org/10.1021/acs.est.0c05279.
Li, Z.H., You, C., Gonzales, M., Wendt, A.K., Wu, F., Brantley, S.L., 2016. Searching for anomalous methane in shallow groundwater near shale gas wells. J. Contam. Hydrol. 207, 50–51. https://doi.org/10.1016/j.jconhyd.2017.09.009.
Mahmud, H.B., Arumugam, S., Mahmud, W., 2019. Potential of low-salinity waterflooding technology to improve oil recovery. In: Enhanced Oil Recovery Processes - New Technologies. IntechOpen. https://doi.org/10.5772/intechopen.88082.
Mariner, C., 2020. Oklahoma City Oil Field. The Historical Marker Database. https://www.hmdb.org/m.asp?m=161376. (Accessed 21 May 2024).
May, J.D., 2023. Burbank. In: The Encyclopedia of Oklahoma History and Culture. Oklahoma Historical Society, Oklahoma City, Oklahoma. https://www.okhistory.org/publications/enc/entry?entry=BU007 (accessed 21 May 2024).
Miller, E.C., 1952. Oily days at cherry grove. Pa. Hist.: A journal of Mid-Atlantic Studies. 19 (1), 33–51. https://www.jstor.org/stable/27769276. (Accessed 21 May 2024).
Mills-Bullard, B.A., 1924. Summary of oil production in Oklahoma by years. Academy of Science. https://ojs.library.okstate.edu/osu/index.php/OAS/article/download/2287/1988. (Accessed 21 May 2024).
Nikulin, A., de Smet, T.S., 2019. A UAV-based magnetic survey method to detect and identify orphaned oil and gas wells. Lead. Edge 38 (6), 447–452. https://doi.org/10.1190/tle38060447.1.
Oklahoma Corporate Commission, 2010. 2010 Report on Oil and Natural Gas Activity Within the State of Oklahoma. https://oklahoma.gov/content/dam/ok/en/occ/documents/og/2010-annual-report.pdf (accessed 21 May 2024).
Oklahoma Demographics, 2024. Oklahoma Counties by Population. https://www.oklahoma-demographics.com/counties_by_population (accessed 21 May 2024).
pa-roots, 1939. The Natural Gas Boom in Jefferson County, What's Historic About Brookville, Pennsylvania?, 1939. pa-roots.com (web archive link, 21 May 2024). https://www.pa-roots.com/jefferson/historicbrookville/a18.html (accessed 21 May 2024).
Pelepko, S., 2020. Abandoned and Orphan Oil and Gas Wells in Pennsylvania. Pennsylvania Bureau of Oil and Gas Planning and Program Management presentation CCAC. http://files.dep.state.pa.us/Energy/Office%20of%20Energy%20and%20Technology/OETDPortalFiles/Climate%20Change%20Advisory%20Committee/2020/10-27-20/Presentation_Abandoned%20Wells_Pelepko_20201027.pdf. (Accessed 4 December 2024).
Pennsylvania Demographics, 2024. Pennsylvania Counties by Population. https://www.pennsylvania-demographics.com/counties_by_population (accessed 21 May 2024).
Pennsylvania Department of Environmental Protection, 2024a. PA DEP GIS. Oil & Gas – Historic Oil & Gas Well Locations. https://newdata-padep-1.opendata.arcgis.com/datasets/PADEP-1::oil-gas-historic-oil-gas-well-locations/explore. (Accessed 20 May 2024).
Pennsylvania Department of Environmental Protection, 2024b. PA*IRIS/WIS Data Portal. https://www.depgis.state.pa.us/PaOilAndGasMapping/OilGasWellsStrayGasMap.html (accessed 21 May 2024).
Pennsylvania Department of Environmental Protection, 2024c. SPUD Data Report/Wells Drilled By County. Pennsylvania Department of Environmental Protection. http://cedatareporting.pa.gov/Reportserver/Pages/ReportViewer.aspx?/Public/DEP/OG/SSRS/Wells_Drilled_By_County. (Accessed 21 May 2024).
Pennsylvania Historical and Museum Commission, 1997. Resources of the Oil Industry in Western Pennsylvania, 1859–1945. Pennsylvania Historical and Museum Commission. https://www.phmc.state.pa.us/Portal/Communities/BHP/MPDFs/Resources_of_the_Oil_Industry_in_Western_PA.pdf (accessed 21 May 2024).
Phillipsfor, M., 2017. Historical markers point to first 'waterflooding' oil site. The Oklahoman. https://www.oklahoman.com/story/lifestyle/2017/08/28/historical-markers-point-to-first-waterflooding-oil-site/60579092007/ (accessed 21 May 2024).
Pianko, M., 2020. California lagged in capping century-old oil wells leaking under homes of LA residents plagued by illness and odors. DeSmog. https://www.desmog.com/2020/02/13/los-angeles-vista-hermosa-cap-orphan-oil-wells-leaking-doggr/ (accessed 21 May 2024).
Raimi, D., Krupnick, A.J., Shah, J.S., Thompson, A., 2021. Decommissioning orphaned and abandoned oil and gas wells: new estimates and cost drivers. Environ. Sci. Technol. 55 (15), 10224–10230. https://doi.org/10.1021/acs.est.1c02234.
Riddick, S.N., Mbua, M., Santos, A., Emerson, E.W., Cheptonui, F., Houlihan, C., Hodshire, A.L., Anand, A., Hartzell, W., Zimmerle, D.J., 2024. Methane emissions

from abandoned oil and gas wells in Colorado. Sci. Total Environ. 922, 170990. https://doi.org/10.1016/j.scitotenv.2024.170990.
Saint-Vincent, P.M.B., Sams, J.I., Reeder, M.D., Mundia-Howe, M., Veloski, G.A., Pekney, N.J., 2021. Historic and modern approaches for discovery of abandoned wells for methane emissions mitigation in Oil Creek State Park, Pennsylvania. J. Environ. Manag. 280, 111856. https://doi.org/10.1016/j.jenvman.2020.111856.
Sams, J.I., Veloski, G.A., Diehl, J.R., Hammack, R.W., 2017. Methods and challenges to locating legacy wells in western Pennsylvania: Case study at Hillman State Park. Environ. Geosci. 24 (2), 95–112. https://doi.org/10.1306/eg.1221161600417009.
Santos, J.E., Fox, Z.R., Mohan, A., O'Malley, D., Viswanathan, H., Lubbers, N., 2023. Development of the Senseiver for efficient field reconstruction from sparse observations. Nat. Mach. Intell. 5, 1317–1325. https://doi.org/10.1038/s42256-023-00746-x.
Schellhammer, M., 2013. Victim of house explosion files lawsuit. The Bradford Era. http://www.bradfordera.com/news/victim-of-house-explosion-files-lawsuit/article_fed27cbe-d7be-11e2-ac81-0019bb2963f4.html. (Accessed 4 December 2024).
Schout, G., Griffioen, J., Hassanizadeh, S.M., de Lichtbuer, G.C., Hartog, N., 2019. Occurrence and fate of methane leakage from cut and buried abandoned gas wells in the Netherlands. Sci. Total Environ. 659, 773–782. https://doi.org/10.1016/j.scitotenv.2018.12.339.
Shappo, M., 2020. Long-Term Consequences of Oil and Gas Extraction: Evidence from the Housing Market. University of Illinois at Urbana-Champaign. Job Market Paper, 2020. https://files.webservices.illinois.edu/9475/job_market_paper_shappo.pdf. (Accessed 4 December 2024).
Short, M.G.F., 1924. State of Oklahoma v. State of Texas, 265 U.S. 493 (1924). https://caselaw.findlaw.com/court/us-supreme-court/265/493.html. (Accessed 21 May 2024).
de Smet, T.S., Nikulin, A., Romanzo, N., Graber, N., Dietrich, C., Puliaiev, A., 2020. Successful application of drone-based aeromagnetic surveys to locate legacy oil and gas wells in Cattaraugus County, New York. J. Appl. Geophys. 186, 104250. https://doi.org/10.1016/j.jappgeo.2020.104250.
Smith, H., 2021. The Story of Oil in Western Pennsylvania: What, How, and Why? Carnegie Museum of Natural History. https://carnegiemnh.org/the-story-of-oil-in-western-pennsylvania/. (Accessed 21 May 2024).
Stephens, S., 2016. Pennsylvania's oil boomtowns of 150 years ago built on fuel of industrial age. The Columbus Dispatch, Pithole City, Pennsylvania. https://www.dispatch.com/story/lifestyle/travel/2016/07/07/pennsylvania-s-oil-boomtowns-150/24195244007/ (accessed 21 May 2024).
Stone, R.W., Clapp, F.G., 1907. Oil and Gas Fields of Greene County, PA. U.S. Geological Survey, U.S. Department of the Interior, Washington. Bulletin no. 304. https://pubs.usgs.gov/bul/0304/report.pdf.
Taliaferro, D.B., Logan, D.M., 1943. History of Water Flooding of Oil Sands in Oklahoma, Report. U.S. Department of the Interior. R. I. 3728. https://digital.library.unt.edu/ark:/67531/metadc38419/m1/1/. (Accessed 21 May 2024).
The McKean County Planning Comm, 1982. A Brief History of the County of Mckean. U. S. Environmental Protection Agency. https://semspub.epa.gov/work/03/2303855.pdf (accessed 21 May 2024).
U.S. Department of Interior, 2022. Department of Interior Orphaned Wells. U.S. Department of Interior, Washington, DC. https://www.doi.gov/orphanedwells (accessed 21 May 2024).
U.S. Energy Information Administration, 2023. Monthly Crude Oil and Natural Gas Production. https://www.eia.gov/petroleum/production/. (Accessed 18 May 2024).
U.S. Environmental Protection Agency, 2022. Inventory of U.S. Greenhouse Gas Emissions and Sinks: 1990–2020, p. 240. https://www.epa.gov/ghgemissions/inventory-us-greenhouse-gas-emissions-and-sinks-1990-2020. (Accessed 21 May 2024).
U.S. Office of Fossil Energy and Carbon Management, 2024. Enhanced Oil Recovery. Office of Fossil Energy and Carbon Management energy.gov. https://www.energy.gov/fecm/enhanced-oil-recovery. (Accessed 21 May 2024).
Washington, 2020. Washington Oil Field. Washington.com (web archive link, 21 May 2024). https://washingtonish.com/washington-oil-field/ (accessed 21 May 2024).
Weaver, B.D., 2023a. Red Fork Field, The Encyclopedia of Oklahoma History and Culture. Oklahoma Historical Society, Oklahoma City, Oklahoma. https://www.okhistory.org/publications/enc/entry.php?entry=RE004 (accessed 21 May 2024).
Weaver, B.D., 2023b. Cleveland Field, The Encyclopedia of Oklahoma History and Culture. Oklahoma Historical Society, Oklahoma City, Oklahoma. https://www.okhistory.org/publications/enc/entry?entry=CL014 (accessed 21 May 2024).
Weaver, B.D., 2023c. Glenn Pool Field. The Encyclopedia of Oklahoma History and Culture. Oklahoma Historical Society. Oklahoma City, Oklahoma. https://www.okhistory.org/publications/enc/entry.php?entry=GL007 (accessed 21 May 2024).
Weaver, B.D., 2023d. Tonkawa–Three Sands Field, The Encyclopedia of Oklahoma History and Culture. Oklahoma Historical Society, Oklahoma City, Oklahoma. https://www.okhistory.org/publications/enc/entry?entry=TO006 (accessed 21 May 2024).
Weaver, B.D., 2023e. Greater Seminole Field, The Encyclopedia of Oklahoma History and Culture. Oklahoma Historical Society, Oklahoma City, Oklahoma. https://www.okhistory.org/publications/enc/entry?entry=GR020 (accessed 21 May 2024).
Wells, B.A., Wells, K.L., 2014. Million Dollar Elm. American Oil & Gas Historical Society.. https://aoghs.org/petroleum-pioneers/million-dollar-elm. (Accessed 21 May 2024)
Wells, B.A., Wells, K.L., 2015. Natural Gas is King in Pittsburgh. American Oil & Gas Historical Society. URL: https://aoghs.org/petroleum-pioneers/pennsylvania-natural-gas/. (Accessed 21 May 2024).
whitehouse.gov., 2021. U.S. Methane Emissions Reduction Action Plan. whitehouse.gov. Washington, DC. https://www.whitehouse.gov/wp-content/uploads/2021/11/US-Methane-Emissions-Reduction-Action-Plan-1.pdf (accessed 21 May 2024).
Williams, J.P., Regehr, A., Kang, M., 2021. Methane emissions from abandoned oil and gas wells in Canada and the United States. Environ. Sci. Technol. 55 (1), 563–570. https://doi.org/10.1021/acs.est.0c04265.
Wintermantel, M., 2012. McDonald Oil Field. The Historical Marker Database, 2012. https://www.hmdb.org/m.asp?m=58541 (accessed 21 May 2024).

Update

Science of the Total Environment

Volume 1032, Issue , 25 May 2026, Page

DOI: https://doi.org/10.1016/j.scitotenv.2026.181871

Science of the Total Environment 1032 (2026) 181871

Contents lists available at ScienceDirect

Science of the Total Environment

journal homepage: www.elsevier.com/locate/scitotenv

Corrigendum

Corrigendum to "Data-driven estimates of undocumented orphan oil and gas wells with implications to the environment"[Sci. Total Environ. Volume 967 (2025) 178746]

Ismot Jahan [a], Mohamed Mehana [a,*], Mary Kang [b], Jade Boutot [b], Andrew Govert [c], Dan O'Malley [a], Hari S. Viswanathan [a]

[a] *Energy and Natural Resources Security Group (EES-16), Earth and Environmental Sciences Division, Los Alamos National Laboratory, Los Alamos, NM, 87545, United States*
[b] *Department of Civil Engineering, McGill University, Montreal, Quebec, H3A 0C3, Canada*
[c] *Methane Mitigation Technologies Division, Office of Fossil Energy Carbon Management, Department of Energy, United States*

The authors wish to remove the last highlight: "Our estimated wells emit 14 times more methane than IOGCC's estimate for all states."

The authors apologize for any inconvenience this may cause.

DOI of original article: https://doi.org/10.1016/j.scitotenv.2025.178746.
* Corresponding author.
E-mail address: mzm@lanl.gov (M. Mehana).

https://doi.org/10.1016/j.scitotenv.2026.181871

Available online 11 May 2026
0048-9697/© 2026 Elsevier B.V. All rights are reserved, including those for text and data mining, AI training, and similar technologies.

EXHIBIT 15

nature COMMUNICATIONS

ARTICLE

DOI: 10.1038/s41467-018-06167-4 OPEN

Physics-based forecasting of man-made earthquake hazards in Oklahoma and Kansas

Cornelius Langenbruch [1], Matthew Weingarten[1,2] & Mark D. Zoback [1]

Reinjection of saltwater, co-produced with oil, triggered thousands of widely felt and several damaging earthquakes in Oklahoma and Kansas. The future seismic hazard remains uncertain. Here, we present a new methodology to forecast the probability of damaging induced earthquakes in space and time. In our hybrid physical–statistical model, seismicity is driven by the rate of injection-induced pressure increases at any given location and spatial variations in the number and stress state of preexisting basement faults affected by the pressure increase. If current injection practices continue, earthquake hazards are expected to decrease slowly. Approximately 190, 130 and 100 widely felt $M \geq 3$ earthquakes are anticipated in 2018, 2019 and 2020, respectively, with corresponding probabilities of potentially damaging $M \geq 5$ earthquakes of 32, 24 and 19%. We identify areas where produced-water injection is more likely to cause seismicity. Our methodology can be used to evaluate future injection scenarios intended to mitigate seismic hazards.

[1] Department of Geophysics, Stanford University, Stanford, CA 94305, USA. [2] Present address: Department of Geological Sciences, San Diego State University, San Diego, CA 92182, USA. Correspondence and requests for materials should be addressed to C.L. (email: langenbr@stanford.edu)

Received by OCD: 6/29/2026

Probabilistic seismic hazard analyses (PSHA) has been used to develop earthquake hazard maps in intraplate areas for several decades[1–4]. Traditionally, PSHA is used to develop maps of the probability of strong ground shaking over relatively long periods of time. It has been widely used by governments and industry in applications such as assessing the safety of nuclear power plants, developing building code requirements and determining earthquake insurance rates. The methodology assumes long-term stationarity of seismicity rates resulting from large-scale geologic processes. Application of these methods to man-made earthquakes, especially those induced by underground injection of fluids, is inherently problematic because injection rates (and thus induced earthquake rates) can vary markedly in space and time[5–7]. For example, over the past 6 years, north-central Oklahoma and southernmost Kansas experienced thousands of widely felt earthquakes ($M \geq 3$) resulting from injection of very large amounts of saltwater that was co-produced with oil[6–9]. The seismicity triggered by the fluid injection corresponds to >2000 years of natural tectonic activity[7] and occurred due to the decrease of frictional resistance to slip on tectonically loaded, preexisting faults[10].

Seismic activity in north-central Oklahoma and southernmost Kansas peaked in 2015, when 943 widely felt $M \geq 3$ (31 $M \geq 4$) earthquakes occurred[11] in response to the dramatic increase in produced saltwater injection rates into the basal sedimentary Arbuckle Group[6,7] (Fig. 1a, b). Driven by market forces and mandated reductions[12], injection rates started to decrease rapidly in mid-2015. Compared to peak injection rates, a reduction of about 50% was reported through March 2018 (Fig. 1b). The earthquake rate responded to decreased saltwater injection rates and reduced by about 80%[7,13] (Fig. 1b). While the overall earthquake rate has decreased markedly over the past 2 years, the seismic hazard remains high[7,13,14]. In 2017, 294 $M \geq 3$ (6 $M \geq 4$) earthquakes were recorded[11]. To date, four induced earthquakes in the study area exceeded $M = 5$, including the September 2016 Pawnee $M = 5.8$ earthquake—the largest in instrumented history in Oklahoma and Kansas.

While the utilization of PSHA has been questioned, in general[15], the main problem when being applied to injection-induced seismicity is that changes of the driving force, and variations of injection rates in space and time, are not considered. More recently, a 1-year seismic hazard model has been developed for Oklahoma and Kansas using last year's seismicity rates to predict the seismic hazard[14]. While a step in the right direction, we argue here that induced seismic hazard should be forecasted based on a physical understanding of induced earthquakes.

In the sections below, we outline a physics-based model for estimating spatial and temporal variations of seismic hazards in Oklahoma and Kansas. The model has two principal components. First, spatial and temporal variations of injection-induced pressure changes are evaluated utilizing the reported injection rates and a regional hydrogeologic model. Second, spatial variations of the seismogenic state are considered, a proxy for number and stress state of preexisting basement faults that are affected by the pressure increase. In this regard, the study reported here departs significantly from our previous analysis of seismicity rates in Oklahoma[7] using a seismogenic index model[16]. First, we integrate a regional hydrologic model into the analysis and second, we assess spatial variability of the seismic hazard. After combining spatial and temporal variations of injection-induced pressure changes and spatial variations of the seismogenic state in a hybrid physics-based statistical model, we create probabilistic seismic hazard maps and an estimate of the earthquake probability throughout the entire region through 2020.

Results

Injection-induced pressure increase at seismogenic depth. To compute injection-induced pore pressure changes at depth, we modelled 809 Arbuckle wells injecting at about 2.1-km depth from Jan 2000 through March 2018 (see Supplementary Fig. 1). The Arbuckle Group is directly overlying the crystalline basement and consists of a pervasively fractured, dolomitic carbonate aquifer with hydraulic continuity over tens to hundreds of kilometres[17]. Reported permeability ranges from core, outcrop and field-scale measurements in Oklahoma and Kansas show permeability as low as 10^{-14} m^2 and as high as 3×10^{-12} m^2[18–22]. As explained in the Methods section, we represent the major lithologic units present across Oklahoma and Kansas with a layered permeability structure. Due to large vertical offsets and regional traps for oil and gas, the north-trending Nemaha fault is a low-permeability barrier to flow across its strike in our model[23]. At the large scale of our model (145,000 km^2), the best-fit Arbuckle Group permeability was found to be 10^{-12} m^2, although we tested models with permeability as low as 10^{-14} m^2 (Supplementary Table 2). This large-scale bulk permeability honours the observation that >60% of wells in the region inject fluid at near-zero wellhead pressure. More importantly, after 6 years of high-volume injection throughout the region, the fluid pressure remains sub-hydrostatic, even near wells injecting tens of thousands of m^3 day^{-1}. Our modelled Arbuckle permeability predicts reservoir pore pressure changes mostly within the range between 0.1 and 2 MPa (Supplementary Fig. 2).

Because of the high permeability of the Arbuckle Group and the wide distribution of injection wells, pressure spreads out quickly and diffuses down into the much lower-permeability crystalline basement, triggering earthquakes on critically stressed faults. The earthquakes are observed at depths that typically range from 4 to 9 km[24,25]. The vertical diffusion of pore pressure is controlled by basement permeability and reflected in the characteristic time delay of several months between changes of injection and earthquake rates in the region (Fig. 1b).

We initially assumed that the permeability of the fractured basement is 10^{-16}–10^{-14} m^2, a range consistent with direct measurements, modelling and induced seismicity in the crystalline basement at other locations around the world[26–28]. To test this, we randomly distributed 25,000 seed points (in the study area shown in Fig. 1a) at a depth of 6.5 km below the surface. These points represent potential locations of preexisting basement faults which, if reactivated by injection-induced pressure increase, produce $M \geq 3$ earthquakes. Following the concept that changes in earthquake activity are caused by changes of the stressing (pressure) rate[29,30], we vary the basement permeability in our model and compare the rate of pressure increase (averaged over all points) to the overall observed earthquake rate ($M \geq 3$). We find that the pressure rate at seismogenic depths is most sensitive to basement permeability (see Supplementary Fig. 3). Pressure rate (and rate of pressure increase) in this publication always refers to monthly pressure accumulation at a given point in space. A basement permeability of 2×10^{-15} m^2 results in the best fit between the shape of observed seismicity rates and modelled pressure rates (see Fig. 1b), consistent with the value range cited above.

Our model computes pressure changes in both time and space. We find that an open-system hydrogeologic model and high

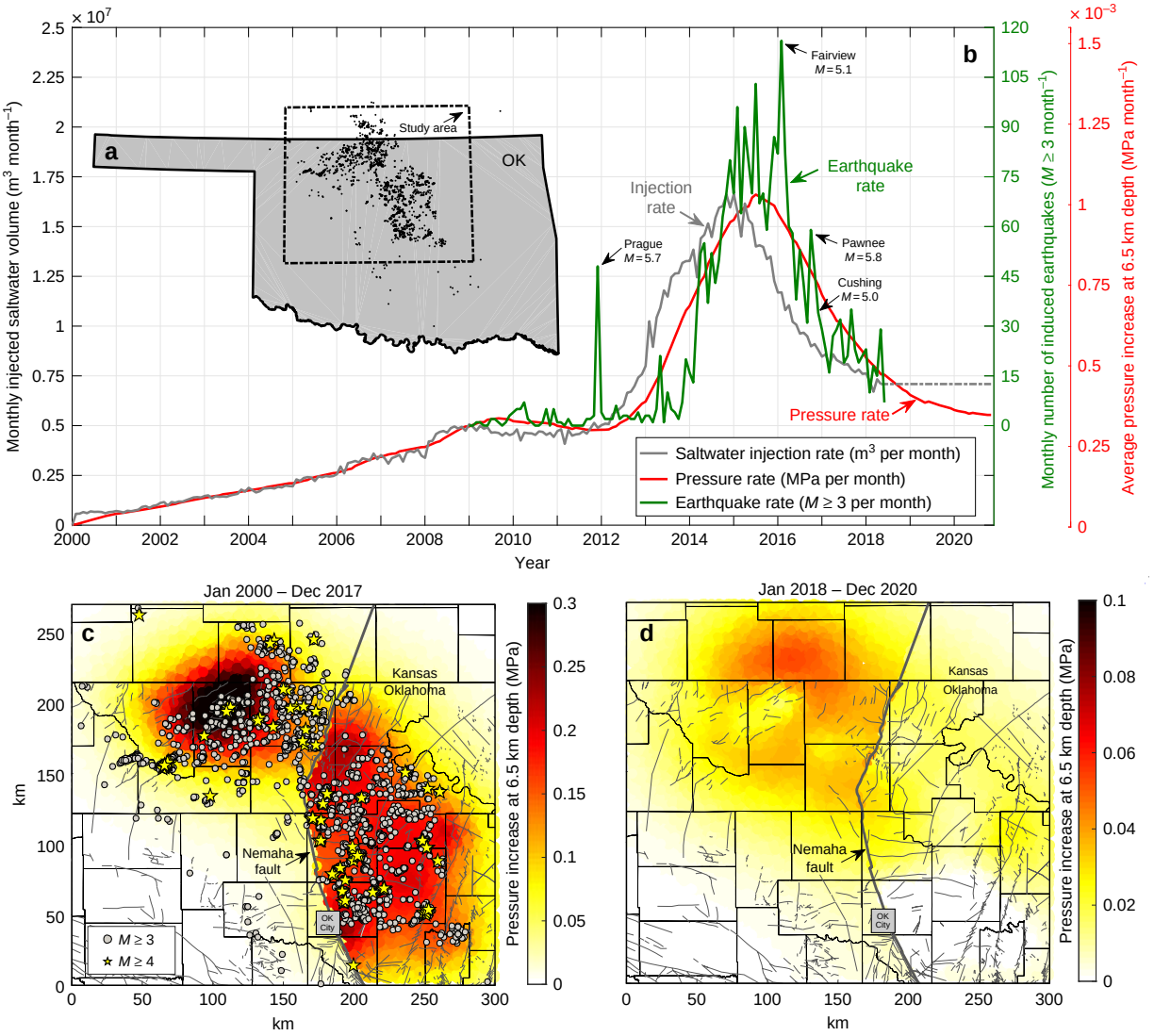


Fig. 1 Saltwater injection, induced earthquakes and pressure increase in Oklahoma and Kansas. **a** The study area is shown by the dashed line. Black dots show $M \geq 3$ earthquakes from Jan 2009 through May 2018. **b** Total monthly saltwater injection rate (grey), observed earthquake rate (green) and average modelled rate of pressure increase (red) in the study area. Our diffusion model predicts increasing pressure at depth through 2020 (red). However, the rate of pressure increase is slowing down to the level observed in 2009, when seismicity began. **c** Map of injection-induced pressure increase at depth (Jan 2000–Dec 2017). Earthquakes ($M \geq 3$ grey dots, $M \geq 4$ yellow stars) generally occurred where injection increased pressure at depth. **d** Projected future pressure increase (Jan 2018–Dec 2020). With the exception of a region east of Oklahoma City, the pressure is expected to further increase through 2020. Note the different range of the colour schemes used in **c** and **d**. Mapped faults in the sedimentary cover[52] (**c** and **d**) are shown as grey lines

Arbuckle permeability is essential to relate seismicity rates to pressure increase. In some local-scale regions in the study area, earthquake rates and injection rates are completely unrelated and time lags of up to 10 years between peak injection and peak seismicity rates are observed (see Supplementary Fig. 4). While local-scale injection and seismicity is unrelated, the observed peak seismicity rates occur at peak pressure rates resulting from our model. Far-field pressurization, caused by high-rate injection wells outside of the considered areas, dominates and explains the high time lags between local injection and seismicity.

The map view of the cumulative injection-induced pressure increase (Jan 2000 through Dec 2017) in the complete study area shows that earthquakes generally occurred where injection increased pressure at depth (Fig. 1c). However, we find that the seismogenic response to a given pressure increase is variable in space (Fig. 1c and Supplementary Figs. 4, 5). In some areas, a relatively small pressure increase results in a high number of earthquakes, while other regions of higher pressure increase show only a low level of seismicity. Such variations are not unexpected, because the seismogenic state, the number and stress state of preexisting basement faults affected by the pressure increase, can vary from one region to another. Based on our observations, we consider a spatially variable seismogenic state in our hybrid physics-based statistical model presented in the next section.

We use the hydrogeologic model to project future pressure changes assuming constant injection rates after March 2018 (Fig. 1b; dashed grey line). Our diffusion model predicts that, with an exception of the area east of Oklahoma City, pressure at

Received by OCD: 6/29/2026

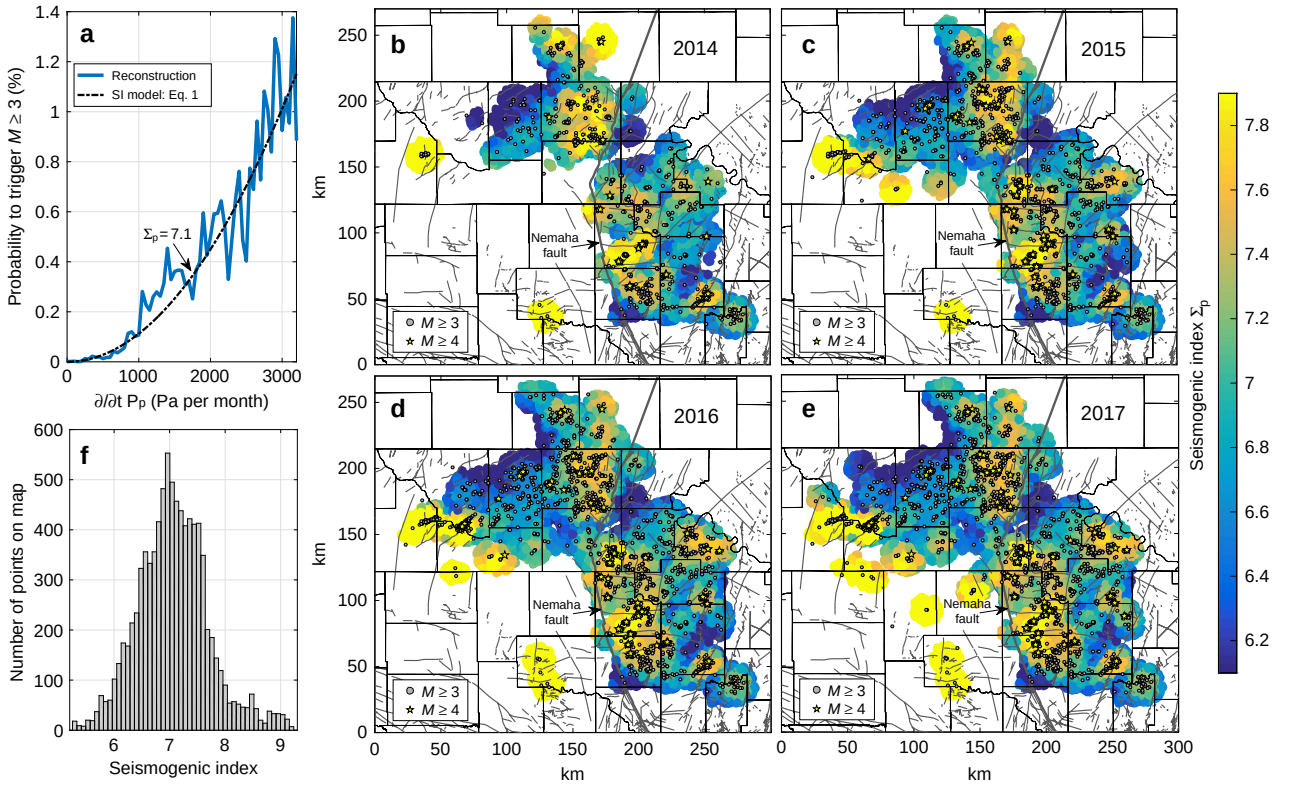


Fig. 2 Reconstructed earthquake-triggering probability ($M \geq 3$), seismogenic index maps and histogram of spatial SI fluctuations. **a** Reconstructed probability to trigger an $M \geq 3$ earthquake at a given pressure rate in our model (see Methods for details). The reconstruction is based on observed earthquakes and modelled pressure rates through Dec 2017 in the complete study area. The probability increases with the square of the pressure rate and a SI of 7.1 (see Eq. 1). **b**–**e** Mapped spatial variability of the SI in north-central Oklahoma and southern Kansas. The SI has been computed in local-scale regions of 10-km radius around the 25,000 seed points and is calibrated through different temporal endpoints between December 2014 and December 2017. The SI shows significant variability in space but it is stable in time. Regions of high and low SI can already be differentiated using earthquakes through Dec 2014 for calibration. More details on the calibration of the SI can be found in the Methods section. **f** Histogram of the calibrated SI shown on the map in panel **e**. The mapped SI fluctuates around a mean value of about 7.1

depth continues to increase through 2020 (Fig. 1d). Increasing pressure will result in further destabilization of faults and seismicity is expected to continue. However, we expect a continuously declining earthquake rate through 2020, because the overall rate of pressure increase (Fig. 1b; red line) is continuously slowing down to the levels observed in 2009, when induced seismicity began.

Modified Gutenberg–Richter relation for induced earthquakes. We set up a model to transfer injection-induced pressure increases in time and space into seismicity rates by reconstructing how triggering probabilities of observed earthquakes are related to modelled pressure rates. High-pressure rates (fast pressure increases) are driving faults faster towards failure by reducing the effective normal stress. Compared to low-pressure rates, more faults are expected to reach the failure stress in a given time and we expect faster pressure increases to be more likely associated with earthquakes. The relation between pressure rate and earthquake probability (Fig. 2a) reconstructed from our model (see Methods for details) confirms the expected increase of earthquake probabilities with the rate of pressure increase. Earthquake probabilities in Oklahoma and Kansas are increasing with the square of the pressure rate (Fig. 2a). Slow pressure increase is causing a disproportionally low percentage of seismicity.

To honour our observations of the increase of the earthquake-triggering probability with the square of the pressure rate (Fig. 2a) and the spatially variable seismogenic state (Fig. 1c and Supplementary Figs. 4, 5), we combine our hydrogeologic model and a modification of the seismogenic index (SI) model[7,16]. In the combined model, we describe monthly earthquake rates $R_{\geq M}(\mathbf{r},t)$ of magnitude M and larger at location $\mathbf{r}$ and time t according to a modified Gutenberg–Richter law for induced earthquakes

$$R_{\geq M}(\mathbf{r},t) = 10^{a(\mathbf{r},t)-bM} = \left[\frac{\partial}{\partial t}P_{\mathrm{p}}(\mathbf{r},t)\right]^2 10^{\Sigma_{\mathrm{p}}(\mathbf{r})-bM} \qquad (1)$$

In Eq. 1, we introduced a space- and time-dependent earthquake productivity $a(\mathbf{r},t) = \log_{10}\left\{\left[\frac{\partial}{\partial t}P_{\mathrm{p}}(\mathbf{r},t)\right]^2\right\} + \Sigma_{\mathrm{p}}(\mathbf{r})$, which is determined by the monthly injection-induced pressure rate $\frac{\partial}{\partial t}P_{\mathrm{p}}(\mathbf{r},t)$ in space and time and the spatially variable SI $\Sigma_{\mathrm{p}}(\mathbf{r})$. The quantity $10^{\Sigma_{\mathrm{p}}(\mathbf{r})}$ in Eq. (1) is a proxy for number and stress state of basement faults at location $\mathbf{r}$. The higher the SI at a location, the higher the earthquake rate caused by a given pressure increase, because a higher number of (or more critically stressed) preexisting faults are affected by the pressure increase. In agreement with the classical Gutenberg–Richter[31] law, 10^{-bM} describes magnitude scaling in our model. The SI and the b-value can be calibrated based on observed earthquakes and modelled

pressure rates up to a given time. The calibrated parameters and modelled future pressure rates can then be used to forecast expected earthquake rates above a given magnitude in space and time according to Eq. (1).

Note that the classical SI model[16] considers injection rates instead of pressure rates and is not (directly) applicable to decreasing injection rates. While Langenbruch and Zoback[7] bypassed this problem by considering a modification of Omori's law[32] to describe the decay rate of seismicity after injection rates start to decrease, in this study, we replace injection rates by pressure rates utilizing a hydrologic model to make our model applicable to arbitrary injection scenarios.

Mapping the seismogenic state. To characterize spatial variability of the seismogenic state throughout the study area, we calibrate $\Sigma_p(\mathbf{r})$ in local-scale regions of 10-km radius around the 25,000 seed points (Fig. 2b–e) by analyzing pressure changes and earthquake rates in each area (see Methods for details). Note that the SI in our model is determined based on observed earthquakes and modelled pressure increases at the fault seed points and is not directly comparable to values determined in other studies using injection volumes[7,16].

We find that $\Sigma_p(\mathbf{r})$ varies by about two units across the study area (Fig. 2b–f). This would mean that in areas of the highest SI, a given pressure increase will cause one hundred times as many earthquakes as in areas characterized by the lowest SI. The SI maps (Fig. 2b–f) can be interpreted as a map of critically stressed faults in the crystalline basement in the areas affected by pressure changes. The areas of highest SI imply one hundred times as many preexisting faults than the areas of lowest SI. Thus, both the local pressure increase and the local seismogenic state must be combined to determine the local rate of induced earthquakes.

To test the concept that spatial variations of $\Sigma_p(\mathbf{r})$ reflect the susceptibility of preexisting faults (formed over geologic time) to pressure changes, we show in Fig. 2b–e that SI maps calibrated through different time periods show only minor fluctuations. This suggests that as soon as the local SI can be determined from local seismicity, Eq. (1) can be used to forecast the expected rate of earthquakes caused by future pressure increase in the considered region.

Physics-based seismic hazard maps. Using our model, we produce 1-year maps of the seismic hazard to assess the probability of potentially damaging induced earthquakes in Oklahoma and Kansas from 2015 through 2020. To produce real forecasts based on knowledge about future injection rates, we only use observed earthquakes and modelled pressures through the end of a given year to calibrate the model (SI map and b-value) (Fig. 2b–e and Supplementary Fig. 7). According to Eq. 1, we then use modelled pressure rates in the coming year to forecast expected seismicity throughout the study area.

Note that fluctuations of the b-value calibrated through different times between Dec 2014 and Dec 2017 are within the uncertainty of the computation (see Supplementary Fig. 7). A spatially constant b-value is applied in the complete area, because b-values computed for small regions, which include a lower number of earthquakes, would show even larger uncertainties and have a high likelihood of being artefacts[33].

Considering that the occurrence of induced earthquakes is a Poisson process[7,13,16,34] the expected annual number ($N_{\geq M}$) of earthquakes of magnitude M or larger can be computed corresponding to Eq. 1 and the probability to exceed magnitude M per year can be determined according to

$$Pr(M) = 1 - Pr(0, M, N_{\geq M}) = 1 - \exp(-N_{\geq M}) \qquad (2)$$

$Pr(0, M, N_{\geq M}) = \exp(-N_{\geq M})$ corresponds to the probability that no earthquake of magnitude M or larger occurs in 1 year, if $N_{\geq M}$ earthquakes of magnitude M or larger are expected.

We choose a magnitude of $M = 4$, because lower magnitudes are very unlikely to cause damage. The resulting prospective 1-year maps of the probability to exceed $M = 4$ (Fig. 3) show how the seismic hazard in time and space is changing in response to spatial and temporal variations of injection rates and spatial changes of the SI. The probabilities shown in Fig. 3 were computed in regions of 20-km radius around the 25,000 seed points. However, the hazard maps can be determined for arbitrary magnitude thresholds, regions and time scales.

We find that earthquakes observed in the year of the predictions occur where our model forecasts enhanced exceedance probabilities (Fig. 3a–d). In total, 64 of 65 $M \geq 4$ earthquakes recorded from Jan 2015 through May 2018 occurred where our model predicts annual exceedance probabilities above 10%. In total, 57 of 65 $M \geq 4$ earthquakes occurred within contours of 30% exceedance probability.

In response to decreased saltwater injection rates, pressure increases are slowing down over a wide range of depths (Supplementary Fig. 8) and our model forecasts a widespread reduction of the seismic hazard in 2017. Even without additional injection rate reductions after March 2018, our model predicts a further decrease of the seismic hazard in 2018, 2019 and 2020. Note that this decrease is caused by the diffusive nature of the pressure migration and the disproportionally low probability of earthquake triggering for slow pressure increases.

East of the Nemaha fault, where injection rates have been reduced most significantly, the strongest decrease is predicted (see Fig. 3). In other parts of northern Oklahoma and southernmost Kansas, $M \geq 4$ probabilities remain on a higher level. Our physics-based maps identify three regions where $M \geq 4$ exceedance probabilities in 2018 remain above 30% (Fig. 3d). Note that most earthquakes observed in 2018 to date occur in or close to these regions. Earthquake probabilities in 2018, 2019 and 2020 are based on the assumption of a constant injection level after March 2018. Further injection rate reductions would accelerate the probability decrease and our model can be updated as soon as new injection data become available.

More importantly, a significant advance of our physics-based method is that it can be used to identify the optimal injection strategy to mitigate the remaining seismic hazard. Alternative scenarios for future injection rates in space and time could easily be considered to evaluate how possible injection regulations would affect the seismic hazard. Not only further reduction in total injection volume, but also a redistribution of injection volumes in the study area could mitigate the seismic hazard. Moving injection volume away from critical regions of high SI could lower the injection-induced seismic hazard without reducing the overall volume of injection.

Retrospective performance evaluation in time and space. To retrospectively evaluate the performance of our model, we compare the observed seismicity rate ($M \geq 3$) in the complete study area to the forecasted seismicity rate resulting from SI models calibrated through different temporal endpoints. We select a magnitude threshold of $M = 3$, because the model performance should be tested based on the highest possible number of observations. Note that while the observed rate of $M \geq 4$

Received by OCD: 6/29/2026

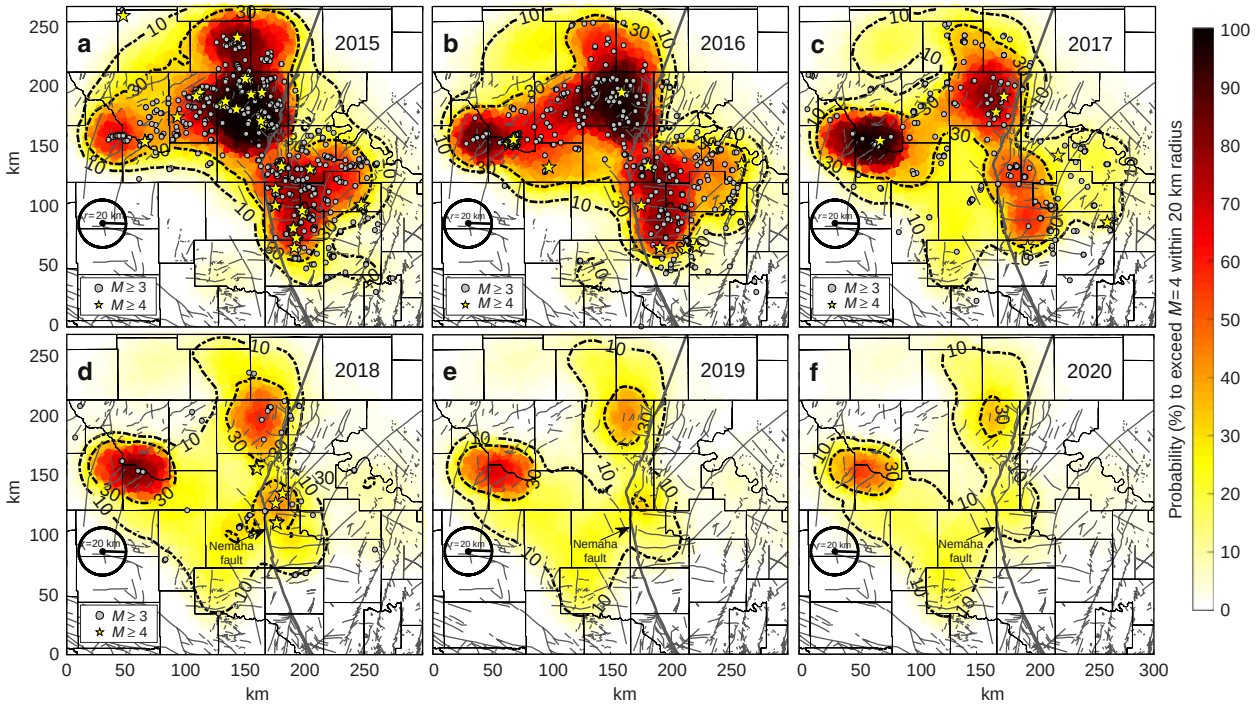


Fig. 3 Physics-based 1-year magnitude ($M \geq 4$) exceedance probability forecasts (2015–2020). Exceedance probabilities are forecasted in areas of 1257 km^2 (20-km radius) and for the time of 1 year. Grey circles and yellow stars show $M \geq 3$ and $M \geq 4$ earthquakes observed in the year of the forecast, respectively. The local seismic hazard is controlled by local pressure increase at depth and the local seismogenic state (the SI Fig. 2b–e). Decrease of magnitude probabilities from 2015 to 2020 is driven by reduced injection rates, which slow down the pressure increase at seismogenic depth. The strongest decrease of the seismic hazard is predicted east of the Nemaha fault, where injection rates were reduced most significantly. Probabilities of 2018–2020 were computed assuming constant injection rates after March 2018. The maps can be produced for arbitrary future injection scenarios to optimize the distribution of fluid injection volumes in space and time for seismic hazard mitigation

earthquakes falls well within the uncertainty range of our model (Supplementary Fig. 9), it does not allow us to draw statistically significant conclusions, because of the high uncertainty caused by the smaller number of $M \geq 4$ observations.

The modelled seismicity rate forecasts of $M \geq 3$ (Fig. 4a) reproduce increase, peak and decrease of the overall observed earthquake rate. However, some short-term spikes peak out of the expected range of seismicity. These spikes are caused by aftershocks of the relatively larger earthquakes such as the $M =$ 5.7 Prague, $M = 5.1$ Fairview and $M = 5.8$ Pawnee earthquakes. In the same way, the slightly under-predicted peak of seismicity in 2015 consists of various spikes of aftershocks following earthquakes of moderate magnitudes (Supplementary Figs. 4, 5). Our model relates long-term trends of produced-water injection to long-term trends of seismicity and is not designed to forecast short-term spikes related to aftershocks. We decided not to remove aftershocks from the catalogue, because declustering depends on a subjective algorithm[35,36] and parameter choices. Moreover, aftershocks contribute to the seismic hazard. Removing them from a hazard assessment seems inappropriate[15].

Figure 4a demonstrates that changing the temporal endpoint of the calibration between Dec 2011 and Dec 2017 has no significant effect on forecasted seismicity rates. Had we only used earthquake information through Dec 2011 to calibrate the SI, our model would have successfully predicted the increase, peak and decrease of the large-scale seismicity rate in response to changes of injection rates.

Ultimately, the most important application of our model is that it can be used to predict local-scale seismicity rates, because the SI is calibrated on the local scale. In Supplementary Fig. 5, we present seismicity rate forecasts in six local-scale study areas of 25-km radius. The areas are selected to represent the full value range of the SI identified across the complete study area (Supplementary Fig. 6). Our results show that our model can be used to forecast local-scale seismicity rates. However, because the local-scale SI can vary significantly from the large-scale average, local-scale model calibration (based on local seismicity and pressure increase) is required to successfully forecast local-scale seismicity rates. We find that compared to the purely observational approach of using last year's earthquakes to predict next year's seismicity, incorporating injection rates and a spatially variable SI through our physics-based approach significantly increases the forecasting performance in time and space (Supplementary Fig. 10).

In Fig. 4a and Supplementary Fig. 5, we compare our results to a recent paper[37] which also considers injection rates to model seismicity rates in Oklahoma and Kansas based on rate and state friction[38]. It considers the Arbuckle group as a closed hydrogeologic system with equally distributed injection rates throughout the region. Because no forecast of the seismicity rate (2018–2020) is presented in the publication, we forecast the seismicity rate through Dec 2020 based on the rate-and-state model[37] assuming constant injection rates after March 2018 as in our analysis.

While the large-scale seismicity rates resulting from the rate-state and the SI models are similar from 2012 through 2015, the rate-state model significantly under-predicts the decay rate following reduced injection rates (Fig. 4a). Moreover, as the rate-and-state model does not consider spatial variability of model parameters, it is not able to describe onset, increase, peak

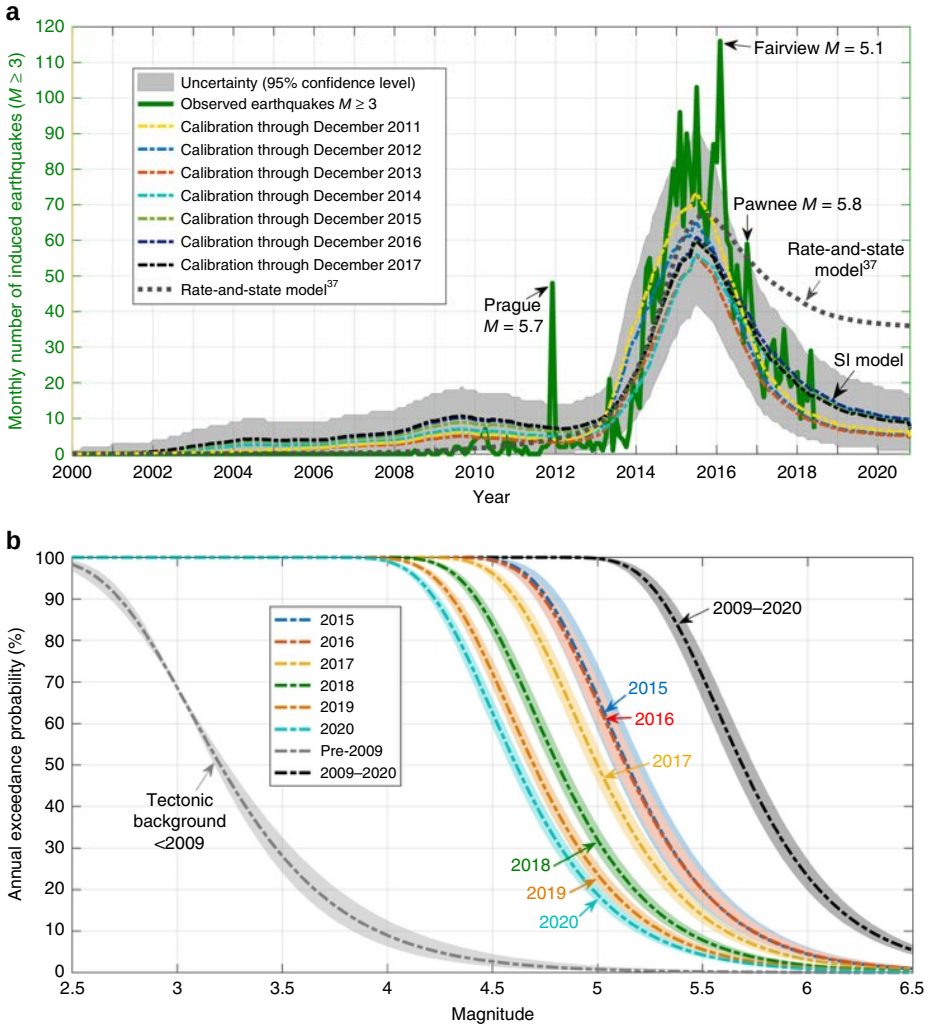


Fig. 4 Forecasted seismicity rate ($M \geq 3$) and magnitude exceedance probability in the complete study area. **a** Observed earthquake rate (solid green line), and forecasted seismicity rates resulting from SI models calibrated through different temporal endpoints (Dec 2011–Dec 2017) (coloured dashed lines). Changing the temporal endpoint of the calibration has only a minor effect on forecasted seismicity rates. A recently published model[37], based on rate and state friction, significantly under-predicts the decrease of the earthquake rate caused by reduced injection (dotted grey line). **b** Forecasted annual exceedance probability of magnitude M in the complete study area. The forecasted probability of potentially damaging earthquakes is significantly enhanced compared to the tectonic background and is the highest in 2015 and 2016. Background probabilities are adopted from Langenbruch and Zoback, 2016[7]. In response to reduced injection rates magnitude exceedance probabilities are decreasing, but still above the tectonic background level through 2020. The overall injection-induced pressure increase from 2009 to 2020 has a potential of 23% to trigger a damaging $M \geq 6$ earthquake (6% of $M \geq 6.5$). Uncertainties (shaded areas) represent *b*-value computations (see Supplementary Fig. 7)

or decay of seismicity in any of the six local-scale regions presented in Supplementary Fig. 5.

Discussion

Based on a physical understanding of injection-induced earthquakes, we developed forecasts of the spatially variable and time-dependent earthquake hazard in Oklahoma and Kansas. In our hybrid physical–statistical model, occurrence probabilities of potentially damaging earthquakes are driven by two factors: (1) the rate of injection-induced pressure increase at depth resulting from the locations and injection rates of the saltwater disposal wells and (2) spatial variations in number and stress state of preexisting basement faults that are affected by the pressure increase.

Other studies[16,32] observe a direct proportionality between pressure increase (injection rates) and earthquake probability during hydraulic stimulation of enhanced geothermal systems and hydraulic fracturing sites. However, we find that earthquake probabilities in Oklahoma and Kansas are increasing with the square of the pressure rate (Fig. 2a). Slow pressure increases cause a disproportionally low percentage of seismicity. Relatively more aseismic fault creep could be occurring when there are slow pressure increases. Moreover, aftershock triggering might contribute to the over-proportional increase of probabilities with the rate of pressure increase.

Our finding of disproportionally low earthquake probabilities at slow pressure increases has important implications for hazard management of induced earthquakes. It underlines the effectiveness of injection rate reductions, which slow down the rate of

Received by OCD: 6/29/2026

pressure increase at seismogenic depth. At the current level of saltwater injection, our model forecasts slowly decreasing earthquake probabilities through 2020. As shown in Fig. 4a, about 190, 130 and 100 widely felt $M \geq 3$ earthquakes are expected in 2018, 2019 and 2020, respectively. This represents a significant reduction compared to 943 earthquakes of $M \geq 3$ observed in 2015.

When communicating probabilistic seismic hazard forecasts to decision-makers or the public, it is important to emphasize that forecasted probabilities strongly depend on the considered scale in time and space. For instance, the annual probabilities to exceed $M = 5$ in 2018, 2019 and 2020 are low (≤5%) in local-scale regions of 20-km radius (Supplementary Fig. 11). However, the annual probability that there will be an $M \geq 5$ somewhere in the affected area is as high as 32%, 24% and 19% in 2018, 2019 and 2020, respectively (Fig. 4b).

Also a longer timescale of interest increases the forecasted probability of earthquake damage. Considering the cumulative injection-induced pressure increase from 2009 to 2020 results in a 24% chance of a damaging $M \geq 6$ (6% of $M \geq 6.5$) earthquake (Fig. 4b). Based on the predicted pressure increase from Jan 2018 through Dec 2020, one additional $M \geq 5$ earthquake is expected to occur (Supplementary Fig. 12). Seismic activity is expected to remain elevated in respect to the tectonic background of about one $M \geq 3$ earthquake and a probability of about 1% to exceed $M \geq 5$ per year[7] observed in the region prior to 2009. Thus, as long as earthquakes are induced by saltwater injection in Oklahoma and Kansas, occurrence of even larger magnitudes (than those observed to date) cannot be ruled out completely. To further mitigate the remaining induced seismic hazard alternative, future injection scenarios could be used as input to our method to identify the optimal injection strategy in time and space.

Methods

Injection well data. We specifically analyzed and utilized Oklahoma Corporation Commission (OCC)[39] and Kansas Corporation Commission (KCC) injection data for Arbuckle Group injection wells operating in the area of interest[12] in north-central Oklahoma as well as Harper and Sumner counties in south-central Kansas. We obtained injection data for wells in Oklahoma and Kansas going back as far as January 2000. Only a handful of wells contain injection information back that far, but we used the most complete dataset of injection data to simulate the largest possible build-up of pressure in the model.

Monthly injection data for most Kansas wells began to be reported in January 2012. Prior to the reporting of monthly injection data, we assumed that annual injection was distributed proportionally across all 12 months of the year. Injection data in Oklahoma and Kansas were collected through March 2018 and December 2016, respectively. All models which project future trends in pressure and seismicity assume that injection wells operated at constant rates are equal to the average of the last three reported months of injection data.

Numerical hydrogeologic model. Our numerical model of the hydrogeologic system of Oklahoma's deepest sediments and crystalline basement is aimed at predicting fluid injection-related pore pressure changes at depth in space and time. Here, we developed a three-dimensional hydrogeologic model which simulates fluid injection from wells operating in the Arbuckle Group from January 2000 through December 2020. We simulate the diffusion of pore pressure using MODFLOW, a modular finite difference numerical code developed by the U.S. Geological Survey[40]. MODFLOW solves for changes in hydraulic head, which are directly proportional to pore pressure, using the groundwater flow equation

$$\begin{aligned} &\tfrac{\partial}{\partial x}\left(K_{xx}\tfrac{\partial h}{\partial x}\right) + \tfrac{\partial}{\partial y}\left(K_{yy}\tfrac{\partial h}{\partial y}\right) + \tfrac{\partial}{\partial z}\left(K_{zz}\tfrac{\partial h}{\partial z}\right) \\ &= S_s\tfrac{\partial h}{\partial t} - Q_i(t)\delta(x-x_i)\delta(y-y_i)\delta(z-z_i), \end{aligned} \quad (3)$$

where h is the hydraulic head [L], K_{ij} are the principal components of the hydraulic conductivity tensor [LT^{-1}], S_s is the specific storage coefficient [L^{-1}] and x, y, z and t are spatial and temporal coordinates. Q_i is the fluid source or sink (T^{-1}). Changes in hydraulic head are directly proportional to changes in pore pressure when accounting for the specific weight of water ($\Delta P_p = \rho g \Delta h$). The hydraulic conductivity tensor is directly proportional to permeability (k) when accounting both for the specific weight (ρg) and dynamic viscosity (μ) of the fluid ($K_{ij} = k_{ij}\frac{\rho g}{\mu}$). The numerical code assumes that injected fluids are of constant density and dynamic viscosity. The fluid density and fluid dynamic viscosity in the model are 1062 kg m^{-3} and 0.547 cP, respectively (Supplementary Table 1). To calculate the fluid density and dynamic viscosity used in the model, we assume a brine TDS of 100,000 ppm[41] and a reservoir temperature of 50 °C derived from a standard geothermal gradient of 25 °C km^{-1}.

Injection in our model occurs into the 2.1-km-deep, 400-m-thick Cambrian-aged, fractured dolomitic carbonate Arbuckle Group and is assumed to be uniform across the entire depth of the interface. The Arbuckle Group is underlain across the entire model domain by a lower-permeability crystalline basement to a depth of 20 km (Supplementary Fig. 13). We explicitly calculate all pressure changes in the model relative to a uniform, hydrostatic pre-injection baseline. The model domain stretches 406 km from east to west and 357 km from north to south, as measured from the model's northwest corner at UTM 409865 E, 4186546 N Zone 14. All model boundaries are of Neumann type (no-flow). Model boundaries in x and y were set intentionally far from the dominant region of injection such that they have no effect on pressure calculations. The upper boundary is reflective to the confined condition of the Arbuckle Group reservoir[8]. The lower boundary of the model domain is set intentionally very deep so as to have no effect on pressure calculations at hypocentral depths. Grid discretization in x–y is 500 × 500 m^2 with some variation as the outer edges of the model are approached. The model contains 12 discretization layers in the z-direction to accurately capture the diffusion of pore pressure in the vertical direction (Supplementary Fig. 13).

Our hydrogeologic model intentionally simplifies and idealizes the three-dimensional hydrogeologic medium by representing the system's large-scale bulk permeability with uniform layered heterogeneity. The initial model parameterizations are based on the reported range of Arbuckle Group permeability, 10^{-14}–10^{-12} m^2, from core, outcrop and monitoring well tests[18–22]. While lacking in direct measurements of crystalline basement permeability in Oklahoma and southern Kansas, we implemented bulk permeabilities of fractured basement rock from the literature (10^{-16}–10^{-14} m^2)[27,28,42]. Due to the inherent uncertainty in model parameterizations, we tested the sensitivity of model outputs to permeability by running several combinations of Arbuckle Group and crystalline basement permeabilities (Supplementary Table 2).

Specific storage in our model is a parameter derived from the porosity, bulk compressibility of water and bulk compressibility of rock reported in the literature for the Arbuckle Group and crystalline basement (Supplementary Table 1). Specific storage combines the bulk compressibility of water (β_w), bulk compressibility of rock (β_r), fluid density (ρ) and porosity (Φ) as described below:

$$S_s = \rho g(\beta_w \Phi + \beta_r), \quad (4)$$

We use a fluid density of 1062 kg m^{-3} reflective of brine with TDS of 100,000 ppm[41] at a reservoir temperature of 50 °C. The bulk compressibility of water of 4.4×10^{-10} Pa^{-1} respects the reservoir temperature. The bulk compressibility and porosity of the Arbuckle Group is 0.16×10^{-10} Pa^{-1} and 0.20 derived from direct observations and core testing[20,22,43]. The bulk compressibility and porosity of the crystalline basement is set from literature value to be 0.7×10^{-11} Pa^{-1} and 0.01, respectively[44]. All of our model sensitivities use specific storage of 1×10^{-6} m^{-1} and 1×10^{-7} m^{-1} for the Arbuckle Group[22,45] and crystalline basement[44], respectively.

Beyond the layered heterogeneity represented in our model, a key feature in our model is the representation of the Nemaha fault as a regional-scale, low-permeability barrier to cross-fault flow ($k = 10^{-20}$ m^2). The Nemaha fault is a structural uplift of Pennsylvanian–Permian age which runs roughly north–south from central Oklahoma through Kansas[23]. The structural uplift has served as a regional trap for oil and gas structures such as the Oklahoma City oil field[46,47].

Two key baseline datasets constrain the large-scale Arbuckle Group permeability: (1) the observed hydraulic underpressure for the deepest hydrostratigraphy in Oklahoma and Kansas, and (2) large-scale trends in reported daily wellhead pressures for Arbuckle injection wells in Oklahoma. The observed hydraulic underpressure, or the difference between the ambient fluid pressure and the land surface elevation, in aquifers of Cambrian–Ordovician–Silurian age in the U.S. mid-continent is well-known[41]. We used hydro-potentiometric surface data for aquifers of Cambrian–Ordovician–Silurian age from Nelson et al. (2015)[41], which were derived from drill-stem tests and calculated hydraulic underpressures at Arbuckle injection well locations (Supplementary Fig. 2a).

In early 2016, the Oklahoma Corporation Commission began mandating daily wellhead pressure measurements for Arbuckle injection wells operating within the area of interest in Oklahoma. Large-scale trends in daily wellhead pressures show that more than half of all Arbuckle injection wells, even wells operating at rates >10,000 m^3 day^{-1}, operate under gravity-feed injection requiring no wellhead pressure. Most of the remaining wells (~40%) operate at wellhead pressures between ~0.3 and 2 MPa[41], well within the pressure range expected simply from wellbore friction. These data indicate that the large-scale, bulk permeability of the Arbuckle Group is likely towards the high end of the reported range.

Injection-induced fault reactivation probability. To compute the probability of triggering M ≥ 3 earthquakes in our model (Fig. 2a), we divide the histogram of pressure rates triggering observed earthquakes (Supplementary Fig. 14a) by the histogram of monthly pressure rates at all 25,000 seed points in the model (Supplementary Fig. 14b). Pressure rates triggering observed earthquakes are extracted in the month of occurrence and at the epicentre locations of all $M \geq 3$ earthquakes in the catalogue through Dec 2017 (depth is fixed at 6.5 km below the surface).

Received by OCD: 6/29/2026

The histogram of earthquakes triggered at a given pressure rate (Supplementary Fig. 14a) does not directly give the probability to trigger an $M \geq 3$ earthquake (fault seed point) in our model. For instance, 90% of all pressure rates in the model are <1000 Pa month^{-1}, but only 15% of earthquakes are triggered in this range (Supplementary Fig. 14b).

Our model suggests that injection-induced pressure rates at seismogenic depths are low. Ninety-nine percent of all pressure rates at the 25,000 fault seed points are below 3000 Pa month^{-1} (Supplementary Fig. 14b). While our modelled rates of pressure increase are low, they fall within the range that has been observed to trigger natural earthquakes. Inter-seismic Coulomb stressing rates on the San Andreas Fault[48,49], for instance, are found to be on the order of 1000 Pa month^{-1}.

Calibration of the seismogenic index. Before calibrating the SI maps (Fig. 2b–e), we precondition the pressure rates resulting from the hydrogeologic model based on the physical understanding of pore pressure changes as the triggering mechanism of induced earthquakes. (1) Only positive pressure rates (pressure increases) are considered in our model, because decreasing pressure results in fault strengthening by increasing the effective normal stress. (2) If the pressure at a given seed point at a considered time is lower than the maximum observed pressure at any earlier time, the pressure rate is not considered. We do this to honour the stress memory effect of rocks (Kaiser effect), describing the necessity to exceed the previous observed maximum pressure (stress) level before seismicity is observed[50,51]. Our results show that including this effect has no large influence on calibrating the SI in Oklahoma and Kansas but might be important for application to other areas, where injection rates show a cyclic behaviour.

The following steps are performed to calibrate the SI maps (Fig. 2b–e) by comparing earthquake and pressure history in circular areas of 10-km radius. (1) Monthly pressure rates $\frac{\partial}{\partial t}P_\mathrm{p}(\mathbf{r}_n, t)$ at all n seed points within a radius of 10 km around a selected seed point up to a given calibration time t_c are extracted, squared and summed up to $\sum_n \left[\frac{\partial}{\partial t}P_\mathrm{p}(\mathbf{r}_n, t \leq t_\mathrm{c})\right]^2$. (2) The number $N_{M\geq 3}(t \leq t_\mathrm{c})$ of $M \geq 3$ earthquakes within 10-km radius around the selected seed point observed up to the given calibration time is determined. (3) The maximum likelihood estimate of the b-value is computed using all $M \geq 3$ earthquakes recorded through the calibration time in the complete study area (Supplementary Fig. 7). (4) The SI at location $\mathbf{r}$ is determined according to

$$\Sigma_\mathrm{p}(\mathbf{r}) = \log_{10}\left\{N_{M\geq 3}(t \leq t_\mathrm{c})\right\} - \log_{10}\left\{\sum_n \left[\frac{\partial}{\partial t}P_\mathrm{p}(\mathbf{r}_n, t \leq t_\mathrm{c})\right]^2\right)\Bigg\} + b(t_\mathrm{c})M. \quad (5)$$

We find that as soon as two earthquakes occurred in the local-scale areas of 10-km radius around a selected seed point, a good estimate of the SI can be obtained. Note that b-values are determined based on earthquakes in the complete study area. Where the number of earthquakes is not sufficient (<2 earthquakes) to directly calibrate the SI based on observed earthquakes and modelled pressure rates, we apply the following rule to obtain a SI value. If no directly calibrated SI value exists within 40-km radius around a selected seed point, the SI is set to the mean value of all directly calibrated SI values. If directly calibrated SI values exist within 40-km radius, the SI is interpolated (using the *griddata* function in Matlab). Dotted areas in Supplementary Fig. 6 show areas where interpolated or averaged SI values are used to create the seismic hazard maps shown in Fig. 3.

Data and code availability

Earthquake catalogue: http://earthquake.usgs.gov/earthquakes/search/. Injection well location and saltwater injection data: http://www.occeweb.com/og/ogdatafiles2.html. Additional data and codes supporting the findings of this manuscript are available from the corresponding author upon reasonable request.

Received: 28 February 2018 Accepted: 22 August 2018
Published online: 26 September 2018

References

1. Cornell, C. A. Engineering seismic risk analysis. *Bull. Seismol. Soc. Am.* **58**, 1583–1606 (1968).
2. McGuire, R. K. FORTRAN computer program for seismic risk analysis: U.S. Geological Survey Open-File Report, 76–67 (1976).
3. Algermissen, S. T., & Perkins, D. M. A probabilistic estimate of the maximum acceleration in rock in the contiguous United States: U.S. Geological Survey Open-File Report 76-416 (1976).
4. Frankel, A. C. et al. National seismic hazard maps - Documentation June 1996: U.S. Geological Survey Open-File Report, 96-532 (1996).
5. Ellsworth, W. L. Injection-induced earthquakes. *Science* **341**, 1225942 (2013).
6. Walsh, F. R. III & Zoback, M. D. Oklahoma's recent earthquakes and saltwater disposal. *Sci. Adv.* **1**, e1500195 (2015).
7. Langenbruch, C. & Zoback, M. D. How will induced seismicity in Oklahoma respond to decreased saltwater injection rates? *Sci. Adv.* **2**, e1601542 (2016).
8. Keranen, K. M., Weingarten, M., Abers, G. A., Bekins, B. A. & Ge, S. Sharp increase in central Oklahoma seismicity since 2008 induced by massive wastewater injection. *Science* **345**, 448–451 (2014).
9. Weingarten, M., Ge, S., Godt, J. W., Bekins, B. A. & Rubinstein, J. L. High-rate injection is associated with the increase in U.S. mid-continent seismicity. *Science* **348**, 1336–1340 (2015).
10. National Research Council. *Induced Seismicity Potential in Energy Technologies* (The National Academies Press, 2012).
11. U.S. Geological Survey. National Earthquake Information Center earthquake catalog; http://earthquake.usgs.gov/earthquakes/search/ last accessed June 2018.
12. Oklahoma Corporation Commission, Earthquake Response Summary, https://www.occeweb.com/News/2017/02-24-17EARTHQUAKE%20ACTION%20SUMMARY.pdf (2017).
13. Langenbruch, C. & Zoback, M. D. Response to Comment on "How will induced seismicity in Oklahoma respond to decreased saltwater injection rates?". *Sci. Adv.* **3**, eaao2277 (2017).
14. Petersen, M. D. et al. One-year seismic-hazard forecast for the central and Eastern United States from induced and natural earthquakes. *Seismol. Res. Lett.* **88**, 772–783 (2017).
15. Mulargia, F., Stark, P. B. & Geller, R. J. Why is probabilistic seismic hazard analysis (PSHA) still used? *Phys. Earth Planet. Inter.* **264**, 63–75 (2017).
16. Shapiro, S. A., Dinske, C., Langenbruch, C. & Wenzel, F. Seismogenic index and magnitude probability of earthquakes induced during reservoir fluid stimulations. *Lead. Edge* **29**, 304–309 (2010).
17. Puckette, J. O. Evaluation of underpressured reservoirs as potential repositories for liquid waste. Oklahoma State University, Ph.D. thesis, 273p (1996).
18. Franseen, E. K. & Byrnes, A. P. Arbuckle Group platform strata in Kansas: a synthesis (eds Derby, J. R., Fritz, R. D., Longacre, S. A., Morgan, W. A., & Sternbach, C. A.). The great American carbonate bank: The geology and economic resources of the Cambrian–Ordovician Sauk megasequence of Laurentia. AAPG Memoir 98, 1031–1047 (2012).
19. Morgan, B. C. & Murray, K. E. Characterizing small-scale permeability of the Arbuckle Group, Oklahoma. Oklahoma Geological Survey Open File Report (OF2-2015). Norman, OK. 12p (2015).
20. Carr, J. E., McGovern, H. E., Gogel, T. & Doveton, J. H. Geohydrology of and potential for fluid disposal in the Arbuckle aquifer in Kansas, Open File Report 86-491, US Geological Survey (1986).
21. Williams, J. *Geologic, Permeability, and Fracture Characterization of the Arbuckle Group in the Cherokee Platform, Oklahoma*. Emporia State University, M. S. Thesis, 75p (2015).
22. Perilla, P. C. *Rock Properties Derived from Analysis of Earth Tide Strain Observed in Continuous Pressure Monitoring of the Arbuckle Group of Oklahoma*. University of Oklahoma, M. S. Thesis, 79p (2017).
23. Gay, S. P. The Nemaha Trend - A System of Compressional Thrust-Fold, Strike-Slip Structural Features in Kansas and Oklahoma, *Shale Shaker*, **54**, 39-49 (2003).
24. Yeck, W. L. et al. Far-field pressurization likely caused one of the largest injection induced earthquakes by reactivating a large preexisting basement fault structure. *Geophys. Res. Lett.* **43**, 1944–8007 (2016).
25. Schoenball, M. & Ellsworth, W. L. Waveform-relocated earthquake catalog for Oklahoma and Southern Kansas illuminates the regional fault network. *Seismol. Res. Lett.* **88**, 1252–1258 (2017).
26. Brace, W. F. Permeability of crystalline and argillaceous rocks. *Int. J. Rock Mech. Min. Sci. Geomech. Abstr.* **17**, 241–251 (1980).
27. Ingebritsen, S. E. & Manning, C. E. Geological implications of a permeability-depth curve for the continental crust. *Geology* **27**, 1107–1110 (1999).
28. Townend, J. & Zoback, M. D. How faulting keeps the crust strong. *Geology* **28**, 399–402 (2000).
29. Toda, S., Stein, R. S. & Sagiya, T. Evidence from the AD 2000 Izu islands earthquake swarm that stressing rate governs seismicity. *Nature* **419**, 58–61 (2002).
30. Dieterich, J., Cayol, V. & Okube, P. The use of earthquake rate changes as a stress meter at Kilauea volcano. *Nature* **408**, 457–460 (2000).
31. Gutenberg, B. & Richter, C. F. *Seismicity of Earth and Associated Phenomenon*, 2nd ed. (Princton Univ. Press, Princton, NJ, 1954).
32. Langenbruch, C. & Shapiro, S. A. Decay rate of fluid-induced seismicity after termination of reservoir stimulations. *Geophysics* **75**, MA53–MA62 (2010).

Received by OCD: 6/29/2026

33. Kamer, Y. & Hiemer, S. Data-driven spatial b value estimation with applications to California seismicity: To b or not to b. *J. Geophys. Res. Solid Earth* **120**, 5191–5214 (2015).
34. Langenbruch, C., Dinske, C. & Shapiro, S. A. Inter event times of fluid induced earthquakes suggest their Poisson nature. *Geophys. Res. Lett.* **38**, L21302 (2011).
35. Reasenberg, P. Second-order moment of central California seismicity, 1969–1982. *J. Geophys. Res.* **90**, 5479–5495 (1985).
36. Gardner, J. K. & Knopoff, L. Is the sequence of earthquakes in Southern California, with aftershocks removed, Poissonian? *Bull. Seis. Soc. Am.* **64**, 1363–1367 (1974).
37. Norbeck, J. H., & Rubinstein, J. L. Hydromechanical earthquake nucleation model forecasts onset, peak, and falling rates of induced seismicity in Oklahoma and Kansas. *Geophys. Res. Lett.* **45**, 2963–2975 (2018).
38. Dieterich, J. A, constitutive law for rate of earthquake production and its application to earthquake clustering. *J. Geophys. Res.* **99**, 2601–2618 (1994).
39. OCC oil and gas data files website. http://www.occeweb.com/og/ogdatafiles2.htm, last accessed April 2018.
40. Harbaugh, A. W. et al. MODFLOW-2000, The U. S. geological survey modular ground-water model-user guide to modularization concepts and the ground-water flow process. *Open-file Report. U. S. Geol. Surv.* **92**, 134 (2000).
41. Nelson, P. H., Gianoutsos, N. J. & Drake., R. M. Underpressure in Mesozoic and Paleozoic rock units in the Midcontinent of the United States Underpressure in Mesozoic and Paleozoic Rock Units in the Midcontinent of the United States. *AAPG Bull.* **99**, 1861–1892 (2015).
42. Shapiro, S. A., Huenges, E. & Borm, G. Estimating the crust permeability from fluid-injection-induced seismic emission at the KTB site. *Geophys. J. Int.* **131**, F15–F18 (1997).
43. Kroll, K. A., Cochran, E. S. & Murray, K. E. Poroelastic properties of the Arbuckle Group in Oklahoma derived from well fluid level response to the 3 September 2016 Mw 5.8 Pawnee and 7 November 2016 Mw 5.0 cushing earthquakes. *Seismol. Res. Lett.* **88**, 963–997 (2017).
44. Freeze, R. A. & Cherry, J. A. *Groundwater* 604pp (Prentice-Hall, Englewood, Cliffs, New Jersey, 1979).
45. Domenico, P. A., & Schwartz, F. W. *Physical and Chemical Hydrogeology* Vol. 506 (Wiley, New York, 1998).
46. Dolton, G. L., & Finn, T. F. Petroleum geology of the Nemaha uplift, central mid-continent (No. 88-450-D). Dept. of the Interior, US Geological Survey (1989).
47. McBee Jr, W. Nemaha strike-slip fault zone. AAPG Mid-Continent Section Meeting (2003).
48. Freed, A. M., Ali, S. T. & Bürgmann, R. Evolution of stress in Southern California for the past 200 years from coseismic, postseismic and interseismic stress changes. *Geophys. J. Int.* **169**, 1164–1179 (2007).
49. Loveless, J. P. & Meade, B. J. Stress modulation on the San Andreas fault by interseismic fault system interactions. *Geology* **39**, 1035–1038 (2011).
50. Kurita, K. & Fujii, N. Stress memory of crystalline rocks in acoustic emission. *Geophys. Res. Lett.* **6**, 9–12 (1979).
51. Simpson, D. W., Leith, W. S. & Scholz, C. H. Two types of reservoir-induced seismicity. Bulletin of the Seismological Society of America **78**, (1988).
52. Darold, A., & Holland, A. Preliminary Oklahoma optimal fault orientations (Tech. rep.): Oklahoma Geological Survey (2015).

Acknowledgements

This study would not have been possible without the Underground Injection Control injection data provided by the Oklahoma Corporation Commission (OCC) and the Kansas Corporation Commission (KCC) and the National Earthquake Information Center earthquake catalogue provided by the U.S. Geological Survey. We thank Justin Rubinstein for providing the digitized injection data obtained from the KCC. The Stanford Center for Induced and Triggered Seismicity provided the financial support for this study.

Author contributions

C.L. conceived the study and performed the analysis except the hydrogeologic modelling part. M.W. implemented and performed the hydrogeologic modelling. M.D.Z. contributed to continual supervision and guidance; C.L. created all figures (except Supplementary Figs. 2, 13 created by M.W.), wrote and revised the manuscript with substantial input from M.W. and M.D.Z.

Additional information

Supplementary Information accompanies this paper at https://doi.org/10.1038/s41467-018-06167-4.

Competing interests: The authors declare that they have no competing interests.

Reprints and permission information is available online at http://npg.nature.com/reprintsandpermissions/

Publisher's note: Springer Nature remains neutral with regard to jurisdictional claims in published maps and institutional affiliations.

Open Access This article is licensed under a Creative Commons Attribution 4.0 International License, which permits use, sharing, adaptation, distribution and reproduction in any medium or format, as long as you give appropriate credit to the original author(s) and the source, provide a link to the Creative Commons license, and indicate if changes were made. The images or other third party material in this article are included in the article's Creative Commons license, unless indicated otherwise in a credit line to the material. If material is not included in the article's Creative Commons license and your intended use is not permitted by statutory regulation or exceeds the permitted use, you will need to obtain permission directly from the copyright holder. To view a copy of this license, visit http://creativecommons.org/licenses/by/4.0/.

© The Author(s) 2018

EXHIBIT 16

Received by OCD: 6/29/2026

International Journal of Greenhouse Gas Control 97 (2020) 103025

Contents lists available at ScienceDirect

International Journal of Greenhouse Gas Control

journal homepage: www.elsevier.com/locate/ijggc

Mechanistic modeling of CO_2 well leakage in a generic abandoned well through a bridge plug cement-casing gap

L. Pan*, C.M. Oldenburg

Energy Geosciences Division, Lawrence Berkeley National Laboratory, Berkeley, CA, 94720, United States

ARTICLE INFO

Keywords:
Mechanistic modeling
CO_2 and brine leakage
Bridge plug failure
Abandoned well

ABSTRACT

Both known and unmapped plugged and abandoned wells are potential leakage pathways for CO_2 from geologic carbon sequestration (GCS) sites. Although many abandoned wells have cement bridge plugs installed to prevent leakage, the seal between the cement and the inner casing wall is subject to failure. In this study, we carried out detailed T2Well simulations of cases of sudden non-Darcy flow of CO_2 and brine leakage up the gap between a cement plug and the inner steel casing wall that becomes a fully connected flow path during the post-injection period. The goal of our study was two-fold: (1) to understand the dynamics, rates, and the characteristic temporal signals associated with the onset of leakage through various gap-aperture sizes, and (2) to suggest potential monitoring strategies based on the findings. Simulation results show that the leakage of CO_2 and brine upward is transient with interesting phase interference behavior. Time-dependent oscillatory flows with varying pressure, temperature, and flow rates of CO_2 and brine show strong dependence on gap aperture. Phase-change and decompression lead to very low temperatures at the top of the well for gap apertures larger than 4 mm suggesting that remote thermal monitoring at the ground surface may be an effective way of monitoring even if well locations are not known a priori. Pressure in the well is also indicative of CO_2 leakage. The temporal patterns of changing temperature and pressure may be useful diagnostic signals for leakage detection. Finally, these transient leakage signals may provide information on the cause of leakage and/or characteristics of the flow path that could inform effective remediation design and execution approaches.

1. Introduction

Both known and unknown (unmapped) plugged and abandoned wells are widely recognized as potential pathways for CO_2 and brine to leak from geologic carbon sequestration (GCS) sites into potable groundwater aquifers and even back into the atmosphere (Gasda et al., 2004). Wells are often abandoned by a procedure involving emplacement of a cement bridge plug at depth, above which the well is filled with fluids such as brine, drilling mud, or corrosion-inhibiting fluid. The purpose of the cement bridge plug is to seal off the well from the reservoir, hydraulic communication to which is provided by perforations. The purpose of the fluid above the bridge plug is to maintain pressure and prevent rapid corrosion of the steel casing. Experience has shown that cement-casing interfaces are subject to debonding and other processes over time that lead to failure to seal that creates a leakage flow path for formation fluids and CO_2 upward past the plug into the fluid-filled well.

Before a plugged and abandoned well that is leaking up its inner casing string to the surface or into shallow soils above a buried well top can be fixed, the leakage must be detected and stopped. Challenges arise because CO_2 leakage rates through degraded cement seals may be small and fluid leakage manifestations on the ground surface from plugged and abandoned wells may be difficult to detect within natural background variations of moisture and CO_2 concentration. In this study, we have carried out detailed non-Darcy flow simulations of the transient period following the onset of CO_2 and brine leakage up the gap in a bridge plug between cement and inner casing wall and into the open fluid-filled column of a prototypical abandoned well. We vary the plug gap aperture and simulate two different bridge-plug lengths (10 m and 30 m) to investigate sensitivity of leakage signals to plug-gap properties. One purpose of this study is to provide information on expected leakage behavior dynamics and the temporal signals associated with non-isothermal CO_2 and brine leakage that can be used to design near-surface monitoring approaches for leakage detection. Through mechanistic modeling of viscous two-phase flow in the well-reservoir system, the reasons for various interesting dynamic behaviors can be explained. The simulation approach is general enough that the plug gap can also be conceived as being a fracture in the cement bridge plug with

* Corresponding author.
E-mail address: lpan@lbl.gov (L. Pan).

https://doi.org/10.1016/j.ijggc.2020.103025
Received 29 July 2019; Received in revised form 21 February 2020; Accepted 24 March 2020
Available online 11 April 2020
1750-5836/ © 2020 Elsevier Ltd. All rights reserved.

Received by OCD: 6/29/2026

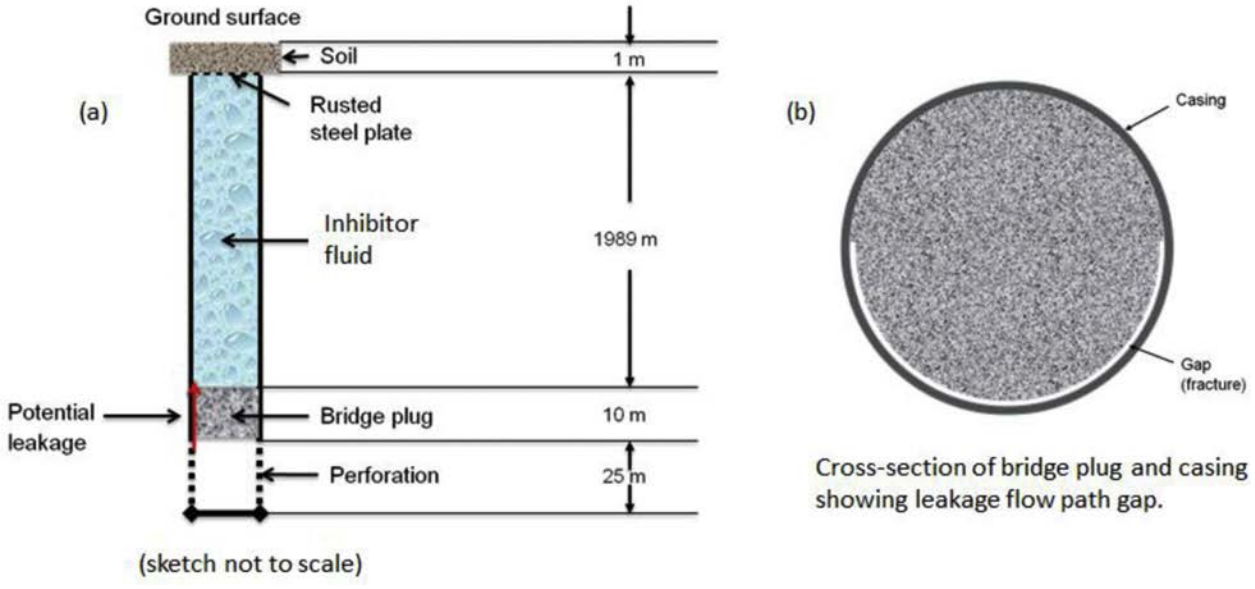


Fig. 1. (a) Conceptual model of prototypical abandoned well with bridge plug below long open section, and (b) cross section of bridge plug showing the gap (over one-half of the circumference) the aperture of which was varied in the simulations shown here. The reservoir and other formations (cap rock, soil etc.) are included in the model (see Fig. 2 and related text for details of the integrated well-reservoir model used in this study).

axial length equal to the plug thickness and horizontal length equal to one-half of the plug perimeter.

2. Background and prior work

Integrity failures in pre-existing wells of all kinds (abandoned, idled, shut-in, operating) completed to reservoir depth within the footprint of the CO_2 free-phase and/or pressure plumes of GCS sites are widely recognized as a potential cause of CO_2 and brine leakage from future large-scale GCS operations. There are several components of wells and critical interface seals that can fail over time and allow leakage to occur as summarized by Gasda et al. (2004). Of the several well integrity failure modes, failures resulting in open gaps and annuli, e.g., between cement and casing or between cement and formation, are considered by researchers studying CO_2 and brine leakage in the GCS context to be most likely to result in large leakage flow (Kutchko et al., 2007; Bachu and Bennion, 2009). Laboratory and field studies in the GCS context have found that chemical reactions between cement and carbonic acid (CO_2 dissolved in water) can degrade cement integrity (net dissolution) and in other cases lead to precipitation and self-sealing of gaps and spaces (Carey et al., 2010; Crow et al., 2010). Nevertheless, the large number of documented cases of sustained casing pressure (SCP) in oil and gas wells (Bourgoyne et al., 1999; Choi et al., 2013; Lackey et al., 2017) suggests that gaps and annuli are generally present in wells (Huerta et al., 2012). At least one example exists in the GCS context of poor bonding of cement to steel casing that can lead to gaps and annular spaces that compromise well integrity (e.g., Oldenburg et al., 2011).

Given the general concern for the integrity of existing wells, a large body of work exists focusing on the evaluation of the leakage rates and total leakage that could occur as a result of well integrity failure, along with remediation approaches (e.g., Wojtanowicz et al., 2001). Early studies were aimed at evaluating and mitigating sustained casing pressure (SCP) in oil and gas wells (e.g., Xu and Wojtanowicz, 2001), and these methods were further developed more recently (Huerta et al., 2012; Tao et al., 2010). As interest in GCS grew in the early 2000's, new semi-analytical approaches to modeling well leakage related to CO_2 and brine were developed and applied (e.g., Nordbotten et al., 2004, 2005). In addition, numerical methods including consideration of two-phase flow were developed and applied (e.g., Pruess, 2003; Celia et al., 2005; Ebigbo et al., 2007). Reduced order models (ROMs) for well leakage and aquifer impact have been developed by the U.S. Department of Energy's National Risk Assessment Partnership (NRAP) for quantification of the uncertainty of estimated leakage impacts (Pawar et al., 2016). Despite the large number of studies and solution approaches, all of the prior well leakage models except for NRAP's open-well leakage ROM (Pan and Oldenburg, 2016) have assumed that well leakage flow was through an effective porous medium, i.e., by the process of Darcy flow. While this assumption may be adequate for many cases involving SCP and/or low-flow-rate or incipient leakage through fine cracks or through tortuous paths in degraded cement, CO_2 and brine leakage through finite-aperture gaps and annuli between cement and casing should formally be modeled as viscous flow rather than Darcy flow.

In the study presented here, we simulate the onset and transient period of well leakage by single-, two-, and three-phase viscous (non-Darcy) flow in gaps or annuli of various apertures along a cement plug at the cement-casing interface within an idealized abandoned well. The conceptual model we assume is that the cement plug was sealing the abandoned well effectively up until some time during the post-injection period of the GCS project when the gap became fully connected across the plug and the well started to leak. Leakage along such a gap leads to reservoir fluid (CO_2 and/or brine) entering the fluid-filled column above the plug where non-Darcy pipe flow occurs by pressure gradient or buoyancy forces. At certain conditions, two types of CO_2-rich phases can exist, namely, gaseous CO_2 and liquid CO_2, which can lead to a three-phase (aqueous, gaseous CO_2 and liquid CO_2) system at different depths in the well. In all cases, we simulate the entire coupled reservoir-well (plug gap and well column) system upward to the top of the well at the ground surface considering coupled reservoir flow (Darcy flow) and open gap and column flow (non-Darcy flow). As it will be shown, these gap-leakage flow processes occur over time scales much smaller than expected chemical reaction time scales which were not included in our model. In order to focus on the flow processes and transient leakage signals, we also neglect for now geomechanical processes. To our knowledge, this is the first study that simulates the mechanistic non-isothermal process of three-phase flow in a narrow gap related to CO_2 and brine well leakage from a hypothetical GCS reservoir.

Received by OCD: 6/29/2026

3. Conceptual model

The prototypical abandoned well system that we simulate is shown in Fig. 1. In the system, a 1989 m-long column of inhibitor fluid (assumed to be pure water in this study) fills an open well above a 10 m-long cement bridge plug with an open gap (e.g., due to debonding) over part of its circumference (50 %). Although the current U.S. regulations require longer cement plugs for abandoned wells (e.g., extending 100 ft above oil bearing strata), many older wells abandoned prior to the 1950s either were not plugged at all or were plugged with very little cement in them (NPC, 2011). The requirement on length of cement plug is rather vague prior to the 1970s in the U.S. The longer the cement plug is, the lower the chance to be subject to through-going gaps and the greater the resistance is to leakage flow if a gap were to develop. We use a 10 m-long cement plug to reflect poor plugs in those older wells that are more vulnerable to leakage without losing the general features of leakage through a failed plug in abandoned wells. Additional results for a 30 m-long plug are presented for comparison.

The perforated bottom section of the well is in hydraulic connection with the permeable CO_2-filled reservoir. As with many plugged and abandoned wells, there is no wellhead and the top of the casing is conceptualized as being covered by a permeable rusted steel plate and 1 m of soil (Fig. 1a), both of which we model as porous media coupled to the open well. The thickness of the semi-circular gap between the cement plug and the casing wall is varied as a parameter in the simulations. Reservoir fluids (CO_2 and brine) have the potential to leak up the gap between the cement of the bridge plug and the inner casing wall into the column of inhibitor fluid and onward to the ground surface through the permeable materials (rusted steel plate and soil) at the top of the well. Note that although this is a coupled well-reservoir model, we do not intend to simulate the full development process of the CO_2-filled reservoir. Instead, we investigate possible dynamic behaviors of leakage when plug failure takes place in an abandoned well connected to a CO_2-filled reservoir during the post-injection period of the GCS reservoir.

The properties of the modeled system for the 10 m-long plug are presented in Tables 1 and 2. We note that all of the layers in the model (Table 2) are assumed to have pore compressibility of 3×10^{-9} Pa^{-1}, and that all layers have thermal conductivities of 3.0 W/(m ºC) and specific heats of 1000 J/(kg ºC).

All formation layers above the reservoir are saturated with water under hydrostatic pressure. The bottom formation layer is modeled (with 25 grid layers) to represent a GCS reservoir with a given initial gas (CO_2-rich phase) saturation (0.5 in this study) and initial pressure at the bottom grid cell equal to the hydrostatic pressure. Because of the existence of gas phase, the initial pressure at the top of the reservoir is slightly (1 bar) larger than the hydrostatic pressure that would exist at the same depth (1986 m below land surface) if the reservoir were fully saturated with water. The wellbore above the reservoir (including the plug) is initially saturated with water under hydrostatic pressure whereas the wellbore below the plug is under the same conditions as the reservoir. The geothermal gradient is 30 °C/km and the ambient temperature at land surface is assumed to be 25 °C. The entire domain is under natural ambient thermal conditions initially. Conditions at the top of the model are held at atmospheric pressure and ambient temperature (25 °C). In all cases we use a radially symmetric (*RZ*) grid with variable radial and vertical grid spacing (Fig. 2). A no-flow boundary is assigned along the lateral boundary at 1000 m away from the well.

Table 1
Well and plug properties.

Feature	Value
Well length	2024 m (from −1 m to −2025 m)
Casing ID	0.15962 m (7-inch casing, wall thickness = 9.09 mm)
Bridge plug	10 m thickness (from −1990 to −2000 m)
Perforation	25 m (from −2000 m to −2025 m)
Wall roughness of well	45×10^{-6} m
Wall roughness of plug gap	100×10^{-6} m
Gap aperture	Various
Effective porosity	Various, a function of aperture
Effective perimeter of gas	Various, a function of aperture
Rusted steel plate at top of the abandoned well	Assumed same permeability as cover soil (100 Darcy)

Table 2
Layer properties.

Layer	Depth (m)	Porosity	Lateral permeability (m^2)	Vertical permeability (m^2)
Reservoir sand	2000 − 2025	0.25	10^{-12}	10^{-12}
Cap rock	1980 − 2000	0.05	10^{-18}	10^{-18}
Overburden	10 − 1980	0.05	10^{-18}	10^{-18}
Soil2	1 − 10	0.45	10^{-15}	10^{-15}
Soil1	0 − 1	0.45	10^{-10}	10^{-10}

4. Methods

We simulate three-phase brine-CO_2 flow in the prototypical leaking well with T2Well, a numerical simulator for solving the equations of non-isothermal, multiphase, and multi-component flows in integrated wellbore-reservoir systems (e.g., Pan et al., 2011a, 2011b; Pan and Oldenburg, 2014). T2Well extends the numerical reservoir simulator TOUGH2 to calculate the non-Darcy flow in open (viscous) flow regions (i.e., not porous media) such as within well tubing, annuli, or cement-casing gaps and in connected porous media simultaneously and efficiently by identifying "wellbore" regions within the numerical grid in which two-phase viscous (non-Darcy) flow is simulated while generalized multiphase Darcy flow is simulated elsewhere. TOUGH2 uses a mass-conserving integral finite difference method with implicit time stepping to solve the multicomponent flow equations, and a residual-based convergence criterion with Newton-Raphson iteration to handle non-linearity (Pruess et al., 2012).

Within the wellbore sub-domains, T2Well solves a 1D momentum equation of the fluid mixture (which may be three-phase) as described by the extended drift-flux model (DFM). The velocity of the mixture is obtained by solving the momentum equation numerically while the individual phase velocities are calculated from the mixture velocity and other fluid-flow parameters as defined by the three-phase DFM. The three-phase DFM is formulated as a two-step extension of the two-phase DFM in which the two-phase DFM is first applied to get the aqueous phase velocity and the non-aqueous (CO_2-rich) phase velocity. If the non-aqueous phase is a mixture of gas and liquid CO_2, the two-phase DFM is then applied to obtain the liquid phase velocity and gas phase velocity with proper parameters from the non-aqueous phase velocity. A mixed implicit-explicit scheme is applied to facilitate the solution of the momentum equation within the Newton-Raphson iteration framework of TOUGH2. Specifically, the pressure gradient, the gravity component, and the time-derivative of momentum are treated fully implicitly while the spatial gradient of momentum is treated explicitly. The friction term is calculated with a mixed implicit-explicit scheme (Pan et al., 2011a). Although the wellbore flow model is one-dimensional and cannot describe two- or three-dimensional flow phenomena, the drift-velocity-model implemented in T2Well does parameterize the two- or three-phase flow instabilities and turbulence and even two-phase counter-flow to model the important multiphase flow phenomena. This wellbore-domain approach is coupled seamlessly with the standard TOUGH2 porous media approach to simulate coupled wellbore-reservoir flow problems. The approach has been demonstrated over the years for problems related to wellbore leakage and injection relevant to geologic carbon sequestration (Pan et al., 2011b), oil

Received by OCD: 6/29/2026

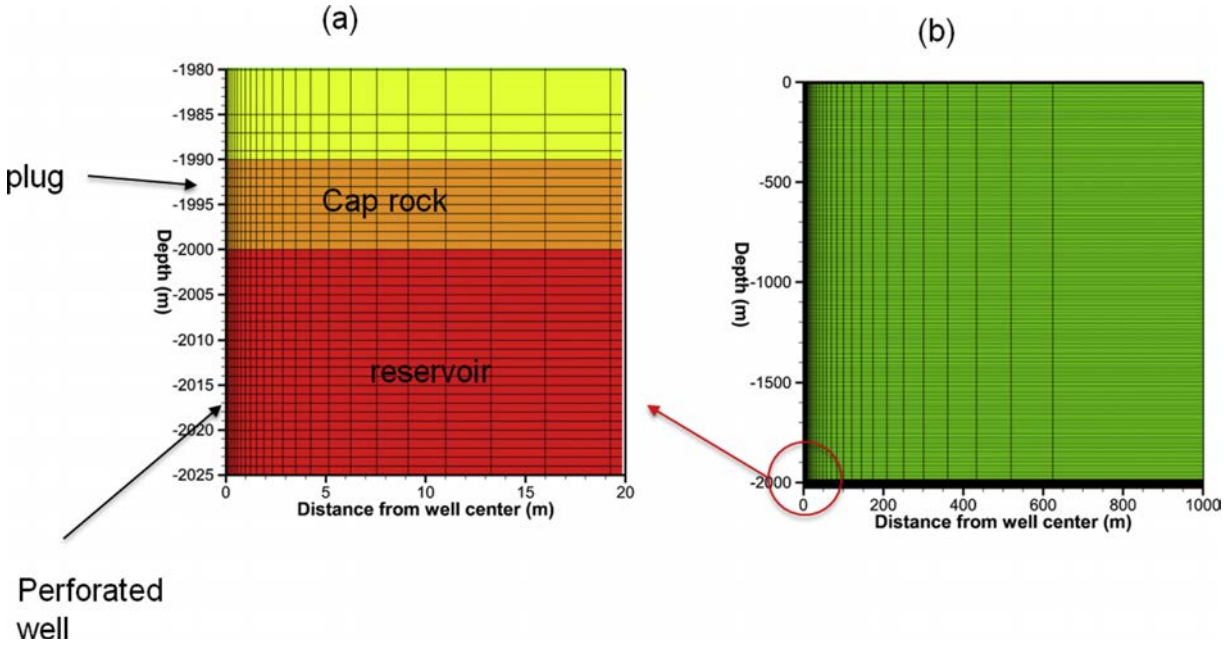


Fig. 2. Radially symmetric *RZ* grid used in the simulations. Horizontal grid resolution varies from 0.1 m near well to ~200 m in the far field while the vertical resolution varies from 1 m below a depth of −1995 m (the top of the plug) to 10 m above −1985 m and 1- ~2 m near land surface. (a) locally zoomed view of the region including the well perforation zone and the plug and (b) overview of entire simulation domain.

reservoir blowout (Oldenburg et al., 2011), and gas reservoir blowout (Pan et al., 2018a). The rigor of the flow modeling in T2Well is complemented by the accuracy of the equation of state (EOS) modules used for the fluid compositions and phase relations. In this study, we make use of a research version of ECO2M (Pruess and Spycher, 2007; Pan et al., 2017) which models three fluid phases (aqueous, gaseous CO_2, and liquid CO_2), and three chemical components (H_2O, CO_2, and salt) with recent improvements and extensions (Pan et al., 2018b). ECO2M is capable of modeling three-phase aqueous systems containing gaseous, supercritical, or liquid CO_2, including two simultaneously co-existing phases of CO_2. Note that the current ECO2M has a lower limit in temperature and cannot simulate the scenarios with frozen or hydrate-forming conditions. As a result, any possible blocking of leakage due to such conditions (forming of ice or hydrate) is not considered in this study. We refer the reader to Pan and Oldenburg (2014) for a complete description of the methods used in T2Well.

5. Results

5.1. Introduction

Before leakage control methods can be applied, leakage must be detected and the well must be located. In order to develop and improve CO_2 and brine leakage detection and abandoned well-locating methods, it is useful to know generally what such leakage signals look like so they can be distinguished from background variations (Oldenburg et al., 2003; Cortis et al., 2008). The mechanistic simulations presented here provide information on the pressure, temperature, and fluid compositional transient signals for the case of an abandoned well leaking CO_2 and brine along a gap in a bridge plug. These results are not meant to be used for quantifying leakage rates from any particular single well nor extrapolated to estimate leakage from multiple wells because the properties of the well modeled are idealized and not site-specific. Instead, the results are meant to be used to gain insight into the signals of leakage originating by this failure mode and to explain the mechanistic origins of the signals including their transient behaviors as a function of well system properties, with a focus on gap aperture. Insights gained from the results can be used to design monitoring and leakage quantification approaches that are especially challenging for unknown and abandoned wells.

The coupled three-phase flow system is complex resulting in the need for many figures to describe the results. We have organized the presentation into three tiers of results. The first tier summarizes the dynamic behaviors in terms of aqueous phase and CO_2-rich phase leakage rates as affected by the fracture aperture in the plug. The second tier analyzes the temporal evolution of well status in each individual well with particular aperture that causes particular characteristics in leakage behaviors. The third tier further analyzes different patterns of the friction and gravity pressure drops along the plug with different apertures which create unique characteristic leakage dynamics in the system that are very promising for leak detection.

5.2. Aqueous and CO_2-rich phase leakage rates

We present in Fig. 3 the aqueous (H_2O-rich) phase and non-aqueous (CO_2-rich) phase flow rates at the top of the well for five different gap apertures. In general, the leakage starts with one or two peaks of water eruption prior to breakthrough of CO_2-rich phase. This erupted water originates as water contained in the well above the plug prior to leakage onset. As shown in Fig. 3, the larger the gap aperture is, the larger the eruption strength and the earlier the eruption occurs. For example, the aqueous mass flow rate reaches 16.97 kg/s at about 130 min for the 8 mm aperture whereas the aqueous mass flow rate only reaches 1.73 kg/s at 290 min in the case of the 1 mm aperture (Fig. 3a). For a 0.5 mm aperture, the aqueous phase flow starts as a strong oscillatory flow with a very small flow rate (Fig. 3c). However, the magnitude of the flow rate during its single peak is larger than that in the 1 mm case although its after-peak aqueous phase flow rate is practically zero. After the short-lived transient water eruption, the aqueous phase flow rate greatly reduces to a small value associated with almost constant non-aqueous phase (CO_2-rich) flow. The non-aqueous phase (i.e., CO_2-rich phase) mass flow rate peaks immediately after breakthrough and then gradually reaches a stable value in most cases except for the cases of 1 or 2 mm gap aperture for which the early peak does not occur. The peak

Received by OCD: 6/29/2026

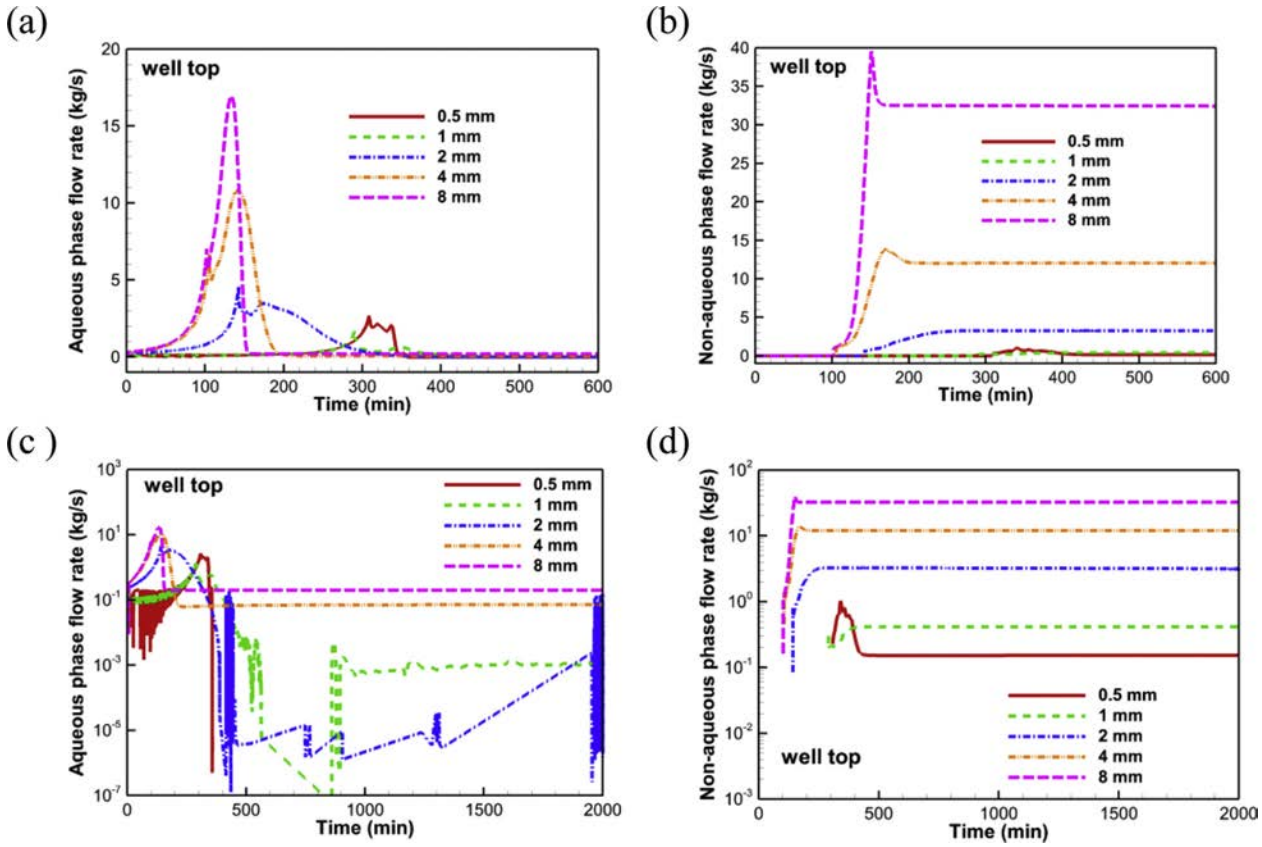


Fig. 3. Simulated mass flow rates of aqueous and non-aqueous phase at the wellhead as a function of time for the five gap apertures. (a) aqueous phase flow rate, (b) non-aqueous (CO_2-rich) phase flow rate, (c) aqueous phase flow rate (log-scale) and (d) non-aqueous phase flow rate (log-scale).

values of non-aqueous phase flow rate are 39.56, 13.88, 3.31 0.42, and 1.03 kg/s for gap apertures of 8, 4, 2, 1, and 0.5 mm, respectively. The corresponding stable flow rates are 32.5, 12.1, 3.3, 0.42 and 0.15 kg/s, respectively. The response in flow rate to gap-size variation is not linear.

The gap size does not only affect the timing and magnitude of aqueous phase eruption but it also regulates the dynamics of the aqueous phase flow rate and the final aqueous phase flow rate (Fig. 3c). As shown in Fig. 3c, the final aqueous phase flow rate decreases quickly with decrease of gap size for all cases in general although it does so in a manner of irregular oscillations in cases with intermediate gap size (e.g., 1 mm and 2 mm). As the aperture is reduced to 0.5 mm, the aqueous phase leakage rate is practically zero after a relatively big eruption at early time associated with the breakthrough of CO_2-rich phase.

Comparing the aqueous phase flow rate at the well top and plug top (Fig. 4) reveals complicated dynamics in phase changes in the well above the plug as a function of gap aperture. For the 8 mm aperture, the aqueous phase flow rate at the wellhead (i.e., well top) is slightly higher than that at the plug top which implies that water vapor has condensed in the well above the plug (Fig. 4a). This difference does not occur for the 4 mm gap in which the aqueous phase flow rates are identical at the wellhead and plug top. When the aperture is reduced to 2 mm, the aqueous phase flow rate out of the plug top is larger than that at the wellhead most of the time although the rate itself is very small. The aqueous phase leak at the wellhead for the 2 mm gap behaves more like a geyser (Fig. 4a) and water may flow downward in the well during those oscillation periods. As the aperture is reduced to 1 mm, the aqueous phase flow rate at the plug top is quite stable but small after early time eruption whereas the aqueous phase flow rate at the wellhead is slightly larger with obvious oscillations (Fig. 4b). However, as the aperture is further reduced to 0.5 mm, the aqueous phase flow rate at the plug top still shows strong oscillations although they tend to decrease with time significantly (Fig. 4b) while the aqueous phase flow rate at the wellhead is practically zero (Figs. 3c & 4 b). In smaller gap-aperture cases (1 and 0.5 mm), the aqueous phase flow rate at the plug top at early time shows strong oscillatory behavior (Fig. 4b).

5.3. Temporal evolution of well status

The complicated leakage behaviors observed to vary with gap aperture originate from variations in the non-isothermal phase change processes occurring in the well as the leakage progresses. In the following paragraphs, we will analyze the temporal evolution of aqueous phase saturation, pressure, temperature, and gaseous CO_2-ratio profiles in the well, case by case, to understand the mechanisms behind the leakage behaviors found in each case.

In the case of the 8 mm gap aperture (Fig. 5a), the initially water-filled well (above 2000 m, i.e., the plug and above) becomes very dry (aqueous saturation ~0.001 or less) after 150 min because the water has been lifted out of the well by the leaking "gas" (CO_2-rich phases) in the big eruption. As a result, the pressure above the plug drops significantly after the big eruption of water (Fig. 5b) although the pressure right above the plug is still around 9 MPa because of small resistance to the flow due to the large aperture (Fig. 6b) and around 3.6 MPa at well top (Fig. 6a). Before the water eruption, the temperature in the well increases in general as warmer fluid flows upward although the trend is complicated by the presence of CO_2-rich phase which is lighter than water (Fig. 5c). The CO_2-rich phase accelerates the upward flow which brings more enthalpy from below resulting in an increase of local temperature shown as the first peak (Fig. 5c) along the aqueous phase saturation line (Fig. 5a or d). However, increases in temperature tend to

Received by OCD: 6/29/2026

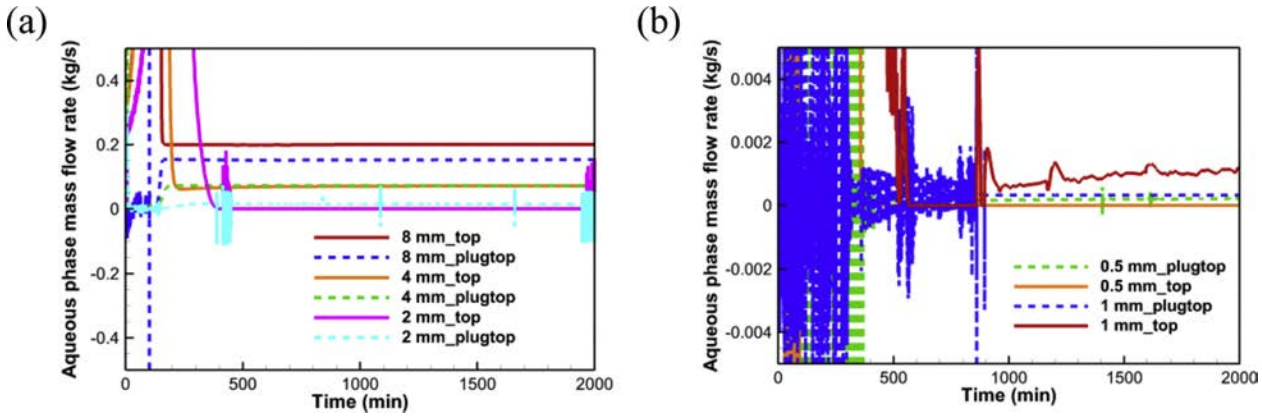


Fig. 4. Simulated mass flow rates of aqueous at wellhead (top) and top of plug (plugtop) as a function of time for the four gap apertures. (a) larger aperture (8, 4, and 2 mm) and (b) smaller aperture (1 and 0,5 mm).

be canceled or suppressed by the expansion cooling of the CO_2-rich phase as the CO_2-rich phase saturation further increases especially in shallow regions of the well until the water flow rate reaches the peak value at eruption when the CO_2-rich phase finally reaches the well top. After that the temperature above the plug drops to below 50 °C (Figs. 5c and 6d) because of expansion cooling. The temperature decreases with elevation (Fig. 5c) and reaches about 3 °C (the lower limit of the equation of state in the simulator) at the well top implying that dry ice or CO_2-hydrate could form under this larger aperture leakage scenario. Furthermore, as shown in Fig. 5d, although CO_2 transforms from supercritical to gas around the depth of 1500 m, there is a large region above the depth of 1000 m where a small amount of liquid CO_2 coexists with gaseous CO_2. This two-phase CO_2 region disappears near the top of the well (< 100 m) and the continuous evaporation of liquid CO_2 at that depth is responsible for the super-cooled condition of the well above this point (the actual temperature could be lower than what is shown considering the 3 °C lower-temperature limitation of the simulator).

If the 8 mm gap aperture is cut in half to 4 mm, the leaking gas is still able to flush the water out of the well to make a very dry well although it takes about 30 min longer time to do so (Fig. 7a). The pressure drop after the water eruption is more severe for the 4 mm gap than for the 8 mm gap (Fig. 7b) because of the larger resistance to leakage flow through the smaller (4 mm) aperture. The pressure right above the plug is reduced to 4.5 MPa while the well top pressure drops to 2.2 MPa (Fig. 6a, b), and pressures at both of these locations are significantly lower than those in the 8 mm case. Although the evolution of the temperature profile before the water eruption for the 4 mm gap

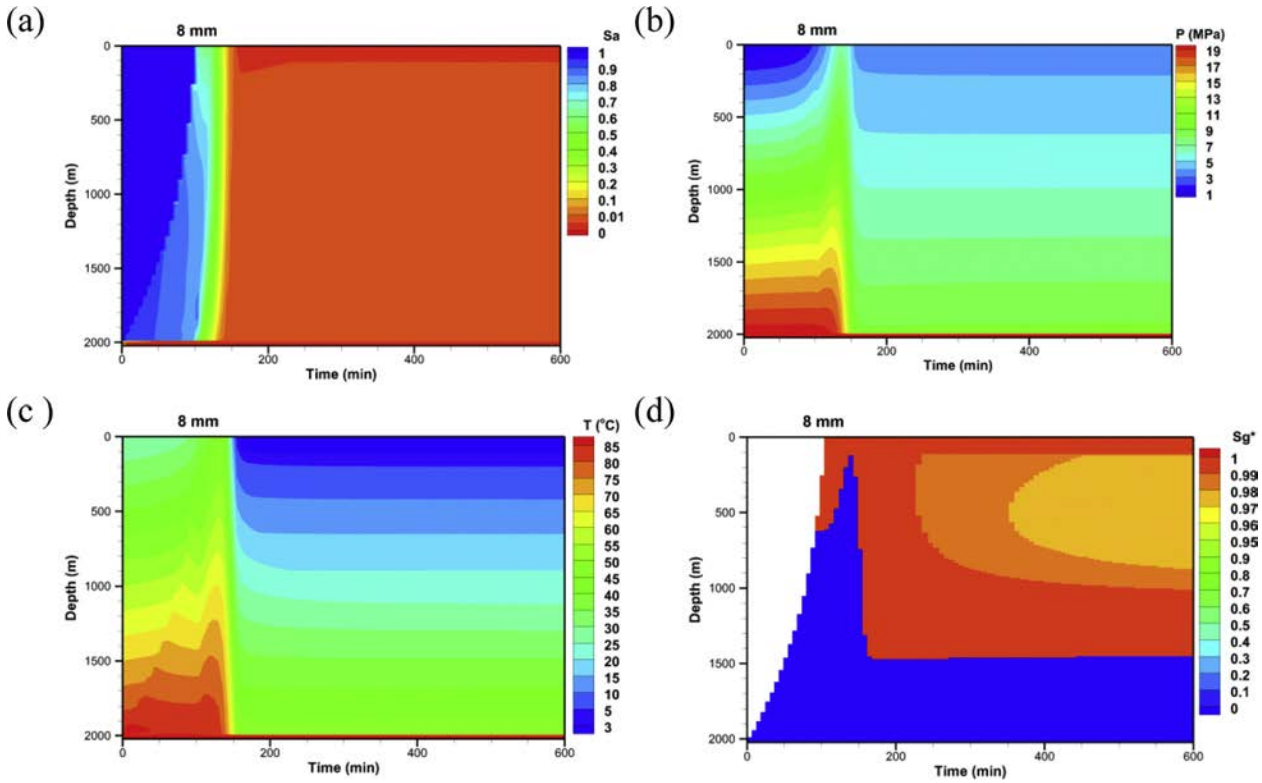


Fig. 5. Evolution of profiles of (a) aqueous phase saturation, (b) pressure, (c) temperature, and (d) the ratio of gaseous CO_2 saturation within CO_2-rich phase ($Sg^* = Sg/(Sg + S_L)$, Sg is the saturation of gaseous CO_2 while S_L is the saturation of liquid or super-critical CO_2) in the well for the 8 mm gap-aperture case. The white region indicates no free CO_2 phase exists (i.e., Sa = 1).

Received by OCD: 6/29/2026

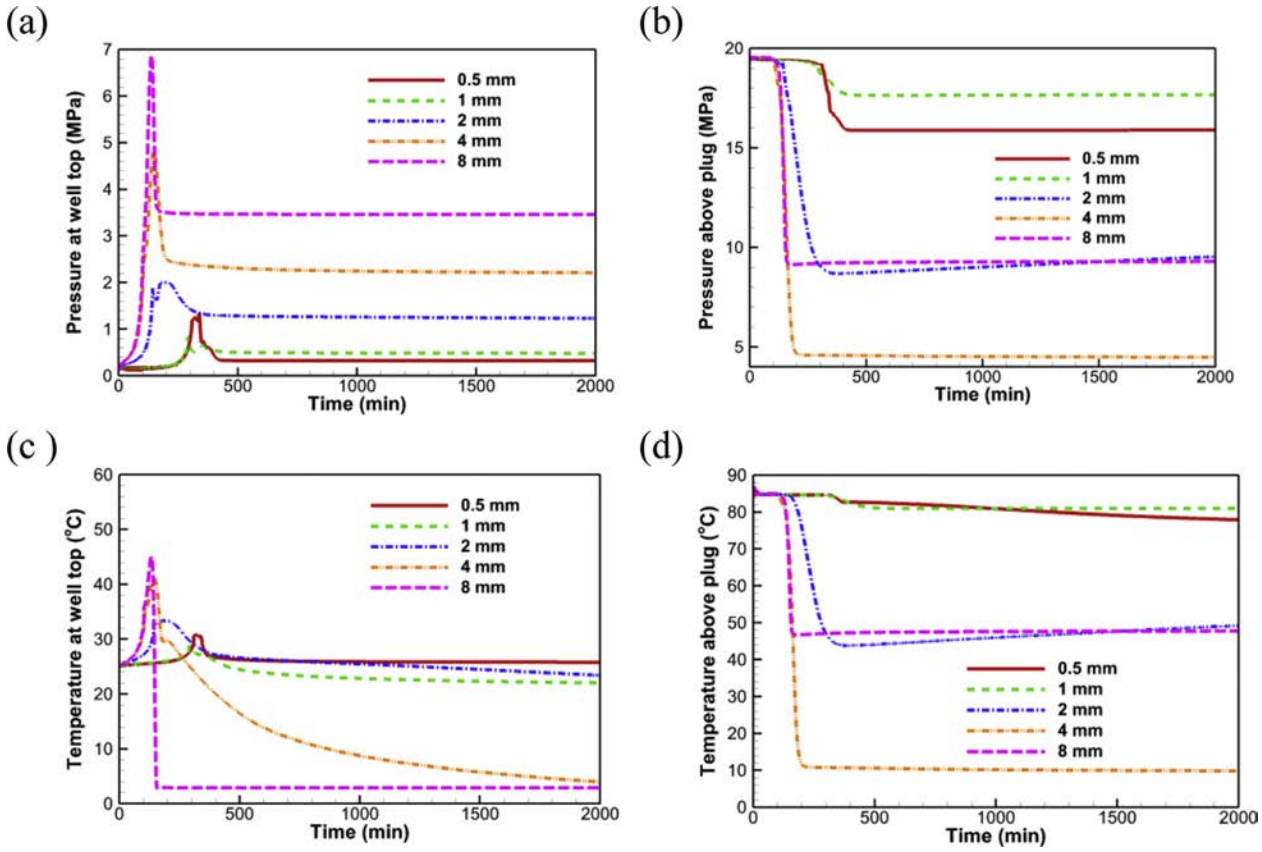


Fig. 6. Simulated (a) pressure at well top, (b) pressure right above plug, (c) temperature at well top, and (d) temperature right above plug for different gap apertures.

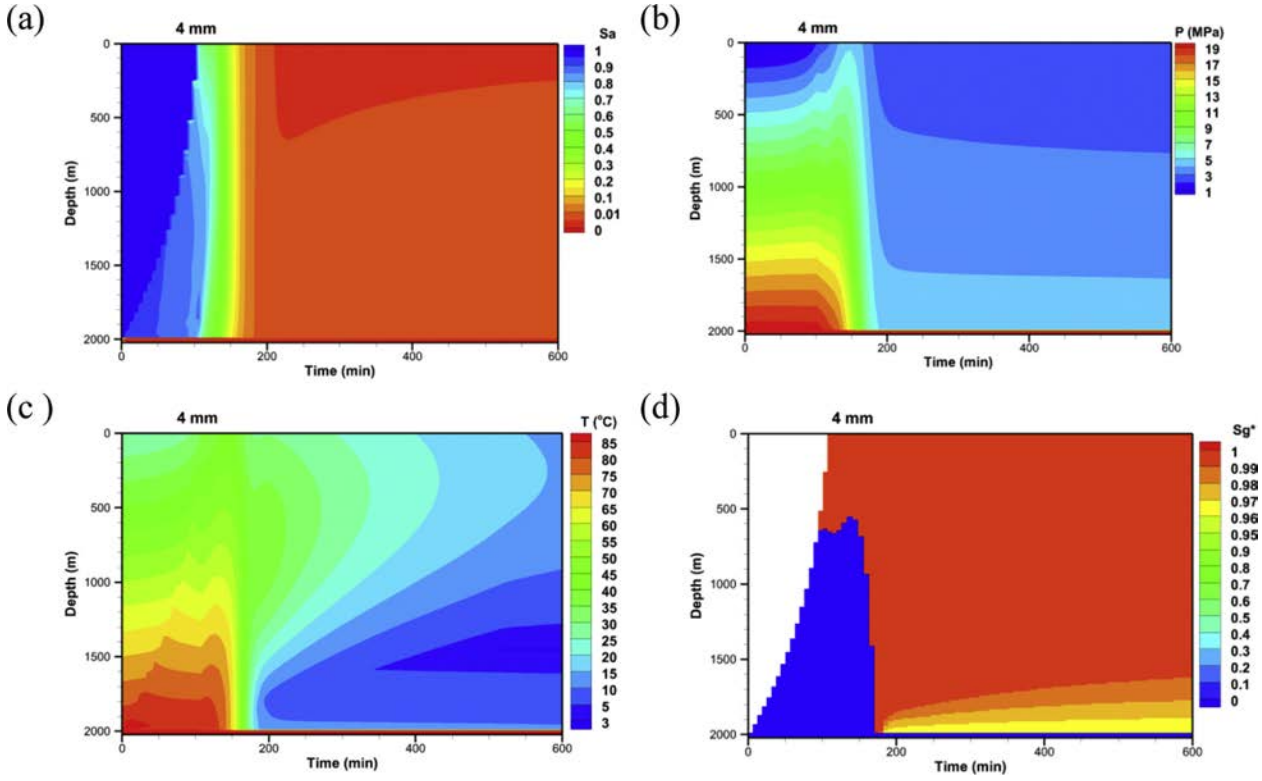


Fig. 7. Evolution of profiles of (a) aqueous phase saturation, (b) pressure, (c) temperature, and (d) the ratio of gaseous CO_2 saturation within CO_2-rich phase ($Sg^* = Sg/(Sg + S_L)$, Sg is the saturation of gaseous CO_2 while S_L is the saturation of liquid or super-critical CO_2) in the well for the 4 mm case. The white region indicates no free CO_2 phase exists (i.e., Sa = 1).

Received by OCD: 6/29/2026

has a similar pattern to that for the 8 mm gap, differences are quite large overall between the two cases (Figs. 6c and 7 c). Whereas the coldest point in the 8 mm case is located at the well top, the coldest point in the 4 mm case is located at about a depth of 1500 m at 600 min, near the upper margin of the two-phase CO_2 region (Fig. 7d). By close inspection of the Sg* (Sg* = Sg/(Sg + S_l) plot (not shown here), we observed that CO_2 evolves from supercritical conditions to enter a two-phase region before reaching the top of the plug in the 4 mm gap-aperture case. The CO_2 temperature continues to decrease as it flows upward because of the drop in pressure (along the phase line). After CO_2 passes the upper margin of the two-phase region, expansion cooling causes further drop in gas temperature. As gaseous CO_2 migrates farther upward, the heat from the surrounding formations is able to overcome the expansion cooling resulting in a gradual increase in temperature as CO_2 flows up to the well top. However, this formation-to-well heating effect is weakening with time so that the cold region shown in Fig. 7c gradually expands upward and reaches the well top at about 2400 min (not shown here) and the well top temperature is eventually approaching 3 °C (Fig. 6c) although the temperature right above the plug is stabilized at 10 °C after 200 min (Fig. 6d).

For the 2 mm gap aperture, the leaking gas is not able to lift all of the water above the plug out of well, unlike in the cases with larger aperture (e.g., 4 and 8 mm). As shown in Fig. 8a, significant aqueous phase still exists in the well after the water eruption around 200 min. Such phase conditions are reflected in the pressure profiles as shown in Fig. 8b. The aqueous phase (denser than CO_2) increases the gravitational pressure gradient along the well. As a result, although the well top pressure is about 1.3 MPa in the 2 mm case, much smaller than 2.2 MPa in 4 mm case or 3.6 MPa in 8 mm case (Fig. 6a), the pressure right above the plug for the 2 mm gap-aperture case is around 9 MPa (Fig. 6b), a level similar to that in 8 mm case, and is much higher than that in 4 mm case (~4.5 MPa). While the well-top pressure is mainly controlled by the final leakage rate, the pressure right above the plug is a result of two interacting factors, the pressure drop through the plug corresponding to the given flow rate from below and the gravity force asserted by the water column in the well above the plug. The significant aqueous phase in the well also alters the temperature profile in the 2 mm case (Fig. 8c). Although the temperature right above the plug drops to below 50 °C due to expansion cooling (Fig. 6d), similar to the 8 mm case, the smaller CO_2-rich aqueous phase saturation (which is under expansion cooling) and smaller leakage rate in the 2 mm case make it possible for the upward flowing fluid to be heated up by the surrounding formations especially in the region below 1000 m (Fig. 8c). As a result, the well top temperature in the 2 mm case is close to the ambient temperature although it is slowly decreasing with time (Fig. 6c) as the surrounding formations gradually cool. Different from the 4 mm case, no two-phase CO_2 regions occur in the 2 mm case (Fig. 8d). Instead, the CO_2 transitions from supercritical into gaseous phase at 1800 m depth.

As the fracture aperture reduces to 1 mm, the resistance to leakage through the gap increases. As a result, the leakage rate of CO_2-rich phase only reaches about 0.42 kg/s (Fig. 3b and d). Although there are two small peaks of aqueous phase flow at the well top associated with the breakthrough of CO_2-rich phase (Fig. 3a and c), the leaking CO_2 is just not able to lift much water out of the well resulting in a very wet well (high aqueous phase saturation) in the 1 mm case (Fig. 9a). Consequently, the pressure gradient in the well (the section above the plug) is only slightly increased from the ambient hydrostatic pressure gradient due to leaking CO_2 (Fig. 9b). The pressure right above the plug only drops by 1.8 MPa to 17.6 MPa (Fig. 6b) while the well-top pressure is slightly below 0.5 MPa (Fig. 6a). The temperature profile changes little except for the small peak that occurs associated with the initial rise of CO_2-rich phase (Fig. 9c). The CO_2 converts from supercritical into gaseous at a depth of 850 m (Fig. 9d) which is about 950 m shallower than that in the 2 mm case.

As gap aperture further reduces to 0.5 mm (five times the 100 μm

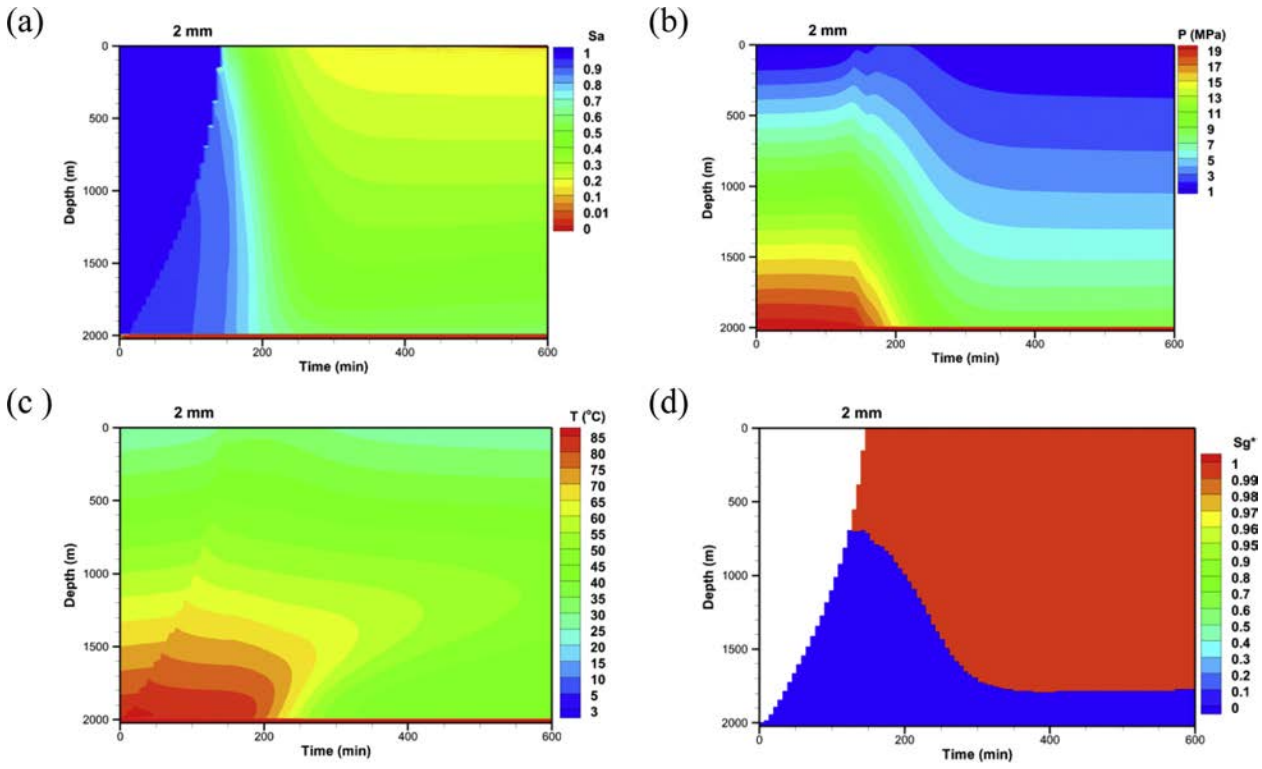


Fig. 8. Evolution of profiles of (a) aqueous phase saturation, (b) pressure, (c) temperature, and (d) the ratio of gaseous CO_2 saturation within CO_2-rich phase (Sg* = Sg/(Sg + S_L), Sg is the saturation of gaseous CO_2 while S_L is the saturation of liquid or super-critical CO_2) in the well for the 2 mm case. The white region indicates no free CO_2 phase exists (i.e., Sa = 1).

Received by OCD: 6/29/2026

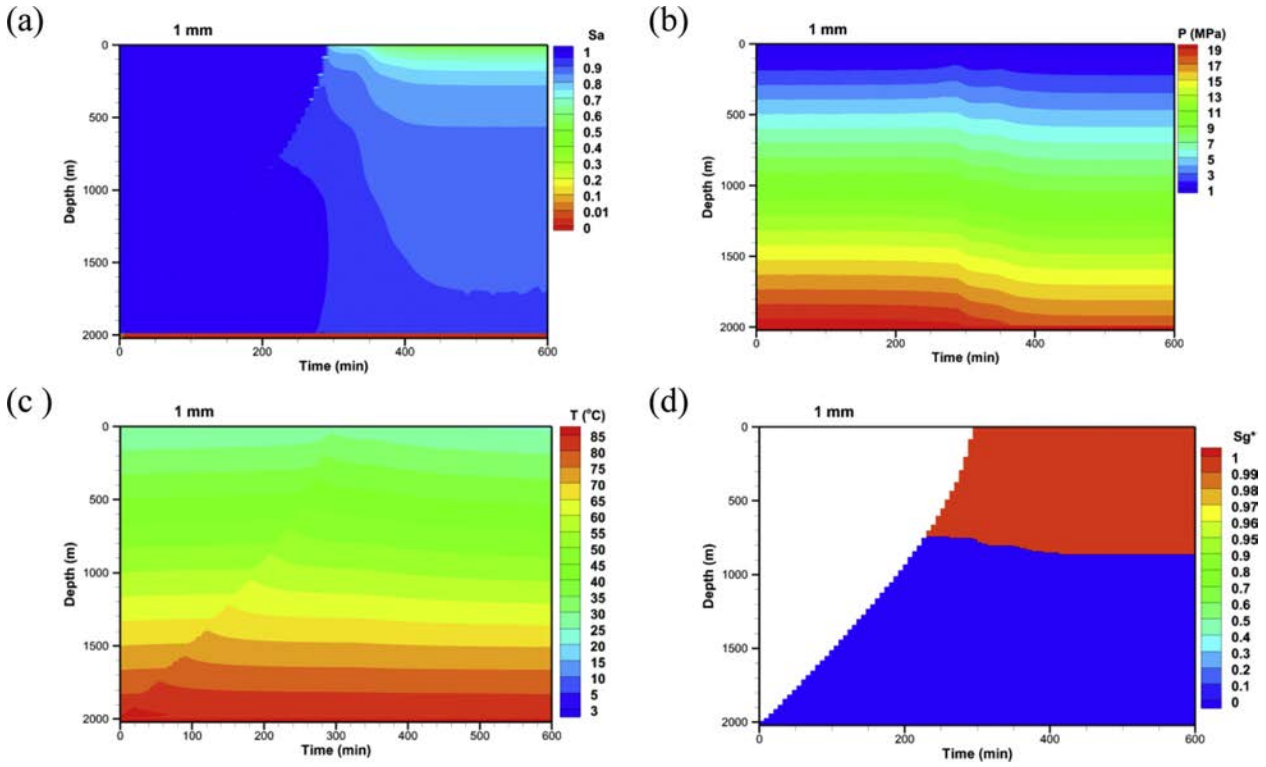


Fig. 9. Evolution of profiles of (a) aqueous phase saturation, (b) pressure, (c) temperature, and (d) the ratio of gaseous CO_2 saturation within CO_2-rich phase ($Sg^* = Sg/(Sg + S_L)$, Sg is the saturation of gaseous CO_2 while S_L is the saturation of liquid or super-critical CO_2) in the well of 1 mm case. The white region indicates no free CO_2 phase exists (i.e., Sa = 1).

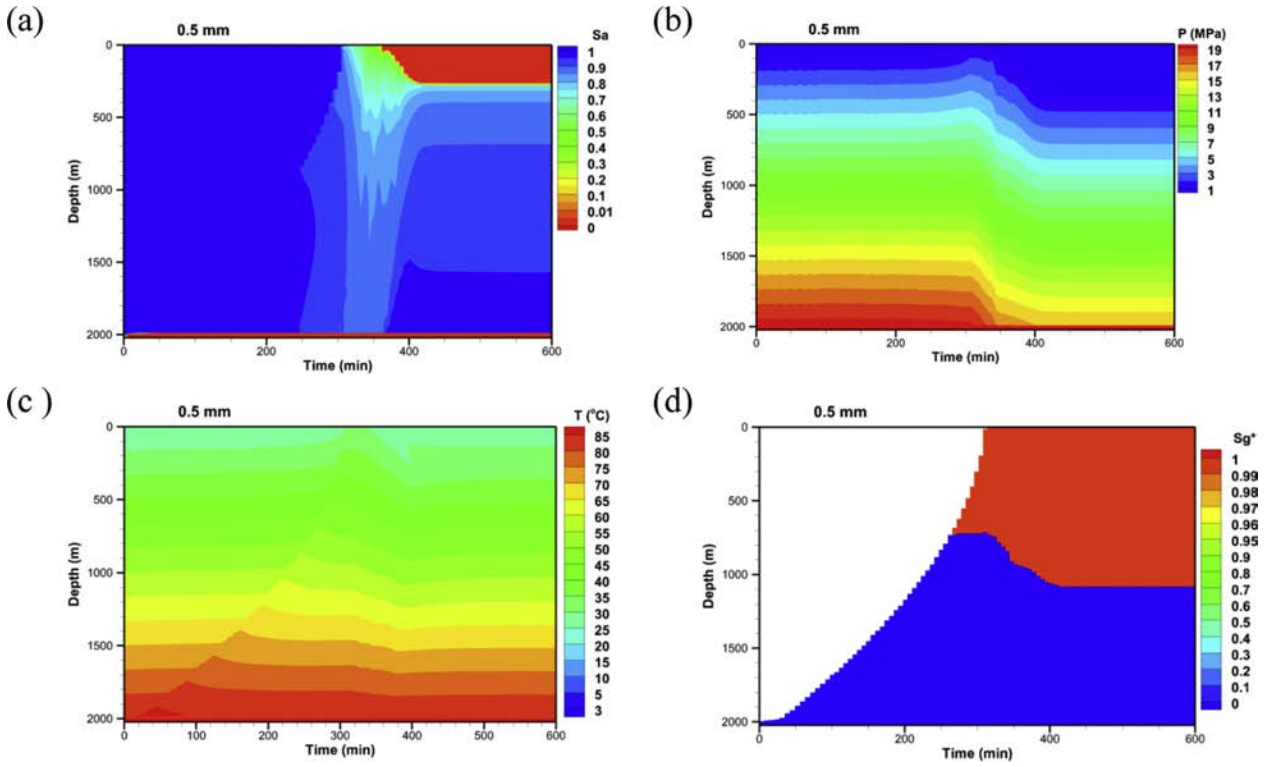


Fig. 10. Evolution of profiles of (a) aqueous phase saturation, (b) pressure, (c) temperature, and (d) the ratio of gaseous CO_2 saturation within CO_2-rich phase ($Sg^* = Sg/(Sg + S_L)$, Sg is the saturation of gaseous CO_2 while S_L is the saturation of liquid or super-critical CO_2) in the well of 0.5 mm case. The white region indicates no free CO_2 phase exists (i.e., Sa = 1).

Received by OCD: 6/29/2026

roughness of the gap walls), the steady-state leakage rate of the CO_2-rich phase is only 0.15 kg/s (Fig. 3b and d), which can barely lift any water out of the well top after the early oscillatory period ends as shown in Figs. 3c or 4b. However, the CO_2 bubbles seem to accumulate to a significant level (Fig. 10a) to cause an eruption of aqueous phase larger than that in the 1 mm case (Fig. 3a). After that, a stable water table at a depth of 260 m forms implying that the flow becomes a scenario of rising CO_2 bubbles through an almost static water column. This can be seen in Fig. 4b where the aqueous phase flow rate at the well top is zero and at the top of the plug is very small with occasional downward flow peaks in the 0.5 mm case, which is different from the 1 mm case where a continue upward aqueous flow exists although at very small magnitude or in a somewhat oscillatory way. The pressure after early eruption is lower in the 0.5 mm case than that in the 1 mm case (Figs. 9b and 10b) although the temperature profiles are very similar (Figs. 9c and 10c). The turning point between gaseous and supercritical CO_2 is located at a depth of 1100 m which is deeper than that in the 1 mm case but shallower than that in the 2 mm case (Figs. 8d, 9d and 10d).

5.4. Patterns of the friction and gravity pressure drops along the plug

The gap in the plug is a narrow flow path which is quite different from the open well above and below the plug from the perspective of flow resistance. We will now inspect the various components of the pressure loss in the plug gap as compared to those in the open well to capture the insights of flow dynamics within the plug. As shown in Fig. 11, the friction loss is orders of magnitude higher than the gravity pressure loss through the plug gap whereas the former is often a fraction of the latter in the well above or below the plug (Fig. 11a and b). In the open-well section (above or below the plug), the friction loss (Fig. 11a) is directly proportional to the mixture velocity squared (Fig. 11e) because the wall roughness is so small (45 microns) compared to the well diameter (16 cm). However, in the plug gap, because the flow path is very narrow (0.5 − 8 mm) compared to the wall roughness (0.1 mm), the larger relative roughness (the ratio of wall roughness to the size of the flow path) starts to alter the relationship between the friction loss and the mixture velocity. For example, although the mixture velocity for the 4 mm gap aperture is smaller than that in the 8 mm case in most of the plug gap (Fig. 11e), the friction loss within the plug in the 4 mm case is significantly larger than that in 8 mm case (Fig. 11a, notice the log scale). Furthermore, even though the mixture velocity within the plug for the 2 mm gap aperture is about a quarter of that in the 8 mm case, the friction loss within the plug is about the same in these two cases. As the aperture is reduced more toward the value of the roughness, although the mixture velocity within the plug in the 1 mm case is slightly larger than that in the 0.5 mm case, the friction loss in the 0.5 mm case is significantly larger than that in the 1 mm case. In reality, the wall roughness, not to mention the aperture, of a gap between cement and casing or of a fracture in the cement plug may be spatially variable resulting in leakage flow behaviors more complicated than those revealed in these idealized simulations.

The gravity pressure loss (Fig. 11b) reflects the fluid density changing with depth. Except for the 4 mm case, the CO_2 within the plug remains in supercritical state as it was in the reservoir (Fig. 11d). As a result, the gravity pressure loss within the plug increases with the gap aperture in these cases because the total pressure loss is proportional to the fracture aperture in the plug in general. The existence of significant aqueous phase in the upper portion of the plug in the smaller aperture cases (2, 1, and 0.5 mm) greatly increases the density of fluid (water-CO_2 mixture) thereby increasing the gravity pressure loss there. In the 4 mm case, larger friction loss causes the pressure in the upper portion of the plug to drop to subcritical levels so that CO_2 there becomes two-phase (Fig. 11d). The transition to gaseous CO_2 greatly reduces the density of the fluid mixture which leads to the smallest gravity pressure loss (Fig. 11b) and the largest mixture velocity (Fig. 11e) in the upper region of the plug gap. The occurrence of two-phase CO_2 also greatly decreases the temperature there in the 4 mm case (Fig. 11f). As a result, the temperature at the top of the plug in the 4 mm case decreases to below 10 °C which is about 40 °C below the cases of the 2 mm and 8 mm gap apertures and 70 °C below the 1 mm and 0.5 mm cases.

6. Discussion

6.1. Discussion of results relative to detection of well leakage

The gap between the cement plug and casing, or an equivalent fracture in the plug, is the limiting feature (bottleneck) for flow of CO_2 leaking up within casing of an abandoned well. In the case of a relatively large aperture (e.g., 4 or 8 mm), the plug offers little resistance to the leaking CO_2. In these cases of minimal flow resistance for sudden opening of the gap, the leaking CO_2 is able to lift the water originally residing in the well above the plug out of the well in a manner of an eruption (Figs. 5a and 7 a). After this initial phase of leakage, water plays little role in regulating the leakage of CO_2 and expansion cooling of CO_2 along the well makes the temperature near the land surface very low, possibly below 3 °C (As shown in Fig. 6c, temperature at the top reached the lower limit of the equation of state in our simulator). Such abnormally low temperatures could be a convenient signal of leakage because of the relative ease of measuring temperature over areas of the ground surface. For example, Fig. 12 shows the temperature deviation from the ambient temperature in the top (1 m) portion of the soil as a function of horizontal distance from the well at the end of 1 day. As shown in Fig. 12, the larger aperture cases (4 and 8 mm) not only have larger temperature drop (> 20 °C) but also a larger anomalously cold region (3 − 4 m in radius) which provides a promising basis for detecting leaking abandoned wells with soil cover by thermal mapping tools. However, as the aperture decreases, both the cold area and the magnitude of the temperature drop decrease. Especially in the case of 0.5 mm, the maximum temperature drop is about 2 °C and the radius of the cold area is only a fraction of a meter. This is because the CO_2 leakage rate is so low in the 0.5 mm case (Fig. 3b) that the flow is unable to lift significant water out of the well (Fig. 10a). Although the CO_2 bubbles are still undergoing expansion cooling as they slowly migrate upward through the water column, the cooling effects of the limited quantity of CO_2 are not enough to cause a large temperature drop in the soil above the well (Fig. 12). The water in the well above the plug becomes an effective barrier for the CO_2 leakage in these small-aperture cases (e.g., 1 and 0.5 mm) by exerting a large pressure on the top side of the plug which greatly reduces the pressure gradient through the plug that drives the upward CO_2 flow.

The effects of water on the CO_2 leakage become more complicated in the case of the medium-aperture gap (2 mm) because the CO_2 leakage rate is large enough to lift some water out of the well resulting in lower water saturation in the well than the smaller-aperture cases but not a dry well as in larger-aperture cases (Fig. 8). As a result, the two-phase interactions between the aqueous phase and the CO_2-rich phase create complicated oscillations in the flow of both the aqueous phase and CO_2-rich phase (Fig. 13). These oscillations in flow and temperature at the top of the well may be a useful target for monitoring for well leakage because they may stand out from natural cycles driven by atmospheric pressure, diurnal effects, or precipitation and runoff. As shown in Fig. 13, for most of the time the oscillations at the plug top are stronger than those at the well top, except for occasional eruption events (e.g., at around 400 min and 2000 min), implying that the well section above the plug acts as a buffer capable of smoothing out the oscillations. During that period, the water flows upward and downward alternately (Fig. 13c) within the well, indicating alternately dominant gas lift (causing upward water flow) and gravity (causing downward water flow) effects. Such alternate upward-downward water flow in the 2 mm case shown in Fig. 13c does not occur or becomes less significant after a

Received by OCD: 6/29/2026

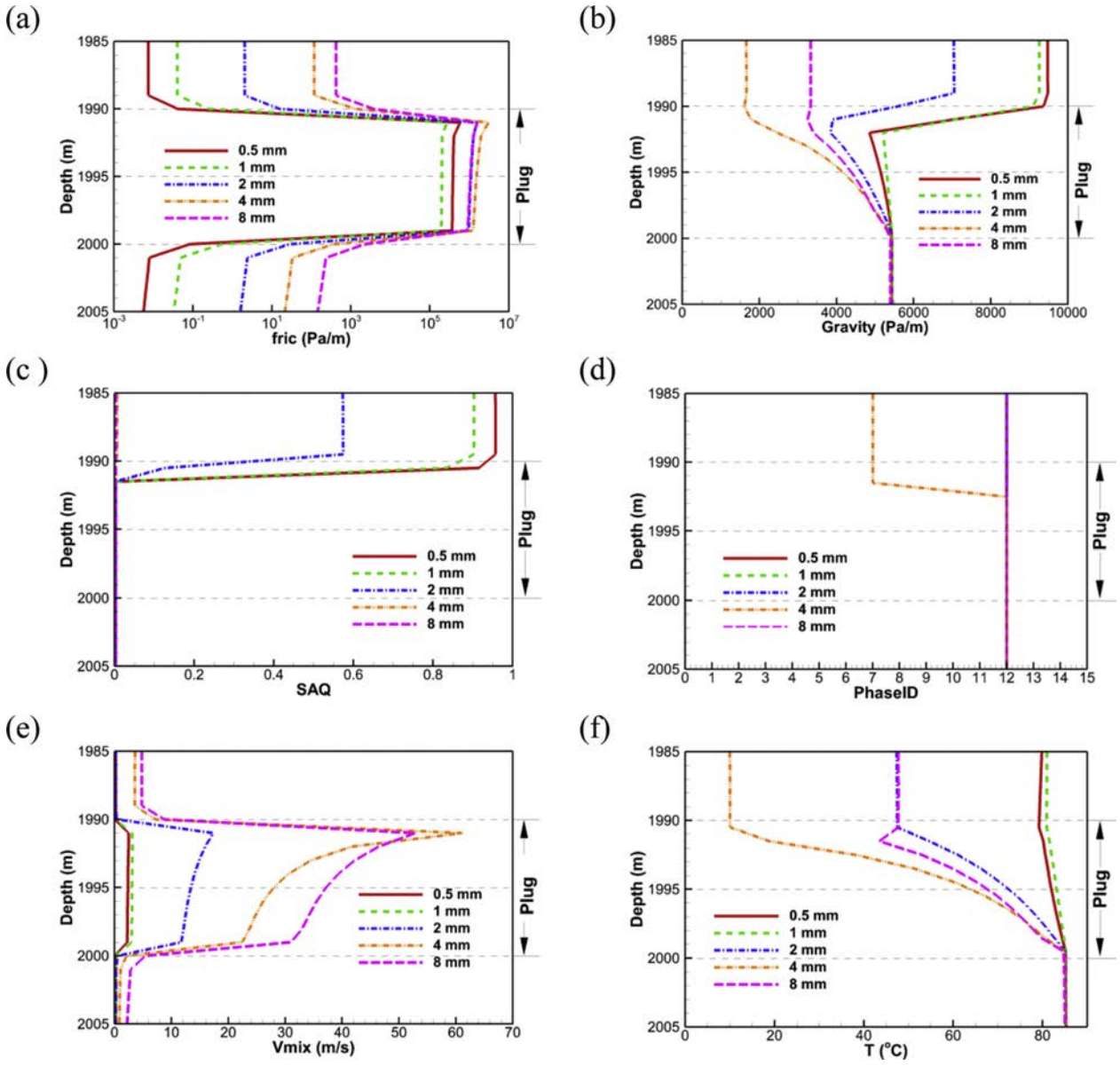


Fig. 11. Profiles of (a) friction pressure gradient, (b) gravity pressure gradient, (c) aqueous phase saturation, (d) Phase ID (12—supercritical CO_2-Aqueous, 7—three phases), (e) mixture velocity, and (f) temperature along the plug (1990-2000 m) at 1440 min (1 day).

certain time as we observed in other cases (not shown here). In larger-aperture cases (4 or 8 mm), almost all of the water is lifted out of the well by the leaking gas within a few hundred minutes resulting in a gas-phase dominant flowing well in which the two-phase interaction is minimum (i.e., small amount of condensed water becomes mist dispersed in gas stream). On the other hand, in smaller aperture cases (1 or 0.5 mm), the gas flow becomes bubble flow through an almost static water column after early time in which the magnitude of water flow caused by the bubble flow is very small. In the 1 mm gap-aperture case, there are some oscillations in magnitude of the upward water flow rate at the well top as shown in Fig. 4b.

Assuming an abandoned well can be located, monitoring the pressures in the well may be an effective way to detect leakage. As shown in Fig. 6a and b, the well top pressure will increase and the plug top pressure will decreases significantly in response to leakage past a bridge plug. The pressure monitoring can detect plug failure even if no CO_2 is released to the atmosphere in the case that the cap of the abandoned well is an effective seal. Of course, the cost to install such monitoring system may be high if large number abandoned wells are involved.

6.2. Discussion of results relative to effects of plug length on leakage

In this study, we conceptualize a prototypical abandoned well system with a 10 m-long plug, which is only about 1/3 of the length required by current U.S. regulation. To understand the effects of the plug length on the leakage dynamics in a failed abandoned well, we performed another set of simulations in which the plug length is changed to 30 m but everything else stays the same. As shown in Fig. 14, a longer plug results in smaller leakage rates in both the 8 mm and 4 mm cases relative to the 10 m-long plug. However, the patterns are similar regardless of plug length. Similar trends can be seen in smaller aperture cases (not shown here). Furthermore, the leakage rate is more sensitive to the aperture than to plug length (Fig. 15). For example, the final (stable) CO_2 leakage rate in the 8 mm case with 10 m-long plug is about 32.3 kg/s. If the plug length increases to 30 m (3 times), the CO_2 leakage rate reduces to about 23.3 kg/s, about 72 % of

Received by OCD: 6/29/2026

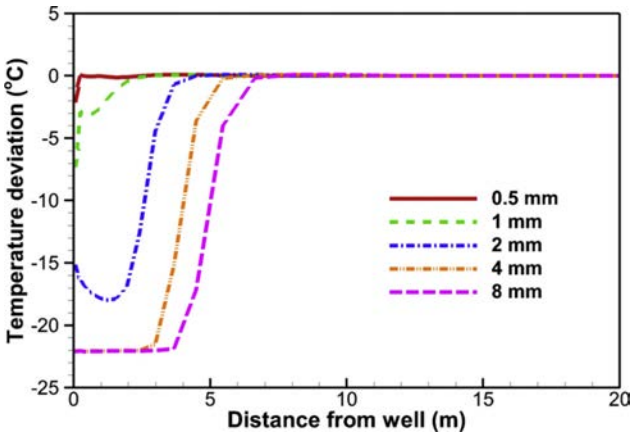


Fig. 12. Temperature deviations from the ambient temperature in top soil above the well as a function of horizontal distance from the well center at 1440 min (1 day).

the original value. However, if the aperture reduces to 4 mm (a half) with the same plug length, the CO_2 leakage rate would reduce to 12.1 kg/s, about 37 %. This is because increase of plug length only increases the resistance to the flow linearly whereas decrease of aperture not only increases the friction through the friction coefficient but also through increase in velocity for the same mass flow rate which would increase the friction proportional to velocity squared.

7. Conclusions

We have used T2Well to simulate the non-Darcy non-isothermal three-phase (aqueous, liquid-CO_2, and gas-CO_2) flow of CO_2 and brine in a prototypical abandoned well suffering a sudden failure of a cement plug during the post-injection period at a GCS site. Results show transient leakage rate and signals of pressure, temperature, and saturation at the top of the well as a result of complicated CO_2-water interactions in the open well sections and in the gap or fracture of a bridge plug. The leakage signals and flow rate show strong dependence on gap aperture. The leakage rate increases with the aperture of the fracture in the plug greatly. In larger aperture cases, the water in the well above the plug will be lifted out of the well by the leaking CO_2, resulting in a dry well in which CO_2 flows freely without interference of the aqueous phase. In these cases the CO_2 expansion cooling effect is extremely strong resulting in a significant cold area around the well forms at land surface which implies that thermal mapping could be an effective monitoring technique to detect possible leakage from abandoned wells. While short-lived two-phase CO_2 regions occur in the 8 mm gap-aperture case, the two-phase CO_2 region exists consistently at the top of the plug (as well as the nearby section above the plug) in the 4 mm case. The strong cooling due to evaporation of the liquid CO_2 in addition to expansion cooling of gaseous CO_2 in the 4 mm case makes the cold region start at the plug and gradually expand to the land surface. For smaller apertures, both the magnitude of the temperature drop and the size of the cold area at the land surface decrease with aperture because the amount of the leaking CO_2 decreases and water saturation increases. As in the 0.5 mm case, such cooling signals become very weak.

During the period with strong interaction between aqueous phase and CO_2-rich phase (usually at early time), the water flow direction can be oscillatory (up and down) at different depths within the well section above the plug, especially in the case of intermediate aperture (e.g., 2 mm) in which case the oscillations never end. In this case, the transient pressure, temperature, and flow rate signals from such a system may stand out from variations arising from natural forcings (barometric pressure, day-night, weather) at the ground surface and provide target strategies for leakage detection monitoring. Furthermore, analysis of

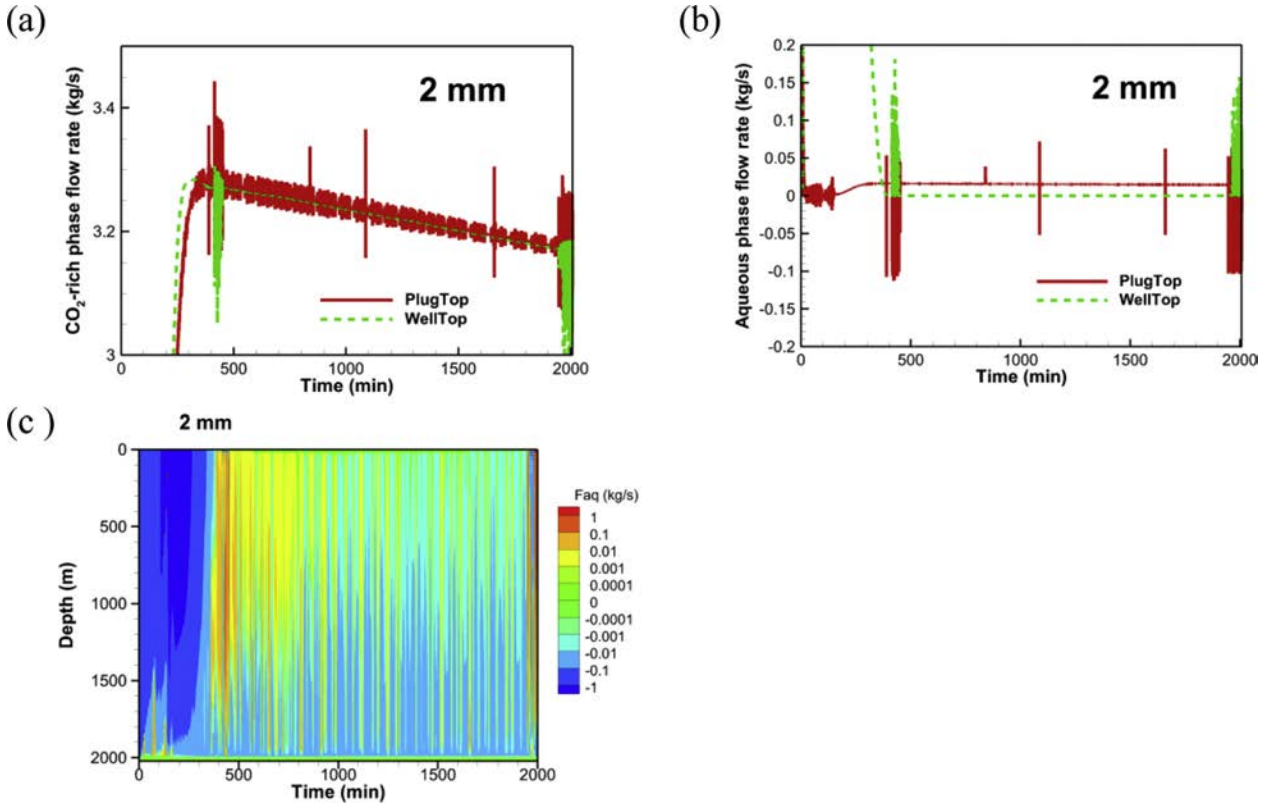


Fig. 13. Evolution of flow rate in 2 mm case: (a) CO_2-rich phase flow rates through well top and plug top, (b) aqueous phase flow rates through well top and plug top, (3) contours of aqueous phase flow rate over depth-time space (positive indicating upward flow and negative indicating downward flow).

Received by OCD: 6/29/2026

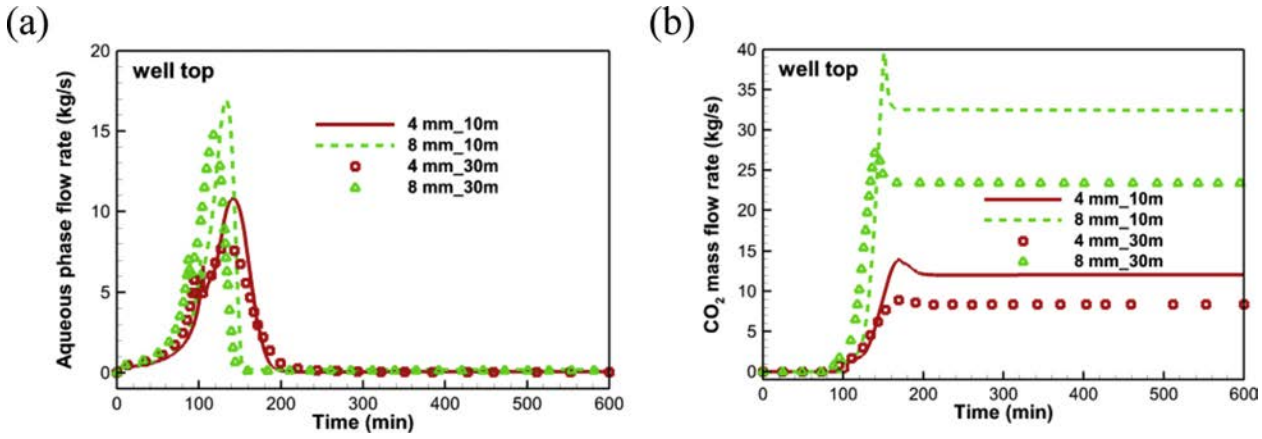


Fig. 14. Comparison of the simulated mass flow rates of aqueous (a) and non-aqueous phase (b) at the wellhead as a function of time for two big gap apertures with different plug length.

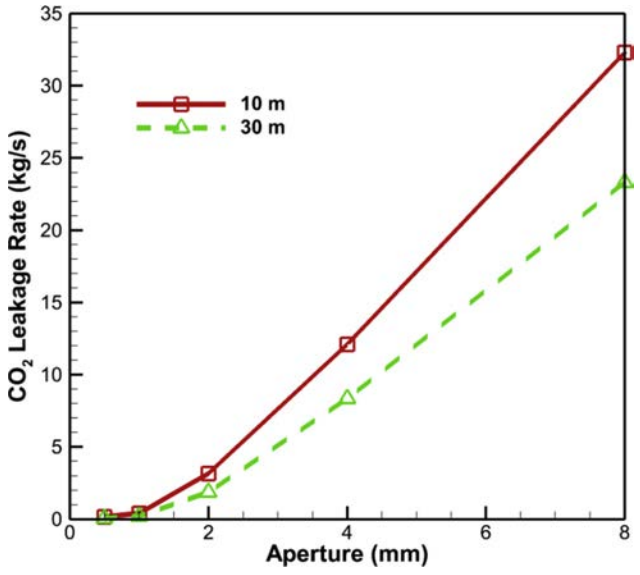


Fig. 15. Comparison of the final CO_2 leakage rates as a function of aperture for two plug lengthes.

the leakage signals may allow diagnosis of the cause and/or source of leakage, characteristics of the flow channel (e.g., its aperture, etc.) that can potentially inform remediation efforts.

The results also show that the well top pressure will increase and the plug top pressure will decrease significantly in response to the leakage. Therefore, pressure monitoring in abandoned wells is an effective way to detect potential leakage although deployment of such monitoring system may be costly if large number of wells are involved.

ECO2M has a lower limit on temperature and cannot simulate scenarios of water ice conditions or hydrate-forming conditions which may interfere or even block further CO_2 leakage in some cases. Therefore, the leakage behaviors may be very different from those reported here if such conditions occur.

CRediT authorship contribution statement

L. Pan: Conceptualization, Methodology, Software, Validation, Writing - original draft. **C.M. Oldenburg:** Conceptualization, Methodology, Writing - review & editing.

Declaration of Competing Interest

The authors declare that they have no known competing financial interests or personal relationships that could have appeared to influence the work reported in this paper.

Acknowledgment

This work was completed as part of the National Risk Assessment Partnership (NRAP) project. Support for this work was provided by the Office of Fossil Energy (DOE), under its Office of Coal CO2 Sequestration R&D Program, through the National Energy Technology Laboratory (NETL), and by Lawrence Berkeley National Laboratory under Department of Energy Contract No. DE-AC02-05CH11231.

This report was prepared as an account of work sponsored by an agency of the United States Government. Neither the United States Government nor any agency thereof, nor any of their employees, makes any warranty, express or implied, or assumes any legal liability or responsibility for the accuracy, completeness, or usefulness of any information, apparatus, product, or process disclosed, or represents that its use would not infringe privately owned rights. Reference herein to any specific commercial product, process, or service by trade name, trademark, manufacturer, or otherwise does not necessarily constitute or imply its endorsement, recommendation, or favoring by the United States Government or any agency thereof. The views and opinions of authors expressed herein do not necessarily state or reflect those of the United States Government or any agency thereof.

Appendix A. Supplementary data

Supplementary material related to this article can be found, in the online version, at doi:https://doi.org/10.1016/j.ijggc.2020.103025.

References

Bachu, S., Bennion, D.B., 2009. Experimental assessment of brine and/or CO_2 leakage through well cements at reservoir conditions. Int. J. Greenh. Gas Control. 3 (4), 494–501.

Bourgoyne, A.T., Scott, S.L., Regg, J.B., 1999. January. Sustained casing pressure in offshore producing wells. Offshore Technology Conference. Offshore Technology Conference.

Carey, J.W., Svec, R., Grigg, R., Zhang, J., Crow, W., 2010. Experimental investigation of wellbore integrity and CO2–brine flow along the casing–cement microannulus. Int. J. Greenh. Gas Control. 4 (2), 272–282.

Celia, M.A., Bachu, S., Nordbotten, J.M., Gasda, S.E., Dahle, H.K., 2005. -Quantitative estimation of CO 2 leakage from geological storage: analytical models, numerical models, and data needs. Greenhouse Gas Control Technologies 7. pp. 663–671.

Choi, Y.S., Young, D., Nešić, S., Gray, L.G., 2013. Wellbore integrity and corrosion of carbon steel in CO_2 geologic storage environments: a literature review. Int. J. Greenh.

Received by OCD: 6/29/2026

Gas Control. 16, S70–S77.
Cortis, A., Oldenburg, C.M., Benson, S.M., 2008. The role of optimality in characterizing CO2 seepage from geologic carbon sequestration sites. Int. J. Greenh. Gas Control. 2 (4), 640–652.
Crow, W., Carey, J.W., Gasda, S., Williams, D.B., Celia, M., 2010. Wellbore integrity analysis of a natural CO2 producer. Int. J. Greenh. Gas Control. 4 (2), 186–197.
Ebigbo, A., Class, H., Helmig, R., 2007. CO 2 leakage through an abandoned well: problem-oriented benchmarks. Comput. Geosci. 11 (2), 103–115.
Gasda, S.E., Bachu, S., Celia, M.A., 2004. Spatial characterization of the location of potentially leaky wells penetrating a deep saline aquifer in a mature sedimentary basin. Environ. Geol. 46 (6–7), 707–720.
Huerta, N.J., Hesse, M.A., Bryant, S.L., Strazisar, B.R., Lopano, C.L., 2012. Experimental evidence for self-limiting reactive flow through a fractured cement core: implications for time-dependent wellbore leakage. Environ. Sci. Technol. 47 (1), 269–275.
Kutchko, B.G., Strazisar, B.R., Dzombak, D.A., Lowry, G.V., Thaulow, N., 2007. Degradation of well cement by CO2 under geologic sequestration conditions. Environ. Sci. Technol. 41 (13), 4787–4792.
Lackey, G., Rajaram, H., Sherwood, O.A., Burke, T.L., Ryan, J.N., 2017. Surface casing pressure as an indicator of well integrity loss and stray gas migration in the Wattenberg Field, Colorado. Environ. Sci. Technol. 51 (6), 3567–3574.
Nordbotten, J.M., Celia, M.A., Bachu, S., 2004. Analytical solutions for leakage rates through abandoned wells. Water Resour. Res. 40 (4).
Nordbotten, J.M., Celia, M.A., Bachu, S., Dahle, H.K., 2005. Semianalytical solution for CO2 leakage through an abandoned well. Environ. Sci. Technol. 39 (2), 602–611.
NPC (National Petroleum Council), 2011. Technology Subgroup of the Operations & Environment Task Group). PLUGGING AND ABANDONMENT OF OIL AND GAS WELLS, White paper #2-25.
Oldenburg, C.M., Lewicki, J.L., Hepple, R.P., 2003. Near-Surface Monitoring Strategies for Geologic Carbon Dioxide Storage Verification, Lawrence Berkeley National Laboratory Report LBNL-54089. . https://escholarship.org/uc/item/1cg241jb.
Oldenburg, C.M., Jordan, P.D., Nicot, J.P., Mazzoldi, A., Gupta, A.K., Bryant, S.L., 2011. Leakage risk assessment of the in Salah CO_2 storage project: applying the certification framework in a dynamic context. Energy Procedia 4, 4154–4161.
Pan, L., Oldenburg, C.M., 2014. T2Well—an integrated wellbore–reservoir simulator. Comput. Geosci. 65, 46–55.
Pan, L., Oldenburg, C.M., 2016. Reduced-Order Model for Leakage through an Open Wellbore from the Reservoir Due to Carbon Dioxide Injection. https://escholarship.org/uc/item/49n090zc.
Pan, L., Oldenburg, C.M., Wu, Y.-S., Pruess, K., 2011a. Transient CO_2 leakage and injection in wellbore-reservoir systems for geologic carbon sequestration. Greenhouse Gases: Sci. and Tech. 1 (4), 335–350 LBNL-5248E.
Pan, L., Oldenburg, C.M., Wu, Y., Pruess, K., 2011b. T2Well/ECO2N Version 1.0: Multiphase and Non-Isothermal Model for Coupled Wellbore-Reservoir Flow of Carbon Dioxide and Variable Salinity Water, Report LBNL-4291E. Lawrence Berkeley National Laboratory, Berkeley, Calif.
Pan, L., Spycher, N., Doughty, C., Pruess, K., 2017. ECO2N V2. 0: a TOUGH2 fluid property module for modeling CO_2-H_2O-NACL systems to elevated temperatures of up to 300° C. Greenh. Gases Sci. Technol. 7 (2), 313–327.
Pan, L., Oldenburg, C.M., Freifeld, B.M., Jordan, P.D., 2018a. Modeling the Aliso Canyon underground gas storage well blowout and kill operations using the coupled well-reservoir simulator T2Well. J. Pet. Sci. Eng. 161, 158–174.
Pan, L., Oldenburg, C.M., Zhou, Q., 2018b. Improving Convergence of ECO2M: Application to Three-phase Systems with Liquid-Gas Phase Change. TOUGH SYMPOSIUM 2018, Berkeley, CA 94720, USA October 8-10, 2018.
Pawar, R.J., Bromhal, G.S., Chu, S., Dilmore, R.M., Oldenburg, C.M., Stauffer, P.H., Zhang, Y., Guthrie, G.D., 2016. The National Risk Assessment Partnership's integrated assessment model for carbon storage: a tool to support decision making amidst uncertainty. Int. J. Greenh. Gas Control. 52, 175–189.
Pruess, K., 2003. Numerical simulation of CO2 leakage from a geologic disposal reservoir including transitions from super-to sub-critical conditions, and boiling of liquid of CO2. Soc. Pet. Eng. J. 9 (2), 237–248.
Pruess, K., Spycher, N., 2007. ECO2N–a fluid property module for the TOUGH2 code for studies of CO_2 storage in saline aquifers. Energy Convers. Manage. 48 (6), 1761–1767.
Pruess, K., Oldenburg, C., Moridis, G., 2012. TOUGH2 User's Guide, Version 2.1, Report LBNL-43134. Lawrence Berkeley National Laboratory, Berkeley, Calif.
Tao, Q., Checkai, D., Huerta, N.J., Bryant, S.L., 2010. January. Model to predict CO2 leakage rates along a wellbore. In: SPE Annual Technical Conference and Exhibition. Society of Petroleum Engineers.
Wojtanowicz, A.K., Nishikawa, S., Rong, X., 2001. Diagnosis and Remediation of Sustained Casing Pressure in Wells. Final Report. Louisiana State University, Virginia. Submitted to: US Department of Interior, Minerals Management Service.
Xu, R., Wojtanowicz, A.K., 2001. January. Diagnosis of sustained casing pressure from bleed-off/buildup testing patterns. In: SPE Production and Operations Symposium. Society of Petroleum Engineers.

EXHIBIT 17

Transport in Porous Media (2024) 151:1199–1240
https://doi.org/10.1007/s11242-023-01972-y

Direct Comparison of Numerical Simulations and Experiments of CO_2 Injection and Migration in Geologic Media: Value of Local Data and Forecasting Capability

Lluís Saló-Salgado[1,2] · Malin Haugen[3] · Kristoffer Eikehaug[3] · Martin Fernø[3,5] · Jan M. Nordbotten[4,5] · Ruben Juanes[1,2]

Received: 20 January 2023 / Accepted: 31 May 2023 / Published online: 23 June 2023
© The Author(s), under exclusive licence to Springer Nature B.V. 2023

Abstract
The accuracy and robustness of numerical models of geologic CO_2 sequestration are almost never quantified with respect to direct observations that provide a ground truth. Here, we conduct CO_2 injection experiments in meter-scale, quasi-2D tanks with porous media representing stratigraphic sections of the subsurface, and compare them to numerical simulations of those experiments. We evaluate (1) the value of prior knowledge of the system, expressed in terms of ex situ measurements of the tank sands' multiphase flow properties (local data), with respect to simulation accuracy; and (2) the forecasting capability of history-matched numerical models, when applied to different settings. We match three versions of a numerical simulation model—each with access to an increasing level of local data—to a CO_2 injection experiment in Tank 1 ($89.7 \times 47 \times 1.05$ cm). Matching is based on a quantitative comparison of CO_2 migration at different times from timelapse image analysis. Next, use the matched models to make a forecast of a different injection scenario in Tank 1 and, finally, a different injection scenario in Tank 2 ($2.86 \times 1.3 \times 0.019$ m), which represents an altogether different stratigraphic section. The simulation model can qualitatively match the observed free-phase and dissolved CO_2 plume migration and convective mixing. Quantitatively, simulations are accurate during the injection phase, but their concordance decreases with time. Using local data reduces the time required to history match, although the forecasting capability of matched models is similar. The sand–water–$CO_{2(g)}$ system is very sensitive to effective permeability and capillary pressure changes; where heterogeneous structures are present, accurate deterministic estimates of CO_2 migration are difficult to obtain.

Keywords CO_2 storage · Geologic carbon sequestration · Two-phase flow · Numerical simulations · History matching · FluidFlower

1 Introduction

CO_2 capture and subsequent geologic carbon sequestration (GCS) is a climate-change mitigation technology that can be deployed at scale to offset anthropogenic CO_2 emissions during the energy transition (Marcucci et al. 2017; European Academies Science Advisory

Extended author information available on the last page of the article

Council (EASAC) 2018; Celia 2021; Intergovernmental Panel on Climate Change (IPCC) 2022). In GCS, reservoir simulation, including coupled flow and geomechanics, is the primary tool used to assess and manage geologic hazards such as fault leakage (e.g., Caine et al. 1996; Ingram and Urai 1999; Nordbotten and Celia 2012; Zoback and Gorelick 2012; Juanes et al. 2012; Jung et al. 2014; Vilarrasa and Carrera 2015; Saló-Salgado et al. 2023) and induced seismicity (e.g., Cappa and Rutqvist 2011; Zoback and Gorelick 2012; Juanes et al. 2012; Ellsworth 2013; Verdon et al. 2013; Alghannam and Juanes 2020; Hager et al. 2021). In response to the inherent uncertainties associated with modeling and simulation of CO_2 storage (Nordbotten et al. 2012), building confidence in the forecasting capabilities of simulation models requires calibration (or, synonymously, history matching), a process that involves updating the reservoir model to match field observations as they become available (Oliver and Chen 2011; Doughty and Oldenburg 2020).

History matching is an ill-posed inverse problem (Oliver and Chen 2011). This means that multiple solutions (i.e., parameter combinations) exist that approximate the data equally well. Automated techniques such as Markov chain Monte Carlo, randomized maximum likelihood or ensemble-based methods can be used to quantify uncertainty in history-matched models, especially in combination with surrogate models to reduce forward model computational time (see Aanonsen et al. 2009; Oliver and Chen 2011; Jagalur-Mohan et al. 2018; Jin et al. 2019; Liu and Durlofsky 2020; Santoso et al. 2021; Landa-Marbán et al. 2023, forthcoming, and references therein). In practice, however, it may be difficult to ensure that the chosen simulation model provides the best possible forecast. This is due to different subsurface conditions, the inability to include all sources of uncertainty in the models, incomplete field data and limited time for history matching.

In the laboratory, intermediate-scale (~meter) experiments have been used to study the physics of petroleum displacement (e.g., Gaucher and Lindley 1960; Brock and Orr 1991; Cinar et al. 2006) and contaminant transport (e.g., Silliman and Simpson 1987; Wood et al. 1994; Lenhard et al. 1995; Fernández-García et al. 2004). Similar 2D and 3D flow rigs have recently been applied to CO_2 storage, providing a link between core-scale measurements and field observations:

Kneafsey and Pruess (2010) found the impact of convective dissolution to be significant, using a page-size Hele–Shaw cell and numerical simulations. Neufeld et al. (2010) studied the scaling of convective dissolution and found it to be an important mechanism in the long-term trapping of injected CO_2 in an idealized site. Wang et al. (2010) used a 3D setup to investigate the ability of electrical resistivity tomography to identify localized leaks. Trevisan et al. (2014, 2017) focused on the impact of structural and residual trapping. In homogeneous sands, they found that previous trapping models, such as the Land (1968) model, can approximate the residually trapped gas saturation ($R^2 > 0.6$). Studying an heterogeneous aquifer characterized by a log-normal distribution of six different sand facies, they report that trapping efficiency increased significantly due to structural trapping. A strong control of sand heterogeneity on upward migration of CO_2 was also found by Lassen et al. (2015). Krishnamurthy et al. (2019, 2022) devised a novel technique to automate the process of beadpack/sandpack deposition and generate realistic depositional fabrics; they concluded that grain-size contrast and bedform architecture significantly impact CO_2 trapping. Subsequently, Ni et al. (2023) presented modified invasion-percolation simulations and reported that bedform architecture can impact CO_2 saturation if enough grain-size contrast is present. Askar et al. (2021) used a ~8-m-long tank to test a framework for GCS monitoring of CO_2 leakage. These studies employed homogeneous glass beads or sands, or focused on heterogeneities and bedform architectures in the aquifer layer; structural complexity was minimal.

In this paper, we use quasi-2D, intermediate-scale experiments of CO_2 storage to evaluate, quantitatively, the forecasting capability of history-matched simulation models against well-defined spatial data. An attempt was made to recreate realistic basin geometries, including stacking of storage reservoirs, faults, caprock and overburden. We simulate each of the three presented experiments with three versions of a numerical model, each with increasing access to local petrophysical measurements. These different versions are denoted Model 1 (M_1), Model 2 (M_2) and Model 3 (M_3). This allows us to assess (1) the value of local information of the system, expressed in terms of sand petrophysical measurements, during history matching, and (2) transferability or forecasting capability of our matched simulation models, when tested against a different experiment. The term *concordance* is used to evaluate agreement between experiments and simulations (Oldenburg 2018).

2 Physical Experiments

The physical experiments of CO_2 injection are conducted using the *FluidFlower* rigs. These rigs are meter-scale, quasi-2D tanks with transparent Plexiglass panels designed and built in-house at the University of Bergen (Fig. 1). Here, we used two tanks, with dimensions $89.9 \times 47 \times 1.05$ cm and $2.86 \times 1.3 \times 0.019$ m (referred herein to as Tank 1 and Tank 2, respectively). Different geologic settings are constructed by pouring unconsolidated sands with desired grain sizes into the water-saturated rigs. The rigs have multiple ports which allow

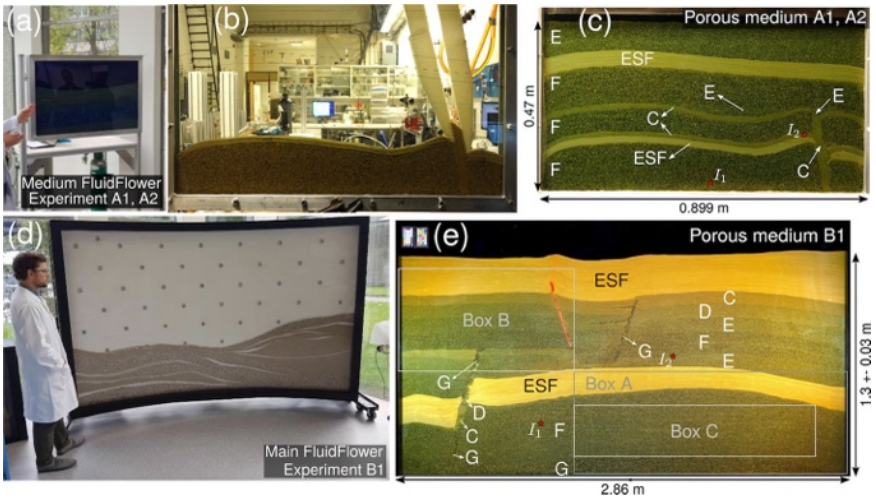


Fig. 1 Overview of the FluidFlower rigs and porous media used in the physical experiments. **a** Medium FluidFlower rig (Tank 1). **b** Snapshot during sand pouring to build the porous medium used in Experiments A1 and A2 in Tank 1 (Haugen et al. 2023, this issue). **c** Front view of porous medium in Tank 1, with lithologies in white and injector location shown with a red star. The length and height correspond to the porous medium. Note the fixed water table at the top. **d** Overview of the main FluidFlower rig (Tank 2), showing the back panel with sensor network. **e** Porous medium in Tank 2, used for Experiment B1, with lithologies in white. Location of injectors and Boxes A, B and C for analysis are shown with a red star and gray boxes, respectively. Length and variable height correspond to the porous medium

Received by OCD: 6/29/2026

flushing out fluids after a given CO_2 injection, such that multiple injections can be conducted in the same setting. The location of the ports can be adjusted to accommodate different injection scenarios. A variety of techniques have been developed by UiB engineers in order to build complex structures such as folds and faults.

Below, we summarize the petrophysical measurements, experimental setup, geologic model/porous media construction and experimental schedule. Details on the conceptualization of the FluidFlower rigs and technical information are given in Fernø et al. (2023, this issue) and Eikehaug et al. (2023, this issue), while the full description of the physical experiment in Tank 1 and ex situ measurements are provided by Nordbotten et al. (2022); Haugen et al. (2023, this issue). Further details on the experiment in Tank 2, as well as results of the international benchmark study (IBS), are provided by Flemisch et al. (2023, this issue).

2.1 Sand Petrophysical Properties

Measurements on the employed Danish quartz sands were conducted using specialized equipment to determine average grain size (d), porosity (ϕ), permeability (k), capillary entry pressure (p_e) and drainage and imbibition saturation endpoints (denoted as connate water saturation, S_{wc}, and trapped gas saturation, S_{gt}). The methodology is described by Haugen et al. (2023, this issue), and obtained values are provided in Table 1. Sands C, D, E and F are very well sorted, sand G is well sorted, and sand ESF is moderately sorted (Haugen et al. 2023, this issue). We verified that Darcy's law is applicable in our system using the Reynolds number (R_e):

$$R_e = \frac{ud}{\nu} \tag{1}$$

where u is the fluid discharge per unit area, d the mean grain diameter, and ν the kinematic viscosity of the fluid. From our simulation results, matched to experimental observations, $\max(R_e) \leq 1$, which ensures the applicability of Darcy's law (e.g., Bear 1972).

Table 1 Petrophysical properties for used quartz sands, as obtained from local, ex situ measurements

Sand type	d (std) (mm)	ϕ (−)	k (D)	p_e (mbar)	S_{wc}	S_{gt}
ESF	0.2 (0.11)	0.435	44	15	0.32	0.14
C	0.66 (0.09)	0.435	473	3	0.14	0.1
D	1.05 (0.14)	0.44	1110	1	0.12	0.08
E	1.45 (0.19)	0.45	2005	–	0.12	0.06
F	1.77 (0.31)	0.44	4259	–	0.12	0.13
G	2.51 (0.63)	0.45	9580	–	0.1	0.06

Porosity and permeability are the average from two measurements for each sand, with a maximum difference between measurements of 0.02 (ϕ) and estimated 20% uncertainty (k). Measured gas column heights for sands E-G were 0, so p_e could not be directly measured. Experimental error in p_e, S_{wc} and S_{gt} was not quantified. A detailed description of the methodology and petrophysical values is provided by Nordbotten et al. (2022); Haugen et al. (2023, this issue)

2.2 Experimental Setup

The front and back panels of the FluidFlower are mounted on a portable aluminum frame, such that boundaries are closed on the sides and bottom (no flow). The top surface is open and in contact with fluctuating atmospheric pressure (Fig. 1). A fixed water table above the top of the porous medium was kept throughout the experiments conducted here. The experimental setup incorporates mass flow controllers to inject gaseous CO_2 at the desired rate, and a high-resolution digital camera with time-lapse function (Haugen et al. 2023, this issue).

Experiments were conducted in 2021 and 2022 in Bergen (Norway) at room temperature ($\approx 23\,^{\circ}C$) and ambient atmospheric pressure. Temperature changes were minimized as much as possible, but maintaining a constant temperature was not possible in the available laboratory space. The fluids and sands were set in the FluidFlowers using the following procedure:

1. The silica sands are cleaned using an acid solution of water and HCl to remove carbonate impurities.
2. The FluidFlower rig is filled with deionized water.
3. Sands are manually poured into the rig using the open top boundary, in order to construct the desired porous medium.
4. A pH-sensitive, deionized-water solution containing bromothymol blue, methyl red, hydroxide and sodium ions is injected through multiple ports until the rig is fully saturated. This enables direct visualization of CO_2 gas (white), dissolved CO_2 (yellowish orange to red), and pure water (dark teal).
5. 5.0 purity (99.999%) CO_2 is injected as gaseous phase at the desired rate. CO_2 is injected through dedicated ports directly into the rig (Fig. 1).
6. After the injection phase, injection ports are closed and CO_2 migration continues.
7. Once the experiment is finished, the rig can be flushed with deionized water and the process can start again from step 4.

Full details on the fluids are given in Fernø et al. (2023, this issue) and Eikehaug et al. (2023, this issue). Below, we refer to the pH-sensitive solution in the rigs as “dyed water".

2.3 Porous Media Geometries

The geometries of the porous media used in this paper aim to recreate the trap systems observed in faulted, siliciclastic, petroleum-bearing basins around the world, given the geometrical constraints of the FluidFlowers and manual sand pouring (Fernø et al. 2023; Eikehaug et al. 2023, this issue). Features such as folds, faults and unconformities were built in both Tanks 1 and 2. The construction of faults, shown in Fig. 1b and detailed in Haugen et al. (2023, this issue), requires a minimum effective “fault-plane” thickness; hence, our fault structures are thicker than natural faults with the same displacement (Childs et al. 2009). Fine sands ($d \approx 0.2$ mm) are used to represent sealing or caprock formations.

The geometry in Tank 1 (Fig. 1c) contains three main high-permeability reservoirs (F sand). The bottom and middle F sand are separated by a seal (ESF sand), while the middle and top are separated by the C sand and connected through a higher permeability fault (refer to Sect. 2.1 for petrophysical properties). The fault separates the bottom section into

Received by OCD: 6/29/2026

two compartments. The bottom and top F sand provide anticlinal traps for the CO_2 to accumulate in.

The geometry in Tank 2 (Fig. 1e) was specifically motivated by the structure of North Sea reservoirs and petroleum basins. From bottom to top, it contains two sections of decreasing-permeability reservoirs capped by two main sealing layers. A fault separates the bottom section into two compartments, while two faults separate the top section into three compartments. Each fault has different petrophysical properties: The bottom fault is a heterogeneous structure containing ESF, C, D, F and G sands, the top-left fault is an impermeable structure made of silicone and the top-right fault is a conduit structure containing G sand.

2.4 Experimental Injection Schedule

The injection schedules for experiments in Tanks 1 and 2 are provided in Table 2. Injection ports have an inner diameter of 1.8 mm.

3 Numerical Simulations

3.1 Model Setup

The isothermal simulations presented in this work were performed with the MATLAB Reservoir Simulation Toolbox, MRST (Krogstad et al. 2015; Lie 2019; Lie and Møyner 2021). Specifically, we used the black-oil module, which is based on fully implicit solvers with automatic differentiation, and assigned properties of water to the oleic phase, such that the gaseous phase (CO_2 only) can dissolve in it. Vaporization of water into the gas phase and chemical reactions are not considered, because they are not primary controls on fluid migration for our operational setup and analysis time.

Table 2 Schedules for the three CO_2 injection experiments simulated in this work

Experiment A1		A2		B1	
I_R (ml/min)	t (hh:mm:ss)	I_R	t	I_R	t
0.1 (I_1)	00:00:00	0.1 (I_1)	00:00:00	10.0 (I_1)	00:00:00
2.0	00:05:00	2.0	00:05:00	10.0	05:00:00
2.0	00:50:00	2.0	04:43:44	0.0	05:00:01
0.0	00:55:00	0.0	04:48:33	10.0 (I_2)	02:15:00
0.1 (I_2)	01:09:11	0.0	05:00:00	10.0	05:00:00
2.0	01:14:11			0.0	05:00:01
2.0	02:29:11			0.0	120:00:00
0.0	02:34:00				
0.0	48:00:00				

I_R is injection rate, while I_i denotes injector (port) number. A five-minute ramp-up and ramp-down was applied in Experiments A1 and A2 in Tank 1. Total duration of conducted experiments and simulations is 48 h (A1), 5 h (A2) and 120 h (B1). Location of injection wells is provided in Fig. 1

In addition to structural and dissolution trapping, we also considered residual trapping (Juanes et al. 2006) to be consistent with local measurements showing nonzero trapped gas saturation (Sect. 2.1). This is achieved through hysteretic relative permeability curves for the nonwetting (gas) phase (see Sect. 3.2). Our implementation in MRST follows ECLIPSE's technical description (Schlumberger 2014), and Killough's (1976) model is used to compute the scanning curves (Saló-Salgado et al. 2023, forthcoming). Physical diffusion was also included through the addition of a diffusive flux term with a scalar, constant coefficient in the computation of the total CO_2 flux (Bear 1972).

The simulator requires very small time-steps (seconds to minutes) due to the buoyancy of CO_2 at atmospheric conditions and high sand permeabilities (Table 1). Linear solver time was reduced by means of AMGCL (Demidov and Rossi 2018; Lie 2019), an external, pre-compiled linear solver. The greatest challenge was the convergence of the nonlinear solver, which required many iterations and time-step cuts. This is consistent with the groups working in the FluidFlower international benchmark study (Flemisch et al. 2023, this issue).

Next, we describe the computational grids for experiments in Tanks 1 and 2, PVT properties and boundary conditions. Petrophysical properties are specific of each model version and are detailed in Sect. 3.2.

3.1.1 Computational Grids

A front panel image of the porous medium was used to obtain layer contact coordinates through a vector graphics software (Fig. 2a). These contacts were then imported into MATLAB to generate the computational grids using the UPR module (Berge et al. 2019, 2021) (Fig. 2b, d). The grids were generated in 2D and then extruded to 3D (using a single cell layer) to account for thickness and volume. Note that, in Tank 1, where the porous

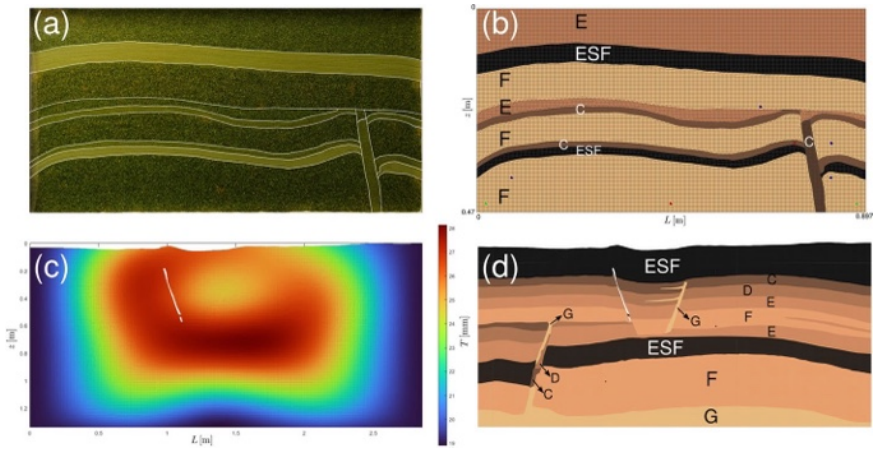


Fig. 2 Simulation grids overview. **a** Front-panel view of Tank 1, where the layer contacts have been highlighted in white. **b** Front view of simulation grid for experiments in Tank 1, with lithologies indicated and colored based on petrophysical properties (see Sect. 3.2). Location of injection wells is shown in red. **c** Thickness map of simulation grid for experiments in Tank 2. **d** Front view of simulation grid for experiments in Tank 2, with lithologies indicated and colored based on petrophysical properties. Location of injection wells is shown in red

medium has dimensions of $89.7 \times 47 \times 1.05$ cm, the thickness (space between the front and back panels) is constant (10.5 mm). Tank 2, which is significantly larger (porous medium dimensions $2.86 \times 1.3 \times 0.019$ m), has a thickness of 19 mm at the sides; however, it varies towards the middle due to forces exerted by the sand and water, to a maximum of 28 mm. A thickness map obtained after initial sand filling was used to generate our variable-thickness mesh via 2D interpolation (Fig. 2c). Also, the top surface of the porous medium is not flat (height $= 130 \pm 3$ cm).

Our composite Pebi grids (Heinemann et al. 1991) have a Cartesian background and are refined around face constraints (contacts and faults) as well as cell constraints (injection wells) (Berge et al. 2019, 2021). We generated multiple grids to test the finest grid we could afford to simulate Experiment B1 in Tank 2 with. Our grid has a cell size $h \approx 5$ mm and 151,402 cells (Fig. 2d). The grid used for Tank 1 has a similar cell size ($h \approx 4$ mm and 27,200 cells), which was chosen to reduce grid-size dependencies when applying our matched models to Experiment B1.

3.1.2 PVT Properties

Consistent with experimental conditions, our simulations are conducted at atmospheric conditions ($T = 25$ C), where the CO_2 is in gaseous state. We employed a thermodynamic model based on the formulations by Duan and Sun (2003) and Spycher et al. (2003); Spycher and Pruess (2005) to calculate the composition of each phase as a function of p, T. The implementation for a black-oil setup is described in Hassanzadeh et al. (2008) and references therein. Given the boundary conditions (Sect. 3.1.3) and dimensions of our experimental porous media, pore pressure changes (Δp) are very small in our simulations (max $\Delta p \ll 1$ bar). Hence, the fluid properties remain similar to surface conditions, where the water and CO_2 have, respectively, a density of 997 and 1.78 kg/m^3, and a viscosity of 0.9 and 0.015 cP. The maximum concentration of CO_2 in water is ≈ 1.5 kg/m^3.

3.1.3 Initial, Boundary and Operational Conditions

Our porous media are fully saturated in water at the beginning of CO_2 injection. No-flow boundary conditions were applied everywhere except at the top boundary, which is at constant pressure and includes a fixed water table a few cm above the top of the porous medium. Injection is carried out via wells completed in a single cell at the corresponding coordinates. The diameter of injection wells is 1.8 mm in both Tank 1 and Tank 2, which operate at a constant flow rate (see Sect. 2). The simulation injection schedule follows the experimental protocol, provided in Table 2. Note that injection rates in our simulations of Experiment A1 and A2 were slightly adjusted during the calibration procedure, as explained in Sects. 3.3 and 4.

3.2 Simulation Model

Three different model versions, denoted Model 1 (M_1), Model 2 (M_2) and Model 3 (M_3), are used throughout this study to evaluate the value of local data in forecasting subsurface CO_2 migration. Each successive model was constructed based on access to an increasing level of local data, with M_1 having access to the least data and M_3 having access to the most data. The model-specific parameters are limited to the following:

- Petrophysical properties (porosity, permeability, capillary pressure and relative permeability), which depend on available local data and are described in this section.
- The molecular diffusion coefficient (D). Models 1–3 were calibrated using the same value, $D = 10^{-9}$ m^2/s. Additionally, Model 3 was also calibrated with $D = 3 \times 10^{-9}$ m^2/s. Accordingly, where required we denote Model 3 as $M_{3,1}$ and $M_{3,3}$.
- Injection rate. Experiments in Tank 1 were conducted at a very low injection rate ($I_R = 2$ ml/min, see Table 2). Given that the mass flow controllers used in Tank 1 may be inaccurate for this rate, the injection rate was also modeled as an uncertain parameter. Model calibration was achieved with $I_R \in [1.6,\ 1.8]$ ml/min for all three models.

All other model characteristics, including the grid and numerical discretization, remain unchanged. Below, we describe the starting petrophysical values for each of our three simulation models. Note that the experimental geometry in Tank 1, used for matching, only contained sands ESF, C, E and F. Properties for sands D and G are also provided because they were required to simulate the experiment in Tank 2 (Fig. 1).

3.2.1 Model 1 (M_1)

For this model, local petrophysical data were limited to a measure of the average grain size (d; see Sect. 2.1 and Table 1). Hence, petrophysical properties were estimated from published data in similar silica sands. Porosity was selected from data in Beard and Weyl (1973) and Smits et al. (2010) for moderately to well-sorted sands. Permeability was obtained from fitting a Kozeny–Carman model to data in Beard and Weyl (1973) and Trevisan et al. (2014). The resulting equation has the form $k = \beta d^2 \phi^3$, where β equals 12,250 in our fit with d in mm and k in D. Obtained porosity and permeability values are provided in Table 3.

Capillary pressure curves were computed as described below:

1. Capillary pressure measurements in a similar system were obtained from the literature. In this case, Plug and Bruining (2007) measured capillary pressure curves on the unconsolidated quartz sand-CO_2-distilled water system at atmospheric conditions. We used their measurements on sand packs with an average particle size between 0.36 and 0.41 mm, which are closest to the C sand in our experiments (Fig. 3a).
2. A Brooks and Corey (1964) model of the form $p_c = p_e (S_w^*)^{-\frac{1}{\lambda}}$ was fitted to these data, where p_e is the nonwetting phase entry pressure at $S_w = 1$, $\lambda = 2.6$ and $S_w^* = \frac{S_w - S_{wc}}{1 - S_{wc}}$ is

Table 3 Initial porosity and permeability for Model 1

Sand type	d (mm)	ϕ (−)	k (D)
ESF	0.2	0.37	25
C	0.66	0.38	290
D	1.05	0.40	930
E	1.45	0.39	1530
F	1.77	0.39	2280
G	2.51	0.42	5720

See main text for estimation details

Received by OCD: 6/29/2026

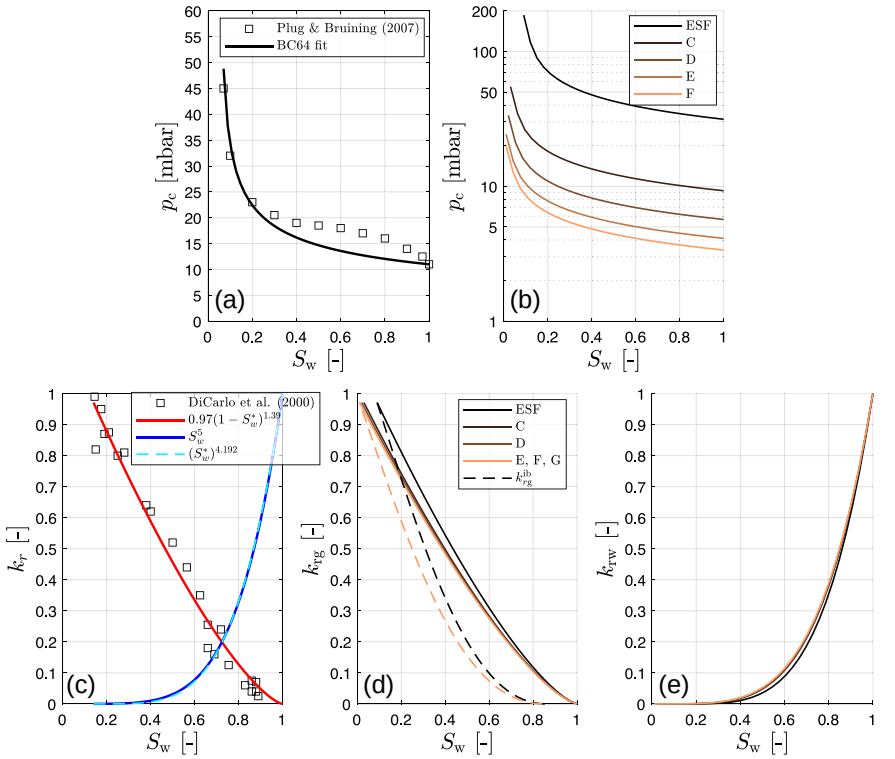


Fig. 3 Multiphase flow properties for Model 1. **a** Capillary pressure measurements and reference curve using a Brooks and Corey (1964) function. **b** Initial capillary pressure curves, computed from the reference curve using Leverett scaling (see main text). **c** Relative permeability data (squares and S_w^5 model) and our fitted Corey model. **d**, **e** Relative permeability of gas and water, respectively. The drainage curve is shown as a solid line, while the bounding imbibition curve is shown for sands ESF and G as a discontinuous line. No relative permeability hysteresis was considered for the water phase

the normalized water saturation with irreducible or connate water saturation S_{wc}. This fit led to our reference curve, p_{cr} (Fig. 3a).

3. The capillary pressure depends on the pore structure of each material, such that sands with different grain sizes require different p_c curves. The capillary pressure variation can be modeled by means of the dimensionless J-function proposed by Leverett (Leverett 1941; Saadatpoor et al. 2010): $J(S_w) = \frac{p_c}{\sigma \cos\theta}\sqrt{\frac{k}{\phi}}$, where σ is the surface tension and θ the contact angle. Assuming the same wettability and surface tension for different sand regions, and the same shape of the p_c curve, the capillary pressure for any given sand (p_{cs}) can be obtained from the reference curve as $p_{cs}(S_w) = p_{cr}(S_w)\sqrt{\frac{k_r\phi_s}{k_s\phi_r}}$ (Fig. 3b).

Drainage relative permeabilities were obtained from CO_2-water measurements by DiCarlo et al. (2000), who used water-wet sandpacks with 0.25 mm grain size. Specifically, we used the data reported in their Figs. 4 and 5 and fitted Corey-type functions (Corey 1954; Brooks and Corey 1964) of the form $k_{rw} = (S_w^*)^a$ and $k_{rg} = c(1 - S_w^*)^b$ (Fig. 3c). The fitted exponents a and b are 4.2 and 1.4, respectively, while c is 0.97. We assumed that the

difference in relative permeability of different sands is the result of different irreducible water saturation only (see Fig. 3d,e). For each of our sands, S_{wc} was obtained from Timur (1968) as $S_{wc} = 0.01 \times 3.5 \frac{\phi^{1.26}}{k^{0.35}} - 1$, where ϕ is in percent and k in mD. This model was used to compute S_{wc} for both the p_c and k_r curves.

In CO_2 storage, secondary imbibition occurs where the water displaces buoyant gas at the trailing edge of the CO_2 plume, disconnecting part of the CO_2 body into blobs and ganglia and rendering them immobile (Juanes et al. 2006, and references therein). This means that the maximum water saturation that can be achieved during imbibition equals $1 - S_{gt}$ (the trapped gas saturation). Here, we used measurements in sandpacks from Pentland et al. (2010) to determine S_{gt}. In particular, we fitted Land (1968)'s model with the form $S^*_{gt} = \frac{S^*_{gi}}{1+CS^*_{gi}}$, where $S^*_g = \frac{S_g}{1-S_{wc}} = 1 - S^*_w$, S_{gi} is the gas saturation at flow reversal, and C is Land's trapping coefficient with a value of 5.2 in our fit. Although Pentland et al. (2010) report that the best fit is achieved with the Aissaoui (1983) and Spiteri et al. (2008) models (cf. their Fig. 5), Land's model was chosen here, given that most relative permeability hysteresis models build on this one (see next paragraph).

Nonwetting phase trapping contributes to irreversibility of the relative permeability and capillary pressure curves (hysteresis). Here, we accounted for this mechanism in the gas relative permeability due to its importance in subsurface CO_2 migration (Juanes et al. 2006, and references therein). In particular, we used Land's (1968) model to compute the bounding imbibition curve (see Fig. 3d), where S_{gt} is obtained as described above, and Killough's (1976) model to characterize the scanning curves. In Killough's model, the scanning curves are reversible, such that the relative permeability at $S_g < S_{gi}$ no longer depends on the displacement type.

3.2.2 Model 2 (M_2)

This model had access to local, ex situ measurements of single-phase petrophysical properties, i.e., porosity and intrinsic permeability (see Sect. 2.1 and Table 1). Comparing with Table 3, it can be seen that our estimation for Model 1 above was correct to the order of magnitude, but resulted in smaller values: porosity $\in$ [85, 93]% and permeability $\in$ [53, 84]% of the local measurements.

Capillary pressures and relative permeabilities were obtained using the same procedure described above for Mdel 1. The slight differences with respect to the curves shown in Fig. 3b, d, e come from the porosity and permeability values used in the Leverett scaling and to determine S_{wc}, which were taken from Table 1 instead. The obtained curves for Model 2 are provided in Fig 4.

3.2.3 Model 3 (M_3)

This model was allowed access to all local, ex situ measurements (see Table 1). Initial porosity and permeability remain unchanged with respect to Model 2. Capillary pressure curves were obtained by scaling the reference curve described in Sect. 3.2.1 and shown in Fig. 3a using the measured entry pressure (Sect. 2.1). The scaling followed the model $p_{cs}(S_w) = p_{cr}(S_w)\frac{p_e}{p_{er}}$, where p_e is the measured entry pressure for each sand, and p_{er} is the reference curve entry pressure. The obtained curves are shown in Fig. 5a.

Received by OCD: 6/29/2026

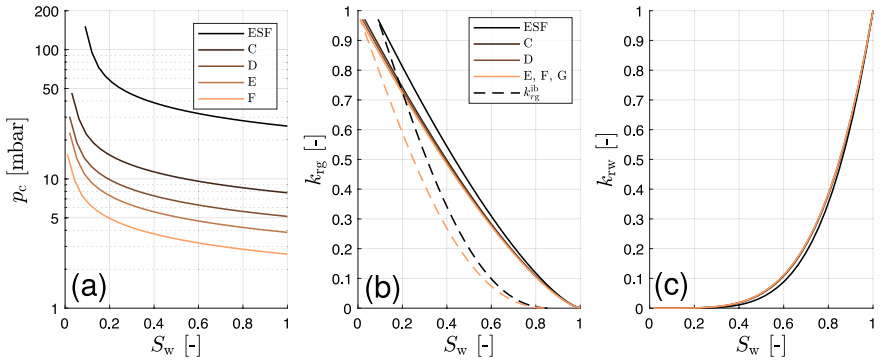


Fig. 4 Multiphase flow properties for Model 2. **b** Initial capillary pressure curves, computed from the reference curve using Leverett scaling (see main text). **b**, **c** Relative permeability of gas and water, respectively. The drainage curve is solid, while the bounding imbibition curve is shown for sands ESF and G as a discontinuous line. No relative permeability hysteresis was considered for the water phase

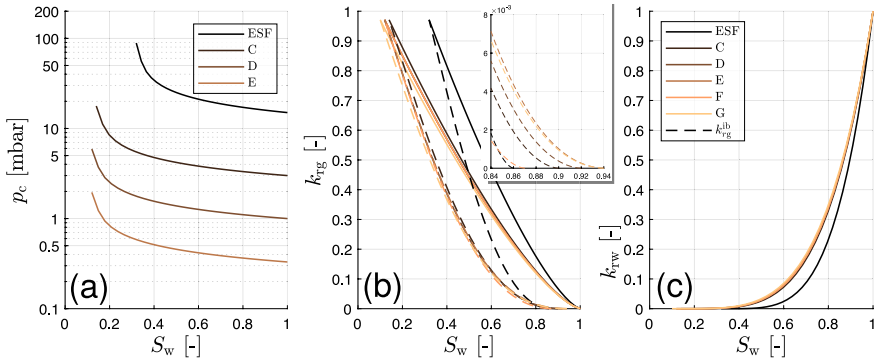


Fig. 5 Multiphase flow properties for Model 3. **b** Initial capillary pressure curves, computed according to the entry pressure determined experimentally (see Sect. 2.1). **b**, **c** Relative permeability of gas and water, respectively, according to the endpoints determined experimentally (Sect. 2.1). The drainage curves are solid, while the bounding imbibition curves are shown as a discontinuous line. The inset in **b** is a zoom view around the trapped gas saturation. No relative permeability hysteresis was considered for the water phase

Relative permeabilities were computed following the same procedure described for Model 1 above. In this case, however, each sand type was assigned the measured S_{wc} and S_{gt} values (see Table 1). This led to differences in both the drainage and imbibition curves, as shown in Fig. 5.

3.3 Model Calibration

Concordance between results obtained with each simulation model (M_1 to M_3) and the validation experiment in Tank 1 (A1, see Sect. 2.4) is quantitatively assessed by comparing the following quantities (see Fig. 6):

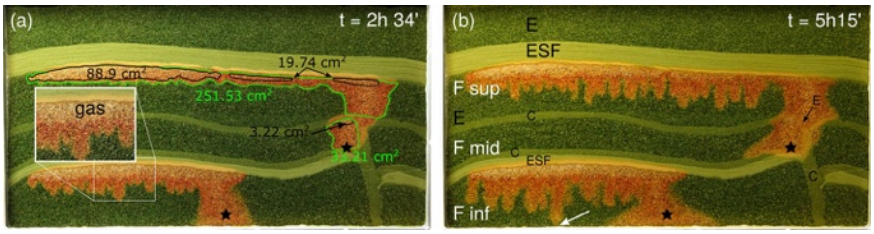


Fig. 6 Front panel view of Tank 1, showing quantities and times for history matching of numerical models to Experiment A1. **a** shows areas with gaseous CO_2 (free-phase, black contours) and dyed water with dissolved CO_2 (green contours) at the end of injection. Location of injection ports is shown with a star. **b** shows the time and location where the first finger touches the bottom of the tank (white arrow), as well as the different lithological units. Note the three F reservoirs labeled 'inf', 'mid' and 'sup', mentioned in the text and other figures

1. At $t = 55$ min (end of injection in port I_1): Areas occupied by free-phase CO_2, and dyed water with dissolved CO_2 in the bottom F reservoir.
2. At $t = 154$ min (end of injection in port I_2): Areas occupied by free-phase CO_2, and dyed water with dissolved CO_2, in the middle and top F reservoirs.
3. Time at which the first finger touches the tank bottom.
4. Time at which the first finger (sinking from the top F reservoir) touches the middle C sand.

Experimental values for points 1–2 were obtained by computing areas from time-lapse images using a vector-graphics software. Careful visual inspection of color-enhanced images was used to distinguish between free-phase CO_2 (white) and dyed water with dissolved CO_2 (yellowish orange to red), and to identify the times for points 3–4 above. Error in experimental values was estimated to be $\leq 5\%$, based on repeated measurements (points 1–2), and ~ 5 min, based on timelapse image comparison (points 3–4). In the simulation models, the threshold gas saturation and CO_2 concentration in water used to compute areas were $S_g > 10^{-3}$ and $C_{CO_2} > 15\%(C^{max}_{CO_2}) \approx 0.2$ [kg/m^3], respectively. The C value was chosen after a shape comparison of the region with dissolved CO_2. A smaller value of $C_{CO_2} > 0.05$ [kg/m^3] was selected to determine finger times for points 3 and 4 above. Figure 6 shows an overview of the experimental values for points 2 and 3, while Fig. 12 in Sect. 4.2 shows the full comparison with the history-matched/calibrated simulation models.

The experiment was conducted first. Afterwards, the process consisted of running Simulation models 1 to 3, in parallel, starting with the petrophysical properties described in Sect. 3.2. Given the number of uncertain variables (four petrophysical properties for each lithological unit, the diffusion coefficient and the injection rate) and the time required to complete a single simulation, a manual history matching method was employed. At the end of each run, quantities 1–4 above were compared and one or more properties were manually changed based on observed concordance and domain knowledge. During the first few runs, only quantities 1 and 2 above were compared. After obtaining a satisfactory areal match, petrophysical properties were further adjusted to match quantities 3 and 4.

4 Results

In Sect. 4.1, we present the results of the first simulation of Experiment A1 with each model and property values detailed in Sect. 3.2. Then, we detail the calibration of simulation models using Experiment A1 and assess the value of local data to history-match CO_2 storage simulation models (Sect. 4.2). Finally, we apply these matched models to Experiment A2, analog for a longer injection in the same geology (Sect. 4.3.1), and to Experiment B1, analog for a larger-scale injection in a different geologic setting (Sect. 4.3.2). We use simulations of Experiments A2 and B1 to assess the forecasting ability of simulation models in different conditions.

4.1 Initial Model Results

Figure 7 shows the comparison between Experiment A1 and the first run with each model, at times indicated in Sect. 3.3. Numerous differences are evident between the experiment and Models 1 and 2, while Model 3 is much closer to the experiment. In particular, models 1 and 2 overestimate the extent of CO_2-rich brine and underestimate the amount of gaseous CO_2 in all F reservoirs (refer to Fig. 6 for location). Model 3 approximates much better the areal extent of gaseous CO_2 in all regions, as well as the CO_2-rich brine in the middle and upper F reservoirs. Model 2 provides the closest finger migration times (points 3 and 4 in Sect. 3.3), although this was not evaluated in the first run, as discussed below.

Petrophysical properties for Models 1 and 2 were obtained from references in Sect. 3.2, which also used silica sands with similar grain sizes. However, despite the relatively homogeneous nature of our quartz sands, Model 3 is significantly more concordant. This result stems from natural sand variability and highlights the difficulty in establishing general,

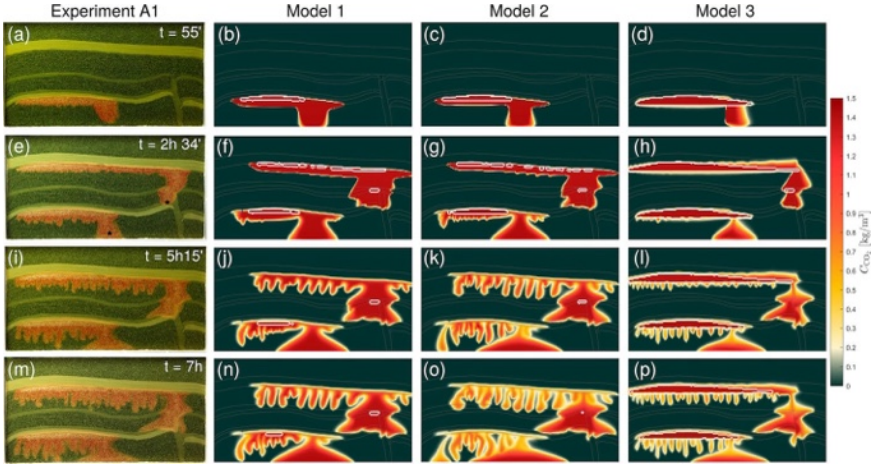


Fig. 7 Comparison between Experiment A1 in Tank 1 (left column) and first-run simulation results with Models 1–3. Color map in simulation plots refers to CO_2 concentration in water, according to color bar. The white contours in simulation plots indicate $S_g = 10^{-3}$. **a–d** End of injection in port 1. **e–h** End of injection in port 2. **i–l** Time at which the first finger touches the tank bottom. **m–p** Time at which the first finger touches the middle C sand

representative elementary volume-scale properties for porous media (see, for instance, Hommel et al. 2018; Schulz et al. 2019, for a discussion on intrinsic permeability). Additionally, results in Fig. 7 highlight the need for conducting sand/rock-specific measurements, even in the case of well-sorted, homogeneous sediments.

4.2 Manual History Matching and Value of Local Data

Figure 8 shows convergence of areas occupied by free gas (A_g) and water with dissolved CO_2 (A_d), according to Sect. 3.3. Each iteration corresponds to a successive model with manually updated parameters, and the different F sand regions evaluated in each panel (a) to (f) are provided in Fig. 6. With the exception of A_d in the lower F sand, Model 3 is accurate since the beginning, and all areas were satisfactorily matched after four iterations. Conversely, Models 1 and 2 were significantly off the experimental reference during the first few iterations. Model 2, however, was accurate after five iterations, while

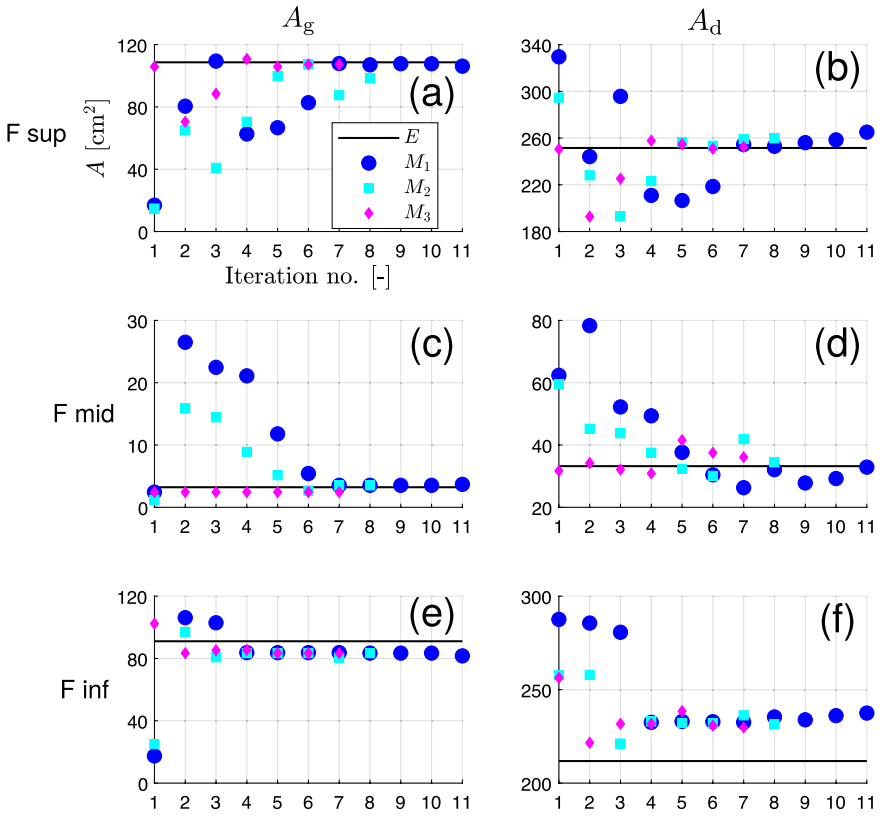


Fig. 8 Convergence of areas occupied by free gas (A_g, left column) and water with dissolved CO_2 (A_d, right column), during the calibration of Models 1–3 with Experiment A1. A_d includes area with gaseous CO_2 (see Fig. 6). Each iteration represents a new simulation run, and the experimental reference (E) is shown as a black line. Refer to Fig. 6 for region location, and to Sect. 3.3 for calibration procedure. **a**, **b**: Upper F sand. **c**, **d**: Middle F sand. **e**, **f**: Lower F sand

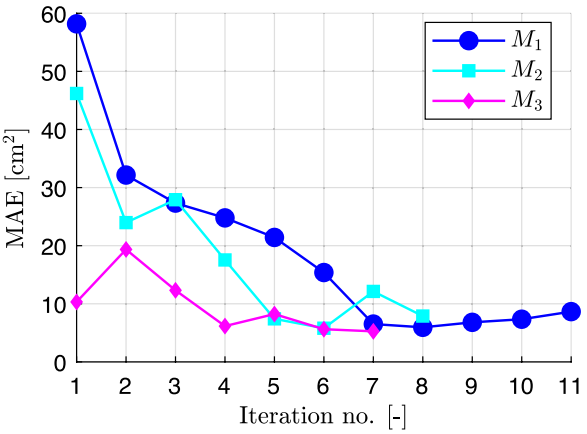


Fig. 9 Convergence of mean absolute error over the six areal quantities measured during the calibration process. The error is computed with respect to experimental values. See Fig. 8 for areas measured, and refer to Sect. 3.3 for calibration procedure

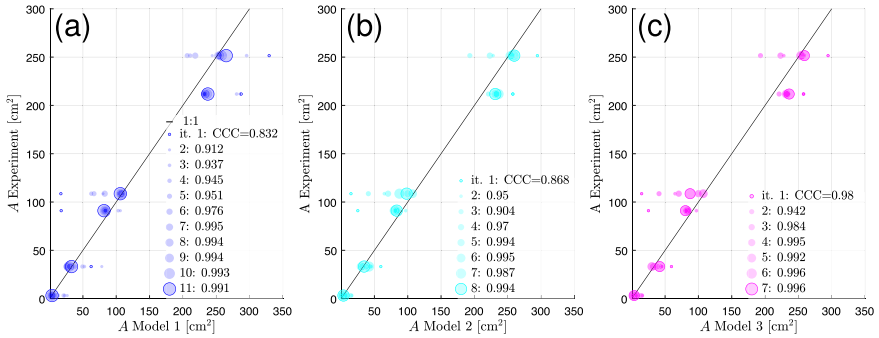


Fig. 10 Concordance between successive model iterations and the experiment, based on six areal measures evaluated during the calibration. Lin's CCC (Lin 1989) is shown in the key of each subplot, computed according to Eq. 2. **a** Model 1. **b** Model 2. **c** Model 3

Model 1 required seven iterations to give satisfactory areal estimates. The mean absolute error (MAE) over the six areal quantities presented in Fig. 8 is evaluated in Fig. 9, where it can be seen that, while all models are accurate towards the end (MAE $\in [5-10]\,\mathrm{cm}^2$), that required a sixfold improvement in Models 1 and 2, but only twofold in Model 3. As mentioned in Sect. 3.3, $C_{\mathrm{CO}_2} > 15\%(C^{\max}_{\mathrm{CO}_2}) \approx 0.2$ [kg/m^3] was used as threshold to determine areas. While the absolute values and error would change with a different C_{CO_2} threshold, we checked that the relative accuracy of our calibrated models does not with both $C_{\mathrm{CO}_2} > 0.01$ and 0.1 [kg/m^3].

Agreement between simulations and experimental observations is readily seen in Fig. 10, where the 1:1 line indicates perfect concordance. The degree of concordance can be quantified by means of Lin's concordance correlation coefficient (CCC) (Lin 1989; Oldenburg 2018), which, for N-valued observation (x) and model (y) vectors (the six areal quantities), is computed as:

Received by OCD: 6/29/2026

$$\mathrm{CCC} = \frac{2\sigma_{xy}}{\sigma_x^2 + \sigma_y^2 + (\bar{x} - \bar{y})^2} \tag{2}$$

where $\bar{x}$ and $\bar{y}$ are the means, σ_x^2 and σ_y^2 the variances, and σ_{xy} the covariance, all calculated using $1/N$ normalization. Results in Fig. 10 show that model calibration results in very good concordance for all models (CCC ≥ 0.99).

Convergence of quantities 3 and 4 in Sect. 3.3, the times at which the first finger touches the rig bottom and the middle C sand, respectively, is provided in Fig. 11. These times were only evaluated after a satisfactory areal match for quantities in Fig. 8 was achieved. Therefore, areas no longer change much in the last few iterations in Fig. 8. In Fig. 11, it can be seen that Models 2 and 3, which incorporated local intrinsic permeability measurements, were significantly closer to our experimental reference than Model 1. Initially, however, we observed that sinking of gravity fingers in the experiment was faster than our model values by a factor of ≈ 2. A satisfactory match of all quantities evaluated was achieved after 11, 8, and 7 iterations for Models 1–3, respectively.

Overall, we find that Model 3, with access to local single-phase and multiphase flow properties, is closer to the experimental reference (i.e., more concordant) from the start. Model 1 started farthest and required significantly more effort for calibration. After the calibration process, all models achieve very good concordance (CCC ≥ 0.99), based on evaluated quantities (Fig. 10). The calibration shown in Figs. 8, 9, 10, 11 employs $D = 10^{-9}$ m^2/s in all model versions (M_1 to M_3). Injection rates (I_R) started at 2.0 ml/min for all three models and were 1.6 ml/min, 1.8 ml/min and 1.75 ml/min, respectively, at the end of the calibration. I_R is slightly different because the goal was to obtain the best match with each model, considering I_R to be an uncertain variable. In Sect. 4.3, the same I_R is used to make forecasts with all three models.

Table 4 compares the starting and final (matched) key petrophysical variables for each model. The models were successfully calibrated by adjusting intrinsic permeability and the capillary pressure curves (same shape, but scaled to higher or lower p_e) only. It was found that CO_2 migration was most sensitive to the properties of the F sand were most of the CO_2 migration occurs, as well as the ESF seal, which structurally traps the CO_2 plume. In our matched models, p_e of ESF is about twice the measured value; this was required because the minimum saturation at which we can define p_e and ensure

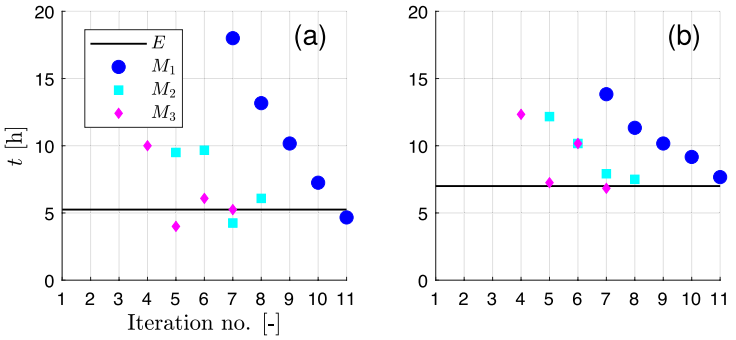


Fig. 11 Convergence of times at which the first finger touches the bottom of the rig (**a**) and the middle C sand (**b**), during the calibration of Models 1–3 with Experiment A1. Refer to Sect. 3.3 for calibration procedure

Received by OCD: 6/29/2026

Table 4 Petrophysical properties for used quartz sands in Experiment A1

Sand type / model	ϕ (−)	k (D)	p_e (mbar)	S_{wc} (−)	S_{gt} (−)
ESF	0.435	44	15	0.32	0.14
M_1^i	0.37	25	31.4	0.09	0.1468
M_1^f	0.37	6	31.4	0.09	0.1468
M_2^i	0.435	44	25.6	0.09	0.1468
M_2^f	0.435	44	25.6	0.09	0.1468
M_3^i	0.435	44	15	0.32	0.14
M_3^f	0.435	15	30	0.32	0.14
C	0.435	473	3	0.14	0.1
M_1^i	0.38	293	9.3	0.03	0.1565
M_1^f	0.38	293, 27	4.6	0.03	0.1565
M_2^i	0.435	473	7.8	0.03	0.1565
M_2^f	0.435	473, 158	2.6	0.03	0.1565
M_3^i	0.435	473	3	0.14	0.1
M_3^f	0.435	473, 118	4.5	0.14	0.1
E	0.45	2005	–	0.12	0.06
M_1^i	0.39	1528	4.1	0.01	0.16
M_1^f	0.39	1528	0.5	0.01	0.16
M_2^i	0.45	2005	3.86	0.01	0.16
M_2^f	0.45	3008	0.58	0.01	0.16
M_3^i	0.45	2005	0.33	0.12	0.06
$M_{3,1}^f$	0.45	2406	0.33	0.12	0.06
$M_{3,3}^f$	0.45	3208	0.33	0.12	0.06
F	0.44	4259	–	0.12	0.13
M_1^i	0.39	2277	3.3	0.01	0.16
M_1^f	0.39	6540, 2907	0	0.01	0.16
M_2^i	0.44	4259	2.62	0.01	0.16
M_2^f	0.44	6814, 4259	0	0.01	0.16
M_3^i	0.44	4259	0	0.12	0.13
$M_{3,1}^f$	0.44	7240, 4685	0	0.12	0.13
$M_{3,3}^f$	0.44	9796, 4259	0	0.12	0.13

Methodology for local measurements is provided by Haugen et al. (2023), while starting property modeling is described in Sect. 3.2. For each sand, measured (first row), initial (superscript i) and final (superscript f) values for each of our models are shown. For sand C, the second permeability value refers to the fault, if different from the rest. For sand F, the second permeability value refers to the middle F layer, if different from the rest. For Model 3, where property values are different, $M_{3,1}$ refers to the calibration with $D = 10^{-9}$ m^2/s and $M_{3,3}$ refers to $D = 3 \times 10^{-9}$ m^2/s

numerical convergence is $S_g \approx 10^{-4}$. Reality, however, is closer to a jump in p_c from 0 to p_e at an infinitesimally small S_g. Additionally, we found that concordance improved when using different values for the C and F sands in different model regions. In the case of the C sand, the explanation lies in the fault construction process, which may

reduce porosity with respect to “natural" sedimentation of stratigraphic layers (Haugen et al. 2023, this issue). The increase in F sand permeability was required to match finger migration times and is possibly compensating the absence of mechanical dispersion in the simulations. This is discussed in Sect. 5. Our calibrated values are within the same order of magnitude of the ex situ measurements (Table 4) and history-matched values for the porous medium in Tank 2 (Landa-Marbán et al. 2023, forthcoming).

Figure 12 shows gas saturation (S_g) and CO_2 concentration (C_{CO_2}) maps at times at which quantities 1–4 described in Sect. 3.3 are evaluated. Snapshots are provided for Model 3 only, since all three calibrated models were qualitatively very similar. It can be seen that CO_2 migration is successfully approximated by our numerical model. In detail, however, some differences are apparent: Firstly, sinking of CO_2-rich water from the bottom injector and horizontal migration along the bottom of the rig is faster in the model. This is due to the higher permeability that our numerical model requires in order to match the gravity fingering advance (cf. Table 4). Secondly, the experiment shows that denser, CO_2-rich water sinks with a rather compact front and closely spaced, wide fingers. Our model with constant $D = 10^{-9}$ m^2/s approximates all gravity-driven migration of the CO_2-rich water through thinner fingers, with the CO_2-saturated region receding with S_g. To better represent fingering widths, we also matched Model 3 with $D = 3 \times 10^{-9}$ m^2/s, used in Sect. 4.3.2.

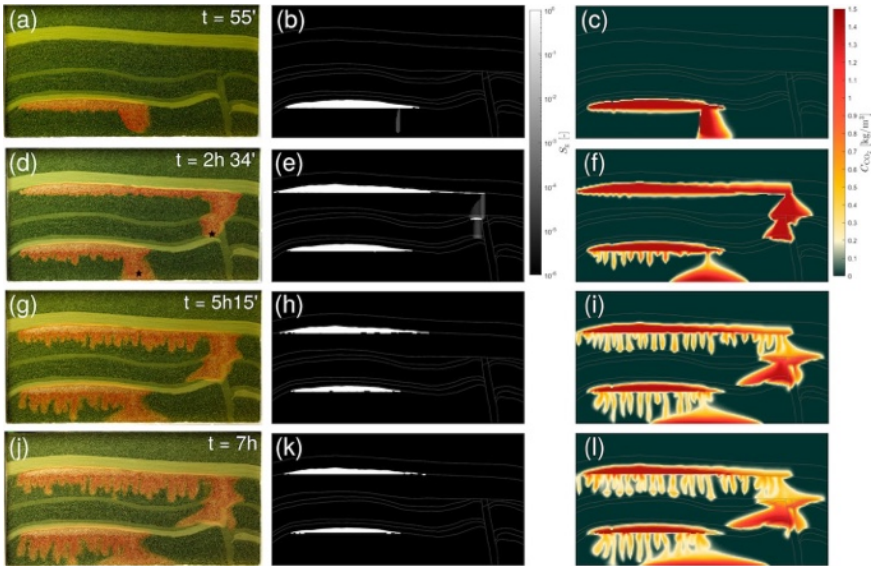


Fig. 12 Comparison between Experiment A1 in Tank 1 (left column) and simulation results with Model 3 after calibration (gas saturation shown in middle column, and CO_2 concentration shown in right column). Location of injection ports shown by black stars in **d**. $D = 10^{-9}$ m^2/s. **a**–**c** End of injection in lower port. **d**–**f** End of injection in upper port. **g**–**i** Time at which the first finger touches the rig bottom. **j**–**l** Time at which the first finger touches the middle C layer

Received by OCD: 6/29/2026

4.3 Transferability: Model Forecasts

A key question after history matching a flow simulation model is whether the physical description has actually been improved, or whether parameters have been modified to match a set of specific observations only. By applying the history-matched models to a different injection protocol (Experiment A2 in Tank 1; refer to Table 2) and subsequently to a different geometry (Experiment B1 in Tank 2), this can be assessed to some extent.

4.3.1 Analog for a Longer CO_2 Injection in the Same Geologic Setting

This case illustrates concordance of our history-matched models in a much longer injection in the same geology (Experiment A2). Before simulating this case, we observed that the trapped gas column against the fault in the experiment was different than what could be achieved with our previous p_e for Models 1–3 (Table 4). Because the capillary properties of the C sand in the fault were not directly involved in Experiment A1, we increased p_e in our calibrated models for that specific region ($p_e = 5$ mbar against the lower F sand, and 3.5 mbar against the middle F sand). All other parameters were taken from the values calibrated to match Experiment A1.

Evaluation was performed at the end of injection, at $t = 4$ h 48 min, with a single run with Models 1–3. I_R and D were set to the same value in all three models: 1.7 ml/min and 10^{-9} m/s^2, respectively. The experimental result is shown in Fig. 13a, while the simulation with Model 3 is depicted in Fig. 13b, c. We observe that the general distribution of CO_2 is close to the experimental truth. However, the experiment shows a compact sinking front of the CO_2-rich water without fingers; in our model, gravity fingering is apparent at this stage and fingers are close to the bottom of the rig. Additionally, CO_2-saturated brine touches the right boundary in the upper F reservoir, which does not occur in the experiment. This is due to capillary breach of the C sand above the middle F reservoir, as shown in Fig. 13b, and can be avoided by reducing the gas saturation value at which p_e is defined, or by increasing p_e.

The comparison of areal quantities is provided in Fig. 14 and demonstrates good-to-very-good concordance. Models 2 (MAE = 16 cm^2, CCC = 0.996) and 3 (MAE = 14.54 cm^2, CCC = 0.996) are similarly accurate and slightly better than Model 1 (MAE = 20.18 cm^2, CCC = 0.988), but there are no marked differences.

4.3.2 Analog for a Larger-Scale CO_2 Injection in a Different Geologic Setting

Finally, we compare the forecasting ability of our calibrated models against Experiment B1, conducted in a larger-scale, more complex geology (Fig. 1e) (Flemisch et al. 2023,

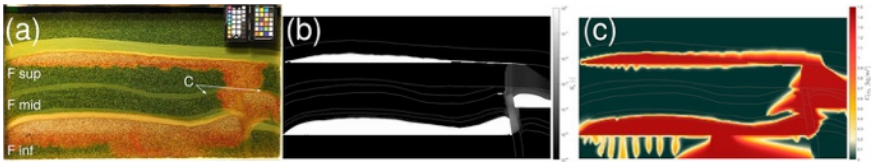


Fig. 13 Comparison between Experiment A2 in Tank 1 (**a**) and simulation results with Model 3 (**b**, **c**) at the end of the injection phase ($t = 4$ h 48 min)

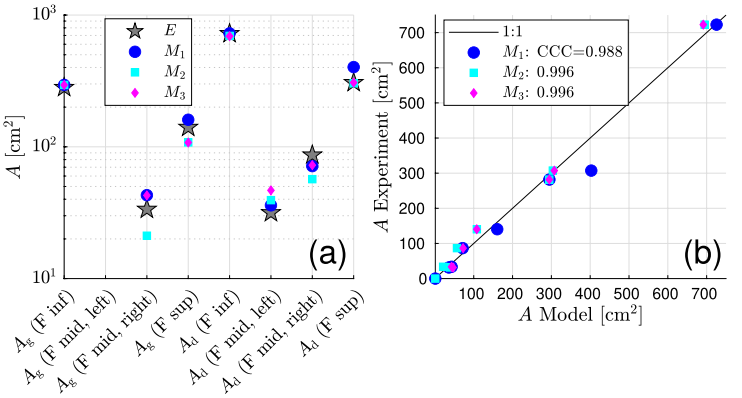


Fig. 14 **a**: Comparison of areas occupied by free gas (A_g) and water with dissolved CO_2 (A_d) for Experiment A2 in Tank 1. Experimental reference shown with a star (E). A_g (F mid, left) not shown because values are very close to 0. Refer to Fig. 6 or Fig. 13a for region location. **b** Concordance plot for each of the three models, using the same areal quantities as in **a**. Lin's CCC (Lin 1989) is shown in the key, according to Eq. 2

this issue). Similar to Sect. 4.3.1, our goal is to assess the forecasting ability of our calibrated models—without changing their properties. However, given that sand D controls migration in the lower fault (see Fig. 2d) and it was not present in our calibrated models, we allowed one change for Models 1 and 2, which did not have access to local p_c measurements. This means that we ran an initial simulation of this experiment with Models 1 and 2 and then adjusted the p_c curve of the D sand. The selected curve lies at $\approx \frac{1}{3}$ of the $p_c(S_w)$ shown in Fig. 3 and Fig. 4, respectively.

Next, we evaluate concordance of Models 1–3 by comparing them to the experimental truth after a single run. Evaluation is performed over the total duration of the experiment (120 h), which is simulated with the same I_R (10 ml/min) and D (10^{-9} m^2/s) in all three models (M_1, M_2, $M_{3,1}$). Additionally, a run with $D = 3 \times 10^{-9}$ m^2/s was completed with Model 3 ($M_{3,3}$) to better approximate finger widths, as noted in Sect. 4.2.

Gas saturation and CO_2 concentration maps at the end of injection with Model 1 are shown in Fig. 15a and Fig. 15b, respectively. The full visual comparison is provided in Fig. 16. We make the following observations:

- At the end of injection ($t = 5$ h), all three models forecast some migration of CO_2 into Box B. Models 2 (Fig. 16c) and 3 (Fig. 16d) underestimate the amount of CO_2, while Model 1 (Fig. 16b) overestimates the amount of CO_2 in the top C sand.
- Also at the end of injection, all models forecast faster sinking of the CO_2-charged water tongue arising from the lower injector. This is due to the higher F sand permeability required to match finger advance (see Sect. 4.2), particularly in Model 3 with $D = 3 \times 10^{-9}$ m^2/s.
- The speed at which CO_2-rich fingers sink is slightly faster in our models, compared to the experiment. As expected, Model 3, with a higher diffusion coefficient, displays thicker fingers, with closer widths to the experiment. Similar to our previous

Received by OCD: 6/29/2026

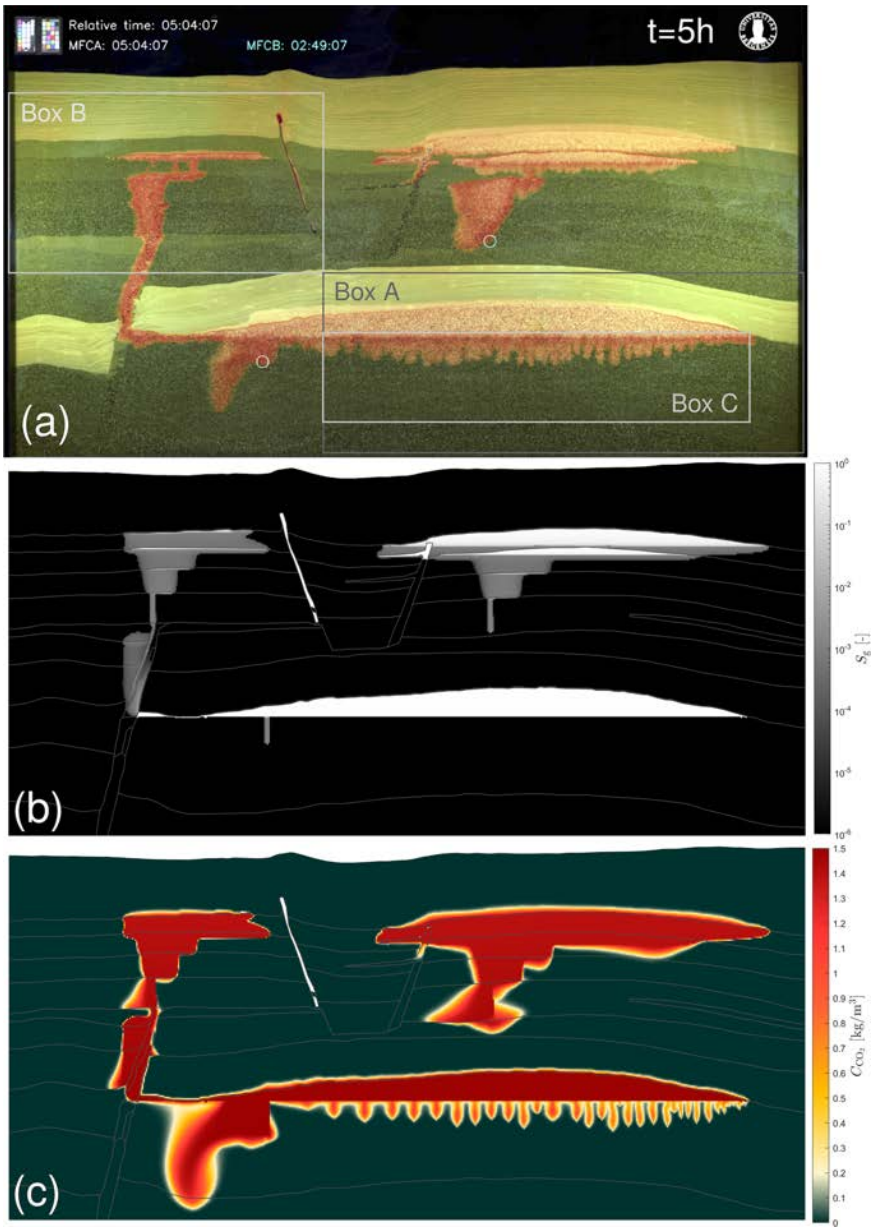


Fig. 15 Comparison between Experiment B1 in Tank 2 (**a**) and simulation Model 1 (**b**, **c**) at the end of injection (t = 5h). Circles in **a** denote the location of injection ports

observations, the numerical models cannot approximate the compact, CO_2-rich water front closely trailing the fingers.

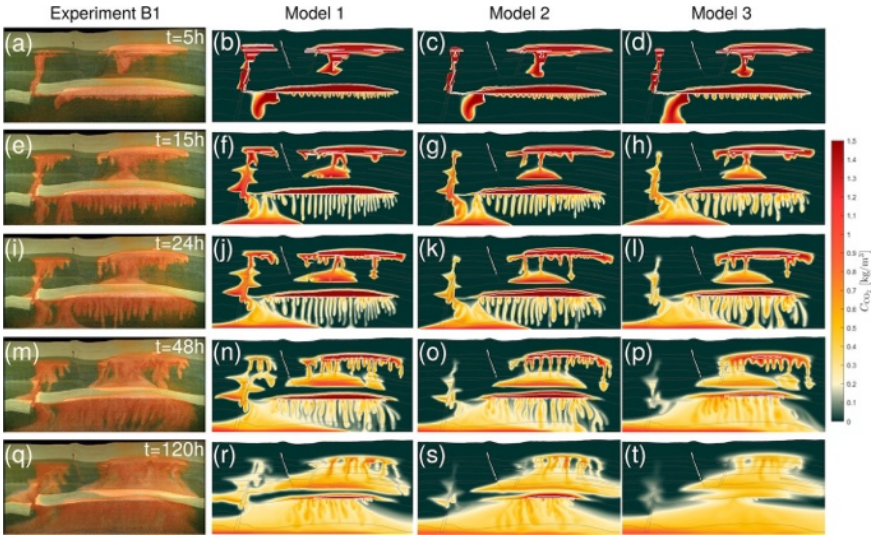


Fig. 16 Comparison between Experiment B1 in Tank 2 (leftmost column) and CO_2 concentration maps for simulation Models 1–3 (middle-left, middle-right and rightmost, respectively). $D = 10^{-9}$ m^2/s (Model 1 and 2), $D = 3 \times 10^{-9}$ m^2/s (Model 3). The white contours in simulation plots indicate $S_g = 10^{-3}$. **a–d** End of injection. **e–h** t = 15h. **i–l** t = 24h. **m–p** t = 48h. **q–t** t = 120h

- Dissolution of CO_2 is underestimated by Models 1 and 2, while it is closer, but overestimated, by Model 3.

Consistent with our approach described in Sect. 3.3, quantitative analysis is provided by means of areal quantities over time in Fig. 17. Experimental values were obtained via segmentation of timelapse images, and the data were reported on a 1 × 1 cm grid where 0 is pure water, 1 is water with dissolved CO_2, and 2 is gaseous CO_2. The segmentation procedure is explained in Nordbotten et al. (2023, this issue). We then obtained the areas of each phase within Box A and B to generate Fig. 17 (refer to Fig. 15a for box location).

In Box A, which contains the main F reservoir and ESF seal, we observe very good concordance (accurate areas) during injection. Afterwards, Model 3 with $D = 3 \times 10^{-9}$ m^2/s continues to follow the experiment closely, whereas the others overestimate gaseous CO_2. Note that the PVT properties of our fluids are the same in all models; differences arise due to (1) higher sand F S_{wc} in Model 3, and higher sand F k in Model 2 and especially Model 3 ($D = 3 \times 10^{-9}$ m^2/s), compared to Model 1, which allow greater convective mixing (Ennis-King and Paterson 2005) (Table 4); and (2) lower p_e and higher k of sand ESF in Model 2 (Table 4), which allows some CO_2 migration into the seal (Fig. 16). In Box B (Fig. 17d–f), Model 1 and Model 3 with $D = 10^{-9}$ m^2/s are able to approximately track the experimental truth during injection. However, our models without dispersion cannot capture the areal increase of CO_2-rich water that occurs afterwards (cf. Fig. 16).

To put these results in perspective, Fig. 18 provides a comparison with results submitted by the international benchmark study (IBS) participants, as well as Experiment B1 (Flemisch et al. 2023, this issue). Figure 18 presents, for each datapoint, mean Wasserstein distances to experiments and forecasts (simulations by IBS participants). Specifically,

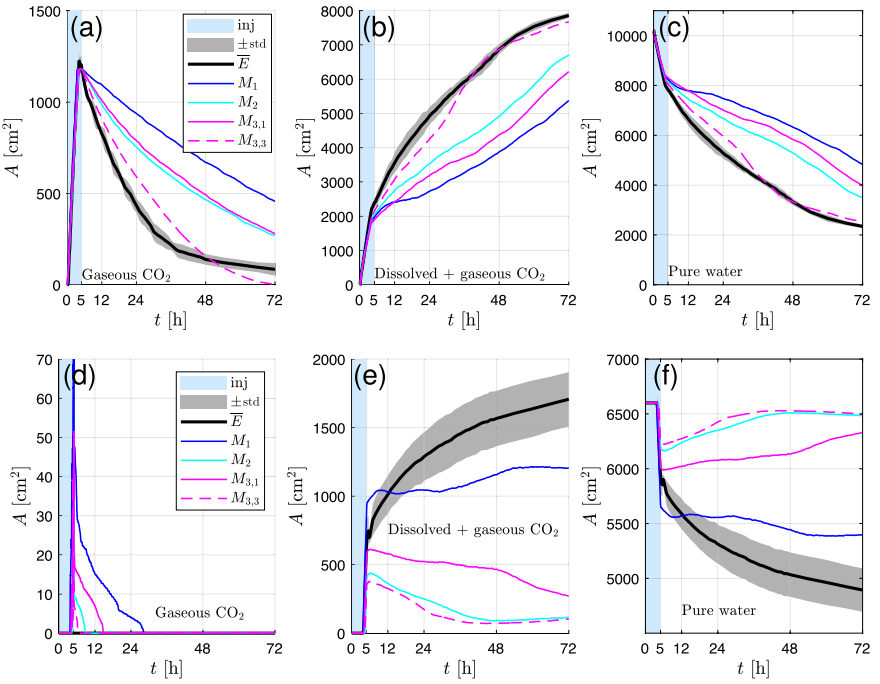


Fig. 17 Comparison of areas occupied by each phase during the first 72 h of case B1. Experimental mean ($\overline{E}$) and standard deviation (std) obtained from four experimental runs with identical protocol, while the results for Models 1–3 are for a single run with each matched model. For M_3, two cases are shown: $D = 10^{-9}$ m^2/s ($M_{3,1}$) and $D = 3 \times 10^{-9}$m^2/s ($M_{3,3}$). Top row shows areas in Box A, and bottom row shows areas in Box B. **a**, **d** Gaseous CO_2. **b**, **e** Dissolved CO_2 (includes area with gaseous CO_2). **c**, **f** Pure water

the Wasserstein metric (W) measures "the minimal effort required to reconfigure the probability mass of one distribution in order to recover the other distribution" (Panaretos and Zemel 2019). We expect $W \to 0$ for two samples from the same distribution, given enough values, and two samples to be more similar or concordant the closer W is to 0. To calculate distances shown in Fig. 18, the cell mass density in a 1×1 cm grid was estimated for all simulations and experiments and then normalized. Therefore, this metric provides a measure of the overall degree of agreement (i.e., in the whole domain). Resulting distances were dimensionalized using the total CO_2 mass in the system, such that the units are grams $\times$ centimeter, with values < 100 gr cm and < 50 gr cm representing good concordance and very good concordance, respectively. Details and code are provided by Flemisch et al. (2023, this issue). In Fig. 18, it can be seen that M_1–M_3 are comparable to or better than the best forecasts by IBS participants. M_1 and $M_{3,1}$, in particular, achieved very good concordance.

Further evaluation of simulation model concordance, including comparison with model results before calibration, mass quantities and error measures, is provided in Appendix A. From this analysis (Sect. 4.3 and Appendix A), we find that:

Received by OCD: 6/29/2026

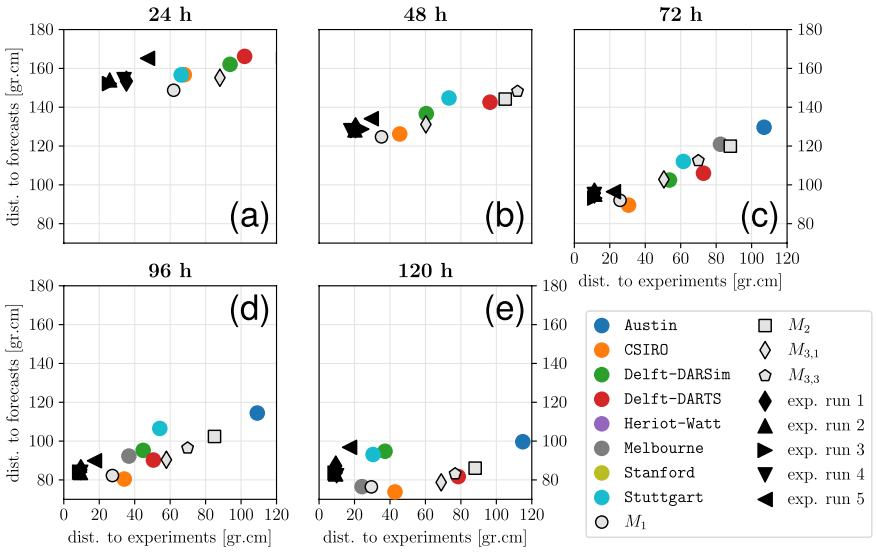


Fig. 18 Wasserstein distances to experiments and forecasts (simulations). Colored circles show forecasts by IBS groups, and results with calibrated Models 1–3 are presented with light gray markers. In each subplot, the vertical axis shows the mean distance between a given datapoint and the forecasts (considering the IBS participants only), while the horizontal axis shows the mean distance between a given datapoint and the experiments. Markers not present fall outside of the axes limits. **a** 24 h. **b** 48 h. **c** 72 h. **d** 96 h. **e** 120 h

- All matched models approximate well CO_2 migration and distribution in the domain, seal capacity, and onset of convective mixing. M_1 and $M_{3,1}$ are most concordant to experiments (Fig. 18).
- Calibrated models are able to accurately estimate specific quantities during the injection phase, yet they accumulate higher errors later on (Fig. 17 and Appendix B).
- Similar to Experiment A1, the calibration procedure significantly improved the concordance of M_1 and M_2 with the experiment (Figs. 19 and 16). In Box A, calibration also improved concordance for M_3 (Figs. 20 and 24). Overall, however, matched $M_{3,1}$ and $M_{3,3}$ are less concordant than their initial versions, which were already in very good agreement with the experiment (Figs. 21 and 18).

In summary, calibrated models are transferable to a different operational setting or geologic structure, as long as sediments and trap systems remain the same (Experiment A2 and Box A in Experiment B1). Where reservoir connectivity is provided by heterogeneous structures with uncertain properties, accurate deterministic estimates of CO_2 migration are unlikely; models calibrated elsewhere (Experiment A1) were not accurate in our test (Box B in Experiment B1). Given unlimited computational time, the forecasting capability of numerical models calibrated with published data appears similar to those having access to local measurements; the main value of local data lies in reducing the time required for history matching. Obtained results suggest that history matching worsened M_3 forecasts in a different setting (Experiment B1). Therefore, forecasts in a given geologic setting may benefit more from local measurements

and accurate physics, rather than history matching, unless historical data of the same setting are available. This is because CO_2-brine flow is very sensitive to variations in petrophysical properties such as capillary pressure, which will change in different areas, even if the geology is similar.

5 Discussion

In the FluidFlower, strong buoyancy and high permeability lead to persistent appearance and disappearance of fluid phases, as the gas migrates upward and dissolves in the water; coupled with other two-phase flow nonlinearities, these aspects make this problem difficult to solve numerically (e.g., Lie 2019). Comparison between the number of nonlinear iterations and the strength of different physical mechanisms (flow rates, buoyancy, capillarity and dissolution) is presented in Appendix B. A clear correlation can be seen between flow rates and number of iterations. However, buoyancy, capillarity and dissolution all appear to be playing a role, and it is not straightforward to discern which effect dominates; hence, this is a topic that requires further study. We note that difficulties with the convergence of the nonlinear solver have been reported by all participants in the international benchmark study (Flemisch et al. 2023, this issue). As hinted in Sect. 3.1, we addressed this by optimizing linear solver time, reducing the time-step length, increasing the number of time-step cuts and relaxing MRST's maximum normalized residual where required.

In a 2D isotropic medium and assuming uniform flow, the hydrodynamic dispersion coefficient ($\underline{\underline{D}}_{\mathrm{h}}$) can be modeled as $\underline{\underline{D}}_{\mathrm{h}} = \begin{bmatrix} \alpha_{\mathrm{L}}\overline{u} & 0 \\ 0 & \alpha_{\mathrm{T}}\overline{u} \end{bmatrix}$, where α_{L} and α_{T} are the longitudinal and transverse dispersivity, respectively, and $\overline{u}$ is the average Darcy velocity (Bear 1972). Assuming dispersivities $\geq 10^{-3} - 10^{-2}$ m (Garabedian et al. 1991; Gelhar et al. 1992; Schulze-Makuch 2005) and $\overline{u} \approx 3 \times 10^{-6}$ m/s (from our simulations), we get $\underline{\underline{D}}_{\mathrm{h}} \in [3 \times 10^{-9}, 3 \times 10^{-8}]\,\mathrm{m}^2/\mathrm{s}$ or larger; this means that $\underline{\underline{D}}_{\mathrm{h}} \geq D$ for the timescales considered (Riaz et al. 2004; Rezk et al. 2022). We also note that numerical dispersivity is on the order of the cell size ($h \approx 4$ mm in Tank 1, and ≈ 5 mm in Tank 2), so it is likely smaller than physical dispersivity. Numerical diffusion can be approximated as uh, which yields maximum values $\sim O(10^{-7}\,\mathrm{m}^2/\mathrm{s})$ (water phase). However, using the mean of the 75$^{\mathrm{th}}$ percentile flow velocity over all time-steps, we obtain $\sim O(10^{-9}\,\mathrm{m}^2/\mathrm{s})$. Therefore, we estimate that numerical diffusion is lower than physical diffusion almost everywhere in our simulations. Previous work suggested that hydrodynamic dispersion in homogeneous sediments can be accounted for by increasing D (Riaz et al. 2004, 2006), as done here. However, our analysis shows that the spreading of CO_2-rich water during convective mixing can be loosely, but not accurately, represented by molecular diffusion. Given (1) the dominance of convective mixing on solubility trapping (Ennis-King and Paterson 2005; Neufeld et al. 2010; MacMinn and Juanes 2013; (2) heterogeneity of many natural reservoirs, which increases the importance of dispersion (Riaz et al. 2006; Bear 2018); and (3) the acceleration of CO_2 dissolution due to dispersion, as observed here and by others (e.g., Hidalgo and Carrera 2009), it is important to quantify the balance between diffusion and dispersion to estimate CO_2 trapping.

Our study of CO_2 injection and migration in unconsolidated sands at atmospheric p, T conditions captures the CO_2-water system dynamics at short to intermediate timescales: buoyancy-driven flow and structural trapping (Bachu et al. 1994; Bryant et al.

2008; Hesse and Woods 2010; Szulczewski et al. 2013), residual trapping (Juanes et al. 2006; Burnside and Naylor 2014) and convective mixing and dissolution trapping (Weir et al. 1996; Ennis-King and Paterson 2005; Riaz et al. 2006; Neufeld et al. 2010; Hidalgo et al. 2012; MacMinn and Juanes 2013; Szulczewski et al. 2013). Due to the very large sand permeability ($10^2 - 10^4$ D), convective mixing and dissolution dominate CO_2 trapping. With respect to values at $\sim$ 1 km depth ($p \sim 100$ bar, $T \sim 40$ C), the dynamic viscosity and density of CO_2 are $\approx 1/3$ and 3×10^{-3}. Conversely, previous studies with similar setups used analogous fluids with density and viscosity ratios similar to supercritical CO_2-brine (Trevisan et al. 2017; Krishnamurthy et al. 2022). Dynamics observed in these systems are similar to ours, with vertical migration of CO_2 dominated by buoyancy and lateral spreading of CO_2 plumes with a main tongue at the top of the aquifer or high permeability layer. A quantitative scaling analysis of the FluidFlower (Tank 2) was performed by Kovscek et al. (2023, this issue), who showed that scaling of physical mechanisms to the field scale is possible. Compared to three CO_2 storage projects (Northern Lights, Sleipner and In Salah) the vertical dimension of the storage reservoir is exaggerated 2 to 3 times. Temporally, 1 h in the FluidFlower is equivalent to $\sim 100 - 400$ y in the field; thus, the experiment in Tank 2 (120 h) covers well the injection and post-injection periods. Similar to the FluidFlower, Kovscek et al. (2023, this issue) estimate the onset of convective mixing to occur during injection in high-permeability formations like the Utsira Sand (Sleipner). This analysis demonstrates that observations made in the FluidFlower can be used to describe field-scale fluid dynamics and quantify forecasting accuracy.

Our models retained some error at the end of the calibration phase, which is a known problem of manual history matching (Oliver and Chen 2011). Consistent with previous findings (e.g., Fisher and Jolley 2007), results show that Model 2 and 3, which had access to local data, achieved faster match to the experimental truth than Model 1 (Sect. 4.2). However, all models seem to have similar forecasting capability (Sect. 4.3). Subsurface heterogeneity and time constraints may explain why, in practice, it is critical to include local data to achieve history matching, and, especially, concordant forecasting (e.g., Gosselin et al. 2003; Fisher and Jolley 2007; Myers et al. 2007; Kam et al. 2015; Avansi et al. 2016). Calibration with Experiment A1 decreased overall concordance of Model 3 to Experiment B1 (but improved concordance in Box A), compared to forecasts with initial (measured) parameter values. We interpret this to be the result of fluid migration in Experiment A1 being controlled by different units than in Box B in Experiment B1. Therefore, local measurements are paramount, especially if historical data in the trap system of interest are not available.

Additionally, we did not quantify uncertainty in history-matched models due to the availability of a ground truth. In general, however, this is necessary to manage reservoir operations (e.g., Aanonsen et al. 2009; Oliver and Chen 2011; Jagalur-Mohan et al. 2018; Jin et al. 2019; Liu and Durlofsky 2020; Santoso et al. 2021, and references therein). It is also important to note that history-matched models may have grid-size dependencies (see Appendix C), which may require that the grid used to make forecasts, if different or encompassing additional regions, maintain a similar resolution. Finally, multiphase flow in poorly lithified sediments is non-unique (Haugen et al. 2023, this issue), which also contributes to uncertainty. Therefore, it seems prudent to adopt a probabilistic perspective when estimating subsurface CO_2 migration. This is consistent with results in Fig. 18 and Flemisch et al. (2023, this issue): in the highly resolved and geologically simple FluidFlower (compared to the subsurface), forecasts by different simulation groups show large spread.

Received by OCD: 6/29/2026

6 Conclusions

We performed experiments (Sect. 2) and numerical simulations (Sect. 3) of CO_2 migration in poorly lithified, siliciclastic sediments at the meter scale. Three simulation model versions, with access to different levels of local data, were manually history-matched to the experiments (Sects. 4.1, 4.2), and then used to make forecasts (Sect. 4.3). The main findings are:

1. The time required to history match Model 3 (access to both single-phase and multiphase measurements) is lower than Model 2 (access to local single-phase measurements), which is lower than Model 1 (no access to local petrophysical measurements).
2. All simulation models achieve a satisfactory qualitative match throughout the experiments. Quantitatively, forecasting capability of Models 1–3 appears similar: in specific domain regions, models were close to the experimental truth during CO_2 injection, and accumulated larger errors afterwards, especially where heterogeneous structures control CO_2 migration.
3. Overall forecasts with Model 3 after calibration in a similar, but not identical, geologic setting were less accurate than forecasts made with measured values. This emphasizes the importance of local measurements and history matching in the same geologic setting.
4. The addition of a constant molecular diffusion coefficient allows matching convective finger widths to experimental observations. However, simulations without dispersion cannot approximate the compact, CO_2-rich sinking front closely trailing convective fingers in our experiments.

Simulation models were not always accurate. Given the degree of control in our study, it seems prudent to quantify uncertainty when assessing subsurface CO_2 migration in the field using numerical models. Obtained results suggest that confidence can be increased by obtaining local data, quantifying petrophysical parameter uncertainty, testing sensitivity to petrophysical parameters in different model regions, using historical data from the same setting and including post-injection data when history matching, and incorporating multiple scenarios of CO_2 migration, particularly where heterogeneous structures are at play.

Appendix A: Additional Analysis of Simulation Model Concordance with Experiment B1

A.1 Results with Initial Model Parameters

Figure 19 compares Experiment B1 and concentration maps from simulations with initial parameters, for each of the three model versions considered. Qualitatively, all models estimate the location of the two main gas plumes correctly, but it is clear that Models 1 and 2 are less concordant to the experiment than Model 3. This is particularly true in the upper left of the domain, where CO_2 migration is controlled by the heterogeneous fault. Similar to results presented in Sect. 4.1, Model 3 is already very close to the experiment, although the advance of convective fingers is slower.

Concordance between our initial models and the simulation is shown in Fig. 20 by means of the ratio between the model and experimental areas for different quantities in Box

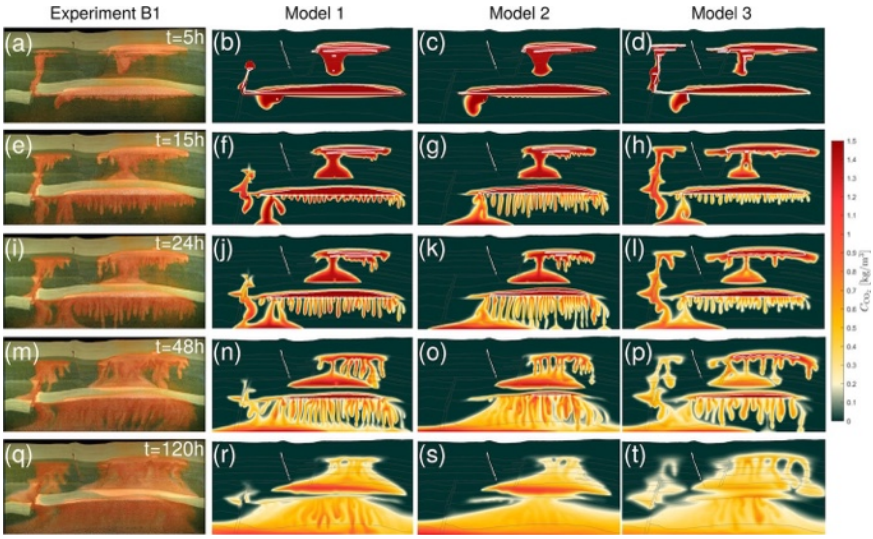


Fig. 19 Comparison between Experiment B1 in Tank 2 (leftmost column) and CO_2 concentration maps for simulation Models 1–3 (middle-left, middle-right and rightmost, respectively) with initial parameters. $D = 10^{-9}$ m^2/s (Model 1 and 2), $D = 3 \times 10^{-9}$ m^2/s (Model 3). **a**–**d** End of injection. **e**–**h** $t = 15$h. **i**–**l** $t = 24$h. **m**–**p** $t = 48$h. **q**–**t** $t = 120$h

A and Box B (see Fig. 15 for box location). Values below 1 indicate that the model underestimates the areal extent of a given quantity, while values above 1 indicate that the model overestimates it. During the first 48–72 h, all models except $M_{3,1}$ are reasonably close to the experiment in Box A. Afterwards, M_1, M_2 and $M_{3,3}$ forecast earlier dissolution of the CO_2 plume, while $M_{3,1}$ forecasts later dissolution. In Box B, concordance is relatively good for M_3 during the first 48 h, but model accuracy diminishes with time for all model versions.

Further comparison between our initial model results and experimental values are provided in Fig. 21, where we evaluate mean Wasserstein distances to the international benchmark study (IBS) participants' forecasts and experiments (Flemisch et al. 2023, this issue). Figure 21 is consistent with Fig. 19, where it can be seen that M_3 is already very close to the experiment and is similarly concordant or more concordant than the best of the IBS participants.

A.2 Calibrated Models

First, we provide the total mass of CO_2 in the computational domain in Fig. 22, and the mass in Boxes A and B in Fig. 23.

Next, in Table 5, the following measures are compared with quantities estimated from the experiment via segmentation of timelapse images (Nordbotten et al. 2023, this issue). These measures correspond to the sparse data requested to participants of the FluidFlower IBS (Flemisch et al. 2023, this issue):

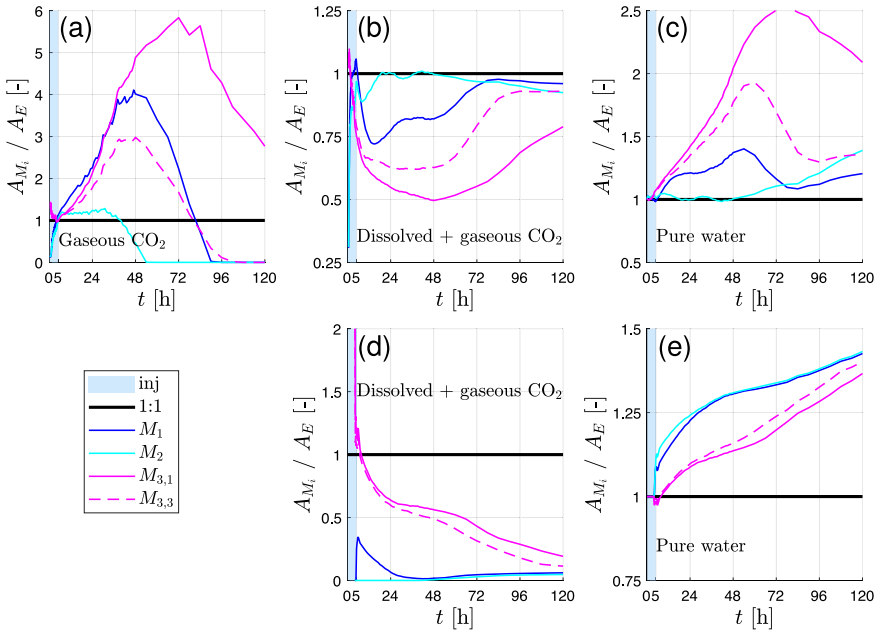


Fig. 20 Ratios between model (A_{M_i}) and experimental mean (A_E) areas occupied by each phase. Experimental mean was obtained from four experimental runs with identical protocol, while the results for Models 1–3 are for a single run. For M_3, two cases are shown: $D = 10^{-9}$ m^2/s ($M_{3,1}$) and $D = 3 \times 10^{-9}$ m^2/s ($M_{3,3}$). Top row shows Box A, and bottom row shows Box B. Ratios for gaseous CO_2 in Box B are not computed because experimental values are 0. **a** Gaseous CO_2. **b**, **d** Dissolved CO_2 (includes area with gaseous CO_2). **c**, **e** Pure water

1. Time of maximum mobile free phase in Box A
2. Mass of mobile $CO_{2(g)}$, immobile $CO_{2(g)}$, dissolved CO_2, and CO_2 in the seal (in any phase), in Box A, 72 h after injection start (2a-d)
3. The same quantities as 2. for Box B (3a-d)
4. time at which m (defined below) exceeds 110% of the width of Box C
5. Total mass of CO_2 in the ESF seal, in Box A, at $t = 120$ h

Convective mixing in Box C (see Fig. 1e) is reported as the integral of the magnitude of the gradient in relative concentration of dissolved CO_2 (Flemisch et al. 2023):

$$m(t) = \int_C \left| \nabla \left(\frac{\chi^{w}_{CO_2}}{\chi^{w,max}_{CO_2}} \right) \right| d\mathbf{x} \tag{A1}$$

where $\chi^{w}_{CO_2}$ is the mass fraction of CO_2 in water, and the dissolution limit is $\chi^{w,max}_{CO_2}$. Note that quantity 4, based on m, cannot be provided with full accuracy based on experimental data, so an uncertain lower and upper bound is provided instead. Therefore, error is not computed in Table 5.

Relative error is evaluated with respect to the experimental mean ($\overline{E}$) as $\varepsilon_i(\%) = 100 \times \frac{|\overline{E_i} - M_{J,i}|}{\overline{E_i}}$, where i is a given measure and J refers to any of the Models 1–3. In

Received by OCD: 6/29/2026

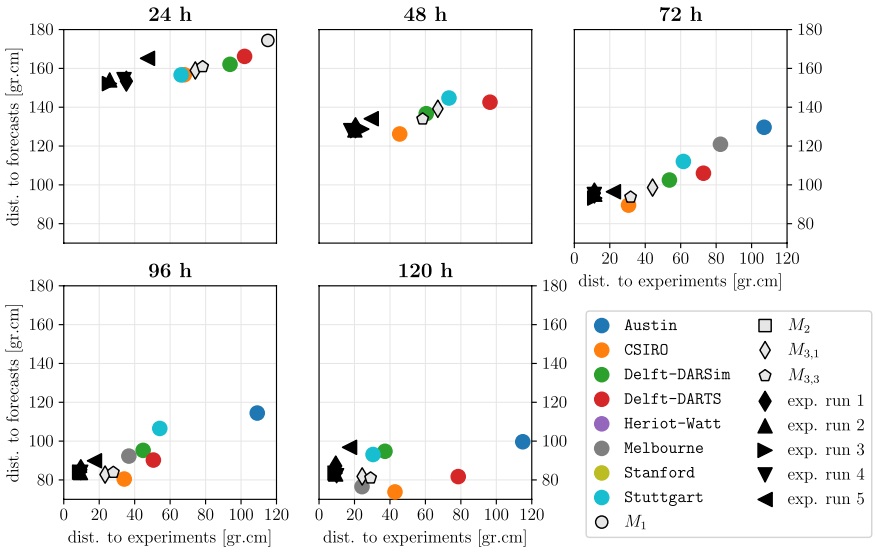


Fig. 21 Wasserstein distances to experiments and forecasts (simulations). Colored circles show forecasts by IBS groups, and results with initial Models 1–3 are presented with light gray markers. In each subplot, the vertical axis shows the mean distance between a given datapoint and the forecasts (considering the IBS participants only), while the horizontal axis shows the mean distance between a given datapoint and the experiments. Markers not present fall outside of the axes limits. See Sect. 4.3.2 for details

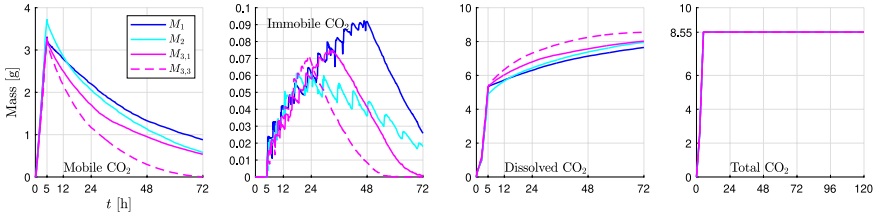


Fig. 22 Total mass of CO_2 for our simulations of Experiment B1 presented in Sect. 4.3.2. Results are provided for Models 1–3. For M_3, two cases are shown: $D = 10^{-9}$ m^2/s ($M_{3,1}$) and $D = 3 \times 10^{-9}$ m^2/s ($M_{3,3}$)

Table 5, it can be seen that all models accumulate some error in most of the quantities reported. The maximum errors are $\approx 140\%$ for Models 1–2 and $< 100\%$ for Model 3. Model 1 is more concordant in the uncertain region (Box B; see Sect. 4.3.2 as well), while Models 2 and 3 are more accurate in Box A, the region where the calibration performed with Experiment A1 is more meaningful. Overall, $M_{3,1}$ does marginally better.

We provide additional analysis in Fig. 24, which shows ratios between model and experimental areas, similar to Fig. 20. As shown in Sect. 4.3.2, $M_{3,3}$ is most concordant in Box A, while M_1 and $M_{3,1}$ do better in Box B. Compared to Fig. 20, the maximum ratio is reduced. In Box A ($t < 72$h), Models 1 and 2 are less accurate than in Fig. 20, but this is not representative of their concordance in the whole domain (Sect. 4.3.2).

Received by OCD: 6/29/2026

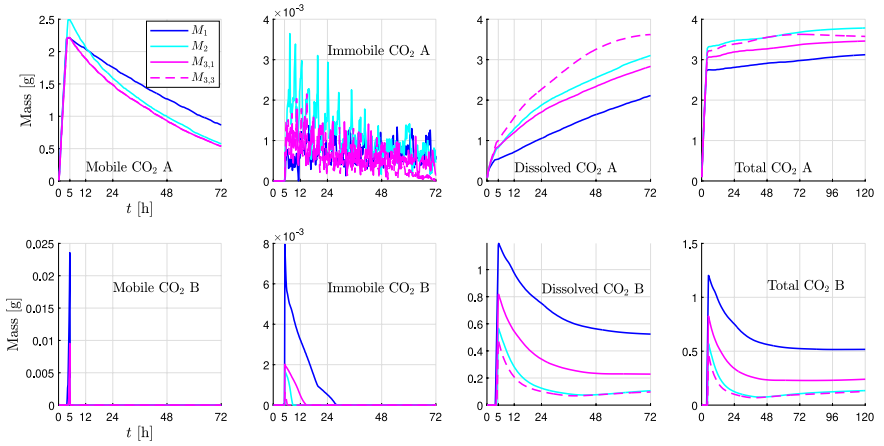


Fig. 23 Mass of CO_2 in Boxes A and B defined in Fig. 1e, for our simulations of Experiment B1 presented in Sect. 4.3.2. Results are provided for Models 1 to 3. For M_3, two cases are shown: $D = 10^{-9}$ m^2/s ($M_{3,1}$) and $D = 3 \times 10^{-9}$ m^2/s ($M_{3,3}$)

Appendix B: Nonlinear Solver Number of Iterations

According to fluid migration in the FluidFlower, flow dynamics are initially dominated by injection rates, then by buoyancy of the gas phase, and finally by capillarity and dissolution. In Fig. 25, we present, for the experiment in Tank 2, the relationship between the number of iterations, the maximum Darcy velocity (u) and the maximum concentration rate ($\dot{C}$), evaluated as $\mathrm{d}C/\mathrm{d}t$, as a function of time. Additionally, we estimated the maximum values of the dimensionless Reynolds (R_e, see Eq. 1), Capillary (C_a) and Bond (B_o) numbers during and after injection (e.g., Bear 1972):

$$C_a = \frac{\mu_\alpha u_\alpha}{\sigma} \tag{B1}$$

$$B_o = \frac{\Delta\rho g k}{\sigma} \tag{B2}$$

where μ is the dynamic viscosity, u the Darcy velocity, σ the interfacial tension, $\Delta\rho$ the density difference, g the gravity, k the permeability, and subscript α denotes a generic fluid phase. Max $B_o \sim O(10^{-3})$ and remains constant in our system. Max $C_a \sim O(10^{-6})$, $\sim O(10^{-7})$ for water and $\sim O(10^{-6})$, $\sim O(10^{-8})$ for gas (during and after injection, respectively), while max $R_e \sim O(10^{-2})$ for water and $\sim O(10^{-1})$, $\sim O(10^{-2})$ for gas (during and after injection, respectively).

From Fig. 25, a correlation between max $|u_{h,g}|$ and the number of iterations is apparent during injection. The number of iterations increases significantly after an injection port becomes active, and also when CO_2 spills out of the lower reservoir and starts migrating along the lower fault (see Fig. 15); this occurs at $t \approx 215$ min and $t \approx 250$ for M_1 and $M_{3,3}$, respectively. Peaks in $\dot{C}$ appear at the onset of injection, but we do not observe significant variations otherwise. Values from the dimensionless groups

Received by OCD: 6/29/2026

Table 5 Sparse data comparison between Experiment B1 in Tank 2 and simulation results with Models 1–3

Measure	$\overline{E}$	$\sigma(E)$	M_1	ε_1 (%)	M_2	ε_2 (%)	$M_{3,1}$	$\varepsilon_{3,1}$ (%)	$M_{3,3}$	$\varepsilon_{3,3}$ (%)
1 (s)	14,880	720	17,700	19	17,160	15.3	17,280	16.1	18,000	21
2a (g)	0.36	0.13	0.87	140.7	0.57	59.7	0.54	48.7	0.005	98.8
2b (g)	0	0	0	0	0	0	0	0	0	0
2c (g)	3.5	0.08	2.11	39.7	3.1	11.3	2.8	19	3.6	3.5
2d (g)	–	–	0.43	n/a	0.97	n/a	0.74	n/a	0.7	n/a
3a (g)	0	0	0	0	0	0	0	0	0	0
3b (g)	0	0	0	0	0	0	0	0	0	0
3c (g)	0.55	0.32	0.52	4.7	0.1	80.7	0.23	58.4	0.1	82.4
3d (g)	n/a	n/a	0.002	n/a	0.006	n/a	0.002	n/a	0.004	n/a
4 (s)	[12,180, 17,990]	[438, 2261]	15,000	n/a	15,000	n/a	18,600	n/a	15,600	n/a
5 (g)	0.38	0.047	0.52	37.1	0.94	148.5	0.73	91.6	0.62	63.1
$\overline{\varepsilon}$ (%)	n/a	n/a	n/a	30.1	n/a	39.4	n/a	29.2	n/a	33.6

Experimental mean and standard deviation were obtained from six experimental runs with identical protocol, while the results for Models 1–3 are for a single run with each matched model. For M_3, two cases are shown: $D = 10^{-9}$ m^2/s ($M_{3,1}$) and $D = 3 \times 10^{-9}$ m^2/s ($M_{3,3}$). Experimental quantity 4 is reported using a lower and upper bound due to high uncertainty, so errors are not computed. See main text for measure description

Received by OCD: 6/29/2026

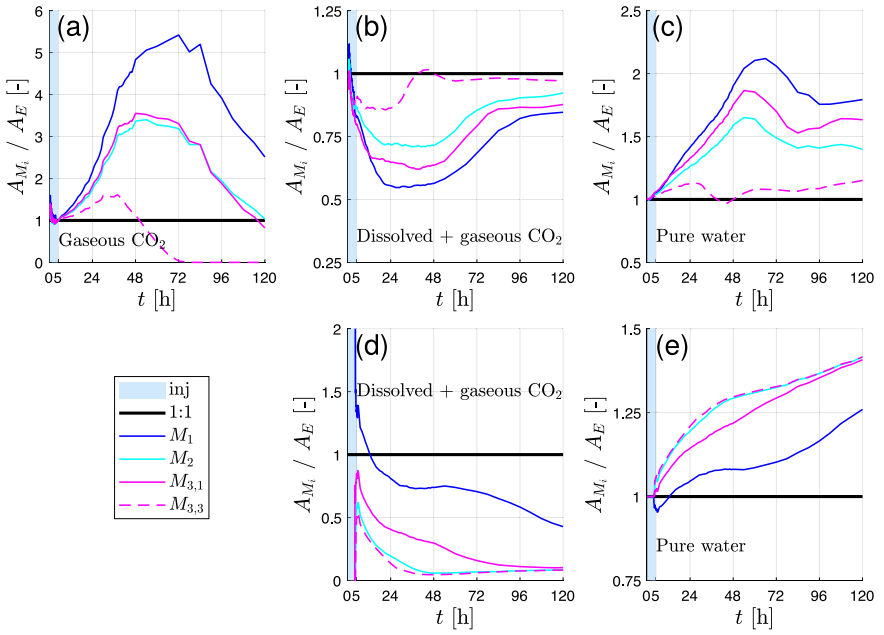


Fig. 24 Ratios between calibrated model (A_{M_i}) and experimental mean (A_E) areas occupied by each phase in case B1. Experimental mean was obtained from four experimental runs with identical protocol, while the results for Models 1–3 are for a single run with each model. For M_3, two cases are shown: $D = 10^{-9}$ m^2/s ($M_{3,1}$) and $D = 3 \times 10^{-9}$ m^2/s ($M_{3,3}$). Top row shows Box A, and bottom row shows Box B. Ratios for gaseous CO_2 in Box B are not computed because experimental values are 0. **a** Gaseous CO_2. **b**, **d** Dissolved CO_2 (includes area with gaseous CO_2). **c**, **e** Pure water

are indicative of high flow rates (R_e close to 1), relatively strong capillary forces, compared to viscous forces ($C_a \sim O(10^{-6})$ or smaller), and appreciable buoyancy. We identify that high flow rates and sudden appearance/disappearance of fluid phases challenge the nonlinear solver during injection. Buoyancy and capillarity forces, which are active throughout the simulation, also impact convergence, but it is not straightforward to identify if one exerts a greater control on the number of iterations. After injection, we observe difficulties between $t \approx 315$ and 1440 min in M_1, and $t \approx 720$ and 1440 in $M_{3,3}$. Our analysis does not reveal why, so this is a topic that warrants further study.

Appendix C: Comparison of Simulation Results with Multiple Grid Resolutions

This section provides two comparisons of concentration maps obtained with Model 3 after the calibration presented in Sect. 4.2:

Received by OCD: 6/29/2026

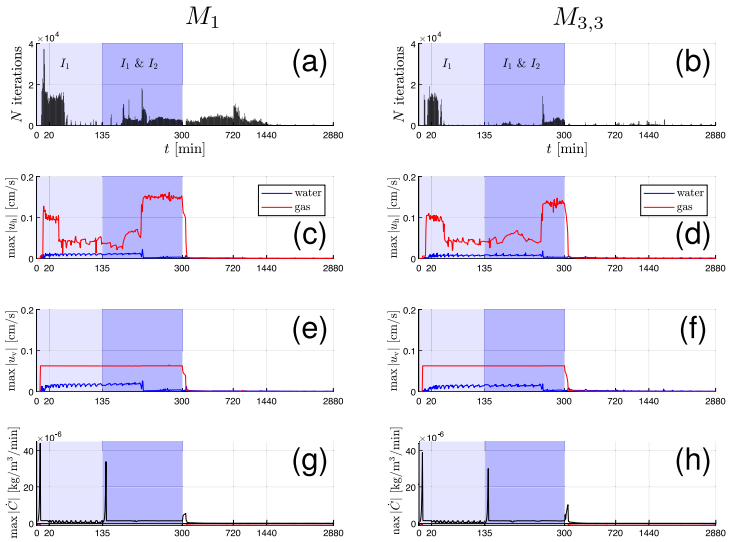


Fig. 25 Number of iterations and maximum values in the simulation domain for various quantities, as a function of time. Results are provided for M_1 (left column) and $M_{3,3}$ (right column). **a,b** Number of nonlinear solver iterations. **c,d** Horizontal Darcy velocity. **e,f** Vertical Darcy velocity. **g,h** Concentration rate ($\dot{C}$)

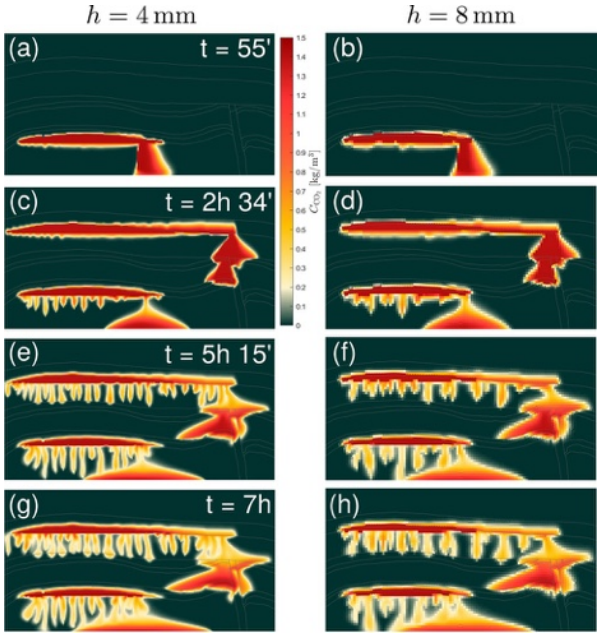


Fig. 26 Concentration maps from our simulations of Experiment A1 with Model 3. Results with two grids are shown: $h = 4$ mm (**a**, **c**, **e**, **g**) and $h = 8$ mm (**b**, **d**, **f**, **h**)

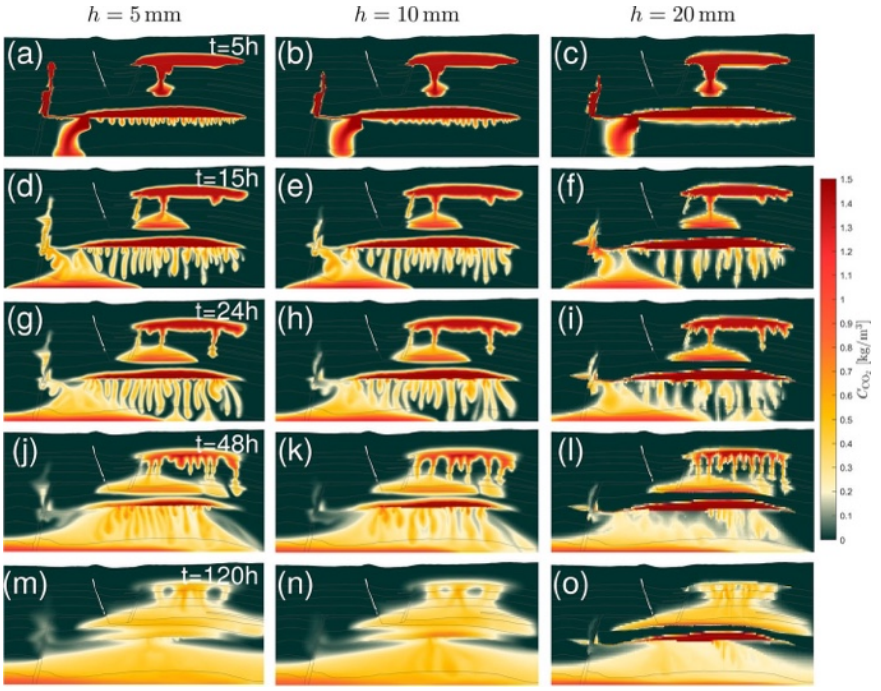


Fig. 27 Concentration maps from simulations of Experiment B1 with Model 3. Results with three grids are shown: $h = 5$ mm (**a**, **d**, **g**, **j**, **m**), $h = 10$ mm (**b**, **e**, **h**, **k**, **n**) and $h = 20$ mm (**c**, **f**, **i**, **l**, **o**)

1. For Experiment A1, we compare two grid sizes: $h = 4$ mm, as shown in the paper, and a coarser grid with $h = 8$ mm (Fig. 26).
2. For Experiment B1, we compare three grid sizes: $h = 5$ mm, used throughout the paper, and two coarser grids with $h = 10$ mm and $h = 20$ mm, respectively (Fig. 27). Note that, in the three simulations in Fig. 27, a total of 8.13 g of CO_2 was injected; this is slightly smaller than the 8.55 g actually injected in the experiment and in our simulations in the rest of the paper.

It can be seen that, for the calibrated parameter set (Table 4), the coarser models maintain a general agreement with the finer ones (and the experimental solution). However, some differences are clear even in this qualitative comparison, including (1) smaller extent of the CO_2 plume, (2) lower dissolution, (3) lower number of fingers and finger widths, and (4) different CO_2-rich finger sinking speed. Therefore, the calibration process is somewhat cell-size dependent, which has implications for applying history matched models from e.g., pilot tests to field-scale CO_2 storage projects.

Acknowledgements LS gratefully acknowledges laboratory support provided by UiB Engineer Emil Bang Larsen and image processing support provided by UiB PhD student Benyamine Benali. LS and RJ are grateful to Olav Møyner and the MRST team at SINTEF for their guidance to implement new functionality and continuous support with the MATLAB Reservoir Simulation Toolbox. A special thanks goes to Robert Gawthorpe, Atle Rotevatn and Casey Nixon for helpful comments on the geology of North Sea reservoirs, which were key to build the geometry in Tank 2, as well as to Bernd Flemisch for sharing scripts to calculate and visualize Wasserstein distances. The authors thank the three anonymous reviewers for thoughtful and

constructive reviews, which helped improve this manuscript significantly. The authors also acknowledge support by the following organizations (refer to 'Funding' below for details): ExxonMobil, "la Caixa" Foundation, Research Council of Norway (RCN), Akademia.

Author Contributions JMN, MF and RJ designed the study and acquired the funding. JMN, MF and KE conceptualized, designed and built the FluidFlower rigs. MH, KE and MF conducted the ex-situ sand property measurements. LS designed the experiments in Tank 1. JMN, MF, MH and KE designed the experiments in Tank 2. MH, KE, LS and MF conducted the experiments. LS developed the simulation models and conducted the simulations. LS, JMN and RJ performed the simulation analysis. LS wrote the paper, with inputs from all authors.

Funding Information This work was supported by ExxonMobil through the project "Modeling and Mitigation of Induced Seismicity and Fault Leakage during CO_2 storage". LS gratefully acknowledges the support of a fellowship from "la Caixa" Foundation (ID 100010434). The fellowship code is LCF/BQ/EU21/11890139. MH is funded by the Research Council of Norway (RCN) Project No. 280341. KE, MH, JMN and MF are partly funded by the Centre for Sustainable Subsurface Resources, RCN Project No. 331841. The work of JMN and MF is funded in part through the Akademia project "FracFlow".

Data Availability The dataset for Experiment B1 and data analysis scripts can be obtained from https://github.com/fluidflower. The remaining experimental and simulation data are available from the corresponding authors on reasonable request.

Declarations

Conflict of interest The authors declare that they have no conflict of interest.

References

Aanonsen, S.I., Nœvdal, G., Oliver, D.S., Reynolds, A.C., Vallès, B.: The ensemble Kalman filter in reservoir engineering—a review. SPE J. **14**(03), 393–412 (2009). https://doi.org/10.2118/117274-PA

Aissaoui, A.: Etude théorique et expérimentale de l'hystérésis des pressions capillaries et des perméabilitiés relatives en vue du stockage souterrain de gaz. Ph. D. thesis, Ecole des Mines de Paris, Paris (1983)

Alghannam, M., Juanes, R.: Understanding rate effects in injection-induced earthquakes. Nat. Commun. **11**(1), 3053 (2020). https://doi.org/10.1038/s41467-020-16860-y

Askar, A.H., Illangasekare, T.H., Ilie, A.M.C.: Monitoring brine leakage from deep geologic formations storing carbon dioxide: design framework validation using intermediate-scale experiment. Water Resources Res. **57**(12), 2021WR031005 (2021). https://doi.org/10.1029/2021WR031005

Avansi, G.D., Maschio, C., Schiozer, D.J.: Simultaneous history-matching approach by use of reservoir-characterization and reservoir-simulation studies. SPE Reserv. Eval. Eng. **19**(04), 694–712 (2016). https://doi.org/10.2118/179740-PA

Bachu, S., Gunter, W., Perkins, E.: Aquifer disposal of CO_2: hydrodynamic and mineral trapping. Energy Convers. Manag. **35**(4), 269–279 (1994). https://doi.org/10.1016/0196-8904(94)90060-4

Bear, J.: Dynamics of Fluids in Porous Media. Dover, Mineola (1972)

Bear, J.: Modeling Phenomena of Flow and Transport in Porous Media, vol. 31. Springer, Berlin (2018)

Beard, D., Weyl, P.: Influence of texture on porosity and permeability of unconsolidated sand. AAPG Bull. **57**(2), 349–369 (1973). https://doi.org/10.1306/819A4272-16C5-11D7-8645000102C1865D

Berge, R.L., Klemetsdal, Ø.S., Lie, K.A.: Unstructured Voronoi grids conforming to lower dimensional objects. Comput. Geosci. **23**, 169–188 (2019). https://doi.org/10.1007/s10596-018-9790-0

Berge, R.L., Klemetsdal, Ø.S., Skaflestad, B., Lie, K.A.: The UPR module. https://github.com/rbe051/UPR (2021)

Brock, D., Orr, F.: Flow visualization of viscous fingering in heterogeneous porous media. SPE Annual Technical Conference and Exhibition (SPE-22614-MS) https://doi.org/10.2118/22614-MS 1991

Brooks, R.H., Corey, A.T.: Hydraulic properties of porous media. Technical report, Colorado State University, Fort Collins, CO (1964)

Bryant, S.L., Lakshminarasimhan, S., Pope, G.A.: Buoyancy-dominated multiphase flow and its effect on geological sequestration of CO_2. SPE J. **13**(04), 447–454 (2008). https://doi.org/10.2118/99938-PA

Burnside, N., Naylor, M.: Review and implications of relative permeability of CO_2/brine systems and residual trapping of CO_2. Int. J. Greenh. Gas Control **23**, 1–11 (2014). https://doi.org/10.1016/j.ijggc.2014.01.013

Caine, J.S., Evans, J.P., Forster, C.B.: Fault zone architecture and permeability structure. Geology **24**(11), 1025–1028 (1996). https://doi.org/10.1130/0091-7613(1996)024<1025:FZAAPS>2.3.CO;2

Cappa, F., Rutqvist, J.: Impact of CO_2 geological sequestration on the nucleation of earthquakes. Geophys. Res. Lett. **38**(17), L17313 (2011). https://doi.org/10.1029/2011GL048487

Celia, M.A.: The role of subsurface engineering in the net-zero energy transition. In: IOP Conference Series: Earth and Environmental Science, vol. 861, IOP Publishing (2021)

Childs, C., Manzocchi, T., Walsh, J.J., Bonson, C.G., Nicol, A., Schöpfer, M.P.: A geometric model of fault zone and fault rock thickness variations. J. Struct. Geol. **31**(2), 117–127 (2009). https://doi.org/10.1016/j.jsg.2008.08.009

Cinar, Y., Jessen, K., Berenblyum, R., Juanes, R., Orr, F.M.: An experimental and numerical investigation of crossflow effects in two-phase displacements. SPE J. **11**(02), 216–226 (2006). https://doi.org/10.2118/90568-PA

Corey, A.T.: The interrelation between gas and oil relative permeabilities. Prod. Mon. **19**, 38–41 (1954)

Demidov, D., Rossi, R.: Subdomain deflation combined with local AMG: a case study using AMGCL library. arXiv preprint. https://doi.org/10.48550/arXiv.1710.03940 (2018)

DiCarlo, D.A., Sahni, A., Blunt, M.J.: Three-phase relative permeability of water-wet, oil-wet, and mixed-wet sandpacks. SPE J. **5**(01), 82–91 (2000). https://doi.org/10.2118/60767-PA

Doughty, C., Oldenburg, C.M.: CO_2 plume evolution in a depleted natural gas reservoir: modeling of conformance uncertainty reduction over time. Int. J. Greenh. Gas Control **97**, 103026 (2020). https://doi.org/10.1016/j.ijggc.2020.103026

Duan, Z., Sun, R.: An improved model calculating CO_2 solubility in pure water and aqueous NaCl solutions from 273 to 533 K and from 0 to 2000 bar. Chem. Geol. **193**(3–4), 257–271 (2003). https://doi.org/10.1016/S0009-2541(02)00263-2

Eikehaug, K., Haugen, M., Folkvord, O., Benali, B., Larsen, E.L., Tinkova, A., Rotevatn, A., Nordbotten, J.M., Fernø, M.: Engineering meter-scale porous media flow experiments for quantitative studies of geological carbon sequestration. Transp. Porous Media (this issue). Preprint available on arXiv through https://doi.org/10.48550/arXiv.2301.09304 (2023)

Ellsworth, W.L.: Injection-induced earthquakes. Science **341**(6142), 1225942 (2013). https://doi.org/10.1126/science.1225942

Ennis-King, J., Paterson, L.: Role of convective mixing in the long-term storage of carbon dioxide in deep saline formations. SPE J. **10**(03), 349–356 (2005). https://doi.org/10.2118/84344-PA

European Academies Science Advisory Council (EASAC). Policy Report 35, 2018. Negative emission technologies: what role in meeting Paris Agreement targets? https://easac.eu/publications/details/easac_net/. Accessed on 20 Jan 2023

Fernández-García, D., Illangasekare, T.H., Rajaram, H.: Conservative and sorptive forced-gradient and uniform flow tracer tests in a three-dimensional laboratory test aquifer. Water Resour. Res. **40**(10), W10103 (2004). https://doi.org/10.1029/2004WR003112

Fernø, M., Haugen, M., Eikehaug, K., Folkvord, O., Benali, B., Both, J.W., Storvik, E., Nixon, C.W., Gawthorpe, R.L., Nordbotten, J.M.: Room-scale CO_2 injections in a physical reservoir model with faults. Transp. Porous Media (this issue). Preprint available on arXiv through https://doi.org/10.48550/arXiv.2301.06397 (2023)

Fisher, Q., Jolley, S.: Treatment of faults in production simulation models. Geol. Soc. Lond. Spec. Publ. **292**, 219–233 (2007). https://doi.org/10.1144/SP292.13

Flemisch, B., Nordbotten, J.M., Fernø, M., Juanes, R., Class, H., Delshad, M., Doster, F., Ennis-King, J., Franc, J., Geiger, S., Gläser, D., Green, C., Gunning, J., Hajibeygi, H., Jackson, S.J., Jammoul, M., Karra, S., Li, J., Matthäi, S.K., Miller, T., Shao, Q., Spurin, C., Stauffer, P., Tchelepi, H., Tian, X., Viswanathan, H., Voskov, D., Wang, Y., Wapperom, M., Wheeler, M.F., Wilkins, A., Youssef, A.A., Zhang, Z.: The FluidFlower international benchmark study: process, modeling results, and comparison to experimental data. Transp. Porous Media (this issue). Preprint available on arXiv through https://doi.org/10.48550/arXiv.2302.10986 (2023)

Garabedian, S.P., LeBlanc, D.R., Gelhar, L.W., Celia, M.A.: Large-scale natural gradient tracer test in sand and gravel, Cape Cod, Massachusetts: 2. Analysis of spatial moments for a nonreactive tracer. Water Resources Res. **27**(5), 911–924 (1991). https://doi.org/10.1029/91WR00242

Gaucher, D., Lindley, D.: Waterflood performance in a stratified, five-spot reservoir—a scaled-model study. Trans. AIME **219**(01), 208–215 (1960). https://doi.org/10.2118/1311-G

Gelhar, L.W., Welty, C., Rehfeldt, K.R.: A critical review of data on field-scale dispersion in aquifers. Water Resour. Res. **28**(7), 1955–1974 (1992). https://doi.org/10.1029/92WR00607

Gosselin, O., Aanonsen, S., Aavatsmark, I., Cominelli, A., Gonard, R., Kolasinski, M., Ferdinandi, F., Kovacic, L., Neylon, K.: History matching using time-lapse seismic (HUTS). In: SPE Annual Technical Conference and Exhibition (SPE 84464). https://doi.org/10.2118/84464-MS (2003)

Hager, B.H., Dieterich, J., Frohlich, C., Juanes, R., Mantica, S., Shaw, J.H., Bottazzi, F., Caresani, F., Castineira, D., Cominelli, A., Meda, M., Osculati, L., Petroselli, S., Plesch, A.: A process-based approach to understanding and managing triggered seismicity. Nature **595**(7869), 684–689 (2021). https://doi.org/10.1038/s41586-021-03668-z

Hassanzadeh, H., Pooladi-Darvish, M., Elsharkawy, A.M., Keith, D.W., Leonenko, Y.: Predicting PVT data for CO_2-brine mixtures for black-oil simulation of CO_2 geological storage. Int. J. Greenh. Gas Control **2**(1), 65–77 (2008). https://doi.org/10.1016/S1750-5836(07)00010-2

Haugen, M., Saló-Salgado, L., Eikehaug, K., Benali, B., Both, J.W., Storvik, E., Folkvord, O., Juanes, R., Nordbotten, J.M., Fernø, M.: Physical variability in meter-scale laboratory CO_2 injections in faulted geometries. Transp. Porous Media (this issue). Preprint available on arXiv through https://doi.org/10.48550/arXiv.2301.07347 (2023)

Heinemann, Z., Brand, C., Munka, M., Chen, Y.: Modeling reservoir geometry with irregular grids. SPE Reserv. Eng. **6**(2), 225–232 (1991). https://doi.org/10.2118/18412-PA

Hesse, M., Woods, A.: Buoyant dispersal of CO_2 during geological storage. Geophys. Res. Lett. **37**(1), L01403 (2010). https://doi.org/10.1029/2009GL041128

Hidalgo, J.J., Carrera, J.: Effect of dispersion on the onset of convection during CO_2 sequestration. J. Fluid Mech. **640**, 441–452 (2009). https://doi.org/10.1017/S0022112009991480

Hidalgo, J.J., Fe, J., Cueto-Felgueroso, L., Juanes, R.: Scaling of convective mixing in porous media. Phys. Rev. Lett. **109**(26), 264503 (2012). https://doi.org/10.1103/PhysRevLett.109.264503

Hommel, J., Coltman, E., Class, H.: Porosity–permeability relations for evolving pore space: a review with a focus on (bio-)geochemically altered porous media. Transp. Porous Media **124**(2), 589–629 (2018). https://doi.org/10.1007/s11242-018-1086-2

Ingram, G.M., Urai, J.L.: Top-seal leakage through faults and fractures: the role of Mudrock properties. Geol. Soc. Lond. Spec. Publ. **158**, 125–135 (1999). https://doi.org/10.1144/GSL.SP.1999.158.01.10

Intergovernmental Panel on Climate Change (IPCC): Climate change 2022: mitigation of climate change. In: Shukla, P.R., Skea, J., Slade, R., Al Khourdajie, A., van Diemen, R., McCollum, D., Pathak, M., Some, S., Vyas, P., Fradera, R., Belkacemi, M., Hasija, A., Lisboa, G., Luz, S., Malley, J. (eds.) Contribution of Working Group III to the Sixth Assessment Report of the IPCC. Cambridge University Press, Cambridge (2022). https://doi.org/10.1017/9781009157926

Jagalur-Mohan, J., Jha, B., Wang, Z., Juanes, R., Marzouk, Y.: Inferring fault frictional and reservoir hydraulic properties from injection-induced seismicity. Geophys. Res. Lett. **45**(3), 1313–1320 (2018). https://doi.org/10.1002/2017GL075925

Jin, L., Lu, H., Wen, G.: Fast uncertainty quantification of reservoir simulation with variational U-Net (2019) https://doi.org/10.48550/arXiv.1907.00718, arXiv:1907.00718

Juanes, R., Hager, B.H., Herzog, H.J.: No geologic evidence that seismicity causes fault leakage that would render large-scale carbon capture and storage unsuccessful. Proc. Natl. Acad. Sci. **109**(52), E3623–E3623 (2012). https://doi.org/10.1073/pnas.1215026109

Juanes, R., Spiteri, E., Orr, F., Jr., Blunt, M.: Impact of relative permeability hysteresis on geological CO_2 storage. Water Resour. Res. **42**(12), W12418 (2006). https://doi.org/10.1029/2005WR004806

Jung, N.H., Han, W.S., Watson, Z., Graham, J.P., Kim, K.Y.: Fault-controlled CO_2 leakage from natural reservoirs in the Colorado Plateau, East-Central Utah. Earth Planet. Sci. Lett. **403**, 358–367 (2014). https://doi.org/10.1016/j.epsl.2014.07.012

Kam, P., Nadeem, M., Novlesky, A., Kumar, A., Omatsone, E.N.: Reservoir characterization and history matching of the Horn River shale: an integrated geoscience and reservoir-simulation approach. J. Can. Pet. Technol. **54**(06), 475–488 (2015). https://doi.org/10.2118/171611-PA

Killough, J.E.: Reservoir simulation with history-dependent saturation functions. SPE J. **16**(01), 37–48 (1976). https://doi.org/10.2118/5106-PA

Kneafsey, T.J., Pruess, K.: Laboratory flow experiments for visualizing carbon dioxide-induced, density-driven brine convection. Transp. Porous Media **82**, 123–139 (2010). https://doi.org/10.1007/s11242-009-9482-2

Kovscek, A.R., Nordbotten, J.M., Ferno, M.A.: Scaling up FluidFlower results for carbon dioxide storage in geological media. Transport in Porous Media (this issue). Preprint available on arXiv through https://doi.org/10.48550/arXiv.2301.09853 (2023)

Krishnamurthy, P.G., DiCarlo, D., Meckel, T.: Geologic heterogeneity controls on trapping and migration of CO_2. Geophys. Res. Lett. **49**(16), e2022GL099104 (2022). https://doi.org/10.1029/2022GL099104

Krishnamurthy, P.G., Meckel, T.A., DiCarlo, D.: Mimicking geologic depositional fabrics for multiphase flow experiments. Water Resour. Res. **55**(11), 9623–9638 (2019). https://doi.org/10.1029/2019WR025664

Krogstad, S., Lie, K., Møyner, O., Nilsen, H.M., Raynaud, X., Skaflestad, B.: MRST-AD—an open-source framework for rapid prototyping and evaluation of reservoir simulation problems. In: SPE Reservoir Simulation Conference, pp. 1–20. https://doi.org/SPE-173317-MS (2015)
Land, C.S.: Calculation of imbibition relative permeability for two-and three-phase flow from rock properties. Soc. Petrol. Eng. J. **8**(02), 149–156 (1968). https://doi.org/10.2118/1942-PA
Landa-Marbán, D., Sandve, T.H., Both, J.W., Nordbotten, J.M., Gasda, S.E.: Performance of an open-source image-based history matching framework for CO_2 storage (2023, forthcoming)
Lassen, R.N., Plampin, M.R., Sakaki, T., Illangasekare, T.H., Gudbjerg, J., Sonnenborg, T.O., Jensen, K.H.: Effects of geologic heterogeneity on migration of gaseous CO_2 using laboratory and modeling investigations. Int. J. Greenh. Gas Control **43**, 213–224 (2015). https://doi.org/10.1016/j.ijggc.2015.10.015
Lenhard, R., Oostrom, M., Simmons, C., White, M.: Investigation of density-dependent gas advection of trichloroethylene: experiment and a model validation exercise. J. Contam. Hydrol. **19**(1), 47–67 (1995). https://doi.org/10.1016/0169-7722(94)00055-M
Leverett, M.C.: Capillary behavior in porous solids. Trans. AIME **142**(01), 152–169 (1941). https://doi.org/10.2118/941152-G
Lie, K.A.: An Introduction to Reservoir Simulation Using MATLAB/GNU Octave: User Guide for the MATLAB Reservoir Simulation Toolbox (MRST). Cambridge University Press, Cambridge (2019)
Lie, K.A., Møyner, O. (eds.): Advanced Modeling with the MATLAB Reservoir Simulation Toolbox. Cambridge University Press, Cambridge (2021)
Lin, L.I-K.: A concordance correlation coefficient to evaluate reproducibility. Biometrics **45**(1), 255–268 (1989). https://doi.org/10.2307/2532051
Liu, Y., Durlofsky, L.J.: Multilevel strategies and geological parameterizations for history matching complex reservoir models. SPE J. **25**(01), 081–104 (2020). https://doi.org/10.2118/193895-PA
MacMinn, C.W., Juanes, R.: Buoyant currents arrested by convective dissolution. Geophys. Res. Lett. **40**(10), 2017–2022 (2013). https://doi.org/10.1002/grl.50473
Marcucci, A., Kypreos, S., Panos, E.: The road to achieving the long-term Paris targets: energy transition and the role of direct air capture. Clim. Change **144**(2), 181–193 (2017). https://doi.org/10.1007/s10584-017-2051-8
Myers, R.D., Allgood, A., Hjellbakk, A., Vrolijk, P., Briedis, N.: Testing fault transmissibility predictions in a structurally dominated reservoir: Ringhorne field, Norway. Geol. Soc. Lond. **292**(1), 271–294 (2007). https://doi.org/10.1144/SP292.16
Neufeld, J.A., Hesse, M.A., Riaz, A., Hallworth, M.A., Tchelepi, H.A., Huppert, H.E.: Convective dissolution of carbon dioxide in saline aquifers. Geophys. Res. Lett. **37**(22), L22404 (2010). https://doi.org/10.1029/2010GL044728
Ni, H., Bakhshian, S., Meckel, T.: Effects of grain size and small-scale bedform architecture on CO_2 saturation from buoyancy-driven flow. Sci. Rep. **13**, 2474 (2023). https://doi.org/10.1038/s41598-023-29360-y
Nordbotten, J.M., Benali, B., Both, J.W., Brattekås, B., Storvik, E., Fernø, M.: DarSIA: an open-source python toolbox for two-scale image processing for porous media. Transp. Porous Media (this issue). Preprint available on arXiv through https://doi.org/10.48550/arXiv.2301.05455 (2023)
Nordbotten, J.M., Celia, M.A.: Geological Storage of CO_2: Modeling Approaches for Large-scale Simulation, p. 242. Wiley, Hoboken (2012)
Nordbotten, J.M., Fernø, M., Flemisch, B., Juanes, R., Jørgensen, M.: Final benchmark description. FluidFlower Int. Benchmark Study (2022). https://doi.org/10.5281/zenodo.6807102
Nordbotten, J.M., Flemisch, B., Gasda, S.E., Nilsen, H., Fan, Y., Pickup, G.E., Wiese, B., Celia, M.A., Dahle, H.K., Eigestad, G.T., Pruess, K.: Uncertainties in practical simulation of CO_2 storage. Int. J. Greenh. Gas Control **9**, 234–242 (2012). https://doi.org/10.1016/j.ijggc.2012.03.007
Oldenburg, C.M.: Are we all in concordance with the meaning of the word conformance, and is our definition in conformity with standard definitions? Greenh. Gases Sci. Technol. **8**(2), 210–214 (2018). https://doi.org/10.1002/ghg.1773
Oliver, D.S., Chen, Y.: Recent progress on reservoir history matching: a review. Comput. Geosci. **15**(1), 185–221 (2011). https://doi.org/10.1007/s10596-010-9194-2
Panaretos, V.M., Zemel, Y.: Statistical aspects of Wasserstein distances. Ann. Rev. Stat. Appl. **6**, 405–431 (2019). https://doi.org/10.1146/annurev-statistics-030718-104938
Pentland, C.H., Itsekiri, E., Al Mansoori, S.K., Iglauer, S., Bijeljic, B., Blunt, M.J.: Measurement of nonwetting-phase trapping in sandpacks. SPE J. **15**(02), 274–281 (2010). https://doi.org/10.2118/115697-PA
Plug, W.J., Bruining, J.: Capillary pressure for the sand-CO_2-water system under various pressure conditions, application to CO_2 sequestration. Adv. Water Resources **30**(11), 2339–2353 (2007). https://doi.org/10.1016/j.advwatres.2007.05.010

Rezk, M.G., Foroozesh, J., Abdulrahman, A., Gholinezhad, J.: CO_2 diffusion and dispersion in porous media: review of advances in experimental measurements and mathematical models. Energy Fuels **36**(1), 133–155 (2022). https://doi.org/10.1021/acs.energyfuels.1c03552

Riaz, A., Hesse, M., Tchelepi, H., Orr, F.: Onset of convection in a gravitationally unstable diffusive boundary layer in porous media. J. Fluid Mech. **548**, 87–111 (2006). https://doi.org/10.1017/S0022112005007494

Riaz, A., Pankiewitz, C., Meiburg, E.: Linear stability of radial displacements in porous media: influence of velocity-induced dispersion and concentration-dependent diffusion. Phys. Fluids **16**(10), 3592–3598 (2004). https://doi.org/10.1063/1.1775431

Saadatpoor, E., Bryant, S.L., Sepehrnoori, K.: New trapping mechanism in carbon sequestration. Transp. Porous Media **82**(1), 3–17 (2010). https://doi.org/10.1007/s11242-009-9446-6

Saló-Salgado, L., Davis, J.S., Juanes, R.: Fault permeability from stochastic modeling of clay smears. Geology **51**(1), 91–95 (2023). https://doi.org/10.1130/G50739.1

Saló-Salgado, L., Møyner, O., Lie, K.A., Juanes, R.: Three-dimensional simulation of geologic carbon sequestration using MRST-ad-blackoil (2023, forthcoming)

Santoso, R.K., He, X., Alsinan, M., Kwak, H., Hoteit, H.: Bayesian long-short term memory for history matching in reservoir simulations. In: SPE Reservoir Simulation Conference (SPE-203976-MS). https://doi.org/10.2118/203976-MS (2021)

Schlumberger: ECLIPSE Technical description (2014.1 ed.). Schlumberger Ltd (2014)

Schulz, R., Ray, N., Zech, S., Rupp, A., Knabner, P.: Beyond Kozeny–Carman: predicting the permeability in porous media. Transp. Porous Media **130**(2), 487–512 (2019). https://doi.org/10.1007/s11242-019-01321-y

Schulze-Makuch, D.: Longitudinal dispersivity data and implications for scaling behavior. Groundwater **43**(3), 443–456 (2005). https://doi.org/10.1111/j.1745-6584.2005.0051.x

Silliman, S., Simpson, E.: Laboratory evidence of the scale effect in dispersion of solutes in porous media. Water Resour. Res. **23**(8), 1667–1673 (1987). https://doi.org/10.1029/WR023i008p01667

Smits, K.M., Sakaki, T., Limsuwat, A., Illangasekare, T.H.: Thermal conductivity of sands under varying moisture and porosity in drainage-wetting cycles. Vadose Zone J. **9**(1), 172–180 (2010). https://doi.org/10.2136/vzj2009.0095

Spiteri, E.J., Juanes, R., Blunt, M.J., Orr, F.M.: A new model of trapping and relative permeability hysteresis for all wettability characteristics. SPE J. **13**(03), 277–288 (2008). https://doi.org/10.2118/96448-PA

Spycher, N., Pruess, K.: CO_2-H_2O mixtures in the geological sequestration of CO_2. II. Partitioning in chloride brines at 12–100 C and up to 600 bar. Geochimica et Cosmochimica Acta **69**(13), 3309–3320 (2005). https://doi.org/10.1016/j.gca.2005.01.015

Spycher, N., Pruess, K., Ennis-King, J.: CO_2-H_2O mixtures in the geological sequestration of CO_2. I. Assessment and calculation of mutual solubilities from 12 to 100 C and up to 600 bar. Geochimica et Cosmochimica Acta **67**(16), 3015–3031 (2003). https://doi.org/10.1016/S0016-7037(03)00273-4

Szulczewski, M., Hesse, M., Juanes, R.: Carbon dioxide dissolution in structural and stratigraphic traps. J. Fluid Mech. **736**, 287–315 (2013). https://doi.org/10.1017/jfm.2013.511

Timur, A.: An investigation of permeability, porosity, & residual water saturation relationships for sandstone reservoirs. Log Anal. **9**(04), 8–17 (1968)

Trevisan, L., Cihan, A., Fagerlund, F., Agartan, E., Mori, H., Birkholzer, J.T., Zhou, Q., Illangasekare, T.H.: Investigation of mechanisms of supercritical CO_2 trapping in deep saline reservoirs using surrogate fluids at ambient laboratory conditions. Int. J. Greenh. Gas Control **29**, 35–49 (2014). https://doi.org/10.1016/j.ijggc.2014.07.012

Trevisan, L., Pini, R., Cihan, A., Birkholzer, J.T., Zhou, Q., González-Nicolás, A., Illangasekare, T.H.: Imaging and quantification of spreading and trapping of carbon dioxide in saline aquifers using meter-scale laboratory experiments. Water Resour. Res. **53**(1), 485–502 (2017). https://doi.org/10.1002/2016WR019749

Verdon, J.P., Kendall, J.M., Stork, A.L., Chadwick, R.A., White, D.J., Bissell, R.C.: Comparison of geomechanical deformation induced by megatonne-scale CO_2 storage at Sleipner, Weyburn, and In Salah. Proc. Natl. Acad. Sci. **110**(30), E2762–E2771 (2013). https://doi.org/10.1073/pnas.1302156110

Vilarrasa, V., Carrera, J.: Geologic carbon storage is unlikely to trigger large earthquakes and reactivate faults through which CO_2 could leak. Proc. Natl. Acad. Sci. **112**(19), 5938–5943 (2015). https://doi.org/10.1073/pnas.1413284112

Wang, S., Lee, M., Park, M.K., Kim, J.M.: Box experiments on monitoring the CO_2 migration in a homogeneous medium using electrical resistivity survey. Geosci. J. **14**, 77–85 (2010). https://doi.org/10.1007/s12303-010-0009-1

Weir, G.J., White, S.P., Kissling, W.M.: Reservoir storage and containment of greenhouse gases. Transp. Porous Media **23**, 37–60 (1996). https://doi.org/10.1007/BF00145265

Wood, B.D., Dawson, C.N., Szecsody, J.E., Streile, G.P.: Modeling contaminant transport and biodegradation in a layered porous media system. Water Resour. Res. **30**(6), 1833–1845 (1994). https://doi.org/10.1029/94WR00434

Zoback, M.D., Gorelick, S.M.: Earthquake triggering and large-scale geologic storage of carbon dioxide. Proc. Natl. Acad. Sci. **109**(26), 10164–10168 (2012). https://doi.org/10.1073/pnas.1202473109

Publisher's Note Springer Nature remains neutral with regard to jurisdictional claims in published maps and institutional affiliations.

Springer Nature or its licensor (e.g. a society or other partner) holds exclusive rights to this article under a publishing agreement with the author(s) or other rightsholder(s); author self-archiving of the accepted manuscript version of this article is solely governed by the terms of such publishing agreement and applicable law.

Authors and Affiliations

Lluís Saló-Salgado[1,2] · Malin Haugen[3] · Kristoffer Eikehaug[3] · Martin Fernø[3,5] · Jan M. Nordbotten[4,5] · Ruben Juanes[1,2]

✉ Martin Fernø
Martin.Ferno@uib.no

✉ Jan M. Nordbotten
Jan.Nordbotten@uib.no

✉ Ruben Juanes
juanes@mit.edu

Lluís Saló-Salgado
lsalo@mit.edu

Malin Haugen
Malin.Haugen@uib.no

Kristoffer Eikehaug
Kristoffer.Eikehaug@uib.no

[1] Department of Civil and Environmental Engineering, Massachusetts Institute of Technology, Cambridge 02139, MA, USA

[2] Earth Resources Laboratory, Department of Earth, Atmospheric and Planetary Sciences, Massachusetts Institute of Technology, Cambridge 02139, MA, USA

[3] Department of Physics and Technology, University of Bergen, 5020 Bergen, Norway

[4] Department of Mathematics, Center for Modeling of Coupled Subsurface Dynamics, University of Bergen, 5020 Bergen, Norway

[5] Norwegian Research Center, Postboks 22 Nygårdstangen, 5020 Bergen, Norway

EXHIBIT 18

ENERGYWIRE

Carbon storage projects hit a hurdle: Corroding steel

EPA has concluded that dozens of planned projects contain dangerous design flaws — a discovery that may slow the rollout of a technology central to the Biden administration's plans to confront climate change.

BY: **ANNIE SNIDER**, **BEN LEFEBVRE** | 10/09/2024 06:35 AM EDT | UPDATED 10/09/2024 03:28 PM EDT



Carbon capture and sequestration technology is a crucial component of President Joe Biden's plans to sharply curb emissions of greenhouse gases.| John Minchillo/AP

ENERGYWIRE | A leak at the country's first commercial carbon dioxide sequestration project was likely caused by corrosion of the steel used in the well, a finding by federal regulators that poses a significant risk to dozens other projects around the country planning to use the same type of metal.

The steel, 13 Chrome, has been used for decades in oil and gas wells, but it appears to be vulnerable to corrosion when exposed to the liquids in carbon sequestration wells. Using an alternate material would likely be more expensive and could delay many of the projects that the agricultural and energy industries are hoping to deploy to access the federal tax credits and address the pollution driving climate change.

Carbon sequestration technology, which typically injects climate-warming carbon dioxide into deep underground saline aquifers, is a nascent technique that the Biden administration has hoped will offer polluting industries a viable path to reducing their impact on the climate. The 2022 Inflation Reduction Act includes billions of dollars in incentives for carbon capture and sequestration as part of its effort to cut greenhouse gas emissions sharply.

Both EPA and the well's owner, Archer-Daniels-Midland, have pointed to the corrosion of the 13 Chrome stainless steel used at the Decatur, Illinois, facility for a leak in a monitoring well that allowed liquid carbon dioxide to escape from the containment reservoir. The company reported a second leak on a separate monitoring well to EPA last week and is running additional tests to shed light on what might have caused it.

EPA moved quickly after being notified of the leak at the first monitoring well by ADM during a site inspection in June, issuing a warning less than two weeks later to the dozens of other companies with projects in the works that they should not rely on that steel. The 13 Chrome pipes have been a go-to material for the oil and gas industry for years and feature in plans for many of the new carbon capture projects pending before the EPA.

In a June 25 email obtained by POLITICO, EPA told companies that are currently applying to EPA for carbon injection well permits that 13 Chrome and a type of cement commonly used by the industry to secure those pipes "are *NOT suitable for construction of these wells in most instances*, particularly under potentially corrosive conditions when both water and CO_2 are present."

The discovery of the vulnerability has prompted EPA to reassess the 150 pending well permit applications that rely on those materials. And it is requiring companies to either switch to more corrosion-resistant materials or justify their use with rigorous technical analyses specific to the site. It is unclear how many of the pending applications at EPA included the use of 13 Chrome, but industry experts say it was likely a large proportion of them.

At least two facilities other than ADM's are currently operating carbon injection wells containing 13 Chrome: Six injection wells operated by Dakota Gasification Company and one injection well operated by Red Trail Energy, both in North Dakota.

The design problems threaten to further slow the rollout of the technology that is crucial to the Biden administration's plans to confront climate change, and that companies are eager to launch, thanks to lucrative tax incentives including in Democrats' Inflation Reduction Act. The mandate to move to stronger materials could also undercut the economics of some projects.

More fundamentally, the issues with the well pipes underscore how novel carbon capture and storage technology is, since emerging research is still reshaping assumptions about how to build projects that can safely and permanently store large quantities of the greenhouse gas more than a mile underground.

"My first reaction when I saw this notice from the EPA was I said, 'Oh my gosh, what about all the [carbon sequestration well] permits that are filed out there right now?' A lot of them are using 13 Chrome," said Jon Grimmer, president of carbon capture company Verde CO2 and a former petroleum engineer who started his career at Exxon Mobil. "The ripple effect here could be very big."

The problems with 13 Chrome stem from the chemical reaction that happens when carbon dioxide is pumped into a saline aquifer, as most carbon injection projects envision. That reaction produces a form of carbonic acid, an extremely corrosive liquid. Until recently there has been very little research into which metals could withstand it over time.

Verde had experienced the problems first hand last year when it tested 13 Chrome steel against the saline conditions in potential reservoirs around the Gulf of Mexico and other areas eyed for carbon sequestration.

After seeing the corrosion that occurred, "we had some real concerns," Grimmer said. The company decided to stockpile more corrosion-resistant Super 25 Chrome — a version of the steel that EPA recommended as an alternative in a June 25 email to companies planning to develop carbon sequestration wells.

But 25 Chrome is both significantly more expensive and harder to obtain than the more common 13 Chrome. A ton of 25 Chrome can cost $40 compared to $7 a ton for 13 Chrome, said Mike Matson, a Boston Consulting Group consultant who specializes in the carbon sequestration industry, citing a recent vendor price. Only one steel mill in the United States makes 25 Chrome, so the vast majority of the material is imported from mills in Asia, and lead times can be up to a year.

Bruce Craig, a metallurgist and corrosion expert who has been consulting for the oil and gas industry for decades through his firm MetCorr, said that while companies like Verde and some of the major oil companies opted to go with higher grade materials, many others plowed ahead with 13 Chrome for their proposed carbon storage projects, concluding it would be sufficient since early projects like the ADM site and a handful of others have used it.

Choosing materials requires an extremely site-specific calculation based on factors such as the impurities in the injection stream and the chemistry and temperature of the reservoir, Craig said. He has conducted laboratory tests and modeling for dozens of projects, he said.

“We haven’t found anywhere 13 Chrome would work. We just don’t think that’s an alloy that’s suitable,” Craig said.

He argued that project developers should run their own analysis rather than immediately reach for one of the other metals EPA recommended.

The EPA regulations governing carbon injection wells require that the materials last for the geologic lifetime of the project and be compatible with all fluids that they are likely to come into contact with, but they don’t spell out which specific materials meet that standard. The Department of Energy, which is preparing to spend more than $1 billion to help launch the initial carbon capture and sequestration projects, said it “is aware” of the memo the EPA sent to permit applicants regarding the corrosion issue. DOE is encouraging project developers to work with regulators to ensure they are using materials appropriate to the specific site conditions, a DOE spokesperson said in an email.

“All DOE projects must comply with all applicable laws and regulations, including the material requirements outlined in EPA-issued Class VI permits,” the spokesperson said, referring to the classification of the carbon sequestration wells. “Should EPA make any changes to the EPA Class VI regulations based on the recent communication, DOE would evaluate the impacts to the cost and timing of affected DOE projects at that time.”

Switching to higher grade materials will add time and expense to projects, but since well metals typically make up only a small slice of a project’s overall costs, it’s not likely to

affect their overall viability, industry experts said.

“Designing and building carbon sequestration projects is so hard in so many other places, that this is a thing I can solve,” said Andrew Duguid, an engineer who consults on carbon storage projects as vice president at Advanced Resources International, Inc.

In fact, the carbon capture industry overall might welcome the EPA’s direction to use the stronger steel because it will take away some guesswork over materials, said Boston Consulting’s Matson.

“There were a lot of things left to the operator’s discretion,” Matson said. “Statements like that were in some ways actually more frustrating to the industry. It's almost like, ‘just tell me what to do, I built this well, but let me know what spec to use.’”

EPA has also been in communication with the three states it has granted the authority to implement the carbon injection well program within their borders — North Dakota, Wyoming and Louisiana — about its concerns regarding 13 Chrome. It is unclear whether or how those states will incorporate EPA’s concerns into their work, though. None of the states’ regulatory offices responded directly to questions about how they would respond to the new 13 Chrome worries when asked.

“North Dakota intends to monitor the situation regarding the ADM site and evaluate the information/science behind the investigation of that incident as it becomes available,” a spokesperson for the North Dakota Department of Mineral Resources said by email.

All of the facilities have testing and monitoring plans in place, she said, and the state “intends to follow those testing and monitoring plans as approved until the science indicates changes are appropriate/necessary.”

A spokesperson for Basin Electric Power Cooperative, which runs the Dakota Gasification project, said the company has not been contacted by either EPA nor North Dakota regulators concerning the material.

CORRECTION: This article has been updated to correct the prices of 13 Chrome and 25 Chrome steel.

UP NEXT IN **THIS EDITION OF ENERGYWIRE**

Renewable energy boom puts tripling target within reach — IEA

BY SARA SCHONHARDT



YOUR ACCOUNT MANAGEMENT TEAM

Caitlin O Hare
Business Development Associate, Pro
cohare@politico.com

© 2024 POLITICO LLC

EXHIBIT 19

Received by OCD: 6/29/2026

Renewable and Sustainable Energy Reviews 179 (2023) 113292



Contents lists available at ScienceDirect

Renewable and Sustainable Energy Reviews

journal homepage: www.elsevier.com/locate/rser





Corrosion challenges in supercritical CO_2 transportation, storage, and utilization—a review

Haofei Sun [a], Haoxiang Wang [a], Yimin Zeng [b,**], Jing Liu [a,*]

[a] University of Alberta, Department of Chemical and Materials Engineering, Edmonton, Alberta, T6G 1H9, Canada
[b] Natural Resources Canada, CanmetMATERIALS, Hamilton, Ontario, L8P 0A5, Canada

ARTICLE INFO

Keywords:
Carbon capture, utilization, and storage (CCUS)
Supercritical CO_2 (s-CO_2)
Impurities
Steel corrosion
Corrosion kinetics

ABSTRACT

Research activities for Carbon capture, utilization, and storage (CCUS) have been rapidly growing due to climate goals and investment opportunities over the past few decades. This work provides an overview of recent corrosion research progress under supercritical CO_2 (s-CO_2) conditions, focusing on the wet s-CO_2 rich phase and s-CO_2-saturated aqueous phase with various impurities. Major corrosion damages on core components of supercritical CO_2 transportation, storage, and utilization systems occur in these environments. In various s-CO_2 environments, the structure and integrity of corrosion layers play a significant role in the overall corrosion kinetics. Moreover, the understanding of corrosion kinetics laws in s-CO_2 environments is currently inadequate, and there is considerable variability in reported corrosion outcomes. Most of the existing studies were conducted in static autoclaves with different exposure durations, making the obtained result lack consistency and high reliability for real operation consideration. In addition, significant knowledge gaps are identified and discussed. Potential research paths, including constructing novel iso-corrosion diagrams, understanding the protection and failure mechanisms of corrosion product layers, improving experimental methods, and developing standards and artificial intelligence approaches from both engineering application and fundamental scientific perspectives, are proposed. This review shall provide useful information and insights for the further development and deployment of the CCUS technology.

1. Introduction

The UN Paris Agreement has established an ambitious target of controlling the increase in the global average surface temperature to "well below" 2 °C relative to preindustrial levels [1]. To achieve the target, global CO_2 emissions (GCE) need to be cut by 50–85% compared to emission levels in 2000 [2,3]. Unfortunately, worldwide CO_2 emissions from the combustion of fossil fuels climbed up to an all-time high of 36.7 billion tons in 2019. According to a report by the Global Carbon Project (GCP), the world is projected to emit 36.4 $GtCO_2$ in 2021, only 0.8% below their pre-pandemic high in 2019 as shown in Fig. 1 [4]. Nevertheless, the recent 2021 World Energy Outlook projects that GCE could rebound past 2019 levels by 2022 or 2023 [5]. As GCE continue to rise, applicable measures and emission reduction technologies are in critical demand. Furthermore, the adoption of economy-wide decarbonization targets for 2050 is stimulating greater carbon capture, utilization, and storage (CCUS) project diversity for industrial applications. One representative pathway is the CO_2-enhanced oil recovery (EOR) combined with CCUS.

The CCUS chain has been applied in EOR for many years, but its application in climate change mitigation has only been seriously considered recently [6–8]. The general process of s-CO_2 transportation, storage and utilization systems is to collect CO_2 from large industrial emitters, transport it under supercritical fluid (s-CO_2), and re-use it for specific field EOR operations. Although leading innovators focus on how to cost-effectively capture CO_2 and design additional applications for CO_2, one cannot ignore the obvious: captured CO_2 is a wasted resource if it cannot be safely and efficiently transported to a storage facility or end-use site. Pipeline transportation of s-CO_2 is recognized as the most efficient and economically feasible method, and has received extensive attention from regulators, policymakers, industries, and researchers. Bonham et al. reviewed regulatory progress, challenges, and key lessons learned from CCUS case studies across Australia, Canada, Europe, and the US [9]. Issues have been identified to exist in relation to CO_2 pipeline

* Corresponding author.
** Corresponding author.
E-mail addresses: Yimin.Zeng@nrcan-rncan.gc.ca (Y. Zeng), jing.liu.arrow@ualberta.ca (J. Liu).

https://doi.org/10.1016/j.rser.2023.113292
Received 14 September 2022; Received in revised form 27 March 2023; Accepted 4 April 2023
Available online 14 April 2023
1364-0321/© 2023 Elsevier Ltd. All rights reserved.

Received by OCD: 6/29/2026

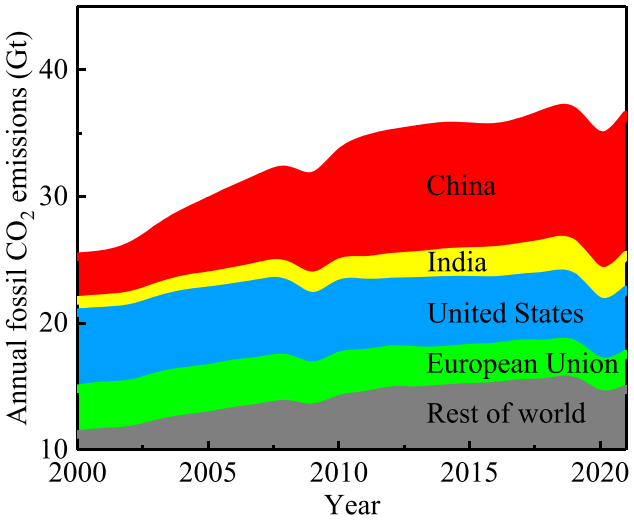


Fig. 1. Global CO_2 emissions from fossil fuels by regions, 2000–2021 [4].

safety regulations and standards [9–15]. CCUS projects developing a transport permit must work closely with regulators to establish appropriate standards. Over the past decades, there have been some significant legal and regulatory developments. For example, in Saskatchewan, Canada, amendments to 'The Oil and Gas Conservation Act' and 'The Pipelines Act' were instated in 2011 and 2012 such that CO_2 injection and storage could be regulated [9]. Two main regulatory considerations for s-CO_2 pipelines and EOR systems are the quality of the CO_2 stream to be transported and the safety risk assessment [10,11]. In each consideration, corrosion is a challenging safety issue in the whole CCUS chain, especially if water is presented in the s-CO_2 stream and steel infrastructure is used.

Steels are the primary materials of construction (MOC) in s-CO_2 transportation, storage and utilization systems and are susceptible to corrosion in s-CO_2 environments due to the presence of impurities (H_2O, O_2, SO_x, H_2S, and NO_x) during transportation and aggressive agents (Cl^-, Br^-, and S^{2-}, *etc*) in EOR environments [3,16]. Several review publications have addressed the corrosion issues under s–CO_2–EOR conditions [17–22]. Sim et al. presented three potential protection strategies, including relevant corrosion inhibitors, corrosion-resistant alloys (CRAs) for s-CO_2 transport pipeline, and the role and physical properties of a protective iron carbonate ($FeCO_3$) layer to mitigate the corrosion damage for reliable and cost-effective transportation [18]. Barker et al. presented a detailed review of CO_2 transmission pipeline incidents (e.g., 74 incidents in the US from 1990 to 2013), industrial experience in handling CO_2 and pipeline incidents, and early corrosion studies in s-CO_2 with impurities [19]. They also discussed the effects of impurities on the critical properties and phase envelope of s-CO_2, as well as the maximum water solubility in s-CO_2. It is worth noting in the case of EOR that there is an economic incentive to reduce certain corrosive impurities down to very low levels to enable optimum s-CO_2 transportation and oil recovery while preventing adverse reactions with hydrocarbons in the reservoir and maintaining the minimum miscibility pressure. Xiang et al. reviewed the existing open literatures, up until 2016, regarding the corrosion of pipeline steel in the CO_2-rich phase, key operating parameters (e.g., impurities, pressure, temperature, flow, exposure time, product layers, and steel chemistry), and the corresponding mechanisms. They pointed out knowledge gaps on localized corrosion and cathodic reaction mechanisms, especially under synergistic conditions with multiple impurities [20]. Wang et al. assessed the corrosion risk of pipelines at different stages of s–CO_2–EOR production from a perspective of multiphase fluids and suggested that tailoring processing parameters, such as shortening the water contact time and reducing the solution corrosivity, could be an effective corrosion control way under CO_2-EOR production conditions [22].

As numerous research papers have focused on studying corrosion under s-CO_2 conditions in recent years, this review work particularly focuses on the publications from 2011 to the present. Appendix Tables A1 and A2 summarize corrosion research in the wet s-CO_2 phase and s-CO_2 saturated aqueous phase, respectively. Different research groups around the world have published systematic research studies with large corrosion datasets, including Choi et al. [23–25], Xiang et al. [26–28], Hua et al. [29–31], Xu et al. [32–34], Sun et al. [35–37], and Gao et al. [38–40]. For example, Fig. 2 displays a data map of corrosion research in the s-CO_2 phase (including water-unsaturated and water-saturated environments) as a function of covered impurity levels. Most of the up-to-date research focused on the corrosion of pipe steels in s-CO_2 systems with around 1000 ppm O_2 and other single or multiple impurities, as indicated in the green zone (Fig. 2). However, despite intensive efforts, solid conclusions have not yet been reached due to controversial results reported by different groups. For instance, researchers adopted various ending exposure times and cleaning methods, which led to diverse corrosion rates (CRs), even with minor differences in experimental factors among some of the studies. The complexity of investigated corrosive environments and the diversity of obtained data make it quite challenging to develop practical operation standards for CCUS industries. In the era of large existing materials data, one should not only create open corrosion data to prevent disasters but should also combine efforts in evaluating corrosion tendencies and mechanisms more concisely, leveraging progress in the Big Data technologies [41].

This work reviews the most recent research papers (published between 2011 and 2021) on corrosion in s-CO_2 transportation, storage and utilization systems. The focus is on the application of corrosion data and the identification of remaining gaps for future research. Firstly, an overview of operating conditions (such as temperature, pressure, and environmental chemistry), as well as current metals of construction (MOC), will be provided. The s-CO_2 corrosion data obtained in both the s-CO_2 phase and s–CO_2–saturated aqueous phase will be analyzed, discussed, and summarized. Finally, the knowledge gaps requiring further investigations will be proposed. The aim of this study is to provide a thorough review of the literature and to communicate the existing corrosion data related to s-CO_2 transportation, storage and utilization systems. It lays a foundation for the future s-CO_2 corrosion research activities and the application of machine learning (ML) on long-term corrosion prediction from a data-oriented perspective.

2. Overview of CCUS operating conditions and metals of constructions

Corrosion is the degradation of materials, usually metals and alloys, due to interaction with their service environments. The investigation of corrosion in s-CO_2 transportation, storage and utilization systems shall start by identifying the operating conditions/environments and MOC. It has been over 40 years since the appearance of gaseous CO_2 pipelines and EOR technologies, and the related technical aspects and thermodynamic data have been thoroughly reviewed [3,42]. CCUS presents a new opportunity to re-purpose pipelines, EOR wells, and depleted reservoirs. However, risks can arise from two aspects in re-purposing: the operating pressure range in existing oil and gas pipelines is much lower than that required for the transport of s-CO_2 as indicated in Fig. 3 [12,43–45]; and existing and future s-CO_2 transportation, storage and utilization systems are likely to deal with s-CO_2 containing various impurities [3]. Fig. 3 presents the pressure and temperature conditions for the whole s-CO_2 transportation, storage and utilization systems [3,17,22,46]. As shown in Fig. 3, CO_2 pipeline transportation is designed to be operated at 20–50 °C and 5–15 MPa for cost-effective consideration. The CO_2 captured from combustion plants is typically compressed to a pressure above its critical point (7.4 MPa, 31 °C) to avoid two-phase flow regimes and consequently achieve optimum transportation

Received by OCD: 6/29/2026

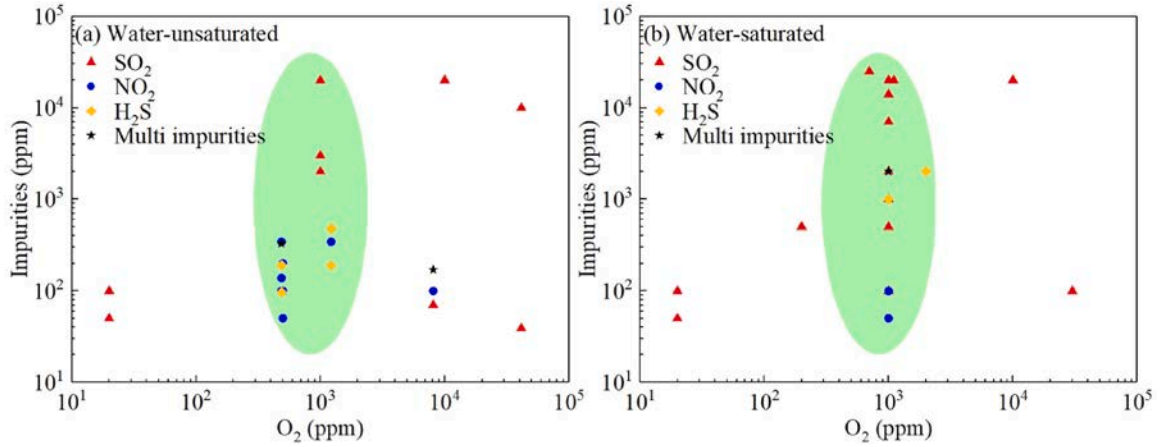


Fig. 2. A data-oriented overview of corrosion research on steels in the s-CO_2 phase with variedimpurity levels, including (a) water-unsaturated and (b) water-saturated environments. "Multi impurities" refers to a mixture of SO_2, H_2S, and NO_2. Data from Appendix Tables A1 and A2.

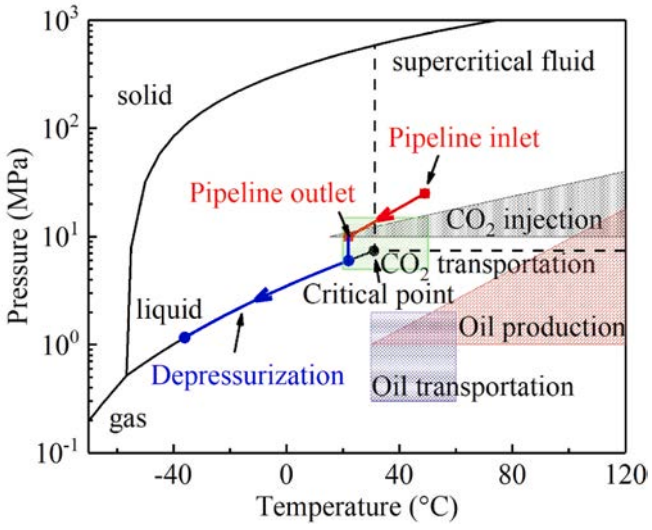


Fig. 3. CO_2 phase diagram with pressure and temperature operation conditions in the whole s-CO_2 transportation, storage and utilization systems [3,17,22,46].

efficiency. The amount of CO_2 transported per unit volume is maximized in the supercritical fluid phase as s-CO_2 possesses the density of a liquid and the viscosity of a gas [47,48]. For instance, the density and viscosity of s-CO_2 at 50 °C and 10 MPa are 395 kg/m^3 and 0.03 cP, respectively [49,50].

For the transportation of s-CO_2 through pipelines, controlling corrosion depends on considering the operating conditions, such as pressure and temperature, and the impurities in the CO_2 streams. Impurities in the s-CO_2 stream can have a significant impact on pipeline network operation and corrosion. Their presence affect the critical point and operating pressure range, which can lead to unwanted two-phase flow as indicated by the phase envelopes for CO_2 mixtures [51]. This can also affect the depressurization distance along the s-CO_2 transport pipeline. A larger pressure drop has been reported for transporting an impure CO_2 stream compared to a pure one along the pipeline [47,48,52–54]. The levels of impurities observed may differ depending on the CO_2 capture and separation technologies used as well as CO_2 sources, as summarized in Table 1. Among all potential impurities, free water (H_2O) is considered the most undesirableas its presence can result in hydrate formation and corrosion problems when interacting with acidic gas components such as CO_x, SO_x, and H_2S. When H_2O is presented over its maximum solubility in s-CO_2, hydrates occur, creating a significant concern for pipeline blockage [3]. Therefore, it is crucial to purify, dehydrate, and compress gaseous CO_2 before pipeline transportation. Although no universal standard exists so far, there are some recommended impurity limits [55–61], which are presented in Table 1.

Table 1
The CO_2 compositions transported in existing pipelines, expected from different CO_2 capture technologies, and with recommendation limits.

Components (%)	Existing pipelines [57–61]				Expected Captures [55]			Recommendation [56]
	Typical pipelines in USA	Canyon Reef Carriers, USA	Weyburn, USA	Sleipner, Norway [57,60]	Post-combustion	Oxy-fuel combustion	Pre-combustion	DYNAMIS
CO_2	95–99.7%	85–98%	96%	93–96%	>99%	>90%	>95.6%	>95.5%
CO	–	–	1000 ppm	–	–	–	–	2000 ppm
O_2	<14 ppm	–	<50 ppm	–	<0.1%	<3%	trace	Aquifer <4% EOR 100–1000 ppm
H_2O	315–630 ppm	50 ppm	<20 ppm	Saturated	0.14%	0.14%	0.14%	500 ppm
H_2	–	–	–	3–5%	trace	trace	<3%	<4%
H_2S	<26 ppm	<200 ppm	9000 ppm	150 ppm	trace	trace	<3.4%	200 ppm
CH_4	0.2–5%	2–15% C_6H_{14}	0.7%	0.5–2.0%	<0.01%	–	<0.035%	Aquifer <4% EOR <2%
N_2	0.3–4%	<0.5%	<300 ppm	3–5%	<0.8%	<1.4%	balance	<4%
Ar	–	–	–	3–5%	trace	<5%	<0.05%	<4%
SO_X	–	–	–	–	<0.001%	<0.25%	–	100 ppm
NO_X	–	–	–	–	<0.001%	<0.25%	–	100 ppm

Received by OCD: 6/29/2026

Not to mention, the quality of transported CO_2 is also important for optimum oil recovery. In CO_2-EOR, there is an economic incentive to reduce certain impurities to very low levels to avoid adverse reactions with hydrocarbons in the reservoir and to lower the minimum miscibility pressure [19]. According to the 'Criteria for Screening Reservoirs for CO_2-EOR Suitability' by the National Energy Technology Laboratory (US) [62], a reservoir that has undergone a successful waterflood is a prime candidate for CO_2-EOR, typically with operating temperatures less than 121 °C and pressures between 8.27 and 10.34 MPa. Millet et al. summarized four corrosion risk scenarios during the process of CO_2 injection and storage: CO_2 injection, short-term shut-in, long-term shut-in, and CO_2 reinjection [63]. As indicated, CO_2 injection requires tubing materials (typically CS) to withstand the corrosion caused by dense dry CO_2, dense wet CO_2, and formation water (FW) and/or saline water (SW) with dissolved CO_2 up to saturation. In summary, the corrosive environment is defined by the near-wellbore conditions, including pressure, temperature, saline properties, and injected CO_2 composition. The CO_2 currently supplied by pipelines to EOR wells is usually of high purity and in a highly dense state. For example, CO_2 compositions at the injection wellhead from the Sheep Mountain Reservoir are 97 vol% CO_2, 1.7 vol% CH_4, 0.7 vol% CH_4^+, 0.6 vol% N_2, and trace amounts of H_2O at 9.6 MPa and less than 24 °C [64]. The chemical properties of FW/SW vary from one reservoir to another, with saltsmainly composed of K^+, Na^+, Ca^{2+}, Mg^{2+}, Cl^-, and HCO_3^-, as shown in Table 2. Moreover, during injection, CO_2 with impurities can partition to the water phase. Acidic gases (e.g., SO_x, NO_x, and other acids) would react with H_2O to form strong acids, which reduces the pH and further increases corrosivity. Therefore, a significant corrosion risk can be expected at the interface between FW/SW and dense CO_2.

In summary, the presence of water is critical to the corrosion of CCUS transportation and EOR components under s-CO_2 conditions [38]. A summary of the commonly used MOC in the two processes is presented in Table 3 with their corresponding corrosive environments. Most EOR systems are constructed with CS. The amount of water and impurities are strictly controlled when s-CO_2 is used for EOR. When these variables cannot be controlled, corrosion-resistant alloys (CRAs), such as high Cr steels and Ni-based alloys, are considered. Appropriate CRAs can be selected based on laboratory evaluations and the limits of their application. As shown in Table 3, corrosive environments can be divided into two categories: s-CO_2 rich phase (wet or dry) and H_2O rich phase saturated with highly dense CO_2. The corrosion data review shall be focused on these two phases accordingly. In addition, standards for relative corrosion resistance (in mm/y) rank CRs of less than 0.02 mm/y as outstanding, 0.02–0.1 mm/y as excellent, 0.1–0.5 mm/y as good, 0.5–1 mm/y as fair, 1–5 mm/y as poor, and greater than 5 mm/y as unacceptable [73]. This ranking system will be adopted in the following discussion.

Table 3
MOC and the corresponding corrosive environments in the s-CO_2 transportation, storage and utilization systems [3,64].

Components	MOC	Environments
CO_2 pipeline	X grade (X60, 65, 70, 80, 100, and 120)	Impure s-CO_2
Upstream Metering, Piping Runs	304, 304 L, and 316 SS	Wet s-CO_2
Injection wellhead, trim, and tubing hanger	316 SS, Incoloy 800, Monel 400/405	Wet s-CO_2
Tubing and casing	Carbon steel, AISI 4140/ P110, Fe steels (with 1-13Cr), and appropriate CRAs	Wet s-CO_2, CO_2-saturated FW/SW

3. Corrosion in s-CO_2 rich phase

s-CO_2 rich phases, unsaturated or even saturated with H_2O, mainly represent the pipeline transportation conditions and upper-level environments in the EOR wells. Studies on steel corrosion in s-CO_2 rich phase have focused on influential parameters such as impurity types and contents, pressure, temperature, service time, steel chemistry, and flow/stirring rate, as shown in Table A1. The influential parameters on the mechanisms of steel corrosion and existing mechanistic prediction models have been summarized well [20]. This section systematically reviews the existing corrosion data, factors which have been overlooked, and contradictory conclusions which are worth re-evaluating.

3.1. Impurities

The CO_2 streams in the future CCUS industry will contain a certain amount of flue gas impurities. A series of studies have assessed the corrosion risks of steels in s-CO_2 with impurities, including H_2O, O_2, SO_x, NO_x, H_2S, HCl, methanol, and monoethanolamine (MEA) [20,74–76]. Among all impurities, H_2O is recognized as the most critical in terms of corrosion in s-CO_2, as it plays a principal role in electrolyte formation. Table 1 shows that most existing CO_2 streams for EOR projects have an upper limit of 630 ppm, except the Sleipner pipeline in Norway that transports s-CO_2 with saturated water [67]. The CO_2 sources from different CO_2 capture technologies are expected to have around 1400 ppm (0.14%) H_2O. Based on the data from existing CO_2 pipelines and experimental findings, the CRs of pipeline steels can be reduced to a safe rate (less than 0.02 mm/y) for long-term operation if the water content in s-CO_2 is insufficient to cause the formation of an acidic aqueous film on pipeline steels [24,29,60,77,78]. In s-CO_2 with impurity H_2O less than its alteration point at designed transportation temperatures and pressures, the steels are likely to experience marginal corrosion damage for long safe operation [77,79]. However, to establish a conclusive

Table 2
The properties of FW and SW.

Water type	Na^+/K^+ mg/L	Mg^{2+} mg/L	Ca^{2+} mg/L	Cl^- mg/L	SO_4^{2-} mg/L	HCO_3^- mg/L	Total salinity mg/L	Refs.
SW	1527	16	113	732	14	3197	5599	[65]
FW	51,810	5241	28,035	112,365	–	–	197,451	[66]
SW	22,353	2648	766	36,585	5015	212	68,358	
FW	54,400	1610	10,610	107,000	370	176	174,156	[67]
SW	16,877	2279	664	31,107	3560	193	54,680	
Aquifer water	1504	66	392	2577	700	192	5436	
FW	60,260	1847	17,480	129,144		147	208,940	[68]
Gulf seawater	13,662	1434	400	23,468	3072	147	42,220	
FW	109,890	11,240	46,070	224,170	140	200	391,850	[69]
SW	848	296	20	1427	87	1	2800	
FW	37,880	760	3280	67,580	3170	–	112,668	[70]
Produced water	11,140/520	630	1610	22,020	4130	–	40,393	
FW	31,275/654	379	5038	60,412	0	–	98,798	[71]
SW	10,890/460	1368	428	19,766	2960	–	35,872	
FW	1720/28	14	35	2150	166	968	5083	[72]
SW	1813/28	0.2	0.5	2150	166	968	5127.5	

Received by OCD: 6/29/2026

upper limit for the water content with the presence of multiple impurities (such as SO_2, O_2 and acids), further investigations are required. In fact, when s-CO_2 is adequately dry, an acidic water film cannot be formed. Thus, the corrosion process is dominated by gas-chemical reactions instead of aggressive electrochemical reactions. The CR of pipeline steels remains excellent (less than 0.1 mm/y) even with the co-presence of small amounts of other impurities. For example, the CR of X65 in the s-CO_2 rich phase was estimated to be 0.025–0.06 mm/y with 650–1770 ppm H_2O, 0–41250 ppm O_2, 39–500 ppm SO_2, and/or 0–191 ppm NO_2 at 8 MPa and 35–50 °C [24,78,80]. Considering the water content and other impurity levels from CO_2 capture technologies, corrosion should not be a huge concern for post-combustion sources [55]. Efforts should be made to reduce the O_2 level down to 1000 ppm (less than 0.1%) for oxy-fuel combustion CO_2 [36,81], and H_2S level down to 100 ppm (trace) for pre-combustion CO_2 [37,82]. It is worth to mention that reducing the O_2 or H_2S level is not a cheap process. Pursuing adequate CRAs may be the ultimate solution.

Moreover, once CCUS pipelines are deployed on a large scale, it is impossible to avoid scenarios with localized spots of saturated H_2O or even a condensed H_2O phase. Several studies have investigated the corrosion of steels in H_2O-saturated s-CO_2 systems, as summarized in Table A1. However,there are contradictory results among different groups on the corrosion of steels in H_2O-saturated s-CO_2 systems. For example, the CR of X65 in H_2O-saturated CO_2 phase with no other impurity was estimated to be 0.4 mm/y with 24 h' exposure time by Choi et al. [83], 0.03 mm/y with 24 h' exposure time by Hua et al. [84], 0.25 mm/y with 240 h' exposure time by Tang et al. at 50 °C and 8 MPa [85], 0.01–0.05 mm/y with 100 h' exposure time by Cabrini at 25–60 °C and 12.3–14.6 MPa [86]. Although factors such as various cleaning methods, exposure times, and angles can lead to data fluctuation, a one-order-of-magnitude fluctuation in CRs under the same conditions is unusual and should be interpreted with caution. Overall, corrosion is not a serious concern in the absence of H_2O for s-CO_2 pipeline transportation, and increasing H_2O content will increase the CR of steels [29,77,83,87]. Noted that the following impurities in the s-CO_2 rich phase are all discussed in the co-presence of H_2O.

3.1.1. Single impurity

Various CO_2 streams contain O_2 from trace to 30,000 ppm, and it is recommended that the O_2 contentbe purified down to 100–1000 ppm for EOR application (Table 1) [56]. The effect of O_2 content as the only impurity on the corrosion of pipeline steels in wet s-CO_2 rich phase has been studied, and results suggest that the CR of pipeline steels remains excellent (less than 0.1 mm/y) in H_2O-saturated s-CO_2 with O_2 addition from 100 to 30,000 ppm at 35–50 °C and 8–10 MPa. Zeng et al. suggested that the influence of O_2 on the steel corrosion in wet s-CO_2 would not be noticeable at an overall pressure lower than 10 MPa [88]. There are contradictory conclusions regarding the effect of increasing O_2 content on the corrosion tendency of steels in H_2O-saturated s-CO_2. Four groups concluded that the presence of O_2 generally increased the CR of steels [23,36,85,89]. For instance, in H_2O-saturated CO_2 phase, the CR increased from 0.005 to 0.01 mm/y on X65 with 2000 ppm O_2 addition and increased from 0.014 to 0.029 mm/y on X70 with 10,000 ppm O_2 addition at 50 °C and 10 MPa. Several researchers proposed that O_2 could provide an additional cathodic reaction pathway and consequently inhibits the formation of a protective iron-carbonate layer, leading to higher CRs [23,36,85,89]. Conversely, another two groups concluded that increasing the O_2 concentration from 0 to 1000 ppm in H_2O-saturated s-CO_2 caused a progressive decrease in the general CRs of X65, 5Cr, and 13Cr steels at 35 °C and 8 MPa [81,90], and of X70 at 40 °C and 10 MPa [91]. The decreased CR was attributed to 1000 ppm O_2 causing the steel substrate to enter the passivation zone [91]. The mechanism behind the corrosion process could be interpreted by two competing theories: electrochemical reactions and gas-chemical reactions. Depending on the presence of H_2O content, impurities such as SO_x, NO_x, and H_2S could either damage the integrity of the surface oxide scale formed on pipe steels and consequently enhance gas-chemical reactions; or react with the water film to form acids and consequently promote electrochemical corrosion by accelerating both the anodic and cathodic processes. For instance, studies by Zeng and Li et al. indicate that corrosion in H_2O-saturated s-CO_2 environments with O_2 shall be a gas-chemical reaction as there is no water film formed on the steel [92], while the corrosion process is likely dominated by electrochemical reaction in SO_2-containing environments as the corrosion rates of X80 are similar in the gas phase and aqueous phase [79,93]. Also, the presence of O_2 and/or other impurities affects the supercritical point and/or influences the water solubility in s-CO_2 [88]. However, it is a puzzle how a separated water film can be formed on steels in the H_2O-saturated s-CO_2 media. Addtionally, it should be noted that the corrosion kinetics in testing environments may not follow linear law. In other words, the exposure time can have a significant impact on the obtained CRs [26,37,40,77,94], which will be discussed in more detail later. Therefore, cautions should be exercised when applying results obtained after a short exposure time [81,90,91], as non-steady state corrosion experiments may not have reached equilibrium in these testing systems. Thus, further investigation and confirmation are still necessary.

Depending on the presence of H_2O content, impurities such as SO_x, NO_x, and H_2S could either damage the integrity of the surface oxide scale formed on pipe steels and consequently enhance gas-chemical reactions, or react with water film to form acids and promote electrochemical corrosion by accelerating both the anodic and cathodic processes. Choi et al. [24] and Farelas et al. [80] investigated the effect of SO_2 as the single impurity on the corrosion of X65 in s-CO_2 at 50 °C and 8 MPa. It was found that the CR of X65 in adequately dry s-CO_2 remained excellent with SO_2 up to 1000 ppm but behaved much worse (3.5 mm/y) when SO_2 reached 10,000 ppm. In H_2O-saturated s-CO_2, the presence of SO_2 can decrease the solubility of H_2O in s-CO_2 and facilitate the formation of a think acidic H_2SO_3 aqueous film on pipe steels [81]. The recommended SO_2 limit for acceptable CR of X70 is lower than 200 ppm [36,91]. NO_x was found to cause very severe corrosion damage to pipeline steels [95,96]. NO_2 can react with H_2O and form an extremely strong acid, HNO_3. Therefore, the tolerable limit for NO_x as a single impurity is expected to be much lower than that of SO_x. Dugstad et al. [77] compared the effects of SO_x and NO_x as a single impurity in s-CO_2 with 1220 ppm H_2O on the corrosion of steels and concluded that adding 191 ppm NO_2 resulted in a significant increase in CR (0.67 mm/y) of X65, while X65 exhibited acceptable CR (0.02 mm/y) with the addition of 344 ppm SO_2. H_2S can promote anodic dissolution/corrosion through sulphide adsorption and lowering of pH in wet s-CO_2 [25,39,97,98]. In H_2O-saturated CO_2 phase, the CR of X65 increased from 0.015 to 0.127 mm/y with 1000 ppm H_2S addition at 50 °C and 10 MPa [97], and increased from 0.17 to 0.24 mm/y with only 50 ppm H_2S addition at 80 °C and 10 MPa [98]. It is believed that a small amount of H_2S can change the absorbability of H_2O on the steel surface, increase the wettability of the steel surface, and thus accelerate the overall corrosion of steels in wet s-CO_2 phase [98]. However, in the case of dry s-CO_2 with less than 100 ppm H_2O, the CR of pipeline steels was ranked as outstanding (less than 0.02 mm/y) with 200 ppm H_2S [25]. The effects of various single impurities have been compared. As shown in Fig. 4a, the corrosivity of single impurities can be ranked as $NO_x > SO_2 > H_2S > O_2$. In summary, O_2 is recommended to be limited to a level of 1000 ppm, and the other three impurities, SO_x, NO_x, and H_2S, are recommended to be limited to 100 ppm levels.

3.1.2. Multiple impurities

Compared to single impurities, steels usually experience more severe corrosion due to the synergistic effects of O_2, SO_2 and H_2S in wet s-CO_2. Previous studies have mainly focused on the synergistic effects of O_2+SO_2, O_2+H_2S, O_2+SO_2+H_2S, and SO_2+H_2S [24,77,99,100]. When O_2 coexists with SO_2 and/or H_2S in H_2O–CO_2 systems, SO_2 can react with O_2+H_2O to form H_2SO_4 which is more corrosive than H_2SO_3. H_2S can be oxidized to SO_2 and S leading to sulphur-initiated pitting

Received by OCD: 6/29/2026

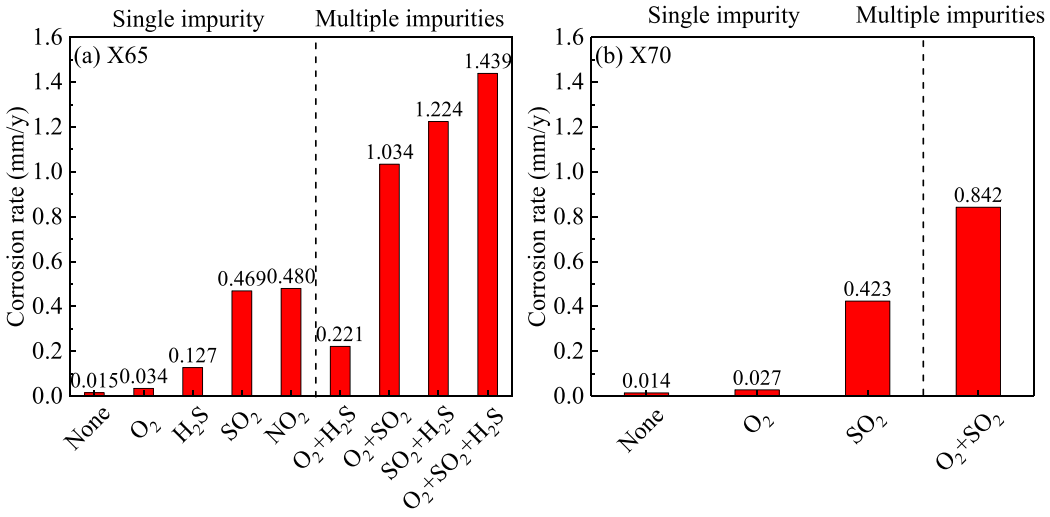


Fig. 4. Impact of gas impurities on the corrosion rates of (a) X65 [97] and (b) X70 [36] steels in H_2O-saturated s-CO_2 containing various impurities of 1000 ppm at 50 °C and 10 MPa.

corrosion. To quantify the synergistic effects in s–CO_2–H_2O–O_2–SO_2–H_2S systems, Sun et al. introduced the synergistic impact factor of multiple impurities (S_m) [97], which was later adopted by other researchers [91].

$$C_i = \frac{V_i - V_o}{V_o} \tag{1}$$

$$S_m = C_m - \Sigma C_s \tag{2}$$

In Equations (1) and (2), V_0 and V_i (mm/y) are the corrosion rates of steels exposed to the H_2O-saturated s-CO_2 environment without and with *i* impurity/impurities, respectively, where *i* is the impurity type. C_i, C_s, and C_m are the corrosion impact factors of the *i* impurity, a single impurity, and multiple impurities, respectively. Fig. 4 clearly demonstrates the synergistic effects in CO_2–H_2O–O_2–SO_2–H_2S systems, where the combinations of O_2 with SO_2, H_2S, or SO_2+H_2S are more aggressive than the cases without O_2. The synergistic effect of SO_2 with H_2O and O_2 is much more noticeable than H_2S on the corrosion rate. Most of the work has focused on the effects of O_2 and SO_2 on the corrosion of steels in wet s-CO_2 environments, while the impact of multiple impurities including NO_x and H_2S has not been well addressed in detail. To the authors' best knowledge, there is no corrosion work done in a comprehensive supercritical system, *i.e.,* CO_2–H_2O–O_2–SO_2-NO_x-H_2S.

3.1.3. Other impurities

Carbon capture processes may also result in residual impurities related to capturing media (amines, catalysts, etc.) and sources (e.g., the flue gas from biomass combustion can contain HCl). The effect of such impurities has not been adequately studied. Russick et al. found that 10 wt% methanol did not cause any adverse effects on CS and SS in s-CO_2 at 50 °C and 24 MPa [76]. Thodla et al. indicated that the presence of 100–1000 ppm H_2O could cause a high CR (greater than 1.0 mm/y) in CS, and the presence of 100 ppm MEA caused a significant decrease in the CR (less than 0.1 mm/y) at 31 °C and 8 MPa [74]. It is also interesting to note that, although adding MDA brought the CR from greater than 1.0 to 0.1 mm/y, 100 ppm MDA addition was more effective than 1000 ppm addition of MDA in decreasing the corrosion rate (0.01 mm/y with 100 ppm MDA vs. 0.1 mm/y with 1000 ppm MDA). There was also an effort to use inhibitors like triethylene-glycol in s-CO_2 transportation. Collier et al. found that the presence of O_2 and DEA (diethanolamine) increased the average CRs of steels in wet s-CO_2 whereas ethylene glycol had no effect [101]. Additionally, CO_2 captured from the flue gas of biomass boilers can contain HCl, and pre-combustion technology can bring CO into the captured CO_2. The adverse effects of HCl and CO have been mentioned [102,103]. Overall, the effects of amines, solvents, HCl, and CO on the corrosion of steels in wet s-CO_2 phase are not well understood and the related corrosion data are limited in numbers.

3.2. Testing parameters

Except for the chemistry of s-CO_2 rich phase, the primary testing parameters of the investigated wet s-CO_2 systems are pressure, temperature, exposure time, steel type, and stirring/flow rate, which are discussed here. The effect of each parameter is summarized in the same system, from the chemistry of s-CO_2 environments to the other testing parameters. However, the experimental data regarding the effect of pressure and temperature are diverse for wet s-CO_2 systems. This could be attributed to the non-ideality of gases and differences in the solubility of various impurities in the condensed phase under supercritical conditions. The difference in corrosion results can also be attributed to the varying consumption rate of impurities by corrosion during exposure. For example, Hua et al. observed a decrease (0.19–0.07 mm/y) in CR on X65 from 8 to 10 MPa at 50 °C with H_2S (1000 ppm) as the single impurity [104], suggesting that the increasing pressure may affect the integrity of the formed FeS layer on the surface and may decrease corrosion rate. Other researchers have reported an increase in CR by increasing the system's total pressure. Xu et al. suggested that increasing pressure from 8 to 10 MPa at 50 °C with multiple impurities (O_2–SO_2–NO_2) resulted in 3 times higher CRs on X70 [34]. A similar conclusion was made by Zeng et al., where increasing pressure from 8.5 to 10 MPa at 45 °C with O_2 as the single impurity resulted in around 3 times higher CRs on various types of X-grade steels [88]. The above-mentioned studies suggested that the effect of various impurities in s-CO_2 streams could surpass the effect caused by increasing pressure from the supercritical point to 10 MPa; however, above 10 MPa, the pressure influence cannot be simply ignored. In H_2O-saturated CO_2 systems with no other impurity, Dugstad et al. reported an increase in CR from 0.8 to 2.7 mm/y on X65 with temperature increasing from 20 to 50 °C at 10 MPa [89]. Another two groups reported a decreasing effect on X65 caused by higher temperatures [29,84,105], yet Cabrini et al. reported an increase followed by a decrease in CR from 20 to 60 °C [86]. Although H_2O-saturated CO_2 will behave differently below or above the critical temperature of 31.5 °C, there is still no solid explanation for the discussed temperature effects.

MOC chemistry plays an important role, and it is generally agreed that SS outperforms CS in resisting corrosion [39,76,101]. Collier et al.

Received by OCD: 6/29/2026

investigated the corrosion of X42, X60, 316 L SS and 304 L SS in both dry and wet s-CO_2 systems [101]. They confirmed that X42 and X60 were more susceptible to corrosion than 304 L and 316 L; there was no significant difference between the CR of X42 and X60, nor significant difference between 316 L and 304 L under all studied conditions. A variety of corrosion studies (listed in Table A1) agreed that X-grade pipeline steels, including X 42, 52, 60, 65, 70, 80, and 100, presented similar CRs under s-CO_2 systems with various impurities [34,79,88,98,101]. Pipeline CS (P110 and X grades) suffered from corrosion problems in H_2O-saturated s-CO_2, while 316 L and 304 L SS presented outstanding corrosion resistance (less than 0.02 mm/y) in the same environment [39,76,101]. It must be mentioned that the main difference between the investigated CS and SS is the Cr content. Usually, X grade CS has less than 0.5 wt% Cr, P110 contains 0.8–1.1 wt% Cr, and 304 L and 316 L SS contain 16–18 wt% Cr. Therefore, efforts have also been made to investigate the effect of Cr contents on steel corrosion in s-CO_2 environments. Studies found that up to 1 wt% of Cr addition brought no significant difference in improving the corrosion resistance of steels [25,94], while 13 wt% of Cr addition significantly improved the CRs of steels [81,106]. However, experimental results regarding the effect of Cr content between 1 and 5 wt% are still diverse in wet s-CO_2 systems. In H_2O-saturated s-CO_2 systems, Hua et al. reported that there was no significant difference in the CR of X65 and 5 wt% Cr steels at 35 °C and 8 MPa [90]. Choi et al. showed that adding 3 wt% Cr significantly improved the CR of steels (0.05 mm/y with 3 wt% Cr vs. 0.44–0.41 mm/y with 0–1 wt% Cr) at 80 °C and 12 MPa with H_2S [25]. Conversely, Gao et al. showed that 3 wt% Cr steel corroded even faster than P110 steel (0.41 mm/y with 3 wt% Cr vs. 0.19 mm/y with 1 wt% Cr) at 80 °C and 10 MPa with H_2S [39]. Thus, the effect of Cr content (up to 5 wt%) requires further investigations.

The CR of steels, except P110, generally decreased as the exposure time was extended [27,29,37,40,86,107], as selectively presented in Fig. 5. There were two potential reasons leading to the decreasing trend of CR vs. exposure time. Firstly, corrosion products gradually accumulated on the steel surface and formed a thick corrosion product layer, which could protect the steel substrate from further rapid corrosion [40]. Besides, as corrosion proceeded, the corrosive species would be gradually consumed, leading to a decrease in CRs with exposure time. Studies presented in Fig. 5 were all performed in H_2O-saturated s-CO_2 systems with or without over 1000 ppm levels of various impurities. When citing corrosion rate results in s-CO streams, it is important to consider the types of impurities present as their consumption rates will

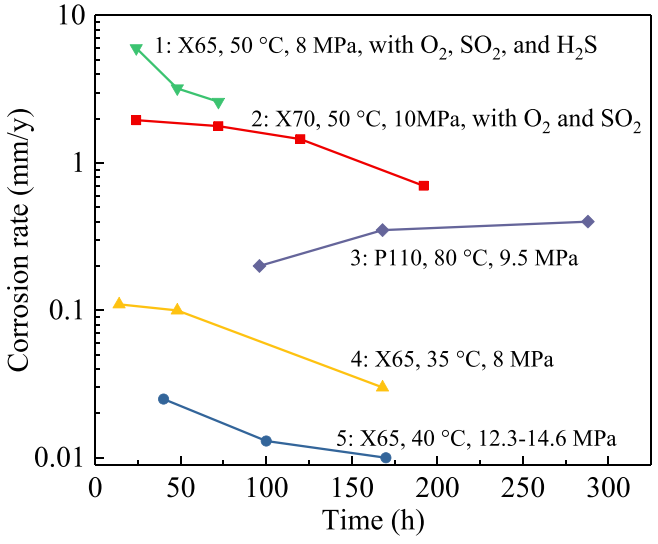


Fig. 5. Effects of exposure time on the corrosion of steels in H_2O-saturated s-CO_2 systems, with data numbered 1 [37], 2 [27], 3 [40], 4 [29,107], 5 [86].

be different and possibly affected by other impurities during corrosion processes. For instance, when H_2S is present in H_2O-saturated s-CO_2, the consumption rate is low due to the formation of relatively stable FeS layers. On the other hand, in the presence of both H_2S and O_2, the consumption rate of H_2S is remarkably higher due to the formation of a very porous and fragile FeS/Fe_3O_4 layer [92]. Therefore, it is believed that the variation in corrosion rate shall depend on both the environmental chemistry and the properties of the corrosion layer grown on pipe steels.

In Fig. 5, the decreasing trend of CR presented a gentler incline as the exposure time exceeded 96 h suggesting an exposure time of at least 96 h for future immersion experiments. Furthermore, Xiang et al. [108] reported that the CR of X70 was 1.16 mm/y, which was higher than that of pure iron (0.59 mm/y) after 454 h of immersion in H_2O-saturated s–CO_2 systems at 50 °C and 10 MPa. This was a different result compared with their previous shorter period experiments [75], attributed to the occurrence of pitting corrosion beneath the corrosion product layers. Wei et al. also reported a significant breakdown of the corrosion product layer integrity on P110 steel after 168 h of immersion in H_2O-saturated s-CO_2 at 80 °C and 9.5 MPa, resulting in an increase in the corrosion rate from 0.2 to 0.4 mm/y with further extending the exposure time from 96 to 288 h [40]. Overall, the structure and integrity of corrosion layers formed on steels determine the overall corrosion kinetics in various s-CO_2 environments. The understanding of corrosion kinetic laws in s-CO_2 environments is currently inadequate, and there is considerable variability in reported corrosion outcomes [109]. The majority of previous investigations were performed in static autoclaves with varying exposure times, resulting in inconsistent and unreliable findings with regard to practical operation considerations.

In addition, most of the summarized studies adopted a closed autoclave system. A few groups investigated the effect of flow/stirring rates on steel corrosion in wet s-CO_2 systems [28,75,79,87,110,111]. Dugstad et al. reported that X65 corroded 10 times faster with a flow rate of 3 m/s than it did with no flow in H_2O-saturated s-CO_2 at 50 °C and 10 MPa [89]. Zeng et al. also reported a 2–3 times increase in corrosion rate on X-grade steels caused by a stirring rate of 150 rpm compared to no flow condition in water-saturated s-CO_2 at 45 °C and 10 MPa [79]. On contrary, Collier et al. noticed that a stirring rate of 100 rpm slightly reduced steel corrosion in H_2O-saturated s-CO_2 at 35 °C and 8 MPa [101]. Later, Sun et al. investigated the influence of flow rate (0–1.5 m/s) on the corrosion of X65 steel in water-saturated s-CO_2 phase containing 1000 ppm H_2S at 35 °C and 8 MPa [110]. As shown in Fig. 6, the CR reached the maximum at 1 m/s and then decreased with a further increase in flow rate to 1.5 m/s. They attributed this trend to the quality of the as-formed corrosion product layer, mainly composed of $FeCO_3$ and FeS. The average size of spherical corrosion products and the percent composition of FeS exhibited the same trend as the CR vs. flow rate. It was believed that the flow rate could affect both the formation process and the characteristics of corrosion product layers on X65. In general, diversities in the impact of flowing rate could be attributed to the properties and integrity of as-formed corrosion product layers.

4. Corrosion in H_2O rich phase

Compared to wet s-CO_2 rich systems, corrosion studies in s–CO_2–saturated aqueous systems are much less extensive. The s–CO_2–saturated H_2O phase mainly exists in localized areas along transportation pipelines where condensation occurs, and in the tubing and casing of s-CO_2-EOR systems. Based on the chemistry of aqueous phases, investigation can be divided into three categories: s–CO_2–saturated H_2O, SW (i.e., NaCl solutions), and FW. Overall, current results suggest that the pipeline steels presented CRs as poor (1–5 mm/y) to unacceptable (greater than 5 mm/y) in s–CO_2–saturated aqueous systems, as shown in Table A2.

Received by OCD: 6/29/2026

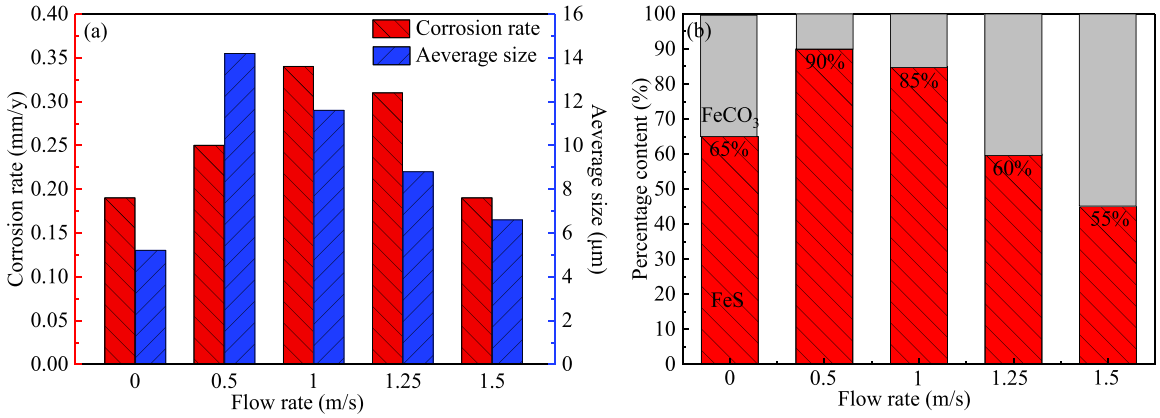


Fig. 6. Impact of flow rate on (a) the CR and average size of spherical corrosion products of X65, and (b) compositions of corrosion products on the steel surface after 72 h' exposure in H_2O-saturated s-CO_2 system containing 1000 ppm H_2S at 35 °C and 8 MPa. Note: figures are re-drawn based on data from Ref. [110].

4.1. s–CO_2–saturated H_2O phase

A study by Choi et al. in 2011 reported the CR of X65 in CO_2-saturated H_2O was in the range of 18–20 mm/y and the increase of overall CO_2 pressure from 4 to 8 MPa in the system did not significantly increase the CR at 50 °C after 24 h [83]. On the other hand, Hua et al. detected a much lower CR (6.6 mm/y) of X65 under the same testing condition (CO_2-saturated H_2O at 50 °C and 8 MPa after 24 h) with the same cleaning solution [84]. Later, researchers from Gao's group studied the corrosion of X65, X70, C75, and 13Cr steels in s–CO_2–saturated H_2O at various temperatures and pressures [82,111–113]. Fig. 7 presents the reported effect of temperature and exposure time on the CR and thickness of the obtained corrosion product layer. As shown there, the thickness of corrosion product layers continuously decreased with increasing temperature while the CR increased from 50 to 80 °C and then decreased from 80 to 130 °C. It was discovered that although corrosion product layers formed at lower temperatures (50–80 °C) were thicker than those at higher temperatures (110–130 °C), the former one had local defects and failures [113]. They also developed a linear relationship between the fracture toughness (K_{IC}) of corrosion product layers and the CR of X65 in s–CO_2–saturated H_2O Phase [112]. The comparison between the measured and calculated CR was also presented in Fig. 7.

It was noticed that the CR of X65 steel generally decreased with the increase in exposure time in s–CO_2–saturated H_2O systems at 80 °C and 9.5 MPa, which may be attributed to the gradual formation of a protective corrosion layer on the steel, which was composed of $FeCO_3$ [112]. Similar trends were reported for X65 steel in s–CO_2–saturated H_2O systems at 50 °C and 8 MPa by Hua et al. [84]. On the other hand, Cabrini et al. observed the CR of X65 steel kept decreasing beyond 100 h' immersion in s–CO_2–saturated H_2O systems at 12.3–14.6 MPa with a stirring rate of 180 rpm [86]. Clearly, the effect of stirring and higher pressures made it difficult to build a relatively compact and protective surface scale on the steel. As to the steel chemistry, it is generally agreed that the s-CO_2-saturated H_2O phase is highly aggressive to CS as their overall CRs are unacceptably high (>5 mm/y) accompanied by intense localized attacks at the reviewed temperatures and pressures. Under such conditions, even 13Cr steel still experienced considerable corrosion damage (0.3–0.8 mm/y) both with and without minor gas impurities [26,111]. Thus, future work is needed to explore the effect of alloy elements (Cr and Mo) on corrosion and identify suitable candidates for application in the s–CO_2–saturated H_2O phase with controlled gas impurities.

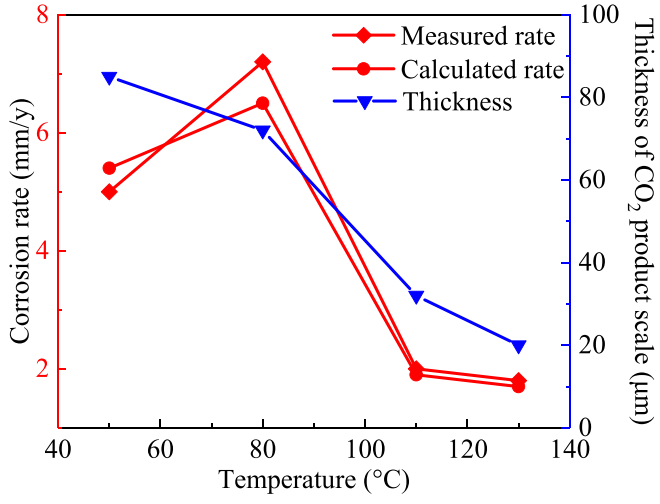


Fig. 7. The CRs and thickness of corrosion product layers of X65 steel as a function of temperature obtained after 168 h [112,113].

4.2. s–CO_2–saturated saline water

Tubing and casing used for injecting CO_2 into saline aquifer reservoirs can encounter SW and FW that contain high concentrations of chloride, and thus, suffer serious corrosion attacks [49,50,94,114]. In s–CO_2–saturated 3.5 wt% NaCl solutions at 9.5–10 MPa, Wei et al. investigated the corrosion mechanism of various steels [39,40,98,106]. Fig. 8a shows the reported average CR of X70 and P110 steels vs. immersion times at 80 °C and 9.5 MPa [40]. In the s–CO_2–saturated saline water, the corrosion process is likely to include three main stages: i) the initial formation of a corrosion layer with a significant decrease in CR, ii) transformation from the initial corrosion layer (Fe_3C) to mixed layers (Fe_3C and $FeCO_3$) with a continuous decrease in CR, iii) further growth of the mixed layer with a slowly decreased and/or constant CR. After about 96 h of immersion, a dense mixed layer with better protectiveness was formed on the steel surface, and both uniform and localized corrosion behaviors slowed down, as indicated in Fig. 8b [106]. To further examine the corrosion process and advance corrosion mechanistic understanding in such corrosive environments, in-situ electrochemical measurement, such as electrochemical impedance spectroscopy (EIS) measurements, can be applied. A three–time constants equivalent electrical circuit (EEC) was used to fit the measured EIS data; where, R_i and Q_i represented the resistance and the constant phase element (CPE) for each layer, respectively [106]. In addition, Xiang et al. and Sun et al. also found similar corrosion behavior of N80 and X65 steels vs. immersion time in s–CO_2–saturated NaCl solutions [26,37].

Since common pipeline steels corrode severely, efforts have been made to search for appropriate CRAs for injection pipelines and tubing

Received by OCD: 6/29/2026

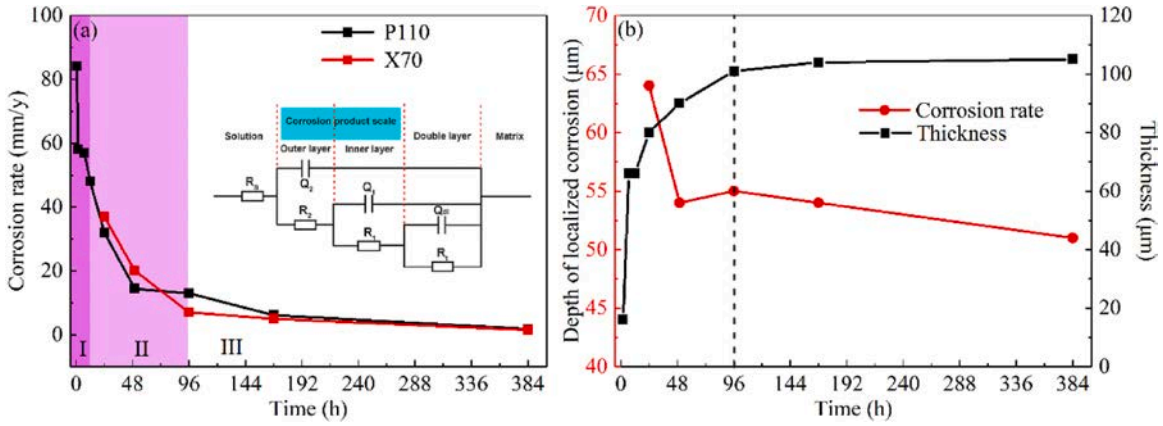


Fig. 8. (a) CRs of pipeline steels vs. immersion time and the EEC used to simulate the as-formed corrosion product layers [40]; (b) variations of the depth of localized corrosion and the thickness of the corrosion product layer formed on X70 steel vs. immersion time; all in s–CO_2–saturated 3.5 wt% NaCl solutions at 9.5 MPa and 80 °C [106].

for s–CO_2–saturated SW applications. Wei et al. studied the effect of Cr additions on improving the corrosion resistance of steels. It was found that the addition of 0.5 and 3 wt% Cr (*i.e.,* P110 and 3Cr steels) could not bring the CR down to an acceptable level, but 316 L (contains around 18 wt% Cr) presented a promising CR to s–CO_2–saturated NaCl solutions with H_2S at 80 °C and 10 MPa [39]. Hua et al. also compared the corrosion behaviors of the steels with Cr content of 1–5%, which were considered as potential injection pipeline/tubing materials [115]. The influence of steel Cr content on the general and localized corrosion was investigated at 60 °C and 10 MPa. Results indicated that prior to the formation of protective films on the steel surface, the resistance of materials to corrosion increased with increasing Cr content. However, with extending immersion time, the protection afforded to different steels significantly varied and decreased with increasing the Cr content. By the end of 192 h experiments, X65 experienced the lowest general CR while 5Cr steel suffered the most severe corrosion. It was found that the localized corrosion was noticeably less on X65 compared to Cr model steels [115]. Overall, results indicate that carbon and low Cr steels (less than 5 wt% Cr additions) are not ideal for s–CO_2–saturated SW applications. More investigations are required to further explore the influence of alloying elements (Cr and Mo) on corrosion and identify the most cost-effective candidates (such as duplex and austenitic stainless steels).

4.3. *s–CO_2–saturated formation water*

Limited research has focused on steel corrosion in s–CO_2–saturated FW, despite the variation in FW chemistry across different reservoir;s it mainly consists of K^+, Na^+, Ca^{2+}, Mg^{2+}, Cl^-, and HCO_3^- (Table 2). Zhang et al. studied the corrosion behavior of N80 in simulated s–CO_2–saturated FW containing NaCl, KCl, $CaCl_2$, Na_2SO_4, $MgCl_2$, and $NaHCO_3$ at 60 °C and 8 MPa [116]. It was found that the CRs under dynamic conditions (265–795 rpm) were consistently higher than those under static conditions, especially in the initial testing period. They also developed an experimental setup composed of two concentric cylinders for *in-situ* electrochemical measurements to investigate the formation and electrochemical behaviors of the as-formed layers under both static and dynamic conditions. Three EECs were used, as shown in Fig. 9(a–c), to explain the electrochemical behaviors on the steel surface: (a) three-time constants EEC in the initial period under static conditions, i.e., one capacitive loop (Q) at high frequency, one inductive loop (L) at an intermediate frequency, and one capacitive loop at low frequency; (b) two-time constants EEC in the initial period under dynamic conditions, i.e., a capacitive loop at high frequency and an inductive loop at low frequency; (c) with the prolongation of exposed time, the impedance spectra were characterized by double capacitive loops under both static and dynamic conditions as the inductive loop shrank gradually and disappeared after 7 h. In the presented EECs, R_s is the solution resistance, Q_{dl} represents the double layer capacitance, R_{ct} is the charge

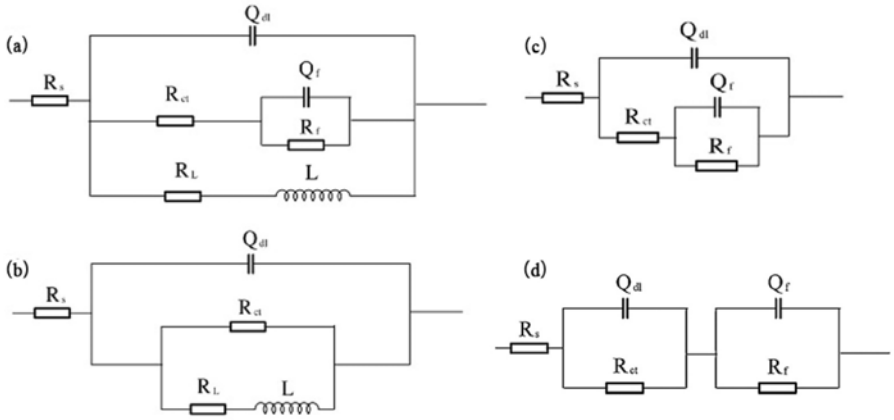


Fig. 9. EECs for EIS results of N80 steel under various conditions: (a) the initial stage under static conditions, (b) the initial stage under dynamic conditions, and (c) the late stage (*i.e.,* after 7 h) under both static and dynamic conditions [116]; EECs for EIS fitting of steels under various conditions: (a) N80 steel after coupled with 13Cr steel for 1 h, (c) N80 steel under other conditions, (d) 13Cr steel [117]. Both studies were performed in the s–CO_2–saturated FW at 60 °C and 8 MPa.

Received by OCD: 6/29/2026

transfer resistance, Q_f represents the capacitance of corrosion product films or passive films, R_f is the resistance of corrosion product films or passive films, L is the inductance, and R_L is the resistance of inductance. In addition, it was found that dynamic conditions (265–795 rpm) could hinder the formation of protective corrosion product films on the steel surface, leading to higher corrosion rates. Later, they modified the experimental setup, and investigated the galvanic effect between N80 and 13Cr steels under static and dynamic s–CO_2–saturated FW conditions at 60 °C and 8 MPa via *in-situ* electrochemical measurements [117]. To determine the electrochemical parameters, EECs (Fig. 9 a, c, and d) were used to fit the EIS data, where Fig. 9a was for the EIS of N80 steel after coupled with 13Cr steel for 1 h, Fig. 9c was for the EIS of N80 carbon steel under other conditions, and Fig. 9d was for the EIS of 13Cr steel. It was confirmed that the corrosion of N80 steel was promoted by the galvanic effect that accelerated under dynamic conditions. The CR of N80 increased and the as-formed corrosion product layer was less protective when N80 steel (serving as the anode) was coupled with 13Cr steel (serving as the cathode). Overall, EIS is considered as a useful method to investigate the formation of protective corrosion products on the steel surface under s-CO_2 conditions.

Hua et al. investigated the individual effects of Cl^-, Ca^{2+}, and Mg^{2+} on the corrosion behavior of X65 steel in simulated FW with 10 MPa CO_2 at 60 °C [30]. The growth of corrosion product layers was monitored and related to the extent of both general and localized corrosion, as in Fig. 10. It was found that increasing Cl^- concentration accelerated the overall corrosion of X65 steel, and the presence of 10,000 ppm Ca^{2+} or Mg^{2+} ions introduced severe pit propagation under the same testing conditions. Accelerated pitting kinetics might be attributed to the co-precipitation of Ca^{2+} and Mg^{2+} ions with $FeCO_3$ forming $Fe_xCa_{1-x}CO_3$ and $Fe_xMg_{1-x}CO_3$, respectively. Compared to Mg^{2+}, Ca^{2+} demonstrated a much greater propensity to co-precipitating with $FeCO_3$, thus resulting in more severe pit propagation. Ultimately, the FW chemistry makes the corrosion of steels under s-CO_2 conditions more complicated. Further work is required to determine the specific reasoning behind accelerated corrosion kinetics under s–CO_2–saturated FW conditions.

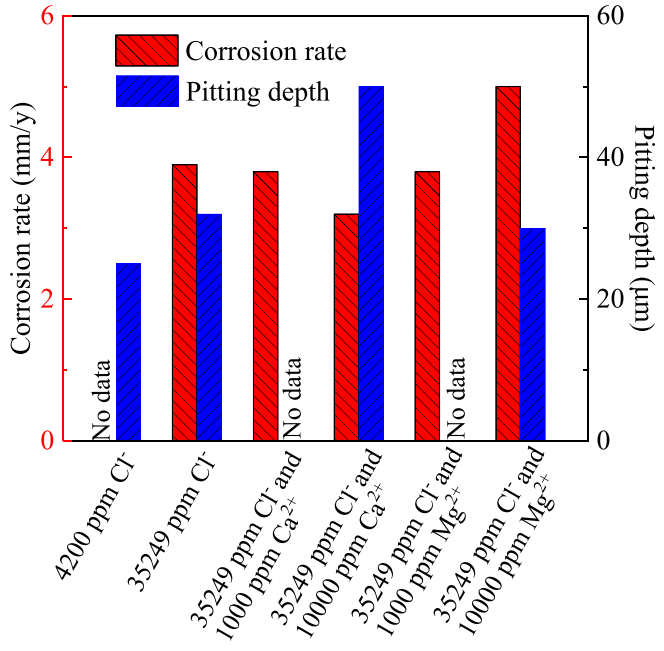


Fig. 10. General CRs and pitting depths of X65 steels exposed to s–CO_2–saturated FW with various contents of Cl^-, Ca^{2+} and Mg^{2+} at 60 °C and 10 MPa for 96 h [30].

5. General discussion and perspective

The capacity of annual CO_2 capture from power and industrial facilities was reported to be 40 Mt in 2021, which is around 4 times more than that in 2010 [118]. The availability of infrastructure to transport and utilize CO_2 safely and reliably is essential for the deployment of CCUS. As reviewed, one major issue delaying the implementation of s-CO_2 transportation, storage, and utilization systems is the corrosion of MOC caused by water and other impurities under s-CO_2 conditions. To date, there is no universal operation or construction standard for the existing and future CCUS facilities, such as pipelines and EOR systems. Although extensive research activities have been conducted and are still ongoing, most of them are done by isolated research groups, and their findings cannot effectively or efficiently contribute to the development of universal CO_2 impurity control and MOC selection standards. For example, researchers adopted various ending exposure times and cleaning methods (in Tables A1 and A2) resulting in diverse CRs. To facilitate the development of standards for CCUS impurity control and MOC strategy, four topics require significant and urgent attention, and they must be investigated from both an engineering and a fundamental perspective.

5.1. Novel iso-corrosion diagrams for quantifying relative corrosion resistance

The iso-corrosion diagram is a popular and useful tool used to recognize high-corrosion situations during the process of equipment design. Many industries have adopted and developed their own iso-corrosion diagrams [119–123]. The diagram consists of lines, each representing an alloy and its CRs at specified values (e.g., 0.1, 0.5, or 1.0 mm/y). A series of detailed and precise iso-corrosion diagrams can serve as a baseline in the early design phase. The style of iso-corrosion diagrams is flexible and can be modified based on the needs of end-users. For instance, there are room temperature iso-corrosion curves for various stainless steels and nickel alloys in H_2SO_4 at a good CR (0.5 mm/y) as a function of temperatures and H_2SO_4 concentrations [123]. As a starting point, one can aim for two types of iso-corrosion diagrams (schematically shown in Fig. 11, modified from Ref. [119]) for X grade CS at various CR levels (0.1, 0.5, and 1.0 mm/y). Diagram I (Fig. 11a) is a function of single impurities (such as 0–1000 ppm SO_2, Y axis) and temperature (35–120 °C, X axis) in H_2O-saturated s-CO_2 system (with other fixed impurities) at 10 MPa, and Diagram II (Fig. 11b) is a function of pressure (7.5–17 MPa, Y axis) and temperature (35–120 °C, X axis) in H_2O-saturated s-CO_2 system with recommended impurity limits (e.g., 1000 ppm O_2, 100 ppm SO_2, 100 ppm NO_2, and 100 ppm H_2S). To the best of the authors' knowledge, there is no iso-corrosion diagram developed related to s-CO_2 applications. Developing such diagrams will be time-consuming and require efforts from research groups around the world. Herein, unified efforts are recommended to develop novel iso-corrosion diagrams for the CCUS industry, which is also in concert with the call for sharing corrosion data [41].

5.2. Understanding the protection and failure mechanisms of corrosion product layers

The reported CRs of steels under wet s-CO_2 conditions are higher than those under gaseous CO_2 conditions although there is not much difference in corrosion mechanisms between these two environments [106]. It is also confirmed that the structure and integrity of corrosion product films formed determine the overall CR of steels under s-CO_2 conditions, which contributes to diverse corrosion data. A few influential parameters with great impact on the protectiveness, morphology, and composition of formed corrosion product layers require further and deeper understanding. One can introduce critical temperature and pressure values (i.e., layer breakdown temperature and pressure) for a specified s-CO_2 environment. For instance, in H_2O-saturated s-CO_2

Received by OCD: 6/29/2026

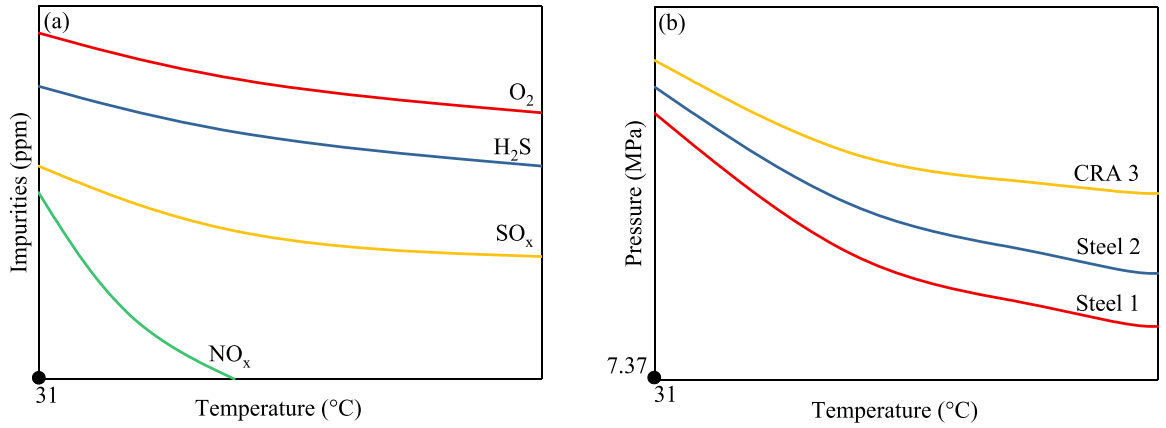


Fig. 11. Potential iso-corrosion diagrams (0.1 mm/y) of MOC. (a) Diagram I of a MOC as a function of single impurities and temperature in the H_2O-saturated s-CO_2 system at 10 MPa, and (b) Diagram II of various MOC as a function of pressure and temperature with recommended impurity limits (e.g., 1000 ppm O_2, 100 ppm SO_2, 100 ppm NO_2, and 100 ppm H_2S).

system with recommended impurity limits (e.g., 1000 ppm O_2, 100 ppm SO_2, 100 ppm NO_2, and 100 ppm H_2S), one can record the CR of steels and as-formed film properties as a function of temperature and pressure to determine thresholds for critical temperature and pressure values. Since steels will experience fast CRs once the formed product layers lose their integrity, the obtained critical temperature vs. pressure line would be presentable and comparable in an iso-corrosion diagram (such as Fig. 11b). In addition, the composition and integrity of the corrosion product layers will be more complicated in the presence of gas impurities in an s-CO_2 stream, and in the case of Cr model alloys. For example, $FeSO_3{\cdot}xH_2O$ and $FeSO_4{\cdot}xH_2O$ crystals are usually detected in the corrosion product layers [87] in the presence of SO_2 and O_2, and the ratio of $FeSO_3{\cdot}3H_2O$ to $FeCO_3$ increases with increasing SO_2 concentration [31]. As reviewed, the effect of Cr content (up to 5 wt%) requires further investigation to elucidate the effectiveness of Cr addition in improving the corrosion resistance of steels under s-CO_2 conditions. Overall, it is fundamentally critical to understand the protection and failure mechanisms of corrosion product layers under s-CO_2 conditions.

In the presence of impurities, corrosion mechanisms in s-CO_2 can be attributed to either electrochemical or gas-chemical processes. In s–CO_2–saturated aqueous solutions, the corrosion process is dominated by electrochemical reactions with potential anodic and cathodic reactions presented below.

Anodic reactions [124]:

$$Fe \rightarrow Fe^{2+} + 2e^- \quad (3)$$

$$Fe \rightarrow Fe^{3+} + 3e^- \quad (4)$$

Cathodic reactions [125]:

$$H_2CO_3 + e^- \rightarrow HCO_3^- + \frac{1}{2}H_2 \ (pH > 4) \quad (5)$$

$$H^+ + e^- \rightarrow H \ (pH < 4) \quad (6)$$

The formed Fe cations could interact with water and form iron oxides/hydroxides. In addition, Fe cations could react with carbonate (CO_3^{2-}) or bicarbonate (HCO_3^-) to form $FeCO_3$ through the following pathways [126]:

$$Fe^{2+} + CO_3^{2-} \rightarrow FeCO_3 \quad (7)$$

$$Fe^{2+} + 2HCO_3^- \rightarrow Fe(HCO_3)_2 \quad (8)$$

$$Fe(HCO_3)_2 \rightarrow FeCO_3 + CO_2 + H_2O \quad (9)$$

Apart from electrochemical reactions, corrosion in s-CO_2 media may occur only through gas-chemical processes as mentioned above. During the gas-chemical corrosion, the formation of liquid water is no longer essential and H_2O dissolved in s-CO_2 could directly react with steels to form iron oxides via [88]:

$$Fe + H_2O(g) \rightarrow FeO + H_2 \quad (10)$$

$$2Fe + 3H_2O(g) \rightarrow Fe_2O_3 + 3H_2 \quad (11)$$

$$3Fe + 4H_2O(g) \rightarrow Fe_3O_4 + 4H_2 \quad (12)$$

As for the formation of $FeCO_3$, it cannot be achieved by direct reactions between Fe and CO_2 since this reaction is thermodynamically unlikely to occur at the temperature ranges of s-CO_2 transportation. The theoretical calculation shows that among different iron oxides, only FeO could react with CO_2 to form $FeCO_3$ [126].

$$FeO + CO_2 \rightarrow FeCO_3 \quad (13)$$

Currently, there is no direct evidence available to determine the dominant corrosion reaction pathway in s-CO_2 environment. Therefore, more work is required to solve this puzzle.

5.3. Improving experimental methods

Improving experimental methodologies is essential for obtaining more accurate and reliable data on corrosion rates in s-CO_2 environments. However, most previous studies have been conducted in static autoclave systems with an impeller to stir the fluid, which may not reflect real-world s-CO_2 transportation conditions accurately. In addition to flow, impurity consumption should also be considered as mentioned above. To improve reliability, experiments in a flow system are recommended to validate the findings from autoclave testing. An in-situ flow experiment setup could also be developed to estimate steel corrosion using mass-loss data, in-situ electrochemical measurements and characterization techniques, and investigate the combined effect of erosion and corrosion in the presence of a moving corrosive fluid, whether single-phase or a worse-case multiple-phase scenario. Moreover, such experiments could facilitate the definition of maximum allowable impurity limits in s-CO_2 captured from different sources. This is particularly important as gas and liquid streams could be encountered when pressure is reduced due to disrupted conditions, undesired environmental cold weather, or high impurity levels. Overall, developing more advanced and innovative experimental methods can help advance our current understanding of corrosion mechanisms in s-CO_2 environments and support the development of applicable corrosion mitigation strategies.

Received by OCD: 6/29/2026

5.4. Developing standards and towards artificial intelligence

The current review work aims to promote data sharing in the field of corrosion in s-CO_2 transportation, storage, and utilization systems. Fig. 12 presents a co-citation network of publications from the period of 2011–2021 and their citation relations using the Web of Science search engine [127]. The search employed the queries of 'Supercritical carbon dioxide' and 'corrosion' in all types of documents under the 'Topic' search. 265 records were obtained and filtered based on domain knowledge, and the resulting cluster highlights extensive research conducted on the corrosion of steels under s-CO_2 conditions. However, the complexity of the s-CO_2 environment, including multiple corrosion-influencing factors such as flow rate, exposure time, impurity types and consumption, and corrosion rate measurement methods, makes it difficult for researchers to compare and establish predictive long-term corrosion kinetic models. Therefore, it is crucial to establish an industry standard to ensure reliable and comparable experimental data.

Coelho et al. recently provided a data-oriented overview of the rapidly growing research field covering ML applied to predict electrochemical corrosion [128]. ML has been gradually applied to corrosion research studies including atmospheric corrosion, pitting corrosion, and MOC (steels and alloys) using various models [128]. Although not the focus of this paper, the corrosion community has benefited far less from developments in Big Data technologies since huge volumes of experiments and traditional predictive models are still relied on for estimating the corrosion performance of MOC. To the best of authors' knowledge, no ML model has been developed to predict the corrosion of steels in s-CO_2 environments despite a huge dataset existing. It is encouraged that corrosion researchers not only work on resolving the above-mentioned knowledge gaps, but also collaborate with computer-oriented scientists to apply ML to corrosion prediction studies. Accurate and reliable ML modelling acquires knowledge from large datasets to continuously improve its performance. Overall, efforts are needed to promote data-sharing practices.

6. Conclusions

This review presents data-driven insights into the current state of corrosion research in s-CO_2 transportation, storage and utilization systems. The following key aspects can be summarized.

1) CCUS operations are carried out under s-CO_2 conditions at varying temperatures (35–20 °C) and pressures (8–17 MPa). X-grade steels are cost-effective for constructing of s-CO_2 transportation, storage and utilization systems, but in severe corrosion scenarios, CRAs such as Cr model steels, SS, and Ni-based alloys should be considered.
2) In the s-CO_2 rich phase, severe corrosion of CS is expected when the amount of water and impurities cannot be strictly controlled. Single impurities ranked by corrosivity are $NO_x > SO_2 > H_2S > O_2$. O_2 plays a critical role in synergistic effects in CO_2–H_2O–O_2–SO_2–H_2S systems, so its level should be controlled below 1000 ppm, and other impurities should be kept below 100 ppm levels. No comprehensive corrosion work has been done in a supercritical system like CO_2–H_2O–O_2–SO_2-NO_x-H_2S.
3) In the s-CO_2 saturated H_2O phase, the corrosion process is dominated by electrochemical reactions, and the formation of a protective corrosion layer on steel is crucial in reducing corrosion. Aqueous chemistry also affects the composition and quality of the corrosion product layer. The corrosion process is either electrochemical or gas-chemical, depending on the water content in the H_2O-saturated s-CO_2 phase. EIS measurements are effective in investigating the formation, protection, and failure mechanisms of corrosion product layers in s–CO_2–saturated aqueous systems.
4) Although extensive research has been conducted on corrosion under s-CO_2 conditions, it has mostly been done in isolation, leading to diverse corrosion rates that cannot efficiently contribute to the development of universal CO_2 impurity and MOC selection standards. Four topics and research paths are discussed to facilitate the development of standards for CCUS impurity control and MOC strategy from both an engineering and fundamental perspective. It is recommended that corrosion researchers collaborate with computer-oriented scientists to develop accurate and reliable ML modelling on the corrosion of steels under s-CO_2 conditions.

Declaration of competing interest

The authors declare that they have no known competing financial interests or personal relationships that could have appeared to influence the work reported in this paper.

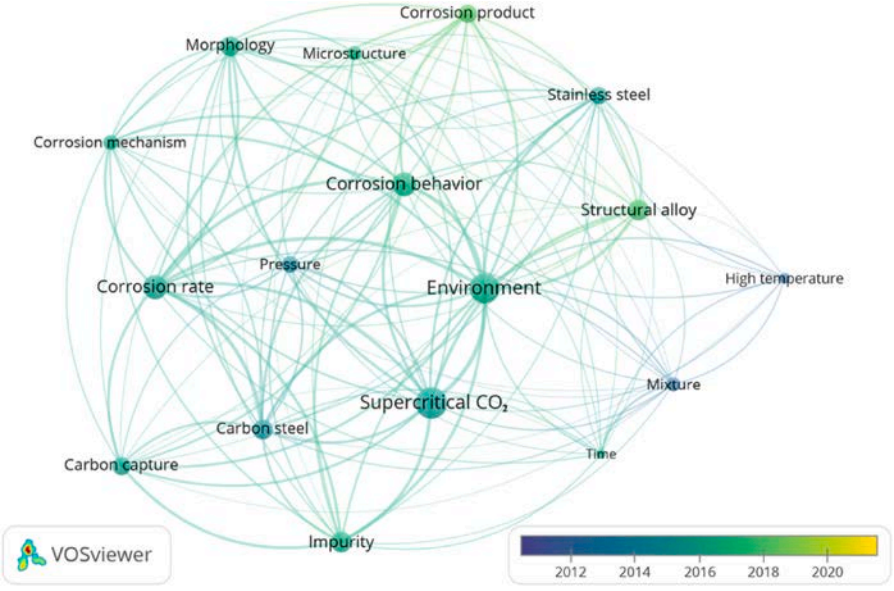


Fig. 12. Visualization of the co-citation network of 'supercritical CO_2' and 'corrosion' publications. Citation relations from 2011 to 2021 (VOSviewer [127]).

Received by OCD: 6/29/2026

Data availability

Data will be made available on request.

Acknowledgements

The authors would like to acknowledge the funding support from Natural Resource Canada Clean Energy Production and CO_2 Capture, Utilization and Storage (CCUS) programs and Natural Sciences and Engineering Research Council of Canada (NSERC).

Appendix

Table A1
Summary of studies for steel corrosion in *S*–CO_2 rich phase with impurities (data since 2011).

Material	T /°C	P /MPa	H_2O /ppmv	O_2 /ppmv	SO_2 /ppmv	NO_2 /ppmv	H_2S /ppmv	Rotation/ r/min	Time/ h	Cleaning process	Rate /mm/y	Refs.
X65	50	8	650–3000	41,250	–	–	–		24	Clarke's solution	<0.01	Choi 2011
X65	50	8	650	–	39	–	–		24		0.032	[24]
X65	50	8	650	–	39	–	–		120		0.019	
X65	50	8	650	41,250	39	–	–		24		0.025	
X65	50	8	650		10,000	–	–		24		3.48	
X65	50	8	650	41,250	10,000	–	–		24		3.70	
X65	50	8	S						24	Clarke's solution	0.4	Choi 2011 [83]
K03014	25	8	S				200		48	Clarke's solution	0.07	Choi 2016
K03014	80	12	S				200		48		0.41	[25]
1Cr	25	8	S				200		48		0.13	
1Cr	80	12	S				200		48		0.44	
3Cr	25	8	S				200		48		0.14	
3Cr	80	12	S				200		48		0.05	
X70	50	10	S	1000	2000			120	288	Clarke's solution	0.2	Xiang 2011
X70	50	10	S	1000	7000			120	288		0.7	[75]
X70	50	10	S	1000	14,000			120	288		0.85	
X70	50	10	S	1000	20,000			120	288		0.9	
99.5% Iron	50	10	S	1000	2000			120	288		0.3	
99.5% Iron	50	10	S	1000	7000			120	288		1.3	
99.5% Iron	50	10	S	1000	14,000			120	288		1.1	
99.5% Iron	50	10	S	1000	20,000			120	288		1.0	
X70	50	10	9% RH	1000	20,000			120	120	Clarke's solution	0	Xiang 2012
X70	50	10	50% RH	1000	20,000			120	120		0.04	[87]
X70	50	10	60% RH	1000	20,000			120	120		0.07	
X70	50	10	70% RH	1000	20,000			120	120		0.33	
X70	50	10	88% RH	1000	20,000			120	120		0.88	
X70	50	10	100% RH	1000	20,000			120	120		1.50	
X70	25	10	S	10,000	20,000			120	120	Clarke's solution	1.1	Xiang 2013
X70	50	10	S	10,000	20,000			120	120		2.5	[28]
X70	75	10	S	10,000	20,000			120	120		3.1	
X70	93	10	S	10,000	20,000			120	120		1.3	
X70	50	10	S	1100	20,000			120	24	Clarke's solution	1.95	Xiang 2013
X70	50	10	S	1100	20,000			120	72		1.78	[27]
X70	50	10	S	1100	20,000			120	120		1.45	
X70	50	10	S	1100	20,000			120	192		0.70	
X70	50	12	S	700	25,000			120	454	Clarke's solution	1.16	Xiang 2013
Iron	50	12	S	700	25,000			120	454		0.59	[108]
13Cr	60	8	S	52	52	52			24	Nitric acid solution	0.15	Xiang 2020
13Cr	60	8	S	52	52	52			120		0.03	[26]
13Cr	60	8	S	52	52	52			480		0.02	
13Cr	60	8	S	52	52	52		120	120		0.005	
X65	20	10	S	0					72	Not mentioned	1.1	Dugstad 2011
X65	20	10	S						336		0.8	[89]
X65	20	10	S	100					336		1.3	
X65	50	10	S						336		2.7	
X65	50	10	S	200					432		0.6	
X65	50	10	S						48–96		3	
X65	50	10	S					1 m/s	48–96		33	
X65	50	10	S					3 m/s	48–96		38	
X65	25	10	488		100			3	336	Not mentioned	<0.005	Dugstad 2013
X65	25	10	488		344			3	336		<0.005	[77]
X65	25	10	1220		344			3	336		0.02	
X65	25	10	1220			478		3	240		1.6	
X65	25	10	1220			191		3	240		0.67	
X65	25	10	488			191		3	480		0.06	

(*continued on next page*)

Received by OCD: 6/29/2026

Table A1 (*continued*)

Material	T /°C	P /MPa	H_2O /ppmv	O_2 /ppmv	SO_2 /ppmv	NO_2 /ppmv	H_2S /ppmv	Rotation/ r/min	Time/ h	Cleaning process	Rate /mm/y	Refs.
X65	25	10	488			96		3	72		0.17	
X65	25	10	488		138	191		3	168		0.017	
L360NB	60	11	100	47,000	70				168		0.003	Paschke 2012
L360NB	60	11	600	47,000	70				168		0.024	[95]
L360NB	60	11	1000	47,000	70				168		0.051	
L485MB	60	11	100	47,000	70				168		0.019	
L485MB	60	11	600	47,000	70				168		0.031	
L485MB	60	11	1000	47,000	70				168		0.072	
X42	35	8							110	10% HCl solution	0.020	Collier 2013
X60	35	8							110		0.021	[101]
316 L	35	8							110		0.0012	
304 L	35	8							110		0.00086	
X42	35	8	S						120		0.016	
X60	35	8	S						120		0.019	
316 L	35	8	S						120		0.0015	
304 L	35	8	S						120		0.0024	
X42	35	8	S					100	120		0.014	
X60	35	8	S					100	120		0.011	
316 L	35	8	S					100	120		0.00052	
304 L	35	8	S					100	120		0.0024	
X42	35	8	1818					100	120		0.0066	
X60	35	8	1818					100	120		0.0073	
316 L	35	8	1818					100	120		0.00080	
304 L	35	8	1818					100	120		0.00046	
X42	35	8	S	30,000				100	120		0.032	
X60	35	8	S	30,000				100	120		0.026	
316 L	35	8	S	30,000				100	120		0.0028	
304 L	35	8	S	30,000				100	120		0.0031	
X42	50	10	S	30,000				100	120		0.099	
X60	50	10	S	30,000				100	120		0.093	
316 L	50	10	S	30,000				100	120		0.0042	
304 L	50	10	S	30,000				100	120		0.0032	
X65	50	8	650		500				24	Clarke's solution	0.05	Farelas 2013
X65	50	8	650		1000				24		0.03	[80]
X65	50	8	650		10,000				24		3.5	
L360NB	60	10	1000	8100	70	100			168	Not mentioned	0.00003	Yevtushenko
Iron	60	10	1000	8100	70	100			168		0.00004	2014 [129]
X52	60	10	1000	8100	70	100			168	Standard DIN 50905	0.025	Yevtushenko
X52	60	10	500	8100	70	100			720		0.004	2014 [94]
X52	60	10	600	8100	70	100			720		0.006	
X52	60	10	1000	8100	70	100			720		0.013	
1Cr	60	10	1000	8100	70	100			168		0.024	
1Cr	60	10	400	8100	70	100			720		0.001	
1Cr	60	10	600	8100	70	100			720		0.003	
1Cr	60	10	1000	8100	70	100			720		0.005	
X65	50	10	500		200			3	168	Acidic stripping solution	<0.005	Brown 2014
X65	50	10	500			50		3	24		0.127	[100]
X65	50	10	500	500		50		3	24		0.116	
X65	50	10	500			100		3	168		0.02	
X65	50	10	500	500		100		3	24		0.182	
X65	50	10	500			200		3	24		0.205	
X65	50	10	500			200		3	72		0.088	
X65	50	10	500			200		3	168		0.025	
X65	50	10	500	500		200		3	24		0.275	
X65	50	10	500	500		200		3	168		0.09	
X65	50	10	500	500				3	168		0.006	
X65	50	10	500	500				3	168		<0.005	
X65	25	12.3–14.6	S						48	HCl solution with	0.09	Cabrini 2014
X65	25	12.3–14.6	S						100	hexamethylenetetramine	0.05	[86]
X65	25	12.3–14.6	S						170		0.03	
X65	40	12.3–14.6	S						48		0.025	
X65	40	12.3–14.6	S						100		0.013	
X65	40	12.3–14.6	S						170		0.01	
X65	60	12.3–14.6	S						100		0.03	
X65	60	12.3–14.6	S						191		0.015	
X65	25	8	600						72	Clarke's solution	0.1	Jiang 2015
X65	25	8	S						72		0.38	[105]
X65	35	8	600						72		0.05	
X65	35	8	S						72		0.28	
X65	35	8	300						48	Clarke's solution	0.003	Hua 2014 [29]
X65	35	8	700						48		0.004	
X65	35	8	2800						48		0.07	
X65	35	8	S						14		0.11	
X65	35	8	S						48		0.10	
X65	50	8	1600						48		–	

(*continued on next page*)

Received by OCD: 6/29/2026

Table A1 (*continued*)

Material	T /°C	P /MPa	H_2O /ppmv	O_2 /ppmv	SO_2 /ppmv	NO_2 /ppmv	H_2S /ppmv	Rotation/ r/min	Time/ h	Cleaning process	Rate /mm/y	Refs.
X65	50	8	2650						48		0.014	
X65	35	8	S						168	Clarke's solution	0.03	Hua 2015 [107]
X65	35	8	S	20	2				48	Clarke's solution	0.105	Hua 2015 [31]
X65	35	8	S	20	50				48		0.35	
X65	35	8	S	20	100				48		0.7	
X65	50	8	S						14	Clarke's solution	0.09	Hua 2015 [84]
X65	50	8	S						24		0.03	
X65	50	8	S						48		0.024	
X65	35	8	300	20	50				48	Clarke's solution	0.0033	Hua 2015 [78]
X65	35	8	300	20	100				48		0.003	
X65	35	8	1200						48		0.01	
X65	35	8	1200	20	50				48		0.01	
X65	35	8	1200	20	100				48		0.04	
X65	35	8	1770						48		0.03	
X65	35	8	1770	20	50				48		0.03	
X65	35	8	1770	20	100				48		0.06	
X65	35	8	S	20	50				48		0.4	
X65	35	8	S	20	100				48		0.7	
X65	35	8	1770	1000					48	Clarke's solution	0.005	Hua 2015 [90]
X65	35	8	2800	1000					48		0.012	
X65	35	8	S	20					48		0.09	
X65	35	8	S	500					48		0.07	
X65	35	8	S	1000					48		0.03	
5Cr	35	8	1770	1000					48		0.002	
5Cr	35	8	2800	1000					48		0.006	
5Cr	35	8	S						48		0.125	
5Cr	35	8	S	20					48		0.12	
5Cr	35	8	S	500					48		0.04	
5Cr	35	8	S	1000					48		0.022	
X65	35	8	S		100				48	Clarke's solution	0.8	Hua 2017 [81]
X65	35	8	S	1000	100				48		1	
13Cr	35	8	S						48		0.003	
13Cr	35	8	S	1000					48		0.001	
13Cr	35	8	S		100				48		0.015	
13Cr	35	8	S	1000	100				48		0.85	
X65	35	8	S				1000		72	10% HCl solution with	0.19	Hua 2018
X65	35	10	S				1000		72	hexamethylenetetramine	0.072	[104]
X65	50	8	S				1000		72		0.032	
X65	35	8	S			50			48	Clarke's solution	0.2	Hua 2018
X65	35	8	S			100			48		0.22	[130]
X65	35	8	S	1000		50			48		0.3	
X65	35	8	S	1000		100			48		0.3	
X65	50	8	S						96	DI water	0.25	Tang 2017
X65	50	8	S	95 mg/ L					96		0.91	[85]
X65	50	8	S	475 mg/L					96		1.48	
X70	50	10	45% RH	10,000	20,000			120	72	Clarke's solution	0.03	Xu 2016 [32]
X70	50	10	50% RH	10,000	20,000			120	72		0.4	
X70	50	10	88% RH	10,000	20,000			120	72		0.9	
X70	50	10	100% RH	10,000	20,000			120	72		1.6	
X70	50	10	45% RH	1000	20,000			120	72	Clarke's solution	0.03	Xu 2017 [33]
X70	50	10	60% RH	1000	20,000			120	72		0.1	
X70	50	10	88% RH	1000	20,000			120	72		1.15	
X70	50	10	100% RH	1000	20,000			120	72		1.61	
X60	50	8	1600	1000	3000			120	72	Clarke's solution	0.02	Xu 2016 [34]
X60	50	8	2000	1000	3000			120	72		0.04	
X60	50	8	2600	1000	3000			120	72		0.1	
X60	50	8	3000	1000	3000			120	72		0.16	
X65	50	8	1600	1000	3000			120	72		0.03	
X65	50	8	2000	1000	3000			120	72		0.09	
X65	50	8	2600	1000	3000			120	72		0.21	
X65	50	8	3000	1000	3000			120	72		0.3	
X70	50	8	1600	1000	3000			120	72		0.04	
X70	50	8	2000	1000	3000			120	72		0.01	
X70	50	8	2600	1000	3000			120	72		0.09	
X70	50	8	3000	1000	3000			120	72		0.12	
X70	50	8	1600	1000	3000			120	72		0.06	
X70	50	8	2000	1000	3000			120	72		0.09	
X70	50	8	2600	1000	3000			120	72		0.30	
X70	50	8	3000	1000	3000			120	72		0.29	
X60, X65,	50	10	3000	1000	3000			120	72		0.81–0.94	

(*continued on next page*)

Received by OCD: 6/29/2026

Table A1 (*continued*)

Material	T /°C	P /MPa	H_2O /ppmv	O_2 /ppmv	SO_2 /ppmv	NO_2 /ppmv	H_2S /ppmv	Rotation/ r/min	Time/ h	Cleaning process	Rate /mm/y	Refs.
X70, X80												
X65	50	10	S						24	10% HCl solution with	0.039	Sun 2016 [97,
X65	50	10	S						120	hexamethylenetetramine	0.015	99]
X65	50	10	S	1000					24		0.078	
X65	50	10	S	1000					120		0.034	
X65	50	10	S				1000		24		0.375	
X65	50	10	S				1000		120		0.127	
X65	50	10	S		1000				24		1.86	
X65	50	10	S		1000				120		0.469	
X65	50	10	S			1000			24		1.76	
X65	50	10	S			1000			120		0.48	
X65	50	10	S	1000			1000		120		0.221	
X65	50	10	S	1000	1000				120		1.034	
X65	50	10	S		1000		1000		120		1.224	
X65	50	10	S	1000	1000		1000		120		1.439	
X65	50	10	S						240	10% HCl solution with	0.005	Sun 2016 [35]
X65	50	10	S	2000					240	hexamethylenetetramine	0.01	
X65	50	10	S				2000		240		0.05	
X65	50	10	S	2000			2000		240		0.34	
X70	50	10	S						120	10% HCl solution with	0.014	Sun 2018 [36]
X70	50	10	S	1000					120	hexamethylenetetramine	0.027	
X70	50	10	S	10,000					120		0.029	
X70	50	10	S		200				120		0.269	
X70	50	10	S		600				120		0.345	
X70	50	10	S		1000				120		0.423	
X70	50	10	S	1000	1000				120		0.842	
X65	35	8	S				1000		72	10% HCl solution with	0.19	Sun 2019
X65	35	8	S				1000	0.5 m/s	72	hexamethylenetetramine	0.25	[110]
X65	35	8	S				1000	1.0 m/s	72		0.34	
X65	35	8	S				1000	1.25 m/s	72		0.31	
X65	35	8	S				1000	1.5 m/s	72		0.19	
X65	50	8	S	1000	1000		1000		1.5	50% HCl solution with	26	Sun 2021 [37]
X65	50	8	S	1000	1000		1000		24	hexamethylenetetramine	6	
X65	50	8	S	1000	1000		1000		48		3.2	
X65	50	8	S	1000	1000		1000		72		2.6	
38Mn6/ C75	50	9.5	S					4 m/s	96	10% HCl solution with hexamethylenetetramine	0.014	Gao's Group 2011 [111]
38Mn6/ C75	80	13.5	S					4 m/s	96		0.033	
38Mn6/ C75	110	16	S					4 m/s	96		0.015	
38Mn6/ C75	130	18.2	S					4 m/s	96		0.013	
X65	50	9.5	S					4 m/s	96		0.016	
X65	80	13.5	S					4 m/s	96		0.045	
X65	110	16	S					4 m/s	96		0.018	
X65	130	18.2	S					4 m/s	96		0.015	
Cr13	50	9.5	S					4 m/s	96		0.0029	
Cr13	80	13.5	S					4 m/s	96		0.0038	
Cr13	110	16	S					4 m/s	96		0.0088	
Cr13	130	18.2	S					4 m/s	96		0.0030	
X65	80	10	S						240	DI water	0.17	Gao's Group
X65	80	10	S				50		240		0.24	2016 [98]
X70	50	10	S						240	10% HCl solution with hexamethylenetetramine	0.04–0.12	Gao's Group 2017 [82]
P110	80	10	S				Uncertain		240	10% HCl solution with	0.19	Gao's group
316 L	80	10	S				Uncertain		240	hexamethylenetetramine	0	2016 [39]
3Cr	80	10	S				Uncertain		240		0.41	
P110	80	9.5	S						96	ASTM G1-03	0.2	Gao's group
P110	80	9.5	S						168		0.35	2018 [40]
P110	80	9.5	S						288		0.4	
X70	40	10	S						48	Clarke's solution	0.06	Wang 2019
X70	40	10	S	200					48		0.09	[91]
X70	40	10	S	1000					48		0.03	
X70	40	10	S		500				48		1.10	
X70	40	10	S	200	500				48		1.24	
X70	40	10	S	1000	500				48		0.60	
X42	45	8.48	S						500	Not mentioned	0.020	Zeng 2015
X60	45	8.48	S						500		0.019	[88]
X80	45	8.48	S						500		0.021	
X100	45	8.48	S						500		0.016	
X42	45	10	S						500		0.033	
X60	45	10	S						500		0.032	
X80	45	10	S						500		0.048	

(*continued on next page*)

Received by OCD: 6/29/2026

Table A1 (*continued*)

Material	T /°C	P /MPa	H_2O /ppmv	O_2 /ppmv	SO_2 /ppmv	NO_2 /ppmv	H_2S /ppmv	Rotation/ r/min	Time/ h	Cleaning process	Rate /mm/y	Refs.
X100	45	10	S						500		0.040	
X42	45	9	S	15,555					500		0.047	
X60	45	9	S	15,555					500		0.039	
X80	45	9	S	15,555					500		0.030	
X100	45	9	S	15,555					500		0.030	
X42	45	10	S	14,000					500		0.119	
X60	45	10	S	14,000					500		0.087	
X80	45	10	S	14,000					500		0.109	
X100	45	10	S	14,000					500		0.086	
X42	45	8.3	S	33,000					500		0.017	
X60	45	8.3	S	33,000					500		0.014	
X80	45	8.3	S	33,000					500		0.017	
X100	45	8.3	S	33,000					500		0.009	
X42	45	9	S	31,250					500		0.052	
X60	45	9	S	31,250					500		0.036	
X80	45	9	S	31,250					500		0.045	
X100	45	9	S	31,250					500		0.033	
X42	45	9.9	S	28,000					500		0.165	
X60	45	9.9	S	28,000					500		0.148	
X80	45	9.9	S	28,000					500		0.163	
X100	45	9.9	S	28,000					500		0.130	
X65	45	10	S	30,000				150	120	10% HCl solution	0.04	Zeng 2020
X65	45	10	S	30,000	100				120		0.39	[79]
X65	45	10	S	30,000	100			150	120		0.55	
X70	45	10	S	30,000				150	120		0.04	
X70	45	10	S	30,000	100				120		0.24	
X70	45	10	S	30,000	100			150	120		0.60	
X80	45	10	S	30,000				150	120		0.05	
X80	45	10	S	30,000	100				120		0.22	
X80	45	10	S	30,000	100			150	120		0.62	

Table A2
Summary of studies for steel corrosion in *S*–CO_2 saturated H_2O rich phase (data since 2011).

Material	T /°C	P /MPa	O_2 /ppmv	SO_2 /ppmv	NO_2 /ppmv	H_2S /ppmv	NaCl	Rotation /r/min	Time/ h	Cleaning process	Rate /mm/ y	Refs.
X65	50	8							24	Clarke's solution	20	Choi 2011 [83]
X65	50	9.5							168	10% HCl solution with	5.0	Gao's Group
X65	80	9.5							0.5	hexamethylenetetramine	27	2011 [112]
X65	80	9.5							7		20	
X65	80	9.5							23		12	
X65	80	9.5							48		8	
X65	80	9.5							168		7.2	
X65	110	9.5							168		2.0	
X65	130	9.5							168		1.8	
38Mn6/ C75	50	9.5						4 m/s	96	Not mentioned	6	Gao's Group 2011 [111]
38Mn6/ C75	80	13.5						4 m/s	96		11	
38Mn6/ C75	110	16						4 m/s	96		8	
38Mn6/ C75	130	18.2						4 m/s	96		5	
X65	50	9.5						4 m/s	96		9	
X65	80	13.5						4 m/s	96		14	
X65	110	16						4 m/s	96		12.5	
X65	130	18.2						4 m/s	96		8.5	
Cr13	50	9.5						4 m/s	96		0.3	
Cr13	80	13.5						4 m/s	96		0.6	
Cr13	110	16						4 m/s	96		0.8	
Cr13	130	18.2						4 m/s	96		0.4	
X70	80	9.5					3.5 wt%		0.5	HCl solution with Sb_2O_3 and	119	Gao's group
X70	80	9.5					3.5 wt%		7	$SnCl_2$	49.5	2015 [106]
X70	80	9.5					3.5 wt%		12		57.4	
X70	80	9.5					3.5 wt%		24		37	
X70	80	9.5					3.5 wt%		96		7	
X70	80	9.5					3.5 wt%		168		5	
X70	80	9.5					3.5 wt%		384		1.5	

(*continued on next page*)

Received by OCD: 6/29/2026

Table A2 (*continued*)

Material	T /°C	P /MPa	O_2 /ppmv	SO_2 /ppmv	NO_2 /ppmv	H_2S /ppmv	NaCl	Rotation /r/min	Time/ h	Cleaning process	Rate /mm/ y	Refs.
X65	80	10					3.5 wt%		240	DI water	8.46	Gao's Group
X65	80	10				50	3.5 wt%		240		15.48	2016 [98]
P110	80	10				S	3.5 wt%		240	10% HCl solution with	10	Gao's group
3Cr	80	10				S			240	hexamethylenetetramine	2.2	2016 [39]
316 L	80	10				S			240		0.018	
X70	50	10							96	10% HCl solution with hexamethylenetetramine	10	Gao's Group 2017 [82]
P110	80	9.5					3.5 wt%		0.5	ASTM G1-03	84.2	Gao's group
P110	80	9.5							12		48	2018 [40]
P110	80	9.5							50		14.4	
P110	80	9.5							168		6.12	
P110	80	9.5							384		1.8	
X65	80	9.5							0.5	10% HCl solution with	28.3	Gao's group
X65	80	9.5							23	hexamethylenetetramine	12.87	2012 [113]
X65	80	9.5							48		8.5	
X65	80	9.5							96		7.35	
X65	50	9.5							168		5.0	
X65	80	9.5							168		7.26	
X65	110	9.5							168		2.0	
X65	130	9.5							168		1.9	
X65	25	12.3–14.6						180	48	HCl solution with	10	Cabrini 2014
X65	25	12.3–14.6						180	100	hexamethylenetetramine	7.5	[86]
X65	25	12.3–14.6						180	170		5.5	
X65	40	12.3–14.6						180	48		18	
X65	40	12.3–14.6						180	100		14	
X65	40	12.3–14.6						180	170		11	
X65	60	12.3–14.6						180	100		20	
X65	60	12.3–14.6						180	191		17	
X65	50	8							6.5	Clarke's solution	10.8	Hua 2015
X65	50	8							14		8.4	[84]
X65	50	8							24		6.6	
X65	50	8							48		5.0	
X65	50	8							96		4.2	
X65	60	10					35,249 ppm Cl^-		6	Clarke's solution	20	Hua 2018
X65	60	10							24		14	[30]
X65	60	10							48		7.5	
X65	60	10							96		3.8	
X65	60	10					1000 ppm Ca^{2+},		6		17.8	
X65	60	10					35,249 ppm Cl^-		24		13	
X65	60	10							48		7	
X65	60	10							96		3.8	
X65	60	10					10,000 ppm		6		16.5	
X65	60	10					Ca^{2+}, 35,249		24		11	
X65	60	10					ppm Cl^-		48		6	
X65	60	10							96		3	
X65	60	10					1000 ppm Mg^{2+},		6		21	
X65	60	10					35,249 ppm Cl^-		24		15	
X65	60	10							48		7.8	
X65	60	10							96		3.8	
X65	60	10					10,000 ppm		6		22	
X65	60	10					Mg^{2+}, 35,249		24		17.8	
X65	60	10					ppm Cl^-		48		9.2	
X65	60	10							96		5.2	
X65	60	10					1.0 wt%		192	Clarke's solution	1.5	Hua 2020
1Cr	60	10							192		1.8	[115]
3Cr	60	10							192		2.0	
5Cr	60	10							192		2.2	
N80	60	8					Simulated		24	DI water	32	Zhang's
N80	60	8					formation water	265	24		75	group 2017
N80	60	8						530	24		82	[116]
N80	60	8						795	24		84	
N80	60	8						0	96		12	
N80	60	8						530	96		24	
N80	80	8					3.0 wt%		1	10% HCl solution with	45	Zhang's
N80	80	8							12	hexamethylenetetramine	29	group 2021
N80	80	8							24		20	[131]
N80	80	8							48		14	
N80	80	8							96		8	
N80	80	8							168		6	
13Cr	60	8	52	52	52				24	Nitric acid solution	0.18	Xiang 2020
13Cr	60	8							120		0.06	[26]
13Cr	60	8							480		0.03	
13Cr	60	8						120	120		0.08	

(*continued on next page*)

Received by OCD: 6/29/2026

Table A2 (*continued*)

Material	T /°C	P /MPa	O_2 /ppmv	SO_2 /ppmv	NO_2 /ppmv	H_2S /ppmv	NaCl	Rotation /r/min	Time/ h	Cleaning process	Rate /mm/ y	Refs.
X65	50	8	1000	1000		1000	3.5 wt%		1.5	50% HCl solution with hexamethylenetetramine	21	Sun 2021 [37]
X65	50	8	1000	1000		1000			24		4	
X65	50	8	1000	1000		1000			72		2.4	

References

[1] Masson-Delmotte V, Zhai P, Pörtner HO, Roberts D, Skea J, Shukla PR. Global warming of 1.5°C. IPCC; 2018.
[2] EEA. EN01 Energy related greenhouse gas emissions. European Environment Agency; 2011.
[3] Onyebuchi VE, Kolios A, Hanak DP, Biliyok C, Manovic V. A systematic review of key challenges of CO_2 transport via pipelines. Renewable Sustainable Energy Rev 2018;81:2563–83.
[4] Hausfather Z. Global CO_2 emissions have been flat for a decade, new data reveals. CarbonBrief: CarbonBrief; 2021.
[5] Januta A. Global carbon emissions rebound to near pre-pandemic levels. Reuters; 2021.
[6] Gaurina-Međimurec N i Pašić B. Design and mechanical integrity of CO_2 injection wells. Rudarsko-Geolosko-Naftni Zb 2011;23:1–8.
[7] Melzer LS. Carbon dioxide enhanced oil recovery (CO_2 EOR): factors involved in adding carbon capture, utilization and storage (CCUS) to enhanced oil recovery. 2012.
[8] Kuuskraa VA, Godec ML, Dipietro P. CO_2 utilization from "Next Generation" CO_2 enhanced oil recovery technology. Energy Proc 2013;37:6854–66.
[9] Bonham S, Chrysostomidis L, Solsbery L. Regulatory challenges and key lessons learned from real world development of CCS projects. CO2 Capture Project 2012: 1–40.
[10] Curson N. Assessing safety risks for CO_2 pipelines. Penspen: Penspen; 2021.
[11] Chrysostomidis I, Geyer TAW, Smith A, Fedorowick J, Bohm M, Beynon E, et al. CO_2 pipeline systems: assessment of the risks and health & safery regulations. IChemE symposium series No 155 2009:411–5.
[12] Johnsen K, Helle K, Røneid S, Holt H. DNV recommended practice: design and operation of CO_2 pipelines. Energy Proc 2011;4:3032–9.
[13] Massicotte MG, Ross AL, Thompson CB. The changing legislation and regulation of carbon capture and storage: impacts on purpose, policy, and projects, vol. 49. Alberta law review; 2011.
[14] Global-Ccs-Institute. Carbon dioxide (CO_2) distribution infrastructure. Global CCS Institute; 2012.
[15] Romasheva N, Ilinova A. CCS projects: how regulatory framework influences their deployment. Resources 2019;8.
[16] Xiang Y. Corrosion issues of carbon capture, utilization, and storage. Mater Perform 2018;57:32–5.
[17] Cole IS, Corrigan P, Sim S, Birbilis N. Corrosion of pipelines used for CO_2 transport in CCS: is it a real problem? Int J Greenh Gas Control 2011;5:749–56.
[18] Sim S, Cole IS, Choi YS, Birbilis N. A review of the protection strategies against internal corrosion for the safe transport of supercritical CO_2 via steel pipelines for CCS purposes. Int J Greenh Gas Control 2014;29:185–99.
[19] Barker R, Hua Y, Neville A. Internal corrosion of carbon steel pipelines for dense-phase CO_2 transport in carbon capture and storage (CCS) – a review. Int Mater Rev 2017;62:1–31.
[20] Xiang Y, Xu M, Choi Y-S. State-of-the-art overview of pipeline steel corrosion in impure dense CO_2 for CCS transportation: mechanisms and models. Corrosion Eng Sci Technol 2017;52:485–509.
[21] Cui G, Yang Z, Liu J, Li Z. A comprehensive review of metal corrosion in a supercritical CO_2 environment. Int J Greenh Gas Control 2019;90:102814.
[22] Wang ZM, Song G-L, Zhang J. Corrosion control in CO_2 enhanced oil recovery from a perspective of multiphase fluids. Frontiers in Materials 2019;6.
[23] Choi YS, Nesic S, Young D. Effect of impurities on the corrosion behavior of CO_2 transmission pipeline steel in supercritical CO_2−Water environments. Environ Sci Technol 2010;44:9233–8.
[24] Choi YS, Nesic S. Effect of water content on the corrosion behavior of carbon steel in supercritical CO_2 phase with impurities. NACE-International Corrosion Conference Series; 2011. NACE-11377.
[25] Choi YS, Hassani S, Vu TN, Nešić S, Abas AZB. Effect of H_2S on the corrosion behavior of pipeline steels in supercritical and liquid CO_2 environments. Corrosion 2016;72:999–1009.
[26] Xiang Y, Song C, Li C, Yao E, Yan W. Characterization of 13Cr steel corrosion in simulated EOR-CCUS environment with flue gas impurities. Process Saf Environ Protect 2020;140:124–36.
[27] Xiang Y, Wang Z, Li Z, Ni WD. Effect of exposure time on the corrosion rates of X70 steel in supercritical $CO_2/SO_2/O_2/H_2O$ environments. Corrosion 2013;69: 251–8.
[28] Xiang Y, Wang Z, Li Z, Ni WD. Effect of temperature on corrosion behaviour of X70 steel in high pressure $CO_2/SO_2/O_2/H_2O$ environments. Corrosion Eng Sci Technol 2013;48:121–9.
[29] Hua Y, Barker R, Neville A. Effect of temperature on the critical water content for general and localised corrosion of X65 carbon steel in the transport of supercritical CO_2. Int J Greenh Gas Control 2014;31:48–60.
[30] Hua Y, Shamsa A, Barker R, Neville A. Protectiveness, morphology and composition of corrosion products formed on carbon steel in the presence of Cl^-, Ca^{2+} and Mg^{2+} in high pressure CO2 environments. Appl Surf Sci 2018;455: 667–82.
[31] Hua Y, Barker R, Neville A. Understanding the influence of SO_2 and O_2 on the corrosion of carbon steel in water-saturated supercritical CO_2. Corrosion 2015;71: 667–83.
[32] Xu M, Zhang Q, Yang X, Wang Z, Liu J, Li Z. Impact of surface roughness and humidity on X70 steel corrosion in supercritical CO_2 mixture with SO_2, H_2O, and O_2. J Supercrit Fluids 2016;107:286–97.
[33] Xu M, Zhang Q, Wang Z, Liu J, Li Z. Effect of high-concentration O_2 on corrosion behavior of X70 steel in water-containing supercritical CO_2 with SO_2. Corrosion 2017;73:290–302.
[34] Xu M, Li W, Zhou Y, Yang X, Wang Z, Li Z. Effect of pressure on corrosion behavior of X60, X65, X70, and X80 carbon steels in water-unsaturated supercritical CO_2 environments. Int J Greenh Gas Control 2016;51:357–68.
[35] Sun J, Sun C, Zhang G, Li X, Zhao W, Jiang T, et al. Effect of O_2 and H_2S impurities on the corrosion behavior of X65 steel in water-saturated supercritical CO_2 system. Corrosion Sci 2016;107:31–40.
[36] Sun J, Sun C, Wang Y. Effects of O_2 and SO_2 on water chemistry characteristics and corrosion behavior of X70 pipeline steel in supercritical CO_2 transport system. Ind Eng Chem Res 2018;57:2365–75.
[37] Sun C, Liu J, Sun J, Lin X, Wang Y. Probing the initial corrosion behavior of X65 steel in CCUS-EOR environments with impure supercritical CO_2 fluids. Corrosion Sci 2021;189:109585.
[38] Wei L, Zhang Y, Pang X, Gao K. Corrosion behaviors of steels under supercritical CO_2 conditions. Corrosion Rev 2015;33:151–74.
[39] Wei L, Pang X, Gao K. Corrosion of low alloy steel and stainless steel in supercritical $CO_2/H_2O/H_2S$ systems. Corrosion Sci 2016;111:637–48.
[40] Wei L, Gao K, Li Q. Corrosion of low alloy steel containing 0.5% chromium in supercritical CO_2-saturated brine and water-saturated supercritical CO_2 environments. Appl Surf Sci 2018;440:524–34.
[41] Li X, Zhang D, Liu Z, Li Z, Du C, Dong C. Materials science: share corrosion data. Nature 2015;527:441–2.
[42] Seevam PN, Race JM, Downie MJ, Hopkins P. Transporting the next generation of CO_2 for carbon, capture and storage: the Impact of impurities on supercritical CO_2 pipelines. 7th International Pipeline Conference; 2008. p. 39–51. 2008.
[43] Dooley JJ, Dahowski RT, Davidson CL. Comparing existing pipeline networks with the potential scale of future U.S. CO_2 pipeline networks. Energy Proc 2009;1: 1595–602.
[44] Koornneef J, Ramírez A, Turkenburg W, Faaij A. The environmental impact and risk assessment of CO_2 capture, transport and storage – an evaluation of the knowledge base. Prog Energy Combust Sci 2012;38:62–86.
[45] Eldevik F, Graver B, Torbergsen LE, Saugerud OT. Development of a guideline for safe, reliable and cost efficient transmission of CO_2 in pipelines. Energy Proc 2009;1:1579–85.
[46] Polytec. Draft report – preparation for workshop 'best practice pipeline transmission of CO_2. Norway: Haugesund; 2008.
[47] Jung W, Nicot JP. Impurities in CO_2 - rich mixtures impact CO_2 pipeline design: implications for calculating CO_2 transport capacity. SPE International Conference on CO2 Capture, Storage, and Utilization; 2010. SPE-139712-MS.
[48] Wetenhall B, Race J, Downie M. The effect of impurities on a simplified CCS network. In: PSIG Annual Meeting; 2013. PSIG-1306.
[49] Global-Ccs-Institute. The global status of CCS. Global CCS Institute; 2017.
[50] Lucci A, Demofonti G, Tudori P, Spinelli CM. CCTS (carbon capture transportation & storage) transportation issues. The Twenty-first International Offshore and Polar Engineering Conference; 2011. ISOPE-I-11-162.
[51] Wang J, Ryan D, Anthony EJ, Wildgust N, Aiken T. Effects of impurities on CO_2 transport, injection and storage. Energy Proc 2011;4:3071–8.
[52] Verma S, Oakes CS, Chugunov N, Ramakrishnan TS. Effect of contaminants on the thermodynamic properties of CO_2 -rich fluids and ramifications in the design of surface and injection facilities for geologic CO_2 sequestration. Energy Proc 2011; 4:2340–7.
[53] Lovseth SW, Skaugen G, Jacob Stang HG, Jakobsen JP, Wilhelmsen Ø, Span R, et al. CO_2 mix project: experimental determination of thermo physical properties of CO_2-rich mixtures. Energy Proc 2013;37:2888–96.
[54] Serpa J, Morbee J, Tzimas E. Technical and economic characteristics of a CO_2 transmission pipeline infrastructure. European Commission Joint Research Centre Report; 2011.

Received by OCD: 6/29/2026

[55] Global-Ccs-Institute. Situation report 2012: a public report outlining the progress, lessons learnt and details of the European CCS Demonstration Project Network. Global CCS Institute; 2012.
[56] Bonis M. Managing the corrosion impact of dense phase CO_2 injection for an EOR purpose. Abu Dhabi International Petroleum Conference and Exhibition; 2012. SPE-161207-MS.
[57] Boot-Handford M, Abanades J, Anthony E, Blunt M, Brandani S, Mac Dowell N, et al. Carbon capture and storage update. Energy Environ Sci 2014;7:130–89.
[58] McCollough DE, Stiles RL. Operation of the central basin CO_2 pipeline system. SPE California Regional Meeting; 1987. SPE-16329-MS.
[59] Gale J, Davison J. Transmission of CO_2—safety and economic considerations. Energy 2004;29:1319–28.
[60] de Visser E, Hendriks C, Barrio M, Mølnvik MJ, de Koeijer G, Liljemark S, et al. Dynamis CO_2 quality recommendations. Int J Greenh Gas Control 2008;2:478–84.
[61] Oosterkamp A, Ramsen J. State-of-the-art overview of CO_2 pipeline transport with relevance to offshore pipelines. 2008.
[62] National-Energy-Technology-Laboratory. Carbon dioxide enhanced oil recovery. National Energy Technology Laboratory U. S. Department of Energy; 2010.
[63] Millet C, Mallick D, Néel G, Faramar L, Amoli AM. Material integrity aspects of CCS: an overview for CO_2 transport and storage. Trondheim CCS Conference; 2021.
[64] Meyer JP, Solutions C. Summary of carbon dioxide enhanced oil recovery (CO_2EOR) injection well technology. 2009.
[65] Yu H, Fu W, Zhang Y, Lu X, Cheng S, Xie Q, et al. Experimental study on EOR performance of CO_2-based flooding methods on tight oil. Fuel 2021;290:119988.
[66] AlQuraishi AA, AlHussinan SN, AlYami HQ. Efficiency and recovery mechanisms of low salinity water flooding in sandstone and carbonate reservoirs. In: Offshore Mediterranean Conference and Exhibition; 2015. OMC-2015-223.
[67] Nasralla RA, Alotaibi MB, Nasr-El-Din HA. Efficiency of oil recovery by low salinity water flooding in sandstone reservoirs. SPE Western North American Region Meeting; 2011. SPE-144602-MS.
[68] Austad T, Shariatpanahi SF, Strand S, Black CJJ, Webb KJ. Conditions for a low-salinity enhanced oil recovery (EOR) effect in carbonate oil reservoirs. Energy Fuels 2012;26:569–75.
[69] Selem AM, Agenet N, Gao Y, Raeini AQ, Blunt MJ, Bijeljic B. Pore-scale imaging and analysis of low salinity waterflooding in a heterogeneous carbonate rock at reservoir conditions. Sci Rep 2021;11:15063.
[70] Shi Y, Miller C, Mohanty K. Surfactant-aided low-salinity waterflooding for low-temperature carbonate reservoirs. SPE J 2021;26:2214–30.
[71] Ayirala SCC, Yousef AAA. A state-of-the-art review to develop injection-water-chemistry requirement guidelines for IOR/EOR projects. SPE Prod Oper 2015;30:26–42.
[72] Jordan M, Mackay E. Predicting and managing inorganic scale associated with produced water from EOR projects. SPE Latin American and Caribbean Petroleum Engineering Conference; 2015. p. D011S05R03.
[73] Denny AJ. Principles and prevention of corrosion. Prentice Hall; 1996.
[74] Thodla R, Francois A, Sridhar N. Materials performance in supercritical CO_2 environments. Corrosion 2009;2009. NACE-09255.
[75] Xiang Y, Wang Z, Xu C, Zhou C, Li Z, Ni W. Impact of SO_2 concentration on the corrosion rate of X70 steel and iron in water-saturated supercritical CO_2 mixed with SO_2. J Supercrit Fluids 2011;58:286–94.
[76] Russick EM, Poulter GA, Adkins CLJ, Sorensen NR. Corrosive effects of supercritical carbon dioxide and cosolvents on metals. J Supercrit Fluids 1996;9:43–50.
[77] Dugstad A, Halseid M, Morland B. Effect of SO_2 and NO_2 on corrosion and solid formation in dense phase CO_2 pipelines. Energy Proc 2013;37:2877–87.
[78] Hua Y, Barker R, Neville A. The influence of SO_2 on the tolerable water content to avoid pipeline corrosion during the transportation of supercritical CO_2. Int J Greenh Gas Control 2015;37:412–23.
[79] Zeng Y, Li K. Influence of SO_2 on the corrosion and stress corrosion cracking susceptibility of supercritical CO_2 transportation pipelines. Corrosion Sci 2020;165:108404.
[80] Farelas F, Choi YS, Nešić S. Corrosion behavior of API 5L X65 carbon steel under supercritical and liquid carbon dioxide phases in the presence of water and sulfur dioxide. Corrosion 2013;69:243–50.
[81] Hua Y, Jonnalagadda R, Zhang L, Neville A, Barker R. Assessment of general and localized corrosion behavior of X65 and 13Cr steels in water-saturated supercritical CO_2 environments with SO_2/O_2. Int J Greenh Gas Control 2017;64:126–36.
[82] Wei L, Pang X, Zhou M, Gao K. Effect of exposure angle on the corrosion behavior of X70 steel under supercritical CO_2 and gaseous CO_2 environments. Corrosion Sci 2017;121:57–71.
[83] Choi YS, Nesic S. Determining the corrosive potential of CO_2 transport pipeline in high pCO_2–water environments. Int J Greenh Gas Control 2011;5:788–97.
[84] Hua Y, Barker R, Neville A. Comparison of corrosion behaviour for X-65 carbon steel in supercritical CO_2-saturated water and water-saturated/unsaturated supercritical CO_2. J Supercrit Fluids 2015;97:224–37.
[85] Tang Y, Guo XP, Zhang GA. Corrosion behaviour of X65 carbon steel in supercritical-CO_2 containing H_2O and O_2 in carbon capture and storage (CCS) technology. Corrosion Sci 2017;118:118–28.
[86] Cabrini M, Lorenzi S, Pastore T, Radaelli M. Corrosion rate of high CO_2 pressure pipeline steel for carbon capture transport and storage. Corrosion 2014;106:21–7.
[87] Xiang Y, Wang Z, Yang X, Li Z, Ni W. The upper limit of moisture content for supercritical CO_2 pipeline transport. J Supercrit Fluids 2012;67:14–21.
[88] Zeng Y, Pang X, Shi C, Arafin M, Zavadil R, Collier J. Influence of impurities on corrosion performance of pipeline steels in supercritical carbon dioxide. Corrosion 2015;2015. NACE-2015-5755.
[89] Dugstad A, Morland B, Clausen S. Corrosion of transport pipelines for CO_2–Effect of water ingress. Energy Proc 2011;4:3063–70.
[90] Hua Y, Barker R, Neville A. The effect of O_2 content on the corrosion behaviour of X65 and 5Cr in water-containing supercritical CO_2 environments. Appl Surf Sci 2015;356:499–511.
[91] Wang W, Shen K, Tang S, Shen R, Parker T, Wang Q. Synergistic effect of O_2 and SO_2 gas impurities on X70 steel corrosion in water-saturated supercritical CO_2. Process Saf Environ Protect 2019;130:57–66.
[92] Li K, Zeng Y, Luo JL. Influence of H_2S on the general corrosion and sulfide stress cracking of pipelines steels for supercritical CO_2 transportation. Corrosion Sci 2021;190:109639.
[93] Xiang Y, Li C, Long Z, Guan C, Wang W, Hesitao W. Electrochemical behavior of valve steel in a CO_2/sulfurous acid solution. Electrochim Acta 2017;258:909–18.
[94] Yevtushenko O, Bä ßler R. Water impact on corrosion resistance of pipeline steels in circulating supercritical CO_2 with SO_2- and NO_2- impurities. Corrosion 2014;2014. NACE-2014-3838.
[95] Paschke B, Kather A. Corrosion of pipeline and compressor materials due to impurities in separated CO_2 from fossil-fuelled power plants. Energy Proc 2012;23:207–15.
[96] Zeng Y, Luo J, Li K, Arafin M. Impacts of impurities on corrosion of supercritical CO_2 transportation pipeline steels. Corrosion 2018;2018. NACE-2018-11481.
[97] Sun C, Sun J, Wang Y, Lin X, Li X, Cheng X, et al. Synergistic effect of O_2, H_2S and SO_2 impurities on the corrosion behavior of X65 steel in water-saturated supercritical CO_2 system. Corrosion Sci 2016;107:193–203.
[98] Wei L, Pang X, Gao K. Effect of small amount of H_2S on the corrosion behavior of carbon steel in the dynamic supercritical CO_2 environments. Corrosion Sci 2016;103:132–44.
[99] Sun C, Wang Y, Sun J, Lin X, Li X, Liu H, et al. Effect of impurity on the corrosion behavior of X65 steel in water-saturated supercritical CO_2 system. J Supercrit Fluids 2016;116:70–82.
[100] Brown J, Graver B, Gulbrandsen E, Dugstad A, Morland B. Update of DNV recommended practice RP-j202 with focus on CO_2 corrosion with impurities. Energy Proc 2014;63:2432–41.
[101] Collier J, Papavinasam S, Li J, Shi C, Liu P, Gravel JP. Effect of impurities on the corrosion performance of steels in supercritical carbon dioxide: optimization of experimental procedure. Corrosion 2013;2013. NACE-2013-357.
[102] Sandana D, Dale M, Charles EA, Race J. Transport of gaseous and dense carbon dioxide in pipelines. Is there an internal stress corrosion cracking risk? Corrosion 2013;2013. NACE-2013-516.
[103] Cole I, Paterson DA, Corrigan P, Sim S, Birbilis N. State of the aqueous phase in liquid and supercritical CO_2 as relevant to CCS pipelines. Int J Greenh Gas Control 2012;7:82–8.
[104] Sui P, Sun J, Hua Y, Liu H, Zhou M, Zhang Y, et al. Effect of temperature and pressure on corrosion behavior of X65 carbon steel in water-saturated CO_2 transport environments mixed with H_2S. Int J Greenh Gas Control 2018;73:60–9.
[105] Jiang X, Qu D, Song X, Liu X, Zhang Y. Impact of water content on corrosion behavior of CO_2 transportation pipeline. Corrosion 2015;2015. NACE-2015-5844.
[106] Wei L, Pang X, Liu C, Gao K. Formation mechanism and protective property of corrosion product scale on X70 steel under supercritical CO_2 environment. Corrosion Sci 2015;100:404–20.
[107] Hua Y, Barker R, Charpentier T, Ward M, Neville A. Relating iron carbonate morphology to corrosion characteristics for water-saturated supercritical CO_2 systems. J Supercrit Fluids 2015;98:183–93.
[108] Xiang Y, Wang Z, Li Z, Ni W. Long term corrosion of X70 steel and iron in humid supercritical CO_2 with SO_2 and O_2 impurities. Corrosion Eng Sci Technol 2013;48:395–8.
[109] Kairy SK, Zhou S, Turnbull A, Hinds G. Corrosion of pipeline steel in dense phase CO_2 containing impurities: a critical review of test methodologies. Corrosion Sci 2023;214:110986.
[110] Sui P, Sun C, Hua Y, Sun J, Wang Y. The influence of flow rate on corrosion behavior of X65 carbon steel in water-saturated supercritical CO_2/H_2S system. CORROSION 2019 2019. NACE-2019-13081.
[111] Zhang Y, Gao K, Schmitt G. Water effect on steel under supercritical CO_2 condition. CORROSION 2011; 2011. NACE-11378.
[112] Zhang Y, Pang X, Qu S, Li X, Gao K. The relationship between fracture toughness of CO_2 corrosion scale and corrosion rate of X65 pipeline steel under supercritical CO_2 condition. Int J Greenh Gas Control 2011;5:1643–50.
[113] Zhang Y, Pang X, Qu S, Li X, Gao K. Discussion of the CO_2 corrosion mechanism between low partial pressure and supercritical condition. Corrosion Sci 2012;59:186–97.
[114] Pfennig A, Kranzmann A. Effect of CO_2 and pressure on the stability of steels with different amounts of chromium in saline water. Corrosion Sci 2012;65:441–52.
[115] Hua Y, Mohammed S, Barker R, Neville A. Comparisons of corrosion behaviour for X65 and low Cr steels in high pressure CO_2-saturated brine. J Mater Sci Technol 2020;41:21–32.
[116] Zhang GA, Liu D, Li Yz, Guo XP. Corrosion behaviour of N80 carbon steel in formation water under dynamic supercritical CO_2 condition. Corrosion Sci 2017;120:107–20.
[117] Li YY, Wang ZZ, Guo XP, Zhang GA. Galvanic corrosion between N80 carbon steel and 13Cr stainless steel under supercritical CO_2 conditions. Corrosion Sci 2019;147:260–72.
[118] IEA. CCUS facilities in operation by application. Paris2021; 1980. 2021.

Received by OCD: 6/29/2026

[119] Mishra A. Performance of corrosion-resistant alloys in concentrated acids. Acta Metall Sin 2017;30:306–18.
[120] Liu J, Alfantazi A, Asselin E. High temperature corrosion of titanium under conditions relevant to pressure leaching: mass loss and electrochemistry. Corrosion 2014;71:352–66.
[121] Robin A, Rosa JL. Corrosion behavior of niobium, tantalum and their alloys in hot hydrochloric and phosphoric acid solutions. Int J Refract Met Hard Mater 2000; 18:13–21.
[122] Dean SW, Reiser DB. Analysis of long-term atmospheric corrosion results from ISO CORRAG program. ASTM Spec Tech Publ; 2002. p. 3–18.
[123] Francis R. The performance of stainless steels in concentrated sulphuric acid. Stainl Steel World 2009:1–4.
[124] Xiang Y, Xie W, Ni S, He X. Comparative study of A106 steel corrosion in fresh and dirty MEA solutions during the CO_2 capture process: effect of NO_3^-. Corrosion Sci 2020;167:108521.
[125] Sun JB, Zhang GA, Liu W, Lu MX. The formation mechanism of corrosion scale and electrochemical characteristic of low alloy steel in carbon dioxide-saturated solution. Corrosion Sci 2012;57:131–8.
[126] Li K, Zeng Y. Advancing the mechanistic understanding of corrosion in supercritical CO_2 with H_2O and O_2 impurities. Corrosion Sci 2023;213:110981.
[127] van Eck NJ, Waltman L. Software survey: VOSviewer, a computer program for bibliometric mapping. Scientometrics 2010;84:523–38.
[128] Coelho LB, Zhang D, Van Ingelgem Y, Steckelmacher D, Nowé A, Terryn H. Reviewing machine learning of corrosion prediction in a data-oriented perspective. npj Mater Degrad 2022;6:8.
[129] Yevtushenko O, Bäßler R, Carrillo-Salgado I. Corrosion stability of piping steels in a circulating supercritical impure CO_2 environment. Corrosion 2013;2013. NACE-2013-372.
[130] Hua Y, Neville A, Barker R. Corrosion behaviour of X65 steels in water-containing supercritical CO_2 environments with NO_2/O_2. Corrosion 2018;2018. NACE-2018-11085.
[131] Li YY, Zhu GY, Hou B, Zhang QH, Zhang GA. A numerical model based on finite element method for predicting the corrosion of carbon steel under supercritical CO_2 conditions. Process Saf Environ Protect 2021;149:866–84.

EXHIBIT 20

Ocean Engineering 362 (2026) 126251

Contents lists available at ScienceDirect

Ocean Engineering

journal homepage: www.elsevier.com/locate/oceaneng

Research paper

Mechanical integrity of cement sheath barriers in deepwater wells under earthquake-induced fault slip: A three-dimensional finite-element study for offshore geohazard conditions

Chuanying Tian [a,b,c], Hu Meng [a,b,c], Jiang Wu [d], Kai Bai [e], Kaide Zhao [a,b,c], Shuangjin Zheng [a,b,c,*]

[a] Hubei Key Laboratory of Oil and Gas Drilling and Production Engineering (Yangtze University), Wuhan, 430100, Hubei, China
[b] School of Petroleum Engineering, Yangtze University, Wuhan, 430100, Hubei, China
[c] State Key Laboratory of Low Carbon Catalysis and Carbon Dioxide Utilization (Yangtze University), Wuhan, 430100, Hubei, China
[d] CNOOC (China) Co., Ltd, Zhanjiang Branch, Zhanjiang, Guangdong, 524000, China
[e] College of Computer Science, Yangtze University, Jingzhou, Hubei, 434023, China

ARTICLE INFO

Keywords:
Deepwater well barrier
Cement sheath integrity
Offshore geohazards
Earthquake-induced fault slip
Submarine landslide
Finite-element analysis

ABSTRACT

Deepwater oil and gas wells deployed in geohazard-prone offshore settings are vulnerable to barrier-integrity degradation when earthquake-induced fault slip and associated submarine slope movement impose asymmetric shear on the casing-cement-formation system. In this study, a three-dimensional finite-element model was established to investigate the mechanical response of the near-wellbore structure under formation slip representative of deepwater seismic events. The model was used to determine radial, circumferential, and shear-related stress redistribution within the cement sheath, and cement-sheath integrity was evaluated using tensile-cracking, Mohr-Coulomb shear-failure, and interfacial-separation criteria. The results show that earthquake-induced formation displacement produces pronounced local stress concentration near the slip plane, which may induce tensile-cracking risk, local compressive-damage tendency, and interfacial separation or sliding. Parametric analyses further demonstrate that the elastic modulus and Poisson's ratio of the cement sheath, formation dip angle, and earthquake magnitude all exert strong controls on stress redistribution and failure risk. The study provides a practical mechanics-based framework for assessing well barrier integrity under offshore geohazard loading and offers guidance for cement-system selection, anti-shear cementing design, and integrity management in deepwater developments.

1. Introduction

As offshore oil and gas development continues to move into deepwater and ultra-deepwater provinces, wellbores are being placed in environments characterized by high hydrostatic pressure, low temperature, weak shallow sediments, and frequent seafloor geohazards. Under these conditions, deepwater wells are exposed to coupled loading throughout drilling, completion, production, injection/withdrawal, and abandonment or storage operations (Li et al., 2024, 2026; He et al., 2023; Wu et al., 2022). The cement sheath serves as a primary barrier for zonal isolation, fluid containment, and casing support, so its mechanical integrity is closely linked to whole-life well safety (De Andrade and Sangesland, 2016; Arjomand et al., 2018; Pandian et al., 2023; Ding et al., 2023; Ibukun et al., 2024). In many deepwater basins, complex seabed morphology, unstable slopes, slump deposits, and active faults coexist (Li et al., 2015). During earthquakes or other strong seabed disturbances, fault reactivation and submarine landslides may impose significant shear on the cement-sheath-casing-formation system. The resulting formation offset can promote shear damage, radial cracking, and interfacial debonding in the cement sheath (Du et al., 2025). If such degradation is not identified and mitigated in time, it may eventually lead to sustained annular pressure, gas migration, and severe offshore well-control consequences (Soroush, 2008; Serfat,2011; Qiao et al., 2023). For this reason, understanding the mechanical response and failure behaviour of cement sheaths under earthquake-related geological loading remains an important issue for deepwater well design and

* Corresponding author. Hubei Key Laboratory of Oil and Gas Drilling and Production Engineering (Yangtze University), Wuhan, 430100, Hubei, China.
E-mail address: 1440716797@qq.com (S. Zheng).

https://doi.org/10.1016/j.oceaneng.2026.126251
Received 9 April 2026; Received in revised form 15 May 2026; Accepted 24 May 2026
Available online 27 May 2026
0029-8018/© 2026 The Authors. Published by Elsevier Ltd. This is an open access article under the CC BY license (http://creativecommons.org/licenses/by/4.0/).

Received by OCD: 6/29/2026

integrity management.

Existing studies on cement-sheath integrity in deepwater wells have mainly examined cement bonding quality, hydrate-related hazards, pressure-temperature effects, and conventional wellbore loading (Gomar et al., 2014; Zhang et al., 2019; Zhang et al., 2021; Wu et al., 2022; Lu et al., 2023; Li et al., 2024). By contrast, the response of the cement sheath to formation-relative displacement induced by offshore fault slip and earthquake-triggered submarine landslides has received far less attention. A systematic evaluation of stress localization, shear transfer, interfacial response, and sealing consequences under such loading is still needed. In the present work, the local stress state and contact response in critical regions of the cement sheath are calculated and interpreted using measured cement strengths and Mohr-Coulomb-based integrity indices. The results are intended to support cement-system selection, anti-shear cementing design, and barrier integrity management for deepwater wells exposed to offshore geohazard loading.

The main contribution of this study is threefold. First, earthquake moment magnitude is converted into an equivalent formation-slip displacement so that offshore seismic geohazard loading can be introduced into a wellbore-scale mechanical model. Second, a three-dimensional casing-cement-formation contact model is established to capture oblique shear-displacement transfer, stress localization, and possible interfacial sliding or separation. Third, cement-sheath integrity is interpreted using combined normal-shear criteria rather than normal-stress comparison alone, thereby providing a clearer link between local mechanical damage tendency and potential well-barrier degradation.

2. Offshore geohazard loading and implications for deepwater well integrity

2.1. Seismotectonic background of deepwater offshore settings

Deepwater seismicity is closely associated with plate motion and the evolution of submarine tectonic structures (Zhao and Toyokuni, 2025; Sallarès and Ranero, 2019). On a global scale, deepwater earthquakes are concentrated mainly in subduction zones, seafloor-spreading centers along mid-ocean ridges, and passive continental margins. Compared with onshore events, earthquakes in deepwater settings occur in a more complex seafloor environment. In subduction zones, marine sediments may reach thicknesses of several kilometres and are commonly saturated with pore water; their high porosity and low shear strength make them especially susceptible to secondary hazards such as submarine sliding and tsunamis (Barnes et al., 2010). The northern continental slope of the South China Sea, which is the geological setting considered in this study, is a deepwater passive-margin system. Although the seismicity there is generally weaker than that of active subduction zones, the combined effects of intraplate extension, deep-seated fault activity, and gravity-driven sediment instability can still generate offshore earthquakes and related seabed deformation (Du et al., 2026; Hui et al.; Yi et al., 2025). Fig. 1 illustrates the recent seismic record of this region and shows that Mw 1-3 events occur repeatedly.

2.2. Fault-slip loading on the well barrier system

Submarine earthquakes along passive continental margins are commonly linked to the reactivation of normal faults developed during extensional tectonic evolution (Deng et al., 2020; Li et al., 2022; Lv et al.). Once fault slip is activated, tectonic stress is released and shear displacement may be transferred to the surrounding seabed and shallow formations, thereby imposing substantial shear loading on the cement sheath and the adjacent well barrier components (Zeng et al., 2024; Zhao et al., 2024; Tuo et al., 2025) (Fig. 2). For deepwater oil and gas developments, such seabed fault motion should be treated as an offshore integrity hazard rather than merely a geological background factor. Its influence needs to be considered explicitly in the design, assessment,

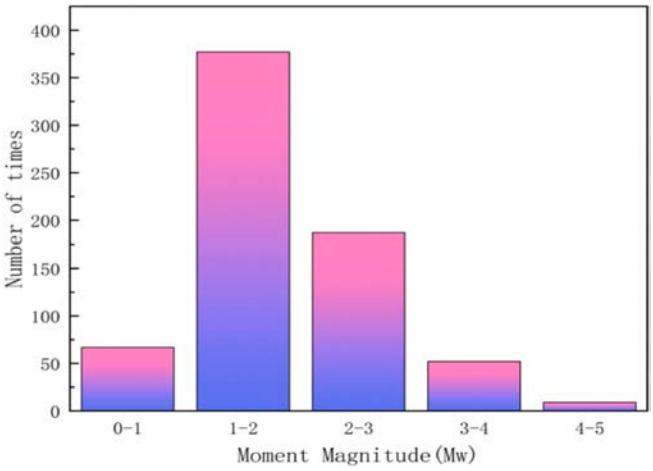


Fig. 1. Seismic records for the Hainan offshore region over the past decade.

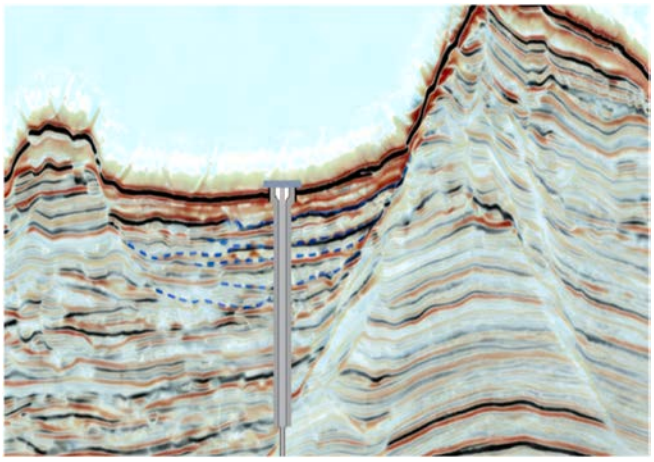


Fig. 2. Schematic illustration of fault-slip loading on the cement sheath.

and risk management of deepwater wells.

The threat posed by fault slip to cement-sheath integrity in deepwater environments is both significant and mechanically complex (Fig. 3). The dominant damage mechanisms include shear-induced failure within the cement sheath and interfacial debonding caused by formation displacement. To quantify the slip loading associated with seismic events, the moment magnitude (Mw), which is analogous in concept to the Richter scale, is used here to estimate the energy released during fault rupture.

According to seismic theory, the key parameter used to characterize fault movement is the seismic moment. The seismic moment, M0, may be defined as the quantity generated by slip within a stratum of rigidity G over a given fault area. If the average fault slip (or displacement) is L and the fault area is S, then

$$M_0 = G\,L\,c\,D^2 \tag{1}$$

where c is the fault shape factor and D is the fault dimension.

For large earthquakes, the fault may be approximated as a rectangular plane, where D is the fault length and c is the ratio of fault width to fault length (Warpinski et al., 2012). The strain generated during fault slip can be expressed as

$$\varepsilon_{xx} = \frac{\partial u_x}{\partial x} = \frac{L}{D} \tag{2}$$

The fault stress drop can then be calculated as

Received by OCD: 6/29/2026

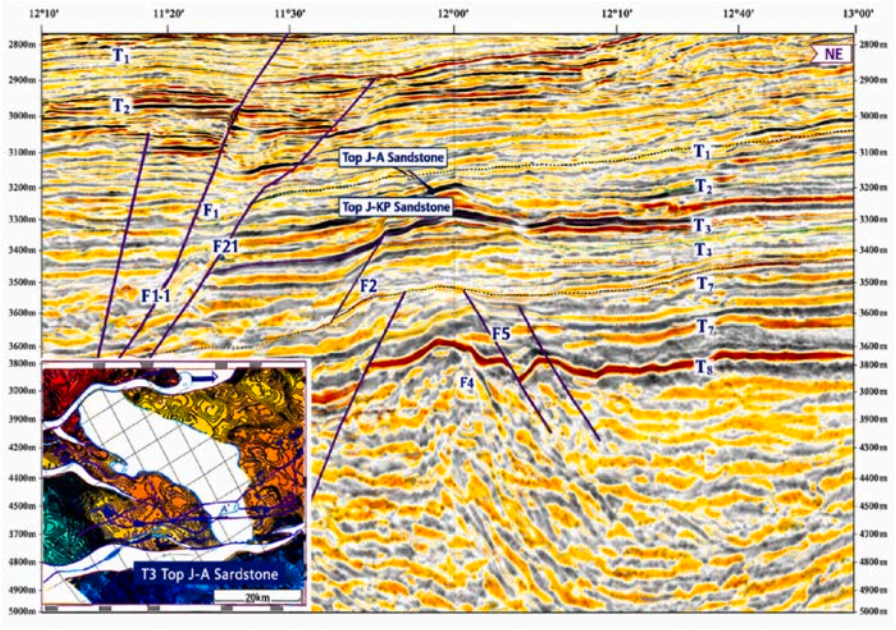


Fig. 3. Actual fault geological data of a certain well location in the South China Sea.

$$\Delta\sigma = G\cdot\varepsilon_{xx} = \frac{GL}{D} \tag{3}$$

The fault shape factor depends on the fault geometry and the slip direction. For a circular fault, the stress drop can be written in terms of the seismic moment and the fault radius as follows (Eshelby, 1957)

$$\Delta\sigma = \frac{7}{16}\frac{M_0}{r^3} \tag{4}$$

where M0 is the seismic moment, in N·m.

During fault activation, strain energy accumulates and is then released abruptly, generating seismic waves that can be used to infer stress changes. The seismic moment may therefore also be estimated from the characteristics of the recorded P- or S-wave field (Stein and Wysession, 2003)

$$M_0 = \frac{4\pi\rho_0 v_0^3 R\Omega_0}{F_c} \tag{5}$$

where ρ is the medium density, kg/m3; v0 is the propagation velocity of the P- or S-wave in the formation at the source, m/s; R is the distance from the source to the receiver, m; Ω0 is the amplitude parameter of the P- or S-wave, m·s; and Fc is the radiation pattern coefficient of the P- or S-wave, generally taken as 0.52 for P-waves and 0.63 for S-waves (Boore and Boatwright, 1984).

To describe the seismic moment on a practical engineering scale, the released energy can be expressed by moment magnitude.

The moment magnitude is calculated using the relation proposed by Hanks and Kanamori (1979):

$$M_w = \frac{2}{3}(\lg M_0 - 9.1) \tag{6}$$

where Mw is the moment magnitude of the earthquake.

By combining Eqs. (4)–(6), the fault radius and slip distance can be related to moment magnitude, stress drop, fault rigidity, and other parameters, as shown in Eqs. (7) and (8) (Stein and Wysession, 2003).

$$r = \sqrt[3]{\frac{7\times 10^{(1.5M_w+9.1)}}{16\Delta\sigma}} \tag{7}$$

$$L = \frac{16\Delta\sigma r}{7\pi G} \tag{8}$$

where r is the fault radius, in m; ρ0 is the density of the formation rock, in kg/m3; v0 is the propagation velocity of seismic waves in the formation, in m/s; R is the distance from the source to the geophone, in m; Ω0 is the displacement at the lowest frequency, in m·s; Fc is the radiation pattern coefficient; Δσ is the stress drop, in MPa; L is the fault slip distance, in m; and G is the fault shear modulus, in GPa.

Using this framework, the fault slip corresponding to moment magnitudes of 0.5, 1.0, 1.5, 2.0, and 2.5 was estimated under different stress-drop conditions. The calculated results are summarized in Table 1. These values are used as an engineering loading matrix for the local wellbore model rather than as deterministic earthquake predictions for a particular future event. In the base case adopted in the finite-element analysis, Mw = 1.0 and a stress drop of 2 MPa correspond to a prescribed formation slip of 17.37 mm. Other stress-drop values in Table 1 are retained for sensitivity analysis because offshore passive-margin earthquakes and reactivated faults may exhibit uncertain stress drops. This equivalent-displacement strategy isolates the mechanical influence of local formation offset on the casing-cement-formation system while avoiding over-interpretation of regional fault-rupture processes.

3. Three-dimensional model for deepwater well barrier integrity assessment

3.1. Model description

Based on the ABAQUS finite-element platform, this study considers a

Table 1
Calculated fault slip under different earthquake magnitudes.

Mw	Slip distance L (mm) under different stress drops				
	2 MPa	4 MPa	6 MPa	8 MPa	10 MPa
0.5	9.77	15.50	20.31	24.61	28.55
1.0	17.37	27.57	36.12	43.76	50.78
1.5	30.88	49.02	64.23	77.81	90.29
2.0	54.91	87.17	114.23	138.37	160.57
2.5	97.65	155.01	203.12	246.07	285.54

Received by OCD: 6/29/2026

local offshore disturbance scenario in which earthquake-triggered submarine slope movement or fault reactivation causes relative formation offset around a cemented casing segment. The associated loading is represented by an equivalent shear-displacement boundary condition applied to the near-wellbore system. Within this controlled loading framework, the model captures stress redistribution in the cement sheath, local deformation compatibility, contact sliding or opening, and the associated damage tendency, thereby providing quantitative support for barrier integrity evaluation and anti-shear cementing design.

A three-dimensional coupled finite-element model of the casing-cement-formation system was established to characterize the load-transfer relationship among the casing, cement sheath, and surrounding formation (Rodriguez et al., 2003; Nabipour et al., 2010). The model represents a 10 m local casing section centered on the slipping formation plane, rather than the entire wellbore. Absolute burial-depth effects are introduced through the initial in-situ stresses and internal hydrostatic pressure, while the finite geometry is used to resolve the local stress concentration and contact response near the slip plane. To retain engineering realism while maintaining computational efficiency, and to isolate the dominant mechanisms governing the response, the following idealized assumptions were adopted:

1. The formation is under a normal-faulting stress regime. The in-situ principal stresses satisfy Sv > SHmax > Shmin; Sv acts vertically, SHmax is aligned with the global X direction, and Shmin is aligned with the global Y direction. This setting reflects the stress anisotropy of deepwater formations dominated by gravity and modified by horizontal tectonic stress (Shaygan et al., 2024).
2. The formation and cement sheath are described by an elastoplastic constitutive framework. Yielding and strength are governed by the Mohr-Coulomb criterion, allowing irreversible deformation and shear-failure tendency under formation-slip loading to be represented (Xu et al., 2022).
3. The formation, cement sheath, and casing are treated as homogeneous isotropic media so that the analysis can focus on the dominant effects of shear displacement and structural/interfacial constraint on the near-wellbore stress field (Zhang et al., 2023).
4. The casing is assumed to be perfectly centralized. The casing-cement and cement-formation interfaces are initially intact, and pre-existing debonding is not introduced. During loading, however, the surface-to-surface contact formulation allows frictional sliding or normal separation to develop if the local contact conditions satisfy the corresponding criteria. This distinction enables the model to identify possible interfacial damage initiation without assuming an initially failed interface (Liu et al., 2018).
5. A hydrostatic internal pressure is applied inside the casing to represent the sustained support provided by wellbore fluids at the local section. Together with the external in-situ formation stresses, this defines the baseline loading state before the incremental earthquake-induced slip displacement is imposed. Coupled thermal, hydration, and production/injection pressure-transient effects are outside the scope of the present quasi-static mechanical model.

Under these assumptions, a three-dimensional numerical model was developed to investigate the shear response of the cement sheath under formation slip (Fig. 4). The model captures the load-transfer path induced by formation offset, the spatial distribution of local stress-concentration zones around the wellbore, and the potential locations at which cracking may initiate and propagate. It therefore provides a unified computational framework for comparing the effects of slip amplitude, loading path, and material properties on barrier integrity.

3.2. Material properties

The engineering and geological parameters used in this study were derived from field data for an oilfield block in the South China Sea. The

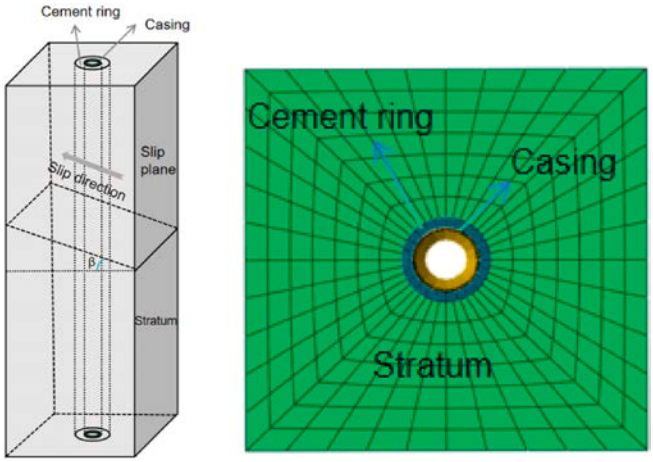


Fig. 4. Three-dimensional model of the cement sheath under formation-slip conditions.

geometric dimensions, material types, and related physical properties of the casing and cement sheath were taken from field design documents and engineering records. The formation mechanical parameters were obtained from laboratory tests on core samples, mainly including Young's modulus and Poisson's ratio. The relevant values are listed in Table 2.

In ABAQUS, the formation, cement sheath, and casing were treated as homogeneous isotropic materials so that parameter input and constitutive implementation remained transparent and controllable, while the dominant response of the near-wellbore structural system under shear loading could be highlighted. The casing was represented by a linear-elastic model described by Young's modulus and Poisson's ratio. For the formation and cement sheath, cohesion and friction angle were used to define the Mohr-Coulomb yield surface and to describe shear resistance under different confinement levels. The compressive strength of 28 MPa and tensile strength of 2.68 MPa are measured laboratory reference values for the cement slurry system; they are used as conservative screening thresholds, whereas confinement-dependent shear failure is evaluated through the Mohr-Coulomb index introduced in Section 3.6.

3.3. Mesh design

The formation domain was modeled as a 3 m × 3 m × 10 m cuboid assembled from two identical obliquely truncated rectangular prisms, so that the displacement-transfer characteristics of the surrounding rock under shear-offset conditions could be represented. The outer boundaries were placed sufficiently far from the wellbore radius to ensure that disturbances induced by loading and constraint decayed before reaching the near-wellbore control zone. In this way, the response around the wellbore becomes effectively insensitive to the exact outer-boundary position, consistent with Saint-Venant's principle.

The casing and cement sheath were idealized as two coaxial concentric cylinders in order to preserve the axisymmetric geometry of the well structure within a three-dimensional framework. Hexahedral elements were adopted and generated through a structured meshing strategy to improve element quality and numerical stability (Lee et al., 2011). Because the cylindrical wellbore had to be transitioned into the external formation block, the mesh transition zone was kept as compact as practicable in order to reduce distortion and suppress numerical amplification of local stress gradients.

After meshing, the formation domain contained 11,520 elements with a global average element size of about 0.2 m. This level of resolution maintained computational efficiency while capturing the transfer of formation shear displacement toward the near-wellbore region. The

Received by OCD: 6/29/2026

Table 2
Wellbore dimensions and material properties.

Material	Size/mm	Wall thickness/mm	Elastic modulus/GPa	Poisson's ratio	Friction angle/°	Cohesive force/MPa
Casing	254	16.13	200	0.3	—	—
Cement sheath	330.2	76.2	4.6	0.17	27.4	11.2
Stratum	3000	—	5	0.45	40.5	1

casing region comprised 4800 elements with a radial characteristic size of 0.1 m, which was sufficient for its elastic response. Because the cement sheath was the primary object of interest, a finer mesh was used in that region. The cement domain contained 22,560 elements with a minimum radial characteristic size of approximately 0.08 m. To balance the need to resolve stress concentrations against the overall computational cost, a non-uniform axial meshing scheme was adopted for the cement sheath, with refinement in the middle section and relatively coarser elements toward both ends (Fig. 5). Under this scheme, the solution showed good convergence and was able to capture local stress peaks and likely damage-initiation locations more reliably.

3.4. Contact properties and boundary conditions

The interactions between the cement sheath and casing, as well as between the formation and cement sheath, were modeled using surface-to-surface contact. This treatment is important in a three-dimensional analysis because interfacial shear transfer, sliding, and possible separation are major sources of nonlinear near-wellbore response. Shear and normal forces were transmitted through the contact interfaces. The tangential behaviour was represented by Coulomb friction, allowing relative sliding once the friction criterion was met, while the normal behaviour was modeled as hard contact to prevent interpenetration under compression and to allow separation when the contact pressure falls to zero.

For tangential contact, the friction coefficient was set to 0.15 at the cement-casing interface and 0.6 at the formation-cement interface, reflecting differences in roughness, bonding condition, and material pairing. These values define representative interface states rather than unique field constants, and their influence was examined through sensitivity analysis. In the normal direction, the hard-contact assumption implies that the interfaces remain closed and continue to transfer normal force under compression, whereas separation is permitted only when the local contact pressure vanishes and opening displacement develops.

The loading and boundary conditions were designed to represent local formation dislocation caused by earthquake-related slip. One end of the formation domain was fully constrained to provide a reference datum, while the opposite end was subjected to prescribed displacement components in the -X and -Z directions, thereby generating an oblique shear-displacement field around the wellbore (Fig. 6). The global Z direction is vertical, and the global X-Z plane contains the imposed slip vector. For a prescribed slip magnitude L and formation or fault dip angle α, the boundary displacement can be decomposed conceptually as UX = -L cos α and UZ = -L sin α; varying α therefore changes the relative horizontal and vertical components of the local shear-transfer path. This loading strategy reproduces the global shear disturbance introduced by boundary slip and provides a clear mechanical path for analysing local stress concentration, interfacial sliding, and likely damage-initiation locations in the cement sheath.

3.5. Validation of the analytical solution and finite-element model

To verify the accuracy of the finite-element model, the numerical results were compared with the composite Kirsch analytical solution. Fig. 7 shows the radial stress distributions along the $\theta = 0^\circ$ and $\theta = 90^\circ$ directions under plane-strain conditions, with both the analytical solution and the ABAQUS results presented. Good agreement is observed near the wellbore. At the casing inner wall, the radial stress matches the internal-pressure boundary condition exactly. Within the cement sheath and formation, the radial stress transitions gradually toward the in-situ formation stress with increasing radius, and the overall trend remains consistent with the analytical solution. In addition, the radial stress is continuous across the casing-cement and cement-formation interfaces, with no non-physical jumps, indicating that the model captures stress transfer in the concentric multi-material system satisfactorily. Small discrepancies appear far from the wellbore and close to the outer boundary because the finite-element model uses a finite square boundary, whereas the analytical solution assumes an infinite formation. Since this difference does not materially affect the wellbore or cement-sheath control zones, the model is considered sufficiently accurate for the present study.

A mesh-convergence analysis was performed to eliminate the

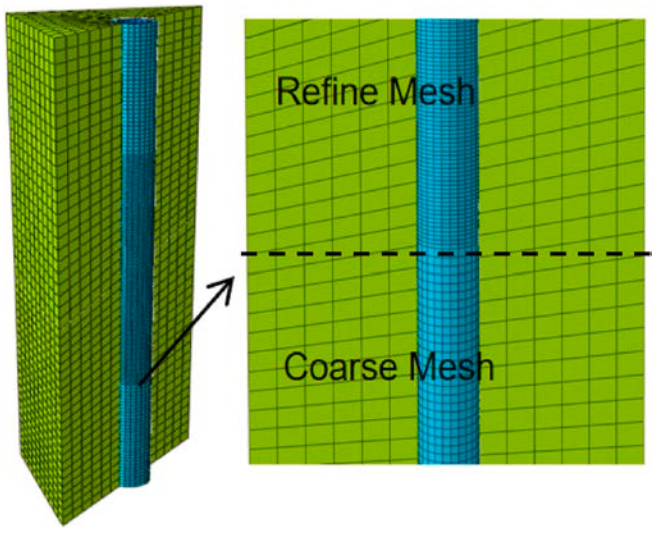


Fig. 5. Mesh model of the cement sheath.

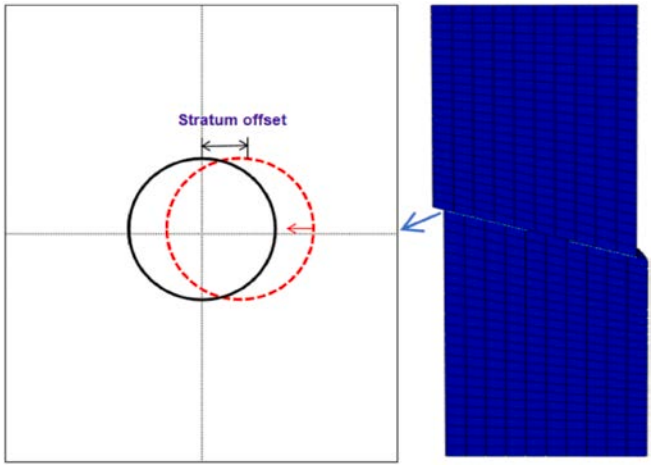


Fig. 6. Schematic diagram of cement sheath movement under prescribed formation slip.

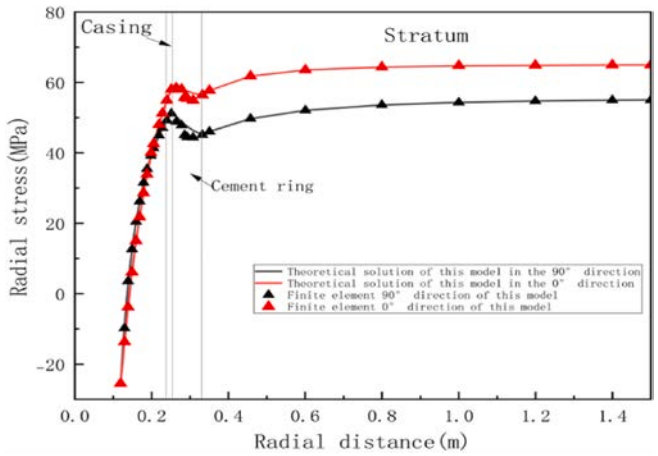


Fig. 7. Verification of the casing–cement annulus model.

influence of mesh density on the results. With the model geometry and boundary conditions unchanged, simulations were carried out using coarse, medium, and fine meshes, and the radial and hoop stresses along critical paths in the cement sheath were compared. When the element size was refined to 0.08 m, as adopted in the present model, variations in the stress response fell below 2%, demonstrating that the discretization satisfies the convergence criterion and that the computed response is essentially mesh independent.

The sensitivity of the model to key material parameters was also examined. Small perturbations of ±10% were applied to selected parameters, including the elastic modulus of the cement sheath and the friction coefficients, after which the stress distributions were recalculated. The results indicate that the model output is relatively sensitive to friction coefficients, whereas the response to reasonable variations in elastic modulus remains stable. This behaviour is physically consistent because interface friction directly controls shear transfer across the casing-cement and cement-formation boundaries. It also supports the use of the present model for comparative risk screening and design-support analysis.

3.6. Failure assessment criteria under combined normal-shear loading

Because earthquake-induced fault slip is a shear-dominated loading process, cement-sheath integrity cannot be assessed using radial or hoop normal stress alone. In this study, the radial and hoop stress components are used mainly to identify the location and extent of stress concentration in the cement sheath. The local damage tendency is further interpreted using combined normal-shear criteria, including tensile cracking, Mohr-Coulomb shear failure, and interfacial separation or sliding.

The tensile-cracking risk is evaluated by comparing the local tensile stress with the measured tensile strength of the cement sheath. The tensile-cracking index is defined as:

$$F_t = \frac{\sigma_{t,max}}{f_t} \tag{9}$$

where σt,max is the local maximum tensile stress, which may be represented by the tensile component of hoop stress or by the maximum principal tensile stress, and ft is the measured tensile strength of the cement sheath. In the present cement system, ft = 2.68 MPa. When Ft ≥ 1, local tensile cracking may initiate.

The shear-failure tendency of the cement sheath is evaluated using a Mohr-Coulomb failure index:

$$F_{MC} = \frac{\tau}{c + \sigma_n^c \tan \varphi} \tag{10}$$

where τ is the resolved shear stress on the potential failure plane, c is cohesion, φ is the internal friction angle, and σn,c is the compressive normal stress on the plane, taken as positive in compression. When FMC ≥1, the local stress state reaches the Mohr-Coulomb shear-failure envelope. Therefore, the laboratory compressive strength of 28 MPa is used only as an unconfined reference value and conservative screening threshold, rather than as a confinement-independent compressive failure strength.

For the interfacial response, separation is interpreted as a potential contact-opening risk rather than an initially assumed defect. At the casing-cement or cement-formation interface, separation is inferred when the normal contact pressure decreases to zero and contact opening develops. Frictional sliding is inferred when the tangential traction approaches the Coulomb limit:

$$\tau_{int} \geq \mu P_n \tag{11}$$

where μ is the interface friction coefficient and pn is the normal contact pressure. It should be emphasized that a local exceedance of one of these criteria indicates damage-initiation risk, but it does not necessarily imply complete loss of well integrity. Whole-well barrier integrity is considered threatened only when tensile cracking, shear damage, local crushing, or interfacial separation develops into a connected leakage path or significantly weakens zonal isolation (Guo et al., 2011; Qiao et al., 2023).

4. Stress response and damage analysis of the cement sheath

4.1. Stress state of the cement sheath

Laboratory tests on the cement-slurry system used in a South China Sea well indicate that the unconfined compressive strength and tensile strength of the cement are 28 MPa and 2.68 MPa, respectively. For a fault dip angle of 20° and a moment magnitude of Mw = 1, the ABAQUS results in Fig. 8 show that the radial and hoop stresses in the cement sheath are strongly non-uniform along the axial direction. The maximum radial compressive stress occurs close to the fault-slip plane and exceeds the unconfined compressive-strength reference value over an interval of approximately 0.45 m on both sides of the slip plane. This result indicates a strong local compression-concentration zone, but it should not be interpreted as direct evidence of compressive failure under confined conditions.

The hoop tensile stress is also concentrated near the slip plane. Within an interval of approximately 0.55 m on both sides of the slip plane, the hoop tensile stress exceeds the measured tensile strength of 2.68 MPa, indicating a local tensile-cracking risk. Therefore, the radial and hoop stress distributions are used here to identify the broader stress-concentration zone around the slip plane, rather than as the sole basis for judging cement-sheath failure.

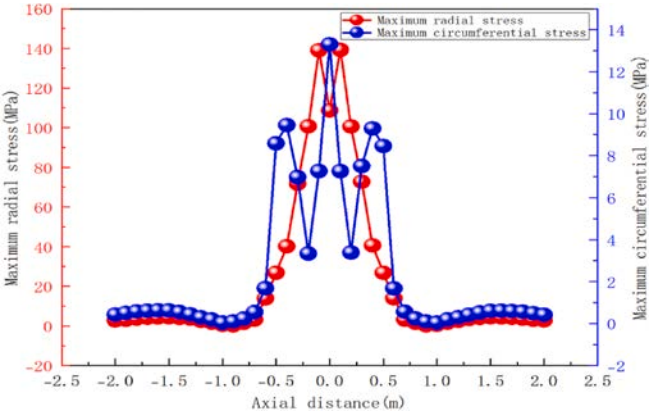


Fig. 8. Radial and hoop stresses for Mw = 1 and a formation dip of 20°.

Received by OCD: 6/29/2026

To further evaluate the shear-dominated failure tendency under fault-slip loading, the Mohr-Coulomb failure index was introduced according to Section 3.6. As shown in Fig. 9, FMC exhibits a pronounced peak near the fault-slip plane and decreases rapidly away from the slip-affected zone. Compared with the normal-stress exceedance zone of approximately 0.45-0.55 m, the zone where FMC approaches or exceeds unity is narrower and more concentrated near the slip plane. This difference occurs because the Mohr-Coulomb index depends not only on shear stress but also on confinement-dependent shear strength. Thus, the normal-stress results identify the broader stress-affected interval, whereas the FMC distribution identifies the core shear-failure risk zone.

These results indicate that even relatively small seismic slip may create localized cement-sheath damage risk through combined tensile, compressive, and shear effects. However, local stress exceedance or a high failure index should be interpreted as damage-initiation risk rather than complete loss of well integrity. Whole-well barrier integrity would be threatened only if the damaged region develops into a connected leakage pathway or significantly weakens zonal isolation.

4.2. Parametric sensitivity analysis

4.2.1. Influence of cement-sheath properties

4.2.1.1. Elastic modulus. To examine the influence of cement-sheath elastic modulus on failure behaviour, the formation dip angle was fixed at 20°, the slip distance was set to 17.37 mm, and six models were analysed with cement elastic moduli of 4, 6, 8, 10, 12, and 15 GPa.To more intuitively show the stress redistribution of cement rings with different elastic moduli, Fig. 10 presents the stress cloud map of the cement sheath. In each case, the upper row shows the radial stress distribution, and the lower row shows the circumferential stress distribution.

To assess the role of elastic modulus in the mechanical response of the cement sheath, the maximum axial radial stress and maximum axial hoop stress were extracted for each modulus case, and the corresponding axial distributions are plotted in Figs. 11 and 12. As the elastic modulus increases, the peak radial stress rises markedly, and the peak generally appears near the contact interfaces and the slip-affected middle section. In this region, geometric discontinuity, material mismatch, and boundary constraint act together to steepen the stress gradient, making it a likely location for damage initiation. By contrast, a low-modulus cement sheath can accommodate displacement incompatibility caused by casing deformation or formation squeezing through greater elastic deformation. This produces a smoother stress distribution and lowers the local risk indices.

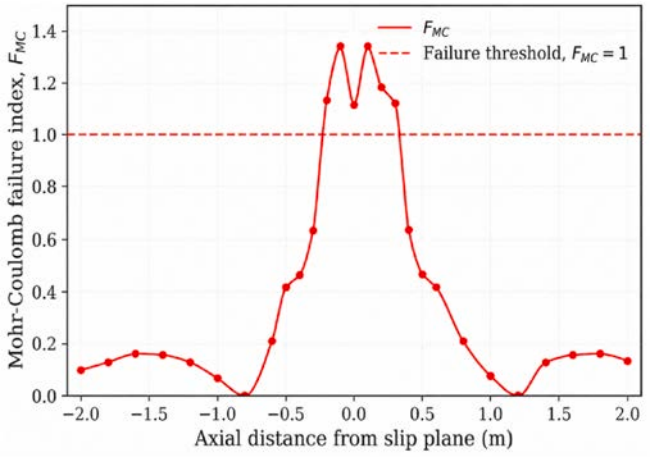


Fig. 9. Apparent Mohr-Coulomb shear-failure index estimated from the radial and hoop stress components under Mw = 1 and a formation dip angle of 20°.

At lower elastic modulus, the overall hoop-stress level is also relatively small. As the modulus increases, hoop stress rises rapidly near the interfaces, and local tensile peaks are more likely to exceed the tensile-strength-based risk threshold, thereby increasing the possibility of circumferential microcracking and sealing degradation. Although a stiffer cement sheath offers greater resistance to deformation, it can also intensify stress concentration and increase brittle-damage tendency, especially when interfacial constraint is strong or material mismatch is pronounced.

4.2.1.2. Poisson's ratio. To evaluate the influence of Poisson's ratio on cement-sheath failure, the dip angle was fixed at 20° and the slip distance at 17.37 mm, while six model groups were analysed with Poisson's ratios of 0.12, 0.15, 0.17, 0.20, 0.22, and 0.25.

The numerical results for different Poisson's ratios are shown in Figs. 13 and 14. From the radial-stress distribution, the overall axial profile remains broadly similar for all cases: a pronounced stress concentration develops near the slip plane, the peak value occurs in the central section, and the stress decays rapidly toward both ends. This indicates that, under a fixed slip boundary condition, the principal load-bearing zone of the cement sheath is controlled mainly by the local compressive load-transfer path induced by formation slip, rather than by changes in Poisson's ratio. However, as Poisson's ratio increases from 0.12 to 0.25, the peak radial stress rises gradually and the response within the high-stress central zone becomes sharper. This suggests that a higher Poisson's ratio reduces the ability of the material to accommodate dislocation through volumetric deformation and causes the compressive load to concentrate more strongly near the slip plane.

Compared with the radial stress, the maximum circumferential stress is more sensitive to changes in Poisson's ratio. In all cases, the curves exhibit a main peak in the middle section together with secondary peaks on both sides. As Poisson's ratio increases, the central peak rises more noticeably, indicating that the effect of Poisson's ratio is expressed mainly through stronger circumferential restraint. Mechanically, a larger Poisson's ratio increases the tendency for lateral deformation under radial compression. Because the cement sheath is simultaneously constrained by the casing and the surrounding formation, that circumferential deformation cannot be released freely, and higher hoop stress therefore accumulates near the slip plane. This means that increasing Poisson's ratio strengthens the additional stress response of the cement sheath under local constraint and increases the driving force for circumferential cracking.

4.2.2. Influence of formation dip angle

As the primary barrier separating formation fluids, the cement sheath must maintain long-term mechanical integrity. This requirement becomes particularly important in inclined formations, where an asymmetric in-situ stress field may substantially modify the loading environment of the cement sheath, activate more complex failure modes, and increase the risk of sustained annular pressure or casing damage. To examine the effect of formation dip on stress distribution and failure tendency, simulations were performed under the same slip loading and cement elastic modulus while the formation dip angle was varied systematically from 10° to 50°. The resulting radial and hoop stress responses were then analysed. To further visualize the stress redistribution on the inclined fault plane, the stress cloud diagrams of the cement sheath are presented in Fig. 15. In each case, the upper row shows the radial stress distribution, while the lower row shows the circumferential stress distribution.

According to the numerical results for different dip angles (Figs. 16 and 17), the maximum radial stress in the cement sheath increases as the dip angle decreases. The radial-stress distribution shows strong axial localization, with the peak occurring near the middle section at approximately 0.5 m and decaying toward both ends. In general, radial stress is much higher than hoop stress. Under the high external pressure

Received by OCD: 6/29/2026

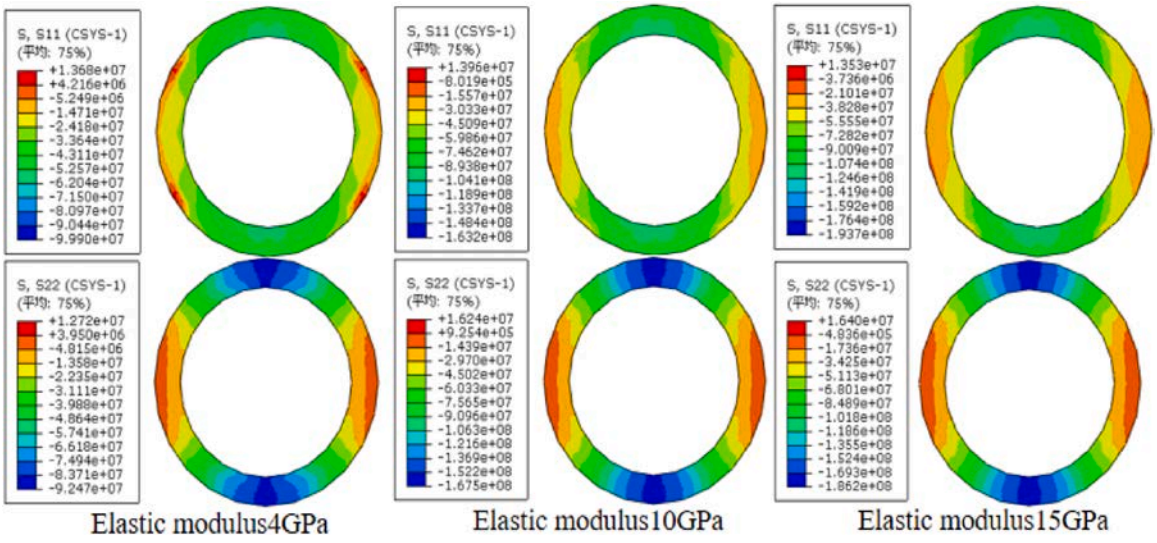


Fig. 10. Stress cloud diagram corresponding to different elastic moduli.

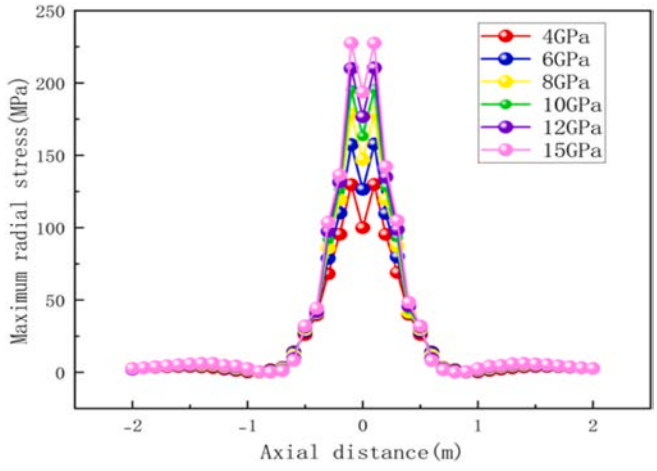


Fig. 11. Maximum radial stress along the axial distance of the cement sheath.

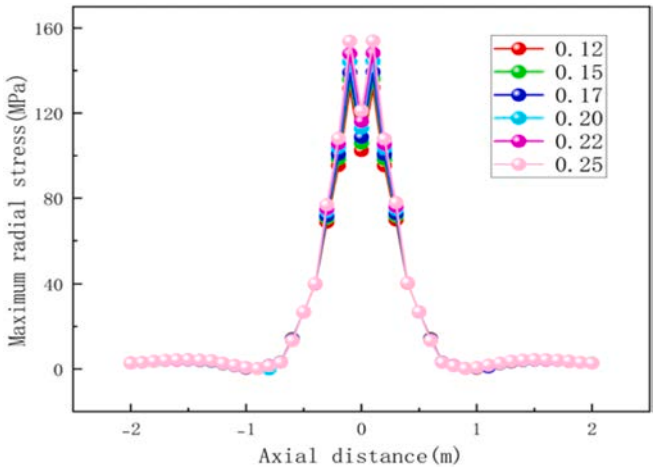


Fig. 13. Maximum radial stress along the axial distance of the cement sheath.

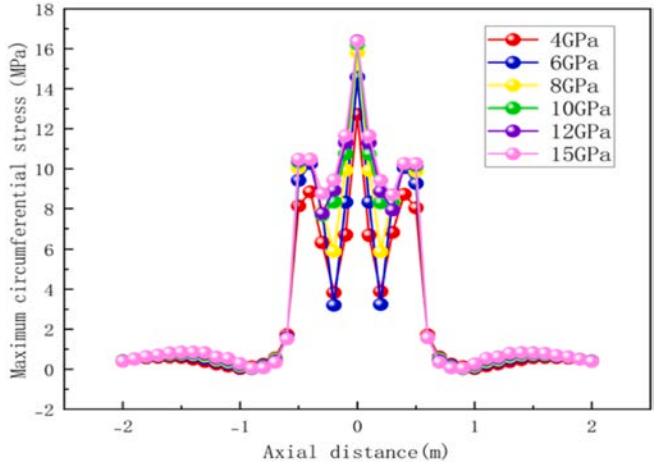


Fig. 12. Maximum circumferential stress along the axial distance of the cement sheath.

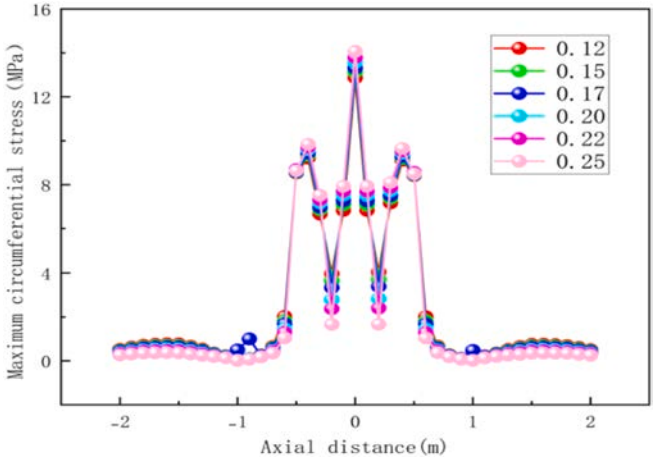


Fig. 14. Maximum circumferential stress along the axial distance of the cement sheath.

characteristic of deepwater environments and the strong confinement provided by the formation, circumferential deformation of the cement

Received by OCD: 6/29/2026

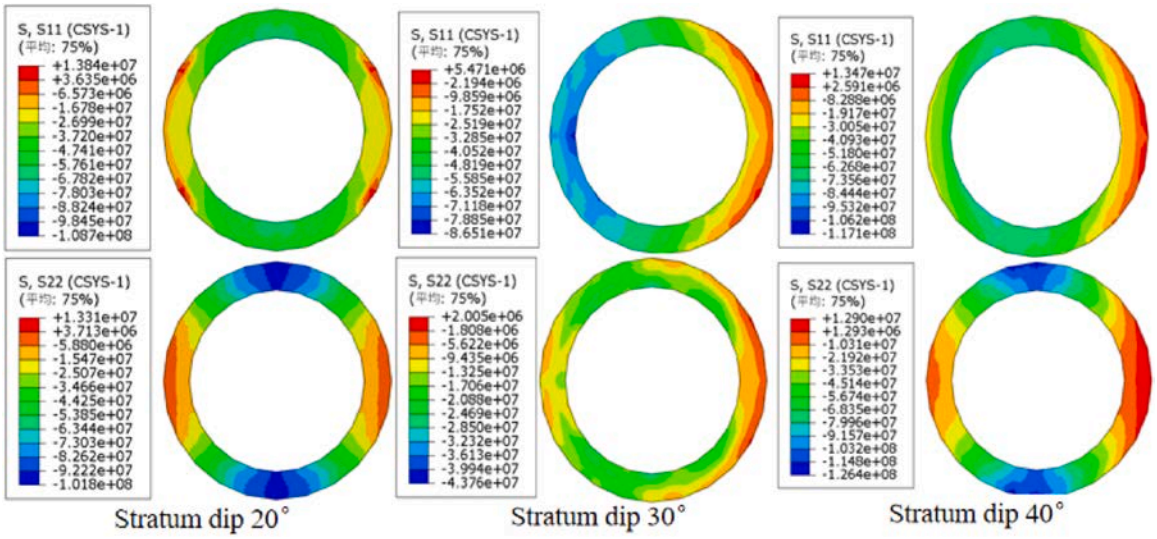


Fig. 15. Stress cloud diagrams corresponding to different inclinations.

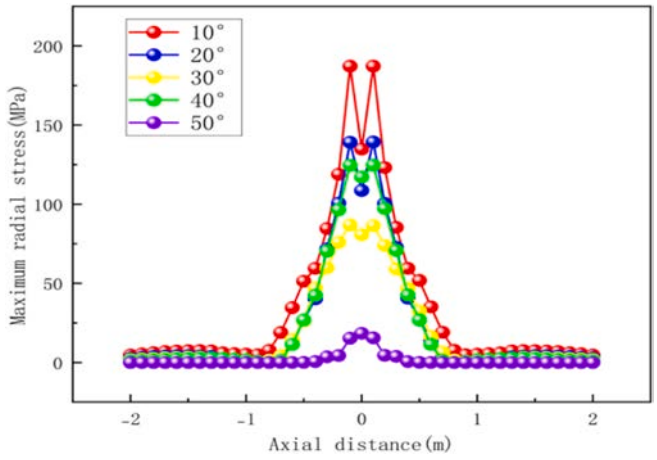


Fig. 16. Maximum radial stress along the axial distance of the cement sheath.

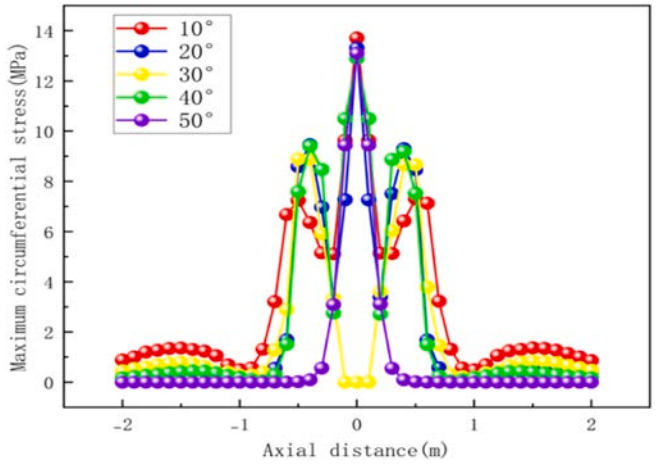


Fig. 17. Maximum circumferential stress along the axial distance of the cement sheath.

sheath is severely restricted, which leads to relatively small hoop strain and thus a lower hoop-stress level.

The middle section of the wellbore experiences the strongest constraints from the upper and lower formations, producing a fixed-end effect that limits radial deformation of the cement sheath and promotes stress concentration. The peak hoop stress shows an overall decreasing trend as the dip angle increases from 10° to 50°, with the minimum value appearing near 30° in the present model. This feature should be interpreted cautiously. A possible explanation is that, at this dip angle, the balance between interface constraint and sliding tendency partially relieves circumferential restraint; however, additional displacement contours and field-scale fault-geometry data would be required before treating this as a general rule. Overall, the stress distribution is clearly axially non-uniform, with the maximum radial stress occurring near the middle section and diminishing toward both ends.

4.2.3. *Influence of earthquake magnitude*

To quantify the effect of seismic loading on cement-sheath integrity, a predefined earthquake-slip relationship was used and finite-element simulations were performed for different moment magnitudes (Mw = 0.5, 1.0, 1.5, 2.0, and 2.5). The resulting relationship between seismic-load intensity and the internal stress state of the cement sheath provides an important basis for evaluating the risk of zonal-isolation failure. To more intuitively show the stress redistribution for different magnitudes, Fig. 18 displays the stress cloud map of the cement sheath. In each case, the upper row shows the radial stress distribution, and the lower row shows the circumferential stress distribution.

The numerical results for different earthquake magnitudes (Figs. 19 and 20) show that radial stress follows a symmetric axial distribution with high values in the middle section and lower values toward both ends, and the peak lies within the 0-0.5 m interval around the slip-affected zone. This pattern reflects the strongest structural constraint occurring near the local slip plane, where deformation is most restricted and stress concentration is therefore most likely to occur. At any given axial position, the radial stress increases monotonically with earthquake magnitude, rising from about 64 MPa at Mw = 0.5 to about 355 MPa at Mw = 2.0 in the modeled cases. Higher magnitudes correspond to larger equivalent formation slip and thus impose stronger lateral compression and shear transfer on the cement sheath.

The peak hoop stress remains lower than the peak radial stress because circumferential deformation of the cement sheath is strongly restrained by high external pressure and tight formation confinement in the local deepwater setting. According to generalized Hooke's law, hoop stress may remain relatively low even when radial stress is high if the corresponding hoop strain is very small. Under these conditions, much

Received by OCD: 6/29/2026

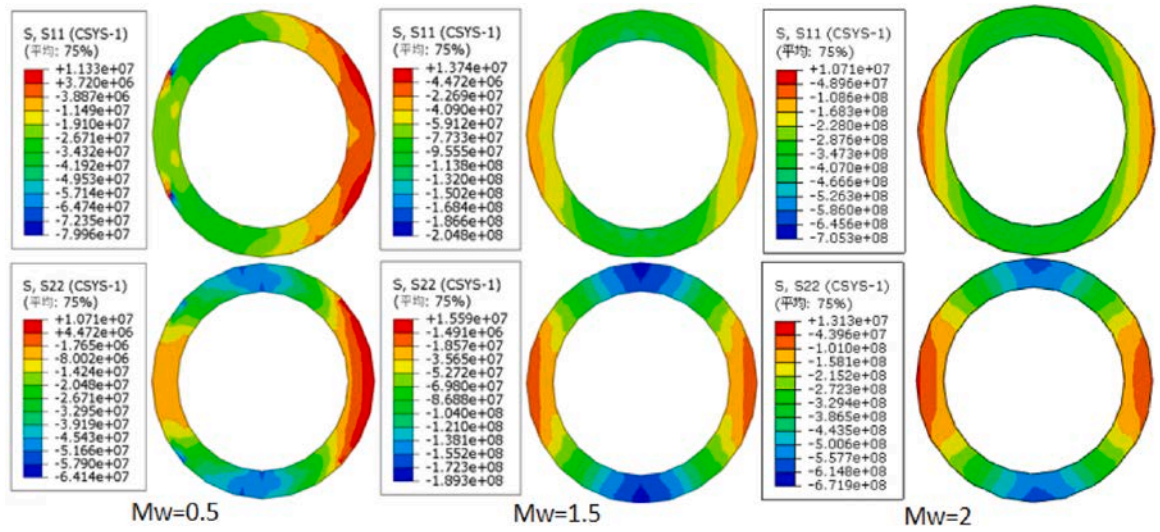


Fig. 18. Stress cloud maps corresponding to different magnitudes.

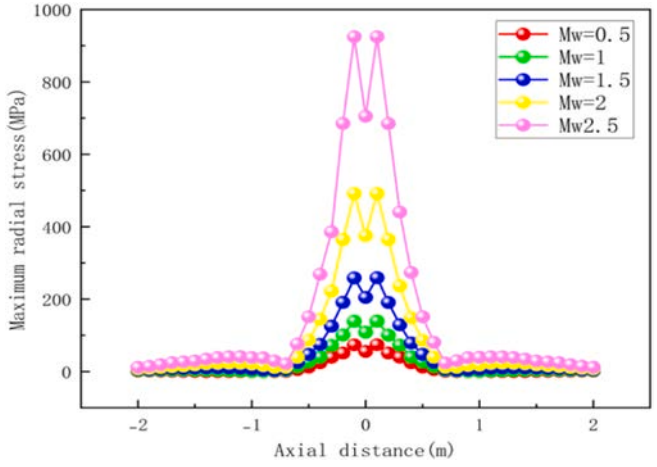


Fig. 19. Maximum radial stress along the axial distance of the cement sheath.

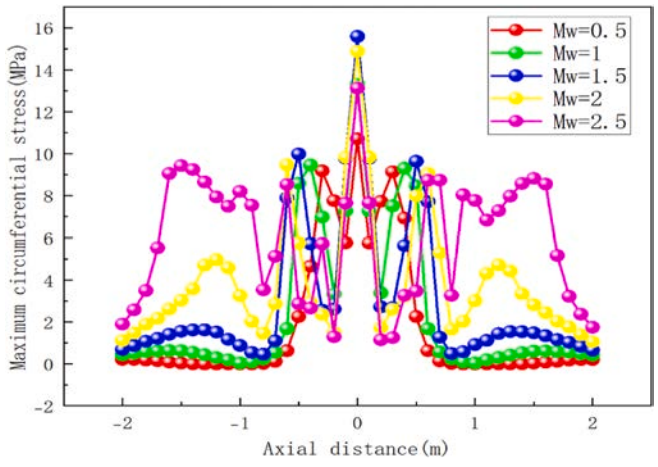


Fig. 20. Maximum circumferential stress along the axial distance of the cement sheath.

of the load is carried by radial compression and contact shear, and tensile or shear risk should be judged using the combined criteria rather than by hoop stress alone.

The hoop stress reaches its maximum at Mw = 1.5 in the present simulations. A reasonable interpretation is that, at lower magnitudes, the cement sheath remains mainly elastic or shows only incipient microdamage. As radial compression and shear transfer increase, the hoop stress required to resist deformation rises accordingly. Once the tensile or shear risk threshold is exceeded, local cracking or contact relaxation may release part of the circumferential constraint and reduce the average hoop stress. This behaviour suggests a threshold-like local damage response under increasing seismic loading, but the exact threshold should be calibrated with field-specific material and interface data.

4.3. Engineering implications and limitations

The results provide several implications for deepwater cementing design and integrity management in areas exposed to offshore geohazards. First, the slip plane and its adjacent interval should be treated as the main design and monitoring target because stress and damage indices localize strongly around this zone. In practice, geohazard screening, fault mapping, and cement-bond evaluation should be integrated before selecting well trajectories or casing-seat depths in potentially unstable slopes or reactivated fault zones.

Second, cement systems with relatively low elastic modulus and low Poisson's ratio are favourable for anti-shear cementing because they can accommodate formation-relative displacement with lower stress concentration. This does not mean that stiffness should be minimized without limit; adequate compressive strength, bonding quality, chemical durability, and long-term sealing ability are still required. The present results therefore support a balanced design strategy in which deformation capacity, interface quality, and strength are optimized together.

Third, the finite-element results can be used as screening guidance for allowable formation-slip thresholds and monitoring priorities. Zones where tensile, Mohr-Coulomb, or contact-separation indices approach unity should receive closer attention in cementing quality control, annular-pressure monitoring, and post-event integrity evaluation. If field evidence indicates larger slip, poor bonding, or strong thermal/pressure cycling, more detailed well-specific analysis is necessary.

Received by OCD: 6/29/2026

5. Conclusions

1. Earthquake-induced fault slip in deepwater offshore settings causes strong non-uniform stress concentration in the cement sheath, especially near the slip plane. This region is the most critical zone for damage initiation, where tensile cracking, local compressive damage, Mohr–Coulomb shear failure, and interfacial sliding or separation may occur. Therefore, the slip plane and its adjacent interval should be the primary focus of well barrier integrity assessment and post-earthquake monitoring.
2. The mechanical integrity of the cement sheath is strongly controlled by cement material properties and formation geometry. Higher elastic modulus and Poisson's ratio intensify radial and hoop stress concentration, increasing brittle-damage tendency. Meanwhile, the formation dip angle changes the local shear-transfer path and affects the distribution of radial and circumferential stresses. Cement systems with relatively low elastic modulus and low Poisson's ratio are therefore more suitable for anti-shear cementing, provided that strength, bonding quality, and long-term sealing performance are maintained.
3. Earthquake magnitude directly controls the equivalent formation-slip displacement and thus governs the stress level and failure risk of the cement sheath. As Mw increases, the radial stress and shear-related damage tendency increase significantly, while the hoop-stress response may show threshold-like behaviour due to local cracking or contact relaxation. The proposed three-dimensional finite-element framework provides a useful mechanics-based method for deepwater cementing design, anti-shear cement-system optimization, and well barrier integrity evaluation under offshore geohazard loading.

CRediT authorship contribution statement

Chuanying Tian: Validation, Supervision, Methodology, Funding acquisition, Formal analysis, Data curation. **Hu Meng:** Validation, Supervision. **Jiang Wu:** Investigation, Funding acquisition. **Kai Bai:** Data curation. **Kaide Zhao:** Methodology. **Shuangjin Zheng:** Resources, Project administration.

Declaration of competing interest

The authors declare that they have no known competing financial interests or personal relationships that could have appeared to influence the work reported in this paper.

On behalf of all authors, the corresponding author confirms that this declaration is accurate and has been approved by all listed authors.

Acknowledgments

This work was supported by the National Natural Science Foundation of China (Grant No. 52404002) and the Open Fund of Hubei Key Laboratory of Oil and Gas Drilling and Production Engineering (Yangtze University) (Grant No. YQZC202515).

Appendix A. Supplementary data

Supplementary data to this article can be found online at https://doi.org/10.1016/j.oceaneng.2026.126251.

References

Arjomand, E., Bennett, T., Nguyen, G.D., 2018. Evaluation of cement sheath integrity subject to enhanced pressure. J. Petrol. Sci. Eng. 170, 1–13. https://doi.org/10.1016/j.petrol.2018.06.013.

Barnes, Philip M., Lamarche, Geoffroy, Bialas, Joerg, Henrys, Stuart, Pecher, Ingo, Netzeband, Gesa L., Greinert, Jens, Mountjoy, Joshu J., Pedley, Katherine, Crutchley, Gareth, 2010. Tectonic and geological framework for gas hydrates and cold seeps on the Hikurangi subduction margin, New Zealand. Mar. Geol. 272 (1–4), 26–48. https://doi.org/10.1016/j.margeo.2009.03.012.

Boore, D.M., Boatwright, J., 1984. Average body-wave radiation coefficients. Bull. Seismol. Soc. Am. 74 (5), 1615–1621. https://doi.org/10.1785/BSSA0740051615.

De Andrade, J., Sangesland, S., 2016. Cement sheath failure mechanisms: numerical estimates to design for long-term well integrity. J. Petrol. Sci. Eng. 147, 682–698. https://doi.org/10.1016/j.petrol.2016.08.032.

Deng, H., Ren, J., Pang, X., et al., 2020. South China Sea documents the transition from wide continental rift to continental break up. Nat. Commun. 11, 4583. https://doi.org/10.1038/s41467-020-18448-y.

Ding, S., Lu, P., Guo, Y., et al., 2023. Progress and prospect on the study of full life cycle sealing integrity of cement sheath in complex environments. Pet. Drill. Tech. 51 (4), 104–113.

Du, Peng, Li, Linlin, Kopf, Achim, Wang, Dawei, Chen, Kejie, Shi, Huabin, Wang, Weitao, Pan, Xiaoyi, Hu, Gui, Zhang, Peizhen, 2025. Earthquake-induced submarine landslides (EQISLs) and a comparison with their terrestrial counterparts: insights from a new database. Earth Sci. Rev. 261, 105021. https://doi.org/10.1016/j.earscirev.2024.105021. ISSN 0012-8252.

Du, P., Li, L., Zeng, F., et al., 2026. Tsunamigenic potential of a newly identified intraplate fault on the passive continental margin of the Northwestern South China Sea. npj Nat. Hazards 3, 30. https://doi.org/10.1038/s44304-026-00185-9.

Eshelby, J.D., 1957. The determination of the elastic field of an ellipsoidal inclusion, and related problems. Proc. Roy. Soc. Lond.: Math. Phys. Eng. Sci. 241 (1226), 376–396.

Gomar, M., Goodarznia, I., Shadizadeh, S.R., 2014. A transient fully coupled thermo-poroelastic finite element analysis of wellbore stability. Arabian J. Geosci. 8 (6), 3855–3865. https://doi.org/10.1007/s12517-014-1461-4.

Guo, Q., Feng, Y.Z., Jin, Z.H., 2011. Fracture aperture for wellbore strengthening applications. Paper Presented at the 45th U. S. Rock Mechanics/Geomechanics Symposium, San Francisco, California.

Hanks, T.C., Kanamori, H., 1979. A moment magnitude scale. J. Geophys. Res. 84 (B5), 2348–2350.

He, Y., Song, B., Li, Q., 2023. Coupling submarine slope stability and wellbore stability analysis with natural gas hydrate drilling and production in submarine slope strata in the South China Sea. J. Mar. Sci. Eng. 11 (11), 2069. https://doi.org/10.3390/jmse11112069.

Gege Hui, Sanzhong Li, Lingli Guo, Pengcheng Wang, Bo Liu, Guangzeng Wang, Xiyao Li, Ian Somerville,A review of geohazards on the northern continental margin of the South China Sea,Earth Sci. Rev.,https://doi.org/10.1016/j.earscirev.2021.103733.

Ibukun, M., Elyan, E., Amish, M., Njuguna, J., Oluyemi, G.F., 2024. A review of well life cycle integrity challenges in the oil and gas industry and its implications for Sustained Casing Pressure (SCP). Energies 17 (22), 5562. https://doi.org/10.3390/en17225562.

Lee, M., Eckert, A., Nygaard, R., 2011. Mesh optimization for finite element models of wellbore stress analysis. Paper Presented at the 45th U. S. Rock Mechanics/Geomechanics Symposium, San Francisco, California.

Gang Li, Lianfu Mei, Qing Ye, Xiong Pang, Jinyun Zheng, Wendi Li,Post-rift faulting controlled by different geodynamics in the Pearl River Mouth Basin, northern South China Sea margin,Earth Sci. Rev.,https://doi.org/10.1016/j.earscirev.2022.104311.

Li, Wei, Alves, Tiago M., Wu, Shiguo, Völker, David, Zhao, Fang, 2015. Recurrent slope failure and submarine channel incision as key factors controlling reservoir potential in the South China Sea (Qiongdongnan Basin, South Hainan Island). Mar. Petrol. Geol. 64, 17–30. https://doi.org/10.1016/j.marpetgeo.2015.02.043. ISSN 0264-8172.

Li, J., Ning, B., Li, B., Qiu, D., 2024. Investigation of wellbore temperature dynamics during cement setting in deepwater shallow formations. Fluid Dynam. Mater. Process. 20 (12), 2927–2939. https://doi.org/10.32604/fdmp.2024.057388.

Li, Y., Wang, H., Yu, L., Shen, Z., Xi, Y., 2026. Failure mechanism and control method of casing shear deformation induced by fault slip during multi-stage fracturing. Petrol. Sci. Technol. 1–24. https://doi.org/10.1080/10916466.2026.2628605.

Liu, Kui, Gao, Deli, Taleghani, Arash, 2018. Impact of casing eccentricity on cement sheath. Energies 11 (10), 2557.

Lu, Z., Li, J., Lian, W., Xie, S., Wang, X., Zhang, H., Song, L., 2023. The failure mechanism and countermeasures of cement sheath in vertical section of well during hydraulic fracturing. Processes 11 (5), 1425. https://doi.org/10.3390/pr11051425.

Liangwei Lv, Zhigang Li, Dawei Wang, Weitao Wang, Xiangming Dai, Fanchang Zeng, Linlin Li, Hao Liang, Gege Hui, Weiwang Long, Peizhen Zhang,The latest activity of the slope fault zone (Pearl River Mouth) in northern South China Sea and implications for earthquake hazard assessments,Mar. Petrol. Geol.,https://doi.org/10.1016/j.marpetgeo.2024.106937.

Nabipour, A., Joodi, B., Sarmadivaleh, M., 2010. Finite element simulation of downhole stresses in deep gas Wells cements. Paper Presented at the SPE Deep Gas Conference and Exhibition, Manama, Bahrain. https://doi.org/10.2118/132156-MS.

Pandian, S., Hazarika, G., Deota, U., Shah, D., Vij, R.K., 2023. Cement-casing shear bond strength: a review of the affecting variables and various enhancement techniques. Petrol. Sci. Technol. 41 (21), 1971–1984. https://doi.org/10.1080/10916466.2022.2105356.

Qiao, Y., Skadsem, H.J., Evje, S., 2023. An integrated modeling approach for vertical gas migration along leaking Wells using a compressible two-fluid flow model. Transport Porous Media 150, 177–213. https://doi.org/10.1007/s11242-023-02005-4.

Rodriguez, W.J., Fleckenstein, W.W., Eustes, A.W., 2003. Simulation of Collapse Loads on Cemented Casing Using Finite Element Analysis SPE, 84566, pp. 1–9.

Sallarès, V., Ranero, C.R., 2019. Upper-plate rigidity determines depth-varying rupture behaviour of megathrust earthquakes. Nature 576, 96–101. https://doi.org/10.1038/s41586-019-1784-0.

Shaygan, K., Haghshenas Lari, S., Mahani, H., Jamshidi, S., 2024. Geomechanical investigation of casing collapse using finite element modeling: the role of cement

Received by OCD: 6/29/2026

sheath integrity. Geomech. Energy Environ., 212579 https://doi.org/10.1016/j.geoen.2023.212579.
Soroush, M., 2008. Underground gas storage in a partially depleted gas reservoir. J. Can. Petrol. Technol. 47 (2).
Stein, S., Wysession, M., 2003. An Introduction to Seismology, Earthquakes and Earth Structure. Blackwell Publishing Ltd., p. 512
Tuo, Y., Yu, H., Lian, Z., Lin, T., Wang, H., 2025. Impact of fault slip induced by water injection on casing deformation: a numerical study. Petrol. Sci. Technol. 43 (14), 1744–1767. https://doi.org/10.1080/10916466.2024.2356734.
W, N.R., D, J., Z, U., et al., 2012. Measurements of hydraulic-fracture-induced seismicity. In: Gas Shales: the SPE Hydraulic Fracturing Technology Conference. Society of Petroleum Engineers, The Woodlands, Texas, USA, 201219.
Wu, Y., Zhou, J., Yang, J., Qin, W., Zhang, T., Wu, Z., 2022. A study on the integrity evaluation of cement sheaths for deep Wells in deep water. Energies 15, 5814. https://doi.org/10.3390/en15165814.
Xu, F., Ren, Q., Ling, H., Yin, H., Zhou, X., Liu, Z., Yang, G., 2022. Analysis of stress state and damage characteristics of the cement sheath. Front. Energy Res. 10, 833388. https://doi.org/10.3389/fenrg.2022.833388.
Yi, H., Zhan, W., Yang, X., Li, J., Wu, X., Sun, J., Yao, Y., Huang, J., Ju, Z., 2025. Shallow structural deformation reveals intraplate seismicity triggered by graben motion in the south China Littoral fault zone. Remote Sens. 17, 2153. https://doi.org/10.3390/rs17132153.
Zeng, F., Wang, D., Li, Z., Wang, W., Dai, X., 2024. The discovery of an active fault in the Qiongdongnan Basin of the northern South China Sea. Mar. Petrol. Geol. 163, 106777. https://doi.org/10.1016/j.marpetgeo.2024.106777.
Zhang, J., Wang, J., Wang, S., Shao, S., Xiao, W., Lin, Z., 2019. Effect of stratum on the interfacial stress and structural integrity of cement sheath. In: IOP Conference Series: Materials Science and Engineering, 611. IOP Publishing, 012044. No. 1.
Zhang, Xiaoyu, Wang, Lei, Bi, Zhenhui, Guo, Yintong, Yang, Chunhe, Yang, Hanzhi, Chang, Xin, 2021. Mechanical analysis on cement sheath integrity under asymmetric load. J. Pet. Explor. Prod. Technol. 12 (1), 135–146.
Zhang, Nan, Wang, Peng, Li, Junliang, Ma, Wenhai, Zhang, Xiaochuan, Zhang, Hongtao, Jiang, Chenggang, Huang, Weiming, Feng, Xinzhu, Liu, Shuwei, 2023. A study on the mechanism of casing deformation and its control strategies in shale oil Hydraulic fracturing. Processes 11 (8), 2437.
Zhao, D., Toyokuni, G., 2025. Seismogenic structures in subduction zones. Surv. Geophys. 46, 1137–1172. https://doi.org/10.1007/s10712-025-09911-w.
Zhao, C., Jin, Y., Wang, X., 2024. Investigation on dynamic mechanism of fault slip and casing deformation during multi-fracturing in shale gas wells. Sci. Rep. 14, 13164. https://doi.org/10.1038/s41598-024-63923-x.

EXHIBIT 21

Received by OCD: 6/29/2026

CrossMark click for updates

Geomechanical behavior of the reservoir and caprock system at the In Salah CO_2 storage project

Joshua A. White[a,1], Laura Chiaramonte[a], Souheil Ezzedine[b], William Foxall[a], Yue Hao[a], Abelardo Ramirez[a], and Walt McNab[a]

[a]Atmospheric, Earth, and Energy Division and [b]Computational Engineering Division, Lawrence Livermore National Laboratory, Livermore, CA 94550

Edited by Mary Lou Zoback, Stanford University, Stanford, CA, and approved May 2, 2014 (received for review September 6, 2013)

Almost 4 million metric tons of CO_2 were injected at the In Salah CO_2 storage site between 2004 and 2011. Storage integrity at the site is provided by a 950-m-thick caprock that sits above the injection interval. This caprock consists of a number of low-permeability units that work together to limit vertical fluid migration. These are grouped into main caprock units, providing the primary seal, and lower caprock units, providing an additional buffer and some secondary storage capacity. Monitoring observations at the site indirectly suggest that pressure, and probably CO_2, have migrated upward into the lower portion of the caprock. Although there are no indications that the overall storage integrity has been compromised, these observations raise interesting questions about the geomechanical behavior of the system. Several hypotheses have been put forward to explain the measured pressure, seismic, and surface deformation behavior. These include fault leakage, flow through preexisting fractures, and the possibility that injection pressures induced hydraulic fractures. This work evaluates these hypotheses in light of the available data. We suggest that the simplest and most likely explanation for the observations is that a portion of the lower caprock was hydrofractured, although interaction with preexisting fractures may have played a significant role. There are no indications, however, that the overall storage complex has been compromised, and several independent data sets demonstrate that CO_2 is contained in the confinement zone.

carbon sequestration | geomechanics

In Salah is an industrial-scale carbon capture and storage project located in central Algeria. Between 2004 and 2011, 3.8 million metric tons of CO_2 were injected into an anticlinal structure at ∼1,800 m depth. Storage integrity at the site is provided by a massive, 950-m-thick caprock that sits above the injection interval (Fig. 1). It consists of a number of low-permeability units that work together to limit vertical fluid migration. These are grouped into main caprock units, providing the primary seal, and lower caprock units, providing an additional buffer and some secondary storage capacity.

In June 2011, injection operations halted at the site to allow reevaluation of the injection strategy (1). At the time, several monitoring observations suggested that pressure, and probably CO_2, had migrated vertically into the lower portion of the caprock. Although there are no indications that overall storage integrity has been compromised, these observations raise interesting questions about the geomechanical behavior of the reservoir and lower caprock system.

Several hypotheses have been put forward by various groups to explain these observations. These include fault leakage, flow through preexisting fractures, or the possibility that injection pressures hydraulically fractured a portion of the lower seal (2–13). In this work, we evaluate these hypotheses in light of the available data. We suggest that the most likely explanation for the observed behavior is that the lower caprock was hydrofractured, although interaction with preexisting fractures may have played a significant role. Previous studies by Bissell and colleagues (4) and Oye and colleagues (8) have shown that injectivity and microseismic data show indications of fracturing behavior, at least in the reservoir and possibly in the overburden. Here, we use well data to constrain the state of stress in the reservoir and lower caprock, providing strong support for the hydrofracture hypothesis.

This work also highlights those monitoring and analysis methods that have been most useful for understanding the field behavior, as well as lessons learned and potential improvements. This perspective can guide future carbon storage projects.

Storage Reservoir

The storage project is colocated with a large natural gas operation. The field, Krechba, has an anticlinal structure with gas accumulation at the cap (Fig. 2). The produced gas has a high CO_2 content, which must be reduced before exporting gas to the European markets (14, 15). A surface separation facility is used to remove the CO_2, after which it is reinjected through three wells into the down-dip water limbs of the anticline. The three CO_2 injectors, denoted KB-501, KB-502, and KB-503, are long-reach horizontal wells that extend for several hundred meters through the ∼20-m-thick reservoir.

Fig. 1 summarizes the major stratigraphic units at the site. The primary storage reservoir is a Carboniferous Tournasian sandstone unit (C10.2), which is overlain by a tight sandstone and siltstone unit (C10.3). Above this lies 900 m of Carboniferous Viséan mudstone (C20 units). The sealing layers below the C20.4 (the Hot Shale) are collectively referred to as the lower caprock, whereas those above are the main caprock. Above the main caprock is the Cretaceous Continental Intercalaire, a pan-Saharan aquifer and key water resource for the region (16, 17). Similar to other CO_2 storage projects, the caprock at In Salah is not a single sealing unit. Instead, a system of low-permeability barriers works together to create the confinement zone.

An advantage of colocating the injection and production wells is that data collection efforts could be leveraged by both operations

Significance

In Salah is one of the largest carbon capture and storage projects to date and has played a central role in demonstrating the feasibility of onshore sequestration of CO_2 in deep saline aquifers. The unique field experience at In Salah provides a valuable case study in managing commercial-scale CO_2 injections. In particular, the current work highlights the importance of geomechanics and integrated monitoring in understanding field behavior and managing storage risk.

Author contributions: J.A.W., L.C., S.E., W.F., Y.H., A.R., and W.M. designed research; J.A.W., L.C., S.E., W.F., Y.H., A.R., and W.M. performed research; J.A.W., L.C., S.E., W.F., Y.H., A.R., and W.M. analyzed data; and J.A.W. wrote the paper.

The authors declare no conflict of interest.

This article is a PNAS Direct Submission.

Freely available online through the PNAS open access option.

[1]To whom correspondence should be addressed. E-mail: jawhite@llnl.gov.

This article contains supporting information online at www.pnas.org/lookup/suppl/doi:10.1073/pnas.1316465111/-/DCSupplemental.

Downloaded from https://www.pnas.org by 146.115.145.114 on June 16, 2026 from IP address 146.115.145.114.

EARTH, ATMOSPHERIC, AND PLANETARY SCIENCES

Received by OCD: 6/29/2026

Downloaded from https://www.pnas.org by 146.115.145.114 on June 16, 2026 from IP address 146.115.145.114.

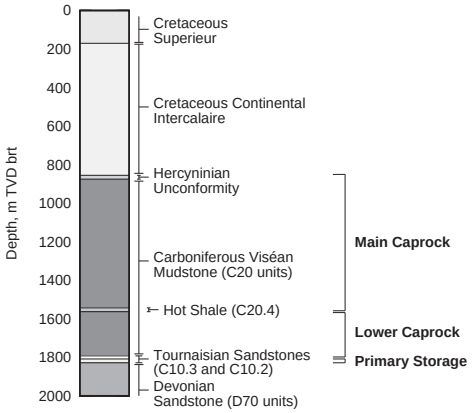


Fig. 1. Stratigraphic column with interval depths at well KB-502. Depth is given as meters of true vertical depth below the rotary table (m TVD brt) of the drilling rig, a common elevation datum in the oil and gas industry.

(3). Available data include well logs, leak-off and formation integrity tests, core measurements, 3D and time-lapse seismic, interferometric synthetic aperture radar (InSAR) monitoring of surface deformations, water quality monitoring of the shallow aquifer, and surface gas monitoring (1, 14, 18). Microseismic recording at the site is limited, however, and only comes from a single geophone string in a shallow well (KB-601). This recording was started in July 2009, well after injection operations had begun (8, 15).

Evidence of Lower Caprock Pressurization

The first interesting observation at Krechba was an earlier-than-expected breakthrough of CO_2 at well KB-5, an abandoned appraisal well 1.3 km to the northwest of KB-502. Injection at KB-502 began in April 2005, and gas reached KB-5 sometime between wellhead inspections in August 2006 and June 2007. Perfluorocarbon tracers injected at KB-502 in June 2007 were detected at KB-5 in March 2008, confirming the source of the CO_2 (19). The early breakthrough suggested that a highly permeable pathway connected the two wells.

The In Salah project was groundbreaking in its use of InSAR satellite data as a storage monitoring technology. A number of groups have demonstrated that surface deformation can be used to monitor pressure migration in the subsurface (2, 10, 20–22). Fig. 3 provides a snapshot of the measured surface deformations in March 2010. The measurements are in terms of the line-of-sight movement toward or away from the satellite (range change). Positive values indicate uplift. Significant uplift was observed above all injectors, but the deformation around KB-502 had an unusual, double-lobe pattern. A central trough is superimposed on the overall uplift, running perpendicular to the well. This trough is also parallel to the estimated present-day maximum horizontal stress (S_{Hmax} at ~135° Az). The operator was able to determine this northwest–southeast stress orientation on the basis of stress indicators in formation microimager (FMI) logs of several wells at the site. The authors have reviewed sections of these logs and concur with this interpretation. Additional stress indicators, such as focal mechanisms, are unavailable in the nearby region to further constrain S_{Hmax} orientation (23).

Vasco and colleagues (2) were the first to suggest that this unusual double-lobe pattern may be indicative of fluids migrating vertically into the lower caprock. As the reservoir was being pressurized, one would expect an approximately elliptical uplift pattern. The unusual pattern at KB-502 suggested that either the reservoir had a highly heterogeneous permeability structure that was compartmentalizing the pressure or, alternatively, pressure was migrating into the caprock. It is known that a vertical, dilating crack in an elastic half space will create trough-like deformations at the surface (Fig. 4) (24). Vasco and coworkers suggested that a plausible explanation for the double-lobe pattern was that pressure was creating dilation along a narrow vertical zone. The resulting trough was then superimposed on the elliptical uplift associated with normal reservoir pressurization.

Although the other two injectors do not show the same double-lobe morphology, a subsequent two-component inversion analysis of the same InSAR data by Rucci and colleagues (10) suggests that surface deformations above all three injectors are consistent with vertical dilation zones in the lower caprock. The estimated dilation magnitudes at the other two injectors are smaller, however, so that the reservoir pressurization overwhelms any double-lobe signature at the surface.

Two 3D seismic surveys were shot at the site: a baseline survey in 1997 and a repeat survey over the northern portion of the field in 2009 (Fig. 2) (15, 18). Using the two surveys, the operator was able to identify time-lapse differences created by injection. It should be noted that the 2009 survey was much higher quality than the 1997 survey, creating processing and interpretation challenges (18). Their analysis revealed a change in the velocity structure above KB-502. In the 2009 data, a NW-SE trending feature crosses the well and extends into the lower caprock (Fig. 5). This feature was not visible in the 1997 survey, suggesting it is a seismic velocity anomaly arising from injection-induced changes. This anomaly and the InSAR trough are perfectly aligned and correlate well with the fast migration pathway from KB-502 to KB-5. A second anomaly was also found near KB-503, with the same orientation (Fig. 5). This anomaly is most visible to the southeast of the injector, near the gas/water contact, but the lineation intersects KB-503 and is parallel to the anomaly at KB-502. KB-501 was not covered by the 2009 survey and therefore could not be analyzed. This second anomaly suggests that at least two, and maybe all three, injectors are behaving similarly. Fig. S1 provides a vertical cross-section through the anomaly at KB-502. The exact vertical extent is difficult to determine, given limited seismic resolution, but it appears to be contained within roughly 200 m of the injection interval, below the Hot Shale.

It is unclear at this point if the seismic velocity changes are caused by excess pressure, CO_2 saturation, or mechanical effects.

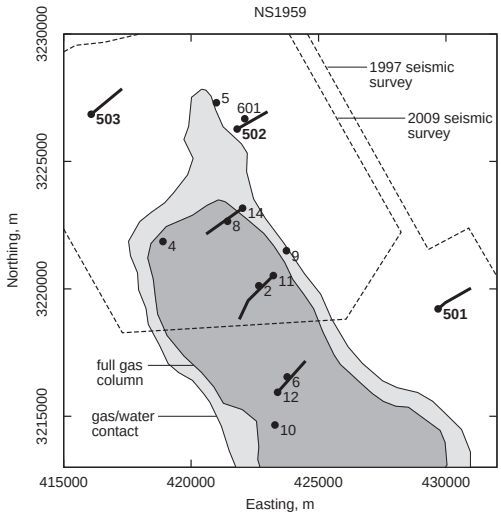


Fig. 2. Map of the Krechba field. Numbered dots denote wellhead locations. Heavy lines indicate trajectories of horizontal wells.

Received by OCD: 6/29/2026

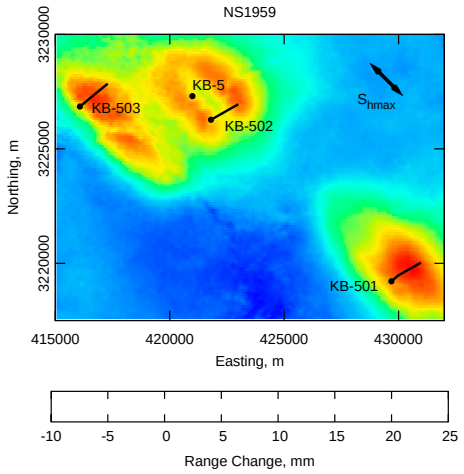


Fig. 3. InSAR measured surface deformations as of March 2010.

At the time of the 2009 survey, KB-502 had been shut-in for approximately 2 years, and the reservoir pressure had nearly returned to background. This suggests that the velocity anomalies are more likely to be a saturation and/or mechanical effect.

These field observations all provide indirect indications that fluids may have migrated vertically, but none is definitive on the mechanism. A variety of hypotheses have therefore been put forward by various groups to explain these observations. Table 1 summarizes four plausible mechanisms, along with published studies relevant to each hypothesis. The remainder of this article examines these hypotheses in greater detail and discusses the supporting and contradictory evidence. Note that these mechanisms are not mutually exclusive (except for hypothesis 1), and more than one may have occurred at the site. For example, injection pressures could have hydrofractured the lower caprock by extending and coalescing preexisting fractures (combining hypotheses 3 and 4). Finally, much of the analysis to date has focused on vertical propagation upward. For many of the proposed mechanisms, however, there are physical grounds to expect that fluids could also migrate downward into the Devonian units. For example, Morris and coworkers (5) considered both downward and upward fluid migration on a preexisting fault. For obvious reasons, however, upward movement presents a greater concern with respect to storage integrity.

It should be emphasized that neither the InSAR nor seismic data suggest that the overall storage integrity has been compromised. In addition, if a significant flow path had formed through the 950 m of caprock, a noticeable drop in reservoir pressures should have been observed (9). This has not been the case. Finally, no water quality degradation has been observed at monitoring wells in the shallow aquifer (17).

Hypothesis 1: Reservoir-Only Behavior

The first hypothesis is that all monitoring observations are consistent with excess pressure and CO_2 saturation contained in the reservoir interval. That is, there has been no vertical migration of fluids into the caprock. As suggested by Vasco and colleagues (20), it is possible that the observed surface deformations above KB-502 could result from a heterogeneous permeability distribution in the reservoir interval alone. A low-permeability zone intersecting the injector and extending to the northwest could partition the reservoir pressurization into two zones, each responsible for one of the uplift lobes. Although inversion models including a vertical dilation zone provide a better fit to the data, one can conclude that InSAR data alone are ambiguous on whether fluid migration has been contained in the reservoir.

The observed velocity anomalies, however, make hypothesis 1 less plausible. The anomalies require a mechanism to change the velocity structure of the lower caprock (i.e., pressure, saturation, and/or mechanical changes). The reservoir-only hypothesis implies the only significant changes to the caprock that have occurred are far-field geomechanical deformations. The diffuse nature of such deformations would not explain the narrow tabular zones that are observed. We therefore conclude that hypothesis 1 has a low probability. Although it cannot definitively be excluded, it does not provide a simple explanation for the similarity of the InSAR and seismic anomalies and requires a complete discounting of the seismic evidence.

Hypothesis 2: Fault Leakage

In response to indications of possible caprock damage around KB-502, much of the initial investigation focused on the potential for leakage through preexisting faults at the site (5–7). This work was motivated by a fault interpretation of the 1997 seismic survey, which suggested a fault or lineation intersecting the horizontal leg of KB-502 (Fig. 6). The strike of this lineation (120° Az) is rotated ~15° with respect to the estimated maximum horizontal stress. A later interpretation of the higher-quality 2009 survey did not pick out this same lineation. The inferred stress regime for the site is strike-slip, with the vertical stress being the intermediate stress (3). Faults with a similar orientation to the "phantom" fault from the 1997 survey could potentially be reactivated by injection pressure.

The fault interpretation was performed by the operator and is briefly described in ref. 18. It is based on reflector offsets in the seismic volume, supplemented with attribute analysis and other methods to help identify smaller features. The 20-m-thick reservoir (C10.2) is never fully offset, and all identified faults were close to the limit of resolution. The same faults are not visible at the C20.1 horizon, ~40 m above the reservoir. No substantial faults are observed in the caprock, suggesting that any faulting in the seals is minor and below seismic resolution. An important caveat is that the caprock in general contains fewer reflectors, making identification more challenging.

Drilling records for KB-502 suggest that the reservoir interval contains unobserved faults. While drilling the horizontal well section through the C10.2, cuttings and logging while drilling revealed that the well suddenly reentered the C10.3 unit. The interpretation was that the well had passed through a vertically

Table 1. Four plausible hypotheses to explain available observations

Hypothesis	References*
1. Reservoir-only behavior: Observations are consistent with excess pressure and CO_2 contained in the reservoir	12, 19, 20
2. Fault leakage: The reservoir intersects one or more faults, providing a vertical migration pathway	1–3, 5–7, 9–12, 18–20
3. Hydrofracture: Injection has created new fracture pathways, through tensile hydrofracture	1, 2, 4, 7–11, 13, 20
4. Preexisting fractures: Preexisting fractures are intrinsically permeable, or reactivated by pressure	1–4, 7–13, 18–20

*Published studies by various groups relevant to each mechanism.

Downloaded from https://www.pnas.org by 146.115.145.114 on June 16, 2026 from IP address 146.115.145.114.

EARTH, ATMOSPHERIC, AND PLANETARY SCIENCES

Downloaded from https://www.pnas.org by 146.115.145.114 on June 16, 2026 from IP address 146.115.145.114.

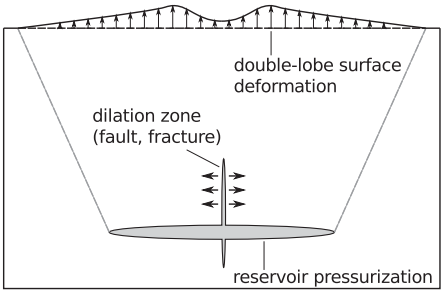


Fig. 4. Plausible mechanism to explain double-lobe deformation.

offset fault. The well was then deviated downward to once again enter the C10.2 a few hundred meters further on. This encounter occurred well away from the observed linear feature, however.

There is no indication of large-scale shear deformations in InSAR. Such deformations would likely induce asymmetric uplift patterns because of opposing lateral displacements on either side of a strike-slipping fault. Only minor asymmetry is observed, all of which can be attributed to the nonvertical look angle of the satellite. The data, rather, indicate a tensile opening mode, which could correspond to a fault zone dilating as pressurization occurs.

It is possible that the reservoir intersects one or more undetected faults that can provide a vertical leakage pathway. The consistency of observations at each injector, however, makes hypothesis 2 problematic. Seismic velocity anomalies are observed at two injectors, and InSAR data suggest all may have tensile opening in the overburden (10). The fault hypothesis would imply that all three have intersected (by chance) leaking faults that are aligned with the in situ stress field. The interpreted faults display a number of orientations but show no preferential alignment with the present-day stress field. Therefore, although still plausible, we conclude that the evidence in support of hypothesis 2 is weaker than for other explanations.

Hypothesis 3: Hydrofracture

The third possibility we examine is that injection pressures caused hydrofracturing in the reservoir and lower caprock units. Leak-off tests and formation integrity tests were performed during the drilling of all wells at the site. A step-rate test was also performed in well KB-9. These well tests can be used to estimate the minimum principal stress and fracture pressure of the formation. A detailed introduction to the test procedures and their interpretation can be found in ref. 25. Compiled test data for production wells 9–14 and injection wells 501–503 are summarized in Fig. 7. Well locations are marked in Fig. 2. To compare tests performed at different depths, all results are presented in terms of equivalent mud weight (EMW); that is, the pressure gradient, rather than the pressure itself. Hydrostatic conditions correspond to an EMW = 1.0 specific gravity (sg) = 0.1 bar/m. Furthermore, because stratigraphic contacts in different wells occur at different depths because of the anticlinal structure, we have converted the vertical depth to a height above the C10.2 interval at the given well. This allows for an easier visual comparison of Viséan and Tournaisian data points. Layer thicknesses are marked using depths from KB-502. There is some variation in layer thicknesses across the site. During drilling, significant wellbore stability issues were often encountered near the base of the C20 units, requiring an increase in mud weight. This "unstable zone" is inferred to be a layer of high tectonic stress.

The most direct measurement of fracturing behavior in the C10.2 interval comes from the step-rate test in KB-9. The raw pressure and flow rate data measured during this test are provided in Fig. S2. Summary results are included in Fig. 7 as an error bar symbol. The lowest bracket is the measured instantaneous shut-in pressure, the middle is the fracture propagation pressure, and the highest is the fracture initiation pressure. The leak-off pressure is approximately the same as the instantaneous shut-in pressure. Hollow symbols denote formation integrity test data; that is, the formation could sustain the applied pressure without leak-off. Filled symbols are tests in which leak-off was observed. There are no leak-off tests for the C10.3 interval. There is also one leak-off test in the C15 interval (filled triangle), a mudstone/limestone unit encountered over part of the field.

It should be emphasized that estimating fracture pressures from well measurements is always difficult, given limited and scattered data. These tests also have considerable uncertainties. They are influenced by drilling performance, wellbore damage, and near-wellbore fractures. They only measure behavior in a small region near the wellbore, and only the step-rate test actually exceeds the fracture initiation pressure. The tests are also performed with drilling mud, which behaves differently from low-viscosity, cold CO_2. Therefore, extrapolating these measurements to kilometer-scale behavior should be done cautiously. They can only be used as a general insight into minimum principal stress and fracturing behavior.

From the data, there appears to be a consistent EMW = 1.35 sg leak-off trend through most of the Viséan C20 caprock. In the unstable zone, there is a noticeable jump, however, to at least 1.55 sg. In the C10.3, only formation integrity test measurements are available, but one could infer a leak-off value of at least 1.6 sg. For C10.2, there is one step-rate test measurement with leak-off observed at 1.25 sg.

The data suggest that fractures could likely be initiated and propagated in sandstone and mudstone units at an EMW somewhere in the range of 1.35–1.70 sg, although the uncertainties mentioned earlier should be kept in mind. For the interval depths at KB-502, this corresponds to a pressure range of 239–301 bar at the top of the C10.2 and 237–298 bar at the top of the C10.3. Fig. 8 shows the estimated bottom-hole pressure (BHP) for KB-502. Daily-averaged values are presented for clarity, as the averaging smooths out hourly fluctuations. BHP was not measured directly, and all BHP measurements are

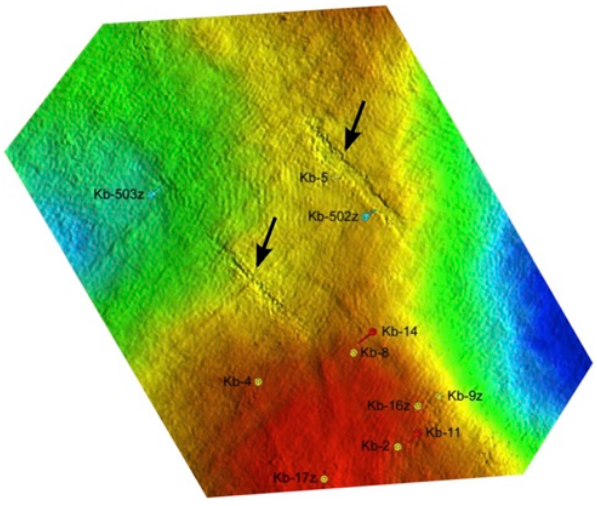


Fig. 5. Two-way time image of the C20.1 top (~40 m above the injection unit) in the 2009 3D seismic volume. Red-to-blue color indicates shallower-to-deeper depth to the anticlinal horizon. Northwest–southeast trending features indicated by black arrows were not seen in the 1997 survey and are interpreted to be seismic velocity anomalies correlated with injection. Image courtesy In Salah Joint Industry Project.

Received by OCD: 6/29/2026

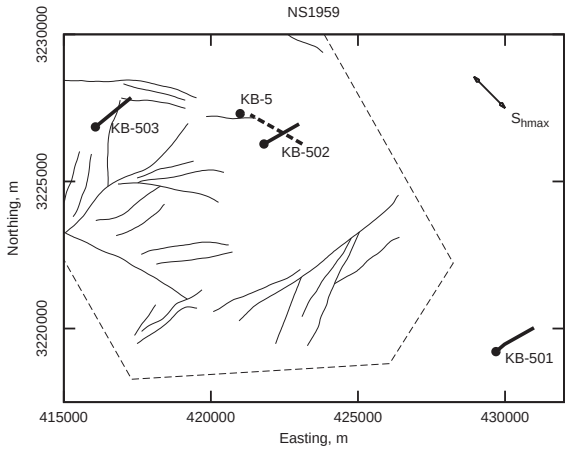


Fig. 6. Fault interpretation at the C10.2 interval, based on the 2009 seismic survey. Dashed trace intersecting KB-502 is a fault interpreted in the earlier 1997 survey but not visible in the higher-quality 2009 survey.

estimated from well head pressure, flow rate, and temperature, using a well model as described in Bissell and colleagues (4). This model was calibrated to three shut-in pressure measurements, one for each well. There is still some uncertainty, however, in the BHP conversion. The model used by the In Salah Joint Industry Project, presented here, is ∼10 bar higher than that of Rinaldi and colleagues (9) and ∼30 bar higher than Shi and colleagues (7), with the discrepancies most likely explained by temperature uncertainties.

A peak BHP of 323 bar occurred in March 2006. Between November 2005 and August 2006, the average BHP was 307 bar. The dashed horizontal lines indicate a fracture gradient range of 1.35–1.70 sg. Even using the reduced BHP estimate from Shi and colleagues (7), one observes that injection pressures are at the upper end of the fracture pressure estimated from the integrity tests. For reference, the first hints of a double-lobe feature appear in the InSAR data in February 2006, with the trough becoming increasingly distinct through shut-in in July 2007. Although there are large uncertainties, the general observation is that the injection pressure at KB-502 is high in comparison with the estimated fracture pressure for both the reservoir and caprock units. A vertical hydrofracture at KB-502, penetrating into the lower caprock, would readily explain the orientation and timing of the InSAR deformations and the appearance of the seismic anomaly.

A portion of the leak-off test and formation integrity test data in Fig. 7 was previously published in Shi and colleagues (7), along with an extrapolated fracture pressure profile. Note that this extrapolation uses the high leak-off test values in the unstable zone to predict fracture pressures below this interval. It therefore overestimates the observed leak-off test in the C20.1 unit and the step-rate test data in the reservoir interval. Using this extrapolation, Shi and colleagues arrive at a fracture pressure of 295 bar at the reservoir depth. Bissell and colleagues (4) estimated a fracture pressure of 286 bar, using log data and a semiempirical calculation. Both of these estimates are within but toward the high end of the uncertainty range inferred from Fig. 7.

As noted in Bissell and colleagues (4) and Oye and colleagues (8), an analysis of the injection rate behavior itself may also provide insight into possible fracturing behavior. For example, Oye and coworkers (8) show, by analyzing the injectivity index, that injectivity increases when pressures exceed ∼297 bar (wellhead pressure, 155 bar). There is significant scatter around this estimate, however, which could be explained in part by an evolution of fracture geometry over time and interaction with preexisting fractures. Interestingly, Oye and colleagues compare this estimate with recorded microseismicity from April to November 2010, using the KB-601 geophones. There is a correlation between measured event frequency and exceedance of a well-head pressure threshold of ∼155 bar. Unfortunately, microseismic was only available late in the field life and did not cover the initial injection period. Event locations are also highly uncertain.

The contrasts in fracture pressure in different layers suggest that the dynamics of hydrofracture growth would be complex. The physics is further complicated by buoyancy and pressure-volume-temperature effects associated with supercritical CO_2. The rate of leak-off of fluids from the fracture into the various units would also play a critical role. The ∼400 m width of the seismic anomaly may correspond to a leak-off zone of pressurized, CO_2-saturated, and/or damaged rock, as the main fracture is likely below seismic resolution.

As mentioned earlier, the seismic and InSAR data suggest that the two other wells may also be hydrofractured. The estimated BHP for both wells approaches and exceeds an EMW of 1.70 sg, although the two wells do not show the same degree of sustained high pressures as seen at KB-502. The surface deformations for these two wells show strong NW-SE trends, suggesting a stress-dependent permeability anisotropy at depth. Unusually, however, the seismic anomaly detected at KB-503 is much stronger to the southeast of the well. One might reasonably argue, therefore, that the evidence for hydraulic fracturing at these two other wells is weaker than at KB-502.

Hypothesis 4: Preexisting Fractures

The reservoir and caprock units contain preexisting fractures, and it is important to consider their role in the observed field behavior. Iding and Ringrose (3) present an extensive fracture characterization for the site, using FMI, core, and mud loss observations. There is a dominant fracture orientation parallel to the maximum horizontal stress (northwest–southeast). In general, fractures are steeply dipping, within 20° of vertical. Fig. S3 provides a rose diagram of fracture strikes observed in the FMI log of well KB-10. This well is some distance from the injectors but may be in a similar structural setting.

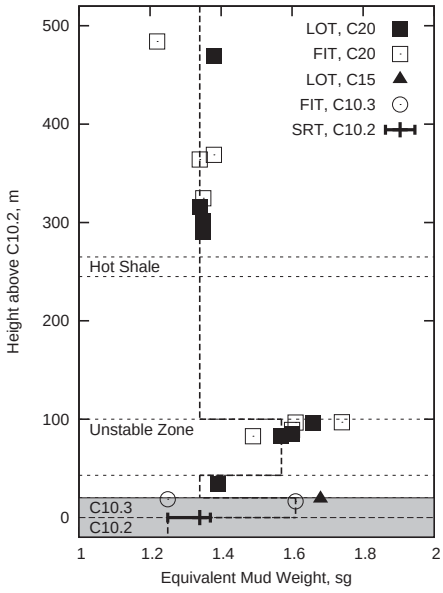


Fig. 7. Leak-off test (LOT), formation integrity test (FIT), and step-rate test (SRT) data compiled from injection and production wells.

Downloaded from https://www.pnas.org by 146.115.145.114 on June 16, 2026 from IP address 146.115.145.114.

EARTH, ATMOSPHERIC, AND PLANETARY SCIENCES

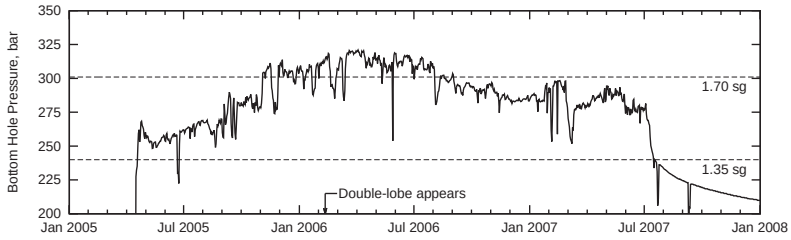


Fig. 8. Time history of estimated BHP at KB-502.

Fractures striking parallel to the maximum horizontal stress would likely be reopened when the fluid pressure exceeded the minimum horizontal stress. Furthermore, there are preexisting fracture orientations that are well-oriented for shear. These fractures could be reactivated at injection pressures lower than the minimum horizontal stress, depending on the cementation and frictional properties of the fractures. In fact, the low leak-off pressure observations at many places in the caprock could be caused by shear along preexisting fractures, rather than tensile initiation of new fractures in intact rock.

Unfortunately, no data are available on the strength and frictional properties of fractures at the site. Nevertheless, it seems likely that peak injection pressures are sufficient to reactivate any existing fractures in both tensile and shear modes. These fractures could also propagate and coalesce through hydrofracture or hydroshearing, improving the connectivity of the initial fracture network. The role that preexisting fractures play in the permeability behavior of the caprock remains a large and important uncertainty.

Summary

In this work, we have explored possible mechanisms to explain observed InSAR deformations, seismic velocity anomalies, and injection behavior. We argue that the evidence favors the hypothesis that injection pressures hydrofractured the reservoir and lower caprock. Vertical hydrofractures provide a simple explanation for the observed narrow, linear features running perpendicular to the minimum in situ stress. An analysis of leak-off and formation integrity test data supports the notion that injection pressures exceeded the fracture pressures for the reservoir and lower caprock units. The timing of the injection pressure increase at KB-502 correlates well with the appearance of the double-lobe in InSAR.

High pressures could also reactivate and coalesce preexisting fracture pathways (a combination of hypotheses 3 and 4), and their role should not be discounted. The evidence in favor of fluid migration from the reservoir along faults is weak, but there are small faults present at the site that could serve as partial migration pathways (7).

In Salah benefitted greatly from the diversity of monitoring techniques applied at the site. Individually, each of the data sets contains ambiguities that make interpretation difficult. Together, however, a clearer picture begins to form. The field experience also highlights the benefits of careful site selection. The 950-m caprock provides a number of thick, resilient seals. As a result, the formation can sustain a breakdown of lower caprock units without compromising the overall storage integrity. This robustness should be a major priority during site selection for future carbon capture and storage projects. At Krechba, robustness is achieved through the massive nature of the seals, but other sites could achieve a similar level of resilience by relying on multiple, thinner seals interleaved with permeable thief zones.

ACKNOWLEDGMENTS. We are grateful for collaboration with the Joint Industry Project, other research partners, and members of the Science Advisory Board. This work was performed under the auspices of the U.S. Department of Energy by Lawrence Livermore National Laboratory under Contract DE-AC52-07NA27344. Data and cofunding were provided by the In Salah Joint Industry Project.

1. Ringrose PS, et al. (2013) The In Salah CO_2 storage project: Lessons learned and knowledge transfer. *Energy Procedia* 37:6226–6236.
2. Vasco DW, et al. (2010) Satellite-based measurements of surface deformation reveal fluid flow associated with the geological storage of carbon dioxide. *Geophys Res Lett* 37(3):L03303.
3. Iding M, Ringrose P (2010) Evaluating the impact of fractures on the performance of the In Salah CO_2 storage site. *Int J Greenh Gas Control* 4(2):242–248.
4. Bissell RC, et al. (2011) A full field simulation of the In Salah gas production and CO_2 storage project using a coupled geo-mechanical and thermal fluid flow simulator. *Energy Procedia* 4:3290–3297.
5. Morris JP, Hao Y, Foxall W, McNab W (2011) A study of injection-induced mechanical deformation at the In Salah CO_2 storage project. *Int J Greenh Gas Control* 5(2):270–280.
6. Morris JP, Hao Y, Foxall W, McNab W (2011) In Salah CO2 storage JIP: Hydromechanical simulations of surface uplift due to CO2 injection at In Salah. *Energy Procedia* 4:3269–3275.
7. Shi JQ, Sinayuc C, Durucan S, Korre A (2012) Assessment of carbon dioxide plume behaviour within the storage reservoir and the lower caprock around the KB-502 injection well at In Salah. *Int J Greenh Gas Control* 7:115–126.
8. Oye V, et al. (2013) Microseismic monitoring and interpretation of injection data from the In Salah CO_2 storage site (Krechba), Algeria. *Energy Procedia* 37:4191–4198.
9. Rinaldi AP, Rutqvist J (2013) Modeling of deep fracture zone opening and transient ground surface uplift at KB-502 CO_2 injection well, In Salah, Algeria. *Int J Greenh Gas Control* 12:155–167.
10. Rucci A, Vasco DW, Novali F (2013) Monitoring the geologic storage of carbon dioxide using multicomponent SAR interferometry. *Geophys J Int* 193(1):197–209.
11. Gemmer L, Hansen O, Iding M, Leary S, Ringrose P (2012) Geomechanics response to CO_2 injection at Krechba, In Salah, Algeria. *First Break* 30(2):79–84.
12. Cavanagh A, Ringrose P (2011) Simulation of CO_2 distribution at the In Salah storage site using high-resolution field-scale models. *Energy Procedia* 4:3730–3737.
13. Verdon JP, et al. (2013) Comparison of geomechanical deformation induced by megatonne-scale CO_2 storage at Sleipner, Weyburn, and In Salah. *Proc Natl Acad Sci USA* 110(30):E2762–E2771.
14. Mathieson A, et al. (2011) In Salah CO_2 storage JIP: CO_2 sequestration monitoring and verification technologies applied at Krechba, Algeria. *Energy Procedia* 4:3596–3603.
15. Eiken O, et al. (2011) Lessons learned from 14 years of CCS operations: Sleipner, In Salah and Snøhvit. *Energy Procedia* 4:5541–5548.
16. Edmunds WM, et al. (2003) Groundwater evolution in the Continental Intercalaire aquifer of southern Algeria and Tunisia: Trace element and isotopic indicators. *Appl Geochem* 18(6):805–822.
17. Darling WG, Sorensen JPR Results and interpretation of hydrogeochemical data from the Krechba borehole sampling of March 2010 and March 2011. Commissioned Report CR/11/121, British Geological Survey; 2011.
18. Ringrose PS, et al. (2011) Characterisation of the Krechba CO_2 storage site: Critical elements controlling injection performance. *Energy Procedia* 4:4672–4679.
19. Ringrose P, Atbi M, Mason D, Espinassous M, Myhrer O Plume development around well KB-502 at the In Salah CO2 storage site. *First Break* 27.
20. Vasco DW, Ferretti A, Novali F (2008) Reservoir monitoring and characterization using satellite geodetic data: Interferometric synthetic aperture radar observations from the Krechba field, Algeria. *Geophysics* 73(6):WA113–WA122.
21. Onuma T, Ohkawa S (2009) Detection of surface deformation related with CO_2 injection by DInSAR at In Salah, Algeria. *Energy Procedia* 1(1):2177–2184.
22. Onuma T, Okada K, Otsubo A (2011) Time series analysis of surface deformation related with CO_2 injection by satellite-borne SAR interferometry at In Salah, Algeria. *Energy Procedia* 4:3428–3434.
23. Heidbach O, et al. (2008) *The World Stress Map Database*. Available at http://dc-app3-14.gfz-potsdam.de/pub/stress_maps/stress_maps.html. Accessed April 17, 2014.
24. Davis PM (1983) Surface deformation associated with a dipping hydrofracture. *J Geophys Res Sol Ea (1978–2012)* 88(B7):5826–5834.
25. Fjaer E, Holt RM, Horsrud P, Raaen AM, Risnes R (2008) *Petroleum Related Rock Mechanics* (Elsevier, New York), 2nd Ed.

Downloaded from https://www.pnas.org by 146.115.145.114 on June 16, 2026 from IP address 146.115.145.114.

EXHIBIT 22

Downloaded from https://www.pnas.org by 146.115.145.114 on June 16, 2026 from IP address 146.115.145.114.

Earthquake triggering and large-scale geologic storage of carbon dioxide

Mark D. Zoback[a,1] and Steven M. Gorelick[b]

Departments of [a]Geophysics and [b]Environmental Earth System Science, Stanford University, Stanford, CA 94305

Edited by Pamela A. Matson, Stanford University, Stanford, CA, and approved May 4, 2012 (received for review March 27, 2012)

Despite its enormous cost, large-scale carbon capture and storage (CCS) is considered a viable strategy for significantly reducing CO_2 emissions associated with coal-based electrical power generation and other industrial sources of CO_2 [Intergovernmental Panel on Climate Change (2005) IPCC Special Report on Carbon Dioxide Capture and Storage. Prepared by Working Group III of the Intergovernmental Panel on Climate Change, eds Metz B, et al. (Cambridge Univ Press, Cambridge, UK); Szulczewski ML, et al. (2012) *Proc Natl Acad Sci USA* 109:5185–5189]. We argue here that there is a high probability that earthquakes will be triggered by injection of large volumes of CO_2 into the brittle rocks commonly found in continental interiors. Because even small- to moderate-sized earthquakes threaten the seal integrity of CO_2 repositories, in this context, large-scale CCS is a risky, and likely unsuccessful, strategy for significantly reducing greenhouse gas emissions.

carbon sequestration | climate change | triggered earthquakes

The combustion of coal for electrical power generation in the United States generates approximately 2.1 billion metric tons of CO_2 per year, ~36% of all US emissions. In 2011, China generated more than three times that much CO_2 by burning coal for electricity, which accounted for ~80% of its total emissions. (According to the Energy Information Agency of the US Department of Energy, total CO_2 emissions in China were 8.38 billion metric tonnes in 2011, with 6.95 billion tons from coal burning, nearly all of which is used electrical power generation.) From a global perspective, if large-scale carbon capture and storage (CCS) is to significantly contribute to reducing the accumulation of greenhouse gases, it must operate at a massive scale, on the order of 3.5 billion tons (1) of CO_2 per year, a volume roughly equivalent (2) to the ~27 billion barrels of oil currently produced annually around the world. (Under reservoir conditions, one billion tons of CO_2 occupies a volume of ~1.3 billion cubic meters, equivalent to 8.18 billion barrels. Thus, 3.5 billion tons of carbon dioxide would correspond to a volume of approximately 28.6 billion barrels. There are currently ~850,000 wells producing oil around the world.) Moreover, a leak rate from underground CO_2 storage reservoirs of less than 1% per thousand years is required for CCS to achieve the same climate benefits as renewable energy sources (3).

Before embarking on projects to inject enormous volumes of CO_2 at numerous sites around the world, it is important to note that over time periods of just a few decades, modern seismic networks have shown that earthquakes occur nearly everywhere in continental interiors. Fig. 1, *Upper* shows instrumentally recorded earthquakes in the central and eastern United States and southeastern Canada. Fig. 1, *Lower* shows instrumentally recorded intraplate earthquakes in south and east Asia (4). The seismicity catalogs are complete to magnitude (M) 3. The occurrence of these earthquakes means that nearly everywhere in continental interiors a subset of the preexisting faults in the crust is potentially active in the current stress field (5, 6). This is sometimes referred to as the *critically stressed* nature of the brittle crust (7). It should also be noted that despite the overall low rate of earthquake occurrence in continental interiors, some of the most devastating earthquakes in history occurred in these regions. In eastern China, the M 7.8, 1976 Tangshan earthquake, approximately 200 km east of Beijing, killed several hundred thousand people. In the central United States, three M 7+ earthquakes in 1811 and 1812 occurred in the New Madrid seismic zone in southeast Missouri.

Because of the critically stressed nature of the crust, fluid injection in deep wells can trigger earthquakes when the injection increases pore pressure in the vicinity of preexisting potentially active faults. The increased pore pressure reduces the frictional resistance to fault slip, allowing elastic energy already stored in the surrounding rocks to be released in earthquakes that would occur someday as the result of natural geologic processes (8). This effect was first documented in the 1960s in Denver, Colorado when injection into a 3-km-deep well at the nearby Rocky Mountain Arsenal triggered earthquakes (9). Soon thereafter it was shown experimentally (10) at the Rangely oil field in western Colorado that earthquakes could be turned on and off by varying the rate at which water was injected and thus modulating reservoir pressure. In 2011 alone, a number of small to moderate earthquakes in the United States seem to have been triggered by injection of wastewater (11). These include earthquakes near Guy, Arkansas that occurred in February and March, where the largest earthquake was M 4.7. In the Trinidad/Raton area near the border of Colorado and New Mexico, injection of produced water associated with coalbed methane production seems to have triggered a number of earthquakes, the largest being a M 5.3 event that occurred in August. Earthquakes seem to have been triggered by wastewater injection near Youngstown, Ohio on Christmas Eve and New Year's Eve, the largest of which was M 4.0. Although the risks associated with wastewater injection are minimal and can be reduced even further with proper planning (11), the situation would be far more problematic if similar-sized earthquakes were triggered in formations intended to sequester CO_2 for hundreds to thousands of years.

Deep borehole stress measurements confirm the critically stressed nature of the crust in continental interiors (12), in some cases at sites directly relevant to the feasibility of large-scale CCS. For example, deep borehole stress measurements at the Mountaineer coal-burning power plant on the Ohio River in West Virginia indicate a severe limitation on the rate at which CO_2 could be injected without the resulting pressure build-up initiating slip on preexisting faults (13). Because of the low permeability of the formations at depth, pore pressure increases would be expected to trigger slip on preexisting faults if CO_2 injection rates exceed approximately 1% of the 7 million tons of CO_2 emitted by the Mountaineer plant each year. Similarly, stress measurements at Teapot Dome, Wyoming, the US government-owned oil field where pilot CO_2

Author contributions: M.D.Z. and S.M.G. wrote the paper.

The authors declare no conflict of interest.

This article is a PNAS Direct Submission.

[1]To whom correspondence should be addressed. E-mail: zoback@stanford.edu.

Received by OCD: 6/29/2026

Downloaded from https://www.pnas.org by 146.115.145.114 on June 16, 2026 from IP address 146.115.145.114.

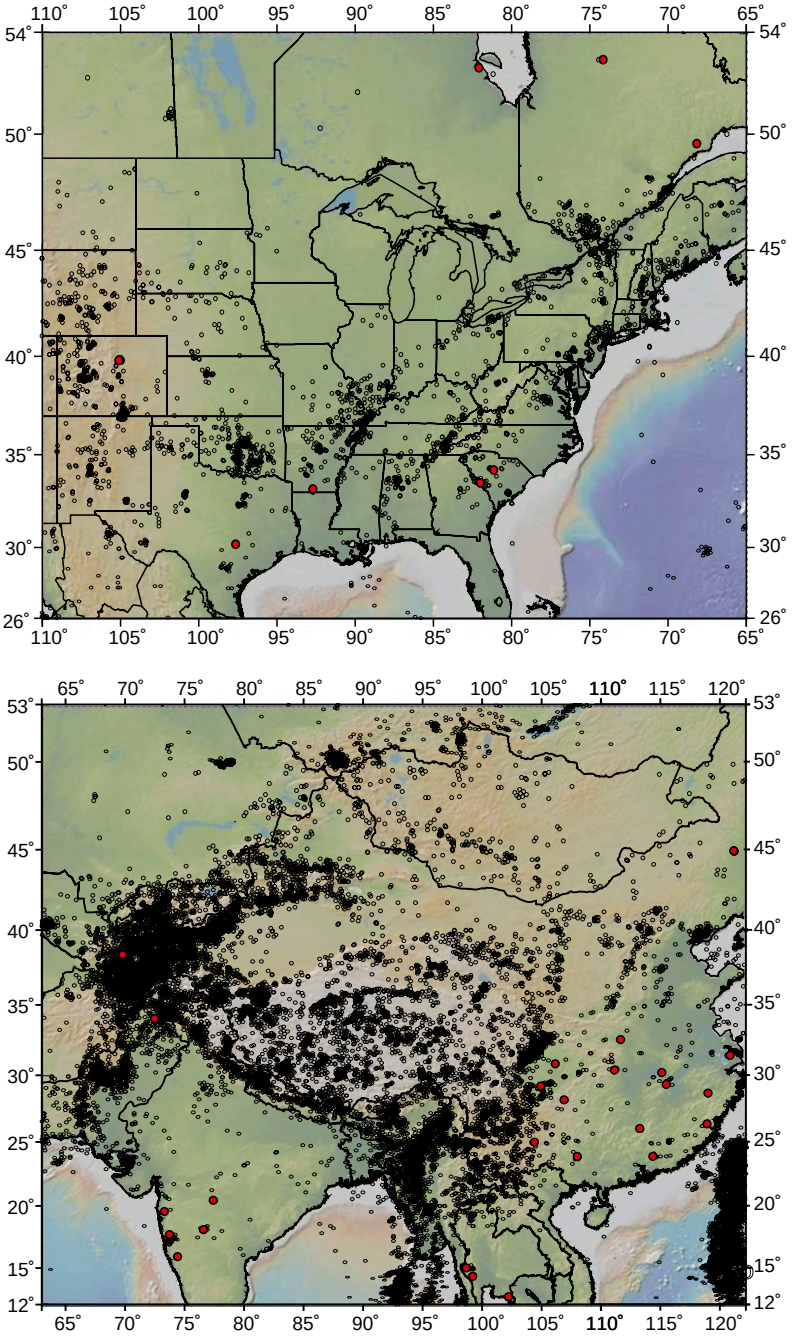


Fig. 1. *Upper*: Instrumentally recorded seismicity and damaging historical earthquakes in the central and eastern United States and southeastern Canada. Red dots indicate sites of reservoir-induced seismicity. *Lower*: Seismicity of south and east Asia and sites of reservoir-induced seismicity. Both data sets are available from the US Geological Survey (4).

injection projects have been considered, show that very small pressure buildups are capable of triggering slip on some preexisting faults (14).

Dam construction and water reservoir impoundment produce much smaller pore pressure changes at depth than are likely to occur with CO_2 sequestration, but many have triggered earthquakes at various sites around the world (15) (red dots in Fig. 1). Except for the much smaller pore pressure increases at depth, reservoir-triggered earthquakes are a good analog for the potential for seismicity to be triggered by CO_2 injection. Both activities cause pore pressure increases that act over large areas and are persistent for long periods. Three reservoir impoundments in eastern Canada (located in the ancient, stable core of the North American continent) triggered earthquakes as large as M 4.1 and M 5 at the two sites (Fig. 1), despite the fact that the pore pressure increases at depth were extremely small.

Triggered Earthquakes and Seal Integrity

Our principal concern is not that injection associated with CCS projects is likely to trigger large earthquakes; the problem is that even small to moderate earthquakes threaten the seal integrity of a CO_2 repository. In parts of the world with good construction practices, it is unusual for earthquakes smaller than approximately M 6 to cause significant human harm or property damage. Fig. 2 uses well-established seismological relationships to show how the magnitude of an earthquake is related to the size of the fault that slipped and the amount of fault slip that occurred (16). As shown, faults capable of producing M ~6 earthquakes are at least tens of kilometers in extent. (The fault size indicated along the abscissa is a lower bound of fault size as it refers to the size of the fault segment that slips in a given earthquake. The fault on which an earthquake occurs is larger than the part of the fault that slips in an individual event.) In most cases, such faults should be easily identified during geophysical site characterization studies and thus should be avoided at any site chosen for a CO_2 repository. (Faults in crystalline basement rocks might be difficult to recognize in geophysical data. We assume, however, that any site chosen as a potential CO_2 repository would be carefully selected, avoiding the possibility of pressure changes in the CO_2 repository from affecting faults in crystalline basement.) The problem is that site characterization studies can easily miss the much smaller faults associated with small to moderate earthquakes.

Although the ground shaking from small- to moderate-sized earthquakes is inconsequential, their impact on a CO_2 repository would not be. Most of the geologic formations to be used for long-term storage of CO_2 are likely to be at depths of approximately 2 km—deep enough for there to be adequate sealing formations to isolate the CO_2 from the biosphere but not so deep as to encounter formations with very low permeability. Given large volumes of CO_2 injected into selected formations for many decades, if a small to moderate earth-

Downloaded from https://www.pnas.org by 146.115.145.114 on June 16, 2026 from IP address 146.115.145.114.

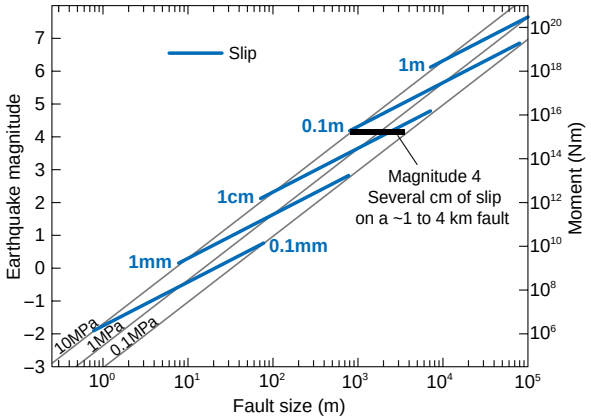


Fig. 2. Relationships among various scaling parameters for earthquakes. The larger the earthquake, the larger the fault and amount of slip, depending on the stress drop in a particular earthquake. Observational data indicate that earthquake stress drops range between 0.1 and 10 MPa.

quake were to be triggered in a geologic formation at approximately 2 km depth, it could jeopardize the seal integrity of the storage formation. For example, if a M ~4 earthquake were to be triggered by CO_2 sequestration (17)—an event that would be widely felt in a populated area but for which shaking would be unlikely to cause harm or damage—it would be associated with several centimeters of slip on a fault several kilometers in size. Because laboratory studies show that just a few millimeters of shear displacement are capable of enhancing fracture and joint permeability (18), several centimeters of slip would be capable of creating a permeable hydraulic pathway that could compromise the seal integrity of the CO_2 reservoir and potentially reach the near surface.

Safe Sequestration

It is important to emphasize that CCS can be valuable and useful for reducing greenhouse gas emissions in specific situations. A good example is the injection of CO_2 into the Utsira formation (19) at the Sleipner gas field in the North Sea, where a significant amount of CO_2 is coproduced with natural gas. After separating the CO_2 from the produced gas, approximately 1 million tons of CO_2 per year has been injected over the past 15 y without triggering seismicity. Assuming isolation from the near surface, injection into highly porous and permeable reservoirs that are laterally extensive would produce small increases in pressure in response to CO_2 injection. Moreover, weak, poorly cemented sandstones are expected to deform slowly in response to applied geologic forces. In such reservoirs, the stresses *relax* over time, and such formations are not prone to faulting (20). In this regard, the Utsira formation is ideal for CO_2 sequestration. It is isolated from vertical migration by impermeable shale formations, and it is highly porous, permeable, laterally extensive, and weakly cemented.

To contribute significantly to greenhouse gas emission reductions (2), roughly 3,500 sites similar to the Utsira formation would have to be found at convenient locations around the world, assuming comparable injection rates of approximately 1 million tons of CO_2 per year. In fact, it would take approximately 85 such sites coming on line each year to reach a goal of storing approximately 1 billion tons of CO_2 by midcentury. Clearly this is an extraordinarily difficult, if not impossible, task if only highly porous and permeable and weakly cemented formations are to be used.

Of course, rather than using potentially problematic geologic formations close to coal-burning power plants for sequestration (as illustrated by the Mountaineer case study cited above), relatively ideal formations for CO_2 storage could be sought on a regional basis to accommodate emissions from a number of plants. One example of this is the potential use of the Mt. Simon sandstone in the Illinois basin. The Mt. Simon is porous, permeable, and regionally extensive. However, models of injection of 100 million tons of CO_2 per year for 40 y predicts (21) increases in pore pressure of several megapascals over a region of ~40,000 km^2. The approximate area of significantly increased pore pressure resulting from injection is shown as the blue-shaded area in Fig. 3, essentially adjacent to the Wabash fault zone, where a series of moderate natural earthquakes occurred in the spring of 2008, the largest being M 5.2. Paleoseismic data indicate the occurrence of much larger nearby earthquakes (some greater than M ~7) in the recent geologic past (22). Importantly, the 100 million ton annual CO_2 injection rate used in the

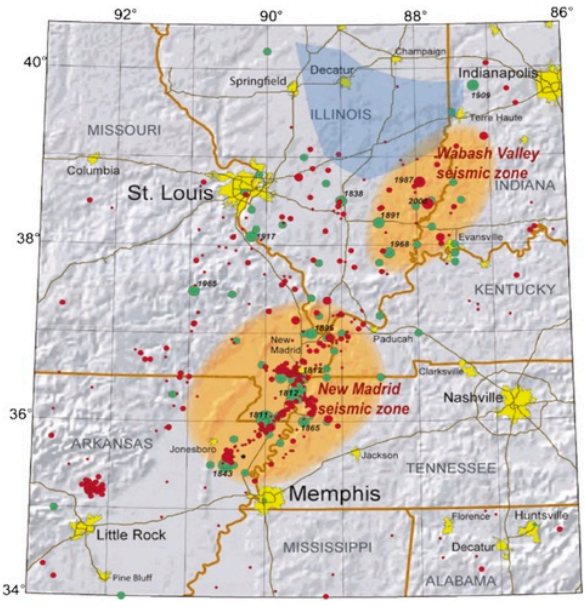


Fig. 3. Instrumentally recorded seismicity in the New Madrid and Wabash Valley seismic zones (modified from ref. 23). Red circles indicate earthquakes that occurred from 1974 to 2002 with magnitudes larger than 2.5 located using modern instruments. Green circles denote earthquakes that occurred before 1974. Larger earthquakes are represented by larger circles. The area shown in blue corresponds to the area where a pressure increase of several megapascals would result from injecting 100 million tons per year of CO_2 into the Mt. Simon sandstone in the Illinois Basin for 40 y (19).

Received by OCD: 6/29/2026

Downloaded from https://www.pnas.org by 146.115.145.114 on June 16, 2026 from IP address 146.115.145.114.

modeling only represents approximately one seventh of the CO_2 generated by the coal-burning power plants in the Ohio River Valley alone.

Because of the need to carefully monitor CO_2 repositories with observation wells, geophysical and geochemical monitoring systems, etc., it is likely that most sites will have to be located on land or very near shore. Otherwise, highly porous reservoirs located offshore, like those adjacent to salt domes along the US Gulf Coast, would be relatively ideal sites because salt formations are known to be excellent seals for hydrocarbons.

Depleted oil and gas reservoirs are potentially suitable for CO_2 storage for a variety of reasons—an infrastructure of wells and pipelines exist, and there is a great deal of geologic and subsurface property data available to characterize the subsurface from decades of study. In addition, from an earthquake-triggering perspective, depleted reservoirs are attractive because at the time injection of CO_2 might start, the pore pressure would be below the value that existed before petroleum production. Thus, there could be significant injection of CO_2 before pressures increase to pre-production values, thereby reducing the potential for triggering earthquakes.

There are a number of potential issues to consider before using depleted oil and gas reservoirs for CO_2 storage, the most important of which are capacity and geographic distribution. The reasons that there is such interest in using saline aquifers for CO_2 storage is that they are potentially well distributed with respect to likely sources of CO_2, and they could presumably accommodate the enormous volumes of CO_2 that need to be stored. If one were only to consider the United States, storing the 2.1 billion tons of CO_2 currently generated annually by coal-burning power plants in depleted oil and gas reservoirs would require injection of CO_2 at a rate of approximately 17 billion barrels per year; a rate equivalent to eight times current US annual oil production and more than four times US peak annual oil production that occurred in the early 1970s. In addition, it is important to make sure that production-related activities, such as water flooding during secondary recovery, did not compromise the seal capacity of the reservoirs. There also needs to be careful study of the wells in the depleted oil or gas field to make sure that poorly cemented well casings, especially in older wells, will not be pathways for release of stored CO_2 (23). Finally, there are likely to be complicated legal questions concerning ownership and liability that will need to be worked out on a case-by-case basis.

Although enhanced oil recovery (EOR) using CO_2 (in which CO_2 is injected to dissolve in oil and reduce its viscosity) would be a beneficial use of CO_2, it is important not to confuse this with CCS. In CCS the goal is to inject large quantities of CO_2 into available pore space and store it there for hundreds to thousands of years. When CO_2 is used for EOR, the CO_2 dissolved in the oil is separated and captured from produced oil and then re-injected. Thus, smaller volumes of CO_2 are used, and the long-term storage capacity of the reservoir is not an issue.

Many CCS research projects are currently underway around the world. Much of this work involves characterization and testing of potential storage formations and includes a number of small-scale pilot injection projects. Because the storage capacity/pressure build-up issue is critical to assess the potential for triggered seismicity, small-scale pilot injection projects do not reflect how pressures are likely to change (increase) once full-scale injection is implemented. Moreover, even though limitations on pressure build-up are among the many factors that are evaluated when potential formations are considered as sequestration sites, this is usually done in the context of not allowing pressures to exceed the pressure at which hydraulic fractures would be initiated in the storage formation or caprock. In the context of a critically stressed crust, slip on preexisting, unidentified faults could trigger small- to moderate-sized earthquakes at pressures far below that at which hydraulic fractures would form.

As mentioned above, sequences of small to moderate earthquakes were apparently induced by injection of waste water near Guy, Arkansas, Trinidad, Colorado, and Youngstown, Ohio in 2011 and on the Dallas-Ft. Worth airport, Texas. Although these earthquakes were widely felt, they caused no injury, and only the Trinidad earthquake resulted in any significant damage. However, had similar earthquakes been triggered at sites where CO_2 was being injected, the impacts would have raised pressing and important questions: Had the seal been breached? Was it still safe to leave previously injected CO_2 in place?

In summary, multiple lines of evidence indicate that preexisting faults found in brittle rocks almost everywhere in the earth's crust are subject to failure, often in response to very small increases in pore pressure. In light of the risk posed to a CO_2 repository by even small- to moderate-sized earthquakes, formations suitable for large-scale injection of CO_2 must be carefully chosen. In addition to being well sealed by impermeable overlaying strata, they should also be weakly cemented (so as not to fail through brittle faulting) and porous, permeable, and laterally extensive to accommodate large volumes of CO_2 with minimal pressure increases. Thus, the issue is not whether CO_2 can be safely stored at a given site; the issue is whether the capacity exists for sufficient volumes of CO_2 to be stored geologically for it to have the desired beneficial effect on climate change. In this context, it must be recognized that large-scale CCS will be an extremely expensive and risky strategy for achieving significant reductions in greenhouse gas emissions.

ACKNOWLEDGMENTS. We thank Owen Hurd and Randi Walters for their help in preparation of the figures, and Mary Lou Zoback, Greg Beroza, Doug Arent, Sally Benson, Franklin Orr, John Bredehoeft, and Larry Goulder for their helpful comments.

1. Pacala S, Socolow R (2004) Stabilization wedges: Solving the climate problem for the next 50 years with current technologies. *Science* 305:968–972.
2. Snieder R, Young R (2009) Facing major challenges in carbon capture and sequestration. *GSA Today* 19:36–37.
3. Shaffer G (2010) Long-term effectiveness and consequences of carbon dioxide sequestration. *Nat Geosci* 3:464–467.
4. US Geological Survey (2011) Rectangular area earthquake search. Available at: http://earthquake.usgs.gov/earthquakes/eqarchives/epic/epic_rect.php. Accessed March 8, 2011.
5. Zoback ML, Zoback MD (1980) State of stress in the coterminous United States. *J Geophys Res* 85:6113–6156.
6. Zoback ML (1992) First- and second-order patterns of stress in the lithosphere: The world stress map project. *J Geophys Res* 97(B8):11,703–11,728.
7. Zoback MD, Townend J, Grollimund B (2002) Steady-state failure equilibrium and deformation of intraplate lithosphere. *Int Geol Rev* 44:383–401.
8. McGarr A, Simpson D, Seeber L (2002) Case histories of induced and triggered seismicity. *Int Handb Earthq Eng Seismol* 81A:647–661.
9. Healy JH, Rubey WW, Griggs DT, Raleigh CB (1968) The Denver earthquakes. *Science* 161:1301–1310.
10. Raleigh CB, Healy JH, Bredehoeft JD (1976) An experiment in earthquake control at rangely, colorado. *Science* 191:1230–1237.
11. Zoback MD (2012) Managing risk associated with earthquakes triggered by fluid injection. *Earth (Waukesha)* 38–43.
12. Townend J, Zoback MD (2008) How faulting keeps the crust strong. *Geology* 28:399–402.
13. Lucier AM, Zoback MD, Gupta N, Ramakrishnan TS (2006) Geomechanical aspects of CO_2 sequestration in a deep saline reservoir in the Ohio River Valley region. *Environ Geol* 13:85–103.
14. Chiaramonte L, Zoback MD, Friedmann J, Stamp V (2008) Seal integrity and feasibility of CO2 sequestration in the Teapot Dome EOR pilot: Geomechanical site characterization. *Environ Geol* 54:1667–1675.
15. Talwani P, Chen L, Gahalaut K (2007) Seismogenic permeability, k_s. *J Geophys Res* 112:B07309.
16. Stein S, Wysession M (2003) *An Introduction to Seismology, Earthquakes and Earth Structure* (Blackwell, Oxford).
17. Cappa F, Rutqvist J (2011) Impact of CO2 geological sequestration on the nucleation of seismic fault ruptures. *Am Rock Mechanics Assoc* 11:paper 471.
18. Chen Z, Narayan SP, Yang Z, Rahman SS (2000) An experimental investigation of hydraulic behaviour of fractures and joints in granitic rock. *Int J Rock Mech Min Sci* 37:1061–1071.

Downloaded from https://www.pnas.org by 146.115.145.114 on June 16, 2026 from IP address 146.115.145.114.

19. Chadwick RA, et al. (2004) Geological reservoir characterization of a CO_2 storage site: The Utsira Sand, Sleipner, northern North Sea. *Energy* 29:1371–1381.
20. Hagin P, Zoback MD (2004) Viscous deformation of unconsolidated sands—Part 1: Time-dependent deformation, frequency dispersion, and attenuation. *Geophysics* 69:731–741.
21. Zhou Q, Birkholzer JT, Mehnert E, Lin YF, Zhang K (2010) Modeling basin- and plume-scale processes of CO2 storage for full-scale deployment. *Ground Water* 48:494–514, 10.1111/j.1745-6584.2009.00657.x.
22. Pond EC, Martin JR (1997) Estimated magnitudes and accelerations of pre-historic earthquakes in the Wabash Valley region of the central United States. *Seismol Res Lett* 68:611–623.
23. Bohnhoff M, Zoback MD (2010) Oscillation of fluid-filled cracks triggered by degassing of CO_2 due to leakage along wellbores. *J Geophys Res* 115:B1130510.1029/2010JB000848.

EXHIBIT 23

Received by OCD: 6/29/2026

International Journal of Greenhouse Gas Control 146 (2025) 104447

Contents lists available at ScienceDirect

International Journal of Greenhouse Gas Control

journal homepage: www.elsevier.com/locate/ijggc

Implications of earthquakes triggered by massive injection of produced water in saline aquifers for large-scale geologic storage of CO_2

Mark D. Zoback [a,*], Peter Hennings [b]

[a] Stanford Center for Induced and Triggered Seismicity, Stanford Center for Carbon Storage, Department of Geophysics Emeritus, Stanford University, United States
[b] Center for Injection and Seismicity Research, Bureau of Economic Geology, Jackson School of Geosciences, The University of Texas, Austin, United States

ARTICLE INFO

Keywords:
Large-scale CO_2 storage
Induced seismicity

ABSTRACT

It is well-established that to significantly decrease greenhouse gas emissions, CO_2 capture and storage in subsurface geologic formations (CCS) must occur at an enormous scale. In this context, large-scale injection of supercritical CO_2 into saline aquifers is an analogous process to the disposal of large volumes of saltwater co-produced with oil and gas (SWD). However, large-scale SWD in saline aquifers over the past 15 years in the mid-continent of North America has caused a remarkable increase in intraplate seismicity. Since 2010, nearly 4 billion m^3 of produced water has been injected into sedimentary layers that are in hydraulic communication with seismogenic geologic basement in Oklahoma and Texas alone, triggering earthquakes as large as magnitude 5.8 and more than 200 $M \geq 4.0$ earthquakes that were widely felt. Every case of large-scale SWD in the mid-continent in deep saline aquifers in hydrologic communication with basement has caused significant induced seismicity. If CO_2 storage projects are associated with induced seismicity, they could be perceived by the public as a hazardous activity which should not be allowed to continue, generally regardless of the magnitudes of the induced events. Thus, among many challenges (operational, geologic and economic), large-scale CCS projects will face, they also will need to minimize the occurrence of injection-induced seismicity. In this paper, we review the extensive research carried out in four regions of the central U.S. with abundant seismicity induced by large-scale SWD in central U.S. as an analogous process to large-scale CO_2 injection. Our primary purpose is to inform non-experts of the key findings of the large body of scientific evidence now available in these areas that help guide decision making related to finding viable options for long-term, large-scale CO_2 storage in geologic formations.

1. Introduction

It has long been recognized that carbon capture and storage in geologic formations (CCS) is an important component of decarbonization strategies to limit global warming (IPCC, 2005). To limit average global warming to 1.5 °C, it is estimated that about 1 GT $scCO_2$/y needs to be stored in the subsurface by 2030 and about 10 GT $scCO_2$/y by 2050 (IPCC, 2018; Jenkins et al., 2023). 1 GT of supercritical CO_2 (with a specific gravity of about 0.6) occupies about 1.3 billion m^3 of pore space in the subsurface. 10 GT of $scCO_2$ is volumetrically equivalent to almost 3 times the volume of current annual global oil production.

It is widely assumed that saline aquifers in North America can accommodate the injection of almost limitless amounts of CO_2 (NETL, 2015). Utilization of saline aquifers for carbon storage at very large scale will require comprehensive site characterization efforts and will be subject to strict regulatory guidelines, before, during and following injection. More challenging will be avoiding the conditions which we now know have been responsible for the numerous cases of injection-induced seismicity over the past 15 years in the mid-continent of North America, especially in the four thoroughly studied areas we review here; north-central Oklahoma and southern Kansas, the Fort Worth Basin in north central Texas and the Midland and Delaware Basins of west Texas and southeast New Mexico. The potential for injection of CO_2 into saline aquifers to induce seismicity was pointed over a decade ago by Zoback and Gorelick (2012) who emphasized the threat of relatively large earthquakes to the seal capacity of potential reservoirs. The M 5.7 and M 5.8 earthquakes triggered by produced water injection in Oklahoma (and multiple earthquakes exceeding M 5 in the Permian Basin) are certainly large enough to cause concern about seal integrity. Recent history, however, has shown that anthropogenically induced seismicity

* Corresponding author.
E-mail address: zoback@stanford.edu (M.D. Zoback).

https://doi.org/10.1016/j.ijggc.2025.104447
Received 1 February 2025; Received in revised form 4 August 2025; Accepted 4 August 2025
Available online 22 August 2025
1750-5836/© 2025 The Authors. Published by Elsevier Ltd. This is an open access article under the CC BY license (http://creativecommons.org/licenses/by/4.0/).

Received by OCD: 6/29/2026

is of great concern to the public. In response to the occurrence of minor earthquakes (the largest of which was a M 3.6 event in 2016), gas production from the Groningen field in The Netherlands has been stopped (Bommer et al., 2024). The occurrence of very small earthquakes associated with hydraulic fracturing of the Preese Hall well in near Blackpool, England (the largest of which was M 2.9) caused the termination of the project (Clarke et al., 2014).

In the sections below, we introduce the basic physical principles associated with injection-triggered seismicity in the context of Coulomb faulting theory and the concept of a critically-stressed faults in the brittle crust. In the sections that follow, we discuss each of the four areas of intense induced seismicity in terms of their unique geological characteristics and history of large-scale saltwater disposal (SWD). Our purpose is to provide an understanding of the relationship between large-scale saltwater injection and seismicity which is directly relevant to the challenge of safely injecting large volumes of CO_2. It is important to emphasize the fact that the cases we discuss here are not unique, as there are a number of other areas in North America where large-scale SWD has triggered seismicity due to similar geologic processes at work. These include the Guy-Greenbrier earthquake sequence in central Arkansas (Horton, 2012) where injection into the basal Ozark formation triggered basement earthquakes, the earthquake sequences in the Dragger Draw area of New Mexico (Litherland, 2023) and earthquake sequences in the Raton Basin of southern Colorado and northern New Mexico (Nakai et al., 2017).

We discuss at length why injection-triggered earthquakes in basement-rooted faults are especially problematic and comment on two relevant small-scale CO_2 injection projects: Quest in Alberta and Decatur, Illinois in the context of implications for induced seismicity. We then discuss how large-scale CO_2 storage in depleted oil and gas reservoirs and geologically young, diagenetically immature formations (such as those found along the Texas/Louisiana Gulf Coast) significantly reduces the probability of triggered seismicity. In the final section of this paper, we summarize optimal geologic conditions for large-scale storage of CO_2. Our goal is to enhance understanding of injection-induced seismicity relevant to large scale CO_2 injection through the lens of the cases we describe. Hence, we make no attempt to summarize the many other global cases of injection related induced seismicity (see compilations by Foulger et al. (2018) and Kivi et al. (2023).

As shown in Fig. 1, the rate of M $\geq$ 3 earthquakes in the mid-continent began to increase anomalously in 2009. 179 M $\geq$ 3.0 earthquakes occurred in the 35 years between 1973 and 2008 (an average of 5 earthquakes per year). In the 15 years between 2009 through 2024, 4262 M $\geq$ 3 earthquakes occurred, a 57-fold increase in the average annual number. As we discuss below, these earthquakes resulted from massive injection of highly saline water (SWD) into deep saline aquifers in each of the four regions considered here. In each case, the saline water was co-produced with oil and gas and not directly related to horizontal drilling and multi-stage hydraulic fracturing. It should be noted that terminology has been proposed that distinguishes between the terms *triggered* and *induced* earthquakes. *Triggering* is a process by which a small perturbation (such as an increase in fluid pressure) reduces frictional resistance to faulting and accelerates the time occurrence of *natural* earthquakes which could have occurred in the geologic future. An induced earthquake is one in which a process such as excavating a mine or tunnel, introduces local stress concentrations that causes an earthquake to occur which would not have naturally occurred otherwise. However, following common usage of the terms, we use *induced* and *triggered* synonymously even though the earthquakes of relevance here are all triggered earthquakes. The pore pressure changes during SWD are

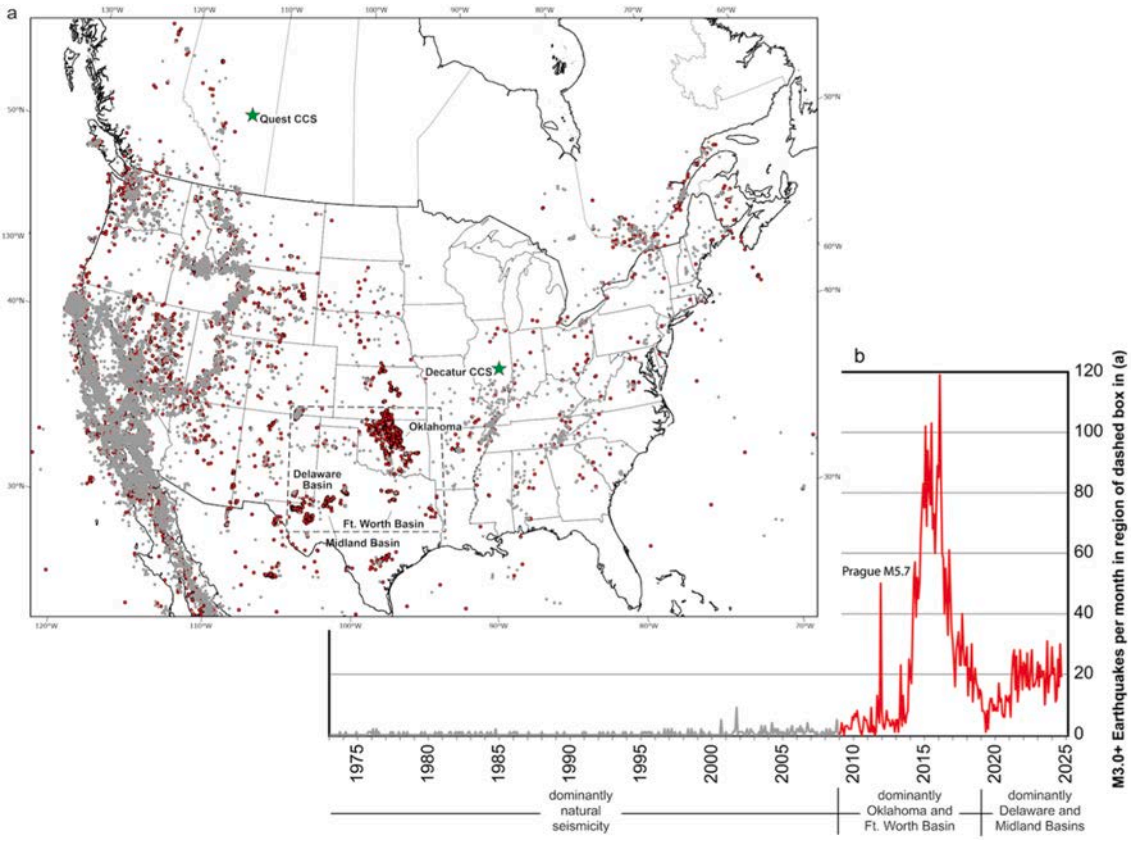


Fig. 1. a) – Earthquakes of M $\geq$ 3 in the contiguous United States and adjacent regions, including the Canadian provinces of Alberta and British Columbia for the period 1973-2008 (gray) plotted on top of 2009-2024 (red). Areas of injection-induced earthquakes and CCS projects as discussed in the text are indicated. b) the monthly number of M $\geq$ 3 earthquakes for the region of the dashed box in (a) using the same color scheme for date range.

Received by OCD: 6/29/2026

extremely small when compared to the energy released in the resultant earthquakes. Thus, the stress released in the earthquakes is already in the earth.

In the central U.S. there are two distinct classes of earthquakes being triggered by SWD into saline aquifers. The first class involves earthquakes occurring in crystalline basement resulting from injection into basal sedimentary formations that are in hydrologic communication with faults in the basement. We refer to these earthquakes as occurring on *basement-rooted* faults. *Crystalline basement* refers to the igneous and metamorphic rocks that underly non-metamorphosed sedimentary rocks within continental areas. In North America, crystalline basement ranges in age from 540 to 3,550 million years and contains complex structural fabrics and densely distributed faults related to craton assembly and other tectonic processes that have acted throughout geologic time. As discussed in the next section, a small fraction of pre-existing faults are active today and thus susceptible to induced slip by injection-related pore pressure increases. Seismicity in basement resulting from injection into the Arbuckle basal saline aquifers is responsible for the relatively large earthquakes in Oklahoma - the 2011 M 5.7 Prague earthquake and the 2016 M 5.8 Pawnee earthquake. Perhaps more relevant is the fact that at the peak of seismicity in 2015, a widely-felt M≥4 earthquakes was occurring each week in north-central Oklahoma. In the Fort Worth, Delaware and Midland Basins of Texas, basal injection has caused seven M ≥ 5.0 earthquakes. Overall, about 200 widely-felt M≥4.0 earthquakes have occurred in the U.S. mid-continent associated with SWD. Minor damage to structures has occurred and many of the largest magnitude earthquakes were reported as felt at distances of >1,000 km.

The second class of injection-induced seismicity involves SWD into stratigraphically bounded reservoirs, meaning that injection-related pressure changes are not transmitted to underlying basement by relatively impermeable strata a greater depth. We discuss these types of earthquakes in the context of induced seismicity in the southern Delaware Basin. In these cases, smaller magnitude induced earthquakes occur (typically M ≤ 3.5) because the vertical extent of fault rupture is restricted by evaporite formations above the injection zone and clay-rich shale below. We refer to these as *strata-bound* faults.

To illustrate the potential challenges associated with linking SWD to seismicity occurring in a region, Fig. 2 (after Hennings and Smye, 2024) presents a generalized regional ~ east-west cross-section across the Permian Basin of west Texas and southeast New Mexico. It illustrates the occurrence of induced seismicity on both basement-rooted and strata-bound earthquakes in different parts of the region. The Central Basin Platform separates the Delaware (sub)Basin, on the west side of the Permian Basin, from the Midland (sub) Basin on the east side. The ~ N-S trending faults associated with the uplift of the Central Basin Platform are shown schematically. The sedimentary sequence above basement is divided into 4 units. At shallow depth there are evaporite deposits (unit 1) that serve as the top seal for injection below. Unit 2, indicated by yellow dots represents shallow SWD, the Delaware Mountain Group in the Delaware Basin and the San Andres Formation and related strata in the Midland Basin. The size of the dot indicates the relative rate of disposal (see legend). Unit 3, shown by the light blue dots indicates the depth at which horizontal drilling and multi-stage hydraulic fracturing are occurring in units including Sprayberry and Bone Spring Formations and the Wolfcamp Group. The purple dots (unit 4) represent deep SWD (scaled by injection rate) relatively close to the top of basement, which is indicated by the dashed red line. Earthquakes catalogued recorded by TexNet (the Texas Seismological Network) are shown by black dots. It should be noted that there can be considerable uncertainty in earthquake depth in this area (*e.g.*, Sheng et al., 2022). In the northern Delaware Basin, there is appreciable deep injection and

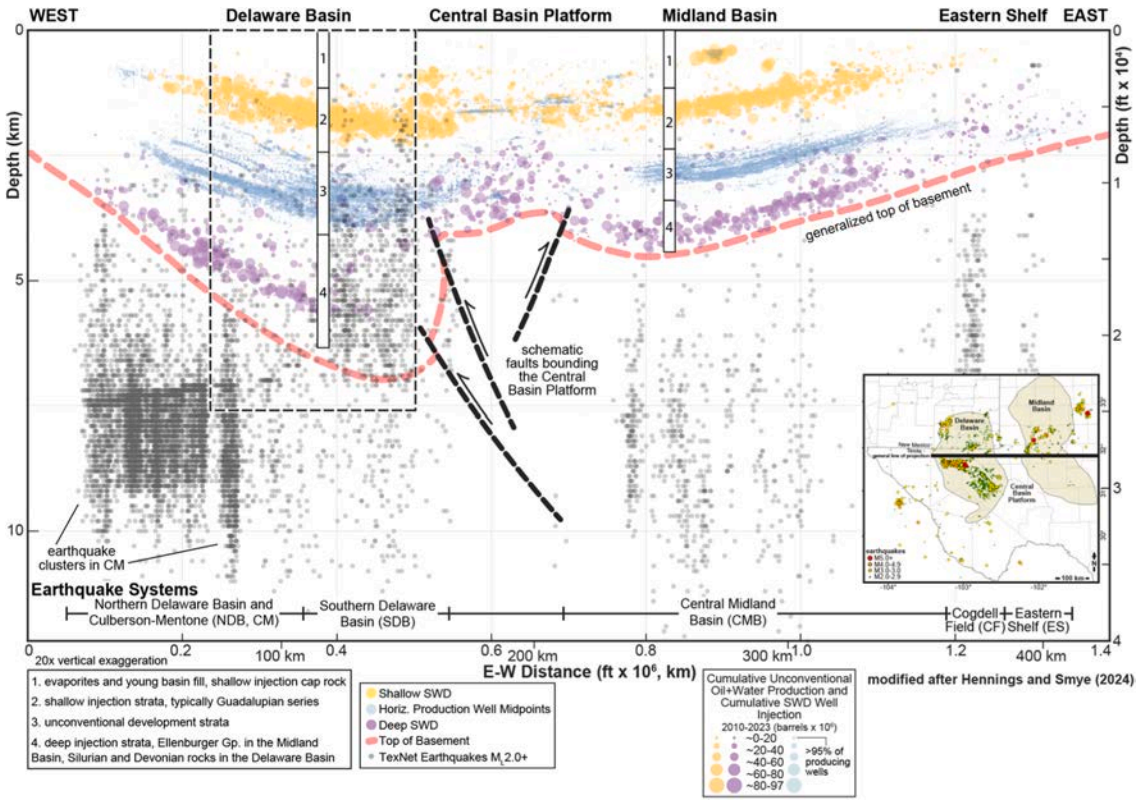


Fig. 2. Subsurface data projection across the Permian Basin of west Texas. As shown in the inset, the schematic data profile is the results of projecting all data, in depth from the surface to a common E-W plane. The section crosses the Delaware Basin on the west side and the earthquakes for that segment of the profile are generally projected into the section from the south. It then crosses the Central Basin Platform which forms the primary structural boundary between the Delaware Basin the Midland Basin to the east. Earthquakes in the Midland Basin are generally projected southward to the profile. Modified after Hennings and Smye (2024).

Received by OCD: 6/29/2026

appreciable seismicity on basement-rooted faults. In the southern Delaware Basin, the great majority of earthquakes are strata-bound earthquakes limited to the injection zone and underlying shale. There is very little seismicity observed on the Central Basin Platform, as there is very little SWD in that area. In the Midland Basin, there is relatively little seismicity at shallow depth even though there is considerable shallow injection. The majority of triggered seismicity is occurring in basement. The geologic reasons for these differences are discussed below. Strata-bound earthquakes resulting from SWD at relatively shallow depth are abundant in the southern Delaware Basin. In marked contrast, relatively shallow, strata-bound faults are essentially absent in the Midland Basin (Horne et al., 2024).

2. Coulomb faulting theory and the critically-stressed crust

As will be discussed, in each of the cases where seismicity was induced by SWD into basal aquifers, relatively small injection-induced pressure changes of about 1 MPa was capable of triggering slip on the subset of pre-existing faults in basement that are most well-oriented for slip in the current stress field. For example, the basement rocks underlying the Arbuckle formation in Oklahoma are approximately 1.2 billion years old. Over that long period of geologic time, these basement rocks have been subjected to multiple episodes of tectonic deformation. Some deformational episodes may have reactivated faults formed at earlier geologic time periods. However, it is only the subset of critically-stressed faults that slip. The faults can be considered as potentially active faults in a geologic sense, as they could be expected to slip sometime in the future as a natural process. Obviously, critically-stressed faults in intraplate areas slip very infrequently. Nonetheless, it is easiest to think of this type of induced seismicity as natural earthquakes that have been advanced in time by injection-induced pressure changes.

Over the past 50 years, many studies have demonstrated the applicability of Coulomb Faulting Theory to the occurrence of injection induced seismicity. These studies began with the now classic studies of earthquakes caused by toxic water disposal in a deep well at the Rocky Mountain Arsenal near Denver, Colorado (Healy et al., 1968) and water injection to enhance oil production in the Rangely oil field, also in Colorado (Raleigh et al., 1976). Slip on faults in the earth is promoted by the shear stress acting parallel to the fault plane (as illustrated in Fig. 3a–e). Slip is resisted by the stress acting normal to the fault plane. The reason injection-related fluid pressure increases can trigger slip on a fault is that the increase in fluid pressure reduces the effective stress acting normal to the fault, thus making fault slip possible (Hubbert and Rubey, 1959) on an already-stressed fault.

The fact that basement seismicity can be triggered by very small pressure changes is consistent with the wide range of observations from intraplate regions around the world that support the concept that suitably-oriented pre-existing faults in basement are in a state of frictional failure equilibrium (see, for example, Zoback et al., 2002; Zoback and Gorelick, 2012). In fact, this was demonstrated experimentally at 9

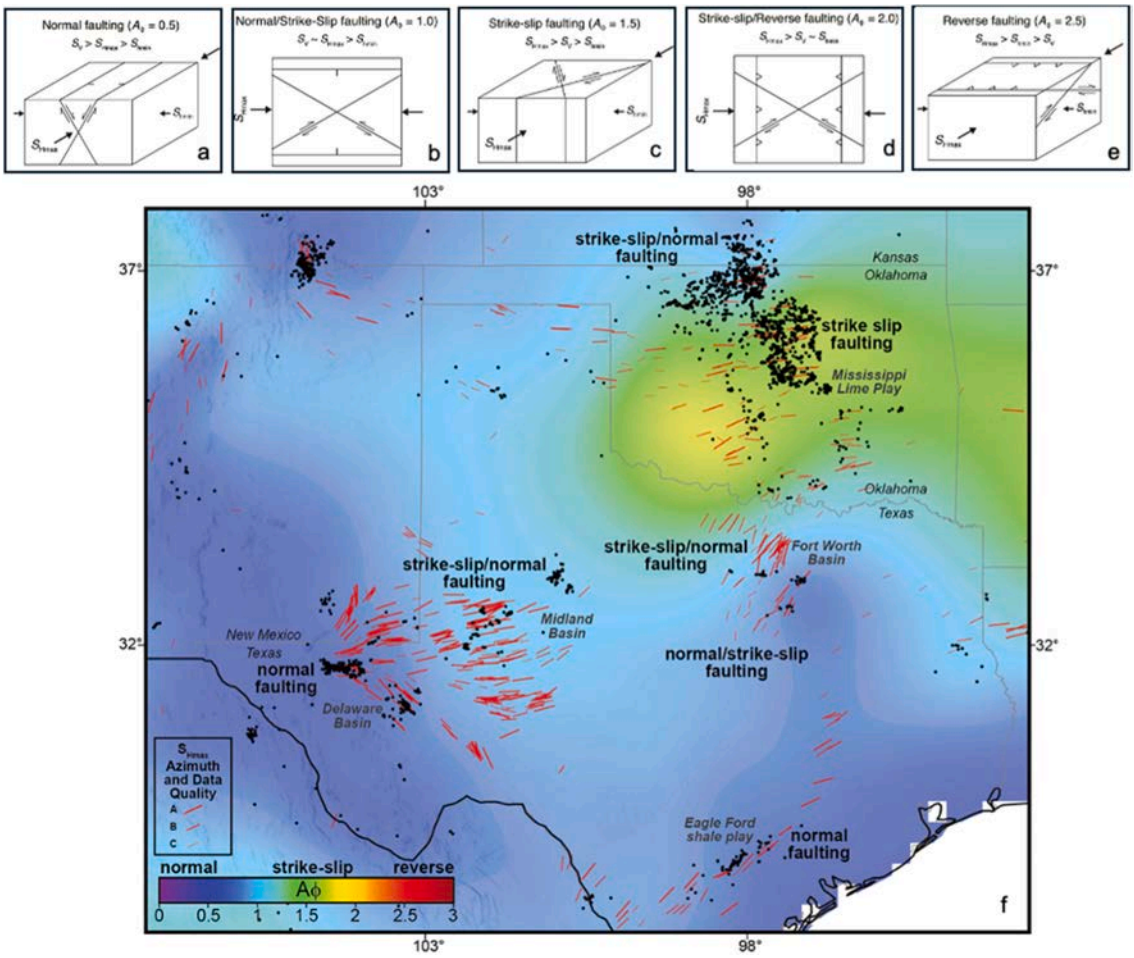


Fig. 3. a-e Five generalized stress states associated with crustal seismicity and the orientation of potentially active faults (see text, Fig. 3b and d are map view). The A_ϕ parameter is a quantitative measure of relative stress magnitudes (after Simpson, 1997). f) State of stress and seismicity in the region encompassing the four study areas considered here. The red lines indicate the azimuth of S_{Hmax} and the background color shows the values of Aϕ. Data from Lund Snee and Zoback (2022). The earthquakes shown are the same as shown in Fig. 1a.

Received by OCD: 6/29/2026

km depth in the deep KTB scientific research well in southeast Germany (Zoback and Harjes, 1997). As summarized by Townend and Zoback (2000), stress measurements made in relatively deep wells in crystalline rock around the world indicate a stress state in frictional faulting equilibrium.

It is helpful to briefly review key principles of Coulomb Faulting Theory that relate the current state of stress and fault slip in earthquakes. Coulomb Faulting Theory predicts a specific relationship between the stress state and the orientation of pre-existing faults in an area that could be induced to slip by fluid pressure change. In other words, even if many faults, potentially with a wide variety of orientations exist in an area (presumably the result of multiple episodes of deformation through geologic time), Coulomb Faulting Theory defines the orientation of which faults are critically stressed and could thus potentially be activated by injection-related pressure increases. Fig. 3a–e represents this graphically. The five stress states shown are an extension of Anderson faulting theory (Anderson, 1951) as described by Zoback and Kohli (2019). The five figures illustrate different configurations of the relative magnitudes of the vertical principal stress, S_V, the maximum horizontal principal stress, S_{Hmax}, and the minimum horizontal principal stress, S_{hmin} as well as the orientation of faults prone to reactivation for each stress state. In order of increasing compression, these stress states range continuously from

- Normal faulting ($S_V \geq S_{Hmax} \geq S_{hmin}$) - Fig. 3a
- Normal/strike-slip faulting ($S_V \approx S_{Hmax} \geq S_{hmin}$) - Fig. 3b
- Strike-slip faulting ($S_{Hmax} \geq S_V \geq$) - Fig. 3c
- Strike-slip/reverse ($S_{Hmax} \approx S_V \geq S_{hmin}$) - Fig. 3d
- Reverse faulting ($S_{Hmax} \geq S_{hmin} \geq S_V$) - Fig. 3e

To be able to map relative stress magnitude we quantify these stress states using the parameter A_ϕ (originally defined by Simpson (1997) which conveniently describes the ratio between principal stress magnitudes using a single, easily interpolated value. As shown in the figures, an A_ϕ value of 0.5 indicates a normal faulting stress state, a value of 1.0 indicates a normal/strike-slip faulting stress state, and so on.

The way to think about the faults shown in Fig. 3a–e, is that even if many faults were present in an area, if the area is characterized by normal faulting (A_ϕ=0.5), as shown in Fig. 3a, a potentially active fault would be expected to strike parallel to the azimuth of S_{Hmax} (S_{Hmax} Az) and dip in the direction of S_{hmin} about 60 ^{o} from horizontal (for expected values of the coefficient of friction). Similarly, as shown in Fig. 3c, potentially active strike-slip faults (A_ϕ=1.5) would be expected to dip steeply and strike $\pm$ 30^o to the direction of S_{Hmax}. Reverse faults would be expected to dip about 30^o and strike normal to the direction of S_{Hmax} as shown in Fig. 3e.

There is high-quality stress orientation and relative magnitude data in each of the four areas discussed in detail below. Fig. 3f is a stress map that encompasses these regions areas (data from Lund Snee and Zoback, 2022). The straight lines indicate S_{Hmax} Az, which is obtained from wellbores in the sedimentary *section* (*e.g.*, Zoback, 2007) and earthquake focal plane inversions in crystalline basement (see Lund Snee and Zoback, 2022 for details). The length of each stress indicator is an indication of the quality of the measurement. The background color of the map shows the relative stress magnitude using A_ϕ. Thus, with knowledge of both stress orientation and relative magnitude, it is possible to identify which faults in a region are critically stressed and could be induced to slip by increasing pore pressure. In addition to the fact that there are differences in the stress fields acting in the four areas considered above, there are also differences in distribution of pre-existing faults in each area (and even within one area) resulting from the unique characteristics of past deformational events.

There are five areas of noteworthy, induced seismicity shown in Fig. 3f. To briefly summarize the state of stress in these regions, the area of appreciable seismicity in north-central Oklahoma has a uniform N~85^{o}E S_{Hmax} Az and a strike-slip faulting stress state (Fig. 3c, A_ϕ = 1.5). The Fort Worth Basin of northeast Texas is characterized by a less compressive normal/strike-slip faulting stress state (Fig. 3b, A_ϕ = 1.0) and a consistent N~25^{o}E S_{Hmax} Az (Hennings et al., 2019). The Midland Basin in west Texas is also characterized by normal/strike-slip faulting stress state and a consistent N~85^{o}E S_{Hmax} Az. The Eagle Ford shale play in south Texas is characterized by a normal faulting stress state (Fig. 3a, A_ϕ = 0.5) and a uniform N~45^{o}E S_{Hmax} Az. As induced seismicity in this area is principally caused by hydraulic fracturing, we do not discuss this case further. The Delaware Basin of westernmost Texas and southeast New Mexico is also characterized by normal faulting. However, there is a pronounced regional variation in the S_{Hmax} Az where it is observed to rotate from N-S In the northernmost part of the basin to E-W near the border with New Mexico, and to NW-SE in the southern part of the basin. To address stress variations within basins, in their study of induced seismicity in the greater Permian Basin, Lund Snee and Zoback, (2018) defined 16 sub-regions of uniform S_{Hmax} Az. Morris et al. (2021) carried out a 3D fault slip hazard assessment in the Delaware Basin and subdivided it into 20 domains of distinct Aϕ and S_{Hmax} Az. Dvory and Zoback (2021) present a map smoothly-varying interpolated S_{Hmax} Az for the Permian Basin.

With knowledge of stress orientation and relative magnitude, Lund Snee and Zoback (2016) demonstrated the applicability of the Coulomb Faulting Theory for several cases of injection-induced seismicity in the Permian Basin. Similarly, (Lund Snee and Zoback, 2018; Hennings et al., 2021) demonstrated the applicability of Coulomb Faulting Theory of injection-induced seismicity in the Delaware Basin. Hennings et al. (2024) did the same for seismicity in the Midland Basin and Hennings et al. (2019) did the same for induced seismicity in the Ft. Worth Basin. Faults slip associated with seismicity triggered by hydraulic fracturing in the Eagle Ford shale play (Fig. 3f) also confirms the predictions of Coulomb Faulting Theory (McKeighan et al., 2022).

As a detailed demonstration of the applicability of Coulomb faulting theory, Fig. 4a is a map showing stress orientation and relative magnitude in Oklahoma (from Lund Snee and Zoback, 2022). The dashed white box is the area encompassing the majority of earthquakes induced by SWD have occurred since 2009. This is area is shown in detail in Fig. 4b. Both maps show faults mapped using public data available to the Oklahoma Geological Survey (Marsh and Holland, 2016). The abundant, high-quality stress data indicate a uniform N85^o±5^{o}E S_{Hmax} Az. This area is principally characterized strike-slip faulting stress regime with a tendency for strike-slip and normal faulting to occur near the border with Kansas. The seismicity in Fig. 4b shows epicentral trends delineating basement faults. This earthquake catalogue was developed using AI and machine learning techniques which locates approximately 400, 000 earthquakes (Park et al., 2022). The histogram in the lower left corner of Fig. 4c illustrates, the great majority of faults delineated by the seismicity strike ±30° from S_{Hmax} direction (as in Fig. 3c), thus confirming the prediction of Coulomb Faulting Theory. It is also important to note that very few of the basement faults defined by lineations of epicenters are correlative with the mapped faults. The seismicity near the site of the 2016 M5.8 Pawnee earthquake (inset in upper right corner of Fig. 4b) shows that the M 5.8 mainshock occurred on a fault striking about N100^{o}E, which was unknown prior to the earthquake. The earthquake epicenters trending about N40^{o}E are mostly aftershocks (and a few foreshocks) that are correlative with the location of a previously mapped fault. Together, the two faults comprise a conjugate fault pair striking ±30° from S_{Hmax} Az, just as predicted by Coulomb faulting theory and illustrated in Fig. 3c.

3. Deep injection and triggered slip on basement-rooted faults in four mid-continent areas

When producing oil from *conventional reservoirs*, saline water co-produced with the oil is typically re-injected into the producing formation. This helps maintain reservoir pressure and water injection wells can be located to drive oil toward production wells. In the case of

Received by OCD: 6/29/2026

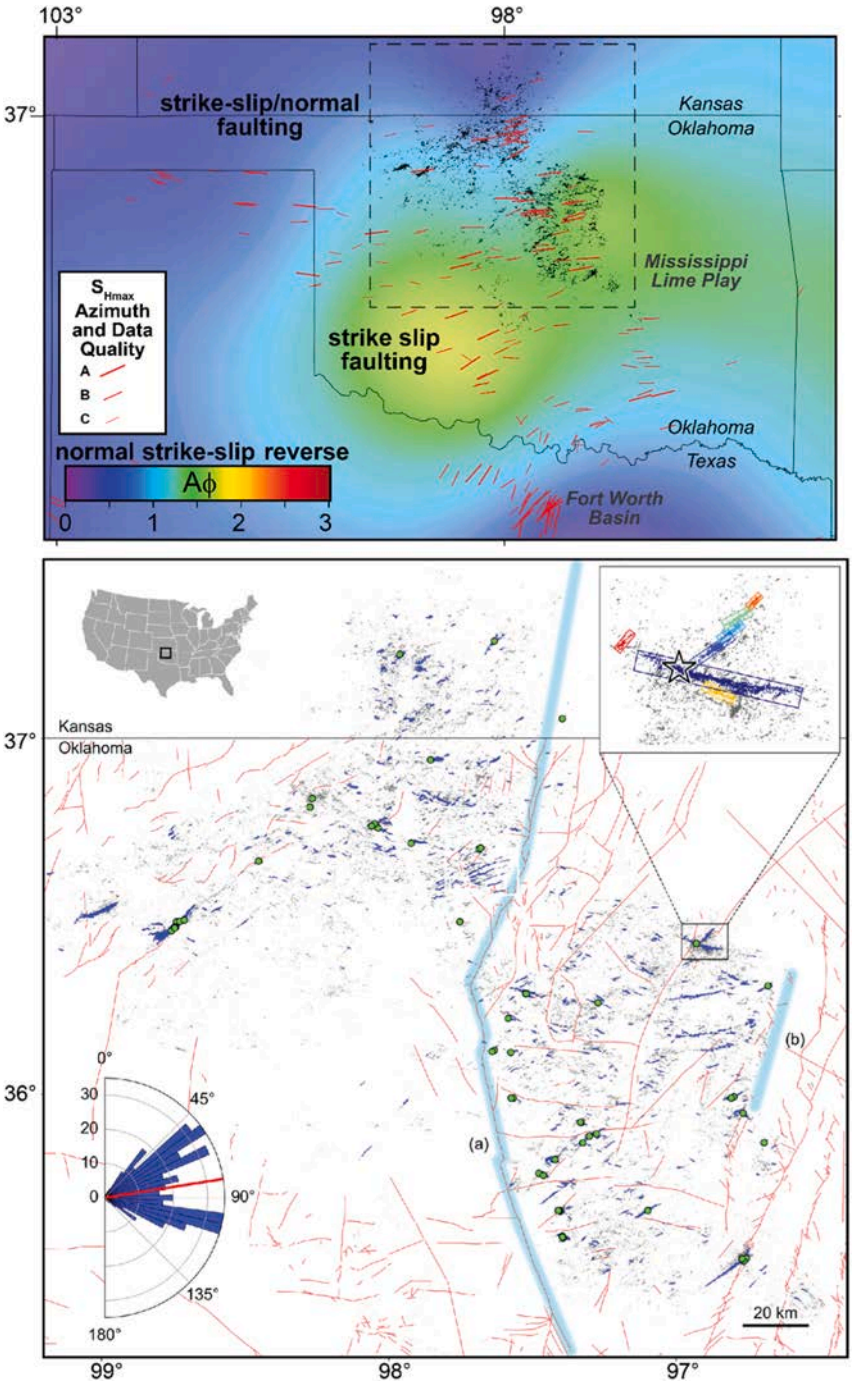


Fig. 4. a) Stress map of Oklahoma (after Lund Snee and Zoback, 2022). Data are obtained from both wellbore observations and the inversion of earthquake focal plane mechanisms. The A_Φ values represented by the background color range between 1.0 and 1.5 indicating a strike-slip (to strike-slip/normal) faulting regime in the area of most seismicity. Earthquakes are M≥2.0 from Park et al. (2022). The region of the dashed box is shown in b) where earthquake epicenters indicate fault trends in crystalline basement from Park et al. (2022) with known faults from Marsh and Holland (2016).

production from horizontal wells in *unconventional reservoirs* (which have extremely low permeability), it is not technically, nor economically, feasible to return the produced water to the hydrocarbon producing zone. Therefore, the produced water becomes wastewater and is injected into more porous and permeable zones either above or below the producing formations, as subject to regulatory requirements. Through 2023, this practice resulted in nearly 4 billion m^3 of wastewater being injected into deep saline aquifers in Oklahoma, southern Kansas, north-central Texas, and the Permian Basin region of west Texas and southeast New Mexico. Each of these areas has experienced significant injection-induced seismicity.

Fig. 5 shows the relationship between deep injection rates and resultant seismicity in each study area. Note that the scale of the figure is the same for each study area. Only earthquakes M ≥ 3 are shown for which the seismic catalogs are complete. In Oklahoma and southern Kansas (Fig. 5a), seismicity was first recorded when injection rates reached about 5.5 million m^3/month in 2008. At this time there were hundreds of injection wells operating throughout the seismically active

Received by OCD: 6/29/2026

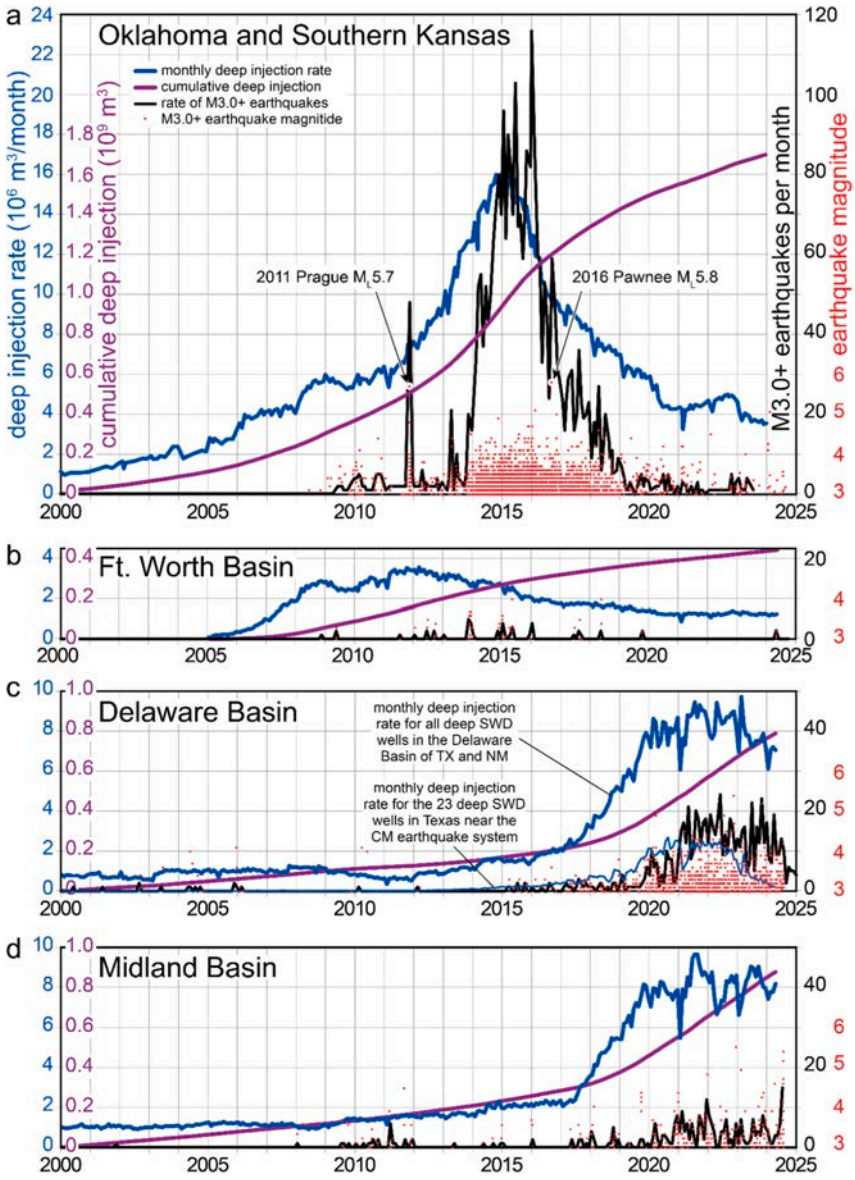


Fig. 5. Comparison of rates of monthly injection for all deep SWD wells, cumulative deep SWD, monthly earthquakes rates (M_L3.0+), and earthquake magnitude (M_L3.0+) for the four cases of deep SWD-induced seismicity we discuss. The plots are shown at the same scale to allow direct comparison of trends.

area. Triggered seismicity was recognized as a significant hazard with the occurrence of the Prague earthquake sequence in Nov. 2011 (Keranen et al., 2013) which included three earthquakes M $\geq$ 5 and numerous aftershocks M $\geq$ 3 as represented by the spike in the number of earthquakes at that time. Other spikes in seismicity rate are associated with aftershocks of larger events. Following the Prague sequence, the injection rate continued to increase through mid-2015 as did the seismicity rate, albeit with a delay of about a year (Langenbruch et al., 2018). At that time, a M $\geq$ 4 earthquakes were occurring about once per week with shaking being felt by the majority of people living in the state. The biggest earthquake to have been triggered to date was the M5.8 Pawnee earthquake in 2016. A marked decrease of seismicity started in the latter part of 2015 when regulators started the first of two restrictions on cumulative injection volumes to those that preceded the marked increase in seismicity in 2012. This is discussed in detail by (Langenbruch and Zoback (2017). Through the end of 2024, approximately 1.7 billion m^3 was injected via more than 700 wells distributed throughout the seismically active area.

Fig. 5b shows that injection rates were much less pronounced in the Fort Worth Basin as was the degree of triggered seismicity. That said, these earthquakes occurred in the region surrounding the Dallas/Ft. Worth metropolitan area with a population of ~ 8 million. Thus, while the earthquake *hazard* was much less (there were fewer and relatively smaller earthquakes than the other areas we discuss here), the potential earthquake *risk* is much greater due to the potential impact of the earthquakes on people and infrastructure earthquakes as large as those in Oklahoma had occurred.

As shown in Fig. 2, the Delaware Basin is a region where there has been appreciable induced seismicity resulting from both shallow and deep injection. Deep injection and earthquakes on basement-rooted faults is principally occurring in the northern part of the basin. Fig. 5c shows a marked acceleration of seismicity coincident with and increase in deep injection rates that started around 2016, leveled off at about 8 million m^3/month in 2020 and began to slowly decrease in 2023 as deep injection rates declined. As in Oklahoma, there is a delay between the time at which deep injection markedly increased and the corresponding increase in seismicity. It should also be noted that M3.0+ earthquakes were catalogued in the area as long ago as 2001, a marked increase in

Received by OCD: 6/29/2026

seismicity was observed when cumulative injection rates reach about 5 million m^3/month in 2018. As in Oklahoma, the rate of seismicity decreased in 2022 associated with the staged curtailment of deep injection in wells that were in closest proximity to the larges induced earthquakes.

The onset of M≥3.0 earthquakes began in the Midland Basin around 2008 (Fig. 5d) and earthquakes occurred intermittently through 2017 while deep injection rates rose gradually from 1 to 2 million m^3/month. Earthquake rates and magnitudes then increased as the rate of injection increased to 8 million m^3/month. The overall relationship between injection rate and seismicity is somewhat different as compared to the Oklahoma and Delaware Basin cases in that the rate of seismicity did not increase to the same degree with sharply increasing injection rate. However, there have been 17 M4.0+ and 3 M5.0+ earthquakes in the Midland Basin since mid-2019.

3.1. North-Central Oklahoma and southern Kansas

Fig. 6 schematically illustrates the key factors responsible for the occurrence of induced earthquakes caused by basal injection in north-central Oklahoma and southern Kansas. Large volumes of co-produced wastewater from the Mississippi Lime and the Hunton Limestone (the black layers in the figure) were injected using hundreds of well into the underlaying Arbuckle Group which is in direct contact with basement. The Arbuckle is thick, porous, permeable and is typically under hydrostatic pressure by as much as ~2 MPa (Allen et al., 2024). These factors seemingly make The Arbuckle ideal for injection. The wastewater diffuses quickly in the Arbuckle due to its high permeability causing elevated pressure to be transmitted directly to faults in the underlying basement over a very large area, resulting in seismicity regionally (Fig. 6c). As shown in Fig. 6b, the seismicity is in the crystalline basement, peaking at a depth of about 8 km below the surface and over 5 km deeper than the contact between the Arbuckle and basement (Park et al., 2022).

An important concept that helps explain why injection-related pressure changes in the Arbuckle triggers seismicity in basement on critically-stressed faults is that these faults have much higher permeability than faults that are mis-oriented for slip in the current stress field. In other words, mechanically dead faults are also hydraulically dead (Barton et al., 1995; Townend and Zoback, 2001; Hennings et al., 2012). Thus, critically-stressed faults that extend from basement up into the sedimentary section provide permeable conduits for pressure transmission to depth in the basement. This is seen in all the cases we discuss in which injection into basal aquifers has triggered seismicity.

Early studies of produced water injection and induced seismicity in Oklahoma found that the increase of pressure in the Arbuckle was surprisingly very small (Walsh and Zoback, 2015). The prevailing sub-hydrostatic condition causes the static water level in an injection well to be ~200 m below ground level and therefore wastewater appears to "fall" into these wells simply due to its weight with injection rates in some cases exceeding 60,000 bbls/day, ~10,000 m^3/day. Despite such high injection rates, whenever injection was terminated, the water level in the well dropped immediately, indicating that pressure remained sub-hydrostatic in the injection reservoir surrounding the well. Even with the large cumulative injection volume from hundreds of wells, modeling indicates the pressure change in the Arbuckle was only about +1 MPa (Langenbruch et al., 2018). Allen et al. (2024) report pressure increases as ranging between 0.3–1.7 MPa below hydrostatic in 15 Arbuckle observation wells in 2016, shortly after the time of peak injection.

Walsh and Zoback (2015) analyzed the correlation between produced water injection and seismicity in north-central and Oklahoma and demonstrated a clear correlation between SWD into the Arbuckle formation and earthquakes in basement. Focusing on 6, 5000 km^2 study areas in Oklahoma, they showed that the three areas with appreciable anomalous seismicity had appreciable SWD into the Arbuckle. Three adjacent areas with almost no SWD had little seismicity. As SWD injection rates increased through 2015, so did the frequency of earthquakes in these areas but, because the pressure change in the Arbuckle was widespread, there was no clear correlation between individual injection wells and individual earthquakes. Instead, the response was observed at a larger system scale.

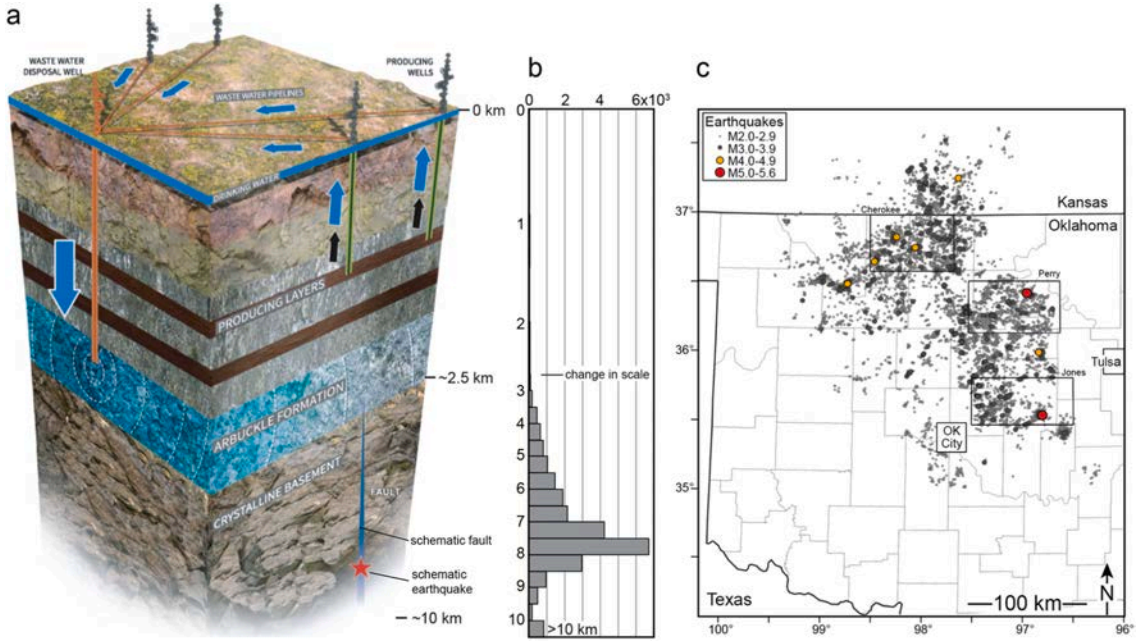


Fig. 6. a) Schematic illustration of produced water from formations such as the Mississippi and Hunton limestones (black layers) being injected into the Arbuckle Group which sits directly on basement (from Zoback and Kohli, 2019). b) Earthquakes triggered by the produced water injection occur in basement. Most seismicity is about 5 km beneath the Arbuckle/basement contact. c) M2.0+ earthquakes were triggered over an extremely large area in north-central Oklahoma and southern Kansas. Data in b) and c) are from Park et al. (2022).

Received by OCD: 6/29/2026

Following the establishment of causation between large-scale SWD into the Arbuckle Group and triggered seismicity, in late 2015 and early 2016 regulators mandated a 40 % reduction of the total volume of produced water to levels that existed prior to the marked increase in seismicity rate. As shown in Fig. 5a, the rate of M3.0+ earthquakes decreased markedly following the reduction in injection rate. In fact, injection rates decreased even more than mandated, and the seismicity rate has since decreased by more than 95 %. Skoumal et al. (2024) discuss the reduction of the earthquake rate in Oklahoma and Kansas as resulting from systemic reduction in injection rate (due both to petroleum commodity price collapse and regulatory actions) and plugging off many SWD wells such that injection was no longer occurring in close proximity to the seismogenic basement.

3.2. Fort Worth Basin

Natural gas development of the Barnett Formation in the Fort Worth Basin of north-central Texas is where unconventional petroleum development of shale reservoirs was first carried out at the basin scale. Wastewater produced along with natural gas comes from the "flowback" of water used hydraulic fracturing as well as formation water. As shown in Fig. 5b, rates of SWD in the Fort Worth Basin began to increase in 2005, reached 2.9 million m^3/month in 2008 as earthquake clusters began to develop, and peaked at 3.5 million m^3/month in 2012 as unconventional development of the basin matured and the rate of induced earthquake cluster development increased. Like the case of Oklahoma and Kansas, deep wastewater injection in the Fort Worth Basin utilized a permeable basal saline aquifer, in the case Ellenburger Group carbonates, which rests stratigraphically on top of seismogenic basement (Horne et al., 2022) (Fig. 7a, b). Most of the seismicity was in the upper ~2 km of the basement, the faults that ruptured are all normal faults that were formed in late Paleozoic time and are linked to older faults in the basement. The current stress state is strike-slip/normal which means $S_{Hmax} \approx S_V$ and both are sufficiently larger than S_{hmin} to satisfy Eqn. 3. The Aϕ value varies systematically across the basin from 1.2 in the north to 0.8 in the south indicating a transition from normal and strike-slip faulting in the north, to normal faulting in the south.

An important aspect of induced seismicity in the Fort Worth Basin is that earthquake clusters developed in close proximity to sites of large-scale injection (proximal) as well as up to 40 km distant. At that great distance (distal), the increase in pore pressure (ΔPp) and the stress change from poroelastic effect (Δσ) must be vanishingly small. Distal earthquake inducement has also been documented for the Oklahoma and Kansas case (Peterie et al., 2018) as well as the Delaware Basin, as discussed below. Integrating the necessary basin-scale components for mechanistic induced seismicity assessment including a 3D Ellenberger Group geological model (Smye et al., 2021), 3D fault interpretation (Horne et al., 2020), in situ stress and fault slip potential analysis (Hennings et al., 2019), Ellenburger Group injection pore pressure model (Gao et al., 2021), and a highly detailed earthquake catalog (Quinones et al., 2019; Hennings et al., 2019, 2021) show that approximately 9 % of the trace length of faults in the basin became seismogenic following an increase in ΔPp from SWD ranging from negligible to 0.36 MPa (≤ 52 psi). This indicates that faults in the Fort Worth Basin can be made unstable with very small pressure or stress perturbations, similar to the Oklahoma example. The faults that ruptured extend from the Ellenburger Group injection zone down into the geologic basement and, as these faults have a wide variation of orientations, there is a correspondingly wide variation in the slip sensitivity of the faults. Once established, reactivation of the earthquake sequences occurred with additional increases of ΔP ranging up to 0.37 MPa. As ΔPp in the basin increased and earthquake sequences formed and evolved, the fault slip potential (FSP; Walsh and Zoback, 2016) increased as well. Fig. 7a shows the maximum ΔPp that the base of the

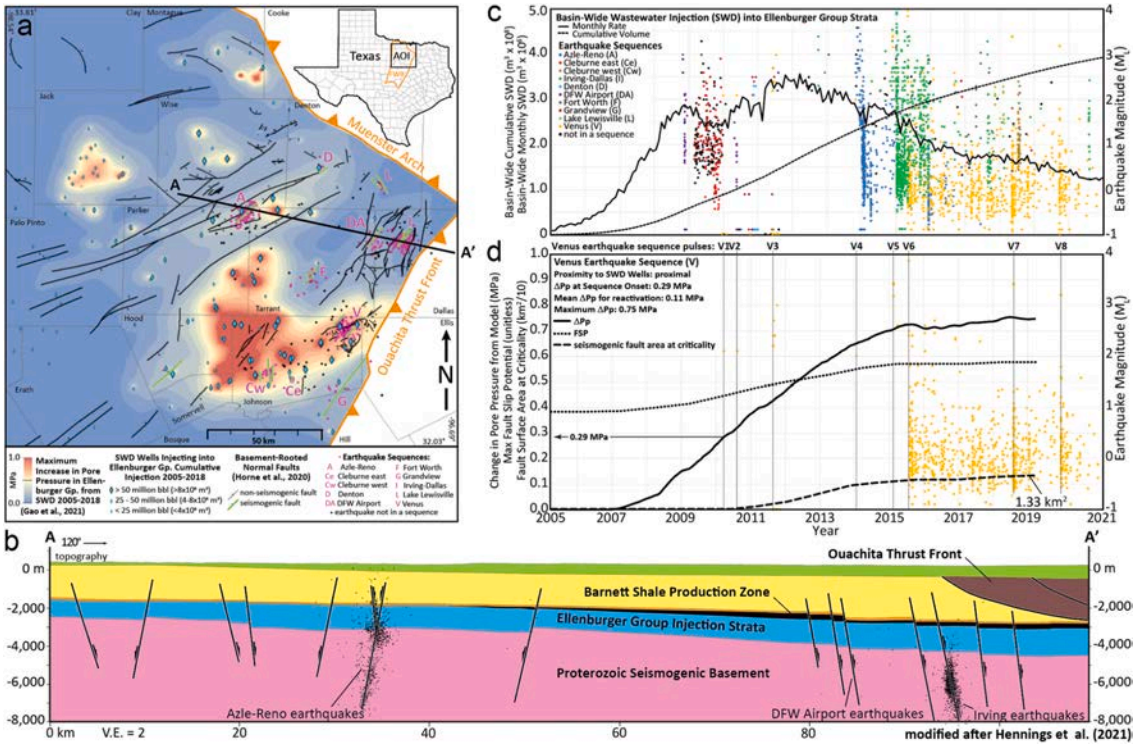


Fig. 7. Mechanistic analysis of deep injection-induced seismicity in the Fort Worth Basin (modified from Hennings et al., 2021). a. Map showing maximum modeled ΔPp from deep injection as experienced at the base of the Ellenberger. b. Cross section showing the architecture of the injection strata in association with normal faults, some of which have become seismogenic (see a) for cross section trace). c. History of monthly and cumulative deep SWD in the Fort Worth Basin along with date and magnitude of prevalent earthquake sequences. d. Time series of pore pressure change from the hydrogeologic model, onset and occurrence of local earthquakes, and evolution of deterministic and probabilistic fault slip potential (FSP, see text).

Received by OCD: 6/29/2026

Ellenberger Group experienced as subject to SWD. Fig. 7b illustrates the structure of the faults in the basin and highlights that some faults experienced extensive ruptures along their surfaces while adjacent faults did not. Fig. 7c shows the overall history of deep SWD in the basin and the temporal character of individual earthquake clusters, some isolated, some lengthy. Fig. 7d highlights the inception of one earthquake cluster in relation to local ΔPp and evolution of probabilistic and deterministic FSP. While the overall seismicity rate in this area was much lower than in Oklahoma, the overall amount of wastewater injection was much less. Approximately 500 million m^3 of wastewater was injected in this area of approximately 22,500 km^2 over the ~4 years prior to the initial onset of seismicity and 2.5 billion m^3 was injected prior to the development of widespread induced seismicity throughout the basin.

Although the number and magnitude of induced earthquakes in the Fort Worth Basin is the least severe of the four cases discussed (*e.g.*, 40 M3.0+, $M_{max} = 4.0$), earthquakes being felt at the surface in a population center with over 8,000,000 people was a significant and widespread concern (Hennings and Young, 2023), more so than the other cases we consider which experienced a far greater number and larger magnitudes of induced events.

3.3. Delaware Basin

Hennings and Smye (2024) describe the seven active induced earthquake systems in the Permian Basin. They define an induced earthquake system to be the earthquakes induced by a specific set of anthropogenic agents that interact uniquely with specific geologic elements in an understandable spatial and temporal context. The case of Oklahoma/Kansas described above has, in general, a single induced earthquake system. Induced seismicity in the Delaware Basin, the western sub-basin of the greater Permian Basin, has three earthquake systems and is the most complex set of cases that we discuss. These three induced earthquake systems include earthquakes hosted on basement rooted faults as induced by proximal deep injection in southeast New Mexico (NDB, Fig. 8); earthquakes hosted on basement-rooted-faults as induced by distal deep injection in the central Delaware Basin of Texas (CM); and shallow, earthquakes hosted on strata-bound faults in the southern Delaware Basin in Texas as induced by a combination of shallow injection, hydraulic fracturing, and possible compaction of oil reservoirs during unconventional production (SDB).

The case of earthquakes hosted on basement rooted faults as induced by distal deep injection in the central Delaware Basin of Texas (CM, Fig. 8) is particularly troubling because it is caused by the stress change from deep injection that occurred at considerable distance to the north of the induced earthquake clusters (Fig. 9a). In this context, Smye et al. (2024a) show the degree of ΔPp associated with development of the CM earthquake system, which in 2021, had a maximum rate of 42 $M_L3.0+$/mo in area of 1,600 km^2. Note that the degree of ΔPp associated with development of the CM system has magnitudes mostly < 0.4 MPa with only 2 clusters as high as 0.8 MPa. As driven by the same deep injection practices in New Mexico, ΔPp achieved magnitudes of > 3.0 MPa in large areas within which few earthquake clusters developed. The basement faults that have hosted seismicity in the CM induced earthquake system must be truly very sensitive to rupture from ΔPp. Another important aspect of both the NDB and CM induced earthquake systems is the deep injection has not occurred in close proximity to seismogenic basement (Smye et al., 2024a,b). For the 23 permitted deep injection wells in the NCR SRA (North Culberson Reeves Seismicity Response Area) in Texas within the CM induced earthquake system, the mean vertical distance between the zones of injection and the top of basement

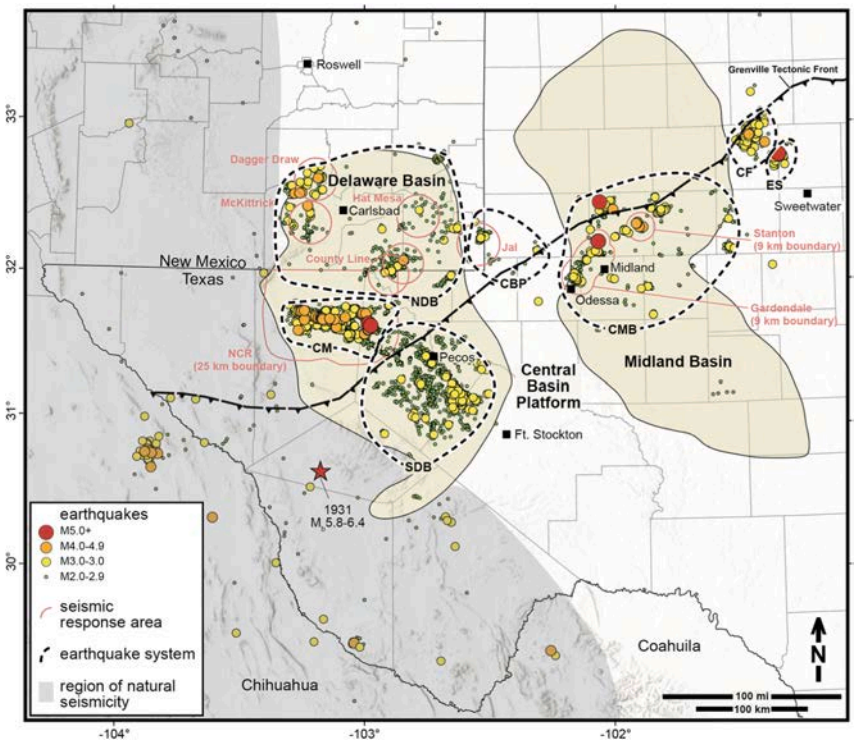


Fig. 8. Generalized map of the Permian Basin showing earthquakes as merged with duplicates removed from the USGS for the period 2000-2023, for 2009-2010, TexNet Earthquake Catalog for 2017-2023, and New Mexico Tech Seismological Observatory for southeast New Mexico for 2019-2023. The Seismic Response Areas (SRAs) are from the Railroad Commission of Texas and the New Mexico Oil Conservation Division and are outlined in red. The SRAs shown for NM are the 16 km (10 mi) boundaries for M3.0+ earthquakes. Earthquake systems as described in the text and outlined in dashed lines include: the Northern Delaware Basin (NDB), Culberson Mentone (CM), Southern Delaware Basin (SDB), Central Basin Platform (CBP), Central Midland Basin (CMB), Eastern Shelf (ES), Cogdell Field (CF). The red star shows the location of the largest earthquake documented for the Permian Basin region which was estimated to be Mb 5.8-6.4 and interpreted to be naturally occurring. Fig. modified after Hennings and Smye (2024).

Received by OCD: 6/29/2026

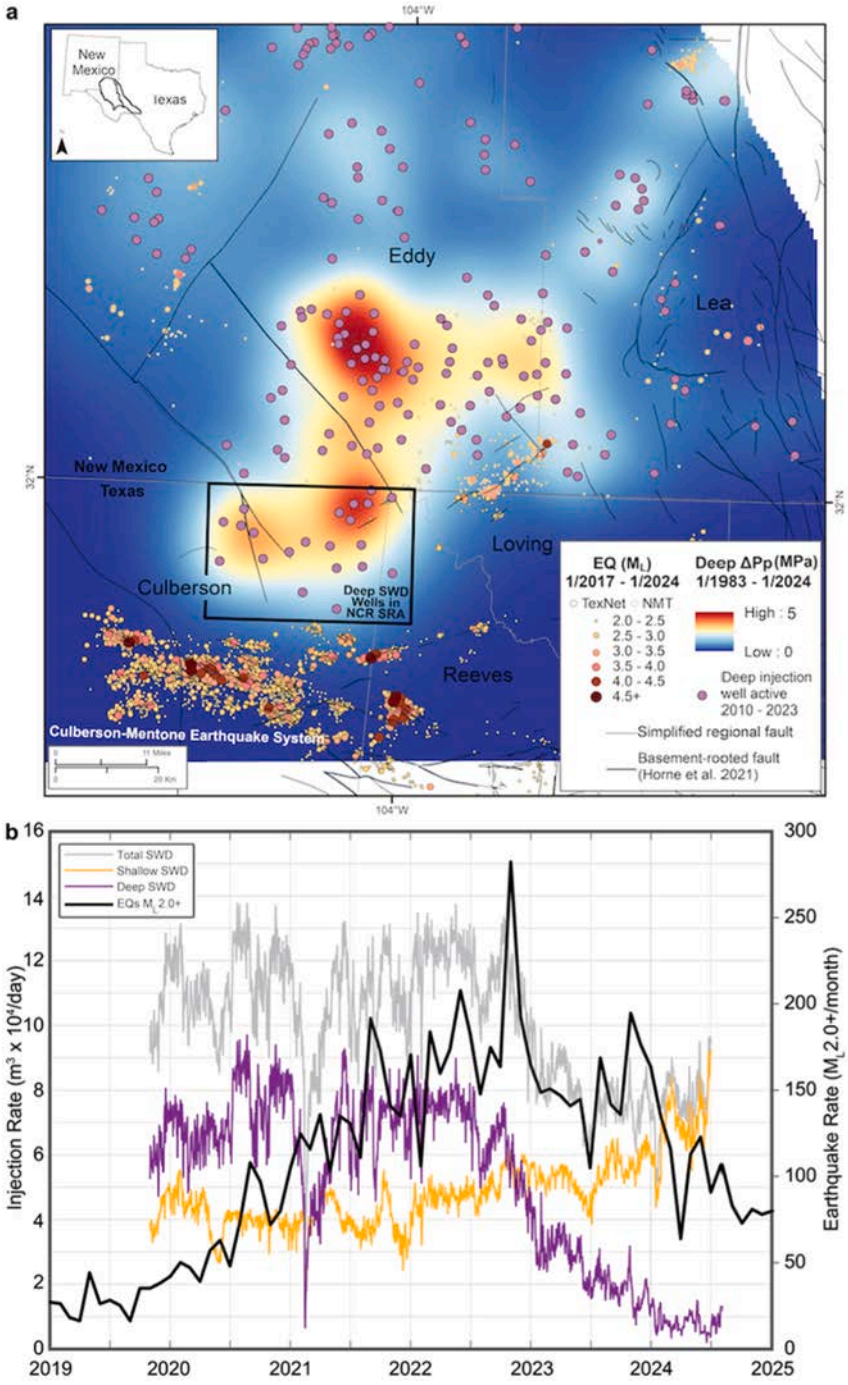


Fig. 9. a). Pore pressure evolution map for deep injection in the northern Delaware Basin showing earthquakes interpreted to be of induced origin (modified after Smye et al., 2024a). Referring to Fig. 9 nomenclature, the two earthquake systems shown in (a) include the NDB, principally in New Mexico and the CM in Culberson and Reeves Counties, in Texas. Note that the degree of ΔPp associated with development of the CM system has magnitudes mostly < 0.4 MPa and 2 clusters as high as 0.8 MPa. b. monthly wastewater injection and earthquake rates in the NCR RRC seismic response area in Texas which focuses on the CM earthquake system. Note the peak earthquake rate in late 2022 the subsequent decrease which is attributed to the decrease in deep injection rate following suspension of 23 deep injection well permits by the RRC. Earthquake data from TexNet and injection data from the TexNet injection reporting tool.

is 500 m. Fig. 9b shows the recent history of daily injection rate and monthly earthquake rate. Note that the earthquake rate peaked in late 2022 and has generally decreased as the monthly rate of deep injection has also decreased following regulatory actions by the Railroad Commission of Texas (RRC) to curtail injection in 23 deep SWD wells in the Texas portion of the Delaware Basin (Fig. 9a).

3.4. Midland Basin

Of the four cases of deep injection-triggered seismicity we discuss, the Midland Basin is unique in that high rates of deep injection occurred for many years prior to the increase in injection rate associated with the development of the widespread earthquake clusters (Fig. 5d). Subsequent to the large increase in injection rate that began in 2013 (Smye

Received by OCD: 6/29/2026

et al., 2024b) and ΔPp that soon followed (Ge et al., 2024), the monthly earthquake rate increased sporadically while ~21 earthquake clusters developed, and there were three earthquakes of M_L5.0+ (Fig. 10; Hennings et al., 2024). Hennings et al. (2024) show how ΔPp from deep injection has interacted with basement-rooted faults mapped by Horne et al. (2024) to cause the cumulative length of critically stressed fault segments to increase from 400 km in 2015 to over 1,300 km in 2023 as the 21 earthquake clusters developed. Sampling the pore pressure increase associated with earthquake cluster onset shows that onset occurred at ΔPp ranging 0.26-3.65 MPa with a mean of 1.5 MPa, and with fault rupture sensitivity that varies regionally and systematically which is similar to the Oklahoma and Fort Worth Basin examples.

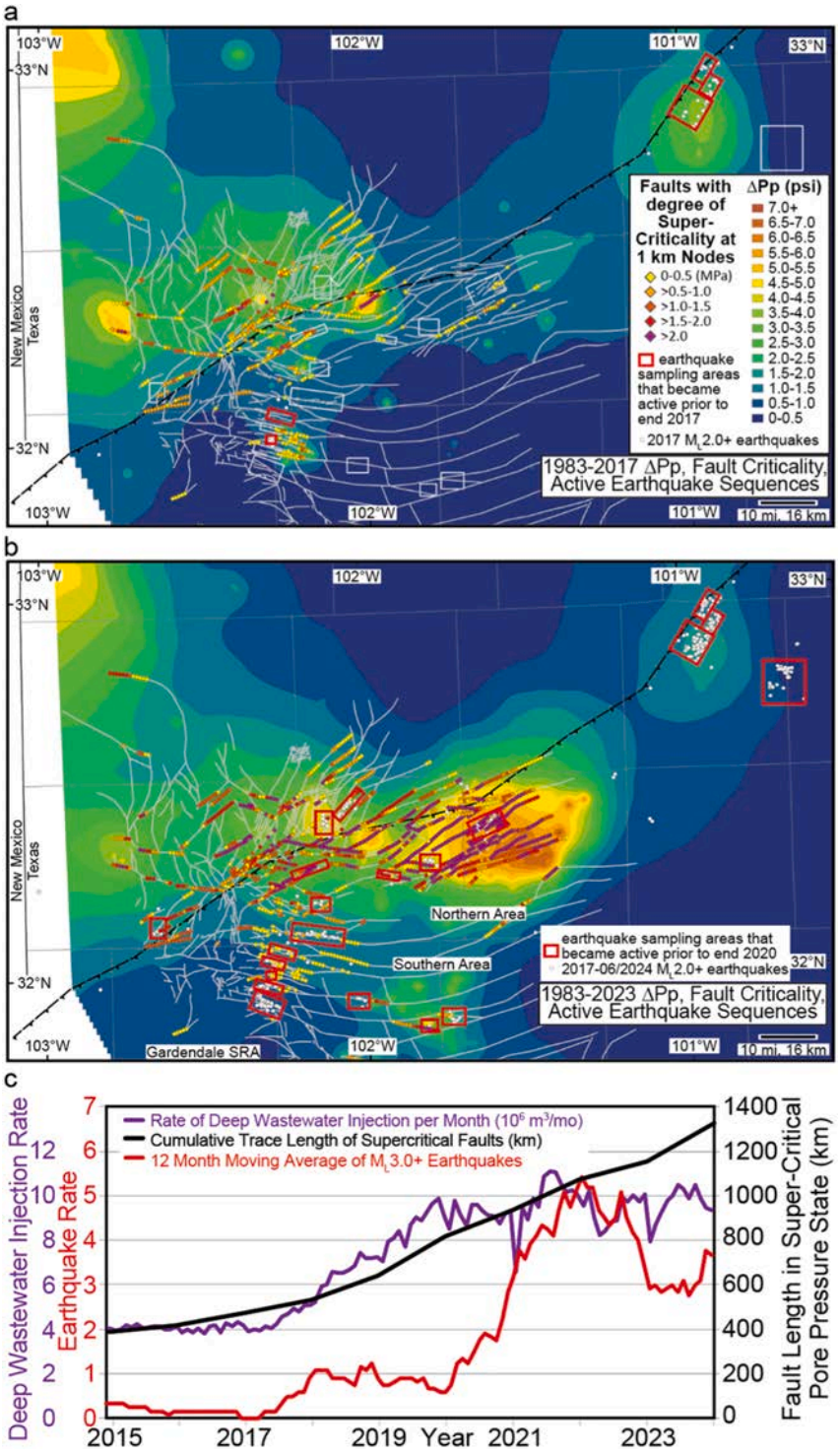


Fig. 10. a. Pore pressure evolution map for deep injection in the central Midland Basin showing ΔPp evolution through 2017, the first earthquake clusters to form associated with ΔPp, and the location of basement-rooted faults that became critically-stressed. b. Map showing the same elements as in (a) but as of the end of 2023 for ΔPp and fault criticality and mid-2024 for earthquakes. c. Graph of the evolution of fault criticality, rate of deep injection, and earthquake rate (modified after Hennings et al., 2024).

Received by OCD: 6/29/2026

3.5. Commonalities among these deep injection induced earthquake systems

There are many important commonalities in the relationship between deep injection and induced earthquakes in the four cases discussed above:

1. Earthquakes are predominantly in crystalline basement beneath the relatively permeable sedimentary formation used for injection. The vertical distance from the level of injection to the sediment/basement contact can be as much as several hundred meters.
2. The faults associated with these earthquakes cut upward from basement up to or into the overlying injection strata, thereby providing discrete hydrologic connection from zones of injection to the seismogenic basement.
3. The faults associated with these earthquakes originated during episodes of geologic deformation that occurred hundreds of millions of years ago, although there might have been periods of reactivation during subsequent tectonic episodes.
4. Nearly all of the seismogenic basement faults were unknown prior to the development of injection-induced seismicity.
5. In each of the four regional cases we discuss, there is clear evidence that the increase in pore pressure in the injection zone that triggered basement seismicity is quite small, on the order of 1 MPa or less. At a representative injection depth of 3 km, hydrostatic pore pressure would be 30 MPa. Thus, a 1 MPa pressure increase represents a very small increase in pressure (a few percent), compared to the frac gradient, for example, that would be on the order of 10 MPa, or more, above ambient pore pressure.
6. In each regional case, the detailed relationship between the distribution of increased pore pressure and the development of the induced earthquake system can seem quite complex, but the presence or absence of *critically-stressed* faults is the principal factor. The concept of a critically-stressed crust in relatively stable continental interiors explains why such small pore pressure increases can trigger intraplate earthquakes of significant size.
7. Given the age and tectonic complexity of the basement in the U.S. mid-continent, it is likely that faults are present everywhere as demonstrated by anthropogenic fault reactivation in all areas subject to large-scale SWD. However, some areas will be more hazardous than others because there are a greater number of critically-stressed faults.
8. In every case of injection-triggered seismicity studied to date where there is knowledge of the orientation and relative magnitude of the current stress field, the subset of pre-existing faults could be identified in a straightforward fashion using Coulomb Faulting Theory. This means that when there is reasonably good knowledge of the state of stress, it is possible to estimate (prior to injection) if known faults have significant fault slip potential.

3.6. Complicating factors

It is important to note that the state of stress varies systematically on a regional scale and knowing the local state of stress is essential for understanding which faults carry a higher rupture hazard. Fig. 3f shows the state of stress in the region of our examples. As noted above, north-central Oklahoma is characterized by a strike-slip faulting stress state with a tendency for strike-slip and normal faulting near the Kansas border. The observed fault ruptures are predominantly strike-slip in that region. The domain of strike-slip faulting in Oklahoma changes to a transitional regime of strike-slip/normal faulting to the south in Texas and the ruptures in the Fort Worth Basin have been predominantly normal faulting along older normal faults (Quinones et al., 2019; Hennings and Young, 2023 and citations therein). Further to the south the stress state becomes pure normal faulting ($A\phi \approx 0.5$) as the neotectonic regime transitions to the Gulf Coast passive margin. In the region of the Eagle Ford shale play along the Texas Gulf Coast where earthquakes are often triggered by hydraulic fracturing, the observed fault ruptures are exclusively normal faulting along preexisting normal faults (e.g. McKeighan et al., 2022 and citations therein). As shown in Fig. 3f, the Midland Basin sits in a broad domain of transitional strike-slip/normal faulting where fault ruptures have been dominantly strike-slip along steeply-dipping faults in basement but with significant normal ruptures as well (Woo and Ellsworth, 2023; Horne et al., 2024; Huang et al., 2024). To the west in the Delaware Basin, the stress state transitions to pure normal faulting associated with the Rio Grande Rift (Lund et al., 2020) and the ruptures observed in both basement and the sedimentary realm occur as normal faulting of existing normal faults and reverse faults.

Within any given region subject to injection-induced seismicity there will typically be some faults that are known prior to the development of induced earthquake clusters but most of the faults that become seismogenic are previously unmapped or unknown in publicly available data. Depending on how the fault geometry and/or the stress field varies, the induced ruptures will usually not cause the entire fault to slip at once but will instead cause limited portions of the fault length or surface area to slip, leading to development of localized earthquake clusters. Due to the concern of the evolving induced hazard in each of the four areas we discuss, the mapping of faults that have and have not ruptured has improved significantly. For example, new mapping of basement rooted faults in the induced seismicity corridor of the Midland Basin by Horne et al. (2024) indicates that there are nearly 800 faults or fault zones that sum to >5,200 km of fault length. However, only about 600 km of that length has become seismogenic. This is despite an analysis that indicates that greater than 1,300 km of fault length has become critically stressed in localized areas that have experienced as much as 3 MPa of pressure increases due to recent injection (Hennings et al., 2024). Thus, it is an important commonality among these four cases of injection induced seismicity that it is the critically-stressed faults that host the induced ruptures but there is significant complexity in the behavior governing which fault segments slip in the presence of pore pressure increase. This typically makes fine-scale spatial and temporal prediction unpractical. What can be said, in general, for the four areas we describe where FSP analysis has been performed using well-constrained input data, is that all of the earthquake clusters have occurred along faults that were stressed critically, natively, or made critical by pore pressure increase from injection. However, it is only a very small percentage of the total length or size of critically stressed faults that slipped in the regions that have experienced pore pressure change. This means that FSP analysis, or any sort of fault rupture assessment or model, is a screening tool, identifying if a fault is, or might reach, a condition of instability, not when or how it might slip.

Another manifestation of spatial variations of the number of critically-stressed faults in an area is how this would affect the rate of triggered seismicity in response to an increase in pore pressure. In Fig. 11, we illustrate a case study of Oklahoma seismicity in which the issue of *fault inheritance* is parameterized in terms of the Seismogenic Index (after Shapiro et al., 2010). The Seismological Index is a statistical modelling procedure based on assumptions of homogenous presence and orientation of pre-existing faults in an area subject to pore pressure increase that diffuses throughout a rock volume from sites of injection. Effectively, a Seismologic Index analysis allows one to separate anthropogenic pressure increases and the geologic inheritance of pre-existing faults in an area of interest. The Seismogenic Index (SI) can be thought of as a statistical measure the number of critically-stressed faults in an area. Thus, any given increase in pore pressure would result in more triggered earthquakes in an area of high SI, compared to an area of low SI.

Langenbruch et al. (2018) carried out a SI study of Oklahoma seismicity based on a relatively simple hydrologic model of injection into the Arbuckle Group and the pressure change at depth responsible for earthquake triggering. Fig. 11a shows the close correlation between

Received by OCD: 6/29/2026

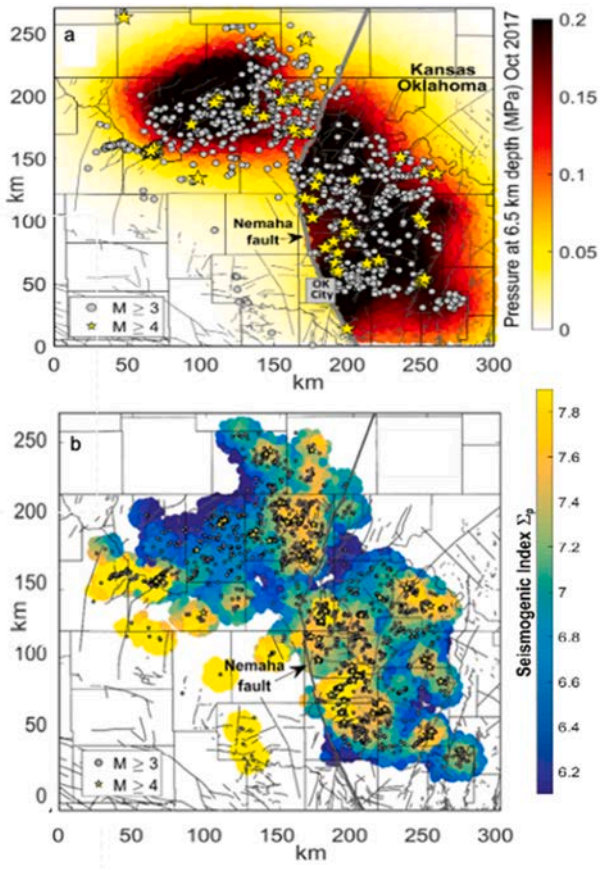


Fig. 11. a) Map of injection-induced pressure increase at the depth of most basement earthquakes (Jan 2000 - Dec 2017). Earthquakes (M ≥ 3 grey dots, M ≥ 4 yellow stars) occurred where injection caused a pressure increase at depth. b) Mapped spatial variability of the Seismogenic Index in north-central Oklahoma and southern Kansas. The SI shows significant variability in space but it is stable in time. Both figures are from Langenbruch et al, (2018).

modelled pore pressure at the average depth of seismicity and the location of injection-induced earthquakes. The approximately north-south trending Nemaha fault (shown by the wide gray line) was assumed to be an impermeable flow barrier based on independent information. The model shows an excellent correlation between the areas of pressure increases at depth and the resultant seismicity. Pressure changes on the east side of the region results from SWD only on the east side of the Nemaha fault which correlates well with the seismicity in that structural domain. Similarly, the pressure change that correlates with the seismicity to the west of the Nemaha fault results from injection wells only on that side of the model.

As shown in Fig. 11b (from Langenbruch et al., 2018), the variation of the SI indicates that there is a spatial variation of about a factor of 20 in the seismicity rate for a given pressure change. Some areas, such as the dark blue area near the Oklahoma/Kansas border, resulted in much less seismicity than more seismically active areas indicated by bright yellow. This likely results from there being relatively more critically-stressed faults in crystalline basement in the high SI areas. Thus, just as the relationship between deep injection and triggered seismicity varies from basin to basin as shown in Fig. 5, there are variations in the seismogenic response to pressure changes within a given basin depending on presence of pre-existing critically-stressed faults. Thus, the importance of geologic inheritance cannot be overestimated in understanding the intensity of seismicity resulting from injection-related pressure increases. With the Oklahoma SI case study as a guide, strong regional variation in fault slip sensitivity can be observed in the other cases we describe, and we assume that this the norm for basement-hosted induced seismicity systems.

4. Injection triggered slip and seismicity on strata-bound faults in the Delaware Basin

As mentioned in the Introduction, a second type of injection-induced seismicity has been well documented in the southern Delaware Basin that is distinct from the deep aquifer injection discussed so far (Fig. 12; Hennings et al., 2023). Recent earthquakes in the southern Delaware Basin occur along steeply-dipping normal faults that are vertically contained in the stratigraphic interval between the base of evaporite-rich ("caprock") strata and the Wolfcamp Shale below (see also Horne et al., 2022). Earthquakes that occur along these faults exhibit exclusively normal fault ruptures along faults made critical principally by pore pressure increase from shallow SWD. Hennings and Smye (2024) review research that demonstrates that the earthquakes that occur along these faults are triggered by shallow SWD in the Delaware Mountain Group, hydraulic fracturing in the underlying shale, and possible differential depletion and compaction associated with unconventional production. We refer to these as *strata-bound earthquakes* because the vertical extent of the faults, and therefore the ruptures, are stratigraphically contained, as compared to induced ruptures that extend many km downward in basement.

Fig. 13 synthesizes many key aspects of seismicity in the Delaware Basin, with an emphasis on earthquakes associated with strata-bound faults. Fig. 13a shows earthquake epicenters and magnitudes recorded between 2010 and 2024 using three independent data sources. All the seismicity shown is documented to be of induced origin by injection, hydraulic fracturing, and hydrocarbon production. Earthquakes for the period 2010-2017 were catalogued using the TXAR seismic array located about 100 km to the south of the figure (Frohlich et al., 2020). While this older seismicity is poorly located due to the large distance between the earthquakes and the TXAR array, it demonstrates that induced seismicity has been occurring in the area prior to the recent dramatic increase in produced water injection in 2017. The TexNet HiRes earthquake catalog is used for the period of 2017 through April 2019 and a proprietary catalog is used for April 2019 through 2024 and both of these catalogs have a low hypocenter error. Fig. 13b uses the proprietary catalog from (a) to indicate earthquake depth relative to the sediment/basement contact. Earthquakes shown as green and amber dots represent earthquakes on strata-bound faults, clearly within the sedimentary section. Note that in northeastern Culberson, Reeves and northeastern Pecos Counties, the shallow earthquakes show prominent lineations that closely follow strata-bound faults (shown as red lines) mapped by Horne et al. (2021) and (Horne and Hennings, 2024). Comparison of Fig. 12a and b shows that the locations of relatively large earthquakes (M_L4.5-5.5) that are shown in yellow and red in Fig. 12a are in the same areas in 12b where the earthquakes are below the sediment/basement contact as shown by black and blue dots in Fig. 12b. In the southern Delaware Basin, the earthquake magnitudes are smaller ($M_L \leq 3.5$) and occur on strata-bound faults above the top of basement. Fig. 12c shows the volumes of produced oil and water from unconventional wells from 2010-2023 and the volumes of shallow (amber) and deep (purple) SWD from 2010-2023 (Smye et al., 2024b). Fig. 13d shows cumulative vertical motion determined via InSAR associated with four 2 yr pairs of measurements of differential uplift or subsidence (Staniewicz et al., 2020; Hennings et al., 2023). Note that the ground elevation changes are quite substantial - as much as 30 cm of subsidence occurring adjacent to areas with 20 cm of uplift. In other words, about 50 cm of differential vertical motion. Hennings et al. (2023) quantitatively relate the causal agents for subsidence, uplift, and lineation to production, injection and fault slip, respectively. Pepin et al. (2022) modelled some of the InSAR changes in ground elevation and concluded that large amounts of aseismic slip on northwest-southeast striking normal faults best explains the elevation changes in the southern Delaware Basin. The

Received by OCD: 6/29/2026

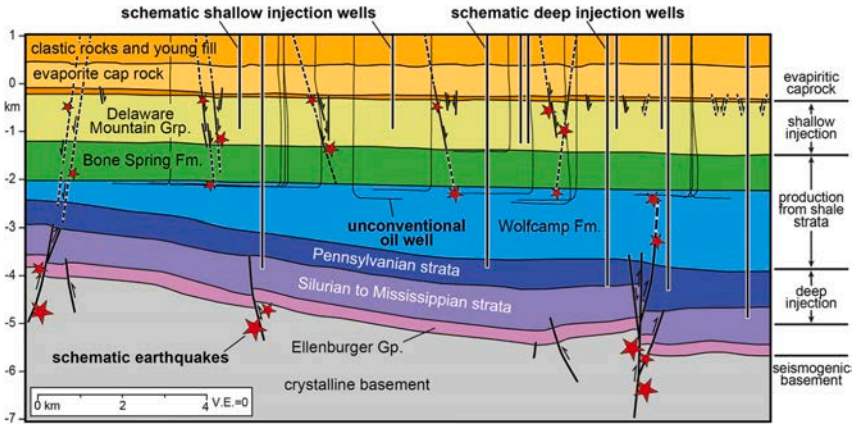


Fig. 12. SW to NE cross section in the central Delaware Basin of west Texas illustrating both types of wastewater injection and triggered earthquakes. In a manner similar to Oklahoma and Kansas, deep injection causes basement-rooted faults to slip. At the same time, shallow injection, principally into the Delaware Mountain Group triggers slip on strata-bound faults (modified from Hennings et al., 2023). See Fig. 13 for the location of the cross section trace.

seismogenic and aseismogenic shallow faults shown in Fig. 12 are (1) mainly restricted to the southern Delaware Basin, (2) strike parallel to S_{Hmax} Az as it changes trend across the region, (3) occur in the extant normal faulting stress regime, (4) are close to being critically stressed (Hennings et al., 2021; Horne and Hennings, 2024), and (5) are easily reactivated by the pore pressure increase from shallow SWD as modeled by Ge et al. (2022). The important observations to draw from this section, and the information in Fig. 13, is that induced basement-rooted and strata-bound fault rupture and seismicity can exist in the same region yet caused by different mechanisms, strata-bound fault rupture can be caused by complex additive or overlapping mechanisms, and strata-bound fault rupture release smaller earthquakes than basement-rooted faults.

Although the principal topic of this paper is triggered seismicity, it is important to recognize that triggered fault slip can be either seismic or aseismic. To describe the seismic and aseismic slip behaviour of faults, Dieterich (1979) and Ruina (1983) developed a theory that explain the sliding velocity dependence of fault friction in terms of material properties of the fault-hosting formations. While it is beyond the scope of this paper to describe this theory in detail, the easiest way to think about it is to visualize a fault that starts to slip. As slips begins, if frictional resistance increases with increasing velocity (which is referred to as velocity-strengthening) it leads to stable fault slip which is often referred to as fault creep. This occurs because friction is increasing as the fault accelerates, it cannot slide at higher velocity unless there is an increase of shear stress to drive slip or increases in pore pressure to decrease the resistance to sliding. However, if frictional resistance decreases with increasing velocity (referred to as velocity-weakening) it leads unstable fault slip because as sliding occurs, less shear stress is required to allow fault slip at higher velocities. Many publications report on velocity-strengthening and velocity-weakening responses in terms of the laboratory constitutive parameters and other factors affecting earthquake propagation. Suffice to say at this point, if the pressure increase associated with SWD or CO_2 injection was sufficient to induce slip on faults, it might induce an earthquake or might result in aseismic fault slip depending on the properties of the fault. Kohli and Zoback (2013) showed that aseismic slip on faults in unconventional oil and gas reservoirs is expected when the fraction of clay and kerogen exceeds 30 %. Aseismic fault slip could pose a risk to wells that cross the slipping fault, but there is little risk of induced seismicity on a velocity strengthening fault.

5. Why basal injection is especially problematic

The case studies described above illustrate that very small pressure increases in both basal and strata-bound saline aquifers have caused fault reactivation and triggered earthquakes. Basal injection is especially problematic because of the potential to trigger sizeable earthquakes in underlaying crystalline basement. Thus far, there have been 15 M5+ earthquakes triggered by injection in the study region shown in Fig. 3e. Some of these have been close to critical infrastructure. The largest of these events was the M5.8 Pawnee earthquake. The Cushing M5.0 event in 2016 occurred within 5 km of the Cushing oil hub which typically stores about 76 million barrels of oil, about 13 % of total U.S. oil storage capacity. If the Pawnee event had occurred closer to the Cushing oil hub there could have been damage to the storage tanks and pipelines. In 2015, when the earthquake rate in Oklahoma and southern Kansas reached its maximum, a M4.0+ earthquake was occurring every week with the shaking felt by the majority of the 4 million people living in Oklahoma. While the largest earthquake to occur in the Fort Worth Basin was only M_L4.0, 8 million people live in the Dallas/Ft. Worth metroplex and many anthropogenically sensitive faults have now been identified throughout the region (Hennings et al., 2019; Horne et al., 2020). As shown in Fig. 5, it is fortunate that the total volume of SWD in the Fort Worth Basin (and resultant seismicity) was considerably less than the other areas we discuss.

It is well known from earthquake seismology that the size of an earthquake correlates with the size of the portion of the fault that slips, the amount of slip and the stress drop (Stein and Wysession, 2003). As summarized in Fig. 14 (modified from Zoback and Gorelick, 2012), independent of the stress drop for an earthquake or the amount of fault slip, M5.0+ earthquakes are associated faults slipping over a characteristic dimensions of 10 km. Note that Cocco et al. (2016) showed that earthquake stress drops are typically 0.1-10 MPa over a very large range of magnitudes. As typical sedimentary thicknesses in intraplate regions are less than 3 km, any fault capable of producing a M5.0+ earthquake must extend down into basement. While the 2016 Pawnee earthquake (M_L5.8) occurred on a fault 10′s of km in size, the strata-bound earthquakes in the southern Delaware have limited magnitudes $M \leq 3.5$ that are consistent with the ≤ 3 km thickness of the sedimentary formations into which injection has occurred and, these faults do not penetrate down into crystalline basement (e.g., Fig. 12). Interestingly, the same arguments have been applied to the maximum size of earthquakes induced by fluid extraction in the Groningen gas field in The Netherlands (Bommer et al., 2024).

It is widely recognized that there is considerable pore volume in basal saline aquifers that would seem to be ideal for large-scale CO_2 storage (NETL DOE Atlas, 2015). Nonetheless, experience to date with SWD in basal saline aquifers, large-scale CO_2 injection into such aquifers has the potential to trigger relatively large, widely felt, and potentially

Received by OCD: 6/29/2026

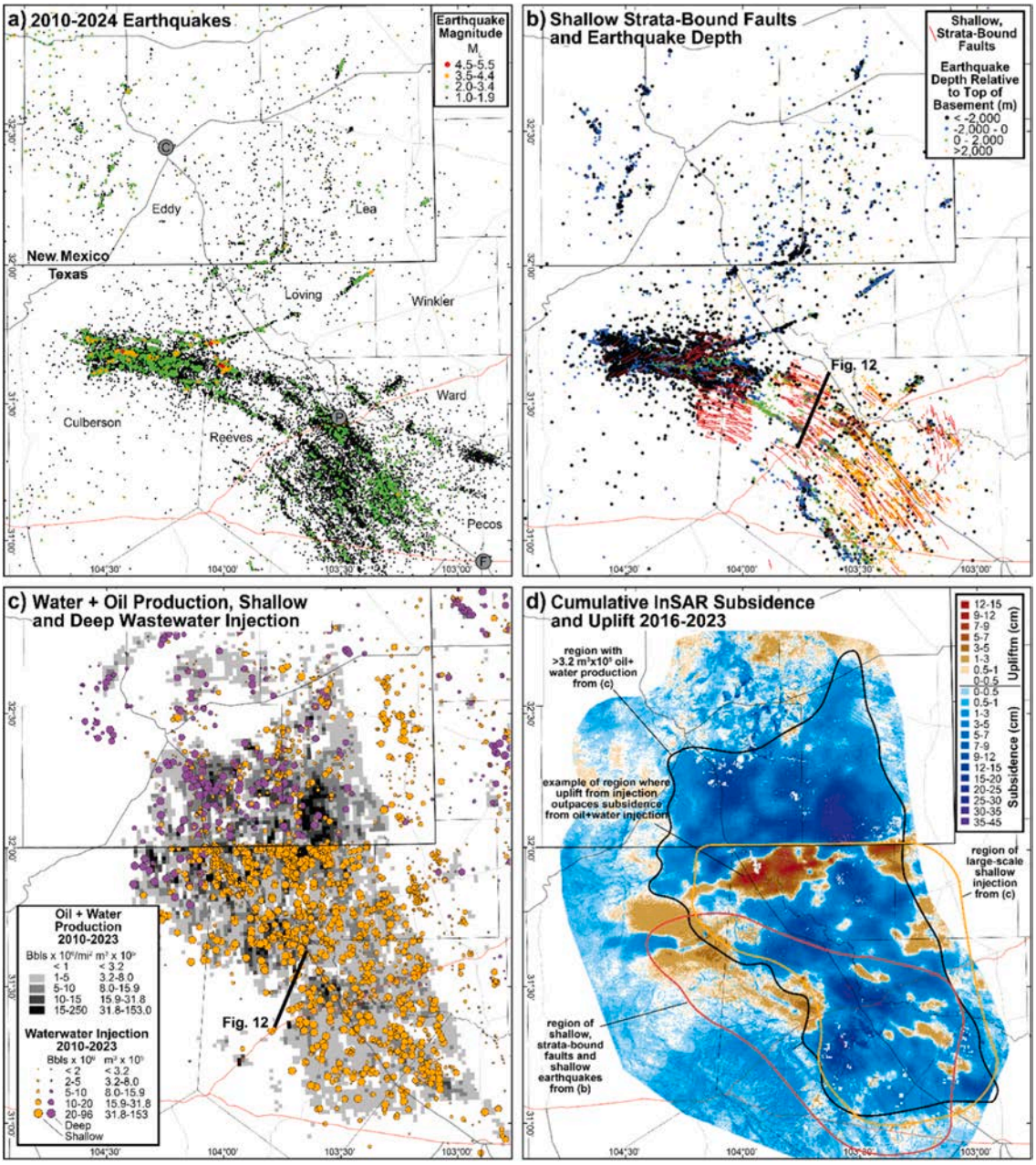


Fig. 13. Maps of the Delaware Basin region showing induced earthquakes, faults, production and injection data, and ground surface uplift and subsidence from InSAR. a). Earthquakes, documented to be of induced origin for the period of 2010 through June 2024. Earthquake sources: 2010-2017 from Frohlich et al. (2020), 2017-Apr 2019 from TexNet HiRes catalog, May 2019-Sep 2024 from a proprietary catalog. C=Carlsbad, NM; P=Pecos, TX; F=Ft. Stockton, TX. b). Earthquakes from the proprietary catalog in (a) shown as depth relative to the basement/sediment interface and published shallow, strata-bound faults. Earthquakes shown as the green and amber dots are at depths suggesting occurring along faults in the sediments. Strata-bound faults mapped by Horne et al. (2021)) and (Horne and Hennings, 2024). c). Volumes of unconventionally produced oil and co-produced water from 2010-2023 and volumes of shallow and deep SWD from 2010-2023 (Smye et al., 2024b). d). Sum of vertical movement of the ground surface determined from four 2-yr InSAR interferograms (2016-2017, 2018-2019, 2020-2021, 2022-2023) after the methods of (Hennings et al., 2023).

damaging earthquakes even when the pore pressure change in the injection zone is relatively small. In addition, it is extremely difficult to identify pre-existing problematic faults in basement. As mentioned above, nearly all the faults responsible for induced seismicity in Oklahoma were unknown prior to large-scale SWD into the Arbuckle.

Two aspects of triggered seismicity in basement are non-intuitive and deserve further discussion. First, is the fact that many M5.0+, potentially damaging earthquakes have been triggered by very small pressure changes. As it turns out, it has been recognized for some time that the maximum magnitude in triggered earthquake sequences correlates with the volume of fluid injected and not the pressure change that triggered the event (*e.g.*, Shapiro et al., 2010; Van Der Elst et al., 2016). The data in Fig. 15 shows that the maximum magnitude of earthquakes triggered by water injection correlates with the volume of injected fluid, regardless of the pressure change resulting from the injection. While there is considerable scatter in the data, the trend is clear; the more fluid injected, the larger the size of the maximum induced earthquake. This does not imply that the pore pressure change is of lesser importance, as it ultimately is the causal factor. With greater injection volume, however, comes a greater volume of rock perturbed which increases the likelihood

Received by OCD: 6/29/2026

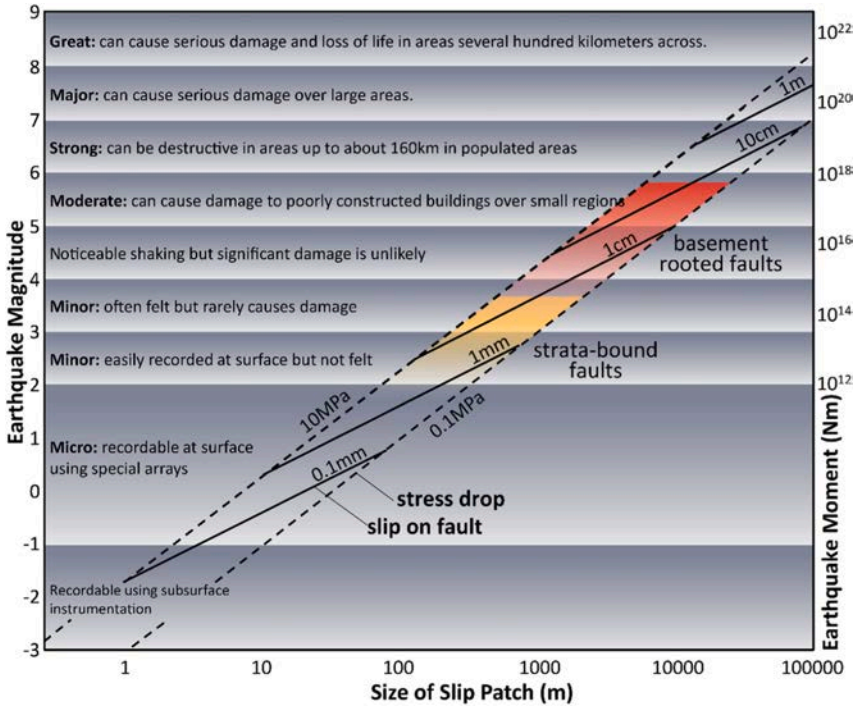


Fig. 14. Generalized representation of earthquake scaling relations between fault size, average slip and stress drop (modified from Zoback and Gorelick, 2012). Regardless of the stress drop or amount of slip in any given earthquake, it is clear that slip in a M5.0+ earthquake must occur on a fault with a spatial dimension of at least 10 km. The vertical axis on the right is earthquake moment, another measure of earthquake energy release. It is defined as the fault area multiplied by the slip in the earthquake multiplied by the rock stiffness.

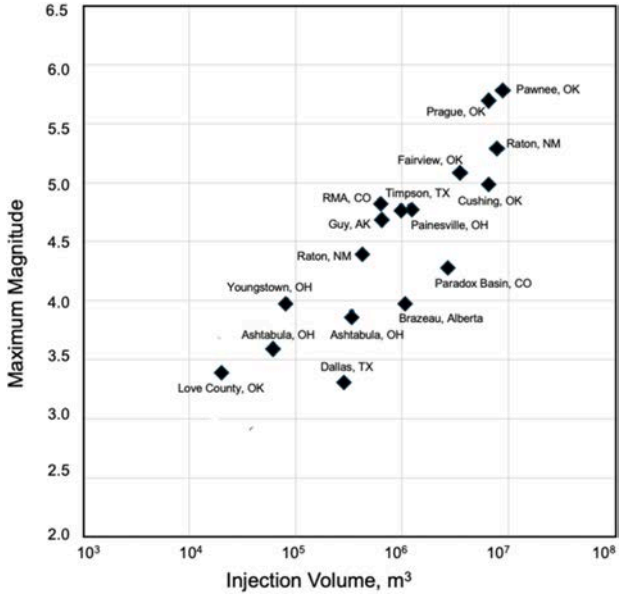


Fig. 15. - The maximum magnitude associated with seismicity induced by water disposal scales with the volume of injected fluid (data modified from Shapiro et al. (2021) which has references to each of the studies represented.

of encountering relatively large critically-stressed faults and thus more earthquakes with larger magnitude. When there are many injection wells in an area, there is a degree of subjectivity in computing how much injection may have been associated with a given earthquake. For example, published estimates of injection volumes in the vicinity of the 2011 M_L5.7 Prague, Oklahoma earthquake varies by about a factor of 2, depending on whether one includes injection wells within a 10 or 20 km of the epicenter. However, this uncertainty does not affect the overall increase in magnitude with injected volume shown in the Fig. 15.

One of the most robust observations in earthquake seismology is the Gutenberg-Richter (G-R) relationship (Gutenberg and Richter, 1944)

$$\log N\,(M \geq m) = a - bM$$

where M is earthquake magnitude, N is the number of earthquakes greater than magnitude M, the parameter "a" is literally the number of M = 0 earthquakes, which is generally an indicator of how seismically active an area is. The parameter "b" (usually referred to as the b-slope), indicates the relative number of earthquakes of different magnitudes.

Gutenberg and Richter found that the b=1 for naturally occurring seismicity in southern California. This means that there are 10 M 5 earthquakes in the region for every M 6, 10 M 4 earthquakes for every M 5, 10 M 3 earthquakes for every M 4, and so on. More recently, Christensen et al. (2002) found b=1 in southern California using a more complete data set (and far more advanced seismic network) than that available to Gutenberg and Richter six decades earlier. Importantly, earthquake seismologists around the world have documented the universal constancy of b≈1, as long as they consider earthquakes occurring throughout crustal volumes with spatial scales several times the 15–20 km thickness of the brittle crust over periods of decades. The reason for this is the fractal distribution of active faults in relatively large regions. As the size of active faults decrease, their number increases exponentially with fractal scaling (Christensen et al., 2002; Shapiro, 2010).

In a statistical study of injection-induced earthquake sequences, Van Der Elst et al. (2016) also interpreted the increase in earthquake magnitude with injected volume as the result of the fractal scaling of faults in the brittle crust. In fact, the title of their paper is *Induced Earthquake Magnitudes are as Large as (Statistically) Expected*, meaning that because the b-slopes of the induced earthquake sequences they considered are approximately 1, they represent natural earthquake sequences, advanced in time by anthropogenic pressure increases. Thus, the larger the crustal volume over which pressure increase occurs due to

Received by OCD: 6/29/2026

larger amounts of injection, the higher the probability of intersecting a fault capable of producing a relatively large earthquake. As discussed further in the next section, this implies that relatively small-scale CO_2 injection projects (which might induce some very small earthquakes) do not test the feasibility of larger scale injection.

One obvious complexity that effects the simple relationship between M_{max} and injected volume is the injection duration. In a recent paper, Langenbruch et al. (2024) have addressed this topic and argue that the maximum magnitudes of induced earthquakes has to be considered in the context of pressure diffusion. Under a constant injection scenario, the pressure-perturbed portion of the brittle crust grows with time as does the nucleation potential of larger-magnitude-induced earthquakes. On the other hand, projects like the CO_2 injection project at Decatur, Illinois (discussed at greater length below) involves injection of relatively small amounts of CO_2 over a long period of time (13 years) with a considerable hiatus between different phases of injection. In such cases, the pressure perturbation in the saline aquifer has time to dissipate as it spreads out effectively limiting the size of the perturbed rock volume that experiences a pore pressure increase above the threshold of fault rupture stability. Thus, fewer and smaller earthquakes than might be predicted by the overall trend of Fig. 15.

As an aside, it might seem that the occurrence of many small, induced earthquakes may relieve accumulated stress in the crust making the probability of inducing a larger earthquake less likely. This is not the case. Each unit of magnitude represents a factor of 33 in energy release (Stein and Wysession, 2003). Thus, a M 3 earthquake releases about one thousand times less energy than a M 5. However, a b-slope of 1 ~ indicates about 100 M 3 earthquakes would occur in a region for every M 5. Thus, if 100 M 3′s, 10 M 4′s and 1 M 5 occurred in the general vicinity of the M 5.8 Pawnee earthquake, those earthquake would have released 6 % of the energy associated with the M 5.8. In other words, if a critically-stressed fault in the subsurface is capable of producing a potentially-damaging M5.0+ earthquake as triggered by an injection-induced pressure increase, the occurrence of smaller earthquakes in the region do not significantly release the strain energy associated with larger events.

5.1. *Basement earthquakes triggered during enhanced geothermal stimulation*

It is well known that earthquakes induced during hydraulic stimulation in enhanced geothermal projects has been a significant problem. Best known are the cases of the M 3.5 earthquake associated with the Basel EGS project in Switzerland (Meier et al., 2015) and the M 5.5 Pohong EGS project in South Korea. Ellsworth et al. (2019) showed successive stimulations stages and associated seismicity during the Pohong EGS project in which injection was occurring in crystalline basement. They show that seismicity began with the first cycle of injection, continued with successive cycles (with increasing magnitudes) until ultimately a M 5.5 earthquake occurred which ended the project. They pore pressure changes responsible for earthquake triggering was only a few tenths of 1 MPa (Ellsworth et al., 2019), similar to the pressure changes at induced earthquake depths in the areas we discuss. One marked difference between Pohong and the cases summarized in Fig. 15 is that the M 5.5 was triggered when very little fluid had been injected prior to the earthquake. As shown by Ellsworth et al. (2019), the bottom of the injection wells were less than 1 km from an unknown, critically-stressed fault of sufficient size to produce a M 5.5 earthquake after relatively little fluid was injected and an extremely small pressure change occurred.

6. Implications of CO_2-induced seismicity at quest and Decatur

The implications of injection triggered seismicity in Oklahoma for large-scale CO_2 storage are significant. CO_2 is a supercritical fluid under typical reservoir conditions with a density of about 700 kg/m^3 at pressures and temperatures expected at a depth of about 2 km. As mentioned above, seismicity in north-central Oklahoma and southern Kansas began to increase markedly when the cumulative injection rate of produced water reached about 6 million m^3/month in 2009. If $scCO_2$ was being injected into the Arbuckle formation instead of water at that rate, 6 million m^3/month of produced water injection would correspond to about 50 million tons $scCO_2$/y . As a single 500 MW natural gas plant emits about 2.5 tonnes of CO_2/y, storing 50 million tons of $scCO_2$/y would accommodate emissions from about 20 natural gas power plants. 40 natural gas power plants are currently operating in Oklahoma (there are about 1000 operating in the U.S.). Thus, if CO_2 storage was occurring in north-central Oklahoma via a process analogous to SWD, it would imply that despite injecting CO_2 in hundreds of wells distributed throughout a very large area (approximately 25,000 km^2) less than half the CO_2 from the natural gas power plants operating in the state could be accommodated before significant seismicity occurred.

In all four of cases of basal injection discussed above, SWD triggered earthquakes on basement faults in response to very small pressure changes. This has important implications for viable sites for large-scale CO_2 storage. In this context, the Quest project northeast of Edmonton, Alberta and the Decatur project in central Illinois are of interest because they have been injecting relatively small amounts of CO_2 into basal aquifers for a number of years.

Quest is located northeast of Edmonton, Alberta. CO_2 is captured at a refinery where bitumen from oil sands is being converted to heavy crude oil. CO_2 injection began in 2015 into a basal, 40 m thick, highly permeable layer immediately above basement. The injection zone is part of a much thicker basal Cambrian sedimentary sequence that is widespread throughout the Western Canadian Sedimentary Basin. The injection interval is overlain by a sequence of shales and evaporites providing effective top seals. Currently, about 1 million tons of $scCO_2$ (a volume of about 1.6 million m^3) is being injected in three wells (Fig. 16a, adapted from Shell Canada, 2024). Bottom-hole pressure in the three wells is about 1–2 MPa higher than native pressure (Harvey et al., 2021). 756 small magnitude earthquakes (nearly all of which are $M < 0$) had occurred in basement by the end of 2023 in the immediate vicinity of the three injection wells (Fig. 16b). These events are recorded on a borehole seismic array deployed in well SCL 8-19 shown in Fig. 16a.

In addition to the very small earthquakes occurring in the vicinity of the injection wells, the Alberta Energy Regulator (part of the Alberta Geological Survey) has located a number of larger (M 1.2 to M 3) earthquakes in the area surrounding the injection wells. The earthquakes shown in Fig. 16c started in 2019, when the cumulative volume injected had reached about four million tons. Because no earthquakes were recorded in the same general region prior to 2015, these earthquakes are possibly induced by pressure changes in the basal Cambrian sandstone. It should be noted that there are about two dozen sites in the region surrounding the Quest project where companies are proposing to inject large volumes of CO_2 in the same basal sedimentary formation as Quest.

CO_2 injection into the basal Mt. Simon formation at Decatur, Illinois began in 2011. The first phase of injection ended in 2014. A second phase of injection began 2017 (Williams-Stroud et al., 2020). In total about 1.3 million m^3 has been injected to date. The first phase of injection was in the lower Mt. Simon close to basement. As illustrated in Fig. 17, this resulted in numerous small earthquakes (all $M \leq 1$) on well-defined near-vertical faults extending down into basement and trending northeast-southwest, as expected for strike-slip faults as $S_{Hmax}Az$ is close to E-W in the Illinois Basin (Lund Snee and Zoback, 2022). The second phase of injection was at shallower depth with several shale baffles (discontinuous shale layers) separating the injection interval from underlaying basement. This resulted in a reduced rate of seismicity, but the events continued to occur along the same faults activated during the first phase of injection (Williams-Stroud et al., 2020). Consistent with many of the other cases we have discussed here for triggered seismicity in basement, pressure increases in the injection

Received by OCD: 6/29/2026

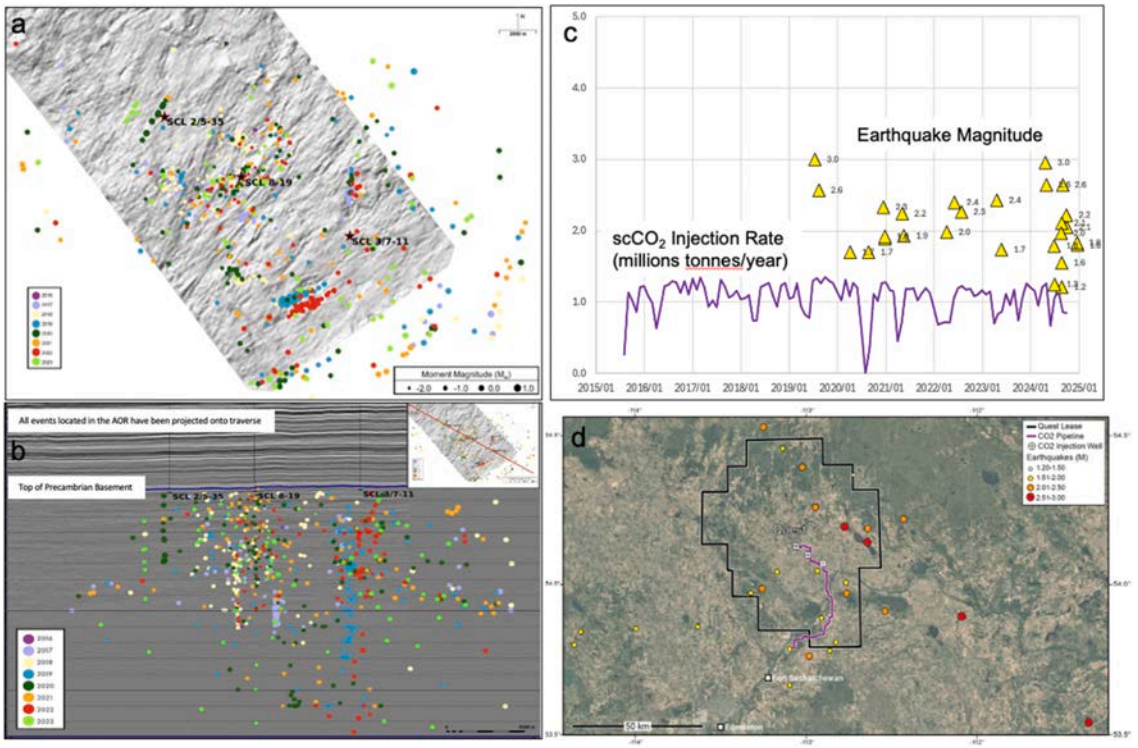


Fig. 16. a) Map view of three injection wells and over 700 locatable seismic events detected within the Quest microseismic through the end of 2024. An eight-level downhole geophone array was deployed in the center well. b) Cross-section from reflection seismic showing the general geologic layering, a seismic monitoring well, and small seismic events along the A-B section line shown in a). Events are coloured by magnitude with a magnitude range between M -2.0 and M 0. The basal Cambrian sandstone storage complex is immediately above Precambrian basement. b). Locations of events in basement colored by time of occurrence a) and b) are adapted Shell Canada (2024). c) The injection rate has been relatively constant since 2015 at about 1 million tons/year with variations caused by routine operational issues. Earthquakes with magnitudes ranging between M 1.2 and M 3 began after approximately 4 million tons of $scCO_2$ had been injected in 2019. d) Map of seismicity surrounding the Quest site from the Alberta Energy Regulator shows the relatively larger (M 1.2-3.0) earthquakes, many occurring at distance of 10′s of km from the injection wells. No events were detected in this region prior to 2015 when injection began.

zone were about 1 MPa. As is the case at Quest, a number of companies have proposed large-scale CO_2 injection into the Mt. Simon sandstone in the vicinity surrounding the Decatur project.

In recognition of the relationship between the magnitude of triggered seismicity and the volume of injection discussed above, relatively small-scale CO_2 storage projects such as Decatur and Quest have not yet tested what could happen if larger volumes of CO_2 are injected and whether there are adequate hydrologic barriers separating the injection zone from basement. Prior to the large amounts of produced water injection that started in the early 2000′s, relatively small-scale disposal of produced water into the Arbuckle in Oklahoma and Ellenburger in the Fort Worth Basin and Midland Basins occurred without noticeably triggering anomalous seismicity. Similarly, the first M 3 earthquakes at Quest did not occur until 4 years after the initiation of injection and more than 4 million tons of $scCO_2$ had been injected.

7. CO_2 storage in geologically young and weak sedimentary formations

Many attributes of geologic formations, such as those along coastal Texas and Louisiana make them ideal for large-scale CO_2 storage (Meckel et al., 2021). Similar geologic formations in other parts of the world should also be attractive areas to consider for large-scale CO_2 storage. These attributes generally apply both onshore and near offshore and in both saline aquifers and depleted oil and gas reservoirs. In addition, there are many point sources of CO_2 at industrial facilities in the area, minimizing source to sink pipeline distances (Callas et al., 2022). As illustrated by Bump and Hovorka (2024) there are structural features such as pervasive normal faults trending sub-parallel to the coastline that accommodate subsidence of the tremendous amount of sediment that has reached the gulf in the last few million years. These faults slip aseismically and are termed *growth faults* they are characterized by increasing displacement with age and depth. There are also pervasive salt diapirs and salt domes, which are primarily offshore. With proper planning, these faults and salt features can be easily avoided. This is facilitated by the widespread availability of 3D seismic data throughout the region associated with oil and gas exploration. However, severe overpressure develops at depth throughout this area due to compaction disequilibrium and potential CO_2 storage reservoirs would have to be located above zones of overpressure.

Recent developments have shed light on another important attribute of clay-rich formations that could potentially bound CO_2 storage reservoirs - they also help limit the vertical extent of fault slip and thus the potential magnitude of induced earthquakes. Viscoelastic stress relaxation (VSR), refers to time-dependent rock deformation observed in laboratory studies of clay rich rocks. It accurately explains observations of lithology-dependent variations of horizontal principal stresses, S_{Hmax} and S_{hmin}, with depth (Sone and Zoback, 2014). As a clay-rich rock deforms over time (viscous deformation), the *differences* between the three principal stresses become smaller. In normal faulting areas, this means that the least principal horizontal stress, S_{hmin}, would be expected to increase in relatively viscous (more ductile) rocks, thus lowering the difference between the vertical principal stress, S_V and S_{hmin} thus inhibiting normal faulting. One example are measurements from a group of wells in the Midland Basin of west Texas (modified from Kohli and Zoback, 2021). Note that there are significant layer-to-layer differences of S_{hmin} with depth by as much as 10 MPa, which are correlative with the relative amounts of clay plus organic content. In the low-clay, relatively

Received by OCD: 6/29/2026

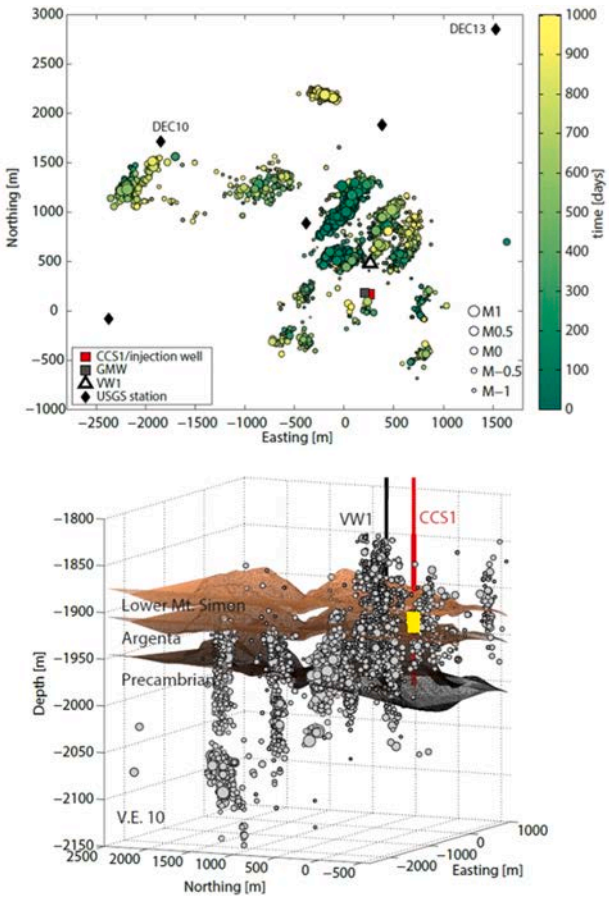


Fig. 17. a) Map shows seismicity trends in the Decatur area triggered by CO_2 injection into the Mt. Simon sandstone (Goertz-Allmann et al., 2017). b) 3-D representation of earthquake hypocenters demonstrate the earthquakes are occurring on faults extending into basement (courtesy of Bettina Goertz-Allman, pers. comm.).

brittle formations, S_{hmin} values are low and consistent with expected values based on normal faulting frictional equilibrium for known values of S_V, pore pressure and expected values of the coefficient of friction. Pore pressure increases in these formations would be expected to potentially trigger slip on well-oriented pre-existing faults. In contrast, S_{hmin} values are much higher in intervals with high clay plus organic content, such that the state of stress is not in frictional equilibrium. Said another way, frac barriers (stress barriers that limit vertical propagation of hydraulic fractures) are also fault barriers (barriers to vertical normal fault propagation). Thus, the presence of relatively ductile clay rich formations above and below an injection zone will be effective both as pressure and flow barriers and mechanical barriers contributing to limiting the vertical extent of triggered fault slip. In the case of potential CO_2 storage reservoirs along coastal Texas and Louisiana the situation is even more favourable, as triggered fault slip would be expected to trigger aseismic slip, not induced seismicity.

8. CO_2 storage in depleted oil and gas reservoirs

It has long been recognized that depleted oil and gas reservoirs offer significant opportunities for large-scale storage of CO_2. This was recently discussed in some detail by Zoback and Smit (2023) in the context of storing large-volumes of CO_2 associated with hydrogen production. They refer to the depleted oil and gas fields of Oman as an example of an oil-producing region that has the potential to store very large volumes of CO_2 in depleted reservoirs. An important benefit is that there is a large portfolio of fields in oil-producing countries because depleted fields with optimal infrastructure can be identified. Of direct relevance in this paper is that the pressure depletion resulting from prior oil and gas production creates a potential for injecting CO_2 without triggering seismicity. An example of this in the Delaware Basin was studied by Dvory and Zoback (2021). They showed that shallow injection into the Delaware Mountain Group and Bone Springs reservoirs responsible for the strata-bound seismicity discussed above is occurring only in the part of the basin which was a saline aquifer prior to injection. There are multiple sources of seismicity in the southern Delaware Basin including shallow SWD, hydraulic fracturing, and differential compaction related to production (Hennings and Smye, 2024) and, of course, seismicity is occurring where there are faults present that are well-oriented for slip in the current the stress field. However, it is apparent in Fig. 18a that while SWD into the Delaware Mountain Group is occurring throughout most of the basin (the size of purple diamonds are scaled by injection rate), Fig. 18b shows that recent seismicity (red dots) are not seen where there had been previous oil and gas production (purple circles are scaled by the volume of previous production). In other words, SWD is triggering seismicity where the Delaware Mountain Group was a saline aquifer. It is not occurring where the Delaware Mountain Group is a depleted reservoir. Dvory and Zoback showed that prior production reduced pore pressure by so much, SWD started at a pressure much less than the original pore pressure. Thus, large volumes of injection (and associated increases in pressure) could be accommodated without inducing seismicity.

An important issue concerning the use of depleted oil and gas reservoirs for CO_2 storage is the experience with injection induced seismicity in the depleted Castor oil field 22 km off the southern coast of Spain. In 2013, a field test was carried out to evaluate the potential use of the reservoir as an underground gas storage facility. Gas injection was terminated only a few days after it started due to the detection of several hundred minor earthquakes in the area. Determination of the exact location of the earthquakes was quite difficult due to the very sparse earthquake monitoring network operating in the region. Resultantly, the pore pressure increase associated with small amount of gas injection was capable of triggering seismicity because, due to the influx of formation or aquifer water, the pore pressure in the field had recovered to near initial values prior to oil production at the time of gas injection. In other words, the pressure decrease associated with oil production had essentially recovered to the pre-production level at the time of gas injection. Hence, when considering the potential of a depleted oil and gas reservoir being used for CO_2 storage, it must be pressure depleted, not just depleted of oil and gas.

9. Summary and conclusions

Based on the arguments above, there are a number of important lessons-learned from produced water injection that are directly applicable to sites of possible large-scale CO_2 injection and long-term sequestration.

1. Basal aquifers in hydraulic communication with crystalline geologic basement may be problematic sites for large-scale CO_2 sequestration. Detailed studies of injection-induced seismicity in the Dallas/Fort Worth area, north-central Oklahoma and southernmost Kansas, and the Midland and Delaware Basins of west Texas all demonstrate marked increases in seismicity in underlying basement when large volumes of produced water were injected in zones communicating pressure to basement-rooted faults. In these areas (and world-wide experience) indicates that cumulative injected volume is a better indicator of the maximum magnitude of triggered seismicity than the injection-induced pressure increase.
2. Essentially all cases of large-scale injection into basal saline aquifers in hydrologic communication with basement have induced problematic seismicity resulting from small pressure changes on the order

Received by OCD: 6/29/2026

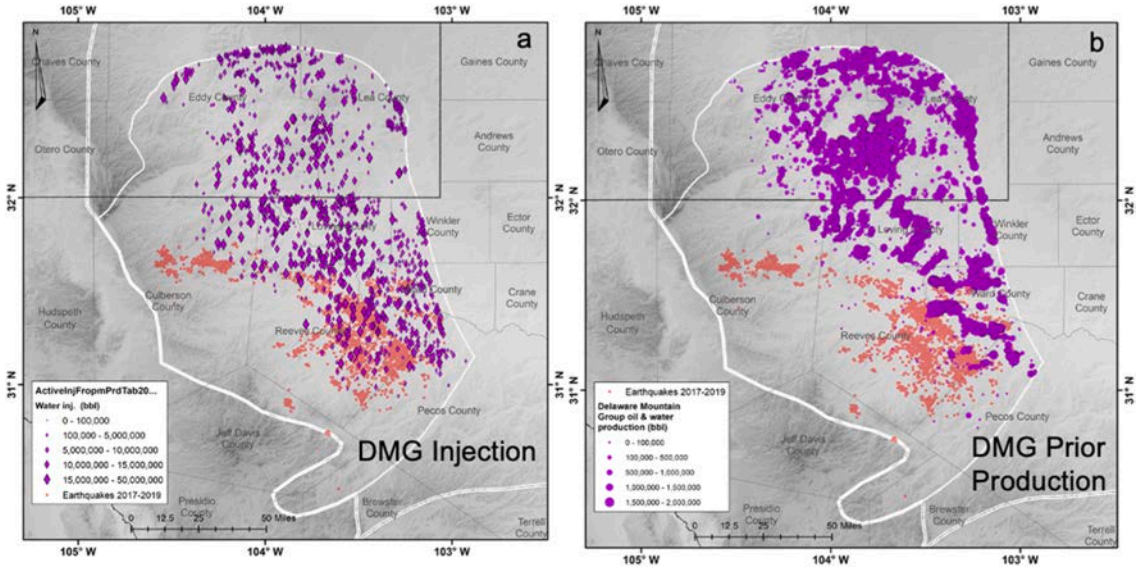


Fig. 18. a) Injection wells in the Delaware Mountain Group (DMG) (purple diamonds, scaled by injection rate). (A–D) Location of wells drilled in the Delaware Basin, western Texas and southeastern New Mexico (USA). Earthquake locations recorded by TexNet (http://coastal.beg.utexas.edu/texnetcatalog) between 2017 and 2020 are shown with red dots. M is the location of the Mentone earthquake sequence. All production and injection values are in oilfield barrels (bbl). b) Production wells in the Delaware Mountain Group (purple dots, scaled by production volume). Adapted from Dvory and Zoback (2021).

of 1 MPa or less. This appears to be occurring at small scales at both the Decatur and Quest CO_2 injection projects, implying that significantly increasing the rate of CO_2 injection at these sites could become problematic. While it is obvious that clay rich shales and mudstone top seals are needed above saline aquifers to prevent upward migration of CO_2, bottom seals are also important to prevent pressure transmission from the injection zone to critically-stressed faults in basement.

3. Geologically young, diagenetically immature (weakly cemented) sedimentary formations such as found along the Texas/Louisiana Gulf Coast (both onshore and offshore) should not be prone to injection-related seismicity. The ubiquitous shales and mud stones in this area provide both flow barriers and barriers to fault rupture. The possibility of triggered aseismic slip on pre-existing growth faults will affect project design.
4. Strata-bound saline aquifers, such as the Delaware Mountain Group in the Delaware Basin have the potential to store large volumes of CO_2 without the occurrence of potentially-damaging earthquakes although numerous relatively small magnitude earthquakes ($M \leq 3.5$) could be triggered.
5. In areas such as the Midland Basin, the absence of critically-stressed faults at shallow depth has precluded the occurrence of induced seismicity that can accompany shallow injection. Verdon et al. (2016) pointed out that the lack of induced seismicity despite SWD in the Williston Basin (despite similarly large disposal volumes), resulted from the hydraulic isolation of disposal formations from the basement.
6. From the perspective of triggered seismicity, CO_2 storage in weakly-cemented sedimentary formations and pressure-depleted oil and gas reservoirs could have significant advantages over deep saline aquifers in hydraulic communication with crystalline basement.

Author statement

This paper was conceptualized, written and reviewed by Mark Zoback and Peter Hennings, working collaboratively.

CRediT authorship contribution statement

Mark D. Zoback: Writing – review & editing, Writing – original draft, Visualization, Project administration, Methodology, Data curation, Conceptualization. **Peter Hennings:** Writing – review & editing, Writing – original draft, Visualization, Methodology, Formal analysis, Conceptualization.

Declaration of competing interest

The authors declare that they have no known competing financial interests or personal relationships that could have appeared to influence the work reported in this paper.

Acknowledgements

We thank our many colleagues associated with the Stanford Center for Induced and Triggered Seismicity (SCITS), Stanford Center for Carbon Storage (SCCS) and the Center for Injection and Seismicity Research (CISR) of the Bureau of Economic Geology at The University of Texas, Austin who made invaluable contributions to the research summarized here. We also thank the corporate sponsors of SCITS, SCCS and CISR.

Data availability

Data will be made available on request.

References

Allen, B., Murray, K., Ogwari, P., Suriamin, F., Walter, J.I., Hayman, N.W., 2024. Pressure monitoring of disposal reservoirs in North-Central Oklahoma: implications for seismicity and geostorage. J. Geophys. Res.: Solid Earth 129 (10), e2024JB029200. https://doi.org/10.1029/2024JB029200.

Anderson, E.M., 1951. The Dynamics of Faulting and Dyke Formation with Applications to Britain. Oliver and Boyd, Edinburgh.

Barton, C.A., Zoback, M.D., Moos, D., 1995. Fluid flow along potentially active faults in crystalline rock. Geology (8), 23. https://doi.org/10.1130/0091-7613(1995)023<0683:FFAPAF>2.3.CO.

Bommer, J.J., Van Elk, J., Zoback, M.D., 2024. Estimating the maximum magnitude of induced earthquakes in the Groningen gas field, the Netherlands. Bull. Seismol. Soc. Am. https://doi.org/10.1785/0120240054.

Received by OCD: 6/29/2026

Bump, A.P., Hovorka, S.D., 2024. Pressure space: the key subsurface commodity for CCS. Int. J. Greenh. Gas Control 136, 104174. https://doi.org/10.1016/j.ijggc.2024.104174.

Callas, C., Saltzer, S.D., Steve Davis, J., Hashemi, S.S., Kovscek, A.R., Okoroafor, E.R., et al., 2022. Criteria and workflow for selecting depleted hydrocarbon reservoirs for carbon storage. Appl. Energy 324, 119668. https://doi.org/10.1016/j.apenergy.2022.119668.

Christensen, K., Danon, L., Scanlon, T., & Bak, P. (2002). Unified scaling law for earthquakes, 90, 2508–2513.

Clarke, H., Eisner, L., Styles, P., Turner, P., 2014. Felt seismicity associated with shale gas hydraulic fracturing: the first documented example in Europe. Geophys. Res. Lett. 41 (23), 8308–8314. https://doi.org/10.1002/2014GL062047.

Cocco, M., Tinti, E., Cirella, A., 2016. On the scale dependence of earthquake stress drop. J. Seismol. https://doi.org/10.1007/s10950-016-9594-4.

Dvory, N.Z., Zoback, M.D., 2021. Prior oil and gas production can limit the occurrence of injection-induced seismicity: a case study in the Delaware basin of western Texas and southeastern New Mexico, USA. Geology 49 (10), 1198–1203. https://doi.org/10.1130/G49015.1.

Ellsworth, W.L., Giardini, D., Townend, J., Ge, S., Shimamoto, T., 2019. Triggering of the Pohang, Korea, Earthquake (M w 5.5) by enhanced geothermal system stimulation. Seismol. Res. Lett. 90. https://doi.org/10.1785/0220190102.

Foulger, G.R., Wilson, M.P., Gluyas, J.G., Julian, B.R., Davies, R.J., 2018. Global review of human-induced earthquakes. Earth-Sci. Rev. 178, 438–514. https://doi.org/10.1016/j.earscirev.2017.07.008.

Frohlich, C., Hayward, C., Rosenblit, J., Aiken, C., Hennings, P., Savvaidis, A., et al., 2020. Onset and cause of increased seismic activity near Pecos, West Texas, United States, from observations at the Lajitas TXAR seismic array. J. Geophys. Res.: Solid Earth 125 (1), e2019JB017737. https://doi.org/10.1029/2019JB017737.

Gao, S., Nicot, J.-P., Hennings, P.H., La Pointe, P., Smye, K.M., Horne, E.A., Dommisse, R., 2021. Low pressure buildup with large disposal volumes of oil field water: a flow model of the Ellenburger Group, Fort Worth Basin, northcentral Texas. AAPG Bull. 105 (9), 2575–2593. https://doi.org/10.1306/03252120159.

Ge, J., Nicot, J.-P., Hennings, P.H., Smye, K.M., Hosseini, S.A., Gao, R.S., Breton, C.L., 2022. Recent water disposal and pore pressure evolution in the Delaware mountain group, Delaware basin, Southeast New Mexico and West Texas. J. Hydrol. - Reg. Stud. https://doi.org/10.1016/j.ejrh.2022.101041.

Ge, J., Nicot, J.-P., Smye, K.M., Calle, A.Z., Hennings, P., Horne, E.A., Leng, J., 2024. Modeling the evolution of pore pressure from deep wastewater injection in the Midland Basin, Texas. Am. Assoc. Pet. Geol. Bull. 108 (12), 2287–2312.

Goertz-Allmann, B.P., Gibbons, S.J., Oye, V., Bauer, R., Will, R., 2017. Characterization of induced seismicity patterns derived from internal structure in event clusters. J. Geophys. Res.: Solid Earth 122 (5), 3875–3894. https://doi.org/10.1002/2016JB013731.

Gutenberg, B., & Richter, C. F. (1944). Frequency of earthquakes in California, 4, 185–188.

Harvey, S., O'Brien, S., Minisini, S., Oates, S., Braim, M., 2021. Quest CCS facility: microseismic system monitoring and observations. SSRN Electron. J. https://doi.org/10.2139/ssrn.3817042.

Healy, J.H., Rubey, W.W., Griggs, D.T., Raleigh, C.B., 1968. The Denver earthquakes. Science 161 (3848).

Hennings, P., Smye, K., 2024. Knowns, questions, and implications of induced seismicity in the Permian Basin, USA. AAPG Bull. 108 (12), 2201–2214. https://doi.org/10.1306/08292424051.

Hennings, P.H., Snee, J.-E.L., Osmond, J.L., Deshon, H.R., Dommisse, R., Horne, E., et al., 2019. Injection-induced seismicity and fault-slip potential in the fort worth basin, Texas. Bull. Seismol. Soc. Am. 109 (5). https://doi.org/10.1785/0120190017.

Hennings, P., Allwardt, P., Paul, P., Zahm, C., Reid, R., Alley, H., et al., 2012. Relationship between fractures, fault zones, stress, and reservoir productivity in the Suban gas field, Sumatra, Indonesia. In: AAPG Bull., 96, pp. 753–772. https://doi.org/10.1306/08161109084.

Hennings, P.H., Dvory, N., Horne, E.A., Li, P., Savvaidis, A., Zoback, M., 2021. Stability of the fault systems that host induced earthquakes in the Delaware basin of West Texas and Southeast New Mexico. Seismic Rec. https://doi.org/10.1785/0320210020.

Hennings, P., Staniewicz, S., Smye, K., Chen, J., Horne, E., Nicot, J.-P., et al., 2023. Development of complex patterns of anthropogenic uplift and subsidence in the Delaware Basin of West Texas and southeast New Mexico, USA. Sci. Total Environ. 903, 166367. https://doi.org/10.1016/j.scitotenv.2023.166367.

Hennings, P., Ge, J., Horne, E.A., Smye, K.M., Nicot, J.-P., 2024. Pore pressure thresholds associated with seismogenic fault slip in the Midland Basin, west Texas, United States. AAPG Bull. 108 (12), 2347–2375.

Hennings, P.H., Young, M.H., 2023. The TexNet-CISR collaboration and steps toward understanding induced seismicity in Texas. In: Buchanan, R.C., Young, M.H., Murray, K.E. (Eds.), Recent Seismicity in the Southern Midcontinent, USA: Scientific, Regulatory, and Industry Responses. Geological Society of America, pp. 53–71. https://doi.org/10.1130/2023.2559(06).

Horne, E., 2024. Quarterly BEG reports to TXRRC for seismic data acquisition and fault mapping project [Data set]. Texas Data Repository. https://doi.org/10.18738/T8/ROWA0Y.

Horne, E.A., Hennings, P.H., Smye, K.M., Staniewicz, S., Chen, J., Savvaidis, A., 2022. Structural characteristics of shallow faults in the Delaware Basin. Interpretation 10 (4), T807–T835. https://doi.org/10.1190/INT-2022-0005.1.

Horne, E.A., Hennings, P.H., Osmond, J.L., DeShon, H., 2020. Structural characterization of potentially seismogenic faults in the greater Fort Worth Basin. Interpretation 8 (2), 74. https://doi.org/10.1190/int-2019-0188.1.

Horne, E.A., Hennings, P., Smye, K.M., Calle, A.Z., Morris, A.P., Huang, G.-C.D., 2024. Interpretation, characterization, and slip hazard assessment of faults in the Midland Basin, west Texas, United States. AAPG Bull. 108 (12), 2313–2346.

Horne, E.A., Hennings, P.H., Zahm, C.K., 2021. Basement-rooted faults of the Delaware Basin and Central Basin Platform, Permian Basin, West Texas and Southeastern New Mexico. In: Callahan, O.A., Eichhubl, P. (Eds.), Geol. Basement Texas: Vol. in Honor of. Peter Flawn, Tex. Bur. Econ. Geol. https://doi.org/10.23867/RI0286C6.

Horton, S., 2012. Disposal of hydrofracking waste fluid by injection into subsurface aquifers triggers earthquake swarm in Central Arkansas with Potential for Damaging Earthquake. Seismol. Res. Lett. 83 (2), 250–260. https://doi.org/10.1785/gssrl.83.2.250.

Huang, G.D., Chen, Y., Savvaidis, A., 2024. Complex seismotectonic characteristics in the Midland Basin of Texas: Constrained by seismicity and earthquake source mechanisms. Seismol. Res. Lett. 95 (3), 1870–1884. https://doi.org/10.1785/0220230269.

Hubbert, M.K., Rubey, W.W., 1959. Role of fluid pressure in mechanics of overthrust faulting. Geol. Soc. Am. Bull. 70, 167–206.

IPCC. (2005), 2005. Carbon Dioxide Capture and Storage. Cambridge University Press, Cambridge, England. Retrieved from. https://www.ipcc.ch/report/carbon-dioxide-capture-and-storage/.

IPCC, 2018. Global Warming of 1.5 °C. Intergovernmental Panel on Climate Change. Retrieved from. https://www.ipcc.ch/sr15/download/.

Jenkins, S., Kuijper, M., Helferty, H., Girardin, C., Allen, M., 2023. Extended producer responsibility for fossil fuels *. Environ. Res. Lett. 18 (1), 011005. https://doi.org/10.1088/1748-9326/aca4e8.

Keranen, K.M., Savage, H.M., Abers, G.A., Cochran, E.S., 2013. Potentially induced earthquakes in Oklahoma, USA: links between wastewater injection and the 2011 Mw 5.7 earthquake sequence. Geology 41 (6), 699–702. https://doi.org/10.1130/G34045.1.

Kivi, I.R., Boyet, A., Wu, H., Walter, L., Hanson-Hedgecock, S., Parisio, F., Vilarrasa, V., 2023. Global physics-based database of injection-induced seismicity. Earth Syst. Sci. Data 15 (7), 3163–3182. https://doi.org/10.5194/essd-15-3163-2023.

Kohli, A., Zoback, M., 2021. Stratigraphically controlled stress variations at the hydraulic fracture test site-1 in the Midland Basin, TX. Energies 14 (24), 8328. https://doi.org/10.3390/en14248328.

Kohli, A.H., Zoback, M.D., 2013. Frictional properties of shale reservoir rocks. J. Geophys. Res.: Solid Earth 118 (9). https://doi.org/10.1002/jgrb.50346.

Langenbruch, C., Zoback, M.D., 2017. Response to comment on "how will induced seismicity in Oklahoma respond to decreased saltwater injection rates? Sci. Adv. 3 (8). https://doi.org/10.1126/sciadv.aao2277.

Langenbruch, C., Weingarten, M., Zoback, M.D., 2018. Physics-based forecasting of man-made earthquake hazards in Oklahoma and Kansas. Nat. Commun. 9 (1), 3946. https://doi.org/10.1038/s41467-018-06167-4.

Langenbruch, C., Moein, M.J.A., Shapiro, S.A., 2024. Are maximum magnitudes of induced earthquakes controlled by pressure diffusion? Philos. Trans. R. Soc. A: Math. Phys. Eng. Sci. 382 (2276), 20230184. https://doi.org/10.1098/rsta.2023.0184.

Litherland, M., 2023. History of monitoring induced seismicity in New Mexico. In: Buchanan, R.C., Young, M.H., Murray, K.E. (Eds.), Recent Seismicity in the Southern Midcontinent, USA: Scientific, Regulatory, and Industry Responses. Geological Society of America, pp. 43–51. https://doi.org/10.1130/2023.2559(05).

Lund Snee, J.E., Zoback, M.D., 2018. State of stress in the Permian Basin, Texas and New Mexico: implications for induced seismicity. *The Leading Edge, Februarry*, pp. 127–134.

Lund Snee, J.-E., Zoback, M.D., 2020. Multiscale variations of the crustal stress field throughout North America. Nat. Commun. 11, 1951. https://doi.org/10.1038/s41467-020-15841-5.

Lund Snee, J.-E., Zoback, M.D., 2022. State of stress in areas of active unconventional oil and gas development in North America. AAPG Bull. 106 (2), 355–385. https://doi.org/10.1306/08102120151.

Marsh, S., & Holland, A. (2016). Comprehensive fault database and interpretive fault map of Oklahoma. *Okla. Geol. Surv. Open-File Rep. (OF2-2016)*, 15.

McKeighan, C., Hennings, P., Horne, E.A., Smye, K., Morris, A., 2022. Understanding anthropogenic fault rupture in the eagle ford region, South-Central Texas. Bull. Seismol. Soc. Am. 112 (6), 2870–2889. https://doi.org/10.1785/0120220074.

Meckel, T.A., Bump, A.P., Hovorka, S.D., Trevino, R.H., 2021. Carbon capture, utilization, and storage hub development on the Gulf Coast. Greenh. Gases: Sci. Technol. 11 (4), 619–632. https://doi.org/10.1002/ghg.2082.

Meier, P.M., Rodríguez, A.A., Bethmann, F., 2015. Lessons learned from Basel: new EGS projects in Switzerland using multistage stimulation and a probabilistic traffic light system for the reduction of seismic risk. Proc. World Geotherm. Congr. *2015*.

Morris, A.P., Hennings, P.H., Horne, E.A., Smye, K.M., 2021. Stability of basement-rooted faults in the Delaware Basin of Texas and New Mexico, USA. J. Struct. Geol. https://doi.org/10.1016/j.jsg.2021.104360.

Nakai, J.S., Weingarten, M., Sheehan, A.F., Bilek, S.L., Ge, S., 2017. A possible causative mechanism of Raton basin, New Mexico and Colorado earthquakes using recent seismicity patterns and pore pressure modeling. J. Geophys. Res.: Solid Earth 122 (10), 8051–8065. https://doi.org/10.1002/2017JB014415.

NETL, 2015. Carbon Storage Atlas, Fifth Edition. Department of Energy.

Park, Y., Beroza, G.C., Ellsworth, W.L., 2022. Basement fault activation before larger earthquakes in Oklahoma and Kansas. Seism. Rec. 2 (3), 197–206. https://doi.org/10.1785/0320220020.

Pepin, K.S., Ellsworth, W.L., Sheng, Y., Zebker, H.A., 2022. Shallow aseismic slip in the Delaware Basin determined by Sentinel-1 InSAR. J. Geophys. Res. Solid Earth 127 (2). https://doi.org/10.1029/2021JB023157 e2021JB023157.

Received by OCD: 6/29/2026

Peterie, S.L., Miller, R.D., Intfen, J.W., Gonzales, J.B., 2018. Earthquakes in Kansas Induced by extremely far-field pressure diffusion. Geophys. Res. Lett. 45 (3), 1395–1401. https://doi.org/10.1002/2017GL076334.
Quinones, L., DeShon, H.R., Jeong, S., Ogwari, P., Sufri, O., Holt, M.M., Kwong, K.B., 2019. Tracking induced seismicity in the Fort Worth Basin: a summary of the 2008–2018 North Texas Earthquake study catalog. Bull. Seismol. Soc. Am. 109 (4), 1203–1216. https://doi.org/10.1785/0120190057.
Raleigh, C.B., Healy, J.H., Bredehoeft, J.D., 1976. An experiment in earthquake control at Rangely, Colorado. Science 191 (4233), 1230–1237. https://doi.org/10.1126/science.191.4233.1230.
Shapiro, S., Kim, K.-H., Ree, J.-H., 2021. Magnitude and nucleation time of the 2017 Pohang earthquake point to its predictable artificial triggering. Nat. Commun. 12 (1), 6397. https://doi.org/10.1038/s41467-021-26679-w.
Shapiro, S.A., Dinske, C., Langenbruch, C., Wenzel, F., 2010. Seismogenic index and magnitude probability of earthquakes induced during reservoir fluid stimulations. Lead. Edge 29 (3), 304–309. https://doi.org/10.1190/1.3353727.
Sheng, Y., Pepin, K.S., Ellsworth, W.L., 2022. On the depth of earthquakes in the Delaware basin: a case study along the Reeves–Pecos county line. Seism. Rec. 2 (1), 29–37. https://doi.org/10.1785/0320210048.
Simpson, R. W. (1997). Quantifying Anderson ' s fault types, 102, 909–919.
Skoumal, R.J., Barbour, A.J., Rubinstein, J.L., Glasgow, M.E., 2024. Reduced injection rates and shallower depths mitigated induced seismicity in Oklahoma. Seism. Rec. 4 (4), 279–287. https://doi.org/10.1785/0320240030.
Smye, K., Banerji, D.A., Eastwood, R., McDaid, G., Hennings, P., 2021. Lithology and reservoir properties of the Delaware mountain group of the Delaware Basin and implications for saltwater disposal and induced seismicity. J. Sediment. Res. 91 (11), 1113–1132. https://doi.org/10.2110/jsr.2020.134.
Smye, K.M., Ge, J., Morris, A., Horne, E.A., Calle, A., Eastwood, R.L., Nicot, J.-P., Hennings, P., 2024a. Role of deep fluid injection in induced seismicity in the Delaware Basin, West Texas and Southeast New Mexico. Geochem. Geophys. Geosyst. https://doi.org/10.1029/2023GC011260.
Smye, K.M., Yut, K., Reedy, R.C., Scanlon, B.R., Nicot, J.-P., Hennings, P., 2024b. Challenges with managing unconventional water production and disposal in the Permian Basin. AAPG Bull. 108.
Snee, J.-E.L., Zoback, M.D., 2016. State of stress in Texas: implications for induced seismicity. Geophys. Res. Lett. 43 (19). https://doi.org/10.1002/2016GL070974.
Sone, H., Zoback, M.D., 2014. Time-dependent deformation of shale gas reservoir rocks and its long-term effect on the in situ state of stress. Int. J. Rock Mech. Min. Sci. 69. https://doi.org/10.1016/j.ijrmms.2014.04.002.
Staniewicz, S., Chen, J., Lee, H., Olson, J., Savvaidis, A., Reedy, R., et al., 2020. InSAR reveals complex surface deformation patterns over an 80,000 km^2 oil-producing region in the Permian Basin. Geophys. Res. Lett. 47 (21), e2020GL090151. https://doi.org/10.1029/2020GL090151.
Stein, S., Wysession, M., 2003. An Introduction to Seismology, Earthquakes, and Earth Structure. John Wiley & Sons. https://doi.org/10.1785/gssrl.74.6.824.
Townend, J., Zoback, M.D., 2000. How faulting keeps the crust strong. Geology 28 (5), 399–402.
Townend, J., Zoback, M.D., 2001. Implications of earthquake focal mechanisms for the frictional strength of the San Andreas fault system. Geol. Soc. Spec. Publ. 186. https://doi.org/10.1144/GSL.SP.2001.186.01.02.
Van Der Elst, N.J., Page, M.T., Weiser, D.A., Goebel, T.H.W., Hosseini, S.M., 2016. Induced earthquake magnitudes are as large as (statistically) expected. J. Geophys. Res.: Solid Earth 121 (6), 4575–4590. https://doi.org/10.1002/2016JB012818.
Verdon, J.P., Kendall, J.-M., Horleston, A.C., Stork, A.L., 2016. Subsurface fluid injection and induced seismicity in southeast Saskatchewan. Int. J. Greenh. Gas Control 54, 429–440. https://doi.org/10.1016/j.ijggc.2016.04.007.
Walsh, F.R., Zoback, M.D., 2015. Oklahoma's recent earthquakes and saltwater disposal. Sci. Adv. 1 (5). https://doi.org/10.1126/sciadv.1500195.
Walsh, F.R., Zoback, M.D., 2016. Probabilistic assessment of potentially active faults in north central Oklahoma. Geology 44 (12), 991–994.
Williams-Stroud, S., Bauer, R., Leetaru, H., Oye, V., Stanek, F., Greenberg, S., Langet, N., 2020. Analysis of microseismicity and reactivated fault size to assess the potential for felt events by CO2 injection in the Illinois Basin. Bull. Seismol. Soc. Am. 110 (5), 2188–2204. https://doi.org/10.1785/0120200112.
Zoback, M.D., Kohli, A.H., 2019. Unconventional Reservoir Geomechanics. Cambridge Univ. Press, ISBN 978-1107087071.
Zoback, M., Smit, D., 2023. Meeting the challenges of large-scale carbon storage and hydrogen production. Proc. Natl. Acad. Sci. 120 (11), e2202397120. https://doi.org/10.1073/pnas.2202397120.
Zoback, M.D., 2007. Reservoir Geomechanics. Cambridge Univ. Press, p. 449.
Zoback, M.D., Gorelick, S.M., 2012. Earthquake triggering and large-scale geologic storage of carbon dioxide. Proc. Natl. Acad. Sci. U. S. A. 109 (26). https://doi.org/10.1073/pnas.1202473109.
Zoback, M.D., Harjes, H.-P., 1997. Injection-induced earthquakes and crustal stress at 9 km depth at the KTB deep drilling site, Germany. J. Geophys. Res. B: Solid Earth 102 (B8).
Zoback, M.D., Kohli, A.H., 2019. Unconventional Reservoir Geomechanics. Cambridge University Press, Cambridge CB2 8BS United Kingdom.
Zoback, M.D., Townend, J., Grollimund, B., 2002. Steady-state failure equilibrium and deformation of intraplate lithosphere. Int. Geol. Rev. 44 (5), 383–401. https://doi.org/10.2747/0020-6814.44.5.383.
Woo, J.-U., Ellsworth, W.L., 2023. Reactivation of Precambrian faults by deep wastewater injection in Midland Basin, Texas, and performance evaluation of seismic response areas. Bull. Seismol. Soc. Am. 113 (6). https://doi.org/10.1785/0120230086.